Proceedings of the XXXVII Summer School – Conference

ADVANCED PROBLEMS IN MECHANICS

A P M 2 0 0 9

St. Petersburg (Repino)

June 30 – July 5, 2009

Preface

Dear Reader,

in this book you will find the Proceedings of the Summer School Conference "Advanced Problems in Mechanics (APM) 2009". The conference had been started in 1971. The first Summer School was organized by Prof. Ya.G. Panovko and his colleagues. In the early years the main focus of the School was on nonlinear oscillations of mechanical systems with a finite number of degrees of freedom. Since 1994 the Institute for Problems in Mechanical Engineering of the Russian Academy of Sciences organizes the Summer School. The traditional name of "Summer School" has been kept, but the topics covered by the School have been much widened, and the School has been transformed into an international conference. Now it is held under the patronage of the Russian Academy of Sciences. The topics of the conference cover now almost all fields of mechanics, being concentrated around the following main scientific directions:

- aerospace mechanics;
- computational mechanics;
- dynamics of rigid bodies and multibody dynamics;
- fluid and gas;
- mechanical and civil engineering applications;
- mechanics of media with microstructure;
- mechanics of granular media;
- nanomechanics;
- nonlinear dynamics, chaos and vibration;
- molecular and particle dynamics;
- phase transitions;
- solids and structures;
- wave motion.

The Summer School – Conference has two main purposes: to gather specialists from different branches of mechanics to provide a platform for cross-fertilization of ideas, and to give the young scientists a possibility to learn from their colleagues and to present their work. Thus the Scientific Committee encouraged the participation of young researchers, and did its best to gather at the conference leading scientists belonging to various scientific schools of the world.

We believe that the significance of Mechanics as of fundamental and applied science should much increase in the eyes of the world scientific community, and we hope that APM conference makes its contribution into this process.

We are happy to express our sincere gratitude for a partial financial support to Russian Foundation for Basic Research, Russian Academy of Sciences, and St. Petersburg Scientific Center. This support has helped substantially to organize the conference and to increase the participation of young researchers.

We hope that you will find the materials of the conference interesting, and we cordially invite you to participate in the coming APM conferences. A part of the papers published in this Volume is planed to be published in Materials Physics and Mechanics Journal by agreement between APM 2009 organizers and Editors of Materials Physics and Mechanics. You may find the information on the future "Advanced Problems in Mechanics" Schools Conferences at our websites:

http://apm-conf.spb.ru

With kind regards,

Co-Chairmens of APM 2009

Dmitri A. Indeitsev, Anton M. Krivtsov

Contents

Contents

Contents

Contents

Contents

Contents

Contents

Contents

Spherical and cylindrical charged dusty particle system response on pulse loading

A. V. Abdrashitov   K. P. Zolnikov   S. G. Psakhie

simoom@sibmail.com

Abstract

Peculiarities of dust particle systems behavior at external confinement field under different types of impulse loading are investigated. The interparticle interaction is described by the Yukawa isotropic pair potential. Structure with cylindrical and spherical symmetry are obtained to investigate wave propagation process. The characteristics of wave propagation generated by external loading are calculated.

1 Introduction

Dusty (or complex) plasma has been the subject of intensive investigation for more than ten years [1, 2]. Now it is well known that microparticles of matter in plasma of different origin can acquire high electric charges and exhibit properties of gas, liquid or a solid. Of particular interest was the discovery of so-called plasma crystals - ordered structures of dust particles [3, 4, 5]. However, attempts to obtain homogenous three-dimensional crystal modifications in gas-discharge devices usually used in laboratories ran into serious difficulties such as chainlike ordering of dust particles in the vertical direction and formation of a void in a dust cloud [6, 7, 8]. The difficulties were overcome in recent experiments [9, 10, 11], which allowed researchers to produce so-called Coulomb balls (CB), i.e. almost spherical systems of dust particles of one size. The rf-discharge device employed in the experiment differed from an ordinary one by the presence of a heated electrode with a glass box mounted on it in which a CB was formed.

More often researchers consider models where particles interacting by one or another law are confined in the harmonic potential $U_{ex}(r) \sim r^2$ whose origin is independent of direction. However, in experiments on the production of CB [9, 10, 11] the situation is aggravated because the dust system is maintained by forces of different origin.

Main purpose of conducted research was investigation of structural response of CB under mechanical loading of outer shell and under instant confinement field changing.
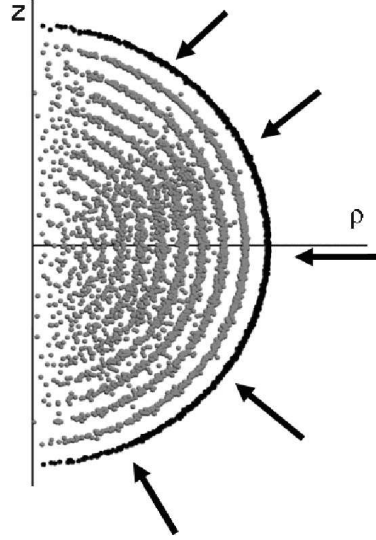
Figure 1: CB with 5000 dust particles in cylindrical coordinates. Outer shell loading scheme.

2 Model

We assume that in all considered cases the dust particle interaction has a purely Debye character. Such interaction is chosen because of a good agreement of the simulation results for the CB structure with experimental data [11]. With regard to the close values of interparticle distance a and screening length λ_d, the choice is well corroborated by the results of a direct experimental study of dust particle interaction in similar cases [12]. Since the dust radius R and length λ_d meet the condition $R \ll \lambda_d$, we represent the potential of any dust particle as

$$\phi = \frac{Q}{4\pi\varepsilon_0 r} e^{\left(-\frac{r}{\lambda_d}\right)} \tag{1}$$

where Q is the particle charge.

The theoretical estimation of the dust particle charge as the particle size function was carried out within an analytical approach [13, 14], which is a generalization of the known charge theory in the orbit motion limited (OML) approximation in case if ion scattering on neutral atoms is taken into account. Such process at buffer gas pressure 20-120 Pa (Ar) [10] causes a significant dust charge reduction as compared to the estimates obtained in the framework of the OML theory [14]. Besides, in the first approximation we considered for a decrease in the concentration of electrons in the plasma volume owing to their localization on the dust particle surface as well as for the quasineutrality condition [2].

The forces acting on a dust particle under the experimental conditions have been studied in detail in [9, 10, 11]. Confinement field have form $\overrightarrow{F_{conf}} = -\alpha Q \overrightarrow{r}$. The analysis based on the measurements and simulation of electrical properties of the experimental setup shows that in the horizontal direction only the electrostatic force acts on the CB, while in the vertical direction the gravitational, thermophoretic, and electrostatic forces act together. The results of [10] have been approximated for the

height dependencies of the temperature gradient and electrostatic force using a third-order polynomial interpolation. The temperature of the dust systems is determined by the below-given values of the coupling parameter $\Gamma = \frac{Q^2}{4\pi\varepsilon_0\, akT}$

3 Method of analysis

It is well known fact that under the conditions of weightlessness for a parabolic confinement field a simulated system of dust particles (DPs) constitutes a sphere Fig. 1. Under laboratory conditions, where the action of the gravitational component on DPs is compensated for by the electrical and thermophoretic forces, a DP system constitutes an ellipsoid of revolution (the axis of revolution is parallel to the gravitational force). In this work, the external pulse loading was applied to crystallized DP systems structured as shells.

An investigation of the DP system response to the external pulse loading relied on the analysis of the outer shell position with respect to time. In the case of a spherical configuration of a DP system, it is essential to know the time variation of one parameter: distance from a shell to the center. While in the case where a DP system was shaped as an ellipsoid of revolution, variation in two semi-axes of an ellipse was needed in order to study its behavior. The volume of the ellipsoid of revolution is determined by the expression: $V_0 = 4/3\pi r_z r_\rho$, where r_z and r_ρ are its semi-axes.

The external loading of a DP system under laboratory conditions was imitated by varying the confinement field strength in the direction perpendicular to the axis of revolution of the ellipsoid. The shape of the ellipsoid was changed and the behavior of this DP system was described accordingly using two functions: variation of volume of the ellipsoid ($W(t)$) and ellipticity variation without changing the volume ($B(t)$). To do so, the dependence of r_z and r_ρ on time could be given as follows:

$$r_z(t) = r_z(0) * W(t) * B(t)^{-2} \tag{2}$$

$$r_\rho(t) = r_\rho(0) * W(t) * B(t) \tag{3}$$

where $W(t)$ is determined from the following expression: $V(t) = V(0) * W(t)^3$.

4 Simulation results

Two types of loading a Coloumb ball (CB) were addressed in this work: imparting a center-oriented momentum to the particles on the outer shell and variation in the confinement field strength. First CB mechanical loading scheme is presented in Fig. 1. Loadings were performed by adding center oriented velocity to particles on the outer shell. These velocities varied in the interval from 0.1 $\frac{sm}{s}$ till 10 $\frac{sm}{s}$, while CB contained from 500 till 5000 dust particles. Dust particles had characteristics of melamine-formaldehyde balls with 4,8 μm diameter and $\rho = 1514\frac{kg}{m^3}$ mass density. Converging spherical waves occur in CB at impulse radial loading. Simulations showed that outer shell oscillations have beat form. The main reason of such response is close values of frequencies of outer shells. Beat amplitude almost decays after few dozen periods. That occurs since synchronization of outer
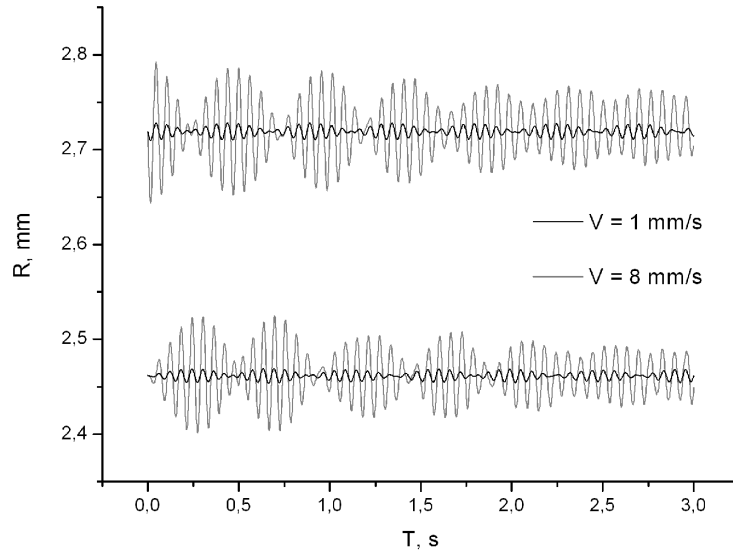
Figure 2: Time dependence of distance from centre of CB for dust particles on outer shell(1) and shell after outer(2) under uniform loading.

shell oscillations Fig. 2. As can be seen from Fig. 2, oscillation amplitude increases with loading intensity, while oscillation frequency remains the same. It should be pointed out, that shell oscillation frequency depends substantially on CB size. This dependence can be written as $T \approx 0.006 + 0.009e^{-\frac{N}{1200}}$. As can be seen from this formula, limiting period is equal to 0.006 s. According to intensity of radial loading two regimes of structure response can be formulated. Shell structure saves under small impulse loading (the first regime) Fig. 3a , while under some greater values of loading the shell structure starts destroying and CB melts (the second regime) Fig. 3b. Variation in the confinement field strength in the DP system results in shell vibration followed by changes in the CB volume but without any changes in its shape. It should be underlined that for this type of loading the shells undergo synchronous oscillation. Also note that their oscillation frequency depends on the finite value of the confinement field strength (Fig. 4). In contrast to the first method of loading, even the external force tripling, connected with corresponding value of the electric field jump, does not lead to the CB failure, since the oscillations of all the CB layers are synchronized from the moment of the external force change. Nevertheless, if the pumping energy leads to the sufficient kinetic energy, the shell structure of CB fails.

Loading of the DP system under laboratory conditions was performed by varying the confinement field strength in the horizontal plane. For the calculations, use was made of a CB consisting of 180 DPs measuring 2.4 μm in diameter with the charge 2013e. The confinement field strength was changed by 10%. The curve describing the outer shell position in terms of time has a complicated shape Fig. 5. Nonetheless, the time dependence of the functions W(t) and B(t) is of a marked harmonic character.
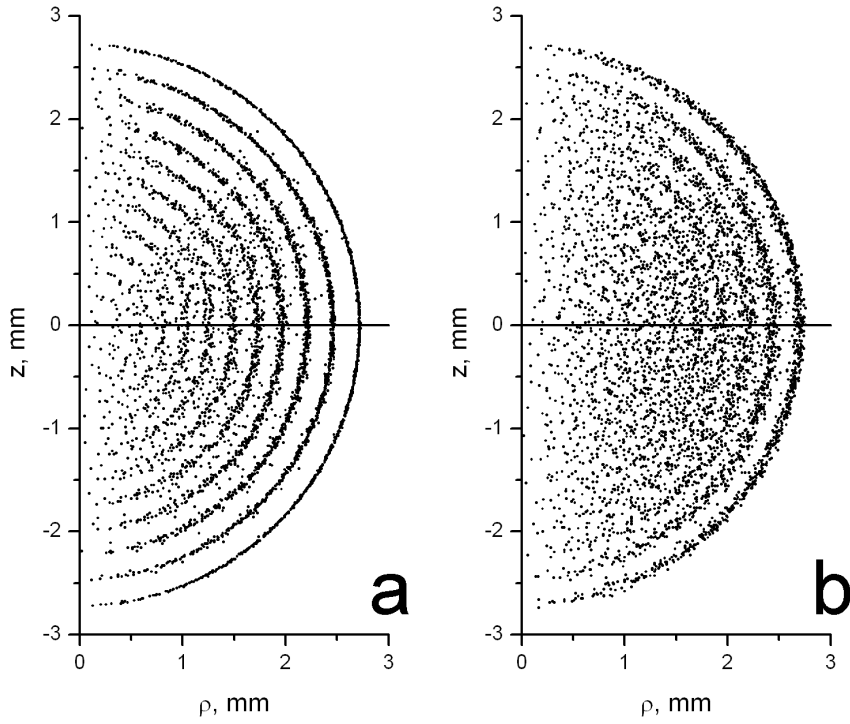
Figure 3: CB with 5000 dust particles in cylindrical coordinates a) before loading , b) after t = 2 s under impulse loading with V = 0.8 sm/s
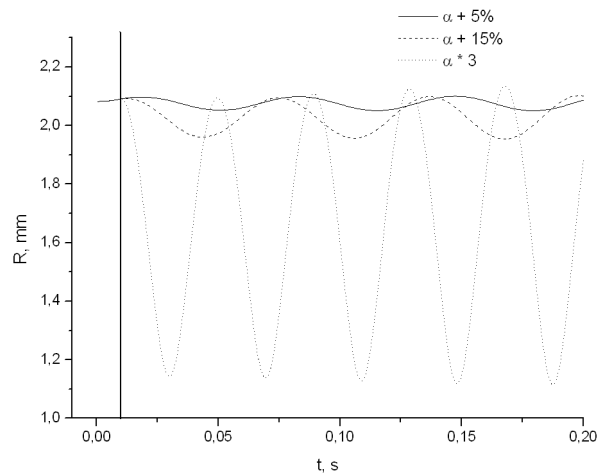
Figure 4: Outer shell oscillation under different confinement field alteration (2000 DP).

16
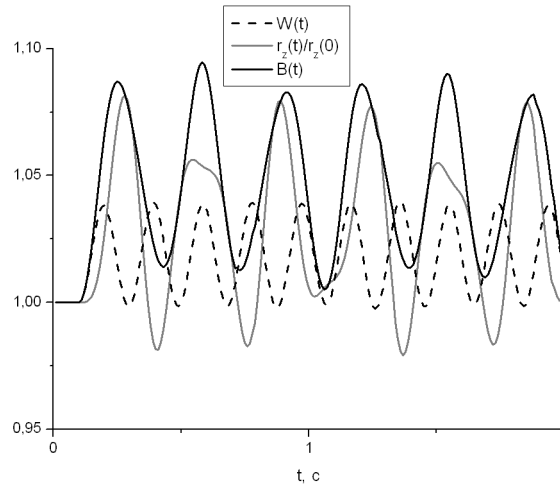
Figure 5: Time dependences of B(t), W(t) and $r_z(t)/r_z(0)$ under anisotropic loading.

5 Conclusions

Outer shell oscillation amplitude increases with loading intensity, while oscillation frequency remains the same. According to intensity of radial loading two regimes of structure response can be formulated. Shell structure saves under small impulse loading (the first regime), while under some greater values of loading the shell structure starts destroying and CB melts (the second regime).

CB shells oscillate after confinement field strength change. Oscillation frequency depends on final confinement field strength while oscillation amplitude depends on value of the confinement field change. In contrast to the first method of loading, even the external force tripling, connected with corresponding value of the electric field jump, does not lead to the CB failure. Nevertheless, if the pumping energy leads to the sufficient kinetic energy, the shell structure of CB fails.

For a CB under laboratory conditions, variation in the confinement field strength in the horizontal plane also gives rise to oscillation motions of its shells. Note again that variation in the shape and volume of a CB in terms of time is harmonic.

References

[1] P. K. Shukla and A. A. Mamun, Introduction to Dusty Plasma Physics (Institute of Physics, Bristol, 2002)

[2] V.E. Fortov, A.G. Khrapak, S.A. Khrapak, V.I. Molotkov, and O.F. Petrov, Phys.Usp. 174, 495 (2004).

[3] J.H. Chu, Phys. Rev. Lett. 72, 4009 (1994)

[4] H. Thomas, G.E. Morfill, V. Demmel, J. Goree, B. Feuerbacher, and D. Mohlmann, Phys. Rev. Lett. 73, 652 (1994)

[5] Y. Hayashi, K. Tachibana, Jpn. J. Appl. Phys. 33, L804 (1994)

[6] W.-T. Juan, Z.-H. Huang, J.-W. Hsu, Y.-J. Lai, and I. Lin, Phys. Rev. E 58, R6947 (1998)

[7] G.E. Morfill, H.M. Thomas, U. Konopka , H. Rothermel, M. Zuzic, A. Ivlev, and J. Goree, Phys. Rev. Lett. 83, 1598 (1999).

[8] H. Rothermel, T. Hagl, G.E. Morfill, M.H. Thoma, and H.M. Thomas, Phys. Rev. Lett. 89, 175001 (2002).

[9] O. Arp, D. Block, A. Piel, A. Melzer, Phys. Rev. Letter 93, 165004 (2004).

[10] O. Arp, D. Block, M. Kindworth, A. Piel, Phys. Plasmas 12, 122102 (2005).

[11] M. Bonitz, D. Block, O. Arp, V.Golubnychiy, H. Baumgartner, P.Ludwig, A.Piel, and A.Filinov, Phys. Rev. Lett. 96, 075001 (2006).

[12] U. Konopka, G.E. Morfill, and L. Ratke, Phys. Rev. Lett. 84, 891 (2000).

[13] M. Lampe, R.Goswami, Z Sternovsky, S. Robertson, V. Gavrishchaka, G. Ganguli, and G. Joyce, Phys. Plasmas 10, 1500 (2003).

[14] S.A. Khrapak, S.V. Ratynskaia, A.V. Zobnin, A. D. Usachev, V. V.Yaroshenko, M. H. Thoma, M. Kretschmer, H. Höfner, G. E. Morfill, O. F. Petrov, V. E. Fortov, Phys. Rev. Lett. 72, 016406 (2005).

Andrey V. Abdrashitov, pr. Academicheskii 2/1, Tomsk, 634021 Rissia
Konstantin P. Zolnikov, pr. Academicheskii 2/1, Tomsk, 634021 Rissia
Sergey G. Psakhie, pr. Academicheskii 2/1, Tomsk, 634021 Rissia

Some dynamical problems for generalized (3+1)-dimensional sine-Gordon equation

E. L. Aero   A. N. Bulygin   Yu. V. Pavlov

bulygin_an@mail.ru

Abstract

The new exact solutions of the three-dimensional sine-Gordon (SG) equation are obtained. These solutions depend on arbitrary function $F(\alpha)$, which argument is some function $\alpha(x, y, z, t)$. The ansatz α is found from the linear equation with respect to x, y, z, t, which coefficients are arbitrary functions depending on α. These coefficients must satisfy a system of algebraic equations. The classical and generalized SG-equations with first derivatives with respect to x, y, z, t are solved by this method. The SG-equation with only first time derivative is considered separately. The approaches for the solutions of SG-equation with variable amplitude are proposed. These methods admit natural generalization in case of integration of the abovementioned types of equations in a space with any number of dimensions.

1   Introduction

A large number of works are devoted to investigating the sine-Gordon (SG) equation, because it appears in various branches of mechanics, mathematics, and theoretical physics. The SG equation describes dislocations in solids [1], deformation of a nonlinear crystal lattice [2], [3], properties of Bloch' walls in ferromagnets [4], propagation of pulses in two levels resonance mediums [5], the orientation structure of liquid crystals [6], commensurability-noncommensurability phase transitions [7], etc. It also arises in simulations of wave processes in geological media [8], in molecular biology [9], in field theory models [10], and in elementary particle physics [11]. Occurrence of soliton, one of the most beautiful and universal objects of modern scientific researches, is connected with SG equation.

Currently, quite effective methods have been developed for solving nonlinear differential equations including the SG equation. These are the method proposed by Lamb for solving the two-dimensional SG equation [12], the Bäcklund transformation [13], the inverse scattering method [14], [15], the Hirota method [16] for finding multi-soliton solutions in explicit form, perturbation theory, and others. But the needs in developing of the theory of nonlinear equations and the problems of practical simulation of various physical phenomena and technological processes stimulate the search for new methods for solving nonlinear equations including the SG equation.

19

2 The transformation and methods for solving the SG equation

We seek solutions of the SG equation

$$\frac{\partial^2 U}{\partial x^2} + \frac{\partial^2 U}{\partial y^2} + \frac{\partial^2 U}{\partial z^2} - \frac{1}{v^2}\frac{\partial^2 U}{\partial t^2} = \sin U \tag{1}$$

in the form Lamb [12] proposed for integrating the two-dimensional SG equation:

$$U = 4\arctan G(x, y, z, t). \tag{2}$$

Earlier such substitution has been used in [17].
Substituting (2) in (1) and using

$$\sin U = \frac{4G}{1+G^2} - \frac{8G^3}{(1+G^2)^2}, \tag{3}$$

we obtain a nonlinear differential equation for G:

$$\frac{4G}{1+G^2}\left[\frac{\partial^2 G}{\partial x^2} + \frac{\partial^2 G}{\partial y^2} + \frac{\partial^2 G}{\partial z^2} - \frac{1}{v^2}\frac{\partial^2 G}{\partial t^2} - G\right] - $$
$$-\frac{8G}{(1+G^2)^2}\left[\left(\frac{\partial G}{\partial x}\right)^2 + \left(\frac{\partial G}{\partial y}\right)^2 + \left(\frac{\partial G}{\partial z}\right)^2 - \frac{1}{v^2}\left(\frac{\partial G}{\partial t}\right)^2 - G^2\right] = 0. \tag{4}$$

Eq. (4) can be easily solved if we assume that the function G simultaneously satisfies the two equations

$$\frac{\partial^2 G}{\partial x^2} + \frac{\partial^2 G}{\partial y^2} + \frac{\partial^2 G}{\partial z^2} - \frac{1}{v^2}\frac{\partial^2 G}{\partial t^2} - G = 0, \tag{5}$$

$$\left(\frac{\partial G}{\partial x}\right)^2 + \left(\frac{\partial G}{\partial y}\right)^2 + \left(\frac{\partial G}{\partial z}\right)^2 - \frac{1}{v^2}\left(\frac{\partial G}{\partial t}\right)^2 - G^2 = 0. \tag{6}$$

Let G have the form

$$G(x, y, z, t) = e^\varphi V(x, y, z, t), \qquad \varphi = a_1 x + a_2 y + a_3 z - v^2\sigma t. \tag{7}$$

Here a_1, a_2, a_3, σ are arbitrary constants. Substituting (7) in Eqs. (5), (6), we verify that they are satisfied if the constants (a_1, a_2, a_3, σ) are related by the condition

$$a_1^2 + a_2^2 + a_3^2 = 1 + v^2\sigma^2, \tag{8}$$

and the function $V(x, y, z, t)$ satisfies the linear equation

$$a_1\frac{\partial V}{\partial x} + a_2\frac{\partial V}{\partial y} + a_3\frac{\partial V}{\partial z} + \sigma\frac{\partial V}{\partial t} = 0, \tag{9}$$

the Hamilton-Jacobi equation

$$\left(\frac{\partial V}{\partial x}\right)^2 + \left(\frac{\partial V}{\partial y}\right)^2 + \left(\frac{\partial V}{\partial z}\right)^2 - \frac{1}{v^2}\left(\frac{\partial V}{\partial t}\right)^2 = 0 \tag{10}$$

and the wave equation

$$\frac{\partial^2 V}{\partial x^2} + \frac{\partial^2 V}{\partial y^2} + \frac{\partial^2 V}{\partial z^2} - \frac{1}{v^2}\frac{\partial^2 V}{\partial t^2} = 0\,. \tag{11}$$

Splitting one differential equation into several equations is justified if there is a constructive method for solving the system of differential equations. Below it will be shown, that the system (9)–(11) supposes functionally invariant solution [18]. There is the next way of construction [19] the function $V(x, y, z, t)$, satisfying system of equations (9)–(11).

Let $V(x, y, z, t)$ is an arbitrary function of ansatz $\alpha(x, y, z, t)$, i.e.

$$V(x, y, z, t) = F(\alpha)\,. \tag{12}$$

An arbitrary function $F(\alpha)$ satisfies Eqs. (9)–(11) if the ansatz $\alpha(x, y, z, t)$ is a solution of the same equations,

$$a_1\frac{\partial \alpha}{\partial x} + a_2\frac{\partial \alpha}{\partial y} + a_3\frac{\partial \alpha}{\partial z} + \sigma\frac{\partial \alpha}{\partial t} = 0\,, \tag{13}$$

$$\left(\frac{\partial \alpha}{\partial x}\right)^2 + \left(\frac{\partial \alpha}{\partial y}\right)^2 + \left(\frac{\partial \alpha}{\partial z}\right)^2 - \frac{1}{v^2}\left(\frac{\partial \alpha}{\partial t}\right)^2 = 0\,, \tag{14}$$

$$\frac{\partial^2 \alpha}{\partial x^2} + \frac{\partial^2 \alpha}{\partial y^2} + \frac{\partial^2 \alpha}{\partial z^2} - \frac{1}{v^2}\frac{\partial^2 \alpha}{\partial t^2} = 0\,. \tag{15}$$

Let's choose the ansatz $\alpha(x, y, z, t)$ from the relation

$$x\,l(\alpha) + y\,m(\alpha) + z\,n(\alpha) - tv^2 p(\alpha) + q(\alpha) = 0\,. \tag{16}$$

Here $l(\alpha)$, $m(\alpha)$, $n(\alpha)$, $p(\alpha)$, $q(\alpha)$ are arbitrary functions. From (16) we obtain

$$\frac{\partial \alpha}{\partial x} = -\frac{l}{\lambda}\,,\quad \frac{\partial \alpha}{\partial y} = -\frac{m}{\lambda}\,,\quad \frac{\partial \alpha}{\partial z} = -\frac{n}{\lambda}\,,\quad \frac{\partial \alpha}{\partial t} = v^2\frac{p}{\lambda}\,,$$
$$\lambda = x\frac{dl}{d\alpha} + y\frac{dm}{d\alpha} + z\frac{dn}{d\alpha} - v^2 t\frac{dp}{d\alpha} + \frac{dq}{d\alpha}\,, \tag{17}$$

$$\frac{\partial^2 \alpha}{dx^2} = \frac{1}{\lambda^2}\left(2l\frac{dl}{d\alpha} - l^2\frac{\nu}{\lambda}\right),$$
$$\frac{\partial^2 \alpha}{dy^2} = \frac{1}{\lambda^2}\left(2m\frac{dm}{d\alpha} - m^2\frac{\nu}{\lambda}\right),$$
$$\frac{\partial^2 \alpha}{dz^2} = \frac{1}{\lambda^2}\left(2n\frac{dn}{d\alpha} - n^2\frac{\nu}{\lambda}\right), \tag{18}$$
$$\frac{\partial^2 \alpha}{dt^2} = \frac{v^4}{\lambda^2}\left(2p\frac{dp}{d\alpha} - p^2\frac{\nu}{\lambda}\right),$$

$$\nu = x\frac{d^2l}{d\alpha^2} + y\frac{d^2m}{d\alpha^2} + z\frac{d^2n}{d\alpha^2} - v^2 t\frac{d^2p}{d\alpha^2} + \frac{d^2q}{d\alpha^2}\,. \tag{19}$$

Substituting (17) and (18) in Eqs. (13)–(15), we conclude that these equations are satisfied if functions $(l,\ m,\ n,\ p)$ are related by the conditions

$$a_1 l + a_2 m + a_3 n = v^2 \sigma p \,,$$

$$l^2 + m^2 + n^2 = v^2 p^2 . \tag{20}$$

Here, we take into account that the relation $l \dfrac{dl}{d\alpha} + m \dfrac{dm}{d\alpha} + n \dfrac{dn}{d\alpha} = v^2 p \dfrac{dp}{d\alpha}$, implied by (15) is a consequence of the second condition in (20).

It can be easily seen that $F(\alpha)$ can be written as a sum of arbitrary functions of the ansatz $\alpha(x, y, z, t)$:

$$\tan \frac{U}{4} = e^\varphi \left[f_1(\alpha) + f_2(\alpha) + \ldots + f_k(\alpha) + \ldots \right] , \tag{21}$$

i.e., $\tan(U/4)$ satisfies the superposition principle.

To demonstrate such method of solving the SG equation, we consider the following case. The solution of system of the equations (20) is expressed through two any functions $p(\alpha)$ and $f(\alpha)$

$$l = x_1 p(\alpha) , \quad m = x_2 p(\alpha) , \quad n = x_3 p(\alpha) , \tag{22}$$

$$
\begin{aligned}
x_1 &= \frac{v}{\sqrt{1 + v^2 \sigma^2}} \left[\cos \delta \cos C \cos f(\alpha) + \sin \delta \sin f(\alpha) + v \sigma \cos A \right] , \\
x_2 &= \frac{v}{\sqrt{1 + v^2 \sigma^2}} \left[\sin \delta \cos C \cos f(\alpha) - \cos \delta \sin f(\alpha) + v \sigma \cos B \right] , \\
x_3 &= \frac{v}{\sqrt{1 + v^2 \sigma^2}} \left[- \sin C \cos f(\alpha) + v \sigma \cos C \right] .
\end{aligned}
\tag{23}
$$

Here

$$
\sin \delta = \frac{a_2}{\sqrt{a_1^2 + a_2^2}} \,, \qquad \cos \delta = \frac{a_1}{\sqrt{a_1^2 + a_2^2}} \,,
$$

$$
\cos A = \frac{a_1}{\sqrt{1 + v^2 \sigma^2}} \,, \quad \cos B = \frac{a_2}{\sqrt{1 + v^2 \sigma^2}} \,, \quad \cos C = \frac{a_3}{\sqrt{1 + v^2 \sigma^2}} . \tag{24}
$$

If we substitute (22) in (16), then one gets the equation for finding ansatz α

$$x x_1 + y x_2 + z x_3 - v^2 t + \frac{q(\alpha)}{p(\alpha)} = 0 . \tag{25}$$

Searching α from Eq. (25) for any functions $f(\alpha)$, $p(\alpha)$, $q(\alpha)$ is complicate problem. The example for a simple case $f(\alpha) = \text{const}$, $q(\alpha)/p(\alpha) = -\alpha$ is given in [20]. Let's consider here a following variant $f(\alpha) = \alpha$, $q(\alpha) = 0$. In this case α is a root of the trigonometrical equation

$$\eta \cos \alpha + \xi \sin \alpha + v \sigma \zeta = 0 \,, \tag{26}$$

$$\begin{aligned}
\eta &= (x - u_1 t)\cos\delta\cos C + (y - u_2 t)\sin\delta\cos C - (z - u_3 t)\sin C\,, \\
\xi &= (x - u_1 t)\sin\delta - (y - u_2 t)\cos\delta\,, \\
\zeta &= (x - u_1 t)\cos A + (y - u_2 t)\cos B + (z - u_3 t)\cos C\,.
\end{aligned} \tag{27}$$

From (26) one finds

$$\alpha = (-1)^{n+1}\left[\arcsin\frac{\eta}{\sqrt{\xi^2 + \eta^2}} + \arcsin\frac{v\sigma\zeta}{\sqrt{\xi^2 + \eta^2}}\right] + n\pi\,, \tag{28}$$

$n = 0, \pm 1, \ldots$

Ansatz α is defined, as it follows from (28), if

$$-1 \le \frac{v\sigma\zeta}{\sqrt{\xi^2 + \eta^2}} \le 1. \tag{29}$$

The domain (29) is outside of cones which axis is directed along the vector $\mathbf{a} = a_1\mathbf{i} + a_2\mathbf{j} + a_3\mathbf{k}$, and the top (at $t = 0$) coincides with the beginning of coordinates. In the course of time cones move in a direction of the vector $\mathbf{a}$ with speed $\mathbf{u} = u_1\mathbf{i} + u_2\mathbf{j} + u_3\mathbf{k}$. The cone opening is defined by parameter $v\sigma$ (see Fig. 1).
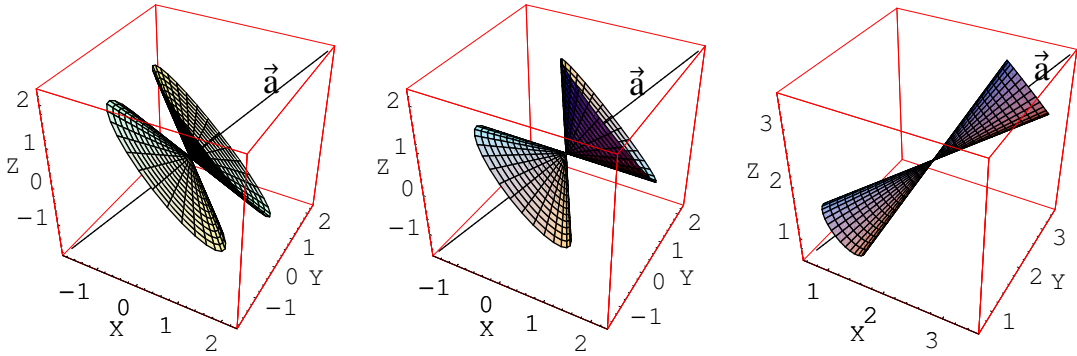
Figure 1: Domains of definitions for solutions (28), if $v\sigma = \sqrt{11}$, $\sqrt{2}$, 0.2828 (on the left, in the center, and on the right).

The graphic representation of the solution appears more evident, if system of coordinates is chosen so that the axis Z coincides with vector $\mathbf{a}$. Then

$$\alpha = (-1)^{n}\left[\arcsin\frac{y}{\sqrt{x^2 + y^2}} + \arcsin\frac{v\sigma(z - u_3 t)}{\sqrt{x^2 + y^2}}\right] + n\pi\,, \tag{30}$$

In this case cones move along an axis Z with a speed u_3. On Fig. 2 the solution corresponding to ansatz (30), is represented at the different time moments: $t = 0$ (at the left), $t = 0.75$ (in the center) and $t = 1.5$ (on the right). At $t = 0$ the top of cones coincides with the beginning of coordinates and the solution $U(x, y, z, t)$ exists in all plane (x, y). If $t > 0$, cones move along an axis Z and "move apart" the solution corresponding to the time moment $t = 0$. In this case, as follows from (29), $U(x, y, z, t)$ is real only outside of cones.

23
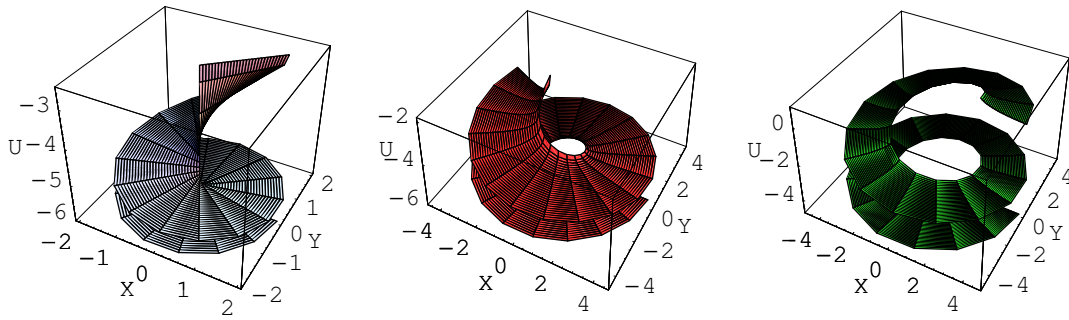
Figure 2: Solutions $U(x, y, z, t)$ for $v\sigma = 0.2828$ and $z = 0$.

3 The transformation and methods for solving the generalized SG equation

Generalized sine-Gordon equation

$$
\gamma \frac{\partial U}{\partial t} + \lambda_1 \frac{\partial U}{\partial x} + \lambda_2 \frac{\partial U}{\partial y} + \lambda_3 \frac{\partial U}{\partial z} + \Delta U - \frac{1}{v^2} \frac{\partial^2 U}{\partial t^2} = \sin U,
$$

$$
\Delta U = \frac{\partial^2 U}{\partial x^2} + \frac{\partial^2 U}{\partial y^2} + \frac{\partial^2 U}{\partial z^2}
$$

(31)

reduces to the classical SG equation if

$$
\lambda_1 = \lambda_2 = \lambda_3 = \gamma = 0.
$$

(32)

Its solution can be received by the method stated above. Then (7) will satisfy the generalized SG equation, if constants a_1, a_2, a_3, σ are connected by a relation (8) and in addition

$$
a_1 \lambda_1 + a_2 \lambda_2 + a_3 \lambda_3 = \gamma \sigma v^2,
$$

(33)

and function $V(x, y, z, t)$ satisfies to two differential equations of the first order

$$
\gamma \frac{\partial V}{\partial t} + \lambda_1 \frac{\partial V}{\partial x} + \lambda_2 \frac{\partial V}{\partial y} + \lambda_3 \frac{\partial V}{\partial z} = 0,
$$

(34)

$$
\sigma \frac{\partial V}{\partial t} + a_1 \frac{\partial V}{\partial x} + a_2 \frac{\partial V}{\partial y} + a_3 \frac{\partial V}{\partial z} = 0,
$$

(35)

and Hamilton-Jacobi equation (10) and the wave equation (11) also.
If we seek $V(x, y, z, t)$ in form (12), then arbitrary function $F(\alpha)$ will be the solution for the system of Eqs. (10), (11), (34), (35), if functions (l, m, n, p, q) are connected by conditions (20) and in addition

$$
\lambda_1 l + \lambda_2 m + \lambda_3 n = \gamma v^2 p.
$$

(36)

It can be easily seen that superposition principle (21) for $\tan(U/4)$ also takes place.

Example of construction of the solution of the generalized SG equation by such method is given in [21] for a case

$$l(\alpha) = x_1 p(\alpha), \quad m(\alpha) = x_2 p(\alpha), \quad n(\alpha) = x_3 p(\alpha), \quad q(\alpha) = -\alpha p(\alpha). \quad (37)$$

In conclusion we shall note, that the presented method, as it can be seen from (33), does not contain a variant $(\lambda_1 = \lambda_2 = \lambda_3 = 0, \ \gamma \neq 0)$. This case deserves special consideration.

4 Solutions of sine-Gordon equation with the first time derivative

Modelling of some physical phenomena and technological processes taking into account dissipation leads to the sine-Gordon with the first time derivative:

$$\gamma \frac{\partial U}{\partial t} + \frac{\partial^2 U}{\partial x^2} + \frac{\partial^2 U}{\partial y^2} + \frac{\partial^2 U}{\partial z^2} - \frac{1}{v^2} \frac{\partial^2 U}{\partial t^2} = \sin U. \quad (38)$$

In the literature there are no effective analytical methods of the Eq. (38) solution. Let

$$U = 2 \arctan G(x, y, z, t). \quad (39)$$

Then the equation (38) will be solved, if G satisfies to the Hamilton-Jacobi equation (6) and

$$\gamma \frac{\partial G}{\partial t} + \frac{\partial^2 G}{\partial x^2} + \frac{\partial^2 G}{\partial y^2} + \frac{\partial^2 G}{\partial z^2} - \frac{1}{v^2} \frac{\partial^2 G}{\partial t^2} = G. \quad (40)$$

If one accepts, that G is any function depending from α: $G = F(\alpha)$, and ansatz α is found from the Eq. (16), then function F should satisfy two equations:

$$F_{\alpha\alpha} \frac{s^2(\alpha)}{\lambda^2} + F_\alpha \left[\frac{1}{\lambda^2} \frac{ds^2(\alpha)}{d\alpha} - \frac{v}{\lambda^3} s^2(\alpha) + \gamma v^2 \frac{p(\alpha)}{\lambda} \right] = F, \quad (41)$$

$$F_\alpha^2 \frac{s^2(\alpha)}{\lambda^2} = 0. \quad (42)$$

Here $s^2(\alpha) = l^2 + m^2 + n^2 - v^2 p^2$, and the bottom index designates a derivative with respect to argument.

The system (41), (42) admits a simple solution

$$F = A \exp \left(\frac{t}{\gamma} - \frac{x x_1 + y x_2 + z x_3}{\gamma v^2 x_4} \right), \quad (43)$$

which appears at the conditions:

$$l(\alpha) = x_1, \quad m(\alpha) = x_2, \quad n(\alpha) = x_3, \quad p(\alpha) = x_4. \quad (44)$$

In (43) A is an arbitrary constant, and constants x_1, x_2, x_3, x_4 satisfy to relation

$$x_1^2 + x_2^2 + x_3^2 = v^2 x_4^2. \quad (45)$$

Solution (43) is a kink, moving with speed v. A width of kink is determined by a product γv. If $\gamma v \to 0$, then (43) tends to disconnected $(0, \pi)$ solution. On Fig. 3 graphics of the solutions $U(x, y, z, t)$ are represented for $x_1 = x_2 = x_3 = A = v = 1$, $z = t = 0$ and $\gamma = 2, \ 1/4$.
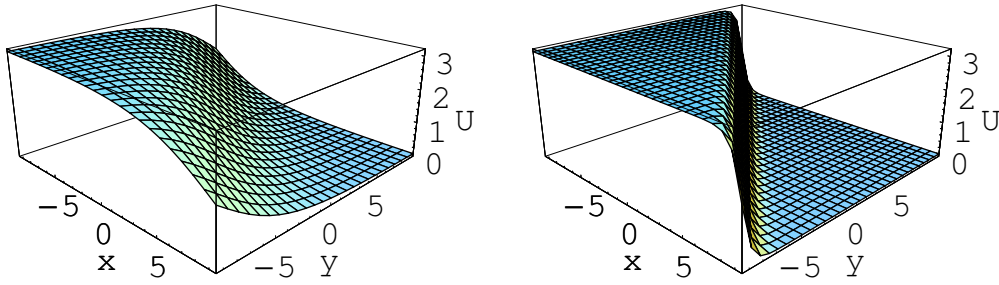
Figure 3: Solutions SG equation with the first time derivative, $\gamma v = 2$ (on the left) and $\gamma v = 1/4$ (on the right).

5 Solution of SG equation with variable amplitude

Let's name the equation

$$\frac{\partial^2 U}{\partial x^2} + \frac{\partial^2 U}{\partial y^2} + \frac{\partial^2 U}{\partial z^2} - \frac{1}{v^2}\frac{\partial^2 U}{\partial t^2} = n_0(x, y, z, t)\sin U \tag{46}$$

as a sine-Gordon equation with variable amplitude. It appears in different areas of natural sciences. In geometry Eq. (46) describes a corner between the coordinate lines forming a Chebyshev's network on pseudo-spherical surfaces [22], in the mechanic of nematic liquid crystals — propagation of waves [23], and also deformation of the curvilinear closed areas which are in variable magnetic field [24]. In the solid-state physics Eq. (46) appears at modelling non-uniform nonlinear crystal lattices [2], [25].

The solution of Eq. (46) is being searched in the form (2). Then $U(x, y, z, t)$ will be solution of (46), if the function G simultaneously satisfies the two equations:

$$\frac{\partial^2 G}{\partial x^2} + \frac{\partial^2 G}{\partial y^2} + \frac{\partial^2 G}{\partial z^2} - \frac{1}{v^2}\frac{\partial^2 G}{\partial t^2} = n_0(x, y, z, t)\, G\,, \tag{47}$$

$$\left(\frac{\partial G}{\partial x}\right)^2 + \left(\frac{\partial G}{\partial y}\right)^2 + \left(\frac{\partial G}{\partial z}\right)^2 - \frac{1}{v^2}\left(\frac{\partial G}{\partial t}\right)^2 = n_0(x, y, z, t)\, G^2. \tag{48}$$

Let's assume

$$G(x, y, z, t) = e^{\varphi(x, y, z, t)}\,. \tag{49}$$

Then the system of Eqs. (47), (48) becomes equivalent to the wave equation

$$\frac{\partial^2 \varphi}{\partial x^2} + \frac{\partial^2 \varphi}{\partial y^2} + \frac{\partial^2 \varphi}{\partial z^2} - \frac{1}{v^2}\frac{\partial^2 \varphi}{\partial t^2} = 0 \tag{50}$$

and classical eikonal equation

$$\left(\frac{\partial \varphi}{\partial x}\right)^2 + \left(\frac{\partial \varphi}{\partial y}\right)^2 + \left(\frac{\partial \varphi}{\partial z}\right)^2 - \frac{1}{v^2}\left(\frac{\partial \varphi}{\partial t}\right)^2 = n_0(x, y, z, t)\,. \tag{51}$$

In optics [26] amplitude $n_0(x, y, z, t)$ is equal to a square of a refractions coefficient of medium.

Solution of Eqs. (50), (51) we shall search in the form

$$\varphi = x a_0(\alpha) + y b_0(\alpha) + z c_0(\alpha) - t v^2 d_0(\alpha) + e_0(\alpha). \tag{52}$$

Here

$$a_0(\alpha) = \int l(\alpha)\, d\alpha, \quad b_0(\alpha) = \int m(\alpha)\, d\alpha, \quad c_0(\alpha) = \int n(\alpha)\, d\alpha,$$

$$d_0(\alpha) = \int p(\alpha)\, d\alpha, \quad e_0(\alpha) = \int g(\alpha)\, d\alpha, \tag{53}$$

and an arbitrary functions (l, m, n, p, q) are connected by relation (16).

Function φ is remarkable due to the fact that its private derivatives of the first order with respect to coordinates and time depend only on ansatz α. Really,

$$\frac{\partial \varphi}{\partial x} = a_0(\alpha), \quad \frac{\partial \varphi}{\partial y} = b_0(\alpha), \quad \frac{\partial \varphi}{\partial z} = c_0(\alpha), \quad \frac{\partial \varphi}{\partial t} = -v^2 d_0(\alpha). \tag{54}$$

That is why the eikonal equation transforms in an algebraic equation

$$a_0^2 + b_0^2 + c_0^2 - v^2 d_0^2 = n_0(x, y, z, t). \tag{55}$$

The second order private derivatives of the function φ depend on ansatz α and actually on coordinates and time which are included in a function λ:

$$\frac{\partial^2 \varphi}{\partial x^2} = -\frac{l^2}{\lambda}, \quad \frac{\partial^2 \varphi}{\partial y^2} = -\frac{m^2}{\lambda}, \quad \frac{\partial^2 \varphi}{\partial z^2} = -\frac{n^2}{\lambda}, \quad \frac{\partial^2 \varphi}{\partial t^2} = v^2 \frac{p^2}{\lambda},$$

$$\lambda = x l' + y m' + z n' - t v^2 p' + g'. \tag{56}$$

However, if one substitutes (56) in the wave equation (50), then it will be carried out independently on λ, if

$$v p(\alpha) = \sqrt{l^2(\alpha) + m^2(\alpha) + n^2(\alpha)}. \tag{57}$$

Taking into account (57) we receive the solution of SG equation with variable amplitude

$$U = 4 \arctan e^{\varphi(x, y, z, t)}, \tag{58}$$

$$\varphi(x, y, z, t) = x a_0(\alpha) + y b_0(\alpha) + z c_0(\alpha) - t v \int \sqrt{l^2(\alpha) + m^2(\alpha) + n^2(\alpha)}\, d\alpha + e_0(\alpha). \tag{59}$$

The arbitrary functions (l, m, n, p, q) are connected by relations

$$x l(\alpha) + y m(\alpha) + z n(\alpha) - t v \sqrt{l^2(\alpha) + m^2(\alpha) + n^2(\alpha)} + g(\alpha) = 0, \tag{60}$$

$$n_0(x, y, z, t) = a_0^2 + b_0^2 + c_0^2 - \left[\int \sqrt{l^2(\alpha) + m^2(\alpha) + n^2(\alpha)} \, d\alpha \right]^2. \qquad (61)$$

Finding (l, m, n, p, q) from integro-functional Eqs. (60), (61) is an uneasy problem and demands special research. However, if (61) is considered as definition of amplitude $n_0(x, y, z, t)$, then (l, m, n, p, q) should satisfy only to one algebraic equation (60). This problem is solved easily. Let's give an example. Let

$$l = vp(\alpha) \cos \Phi_0 \cos 2\delta, \quad m = vp(\alpha) \sin \Phi_0 \cos 2\delta, \quad n = vp(\alpha) \sin 2\delta,$$

$$\delta = vd_0(\alpha), \quad \Phi_0 = \text{const}. \qquad (62)$$

In addition, let's accept, that $g(\alpha) = 0$, then from (60) we find

$$2\delta = (-1)^k \left[\arcsin \frac{tv}{R} - \arcsin \frac{x \cos \Phi_0 + y \sin \Phi_0}{R} \right] + k\pi, \quad k = 0, \pm 1, \ldots \ (63)$$

$$R = \sqrt{z^2 + (x \cos \Phi_0 + y \sin \Phi_0)^2}.$$

Substituting (57) in (53), we find

$$a_0(\alpha) = \cos \Phi \sin \delta \cos \delta, \quad b_0(\alpha) = \sin \Phi \sin \delta \cos \delta, \quad c_0(\alpha) = \sin^2 \delta, \quad (64)$$

$$n_0(x, y, z, t) = \sin^2 \delta - \delta^2. \qquad (65)$$

Therefore, solution of Eq. (46) with amplitude (65) will be (58) with

$$\varphi(x, y, z, t) = (x \cos \Phi_0 + y \sin \Phi_0) \sin \delta \cos \delta + z \sin^2 \delta - tv\delta. \qquad (66)$$

On Fig. 4 graphics of the amplitute n_0 and solution U corresponding SG equation with such variable amplitude are represented for $\Phi_0 = y = 0$, $v = z = 1$.
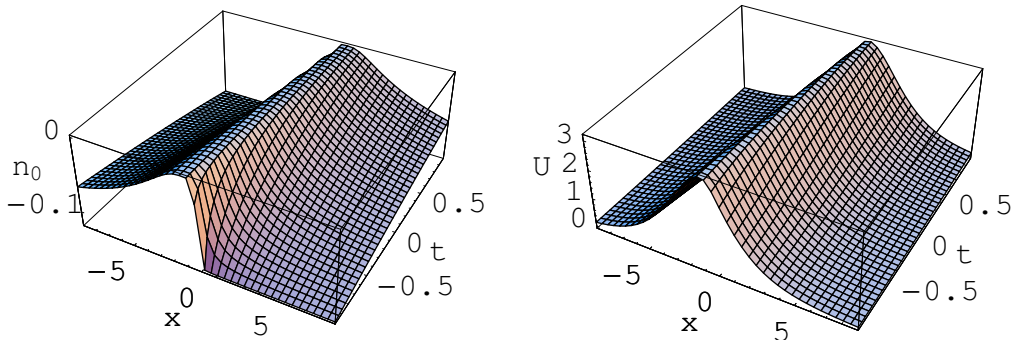
Figure 4: The amplitude n_0 (on the left) and solution of SG equation (on the right).

The equation (46) can be solved and in another way. Let's accept, that

$$U = 2 \arctan G(x, y, z, t). \qquad (67)$$

The equation (46) will be solved, if $G(x, y, z, t)$ is a solution of Eq. (47) and

$$\left(\frac{\partial G}{\partial x} \right)^2 + \left(\frac{\partial G}{\partial y} \right)^2 + \left(\frac{\partial G}{\partial z} \right)^2 - \frac{1}{v^2} \left(\frac{\partial G}{\partial t} \right)^2 = 0. \qquad (68)$$

28

The system (47), (68) proves to be equivalent to the non-uniform wave equation

$$\frac{\partial^2 \varphi}{\partial x^2} + \frac{\partial^2 \varphi}{\partial y^2} + \frac{\partial^2 \varphi}{\partial z^2} - \frac{1}{v^2} \frac{\partial^2 \varphi}{\partial t^2} = n_0(x, y, z, t) \tag{69}$$

and the Hamilton-Jacobi equation

$$\left(\frac{\partial \varphi}{\partial x}\right)^2 + \left(\frac{\partial \varphi}{\partial y}\right)^2 + \left(\frac{\partial \varphi}{\partial z}\right)^2 - \frac{1}{v^2}\left(\frac{\partial \varphi}{\partial t}\right)^2 = 0\,, \tag{70}$$

if G is represented in form (49).

We shall search a solution of Eqs. (69), (70) by the method stated above. Then (l, m, n, p, q) prove to be connected by relations

$$a_0^2 + b_0^2 + c_0^2 - v^2 d_0^2 = 0\,, \tag{71}$$

$$l^2 + m^2 + n^2 - v^2 p^2 = -\lambda\, n_0(x, y, z, t). \tag{72}$$

One can split Eq. (72) on two equations

$$l^2 + m^2 + n^2 - v^2 p^2 = r^2(\alpha)\,, \tag{73}$$

$$n_0(x, y, z, t) = -r^2(\alpha)/\lambda\,. \tag{74}$$

Here $r^2(\alpha)$ is an arbitrary function of ansatz α. Such transformation turns out to be appropriate, since in this case the functions (l, m, n, p, q) are found from two relations (71) and (73) which contain quantities depending on α only, and one can consider the relation (74) as definition of the amplitude $n_0(x, y, z, t)$.

One more special case is considered in work [24], where the amplitude n_0 is given in the form $n_0 = \text{grad}^2 \mu(x, y)$. Here $\mu(x, y)$ is arbitrary function.

6 Conclusion

The proposed approach transforms the problem of integration of classical SG equations and its generalizations to searching of unknown functions from the system of algebraic equations.

Finding of ansatz $\alpha(x, y, z, t)$ from the corresponding equation and choice of arbitrary functions $F(\alpha)$ actually mean finding of particular solution satisfying to the definite initial and boundary conditions. Such problems appear in modelling of specific physical phenomena or technological processes and they are worthy of special research.

In conclusion we shall note, that the abovementioned approach supposes natural generalization in case of integration of the considered equations in the space of any number of dimensions, and this approach also allows to receive the solution of sinh-Gordon equations if one accepts, that

$$U = 4\tanh^{-1} G(x, y, z, t)\,. \tag{75}$$

Acknowledgements

References

[1] J. Frenkel, T. Kontorova. J. Phys. Acad. Sci. USSR **1**, (1939) 137–149.

[2] E. L. Aero, A. N. Bulygin. Izv. Ross. Akad. Nauk. Ser. Mekh. Tverd. Tela No. 5, (2007) 170–187.

[3] E. L. Aero. J. Engineering Math. **55**, (2006) 81–95.

[4] P. Guéret. IEEE Trans. Magnetics **11**, (1975) 751–754.

[5] Solitons in Action. Eds. K. Lonngren, A. Scott. Academic Press, New York, 1978.

[6] P. G. de Gennes. The Physics of Liquid Crystals. Clarendon Press, Oxford, 1974.

[7] W. L. McMillan. Phys. Rev. B **14**, (1976) 1496–1502.

[8] V. G. Bykov. Nonlinear Wave Processes in Geological Media. Dalnauka, Vladivostok, 2000.

[9] A. S. Davydov. Solitons in Bioenergetics. Naukova Dumka, Kiev, 1986.

[10] L. A.Takhtadzhyan, L. D. Faddeev. Hamiltonian Approach in the Theory of Solitons. Nauka, Moscow, 1986.

[11] L. A. Takhtadzhyan., L. D. Faddeev. Theor. Math. Phys. **21**, (1974) 1046–1057.

[12] G. L. Lamb, Jr. Rev. Mod. Phys. **43**, (1971) 99–124.

[13] R. M. Miura (ed.) Bäcklund transformations, the Inverse Scattering Method, Solitons, and Their Applications (Lecture Notes Math. Vol. 515). Springer, Berlin, 1976.

[14] M. J. Ablowitz, H. Segur. Solitons and the Inverse Scattering Transform. SIAM, Philadelphia, 1981.

[15] V. E. Zakharov, S. V. Manakov, S. P. Novikov, L. P. Pitaevskii. Theory of Solitons: The Inverse Scattering Method. Nauka, Moscow, 1980.

[16] R. Hirota. J. Phys. Soc. Japan **33**, (1972) 1459–1463.

[17] R. Steuerwald. Abh. Bayer. Akad. Wiss., N. F. No. 40, (1936) 1–106.

[18] S. L. Sobolev. Trudy Fiz.-Mat. Inst. V.A. Steklova **5**, (1934) 259–264.

[19] H. Bateman The Mathematical Analysis of Electrical and Optical Wave–Motion: On the Basis of Maxwell's Equations. Dover, New York, 1955.

[20] E. L. Aero, A. N. Bulygin, Yu. V. Pavlov. Teor. Matem. Fiz. **158**, No. 3, (2009) 370–377 [English transl.: Theor. Math. Phys. **158**(3), (2009) 313–319].

[21] E. L. Aero, A. N. Bulygin, Yu. V. Pavlov. A new approach to solution of sine-Gordon equation. *In* Proceedings of the 4-th European Conference on Structural Control. Eds. A.K.Belyaev, D.A.Indeitsev. St.Petersburg, 2008. Vol. 1, 117–124.

[22] P. L. Chebyshev. Uspekhi Matem. Nauk **1**, N 2, (1946) 38–42.

[23] E. L. Aero. Prikladn. Matem. Mekh. **66**, (2002) 102–108.

[24] E. L. Aero. Vysokomolekul. Soedineniya. Ser. A **37**, (1995) 1286–1299.

[25] E. L. Aero. Uspekhi Mekhaniki **1**, (2002) 130–176.

[26] M. Born, E. Wolf. Principles of Optics. Pergamon Press, New York, 1968.

E. L. Aero, A. N. Bulygin, Yu. V. Pavlov,
Institute of Problems in Mechanical Engineering, RAS,
61 Bol'shoy, V.O., Saint Petersburg, 199178, Russia

Fundamental Forms of Strength Hypotheses

Holm Altenbach   Vladimir A. Kolupaev

holm.altenbach@iw.uni-halle.de

Abstract

The equivalent stress concept is an engineering tool allowing the solution of multiaxial problems in the mechanics of deformable bodies. The basic idea is that the phenomenological constitutive equations can be formulated for arbitrary stress states which are presented by one scalar variable. This variable can be equated to the respective value of the uniaxial stress state and named by equivalent stress.

Various suggestions for equivalent stress expressions are formulated and applied with different success in the practice. The main disadvantage of the equivalent stress concept is that it cannot be founded on some physical principles. Hence, for the formulation of models no sufficient conditions exist. This results in a big number of models. These models do not take into account the microstructure of the material.

In the present work the existing models are discussed from the point of view of four basic forms of incompressible material behavior. After that a similar form of compressible extension is presented. Some necessary conditions of a successful modeling will be established and added by plausibility conditions. As an application example a new model (the geomechanical model) satisfying these demands is introduced.

For comparison and for the identification of the material parameters in different models some significant ratios are introduced. The relevant range of the model parameters can be limited by these rations. By this approach the error in the material description can be minimized.

1   Introduction

With help of a strength criterion one compares the multiaxial material behavior with a single property of the material, which is specific and significant in each application. At the same time all other material properties are ignored. The comparison is based on scalar variable - the equivalent stress σ_{eq}. This variable can be explicitly estimated for any arbitrary stress state and compared with a uniaxial state, for example tension state (material parameter σ_{+})

$$\sigma_{\mathrm{eq}} = \sigma_{+}. \tag{1}$$

Three hypotheses (normal or shear stress, energy at the limit stress states) result in formulation of three criteria: the hypothesis of the maximum of normal stress,

the hypothesis of the maximum of shear stress and the maximum of the distorsion energy. The development of strength criteria should be coincide with images about the material behavior: it is impossible to make conclusions on the arbitrary stress states, which are based on one test only.

The further development was characterized by the formulation of phenomenological criteria including beside the reference property σ_{eq} additional parameter or parameters. By these parameter more information on the material behavior can be taken into account. Some well-known criteria are maximum strain criterion suggested by MARIOTTE, ST. VENANT among others (with the POISSON's ratio as an additional parameter), the MOHR-COULOMB and the DRUCKER-PRAGER criteria. These and other criteria approximate the given experimental data and extrapolate the experiences in the whole range of validity. An "exact" solution cannot be presented in general since one has a problem with insufficient input information.

Any strength criterion can be given as

$$\Phi(\sigma_I, \sigma_{II}, \sigma_{III}, \sigma_{eq}) = 0. \tag{2}$$

Assuming isotropic material behavior this function depends on three independent invariants of the stress tensor, e.g. on the first invariant I_1 and the second and the third invariant I_2', I_3' of the stress deviator [1, 13, 21]

$$\Phi(I_1, I_2', I_3', \sigma_{eq}) = 0 \tag{3}$$

with

$$I_1 = \mathbf{I} \cdot\cdot\, \boldsymbol{\sigma}, \qquad I_2' = \frac{1}{2}\mathbf{s} \cdot\cdot\, \mathbf{s}, \qquad I_3' = \frac{1}{3}(\mathbf{s} \cdot \mathbf{s}) \cdot\cdot\, \mathbf{s}. \tag{4}$$

Here $\mathbf{I}$ is the second rank unit tensor and $\mathbf{s} = \boldsymbol{\sigma} - \frac{1}{3}\mathbf{I} \cdot\cdot\, \boldsymbol{\sigma}\mathbf{I}$ is the stress deviator. Instead of I_3' the stress angle θ is frequently applied

$$\Phi(I_1, I_2', \theta, \sigma_{eq}) = 0 \tag{5}$$

with

$$\cos 3\theta = \frac{3\sqrt{3}}{2}\frac{I_3'}{(I_2')^{3/2}}. \tag{6}$$

The two sets (3), (5) achieve acceptance in the theory of plasticity and in strength of materials since the split into incompressible or compressible material behavior is obvious. In addition, the invariants in Eq. (5) have a straightforward geometric interpretation.

The phenomenological criteria result a simple and complete description of experimental data. They can be improved or corrected by experiences. In the case of new materials they have simple engineering applications. The aim of this paper is to show that the number of admissible shapes of the surfaces Φ is limited. This allows to simplify the choice of a suitable criterion.

2   Extension to Compressible Material Behavior

The modeling of incompressible material behavior is based on neglecting of the first invariant [17, 21]

$$\Phi(I_2', I_3', \sigma_{eq}) = 0 \qquad \text{or} \qquad \Phi(I_2', \theta, \sigma_{eq}) = 0. \tag{7}$$

Such an idealization cannot be accepted in many cases. The models (7) can be extended by a linear transform [16]

$$\sigma_{eq} \to \frac{\sigma_{eq} - \gamma_1 I_1}{1 - \gamma_1} \tag{8}$$

or in dependence of the available power of the equivalent stress σ_{eq} in the terms of the criteria by a quadratic transform

$$\sigma_{eq}^2 \to \frac{\sigma_{eq} - \gamma_1 I_1}{1 - \gamma_1} \frac{\sigma_{eq} - \gamma_2 I_1}{1 - \gamma_2} \tag{9}$$

and a cubic transform

$$\sigma_{eq}^3 \to \frac{\sigma_{eq} - \gamma_1 I_1}{1 - \gamma_1} \frac{\sigma_{eq} - \gamma_2 I_1}{1 - \gamma_2} \frac{\sigma_{eq} - \gamma_3 I_1}{1 - \gamma_3} \tag{10}$$

to compressible behavior (3), (5). The parameters γ_i are related to the position of the hydrostatic nodes (surface points on the hydrostatic axis) [8, 9].

3   Ratios of Material Parameters

For better comparison of the criteria and the material behavior the following ratios are introduced, cf. [1]:

- the uniaxial compression - uniaxial tension ratio ($\boldsymbol{\sigma} = -d\,\sigma_+\,\mathbf{pp} = \sigma_-\,\mathbf{pp}$, $\mathbf{p}$ is the unit vector characterizing the loading direction at uniaxial tension) [20]

$$d = |\sigma_-|/\sigma_+. \tag{11}$$

  σ_- is the limit value at compression.

- the torsion - uniaxial tension ratio ($\boldsymbol{\sigma} = k\,\sigma_+(\mathbf{pm} + \mathbf{mp}) = \sqrt{3}\tau_*(\mathbf{pm} + \mathbf{mp})$, $\mathbf{m}$ is a othogonal to $\mathbf{p}$ unit vector) [2]

$$k = \sqrt{3}\tau_*/\sigma_+. \tag{12}$$

  τ_* is the limit value at torsion.

- biaxial compression - uniaxial tension ratio ($\boldsymbol{\sigma} = -b_D\,\sigma_+(\mathbf{pp} + \mathbf{mm}) = \sigma_{BD}(\mathbf{pp} + \mathbf{mm})$)

$$b_D = |\sigma_{BD}|/\sigma_+. \tag{13}$$

34

σ_{BD} is the limit value at biaxial compression. Applying the transforms (8), (9) and (10) to Eqs (7) one obtains

$$b_{\mathrm{D}} = \frac{1 + 2b_{\mathrm{D}}\gamma_1}{1 - \gamma_1} \qquad \text{oder} \qquad b_{\mathrm{D}} = 1/(1 - 3\gamma_1), \tag{14}$$

$$b_{\mathrm{D}}^2 = \frac{1 + 2b_{\mathrm{D}}\gamma_1}{1 - \gamma_1} \frac{1 + 2b_{\mathrm{D}}\gamma_2}{1 - \gamma_2}, \tag{15}$$

$$b_{\mathrm{D}}^3 = \frac{1 + 2b_{\mathrm{D}}\gamma_1}{1 - \gamma_1} \frac{1 + 2b_{\mathrm{D}}\gamma_2}{1 - \gamma_2} \frac{1 + 2b_{\mathrm{D}}\gamma_3}{1 - \gamma_3}, \tag{16}$$

respectively. The smallest positive roots in (15) and (16) are physically reasonable.

- hydrostatic tension - uniaxial tension ratio ($\boldsymbol{\sigma} = a_+^{\mathrm{hyd}}\sigma_+\mathbf{I} = \sigma_+^{\mathrm{hyd}}\mathbf{I}$) and the hydrostatic compression - uniaxial tension ratio ($\boldsymbol{\sigma} = -a_-^{\mathrm{hyd}}\sigma_+\mathbf{I} = \sigma_-^{\mathrm{hyd}}\mathbf{I}$)

$$a_+^{\mathrm{hyd}} = \sigma_+^{\mathrm{hyd}}/\sigma_+, \qquad a_-^{\mathrm{hyd}} = |\sigma_-^{\mathrm{hyd}}|/\sigma_+. \tag{17}$$

σ_+^{hyd} and σ_-^{hyd} are the limit values at hydrostatic tension and hydrostatic compression, respectively. Applying again the transforms (8), (9) and (10) to Eqs (7) one obtains

$$1 - 3\gamma_1 a^{\mathrm{hyd}} = 0, \tag{18}$$

$$(1 - 3\gamma_1 a^{\mathrm{hyd}})(1 - 3\gamma_2 a^{\mathrm{hyd}}) = 0, \tag{19}$$

$$(1 - 3\gamma_1 a^{\mathrm{hyd}})(1 - 3\gamma_2 a^{\mathrm{hyd}})(1 - 3\gamma_3 a^{\mathrm{hyd}}) = 0. \tag{20}$$

The distinction a_+^{hyd} and a_-^{hyd} depends on the the sign of the relevant parameters γ_i.

- The plastic POISSON's ratio

$$\nu^{\mathrm{pl}} = -\frac{\partial\,\Phi}{\partial\,\sigma_{22}} \bigg/ \frac{\partial\,\Phi}{\partial\,\sigma_{11}} \tag{21}$$

can be estimated from the normality rule with $\sigma_{\mathrm{II}} = \sigma_{\mathrm{III}} = 0$ [11, 21]. One distinguishes the POISSON's ratio at tension ν_+^{pl} with $\sigma_{\mathrm{I}} = \sigma_{\mathrm{eq}}$ and at compression ν_-^{pl} with $\sigma_{\mathrm{I}} = -d\,\sigma_{\mathrm{eq}}$ [9]. For the strength criteria this ratio has a formal meaning, but it allows to restrict the model parameters. Independently of the model one gets with the help of the transforms (8), (9) and (10)

$$\nu_+^{\mathrm{pl}} = \frac{1}{2}(1 - 3\gamma_1), \tag{22}$$

$$\nu_+^{\mathrm{pl}} = \frac{-1 + 2(\gamma_1 + \gamma_2) - 3\gamma_1\gamma_2}{-2 + \gamma_1 + \gamma_2}, \tag{23}$$

$$\nu_+^{\mathrm{pl}} = \frac{3 - 5(\gamma_1 + \gamma_2 + \gamma_3) + 7(\gamma_1\gamma_2 + \gamma_1\gamma_3 + \gamma_2\gamma_3) - 9\gamma_1\gamma_2\gamma_3}{6 - 4(\gamma_1 + \gamma_2 + \gamma_3) + 2(\gamma_1\gamma_2 + \gamma_1\gamma_3 + \gamma_2\gamma_3)}, \tag{24}$$

respectively. The expressions ν_-^{pl} are in the general case to large.

- By analogy to the POISSON's ratio the elongation/contraction ratio for a torsion bar can be established

$$\chi = \frac{\partial \, \Phi}{\partial \, \sigma_{11}} \bigg/ \frac{\partial \, \Phi}{\partial \, \sigma_{12}} \qquad (25)$$

with $\sigma_{12} = k\sigma_{eq}/\sqrt{3}$ and $\sigma_{11} = \sigma_{22} = \sigma_{33} = \sigma_{13} = \sigma_{23} = 0$. With the help of this ratio similar to the POYNTING-effect, the POYNTING-SWIFT-effect and KELVIN-effect [1, 2] can be characterized by further properties.

The material behavior of the VON MISES-type

$$\sigma_{eq}^2 = 3I_2'. \qquad (26)$$

results in the following ratios $d = k = b_D = 1$, $a_+^{hyd}, a_-^{hyd} \to \infty$, $\nu_-^{pl} = \nu_+^{pl} = 1/2$ and $\chi = 0$. In the case of the maximum normal stress hypothesis it follows $k = \sqrt{3}$, $d = \infty$, $a_+^{hyd} = 1$, $\nu_+^{pl} = 0$ and $\chi = 1/2$. Similar values are introduced in [1].

4 Requirements to the Models

The correctness of any hypothesis can be verified by experimental data [5]. On the other hand, there are not enough and accurate data at combined stress states. For example, the scattering of the data allows the fitment of different models by the same experimental data. From this it follows that the uniqueness of the choice of a criterion cannot be established. With other words, there are no sufficient conditions for the choice. The necessary conditions can be formulated as it follows:

- convexity
  This requirement is not necessary for all failure criteria.

- trigonal or hexagonal symmetrie of the surface in the π-plane
  The rotational symmetry can be obtained for models with smooth surfaces as an interim solution.

- bounds of the plastic POISSON's ratio at tension $\nu_+^{pl} \in]-1, 1/2]$

- bounds of the plastic POISSON's ratio at compression $\nu_-^{pl} \in]-1, 1/2]$ for materials with restricted hydrostatic compression, otherwise if $a_-^{hyd} \to \infty$ it follows $\nu_-^{pl} \geq 1/2$

- bounds of the hydrostatic tension (17) $a_+^{hyd} \in]1/3; 1/(1 - 2\nu_+^{pl})]$
  The upper bound follow from the DRUCKER-PRAGER criterion. The lowest bound $a_+^{hyd} = 1/3$ yields from the plane $I_1 = \sigma_{eq}$.

The necessary conditions are not enough for the choice of a criterion. In this case some plausibility conditions can be introduced allowing shortening the number of models [4, 14, 20]:

- adequate description of the experimental data,

- reliability and trustworthiness of the predictions,

- simple and confident application,

- understandability of the models,

- clear geometric background,

- physical basis, not only abstract mathematical formulation,

- account of the medial stress,

- minimal number of parameters,

- dimensionless parameters,

- continuous differentiability even for limit surfaces,

- continuous differentiability in the hydrostatic nodes ("rounded apex" after FRANKLIN), and

- the models should contain well-known hypotheses as spacial cases.

Additional requirements are [8, 9]:

- explicit resolution with respect of σ_{eq},

- wide as possible range of convex shapes in the π-plane, which can result in singular edges,

- no change of the shape in the π-plane for all intersections $I_1 = \mathrm{const}$,

- no formulation of model surfaces with partial surfaces, which result in singular meridians (only models with planes or smooth surfaces can be used),

- dependence of the models for Φ of all three invariants,

- only rational functions of the invariants I_1 and I_3' should be introduced, and

- maximum of the stress power is in all known models not higher than 12 [8].

Considering the big number of models suggested [1, 2, 14, 18, 19, 21], up to now there are no physical statements for the shape of the surface Φ [14]. From this it follows that the models can be only formulated empirically [12].
In the next two sections five models are presented, which satisfy the necessary and several plausibility conditions. With the help of these models one can describe arbitrary behavior of isotropic materials. These models are simple, understandable and they can be implemented in standard Finite-Element codes.

5 Models of Incompressible Material Behavior

5.1 Cubic Model of Sayir I

The cubic model of SAYIR I has a trigonal symmetry in the π-plane [3, 16]

$$\frac{3I_2'\,\sigma_{\mathrm{eq}} + c_3 I_3'}{1 + 2c_3/3^3} = \sigma_{\mathrm{eq}}^3 \tag{27}$$

and can be resolved with respect to σ_{eq}. The admissible range of parameters follows from the convexity condition

$$-3^2 \le c_3 \le 3^2/2. \tag{28}$$

The ratios k and d results in

$$k^2 = 1 + \frac{2}{3^3}c_3, \qquad d = \frac{3^3 + 2c_3 - \sqrt{3(3^2 - 2c_3)(3^3 + 2c_3)}}{2^2 c_3}. \tag{29}$$

The bounds for the elongation/contraction ratio for torsion bars $\chi \in [-\frac{1}{6}; \frac{1}{6}]$ one gets from

$$\chi = \frac{c_3}{2 \cdot 3^2\,\sqrt{3}} \sqrt{1 + \frac{2}{3^3}c_3} = \frac{c_3}{2 \cdot 3^2\,\sqrt{3}}\,k. \tag{30}$$

5.2 Irregular Hexagonal Prism of Sayir II

This model has a trigonal symmetry in the π-plane [16]

$$\alpha_{41}\sigma_{\mathrm{eq}}^4 I_2' + \alpha_{31}\sigma_{\mathrm{eq}}^3 I_3' + \alpha_{21}\sigma_{\mathrm{eq}}^2 I_2'^2 + \alpha_{11}\sigma_{\mathrm{eq}} I_2' I_3' + \beta_{21} I_2'^3 + \beta_{31} I_3'^2 = \sigma_{\mathrm{eq}}^6 \tag{31}$$

with

$$\alpha_{41} = \frac{2 \cdot 3(1 + b_1 + b_1^2)}{(1 + b_1)^2}, \qquad \alpha_{31} = \frac{3^3 b_1}{(1 + b_1)^2},$$

$$\alpha_{21} = -3^2\frac{(1 + b_1 + b_1^2)^2}{(1 + b_1)^4}, \qquad \alpha_{11} = -3^4 b_1\frac{1 + b_1 + b_1^2}{(1 + b_1)^4},$$

$$\beta_{21} = \frac{(-1 + b_1)^2(2 + b_1)^2(1 + 2b_1)^2}{(1 + b_1)^6}, \qquad \beta_{31} = -\frac{3^3(1 + b_1 + b_1^2)^3}{(1 + b_1)^6}. \tag{32}$$

For $b_1 = 0$ one gets the TRESCA's criterion. With $b_1 \to -1/2$ and $b_1 \to 1$ this model degenerates to the limit cases of the model SAYIR I, Eq. (27). The presentation in the principal stresses results in six planes [20]

$$\sigma_{\mathrm{I}} - \frac{1}{1 + b}(b\sigma_{\mathrm{II}} + \sigma_{\mathrm{III}}) - \sigma_{\mathrm{eq}} = 0. \tag{33}$$

Additional equations follow by cyclic permutation of the indices. At the corners one gets singularities. The ratios of k and d can be computed

$$k = \sqrt{3}\frac{1 + b}{2 + b}, \qquad d = 1 + b. \tag{34}$$

5.3 Irregular Hexagonal Prism after Haythornthwaite

This model with trigonal symmetry in the π-plane can be deduced with the help of two conditions (27) with the bounds $c_3 = -3^2$, $c_3 = 3^2/2$ from Eq. (28) [7, 9]

$$\left(\frac{3(2d\sigma_{\text{eq}})I_2' + (-3^2)I_3'}{1 + 2(-3^2)/3^3} - (2d\sigma_{\text{eq}})^3 \right) \left(\frac{\sigma_{\text{eq}}3I_2' + (3^2/2)I_3'}{1 + 2(3^2/2)/3^3} - \sigma_{\text{eq}}^3 \right) = 0. \qquad (35)$$

With $d = 1/2$ and $d = 2$ one gets triangles in the π-plane, with $d = 1$ one gets the SCHMIDT-ISHLINSKY-HILL criterion. The ratio k can be computed

$$\begin{aligned} &\text{HAYTHORNTHWAITE I:} \quad k = \frac{2}{\sqrt{3}} \qquad \text{für} \qquad d \in [1, 2], \\ &\text{HAYTHORNTHWAITE II:} \quad k = \frac{2d}{\sqrt{3}} \qquad \text{für} \qquad d \in [\frac{1}{2}, 1]. \end{aligned} \qquad (36)$$

5.4 Bicubic Model

This model has a hexagonal symmetry ($d = 1, \chi = 0$) in the π-plane [8, 9]

$$\frac{b_6 I_2'^3 + c_6 I_3'^2 + b_4 I_2'^2 \sigma_{\text{eq}}^2 + b_2 I_2' \sigma_{\text{eq}}^4}{b_6/3^3 + 2^2 c_6/3^6 + b_4/3^2 + b_2/3} = \sigma_{\text{eq}}^6 \qquad (37)$$

In addition, σ_{eq} can be explicitly calculated. The ratio k results from

$$\frac{\frac{1}{3}b_2 k^2 + \frac{1}{3^2}b_4 k^4 + \frac{1}{3^3}b_6 k^6}{b_6/3^3 + 2^2 c_6/3^6 + b_4/3^2 + b_2/3} = 1. \qquad (38)$$

This model contains the model of TRESCA [2, 15, 21] with

$$b_2 = 3, \quad b_4 = -\frac{3^2}{2}, \quad b_6 = 2, \quad c_6 = -\frac{3^3}{2}. \qquad (39)$$

For the model of SCHMIDT-ISHLINSKY-HILL [2, 6, 20] should be fulfilled

$$b_2 = 3, \quad b_4 = -\frac{3^3}{2^3}, \quad b_6 = 0, \quad c_6 = \frac{3^5}{2^5}. \qquad (40)$$

As the special case the model (37) contains the model DRUCKER I [2] with

$$b_2 = 0, \quad b_4 = 0, \quad b_6 = 3^3, \quad -\frac{3^5}{2^2} \le c_6 \le \frac{3^6}{2^3}. \qquad (41)$$

The general form (37) contains three parameters b_4, b_6, c_6 (if $b_2 = 3$). This is for the application not acceptable. The model can be expressed as a function of one parameter $-1 \le \xi \le 1$. Now one obtains a continuous transition from TRESCA's model ($\xi = 1$) to the model of SCHMIDT-ISHLINSKY-HILL ($\xi = -1$). With $\xi = 0$ it follows the VON MISES model.
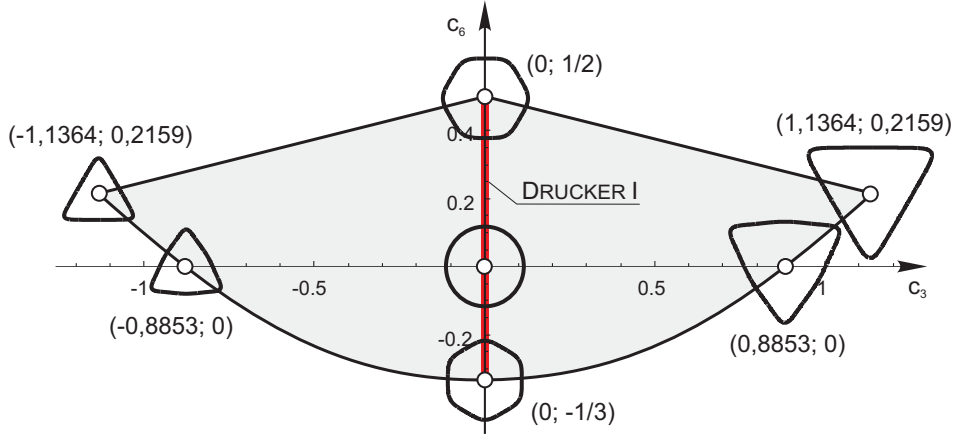
Figure 1: Convexity range c_3-c_6 for the geomechanical model (43) (the intersections in the π-plane are presented for identical values σ_{eq} [9]

.

Taking into account the conditions of EDELMAN-DRUCKER [11] and KOVAL'CHUK [10] one can formulate

$$
\sigma_{eq}^6 = \begin{cases}
\dfrac{3I_2'\sigma_{eq}^4 + \xi(b_6 I_2'^3 + c_6 I_3'^2 + b_4 I_2'^2 \sigma_{eq}^2)}{1 + \xi(b_6/3^3 + 2^2 c_6/3^6 + b_4/3^2)}, & \xi \in [0,1]; \\[4mm]
\dfrac{3I_2'\sigma_{eq}^4 - \xi(b_6 I_2'^3 + c_6 I_3'^2 + b_4 I_2'^2 \sigma_{eq}^2)}{1 - \xi(b_6/3^3 + 2^2 c_6/3^6 + b_4/3^2)}, & \xi \in [-1,0[.
\end{cases}
\tag{42}
$$

Now for the first equation the parameters (39) must be considered, for the second equation - (40). The model DRUCKER I (41) can be obtained for $k \in [(2/3)^{1/6}, (3/2)^{1/6}]$ with $\xi \in [-0,7533; 0,9156]$.

6 "Geomechanical" Model

The geomechanical model [8, 9] is formulated on the basis of the stress angle (6)

$$
(3I_2')^{n/2}\frac{1 + c_3 \cos 3\theta + c_6 \cos^2 3\theta}{1 + c_3 + c_6} = \sigma_{eq}^n.
\tag{43}
$$

The maximum field of convex solutions one gets if $n = 6$. Then three curves restrict these solutions (Fig. 1)

$$
c_6 = \frac{1}{4}(2 + c_3), \qquad c_6 = \frac{1}{4}(2 - c_3), \qquad c_6 = \frac{1}{\sqrt[3]{13}}c_3^2 - \frac{1}{3}.
\tag{44}
$$

With the parabola (44) the numerical part of the solutions is approximated. With $c_3 = 0$ one gets the model of DRUCKER I (41). The ratios k, d and χ can be computed as it follows

$$
k^n = 1 + c_3 + c_6, \qquad d^n = \frac{k^n}{1 - c_3 + c_6}, \qquad \chi = \frac{\sqrt{3}\,c_3}{2\,n}.
\tag{45}
$$

With the transform (9) and (10) for $n = 6$ one gets

$$(3I_2')^3 \frac{1 + c_3 \cos 3\theta + c_6 \cos^2 3\theta}{1 + c_3 + c_6} = \left[\frac{\sigma_{eq} - \gamma_1 I_1}{1 - \gamma_1} \frac{\sigma_{eq} - \gamma_2 I_1}{1 - \gamma_2} \right]^3 \tag{46}$$

and

$$(3I_2')^3 \frac{1 + c_3 \cos 3\theta + c_6 \cos^2 3\theta}{1 + c_3 + c_6} = \left[\frac{\sigma_{eq} - \gamma_1 I_1}{1 - \gamma_1} \frac{\sigma_{eq} - \gamma_2 I_1}{1 - \gamma_2} \frac{\sigma_{eq} - \gamma_3 I_1}{1 - \gamma_3} \right]^2 . \tag{47}$$

The last one allows a more satisfying description of the material behavior. It holds true

$$k^6 = \frac{1 + c_3 + c_6}{(1 - \gamma_1)^2 (1 - \gamma_2)^2 (1 - \gamma_3)^2}, \qquad \chi = \frac{3\,c_3 + 2^2\,k\,(\gamma_1 + \gamma_2 + \gamma_3)}{12\sqrt{3}} \tag{48}$$

and

$$\frac{1 - c_3 + c_6}{(1 + d\gamma_1)^2 (1 + d\gamma_2)^2 (1 + d\gamma_3)^2} = \frac{k^6}{d^6}. \tag{49}$$

7 Discussion of the Models

There exist a big number of models and it is not so easy to make a satisfying choice in applications. The following discussion can be helpful. At first, let us focus our attention on the intersections of the model surfaces in the π-plane: the convex shape is restricted by the models (31) and (35). The bounds can be presented in the diagram of the ratios d vs. k for incompressible material behavior (Fig. 2). At second, two other models (27) and (37) show irreducible trigonal and hexagonal symmetries, respectively.

Since one obtains several shapes in the π-plane which are convex for incompressible material behavior, it is necessary to apply a criterion with a minimal number of parameters. The geomechanical model (43) can be preferred, because there are only two parameters c_3 and c_6 for a big amount of diagram d vs. k.

In [1] a systematization of the models by the number of parameters is suggested. That means the maximum normal stress hypothesis, the VON MISES, and the TRESCA criterion does not need additional parameters if the reference property σ_{eq} is given. These models and the models with one parameter (e.g. the maximum strain hypothesis, the BELTRAMI and the MOHR-COULOMB criterion) are mostly used in practice if a first estimate is necessary.

For materials with $a_-^{hyd} \to \infty$ the models with trigonal symmetry and two parameters are optimal. The parameters control the behavior in the π-plane and the influence of the compressibility. The criteria SAYIR I, SAYIR II and HAYTHORN-THWAITE with the help of the linear transform (8) belong, for example, to this group.

Compressible models with hexagonal symmetry can be obtained from (37) and (42) with the quadratic transform (9). For $\xi = 0$ one gets the rotational symmetric model

$$3I_2' = \frac{\sigma_{eq} - \gamma_1 I_1}{1 - \gamma_1} \frac{\sigma_{eq} - \gamma_2 I_1}{1 - \gamma_2} \tag{50}$$
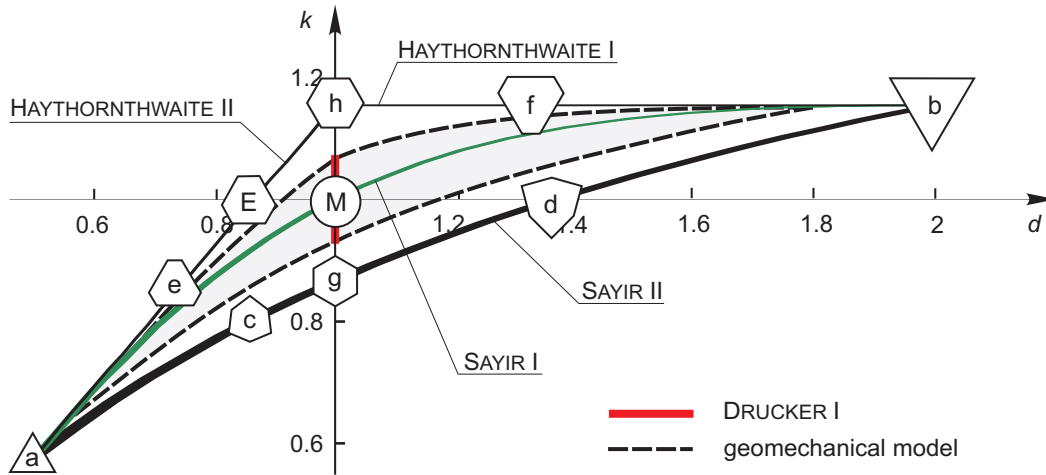
Figure 2: Ratios $\mathsf{d} - \mathsf{k}$ for convex models in the case of incompressible material behavior, for comparison purposes the VON MISES hypothesis [9]

a. $\mathsf{k} = 1/\sqrt{3}$, $\mathsf{d} = 1/2$

b. $\mathsf{k} = 2/\sqrt{3}$, $\mathsf{d} = 2$

c. $\mathsf{k} = 3(2 - \sqrt{3})$, $\mathsf{d} = -\sqrt{3}/2$

d. $\mathsf{k} = 1$, $\mathsf{d} = (1 + \sqrt{3})/2$

e. $\mathsf{k} = \sqrt{3}/2$, $\mathsf{d} = 3/4$

f. $\mathsf{k} = 2/\sqrt{3}$, $\mathsf{d} = 4/3$

g. $\mathsf{k} = \sqrt{3}/2$, $\mathsf{d} = 1$

h. $\mathsf{k} = 2/\sqrt{3}$, $\mathsf{d} = 1$

E. $\mathsf{k} = 1$, $\mathsf{d} = \sqrt{3}/2$

M. $\mathsf{k} = 1$, $\mathsf{d} = 1$ (VON MISES)

with

- cone of DRUCKER-PRAGER (MIROLYUBOV) if $\gamma_1 = \gamma_2 \in]0; 1[$,

- paraboloid of BALANDIN if $\gamma_1 \in]0; 1[, \gamma_2 = 0$,

- ellipsoid of BELTRAMI if $\gamma_1 = -\gamma_2 \in]0; 1[$ or $\nu_-^{\mathrm{pl}} = \nu_+^{\mathrm{pl}} \in]-1; 1/2]$,

- ellipsoid of SCHLEICHER if $\nu_-^{\mathrm{pl}} \neq \nu_+^{\mathrm{pl}} \in]-1; 1/2]$ (other ellipsoids can be presented if $\nu_-^{\mathrm{pl}} > 1/2$),

- hyperboloid of BURZIŃSKI-YAGN if $\gamma_1 \in]0; 1[, \gamma_2 \in]0; \gamma_1[$.

If $\gamma_1 = \gamma_2 \in]0, 1[$ one obtains from (37)

- pyramid of DRUCKER II with the parameters (39) and

- pyramid after SCHMIDT-ISHLINSKY-HILL with parameters (40).

It can be additionally obtained a paraboloid, an ellipsoid, and a hyperboloid for $\xi \in [-1; 1]$. But there is a problem - models with hexagonal symmetry restrict the possibilities to describe real material behavior.

For the application the geomechanical model (47) can be recommended. It allows the best possibilities to present the material behavior. The following set of parameters γ_i for materials with $\mathsf{a}_-^{\mathrm{hyd}} \to \infty$ must be used

- $\gamma_1 = \gamma_2 = \gamma_3$,

- γ_1 with $\gamma_2 = \gamma_3 = 0$ or

- $\gamma_1 = \gamma_2$ with $\gamma_3 = 0$.

For closed criteria, which restrict in addition to the hydrostatic tesion the hydrostatic compression too, the following parameters γ_i should be considered

- $\gamma_1 \in [0, 1[, \gamma_2 = \gamma_3 < 0$,

- $\gamma_1 = \gamma_2 \in [0, 1[, \gamma_3 < 0$ oder

- $\gamma_1 \in [0, 1[, \gamma_2 < 0, \gamma_3 = 0$.

The parameters must be restricted if the experimental data are fitted. For tension of ductile materials the following restriction holds true

$$\nu_+^{el} < \nu_+^{pl} \leq 1/2, \tag{51}$$

This restriction follows only from the experience and allows an estimate of the fitting quality. For a "very" ductile material behavior [11] an additional requirement occurs

$$\nu_+^{pl} \to 1/2. \tag{52}$$

In the case of brittle materials one states formally

$$\nu_+^{pl} \in] -1, \nu_+^{el}]. \tag{53}$$

This restriction can be deduced from the normal stress hypothesis ($\nu_+^{pl} = 0$) and the maximum strain hypothesis ($\nu_+^{pl} = \nu_+^{el}$).

From the experience additional restrictions can follow. The convexity range (44) is restricted by $c_3 \geq 0$ for several materials. During the fitting procedure based on Eq. (44) it is helpful to control the function $c_6(c_3)$.

In most of the cases the optimization yields solutions for $(c_3; c_6)$ in the corners $(0; 1/2)$, $(0; -1/3)$ and $(1, 1364; 0, 2159)$. The last solution if

$$\gamma_1 = \gamma_2 = \gamma_3 = \frac{1}{3} \tag{54}$$

approximates with $k = 1,73$, $d = 21,86$, $a_+^{hyd} = 1$ and $\chi = 0.5$ the maximum stress hypothesis. Other values for $(1, 1364; 0, 2159)$ with

- $\gamma_1 = \gamma_2 = \frac{3}{7}, \gamma_3 = 0$ und

- $\gamma_1 = \frac{3}{5}, \gamma_2 = \gamma_3 = 0$

describes a "weak" brittleness at $\nu_+^{pl} = 0$ and results in $k = 1,67$, $d = 5,94$, $a_+^{hyd} = 7/9$, $\chi = 0.36$ and $k = 1,57$, $d = 3,47$, $a_+^{hyd} = 5/9$, $\chi = 0,25$.

Ductile behavior at present is described by models with hexagonal symmetry. In the case of (47) this yields $c_3 = 0$. For "weak compressibility" with $\nu_+^{pl} = 0.48$ it follows $d = 1,03$. This value should be preferred for several constructional steels (instead of $d = 1$).

8   Conclusion

During the last century various advanced equivalent stress expression were suggested, but the implementation in the construction rules and norms mostly failed. One of the reasons is the conservative design procedures and the incomplete didactic concepts. These and other conclusion are underlined in [18] among others.

The number of criteria increases dramatically during the last century, but up to now the maximum normal stress hypotheses, the VON MISES and TRESCA criteria are mostly used by engineers. These hypotheses yield acceptable results at uniaxial tension and compression superposed by torsion $-d\sigma_{eq} \leq I_1 \leq \sigma_{eq}$. These results can be applied to not very important structural elements. The models presented by (50) are used in many practical cases since the identification of the parameters is not too complicated and the criterion is verified by many tests.

The geomechanical model (47) allows a better prediction of the failure limits. It is simple in application and several special criteria are included (for example, the DRUCKER I model). In addition, a good agreement with experimental data can be observed. The surface is presented in a unique manner by the hydrostatic nodes and the shape in the π-plane. The hydrostatic nodes are restricted in dependence of the material and the POISSON ratio ν_+^{el}.

Applying optimization procedures this model allows to account in a very simple manner additional information and restrictions. By this model a unified solution procedure for various materials can be suggested. The possibilities of incorrect predictions can be minimized if the ratios $d, k, \nu_+^{pl}, \nu_-^{pl}$ are controlled.

The presented in this paper fundamental forms can be helpful since they contains clear an interpretation of the effects of material behavior under consideration. Further developments of strength criteria should be based on some mathematical structures.

References

[1] Altenbach, H.; Altenbach, J.; Zolochevsky, A.: Erweiterte Deformationsmodelle und Versagenskriterien der Werkstoffmechanik. Deutscher Verlag für Grundstoffindustrie, Stuttgart, 1995.

[2] Backhaus, G.: Deformationsgesetze. Akademie-Verlag, Berlin, 1983.

[3] Betten, J.: Kontinuumsmechanik: Elastisches und inelastisches Verhalten isotroper und anisotroger Stoffe. 2. erw. Auflage, Springer, Berlin, 2001.

[4] Burzyński, W.: Theoretical foundations of the hypotheses of material effort. Engineering Transactions, Polish Academy of Sciences, Warsaw, 56, Special Issue, 2008, 9 – 45.

[5] Filonenko-Boroditsch, M. M. (Ed.): Cours in Strength of Materials (in Russ.). Gos. izd. tekh.-teor. lit., Moskwa, 1955.

[6] Ishlinsky, A.; Ivlev, D.: Mathematical Theory of Plasticity (in Russ.). Fizmatlit, Moskau, 2003.

[7] Haythornthwaite, R.: Range of yield condition in ideal plasticity. Journal of the Engineering Mechanics Division, Proceeding of the American Society of Civil Engineers, EM6, 12, 1961, 117 – 133.

[8] Kolupaev, V.A.; Bolchoun, A.: Kombinierte Fließ- und Grenzbedingungen. Forschung im Ingenieurwesen, 72, 2008, 209 – 232.

[9] Kolupaev, V.A.; Altenbach H.: Einige Überlegungen zur Unified Strength Theory von Mao-Hong Yu. Forschung im Ingenieurwesen, 2009 (submitted).

[10] Lebedev, A.A. (Ed.); Koval'chuk, B.I.; Giginjak, F.F., Lamashevsky, V.P.: Handbook of Mechanical Properties of Structural Materials at a Complex Stress State. Begell House, New York, 2001.

[11] Lemaitre, J.; Chaboche, J.-L.: Mechanics of Solid Materials. Cambridge University Press, Cambridge, 1990.

[12] Malmeisters, A.; Tamužs, V.; Teters, G.: Strength of Polymers and Composites (in Russ.). Zinatne, Riga, 1980

[13] Naumenko, K.; Altenbach, H.: Modeling of Creep in Structural Analysis. Springer, Berlin, 2007

[14] Pisarenko, G.; Lebedev, A.: Deformation and Strength of Material at Complex Stress States (in Russ.). Naukowa Dumka, Kiew, 1976

[15] Prager, W.; Hodge, P.: Theory of perfectly plastic solids. Wiley, New York, 1965.

[16] Sayir, M.: Zur Fließbedingung der Plastizitätstheorie. Ing. Arch., 39, 1970, 414 – 432.

[17] Skrzypek, J.: Plasticity and Creep: Theory, Examples and Problems. CRC Press, Boca Raton, 1993.

[18] Yagn, Yu. I.: New methods of strength prediction (in Russ.). Vestnik inzhenerov i tekhnikov, 6, 1931, 237 – 244.

[19] Yu, M.-H.: Advances in strength theories for materials under complex stress state in the 20th century. Appl. Mech. Rev., 55(5), 2002, 169 – 218.

[20] Yu, M.-H.: Unified Strength Theory and its Applications. Springer, Berlin, 2004.

[21] Życzkowski, M.: Combined Loadings in the Theory of Plasticity. PWN-Polish Scientific Publ., Warszawa, 1981.

Holm Altenbach, Martin-Luther-Universität Halle-Wittenberg, Lehrstuhl für Technische Mechanik, D-06099 Halle (Saale), Germany

Vladimir A. Kolupaev, German Institute for Polymers (DKI), Schloßgartenstr. 6, D-64289 Darmstadt, Germany

Friction factor in smooth circular microchannels

V. M. Aniskin   K. V. Adamenko

aniskin@itam.nsc.ru

Abstract

The paper presents the results of the experimental determination of the flow friction factor in circular-section microchannels. Demineralized degassed water was used as a working liquid. Under study were the glass microchannels with the inner diameter of 34.5, 33.6, 25.4, and 16.3 μm and length from 85 to 600 diameters. The experiments were carried out within the Reynolds numbers range from 15 to 350. Experimentally obtained friction factor and its theoretical value were compared.

1 Introduction

Recently, the microfluidics systems become more and more spread in many fields of science. Among the applications of the microfluidics devices are biomedical processes (chemical analysis, DNA analysis), micro-scale mixing and separation and also high-effective systems of electron components cooling. To optimize the design of such devices, it is necessary to study in details the behavior of the liquid at the micro-level.

The liquid flow in a straight microchannel has a number of peculiarities which should be taken into account. One important characteristic of the liquid flow at the micro-level is the value of pressure drop in the microchannel. This value consists of the pressure drop in the areas of microchannel enter and exit and also the pressure drops in the areas of developing and developed liquid flow. But, because of the complicity and sometimes impossibility to measure the pressure drop in the microchannel in the developed-flow area, the method of two or more microchannels of the same inner diameter but different length is applied [1], [2]. Two microchannels enable, with the liquid flow rate being the same, to exclude the influence of the end effects and to calculate the friction factor of the microchannel.

The purpose of this work was to define the friction factor of the microchannles with the inner diameters of 34.5, 33.6, 25.4, and 16.3 μm by the above method.

2 Experiment

In the experiments, demineralized water was used as a process liquid. The water was preliminary degassed by means of helium, a small but constant amount of which

was passed through it during 30 minutes (the water volume was of 0.5 l). Schematic of the experiment is shown in Fig.1. The liquid under the gas (helium) pressure was pumped through the microchannel. The pressure at the microchannel entrance, pressure drop in the microchannel, and also the temperature at the microchannel entrance and exit were measured. The liquid flow rate was found from the liquid level in the calibrated tank. The maximum entrance pressure for each microchannel was 11 atm, which was determined by the strength of metal and polymer tubes connection.
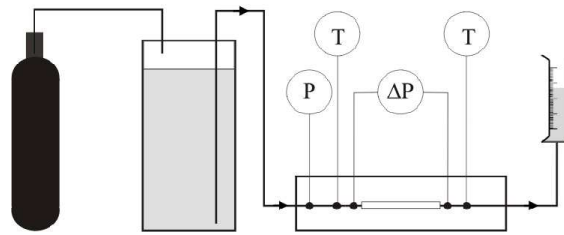
Figure 1: Schematic of the experiment

The temperature was measured with T-type thermocouples. The thermocouples were made of copper and constantan wire of 20 - 30 μm in diameter and were set directly ahead of the microchannel entrance and at the exit. Glass microcapillaries with the inner diameter of 34.5, 33.6, 25.4, and 16.3 μm were used as objects under study. To approve the above method of the -friction factor definition for each diameter, we used 4 microchannels with the length from 85 to 600 diameters.

The studied microchannels were produced by gradual cutting from a microcapillary billet of the proper diameter. Precise determination of the diameter is stupendous because of its essential influence on the measurement results. To define precisely the microchannel diameter, the entrance and exit planes of the microcapillary billets were photographed. It turned out that for the diameter of 34.5 μm, the hydraulic diameter changes for about 1.3 μm over the total length of the microcapillary billet of 45.52 mm. Moreover, in the case of this diameter we observed the ellipticity of the microchannel section, which was taken into account at its hydraulic diameter definition. For the diameters of 33.6, 25.4, and 16,3 μm, no ellipticity was observed. The diameter variation over the length of the microcapillary billets of 33.6 and 25.4 μm was 0.4 and 1.39 μm correspondingly. For the diameter of 16.3 μm, no diameter change over the length took place. Fig.2 presents the average values for the microchannels diameters and their lengths. The error of the microchannel diameters definition is the sum of the error defined by the photos and the error related with the diameter variation over the length.

The photos of the entrance cross-sections for 4 microchannels are given in Fig.3.

The roughness of the microchannel inner surface was defined by the help of a 3D surface-structure analyzer ZYGO NewView 6300; it is 5 nm.

D_h, μm	ΔD_h, μm	L, mm	ΔL, mm	L/D_h
34.5	1.2	20.23	0.06	600
		12.2	0.04	365
		8.43	0.03	250
		4.66	0.03	138
33.6	0.5	11.72	0.04	349
		8.89	0.03	265
		5.88	0.03	175
		2.87	0.03	85
25.4	1.2	8.74	0.03	344
		6.06	0.03	239
		4.12	0.03	162
		2.25	0.03	89
16.3	0.3	4.78	0.03	294
		3.71	0.03	228
		2.83	0.03	174
		1.41	0.03	87

Figure 2: Diameters and lengths of microchannels
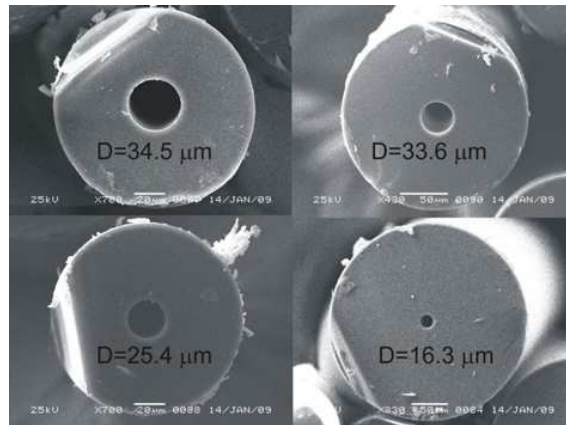
Figure 3: Photos of the microchannels cross-section made by the electronic-scanning microscope

3   Experimental results

The maximum value of the liquid temperature difference at the microchannel entrance and exit was 0.4 Celsius degree. This value was reached in the maximum extension microchannel and with the maximum Reynolds number for this channel. For the microchannels of small extension, we failed to register the liquid heating. The phenomenon of the viscous heating of the liquid was ignored at the flow-friction factor definition because of its negligible influence.

Fig. 4 shows the data obtained for the friction factor in the microchannels of various lengths, each with the diameter of 33.6 μm. Evident that, as the length reduces, the total drag of the microchannel increases, however, for two smallest microchannels, the total drag turned out to be similar.

From the obtained data, using the method of two channels, the flow-friction factor was calculated. With 4 microchannels of one diameter but various length, we can use their different combinations. Having the following designations: 1-11.72 mm, 2-8.89 m, 3-5.88 mm and 4-2.87 mm, we can involve the following combinations of the microchannels 1-2, 1-3, 1-4, 2-3, 2-4, and 3-4. Fig. 5 presents the data for the

microchannels combinations 1-2, 1-3, and 1-4.
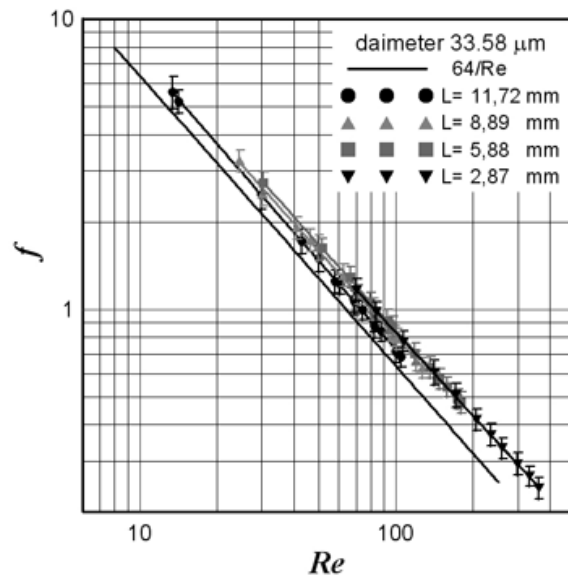
Figure 4: Total flow friction factors
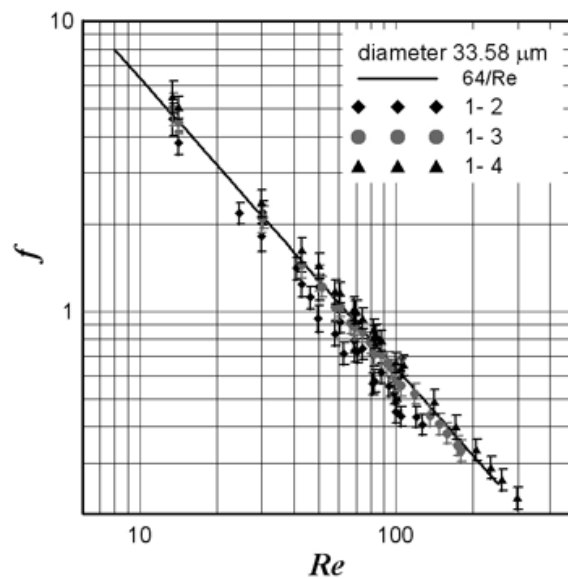
Figure 5: Friction factors found by the two-channel method

The analysis of the obtained results has revealed that the good agreement between the experimental friction factor and theoretical value 64/Re is observed in the case when the difference of two channels lengths is above 100 - 150 diameter calibers.

Acknowledgements

References

[1] Gh. Mohiuddin Mala, Dongqing L. Flow characteristics of water in microtubes. // International Journal of Heat and Fluid Flow. 1999. V. 20, P. 142-148.

[2] G.P. Celata, M. Cumo, S. McPhail, G. Zummo. Characterization of fluid dynamic behaviour and channel wall effects in microtube. International Journal of Heat and Fluid Flow. 2006. V. 27, P. 135-143.

Aniskin Vladimir, Institutskaja str., 4/1, Khristianovich's Institute of Theoretical and Applied Mechanics SB RAS, 630090, Novosibirsk, Russian Federation
Adamenko Kseniya, Pirogova str., 2, Novosibirsk State university, 630090, Novosibirsk, Russian Federation

Micro hot-tubes array: measurements and flow control

V. M. Aniskin   A. A. Maslov   A. N. Shiplyuk   V. A. Seleznev
V. Ya. Prinz
aniskin@itam.nsc.ru, maslov@itam.nsc.ru, shiplyuk@itam.nsc.ru,
seleznev@isp.nsc.ru, prinz@isp.nsc.ru

Abstract

The present article is dedicated to the creation of an array of microtubes to control boundary flow. The method of micro- and nanotube production is based on self-rolling of thin heterofilms detached from the substrate under inner mechanical stress. The peculiarity of such micro- and nanotubes is nanosized wall thickness. Each of the microtube of array is a current conducting microtube with diameter of 10 μm and wall thickness of less than 0.1 μm. The work represents data of elaboration of the model surface with an array of microtubes for boundary layer control. A flat plate model was used, in which the surface of a chip of 3x4 mm with microtubes was fixed flush. Part of the microtubes were probes, and the rest were actuators. The tube-actuators could be heated impulsively with the frequency defined by supplying them an electrical signal from a generator. It was shown, that impulsive thermal influence affected the boundary layer with the frequency defined in the case of subsonic velocities.

1   Introduction

Modern nanotechnology provides new opportunities for creating materials and equipment. Nanosize allows for the considerable enhancement of performance characteristics of probes and makes it possible to create conceptually new equipment.
One of such tehnology is the method of micro- and nanotube production based on self-rolling of thin heterofilms detached from the substrate under inner mechanical stress described [1],[2],[3],[4].
One useful application of micro- and nanotubes is when they are used as sensors of thermo-anemometer probes [5] . The main advantage of the tube is that it weights considerably less in comparison with a wire with an equal value of surface area. This reduces heating and cooling inertia and, consequently, significantly increases operating speed. Besides that the tubes can be used not only as flow pulsation probes in the thermo-anemometer circuit, but as point heat-producing elements at impulse electro-charge.   Joined to the regular arrays on the surface with an appropriate

supervision system, they can serve as a self-regulating surface that prevents the appearance of instability in the boundary layer. Such controlled surfaces do not have any moving parts, which has an advantage over mechanical systems of influence on the flow.

The aim of the present work is designing and creating a model surface with an array of microtubes for controlling the flow.

2   Fabrication of Arrays of Microtubes

For the first step we decided to limit the chip size to 3x4 mm.

The chip construction with microtube array is represented in Fig. 1(a). The chip contains nine tubular sensors 1 fixed on low-resistance conducting paths 2 and on substrate 3. Low-resistance conducting paths are set on each microtube to the edges of the chip, which is needed for further insertion of the chip into the researched model and for the switching to the measuring system. Every tubular element consists of compressed layer 5, extended layer 6 and conducting layer 7. Layers 5 and 6 provide rolling for conducting layer 7 that is coated on them with selective extraction of the substrate under them or with extraction of sacrificial layer 4.

The length of the microtubes is 500 μm, the distances between the microtubes along their axis is 600 μm, between the rows 900 μm.

To produce the chips with microtubes we used two different heterostructures: GaAs/AlAs/InGaAs/GaAs and Si/SiO2/Si3N4.

In the heterostructure GaAs/AlAs/InGaAs/GaAs the layer AlAs is used as a sacrificial layer, the heterolayer InGaAs/GaAs is used for forming the tube (Fig. 1(a), layers 5 and 6). The structure that contains layers AlAs (10 nm), In0.2Ga0.8As (16 nm), GaAs (16 nm), was coated with a layer of gold (50 nm). Low-resistance paths to the microtubes were formed with additional gold spraying (300 nm).
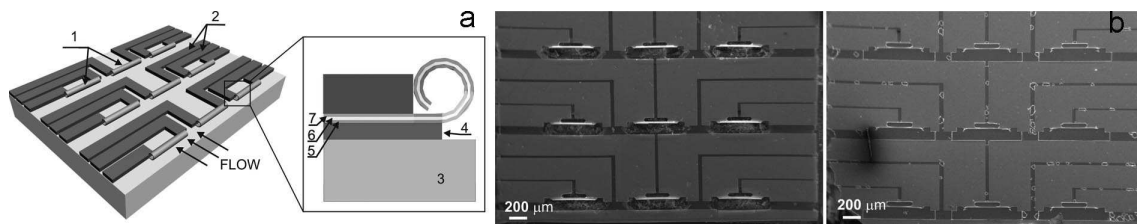
Figure 1: Main elements of the chip construction with array of microtubes (a) and photograph of the chips manufactured with arrays of electroconducting microtubes (b): left - arrays of microtubes rolled from the heterofilm SiO2/Si3N4/Au, with the tubes suspended above the holes etched out in the substrate; right - arrays of microtubes rolled from the heterofilm InGaAs/GaAs/Au without etched holes.

The thickness of the layers in the heterostructure Si/SiO2/Si3N4 was compressed layer of SiO2 (20 nm), an extended layer of Si3N4 (20 nm) and conducting layerof Au (50 nm).

The total volume of wall thickness InGaAs/GaAs/Au of the microtubes is 82 nm, SiO2/Si3N4/Au of the microtubes is 90 nm. The diameters of produced microtubes were 10 μm.

A special feature of the chips manufactured upon silicon is the presence of holes from etching the substrate under the tubes (Fig. 1(b)). In this case the microtube is fixed only on the edges and is available for air blowing from all sides. When the heterostructure GaAs/AlAs/InGaAs/GaAs/Au is used, the tubes are set up above the substrate GaAs for the thickness of the sacrificial layer AlAs. It becomes possible to set precisely the thickness of the sacrificial layer from several tens of nanometers to micrometer units. In such a manner, the chips manufactured on the GaAs substrates have a smoother surface, which is attractive for aerodynamic research.

We should note that after forming the microtubes the semiconducting or dielectric layers are located outside of the tube, and heat occurs when electric current is passed through the gold film. This fact is very important for stability of the characteristics during probe operation, because the pollution of the surface by the particles from the flow results in change of the probe characteristics. In our case the problem of protective coating is solved automatically.

3   Test of Model Surfaces with an Array of Micro-tubes in Subsonic Flow

The tests were carried out in a small subsonic wind tunnel T-324M of ITAM of SB RAS on the model of a plane plate 200x500 mm size. The velocity of selected air flow was 10 m/s. Figure 2(a) shows the design of the wind tunnel's operational part. The chip with 9 probes (Fig. 1(b)) was flush-mounted on the model's surface. The chip was placed in such a manner, that the rows of microtubes were perpendicular to the air flow (Fig. 2(b)).
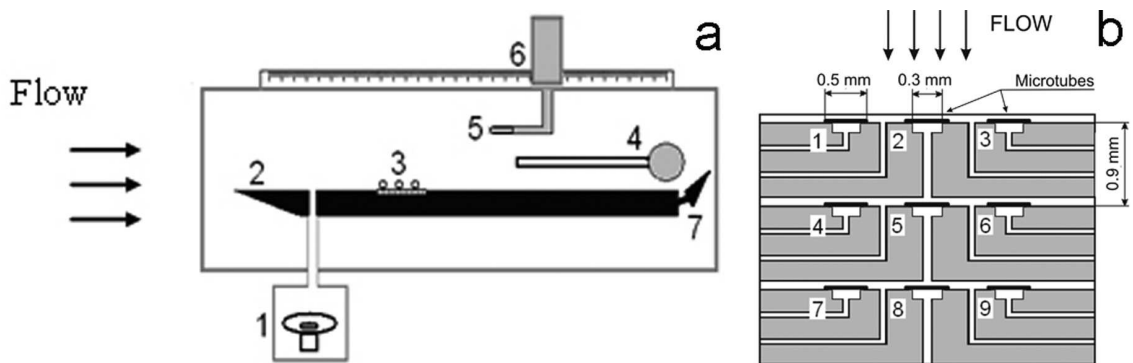
Figure 2: The design of the wind tunnel's operational part (a) and the design of the microchip with the numeration of the tubes (b). 1 - the dynamic, which introduced perturbations into the flow; 2 - the model of the plane plate; 3 - the array of the microtubes; 4 - Pitot's tube; 5 - hot-wire probe; 6 - coordinate spacer; 7 - wing flap.

The experiments were aimed at checking whether the microtube on the model's surface registers perturbations generated upstream.

Perturbations were introduced in the flow through a gap 0.5 mm wide and 50 mm long by periodical blowing-exhaust, made by the dynamic at the frequency of 267

Hz. The distance from the gap to the microchip that was fixed downstream was 123 mm. Perturbations generated by the dynamic were registered by a standard hot-wire probe with an AN-1003 constant resistance thermo-anemometer. Signals from hot-tubes were measured with a constant voltage thermo-anemometer.

For convenience, as a central point of coordinates we selected the first row of tubes on the chip. The coordinate X is normalized for the distance between the first and last rows of tubes.

The results of measurements of characteristics introduced by the perturbations dynamic and obtained by the hot-wire probe and hot-tubes on the surface, are represented below. The hot-wire probe was fixed above the surface at a height of 0.5 mm. The measurements by hot-wire probe were performed immediately behind the array of microtubes at a distance range X from 1.5 to 4.5.

The spectra of perturbations generated and spectra measured by the hot-wire probe and hot-tubes are represented in Fig. 3. It is possible to see that the array of microtubes placed flush with the surface of the model tracks the perturbations introduced.
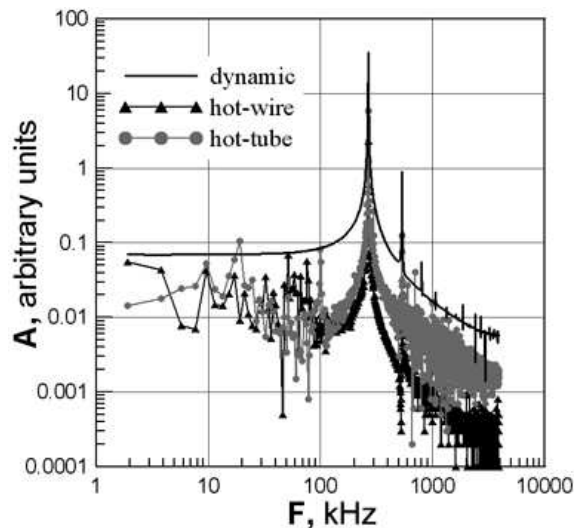
Figure 3: Pulsation spectra.

Fig. 4(a) shows the dependence of the phase of periodical perturbations generated downstream. Line 1 shows the dependence of the phase obtained by the hot-wire probe. Lines 2 and 3, consequently, show the phase obtained by the rows of hot-tubes 1, 4, 7 and 2, 8 (Fig. 2(b)). The results show that the regularity of changing signal phase with the distance passed is close to linear. The regularities obtained by hot-wire and hot-tubes coincided. As a consequence, we can conclude that it is possible to use arrays of hot-tubes for measuring flow velocity.

Fig. 4(b) shows the dependences of velocity pulsation amplitude of periodical perturbations generated by the dynamic. Line 1 shows the dependence of velocity pulsation amplitude obtained by the hot-wire probe, and lines 2 and 3 show the dependence of amplitude obtained by hot-tubes 1, 4, 7 and 2, 8 (Fig. 2(b)). Apparently, the laws of changing perturbation amplitude coincide well with the distance passed.

It was a very important requirement of the tests to find out whether the microtube
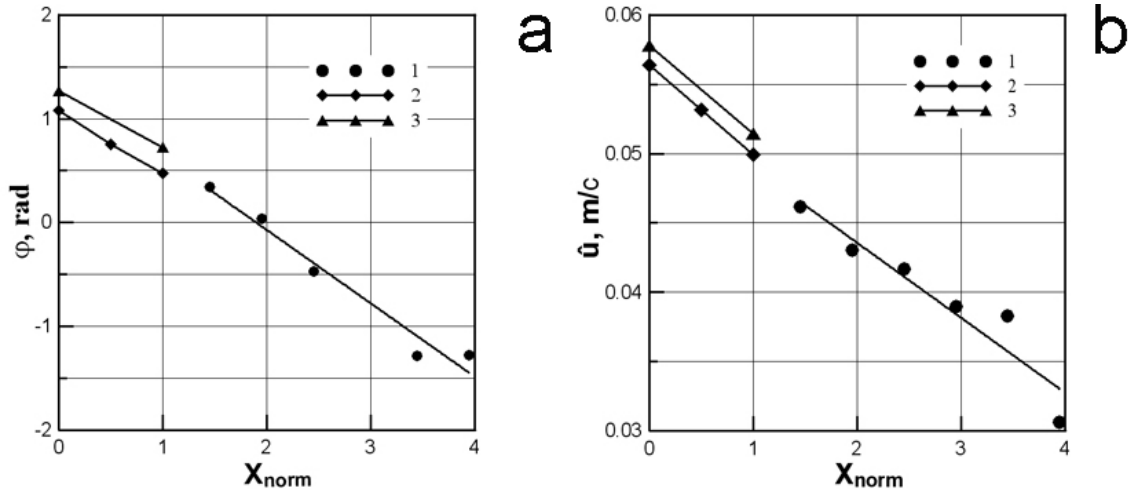
Figure 4: Dependences of the perturbation phase (a) and of the velocity pulsation amplitude (b).

generates perturbations in the case of periodic impulse heating.

For this, periodic rectangular impulse with an amplitude of 0.45 V was transmitted in the flow from the controlling system to tube 1 at the frequency of 267 Hz. Perturbations introduced were registered by the hot-wire probe and by microtubes 4 and 7 (Fig. 2(b)).

Measurements with a hot-wire probe that was placed downstream, showed that the microtube in fact introduces perturbations in the flow. Fig. 5(a) shows the spectrum of the signal of the standard probe (blue line) where the peak at the frequency of perturbation generation is clearly seen.

Fig. 5(b,c) shows the spectra of pulsations registered by microtubes 4 and 7. The graphs correspond to various mutual placements of the tube-generator and tube-probe: b) - the generator is placed directly in front of the probe (microtubes 1 and 4), c) - the generator is placed over one tube in front of the probe (microtubes 1 and 7) (Fig. 2(b)).
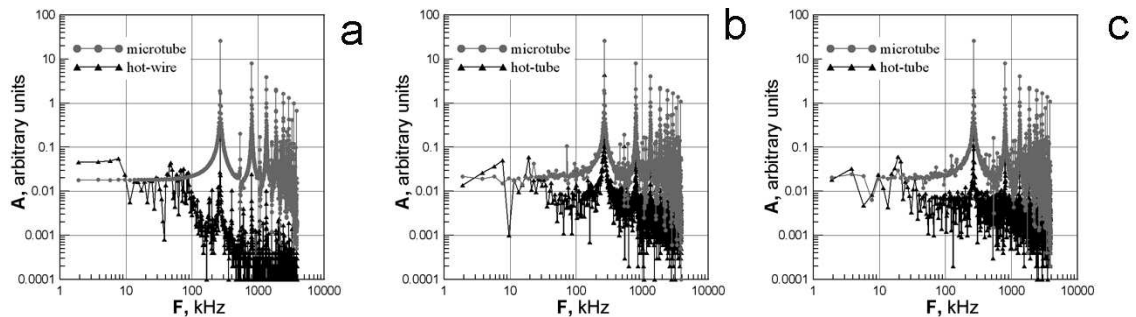
Figure 5: Spectrum of pulsations obtained by hot-wire (a) and hot-tube (b,c) probes.

It is clearly seen that in both cases the tube follows the perturbations introduced.

4   CONCLUSIONS

Aerodynamic experiments with microtubes fixed on the chip showed that it is possible to measure flow perturbation by hot-tubes directly on the surface of the model. It is shown that it is possible to introduce disturbances in the flow with microtubes by their impulse electro-charging. The frequency of the disturbances introduced to the flow corresponds to the frequency of the impulse heating of the microtubes.

Acknowledgements

References

[1] V.Ya. Prinz, V.A. Seleznev, A.K. Gutakovsky, A.V. Chehovskiy, V.V. Preobrazhenskii, M.A. Putyato, T.A. Gavrilova (2000). Free-standing and Overgrown InGaAs/GaAs Nanotubes, Nanohelices and Their Arrays, Physica E., vol. 6, pp. 828-831.

[2] V.Ya. Prinz, D. Grutzmacher, A. Beyer, C. David, B. Ketterer, E. Deckardt (2001). A New Technigue for Fabricating Three-dimensional Micro- and Nanostructures of Various Shapes, Nanotechnology, vol. 12, pp. 399-402.

[3] S.V. Golod, V.Ya. Prinz, V.I. Mashanov, A.K. Gutakovsky (2001). Fabrication of Conducting GeSi/Si Micro- and Nanotubes and Helical Microcoils, Semicond. Sci. Technol., vol.16, pp. 181-185.

[4] A.B. Vorob'ev, V.Ya. Prinz (2002). Directional Rolling Ofstrained Heterofilms, Semicond. Sci. Technol., vol. 17, pp. 614-616.

[5] V.M. Fomin, A.N. Shiplyuk, V.M.Aniskin, A.A. Maslov, V.V. Pay, V.Ya. Prinz, V.A. Seleznev, Hot-tube probes of thermal anemometers with high spatial and temporal resolution , Doklady. Physics. - 2006. - V.51, N 3. - P.132-135.

Aniskin Vladimir, Institutskaja str., 4/1, Khristianovich's Institute of Theoretical and Applied Mechanics SB RAS, 630090, Novosibirsk, Russian Federation
Maslov Anatoliy , Institutskaja str., 4/1, Khristianovich's Institute of Theoretical and Applied Mechanics SB RAS, 630090, Novosibirsk, Russian Federation
Shiplyuk Aleksandr, Institutskaja str., 4/1, Khristianovich's Institute of Theoretical and Applied Mechanics SB RAS, 630090, Novosibirsk, Russian Federation
Seleznev Vladimir, Lavrent'ev st., 13, Institute of Semiconductor Physics SB RAS, 630090, Novosibirsk, Russian Federation
Prinz Viktor, Lavrent'ev st., 13, Institute of Semiconductor Physics SB RAS, 630090, Novosibirsk, Russian Federation

Equilibrium cylindrical new phase inclusion

Mikhail Antimonov   Alexander Freidin

mike.antimonov@gmail.com afreidin@yandex.ru

Abstract

We consider an elastic body undergoing stress-induced phase transformations of martensite type. We examine an existence of cylindrical new phase inclusions. We prove characteristic properties of the equilibrium cylindrical inclusion and construct the existence surfaces in strain space. We relate the surfaces with phase transition zones and new phase nucleation surfaces.

1 Introduction

Description of phase transitions in solids remains the open problem of mechanics. Roughly speaking, there are two approaches. The first one introduces internal parameters, such as a new phase concentration, and describe new phase evolution basing on formulated constitutive equations (see [1] and reference therein). This gives proper tools for quantitative descriptions "on average", but does not consider an interface as it is and remains undetermined the local strains and stresses which are important for example in related fracture problems. The second approach is based on the consideration of the conditions on the interfaces and meet the problem of finding unknown interfaces and stability analysis (see e.g. [9, 10, 11] and reference therein).

The present work represents results obtained within the framework of the second approach. Various two phase structures were described earlier. For example, ellipsoidal new phase inclusions were considered in [2, 12, 14, 5, 7], spherically symmetric two-phase deformations were studied (see [3] and reference therein), heterogeneous deformation due to multiple appearance of new phase domains was presented for laminates and ellipsoidal new pase inclusions [6, 7]. Irrespectively of new phase domain examinations, the concept of phase transition zones (PTZ) formed by of all strains which can coexist on the equilibrium two phase interface was developed (see, e.g., [6, 8]and reference therein).

The PTZ boundary acts as a transformation surface if a new phase nucleates in a form of layers (laminates). In this paper we supplement the PTZ with surfaces of ellipsoidal and cylindrical new phase domains of existence. We use previous results in the case of ellipsoids [14, 5] and we present new results for cylindrical domains, briefly mentioned in [5]. As a result we construct a transformation surfaces and demonstrate that the type of new phase domains on the direct and reverse phase transformations depends on the strain state.
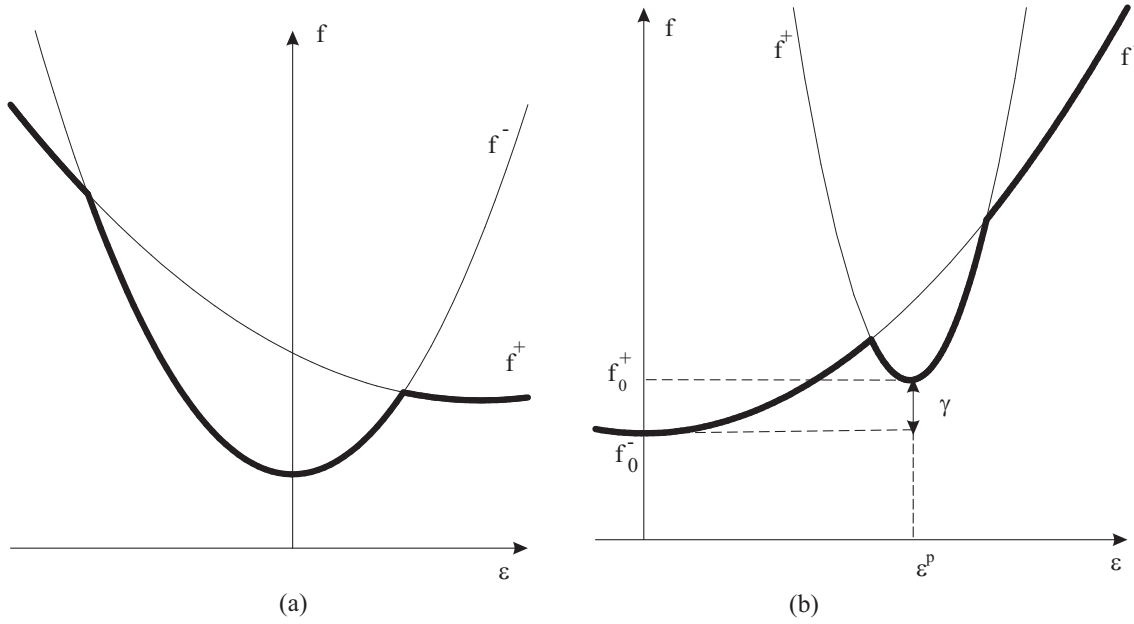
Figure 1: One-dimensional two-well energy. a – the new phase is softer. b – the parent phase is softer.

2 Cylindrical new phase inclusion

Suppose that a cylindrical inclusion with the ellipse in the base exists in an infinite body made of a material capable of undergoing stress-induced phase transformations. External strain $\boldsymbol{\varepsilon}_0$ (prescribed by conditions at infinity) is uniform. Describing phase transformations, we deal with materials characterized by a multi-well free energy density sketched for a two-well case in Fig. 1 and represented in a case of small deformations by quadratic functions

$$
\begin{aligned}
f(\boldsymbol{\varepsilon}, \theta) &= \min_{-,+} \{ f_-(\boldsymbol{\varepsilon}, \theta), f_+(\boldsymbol{\varepsilon}, \theta) \}, \\
f_\pm(\boldsymbol{\varepsilon}, \theta) &= f_\pm^0(\theta) + \frac{1}{2}(\boldsymbol{\varepsilon} - \boldsymbol{\varepsilon}_\pm^p) : \mathbf{C}_\pm : (\boldsymbol{\varepsilon} - \boldsymbol{\varepsilon}_\pm^p),
\end{aligned}
\tag{1}
$$

where "–" and "+" denote the parent and new phases, $\mathbf{C}_\pm$ is a tensor of the elastic modules of the phases, $\boldsymbol{\varepsilon}$ is a strain tensor, $\boldsymbol{\varepsilon}_\pm^p$ are strains in stress-free states, $[\boldsymbol{\varepsilon}^p] \equiv \boldsymbol{\varepsilon}_+^p - \boldsymbol{\varepsilon}_-^p$ is a transformation strain tensor, $f_\pm$ are strain energy densities of the stress free phases, θ is the temperature. The problem of the two phase equilibrium of the elastic body is reduced to the problem of equilibrium of the composite material with the unknown interface and to the problem of finding the phase interface Γ and the displacement fields $\mathbf{u}$ which are sufficiently smooth when $\mathbf{x} \notin \Gamma$ and continuous when $\mathbf{x} \in \Gamma$:

$$
\mathbf{x} \notin \Gamma \;:\; \nabla \cdot \boldsymbol{\sigma} = 0, \quad \theta = \text{const}, \tag{2}
$$

$$
\mathbf{x} \in \Gamma \;:\; [\mathbf{u}] = 0, \tag{3}
$$

$$
[\boldsymbol{\sigma}] \cdot \mathbf{n} = 0, \tag{4}
$$

$$
[f] - \boldsymbol{\sigma} : [\boldsymbol{\varepsilon}] = 0 \tag{5}
$$

Traction and displacement continuity across the interface is reduced to [14, 5]

$$
\begin{aligned}
&[\boldsymbol{\varepsilon}] = \mathbf{K}_{\mp}(\mathbf{n}) : \mathbf{q}_{\pm}, \mathbf{q}_{\pm} = -\mathbf{C}_1 : \boldsymbol{\varepsilon}_{\pm} + [\mathbf{C} : \boldsymbol{\varepsilon}^{\mathrm{p}}], \\
&\mathbf{K}_{\pm}(\mathbf{n}) = \{\mathbf{n} \otimes \mathbf{G}_{\pm} \otimes \mathbf{n}\}^{\mathrm{s}}, \mathbf{G}_{\pm} = (\mathbf{n} \cdot \mathbf{C}_{\pm} \cdot \mathbf{n})^{-1}, \mathbf{C}_1 = \mathbf{C}_+ - \mathbf{C}_-
\end{aligned}
\tag{6}
$$

where the jump in trains is determined by the normal to the interface, the strains on one side of the interface and the elastic modules on the other one.
In the case of isotropic phases

$$
\mathbf{K}_{\pm} = \frac{1}{\mu_{\pm}} \left((\mathbf{n}\mathbf{E}\mathbf{n})^{\mathrm{s}} - \frac{1}{2(1 + \nu_{\pm})}\mathbf{n}\mathbf{n}\mathbf{n}\mathbf{n} \right),
\tag{7}
$$

where $\nu_{\pm}$ and $\mu_{\pm}$ are Poisson's coefficients and the shear modules of the phases.
Using (1) and (6) one can reduce the thermodynamic equilibrium equation (5) to the equation

$$
\gamma + \frac{1}{2}[\boldsymbol{\varepsilon}^{\mathrm{p}} : \mathbf{C} : \boldsymbol{\varepsilon}^{\mathrm{p}}] + \frac{1}{2}\boldsymbol{\varepsilon}_{\pm} : \mathbf{C}_1 : \boldsymbol{\varepsilon}_{\pm} - \boldsymbol{\varepsilon}_{\pm} : [\mathbf{C} : \boldsymbol{\varepsilon}^{\mathrm{p}}] \pm \frac{1}{2}\mathbf{q}_{\pm} : \mathbf{K}_{\mp}(\mathbf{n}) : \mathbf{q}_{\pm} = 0, \tag{8}
$$

(see, e.g., [5]) that can be rewritten as

$$
\varphi(\boldsymbol{\varepsilon}_{\pm}) = \mp\frac{1}{2}\mathbf{q}_{\pm} : \mathbf{K}_{\mp}(\mathbf{n}) : \mathbf{q}_{\pm},
\tag{9}
$$

where

$$
\varphi(\boldsymbol{\varepsilon}_{\pm}) = \gamma + \frac{1}{2}[\boldsymbol{\varepsilon}^{\mathrm{p}} : \mathbf{C} : \boldsymbol{\varepsilon}^{\mathrm{p}}] + \frac{1}{2}\boldsymbol{\varepsilon}_{\pm} : \mathbf{C}_1 : \boldsymbol{\varepsilon}_{\pm} - \boldsymbol{\varepsilon}_{\pm} : [\mathbf{C} : \boldsymbol{\varepsilon}^{\mathrm{p}}]
\tag{10}
$$

Since external strains are uniform, strains inside the elliptical cylinder are also uniform [4]. Then the function $\varphi(\boldsymbol{\varepsilon}_{\pm})$ is uniform inside the cylinder. Thus, the thermodynamic condition (9) can be satisfied only if the strains $\boldsymbol{\varepsilon}_+$ are such that $\mathbf{q}_+ : \mathbf{K}_- : \mathbf{q}_+$ does not depend on the normal $\mathbf{n}$. This fact leads to the following theorem.
Theorem. *If an equilibrium new phase domain is an elliptical cylinder in an isotropic homogeneous parent phase "–", and the tensors $\boldsymbol{\varepsilon}_+^{\mathrm{p}}$ and $\mathbf{C}_+$ are constant inside the cylindrical inclusion and the tensor $\mathbf{C}_1$ exists, and the strain $\boldsymbol{\varepsilon}_+$ is uniform inside the inclusion, then the tensor $\mathbf{q}_+$ is axially-symmetric,*

$$
\mathbf{q}_+ = q_1\mathbf{k}\mathbf{k} + q_*(\mathbf{E} - \mathbf{k}\mathbf{k}),
\tag{11}
$$

where $\mathbf{k}$ is the axe of the cylinder. The jump in strains on the phase interface is

$$
[\boldsymbol{\varepsilon}] = \frac{1 - 2\nu_-}{2\mu_-(1 - \nu_-)}q_*\mathbf{n}\mathbf{n}.
\tag{12}
$$

In the case of isotropic parent phase "–" the thermodynamic equilibrium equation (8) is reduced to

$$
2\gamma_* + \frac{(q_1 + 2q_*)^2}{9k_1} + \frac{(q_1 - q_*)^2}{3\mu_1} + \frac{1 - 2\nu_-}{2\mu_-(1 - \nu_-)}q_*^2 = 0,
\tag{13}
$$

where $\gamma_* = \gamma + \dfrac{1}{2}[\boldsymbol{\varepsilon}^{\mathrm{p}}] : \boldsymbol{B}_1^{-1} : [\boldsymbol{\varepsilon}^{\mathrm{p}}]$, $\boldsymbol{B}_\pm = \boldsymbol{C}_\pm^{-1}$, $\boldsymbol{B}_1 = \boldsymbol{B}_+ - \boldsymbol{B}_-$, μ_1 and k_1 are the differences between the share and volume elastic modules of the new phase and the parent one.

Proof. By (7),

$$\mathcal{K}(\mathbf{q}, \mathbf{n}) \equiv \mathbf{q} : \mathbf{K}(\mathbf{n}) : \mathbf{q} = \frac{1}{\mu}(\mathbf{n} \cdot \mathbf{q}^2 \cdot \mathbf{n} - a(\mathbf{n} \cdot \mathbf{q} \cdot \mathbf{n})^2) \tag{14}$$

where $a = \dfrac{1}{2(1 - \nu)}$.

First, we prove that the quadratic form $\mathcal{K}(\mathbf{q}, \mathbf{n})$ does not depend on the normal $\mathbf{n}$ to cylindrical interface if and only if the tensor $\mathbf{q}$ is axially-symmetric,

$$\mathbf{q} = q_1 \mathbf{kk} + q_*(\mathbf{E} - \mathbf{kk}) \tag{15}$$

where $\mathbf{k}$ is the cylinder axe.

To prove the sufficiency we substitute (15) into (14) and obtain the expression independent on the normal to the interface,

$$\mathbf{q} : \mathbf{K} : \mathbf{q} = \frac{1}{\mu} q_*^2 (1 - a). \tag{16}$$

To prove the necessity we note that $\mathbf{n} = \mathbf{P} \cdot \mathbf{n}$ where $\mathbf{P} = \mathbf{E} - \mathbf{kk}$ is a projector onto the plane of the base of the cylinder. Then

$$\mathcal{K}(\mathbf{n}) = \mathbf{n} \cdot \widetilde{\mathbf{q}}^2 \cdot \mathbf{n} + (\mathbf{n} \cdot \mathbf{q} \cdot \mathbf{k})^2 - a(\mathbf{n} \cdot \widetilde{\mathbf{q}} \cdot \mathbf{n})^2 \tag{17}$$

where $\widetilde{\mathbf{q}}^2 = \mathbf{P} \cdot \mathbf{q} \cdot \mathbf{P}$. The necessity condition takes the form

$$\frac{d\Phi(\mathbf{n})}{d\mathbf{n}} = 0 \tag{18}$$

where the Lagrange function

$$\Phi(\mathbf{n}) = \mathcal{K}(\mathbf{n}) + \mathcal{A}(\mathbf{n} \cdot \mathbf{n} - 1) + \mathcal{B}\mathbf{n} \cdot \mathbf{k}, \tag{19}$$

$\mathcal{A}$ and $\mathcal{B}$ are the Lagrange multipliers. By (18) and (19),

$$2\widetilde{\mathbf{q}}^2 \cdot \mathbf{n} + 2(\mathbf{q} \cdot \mathbf{k})(\mathbf{n} \cdot \mathbf{q} \cdot \mathbf{k}) - 4a(\widetilde{\mathbf{q}} \cdot \mathbf{n})(\mathbf{n} \cdot \widetilde{\mathbf{q}} \cdot \mathbf{n}) + 2\mathcal{A}\mathbf{n} + \mathcal{B}\mathbf{k} = 0. \tag{20}$$

Multiplying (20) by $\mathbf{t} = \mathbf{k} \times \mathbf{n}$ we obtain

$$\mathbf{t} \cdot \widetilde{\mathbf{q}}^2 \cdot \mathbf{n} + (\mathbf{t} \cdot \mathbf{q} \cdot \mathbf{k})(\mathbf{n} \cdot \mathbf{q} \cdot \mathbf{k}) - 2a(\mathbf{t} \cdot \widetilde{\mathbf{q}} \cdot \mathbf{n})(\mathbf{n} \cdot \widetilde{\mathbf{q}} \cdot \mathbf{n}) = 0. \tag{21}$$

Since the ellipse is a closed figure, $\mathbf{n}$ is an arbitrary unit vector perpendicular to the vector $\mathbf{k}$, and vectors $\mathbf{n}, \mathbf{t}$ represent an arbitrary pair of orthogonal unit vectors lying in the plane of the cylinder base. Let $\mathbf{i}_1$, $\mathbf{i}_2$ in a pair of arbitrary orthogonal unit vectors in the base plane. Let take $\mathbf{n} = \mathbf{i}_1, \mathbf{t} = \mathbf{i}_2$ and then take $\mathbf{n} = \mathbf{i}_2, \mathbf{t} = -\mathbf{i}_1$. By (21), the following equalities must hold

$$\mathbf{i}_2 \cdot \widetilde{\mathbf{q}}^2 \cdot \mathbf{i}_1 + (\mathbf{i}_2 \cdot \mathbf{q} \cdot \mathbf{k})(\mathbf{i}_1 \cdot \mathbf{q} \cdot \mathbf{k}) - 4a(\mathbf{i}_2 \cdot \widetilde{\mathbf{q}} \cdot \mathbf{i}_1)(\mathbf{i}_1 \cdot \widetilde{\mathbf{q}} \cdot \mathbf{i}_1) = 0, \tag{22}$$

$$\mathbf{i}_1 \cdot \widetilde{\mathbf{q}}^2 \cdot \mathbf{i}_2 + (\mathbf{i}_1 \cdot \mathbf{q} \cdot \mathbf{k})(\mathbf{i}_2 \cdot \mathbf{q} \cdot \mathbf{k}) - 4a(\mathbf{i}_1 \cdot \widetilde{\mathbf{q}} \cdot \mathbf{i}_2)(\mathbf{i}_2 \cdot \widetilde{\mathbf{q}} \cdot \mathbf{i}_2) = 0. \tag{23}$$

From (22) and (23) it follows that

$$\mathbf{i}_1 \cdot \widetilde{\mathbf{q}} \cdot \mathbf{i}_1 = \mathbf{i}_2 \cdot \widetilde{\mathbf{q}} \cdot \mathbf{i}_2 \quad \text{or/and} \quad \mathbf{i}_1 \cdot \widetilde{\mathbf{q}} \cdot \mathbf{i}_2 = 0 \quad \forall \mathbf{i}_1, \mathbf{i}_2 : \; \mathbf{i}_1 \perp \mathbf{i}_2, \mathbf{i}_1 \perp \mathbf{k}, \mathbf{i}_2 \perp \mathbf{k}.$$

Thus,

$$\widetilde{\mathbf{q}} = q_* \mathbf{P}. \tag{24}$$

Then, by (22),

$$(\mathbf{i}_2 \cdot \mathbf{q} \cdot \mathbf{k})(\mathbf{i}_1 \cdot \mathbf{q} \cdot \mathbf{k}) = 0 \quad \forall \mathbf{i}_1, \mathbf{i}_2 : \; \mathbf{i}_1 \perp \mathbf{i}_2, \mathbf{i}_1 \perp \mathbf{k}, \mathbf{i}_2 \perp \mathbf{k}. \tag{25}$$

Thus, the vector $\mathbf{k}$ is a eigenvector of the tensor $\mathbf{q}$ and the tensor $\mathbf{q}$ is axially-symmetric.

Formula (12) for the jump in strain immediately follows from (15) and (6). Finally, substituting (11) into (8) we obtain (13). □

Strain tensor $\boldsymbol{\varepsilon}_+$ inside the cylinder is related with the external strain $\boldsymbol{\varepsilon}_0$ as [4, 13]

$$\boldsymbol{\varepsilon}_+ = \boldsymbol{\varepsilon}_0 + \mathbf{A} : \mathbf{q}_+, \tag{26}$$

where $\mathbf{A}$ is the Eshelby tensor which characterizes the geometrical parameters of the ellipsoidal inclusions. Its components are given by the integrals (see [13])

$$A_{pppp} = \frac{\chi_-}{8\pi\mu_-}(3J_{pp} + (1 - 4\nu_-)J_p),$$

$$A_{ppqq} = \frac{\chi_-}{8\pi\mu_-}(J_{qp} - J_p),$$

$$J_p = \frac{3}{2}\nu a_p^2 \int_0^\infty \frac{du}{(a_p^2 + u)(a_q^2 + u)\Delta(u)}, \tag{27}$$

$$\Delta(u) = \sqrt{(a_1^2 + u)(a_2^2 + u)(a_3^2 + u)},$$

$$\nu = \frac{4}{3}\pi a_1 a_2 a_3, \quad \chi_- = \frac{1}{2(1 - \nu_-)}, \quad p, q = 1, 2, 3.$$

where a_1, a_2 and a_3 are the semiaxises of the ellipsoid. In the case of a cylindrical inclusion $a_1 \to \infty$ and we obtain

$$A_{1111} = A_{1122} = A_{1133} = A_{2211} = A_{3311} = 0,$$

$$A_{2222} = \frac{\chi_-}{2\mu_-(1 + \xi)^2}(3\xi + 2 - 4\nu_-(1 + \xi)),$$

$$A_{2233} = A_{3322} = -\frac{\chi_- \xi}{2\mu_-(1 + \xi)^2}, \tag{28}$$

$$A_{3333} = \frac{\chi_- \xi}{2\mu_-(1 + \xi)^2}(3\xi + 2 - 4\nu_-(1 + \xi)),$$

where $\xi = \dfrac{a_2}{a_3}$ is the ratio of the semiaxes of the elliptical base of the cylinder. Substituting (28) into (26) and using the fact that $\boldsymbol{\varepsilon}_+ = \varepsilon_1^+ \mathbf{e_1 e_1} + \varepsilon_*^+(\mathbf{e_2 e_2} + \mathbf{e_3 e_3})$ we obtain that

$$
\begin{aligned}
\varepsilon_1^0 &= \varepsilon_1^+, \\
\varepsilon_2^0 &= \varepsilon_*^+ - \frac{\chi_-}{2\mu_-(1+\xi)}(3k_+\varepsilon_p - \lambda_1(2\varepsilon_*^+ + \varepsilon_1^+) - \mu_1\varepsilon_*^+), \\
\varepsilon_3^0 &= \varepsilon_*^+ - \frac{\chi_-\xi}{2\mu_-(1+\xi)}(3k_+\varepsilon_p - \lambda_1(2\varepsilon_*^+ + \varepsilon_1^+) - \mu_1\varepsilon_*^+).
\end{aligned}
\tag{29}
$$

The domains of existence of the cylindrical new phase inclusions can be constructed in the external strains space if we substitute (29) into (13) taking into account that

$$
\mathbf{q}_+ = -\mathbf{C_1} : \boldsymbol{\varepsilon}_+ + [\mathbf{C} : \boldsymbol{\varepsilon}^p].
\tag{30}
$$

Substituting (15) into (26) we obtain

$$
\boldsymbol{\varepsilon}_+ = \boldsymbol{\varepsilon}_0 + q_*\boldsymbol{\omega},
\tag{31}
$$

where $\boldsymbol{\omega} = \mathbf{A} : \mathbf{E}$. The eigenvectors of $\boldsymbol{\omega}$ coincide with the cylinder axes and its eigenvalues are positive. Then

$$
\frac{1}{q_*}(\varepsilon_*^+ - \mathbf{n} \cdot \boldsymbol{\varepsilon}_0 \cdot \mathbf{n}) \geqslant 0,
\tag{32}
$$

where $\mathbf{n}$ is a arbitrary normal to the cylinder surface. The inequality (32) is a restriction on the domain of existence of equilibrium new phase cylinders.

From (31) it also follows that, since tensors $\boldsymbol{\omega}$ and $\boldsymbol{\varepsilon}_+$ are coaxial to the new phase cylinder, the external strain tensor $\boldsymbol{\varepsilon}_0$ is coaxial to the cylinder too. It means that in the media loaded by external strains coaxial to the external strains cylinder appears. In Fig.2 axisymmetric sections of phase transition zones and domains of new phase ellipsoids and cylinders existence are presented. Filled areas are the phase transition zones (see, e.g., [8, 6]). PTZ boundaries correspond to the laminates of infinitesimal concentration of the new phase. Dotted lines correspond to the appearance of cylindrical inclusion, dashed lines a constructed according to [14] and correspond to the appearance of ellipsoidal inclusions.

At the points where dashed lines touch the dotted lines one of the axes of the ellipsoidal inclusion tend to infinity and the ellipsoid becomes the cylinder. At the points where dashed and dotted lines touch the solid lines two axes of the ellipsoids and one of the axes of the ellipse in the base of the cylinder tends to infinity and both the ellipsoid and the cylinder become simple laminates. At the points where dotted lines touch the solid lines one of the axes of the ellipse in the base of the cylinder tends to infinity and the cylinder becomes the simple laminates.

The limit transformation surface is an envelope of all existence domains. Various parts of the transformation surface on the one hand correspond to various two-phase structures and on the other hand correspond to various strain states. Thus, on the different straining paths one can expect the appearance of the different equilibrium two phase structures.

Note that the PTZ boundaries are not convex everywhere. Cylinders and ellipsoids allowed us to construct the convex envelope almost everywhere. We expect that the remained nonconvex part will be covered after examinations of high-order laminates.
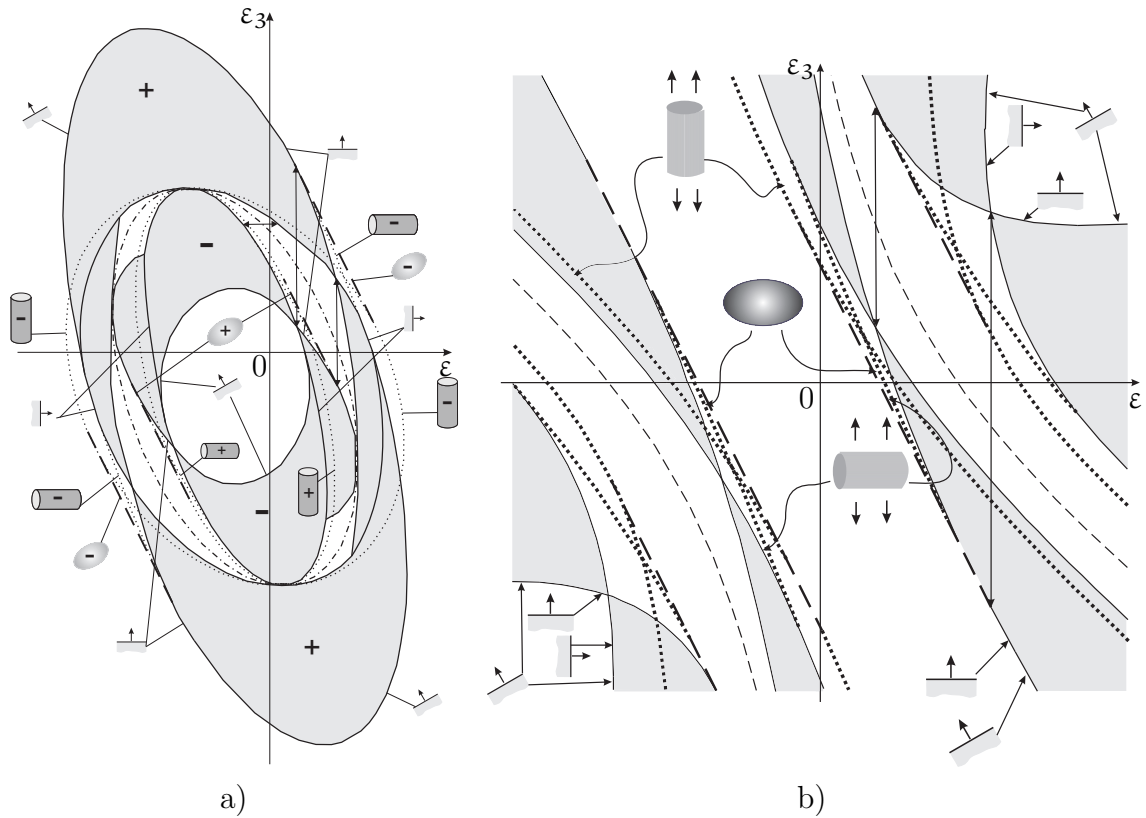
Figure 2: Axisymmetric section of the external strain space, $\varepsilon_1=\varepsilon_2=\varepsilon$. a) is a case when $\mu_1 < 0$, b) is a case when $\mu_1 > 0$.

Acknowledgements

References

[1] *S. P. Belyaev, A. E. Volkov et al.* Materials with effect of shape memory. /Ed. by V. A. Likhachev. SPb.: NIIH SPbSU, V.1. 1997. pp.424; V. 2., 1998. pp.374; V. 3, 1998. pp.474; V. 4, 1998. pp.268.

[2] *V. L. Berdichevsky.* Seed of a melt in a solid, Dokl. Acad. Nauk SSSR 27 (1983) 80–84.

[3] *V. A. Eremeyev, A. B. Freidin, L. L. Sharipova.* The stability of the equilibrium of two-phase elastic solids, J. Appl. Math. Mech. (PMM) 71 (2007) 61–84.

[4] *J. D. Eshelby.* The determination of the elastic field of an ellipsoidal inclusion and related problems, Proc. R. Soc. Lond. A 241 (1957) 376–396.

[5] *A.B. Freidin.* On new phase inclusions in elastic solids. ZAMM - Z. Angew. Math. Mech. 87, No. 2, pp.102–116 (2007).

[6] *A.B. Freidin, L.L. Sharipova.* On a Model of Heterogenous Deformation of Elastic Bodies by the Mechanism of Multiple Appearance of New Phase Layers. Meccanica (2006) 41: 321–339.

[7] *A. B. Freidin, E. N. Vilchevskaya.* Multiple development of new phase inclusions in elastic solid, Int. J. Engineering Sciences. 2009. V. 47. P. 240-260.

[8] *A. B. Freidin, E. N. Viltchevskaya, L. L. Sharipova.* Two-phase deformations within the framework of phase transition zones, Theor. Appl. Mech. 28 – 29 (2002) 149–172.

[9] *M. A. Grinfeld.* Thermodynamic methods in the theory of heterogeneous systems (Longman, New York, 1991).

[10] *M. E. Gurtin.* Two-phase deformations of elastic solids, Arch. Rat. Mech. Anal. 84 (1983) 1–29.

[11] *R. D. James.* Finite deformation by mechanical twinning, Arch. Rat. Mech. Anal. 77 (1981) 143–177.

[12] *I. M. Kaganova, A. L. Roitburd.* Equilibrium of elastically interacting phases, Sov. Phys. JETP 67 (1988) 1174–1186.

[13] *S. K. Kanaun, V. M. Levin.* Self-consistent methods for composites, Static Problems, vol. 1, Springer, 2007.

[14] *L. B. Kublanov and A. B. Freidin.* J. Appl. Math. Mech. (PMM USSR) 52, 382–389 (1988) (translation of Prikl. Matem. Mekhan., 52, 493–501).

Mikhail Antimonov, Alexander Freidin, Institute for Problems in Mechanical Engineering, Russian Academy of Sciences, 61, Bolshoj pr., V.O., Saint-Petersburg, Russia, 199178

Regimes of drops and bubbles deformation in two-phase flows

V. A. Arkhipov   V. F. Trofimov   A. S. Usanina

leva@niipmm.tsu.ru

Abstract

The processes of drop and bubble deformation and instability resulting in their breakup play an important role in hydro- and gas dynamics of two-phase flows. These processes are of obvious practical importance in meteorology (the formation of the size spectrum of atmospheric precipitations), in propulsion engineering (the dispersibility of fuel drops in internal-combustion and rocket engines), in ecological problems (the emission of toxic fluid-propellant components at the stage separation of a launch vehicle) and in quite a number of other branches of technics and technology.

It is known that there are two mechanisms of drop and bubble instability in a flow: the Kelvin-Helmholtz instability and the Rayleigh-Teylor instability [1]. The breakup occurs at sufficiently high Weber numbers We and Bond numbers Bo, respectively. The results of the experimental investigation and theoretical study of drop and bubble instability and breakup in the range of Reynolds numbers $\text{Re} \sim 1$ according to the Rayleigh-Teylor mechanism, at the Bond numbers Bo close to the critical value $\text{Bo}_* = 40 \div 90$ have been presented in the paper [1, 2, 3]. The Bond number is defined as

$$\text{Bo} = \rho_l \omega D^2 / \sigma.$$

Here ρ_l is the density of a fluid phase; σ is the surface tension coefficient; D is the diameter of the equivalent spherical drop (bubble), which has the same volume as the deformed drop (bubble); ω is the acceleration of mass forces. The choice of such a regime of drops sedimentation (and bubbles rising) is caused by the fact that flows at $\text{Re} \gg 1$ were considered in the well-known publications [1, 2, 3].

In the majority of works, the Weber number is considered as the principal parameter determining the drop deformation and crash in a flow, i.e. the breakdown occurs due to the Kelvin-Helmholtz instability. The Weber number is defined as

$$\text{We} = \rho U D / \sigma.$$

Here ρ is the density of a medium, in which the drop moves; U is the relative velocity. The critical value We_* may vary widely ($1.2 < \text{We}_* < 60$) depending on the drop motion regime.

1 Theoretical analysis

As it follows from the Hadamard's solution for a drop falling down in a viscous liqiud under gravity at low Reynolds numbers, the difference between normal stresses is stable all over its spherical surface and does not tend to deform the drop. In view of the above, the conclusion was made in Batchelor's works [4] that if the viscosities and densities of two liquids are such that at low Reynolds numbers it is possible to neglect the inertial forces, there are no size limit of a spherical drop.

The possibility of solving this problem for axisymmetric perturbations of a spherical drop or bubble restrained by surface tension forces in case of axisymmetric perturbations in an external flow was theoretically studied

$$r[N''_{\varphi\varphi} + N'_{\varphi}\cos\varphi/(\sin\varphi) + (r + \mathrm{Bo}\cos\varphi)N] - Cr = \delta F,$$

$$N'_{\varphi}|_{\varphi=0} = 0, \quad N'_{\varphi}|_{\varphi=\pi} = 0, \quad \int_0^{\pi} Nr\,d\varphi = 0,$$

where N is the small perturbation of a drop shape in the direction normal to the surface; φ is a latitudinal angle in the spherical coordinate system; r is the radius of an undisturbed drop; δF is the axisymmetric perturbation of the forces (including viscous) acting normal to the surface; C is constant.

For the operator in the left side of the differential equation the eigenvalue problem was solved. It has been shown that for the least eigenvalue the problem is solvable due to the equation of motion of the drop mass center. For other eigenvalues the solvability condition follows from self-adjointness of the differential operator. It consists in the orthogonality of eigenfunctions and an arbitrary function δF. As the eigenfunctions are not connected with the functions of perturbation of an external flow, for arbitrary perturbations the condition of orthogonality will not be satisfied and, hence, the problem will not have the solution. The calculation of the least nonzero eigenvalue allowed the critical value of the Bond number, $\mathrm{Bo}_* = 90$, to be found.

2 Experimental investigation

Drop and bubble deformation and breakup are extremely complicated processes and they are characterized by interaction of surface tension forces, viscosity and inertia. The condition of the breakup initiation is to be obtained by analyzing the liquid sphere stability in a flow of another liquid. The experimental investigation of deformation of a single initially spherical drop moving in another liquid under gravity at the Reynolds numbers $\mathrm{Re} \sim 1$ and the Bond numbers close to $\mathrm{Bo}_* = 90$ was conducted for a pair of modeling liquids (falling down of a mercury drop in glycerin).

It has been ascertained that the mercury drop is stable and keeps the spherical form while falling down if the diameter of the mercury drop moving in glycerin at low Reynolds numbers is less than 8 mm. Corresponding Bo_* equals 26. If the drop

Table 1:

Solution	87%	100%	100%
T, ^{0}C	21	22.5	10
μ, Pa · s	$0.09 \div 0.01$	$1.09 \div 0.08$	$3.60 \div 0.25$
ρ, kg/m^3	1230	1260	1270
σ, N/m	$65 \cdot 10^{-3}$	$63 \cdot 10^{-3}$	$64 \cdot 10^{-3}$

diameter is about 10 mm, the drop is unstable and breaks into fragments when moving. Corresponding Bo_* is equal to 40.

Simultaneous fulfillment of the conditions $Bo_* \sim 90$ and $Re \sim 1$ in the experiment is difficult because of the production complexity of large mercury drops. To study the drop motion at $Bo \sim 90$, it is necessary to produce an initial spherical drop of about 15 mm in diameter. No modifications of the capillary-based device for drop production gave positive results. However, the results of the experiments conducted confirm the existence of the range of the Bond numbers, $Bo = 26 \div 40$, where the drop moving at low Reynolds numbers collapses and breaks into fragments. The theoretically predicted $Bo_* = 90$ qualitatively verifies the existence of the range.

The evaluations performed in the work revealed that the regime could be realized by means of bubble rising. The results of the experimental investigation of stability of a single initially spherical air bubble in water-glycerin solution were obtained. Depending on the temperature and percentage of water, characteristics of the solutions investigated are shown in the table 1 [5].

The calculation of the Bond and Reynolds numbers was performed for each series of experiments by formula:

$$Re = \rho_l U D / \mu.$$

Here μ is the viscosity coefficient of a fluid phase. Corresponding similarity criteria and other parameters being estimated for the experiments conducted vary in the range of $Re = 0.008 \div 34$, $Bo = 0.2 \div 448$, $D = 0.1 \div 4.8$ sm, $U = 0.6 \div 19$ sm/s.

Depending on the similarity criteria being varied, the shape, size and rising velocity were fixed by means of the video camera Panasonic NV-DA1. Quantitative characteristics of the process (rising velocity, geometrical size of a bubble) were determined by processing with Adobe After Affect. Taking into account the resolution of the video camera, the geometrical size of a bubble was determined with the uncertainty of 1% and the uncertainty of measurement of rising velocity was accounted for, mainly, by the dispersion of the data of backup tests and did not exceed 10%.

The analysis of the experimental results showed that there were some steady bubble shapes in the investigated range of the similarity criteria: sphere, ellipsoid, a segment of sphere.

3 Conclusions

The drop and bubble instability at low Reynolds numbers in the range of the Bond numbers larger than 40 has been experimentally verified. In the investigated range of Re and Bo bubbles have not been found to break into fragments in contrast to drops.

Acknowledgements

References

[1] Nigmatulin R.I. Dynamics of multiphase media. Part 1 – M.: Science, 1987. – 464p.

[2] Vasenin I.M, Arkhipov V.A., Butov V.G., Glazunov A.A., Trofimov V.F. Gas dynamics of two-phase flows in nozzles. – Tomsk: TSU, 1986. – 286p.

[3] Harper E.Y., Grube G.W., I-Dee Chang. On the breakup of accerating liquid drops. Part 2 // J. Fluid Mech. – 1972. – Vol. 52. – P. 565–591.

[4] Batchelor G. Introduction into fluid dynamics [Russian translation]. – Moscow, 1973. – 760p.

[5] Nevolin F.V. Chemistry and tecnology of glycerin producing. – M.: Chemistry, 1954.

Vladimir A. Arkhipov, 634050, Lenina av. 36, Tomsk, Russia
Vyacheslav F. Trofimov, 634050, Lenina av. 36, Tomsk, Russia
Anna S. Usanina, 634050, Lenina av. 36, Tomsk, Russia

Thermodynamic creep fracture law for aging polymer materials

Robert A. Arutyunyan   Anna V. Vardanyan

Robert.Arutyunyan@paloma.spbu.ru

Abstract

The modified elastic-viscous equations expressed in the scale of the effective time are considered to describe the deformation, climate and radiation aging of polymer materials. The concrete differential relations for the parameter of effective time are suggested. Using the received constitutive equations and the energy conservation law the creep fracture criterion is formulated. The criterion can be applied to describe the time to fracture of polymer materials undergoing UV irradiation. It is known, that UV irradiation promotes the degradation and fracture of polymer materials. In the thermodynamic creep fracture criterion these effects are connected with the increase of internal and, consequently, with the increase of the stored energy. The received results can be applied to predict the destruction of polymer materials and structures, also to optimize the human skin sunburn process. In the last case the effect of deformation aging (massage) will be very important and it was not considered in the world medicine practice.

Financial support of the Russian Foundation for Basic Research (Grant N 09-01-90900) is gratefully acknowledged.

Numerous publications [1-3] are devoted to the experimental investigations of thermal and climatic aging of polymers. For example, in [1] the results of creep experiments on quenched and aged during 4 years specimens made of different polymer materials in amorphous state are presented. To describe the results of such experiments generally the principle of time temperature superposition is applied. This principle leads to the horizontal shifting of the compliance curves and describes the behavior of rheologically simple materials. To model the behavior of complex materials and deformation and radiation aging materials it is necessary to operate with the principles capable to consider both horizontal and vertical shifting. For this purpose the parameter of effective time ω is introduced by the following relation

$$d\omega = f_1(\omega, \varepsilon, r, T, t)dt + f_2(\omega, \varepsilon, r, T, t)d\varepsilon, \qquad (1)$$

where ε is the value of deformation, r is radiation dose, t is the real time, T is temperature.

As it follows from the definition, the parameter of effective time ω is defined so that at "instant", active loading it corresponds to the "deformation" time. In unloading

condition this parameter is reduced to the real time and may describe the chemical processes due to aging, so we may call it as the chemical time. Thus, in a scale of the effective time the behavior of quenched, deformation and radiation aged materials are described.

To describe the deformation behavior of polymer materials, elastic viscous models (Maxwell, Voigt, Boltzmann-Volterra and others) are introduced. Rheological equation for aging medium based on Maxwell's model is formulated. In the classical case the model is linear and is not capable to describe the aging behavior of polymer materials. To cover the aging effects the Maxwell's equation is expressed through the effective time ω.

To describe the process of deformation aging of polymer materials we will consider the Maxwell's elastic viscous model

$$E\sigma + \eta\dot{\sigma} = E\eta\dot{\varepsilon}. \tag{2}$$

In the classical approach the viscous and elastic coefficients η, E in equation (2) are considered as constants. Such assumptions are valid for the stable viscous-elastic media. For the unstable, aging materials these coefficients are time dependent functions and must be defined experimentally.

At first, let's consider the case when viscous and elastic coefficients are functions of real time. If we use the physical relation $\eta \approx E\tau$ where τ is the relaxation time, the modified Maxwell equation (2) can be written in the form

$$\frac{d\varepsilon}{dt} = \frac{d}{dt}\left[\frac{\sigma}{E(t)}\right] + \frac{\sigma}{E(t)\tau}. \tag{3}$$

The experimental relation for elasticity modulus are usually expressed through the real time [4] as

$$E = E_0(1 + (1 - e^{-kt})), \tag{4}$$

where E_0, k are constants.

The solution of equation (3) is presented in [4] and the theoretical creep curves are compared with the corresponding experimental creep and aging curves (compliance $D = \varepsilon/\sigma_0$) for different polymer materials. It is shown that the Maxwell equation expressed through the real time can be used to describe the processes of aging of polymers due to heat and weathering. However to describe the deformation aging of polymers we will used the parameter ω given by the relation (1).

Let's consider the simple relation for the parameter ω

$$d\omega = kt^n dt, \tag{5}$$

where k, n are constants.

The equation (2), written through parameter ω , have the following form

$$\frac{d\varepsilon}{d\omega} = \frac{d}{d\omega}\left(\frac{\sigma}{E(\omega)}\right) + \frac{\sigma}{\eta(\omega)}. \tag{6}$$

Introducing (5) into (6), assuming $\sigma = \text{const}$, E, $\eta = \text{const}$ and taking the initial conditions $\omega = 0$, $t = 0$, $\varepsilon = \sigma/E$, the solutions of the received equations can be written as

$$D = \frac{\varepsilon}{\sigma} = \frac{1}{E}\left(1 + \frac{Ekt^{n+1}}{\eta(n+1)}\right). \qquad (7)$$

To describe the effect of deformation aging of polymer materials we shall consider the following kinetic equation of effective time

$$d\omega = ae^{kt}dt + bd\varepsilon, \qquad (8)$$

where a, k, b are constants.

Writing down Maxwell equation (6) in view of the formula (8) and solving the received equation at $\sigma = \text{const}$ and initial conditions $\omega = 0$, $t = 0$, $\varepsilon = \sigma/E$, we have the following creep solution

$$\varepsilon = \frac{\sigma}{E}\left[1 + \frac{a(e^{kt}-1)}{k\tau(1-\frac{\sigma b}{E\tau})}\right]. \qquad (9)$$

In order to evaluate the value of energy consumed for the creep fracture the energy conservation law will be used to formulate the thermodynamic fracture criterion for heterogeneous materials Applied to the problem of creep deformation and fracture of a specimen, this law can be formulated in the following manner [5]. When an element of a system (specimen) goes from the initial state (initial loading) to the final state (fracture) a small increment of internal energy du is equal to the sum of increments of strain energy dw, radiation energy δR and the heat δq removed from the element of the system

$$du = \delta w - \delta q + \delta R, \qquad (10)$$

where $\delta w = \sigma_{ij}d\varepsilon_{ij}$ ($d\varepsilon_{ij} = \dot{\varepsilon}_{ij}dt$), σ_{ij} are components of stress tensor, $d\varepsilon_{ij}$ are components of strain increment tensor.

Integrating (10) from initial (marked 0) to the fractured state (marked *), we will receive

$$\Delta u_* = w_* - \Delta q_* + \Delta R_*, \qquad (11)$$

where

$$\Delta u_* = \int_{u_0}^{u_*} du = u_* - u_0, w_* = \int_0^{w_*} \delta w, \Delta q_* = \int_{q_0}^{q_*} \delta q, \Delta R_* = \int_{R_0}^{R_*} \delta R. \qquad (12)$$

Introducing notations $\Delta q_* = w_{*1}$, $\Delta u_* = w_{*2}$, $\Delta R_* = w_{*3}$ the energy conservation law (11) can be rewritten as $w_* + w_{*3} = w_{*1} + w_{*2}$. So the summary of deformation and radiation energy is the summary of the heat energy w_{*1} and the energy w_{*2} consumed for the fracture of a specimen. The energy w_{*2} is the latent or stored energy and it represents the change in internal energy of the material.

For pure tension $\varepsilon_{ij} = \varepsilon$, $\sigma_{ij} = \sigma$, where $\sigma = const$, the deformation energy can be calculated as $w_* = \sigma\varepsilon_*$, from which follows

$$\varepsilon_* = \frac{w_*}{\sigma} = \frac{w_{*1} + w_{*2} - w_{*3}}{\sigma}. \tag{13}$$

If we compare the value of creep deformations $\varepsilon = \varepsilon_*$ in relations (7), (9) at the fracture time $t = t_p$ with (13) we will receive the following creep fracture laws

$$t_p = \left[\frac{\eta(m+1)}{kE} \left(\frac{E(w_{*1} + w_{*2} - w_{*3})}{\sigma^2} - 1 \right) \right]^{1/n+1}, \tag{14}$$

$$t_p = \frac{1}{k} \ln \left[1 + \frac{k\tau}{a} \left(\frac{E(w_{*1} + w_{*2} - w_{*3})}{\sigma^2} - 1 \right) \left(1 - \frac{b\sigma}{E\tau} \right) \right]. \tag{15}$$

The received thermodynamic creep fracture criterions (14), (15) will be applied to describe the creep fracture curves for polymer materials subjected to heat and ultraviolet radiation. In this case, in accordance with the experiments, the proposed relations predict the intensification of creep rate and the significant decrease of the time to fracture. These criterions contain the summary of heat, stored and radiation energies. Assuming that the heat energy is given out so it has no effect on the fracture process, the creep fracture criterion is simplified. So the latent and radiation energies are responsible for the aging, degradation and fracture of polymer materials. This version of the criterion will be applied to describe the experimental creep fracture curves of different polymer materials undergoing UV irradiation. It is known [6], that UV irradiation promotes the degradation and fracture of polymer materials. As it was shown, these effects are connected with the increase of internal, and consequently, with the increase of the stored energies. The received results can be applied to predict the destruction of polymer materials and structures, also to optimize the human skin sunburn process. In the last case the effect of deformation (massage) and UV radiation aging will be very important and it was not considered in the world medicine practice.

References

[1] Struik L.C.E. Physical aging in amorphous polymers and other materials. Amsterdam, Oxford, New York: Elsevier Sci. Publ.Comp. 1978. 229p.

[2] Bruijn de J.C.M. The failure behavior of high density polyethylene with an embrittled surface layer due to weathering. Delft: Delft University press. 1992. 167p.

[3] Kulich D.M., Gaggar S.K. Weathering of Acrylonitile Butadiene-Styrene Plastics: compositional effects on impact and color // Polymer durability. Advances in Chemistry. Series 249. American chemical society. Washington, DC. 1996. P. 483-501.

[4] Arutyunyan R.A. The problem of deformation aging and prolonged fracture in material sciences. Sankt-Petersburg: S.-Petersburg university press. 2004. 252p. (in Russian).

[5] Robert A. Arutyunyan. Energy consumption for creep fracture of metallic materials // Acta Mechanica Sinica. 2008. vol. 24. N4. P. 469-472.

[6] Regel V.R., Boboev T.B., Cherniy N.N. Strength time-temperature dependence of polymers undergoing ultraviolet radiation // Mechanica polymerov. 1969. N3. P. 442-448. (in Russian).

Robert A. Arutyunyan, St.-Petersburg State University, Faculty of Mathematics and Mechanics, Sankt-Petersburg, Petrodvoretz, Universytetskii prospect, 28, 198504, Russia,
Anna V. Vardanyan, Institute of Mechanics National academy of science of Armenian, pr. Marshala Bagramyana, 24b, Erevan, Republic of Armenia

Degradation of high elastic thin layer subjected to cyclic compression

Robert A. Arutyunyan   Kira S. Yakimova

Robert.Arutyunyan@paloma.spbu.ru

Abstract

In engineering applications, for example, pressure cylinders employed in paper industry, as a material of thin layer, polyurethane or natural and artificial rubbers in high elastic state is used. To define the stresses interval, where the material behavior can be considered as uncompressible and to specify the mechanical characteristics, the experiments on deep pressure and creep under the specimens made of polyurethane were carried out. The problem of thin layer made of incompressible viscous material subjected to compression by two parallel plates is considered. The analytical expressions for current lines, the rates of displacements, the deformations and stresses are derived and the corresponding diagrams are constructed. The dimensions of thin stratum near the contact planes are determined in which the stress condition can be considered as the state of hydrostatic pressure. This state may be responsible for degradation of the structure and the failure of thin layer and the construction as a whole. The results can be applied to estimate the fatigue life of different elastic viscous materials and the items where these materials are used as working elements.

1 Definition of the mechanical properties of polyurethane in the experiments on deep pressure and creep

The purposes of these experiments are construction of deep pressure stress - strain curves and the definition of the Young modulus of polyurethane. As it is known, the Young modulus is a very important mechanical characteristic of material since it defines the initial rigidity of a material. Moreover this characteristic plays important role in the contact problem when calculating the contact stresses. So we will direct our attention on the methods of calculating of this characteristic.

In the deep pressure experiments the specimens of square cross section made of polyurethane were used. The specimens have the following dimensions:

20x20x30 *mm*. Experiments were carried out on the Instron 1231U-10 test machine with the loading velocity equals to $3,5$ mm/min.

At the first loading (on the 200 kg base of the force measurer) the value of force at maximal pressure was equal to 190 kg. The deformation on this force level was equal to 56,3%. Immediately following the unloading the specimen has the dimensions: 20,5x20,5x29,5 *mm*. The specimen recovered its original shape after three minutes of "rest".

The second loading was carried out on the 1000 kg base of the force measurer. At the maximal pressure value of force 850 kg the pressure deformation was 78,5%. At this level of pressure the specimen has the following dimensions: 40x40x28 *mm*. Immediately following the unloading the specimen has the dimensions: 21,7x21,7x28 *mm* and after ten minutes of "rest" - 20,7x20,7x28,5 *mm*. After the long period of "rest" the dimensions of the specimen were stabilized on the level: 20x20x29 *mm*.

In the experiment the current value of specimen length were measured. The current value of the cross section area was calculated using the incompressibility condition: $l_0 F_0 = l F$ (l_0, F_0 are the initial and l, F are the current length and cross section area of the specimen).

The diagrams $\sigma - \varepsilon$ ($\sigma = P/F$, $\varepsilon = (l - l_0)/l_0$), $\sigma - \lambda$ ($\lambda = l/l_0$, $\lambda = 1 + \varepsilon$) are shown in Figures 1, 2.
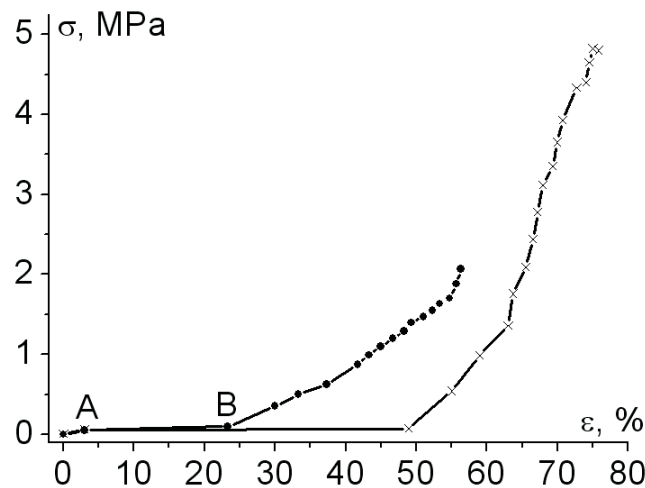
Figure 1: The diagrams $\sigma - \varepsilon$.

The "conventional" elastic modulus E was defined on the deformation base about 20% according to the initial part of $\sigma - \varepsilon$ diagram (Fig. 1). The value of the modulus is equal to $0,4$ MPa. The real value of the elastic modulus E can be found on the deformation base less than 1% of $\sigma - \varepsilon$ diagram, marked OA in Fig. 1.

If λ is the relative deformation then, according to the statistical theory of high elastic deformation, the relation between λ and stress has the form [1]

$$\sigma = \frac{E}{3}(\lambda^2 - \frac{1}{\lambda}).$$
(1.1)

Introducing the relation $\lambda = 1 + \varepsilon$ into (1.1), we will receive
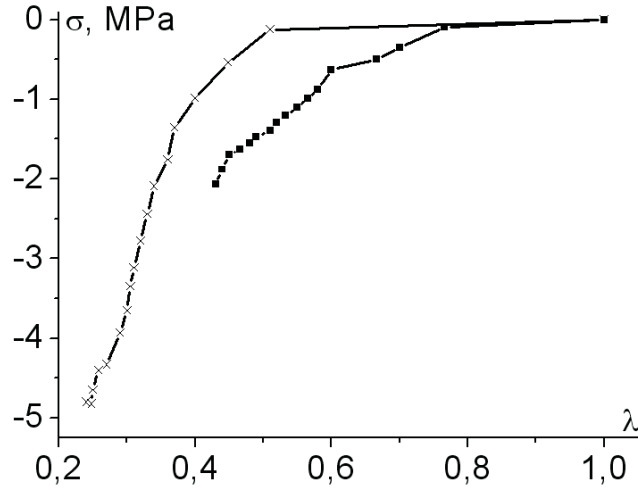
Figure 2: The diagrams $\sigma - \lambda$.

$$\sigma = \frac{E}{3}\left[(1+\varepsilon)^2 - \frac{1}{1+\varepsilon}\right]. \tag{1.2}$$

The value of the elastic modulus follows from the condition

$$E = \lim_{\varepsilon \to 0}\left(\frac{d\sigma}{d\varepsilon}\right). \tag{1.3}$$

and in the case of relation (1.2) we have

$$E = \lim_{\varepsilon \to 0}\left(\frac{d\sigma}{d\varepsilon}\right) = \lim_{\varepsilon \to 0}\frac{E}{3}\left[2(1+\varepsilon) + \frac{1}{(1+\varepsilon)^2}\right] = E. \tag{1.4}$$

If $E = 0,4 \text{MPa}$, $\varepsilon = 23\%$, from (1.2) follows $\sigma = 0,1 \text{MPa}$. This value of stress is equal to the experimental data according to the $\sigma - \varepsilon$ diagram (Fig. 1).

To define the value of elastic modulus on the initial part of $\sigma - \varepsilon$ diagram the following relations can be also used

$$\sigma = \frac{E}{b}(e^{b\varepsilon} - 1). \tag{1.5}$$

$$\sigma = E\varepsilon + E_1^0\varepsilon^2 + E_2^0\varepsilon^3 + ... \tag{1.6}$$

where b, E_1^0, E_2^0, ... are constants.

For the functions (1.5), (1.6) the following condition $E = \lim_{\varepsilon \to 0}\left(\frac{d\sigma}{d\varepsilon}\right)$ is valid.

In application to the problem of pressure cylinders one need to calculate the value of contact stresses and the pressure strip. Using these values and the experimental pressure curve we can choose the rheological elastic viscous relation and the calculation model of loading.

The Hertz's solution [2] for the pressure of two steel cylinders, one of which is covered by thin layer made of polyurethane will be applied for the calculation of the contact stresses and the pressure strip.

Let's P is the force intensity on the unit length and $E_1, E_2, \upsilon_1, \upsilon_2, R_1, R_2$ are, correspondingly, the elastic modulus, the Poisson ratios and the radii of cylinders. The maximum value of pressure stress in the middle of contact layer σ_{max} and the value of pressure strip a are defined [2] as

$$\sigma_{max} = \sqrt{\frac{P(R_1 + R_2)}{\pi R_1 R_2 \left(\frac{1-\upsilon_1^2}{E_1} + \frac{1-\upsilon_2^2}{E_2} \right)}}, \qquad (1.7)$$

$$a = \sqrt{\frac{4 P R_1 R_2}{\pi(R_1 + R_2)} \left(\frac{1-\upsilon_1^2}{E_1} + \frac{1-\upsilon_2^2}{E_2} \right)}. \qquad (1.8)$$

If $R_1 = R_2 = R$, $E_2 \to \infty$, from (1.7), (1.8) follow

$$\sigma_{max} = \sqrt{\frac{2 P E_1}{\pi R (1 - \upsilon_1^2)}}, \qquad (1.9)$$

$$a = \sqrt{\frac{4 P R}{2 \pi} \left(\frac{1-\upsilon_1^2}{E_1} \right)}. \qquad (1.10)$$

Using in (1.9), (1.10) the real values of the parameters of the considered problem: $P = 130$ kg/sm, $R = 39$ sm, $E_1 = 0,4$ MPa, $\nu_1 = 0,5$, we will receive $\sigma_{max} = 0,336$ MPa, $a = 24,6$ sm.
In accordance with the $\sigma - \varepsilon$ diagram of Fig. 1 for the value of stress $0,336$ MPa the deformation is about 30%. On this level of stress the deformation is reversible and the material of the tin layer can be considered as linear viscous. So it can be also supposed that the layer under the pressure is in plane strain condition.
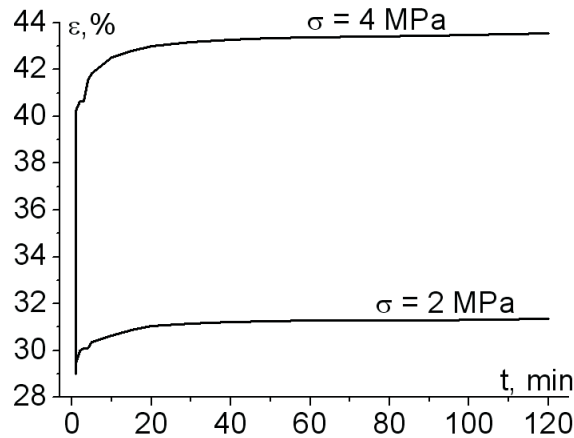
Figure 3: Creep curves for the stresses $\sigma_x = 2$ MPa and $\sigma_x = 4$ MPa.

To carry out the numerical calculation it is necessary to know the value of viscosity coefficient. It was defined in the creep experiments at the two pressure stress levels $\sigma = 2$ MPa and $\sigma = 4$ MPa. The received creep curves are shown in Fig. 3. As it follows from the Fig. 3, at the initial parts of creep curves up to 30% of deformation

the material behavior is linear viscous. So the viscosity coefficient will be calculated from the following relations

$$\dot{\varepsilon} = \frac{1}{2\eta}(\sigma_x - \sigma), \ \sigma_y = 0, \sigma_z = 0, \sigma = \frac{1}{3}\sigma_x,$$

$$\dot{\varepsilon} = \frac{1}{3\eta}\sigma_x, \eta = \frac{\sigma_x}{3\dot{\varepsilon}_x}.$$

According to the creep curve for the stress $\sigma_x = 2\,\mathrm{MPa}$ the creep rate $\dot{\varepsilon}_x$ was defined on the creep deformation base $(0, 0 - 0, 2943)$ in the time interval $(0, 0 - 1, 0)$ min. as $\dot{\varepsilon}_x = \frac{\varepsilon_2 - \varepsilon_1}{t_2 - t_1}$, $\dot{\varepsilon}_x = 0,2943\frac{1}{\mathrm{min.}}$. The corresponding value of viscosity coefficient is $\eta = 2,265\,\mathrm{MPa}\cdot\mathrm{min}$.

2 Compression of thin layer made of high elastic materials subjected to two long parallel plates

We will consider the problem of cyclic compression of thin layer made of high elastic materials subjected by two long parallel plates. It is assumed that the incompressibility condition for elastic and viscous materials is conformed. So the mathematical solutions, which satisfy the same boundary conditions, also must be identical, when the viscous coefficient is equal to the elastic shearing modulus. If the width $2a$ of the layer is much less then its length $2b$, as shown in Fig. 4, the problem can be considered as plane strain problem [2, 3].
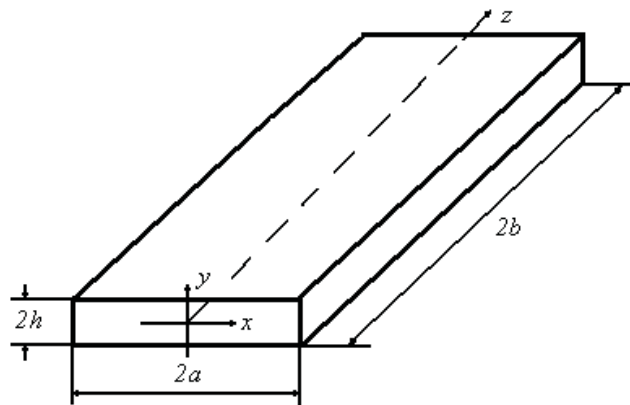
Figure 4: Plane strain state.

As a material for the layer we will consider the high elastic materials, for example, polyurethane in high elastic state. As it follows from the results of creep and compression experiments in the required force and time intervals the material behavior can be considered as linear viscous. The rate components u, v satisfy the inequalities $u \neq 0$, $v \neq 0$, and the rate component in z direction is equal to zero $w = 0$.

The following deformation rates and components of stresses also are equal to zero $\dot{\varepsilon}_z = 0$, $\dot{\gamma}_{yz} = 0$, $\dot{\gamma}_{zx} = 0$, $\dot{\gamma}_{yz} = 0$, $\tau_{xz} = 0$, $\tau_{yz} = 0$.

In the case of plane strain the linear viscous equations [4] is written in the form

$$\sigma_x - \sigma = 2\eta\dot{\varepsilon}_x, \ \tau_{x\,y} = \eta\dot{\gamma}_{x\,y}, \sigma_y - \sigma = 2\eta\dot{\varepsilon}_y, \tag{2.1}$$

$$\sigma = 1/2(\sigma_x + \sigma_y) = \sigma_z. \tag{2.2}$$

In equations (2.1), (2.2) the following notations are introduced: σ_x, σ_y, σ_z, τ_{xy} are the components of stresses, $\sigma = 1/3(\sigma_x + \sigma_y + \sigma_z)$ is the mean stress, $\dot{\varepsilon}_x$, $\dot{\varepsilon}_y$, $\dot{\gamma}_{xy}$ are the components of rate deformations, η is the viscosity coefficient.

For the incompressible materials the equations (2.1) are similar in form to the relations for linear elastic incompressible material. If $E = 3\eta$ (E is Young modulus), we have identical equations for elastic and viscous media.

The following Cauchy relations are satisfied for the components of the rate displacements u, v

$$\dot{\varepsilon}_x = \frac{\partial u}{\partial x}, \dot{\varepsilon}_y = \frac{\partial v}{\partial y}, \dot{\gamma}_{x\,y} = \frac{\partial u}{\partial y} + \frac{\partial v}{\partial x}. \tag{2.3}$$

The system of equilibrium equations can be written through the rate components u, v, w in the form of the Navier differential equations

$$\eta\Delta u + \frac{\partial \sigma}{\partial x} = 0, \eta\Delta v + \frac{\partial \sigma}{\partial y} = 0,$$

$$\Delta u = \frac{\partial^2 u}{\partial x^2} + \frac{\partial^2 u}{\partial y^2}, \Delta v = \frac{\partial^2 v}{\partial x^2} + \frac{\partial^2 v}{\partial y^2}, \tag{2.4}$$

$$\frac{\partial^2 \sigma}{\partial x^2} + \frac{\partial^2 \sigma}{\partial y^2} = 0, \tag{2.5}$$

where $\Delta = \frac{\partial^2}{\partial x^2} + \frac{\partial^2}{\partial y^2}$ is the Laplace operator.

The incompressibility equation will be written as

$$\dot{\varepsilon}_x + \dot{\varepsilon}_y = \frac{\partial u}{\partial x} + \frac{\partial v}{\partial y} = 0. \tag{2.6}$$

It is known that the system of equations (2.4)-(2.6) are solved by introducing the current function φ, satisfying the following relations

$$u = \frac{\partial \varphi}{\partial y}, v = -\frac{\partial \varphi}{\partial x}. \tag{2.7}$$

For the function φ we will have the linear differential equation of the fourth order, so called bi-harmonic equation

$$\frac{\partial^4 \varphi}{\partial x^4} + 2\frac{\partial^4 \varphi}{\partial x^2 \partial y^2} + \frac{\partial^4 \varphi}{\partial y^4} = 0, \Delta\Delta\varphi = 0. \tag{2.8}$$

Considering the concrete problems, the solutions of equation (2.8) can be found for the boundary conditions for the functions u, v.

Let's consider the case when the viscous layer is compressed without slip by two plane plates moving with the velocity v_0. For these limitations the components u, v on the planes $y = \pm h$ are equal

$$u = 0, v = -v_0 = \mathsf{Const} \text{ at } y = h,$$

$$u = 0, v = v_0 = \mathsf{Const} \text{ at } y = -h. \tag{2.9}$$

According (2.7) for the current function φ we have the following boundary conditions

$$\varphi = v_0 x, \frac{\partial \varphi}{\partial y} = 0 \text{ at } y = h,$$

$$\varphi = -v_0 x, \frac{\partial \varphi}{\partial y} = 0 \text{ at } y = -h. \tag{2.10}$$

For the long rectangular plate the solution of equation (2.8) is expressed in the form of polynomial [3], particularly in the form of polynomial of fourth degree $\varphi = ax^4 + bx^3 y + cxy + dxy^3 + ey^4$. Taking into account the boundary conditions, the coefficients of polynomial will be found as $a = 0$, $b = 0$, $e = 0$, $c = 3v_0/2h$, $d = -v_0/2h^3$. So the equation (2.8) is satisfied by the current function of the form

$$\varphi = \frac{v_0 x}{2h^3} \left(3h^2 y - y^3 \right). \tag{2.11}$$

According to the relations (2.7) for the rates u, v the following expressions can be found

$$u = \frac{3v_0 x}{2h^3} \left(h^2 - y^2 \right), v = -\frac{v_0}{2h^3} \left(3h^2 y - y^3 \right). \tag{2.12}$$

Current lines, defined according to the condition $\varphi = \mathsf{Const}$, are shown in Fig. 5.
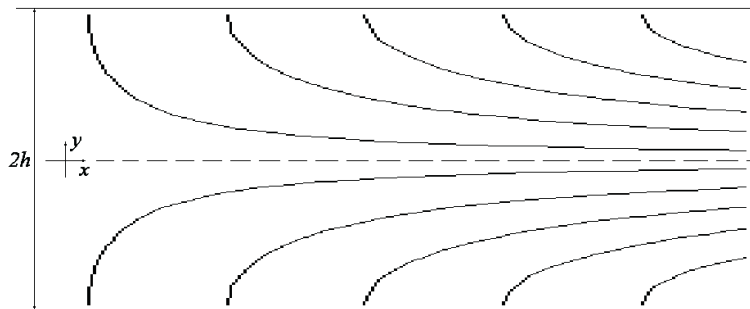
Figure 5: The current lines $\varphi = \mathsf{Const}$.

At the first moment the current lines are perpendicular to the guiding plates then they turn down very quickly into the direction of main motion, parallel to the plates. If the compressed polymer layer posses the sufficiently high value of initial elastic and viscous characteristics or if the surface residual stresses are favourable in sign with the acting stresses, then in the initial moment it is possible that the over stresses

will be develop, which are the cause of breaks and microcrack, providing the viscous flow into the direction of x axis.

Let's consider the distribution off the stress components. The mean stress σ or the pressure $P = -\sigma$ is calculated according to the formulae (2.4)

$$\eta \Delta u = -\frac{\partial \sigma}{\partial x} = \frac{\partial P}{\partial x} = -\frac{3\eta v_0 x}{h^3},$$

$$\eta \Delta v = -\frac{\partial \sigma}{\partial y} = \frac{\partial P}{\partial y} = \frac{3\eta v_0 y}{h^3}. \tag{2.13}$$

From the system (2.13) follows

$$P = P_0 + \frac{3\eta v_0}{2h^3}\left(y^2 - x^2\right), \tag{2.14}$$

where P_0 is the value of pressure at the point $x = 0$, $y = 0$. This value can be approximated using the condition $P \approx 0$ at $x = \pm a$, $y = 0$. So from the relations (2.14) follows

$$P_0 = \frac{3\eta v_0 a^2}{2h^3}. \tag{2.15}$$

Introducing (2.15) into (2.14), we will receive

$$P = \frac{P_0}{a^2}(a^2 + y^2 - x^2). \tag{2.16}$$

The maximum value of pressure $P = P_0$ will be observed along the line $x = 0$, $y = 0$. At a point $x = a$, $y = 0$ the pressure drops to the zero value.

According to Cauchy formulae the deformation rates are given by the relations

$$\dot{\varepsilon}_x = \frac{\partial u}{\partial x} = \frac{3v_0}{2h^3}\left(h^2 - y^2\right),$$

$$\dot{\varepsilon}_y = \frac{\partial v}{\partial y} = -\frac{3v_0}{2h^3}\left(h^2 - y^2\right),$$

$$\dot{\gamma}_{xy} = \frac{\partial u}{\partial y} + \frac{\partial v}{\partial x} = -\frac{3v_0 xy}{h^3}. \tag{2.17}$$

Taking into account (2.1) the stress components will be calculated as

$$\sigma_x = -P + 2\eta\dot{\varepsilon}_x = \frac{P_0}{a^2}\left(x^2 - 3y^2 - a^2 + 2h^2\right),$$

$$\sigma_y = -P + 2\eta\dot{\varepsilon}_y = \frac{P_0}{a^2}\left(x^2 + y^2 - a^2 - 2h^2\right),$$

$$\tau_{xy} = -\eta\dot{\gamma}_{xy} = -\frac{3\eta v_0 xy}{h^3}. \tag{2.18}$$

In accordance with the relations (2.18), in arbitrary cross section plane $x = \text{Const}$ the normal stresses are distributed by parabolic law. Along the length and in the cross section plane the shear stresses are distributed by linear law.

3 The diagrams of the rates displacements and the stresses.

The diagrams of the rates displacements u, v were built using the formulae (2.12) where the following values of coefficients: $v_0 = 1$ mm/min., $2h = 25$ mm, $2a = 10, 8$ mm are introduced. The diagrams for the rates u are shown in Fig. 6. In the direction of the x axis the rates u are distributed as parabola with the maximum at the points: $y = 0$. The value of particles rate are increased when moving off from the zero coordinate point. If $2a = 10$ mm, $u_{max} = 0, 12$ mm/min., and for $2a = 30$ mm, $u_{max} = 1, 8$ mm/min. So with the increasing the with of the layer the value u will increase.
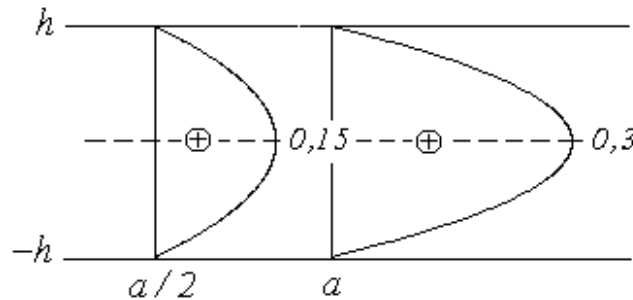
Figure 6: The diagrams of the rate component u.

The diagrams of the rate v in direction of axis y are not dependent of coordinate x and are distributed similarly on any cross section $x = \text{Const}$ (Fig. 7). On the planes $y = \pm h$ the rates v reach the maximum value $v_{max} = 1$ mm/min.
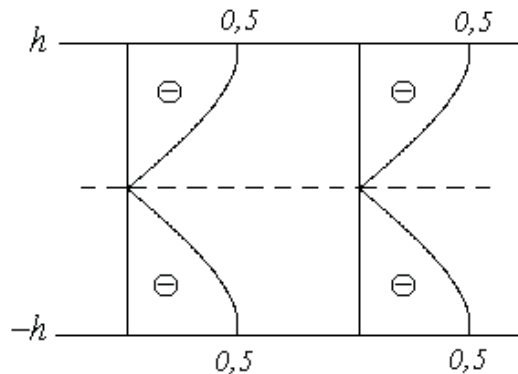
Figure 7: The diagrams of the rate component v.

The diagrams of the stresses were built using the formulae (2.18) where the following values of coefficients $v_0 = 1$ mm/min., $2h = 25$ mm, $2a = 10, 8$ mm, $\eta = 2, 265$ MPa$\cdot$min. are introduced. As follows from the formulae (2.18) the functions for σ_x and σ_y have maximums at the point $(0, 0)$.

The diagrams of the stresses σ_x they are shown in Fig. 8 for the two cross sections $x = 0$ and $x = a$. The maximum stresses are positive and at $x = a$ they are $\sigma_x = 0,54$ MPa. With approaching to the planes $y = \pm h$ the stress σ_x changes the sign into the negative and at $y = \pm h$ $\sigma_x = -0,27$ MPa. As it follows, the negative values of σ_x are observed in the thin stratum about 3 mm in thickness near the contact planes.
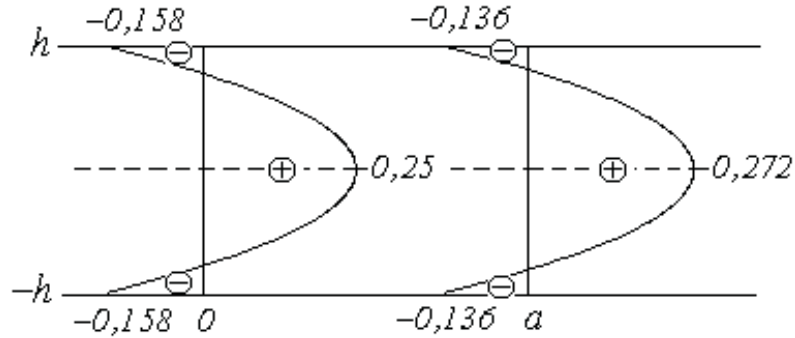
Figure 8: The diagrams of stresses σ_x.

The values of the stress σ_y are negative with the maximum at the point $(0,0)$ equal $\sigma_y = -0,93$ MPa. With the moving off from the plates $x = 0$ the stresses σ_y will be decreased and for the big values of a they will tend to zero. The diagrams of the stresses σ_y for the two cross sections $x = 0$ and $x = a$ are shown in Fig. 9.
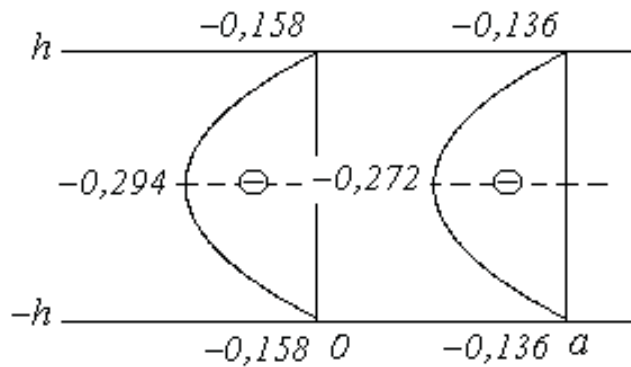
Figure 9: The diagrams of stresses σ_y.

In accordance with the introduced suppositions $\sigma_z = 1/2(\sigma_x + \sigma_y)$, so comparing the values of three normal stresses, one can come to the following conclusion. On the surface of pressed plane and in the inside points of the thin stratum about 3 mm in thickness near the contact planes the stress condition approaches to the state of hydrostatic pressure. So in these regions the brittle fracture will be appeared.

The diagrams of the stresses τ_{xy} are shown in Fig. 10. As it follows, on the central cross section $x = 0$ $\tau_{xy} = 0$. On an arbitrary cross section $x \neq 0$, $x = \mathsf{Const}$ the shear stresses are distributed according to the linear law. Also the linear distribu-

tions of the shear stresses are observed on the planes $y = \mathtt{Const}$. At the points $x = a$, $y = \pm h$ they reach the maximum values $\tau_{xy} = 0,214$ MPa.
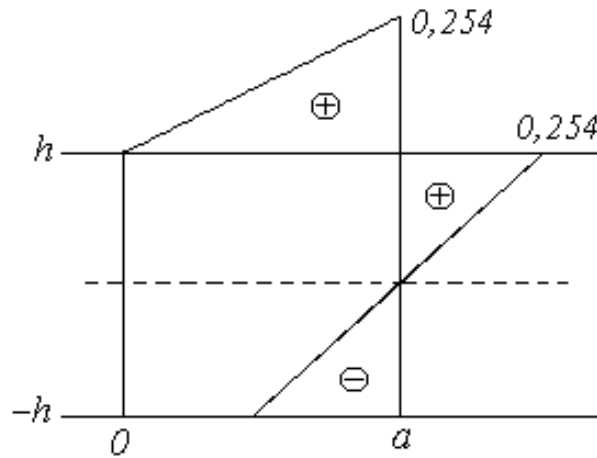
Figure 10: The diagrams of stresses τ_{xy}.

The receive results we will use to estimate the cyclic strength of layer made of high elastic materials, for example, polyurethane in high elastic state. This polymer is used as a cover of pressure cylinders employed, for example, in paper industry. The very thin paper layer is rolled between the two pressed to each other rotating steel cylinders with the frequency about two revolution per minute. One of cylinders is covered by thin polyurethane layer. In engineering practice three are many observations of cyclic failure of polyurethane layer so the estimation of the cyclic strength of this layer will be very useful for the practical applications.

References

[1] Gul E.V., Kulesnyov V.N. Structure and mechanical properties of polymers. M.: High School Press. 1972. 320p. (in Russian).

[2] Katz A.M. Theory of elasticity. M.: Technical - Theoretical Literature Press. M.: 1956. 207p. (in Russian).

[3] Timoshenko S.P., Goodier J.N. Theory of elasticity. M.: Nauka. 1975. 576p. (in Russian).

[4] Nadai A. Plasticity and fracture of solids. M.: Foreign literature press. 1954. 648p. (in Russian).

Robert A. Arutyunyan, St.-Petersburg State University, Faculty of Mathematics and Mechanics, Sankt-Petersburg, Petrodvoretz, Universytetskii prospect, 28, 198504, Russia

Evolution of scale levels of the materials structure rearrangements during cyclic loadings

A. R. Arutyunyan   B. A. Zimin   Yu. V. Sud'enkov

Robert.Arutyunyan@paloma.spbu.ru

Abstract

The results of investigations of materials elastic properties changes on cyclic bending are presented using the method of optical-acoustic spectroscopy. It is shown that the optical-acoustic spectroscopy method allows receiving information about the elastic modules changes defined by structure rearrangements and information about the scale levels of such rearrangements. It is known that essential changes on character of frequency dependent attenuation of acoustic waves are defined by dispersion process on internal materials structures. So analysis of the frequency dependent attenuation of acoustic waves based on well known dispersion models, in particular the Rayleigh's model, allows restoring the function of structure elements distribution on scales. The frequency dependent attenuation analysis during cyclic tests in metals, polymers and composites allows estimating the character of evolution of the scale levels of materials structure rearrangements on different stages of experiment. For materials, which have pronounced structure, such as steel and glass-fiber plastic, basic structure rearrangements are observed on scales comparable with scales of character structure elements in these materials. In metals it is the grain size and in composites materials it is the size of braid. In PMMA there is no pronounced structure, so the changes are occurred in all scales of the structure elements. The correlation of materials elastic properties changes and the function of structure elements distribution changes during cyclic experiments is notice. On a damage accumulation stage when the number of loading cycles is increased the number of structure elements in greater scales is growing.

Financial support of the Russian Foundation for Basic Research (Grant N 06-01-00202) is gratefully acknowledged.

During last 30 years the investigations of optical-acoustic (OA) effect [1-5], which based on thermo elastic reaction of continuous medium were intensively carried out. These investigations show the possibilities of using of the effect to solve some research and technical problems, in particular the non breakable control of materials.

Application of laser methods of excitation of acoustic pulses has some advantages compared with the traditional methods of acoustic defectoscopy and spectroscopy. Permission of optical-acoustic defectoscopy is defined by a minimum duration of excitation acoustic pulses, which is easy realized in the range $\sim (1-3) \cdot 10^{-8}$s.

This allows us to receive information about internal material structure in a wide frequency range up to ~ 100MHz. The possibility of easily rise of amplitude of acoustic pulses makes this method very perspective for investigation of properties and defectoscopy of high absorb materials.

In papers [6, 7] the optical-acoustic (OA) cell was proposed, which is a main element of optical-acoustic defectoscop (OAD). OA cell allows overcoming a number of technical limitations of optical-acoustic effect in defectoscopy of materials and structural elements and combines the functions of optical and acoustic waveguides and also the function of effective thermo acoustic transformer light-sound. It allows to carry the measurements, when only one side access to the object is available or in the case of simultaneous control of passed and reflected pulses.

In papers [8, 9] the investigations of acoustic properties of specimens ($\sim 3 \times 30 \times 150$mm) made by tool steel, PMMA and glass-fiber plastic on cyclic bending with frequencies 15Hz and 27Hz was carried out. The time of load influence was equal to $\sim (10-15)\mu$s.

Acoustic properties evolution of specimens controls by OAD on a distance ~ 10mm from the doing up. Block scheme of OAD is shown on fig. 1. Laser with modulated durability on neodymium glass with duration of radiation pulses $15 \cdot 10^{-9}$s and energy in one pulse ~ 1mJoule is used.

Values of stresses for investigated specimens were in elastic region of materials reaction. The number of cycles to fracture for the tool steel specimens is equal to $\sim (8-9) \cdot 10^5$ and for PMMA is equal to $\sim (8-9) \cdot 10^6$. For glass-fiber plastic specimens the experiments were stopped at $\sim (12-13) \cdot 10^6$ cycles when the initiation of layering is occurred.

Every $\sim 5 \cdot 10^4$ loading cycles the dependences of sound velocity and attenuation of acoustic pulses in specimens was measured and the changes of there spectral characteristics were analyzed.

Receiving and analyzing possibilities of dependences of attenuation of acoustic pulses in a wide frequency range gives additional information about structure rearrangements of materials during cyclic loadings. This allows estimating the character of evolution of scale levels of structure rearrangements during loadings.

With a sufficient basis [10] we can suppose that observed essential evolution of character of frequency dependent attenuation of acoustic pulses for different number of loading cycles are defined significantly by dispersion process on internal material structure. Using the Rayleigh's model as a dispersion model the frequency dependent attenuation can be connect with the scales of structure elements using the following relation [11]

$$\alpha(\lambda) = \frac{n(D)D^3}{\lambda^4}, \tag{1}$$

where $n(D)$ is structure elements distribution, D is their size, λ is wave length.

Analysis of spectrum of acoustic pulses on different loading stages was carried out. Frequency dependent attenuation was defined using the following relation

$$\alpha(f) = \ln\left(\frac{P(f)}{P_z(f)}\right), \tag{2}$$
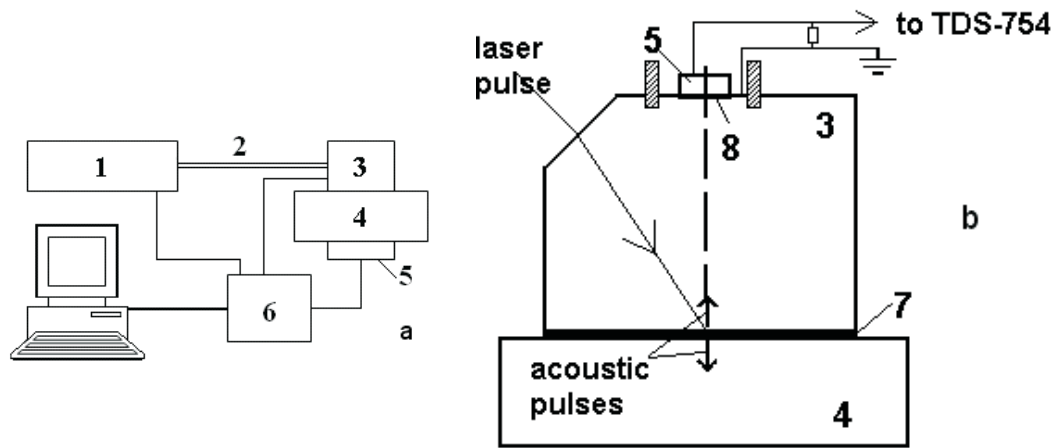
Figure 1: Block-scheme of optical-acoustic defectoscop (OAD) (a) and optical-acoustic (OA) cell (b): 1 - laser, 2 - optical fiber, 3 - optical-acoustic cell, 4 - specimen, 5 - piezo sensing element, 6 - oscillograph, 7 - absorption layer, 8 - reflection layer.
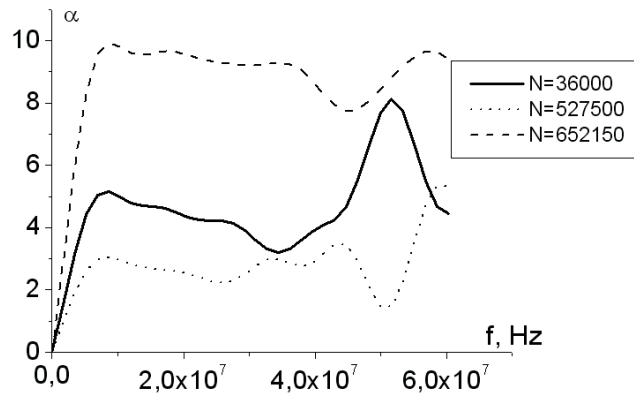
Figure 2: Frequency dependent attenuation for different number of loading cycles for tool steel specimens.

where $P(f)$ and $P_z(f)$ are the power spectrum of passed and probe acoustic pulses. The received dependencies of $\alpha(f)$ for tool steel specimens are given on fig. 2.

Taking the size of structure elements for tool steel specimens in a range from 0 to $100\mu m$, which is closed to a real values for steel [11] and using well known relation $\lambda = c/f$ (where c is sound velocity) the distribution function $n(D)$ can be restored. The received distributions of structure elements for different loading cycles for tool steel specimens are shown on fig. 3.

These curves are well approximated by the function $n(D) \sim n_0 e^{-D/D_0}$ which is usually used to describe the defect distribution in different materials [12].

More informative and obvious is the relative changes of function $n(D)$ during cyclic experiments: $n_{otn}(D) = (n(D) - n_0(D))/n_0(D) \cdot n_{max}(D)$, where $n_0(D)$ is defects distribution in specimen without loadings, $n_{max}(D)$ is maximum value of defects distribution.

The relative changes of function of structure elements distribution for tool steel
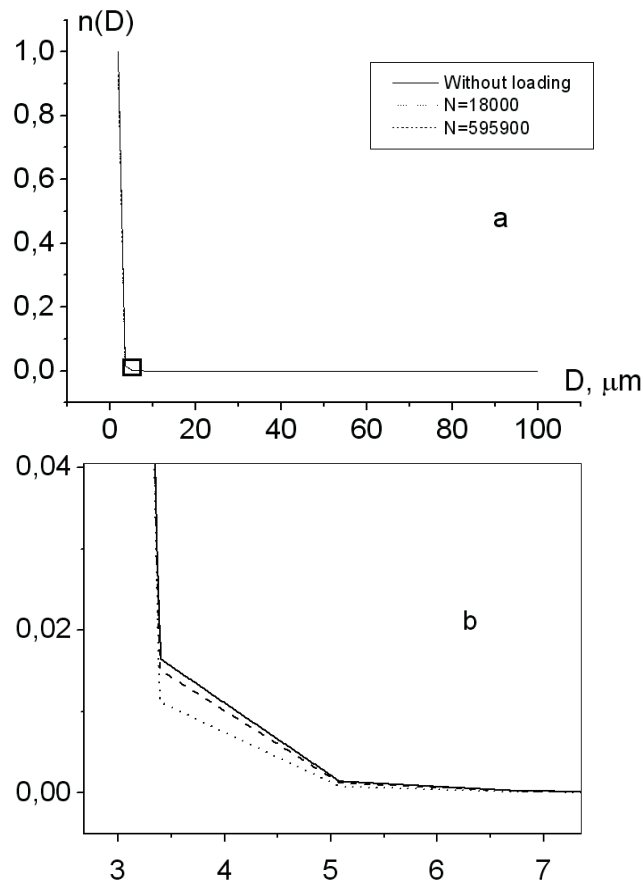
Figure 3: Distribution of structure elements from their size (a) and magnificated fragment of picked out region (b) for different loading cycles for tool steel specimens.
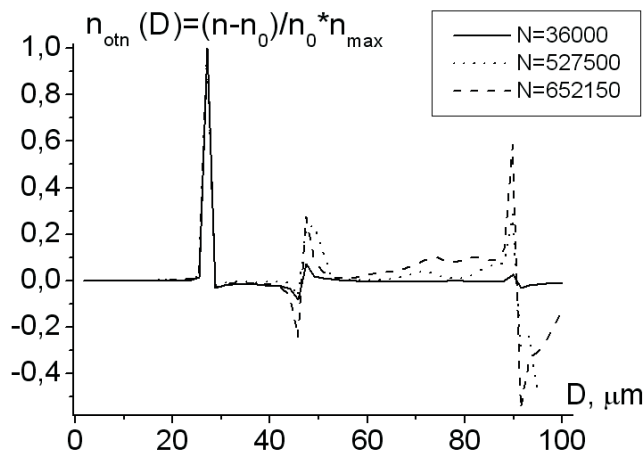
Figure 4: Relative changes of structure elements distribution from their size for tool steel specimens for different number of loading cycles.

specimens for different number of loading cycles are given on fig. 4.

It is seen that the fundamental processes of rearrangements for tool steel specimens
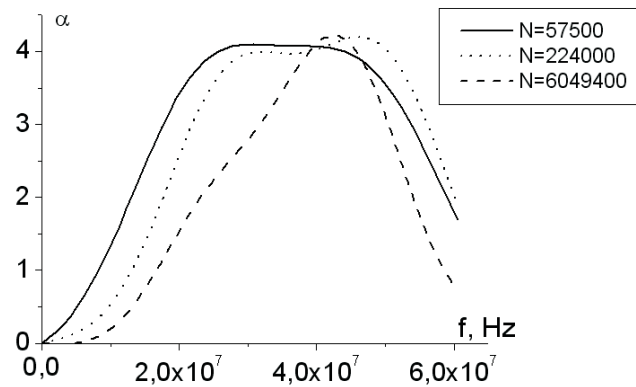
Figure 5: Frequency dependent attenuation for different number of loading cycles for PMMA specimens.
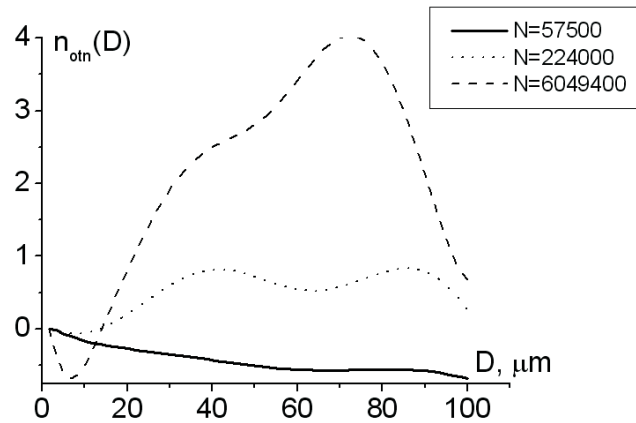
Figure 6: Relative changes of structure elements distribution from their size for PMMA specimens for different number of loading cycles.

are observed on sizes which are compared with grain size $\sim 27\mu m$. When the number of cycles is increased, substantial changes become apparent in bigger scales of structure elements.

The frequency dependent attenuation for different number of loading cycles for PMMA specimens are shown on fig. 5.

The relative changes of structure elements distribution from their size for PMMA specimens for different number of loading cycles are given on fig. 6.

In PMMA there is no pronounced structure, so the changes are occurred in all scales of the structure elements.

For glass-fiber plastic specimens like a tool steel specimens essential changes of distribution function are observed on scales of character structure elements - size of glass fiber braid ($\sim 180\mu m$) [13].

The conducted investigations shown that the behavior of all investigate materials during cyclic experiments are characterized by non monotonic evolution of function of structure elements distribution, which correlate with non monotonic evolution
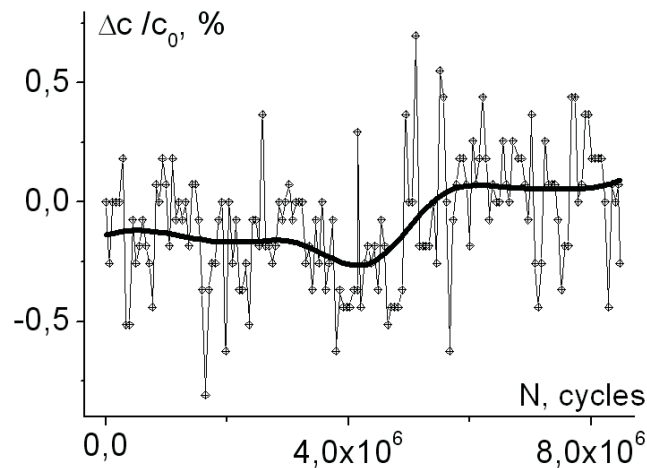
Figure 7: Dependence of sound velocity from number of loading cycles for PMMA specimens.

of such acoustic properties of materials as a sound velocity and attenuation. The dependence of sound velocity from number of loading cycles for PMMA specimens is shown on fig. 7 [8, 9].

Also the common for all investigate materials are essential evolution of distribution function in bigger scales when the number of cycles is increased.

So, in spate of the range of sizes evolution of structure elements D was selected arbitrary, the used approach allowed to reveal the evolution of scales of materials structure rearrangements during cyclic experiments.

Conclusions

1. Optical-acoustic method using the attenuation dependencies in a wide frequency range allows receiving the evolution of character scale levels of structure rearrangements.

2. The non monotonic character of evolution of function of structure elements distribution during cyclic experiments is observed, which correlate with the elastic properties evolution of materials.

3. The basic evolution of structure for materials with pronounced structure elements size (steel, glass-fiber plastic) is observed on sizes compared with the character size of these materials.

4. On initial stages of loadings main evolution of structure occurred in small scales of structure elements. When the number of cycles is increased the growth of big scale structure elements is observed. This fact takes place for three types of investigated materials: metals, polymers and composites.

References

[1] Gusev V.E., Karabutov A.A. Laser optoacoustics. Moscow. Nauka. 1991. 304p. (in Russian).

[2] Zarov V.P., Letohov V.S. Laser optic-acoustic spectroscopy. Moscow. Nauka. 1984. 128p. (in Russian).

[3] Liamshev L.M. Lasers in acoustic. Uspehi fizicheskih nauk. 1987. V. 151. N 3. P. 479-527. (in Russian).

[4] Scruby C. B. Some applications of laser ultrasound. Ultrasonics. 1989. 27. N 4. P. 195-208.

[5] Bondarenko A. H. Laser methods of excitation and recording of acoustic signals. Moscow. Izd-vo standartov. 1989. 115p. (in Russian).

[6] Sud'enkov Yu. V., Ivanov Ed. V., Nikitin D. Yu. Optic-acoustic cell to defectoscopy of materials and biological objects. Proceedings of X Session of Russian Acoustic Association. Moscow. 2000. V. 2. pp. 345-348. (in Russian).

[7] Yu. V. Sud'enkov, Z. A. Valisheva, B. A. Zimin. Time-resolved optical-acoustic defectoscope. 34th International Conference and NDT Exposition, Defectoscopy 2004, November 3-5, 2004. Špindlerův Mlýn - Czech Republic. 2004. P. 277-284.

[8] Arutyunyan A.R., Zimin B.A., Sud'enkov Yu.V. Application of optic-acoustic spectroscopy method to investigate the fatigue of construction materials. Proceedings of International Conference "Topical Problems of Continuum Mechanics" September 25-28, 2007, Tsahkadzor, Armenia. Yerevan. Institute of Mechanics NAS of Armenia. 2007. P. 63-68. (in Russian).

[9] Arutyunyan A.R., Zimin B.A., Sud'enkov Yu.V. Investigation of cyclic durability of constructive materials using method of optic-acoustic spectroscopy. Vestnic of St.-Petersburg University. 2008. Ser. 1. N. 3. P. 88-96. (in Russian).

[10] Ultrasound. Small encyclopedia. Edited by I.L. Goliamin. Moscow. Sovetskaya encyclopedia. 1979. 400p. (in Russian).

[11] Botvina L.R. Kinetics of construction materials fracture Moscow. Nauka. 1989. 230p. (in Russian).

[12] Shock waves and phenomenon of high velocity metals deformation. Edited by M.A. Meiers and L.E. Mur. Moscow. Metallurgia. 1984. 512p. (in Russian).

[13] Plastic reference book. In two volumes. Edited by V.M. Kataev and others. Moscow. Himija. 1975. V. 1. 448p. V. 2. 568p. (in Russian).

Alexander R. Arutyunyan, Boris A. Zimin, Yury V. Sud'enkov, St.-Petersburg State University, Faculty of Mathematics and Mechanics, Sankt-Petersburg, Petrodvoretz, Universytetskii prospect, 28, 198504, Russia

The possibility of diagnosing imperfection of nanosized ceramic coatings on the base of tribospectral analysis

Sergey V. Astafurov   Evgenii V. Shilko   Valentin L. Popov

Sergey G. Psakhie

astaf@ispms.tsc.ru

Abstract

In the paper the possibility of application of tribospectral analysis for diagnosis of nanosized heterogeneities and discontinuities on the interface between nanosized coating and substrate is theoretically investigated. The main idea of the suggested approach consists of measurement of sliding resistance force of counterbody along the specimen surface and following Fourier analysis of its frequency spectrum. This new approach was called nanotribospectroscopy. Theoretical investigation of possibility of application of nanotribospectroscopy was based on computer-aided simulation. Movable cellular automaton method was used. Results of investigation showed the possibility of estimation of some parameters of nanosized discontinuities in coatings and interfaces coating/substrate. For example, nanotribospectroscopy allows to estimate linear dimension and period of distribution of such defects. In the paper realization of experimental setup (nanotribospectrometer) is also described. Resolution of suggested device is equal to 8 nm. Theoretical and experimental result shows that nanotribospectroscopy could be a perspective method of nondestructive testing of imperfection of nanosized coatings and surface layers.

1 Introduction

A great number of new electron-ion plasma technologies of surface hardening are widely developed during last years. This techiques allow to form nanostructured ceramic coatings which have relatively high hardness (up to 70 GPa) [1, 2, 3]. Generally these coatings are intended for strength details of mechanisms and machines. So they have to possess high operational characteristics. First of all this refer to nanoporosity and defects which are formed during formation coating and exploitation processes. Nanoscale injuries on the coating/substrate interface are also hazardous. Thus, development of new techniques for diagnosis quality of coatings is very actual problem. It is necessary to mention that these techniques must have high resolution (up to nanoscale level) and provide high production. One of perspective direction of investigation is analysis of dependence of friction force on structure features of coating.

For example spectral analysis of results of high-precision measurement of friction force of one of tribopartner allows to define features of microscopic interactions in tribological contact [4].

This paper is devoted to investigation of possibility of application of tribospectral analysis for diagnosis of quality of nanosized ceramic coatings. It is clear that for defining of correlation of macroscopic friction force and such nanoscale parameters as imperfection and defect structure of nanostructured coatings it is necessary to use suitable multiscale methods of computer-aided simulation. It is necessary to use multiscale approaches of investigation because typical scale of system (size of damages, thickness of coating, and length of relative displacement of tribopartners) could differ substantially. So, for computer-aided simulation of process of tribospectral diagnosis of defect structure of coatings movable cellular automaton method was used [5, 6, 7].

2 Procedure and parameters of computer-aided simulation

In the paper movement of counterbody along steel specimen with ceramic coating was simulated (fig. 1a). Thickness of coating was equal to 100 nm, diameter of structural discrete element (movable cellular automaton) d was equal to 3 nm, and length of specimen was equal to 1 mkm. Mechanical properties of substrate and coating corresponded to rail steel and nonporous ceramic ZrO_2 respectively. Cohesion of coating and substrate was ideal or in other words strength of cohesion in the interface between steel and ceramic was equal to strength of steel. In the framework of movable cellular automaton method mechanical properties of simulated materials are defining by so-called response function of automata [5, 6, 7]. For simplicity of interpretation on figure 1 b response function are represented as loading diagrams ($\sigma - \varepsilon$ curves).
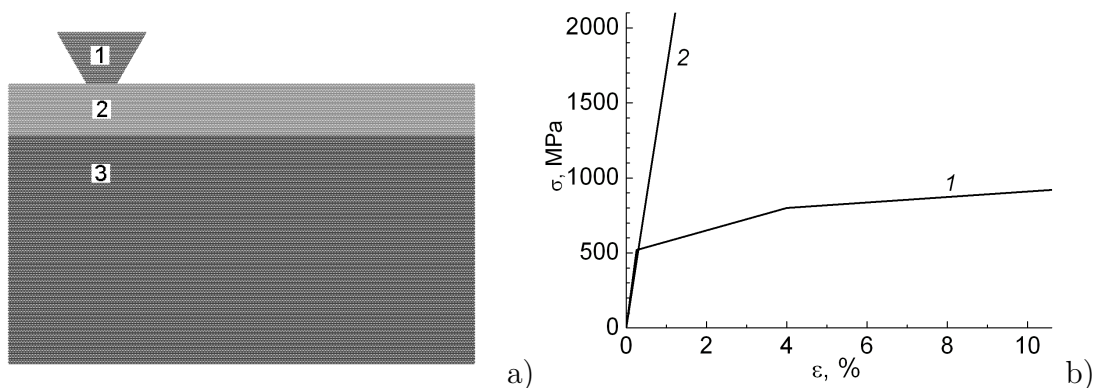
Figure 1: fig. 1. a) Structure of simulated system (1 - counterbody, 2 - ceramic coating, 3 - steel substrate); b) response functions of movable cellular automata of ceramic coating (1) and steel substrate (2).

Counterbody had trapezoidal shape. Length of its smallest base was equal to 60 nm. Its movement was simulated by setting to upper automata of counter body

of horizontal constant velocity which was equal to $V_{sl} = 1,5$ mps. Bottom surface of specimen was immovable, and its lateral surfaces were free. During simulation of counterbody movement calculation of resistance force to its sliding along the specimen was carried out. Horizontal component of this force which act on counterbody from the specimen corresponds to sliding friction force F_{fr}. Discrete Fourier transform was used for spectral analysis of obtained time dependences $F_{fr}(t)$ [8].

In connection with limitations which are constrained by discrete Fourier transform following main requirements were took into account in computer model:

1. Time period of record of value F_{fr} should be relatively small to ensure that Fourier estimation of its spectral density will contain all frequencies expecting in the investigated system.

2. Length of counterbody displacement should be no less the two relevant distances between defects in nanosized coating (in this paper it was up to 10 relevant distances).

It is necessary to mention that these requirements are valid for real experiments.

Defect structure/imperfection of coating was simulated by means of generation of nanosized continuity violations. Stretched defects such as nanocracks at the coating/substrate interface were analyzed (fig. 2). Quasiperiodic distribution of nanosized cracks was investigated. Relevant distance between cracks (P_{icr}) was equal to 90 nm, length of cracks varied from 12 to 36 nm. Width of cracks was equal to 2,5 nm.

Figure 2: Fragment of simulated system with defect structure at the interface coating/substrate (length of cracks is equal to 24 nm)

The possibility of determining of main features of defect structure of nanosized coatings was analyzed. Among this features could be mentioned average size of nanocracks an average distance between them.

3 Results of computer-aided simulation and experimental realization of nanotribospectroscopy

Specimen with ideal (undamaged) coating/substrate interface was used as base sample. Fourier-estimation $F_{fr}(\nu)$ of spectral density time dependence of sliding friction force shown on figure 3. Main peak on the $F_{fr}(\nu)$ curve corresponds to periodical component of artificial roughness of specimen surface (this artificial roughness associated with discreteness movable cellular automata). Frequency of this periodical component is equal to $\nu_d = V_{sl}/d = 5 * 10^8$ Hz. Peaks with frequencies n d (here n is integer number) are also attend on the curve $F_{fr}(\nu)$. Amplitude of this peaks

decreases with increasing of n number. In the region $\nu < \nu_d$ the curve $F_{\text{fr}}(\nu)$ is smooth and there are no any other peaks (or periodical components).
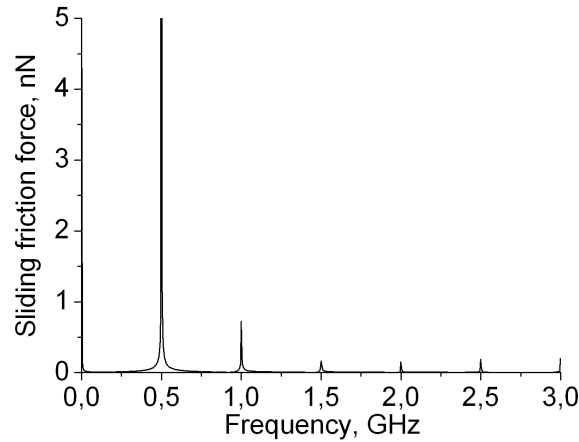
Figure 3: Fourier-estimation of spectral density of time dependence of sliding friction force for ideal sample (sample without defects at the coating/substrate interface).

Existence of quasiperiodically distributed nanocracks at the coating/substrate interface leads to formation of new low-frequency peak on the $F_{\text{fr}}(\nu)$ curve (this peak is marked by arrow on figure 4). Frequency of this peak is equal to $\nu_{icr} = 1,8*10^7$ Hz and it corresponds to average interval of quasiperiodic spatial structure formed by interfacial nanocracks ($V_{\text{sl}}/P_{\text{icr}} = 1,7*10^7$ Hz). Thus, obtained results allowed to estimate average distance between nanocracks.
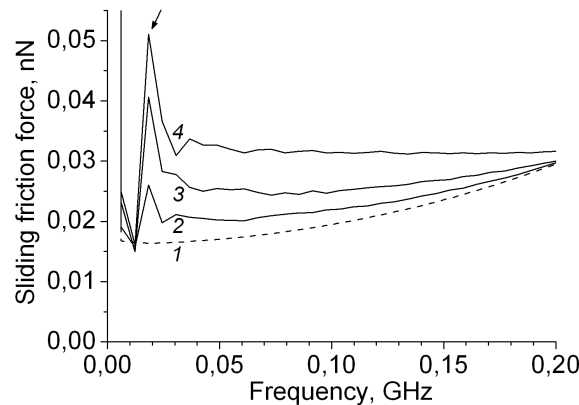
Figure 4: Fourier-estimation of spectral density of time dependence of sliding friction force for ideal sample (1) and for samples with interfacial nanockracks: . Length of nanocracks (licr) is equal to 12 nm (2), 23 nm (3) and 36 nm (4).

Existence of nanocracks at the coating/substrate interface leads to changing of view of $F_{\text{fr}}(\nu)$ curve in correspondent frequency interval. So we can diagnosis these defects. For investigation of opportunity of defining of nanocracks sizes samples with different length of cracks were examined. It is necessary to mention that average distance between cracks in different sample was the same (P_{icr}=90 nm). Results of analysis of spectral density of sliding friction force counterbody showed that increase of nanocracks length led to:

1. increasing (up to 2 times) of absolute and relative amplitude of the peak corresponding to quasiperiodic spatial structure formed by interfacial nanocracks ($\nu_{icr} = 1,83 * 10^7$ Hz);

2. increasing (up to 1,5 times) of average value of the $F_{\text{fr}}(\nu)$ curve in the vicinity of ν_{icr}. In other word increasing of nanocracks length leads to increasing of energy of the signal in the vicinity of ν_{icr}.

It is necessary to mention that value of ν_{icr} didn't change for all samples with nanocracks (fig. 4). So, on the base of analysis of spectral density of time dependence of sliding friction force we could estimate length of nanocracks and average distance between them.

Results of computer-aided simulation allow to suspect that heterogeneities with size about 10-100 nm could be identified in real experiments on the base of analysis of spectral density of sliding friction force. So, resolution of experimental equipment should be more than 10 nm. Systems with this resolution we will call nanotribospectrometers. This equipment could based on experimental realization of tribospectrometer suggested in [9]. In this paper we suggest following realization of experimental setup. Counterbody moves along the specimen surface and special sensors measure with high precision displacement of counterbody and sliding friction force acting on it.
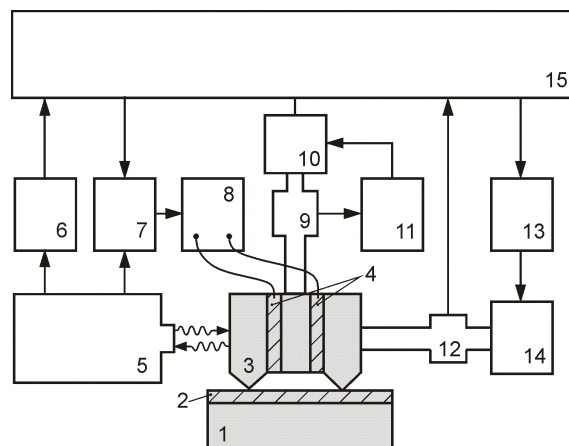
Figure 5: Scheme of nanotribospectrometer: 1 - specimen, 2 - coating, 3 - head of tribospectrometer, 4 - integrated piezoelectric elements, 5 - laser vibrometer with clock rate 1 MHz, 6 - high-speed information tank (intermediate memory), 7 - controller of generator of alternating voltage, 8 - generator of alternating voltage, 9 - force sensor for normal force, 10 - step motor for vertical displacement, 11 - controller of step motor for vertical displacement, 12 - force sensor for tangential force, 13 - controller of step motor for tangential displacements, 14 - step motor for tangential displacements, 15 - computer.

Scheme of realized nanotribospectrometer is shown on figure 5. Main part of system is tribological contact between coating (2) and detection head of tribometer (3). The head could have one contact and two contacts with coating (fig. 5). Head of tribometer is pressed to coating by engine (10) through force sensor (9). The force keeps constant by means of feedback system (11). Head of tribometer moves

horizontally along coating surface by means of engine (14). Force acting on head measures by sensor (12) and all data transfer on computer (15).

Laser vibrometer (5) measures displacement of head of tribometer with clock rate 1 MHz. Displacements are controlled by means of feedback systems on the base of chosen program. Special high-speed memory (6) used for recording of large volumes of information. This data transfer to computer (15) for post processing.

4 Conclusions

Obtained results of investigations let us justify opportunities of nanotribospectroscopy as the method for diagnosis of defect structure of nanostructured coating/substrate interface. Keystone of this approach is measurement of sliding friction force and analysis of its frequency spectrum. On the base of analysis of Fourier-transform of time dependence of sliding friction force it is possible to estimate average spatial period between nanocracks and their linear dimensions. It is necessary to mention that spectroscopic methods don't allow us to define structure of defects ant their spatial location. So, for obtaining of exhaustive information about defect structure it is ought to use nanotribospectroscopy jointly with other methods. Thus, nanotribospectroscopy could be suggested as perspective nondestructive method for nanodiagnosis of defect structure of coatings and surface layers of materials. It is possible to use this method for estimation of porosity of nanostructured coating, for defining of typical scales of friction processes behavior, and so on.

Acknowledgements

References

[1] Veprek S., Argon A.S. Mechanical properties of superhard nanocomposites // Surf. Coat. Technol. - 2001. - V. 146-147. - P. 175-182.

[2] Lee Eung Alu, Kim Kwang Ko. Deposition and mechanical properties of Ti-Si-N coated layer on WC-Co by RF inductivity coupled plasma-enhanced chemical vapor deposition // Thin Solid Films. - 2002. - V. 420-421. - P. 371-376.

[3] Korotaev A.D., Borisov D.P., Moshkov V.Yu. et. al. Nanocomposite and nanostructured superhard Ti-Si-B-N coatings // Russian Physics Journal. -V.50. - No.10. -P. 969-979.

[4] Dudko O.K., Popov V.L., Putzar G. Tribospectroscopy of randomly rough surfaces // Tribology Int. - 2006. - V. 39. - No. 5. - P.456-460.

[5] Psakhie S.G., Horie Y., Ostermeyer G.P. et al. Movable cellular automata method for simulating materials with mesostructure // Theor. Appl. Fract. Mech. - 2001. - V. 37. - Nos. 1-3. - P. 311-334.

[6] Dmitriev A.I., Popov V.L., Psakhie S.G. Simulation of surface topography with the method of movable cellular automata // Tribology Int. - 2006. - V. 39. - No. 5. - P. 444-449.

[7] Popov V.L., Psakhie S.G. Numerical simulation methods in tribology // Tribology Int. - 2007. - V. 40. - P. 916-923.

[8] Marple S.L. Digital Spectral Analysis: With Applications. -Prentice Hall, 1987. -492 p.

[9] Popov V.L., Starcevic J., Filippov A.E. Reconstruction of potential from dynamic experiments // Phys. Rev. E. - 2007. - V. 75. - 066104 (6 pp).

Sergey V. Astafurov, ISPMS SB RAS, Akademicheskii pr., 2/4, Tomsk, Russia, 634021
Evgenii V. Shilko, ISPMS SB RAS, Akademicheskii pr., 2/4, Tomsk, Russia, 634021
Valentin L. Popov, Berlin Technical University, Sekr. C 8-4, Gebaude M, Strasse des 17 Juni 135, 10623, Berlin, Germany
Sergey G. Psakhie, ISPMS SB RAS, Akademicheskii pr., 2/4, Tomsk, Russia, 634021

Surface waves in transversely isotropic media

Mels V. Belubekyan   Davit H. Mheryan

mbelubekyan@yahoo.com davidmher@mail.ru

Abstract

The beginning of research of surface waves is connected with work Reyleight [1]. In this work existence of the elastic waves propagating along free surface of semi-space and with amplitude which exponentially attenuate along depth of semi-space is established. The solution of a three-dimensional problem generalizing Reyleight problem, is received in [2], results of this article are also brought in the monograph [3]. In [4] three-dimensional problems of propagation of elastic surface waves in isotropic semi-space with two variants of conditions on the surface of semi-space are considered: free from stresses surface and when on the surface of semi-space the normal component of stresses, one of tangential stresses and one of tangential displacements are equal to zero. In the work [5] the problem of propagation of elastic surface waves in a transversally isotropic semi - space with two variants of conditions on the surface of semi - space is considered, here was assumed, that the surface of semi-space is a plane of isotropy.

In [6] the plane problem of propagation of elastic surface waves in hexagonal piezoelectric semi-space is considered, generalization of this problem, from the viewpoint of three-dimensional problem is brought in [7]. Herein it is also supposed, that the plane of isotropy is parallel to a plane limiting semi-space.

The offered work is devoted to research of surface waves in transversally isotropic semi-space when the plane of isotropy is perpendicular to a plane, limiting semi-space. It is supposed that the plane limiting semi-space is free from stresses. The new dispersion equation for surface wave finding is obtained, which particularly in the case of isotropic medium is brought to the equation of Reyleight. Conditions of surface waves damping are investigated, parameters of phase speed of a surface wave for known transversally isotropic materials are received.

1 Problem statement

The transversely isotropic semi-space is considered. It is supposed, that from each point of medium the parallel planes of elastic symmetry pass, in which all directions are elastic-equivalent (planes of isotropy). It is supposed, that the surface of semi-space is perpendicular to a plane of isotropy. The direction of axis z is perpendicular to plane of isotropy, axes x and y are situated in the planer of isotropy ($-\infty < x < +\infty, 0 \leqslant y < +\infty, -\infty < z < \infty$)

The system of differential equations determining wave process in this medium has the form:

$$c_{11}\frac{\partial^2 u}{\partial x^2} + \frac{1}{2}(c_{11} - c_{12})\frac{\partial^2 u}{\partial y^2} + c_{44}\frac{\partial^2 u}{\partial z^2} + \frac{1}{2}(c_{11} + c_{12})\frac{\partial^2 v}{\partial x \partial y} +$$

$$+(c_{13} + c_{44})\frac{\partial^2 w}{\partial x \partial z} = \rho\frac{\partial^2 u}{\partial t^2}$$

$$\frac{1}{2}(c_{11} - c_{12})\frac{\partial^2 v}{\partial x^2} + c_{11}\frac{\partial^2 v}{\partial y^2} + c_{44}\frac{\partial^2 v}{\partial z^2} + \frac{1}{2}(c_{11} + c_{12})\frac{\partial^2 u}{\partial x \partial y} + \qquad (1.1)$$

$$+(c_{13} + c_{44})\frac{\partial^2 w}{\partial y \partial z} = \rho\frac{\partial^2 v}{\partial t^2}$$

$$c_{44}\Delta_2 w + c_{33}\frac{\partial^2 w}{\partial z^2} + (c_{13} + c_{44})\frac{\partial}{\partial z}(\frac{\partial u}{\partial x} + \frac{\partial v}{\partial y}) = \rho\frac{\partial^2 w}{\partial t^2}$$

u, v, w - are components of displacement vector, c_{ij}- are five elastic characteristics of the transversely isotropic medium, Δ_2- is two-dimensional operator of Laplas. To solve the problem of propagation of surface waves, we have to satisfy the conditions of damping:

$$\lim_{y\to\infty} u = 0, \lim_{y\to\infty} v = 0, \lim_{y\to\infty} w = 0 \qquad (1.2)$$

It is supposed, that the surface of semi-space is free from stresses:

$$\sigma_{yy} = 0, \ \sigma_{yz} = 0, \ \sigma_{yx} = 0 \ \text{ when } \ y = 0 \qquad (1.3)$$

It is necessary to note, that the surface wave is also exist, when on the surface of semi-space the normal component of stresses, one of tangential stresses and one of tangential displacements are equal to zero, this problem is solved for isotropic semi-spaces in work [4], and for transversely isotropic semi-spaces, when the plane of isotropy is parallel to the surface of semi-space [5].

2 Problem solution

Let's assume that the surface wave extends in a direction of an axis z. Such wave can arise, if perturbation causing of it does not depend on a variable x. Here we deal with the plan deformation state. The system of differential equations (1.1) is brought to the form:

$$c_{11}\frac{\partial^2 v}{\partial y^2} + c_{44}\frac{\partial^2 v}{\partial z^2} + (c_{13} + c_{44})\frac{\partial^2 w}{\partial y \partial z} = \rho\frac{\partial^2 v}{\partial t^2}$$

$$c_{44}\frac{\partial^2 w}{\partial y^2} + c_{33}\frac{\partial^2 w}{\partial z^2} + (c_{13} + c_{44})\frac{\partial^2 v}{\partial y \partial z} = \rho\frac{\partial^2 w}{\partial t^2} \qquad (2.1)$$

The case, when the surface wave extends in a direction of an axis x is not considered, because in this case the analogues problem for isotropic media is obtained. The solutions of the system of differential equations (2.1) are represented in the form:

$$v = Be^{-pky} \times \exp i(\omega t - kz)$$

$$w = Ce^{-pky} \times \exp i(\omega t - kz) \qquad (2.2)$$

Substituting (2.2) in (2.1), the system of homogeneous algebraic equations with respect to arbitrary B, C is obtained:

$$\left[p^2 - \theta + \theta\eta\right] B + \left[C_1 + \theta\right] ipC = 0$$
$$\left[C_1 + \theta\right] ipB + \left[\theta p^2 - C_2 + \theta\eta\right] C = 0$$

(2.3)

The following denotations are done:

$$\eta = \frac{\rho\omega^2}{c_{44}k^2}, \ \theta = \frac{c_{44}}{c_{11}}, \ C_1 = \frac{c_{13}}{c_{11}}, \ C_1 = \frac{c_{33}}{c_{11}}$$

(2.4)

Particularly, in the case of isotropic medium:

$$c_{11} = c_{33} = \lambda + 2\mu, \ c_{44} = \mu, \ c_{12} = c_{13} = \lambda, \ C_1 = 1 - 2\theta, \ C_2 = 1.$$

It is supposed, that the determinant of the system (2.3) is equal to zero, and the following equation is obtained:

$$p^4 + [\eta + \theta\eta + 2C_1 + \theta^{-1}(C_1^2 - C_2)]p^2 + (1 - \eta)(C_2 - \theta\eta) = 0$$

(2.5)

Particularly in the case of isotropic medium the equation (2.5) to the analogues equation for isotropic media is brought:

$$p^4 + [\eta - 1 + \theta\eta - 1)]p^2 + (1 - \eta)(1 - \theta\eta) = 0$$

Considering roots of the equation (2.5) it is possible to find conditions of damping for surface waves. It is established, that conditions of damping for all considered transversely isotropic materials is interval $(0, 1)$. From the first equation of the system (2.3) we shall obtain:

$$C = -\frac{p^2 - \theta + \theta\eta}{[C_1 + \theta] ip}B$$

From the equation (2.5) the roots p_1, p_2, p_3, p_4 are obtained. From these roots only $p_1 \, and \, p_2$ satisfy to the damping conditions, so the displacements have the form:

$$v = B_1 e^{-p_1 ky} \times \exp i(\omega t - kz) + B_2 e^{-p_2 ky} \times \exp i(\omega t - kz)$$
$$w = -\frac{p_1^2 - \theta + \theta\eta}{[C_1 + \theta] ip_1} e^{-p_1 ky} \times \exp i(\omega t - kz)B_1 -$$
$$-\frac{p_2^2 - \theta + \theta\eta}{[C_1 + \theta] ip_2} e^{-p_2 ky} \times \exp i(\omega t - kz)B_2$$

(2.6)

3 Dispersion equation and numerical results

The boundary conditions (1.3) in the term of displacements have the form:

$$c_{11}\frac{\partial v}{\partial y} + c_{13}\frac{\partial w}{\partial z} = 0$$
$$\frac{\partial v}{\partial z} + \frac{\partial w}{\partial y} = 0$$

(3.1)

Substituting the expressions for v, w in (3.1) the system of homogeneous algebraic equations with respect to arbitrary B_1, B_2 is obtained:

$$\left[\frac{[p_1^2 - \theta + \theta\eta]\, C_1}{(C_1 + \theta)p_1} - p_1\right] B_1 + \left[\frac{[p_2^2 - \theta + \theta\eta]\, C_1}{(C_1 + \theta)p_2} - p_2\right] B_2 = 0$$

$$\left[\frac{p_1^2 - \theta + \theta\eta}{C_1 + \theta} + 1\right] B_1 + \left[\frac{p_2^2 - \theta + \theta\eta}{C_1 + \theta} + 1\right] B_2 = 0 \tag{3.2}$$

It is supposed, that the determinant of the system (3.2) is equal to zero, and the following equation is obtained:

$$\frac{\theta(p_1 - p_2)\left\{C_1(\eta - 1)(\theta\eta + C_1 + p_1^2) + \eta(\theta + C_1)p_1 p_2 + \left[(\eta - 1)C_1 - p_1^2\right] p_2^2\right\}}{(\theta + C_1)^2 p_1 p_2} = 0 \tag{3.3}$$

If $p_1 - p_2 = 0$ then $B_1 + B_2 = 0$ (see (3.2)) and $v = w = 0$ (see (2.6)).

So to find the dimensionless parameter of speed of surface wave, we have to solve the following equation:

$$R(\eta) = \eta(\theta + C_1)\sqrt{C_2 - \theta\eta}+$$
$$+\sqrt{1 - \eta}\left[\theta\eta - C_2 + C_1\left[\theta^{-1}(C_1^2 - C_2) + \eta + C_1\right]\right] = 0 \tag{3.4}$$

Particularly in the case of isotropic medium the equation (3.4) to Reyleight equation is brought:

$$\eta - \frac{4\sqrt{1 - \eta}(1 - \theta)}{\sqrt{1 - \eta} + \sqrt{1 - \theta\eta}} \tag{3.5}$$

The significance of the function $R(\eta)$ in the corners of interval $[0, 1]$ have the form:

$$R(1) = (\theta + C_1)\sqrt{\frac{c_{33} - c_{44}}{c_{11}}} \tag{3.6}$$

The expression $c_{33} - c_{44}$ is positive for all materials, observed by us, so $R(1) > 0$.

$$R(0) = \frac{(\theta + C_1)}{\theta}\frac{c_{13}^2 - c_{33}c_{11}}{c_{11}^2} \tag{3.7}$$

The expression $c_{13}^2 - c_{33}c_{11}$ is negative for all materials, observed by us, so $R(0) < 0$. The value of dimensionless parameter for some transversally isotropic materials is brought in the Tab.1. The characteristics of materials are taken from [8], [9].

Table1

material	η	θ	η for isotropic materials
Be	0.7563	0.5559	0.7206
PZT-4	0.88011	0.1841	0.8843
ZnO	0.9132	0.2026	0.8805
CdS	0.9391	0.1739	0.8863
Ti	0.8804	0.2875	0.8595
Zn	0.6556	0.2370	0.8727
Y	0.8658	0.3225	0.8488
Cd	0.8078	0.1762	0.8858

Tab.1 shows, that there are materials for which dimensionless parameter of speed of surface wave increases in compare with isotropic case, and there are materials for which it decreases.

Let's considered the coefficient of anisotropy in the following way:

$$\alpha = \frac{v_{p\ max} - v_{p\ min}}{v_{p\ min}} \times 100\%$$

Where $v_{p\ max}$ is the maximal speed of longitudinal wave and $v_{p\ min}$ is the minimal. The significance of α for some transversally isotropic materials is brought in the Tab.2.

Table2

material	α
Be	7.2787%
PZT-4	9.94069%
Zno	0.28571%
CdS	4.53801%
Ti	5.48387%
Zn	60.56004%
Y	2.03913%
Cd	50%

Tables 1 and 2 show, that for materials, which have small coefficient of anisotropy, parameter of speed of surface wave increases in compare with isotropic case and decreases for materials with big coefficients of anisotropy. Only Be is opposition.

References

[1] J. W. Reyleight. On waves propagated along the plane surface of an elastic solid. Proc. Math. Soc. London 17, 1885.p. 4-11.

[2] J. K. Knowles. A note on surface waves. J. of Geophysical Research. V.21. N22, 1966, p. 5480-5481.

[3] J. D. Achenbach. Wave propagation in elastic solids. NORTH-HOLLAND, 1984, 425 p.

[4] V. M. Belubekyan, M. V. Belubekyan. Three dimensional problem of Reyleight wave propagation. //Rep. NAS of Armenia, V. 105. N. 4, 2005, p.362 - 368.

[5] D. H. Mheryan, V. M. Belubekyan. On the problem of propagation of surface waves in transversally isotropic medium. Proceedings of XXXIV Summer School - Conference Advanced Problems in Mechanics June 25 - July 1, 2006, St. Petersburg (Repino). p. 363-370.

[6] D. I. Barzokas, B. A. Kudryavcev, N. A. Sennik. Wave propagation in electro-magnitoelastic media. M.:URSS 2003, 334p.

[7] D. H. Mheryan. Three dimensional problem of surface wave propagation in hexagonal piezoelectric semi-space. Proceedings of International Conference dedicated to the 95th Anniversary of Academician Nagush Kh. Arutyunyan, September 25 - September 28, 2007, Tsaxkadzor, Armenia. p. 275-279.

[8] T. D. Shermergor. Theory of elasticity of microinhomogeneous medium. M.:Nauka, 1997, 399p.

[9] E. Delesan, D. Ruaye. Elastic waves in solids. M.:Nauka, 1982, 424 p.

Mels V. Belubekyan, Republic of Armenia, NAS, Institute of Mechanics, 24B, Marshal Baghramian Ave., Yerevan, 0019
Davit H. Mheryan, Republic of Armenia, NAS, Institute of Mechanics, 24B, Marshal Baghramian Ave., Yerevan, 0019

Vibrational displacement produced due to deformability of the system elements

I. I. Blekhman   L. I. Blekhman   K. S. Ivanov   V. S. Sorokin
V. B. Vasilkov   K. S. Yakimova
blekhman@vibro.ipme.ru

Abstract

The effect of vibrational displacement means the appearance of the "directed on the average" change in the position (particularly of motion) of a system under the influence of the undirected on the average (oscillatory) excitation [1]. We consider here the specific class of such systems, in which the vibrational displacement is produced due to deformability of their elements. The paper [2] pioneered work in this direction. It is concerned with the problem of the motion of a solid body over a rough plane. A solid body contains an additional mass attached to a spring mounted at some angle about the plane. It was found that the body can move along the plane even in the case of symmetrical vibration. The direction of the motion, in this case, is controlled by the magnitude of the vibration frequency, whereas the velocity increases near the resonance. In this presentation, several new problems are considered:

1. The motion of a washer, planted on an elastic rod (Chelomei's pendulum). It is shown, that the washer can move along the rod even in the case of its pure harmonic longitudinal oscillations. This effect occurs due to the periodical changing of the diameter of the cross section of the rod caused by its longitudinal deformation.

2. The motion of a deformable particle (for example, a gas bubble) in an incompressible harmonically oscillating fluid. In this case, the vibrational displacement of the particle can be caused by the periodical changing of its size due to pressure pulsation in the fluid. In particular, the bubble can sink in the fluid, rather than rise or float.

Analytical solutions are obtained by the method of direct separation of motions. They are verified numerically and experimentally.

1   Introduction

The following phenomena are based on the effect of the vibrational displacement: vibrational transportation of single bodies and granular materials in vibrating trays and vessels; the work of the devices called vibrational transformers of motion and vibrating motors, vibrational sinking of piles, sheet piles and shells; vibrational

separation of particles of granular material according to their density, size and some other parameters; the motion of vibrationalcoaches; the flight and swimming of living organisms. A harmful effect of vibrational displacement can be exemplified by the appearance under the action of vibration of the mobility of the normally immobile parts of machines (such as self-unscrewing nuts).

From physical point of view the vibrational displacement is always the result of system or excitation mode asymmetry. Six possible types of such a system are indicated in reference [1]. We consider here the specific class of such system asymmetry, in which the vibrational displacement is produced due to deformability of the elements. The majority of problems on the theory of vibrational displacement are reduced to the investigation of solutions of nonlinear differential equations with periodic over the fast time $\tau = \omega t$ right sides (ω is the frequency of vibration), for which the velocities of the change of the generalized coordinates have the form

$$\dot{x} = \dot{X}(t) + \dot{\psi}(t, \omega t), \tag{1}$$

where $\dot{X}(t)$ is a slowly changing component, and $\dot{\psi}$ is a fast changing component, with

$$\langle \psi(t, \omega t) \rangle = 0, \tag{2}$$

where brackets $\langle \rangle$ indicate averaging for period 2π for fast time ωt. The component $\dot{X}(t)$ is called the *velocity of vibro-displacement*; in most cases its determination in the stable stationary motions (that is when $\dot{X} = \text{const}$) is of utmost interest for applications.
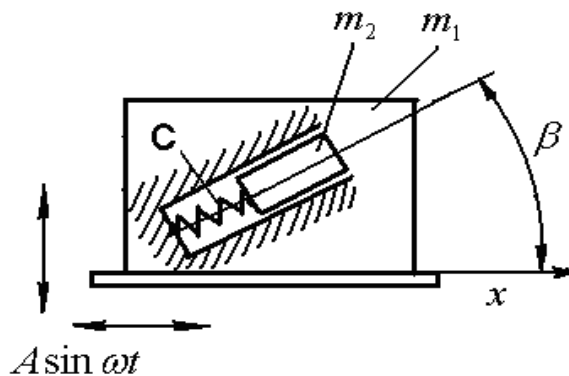
Figure 1: Solid body with inner degree of freedom.

2 Vibrational displacement of a body with inner degree of freedom

The paper of K.S. Yakimova [2] was the first work in this direction. It is concerned with the problem of the motion of a solid body of mass m_1 over a rough plane (Fig. 1). The solid body contains an additional mass m_2 attached to a spring c mounted

at some angle β to the plane. It was found that the body can move along the plane even in the case of symmetrical (horizontal or vertical harmonic) vibration. The direction of the motion (sign of $\dot{X}$) in this case is controlled by the magnitude of the vibration frequency, whereas the velocity increases near the resonance. These analytical results were confirmed experimentally on the model, given in Fig. 2.
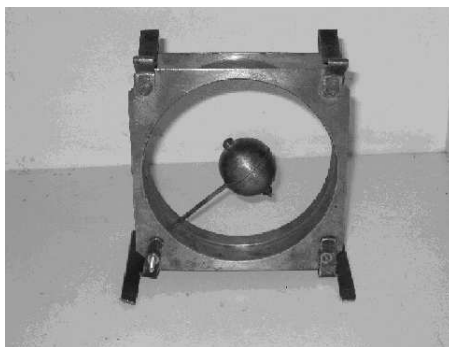
Figure 2: Experimental model.

An interesting system in which the deformability of the element also plays a significant part in formation of vibrational displacement of the body along a rough surface was investigated in paper [3].

3   Vibrational displacement of a washer placed on an elastic rod (Chelomey's pendulum)

A discussion has sprung up in connection with the publication of Chelomey's paper [4] whether purely lengthwise harmonic vibrations of a flexible rod (Fig. 3) can induce a vibrational lengthwise displacement of a rigid washer in condition of a dry or viscous friction between the rod and the washer. (see reviews in [1] and [5]).
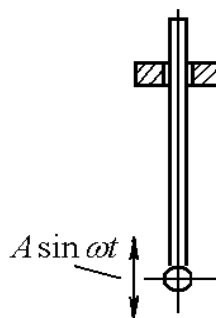
Figure 3: Chelomey's pendulum.

Most of the researchers were inclined to the opinion that such lengthwise displacement of the washer can be achieved only on condition of transverse vibrations of the rod. An idea has been proposed by K.S. Ivanov that vibrational displacement

of the washer in this case may be induced by periodic expansion and constriction of the rod cross-section in step with the compressing and tensile stress. The result of such deformations is that during a certain part of the cycle the washer is in close contact with the rod while during the other part of the cycle the contact is loosened (the washer is supposed to be put on the rod with a drive fit). The result of this is that the force of dry friction between the washer and the rod during one part of the cycle is greater than that during the other part. This circumstance is the cause of the asymmetry indispensable for obtaining the effect of vibrational displacement. Let us consider a simplest model of the above described process.

Fig. 4 shows a flexible rod with its left end vibrating according to the law:

$$\xi = A \sin \omega t, \tag{3}$$

where A - is amplitude, ω - vibration frequency. To simplify the investigation let us assume that the right end of the rod carries some mass m_1. If we suppose that the least eigenfrequency of the mass m_1 on the rod is sufficiently higher that frequency ω then the deformation of the rod may be considered as identical along the whole rod length and caused by the action of force $F = -m_1 \ddot{\xi} = m_1 A \omega^2 \sin \omega t$.
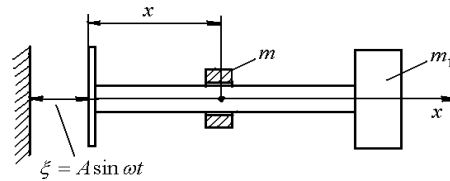
Figure 4: Simplest model of the system.

Washer movement in this assumption can be described by the following equation:

$$m\ddot{x} = -m\ddot{\xi} - f(N_0 + \eta m_1 \ddot{\xi})\operatorname{sign}\dot{x}, \tag{4}$$

where m - is the mass of the washer, f - dry friction coefficient, N_0 - normal reaction between the washer and the rod in static state, and η - a positive coefficient depending on washer and rod elasticities. Sign $+$ standing before the second addend within the brackets of equation (4) is of great significance: at a positive acceleration $\ddot{\xi}$ the rod is compressed so that normal reaction is increased as compared to N_0. We suppose that magnitude of N_0 is such that the sum $N_0 + \eta m_1 \ddot{\xi}$ will be always positive.

A more complicated model is show in fig. 5. In this case the least frequency of free rod vibrations is assumed to be not higher than excitation frequency and the washer motion is represented by the following equation:

$$m\ddot{x} = -m\ddot{\xi}_0 - f(N_0 - \eta_1 \frac{\partial \xi}{\partial x})\operatorname{sign}\dot{x} \tag{5}$$

where $\xi = \xi(x, t)$ - is bias of the rod point with coordinate x , corresponding to standing wave excited in the rod, $\eta_1 > 0$ - is a certain coefficient.

Equations (4) and (5) were solved by the method of direct separation of motions [1]. In this case the fast motion equation was solved by a simplest assumption
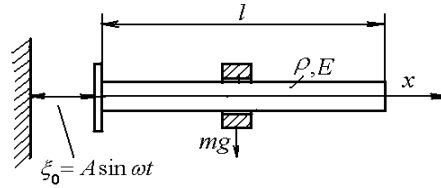
Figure 5: Model of the system taking into account arising the longitudal standing wave.

that inertia forces by far exceed dry friction forces. With such an approximation the method given failed to detect the effect of the washer vibrational displacement. Quite a different result has been obtained with a numerical modelling of equations (4) and (5) and in exact solution. Such an solution can be obtained if one observes that equations (4) and (5) can be considered as a particular case of the equation describing movement of a body along an harmonically vibrating flat surface which is an equation describing behaviour of a quite different physical system [6]. This latter system does not include any elastic elements though the normal reaction in it changes in accordance with the harmonic law.

In more detail the problem is considered in K.Ivanov's paper.

4 Vibrational displacement of a solid and deformable particle in compressible and noncompressible media

The problems concerning vibrational displacement of particles in oscillating media are apt to rouse significant applied and principal interest. In all cases deformability of a particle or compressibility of medium play a definite role in arising of vibrational displacement. In particular, particles of density less than that of the medium can sink while the denser than the medium particles can float (see monograph [7] and paper [4] containing also surveys of published papers).

Equation of particle motion in compressible medium in a system of coordinates associated with a vibrating vessel with certain assumptions can be represented by the following form (where axis x is directed vertically downward).

$$(m + qm_0)\ddot{x} = -F(\dot{x}) + \left[g + \ddot{\xi}(x, \omega t)\right](m - m_0) \tag{6}$$

Here m - is particle mass, m_0 - medium mass in particle volume, q - coefficient of attached mass, $F(\dot{x})$ - resistance force, $\ddot{\xi}$ absolute acceleration of medium in the point of particle disposition.

Vibrational displacement in this case can be caused by the following:

1) Deformability (compressibility) of medium. Value $\ddot{\xi}(x, \omega t)$-in this case corresponds to standing or running wave [7, 8].

2) Deformability of particle. Periodic excitation of medium under the action of pulsing pressure can involve the change of particle size with consequent periodic

change of the attached mass m_0 and resistance force $F(\dot{x})$.

In both cases after transition to the slow motion equation vibrational forces causing vibrational displacement will arise due to non-linearity and parametricity.

It is worthwhile to mention the second case when the oscillating medium such as liquid is practically nondeformable whereas vibrational displacement effects are caused by deformability of the particle itself. This case is discussed in V. Sorokin's paper at this school.

5 On vibrational displacement of liquid layer

Possibility of directed shift of liquid along a horizontal plane vibrating at some angle to it has been found by these authors' experiments. There is reason to believe that in this case vibrational displacement is caused by emergence of non-linearity manifesting itself as certain cellular structures resembling known Benar's cells (Fig. 6). This effect may be explained also as caused by "introduction" of additional degree of freedom containing some elastic element.

Figure 6: Cells on the surface of vibrational water.

6 Conclusion

The examples cited give evidence that presence of deformable elements in a non-linear system can cause or enhance vibrational displacement effects i.e. generation of directed slow motions under the influence of fast vibrational action.

Acknowledgements

110

References

[1] Blekhman I.I. Vibrational Mechanics. World Scientific Publishing Co. Pte. Ltd. Singapore, New Jersey, Hong Kong, 2000. - 509 p.

[2] Yakimova K.S. Vibrational Displacement of a two-mass oscillating system - Izvestiya Academii nauk SSSR, 1969, N 5, pp. 20-30.

[3] Zimmerman K., Zeidis I., Steigenberg J. An approach to worm-like motion. Proc. of the XXI ICTAM. Warshaw, 2004.

[4] Chelomey V.N. Paradoxes in mechanics due to vibrations. Doklady Academii nauk SSSR. Mechanics - 1983. v. 270, N 1. - pp. 62-67.

[5] Myalo E.V. Dynamics of a flexible rod with an easy fitted ring in parametric excitation. Master of Sciences dissertation. Russian Academy of Sciences. 2008.

[6] Blekhman I.I. and Dzhanelidze G. Yu. Vibrational Displacement. - Moscow, Nauka, 1964. 410 p. (in Russian).

[7] Ganiyev R.F., Ukrainsky L.E. Non-linear wave mechanics and technology. M.: Publishing House "Regular and chaotic dynamics". 2008, 712 p.

[8] Blekhman I.I., Vaisberg L.A., Blekhman L.I. Vasilkov V.B., Yakimova K.S. "Anomalous" phenomena in fluid under vibration influence. - Doklady Academii nauk, 2008, v. 422, N 4, pp. 470-474.(in Russian). (In English: Doklady Physics, Pleiades Publishing, 2008, v. 53, N 10, pp. 520-524).

Blekhman I.I., V.O., Bolshoy av., 61, Saint-Petersburg, 199178, Russia

On a Chelomey pendulum problem

I. I. Blekhman   K. S. Ivanov

ivanoff.k.s@gmail.com

Abstract

Possibility of a vibrational translation washer along a rod influenced with longitudial symmetric vibration and symmetric friction is widely discussed in a current literature. The work provides a possibly case of such motion caused by longitudial deformation of the rod. Problem is considered in terms of motions separation method and numerically.

1   Introduction

A deep resonance was made in the early 80-s of the previous century by an article by V.N. Chelomey describing a system consisting of hingedly mounted rod and "washer" planted on it with lengthwise moving ability. Chelomey observed that influenced by vertical vibration of joint while as the upper equilibrium position becomes stable (Stephenson-Kapitsa pendulum), washer shifts from the base and takes some fixed position. Practically right away were published articles by some authors explaining the effect. Some review of this question is given at I.I. Blekhmans book "Vibrational mechanics" [2]. One could distinguish major trends in research of this problem right by that time (1994):

- rod was considered perfectly rigid (in this case vibrations were induced either purely by vertical oscillations of joint [3] or by vertical and horizontal ones [4])

- rod was considered to be deformable, vacillating in lateral standing wave mode[5,6].

Figure 1: Variants of the task consideration.

Somehow or other all variants contained horizontal displacement of a washer, and the problem of possibility of washer transition during purely longitudal vibration

subject to dry or viscous friction between washer and rod had became a subject of argument. In this work is made a supposition of a washer movement possibility emerging under the influence of purely longitudal rod oscillations. For this purpose the deformation of cross-section of rod originating of stress-strain is taken into consideration. Oscillations of the end of the rod are considered harmonic. Fixing is assumed to not oppose stress-strain of the rod.
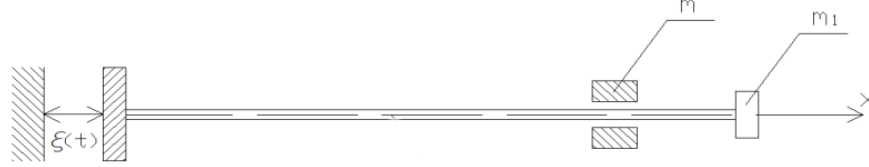
Figure 2: Model diagram.

2 Model of a system. Motion equations and their solutions.

First consideration took place under the assumption that sonic speed inside the rod is big enough to regard it as being statically deformed at each point of time during the pinning point dislocation. Then an equation can be written down in a reference frame attached to fixing, holding that washer is planted sufficiently tight,

$$m\ddot{x} = -m\ddot{\xi} - fN(t)\text{sign}(\dot{x}), \tag{1}$$

were f - constant of dry friction,

$$N(t) = \begin{cases} (N_0 + \eta m_1 \ddot{\xi}), & (N_0 + \eta m_1 \ddot{\xi}) \geq 0 \\ 0, & (N_0 + \eta m_1 \ddot{\xi}) < 0 \end{cases}, \tag{2}$$

reacting force between washer and fixing and N_0 its value when $\ddot{\xi} = 0$. If we keep in mind that expression $\ddot{\xi} = -A\omega^2 \sin(\omega t)$ is negative when weight is on the top and positive at the bottom. Let us think that initial tension is sufficient for contact between washer and rod not to break when the rod is stretched i.e. inequality $N_0 > f\eta m_1 A\omega^2$ always holds true. Thus

$$N(t) = (N_0 + \eta m_1 \ddot{\xi}), \tag{3}$$

Let us solve the equation numerically: For the parameters $N_0 = 1N$, $f = 0.5$, $\eta = 1$, $m = 1kg$, $m_1 = 1kg$, $A = 0.01m$, $\omega = 30s^{-1}$ we got clearly observable result One can approach a solution of the problem slightly different - with the help of step-by-step integration method. When using this method the washer moving is divided into stages concerning rest and sliding. First stage corresponds to "relative
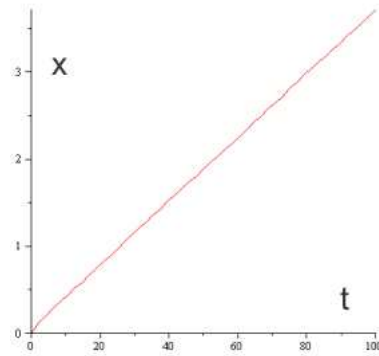
Figure 3: "Slow" coordinate time dependence for a particular trial.

rest" of the washer, on this stage the equation is integrated taking account of the force of friction equal to and applied in the line of force of inertia. Second stage - stage of "sliding" - force of friction is calculated by formula (2). Third stage - similar to the first, and so on. The main difficulty of analytical examination by such method is in determination of moments of stage interchange, however during numerical examination at each step one can verify conditions of stage continuation and find moments of stage interchange. Eventually phase-plane portrait would look like Fig.4.
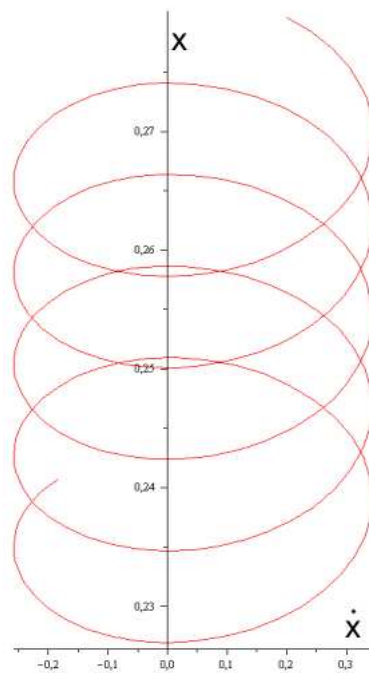
Figure 4: Phase-plane portrait of steady-state washer movement.

Remarkably, the use of traditional "movement separation" method will not allow to locate any moving. In supposition that there exists an average uniform moving we will apply "movement separation" method assuming that.

$$x = X + \Psi, \tag{4}$$

Where X and Ψ is a "slow" and "fast" movement components correspondingly. Than the equation of slow motion becomes:

$$m\ddot{X} = -f < (N_0 - \eta m_1 A\omega^2 \sin(\omega t))\text{sign}(\dot{X} + \dot{\Psi}) >, \tag{5}$$

Where angle brackets point at averaging over a period from 2π to ωt. Fast motion is determined from approximate equation

$$m\ddot{\Psi} = -m\ddot{\xi}, \tag{6}$$

from which

$$\begin{aligned} \ddot{\Psi} &= A\omega^2 \sin(\omega t) \\ \dot{\Psi} &= -A\omega \cos(\omega t) \end{aligned}, \tag{7}$$

Taking obtained $\dot{\Psi}$ and the conditions of $\dot{\Psi} + \dot{X}$ sign change into consideration we convert the right hand side component, being averaged

$$< (N_0 - \eta m_1 A\omega^2 \sin(\omega t))\text{sign}(\dot{X} + \dot{\Psi}) >=$$
$$= N_0 - \frac{\eta m_1 A\omega^2}{2\pi} \left(-\int_0^{\omega t_1} \sin(\omega t)d\omega t + \int_{\omega t_1}^{2\pi - \omega t_1} \sin(\omega t)d\omega t - \int_{2\pi - \omega t_1}^{2\pi} \sin(\omega t)d\omega t \right)$$

The first and last integrals compensate each other and the middle one:

$$\int_{\omega t_1}^{2\pi - \omega t_1} \sin(\omega t)d\omega t = -\cos(\omega t)|_{\omega t_1}^{2\pi - \omega t_1} = -\cos(\omega t_1) + \cos(\omega t_1) = 0$$

Finally:

$$< (N_0 - \eta m_1 A\omega^2 \sin(\omega t))\text{sign}(\dot{X} + \dot{\Psi}) >= \frac{\pi - 2\omega t_1}{\pi} N_0, \tag{8}$$

Using the condition of friction force's direction change $\dot{X} - A\omega \cos(\omega t_1) = 0$ we get

$$\cos(\omega t_1) = \frac{\dot{X}}{A\omega}, \quad \sin(\frac{\pi}{2} - \omega t_1) = \frac{\dot{X}}{A\omega}, \tag{9}$$

Taking $\frac{\dot{X}}{A\omega}$ minor as compared to one, one can write down an equation for slow motion as:

$$m\ddot{X} = \frac{2fN_0}{\pi A\omega}\dot{X}, \tag{10}$$

This implies that in steady state washer is in relatively indifferent equilibrium, which contradicts the accurate development exact solution Equation (1) is absolutely similar accurate to coefficients to motion equation of a body on a vibrating inclined plane, vibrational translation for which is studied in [7].
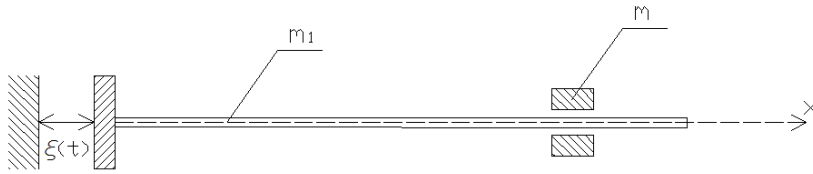
Figure 5: Model diagram for a standing wave case.

At the next stage of research were taken into consideration longitudal elastic oscillations with the establishment of standing wave (Fig.5).

Assuming the least frequency of rods free oscillations greater than forcing frequency, the motion equation can be written down as follow

$$m\ddot{x} = -m\ddot{\xi}_0 - fN(x,t)sign(\dot{x}),$$ (11)

where $\xi_0 = A\sin\omega t$ and

$$N(t) = (N_0 + \eta_1 \frac{\partial\xi}{\partial x}),$$ (12)

$\xi(x,t)$ offset of rods axis point with relative coordinate x, corresponding to the standing wave. Let us write down the standing wave equation:

$$\begin{aligned}\rho\frac{\partial^2\xi}{\partial t^2} &= E\frac{\partial^2\xi}{\partial x^2} - \rho\ddot{\xi}_0 \\ \xi|_{x=0} &= 0 \\ \frac{\partial\xi}{\partial x}\Big|_{x=l} &= 0\end{aligned},$$ (13)

Let us find the solution in $\xi(x,t) = B(x)\sin\omega t + C\sin\omega t$ form, we will get:

$$\xi(x,t) = \left(\frac{\cos\frac{\omega}{c}(l-x)}{\cos\frac{\omega}{c}l} - 1\right) A\sin\omega t = \Phi(x)\sin\omega t,$$ (14)

Where $c = \sqrt{\frac{E}{\rho}}$ sonic speed inside the rod. Let us substitute the acquired expression into the slow motion equation and resolve by fast motion solution.

$$m\ddot{X} = -f < (N_0 + \eta_1\Phi(X)\sin(\omega t) + \eta_1\Psi\Phi'(X)\sin(\omega t))sign(\dot{X} + \dot{\Psi}) >,$$ (15)

As in solution of problem with uniform deformation - the first component to be averaged with $\Phi(X)$ becomes zero. However, by averaging the new component we obtain $\frac{2}{\pi}\frac{\dot{X}}{A\omega}$ and the equation for slow movements becomes:

$$m\ddot{X} = C\dot{X},$$ (16)

This again does not allow drawing a correct conclusion on vibrational translation At a more accurate examination it is possible to find out that areas of indifferent

equilibrium may appear around nodes of deformation wave. Outside those areas vibrational translation will take place, which will move the washer towards certain areas and away from other areas. This phenomenon is similar to stability and instability of nodes and loops in certain other modifications of problem examination based on other types of waves.

Acknowledgements

References

[1] Chelomey V.N. Paradoxes in mechanics due to vibrations. Doklady Academii nauk SSSR. Mechanics - 1983. v. 270, N 1. - pp. 62-67.

[2] Blekhman I.I. Vibrational Mechanics. World Scientific Publishing Co. Pte. Ltd. Singapore, New Jersey, Hong Kong, 2000. - 509 p.

[3] Kurbatov A.M., Chelomey S.V., Khromushkin A.V. On a Chelomey pendulum issue. Izvestiya Academii nauk SSSR, 1986, N 6, pp. 63-65.

[4] Menyaylov A.I., Movchan A.V. On a rod-washer systems stabilization with vibration influenced hinge. Izvestiya Academii nauk SSSR, 1984, N 6, pp. 35-40.

[5] Blekhman I.I., Malachova O.Z. On a quasi-equilibrium Chelomey pendulum states. - Doklady Academii nauk, 1988, v. 287, N 2, pp. 290-294.

[6] Myalo E.V. Dynamics of a flexible rod with an easy fitted ring in parametric excitation. Master of Sciences dissertation. Russian Academy of Sciences. 2008.

[7] Blekhman I.I. and Dzhanelidze G. Yu. Vibrational Displacement. - Moscow, Nauka, 1964. 410 p. (in Russian).

Blekhman I.I., V.O., Bolshoy av., 61, Saint-Petersburg, 199178, Russia

Transient regimes in inertially excited postresonance vibrational devices with several degrees of freedom of the carrying system

I. I. Blekhman   N. P. Yaroshevich

blekhman@vibro.ipme.ru, m_yaroshevich@mail.ru

Abstract

Regimes of start and run - out of trans-resonant vibration devices with inertial (rotational unbalance) excitation of oscillations are considered. The problem of passage through the resonance zone arises in such devices. As a result, increased power of the motor is required. Moreover, the near-resonant locking effect ("Sommerfeld effect") can occur. The intensive oscillations in the start and run - out regimes are undesirable.

Blekhman I.I., Indeitsev D.A. and Fradkov A.L. [7] analyzed dynamics of start process by means of an iterative method combined with the method of direct separation of motions. An elementary model with one oscillatory degree of freedom of the carrier system was considered. A review of the problem and a list of references were also given in this reference.

This paper presentation extends the results of abovementioned article to a system with three oscillatory degree of freedom of the carrier system. The expression for the braking vibration moment and the equation for the semi - slow oscillations of the internal pendulum are derived. These relations generalize previously obtained results. Some differences are also highlighted. In particular, the complicated behavior of the system in the frequency range, which contains natural frequencies of the carrier system, is possible.

1 Introduction

Inertial (unbalanced) drive is widely practiced in vibrational machines and devices owing to its simplicity and possibility of obtaining considerable motive forces at small overall dimensions and relatively small mass. Machines with inertial vibraexciters are mostly postresonance ones. Their operation is stable enough in stationary regime. However in start and run-out periods a problem of passing through resonance frequencies zone arises. In particular, sticking of rotor rotating frequency close by one of its own frequencies may occur at starting, that is Zommerfield's effect may develop. Passing through resonance zone in these cases involves considerable oscillations in the system and, correspondingly, dynamic loads on the construction elements. Besides, uprated engine power is needed.
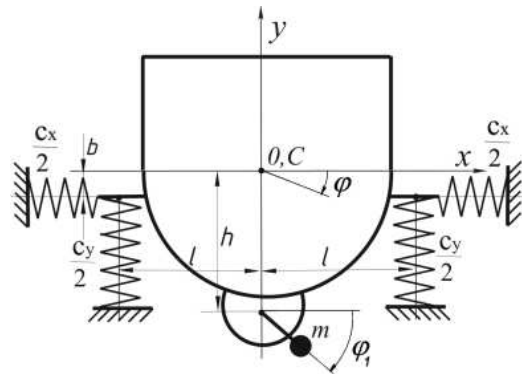
Figure 1: Scheme of oscillatory system with plane motion of the working head.

Zommerfield's effect is considered with the application of various methods in a number of works (books [1-6], paper [7], see also works [8-10]). Rigorous investigation of Zommerfield's effect by Poincare's method was carried out in work [1].Book [4] shows that theoretical explanation and numerical description of the known appropriateness of Zommerfield's effect may be easily obtained by means of the method of direct separation of motions. In [7] The problem for the case of oscillating system with one degree of freedom is solved by the method of successive approximation coupled with the method of direct separation of motions. It is shown that such approach, rougher than in known works, allows to comparatively easier describe the system behavior in both pre-and post- resonance zones of rotor rotation frequencies. Such approach is used in the offered work for systems whose oscillating part is a rigid body with plane-parallel motion. Expression for retarding vibrational moment and equation of internal pendulum semislow oscillation which generalizes previous results are obtained.

Attention has been paid to a number of differences, in particular, to the possibility of complicated behanour of the system in the range between the frequencies of carrying system free oscillations.

Consideration of dynamics of passing though resonance in vibrational machines with inertial excitation of oscillations is essensial at designing start control systems. Such systems allow to considerably reduce the driving engine power necessary for passing though resonance zone [11].

2   Scheme of the system and motion equations

A wide range of vibrational machines may be idealized in the form of a system schematically presented in Fig. 1. Carrying body(vibrating member of machine) is considered to be a rigid body capable to execute small plane-parallel oscillations, that is, has, in general case, three degrees of freedom. It is linked with stationary base by the system of elastic and damping elements. An umbalanced rotor, set to rotation by asynchronous electric motor or by d.c. current motor, is mounted on the carrying body.

The axis of the exciter rotor is perpendicular to the plane, parallely to which the carrying body motion is executed.

Let x and y be masses C centre coordinates in the rest system xOy and φ, φ_1 be correspondingly angles of rotation of carrying body and rotor exciter. Differential equations of motion of the system under consideration are presented as.

$$I\ddot{\varphi} = L(\dot{\varphi}_1) - R(\dot{\varphi}_1) + m\varepsilon(\ddot{x}\sin\varphi_1 + \ddot{y}\cos\varphi_1 - \ddot{\varphi}h\sin\varphi_1), \tag{1}$$

$$M\ddot{x} + \beta_x\dot{x} + c_x x = m\varepsilon(\ddot{\varphi}_1\sin\varphi_1 + \dot{\varphi}_1^2\cos\varphi_1),$$

$$M\ddot{y} + \beta_y\dot{x} + c_x x = m\varepsilon(\ddot{\varphi}_1\cos\varphi_1 - \dot{\varphi}_1^2\sin\varphi_1),$$

$$J\ddot{\varphi} + \beta_\varphi\dot{\varphi} + c_\varphi\varphi = -m\varepsilon h(\ddot{\varphi}_1\sin\varphi_1 + \dot{\varphi}_1^2\cos\varphi_1), \tag{2}$$

where M-is total mass of the system; J - is a moment of inertia in respect to the axes passing through the masses centre; I - is a total moment of vibroexciter rotor inertia in respect to its axis of rotation; m, ε - are, correspondingly, vibroexciter mass and its eccentricity; $\beta_x, \beta_y, \beta_\varphi$ - are coefficients of viscous resistance, c_x, c_y -are longitudinal rigidities of vertical and horizontal springs; $c_\varphi = c_y l^2 + c_x b^2$; l, b - parameters determining attaching point of the upper spring ends in respect to exciter rotor axis; $L(\dot{\varphi}_1), R(\dot{\varphi}_1)$ - are correspondingly, motor torque and a moment of forces resistant to rotation.

Writing down equation (2) we assume, for simplification, that axes x and y are "main" both in respect to rigidities and to the coefficient of viscous resistance, that is, "cross" values of parameters $c_{xy}, ..., \beta_{xy}, ...$ are equal to zero; it is also assumed that lateral rigidity of elastic elements are negligible.

Consideration of more general case by means of the used below method does not cause difficulties, but, however, its bound with more awkward computations.

3 The first approximation, peculiarities of Zommerfield's effect manifestation in the system

To study motion of unbalanced excites rotor at passing through the resonance zone the method of direct separation of motions is used [4], according to the main precondition of the method let us assume that motions under consideration may be presented in the form:

$$\varphi_1 = \omega t + \psi(t, \omega t), q_i = q_i(t, \omega t) \tag{3}$$

where $\omega = \omega(t)$ is slow and ψ and $q_1 = x, y, \varphi$ are fast time functions, they are 2π - periodical at $\tau = \omega t$ and they value average equals zero;

$$\langle\psi(t, \tau)\rangle = 0, \langle q_i(t, \tau)\rangle = 0 \tag{4}$$

It is also assumed that $\dot{\psi} << \omega$. French quotes in formula (4) and further indicate time averaging for the period $T = 2\pi$ in fast time $\tau = \omega t$.

Such presentation of equations (1),(2) at studying the vibroexciter rotor passing through resonance zone, when Zommerfield's effect is taking place and, correspondingly, the frequency of rotor rotation $\dot{\varphi}_1$ changes slowly enough seems to be rightful. It will be checked "a posteriory" below.

Let us substitute the first expression (3) into assumed differencial equation (1) and average its left and right part in fast time τ. To continue, we subtract the obtained relationship from the assumed one and come to the following system of integro - differencial equations of slow and fast motion of vibroexciter rotor:

$$I\dot{\omega} = L(\omega) - R(\omega) + \langle \Phi(\ddot{x}, \ddot{y}, \ddot{\varphi}, \varphi_1) \rangle \tag{5}$$

$$I\ddot{\psi} + k\dot{\psi} = \Phi(\ddot{x}, \ddot{y}, \ddot{\varphi}, \varphi_1) - \langle \Phi(\ddot{x}, \ddot{y}, \ddot{\varphi}, \varphi_1) \rangle \tag{6}$$

where

$$\Phi\langle (\ddot{x}, \ddot{y}, \ddot{\varphi}, \varphi_1) \rangle = m\varepsilon[(\ddot{x} - h\ddot{\varphi})\sin\varphi_1 + \ddot{y}\cos\varphi_1]$$

At obtaining this system lineariration of expressions $L(\dot{\varphi}_1), R(\varphi_1)$, as in [1], close by value $\dot{\varphi}_1 = \omega$(where ω - is frequency of rotor "sticking") is performed,$k = -\frac{d(L-R)}{d\dot{\varphi}_1}|_{\dot{\varphi}=\omega} > 0$ being a total damping coefficient).

First, according to the method of direct separation of motions, approximate periodic solution of fast motions (2), (6) equations at constant ("frozen") $\omega(t), \dot{\omega}(t)$ are found.

As in works [4, 7], we adopt $\psi = \psi^{(1)} = 0$, $\varphi_1 = \varphi_1^{(1)} = \omega t$ as the first approximation and corresponding periodic solution of equations (2)

$$x = x^{(1)} = A_x^{(1)}\cos(\omega t + \gamma_x), y = y^{(1)} = A_y^{(1)}\cos(\omega t + \gamma_y), \varphi = \varphi^{(1)} = A_\varphi^{(1)}\cos(\omega t + \gamma_\varphi) \tag{7}$$

where

$$A_x^{(1)} = \frac{m\varepsilon}{MB_x}, B_x = \sqrt{(1-\lambda_x^2)^2 + 4n_x^2}, \lambda_x = \frac{p_x}{\omega}, p_x = \sqrt{\frac{c_x}{M}}, n_x = \frac{\beta_x}{2M\omega}, \sin\gamma_x = -\frac{2n_x}{B_x},$$

$$A_y^{(1)} = -\frac{m\varepsilon}{MB_y}, B_y = \sqrt{(1-\lambda_y^2)^2 + 4n_y^2}, \lambda_y = \frac{p_y}{\omega}, p_y = \sqrt{\frac{c_y}{M}}, n_y = \frac{\beta_y}{2M\omega}, \sin\gamma_y = -\frac{2n_y}{B_y},$$

$$A_\varphi^{(1)} = -\frac{m\varepsilon h}{JB_\varphi}, B_\varphi = \sqrt{(1-\lambda_\varphi^2)^2 + 4n_\varphi^2}, \lambda_\varphi = \frac{p_\varphi}{\omega}, p_\varphi = \sqrt{\frac{c_\varphi}{J}}, n_\varphi = \frac{\beta_\varphi}{2J\omega}, \sin\gamma_\varphi = -\frac{2n_\varphi}{B_\varphi}. \tag{8}$$

Having substituted solutions (7) into the right part of slow motions equation (5) and having performed averaging, we obtain approximated formula of, so called, vibrational moment [1, 2, 4].

$$V^{(1)}(\omega) = -(m\varepsilon\omega)^2[\frac{n_x}{MB_x^2} + \frac{n_y}{MB_y^2} + \frac{h^2}{J}\frac{n_\varphi}{MB_\varphi^2}] \tag{9}$$

At $\lambda_y = \lambda_\varphi \to \infty$ that is, in the case of carrying body with one degree of freedom, formula (9), as it should be, coincides with the corresponding formula of work [7] (it should be taken into account that $n_x = n/\omega$, that , where n, according to work [7], is written for the value $\beta/2M$).

All components in formula (9) are negative. Thus, as it is for the system with one oscillatory degree of freedom, vibrational moment is always retarding, i.e., it is an additional load upon the engine rotor, its dependency on frequency is of resonance character, and, therefore, its retarding effect manifests itself in comparatively narrow frequency range.

With account of uniformity of components in (9) and by analogy with [1, 4] expression (9) for the vibrational moment affecting vibroexciter rotor may be considered as the sum

$$V^{(1)}(\omega) = \sum_{q=x,y,\varphi} \nu_q$$

summands of which

$$\nu_q = -(m\varepsilon\omega)^2 \frac{n_q}{M_q B_q^2}, \tag{10}$$

are "particular" vibrational moments characterizing the effect of q-oscillatory motion (oscillatory coordinate) on the rotation of exciter rotor. (Here, if $q = x$, or $q = y$, then $M_q = M$, if $q = \varphi$, then $M_q = M\frac{\rho^2}{h^2}$).

If should, be noted that expression (10) for "particular" vibrational moment may be presented in the form

$$\nu_q = \frac{1}{2}Fa_q \sin\gamma_q,$$

where $F = m\varepsilon\omega^2$-is an amplitude of driving force developed by exciter rotor at stationary carrying body, $a_q = \frac{m\varepsilon}{M_q \sqrt{(1-\lambda_q^2)^2 + 4n_q^2}}$-is an amplitude of platform oscillations, corresponding to q-oscillatory coordinate.

Both particular and general vibrational moments characterize vibrational link between carrying body oscillatory motions and rotating motions of vibroexciter rotor. According to formulas (9), (10) the retarding effect of vibration at starting is the less, the stronger the resistance of the system in coordinates x, y, φ is (as it is for the system with one degree of freedom).

Fig.2 shows the dependency of vibrational moment on viscous resistance coefficient β ($\beta = \beta_x = \beta_y/1, 1 = \beta_\varphi/0, 05$) at passing through the resonance zone of frequencies x, y, φ for the system with three oscillatory degrees of freedom.

The diagram shows that vibrational moment increases not so sufficiently in the region of resonance frequencies ($p_x = 30\text{sec}^{-1}, p_y = 35\text{sec}^{-1}, p_\varphi = 44\text{sec}^{-1}$) at relatively great damping coefficients ($\beta \geq 300\text{kg/sec}$) than it does at small ones

122
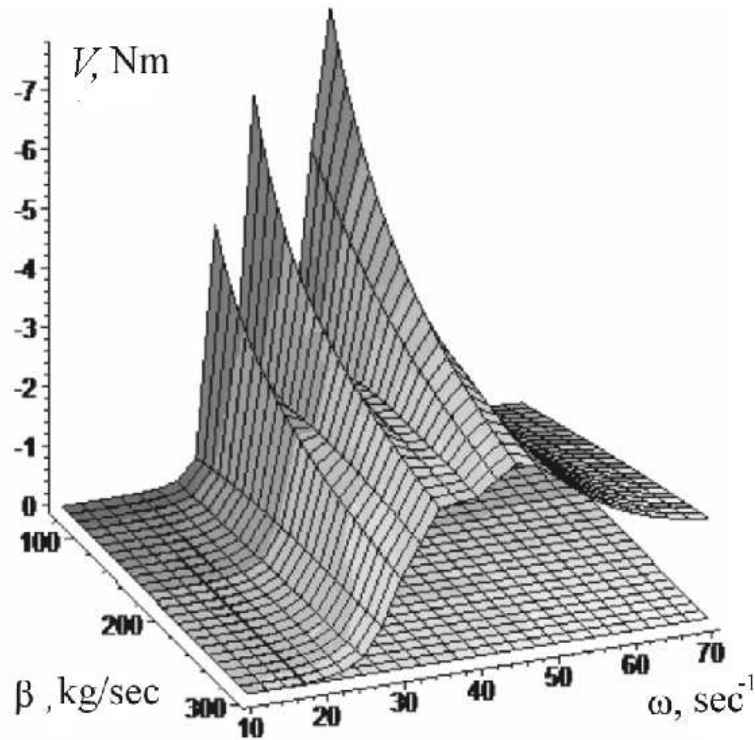
Figure 2: Dependency of vibrational moment on frequency and resistance coefficient β.

($\beta \leq 100 \text{kg/sec}$); resonance maxima corresponding each coordinate are almost imperceptible.

It should be emphasized that the value of maximal retarding vibrational moment sufficiently depends, according to (8) and (9), on the frequencies of natural oscillations of the system; decreasing natural frequency we may decrease the retarding moment and, in consequence, decrease resonance amplitudes of oscillations as well as the power of the engine necessary for passing through the resonance zone.

Taking into account dependency of vibrational moment on natural frequencies we may assume that the most significant retarding effect is exerted by a particular vibrational moment , whose frequency is , as a rule, the highest for the range of machines under consideration (usually $p_\varphi > p_x \approx p_y; p_\varphi \approx p_y l / \rho, l > \rho$).

Thus, for instance, in the case of damper application for decreasing the level of oscillations at passing through the resonance the mounting of only one damper of rotational oscillations will be enough.

Since the changing of vibrational moment components is of strongly resonant character, it is advisable to choose (9) frequencies p_x, p_y, p_φ different, to separate corresponding to horizontal, vertical and rotational carrying body oscillations maxima of retarding vibrational moment in time.

Let us consider a particular case of the system when the axle of unbalanced rotor passes through the centre of the working camera masses (Fig. 3). The exciter axle and attaching chamber spring points are in the same plane ($\beta \approx 0$). Thus, carrying body performs only transitional motion in plane $x0y$.

In this case, according to (9), we have the following expression of vibrational mo-

ment.

$$V^{(1)}(\omega) = -\frac{(m\varepsilon\omega)^2}{M}[\frac{n_x}{B_x^2} + \frac{n_y}{B_y^2}]. \tag{11}$$

In particular, when $c_x \approx c_y, \beta_x \approx \beta_y$, we have.

$$V^{(1)}(\omega) = -2\frac{(m\varepsilon\omega)^2}{M}\frac{n_x}{(1-\lambda_x^2)^2 + 4n_x^2}. \tag{12}$$

This formula differs from that presented in work (4) only by coefficient 2. Hence, the value of vibrational moment in the case of plane oscillations of symmetric system is two times as much as at rectilinear ones.

4 Second approximation. Semislow oscillations of exciter rotor.

For further analysis of rotor motion at passing through the resonance zone we shall use methods offered for investigation of the simplest system in work [7].
We assume $\varphi_1 = \varphi_1^{(2)} = \omega t + \psi, x = x^{(1)} + x^{(2)}, y = y^{(1)} + y^{(2)}, \varphi = \varphi^{(1)} + \varphi^{(2)}.$
Then we come to the following system of equations for ψ and $x^{(2)}, y^{(2)}, \varphi^{(2)}$:

$$
\begin{aligned}
I\ddot{\psi} + k\dot{\psi} &= m\varepsilon\{[\ddot{x}^{(1)} + \ddot{x}^{(2)} - (\ddot{\varphi}^{(1)} + \ddot{\varphi}^{(2)})h]\sin(\omega t + \psi)+ \\
&\quad + (\ddot{y}^{(1)} + \ddot{y}^{(2)})\cos(\omega t + \psi)\} - m\varepsilon\langle(\ddot{x}^{(1)} - \ddot{\varphi}^{(1)}h)\sin\omega t + \ddot{y}^{(1)}\cos\omega t\rangle, \\
M\ddot{x}^{(2)} &+ \beta_x\dot{x}^{(2)} + c_x x^{(2)} = \\
&= m\varepsilon[(\dot{\omega} + \ddot{\psi})\sin(\omega t + \psi) + (\omega + \dot{\psi})^2\cos(\omega t + \psi) - \omega^2\cos\omega t], \\
M\ddot{y}^{(2)} &+ \beta_y\dot{y}^{(2)} + c_y y^{(2)} = \\
&= m\varepsilon[(\dot{\omega} + \ddot{\psi})\cos(\omega t + \psi) + (\omega + \dot{\psi})^2\sin(\omega t + \psi) + \omega^2\sin\omega t], \\
J\ddot{\varphi}^{(2)} &+ \beta_\varphi\dot{\varphi}^{(2)} + c_\varphi\varphi^{(2)} = \\
&= m\varepsilon h[(\dot{\omega} + \ddot{\psi})\sin(\omega t + \psi) + (\omega + \dot{\psi})^2\cos(\omega t + \psi) - \omega^2\cos\omega t].
\end{aligned} \tag{13}
$$

For the solution of system (13) we shall use the method of direct separation of motions assuming that

$$\psi = \Psi + \gamma, x^{(2)} = X + \delta_x, y^{(2)} = Y + \delta_y, \varphi^{(2)} = \Phi + \delta_\varphi, \tag{14}$$

where Ψ, X, Y, Φ are slow and $\gamma, \delta_x, \delta_y, \delta_\varphi$ -fast 2π-periodic in fast time $\tau = \omega t$ components with average zero values.
Now let us come to slow and fast motions equations. In the bounds of the applied method fast motions equations may be solved approximately, without committing a serious error in slow motions equations. It is enough to reduce the problem after having obtained slow motions equations for variable Ψ in assumption that fast

variable γ is small in comparison with Ψ and values $x^{(2)}, y^{(2)}, \varphi^{(2)}$ -are small in comparison with $x^{(1)}, y^{(1)}, \varphi^{(1)}$ [7]. Having substituted the first expression (14) into the first equation of system (13) we shall come to the following equation for the slow (to be more exact, semislow) component Ψ:

$$
I\ddot{\Psi} + k\dot{\Psi} = m\varepsilon\langle(\ddot{x}^{(1)} - h\ddot{\varphi}^{(1)})\sin(\omega t + \Psi) + \ddot{y}^{(1)}\cos(\omega t + \Psi) -
$$
$$
-\langle(\ddot{x}^{(1)} - h\ddot{\varphi}^{(1)})\sin\omega t + \ddot{y}^{(1)}\cos\omega t\rangle\rangle.
$$
(15)

Having performed averaging in the right part (15) with account of expression (7) and (8) we present the equation in the form obtained in [7] for the system with rectilinear oscillations of carrying body

$$
\ddot{\Psi} + 2n_1\dot{\Psi} + B\sin\Psi - P\sin^2\frac{\Psi}{2} = 0,
$$
(16)

here

$$
2n_1 = k/I, \, B = b_x + b_y + b_\varphi, \, P^2 = \rho_x^2 + \rho_y^2 + \rho_\varphi^2,
$$
$$
b_x = \frac{(m\varepsilon\omega^2)^2}{2MI}\frac{p_x^2 - \omega^2}{(p_x^2 - \omega^2)^2 + 4n_x^2\omega^4}, \rho_x^2 = \frac{(m\varepsilon\omega^2)^2}{2MI}\frac{2n_x\omega^2}{(p_x^2 - \omega^2)^2 + 4n_x^2\omega^4},
$$
$$
b_y = \frac{(m\varepsilon\omega^2)^2}{2MI}\frac{p_y^2 - \omega^2}{(p_y^2 - \omega^2)^2 + 4n_y^2\omega^4}, \rho_y^2 = \frac{(m\varepsilon\omega^2)^2}{2MI}\frac{2n_y\omega^2}{(p_y^2 - \omega^2)^2 + 4n_y^2\omega^4},
$$
$$
b_\varphi = \frac{(m\varepsilon\omega^2)^2h^2}{2JI}\frac{p_\varphi^2 - \omega^2}{(p_\varphi^2 - \omega^2)^2 + 4n_\varphi^2\omega^4}, \rho_\varphi^2 = \frac{(m\varepsilon\omega^2)^2h^2}{2JI}\frac{2n_\varphi\omega^2}{(p_\varphi^2 - \omega^2)^2 + 4n_\varphi^2\omega^4}.
$$
(17)

It should be noted that equation (16), as in [7], is an equation of semislow (or semi-fast) oscillations of exciter rotor angular velocity with respect to uniform rotation (equation of "internal pendulum" oscillations); in the case of consideration of small oscillations, having linearized equation (16) we may present it in classical form

$$
\ddot{\Psi} + 2n_1\dot{\Psi} + B\Psi = 0.
$$

At satisfaction of condition $\dot{\omega} << \omega^2$ frequency of rotor rotational speed ω changes slowly and value $q = \sqrt{|B|}$ is frequency of small free oscillations of the linearized model of internal pendulum (without account of the force of resistance).
Let $n_x \approx n_y, p_x \approx p_y$; then the expression for coefficicul B may be presented in the form

$$
B = b_x(2 + z_b\frac{h^2}{\rho^2})
$$
(18)

where

$$
z_b = \frac{p_\varphi^2 - \omega^2}{p_x^2 - \omega^2}\frac{(p_x^2 - \omega^2)^2 + \beta_x^2\omega^2/M^2}{(p_\varphi^2 - \omega^2)^2 + \beta_\varphi^2\omega^2/J^2}.
$$

It should be noted that if p_x-is the small of natural frequency, $z_b \leq 1$. It follows from the analysis of formulas (17), (18), that frequency q of semislow free oscillations of rotor speed in case of relative proximity of all natural frequencies for the system with plane motion of the working head is, approximately, $\sqrt{3}$ times higher that the frequency q_x for the system with one oscillatory degree of freedom. It is easy to establish that the higher any of natural frequency is, the less its contribution to value q is; acquires its maximal frequency q value in the case of equality of all natural frequencies. Fig. 4. presents plots of variations of frequency q in preresonance zone $(p_x = 30\sec^{-1}, p_y = 30\sec^{-1}, p_\varphi = 44\sec^{-1})$ for the systems with one, two and three oscillatory degrees of freedom.

Fig. 5. presents plots of variations of frequency q in preresonance zone for the systems with three oscillatory degrees of freedom for different values of viscous resistance coefficients $\beta = \beta_x = \beta_y/1, 1 = \beta_\varphi/0,05$.

Conclusions, made in work [7], about the validity of equation (16) for the system with one oscillatory degree of freedom apply to the cases with two or three degrees of freedom as well.

So, according to [7], it is necessary for the validity of equation (16) that frequency q should be considerably lower than ω, that is, assumption, of relative rates of variables Ψ and $x^{(2)}, y^{(2)}, \varphi^{(2)}$, changing should be of satisfied. Practically, the satisfaction of inequality $q/\omega < 1/3$ will be enough. Then, for the considered system with two oscillatory degree of freedom, for example, it will be easy to come to the condition of validity of equation (16) for any $\lambda = \omega/p$ in the form

$$\frac{2}{9}\nu(1 + \nu) > \eta^2,$$

where

$$\nu = \frac{n_x}{p_x}, \eta = \frac{m\varepsilon}{\sqrt{2MI}}.$$

The last inequality in dimential form looks as follows

$$\frac{m^2\varepsilon^2}{2MI} < \frac{2}{9}\frac{\beta_x}{Mp_x}, \tag{19}$$

It should be noted that this inequality differs from that obtained in [7] only by numerical coefficient.

Let us go on with the analysis of equation (16). At $B > 0$ the solution $\Psi = \Psi_1 = 0$, corresponding to "lower" position of internal pendulum, is stable and at $B < 0$ the solution $\Psi = \Psi_2 = \pi$ corresponding to "upper" position is stable.

Therefore, solution $\Psi_1 = 0$ is stable in preresonance zone of variations of frequency $\omega < p_{min}$ where p_{min}-is the smallest of values p_x, p_y, p_φ-and in postresonance zone solution $\Psi_2 = 0$ is stable. Therefore, as in the case of oscillatory system with one degree of freedom, we may say that the internal pendulum turns over in the postresonance zone of frequencies $\omega > p_{max}$.

Sufficient distinction of the system under consideration is the fact that in intermediate zone $p_{min} < \omega < p_{max}$ pendulum may have time to turn over several times. In other words, complicated behavior of the system may be expected in the mentioned

zone. It is natural, that such effect may tace place in the system with any number
of oscillatory degrees of freedom.

The obtained results are corroborated by numerical experiment. Fig. 6. shows the
effect of the origin of semislow oscillations of exciter rotor angular velocity close by
resonance zone in the case of the rotor "sticking" in resonance zone for the systems
with one and two oscillatory degrees of freedom with parameters $M = 39kg, m =
3.2kg, \varepsilon = 0.037m, l = 0.23m, I = 0.006kg \cdot m^2, c_x = c_y = 45000N/m, \beta_x = \beta_y =
135kg/sec$

According to the presented plots, the ratio of frequencies of semislow free oscillations
of exciter rotor speed for such oscillatory systems is roughly, 1.4 as it should be,
according to formula (17)

In Fig. 7. plots of semislow free oscillations of rotor speed in preresonance zone
of at different values of coefficient of viscous resistance β. According to the plots,
a tenfold increase of resistance along the coordind q leads to 1.4 fold decrease of
frequency.

Along with it, more pronounced increase of oscillations damping rate is observed.

It should be noted that fast oscillations of angular velocity of rotor rotation with
frequency 2ω are absent in the considered symmetrical system with two degrees of
freedom while they are well visible for the system with one degree of freedom (Fig.
6). It is easy to establish that corresponding oscillations for the last system are
determined by expression $\dot{\psi} = \dfrac{m^2\varepsilon^2\omega}{4IM\sqrt{(1-\lambda_x^2)^2+\beta_x^2/M^2\omega^2}}\cos 2\omega t$; the system with two
degrees (case $n_x = n_y, p_x = p_y$)-$\dot{\psi} = 0$.

5   Findings

The work deals with the problem of passing the resonance frequency zone at start
and run-out of vibrational machine with inertial exciter of oscillations. The case have
been studied when oscillatory part of the system is linear and is a plane-parallely
oscillating rigid body. As in the simplest case of the system with one oscillatory
degree of freedom, the problem is comparatively, simply solved, by application of
the method of direct separation of motions coupled with the method of successive
approximations.

Expression for the retarding vibrational moment which must be overcome by the
engine at passing through the resonance zone consists in the considered case with
three components, corresponding to each of three frequencys of free oscillations of
the body.

These components are of pronouncedly manifested resonance character. Accord-
ingly, the obtained expression for the square of the frequency of semislow oscillations
of the internal pendulum (rotor "swinging") also consists of tree components.

As in the simples system, this pendulum as if turns over at passing through reso-
nance frequency: its "lover" position is stable in postresonance zone. In the interval
between the smallest and the greatest resonance frequencies stable positions may
alternate. A complicated behavior of the system may be expected in this interval.

Absence of fast oscillations of rotor with doubled frequency of rotation in the case of
symmetry of the oscillatory part of the system is a peculiar feature of the considered

system.

The carried out analytical investigation showed good conformity to the results of numerical modeling.

References

[1] Blekhman I.I. Synchronization in Nature and Technology. Moscow: Nauka, 1981. - 351 p. (in Russian).

[2] 2. Oscillations of nonlinear mechanical systems. Vibration in technology: Handbook in 6 vol., 2 (Mashinostrojenie, Moskow, 1978). - 551 p. (in Russian).

[3] F.F. Alifov, K.V. Frolov. Interaction of nonlinear oscillatory systems with sources of power. Moscow: Nauka, 1985. - 328 p.(in Russian).

[4] Blekhman I.I.Vibrational mechanics, Fizmatlit, Moscow - 400 (in Russian). English translation : Vibrational mechanics. Singapore, world Scientific, 2000. -509 p. (in Russian).

[5] Fildin A. Nonlinear Oscillations in Mechanical Engineering. Berlin, Heidelberg. Springer-Verlag. 2006. - 358 p.

[6] Krasnopolskaya T.Z., Shvets A. Yu. Regular and random dynamics of the system with limited excitation. Moscow - Izhevsk, 2008. - 280 p. (in Russian).

[7] Blekhman I.I., Indieytshev D.A., Fradkov A.I. Slow motions in systems with inertial excitation of oscillations // Problems of machine building and reliability of machines, Ni1 2008. 25-31. (in Russian).

[8] Rand R.H., Kinsey R.J., Mingori D.L. Dynamics of spin-up through resonance //Intern. J. of Nonlinear Mechanics, vol. 27, Ni. 3, 1992, pp. 489-502.

[9] Balthazar J.M., Mook D.T., Weber H.I. et al. An overview on non-ideal vibrations // Meccanica 38 (6): 613-621, 2003.

[10] Zniber A. Quinn D.D. Resonance capture in a damped three-degree-of-freedom system: Experimental and analytical comparison // Intern. Of Nonlinear Mechanics, 41 (10): 1128-1142, 2006.

[11] Tomchin D.A., Fradkov A.I. Control of rotor passing through the resonance zone on the basis of the method of velocity gradient// Problems of machine building and reliability of machines, Ni5 2005. 66-71. (in Russian).

Influence of processing conditions on the phase composition and the chemical properties

Natalia V. Bukrina   Anna G. Knyazeva

bookr@mail.ru

Abstract

In this work we are investigated numerically the model of TiN coating modification during Al and B ion bombardment. The phase and chemical composition of coating in the arbitrary moment of time and the end of treatment is investigation results by the change of technology parameters. We showed that the diffusion and thermal stresses are segregated obviously only in the separated particular cases, based on idea of generalized plane stress. In the simple case the task is reduced to that on the stress state of a plate with properties varying with thickness. For the first approximation we used the known problems of thermoelasticity, including the existing analytical solutions for the estimation of thermal stresses in the material in different particular cases. There is qualitative agreement for the numerical investigation results of the model with experimental date.

1   Introduction

Coatings based on titanium nitride TiN have been widely used in practice for the purpose of increasing the wear resistance of cutting tools. However, more detailed investigations of the properties of these coatings have revealed a number of disadvantages that have limited the prospects of their use in industry. In particular, TiN-based coatings exhibit a low oxidation resistance.

The use of high-energy ion beam bombardment makes it possible to synthesize coatings with a structure and phase composition varying in depth, i.e. the so-called gradient coatings [1-3].

Experimental investigations of the structure of the coating subjected to ion beam treatment cannot provide detailed information that is necessary for revealing the processes responsible for the formation of a particular structure. In this case, additional information can be obtained from the mathematical simulation. Furthermore, the appropriate simulation of the technological process is necessary for the optimization of the technological procedures and for the proper choice of their parameters.
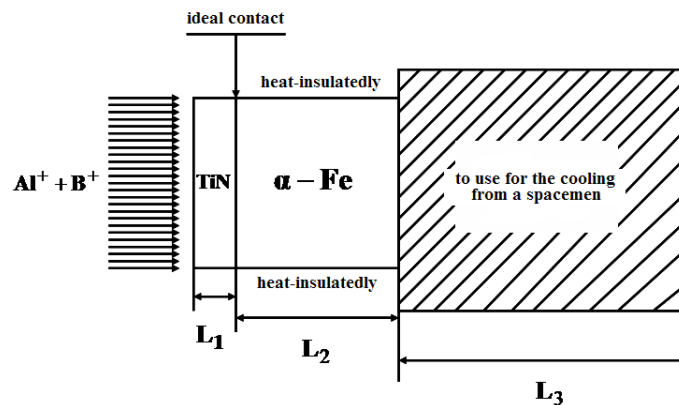
Figure 1: Conventional scheme of coating modification by a combined ion beam.

2 Mathematical formulation of the problem

Let us assume that a titanium nitride (TiN) coating is deposited in some way or another on a sample of α iron (Fig. 1). Then, the sample is treated with a beam of Al+ and B+ ions. The ion beam treatment leads to the implantation of ions into the surface layer of the coating followed by its heating. The substrate is also heated as a result of heat conduction. A more intensive heat removal can be achieved when the substrate contacts a material with high thermal conductivity, which is not always the case. Additional heat losses occur through radiation from the surface. The ion beam treatment is accompanied by the redistribution of elements and the formation of different compounds and phases in the surface layer of the coating.

If heating surface is homogeneous, lateral surfaces are heat-insulated and the sample has sufficiently large thickness then the heat conduction and diffusion problems can be considered as one-dimensional. Due to smallness of the coating and the substrate (L_1 and L_2) in comparison with heat penetration width which can be formed in the sample during the observation period the model is simplified and instead of the heat conduction equation we get the heat-balance equation. Full mathematical formulation of the problem is described in [4].

The problem is solved numerically with the use of the special algorithm described in [5]. According to this algorithm, the heat conduction and the diffusion problems are solved using different but matched difference schemes. Since the temperature distribution over the coordinate is ignored in the model under consideration, the algorithm is reduced to the matching of the time steps in the diffusion and heat sub-problems according to the characteristic rates of the heat conduction and diffusion processes. The system of kinetic equations is solved independently by the Runge-Kutta method with the automatic choice of the step at each step of solving the heat problem.

3 Analysis of numerical results

The time dependencies of the average temperature of the sample for varying irradiation modes are plotted in Fig.2. It is evident that the higher the irradiation
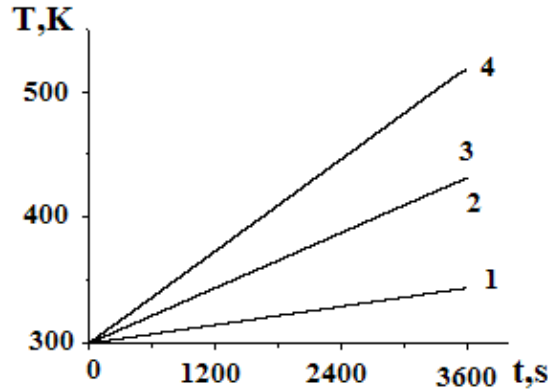
Figure 2: Time dependencies of the sample temperature at different irradiation doses $1. - D = 10^{17}$ ions/cm^2, $2. - D = 3.25 \cdot 10^{17}$ ions/cm^2, $3. - D = 4 \cdot 10^{17}$ ions/cm^2, $4. - D = 6 \cdot 10^{17}$ ions/cm^2.

dose, the higher the temperature. At the irradiation dose $D = 10^{17}$ ions/cm^2, the temperature doesn't exceed 30-40ºC, which is in agreement with the experimental data.

Each calculation provides complete information on the dynamics of the distribution of the molar concentration of the "unbound" elements and chemical compounds, as well as the distribution of atomic concentrations of the Ti, Al, B, and N elements at an arbitrary instant of time and toward the end of the treatment process.

Numerical results and the experimental data at irradiation dose $D = 10^{17}$ ions/cm^2 are presented in Table 1. It is seen, that agreement of the results is rather satisfactory. Numerical concentration values do not agree with the experimental data as far as parameters of the model have been assessed with a certain error. For instance, the diffusion coefficients used in our calculations are most likely underestimated and do not correspond to the diffusion coefficients D_k in the solid solution. In the real experiment, the treatment depth increases with an increase in the irradiation dose. This can be explained by acceleration of diffusion, for example, due to the activation of the elements in the surface layer [6, 7], which is ignored in the model.

Table 1. Comparison of the calculation data of relative atomic concentrations of pure elements Ti, N, Al, B with the experimental data [4] at irradiation dose $D = 10^{17}$ ions/cm^2

elements	Ti	N	Al	B
$C_{at}, \%$, experiment	50	38	9	5
$C_{at}, \%$, theory	56	28	9.2	6.8

It should be noted that in the result of irradiation by an ion beam at $D = 4 \cdot 10^{17}$ ions/cm^2 the content of the TiAlBN new phase amounts to 37% what also agrees with the experimental data [4].

4 Evaluation of stresses and deformations in the diffusion zone

Assuming that deformations are small, we have used known models of thermo- and masselasticity to evaluate stresses and deformations [8, 9].

In the general case a stress problem includes equilibrium equations, Duamel-Neumann relations and compatibility equations incurring from Cauchy equations [10, 11].

We will examine the particular case of a slab with thickness graded properties. The slab is completely free from volume surface forces. The temperature and the concentrations are varying with the thickness only, i.e. $\mathsf{T} = \mathsf{T}(z)$.

Formulation of the problem is described in [12].

Finally, we have different relations for different layers.

Thus, stresses in the coating can be evaluated by the following formula:

$$
\begin{aligned}
\sigma_{xx,1} = \sigma_{yy,1} = \frac{\mathsf{E}_1}{1 - \nu_1}\Big[-\alpha_{\mathsf{T},1}(\tilde{\mathsf{T}} - \mathsf{T}_0) - \\
- \sum_{k=1}^{n} \alpha_k(y_k - y_{k0}) + \mathsf{C}_1 + \mathsf{C}_2 z \Big], \quad 0 \leq z \leq \mathsf{L}_1.
\end{aligned}
\tag{1}
$$

The first term in (1) is a function of t only, the rest of the terms are functions of t, z. This formula is for stresses in the diffusion zone.

In two other layers we have

$$
\sigma_{xx,2} = \sigma_{yy,2} = \frac{\mathsf{E}_2}{1 - \nu_2}(-\alpha_{\mathsf{T},2}(\tilde{\mathsf{T}} - \mathsf{T}_0) + \mathsf{C}_1 + \mathsf{C}_2 z), \quad \mathsf{L}_1 \leq z \leq \mathsf{L}_1 + \mathsf{L}_2,
\tag{2}
$$

$$
\sigma_{xx,3} = \sigma_{yy,3} = \frac{\mathsf{E}_3}{1 - \nu_3}(-\alpha_{\mathsf{T},3}(\tilde{\mathsf{T}} - \mathsf{T}_0) + \mathsf{C}_1 + \mathsf{C}_2 z), \quad \mathsf{L}_1 + \mathsf{L}_2 \leq z \leq \mathsf{L}_1 + \mathsf{L}_2 + \mathsf{L}_3.
\tag{3}
$$

Taking into account the above we can write

$$
\begin{aligned}
\tilde{\sigma}_{xx,2} = \tilde{\sigma}_{yy,2} &= \frac{\mathsf{E}_2}{1 - \nu_2}\Big[-\alpha_{\mathsf{T},2}(\tilde{\mathsf{T}} - \mathsf{T}_0) + \frac{1}{\mathsf{L}_2}\int_{\mathsf{L}_1}^{\mathsf{L}_1 + \mathsf{L}_2}(\mathsf{C}_1 + \mathsf{C}_2 z)\mathrm{d}z \Big] = \\
&= \frac{\mathsf{E}_2}{1 - \nu_2}\Big[-\alpha_{\mathsf{T},2}(\tilde{\mathsf{T}} - \mathsf{T}_0) + \mathsf{C}_1 + \frac{\mathsf{C}_2}{\mathsf{L}_2}\Big(\frac{(\mathsf{L}_1 + \mathsf{L}_2)^2}{2} - \frac{\mathsf{L}_1^2}{2}\Big) \Big],
\end{aligned}
\tag{4}
$$

$$
\begin{aligned}
\tilde{\sigma}_{xx,3} = \tilde{\sigma}_{yy,3} &= \frac{\mathsf{E}_3}{1 - \nu_3}(-\alpha_{\mathsf{T},3}(\tilde{\mathsf{T}} - \mathsf{T}_0) + \frac{1}{\mathsf{L}_3}\int_{\mathsf{L}_1 + \mathsf{L}_2}^{\mathsf{L}_1 + \mathsf{L}_2 + \mathsf{L}_3}(\mathsf{C}_1 + \mathsf{C}_2 z)\mathrm{d}z) = \\
&= \frac{\mathsf{E}_2}{1 - \nu_3}\Big[-\alpha_{\mathsf{T},3}(\tilde{\mathsf{T}} - \mathsf{T}_0) + \mathsf{C}_1 + \frac{\mathsf{C}_2}{\mathsf{L}_3}\Big(\frac{(\mathsf{L}_1 + \mathsf{L}_2 + \mathsf{L}_3)^2}{2} - \frac{(\mathsf{L}_1 + \mathsf{L}_2)^2}{2}\Big) \Big].
\end{aligned}
\tag{5}
$$

These expressions describe the macroscopic stresses which incorporate the contribution of the diffusion zone via C_1 and C_2.

In a similar manner we proceed with evaluation of deformations in layers 1–3:

$$\varepsilon_{xx,1} = \varepsilon_{yy,1} = C_1 + C_2 z, \tag{6}$$

$$\tilde{\varepsilon}_{xx,2} = \tilde{\varepsilon}_{yy,2} = C_1 + \frac{C_2}{L_2}\left[\frac{(L_1 + L_2)^2}{2} - \frac{L_1^2}{2}\right],$$

$$\tilde{\varepsilon}_{xx,3} = \tilde{\varepsilon}_{yy,3} = C_1 + \frac{C_2}{L_3}\left[\frac{(L_1 + L_2 + L_3)^2}{2} - \frac{(L_1 + L_2)^2}{2}\right].$$

and

$$\varepsilon_{zz,1} = \frac{K_1\left(3\alpha_{T,1}(\tilde{T} - T_0) - \sum_{k=1}^{n}\alpha_k(y_k - y_{k0})\right) - 2\lambda_1\varepsilon_{xx,1}}{2\mu_1 + \lambda_1}$$

$$\tilde{\varepsilon}_{zz,2} = \frac{K_2\left(3\alpha_{T,2}(\tilde{T} - T_0)\right) - 2\lambda_2\tilde{\varepsilon}_{xx,2}}{2\mu_2 + \lambda_2} \qquad \tilde{\varepsilon}_{zz,3} = \frac{K_3\left(3\alpha_{T,3}(\tilde{T} - T_0)\right) - 2\lambda_3\tilde{\varepsilon}_{xx,3}}{2\mu_3 + \lambda_3}$$

For numerical evaluation of stresses in the diffusion zone and the macroscopic stresses we need to know mechanical properties E_j, ν_j, $j = 1.2.3$ and coefficients $\alpha_{j,k}$ and α_T. Obviously, E_1, ν_j change with change in composition, but dependencies $E_1(y_k)$, as a rule, are undetermined. Hence, we will limit ourselves to certain effective values (as it was taken into account in deriving of formulas). Let us assume

$$E_1 = 65 \cdot 10^3, E_2 = 195 \cdot 10^3, E_3 = 205 \cdot 10^3 \mathrm{N/cm}^2; \nu_1 = 0.3, \nu_2 = 0.28, \nu_3 = 0.3$$

We will use the approximate approach described in [13, 14] for evaluation of $\alpha_{j,k}$. According to this approach the most widely used evaluation of a solute lattice contraction coefficient has the next form

$$\alpha_k = \frac{1}{3}\frac{\omega}{\sum_{(i)}\omega_i} \tag{7}$$

Here ω is the atomic (molecular, molar) volume of the component with the number k in its phase.
Evaluation of the coefficients $\alpha_{j,k}$ by the formula (7) gives

$$\alpha_{Ti} \approx 0.083, \alpha_N \approx 0.136, \alpha_{Al} \approx 0.078, \alpha_B \approx 0.036.$$

For given experimental conditions the numerical stress analysis showed that an increase in the irradiation dose leads to an increase in the stresses in the coating. The
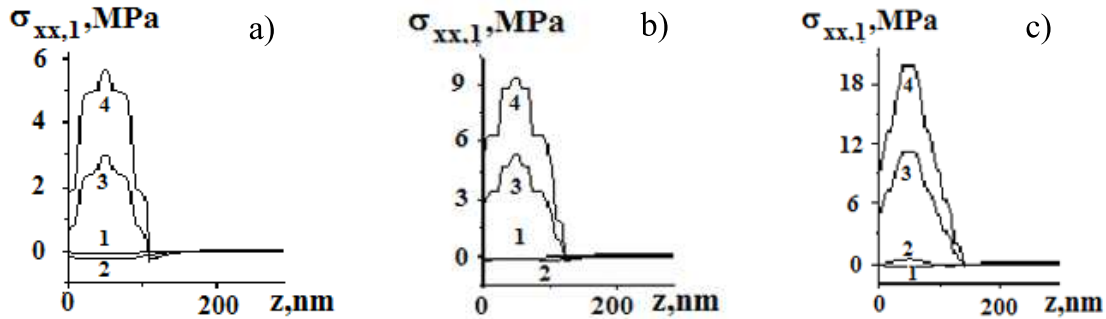
Figure 3: Spatial distributions of the stresses in the coating for a varying the irradiation dose for the initial temperature of the surface $T_0 = 300K$ at instants of time $t : 1. - 0.25; 2. - 1.25; 3. - 6; 4. - 10$ s. a). $q_{m3} = 2 \cdot 10^{-10}$, $q_{m4} = 1.5 \cdot 10^{-10}$ mol/(cm^{2}s); b). $q_{m3} = 4 \cdot 10^{-10}$, $q_{m4} = 3 \cdot 10^{-10}$ mol/(cm^{2}s)); c). $q_{m3} = 8 \cdot 10^{-10}$, $q_{m4} = 6 \cdot 10^{-10}$ mol/(cm^{2}s)
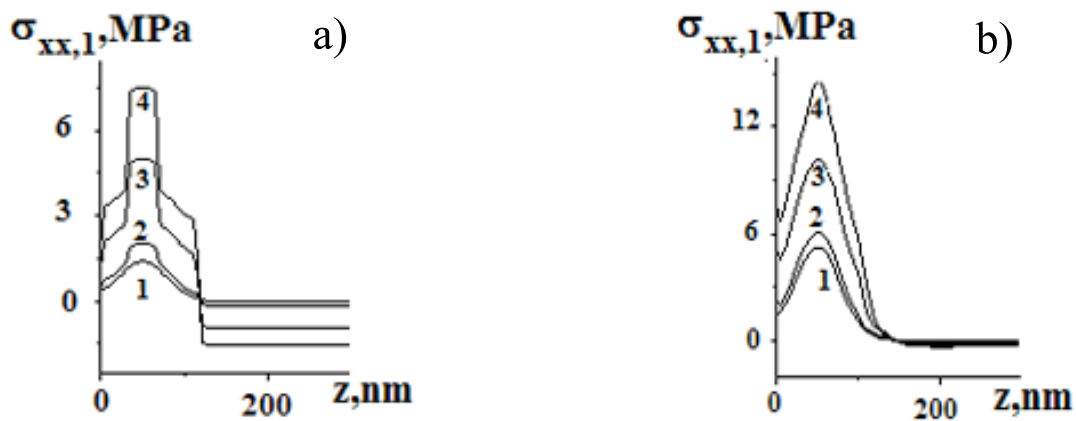
Figure 4: Spatial distribution of the stresses in the coating for a varying the irradiation dose for the initial temperature of the surface $T_0 = 773$ K at instants of time $t : 1. - 0.25; 2. - 1.25; 3. - 6; 4. - 10$ s. a). $q_{m3} = 2 \cdot 10^{-10}$, $q_{m4} = 1.5 \cdot 10^{-10}$ mol/(cm^{2}s); b). $q_{m3} = 4 \cdot 10^{-10}$, $q_{m4} = 3 \cdot 10^{-10}$ mol/(cm^{2}s).

maxima in the stress distributions are observed in the region corresponding to the maxima of implanted ions (fig. 3, a-c).

For high irradiation doses the maximum in the stress distribution diffuses (fig. 3,c). This is connected with redistribution of the elements as a result of the diffusion.

For an increasing in the initial temperature up to $T_0 = 773$ K and fixed flow q_{m3}, q_{m4} a qualitative change in behavior of stresses connected with the preceding activation of the diffusion and chemical transformations is observed (fig. 4).

Complete calculation corresponding to the real time of treatment (1 hour) shows that the values of stresses in the diffusion zone are very high (about 6000 MPa) and it correlates with the experimental data [15]. Numerical calculations of stresses can disagree with stresses observed in reality as far as there is a number of effects (such as change of thermophysical and mechanical properties) which have not been taken into account in the model under consideration.

5   Conclusion

We have examined the problem of modification of nitride coating by a combined ion beam accounting for formation of chemical compositions and phases with ions.

It was revealed that values of the diffusion coefficients corresponding to the reference data which was taken in our calculations are understated and do not correspond to values of these coefficients under conditions of high-energy treatment.

We have proposed a method of evaluation of stresses which appear in the diffusion zone during the process of material treatment by ion beams. Our evaluations take into account a contribution of not only diffusion but also chemical processes to irreversible deformations.

Theoretical results agree sufficiently with the experimental data.

References

[1] V. P. Sergeev. Superhard nanocomposite coatings based on titanium nitride alloyed by Cu, Al or C. / In book: Deformation, localization, fracture. Collected articles / Ed. by .L.B. Zuev (NTL Press, Tomsk, 2005). 1183-1193, 2002.

[2] V.E. Panin, V.P. Sergeev, M.V. Fedorisheva, et al. Structure and mechanical properties of nanocrystalline coatings based on titanium and aluminum carbides and nitrides // Fiz. Mezomekh. 2004, 7 (2) - pp.321-324.

[3] G.E. Remnev, V.A. Tarbokov Hardening of a carbide by method of preparatory treatment by high-energy ion beam and by deposition of nitride-titan coating // Fiz. Mezomekh. 2004, 7 (2) - pp. 329-332.

[4] N.V. Bukrina, A.G. Knyazeva and V.P. Sergeev Experimental and numerical studies of the formation of transient regions in nitride coatings under bombardment by a combined ion beam // Poverkhnost. Rentgenovskie, sinkhrotronnye i neitronnye issledovaniya. 2009, 1 - pp. 83 - 92.

[5] N.V. Bukrina, A.G. Knyazeva Numerical problem algorithms for nonisothermic diffusion occurred in processes of surface treatment // Fiz. Mezomekh. 2006, 9 (2) - pp. 55-62.

[6] A.G. Knyazeva, S.G.Psakh'e Diffusion of elements in activated surface layer // Fiz. Mezomekh. 2006, 9 (2) - pp. 49-54.

[7] A.G. Knyazeva, S.G.Psakh'e Simulation of non-equilibrium diffusion accompanied by internal stresses // Fiz. Mezomekh. 2005, 9 (8 Special Issue) - pp. 41-44.

[8] PalDey S., Deevi S.C. Single layer and multilayer wear resistant coatings of (Ti, Al) N: a review // Materials Science and Engineering. 2003; 342 - pp. 58 - 79.

[9] A.G. Knyazeva On simulation of irreversible processes in materials with a great number of inner interfaces // Fiz. Mezomekh. 2003; 6 (5) - pp.11-27.

[10] V.S. Eremeev Diffusion and stresses. Energoatomizdat (Moscow) 1984.

[11] B. Boley, J. Weiner Theory of thermal stresses. Mir (Moscow) 1964.

[12] N.V. Bukrina, A.G. Knyazeva About estimation of stress in the composite during impulsive energy source treatment // Mathematical modeling of the system and the process. Herald of the Permian state technical university. 2008, 16 - pp. 17-27.

[13] A.G.Knyazeva, I.L. Pobol, V.A. Romanova Stress field in diffusion zone of compound obtained by an electron-beam soldering. Fiz. Mezomekh. 2001; 4 (5) - pp. 41-53.

[14] A.G. Knyazeva Introduction in locally equilibrium thermodynamics of physico-chemical transformations in deformable mediums. Tomsk. Gos. Univ. (Tomsk) 1996

[15] V.P. Sergeev, M.V. Fedorischeva et al. Structure and mechanical properties on basis of titanium carbonitride by magnetron deposition during ion beam treatment. Perspekt. Mater. 2005; 5 - pp. 72-77.

Natalia. V. Bukrina, Academichesky Ave., 2/4, Tomsk, Russia
Anna. G. Knyazeva, Academichesky Ave., 2/4, Tomsk, Russia

Hybrid sliding mode control for motorised space tether spin-up when coupled with axial oscillation

Yi Chen   Matthew P. Cartmell

yichen@mech.gla.ac.uk, matthewc@mech.gla.ac.uk

Abstract

A specialised hybrid controller is applied for the control of motorised space tether spin-up coupled with an axial oscillation phenomenon. A six degree of freedom dynamic model of a motorised momentum exchange tether is used as the basis for interplanetary payload exchange in the context of control. The tether comprises a symmetrical double payload configuration, with an outrigger counter inertia and massive central facility. It is shown that including axial elasticity permits an enhanced level of performance prediction accuracy and a useful departure from the usual rigid body representations, particularly for accurate payload positioning at strategic points. A simulation with a given initial condition data has been devised in a connecting programme between control code written in MATLAB and dynamics simulation code constructed within MATHEMATICA. It is shown that there is an enhanced level of spin-up control for the six degree of freedom motorised momentum exchange tether system using the specialised hybrid controller.

1   Introduction

The concept of the motorised momentum exchange tether (MMET) was first proposed by Cartmell [1], and its modelling and conceptual design were developed further, in particular modelling of the MMET as a rigid body by Ziegler and Cartmell [2], and modelling of the MMET with axial elasticity by Chen and Cartmell [3]. A conceptual schematic of the MMET system with axial elasticity included is shown in Figure 1. The system is composed of the following parts: a pair of braided propulsion tether tube sub-spans, a corresponding pair of braided outrigger tether tube sub-spans, the launcher motor mass within the rotor, and the launcher motor mass within stator, the outrigger masses, and the two payload masses. The MMET is excited by means of a motor, and the model uses angular generalised co-ordinates to represent spin and tilt, together with an angular co-ordinate for circular orbital motion. Another angular co-ordinate defines backspin of the propulsion motor's stator components. The payload masses are fitted to each end of the tether sub-spans, and the system orbits a source of gravity in space, in this case, the Earth. The use of a tether means that all constituent parts of the system have the same angular velocity as the overall centre of mass (COM). As implied in Figures 1 and

2, the symmetrical double-ended motorised spinning tether can be applied as an orbital transfer system, in order to exploit momentum exchange for propelling and transferring payloads in space.
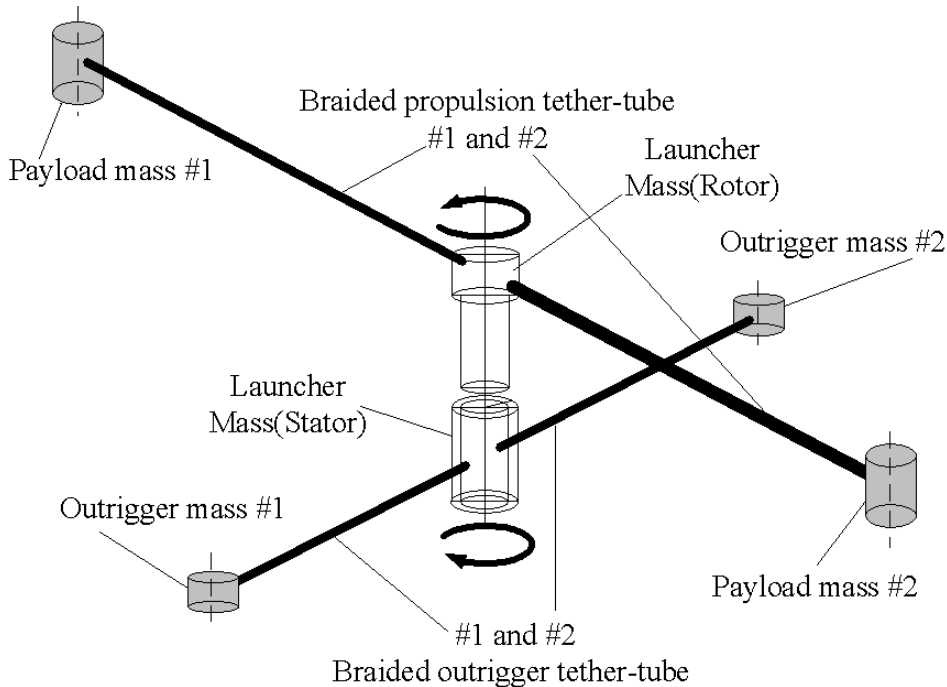
Figure 1: Conceptual Schematic of the Motorised Momentum Exchange Tether with Axial Elasticity

It has been well recognized that fuzzy logic control (FLC) is an effective and potentially robust control method for various diverse applications The FLC rule-base is generally based on practical human experience, however, the intrinsic linguistic format expression required to construct the FLC rule base makes it difficult to guarantee the stability and robustness of the control system [4].

Variable structure control (VSC) with sliding mode control was introduced in the early 1950s by Emelyanov and subsequently published in the 1960s [5], and then further developed by several other researchers [6][7]. Sliding mode control (SMC) is recognised as a robust and efficient control method for complex, high order, non-linear dynamical systems. The major advantage of sliding mode control is its low sensitivity to a system's parameter changes under various uncertainty conditions. Another advantage is that it can decouple system motion into independent partial components of lower dimension, which reduces the complexity of the system control and feedback design. However, a major drawback of traditional SMC is a propensity for chattering, which is generally disadvantageous within control systems.

In recent years, a lot of literature has been generated in the area of fuzzy sliding mode control (FSMC), and this has also covered the chattering phenomenon. The involvement of FLC in the design of a FSMC based controller can be harnessed to help to avoid the chattering problem. The smooth control feature of fuzzy logic can be helpful in overcoming the disadvantages of chattering. This is why it can be useful to merge FLC with SMC to create the FSMC hybrid [8][9][10][11][12], and the
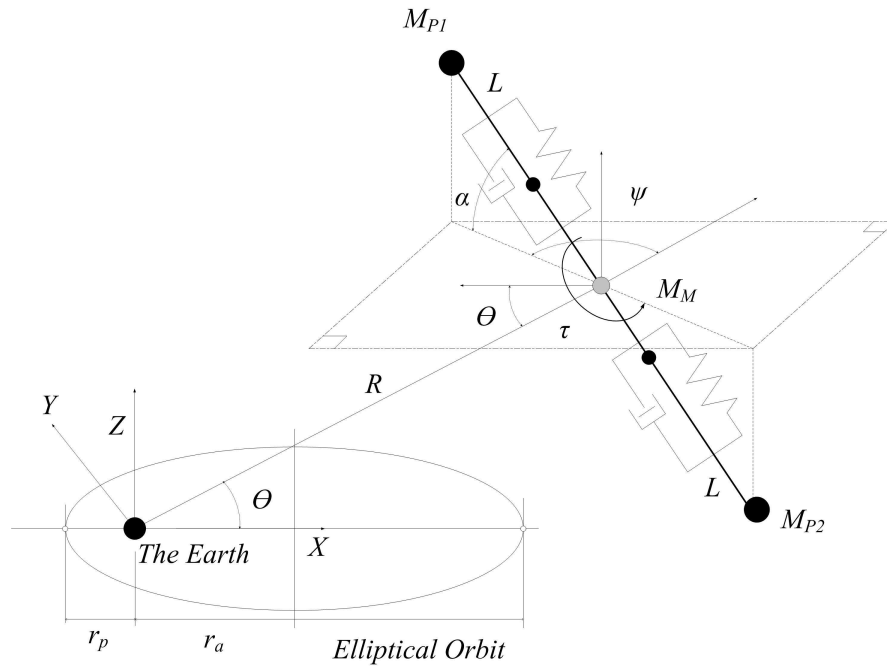
Figure 2: Modelling of the Motorised Momentum Exchange Tether with Axial Elasticity

hybrid fuzzy sliding mode control is defined as FαSMC [13], with a skyhook surface (SkyhookSMC) is applied here to control the tether sub-span length for spin-up control of the MMET system.

2 Six degree of freedom MMET Model

A six degree of freedom non-planar tether model, which includes an axial elasticity coordinate and a solid rolling coordinate, is proposed as an interim model of moderate accuracy for the MMET 6-DOF system, as shown in Figure 2. This discretised MMET system comprises a symmetrical and cylindrical double payload configuration, a cylindrical motor facility, and two axially flexible and essentially tubular tether sub-spans. In the discretised non-planar tether model, environmental effects such as solar radiation, residual aerodynamic drag in low Earth orbit and electro-dynamic forces, that may also influence the modelling, are reasonably assumed to be negligible in this context. The motor consists of a central rotor, which is attached to the propulsion tethers, and a stator which locates the rotor by means of a suitable bearing. The power supplies, control systems, and communication equipment are assumed to be fitted within the surrounding stator assembly in a practical installation. The stator also provides the necessary reaction that is required for the rotor to spin-up in a friction free environment. The motor torque acts about the motor drive axis, and it is assumed here that the motor drive axis will stay normal to the spin plane of the propulsive tethers and payloads.

The elasticity of the tether system is considered to be distributed symmetrically along each tether sub-span. The tether and the motor are connected by discrete

139
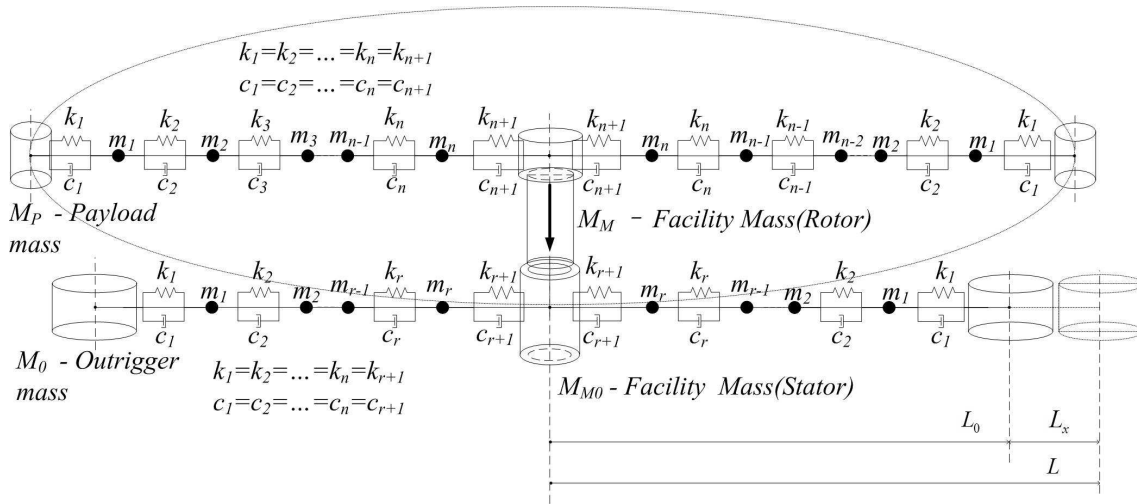
Figure 3: Modelling of Axial Elasticity for Motorised Momentum Exchange Tether [3]

spring-damper groups as shown in Figure 3. When the tether moves out of the orbital plane, the motor drive axis remains orthogonal to the spin plane, meanwhile, the motor torque will act about the principal axis through its centre of mass. The length of the discretised MMET from payload to COM, where the time variant length $L(t)$ of the tether is the sum of L_0 and $L_x(t)$, the static length and the variable elastic length of the discretised tether, respectively. There are six generalised coordinates in this model, in the form of four rotational coordinates (ψ, θ, α, γ) and two translational coordinates ($L_x(t)$, R). Coordinate ψ defines the spin-up performance of the MMET system and is the 'in-plane pitch angle'. This denotes the angle from the x_0 axis in Figure 2 to the projection of the tether onto the orbit plane. θ is the circular orbit angular position, effectively the true anomaly. α is an out-of-plane angle, from the projection of the tether onto the orbit plane to the tether, and is always within a plane normal to the orbit plane. γ defines rolling, and lies between the torque-plane and the tether-spin-plane. R is the distance from the Earth to the MMET COM, and L_x is the axial elastic length. Lagrange's equations are used to obtain the dynamical equations of motion based on the six generalised coordinates [3].

3   Hybrid Control Strategy

To make the necessary enhancement required to obtain the FαSMC method, a hybrid control law is introduced. This combines the fuzzy logic control with sliding mode control in which a sliding hyperplane surface is generated by use of a skyhook damping law. Meanwhile, because the chattering phenomenon is an acknowledged drawback of sliding mode control and is usually caused by unmodelled system dynamics, a special boundary layer is proposed around the sliding surface is also taken to solve the chattering problem [14].

A flow diagram for the FαSMC, and applying the SkyhookSMC approach, is given in
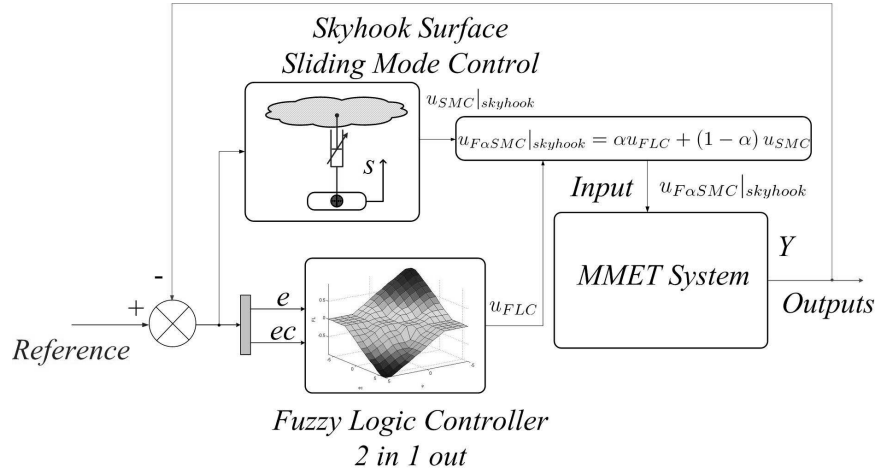
Figure 4: FαSMC flow diagram

Figure 4. The hybrid control effects of the FLC and the SkyhookSMC are combined by equation (1). In equation (1), α is a switching factor which balances the weight of the fuzzy logic control to that of the skyhook surface sliding mode control. Clearly, $\alpha = 0$ represents for SkyhookSMC, and $\alpha = 1$ represents for FLC, $\alpha \in [0,1]$.

$$u_{F\alpha SMC}|_{skyhook} = \alpha u_{FLC} + (1 - \alpha)\, u_{SMC}|_{skyhook} \tag{1}$$

3.1   Fuzzy Logic Controller Design

Fuzzy control is a practical alternative for a variety of challenging control applications since it provides a convenient method for constructing nonlinear controllers via the use of heuristic information. This may come from an operator that acts as a human-in-the-loop controller and from whom experiential data is obtained. The structure of the FLC for the the MMET system is shown in Figure 5. An 'If-Then' rule-base is then applied to describe the expert knowledge. The FLC rule-base is characterised by a set of linguistic description rules based on conceptual expertise which arises from typical human situational experience. Table 2 is the 2-in-1-out FLC rule-base table which can drive the FLC inference mechanism, and this came from previous experience gained from examining dynamic simulations for tether length changes during angular velocity control. Briefly, the main linguistic control rules are: (1) when the angular velocity decreases, the length tether increases; Conversely, when the angular velocity increases, the tether length decreases. (2) When the angular acceleration increases, the tether length increases can reduce the error between the velocity and the reference velocity; otherwise, when the angular acceleration decreases, the tether length decreases as well. A membership function (MF) is a curve that defines how each point in the input space is mapped to a membership value between 0 and 1. The MF for the MMET 6-DOF system is a Gaussian combination membership function. The inputs e and ec are interpreted from this fuzzy set, and the appropriate degree of membership is obtained [13].
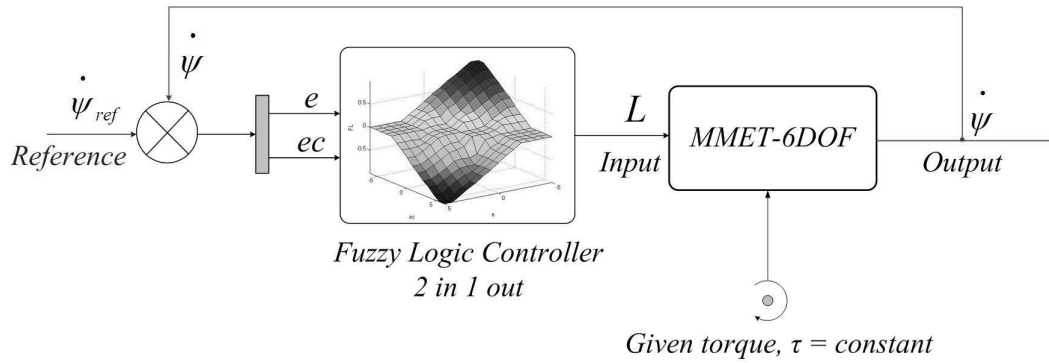
Figure 5: FLC flow diagram

Table 2: 2-in-1-out FLC rule table for MMET 6-DOF

U		EC							
		NB	NM	NS	NZS	ZE	PZS	PS	PM	PL
	NB	NB	NM	NS	NZS	PZS	PZS	PS	PM	PB
	NM	NM	NM	NZS	NZS	PZS	PZS	PZS	PM	PM
	NS	NS	NS	NZS	NZS	PZS	PZS	PZS	PS	PS
	NZS	NZS	NZS	NZS	NZS	ZE	PZS	PZS	PZS	PZS
E	ZE	PZS	PZS	PZS	ZE	ZE	ZE	PZS	PZS	PZS
	PZS	PZS	PZS	PZS	PZS	ZE	NZS	NZS	NZS	NZS
	PS	PS	PS	PZS	PZS	PZS	NZS	NZS	NS	NS
	PM	PM	PM	PS	PZS	PZS	NZS	NS	NM	NM
	PB	PB	PM	PS	PZS	PZS	NZS	NS	NM	NB

3.2 Sliding Mode Control with Skyhook Surface Design

The objective of the SkyhookSMC controller is to consider the nonlinear tether system as the controlled plant, and therefore defined by the general state-space in equation (2):

$$\dot{x} = f(x, u, t) \tag{2}$$

where $x \in R^n$ is the state vector, n is the order of the nonlinear system, and $u \in R^m$ is the input vector, m is the number of inputs. $s(e, t)$ is the sliding surface of the hyperplane, which is given in equation (3) and shown in Figure 6, where λ is a positive constant that defines the slope of the sliding surface.

$$s(e, t) = \left(\frac{d}{dt} + \lambda \right)^{n-1} e \tag{3}$$

where λ is a positive constant that defines the slope of the sliding surface. The MMET system is a second-order system, so by letting n = 2, one obtains a second-order system in which s defines the position error (e) and velocity error ($\dot{e}$) in equation (4).

142
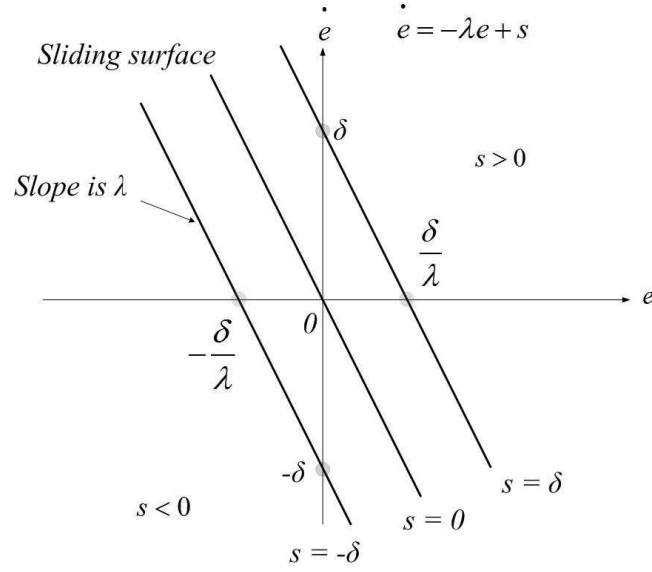
Figure 6: Sliding surface

$$s = \dot{e} + \lambda e \tag{4}$$

From equations (3) and (4), the second-order tracking problem is now replaced by a first-order stabilization problem in which the scalar s is kept at zero by means of a governing condition. This is obtained from use of the Lyapunov stability theorem, given in equation (5), and it states that the origin is a globally asymptotically stable equilibrium point for the control system. Equation (5) is positive definite and its time derivative is given in inequality (6), to satisfy the negative definite condition, that the system should satisfy the inequality in (6).

$$V(s) = \frac{1}{2}s^2 \tag{5}$$

$$\dot{V}(s) = s\dot{s} < 0 \tag{6}$$

Skyhook control strategy was introduced in 1974 by Karnopp et al [15]. In Figure 7 the basic idea is to link a vehicle body's sprung mass to the the 'stationary sky' by a controllable 'skyhook' damper, which can then reduce vertical vibrations due to all kinds of road disturbance. Skyhook control can reduce the resonant peak of the sprung mass quite significantly and thus achieves a good ride quality in the car problem. By borrowing this idea to reduce the sliding chattering phenomenon, in Figure 8, a soft switching control law is introduced for the major sliding surface switching activity in equation (7), in order to reduce the chattering and to achieve good switch quality for the FαSMC combined with SkyhookSMC.

$$u_{\text{SMC}}|_{\text{skyhook}} = \begin{cases} -c_0 \tanh\left(\frac{s}{\delta}\right) & s\dot{s} > 0 \\ 0 & s\dot{s} \leq 0 \end{cases} \tag{7}$$
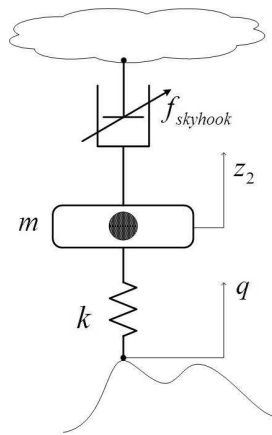
Figure 7: Ideal skyhook damper
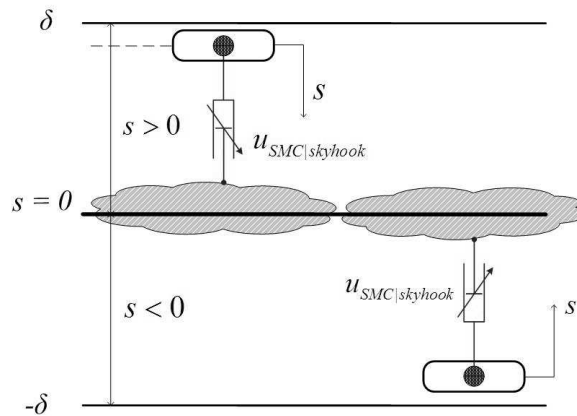
Figure 8: Sliding skyhook surface

where c_0 is an assumed positive damping ratio for the switching control law. This law needs to be chosen in such a way that the existence and the reachability of the sliding-mode are both guaranteed. Noting that δ is an asssumed positive constant which defines the thickness of the sliding mode boundary layer [14].

4   Simulation and Conclusion

Numerical results are obtained using a specially devised co-simulation toolkit of MATLAB and MATHEMATICA functions in an integrated programme to provide a new toolbox, known henceforth here as SMATLINK. This integrates the control in MATLAB/SIMULINK and the MMET modelling in MATHEMATICA. The velocity and acceleration of ψ are selected as error (e) and change-in-error (ec) feedback signals for the the MMET system's spin-up control. Unless stated otherwise all the results are generated using the following parameters for the MMET 6-DOF system and controller in Table 3.

It is easy to switch the controller between the SkyhookSMC and the FLC modes when a proper value of α is selected ($0 < \alpha < 1$), and the hybrid fuzzy sliding mode controller is generated combining FLC with a soft continuous switching Sky-

Table 3: MMET 6-DOF system parameters

N	number of mass points	20
μ	gravitational constant	3.9877848×10^{14} $m^3 s^{-2}$
M_P	propulsion tether payload mass	1000 Kg
M_M	mass of motor facility	5000 Kg
r_{Tinner}	radius of tether inner tube	0.08 m
r_{Touter}	radius of tether outer tube	0.1 m
r_M	radius of motor facility	0.5 m
r_P	radius of payload	0.5 m
r_{per}	periapsis distance	6.890×10^6 m
r_{apo}	apoapsis distance	1.0335×10^7 m
L_0	static length tether sub-span	50000 m
A	undeformed tether tube cross-sectional area	1.13097×10^{-2} m^2
ρ	tether density	970 kg/m^3
e	orbit eccentricity	0.2
ψ_0	initial angular	0.0 rad
$\dot{\psi}_0$	initial angular velocity	0.0 rad/s
τ	motor torque	2.5×10^6 Nm
c_i	tether sub-span axial damping coefficient	2×10^6 Ns/m
k_i	tether sub-span axial stiffness	2×10^9 N/m
Ke	FLC scaling gains for e	1
Kec	FLC scaling gains for ec	1
Ku	FLC scaling gains for u	21000
α	FαSMC switching factor	$\{0, 0.5, 1\}$
c_0	SkyhookSMC damping coefficient	-3000
δ	thickness of the sliding mode boundary layer	0.8
λ	slope of the sliding surface	0.0014

hookSMC law based on equation (7). All the control methods have an effect on the spin-up of the MMET 6-DOF system from the given initial conditions. The FαSMC hybrid fuzzy sliding mode control system parameters require a judicious choice of the FLC scaling gains of $\{Ke, Kec\}$ for fuzzification, Ku is the defuzzification gain factor which is used to map the control force to the range that actuators can generate practically. Similarly, the SkyhookSMC damping coefficient c_0 is required to expand the normalised controller output force into a practical range. The thickness of the sliding mode boundary layer is given by δ, and the slope of the sliding surface λ. Both data came from the previous MMET 6-DOF system spin-up simulation results without control, which are given in Table 3. In this simulation the FαSMC is used, with $\alpha = 0.5$ to balance the control weight between the FLC and the SkyhookSMC modes.

Different values of $\alpha = \{0.0, 0.5, 1.0\}$ can be used for $\{SkyhookSMC, F\alpha SMC, FLC\}$ control, respectively, for the MMET 6-DOF system. Figure 9 gives the time responses for the spin-up velocity $\dot{\psi}$, with different values of α, for the spin-up. These results show that all the control methods have an effect on the spin-up of the MMET system from the given initial conditions.
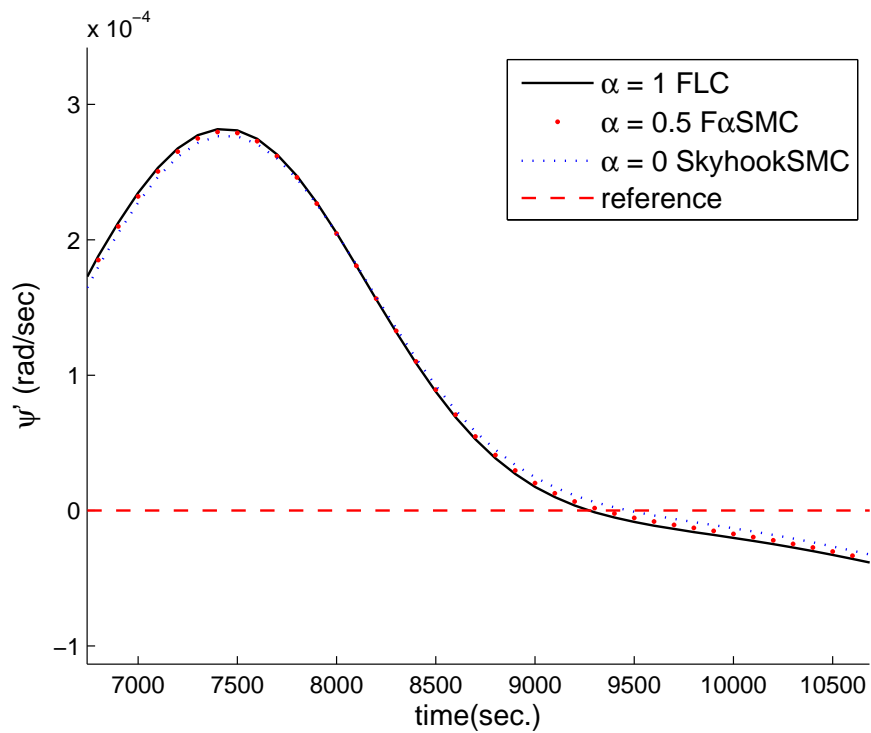
Figure 9: Spin-up velocity with different values of α
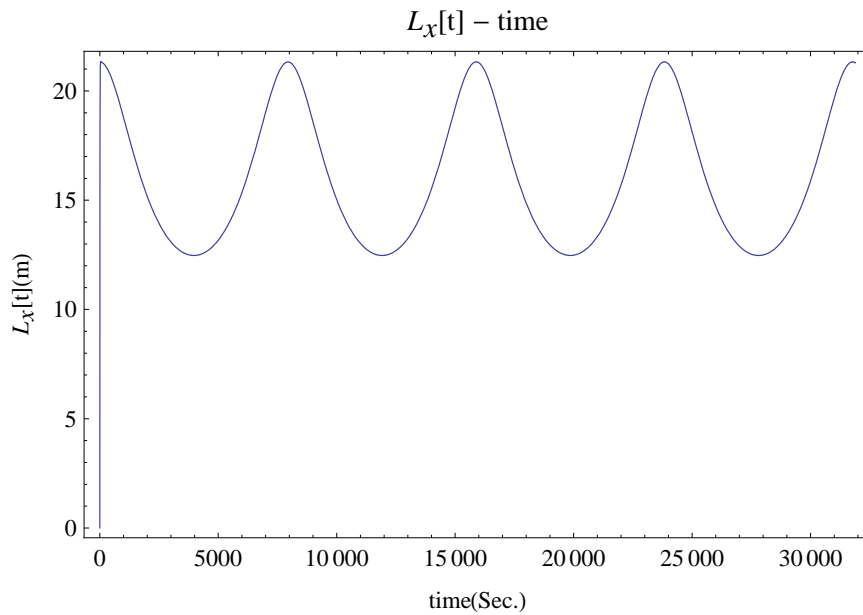
Figure 10: MMET axial elastic behaviour

Figure 10 gives the axial elastic behaviour of the MMET in the simulation with the appearance of stable axial oscillation.

The phase plane plots with different values of α are shown in Figure 11 as limit cycles whose behaviour for the spin-up coordinate ψ clearly corroborates interpretations of steady-state.

146
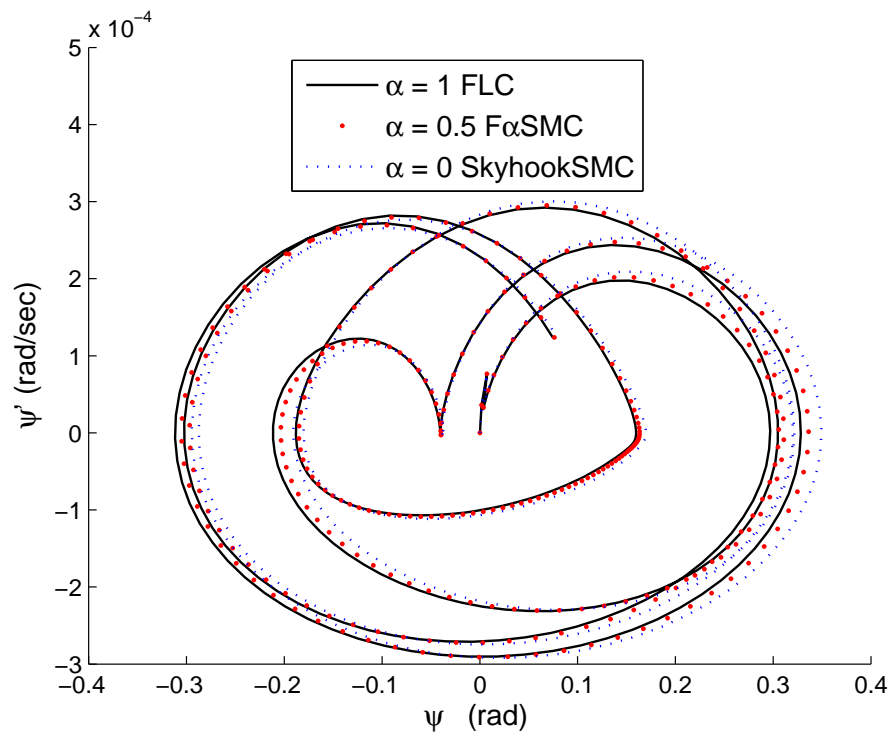
Figure 11: MMET spin-up phase plane plots with different values of α
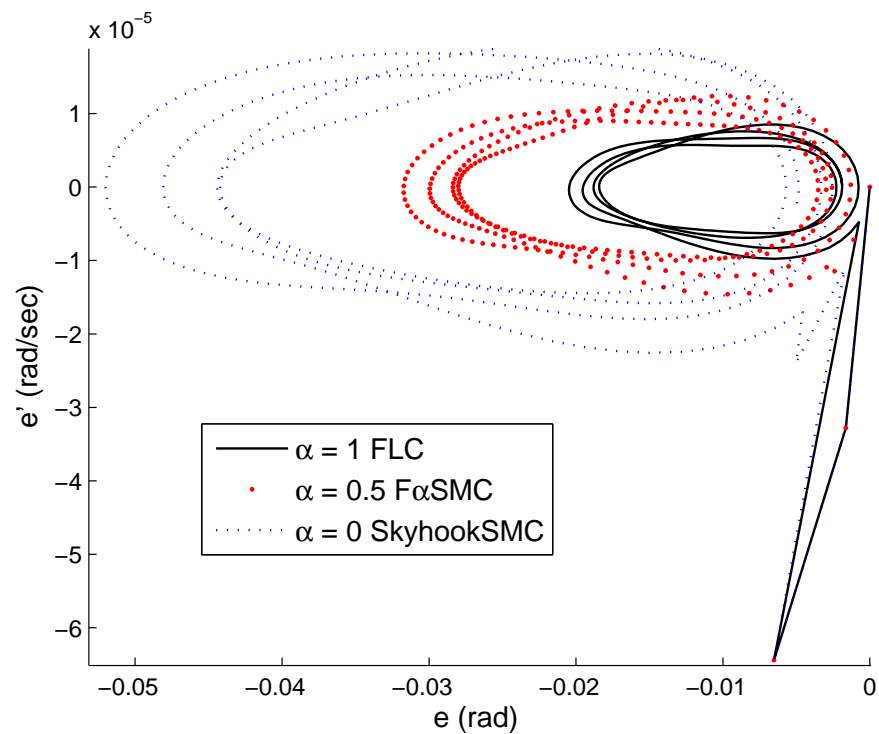
Figure 12: MMET spin-up errors phase plane plots with different values of α
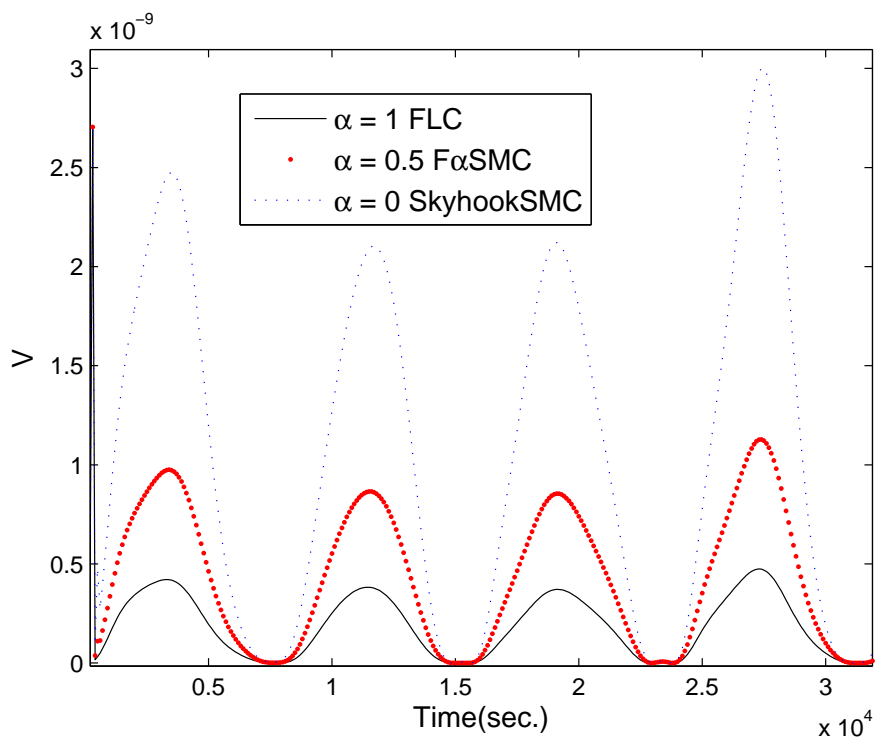
Figure 13: Lyapunov function for spin-up control methods with different α
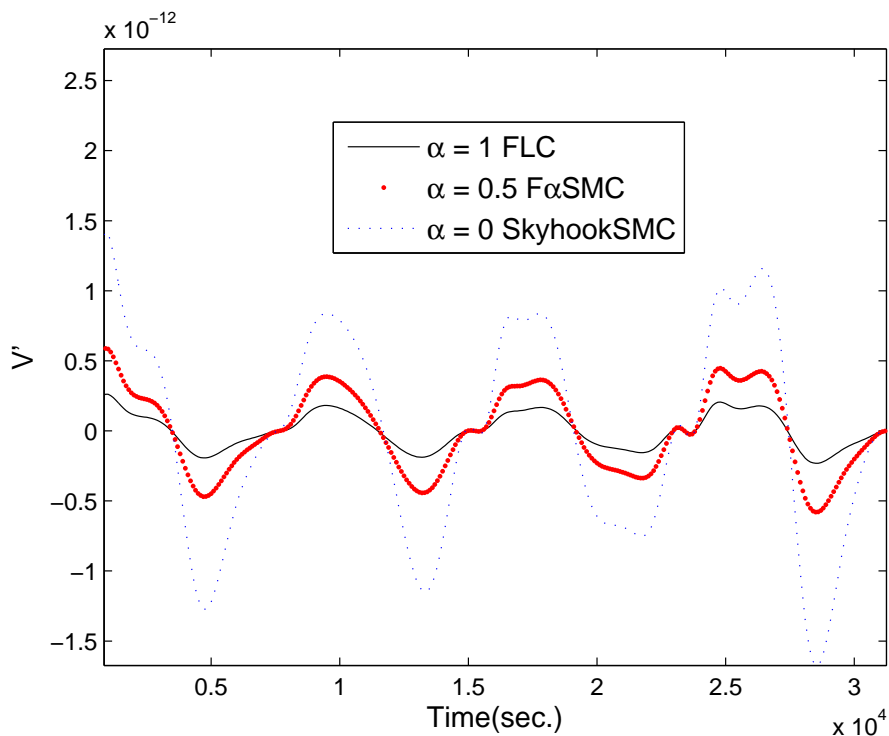
Figure 14: Sliding surface switching plot

In Figure 12, the MMET spin-up error phase plane plots with different α are given, and these shows that all the control methods offer limit cycles. The FLC caused generally faster response behaviour than the two other control methods for the spin-up coordinate ψ.

Figures 13 and 14 show the plots for the Lyapunov function and its derivative and this shows the effect of FαSMC control for different values of α. SkyhookSMC has higher energy activities than the two other control methods, and FLC has the lower associated energy around $V' = 0$, with the FαSMC's energy in the middle of the three. FαSMC can balance the control effects of FLC and SkyhookSMC for stable MMET 6-DOF spin-up outputs and associated energy activities.

5   Future work

The work in this paper has shown that by including the switching factor α, the FαSMC hybrid controller can switch and combine control from FLC to the SkyhookSMC rapidly, according to design requirements. This can balance the weight of the FLC and SkyhookSMC to override spin-up enhancement for the MMET 6-DOF system. The parameter settings for the FαSMC need further consideration because the current simulation results come from manual parameter tests. In order to enhance the parameter selection process and validation, some computational intelligence (CI) optimisation tools, such as Genetic Algorithms (GA) and Artificial Neural Networks (ANN), could be applied for parameter selection for the FLC, SMC and FαSMC. This would give some useful reference sets for parameter settings. A GA has already been used as an optimisation tool for parameter selection of the MMET system when applied to payload transfer from low Earth orbit (LEO) to geostationary Earth orbit (GEO), and the GA's optimisation ability has, in that case, been reasonably demonstrated [16].

Acknowledgements

References

[1] M. P. Cartmell, (1998), "Generating Velocity Increments by means of a Spinning Motorised Tether", 34th AIAA/ASME/SAE/ASEE Joint propulsion Conference and Exhibit, Cleveland Conference Centre, Cleveland, Ohio, USA, AIAA-98-3739.

[2] S.W. Ziegler,and M. P. Cartmell, (2001), "Using Motorised Tethers for Payload Orbital Transfer", Journal of Spacecraft and Rockets, 38 (6), November / December, pp 904-913.

[3] Y. Chen, M.P. Cartmell, (2007) "Dynamical Modelling of The Motorised Momentum Exchange Tether Incorporating Axial Elastic Effects", Advanced Problems in Mechanics , 20-28 June, Russian Academy of Sciences, St Petersburg, Russia.

[4] Kevin M. Passino , Stephen Yurkovich, (1998), "Fuzzy Control", Addison Wesley Longman, Menlo Park, CA.

[5] S. V. Emelyanov, (1967), "Variable Structure Control Systems (in Russian)", Moscow: Nauka.

[6] Y. Itkis, (1976), "Control Systems of Variable Structure", New York: Wiley

[7] V. A. Utkin, (1978), "Sliding Modes and Their Application in Variable Structure Systems", Moscow: Nauka (in Russian) (also Moscow: Mir, 1978, in English)

[8] J.J.E. Slotine, and W.P. Li, (1991), "Applied Nonlinear Control", Prentice-Hall International.

[9] K. C. Ng, Y. Li, D. J. Murray-smith, K. C. Sharman, (1995), "Genetic Algorithm applied to Fuzzy Sliding Mode Controller design", First International Conference on Genetic Algorithms in Engineering Systems: Innovations and Applications, GALESIA, 12-14 Sep 1995 Page(s):220 - 225.

[10] Brian O'Dell, (1997), "Fuzzy Sliding Mode Control: A Critical Review", Oklahoma State University, Advanced Control Laboratory, Technical Report ACL-97-001.

[11] S. G. Tzafestas1 ,G. G. Rigatos1, (1999), "A Simple Robust Sliding-Mode Fuzzy-Logic Controller of the Diagonal Type", Journal of Intelligent and Robotic Systems, Volume 26, Numbers 3-4 , pp 353-388.

[12] E.H. Mamdani, (1977), "Applications of fuzzy logic to approximate reasoning using linguistic synthesis", IEEE Transactions on Computers, Vol.26, No. 12, pp. 1182-1191.

[13] Y. Chen, M.P. Cartmell, (2009), "Hybrid fuzzy and sliding-mode control for motorised tether spin-up when coupled with axial vibration", 7th International Conference on Modern Practice in Stress and Vibration Analysis, New Hall, Cambridge, UK.

[14] J.J. E. Slotine, (1982), "Tracking control of nonlinear systems using sliding surfaces with application to robot manipulations", PhD Dissertation, Laboratory for Information and Decision Systems, Massachusetts Institute of Technology.

[15] D. C. Karnopp, M. J. Crosby , R. A. Harwood, (1974), "Vibration Control Using Semi-Active Force Generators", Journals of Engineering for Industry, Transactions of the ASME, 94:619-626.

[16] Y. Chen, M.P. Cartmell, (2007), "Multi-objective optimisation on motorised momentum exchange tether for payload orbital transfer", IEEE Congress on Evolutionary Computation, Publication Date: 25-28 Sept. 2007, pp. 987-993.

Yi Chen, Matthew P. Cartmell, Department of Mechanical Engineering, University of Glasgow, Glasgow, G12 8QQ, Scotland, UK.

Diffusion controlled evolution of nanorolls ensemble

S. A. Chivilikhin   E. N. Korytkova   T. P. Maslennikova
I. Yu. Popov   D. S. Chivilikhin   V. V. Gusarov

sergey.chivilikhin@gmail.com

Abstract

Present paper is devoted to the construction of the model of formation and evolution of nanorolls from compositions with layered structures and to experimental justification of the model. The dynamics of formation and diffusion growth of nanorolls in hydro-thermal medium is considered. The source of nanorolls is a system of nanoplates distributed in the fluid. Intercalation lead to separation of the upper layer which transforms to nanoroll. This transformation takes very small time in comparison with the time of the diffusion growth.

1 Introduction

Nanorolls are a wide class of nanotubes of different morphology. Its form as a nanoheterostructures [1, 2] or by rolling layers of nanocrystals [7]. Models of nanorolls formation are suggested in [6, 7, 8]. Experimental justification is also made. The models give values of rolling speed, but it is not unique parameter which determines form and size of nanotube [10, 5, 3]. The structure and evolution of nanoplates- the predecessors of nanorolls play an important role. There is also a process of morphological transformation of nanotubes due to recrystallization [12]. For different applications it is important to know not only the the morphology and composition of nanotubes, but also the distribution of nanoparticles in respect to length and diameter. Up to now there is no investigation of influence of synthesis parameters on this distribution.

2 Model description

Let $f_p(L_p, H, t)$ and $f_r(L_r, S, t)$ be the distribution density of plates and rolls, L_p, H are the diameter and width of the plate, L_r, S are the length and the area of the cross-section of the roll. The growth (solution) of the plates and rolls is determined by the mass transport at the surface. The conservation of mass takes place for densities: $\rho_s(t) + \rho_p(t) + \rho_r(t) = \rho_s(0) + \rho_p(0)$. Here

$$\rho_p = \rho_m \int f_p(L_p, H, t) L_p^2 dL_p H dH,$$

$$\rho_r = \rho_m \int f_r(L_r, S, t) L_r dL_p S dS,$$

ρ_m is the density of matter of plates and rolls, ρ_s -density of solute matter. The initial condition is $\rho_r(0) = 0$.

The speed of variation of the length and width of the plate is determined by the gradient of the density of the solute matter, which is related with the boundary value of the normal derivative of the corresponding solution of external Dirichlet problem around any nanoparticle

$$\Delta\rho = 0,$$

$$\rho|_{\partial\Omega} = \rho_e,$$

$$\rho|_{r\to\infty} = \rho_s,$$

We obtain the numerical solution of this problem. Using determined boundary value of the normal derivative of the density one can find the density of the mass flux:

$$j = -D\frac{\partial\rho}{\partial\nu} \sim \rho_e - \rho_s,$$

where D is the diffusion coefficient for the solute matter, ρ_e is the equilibrium concentration of the solute matter at the surface of the solid phase.

This question is analogous to the problem of construction of Dirichlet-to-Neuman map. The normal velocity of particle surface growth V is proportional to the mass flux:

$$V = -\frac{1}{\rho_m}j.$$

In this work we assume the nanoparticles can vary size but keep the shape. We describe the rate of particles size changing using the average normal velocity over the corresponding part of the surface. So $V_{L_p}, V_H, V_{L_r}, V_S$ are the speeds of the corresponding parameters variation due to the diffusion. For example, we use the normal velocity averaged over the edge of the nanotube for calculation of the velocity of nanotube length changing V_{L_r}. We use the normal velocity averaged over lateral surface of the nanotube for calculation of the velocity of nanotube surface changing $V_S = 2\pi R\overline{V}$ (R is the external radius of the nanotube). We assume that ρ_e is a function of the surface density of energy of the stressed layer:

$$\rho_e = \rho_e^0 \left(1 + \gamma e^2\right),$$

where ρ_e^0 is the corresponding concentration for unstressed layer, γ is some constant. Density of elastic energy for nanoplates e_p is greater than the corresponding one for nanotubes. Decreasing of mechanic stress and, correspondingly, the elastic energy is the reason for rolling of flat layers and forming of nanorolls. Note that we use a basic assumption that the mass transfer from liquid to solid state is due to the diffusion only (we don't take into account the kinetic effects of solution and crystallization at the surface).

The energy density for preliminary stressed double layer of width δ' and curvature radius r can be written in the following form:

$$e_r = \frac{E\delta'^3}{24}\left(\frac{1}{r} - \frac{1}{R_0}\right)^2 \tag{1}$$
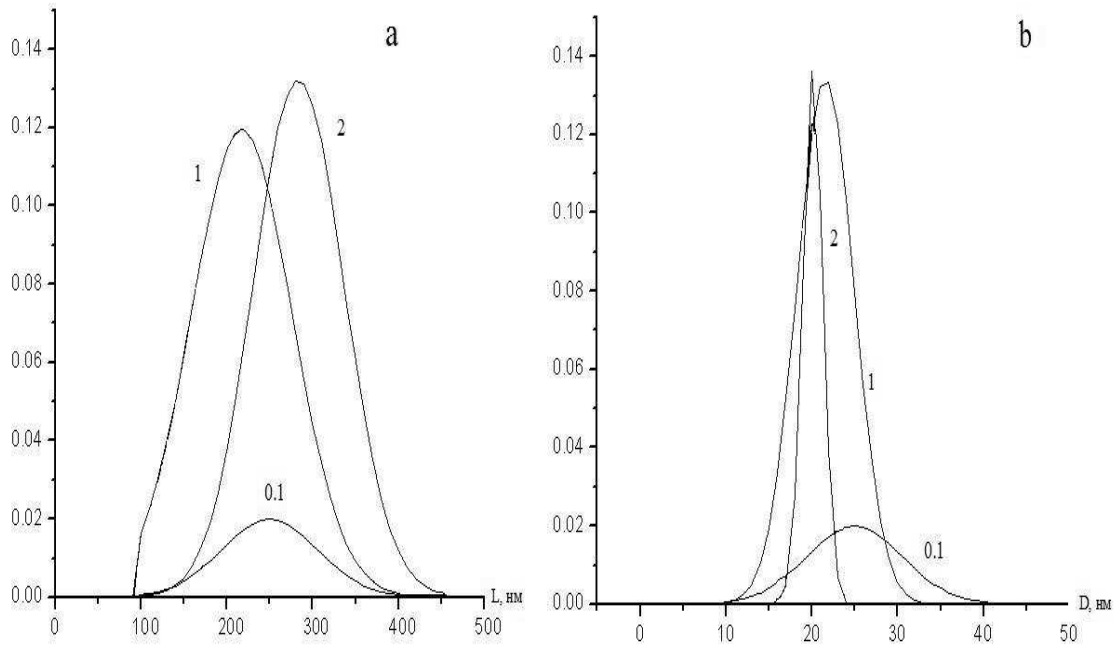
Figure 1: Distribution density for nanoplates (a)and nanorolls (b) at the moments of the dimensionless time $\nu t = 0.1,\ 1,\ 2$

where R_0 is the equilibrium curvature radius of the layer, E is the Young constant. The energy density for nanoplate is obtained from (1) when $r \to \infty$:

$$e_p = \frac{E\delta'^3}{24R_0^2}. \tag{2}$$

At the surface of the nanoroll $(r = R$) the energy density is

$$e_R = \frac{E\delta'^3}{24}\left(\frac{1}{R} - \frac{1}{R_0}\right)^2 \approx \frac{E\delta'^3 h^2}{192R_0^4}. \tag{3}$$

The mean value of the energy density for the cross section of the nanoroll is

$$\overline{e} = \frac{1}{h}\int_{R-h}^{R} e(r)dr \approx \frac{E\delta'^3 h^2}{288R_0^4}. \tag{4}$$

One can see by comparing of (2), (3) and (4) that

$$e_R \sim \overline{e} \ll e_p$$

The evolution of the distribution density for nanoplates (nanorolls) is determined by the kinetic equations:

$$\frac{\partial f_p}{\partial t} + \frac{\partial}{\partial L_p}\left(V_{L_p}f_p\right) + \frac{\partial}{\partial H}\left(V_H f_p\right) = \nu\left[f_p\left(L_p, H + a, t\right) - f_p\left(L_p, H, t\right)\right],$$

$$\frac{\partial f_r}{\partial t} + \frac{\partial}{\partial L_r}\left(V_{L_r}f_r\right) + \frac{\partial}{\partial S}\left(V_S f_r\right) = \nu\delta\left(S - aL_r\right)\int_0^\infty f_p\left(L_r, H, t\right)dH,$$

where $\delta(x)$ is the Dirac δ-function, a is the width of the double layer, ν is the frequency of the separation of double layers from a plate.

The terms in the right hand sides of the equations describe the separation of the external layers from plates and the appearance of new rolls (by rolling of these separated double layers).

Computations show that after some moment the nanoplates disappear. As for rolls, they transform to rolls of radius close to the equilibrium one (R_0) [4]. On the Fig.1 we can see the distribution density for nanoplates (a) and nanorolls (b) at the moments of the dimensionless time $\nu t = 0.1, 1, 2$.

Acknowledgements

References

[1] Schmidt O.G., Eberl K. // Nature. 2001. V.410. P.168.

[2] Prinz V.Y. // Russian Physics Journal. 2002. V.46, N6. PP.568-576

[3] Korytkova E.N., Maslov A.V., Pivovarova L.N., Drozdova I.F., and Gusarov V.V. // Glass Physics and Chemistry. 2004. V.30. N1. PP.51-55.

[4] Korytkova E.N., Maslov A.V., Pivovarova L.N., Polegotchenkova Yu. V., Povinich V. F., Gusarov V. V. // Inorganic Materials. 2005. V.41, N7. PP.743-749

[5] Deneke Ch., Schmidt O.G. // Appl. Phys.Lett. 2004. V.85. N.14. PP. 2914-2916.

[6] M.Yu.Gutkin, A.M.Krivtsov, N.F.Morozov, B.N.Semenov. Provlemi nanotehnologii // V sb.: Problemi mehaniki deformiruemih tverdih tel I gornih porod. Sbornik statei k 75-letiu E.I.Shemiakina/ Pod red. D.D.Ivleva b N.F.Morozova; Fizmatlit, 2006. 221-242.

[7] Chivilikhin S.A., Popov I.Yu., Gusarov V.V. // Doklady Physics, 2007. V.52. N1, PP.60 – 62

[8] Chivilikhin S. A., Popov I. Yu., Blinova I. V., Kirillova S. A.,Konovalov A. S., Oblogin S. I., Tishkin V. O., Chernov I. A., Gusarov V. V. //Glass Physics and Chemistry. 2007. V.33. N4. PP.315-319

[9] Chivilikhin S.A., Gusarov V.V., Popov I. Yu. , Svitenkov A.I. // Russ. J. Math. Phys. 2008. V.15. N3. PP.409–411

[10] Pauling L. // Proc. Natl. Acud. Sci. U.S.A. 1930. V.16. P.578-582. 6. Deneke Ch., Schmidt O.G. // Appl. Phys.Lett. 2004. V.85. N.14. P.2914-2916.

[11] Yaob B.D., Chan Y.F., Zhang X.Y., Zhang W.F., Yang Z.Y., Wang N. // Appl.Phys.Lett. 2003. V.82. N2. P.281-283.

[12] Jancar B., Suvorov D. // Nanotechnology. 2006. V. 17. P.25-29.

S.A. Chivilikhin, I.Yu. Popov,D.S. Chivilikhin. St.-Petersburg State University of Information Technologies, Mechanics and Optics. Kronverkskii, 49, St.-Petersburg, Russia
E.N. Korytkova,T.P. Maslennikova. Institute of Silicate Chemistry of Russian Academy of Sciences, Adm. Makarova emb., 2, St.-Petersburg, Russia
V.V. Gusarov. St.-Petersburg State Institute of Technology, Moscovskii av., 26,Saint-Petersburg, Russia

Residual stress state behaviour under fatigue loading in duplex stainless steel

P. D. Pedrosa   J. M. A. Rebello   M. P. Cindra Fonseca
jmarcos@metalmat.ufrj.br mcindra@vm.uff.br

Abstract

The lifetime of duplex stainless steel parts experiencing cyclic fatigue is directly influenced by the residual stresses present in the ferrite and austenite phases. The motivation for this work was to analyze the behaviour of the residual stresses fields introduced by shot peening treatment in both phases, in the sample surface as in the subsurface layers, in low fatigue cycles, using the X-rays diffraction technique. The results shows that the compressive residual stresses introduced by the shot peening treatment in both phases improved fatigue life of the material. However, the cyclical loads produce partial or total relief in these residual stresses fields. It was verified that the shot peening process induced the formation of microcracks only in the ferrite phase. The largest variations in the total compressive residual stresses fields also occurred in this phase. The samples surfaces were analyzed by scanning electron microscopy (SEM).

Key words: residual stresses, duplex steel, fatigue, X-ray diffraction technique.

1   Introduction

Duplex stainless steels present an austenite-ferrite biphasic microstructure, the exact amount of each phase being a function of the chemical composition and the thermal treatment employed. The main reason to use duplex stainless steels is their high resistance to oxidation, corrosion and corrosion under stress, associated to good mechanical properties. Due to this original combination of properties they have been widely used in the chemical and petrochemical industries, paper industry and power generation [1].

Many works have been published approaching duplex stainless steel mechanical and physical properties, such as yield and tensile strength and corrosion resistance [2]. However, the behaviour of residual stresses present in the different phases of these steels, under fatigue cycles, has not yet been well established.

Fatigue resistance of metallic alloys is highly dependant on the residual stress state induced in the surface layers while compressive residual stresses have proved to be beneficial to fatigue life and stress corrosion besides inhibiting crack nucleation and propagation.

An excellent method to introduce residual stresses aiming to improve the fatigue life of materials is the shot peening process. However, the introduced residual stresses may be reduced or wholly relieved applying mechanical or thermal loads, mostly cyclic.

Residual stresses are self-balanced stresses present in materials or body at uniform temperature conditions and in the absence of external load [3].

In multiphase and/or polycrystalline materials, residual stresses may be micro stresses arisen due to elastic incompatibility among grains or phases and/or macro stresses formed by differential plastic deformation, for example, surface and inside, that suffer uneven deformation during cooling and are forced to adjust jointly [4,5].

It is well established that the presence of residual stresses may highly influence the mechanical properties of the material and particularly, its properties under fatigue. Therefore, evaluation of residual stresses is an important quality control method in the manufacture of structures, pieces and components.

Several methods are available for residual stress measuring. Among them, X-ray diffraction technique, a well established and reliable non-destructive method is one of the most widely applied [1,6].

2   Materials and Experimental Techniques

In the present work, UNS S31803 duplex stainless steel manufactured according to ASTM A240 standard was used. The microstructure of the plates, as show in figure 1, was composed of 49% austenite and 51% ferrite and the chemical composition is shown in table 1. The shot peening treatment was performed at two Almen intensities (A) of 0.25A and 0.39A, using metallic shot with diameter between 0.59 – 0.71 and 1.0 – 1.41mm respectively.
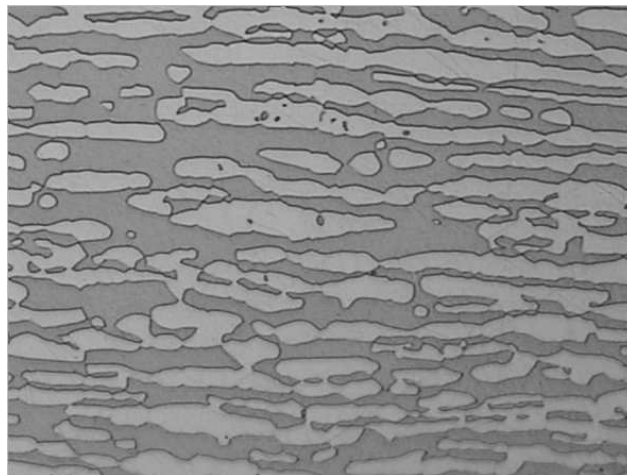
Figure 1: Biphasic microstructure of duplex stainless steel (magnified 500X with attack).

Residual stresses were measured by X-ray diffraction technique by double exposure method, using portable equipment.

Table 4: Chemical composition of UNS S31803 stainless steel (weight %).

Fe	C	Ni	Mo	N	Cr
Balance	0.020	5.44	2.49	0.16	22.30

Thin layers were removed by electrolytic polishing to study the residual stress state variations through thickness, in order to evaluate the depth of the layer attained by the shot peening treatment, and thickness of the removed layers was checked with a digital comparator.

The influence of the shot peening treatment on the mechanical properties of duplex stainless steel was verified through tensile tests conducted in an Instron machine with 10^{-3} s^{-1} deformation rate, in samples as received and after shot peening treatment with Almen intensity of 0.39A. Test specimens were manufactured according ASTM A370 standard, with 3.0mm thickness.

Fatigue tests were conducted in a PWO Carl Schenck AG alternate flexure testing machine, with constant frequency cycles at 60Hz. The samples were analyzed after polishing and at the two shot peening intensities (0.25A and 0.39A), based on S-N curves, for each of these conditions, with load rate R $= -1$, at different stress levels for low-cycle fatigue regime. The maximum load applied during fatigue tests was supported by the middle of the sample.

Residual stresses were measured in low cycle fatigue, with 10^3 cycles, in the longitudinal (L) and transversal (T) direction of the test specimen, as shown in figure 2. Residual stresses were measured on the surface and through the thickness. For this end, several electrolytic polishing were carried on for each sample and the residual stresses were measured after each polishing on both steel phases (austenite and ferrite) up to 0.45mm depth.
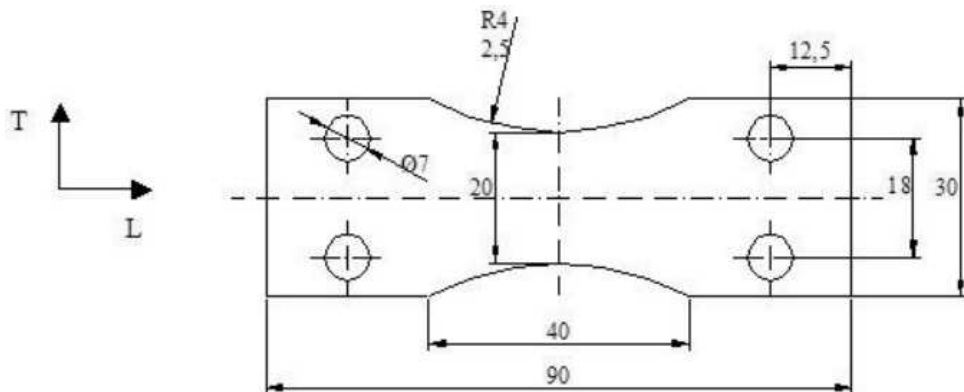
Figure 2: Test specimen used for fatigue tests.

Scanning electron microscopy (SEM) was conducted on the transversal surfaces of non-fractured samples at both shot peening intensities (0.39A and 0.25A) without fatigue.

3   Results and Discussion

The results are presented in three steps. On the first step, the main objective was to study the effect of the two different shot peening intensities on UNS S 31803 duplex stainless steel mechanical properties, mainly fatigue resistance. On the second step, the behaviour of compressive residual stresses was assessed after cyclic loading of 10^3 cycles in both steel phases, austenite and ferrite, in the longitudinal and transversal directions. On the third step, the efficiency of shot peening process on the recovery of fatigue life was assessed in correlation with crack initiation points, after shot peening and after shot peening plus cyclic load up to 10^3 cycles.

Table 2 presents the values obtained for yield strength, tensile strength and percentage elongation in the samples as received and with 0.39A shot peening intensity.

Table 5: Mechanical properties of steel before and after shot peening.

Material condition	σ_Y (MPa)	σ_T (MPa)	ε (%)
As received	565	757	35.3
Peened at 0.39A	650	784	21.3

Figure 3 shows that yield and tensile strength increase with shot peening treatment while elongation decreases. This behaviour is due to sample surface hardening caused by the treatment.
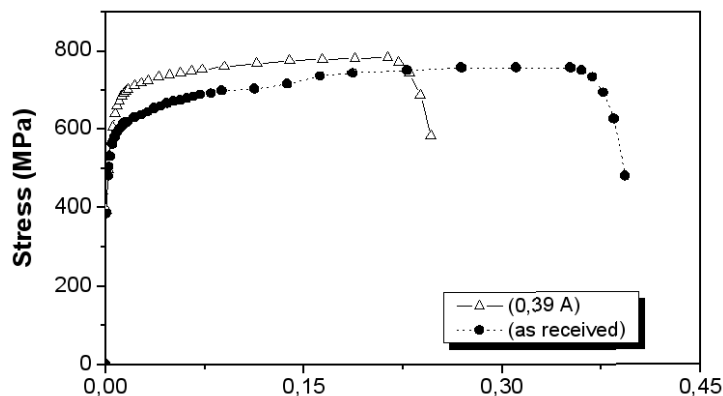
Figure 3: Stress *vs* deformation curve of samples as received and after 0.39 Almen intensity shot peening.

Figure 4 presents the *S x N* curve obtained for the as received condition samples, peened at 0.25A and 0.39A intensities samples.

The hot peening treatment increased fatigue life in low and middle cycle regime in both shot peening conditions (0.39A and 0.25A). However, in high cycle regime,

fatigue life of samples that received a lower shot peening intensity decreased in relation to as received condition samples. This behaviour may be explained by the fact that samples that received a lower shot peening intensity induced maximum total compressive residual stresses mainly in the surface, on both phases, as shown in figures 5 and 6.
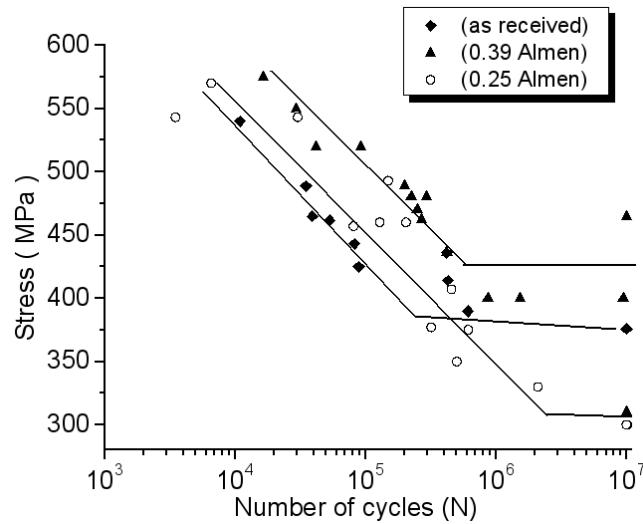
Figure 4: Comparison of S-N curves of UNS S 31803 steel in the condition as received and peened at 0.25A and 0.39A.

Figures 5 and 6 present a depth profile of total compressive residual stresses (TCRS) for both used shot peening conditions, in the longitudinal and transversal directions of the test specimen, in both phases, austenite and ferrite, before fatigue.
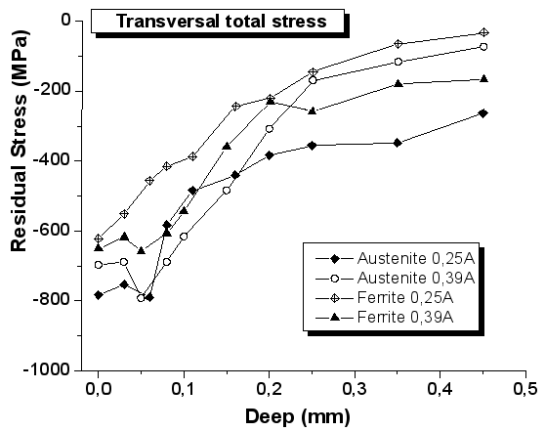
Figure 5: Total residual stresses for both shot peening intensities, before fatigue, in the transversal direction.
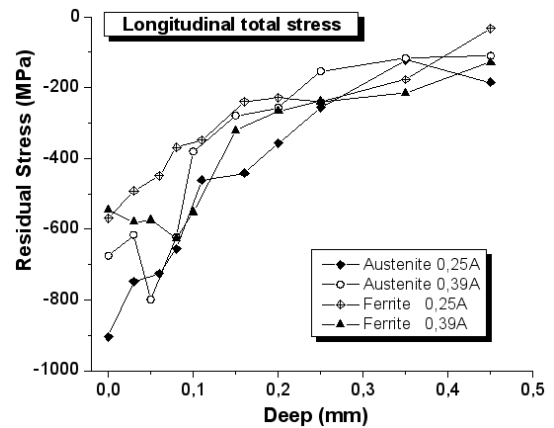
Figure 6: Total residual stresses for both shot peening intensities, before fatigue, in the longitudinal direction.

Another point that should be discussed, as a probable explanation to fatigue results in figure 4, involves the greater hardening of the austenite phase when compared to ferrite for monotonic and cyclical loading [7,8]. Indeed, the 758MPa endurance
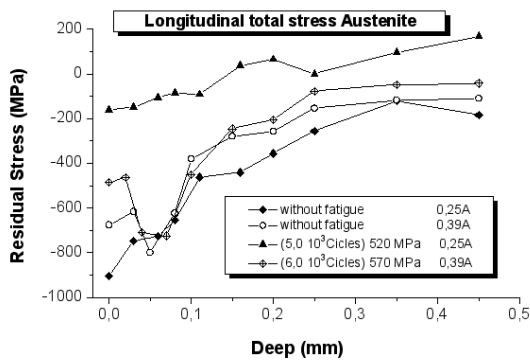
Figure 7: Total austenite residual stresses, longitudinal direction before fatigue and in low cycle conditions
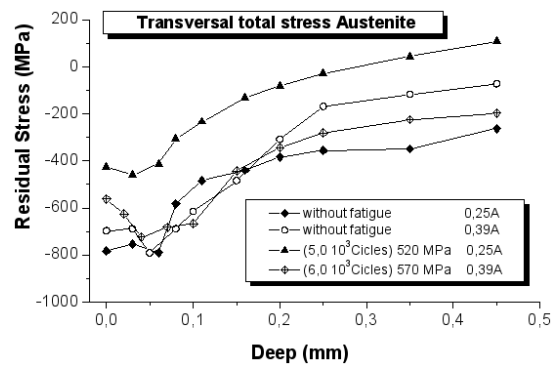
Figure 8: Total austenite residual stresses, transversal direction before fatigue and in low cycle conditions.

limit value for samples peened at 0.39A and 505MPa for samples of the material as received evidence such fact, particularly for monotonic loading, though also for all samples.

This austenite hardening, occurring at low cycle fatigue, is supposed to contribute and explain the better performance of the samples with high shot peening intensity, because the load levels are high. For samples with peening of 0.25A, this monotonic hardening would be less and, in fatigue, because of similar low load, the fatigue life would be reduced, and those samples would not have the benefit of austenite hardening shown by the samples with higher shot peening intensity (0.39A).

Figures 7 and 8 show that austenite total compressive residual stress fields (TCRSF) of samples submitted to 0.25A intensity in low cycle (10^3) regime, presented greater relaxation in the longitudinal direction. However, high stress relief was also observed in the transversal direction. Nothing was observed on austenite TCRSF for 0.39A intensity, where there was stress relaxation on the surface and near it, up to 0.08mm depth, even when submitted to a greater cyclic loading when compared to samples with lower shot peening intensity, both in the longitudinal and transversal direction.

Figures 9 and 10 shows that ferrite TCRSF in the samples with lower shot peening intensity (0.25A) in low cycle regime, suffered relaxation in both longitudinal and transversal directions. However, in samples with higher shot peening intensity (0.39A) TCRSF relaxation occurred only in the longitudinal direction, while in the transversal direction there was only total compressive residual stress relief in the surface and near it, up to 0.08mm depth.

The analysis of figures 7 to 10 shows that the TCRSF is more stable for a higher shot peening intensity (0.39A). This behaviour may be explained because the induction of TCRSF in this intensity demands a higher energy and then a higher energy will also be needed to remove this stress field originally created by blasting.

In the same way, a lower energy is expected to be used to remove a TCRSF for a lower (0.25A) shot peening intensity.

The austenite presented a more stable TCRSF: only relief of total compressive residual stresses (TCRS) was observed in the surface and below up to 0.08mm depth, mainly in the longitudinal direction, coinciding with the direction of the cyclic load.
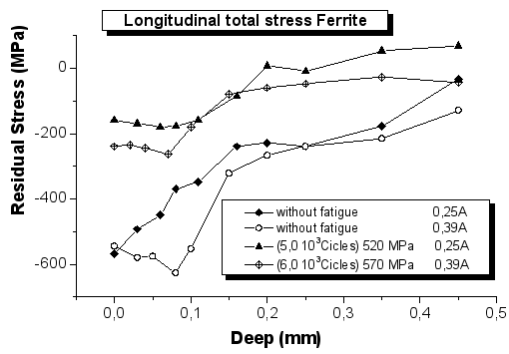
Figure 9: Ferrite longitudinal total residual stress field before fatigue and in low cycle.
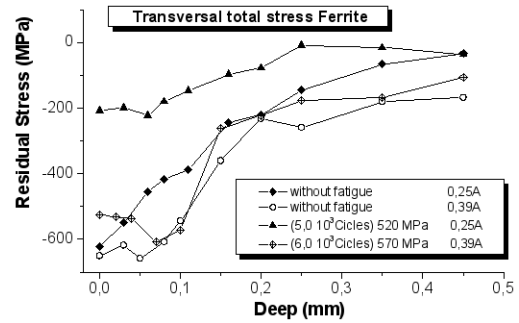
Figure 10: Ferrite transversal total residual stress field before fatigue and in low cycle.
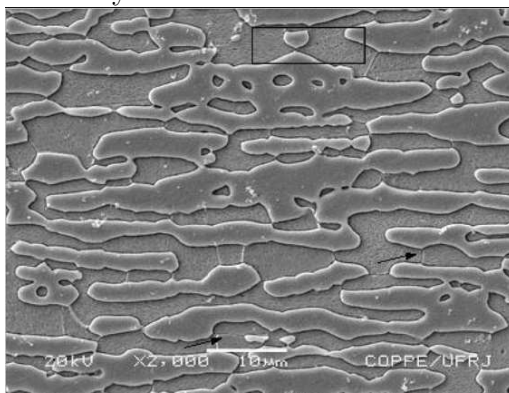
Figure 11: SEM. Microcracks inside the ferrite transversal surface after 0.39 A shot peening.
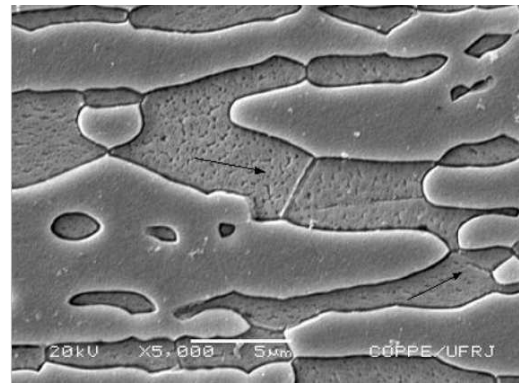
Figure 12: SEM. Microcracks inside the ferrite transversal surface after 0.39 A shot peening.
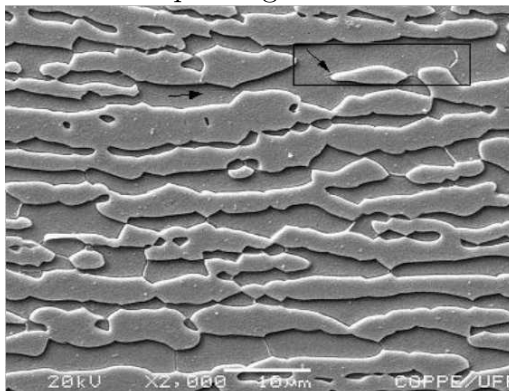
Figure 13: SEM. Microcracks inside the ferrite transversal surface after 0.25 A shot peening.
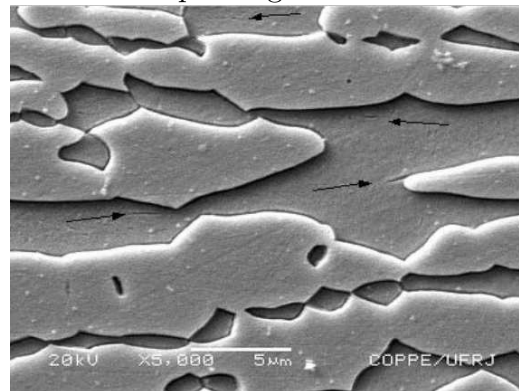
Figure 14: SEM. Microcracks inside the ferrite transversal surface after 0.25 A shot peening.

This behaviour may be attributed to the easier hardening of the austenite phase when compared to ferrite due to cyclic loading higher or equal to the material yield limit.

Scanning electron microscopy (SEM) with attack was used to observe the samples

peened in both conditions. These observations show that the shot peening process introduce microcracks in the ferrite phase near the surface of the samples, effect that is accentuated in the 0.39A shot peening (figure 7 and 8). However, microcracks were also observed in some samples with lower shot peening intensity (0.25A), though in a smaller scale (figures 9 and 10).

Figures 11 to 14 show the surfaces of the samples in the transversal direction, in the middle of their length, after shot peening, in the same place where residual stresses were measured and the higher cyclic load was applied.

Most of the microcracks found after shot peening are in the 0,5mm range. However, 1,5mm length microcracks were found in smaller amounts inside the ferrite phase. None of the samples presented microcracks in the austenite phase.

4   Conclusions

The study of the variation of residual stresses induced by shot peening in duplex stainless steel fatigue life showed that:

1. The higher intensity (0.39A) shot peening treatment used conducted to better result under fatigue.

2. TCRSF relaxation occurred in both directions, longitudinal and transversal, and in both phases present in duplex stainless steel for low cycle fatigue regime. However, this TCRSF relief was more accentuated in the longitudinal direction, fact that may be related to cyclic load being applied in this direction.

3. The samples that showed better behavior under fatigue were those that had maximum compressive residual stresses under the surface.

4. The highest variations in total compressive residual stress fields occurred in the ferrite phase.

5. The shot peening process induced microcrack formation only in the ferrite phase.

5   Acknowledgements

References

[1] Lindgren, M., Lepisto, T., "Relation between residual stress and Barkhausen noise in a duplex steel", *NDT&E International*, 36, pp. 279-288, 2003.

[2] Johansson, J., Odën, M., "Evolution of Residual Stress State in a Duplex Stainless Steel During Loading", *Acta Materialia*, pp 2669-2684, vol 47, 1999.

[3] Macherauch, E., Kloos, K. H., "Origin, Measurements and Evaluation of Residual Stress in Science and Technology", Ed. By E. Macherauch, V. Hauk, *DGM VERLAG*, 1987.

[4] Almer, J.D., Cohen, J.B., Winholtz, R. A., "The Effects of Residual Macrostresses and Microstresses on the Fatigue Crack Propagation", *Metallurgical and Materials Transactions A*, pp 2127-2136, Aug. 1998.

[5] Almer, J.D., Cohen, J.B., Moran, B., "The Effects of Residual Macrostresses and Microstresses on the Fatigue Crack Initiation", *Materials Science and Engeneering A*, pp 268-279, vol 284, 2000.

[6] Benning, O.I., "Non-destructive determination of load and residual stresses by the X-ray stress method", *The Rigaku Journal*, vol 6, N 2, pp 15-20, 1989.

[7] Chai. G., "Fatigue behaviour of duplex stainless steels in the very high cycle regime", *International Journal of Fatigue*, vol 28, pp 1611-1617, 2006.

[8] Inal K., Gergaud. P., François. M., "X-ray diffraction methodologies of macro and pseudo-macro stress analysis in a texture duplex stainless steel", *Scandinavian Journal of Metallurgy*, pp 139-150, vol 28, 1999.

Cindra Fonseca, M. P., Mechanical Dept., Federal Fluminense University - UFF/TEM/ PGMEC, Rua Passo da Pátria, 156, Bl. D, S/302, CEP 24210-240, Niterói, RJ - Brazil. E-mail: mcindra@vm.uff.br

To one approach to the construction of exact solution of one dimensional dynamics equations of elasticity theory for stratified media

Valery N. Demidov

vn_demidov@mail.ru

Abstract

Initial-boundary problem for one-dimensional equations of elastic media dynamic is studied for multi-layer region which is finite and is in the conditions of one-axis deformation state. From physical point of view the solution of this problem is interpreted as wave process initiated by initial (or boundary) conditions and developed in time. The algorithm is sug-gested to find exact solution of this problem. This algorithm is based on the idea of inverse characteristic and com to following. Two characteris-tics are directed in the opposite of time axis to internal or external boundary in the point of plane where it is necessary to calculate the cur-rent parameters. From new occurring points new characteristics are di-rected to neighboring boundaries etc. Finally we fall to initial time, where the medium state is known from initial conditions. Intervals of the characteristics form oriented graph - binary root tree. Moving now into the time direction and using the relations on the characteristics, one can to calculate the values of required functions for all vertexes of graph, including its root, where it is necessary to obtain the solution. The con-structed graph is the region of solution that corresponds to physical sense of hyperbolic equations. Described algorithm is generalized simple for arbitrary hyperbolic equation system. Exact solution is god test for nu-merical methods. The examples are presented in the paper for compari-son of exact and numerical solutions obtained using explicit difference schemes of first and second steeps of approximation.

1 Introduction

One-dimensional problem is studied in this paper on plane elastic waves propagation in the finite sizes region made of some number of different materials. One can construct easily the analytical solution of this problem when region is homogeneous using known Dalamber formulae and superposition principle. However, this problem becomes more complex for stratified medium because reflected and refracted waves appear on each interface during process development. Any wave appearing once begins "exist his life", tested multiple reflections and refractions generating new and

To one approach to the construction of exact solution of one dimensional dynamics equations of elasticity theory for stratified media
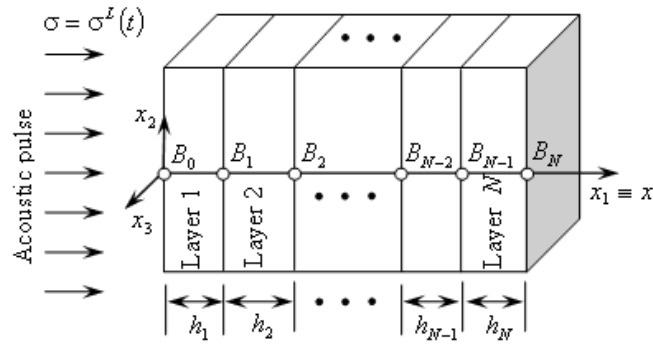
Figure 1: Scheme of one dimensional problem on mechanical loading of multi-layer specimen by acoustic pulse.

new waves that leads to extremely complex and tangled wave picture. Certainly, one can investigate this problem using numerical methods. However, whatever numerical method possessing certain internal dissipative and dispersion properties no inherent to initial differential problem, distorts the solution by some way. That distortion can be very appreciable for large times. This question is touched in p. 4.

One can to construct exact solution of problem under study no using analytical recording. The original simply programmed algorithm is suggested in this paper. The essence of this algorithm consist of employment of method of inverse characteristics that is described in p.2.

2   Problem formulation

Scheme for studied problem is presented on Fig.1. Multilayer specimen containing N plane layers of different materials is shown here. It is assumed that specimen sizes in the axes x_2, x_3 directions are larger essential of its size in the axis x_1 direction, and external actions given in vertical planes traversing the points B_0 and B_N are uniform that is do not depend on x_2, x_3 - coordinates. Besides, it is believed that ideal mechanical contact conditions are correct in the interfaces (that is in the planes traversing the points $B_1, B_2, \ldots, B_{N-1}$). It follows from above that one axis deformation state will realize in this problem and all required functions would depend on unique space variable - x_1. We assume next designations:

$$x \equiv x_1, \quad \sigma \equiv \sigma_{11}, \quad \varepsilon \equiv \varepsilon_{11}, \quad v \equiv v_1, \quad u \equiv u_1, \quad v = \frac{\partial u}{\partial t}, \quad \varepsilon = \frac{\partial u}{\partial x}.$$

Here σ, ε, v and u - are components of stress and strain tensors, velocity and displacement vector correspondingly in the direction x - axis. It is convenient in this problem to use stress $\sigma(x, t)$ and $v(x, t)$ as studied functions. Denote the coordinated of the points $B_1, B_2, \ldots, B_{N-1}$ on the Fig.1 as $x_1, x_2, \ldots, x_{N-1}$. Eventually we come to the following initial – boundary problem for one-dimensional equations of elastic media dynamics in multilayer region of finite size:

$$\rho \frac{\partial v}{\partial t} = \frac{\partial \sigma}{\partial x}, \quad \frac{\partial \sigma}{\partial t} = \rho a^2 \frac{\partial v}{\partial x}, \tag{1}$$

$$v(x, 0) = v_0(x), \quad \sigma(x, 0) = \sigma_0(x), \quad x_0 \leq x \leq x_N \tag{2}$$

$$\sigma(x_0, t) = \sigma^L(t), \quad \sigma(x_N, t) = \sigma^R(t), \quad t \geq 0 \tag{3}$$

$$\sigma(x_k^+, t) = \sigma(x_k^-, t), \quad v(x_k^+, t) = v(x_k^-, t), \quad k = 1, 2, \ldots, N-1, \quad t \geq 0. \tag{4}$$

Fist equation (1) is law of impulse conservation for element of elastic medium, second results after Gook law differentiation

$$\sigma_{ij} = \lambda \varepsilon_{kk} \delta_{ij} + 2\mu \varepsilon_{ij},$$

Which takes the form

$$\sigma = (\lambda + 2\mu)\varepsilon.$$

for studied one-dimensional case.

Appearing in (1) parameters - density ρ and sound rate $a = \sqrt{(\lambda + 2\mu)/\rho}$ are material parameters as it is assumed in linear elasticity theory.

Let reduce the equation system (1) to some canonical form. For this purpose, we divide second equation on ρa. Then we add obtained equation to the first equation (1) and then deduct from it. As a result, we obtain two equations:

$$\frac{\partial}{\partial t}\left(v + \frac{\sigma}{\rho a}\right) - a\frac{\partial}{\partial x}\left(v + \frac{\sigma}{\rho a}\right) = 0,$$

$$\frac{\partial}{\partial t}\left(v - \frac{\sigma}{\rho a}\right) + a\frac{\partial}{\partial x}\left(v - \frac{\sigma}{\rho a}\right) = 0,$$

or after designations

$$R^{\pm} = v \mp \frac{\sigma}{\rho a}, \tag{5}$$

- the equations

$$\frac{\partial R^+}{\partial t} + a\frac{\partial R^+}{\partial x} = 0, \quad \frac{\partial R^-}{\partial t} - a\frac{\partial R^-}{\partial x} = 0. \tag{6}$$

This system, in comparison with (1), contains the equations for new unknown quantities independent from each other, that allows to write the general solution in the form

$$R^+ = f^+(x - at), \quad R^- = f^-(x + at), \tag{7}$$

where f^+, f^- are arbitrary functions the view of which depends on initial and boundary conditions. The values $R^{\pm}$ are Ryman invariants and straight lines

$$C^+ : x - at = \text{const}, \quad C^- : x + at = \text{const} \tag{8}$$

are the characteristics of the equation system (1).

The solution (7) has clear physical and geometrical sense. It is follows from (6), (7), R^+ conserves a constant value along the line $C^+ : x - at = \text{const}$, that is the plot of the function $R^+(x)$ shifts in time to the right with the sound rate a, no changing their form. Analogously R^- conserves its value along the line $C^- : x + at = \text{const}$ and shifts with the same rate a to the left. So, there are two plane waves propagating into opposite directions. One wave transfers constant value of Ryman R^+, and second - constant value of Ryman R^-.
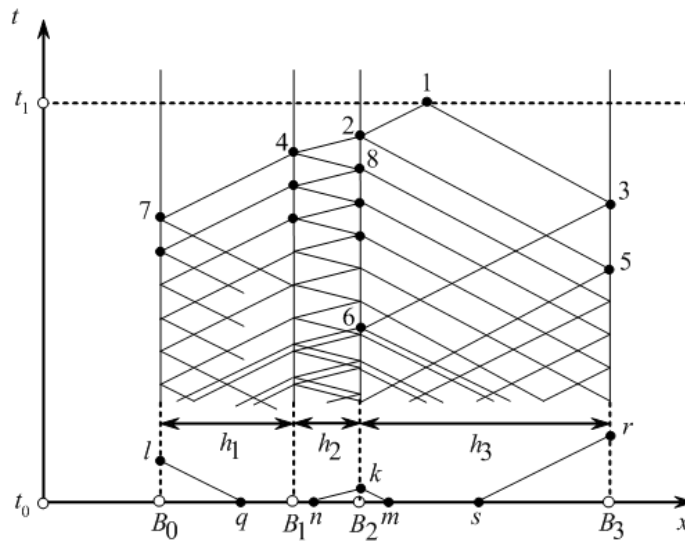
Figure 2: Scheme explaining the calculation algorithm of the current in the point 1 using reverse characteristic approach. The sense of the point B_0, B_1, B_2, B_3 is the same that it was on the Fig.1.

3 Algorithm of exact solution construction

We describe algorithm of exact solution construction using three-layer specimen, shown on the Fig.2, the stress $\sigma^L(t)$ is given in the left boundary, and right boundary is free $\sigma^R(t) \equiv 0$. Let suppose that it is necessary to calculate the solution in some time moment $t = t_1$. Take arbitrary point corresponding to given time moment; it has the coordinates (x_1, t_1) and is designed by number 1 on the Fig.2. Our purpose consists in the finding of the $\sigma_1 \equiv \sigma(x_1, t_1)$ and $v_1 \equiv v(x_1, t_1)$ in this point.

We divide the calculating algorithm in two independent steps.

The first step includes following geometrical structures. Let draw the characteristics with positive and negative slopes through points 1 in reverse (relatively to time axis) direction to their intersections with one of boundary of calculating region. It can be external (free) or internal (contact) boundary. Design the corresponding intersection points as 2 and 3, as it is shown on Fig.2. If rate and stress values would be known in these points, using the relations in the characteristics, one could be calculate the values σ_1, v_1. But to calculate σ_2, v_2 it is necessary to know the values σ_4, v_4 and σ_5, v_5; here 4 and 5 are the intersections points with contact and free boundary correspondingly for characteristic straight lines emerging from point 2. Then analogous reasoning repeat for the points 3, 4, 5, etc. Moving in the reverse in t direction, we come sooner or later to time $t = t_0$, where initial data are given. Here straight-line course ends. It is shown, that it consists in the calculation of the coordinates of the points $(x_i, t_i), i = 1, 2, 3, \ldots$, and organization of certain connection between them.

Notice, that different situations are possible on the finally stage of first step, that is shown in the Fig.2. Really, we can reach to line $t = t_0$ sinking from left external boundary of calculation region (from point l to q), from right external boundary (from point r to s) and from interface (from point k to m and n).

Preparatory to go to second step, notice that using initial data and boundary conditions, one can calculate the motion parameters in the points l, k, r. Present corresponding formulae.

Equaling the values of Ryman invariant R^+ in the points n and k, and invariant R^- in the points m and k, we obtain the equation system

$$v_k - \frac{\sigma_k}{\rho_n a_n} = v_n - \frac{\sigma_n}{\rho_n a_n}, \quad v_k + \frac{\sigma_k}{\rho_m a_m} = v_m + \frac{\sigma_m}{\rho_m a_m},$$

whence we have

$$\sigma_k = \frac{\rho_n a_n \sigma_m + \rho_m a_m \sigma_n + \rho_n a_n \rho_m a_m (v_m - v_n)}{\rho_n a_n + \rho_m a_m}, \tag{9}$$

$$v_k = \frac{\rho_n a_n v_n + \rho_m a_m v_m + \sigma_m - \sigma_n}{\rho_n a_n + \rho_m a_m}. \tag{10}$$

To calculate the values σ_l, v_l we use given boundary condition and the constancy condition of invariant R^- along the characteristic straight line ql:

$$\sigma_l = \sigma^L(t_l), \quad v_l + \frac{\sigma_l}{\rho_l a_l} = v_q + \frac{\sigma_q}{\rho_q a_q}. \tag{11}$$

Hereof the equalities

$$\sigma_l = \sigma^L(t_l), \quad v_l = v_q + \frac{\sigma_q - \sigma_l}{\rho_q a_q}. \tag{12}$$

follow taking into account the equality $\rho_q a_q = \rho_l a_l$.

Analogously we obtain for right (free) boundary

$$\sigma_r = 0, \quad v_r = v_s - \frac{\sigma_s}{\rho_s a_s}. \tag{13}$$

Second step of calculating algorithm consist in that rising from time moment $t = t_0$ to $t = t_1$, we pass step-by-step all points which were fixed in the first step and calculate there the values of the parameters σ, v, using every time one of presented formulae. For example, the formulae (13) are employed in the point 3 for $r = 3$, $s = 6$, the formulae (9), (10) in the point 4 for $k = 4$, $n = 7$, $m = 8$ etc. Moving by similar way, we come eventually to the point 1 and calculate σ_1, v_1. Here second step finishes.

When calculating process is organized and data structure (which are stored in the computer) is chosen, the interpretation of presented algorithm with point of view of graph theory. On the first step, moving from t_1 to t_0, we from graph: the points 1, 2, 3,... are graph tops, and the segments of the characteristic are ribs of graph. According to terminology assumed in the graph theory the depicted on the Fig.2 graph is binary root tree or, in other words, oriented bound graph without cycles, the degree of each top of which does not two. The top 1 is tree root, the tops 2,3 are successors of root (right and left correspondingly); analogously, the points 4 and 5 are left and right successors of tops 2 etc. The pops of root tree no possessing the successors call leafs. As it is shown from Fig. 3, the tree leafs locate on the segment
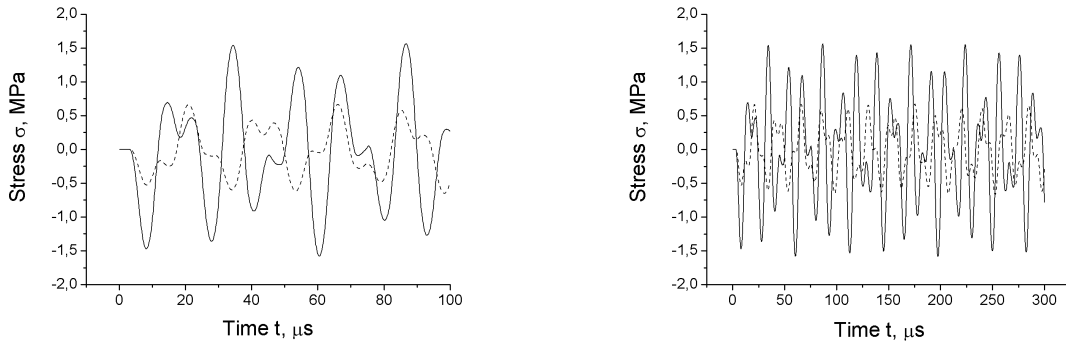
Figure 3: Stress state change in the interface of double specimens AB (solid line) and BA (dotted line).
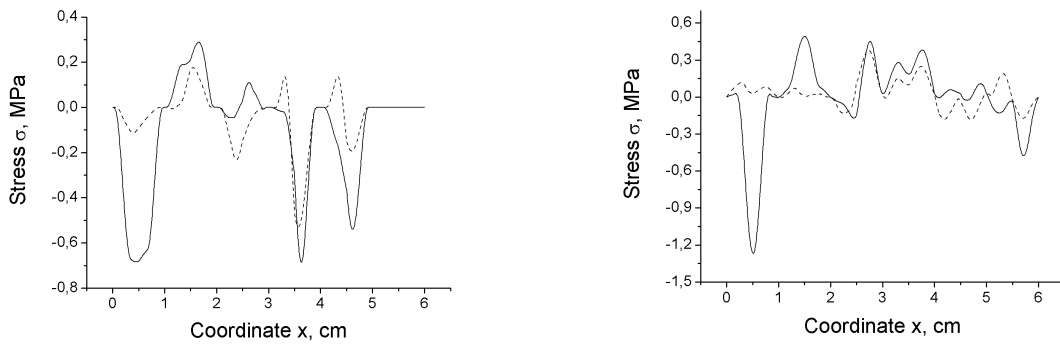
Figure 4: Stress distribution along the thickness 12-layer specimens ABAB... (solid line) and BABA... (dotted line) for time moments $t = 8$ μs (on the left) and $t = 40$ μs (on the rigth).
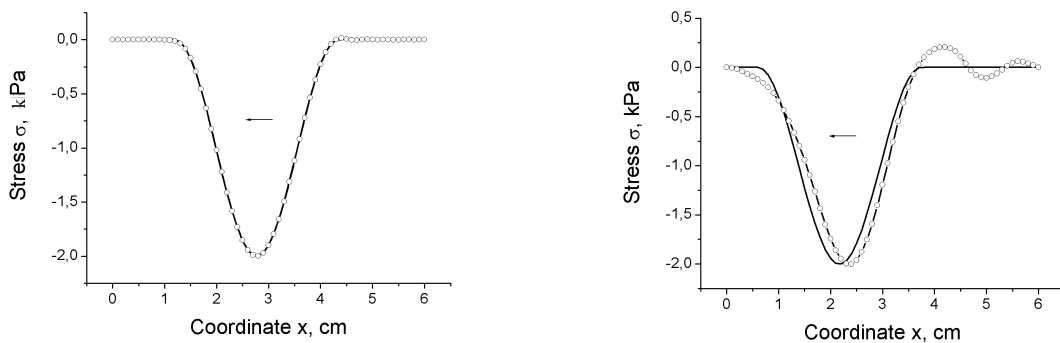
Figure 5: The comparison of analytical (solid line) and numerical (circles) solution obtained using difference scheme of second step of accuracy.

$t = t_0$ with initial data. Each top of graph settling in the interface has two successor - left and right; the tops locating on the external boundaries have one successor - right for left boundary and left for right boundary.

Using this terminology, one can say, that tree leafs possess full information (the velocity, stress are known here from initial data), the tops with one successor possess partly information (in the form of boundary condition), the tops with two successors have not information. During reverse course of numerical algorithm, each top could receive full information. When we calculate σ_1, v_1, information flows from leafs to tree root. In passing, cause-effect relation appears here in the development of studied wave picture of the motion: each top of the graph is the point of origin of refracted and/or reflected waves, and each rib of graph is trajectory of corresponding wave. According to known interpretation of physical sense of linear hyperbolic equations, only these waves effect on medium state in the point 1. So, depicted in the Figure graph is dependence region for point 1.

4   Examples

We illustrate the practical employment of described algorithm with the help of various specimens made from two materials (A and B) with the parameters:

$$\rho_A = 2.71 \mathrm{g \cdot cm^{-3}}, \quad a_A = 6275 \mathrm{m \cdot s^{-1}}, \quad \rho_A = 7.85 \mathrm{g \cdot cm^{-3}}, \quad a_A = 6022 \mathrm{m \cdot s^{-1}}$$

Let consider two layer specimens AB and BA, consisting of plane layers of equal thickness $h_1 = h_2 = 3$ cm. Mechanical exciting of model specimens was carried out by acoustic pulse

$$\sigma^L(t) = \sigma_M \Big(1 + \cos\Big(\pi\Big(\frac{t}{t_M} - 1 \Big) \Big) \Big), \quad 0 < t < 2t_M, \tag{14}$$

acting on the left boundary. Here $t_M = 5$ μs is maximum point, and $\sigma_M = 1.0$ MPa is half of amplitude in the point $t = t_M$. Let assume that development of oscillating process in the interface and the evaluation of maximal stresses acting there are interested for us.

Exact analytical solution constructed on the base of described above algorithm is shown in the Fig.3. Stress variation is demonstrated on the left to time moment 100 μs. It is obvious that compressing and tension stresses acting in the interface of AB-specimen are two double the contact stresses in BA-specimen. Right graph authenticates that this regularity remains in time.

Let examine, as second example, twenty-layer specimen made from interlaced layers ABAB... with equal thickness $h_1 = h_2 = \cdots = h_{12} = 0.5$ cm and analogous specimen with other layer arrangement - BABA... The pulse (14) with the parameters $t_M = 0.5$ μs, $\sigma_M = 1.0$ MPa acts on the left boundary of these specimens. Fig. 4 illustrates essential difference in the stress distribution along the specimen thickness for two time moments.

Suggested algorithm is rewarding for testing of finite-difference methods used when wave processes in solids have been studied. Appropriate example is disclosed in the Fig. 5. Stress impulse is demonstrated after single run along specimen and

after reflection from right free boundary placed in the point $x = 6$. Coincidence of exact and approximate exact solution (it was obtained using difference scheme of second step of approximation) is very well. Numerical solution is distorted with the time. The impulse after 74 running along specimen thickness is shown in the right picture that allows to estimate the difference between exact and approximate solutions accumulating to this time.

5   Conclusion

So, the algorithm of exact analytical solution construction is suggested for one-dimensional initial - boundary dynamic problem of elasticity theory in multilayer region of finite size. From Physical point of view, the solution of this problem is interpreted as developed in time wave or oscillation process initiated by initial or boundary conditions. The interpretation of this algorithm is given from point of view of graph theory, which allows arranging corresponding computer program rationally. Note that algorithm is efficient: it indicates exactly the region of solution dependency and leads to minimum the calculating work. Algorithm could be generalized by obviously way to arbitrary linear system of hyperbolic type.

Valery. N. Demidov, Academichesky Ave., 2/4, Tomsk, Russia

Numerical modeling of dry friction sliding in pad-disc interface at the nanoscale

Andrey I. Dmitriev   Werner Oesterle

dmitr@ispms.tsc.ru

Abstract

The frictional behaviour at local contacts in an automotive brake system was analysed on the basis of computer simulation with the aid of the method of Movable Cellular Automata (MCA). The boundary conditions of the model were adjusted to experimental observations obtained by Transmission Electron Microscopy (TEM). The impacts of friction layer composition, pressure and velocity changes on friction evolution, friction level and regime of sliding were investigated. Thus it could be shown that only under certain conditions, when a mechanically mixed layer had formed, the coefficient of friction (CoF) was stabilized with a minimum of fluctuations. Obtained results are in agreement with conventional friction theories and they characterize well the considered types of contacts. This result suggests that the MCA-model can help a lot to improve our basic understanding of the micro-processes taking place at the pad-disc interface.

1 Introduction

Understanding the basic friction mechanisms occurring at the interface between the fixed brake pad and rotating brake disc is still a challenging area of research. Theoretical considerations as well as experimental studies suggest the formation of surface layers with properties distinctly different from the properties of basic materials [1, 2]. Composition, structure and thickness of the modified layers depend on properties of initial material, loading conditions, temperature and the environment in which the process of friction is taking place. Essential progress in our understanding of dry friction was outlined by the work of M.Godet et al. [3] with the introduction of the third body concept. In the framework of this concept it is supposed that the modified surface layers which have formed during mutual sliding of bodies as a result of mechanical, chemical, thermal and other processes have a determinative influence on the friction and wear behaviour of the couple. Later this concept was also predicted for brake materials by Jacko et al. in [4].

Despite of permanent development of new experimental methods in material science, direct observation of friction layers during a brake application is not possible. We only can investigate surfaces and cross-sections at the end of a braking cycle after the pressure has been released and the pads have been removed from the disc. On

the other hand, modeling on the nanometer scale can be effectively used for the description of friction and wear [5, 6] at single asperity contacts. The results received during modeling, can provide a basis of forecasting the behavior of interacting materials and can also provide a measure for optimization of tribotechnical materials. The aim of our investigations was to obtain a feeling of the frictional behavior at the pad-disc interface and to find correlations between characteristics of friction and properties of contacting materials and loading conditions.

2 Numerical model of a friction layer

The researches were done by modeling on the nanometer scale with the aid of the method of Movable Cellular Automata (MCA) [7]. Previously the MCA method was successfully used for the investigation of similar processes in contact areas [8, 9, 10]. The MCA method is a kind of discrete approach where all objects are represented as an ensemble of interacting particles (movable automata). The principles of MCA-modeling have been described in [7] and briefly formulated as follow: Velocity accommodation between the stationary pad and the rotating disc can be accomplished by assuming a flow of granular wear debris (third body) in the gap between the two first bodies. Observation of the friction layer (Fig. 1,a) and its structure [10] imply that the granular particles must be very small, i.e. of the order of 10 nm in diameter. The friction layers on both first bodies might be interpreted as sintered layers of wear debris, formed after milling and mechanical mixing of larger wear particles. In the model the particles correspond to interacting elements of finite size (10 nm) which are linked to each other within the friction layers. The bonding state can be switched from linked to unlinked and vice versa depending on stress-intensity in pair and contact stress, respectively. Thus it is possible to simulate not only asperity deformation, wear mechanisms, mechanical mixing, detachment of particles and granular flow, but also the recombination of particles, e.g. nano-welding or adhesive bonding of metallic asperities.

The different materials involved in third body formation enter the model by attributing their stress-strain characteristics to individual automata. Since in reality the situation is very complex, some simplifications had to be introduced, as shown schematically in Fig. 1,b.

According to chosen automaton diameter the cross-sectional area during simulation was of the order of 1×1 μm^2. Actually, we regard only one very small contact in two dimensions defining a micron-sized cross-section similar to the one shown in Fig. 1,a, but comprising both sides of the interface i.e. pad and disc. On the pad side we assume a primary contact site according to Eriksson et al. [11] which is provided by the section of one of the steel fibers used in low-met pads as reinforcing elements. The supporting material on the disc side is pearlitic steel. The friction layer is modeled with a random distribution of single graphite particles in a matrix of iron oxide. Graphite was chosen as a representative of any other solid lubricant because its mechanical properties are well known. The mechanical properties of the different bulk materials (see Table 6) were allocated to each element (particle) in the model. The following boundary conditions for modelling as depicted in Fig. 1,b were used. A constant sliding velocity (V) equal to 10 m/s, corresponding to the rotational
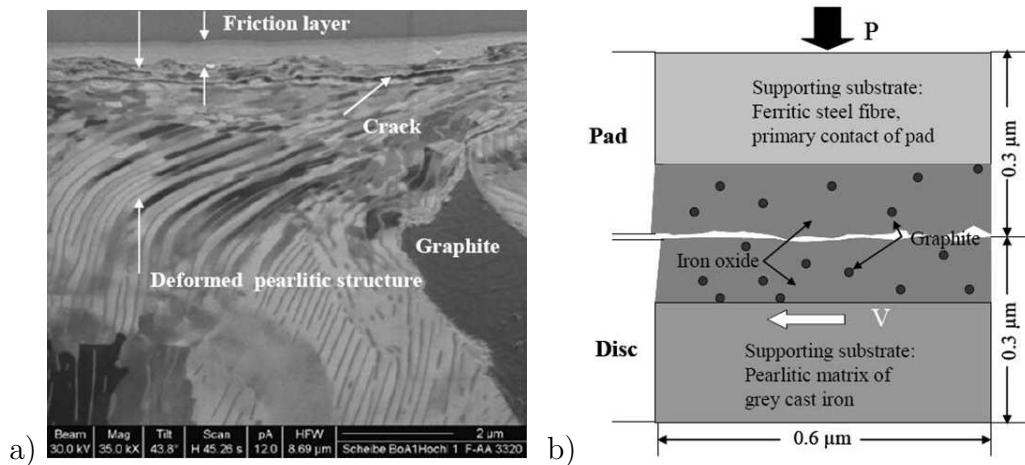
Figure 1: a) Cross-section of friction layer on brake disc. b) The modelled scheme

Table 6: Parameters of the model material

	Young modulus E, GPa	Poisson ratio ν	Elastic limit σ_{y1}, MPa	Yield strength σ_{y2}, MPa	Ultimate tensile strength σ_s, MPa	Strain at σ_{y2} ϵ_{y2}	Breaking strain ϵ_s
Ferritic steel	206	0.28	450	500	550	0.04	0.106
Pearlitic steel	206	0.28	520	800	920	0.04	0.106
Iron oxide	380	0.3	290	305	340	0.008	0.009
Graphite	20	0.3	15	35	45	0.05	0.15

speed of the disk before braking was applied on all particles of the bottom layer of disk. At the same time their position in vertical direction was fixed. A constant normal force corresponding to the contact pressures (P) in the range between 5 MPa and 50 MPa for different calculations was acted upon all the elements of the upper layer of the pad. For both types of loading a linear procedure of value increasing was used. At the left and right side of the setup, periodic boundary conditions were used, i.e. material ejected at one side was reintroduced on the other side. The time step $\Delta t = 10^{-13}$ s for simulation is determined by automata size and elastic modulus of interacting materials. A surface profile with roughness on the nanometer scale was set deliberately prior to simulation. The model calculates position and binding state of each automaton (particle) as well as resulting tangential forces at the micro-contact for each time step.

3 Results of simulation

3.1 Observation of mechanically mixed layer formation

As it was shown in our previous papers [8, 10, 12] beginning of relative motion of the interacting bodies is accompanied by formation of superficial layer which structure

and properties are different from the structures of the bulk materials. The generation of the layer where processes of deformation, fracture and intensive mass mixing are taking place can be associated as a third-body formation which does not propagate to bulk of the contacting bodies. Due to mixing of material from pad and disc within this layer, it can be associated with formation of so called mechanically mixed layer (MML). This layer is realized mostly in conditions of dry sliding friction and plays an important role in determining the tribological behaviour of the material. Let consider the particles behaviour in the layer in more detail.

3.2 The influence of solid lubricant

To analyze the macroscopical properties of modelling local contact the coefficient of friction (CoF) for interacting bodies was used. For it evaluation the normal and tangential forces were calculated during the simulation. The overall forces were determined as the sum of all the tangential and normal forces, which act at the current time step on the boundary layer of the disc. The quotient of both gives the friction coefficient. Calculation of CoF for mating pair with concentration of graphite about 17.5 vol% and the value of external pressure about 30 MPa gives the value 0.35. Expectedly, increasing of concentration of solid lubricant particles in the friction layer reduces the coefficient of friction. The results of the modelling with various graphite concentrations are shown in Fig. 2. For the layer with graphite concentration about 27.5 % (Fig. 2,a) the mean CoF feebly fluctuated at a value of 0.3 after a short running-in period, whereas for the layer with only 5.5% graphite (Fig. 2,b) the CoF increases gradually with time exceeding 0.5 at the end of the simulation. In figures strong fluctuation of calculated momentary coefficient of friction is explained by realization of various situations in local contact at each time step. In spire of this the CoF-fluctuations between successive time steps are very different for the two cases, implying different conditions at the sliding interface.
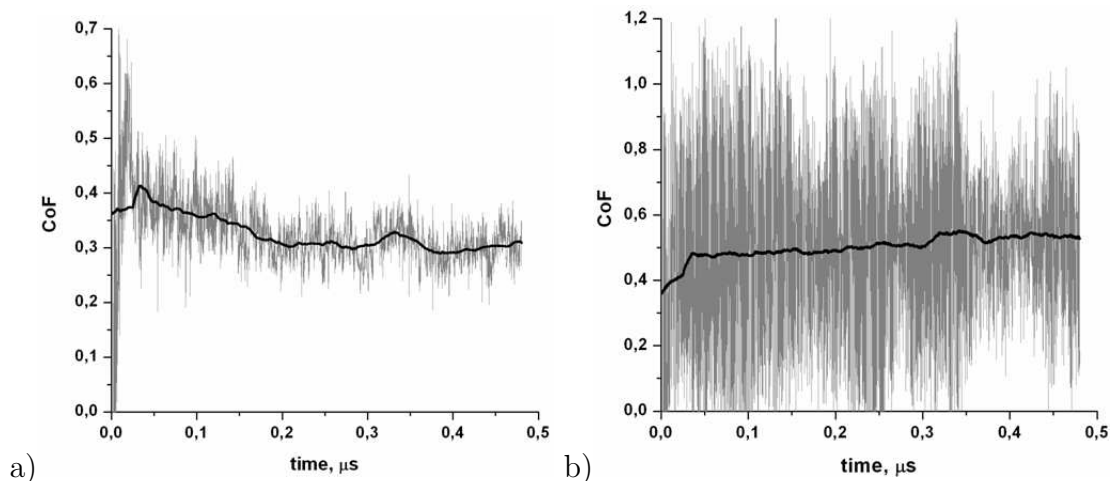
Figure 2: Simulation of CoF evolution at P = 35 MPa for two graphite concentrations: a) 27%; b) 5%

Fig. 3 depicts the results of a series of simulations with systematically changed

graphite concentrations. The steep increase of the CoF starting at approximately 10 % graphite corresponds to the situation without MML-formation. Between 13 and 27.5 % the CoF decreases moderately and an increase of MML-thickness was observed. The graph also contains simulation results with 0 % and 100 % graphite. The pure oxide showed cracks but no loose particles and very high fluctuations of the CoF. The lowest CoF (0.2) was simulated assuming steel sliding against steel covered by a graphite layer. In this case no MML had formed, but all bonds between graphite particles had been broken thus imitating the real graphite's behavior. This situation led to the lowest CoF-fluctuations.
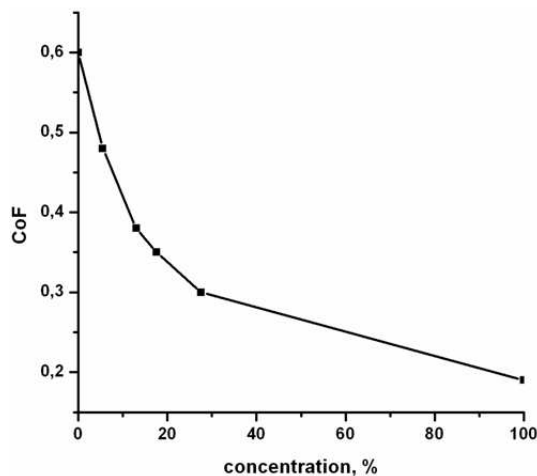
Figure 3: Impact of graphite concentration on CoF (35 MPa).

3.3   Impact of external pressure

As the next step of pad-disc interface investigation, we analyse the influence of applied pressure on tribotechnical properties of mating pair. For this at given concentrations of graphite the MML-thickness and corresponding friction response were calculated with varying of applied pressure (P). The structure analysis has shown that at small P with growth of pressure the increase in MML thickness is compensated by layer compression. What occurs thus with friction force? According to results of simulation the CoF-value shows non-linear decreasing with pressure and with the subsequent attainment of some constant value. This result is in good correlation with experimental data obtained in [13], where CoF versus pressure dependence divides on three parts. For other graphite concentration the same dependencies of the MML-thickness and CoF on applied loading were obtained. In Fig. 4 we try to represent all these results as three-dimensional histograms. The height of each bar corresponds to the value of corresponding parameter. It is seen that the increasing pressure and the concentration of graphite in a friction layer leads to increase the thickness of mechanically mixed layer and reduce coefficient of friction. The exception is the point of a high pressure with volume concentration of graphite 5.5%. The applied normal pressure is sufficient to destroy the layer of iron oxide and generate the mixed layer from oxide particles.
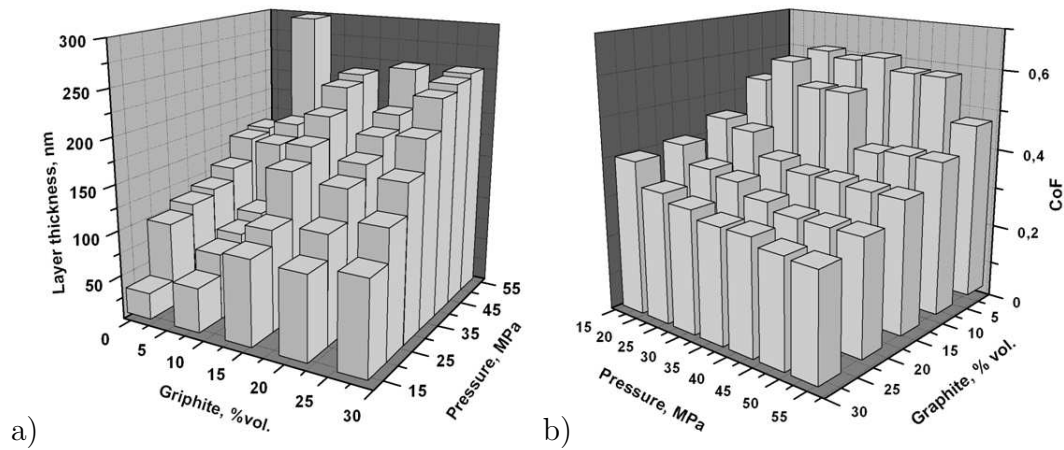
Figure 4: MML-thickness (a) and CoF (b) versus pressure and graphite concentration in friction layer

Thus, it is possible to say about the existence of a critical pressure needed to initiate MML-formation and therefore responsible of friction forces stabilization at low graphite concentrations.

3.4   Simulation of metal-on-metal contact

Since commercial brake pads contain a large number of ingredients a large variety of different contact situations can occur. In papers [10, 12] we also considered metal-on-metal contact which seems to be relevant, because uncovered metallic surfaces were observed frequently for both: the steel fibres of the pads and the cast iron discs. Since it is well known that metal particles will recombine by micro-welding during a milling process the possibility of re-bonding of automata was accounted for in the model. For such transition from unlinked to linked state a critical value of normal stress in the contacting pair equal to $(\sigma_s - \sigma_{y2})/2$ was selected (see Tab. 6).
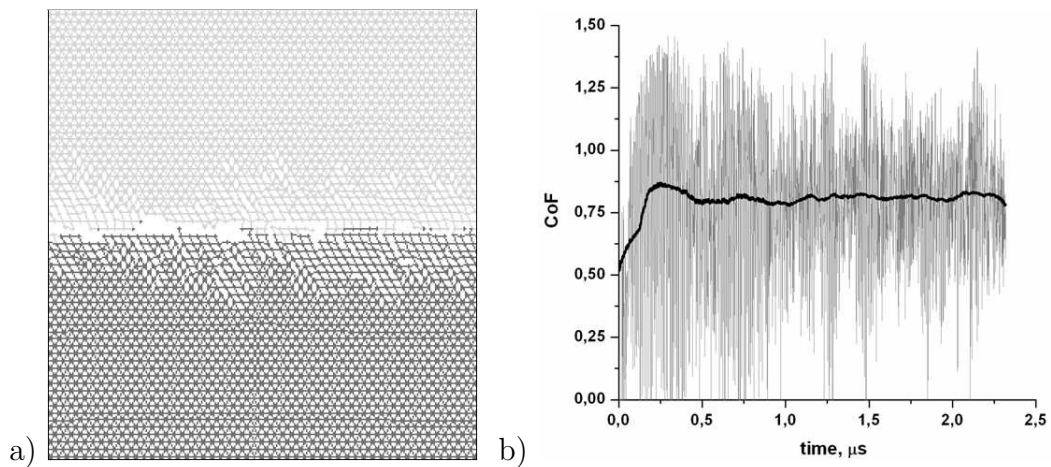
Figure 5: a) Final structure of friction layer. b) CoF evolution

The resulting structure and CoF-evolution is shown in Figures 5,a and 5,b, respectively. No MML was formed during this simulation. Accordingly, the calculated momentary CoF shows very unstable behavior from step to step which is due to velocity accommodation by breaking of inter-particle bonds, leading to a stick-slip kind of sliding behavior. Furthermore, the mean CoF value is higher as desired for brake applications. At the snapshot-structure presented in Figure 5,a it is visible that many automata pairs at the interface of both interacting bodies have been able to restore links with their nearest neighbors and form a modified surface structure which is characterized by a large number of defects.

The goal of further investigation was to compare results of metal-on-metal contact with assumptions suggested by Bowden and Tabor in [14]. As was mentioned above, the actual area of contact (A) increases with nominal pressure and quotient of applied loading (N) and yield stress (q). Taking into account that the real area of contact is 1-2 orders smaller than the nominal contact area we also have to conclude that the values of local pressure realized on A will be much higher than the nominal applied normal pressure. Thus, nominal pressures of 10 or 100 times smaller than q can lead to plastic deformation of materials in contact points (asperities) [15]. This assumption is confirmed by results of MCA simulation. Fig. 6 shows the distribution of irreversible deformation in modeled assembly at different moments of time. It is well visible, that while initially only small fragments of material are involved in plastic deformation near to local contact points, only few time steps later the field of irreversible deformation extents to the whole modeled microcontact. Comparing Fig. 5,a and 6 suggests that the formation of the modified layer corresponds to a zone of irreversible deformation of particles in that area.
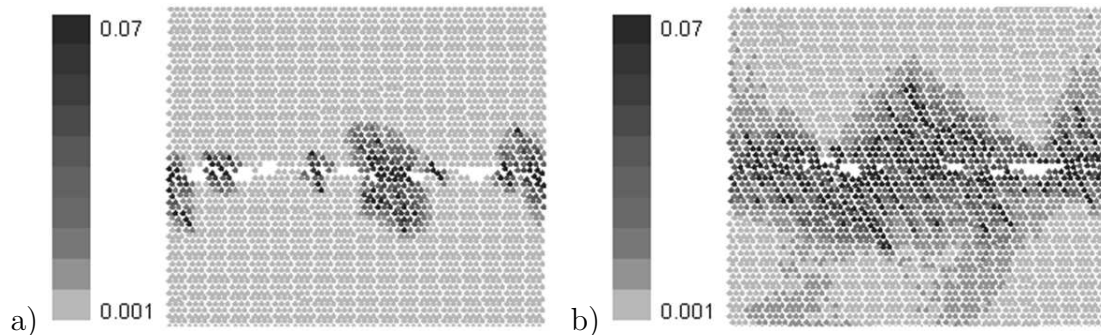
Figure 6: Distribution of irreversible deformation in contact area: a) initially; b) at running-in stage

Thus, as actual pressure on contact is approximately constant and equal to the yield stress of the modeled material formation of the modified layer does not depend on applied loading. Realization of various processes in contact zone is mostly not defined by the value of nominal pressure, but rather by microgeometry of the surface and mechanical properties of superficial layers present on the area of real contact. With the increase of nominal pressure the area of real contact increases, basically due to involving more and more asperities. Thus, the average area of contact of individual roughness remains practically constant [15].

So, it is possible to conclude that these results are in agreement with a formalism of Bowden and Tabor and they are correct for various type contacts. For instance, in case of oxide-on-oxide contact it is reaching of constant value of CoF after some value of loading, in case of two metals contact - achievement of the local pressure corresponding to yield stress at any nominal pressure. Certainly, both variants suppose the sliding regime conservation. Obtained agreement suggests that the MCA model can be considered as an effective tool for the qualitative study of the influence of the surface layer structure and load conditions to change the friction parameters, as well as more detailed understanding of the causes of some processes in friction layer.

4   Conclusion

The results of direct simulation of various local contact situations at the surfaces of pad and disc of the automotive brake revealed the complexity and diversity of the processes taking place under contact interaction. Despite of the fairly simple two-dimensional model, some very important features of braking, namely velocity accommodation between fixed pad and rotating disc, constant friction level and reduction of CoF-fluctuations could readily be explained by mechanically mixed layer formation at dry friction. The structure of the layer is determined by the intensity of the processes occurring in the surface layers of interacting first bodies. The obtained results help to obtain a better understanding of the processes and mechanisms occurring in the surface layers. They especially can be used to predict tendencies of CoF-changes induced by changes of the composition, structure of contact surfaces and loading conditions. According to aforesaid MCA-modeling provide an opportunity to find new ways of improving the tribological properties of materials of a friction pair.

Acknowledgements

References

[1] Panin V.E., Fomin V.M. and Titov V.M. Physical principles of mesomechanics of surface layers and internal interfaces in a solid under deformation, Phys. Mesomech., 6, N.3.- 2003. pp.5-13

[2] Oesterle W., Urban I., Severin D., Trepte S. Correlations between surface modification and tribological performance of brake pads // Surface engineering, V.17, N.2.- 2001. pp. 123-125

[3] Godet, M. The third body approach: a mechanical view of wear, Wear, 100.- 1984. p. 437-452.

[4] Jacko, M.G., P.H.S. Tsang, S.K. Rhee, Wear debris compaction and friction film formation of polymer composites, // Wear, 133.- 1989, p.23-38

[5] Zhang L.C. Johnson K.L, Cheong W.C.D. A molecular dynamics study of scale effects on the friction of single-asperity contacts // Tribology Let. Vol. - 2001. -V.10. - N.1-2. - P. 23-28

[6] Kemmer, H.A., "Investigation of the friction behaviour of automotive brakes through experiments and tribological modeling", PhD-thesis University Paderborn 2002, Robert Bosch GmbH, Schriftenreihe ISBN 3-00-011230-8.

[7] Psakhie S.G., Horie Y., Ostermeyer G.-P., Korostelev S.Yu., Smolin A.Yu., Shilko E.V., Dmitriev A.I., Blatnik S., Spegel M., Zavsek S. Movable Cellular Automata method for simulating materials with mesostructure // Theor. Appl. Fracture Mech.- V.37.- 2001. P.311-334

[8] Popov V.L., Psakhie S.G., Shilko E.V., Dmitriev A.I., Quasi-fluid nano-layers at the interface between rubbing bodies: simulation by movable cellular automata, Wear 254.- 2003. pp.901-906

[9] Bucher F., Dmitriev A.I., Ertz M., Knothe K., Popov V.L., Psakhie S.G., Shilko E.V. Multiscale simulation of dry friction in wheel/rail contact // Wear V.261 N7-8.- 2006. pp. 874-884

[10] Oesterle W., Kloss H., Urban I., Dmitriev A.I. Towards a better understanding of brake friction materials // Wear 2007.- V.263. Pp.1189-1201

[11] Eriksson, M., Lord J., Jacobson S. Wear and contact conditions of brake pads: dynamic in situ studies of pad on glass, Wear, 249, (2001), 272-278.

[12] Dmitriev, A.I., Oesterle W., Kloss H. Numerical simulation of typical contact situations of brake friction materials, Tribology Int., 41.- 2008, pp. 1-8

[13] K.-H.Zum Gahr, Modelling and microstructural modification of alumina ceramics for improved tribological properties. Wear 200 (1996) pp.215-224.

[14] F. P Bowden, D. Tabor. The friction and lubrication of solids. Oxford University Press, 2000.

[15] Demkin N.B. Multilevel model of friction contact. Journal of friction and wear.- V.21. 2 (2000) Pp.1-6.

Andrey I. Dmitriev, pr. Academicheskii 2/4, Tomsk, 634021 Russia
Werner Oesterle, Unter den Eichen 87, Berlin, D-12200 Germany

Peculiarities determining generation of elastic waves in friction. Computer simulation using discrete-continual approach

Serguei A. Dobrynin   Aleksey Yu. Smolin   Igor S. Konovalenko

laesod@ms.tusur.ru

Abstract

A model of mechanical interaction in the sliding friction contact zone was considered on the basis of discrete-continual approach. Frequency spectrum of the elastic waves generated was studied. The frequencies depending on roughness of the surface profiles were shown. Fourier and wavelet analysis of the registered signals allowed revealing the complex structure of elastic waves taking place in sliding friction. It is concluded, that mechanisms of wear could be studied on the basis of corresponding acoustic spectra.

Introduction

Machine and device wear is the most nagging problem concerned with sliding friction. Friction and wear are complex and essentially dynamic phenomena, this feature makes their investigation very difficult. For example the continuous measurements of coefficient of friction show that this characteristic is not constant value even in steady-state regime. It alternates, varying from minimum to maximum and vice versa [1, 2]. Producing of acoustic vibrations in sliding friction is also one more evidence of dynamic character of this process. These vibrations play important role in mechanical behavior of interacting bodies including its wearing. The life time of a tribotechnical system could be significantly increased by means of only vibration cancellation using absorbers, coating or certain fitting of geometry of parts to damp rapidly oscillation of dangerous frequency [3].

In case of experimental investigation of friction and wear phenomenon, observations and measurements of material directly in the contact patch are performed after completion of the test. Therefore some results of this study could be the consequence of completion of process, but not process itself. Using of computer simulation let us to study dynamics of the process.

It was shown [4, 5] that using of discrete-continual approach is very effective in modeling of sliding friction [6]. In this case a narrow contact zone of interacted bodies is described by discrete approach of movable cellular automaton method and the rest material, which is under elastic loading, is described by a numerical method of continuum mechanics.

183

The goal of this paper is investigation of time-frequency characteristics of elastic waves, generated in the model friction pair, and to reveal dependency between the frequencies of these waves and roughness of interacting surfaces.

1 Time-and-frequency analysis of elastic waves in model friction pair

It is known, that real contacts take only a few percent of nominal surface of interacting bodies [7]. A schematic drawing of contact region of two surfaces in friction is presented in fig. 1,a. At this scheme the regions of real contact is marked by squares. In this paper the simulation of a certain part of real contact was performed. The mentioned part of the contact belongs to nano-scale level and is represented between two vertical lines on the right side of fig. 1,a. Such choice of the region allows to apply periodic boundary conditions in the displacement line of interacting bodies and to simplify slightly the task of simulation.

a) b) c)
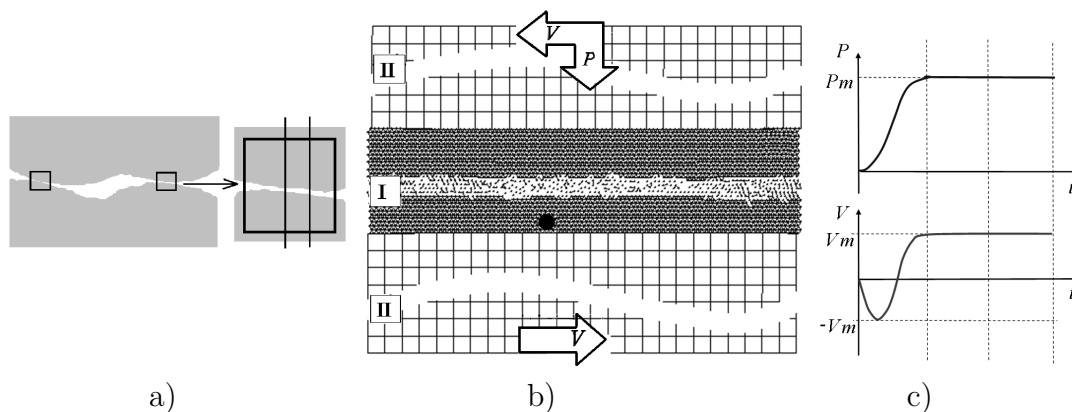
Figure 1: Contact zone in sliding-friction and the region under investigation (a), general view of the model sliding friction pair (b) and scheme of its loading (c).

Simulation of sliding friction was performed according to the scheme proposed in [8] (fig. 1,b). The friction zone was described on the basis of the movable cellular automaton method (region I in fig. 1,b). The rest part of interacting bodies was described by the approach of continuum mechanics (regions II in fig. 1,b), that allowed to decrease computation time. Location of a sensor for registration of elastic wave propagation is marked by the circle in the region I. The velocity V of the outside surface of the blocks (the upper surface for the upper block and the bottom surface for the bottom block) was increased step-by-step, according to time t, from 0 to $V_m = 10$ m/s (fig. 1,c). At the same time the upper surface was subjected by pressure P, which was increased up to its maximum $P_m = 127.5$ MPa. The bottom surface was fixed to exclude the displacement in the line of axis Y. In horizontal direction the model blocks were under periodic boundary conditions. Automaton size was 2.5 nm, step of the grid was 10 nm. A detail procedure of coupling discrete movable cellular automaton method with continuum mechanics approaches is considered in detail in [6].

A certain roughness was specified in the contact zone initially. The three typical
specimens of friction pairs studied are presented in fig. 2. Specimens (a) and (b) had
the same width (450 nm), but different initial surface profiles. The main difference
between these specimens was as follows. Surface irregularities of the specimen (a)
had two maxima and two minima. The specimen (b) had three mentioned surface
irregularities with lower height than one of the specimen (a). Width of the specimen
(c) was two times greater than one of the specimens (a) and (b). Surface profile of
this specimen corresponded to the surface profile of the specimen (b). The surface
profiles were specified by means of pseudorandom function.
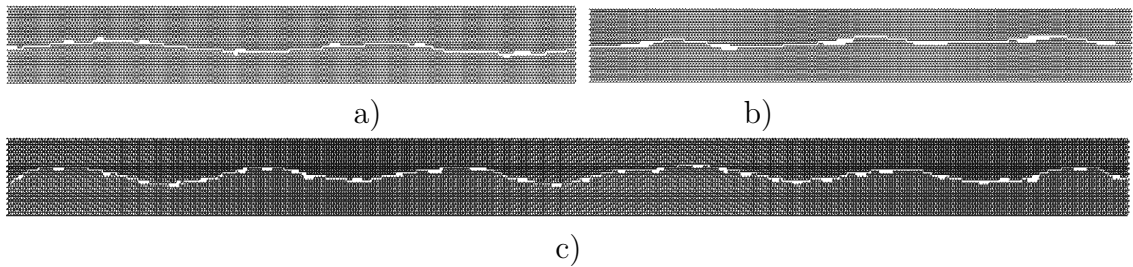
Figure 2: The initial specimens of the model friction pair. Only the regions described
by the movable cellular automaton method are presented.

Elastic wave recording was performed by means of a sensor, which marked as the
black dot in fig. 1,b. The sensor consisted of two automata. The following charac-
teristics of this pair were recorded: the components of velocities V_X and V_Y, stress
tensor intensity I and pressure P. The methods of recorded data processing and
analysis of the obtained results is described in detail in [8]. In particular, the factors
determining natural frequency of the mentioned system were indicated there. It
was noted, that peaks of Fourier-spectrum, corresponding to these frequencies, took
place for all recorded data. Additionally, it was shown that Fourier-spectra, plotted
for different time intervals, changed (the peaks changed its amplitude and location).
It is well known, that to analyze frequency variation in time they use the method
of signal processing like window Fourier method and wavelet transform [9].
In this paper we use wavelet transform of the signals studied, which performed by
means of shareware signal processing package "Last Wave" [10]. The most common
"Mexican hat" and Morlet functions were chosen as wavelets. To understand the
results obtained let's analyze two simple signals, namely amplitude-modulated and
frequency-modulated harmonic signals, using the mentioned wavelets.
The ordinate axis in a wavelet image is represented by nondimensional scale a which
is in the inverse proportion with frequency f. That is why low frequencies are shown
at the top and high frequencies at the bottom of the plot. Abscissa corresponds to
time (record number of a discrete signal). It should be noted, that a wavelet image
explicitly shows time variation of the signals with the frequency and the amplitude
in case of frequency and amplitude modulation respectively. Fourier analysis does
not allow to reveal such peculiarity of the studied signals. Sometimes in the upper
corner of images, corresponding to the end and to the beginning of a signal, one can
see strips (fig. 3), which are artifacts (interference induction) induced by finiteness
of a signal likewise the lobes at the Fourier-spectrum for the finite length sine-wave

185
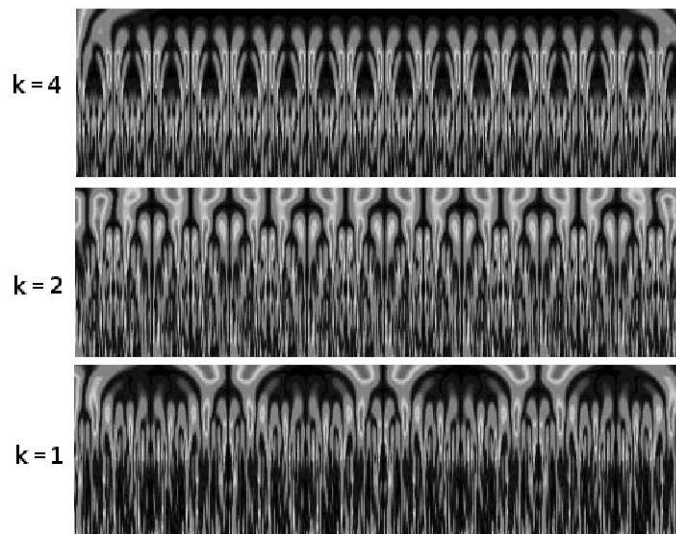
Figure 3: Wavelet transform of signals with various modulating frequencies.
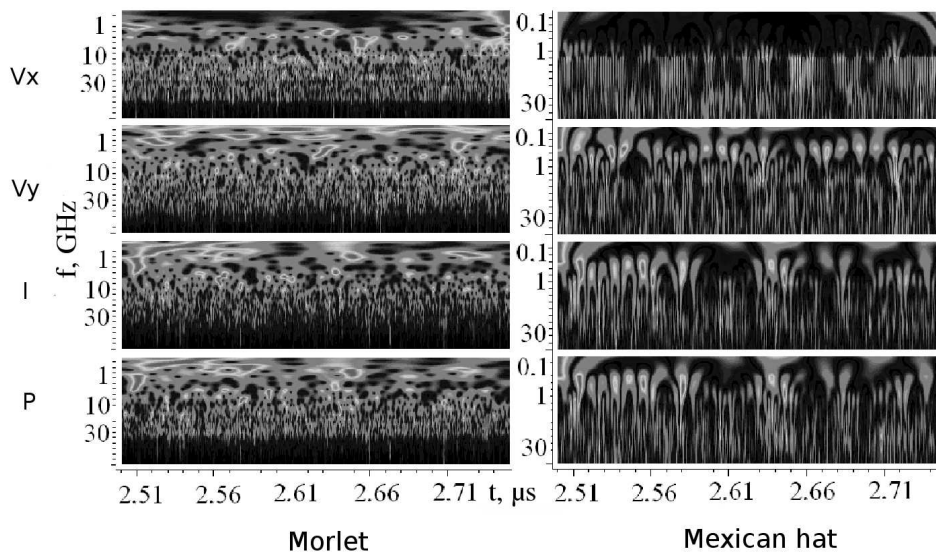
Figure 4: Wavelet transforms of the recorded data for the specimen (b) in fig. 2.

signal.

Mathematical notation of a frequency-modulated signal is $\sin[w \cdot x + d(x)]$, where w is a carrier frequency, d is modulating function of a signal, x is time. In this paper $w = 64\pi$, $d(x) = 8\sin(u \cdot x)$, where u is modulating frequency. The wavelet transform of frequency-modulated signals with different modulating frequencies $u = 4k\pi$ by means of "Mexican hat" function are shown in fig. 3. It is seen that appearance of the wavelet image significantly changes with increase of modulating frequency. It should be noted that transform by means of Morlet function holds a zigzag that is the characteristic feature of frequency-modulated signals.

Now, let's consider wavelet transform of registration signals, obtained from simula-

tion of sliding-friction (fig. 4). The comparison of fig. 3 and fig. 4, allows to reveal that elastic waves, generated in friction, probably are frequency- and amplitude-modulated.

In fact, as was shown in [8], natural frequencies of the studied system vary depending on the height of blocks. This height stochastically changes in sliding friction (even under steady-state behavior) as a result of particles separation from interacting surfaces (wear) and adhering of another particles from the friction zone on these surfaces (micro-welding). The simulation data clearly show the changing of corresponding frequencies due to small block sizes. Thus, little changing in height of quasi-liquid layer (i.e. the region of material mixture, where movable cellular automata are generally unbonded [4]) essentially affects the natural frequencies. This effect would be less noticeable in the case of greater block sizes.

The amplitude of the studied elastic waves depends on the force of interaction of upper and bottom blocks. As was mentioned above, friction coefficient, which is a ratio of resistant force of interacting bodies to the compressing force, permanently varies even under steady-state regime. It is observed not only in practice [1, 2] but in calculations also. Thus, alternating coefficient of friction leads to amplitude modulation of the registered signals.

2   Influence of surface roughness on elastic waves generated in friction pair

It was shown [8], that not only the natural frequencies of the system but also the frequencies related to the model sizes (width of the area investigated and the automaton size) and to the velocity of relative motion of blocks are represented at the spectra. It was noted the presence of unidentified peaks in the low-frequency region of the spectra as well. Location and height of these peaks are changed in time (fig. 5).

Additional analysis of the simulation results showed that surface profiles, separated a pseudo-liquid layer and a rigid part of specimens changed in sliding-friction. It allowed to assume that characteristic roughness of such surface profiles could correspond to these peaks at the spectra.

The algorithm presented in [11] with some changes was used for build up a surface profile, separating pseudo-liquid layer and rigid part of specimens. The changes consisted in the cutting of high-frequency spectrum components due to discreteness of the simulation model. The functions, describing profile of the bottom surface of the model friction pair, plotted on the basis of different algorithms, are shown in fig. 6. The function, plotted on the basis of the algorithm, described in [11], is shown in fig. 6,a. The result of the algorithm, proposed in this paper, is shown in fig. 6,b. The last function smooths away chains of inter automaton bonds protruded from the rigid surface, because it considers they belong to quasi-liquid layer.

The scheme of discrete representation of sought function $h(x)$ is shown in fig. 7. A value of discretization step δ corresponds to the automaton radius (minimum distance between vertical projections of automaton centers in close packing).

Surface profiles of friction pairs under consideration plotted at different times are
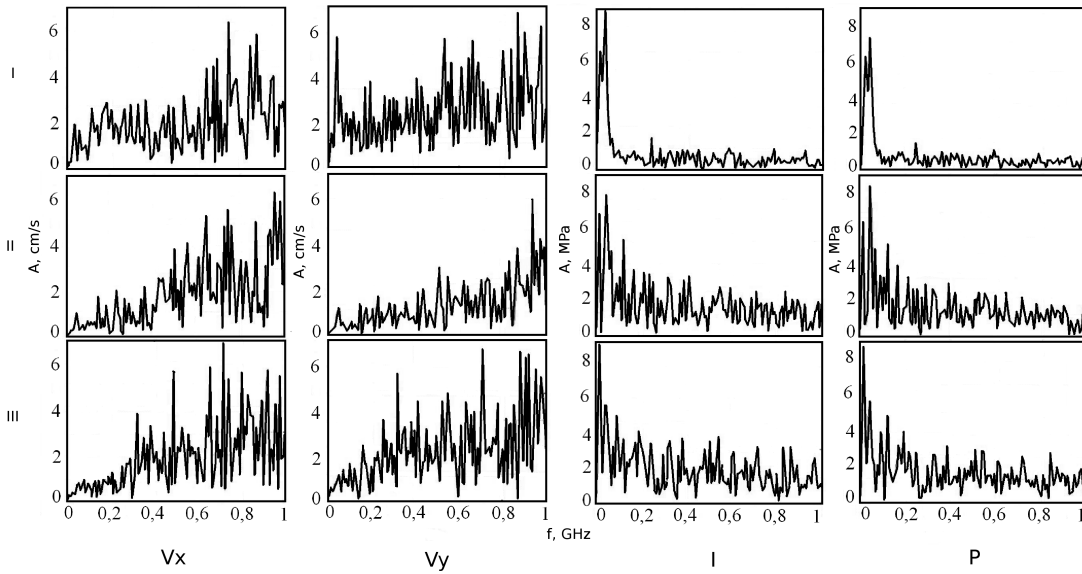
Figure 5: Fourier-spectra of analyzed data in the different time periods of interaction for the specimen in fig.2,b: I) 0.025..1.33; II) 1.33..2.64 III) 2.64..3.95 μs.
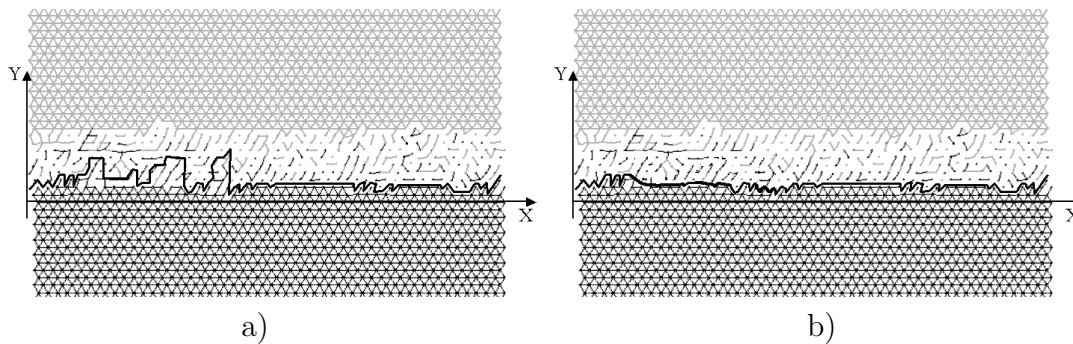
Figure 6: Example of functions describing the bottom surface profile of the model friction pair.
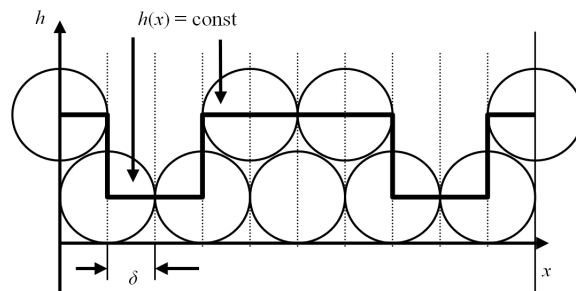
Figure 7: The scheme of discrete representation of function describing surface profile.

presented in fig. 8. The labels of the columns corresponds to the specimens shown in fig. 2. One can see that the thickness of friction layer increases in time, and the surface of blocks become smoother.

The periodicity of interacting surface profiles has to appear in corresponding frequencies of elastic waves, generated under relative displacement of the surfaces. Ex-
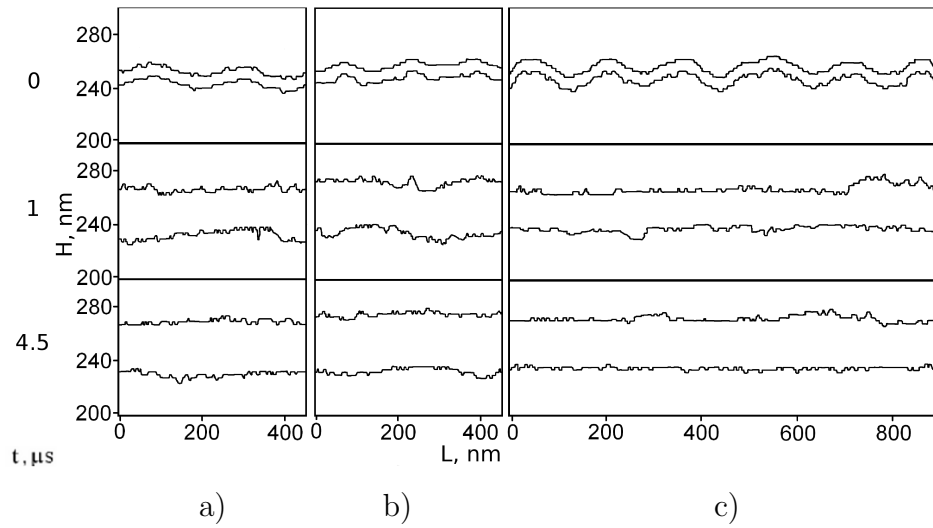
Figure 8: The surface profiles of the upper and the bottom blocks for the specimens
(a-c) in fig. 2 in different times t.
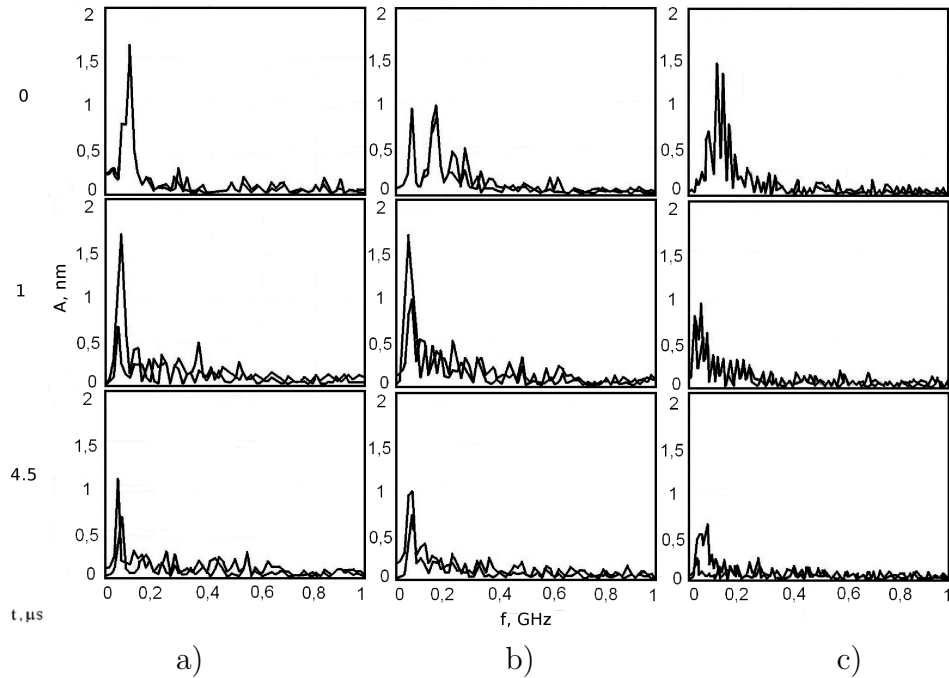
Figure 9: Spectra of the expected signals in different time moments t.

pected frequency of corresponding signal is calculated according to formula $f = v/l$,
where v is relative velocity of blocks, l is the distance between surface profile peaks.
Fourier-spectra of the expected signals were plotted on the basis of the obtained
surface profiles. These Fourier-spectra are shown in fig. 9. Whereas the fast Fourier
transform was used in this work, we would need data sample with the size as 2 in
some power to analyze the simulation results. The data describing the surface profile
had the size different from 2 in any power. Therefore, owing to periodic boundary
conditions of the model, the initial data sample was extended up to the needed size
using periodic repeating of the initial data.

As one can see from the presented spectra, one or another frequency would be stronger appeared in different time moments for these profiles. In addition, the peaks that insignificantly change their location (frequency) and the peaks that insignificantly change their amplitude were discovered.

The frequencies equal to 70, 90, 110 and 160 MHz are the most evident peaks in the spectra of expected signals. These frequencies were revealed in data spectra of the sensors of the model friction pairs shown in fig. 5. Moreover the accordance was more clear for pressure and stress intensity registration. Owing to changeability of friction coefficient during interaction, it should be expected that appearing oscillations would be amplitude-modulated.

Conclusions

The analysis of simulation results shows that the frequencies depending on the roughness of the surfaces separating quasi-liquid layer and interacting rigid bodies are present in the spectra of elastic waves generated under sliding-friction. The other peaks in these spectra are the natural frequencies of the specimen and the frequencies determined by the geometric sizes of the model and the velocity of relative motion. Furthermore, spectrum-and-frequency and time-and-frequency analyses, performed on the basis of Fourier and wavelet transforms, allowed revealing the complex structure of oscillations taking place in sliding friction. So, it is shown, that the change of friction surface profiles results in frequency modulation of generated elastic waves, in spite of apparent random manner of elementary events of wear fragments separation and their following welding in the friction zone. Amplitude modulation of the recorded signals may be explained by corresponding oscillations of the interaction force of the upper and bottom blocks and, accordingly, friction coefficient. So, one can conclude, that wear occurs according to certain laws, which may be studied on the basis of the corresponding acoustic spectra analysis.

Acknowledgements

References

[1] Mashkov Y.K., Ovchar Z.N., Baybarickaya M.Y., Mamaev O.A. Polymeric composition matirials in tribological engineering. M.: Nedra-Bisnescentr, 2004, 262 p.

[2] Gardos M.N., Gabelich S.A. Atmospheric effects of friction, friction noise and wear with silicon and diamond. Part I. Test methodology // Tribology Letters, 1999, No6, P. 79–86.

[3] Gritsenko B.P. Role of the acoustic oscillations generated by friction in fracture
of tribosystems // Trenie I iznos, 2005, V.26,No5, P. 481–488. (In Russian)

[4] A.I. Dmitriev, A.Y. Smolin, V.L. Popov, S.G. Psakhie Mnogourovnevoe mod-
elirovanie processov treniya i iznosa na osnove chislennikh metodov diskretnoy
mekhaniki i fenomenologicheskoy teorii // Physical mesomechanics, 2008, V.11,
No4, P. 15–24. (in Russian)

[5] Smolin A.Y., Konovalenko I.S. On the generation and propagation of elastic
waves in friction. Computer simulation. // Physical mesomechanics, 2006, V 9,
Spec. Issue, P. 45–48. (in Russian)

[6] S.G. Psakhie, A.Yu. Smolin, Yu.P. Stefanov, P.V. Makarov, E.V. Shilko, M.A.
Chertov, and E.P. Evtushenko, Simulation of behavior of complex media on
the basis of a discrete-continuous approach // Physical mesomechanics, 2003,
V. 6, No 5–6, P. 47–57.

[7] Persson B.N. J. Sliding Friction. Physical Principles and Applications. 2rd ed.
Berlin: Springer, 2000, 515 p.

[8] Smolin A.Yu, Dobrynin S.A., Psakhie S.G. Time-and-frequency analysis of elas-
tic waves in model friction pair // Vestnik of Tomsk state university. Mathe-
matics and mechanics, 2009, No1(5), P. 96–111. (in Russian)

[9] Mala S.A Wavelet Tour of Signal Processing N.Y:Academic Press, 1999. 671 p.

[10] URL: http://www.cmap.polytechnique.fr/ lastwave/.

[11] S.G. Psakhie, A.Yu. Smolin, Yu.P., Korostelev S.Yu., Dmitriev A.I., Shilko
E.V., Alekseev S.V. On peculiarities of establishment of deformation steady-
state condition of solid bodies // Journal of Technical Physics, 1997, V. 67,
No9, P. 34–37.

Serguei A. Dobrynin, pr. Academicheskii 2/4, Tomsk, 634021 Rissia
Aleksey Yu. Smolin, pr. Academicheskii 2/4, Tomsk, 634021 Rissia
Igor S. Konovalenko, pr. Academicheskii 2/4, Tomsk, 634021 Rissia

Analytical synthesis of crank-rocker and double-crank mechanisms with minimax link-length ratios

Abdullah F. Al-Dwairi   Suleiman E. Al-Lubani
Mohammad A. Al-Nawafleh
dwairy@just.edu.jo slubani@huson.edu.jo m_nawafleh@hotmail.com

Abstract

This paper presents analytical procedures for the synthesis of centric crank-rocker and double-crank four-bar mechanisms. The procedures are based on minimizing the longest-to-shortest link-length ratio and finding the corresponding extreme transmission angle. The addressed problems include designing the crank-rocker to convert a full-rotation input into a re-rocking motion of a desired stroke angle, and designing the double-crank mechanism to convert uniform rotation into a non-uniform, cyclically varying rotation with a given non-uniformity characteristic. The proposed approach has led to simple closed-form solutions for the two design problems.

1 Introduction

Crank-type inversions of a Grashofian four-bar chain include the simple crank-rocker and the double-crank (drag-link) mechanisms. In their simplest use as function generators, the crank-rocker converts full input rotation into a re-rocking output, while the double-crank linkage converts uniform full-rotation input into a full, but non-uniform, rotational output. According to Grashof's criterion, a four-link chain yields a linkage mechanism with at least one fully-rotatable link if the sum of the shortest and the longest links of the chain is less than the sum of the remaining two. Furthermore, if the shortest link is chosen as the ground link, the result is a double-crank mechanism. A crank-rocker mechanism results, on the other hand, if the shortest link is adjacent to the ground link.

Dimensional synthesis of linkage mechanisms usually involves two design criteria that are used to assess the design performance. The first criterion pertains to the quality of motion transmission in the mechanism and the other is related to the requirement that mechanism links be of comparable lengths (see for instance, [1 - 5]).

Quality of motion transmission in a four-bar linkage is assessed using the transmission angle - the included angle between the coupler link and the output link. The

closer the extreme value of this angle is to 90 deg, the better is the quality of motion
transmission in the mechanism. Linkages with extreme transmission angles less than
45 deg (or larger than 135 deg) are considered impractical, especially for high-speed
applications.

On the other hand, it is often desirable that the links of a linkage be of comparable
lengths to create conditions for better realization of the mechanism. In a crank-
rocker mechanism, too short a crank is undesirable due to many reasons, among
which is the increased sensitivity to length variation caused by manufacturing errors
and joint clearances. In a drag-link mechanism, on the other hand, too long a crank
leads to larger mechanism size and increased inertia effects.

Mechanism designers usually place limitations on minimum and maximum link
lengths. The limitations often take the form of inequalities that are fulfilled through
design iteration.

In this paper, design equations are developed for crank-rocker and double-crank
linkages based on analytically minimizing the longest-to-shortest link-length ratio
Developments are restricted to centric crank-type linkages, in which case the in-
put displacement between the two limiting positions of a mechanism is 180 degrees.
Hereafter, the term "drag-link" will be used instead of "double-crank," for conve-
nience.

2   Crank-rocker mechanism

Figure 1 shows a crank-rocker 4-bar in its limit positions in which the crank and
the coupler links are inline. Angles φ and ψ denote input and output displacements
measured from position 1 of the linkage and $\Delta\varphi$ and $\Delta\psi$ denote total input and
output displacements between the two limit positions. If angle $\Delta\varphi$ is 180 degrees,
the crank-rocker is said to be centric.
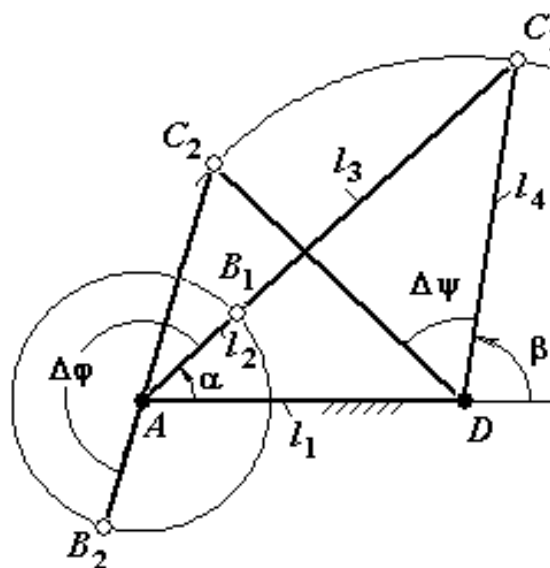
Figure 1: Crank-Rocker Limit Positions

Let it be desired to design a centric crank-rocker to generate a re-rocking motion with a given re-rocking stroke $\Delta\psi$. We need to specify a suitable set of link lengths that correspond to the specified $\Delta\psi$ and, at the same time, fulfill other design objectives. The two main design objectives addressed here are those of quality of motion transmission and of the highest link-length ratio.

In Fig. 1, the link lengths are l_1, l_2, l_3, and l_4, which are lengths of the fixed link, the input crank, the coupler link, and the output link, respectively. Following the traditional course of action, we switch from these metric dimensions to non-dimensional link-length ratios. This can be done by taking the fixed link length l_1 for the unit of length and relating the remaining lengths to it. This yields the following link-length ratios.

$$a = \frac{l_2}{l_1}, \quad b = \frac{l_3}{l_1}, \quad c = \frac{l_4}{l_1}, \quad \text{and } d = 1 \tag{1}$$

Synthesis equations are developed from geometrical relations of Figs. 1 and 2. As Figure 2 illustrates, the transmission angle reaches its extreme values when the input crank becomes coincident with the fixed link. Since the input displacement between the two limit positions (Fig. 1) is $\Delta\varphi = 180$ deg., the extreme values of the transmission angle, μ_{min} and μ_{max}, are deviated equally from 90 deg. [2 – 7]. With this fact in mind, it can be shown from the triangles B'C'D and B"C"D that the link-length ratios fulfill the following two equations.
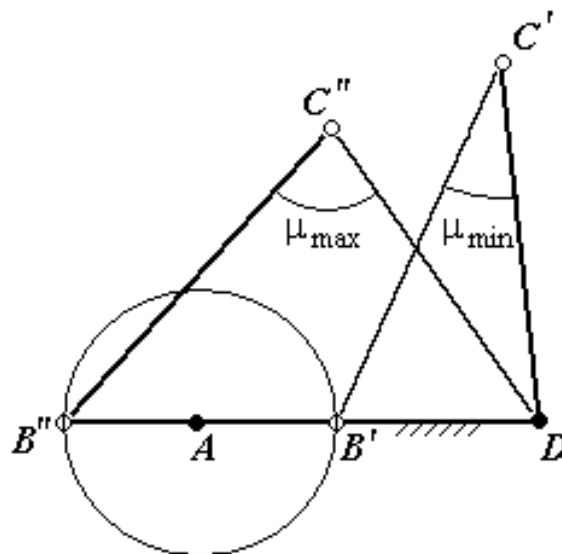
Figure 2: Extreme Transmission Angles of Crank-Rocker

$$a^2 + 1 = b^2 + c^2 \tag{2}$$

and

$$a = b\,c\cos\mu_{min} \tag{3}$$

Based on Grashof's criterion, the input link AB must be the shortest among the four links. From Eq.(2), it then follows that the ground link AD, which is represented by the unity, is the longest. Consequently, parameter a is the shortest-to-longest link-length ratio in a centric crank-rocker mechanism. To ensure link lengths of comparable magnitudes, this ratio should be maximized.

Equations (2) and (3) involve the sought-for link-length ratios and the extreme transmission angle. Since there are four unknowns in two equations, any two of the unknowns can be assigned arbitrarily. The usual approach is to assign a least-acceptable transmission angle μ_{min} and one of the link-length ratios and solve for the remaining two ratios. The resulting from this approach solution might turn to be unsatisfactory due to unacceptable link-length ratios. Usually, iteration is necessary to find an acceptable solution.

To avoid iteration, the approach proposed here suggests looking for an analytical solution to Eqs.(2) and (3) that maximizes link-length ratio a. We add the condition:

$$a \rightarrow maximum \tag{4}$$

Brodell and Soni [6] provided formulae for a, b, and c that fulfill Eqs.(2) and (3) and the desired re-rocking stroke $\Delta\psi$. The formulae are:

$$b = \sqrt{\frac{1 - \cos\Delta\psi}{2\cos^2\mu_{min}}} \tag{5}$$

$$c = \sqrt{\frac{1 - b^2}{1 - b^2\cos^2\mu_{min}}} \tag{6}$$

$$a = \sqrt{b^2 + c^2 - 1} \tag{7}$$

It is seen from the above equations that for given $\Delta\psi$ and μ_{min}, link-length ratio a is a function of b (since c is given in terms of b). To maximize a, therefore, the derivative of a with respect to b must be zero. That is:

$$\frac{\partial a}{\partial b} = 0 \tag{8}$$

One approach here is to substitute from Eqs.(5) and (6) into (7), carry out the differentiation, and solve Eq.(8) for b. This procedure, however, may be skipped by directly noticing from Eqs.(2) and (3) that the dependence of a on b is the same as on c. Based on known concepts from differential calculus, function a will be maximum or minimum if b and c are equal to each other. Equation (8) therefore implies that:

$$b = c \tag{9}$$

Substituting this result into Eq.(6) and rearranging terms gives:

$$b^4\cos^2\mu_{min} - 2b^2 + 1 = 0 \tag{10}$$

Equation (10) is a bi-quadratic in b leading to four possible solutions for b. However, only two of the four solutions are positive and are:

$$b = \frac{1}{\sqrt{1 - \sin \mu_{min}}} \tag{11}$$

and

$$b = \frac{1}{\sqrt{1 + \sin \mu_{min}}} \tag{12}$$

By recalling that link-length ratio b cannot be greater than unity, only solutions by Eq.(12) apply here. Substitution from Eq.(12) into (5) and rearranging yields:

$$\sin \mu_{min} = \cos^2 \frac{\Delta \psi}{2} \tag{13}$$

Equation (13) relates μ_{min} to $\Delta \psi$ and involves no link-length ratios. Choosing μ_{min} in accordance with this equation ensures maximization of the link-length ratio a. Back substitution from Eq.(9) and (12) into Eq.(7) gives the maximum link-length ratio a as:

$$a = \frac{\cos \mu_{min}}{1 + \sin \mu_{min}} \tag{14}$$

Substituting from Eq.(13) into (14) and (12) yields the link-length ratios in terms of the desired stroke $\Delta \psi$ in the form:

$$a = \frac{\sin(\frac{\Delta \psi}{2})}{\sqrt{1 + \cos^2(\frac{\Delta \psi}{2})}} \tag{15}$$

$$b = c = \frac{1}{\sqrt{1 + \cos^2(\frac{\Delta \psi}{2})}} \tag{16}$$

Equations (15) and (16) can be used instead of Eqs.(5), (6), and (7) whenever a maximized shortest-to-longest link-length ratio is desired. The extreme transmission angle in this case cannot be assigned arbitrarily and should be obtained from Eq.(13). To illustrate the above results, Equations (5), (6), and (7) have been plotted in Fig. 3 against $\Delta \psi$ for a number of values of μ_{min}. Note from this figure that in all cases, the curve for link-length ratio a reaches its maximum point when the curves for b and c intersect with each other, i. e., when $b = c$, as given in Eq.(9).
Figure 3 also illustrates that μ_{min} and $\Delta \psi$ must fulfill the inequality:

$$\Delta \psi + 2\mu_{min} \leq 180^\circ \tag{17}$$

At strict equality in Eq.(17), link-length ratios a and c become zero and link-length ratio b becomes unity.

196
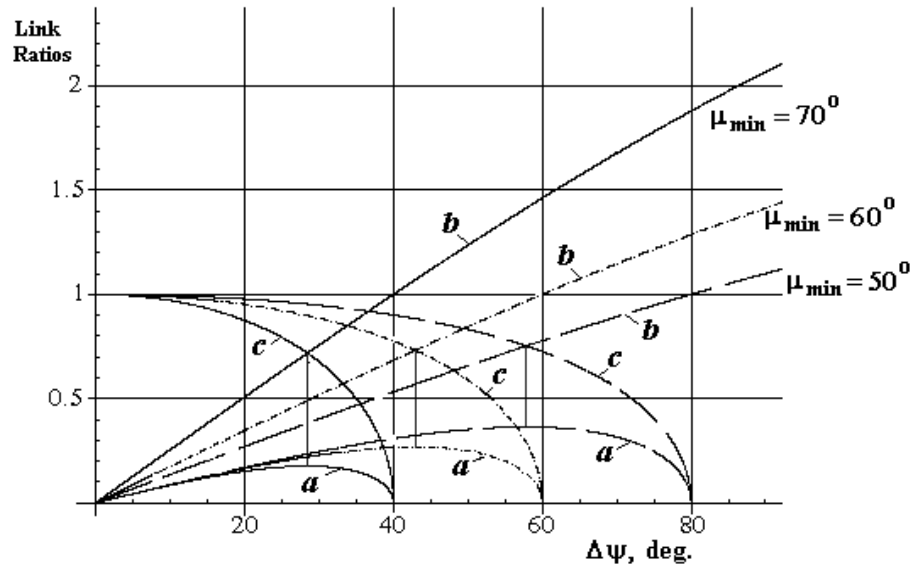
Figure 3: Link-Length Ratios of Crank-Rocker vs. Rocking Stroke

3 Drag-link mechanism

Figure 4 shows a drag-link mechanism in two finitely separated positions in which coupler link BC is parallel to ground link AD. A velocity analysis of this mechanism would show that in the two positions shown, the input and output links instantaneously rotate at the same speed and the velocity ratio, $d\psi/d\varphi$, hence is unity.

Drag-link motion may be described using the generated difference between angular positions α and β of the input and the output links, respectively. Because the coupler link BC must be longer than the ground link AD, angle α is always greater than β and the output link CD hence always "lags" behind the input link AB. A lag angle, L, therefore is introduced as:

$$L = \alpha - \beta \tag{18}$$

Tsai [7] showed that the lag L reaches its minimum value, L_{min}, in the position AB_1C_1D where $\varphi = 0$ and reaches its maximum value, L_{max}, in the position AB_2C_2D where $\varphi = \Delta\varphi$. A typical shape of the drag-link displacement function, $\varphi = f(\psi)$, is shown in Fig. 5.

The change in lag, dL, is the delay generated in the output displacement relative to the input displacement. The delay generation can be viewed from Fig. 5 as the deviation of the displacement curve from the diagonal line. The maximum delay, ΔL, therefore, is given by:

$$\Delta L = \Delta\phi - \Delta\psi \tag{19}$$

This work is limited to the case $\Delta\varphi = 180$ deg so that:

$$\Delta L = 180^\circ - \Delta\psi \tag{20}$$

197
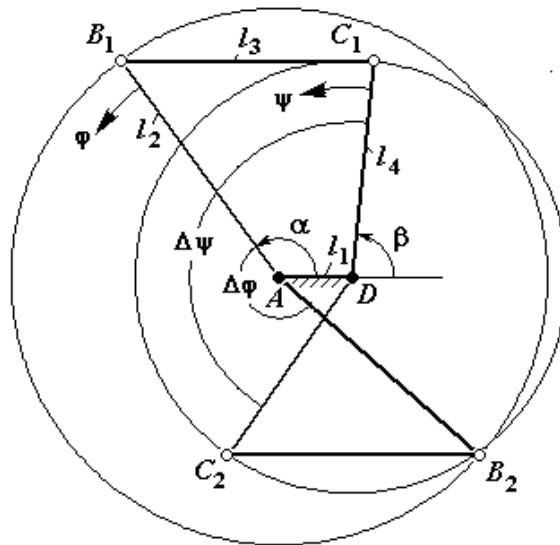
Figure 4: Drag-Link Mechanism in parallel and Anti-parallel Positions

One kind of drag-link synthesis problems is to design the mechanism to generate a specified maximum delay ΔL. We seek a drag-link mechanism to generate the desired ΔL while achieving a good quality of motion transmission and a minimum longest-to-shortest link-length ratio. Al-Dwairi [3] showed that minimizing this ratio means minimization of the space occupation of the drag-link.

To synthesize the drag-link, we begin by analyzing the drag-link positions to obtain relationships among the mechanism parameters and characteristics. By referring to Fig. 4, we use the same notation $\{a, b, c\}$ for the drag-link ratios as given in Eq.(1). With the preserved notations, it can be shown that Eqs.(2) and (3) hold for the drag-link mechanism and can be derived from the triangles DB'C' and DB"C" of Fig. 6, which shows the drag-link in its extreme-transmission-angle positions. As with the centric crank-rocker, angles μ_{max} and μ_{min} are deviated equally from 90 deg.

Design equations for synthesizing centric drag-link mechanisms to generate a specified maximum delay ΔL with an assigned μ_{min} were derived by Tsai [7] who arrived at the following results for the link-length ratios:

$$c = \frac{1}{\sin(\frac{\Delta L}{2})} \tag{21}$$

$$b = \sqrt{\frac{c^2 - 1}{c^2 \cos^2 \mu_{min} - 1}} \tag{22}$$

$$a = b\,c\,\cos\mu_{min} \tag{23}$$

In order to minimize the longest-to-shortest link ratio a, we notice that the dependence of a on b is similar to the dependence of a on c in both Eq.(2) and (3) and conclude directly that ratio a becomes extreme when b and c are equal to each other. This fact is illustrated in Fig. 7 which depicts the link-length ratios from

198
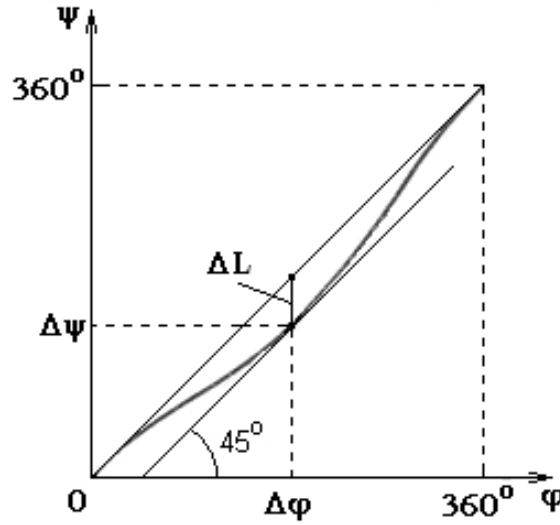
Figure 5: Typical Drag-Link Displacement Function

Eqs.(21), (22), and (23) versus the maximum delay ΔL for various values of $\mu_{\min}$. Note that for any given $\mu_{\min}$, link-length ratio a reaches its minimum at the same ΔL at which the curves for b TRIAL RESTRICTION and c intersect with each other.

Based on this result, we replace the left-hand side of Eq.(22) with c and rearrange terms to obtain:

$$c^4 \cos^2 \mu_{\min} - 2c^2 + 1 = 0 \tag{24}$$

Equation (24) is similar to Eq.(10) derived for the link-length ratio b of the crank-rocker. Solution of this equation yields two possible solutions: either

$$c = \frac{1}{\sqrt{1 - \sin \mu_{\min}}} \tag{25}$$

or

$$c = \frac{1}{\sqrt{1 + \sin \mu_{\min}}} \tag{26}$$

Solution by Eq.(26) yields values of c less than unity and is unacceptable here. The only valid solution is by Eq.(25). Hence:

$$b = c = \frac{1}{\sqrt{1 - \sin \mu_{\min}}} \tag{27}$$

Substituting from Eq.(27) into Eq.(23) yields the minimum of the link-length ratio a in the form:

$$a = \frac{\cos \mu_{\min}}{1 - \sin \mu_{\min}} \tag{28}$$
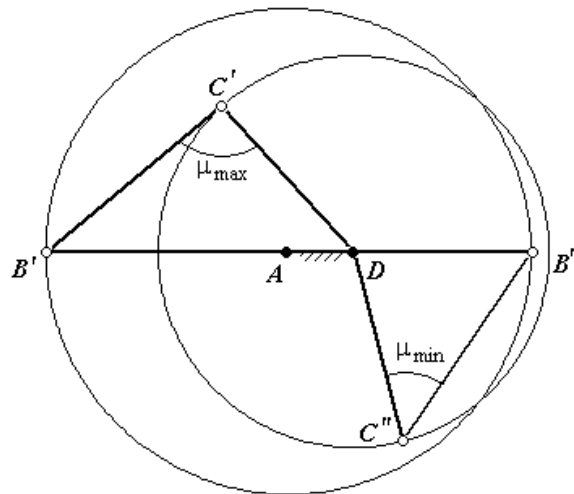
Figure 6: Extreme Transmission Angles of Drag-Link

To express the drag-link ratios in terms of the desired maximum delay ΔL, equate the left-hand side of Eq.(26) to that of Eq.(21) to arrive at:

$$\sin \mu_{\min} = \cos^2 \frac{\Delta L}{2} \tag{29}$$

Incorporating this result into Eqs.(27) and (28) yields:

$$b = c = \frac{1}{\sin(\frac{\Delta L}{2})} \tag{30}$$

and

$$a = \frac{\sqrt{1 + \cos^2(\frac{\Delta L}{2})}}{\sin(\frac{\Delta L}{2})} \tag{31}$$

A drag-link mechanism designed using Eqs.(30) and (31) generates the specified delay ΔL with a minimum transmission angle found from Eq.(29) and has the least possible longest-to-shortest link-length ratio a.

4 Conclusions

An examination of the equations derived above for centric crank-rocker and drag-link mechanisms shows a strong analogy between the two designs. This analogy is due to the fact that both designs are inversions-on-the-input of each other. This analogy was analyzed by Tsai [8] who expressed it as a one-to-one-correspondence between the two mechanisms. Reflecting this correspondence onto the material of this paper allows constructing the table shown below, which contains unified design formulae that can be used for both inversions. In the table below, the variable x denotes $\Delta\psi/2$ for the crank-rocker and $\Delta L/2$ for the drag-link. This implies that if

200
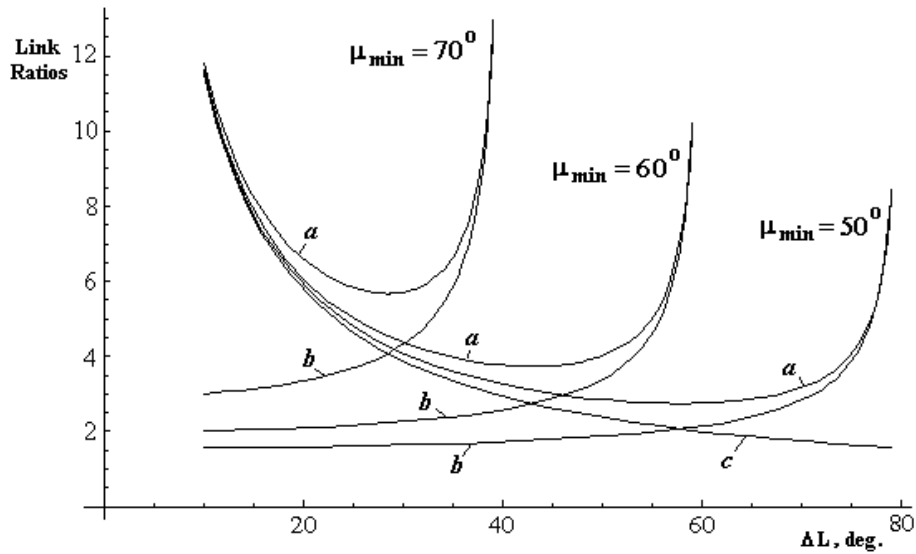
Figure 7: Link-Length Ratios of Drag-Link vs. Maximum Delay

a crank-rocker that generates a given rocking stroke $\Delta\psi$ is inverted on its input, the resulting drag-link will generate a maximum delay ΔL that is equal to the rocking stroke $\Delta\psi$ of the original crank-rocker, and vise versa.

Another point worth of clarification here is the cost of optimizing the highest link-length ratio in the two inversions. This cost can be recognized by comparing Eq.(17) with Eq. (13). From Eq.(17), if we were not to optimize the link-length ratio a, we could select any μ_{min} up to (90 deg-$\Delta\psi$/2) or (90 deg - ΔL/2). A designer would usually select μ_{min} some 4-5 degrees below these limits. To optimize a, however, angle μ_{min} is now constrained to Eq.(13).

Crank-rocker	Drag-Link	Formula
$\dfrac{\text{input crank}}{\text{ground link}}$	$\dfrac{\text{ground link}}{\text{input crank}}$	$\dfrac{\sin x}{\sqrt{1+\cos^2 x}}$
$\dfrac{\text{input crank}}{\text{coupler link}} \dfrac{\text{input crank}}{\text{rocker}}$	$\dfrac{\text{ground link}}{\text{coupler link}} \dfrac{\text{ground link}}{\text{output crank}}$	$\sin x$
$\sin \mu_{min}$	$\sin \mu_{min}$	$\cos^2 x$

To illustrate this point, Figure 8 is provided which is a plot of Eqs.(13) and (17). As this figure shows, optimization is achieved at the expense of some decrease in the quality of motion transmission.

5   Illustrative example

Let it be desired to design a centric crank-rocker to generate a re-rocking stroke of $\Delta\psi = 30$ deg with a ground link length of $l_1 = 200$ mm. The input-crank length is desired to be the maximum possible.

Solution
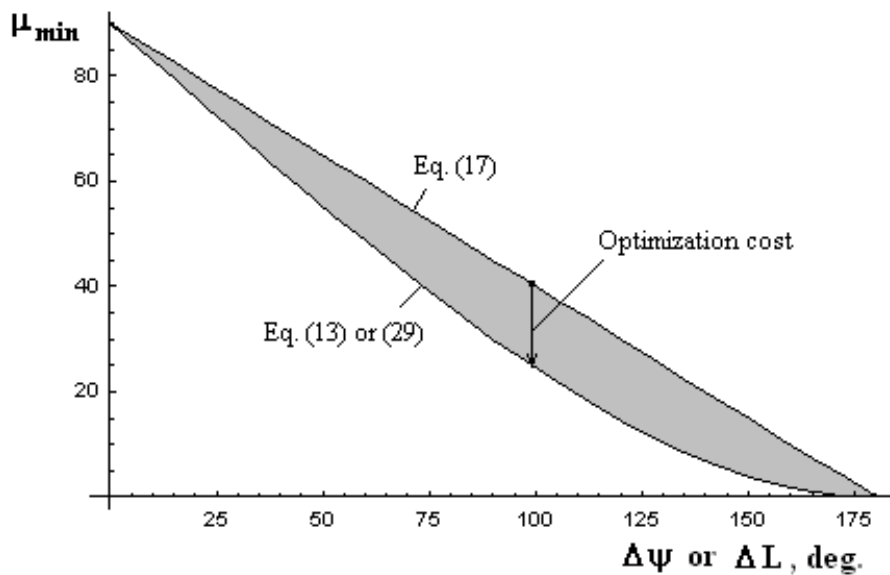
Figure 8: Optimizing the highest link-length ratio at the expense of some loss in the quality of motion transmission

Using the formulae given in Table 1 with $x = \Delta\psi/2 = 15$ deg and ground link = 200 mm, the required mechanism dimensions are found to be:

$$\text{input crank} = 200 \frac{\sin 15^{\circ}}{\sqrt{1 + \cos^2 15^{\circ}}} = 37.23 \text{mm}$$

$$\text{coupler link} = \text{output rocker} = 37.23/\sin 15^{\circ} = 143.85 \text{mm}$$

Upon inverting this crank-rocker on its input, a drag-link mechanism results with the following dimensions (see Table 1):
ground link = 37.23 mm;
input crank = 200 mm;
coupler link = output crank = 143.85 mm.
The drag-link generates a maximum delay of $\Delta L = \Delta\psi = 30$ deg.
The extreme transmission angle in both inversions is found to be:

$$\mu_{\min} = \sin^{-1}(\cos^2 15^{\circ}) = 68.91^{\circ}.$$

Summary

The paper provided closed-form solutions to the position synthesis of centric crank-rocker and drag-link mechanisms based on minimizing the longest-to-shortest link-length ratio. By introducing this minimization constraint, no optimization search is required and the extreme transmission angle is defined uniquely. The paper demonstrated that this minimization is achievable at the expense of some decrease in the achievable quality of motion transmission. Using kinematic inversion, a unified set of design equations is developed that can be used for both crank-rocker and drag-link mechanisms.

References

[1] Paul B., 1979, Kinematics and Dynamics of Planar Machinery, Prentice Hall, 670 p.

[2] Balli S. and Chand S., 2002, "Transmission Angle in Mechanisms (Triangle in Mech)", Mech. Mach. Theory, 37(2), pp. 175 – 195.

[3] Al-Dwairi, A. F., 2009, Design of Centric Drag-Link Mechanisms for Delay Generation with Focus on Space Occupation, ASME Journal of Mechanical Design, Vol. 131, 011015.

[4] Peisach, E. E. and Nesterov, V. A., 1988, *A System of Designing of Planar Linkages*, Machinostroenie, Moscow, in Russian

[5] Ming, L. and Younghu L., 1996, "Design of Crank-Rocker Mechanisms with Optimum Transmission Angle over Working Stroke", Mechanism and Machine Theory, 31(4), pp. 501-511.

[6] Brodell, R. J., and Soni, A. H., 1970, Design of the crank rocker mechanism with unit time ratio. *J. Mech.* **5**, pp. 1–4.

[7] Tsai, L. W., 1983, "Design of Drag-Link Mechanisms with Optimum Transmission Angle", ASME J. Mechanical Design, 105(2), pp. 254-259.

[8] Tsai, L. W., 1983, "Design of Drag-Link Mechanisms with Minimax Transmission Angle Deviation", ASME J. Mechanical Design, 105(4), pp. 686-691.

Abdullah F. Al-Dwairi, Industrial Engineering Department, Jordan University of Science and Technology, P.O. Box (3030), Irbid 22110, Jordan, dwairy@just.edu.jo

Suleiman E. Al-Lubani, Mechanical Engineering Department, Al-Huson University, College, Al-Balqaa Applied University, slubani@huson.edu.jo

Mohammad A. Al-Nawafleh, Al-Hussein Bin Talal University, Jordan, m_nawafleh@hotmail.com

On the problem of analysis of the stress-strained state of the tape during it's winding around the solids

Polina Dyatlova   Marina Rudaya   Alexandr Majorov

dyatlovaspb@hotbox.ru

Abstract

In present work the causes of heterogeneity of strain-stressed state of textile tape winded up on the solid are analyzed. Influence of geometric shapes of objects which are reinforced by the tape on localization and character of heterogeneity is considered. Methods of strains and stresses calculation in the process of reinforcing of complex shape objects by elastic textile materials are proposed. As example of the problem of reinforcing objects by materials with hereditary properties, a problem of the tape winding on the cylindrical tube and corresponding to constitutive equations of differential type is investigated. The tape is supposed to have canvas structure.

1 Introduction

Tape winding is the widespread operation in manufacture and reinforcing of many products. From the point of view of quality improving of a created product significant interest has development of calculation methods which allow to find way for elimination of heterogeneities stress-strained state of the tapes. Therefore development of the theory predicting deformations and the pressure arising during winding in the tapes, possessing various rheological characteristics, is an actual problem. Successes in solution of this problem can form a basis for development of recommendations on selection of materials and textile structures of used tapes and on designing technologies of winding [2], [3].

2 Various causes of the tapes heterogeneity

Studying the tape winding processes lead us to a lot of difficult problems of shell mechanics. In particular, questions of deformation and laying the tapes quite often can be considered within the limits of the theory of soft shells, i. e. the shells not resisting to bending.

Thus it is easy to reveal some typical conditions of occurrence of heterogeneity of deformations and tape pressure. These heterogeneities can be caused by geometrical

204

properties of wind-up object. Lets point out some examples. It is possible to specify the heterogeneity, arising at tape winding on bent parts of the tubes represented in figures 1 and 2 [4].
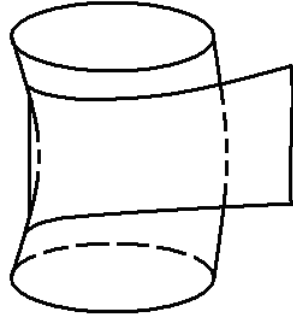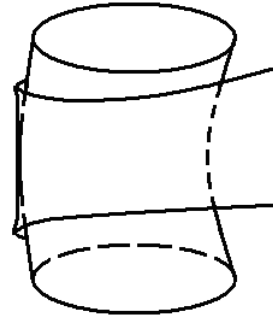
Figure 1. Tube 1   Figure 2. Tube 2

As you can see at figure 1 with growing of tension of the tape its edges will draw together, sliding on the surface of the tube. Thus the longitudinal folds on the tape concentrating in a hollow (in the saddle or the hyperbolic part) of tubes are formed.

As to the tape represented on figure 2 the cross tucks near its edges (if edges do not adjoin to the surface of the tube) can be formed. At winding on such edges of the next coil of the tape formation of the specified cross tucks cannot be avoided. Such mechanism of wrinkles formation can be excluded if to provide edges fitting to the tube, using elastic tapes and pulling them with sufficient strain. But also in this case heterogeneity of the stress-strain state of the tape takes place because its edges are strained less than its middle part.

Calculation methods for investigation of axisymmetric problems about stress-strained state of the elastic shells covering cylindrical solids are developed in [4], [5], [6]. In these works the approached calculation methods of axisymmetric elastic shells covering the cylindrical solids are given. Complexity of problems increases, at deviations from axial symmetry as in this case fibres or the threads forming textile structures of tapes, cannot be located all along geodetic lines of the reinforced solid, and slide on its surface, being displaced to such lines. This phenomenon observed already in such simple cases as tape winding on a circular cone, can lead to essential heterogeneities of pressure and deformations fields of the tapes.

For elastic tapes small axial symmetry infringements of problems on the basis of application asymptotic analysis methods can be considered.

Rather successful development of the nonlinear theory of elastic shells is caused by that in this case the research problem and the equations of shells in displacements can be replaced by an equivalent problem of minimization energy functional. For such case effective numerical methods of research are developed.

3 On the winding of the tapes with hereditary properties

Research of inelastic shells cannot in any natural way be reduced to variational problems as for such shells, unlike elastic shells, it is impossible to enter analogue of strain energy of their deformation convenient enough for research [1], [6]. Because of that mathematical research methods of products reinforcing problems by means of inelastic tapes winding on their surface, even with simple hereditary properties, till now have not received essential development.

Some promotion in research of these problems can be received with reference to tubes reinforcing at some simplifying assumptions concerning textile structure of the tape, it constitutive equations and its winding mode.

Let's suppose that the thread has textile structure of the canvas, and warps are directed along the tape and located, as well as cross-section wefts, so rarefied, that in zero approximation, it is possible to neglect weft influence on the tension of warps. Rheological properties of the warps are assumed to be defined by linear constitutive equations of differential type

$$P_n\left(\frac{\partial}{\partial t}\right)T = Q_m\left(\frac{\partial}{\partial t}\right)\varepsilon, \tag{1}$$

where $P_n\left(\frac{\partial}{\partial t}\right)$ and $Q_m\left(\frac{\partial}{\partial t}\right)$ are differential operators of the order n and m accordingly, T is a tension of the thread, ε is its relative elongation.

Let's consider that winding is realized under the scheme represented in figure 3. On this scheme the tube 1 of radius R which rotates around the axis Z with angular velocity Ω and, at the same time moves along this axis with velocity V. The tape 2 constituting the angle φ with a vertical is reeled up on the tube. The tape moves on the tube with feeding package 3 which rotates with angular velocity ω around of fixed axis and has radius r. Through $L(h)$ the length free (being between the package and the tube) parts of the warp located on distance h from the bottom thread which length is equal $L_0 = L(0)$, $\Delta L(h) = L(h) - L_0$ is designated.

Relaxation processes most actively occur at part of the tape which is between the feeding package and the tube. During movement in this area the basic and remaining in the final product differences in the stress-strain states of the tape parts are formed. These differences arise because of inequality of movement time of different tape parts between the package and the tube.

That the tape did not slide on surfaces of the feeding package or tubes, warps should leave from the package in a direction perpendicular to its axis, and on the tube these treads should settle down on geodetic lines. These conditions will be executed, if parameters of process will satisfy to equality:

$$V = R\Omega \cot\varphi. \tag{2}$$

The specified scheme of the tape winding leads to an inequality of warps tension. This inequality is connected with distinction $\Delta L(h)$ of lengths of those (free) sites of these threads which settle down between the package surfaces and tubes.
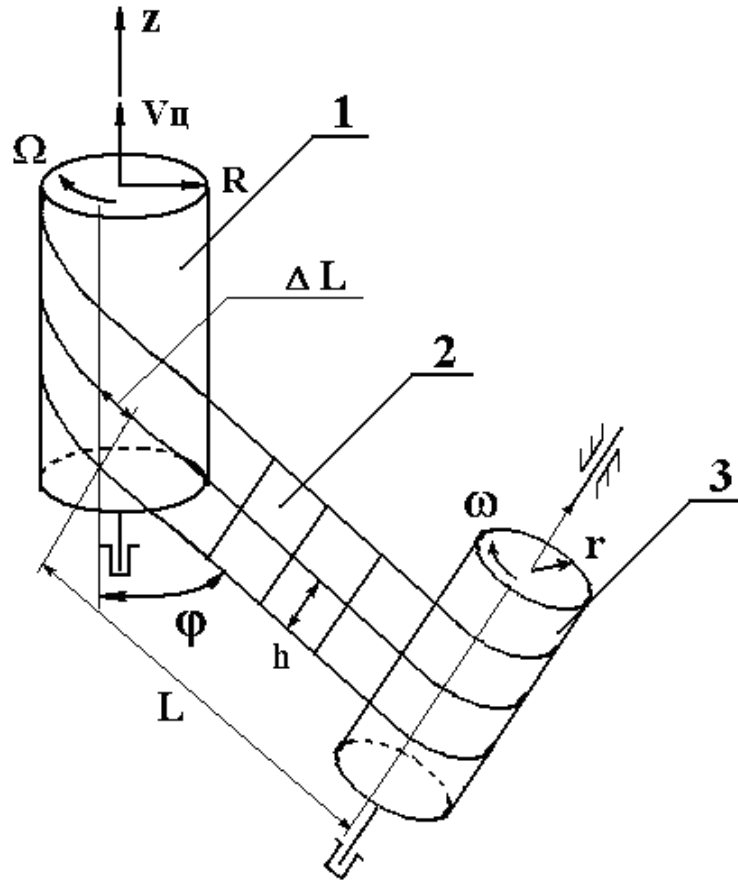
Figure 3.

Studying of heterogeneity of the tension of the warps is reduced to the analysis of
the calculation of the equation (1) satisfying to boundary conditions of leaving of the
tape from the feeding package and its receipts on the reinforced tube. Such analysis
is fulfilled at a simplifying assumption, that inertness of the tape is negligibly small,
and the value T along each warp remains constant though varies at transition from
one yarn to another, being, thus, function of parameter h defining position of the
yarn in the tape. In this case the analysis of movement and deformations of the
tape can be absolutely completed by numerical methods on the basis of the common
solution of the equation (1).

The certain notion about obtained results give us the studying of the tape corre-
sponding constitutive Fohgt equation, i. e. to the equation

$$T(h) = E\varepsilon(l, h, t) + \mu \partial \varepsilon(l, h, t)/\partial t, \tag{3}$$

where E and μ are coefficients of elasticity and viscosity, l is Lagrange coordinate of
the thread particle, entered on uniformly stretched threads having relative elongation
ε_0 by the formula

$$l = (1 + \varepsilon_0)s. \tag{4}$$

Here s is Lagrange coordinate entered on non deformed threads as it is specified in [1].

Positions of the thread particles in space are characterized by Euler coordinates x which are counted along threads in direction of its movement from package. The coordinate x of any section of some threads which are at distance h from the bottom edge of the tape can be considered either as function from h, s, t or as function from h, l, t.

In the latter case we receive

$$
x(h,l,t) = \frac{1}{1+\varepsilon_0} \times \tag{5}
$$
$$
\times \left(\left(1 + \frac{T(h)}{E}\right)(l+\omega rt) - \left(\varepsilon_0 - \frac{T(h)}{E}\right)\frac{\mu\omega r}{E}\left(e^{-\frac{E}{\mu\omega r}(l+\omega rt)} - 1\right)\right).
$$

Velocities of movement of the tape particles are defined by the equation

$$
V = \frac{\partial x(h,l,t)}{\partial t} = \frac{\omega r}{1+\varepsilon_0}\left(1 + \frac{T(h)}{E} + \left(\varepsilon_0 - \frac{T(h)}{E}\right)e^{-\frac{E}{\mu\omega r}(l+\omega rt)}\right). \tag{6}
$$

Distribution of relative elongations of warps in the tape can be calculated by the formula

$$
\varepsilon(l,h,t) = \frac{T(h)}{E} + \left(\varepsilon_0 - \frac{T(h)}{E}\right)e^{-\frac{E}{\mu\omega r}(l+\omega rt)} \tag{7}
$$

4 Stress distribution at the tape

The value $T(h)$ defining the tension of the thread, at distance h from the bottom edge of the tape, can be calculated on the basis of boundary conditions characterizing the tape from package and its receipts on the tube at arbitrary fixed parameters of process: R, r, Ω, ω, φ, ε_0 and also material characteristics of warps μ and E. These calculations are easily realized by means of rather simple program. Typical for any values of parameters R, r, Ω, ω, ε_0, μ and E the picture of dependence of value $T(h)$ from the angle φ and distances h from the considered point of the tape up to its bottom edge is given on figure 4.

It is possible to note, that at an insignificant spinning degree of the tapes at winding the approached formula is fair

$$
T(h) = E\varepsilon_0 + (1+\varepsilon_0)\frac{\mu}{L + h\cot\varphi}\left(\frac{R\Omega}{\sin\varphi} - \omega r\right), \tag{8}
$$

Which together with formulas (5) – (7) allows to make full and elementary calculation water deformations, pressure and speeds of the tape movement.
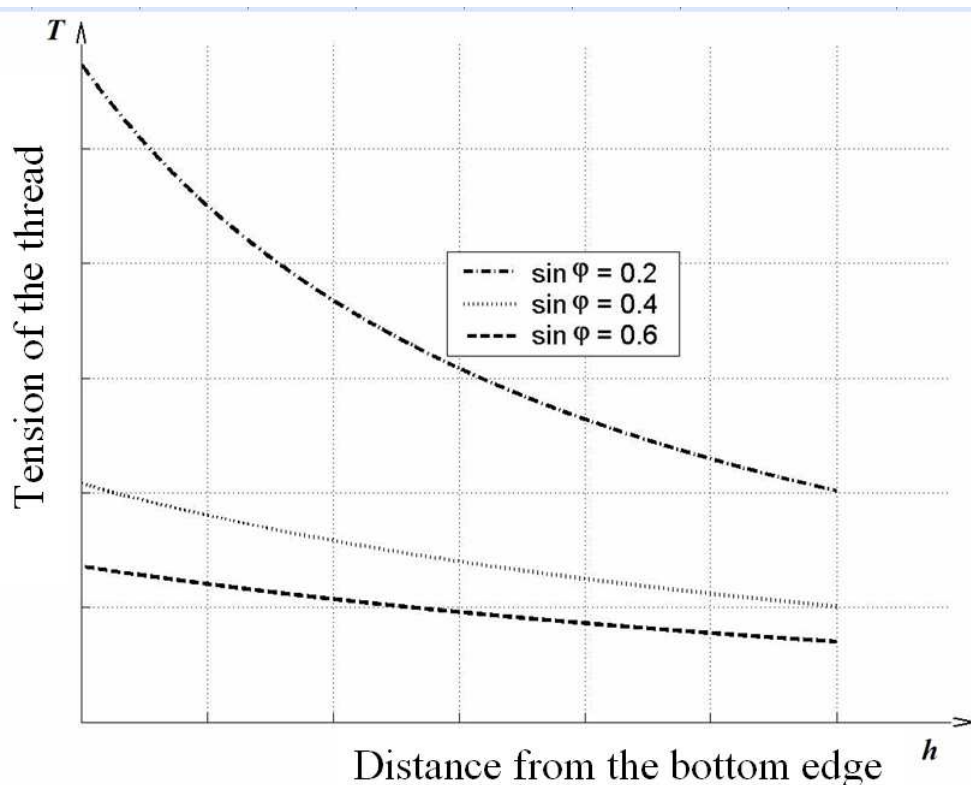
Figure 4. Tension dependence

5   Conclusion

The basic causes of irregularity the stress-strain state of the composites obtained by tape winding are considered. The solution of a problem of definition of stress and velocity distributions along the tape with linear hereditary properties during its winding around a cylindrical tube at stable process is given. The obtained solution can be used for asymptotical investigations of problems of reinforcing products by inelastic tapes winding.

Acknowledgements

References

[1] V. Chaikin Applied problems of threads theory - Saint-Petersburg: SPSUTD. 2001. P. 178

[2] Akasaka T. Structural mechanics of radial tires // Rubber Chemistry and Technolodgy. 1981. Vol. 54, N3. P.461-492.

[3] Ames W. F. Stresses in cylindrically symmetric membranes reinforced with extensible cords // Journal of the Franklin Institute. 1961. Vol. 272, N 3. P. 185-190.

[4] Dyatlova P. Numerical methods of investigation of interaction of tubular knitted fabric shells with enveloped solids. // Proceedings of 44 Congress IFKT "Knitting round the clock", Saint-Petersburg, 2008. P. 1 - 8.

[5] Dyatlova P. Nonlinear problems of fibre reinforced soft shells. // Book of abstracts of 11th EUROMECH-MECAMAT conference. Mechanics of microstructured solids: cellular materials, fibre reinforced solids and soft tissues. Torino, 2008. P. 29.

[6] E. Polyakova, P. Dyatlova, V. Chaikin On the finite elements method for investigation of the interaction of soft shells with solids' surfaces. // Proceedings of XXXV Summer School - Conference "Advanced problems in Mechanics. St. Petersburg, 2007. P. 85 - 92.

Polina Dyatlova, St. Petersburg State University of Technology and Design, Bolshaya Morskaya St. 18, St.-Petersburg, 191186, Russia

Structural model of the time dependence of elastomeric nanocomposites

Svetlana E. Evlampieva   Valery V. Moshev

evl@icmm.ru

Abstract

A mathematical model of elastomeric nanocomposites taking into account the composite microstructure rearrangement and its influence on the macroscopic behavior of the composite is proposed. The structure of the model includes an elastic spring simulating a macromolecule, two substrates simulating the surface of adjacent filler particles, and a space between the particles simulating particle concentration (the more the space, the less the concentration of particles). The elastic nonlinear resistance of the spring simulates the properties of elastomeric molecules with freely jointed segments. It is assumed that high attraction peculiar to small-size particles prevents normal disruption of the macromolecule from the particles, while the longitudinal slip of macromolecules over the surface of particles is presumed possible. The resistance to such an interaction is considered to be a kind of friction that depends on the slip velocity. A closer examination of the properties of the proposed mathematical model shows that it adequately simulates the behavior of real materials examined experimentally. The physical essence of the relaxation mechanism simulated by the model is as follows. The specimen is stretched to a prescribed magnitude, which remains fixed hereafter. The spring begins to slip from the substrates into the space between them, decreasing thus the elastic resistance of the the model. The process comes to equilibrium between the dragged and non-dragged parts of the spring. The decay of stress in time simulates the relaxation process observed experimentally. The model operates on elements having physical meaning and can be used by materials scientists who design new composite materials.

1   Structure of the model

The mechanical behavior of disperse-filled elastomeric composites is known to be time-dependent. This specific feature of composites is formed under the joint action of such independent structural mechanisms as the intrinsic viscoelasticity of the elastomer, filler-matrix debonding during deformation of the composite system, plasticizer migration in micro-volumes subjected to nonuniform loading, and, probably, by some other mechanisms still to be discovered. In the construction of models of the mechanical behavior of composites within the framework of continuum mechanics, the time sensitivity is generally considered as some integral effect.
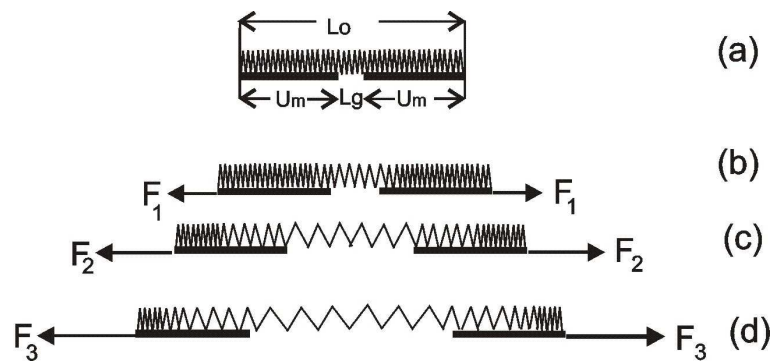
Figure 1: Geometry of the structural cell of the proposed model.

However, such an approach cannot satisfy the materials scientists who need the understanding of peculiarities of the internal structure that predetermine the continuum behavior of composites.

Consideration of relaxation mechanisms, which is a topic of this communication, is of great interest to materials scientists. It allows one to find optimal solutions in the arrangement of composites with prescribed mechanical properties. The aforesaid is fully applicable to elastomeric nanocomposites. It has been found experimentally that the structural peculiarities of these composites notably affect the formation of their continuum behavior.

In the present paper, a mathematical model that is able to take into account the above mentioned peculiarities of elastomeric nanocomposites is considered. The structure of composites is characterized by very small sizes of particles and their high concentration. The spaces between the neighboring particles are less than the length of a rubber macromolecule, and hence each macromolecule is adsorbed by several filler particles from the nearest surrounding.

This circumstance is accounted for by the geometrical structure of the proposed mathematical model (Fig.1). The model includes an elastic spring of length L_0 simulating the macromolecule, two substrates of length D simulating the surface of adjacent filler particles, and an interparticle space L_g simulating the concentration of particles in the composite.

The elastic resistance of the spring is simulated as close as possible to the properties of elastomeric molecules with freely jointed segments. Its elongation is represented by expression [1]

$$\lambda = \sqrt{L_0}(Cthf - \frac{1}{f}) + 1.0,$$

where L_0 is the spring length expressed through the number of segmental units, and f is the tensile force in arbitrary units. The formula takes into account two basic features of elastomeric macromolecules: dependence of their elastic strength on the length L_0 and their nonlinear increasing resistance to deformation. It is essential that the elastic resistance of the elastomeric macromolecules increases rapidly as their length decreases.

It is suggested that the significant adhesive attraction peculiar to small-size particles
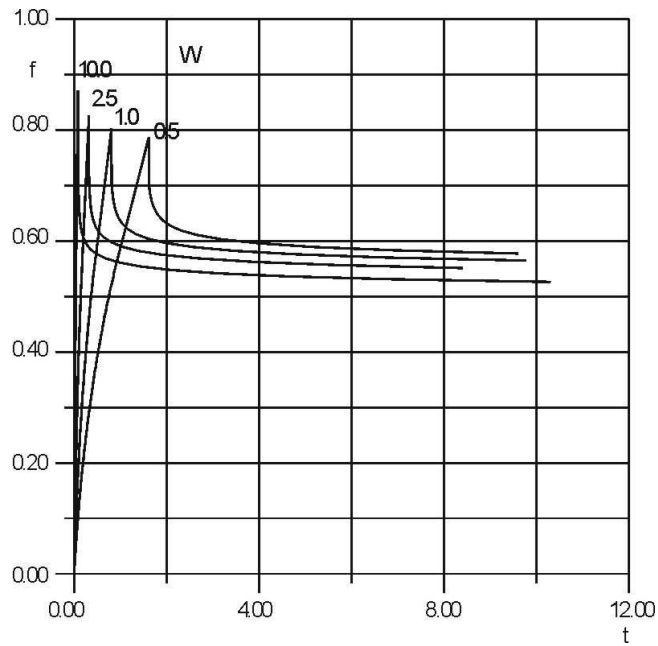
Figure 2: Tensile curves for different extension rates W.

prevents normal separation of the macromolecule from the particles [2], but the longitudinal slip of macromolecules (spring) over the surface of particles (substrates) is retained. The resistance to such a longitudinal slip can be treated as adhesive friction, and it can be represented as a binomial expression

$$T = T_0 + qV^m,$$

in which T is the frictional resistance per unit length of the substrate, is the frictional force at zero sliding velocity (friction at rest), V is the rate of interfacial sliding, T_0, q and m are the empirical constants [3].

The analysis of the properties of the proposed mathematical model shows that it can be successfully used for simulating the behavior of real materials observed in a series of experiments. The proposed approach gives more reliable data concerning the influence of testing regimes and separate material parameters on the mechanical behavior of elastomeric composites.

Figure 2 presents the tensile curves obtained using the developed model at various extension rates. It is seen that the resistance to extension increases with increasing extension rate obtained experimentally.

The physical essence of the relaxation mechanism is simulated by the model as follows (Fig.3). The specimen is stretched to a prescribed magnitude, which remains fixed. At the moment of stop, the spring in the space between the substrates experiences the maximum load. This leads to the slipping of the spring from the substrates into the gap between them, decreasing thus the elastic resistance of both the bridge and the model. The process comes gradually until the equilibrium between the dragged and non-dragged parts of the spring takes place. The decay of stress over time simulates the relaxation process.
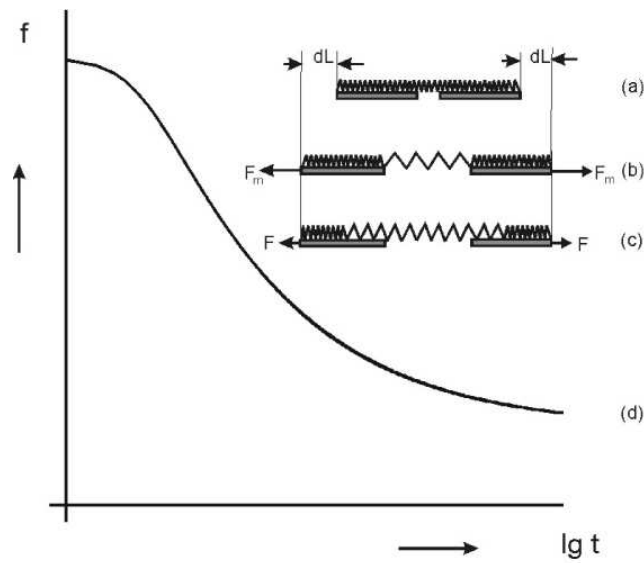
Figure 3: Relaxation curve.
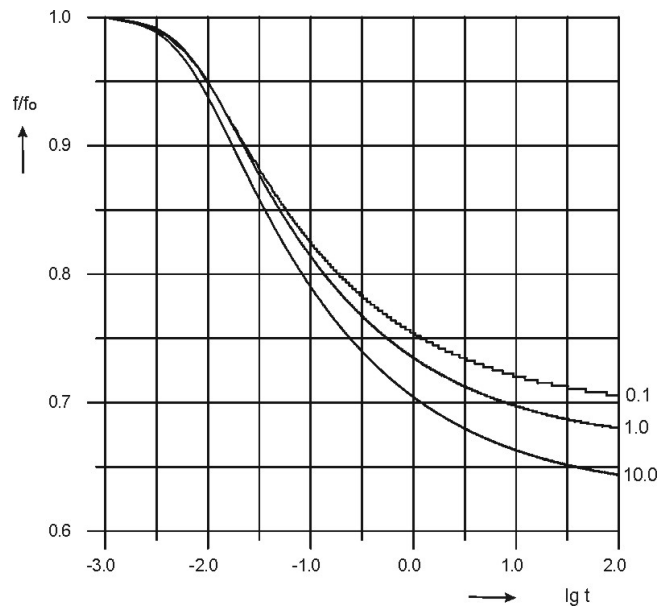
Figure 4: Nonlinearity dependence of relaxation curves on the prescribed deformation.

A complete form of the relaxation curve has the shape shown in the scheme (Fig.3g), where the upper plateau represents short time intervals close to the initial state of the system, the lower plateau - the state close to equilibrium, and the middle part - transition from one state to another.

Figure 4 presents the dependence of the relative relaxation modulus on the prescribed strains. Unlike the classical linear elasticity, the obtained relaxation curves are different, which is attributed to the fact that the structural rearrangements in

214
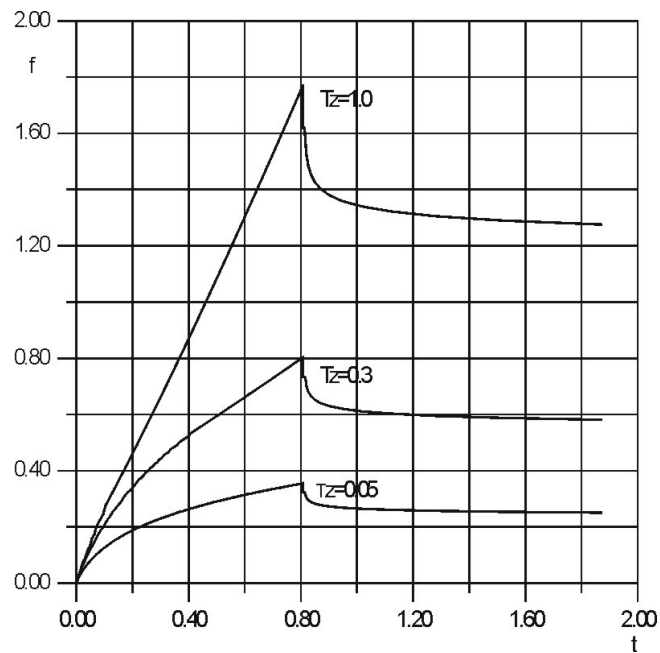
Figure 5: Influence of the parameter T_z on the shape of relaxation curves.
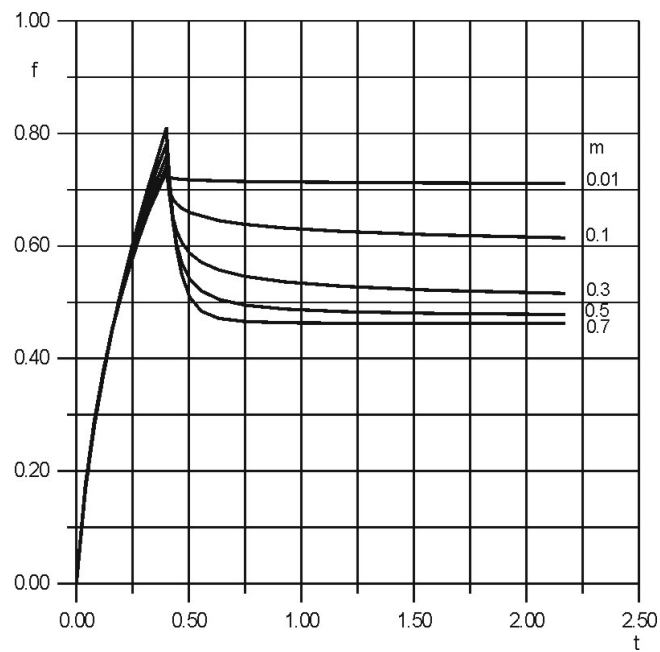
Figure 6: Influence of the parameter m on the shape of relaxation curves.

depth are different [4]. The form of relaxation curves also depends on the prior extension rate. The equilibrium relaxation elasticity moduli decrease in the case when the prior extensions are carried out at higher rate.

Figures 5 and 6 illustrates how the static friction and its rate sensitivity to extension of specimens (preceded the relaxation tests) affect the properties of composites.

Composite specimens do not recover their primary state after relaxation testing, and repeated extensions show that their initial modulus increases significantly. However, this result cannot be considered as an indication of irreversible changes in the behavior of the material. Upon warming-up of the specimens, their initial properties are recovered, and no structural changes caused by prior actions are observed [5]-[10]. Higher temperatures loosen adhesive bonds and let the thermal motion draw back the structure to the original state.

2 Conclusions

The structural model of elastomeric composites has been developed which takes into account structural rearrangements of the composite and their influence on its macroscopic behavior of the composite.

The proposed relaxation mechanism may be thought of as reversible, since the structural rearrangements caused by deformation can be removed by simple heating of the material, which results in restoring its initial properties.

The model operates on elements having physical meaning and, therefore, can be used by materials scientists in the design of new composite materials.

References

[1] Moshev, V.V. and Evlampieva S.E. Filler-reinforcement of elastomers viewed as a triboelastic phenomenon. Int. J. Solids Struct. 2003. V. 40, P. 4549-4562.

[2] Persson D.N.J. Sliding friction //Surface Science Reports. 1999. V. 33, P. 83-119.

[3] Kovrov V.N., Moshev V.V., Mechanical hysteresis in rubbers and its relation with strength // Structural-mechanical investigation of composite materials and structures. Sverdlovsk: USC AS USSR. 1984, P. 19-22.

[4] Drozdov A.D., Dorfmann A. Modeling the response of filled elastomers at finite strains by rigid-rod networks // Archive of applied mechanics. 2002. V. 72, P. 52-76.

[5] Aleksandrov A.P. Lazurkin Yu.S., 1944, Strength of amorphous and crystallizing rubber polymers // FEB AS USSR . V.45, No 7, P.308-311.

[6] Dannenberg E.M. Molecular slippage mechanism of reinforcement // Trans. Inst. Rub. Ind. 1966. V. 42, P.26-42.

[7] Edwards D.C. Polymer-filler interactions in rubber reinforcement // J. Mater. Sci. 1990. V. 25, P.4175-4185.

[8] Medalia A.I. Effect of carbon black on ultimate properties of rubber vulcanizates // Rubber chem. technol. 1987. V.60, P. 45-61.

[9] Rigbi Z. Reinforcement of rubber by carbon black // Adv. Polym. Sci. 1980. V. 36, P. 21-68.

[10] Soos I. Charakterisierung des Verstakungeffektes von Fullstoffen aufgrund der Auswertung der Spannungs-Deformations-Kurve // GAK. 1984. V. 37, PP. 232-238, 300-303, 509-512.

Svetlana E. Evlampieva, Institute of Continuous Media Mechanics, Korolev Str., 1, 614013, Perm, Russia

Valery V. Moshev, Institute of Continuous Media Mechanics, Korolev Str., 1, 614013, Perm, Russia

Propagation of solid-phase chemical reaction in a plate under mechanical loading

N. K. Evstigneev   A. G. Knyazeva

evstigneev.nk@rambler.ru anna@ispms.tsc.ru

Abstract

Mathematical model of solid-phase chemical reaction in a plate under mechanical loading was suggested. Numerical simulation demonstrated that coupling effect influences process behavior essentially. Uniaxial mechanical load less than one half of material ultimate strength does not make a material effect on process propagation.

1   Physical problem definition
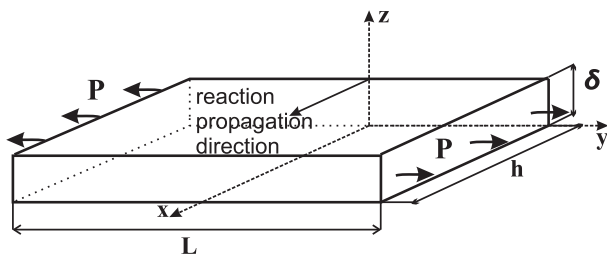
Figure 1: Problem definition illustration

Let us consider a rectangular plate made from reactive material. The width of the plate is h, the length is L and the height is δ. The plate is subjected to mechanical loading, the direction of which is perpendicular to the direction of chemical reaction propagation. Axes of coordinates are placed as it is shown on fig.1. Chemical reaction in the plate spreads in the direction of x axis. It is suggested that melting temperature is not reached and the reaction is solid-phase. Heat exchange with the environment takes place according to Newton law. Inertial forces are neglected considering that solid-phase reaction propagation velocity is much less than mechanical disturbance propagation speed. It is required to determine the influence of external load value and coupling effect on the process flow.

The problem consists of two parts which are solved partly independently if above mentioned assumptions are taken into consideration. Really, supposing that temperature and concentration distributions are known at every point of time, the problem of mechanical equilibrium of a plate can be investigated separately [1]. In this problem time t is a parameter. From the other hand if relations between stress and

strain tensor components and temperature and concentration are known, we can investigate the problem of solid-phase reaction propagation with a "given" additional heat source or heat sink [2]. Let's study both problems separately.

2 The problem of mechanical equilibrium of a plate

If temperature field in a plate is uniform, we may consider that stress tensor component perpendicular to xy plane is $\sigma_{zz} = 0$, i.e. stress state is the state of plane stress. Therefore all nonzero stress and strain tensors components depend on coordinates x and y only. If nonuniform compound and $T = T(x, y)$ are given, then under fulfillment of conditions $h << L$, $\delta << L$ we may suppose that

$$\frac{1}{h}\int_0^h \sigma_{yy}(x, y)dx = P, \quad \frac{1}{h}\int_0^h \sigma_{yy}(x, y)dx = 0. \tag{1}$$

It follows from generalized Hooke's law that

$$\sigma_{ij} = 2\mu\varepsilon_{ij} + \delta_{ij}(\lambda\varepsilon_{kk} - Kw), \tag{2}$$

where $w = 3\left[\alpha_T(T - T_0) + \sum_{k=i}^n \alpha_k(C_k - C_{k0})\right]$, C_k - mass concentrations of components, α_T - thermal expansion coefficient, α_k - coefficients of volume expansion, index "0" corresponds to unstrained state.

If we are interested only in stresses in reaction zone, which is far from load-bearing faces, we may confine ourself to one-dimensional problem and suppose that all quantities depend only on x coordinate. Then equilibrium equations are satisfied identically and we should use compatibility equations. Two of them are left: $\frac{\partial^2\varepsilon_{yy}}{\partial x^2} = 0$, $\frac{\partial^2\varepsilon_{zz}}{\partial x^2} = 0$.

$$\text{So,}\ \varepsilon_{yy} = Ax + B,\ \varepsilon_{zz} = Cx + D. \tag{3}$$

We suppose there is no shearing. It means that

$$\frac{1}{h}\int_0^h \sigma_{yy}(x)xdx = 0, \quad \frac{1}{h}\int_0^h \sigma_{zz}(x)xdx = 0. \tag{4}$$

Substituting (3) into (2) and using (1) and (4) we get a set of equations to determine constants A, B, C and D. As a result we have expressions for calculating all nonzero stress and strain tensor components — σ_{xx}, σ_{yy}, ε_{xx}, ε_{yy}, ε_{zz}. Formulae are omitted because of their unhandiness.

3 The problem of chemical reaction propagation in a solid phase

In dimensionless variables

$$\theta = \frac{T - T_0}{T_* - T_0}, \tau = \frac{t}{t_*}, \overline{w} = \frac{w}{w_*}, \overline{e}_{kk} = \frac{\varepsilon_{kk}}{\varepsilon_*}, \overline{s}_{kk} = \frac{\sigma_{kk}}{\sigma_*}, \xi = \frac{x}{x_*}, \overline{P} = \frac{P}{P_*},$$

where $T_* = T_0 + \dfrac{Q}{c\rho}$, $t_* = \dfrac{c\rho R T_*^2}{E Q k_0} exp\left(\dfrac{E}{R T_*}\right)$, $w_* = 3\alpha_T(T_* - T_0)$, $x_* = \sqrt{\dfrac{\lambda t_*}{c\rho}}$,

$$\varepsilon_* = \frac{3K\alpha_T(T_* - T_0)}{\lambda + 2\mu}, \sigma_* = 3K\alpha_T(T_* - T_0), P_* = \mu\alpha_T(T_* - T_0),$$

the problem takes form

$$\frac{\partial\theta}{\partial\tau} = \frac{\partial^2\theta}{\partial\xi^2} + \frac{\partial y}{\partial\tau} - \delta(\theta + \sigma_T)\frac{\partial\overline{e}_{kk}}{\partial\tau}, \tag{5}$$

$$\frac{\partial y}{\partial\tau} = \frac{1}{\theta_0}(1 - y)exp\left(\frac{\theta - 1 + (1 + \sigma_T)A\delta\Pi}{\beta(\theta + \sigma_T)}\right). \tag{6}$$

Initial conditions: $\tau = 0$: $\theta = 0$, $y = 0$.
Boundary conditions:
$\xi = 0 : \dfrac{\partial\theta}{\partial\xi} = Nu(\theta - \theta_e) - \overline{q}$,

$\xi = L : \dfrac{\partial\theta}{\partial\xi} = -Nu(\theta - \theta_e)$,

where
$$\frac{\partial\overline{e}_{kk}}{\partial\tau} = \frac{1}{1 - h_1}\frac{\partial\overline{w}}{\partial\tau} + \frac{6h_1}{(3 - 2h_1)(1 - h_1)}\frac{1}{L}\left\{\left(\frac{\xi}{L} - \frac{2}{3}\right)\frac{\partial\overline{I}_1}{\partial\tau} - \frac{2}{L}\left(\frac{\xi}{L} - \frac{1}{2}\right)\frac{\partial\overline{I}_2}{\partial\tau}\right\},$$

$\Pi = -(\overline{s}_{xx}\overline{e}_{xx} + \overline{s}_{yy}\overline{e}_{yy})$, $\overline{I}_1 = \int\limits_0^L \overline{w}d\xi$, $\overline{I}_2 = \int\limits_0^L \overline{w}\xi d\xi$, $\overline{w} = \theta + g \cdot y$.

Dimensionless parameters are as follows: $A = \dfrac{k_\sigma Q}{E}$, $\delta = \dfrac{(3K\alpha_T)^2(T_* - T_0)}{c\rho(\lambda + 2\mu)}$, $\sigma_T = $

$\dfrac{T_0}{T_* - T_0}$, $\beta = \dfrac{RT_*}{E}$, $\theta_0 = \dfrac{E}{RT_*^2}(T_* - T_0)$, $h_1 = \dfrac{2\mu}{\lambda + 2\mu}$, $g = \dfrac{\alpha_p - \alpha_r}{\alpha_T(T_* - T_0)}$, $\theta_e = \dfrac{T_e - T_0}{T_* - T_0}$,

$\overline{q} = \dfrac{q_0 x_*}{\lambda_T(T_* - T_0)}$, $Nu = \dfrac{\alpha x_*}{\lambda_T}$, $L = \dfrac{h}{x_*}$.

Here T is temperature, y — conversion degree, ε_{kk} — sum of nonzero strain tensor components, σ_{kk} — sum of nonzero stress tensor components, ξ — coordinate, Q — thermal effect of chemical reaction, c — heat capacity, ρ — density, E — activation energy, R — universal gas constant, k_0 — pre-exponential factor, λ and μ — Lame coefficients, K — bulk modulus, k_σ — coefficient of chemical reaction sensitivity to the work of tensions, q_0 — heat flow density, λ_T — thermal conductivity coefficient, α — heat exchange coefficient.

Resulting parameters characterize: σ_T — ratio of initial temperature to the value of heating, g — relative volume change (ratio of concentration deformation to the thermal one), h_1 — mechanical properties of substance, β — chemical reaction activation energy, θ_0 — temperature drop, $\overline{P}$ — external load value, δ — coupling coefficient, A — sensitivity of chemical reaction to the work of stresses.

4   Computation results

The problem was solved by double-sweep method using implicit difference scheme and linearization of kinetic term. Physical parameters ranges were chosen typical for

intermetallic compounds and it was fixed in calculations that $\delta = 0.03$, $\sigma_T = 0.15$, $\beta = 0.1$, $L = 50$, $Nu = 0$, $g = 0.5$, $\overline{P} = 0.01$. Plate length, L, was chosen to be 10 times larger than heat penetration zone width, which was estimated as $1/\overline{u}$, where $\overline{u}$ is chemical reaction propagation velocity. External load value, $\overline{P}$, was selected as $10^{-3} - 10^{-2}$ of ultimate tensile strength of concerned material.

Program was tested to check its accuracy. Equation (5) can be solved analytically in the next extreme case: inert problem without mechanical loading and without chemical reaction, $L \to \infty, Nu = 0$. The solution takes form $\theta(\xi, \tau) = 2q\sqrt{\dfrac{\tau}{\pi}}exp\left(-\dfrac{\xi^2}{4\tau}\right) - q\xi erfc\left(\dfrac{\xi}{2\sqrt{\tau}}\right)$, which was replicated numerically accurate within 1%.

Grid convergence was also investigated. Plate temperature at $\xi = 0$ at the point of time $\tau = 30$ was calculated using different values of time and coordinate steps. It was found out that if $\Delta\xi \le 0.2$ and $\Delta\tau \le 0.005$ the results differ less than by 1%. So, time and coordinate steps were chosen to be $\Delta\xi = 0.2$, $\Delta\tau = 0.005$.

In the process of numerical investigation of full model the distributions of temperature, conversion degree, stress and strain tensor components, chemical reaction propagation velocity at every point of time and surface temperature evolution were determined and analyzed.
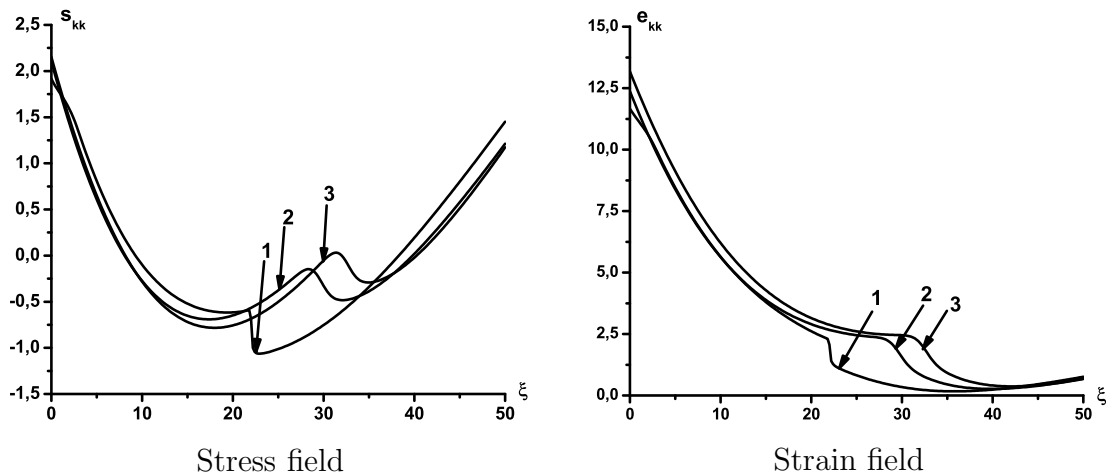
Figure 2: 1— $\delta = 0.03$, $A = 0$, 2— $\delta = 0.03$, $A = 0$, 3— $\delta = 0$, $A = 20$

Fig.2 describes stress and strain fields. It can be seen that taking into consideration connectivity effect results in differences of stress and strain fields in the area of intensive chemical transformations.

Chemical reaction propagation velocity was determined as follows: after chemical reaction initiation a point was searched where conversion degree amounted $y_{1/2} = 0.5$. Linear approximation of y function values was used. After 10-20 time steps a new point corresponding to half reaction was detected. Flame propagation velocity was calculated according to $\overline{u} = \dfrac{\xi_2 - \xi_1}{N\Delta\tau}$, where N is the number of time steps passed since the moment of last calculation. Dependencies of flame propagation rate on sensitivity coefficient and on time are shown on fig.3. Increasing of values after $\tau > 90$ (curves 3 and 4) is caused by the fact that reaction front has spread
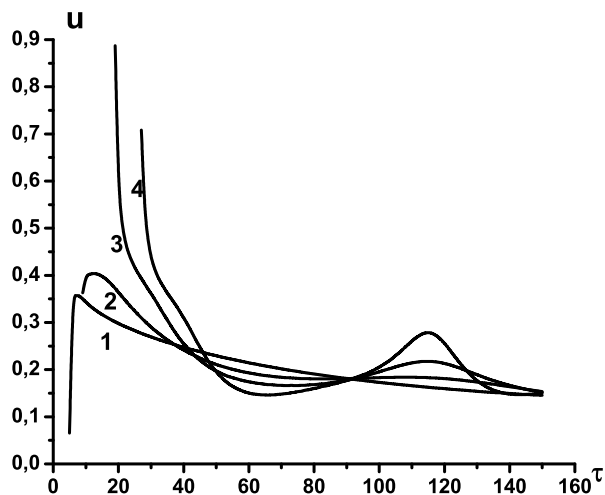
Figure 3: Evolution of flame front speed. 1— A=0, 2— A=3, 3— A=6, 4— A=9

deep into the plate and reactant near the right border had enough time to warm up by the heat emitted from reacting layers. Enlarging plate length it is possible to get rid of border influence and to get a stationary reaction propagation.

Variation of external load value does not result in variation of flame propagation velocity. Differencies in values are about calculation accuracy.

Let us consider average value of conversion degree: $\langle y \rangle = \dfrac{1}{L} \int_0^L y \, d\xi$. Its evolution is shown on fig.4. Increasing of sensitivity coefficient results in slowing down the reaction at the beginning of the process, but in the course of time this difference disappears.
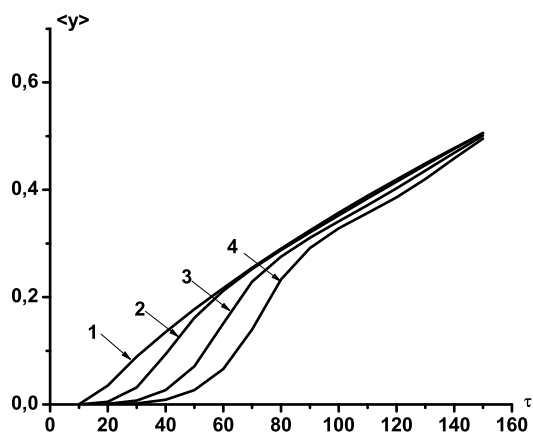
Figure 4: Average conversion degree. 1— A=0, 2— A=5, 3— A=10, 4— A=15

Time of half reaction $\tau_{1/2}$, that is the moment of time when average value of conversion degree $\langle y \rangle = 0.5$ depends on sensitivity coefficient in a non-linear way. It surges considerably with the increase of A. Increasing of external load value up to one half of material ultimate strength leads to variation of $\tau_{1/2}$ within the scope of only 10 %.

222
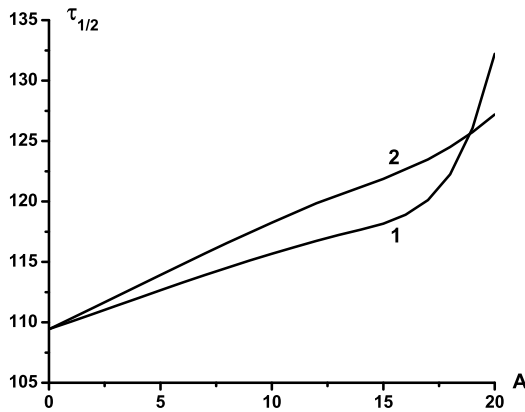
Figure 5: Time of half reaction. 1— $P = 0.01$, 2— $P = 0.5$

In view of absence of typical temperature surge near the hot surface, ignition moment was fixed when conversion degree in a certain point reached the value $y = 0.01$. It was determined that increasing of sensitivity coefficient slows down surface temperature growth. It is caused by penetration of ignition point deep into the plate. Thus, for example, for $\delta = 0.03, A = 20$ coordinate of ignition point is $\xi_{ign} = 4.2$. If $A = 0$, then ignition always occurs on the plate surface.

5 Conclusion

The coupling model of reaction propagation under mechanical loading was suggested. The algorithm of numerical investigation of non-linear model was developed; parametric investigation of the problem was carried out; the influence of coupling effect on reaction propagation was shown. It was ascertained that uniaxial mechanical load less than one half of material ultimate strength does not make a material effect on reaction propagation.

References

[1] B. Boley, J. Weiner. Theory of thermal stresses. Moscow: Mir, 1964 (in Russian)

[2] A. Knyazeva. On the explosive crystal ignition // Fizika goreniya i vzryva, 2001. - V.37, No 3. (in Russian)

[3] M. Brown, D. Dollimore, A. Galwey. Reactions in the solid state. Moscow: Mir, 1983. (in Russian)

N.K. Evstigneev, 36 Lenina pr., Tomsk, Russia
A.G. Knyazeva, 2/1 Akademicheskii pr., Tomsk, Russia

Application of method of special series for solution of nonlinear problems of continuum mechanics

Mikhail Yu. Filimonov

fmy@imm.uran.ru

Abstract

Different constructions of special series with coefficients calculated recurrently are presented. This approach is used for the representation of solutions of a wide class of nonlinear problems of continuum mechanics.

1 Introduction

One of the most perspective ways to construct solutions of nonlinear partial differential equations is combination of numerical and analytical methods. I n this presentation analytical method of special series is used. Essence of this method is in expansion of solutions into a series by the powers of one or several special functions provided the coefficients of the series to be computed recurrently.

In contrast to Fourier method, which also used for solving nonlinear partial differential equations, method of special series allows to obtain solutions with preliminary assigned accuracy because the developed approach leads to a sequence of finite systems of ordinary differential equations. The obtained sequence turns out to be linear even for nonlinear initial equation. This fact allows to obtain new results: in a number of cases it is possible to prove global convergence of constructed series including for unbounded domains, where numerical methods occur principal difficulties. This approach allows to obtain constructive solutions in the form of convergent series also for boundary-initial problems for a certain class of nonlinear equations. Some numerical results are presented for nonlinear equation.

The method of special series, whose development has been stimulated by the work of A.F. Sidorov [1], is included into another group of analytical approaches. The main idea is to expand a solution in a power series with respect to one or several functions chosen in a special way [2, 3] (in the sequel, we call these functions basic). Such a choice, in contrast to the methods of Galerkin type, allows one to find solutions with a check accuracy because the used approaches leads to a chain of finite systems of differential equations, which are, as a rule, linear even for nonlinear equations to be solved, that allows one to obtain new results: in a number of cases it is possible to prove the global convergence even in nonrestricted domains [4, 5], where numerical methods meet essential difficulties. In constructing like this one only the first term of the series may be found as a solution of a nonlinear differential equation. In contrast

to Taylor power series, which locally converge for equations of Kovalevskaya type [6] under assumption of analyticity of the problem initial conditions, the constructed special series may converge for wider classes of equations and systems. This special series may be also used for representation of solution of Kovalevskaya type equations but with nonanalytical initial conditions [7].

Another field of application of special series is connected with the possibility of using them to solve initial-boundary value problems. In case zero boundary conditions are given, for a wide class of nonlinear equations it is possible to construct series converging to a solution of the problem and exactly satisfying the boundary condition [4] including two-dimensional complex domains [8].

Thus, the considered different constructions of special series turn out to be convenient apparatus for constructive investigation of the structure of solutions of nonlinear partial differential equations and allow one to prove theorems of the existence of solutions of initial-boundary value problems.

2 Statement of a problem and construction of the solution

Let us describe certain possible approaches to construct special series on the example of the following initial-boundary value problem:

$$u_{tt} = G(t, u, u^2 u_{xx}, u^2 u_x^2), \tag{1}$$

$$u_t(x, 0) = u_1(x), \quad u(x, 0) = u_0(x), \tag{2}$$

$$u(0, t) = u(\pi, t) = 0, \quad t \geq 0. \tag{3}$$

Here G is an analytical function, besides, probably, the first one. Let G be represented for $|u|, |u_x^2|, |u_{xx}| \leq D$ $(D > 0)$ in the form of absolutely convergent series

$$G = \sum_{q=1}^{\infty} \sum_{m+k+l=q} \beta_{mkl}(t) u^{m+k+l} u_{xx}^k u_x^{2l}.$$

Assume, that $\beta_{100}(t) \equiv 0$, $\beta_{mkl}(t) \in C[0, \infty)$ and the following conditions are fulfilled:

$$\sum_{m+k+l=q} |\beta_{mkl}(t)| \leq b_q, \quad \sum_{q=1}^{\infty} b_q = B, \quad b_q, B = \text{const}.$$

The following theorem is valid:

Theorem 1. *Let the initial conditions* $u_\nu(x)$, $\nu = 0, 1$ *is represented in the form of series*

$$u_\nu(x) = \sum_{n=1}^{\infty} g_{\nu n} S^n(x), \quad g_{\nu n} = \text{const} \tag{4}$$

and function $S(x)$ *satisfies equation*

$$\left(\frac{dS}{dx}\right)^2 = \sum_{k=0}^{\infty} \alpha_k S^k, \quad \alpha_k = \text{const}, \tag{5}$$

225

where the series (4), (5) *are assumed to be convergent for* $|S| \leq A$, $A > 0$ *and conditions are fulfilled* $g_{01} = g_{11} = 0$ *and* $|g_{0n}| + |g_{1n}| + |\alpha_n| \leq 0.5n^{-4}M^n$, $0 < M < A^{-1}$. *Then series*

$$u(x,t) = \sum_{n=1}^{\infty} u_n(t)S^n(x) \tag{6}$$

is a solution of Cauchy problem (1), (2) *for all* $0 \leq t \leq T$, $T = -b^{-1}\ln(AM)$, $b \geq b_0 > 1$ *and* x, *such that* $|S(x)| \leq A$.

P r o o f.

Let check probability of recurrence in calculating coefficients of series (6) $u_n(t)$. At the beginning we find $u^2 u_{xx}$.

$$u_{xx} = \sum_{n=1}^{\infty} n(n-1)u_n(t)S^{n-2}(x)S_x^2(x) + \sum_{n=1}^{\infty} nu_n(t)S^{n-1}(x)S_{xx}(x) =$$

$$\sum_{n=1}^{\infty} n(n-1)u_n(t)S^{n-2}(x) \sum_{k=0}^{\infty} \alpha_k S^k(x) + \sum_{n=1}^{\infty} nu_n(t)S^{n-1}(x)0.5\sum_{k=1}^{\infty} k\alpha_k S^{k-1}(x).$$

Finally we have

$$u^2 u_{xx} = \sum_{n \geq 4} \left[\sum_{m_1+m_2+m_3-2+k=n} u_{m_1}(t)u_{m_2}(t)m_3(m_3-1)u_{m_3}(t)\alpha_k + \right.$$

$$\left. 0.5ku_{m_1}(t)u_{m_2}(t)m_3 u_{m_3}(t)\alpha_k \right] S(x)^n.$$

Similarly

$$u^2 u_x^2 = \sum_{n \geq 4} \sum_{m_1+m_2+m_3+m_4+k=n} u_{m_1}(t)u_{m_2}(t)m_3 u_{m_3}(t)m_4 u_{m_4}\alpha_k S^n(x).$$

Further, substituting the found expressions to function G and equating expressions at the same powers of $S(x)$, to calculate coefficients of series (6) $u_n(t)$ we obtain a sequence of ordinary second order differential equations

$$u_n''(t) = G_n(t, u_m(t)), \quad m < n, \tag{7}$$

with initial conditions

$$u_n'(0) = g_{1n}, \quad u_n(0) = g_{0n}, \quad n > 1. \tag{8}$$

For solutions of equations (7), (8) the following estimations are valid:

$$|u_n(t)| \leq n^{-4}M^n \exp(btn), \quad n \geq 2, \quad 0 \leq t \leq T. \tag{9}$$

To prove estimations (9) method of induction is used. To estimate coefficients of series (6) condition $g_{01} = g_{11} = 0$ is used. In this case $u_1(t) \equiv 0$ and we have sequence of equations (7) with $m < n$ (in the opposite case we also have a sequence

of linear equations with $m \leq n$ and the question of estimations of coefficients is still open).

Now with using estimations (9) it is possible to prove convergence of series (6) to solution of Cauchy problem (1), (2). Theorem 1 is proved.

R e m a r k 1.

If the consistent basic function $S(x)$ satisfies an additional condition $S(0) = S(\pi) = 0$ then series (6) is a solution of initial–boundary value problem (1) – (3) also.

For example such a function is $S(x) = S_1(x) = \sin x$ for which equation (5) has the form $(S_1')^2 = 1 - S_1^2$. The corresponding series (6) has written in the form

$$u(x, t) = \sum_{n=1}^{\infty} u_n(t) \sin^n x. \tag{10}$$

If $S(x) = S_2(x) = x(x - \pi)$, then equation (5) has the form $(S_2')^2 = \pi^2 + 4S_2$. The corresponding series (6) is written in the form

$$u(x, t) = \sum_{n=1}^{\infty} u_n(t) x^n (x - \pi)^n.$$

Let show application of special series (10) for the following model problem for which numerical computations will be carred out

$$u_{tt} = u^2 u_{xx}, \tag{11}$$

$$u_t(x, 0) = 0, \quad u(x, 0) = u_0(x), \tag{12}$$

$$u(0, t) = u(\pi, t) = 0, \quad t \geq 0. \tag{13}$$

After substitution of series (10) into equation (11) to find the coefficients we get a sequence of equations

$$u_n''(t) = u_1(t)^2 n(n-1) u_n(t)) + \sum_{m+k+l-2=n} u_m(t) u_k(t) l(l-1) u_l(t)$$
$$- \sum_{m+k+l=n} u_m(t) u_k(t) l^2 u_l(t), \tag{14}$$

Formulation of Theorem 1 is better to be defined concretely for this particular problem.

The following theorem is valid.

Theorem 2. *Let initial conditions* (12) *be represented in the form*

$$u_0(x) = \sum_{n=2}^{\infty} g_{0n} \sin^n(x), \tag{15}$$

and $|g_{0n}| \leq M^n n^{-4}$ $M = \text{const}, \quad 0 < M < 1.$
Then series (10) *is a solution on initial–boundary problem* (11) *–* (13) *for all* $0 \leq t \leq T$, $T = -b^{-1} \ln M > 0, b \geq b_0 > 1$ *and* $0 \leq x \leq \pi.$

Proof of Theorem 2 is similarly to the proof of Theorem 1. In this case we note that boundary conditions (13) are automatically fulfilled by basic function choosing. Coefficient of series (10) are found as follows from equations (14):

$$u_n(t) = \int_0^t \int_0^\tau \left[\sum_{m+k+l-2=n} u_m u_k l(l-1) u_l - \right.$$

$$\left. \sum_{m+k+l=n} u_m u_k l^2 u_l \right] d\tau d\tau + g_{0n}. \tag{16}$$

Here we used condition that $g_{01} = 0$ and, consequently, $u_1(t) \equiv 0$. Thus series (13) is solution ob initial–boundary value problem in all of area on x and for all $0 \le t \le T$.

3   Numerical results

Numerical results are presented for model problem (11) – (13) with initial conditions $u_0(x) = 0.1 \sin^2 x$ (fig. 1) and with $u_0(x) = 1/15 \sin^2 x - 1/20 \sin^3 x$ (f. 2). Computations have been carried out by using MAPLE. First 12 coefficients of series (10) is found from equation (16) and an approximate solution was summarized

$$u_m(x,t) = \sum_{k=1}^m u_k(t) \sin^k x, \quad m \le 12.$$
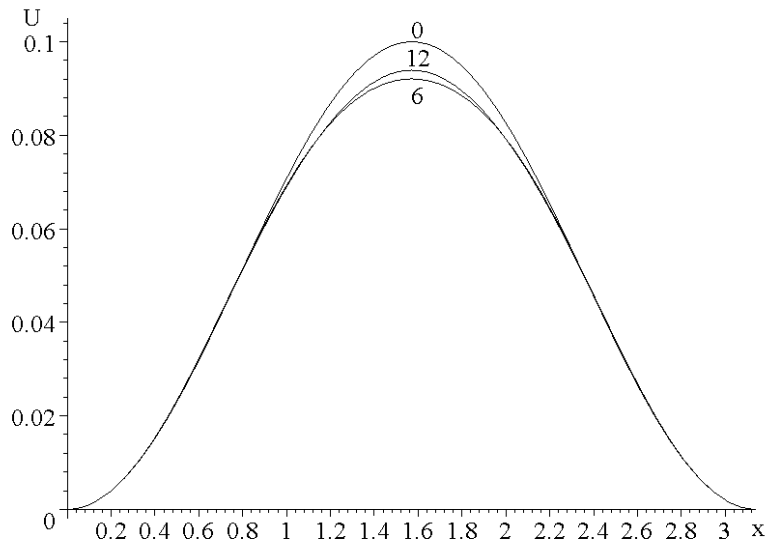
Figure 1: (0) – initial condition $u_0(x) = 0.1 \sin^2 x$; (6) – approximate solution $u_6(x,3)$; (12) – approximate solution $u_{12}(x,3)$.

Presented computations verify that series (10) converges rapidly. The differences between $|u_{12}(x,t) - u_6(x,t)|$ (fig. 1) and $|u_{12}(x,t) - u_{10}(x,t)|$ (fig. 2) is about 1% with respect to $\max u_{12}(x,t)$.

228
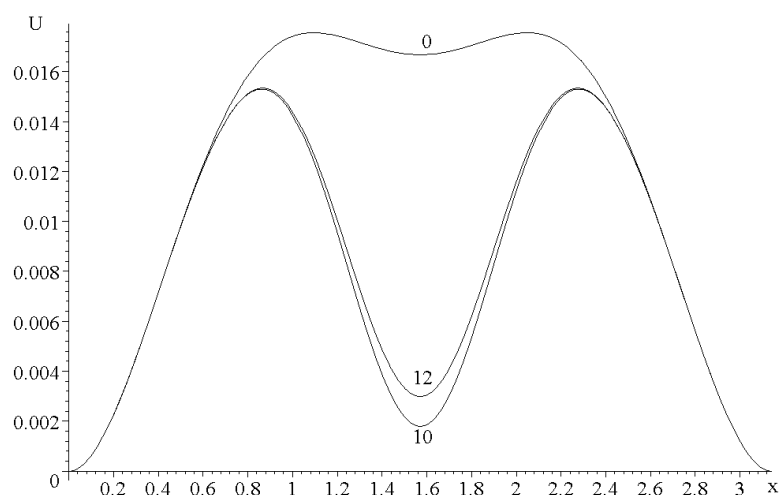
Figure 2: (0) – initial condition $u_0(x) = \frac{1}{15}\sin^2 x - \frac{1}{20}\sin^3 x$; (10) – approximate solution $u_{10}(x, 1.5)$; (12) – approximate solution $u_{12}(x, 1.5)$.

Thus, presented constructions of special consistent series by the powers of new basic functions may be used not only for solutions of Cauchy problems only, but also for solutions of initial–boundary value problems for a wide class of nonlinear equations and systems which occur in continua media mechanics.

Acknowledgements

References

[1] A. F. Sidorov. On Some Representations of Solutions of Quasilinear Hyperbolic Equations. Chislen. metody mekhan. sploshnoi sredy. Vychisl. Tsentr Inst. Teor. Prikl. Mekh. Sibir. Otdel. Acad. Nauk SSSR, Novosibirsk, **6**, 4, 1975.

[2] V. V. Vasin and A. F. Sidorov. On Some Methods of Approximate Solution of Differential and Integral Equations. Izv. Vyssh. Uchebn. Zav. Mat., 7, 1983.

[3] M. Yu. Filimonov, L. G. Korzunin, and A. F. Sidorov. Russ. J. Num. Anal. Math. Mod., **8**, 2, 1993.

[4] M. Yu. Filimonov. Representation of Solutions of Mixed Problems for Nonlinear Wave Equation by Special Double Series. Diff. Uravn., **27**, 9, 1991.

[5] M. Yu. Filimonov. Application of Special Coordinated Series to the Solution of Nonlinear Partial Equations in Unbounded Domains. Diff. Uravn., **36**, 11, 2000.

[6] S. V. Kovalevskaya. Scientific Works. To the Theory of Partial Differential Equation, Izd. AN SSSR, Moscow, 1948.

[7] M. Yu. Filimonov. On the Representation of Solutions of Nonlinear Equations of Cauchy–Kovalevskaja Type with Nonanalytic Initial Data by Special Series. Sib. Zh. Ind. Mat., **2**, 2001.

[8] M. Yu. Filimonov. Application of Method of Special Series to Representation of Solutions of Initial-Boundary Value Problems for Nonlinear Partial Differential Equations. Diff. Uravn., **39**, 8, 2003.

[9] M. Yu. Filimonov. Proc. of Steclov Inst. of Math. (Suppl. 1), 2004.

Mikhail Yu. Filimonov
Institute of Mathematics and Mechanics UrB RAS, S. Kovalevskaya str. 16, Ekaterinburg, 620219, Russia

On chemical reaction fronts in nonlinear elastic solids

Alexander B. Freidin

alexander.freidin@gmail.com

Abstract

We consider a nonlinear elastic solid in which chemical reactions of oxidizing type take place. We suppose that the chemical reaction is localized at the chemical reaction front, and the reaction is sustained by the diffusion of an oxidizing gas constituent through the solid oxide. Basing on introducing an intermediate configuration reflected chemical transformations of solid constituents we derive an expression of the potential energy release due to the reaction front propagation. As a result we obtain the input of solid phases into a chemical affinity tensor as a combination of Eshelby stress tensors determined with respect to stress free configurations of the initial and chemically produced solid constituents and multiplied by chemical reaction parameters. Finally we consider an input of a gas constituent and formulate a simplest kinetic relation for the front propagation.

1   Kinematics

Let $v_t = v_- \cup v_+$ is a current configuration of a body at time t, and volumes v_- and v_+ are occupied by materials A_- and A_+, respectively, and A_+ is produced as a result of a chemical reaction

$$\nu_- A_- + \nu_* A_* \rightarrow \nu_+ A_+ \tag{1}$$

where A_-, A_* and A_+ are chemical formulae of reacting constituents, ν_-, ν_* and ν_+ are stoichiometric coefficients. We assume that A_- and A_+ are solids and A_* is a gas. An example of the reaction (1) is the oxidation of silicon

$$\mathrm{Si} + \mathrm{O}_2 \rightarrow \mathrm{SiO}_2 \quad (\nu_- = \nu_* = \nu_+ = 1) \tag{2}$$

We suppose that the chemical reaction is localized at the interface Γ_t between v_- and v_+ (i.e. at the chemical reaction front), and the reaction is sustained by the diffusion of A_* to Γ_t through v_+. We assume that the diffusion of A_* occurs only in v_+ until the chemical reaction front is reached by molecules of A_*. For simplicity sake we assume that diffusion of A_* does not affect strains of the skeleton.

Let $\mathbf{x}_-$ and $\mathbf{x}_+$ are positions of material points A_- and A_+ in a current configuration v_t, and let $\mathbf{X}_- \in V_-$ and $\mathbf{X}_g^+ \in V_g^+$ are their positions in unloaded reference configurations V_0 and V_g, respectively (Fig. 1).

Material segments $d\mathbf{x}_-$ and $d\mathbf{x}_+$ from ν_- and ν_+ can be related with corresponding segments $d\mathbf{X}_- \subset V_-$ and $d\mathbf{X}_g^+ \subset V_g^+$ by transformations $\mathbf{F}_-^e$ and $\mathbf{F}_+^e$,

$$d\mathbf{x}_- = \mathbf{F}_-^e \cdot d\mathbf{X}_-, \quad d\mathbf{x}_+ = \mathbf{F}_+^e \cdot d\mathbf{X}_g^+ \tag{3}$$

Let ρ_-^t and ρ_0 are densities of A_- in the current configuration ν_t and the reference
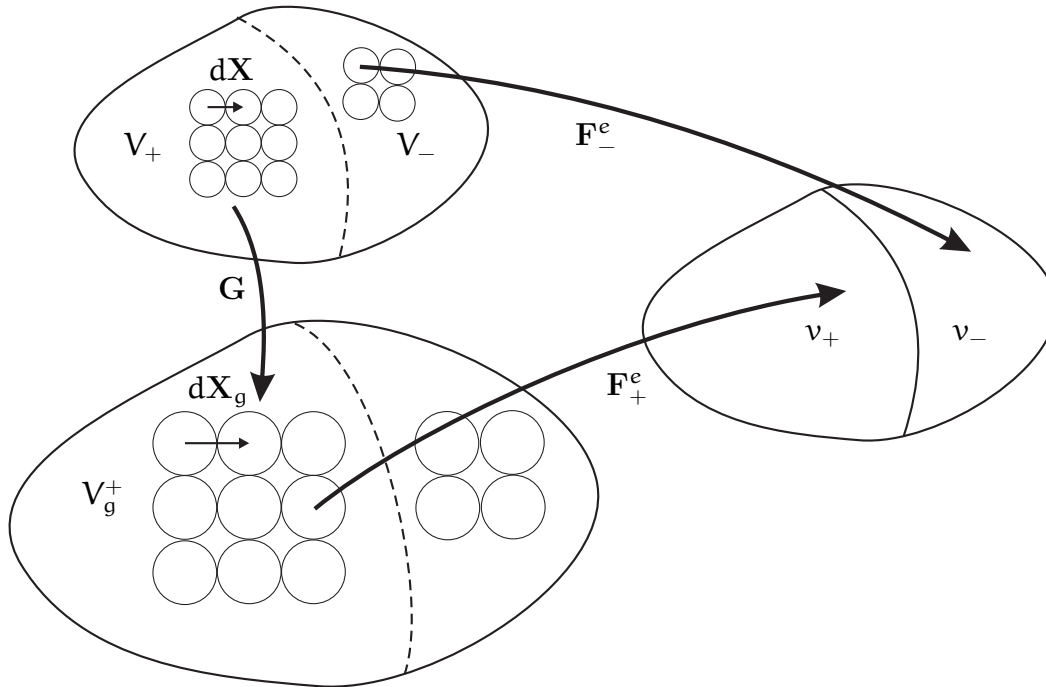
Figure 1: Configurations resulting from chemical transformation and deformation

configuration V_0, respectively. Let ρ_+^t and ρ_*^t are the partial densities of A_+ and A_* in the current configuration ν_t, and let ρ_g and ρ_* are the partial densities of A_+ and A_* in the reference configuration V_g. Then

$$\det \mathbf{F}_-^e = \frac{d\nu_-}{dV_-} = \frac{\rho_0}{\rho_-^t}, \quad \det \mathbf{F}_+^e = \frac{d\nu_+}{dV_g^+} = \frac{\rho_g}{\rho_+^t} \tag{4}$$

where the conservation of mass is taken into account for the transformations linking the reference volume elements $dV_- \subset V_-$ and $dV_g^+ \subset V_g^+$ with spatial volume elements $d\nu_- \subset \nu_-$ and $d\nu_+ \subset \nu_+$ respectively

Although material points in V_+ and V_g^+ present different materials, they are related by the chemical reaction (1), and segments $d\mathbf{X}$ and $d\mathbf{X}_g$ which consist of corresponding points A_- and A_+ can be related by the transformation tensor $\mathbf{G}$,

$$d\mathbf{X}_g = \mathbf{G} \cdot d\mathbf{X} \tag{5}$$

To construct $\mathbf{G}$ note that if M_- and M_+ are the molar masses of A_- and A_+ respectively then, due to the chemical reaction, the volume element $dV_0 = \nu_- M_- / \rho_0$ transforms into the volume element $dV_g = \nu_+ M_+ / \rho_g$. Then

$$\det \mathbf{G} = \frac{dV_g}{dV_0} = \frac{\nu_+ M_+ \rho_0}{\nu_- M_- \rho_g} \equiv g^3 \tag{6}$$

Note that $\det \mathbf{G} \neq \rho_0 / \rho_g$ (cf. with (4)). Further we suppose that the transformation tensor is isotropic. Then

$$\mathbf{G} = g\mathbf{E}, \quad g = \left(\frac{\nu_+ M_+}{\nu_- M_-} \frac{\rho_0}{\rho_g} \right)^{1/3} \tag{7}$$

where $\mathbf{E}$ is the unit tensor.

One may also consider a transformation

$$d\mathbf{x}_+ = \mathbf{F}_+ \cdot d\mathbf{X}_+, \quad \mathbf{F}_+ = \mathbf{F}_+^e \cdot \mathbf{G}, \quad d\mathbf{x}_+ \subset \nu_+, \quad d\mathbf{X}_+ \subset V_+ \tag{8}$$

where ν_+ is treated as a volume occupied by material points A_+ which are produced from corresponding points A_- contained in V_+.

Representation (8) is the Lee decomposition if $\mathbf{G}$ presents plastic strains [4], and have been used in mechanins of biological growth with $\mathbf{G}$ as a growth ("transplant") tensor (see, e.g. [1, 5, 2] and reference therein). Our case is more simple in some way. $\mathbf{G}$ is a constant tensor determined by the densities and molar masses of the constituents A_-, A_+ and the stoichiometric coefficients, $\mathbf{F}_-^e$ and $\mathbf{F}_+^e$ are deformation gradients which correspond to deformations $\mathbf{x}_- = \mathbf{x}_-(\mathbf{X}_-)$ and $\mathbf{x}_+ = \mathbf{x}_+(\mathbf{X}_g^+)$ from V_- and V_g^+ to ν_t, and

$$\mathbf{F}_+ = g\mathbf{F}_+^e \tag{9}$$

2 Stresses

Further we assume that $\mathbf{F}_-^e$ and $\mathbf{F}_+^e$ correspond to the elastic deformations of A_- and A_+. Then the Piola-Kirhgoff stress tensors $\mathbf{S}_-$ and $\mathbf{S}_+^g$ referred to V_0 and V_g configurations are given by the constitutive equations

$$\mathbf{S}_- = \rho_0 \frac{\partial f_-}{\partial \mathbf{F}_-^e}, \quad \mathbf{S}_+^g = \rho_g \frac{\partial f_+}{\partial \mathbf{F}_+^e} \tag{10}$$

where $f_- = f_-(\mathbf{F}_-^e, T)$ and $f_+ = f_+(\mathbf{F}_+^e, T)$ are free energies of A_- and A_+ per unit mass, T is the temperature.

The mechanical equilibrium equation in regular points of the body takes the form:

$$\nabla \cdot \mathbf{S}_-^T = 0 \quad (\mathbf{x} \in V_-), \quad \overset{g}{\nabla} \cdot (\mathbf{S}_+^g)^T = 0 \quad (\mathbf{x}_g \in V_g^+) \tag{11}$$

where ∇ and $\overset{g}{\nabla}$ are nabla-operators in V_0 and V_g configurations.

Let Γ and Γ_g are the images of Γ_t in V_0 and V_g configurations, $\mathbf{N}$, $\mathbf{N}_g$ and $\mathbf{n}$ are the normals to Γ, Γ_g and Γ_t respectively, directed from "+" to "−". Since $\boldsymbol{\sigma}_- \cdot \mathbf{n}\, d\Gamma_t = \mathbf{S}_- \cdot \mathbf{N}\, d\Gamma$, $\boldsymbol{\sigma}_+ \cdot \mathbf{n}\, d\Gamma_t = \mathbf{S}_+^g \cdot \mathbf{N}_g\, d\Gamma_g$, it follows from the traction continuity condition written for the solid skeleton that

$$\mathbf{S}_- \cdot \mathbf{N}\, d\Gamma = \mathbf{S}_+^g \cdot \mathbf{N}_g\, d\Gamma_g \tag{12}$$

Since by the Nanson's formula

$$\mathbf{N}_g\, d\Gamma_g = (\det \mathbf{G})\, \mathbf{G}^{-1} \cdot \mathbf{N}\, d\Gamma = g^2 \mathbf{N}\, d\Gamma \tag{13}$$

the traction continuity condition takes the form:

$$\mathbf{S}_- \cdot \mathbf{N} = g^2 \mathbf{S}_+^g \cdot \mathbf{N} \quad (\mathbf{X} \in \Gamma,\ \mathbf{X}_g = \mathbf{X}_g(\mathbf{X}) \in \Gamma_g) \tag{14}$$

3   Energy release due to the chemical reaction front propagation

The free energy of the body

$$\mathsf{F} = \mathsf{F}_s + \mathsf{F}_*$$

$$\mathsf{F}_s = \int\limits_{\nu_-} \rho_- f_-\, d\nu + \int\limits_{\nu_+} \rho_+^t f_+\, d\nu = \int\limits_{V_-} \rho_0 f_-\, dV_0 + \int\limits_{V_g^+} \rho_g f_+\, dV_g \tag{15}$$

$$\mathsf{F}_* = \int\limits_{\nu_+} \rho_*^t f_*\, d\nu = \int\limits_{V_g^+} \rho_* f_*\, dV_g$$

where f_* is free energy of A_* per unit mass By (10),

$$\dot{\mathsf{F}}_s = \int\limits_{V_-} \mathbf{S}_- : (\dot{\mathbf{F}}_-^e)^\mathsf{T}\, dV_0 + \int\limits_{V_g^+} \mathbf{S}_g^+ : (\dot{\mathbf{F}}_+^e)^\mathsf{T}\, dV_g - \tag{16}$$

$$- \int\limits_{\Gamma} \rho_0 f_- \mathbf{v}^\Gamma \cdot \mathbf{N}\, d\Gamma + \int\limits_{\Gamma_g} \rho_g f_+ \mathbf{v}_g^\Gamma \cdot \mathbf{N}_g\, d\Gamma_g$$

where $\mathbf{v}^\Gamma$ and $\mathbf{v}_g^\Gamma$ are the reaction front velocities with respect to V_0 and V_g configurations.

Let the displacement is given on Ω_1 and the traction $\mathbf{t}_0$ is given on Ω_2 where $\Omega_1 \cup \Omega_2 = \Omega \equiv \partial V_0$, and points of Ω_1 as well as points of Ω_2^a where $\mathbf{t}_0 \neq 0$ (the "active" part of Ω_2) do not undergo chemical transformations. Then

$$\int\limits_{V_-} \mathbf{S}_- : (\dot{\mathbf{F}}_-^e)^\mathsf{T}\, dV = \int\limits_{\Omega_2^a} \mathbf{t}_0 \cdot \mathbf{v}_-\, d\Omega - \int\limits_{\Gamma} \mathbf{N} \cdot \mathbf{S}_-^\mathsf{T} \cdot \mathbf{v}_-\, d\Gamma \tag{17}$$

$$\int\limits_{V_g^+} \mathbf{S}_g^+ : (\dot{\mathbf{F}}_+^e)^\mathsf{T}\, dV = \int\limits_{\Gamma_g} \mathbf{N}_g \cdot (\mathbf{S}_g^+)^\mathsf{T} \cdot \mathbf{v}_+^g\, d\Gamma$$

where the velosities

$$\mathbf{v}_- = \frac{\partial \mathbf{x}_-(\mathbf{X}, \mathbf{t})}{\partial \mathbf{t}}, \quad \mathbf{v}_+^g = \frac{\partial \mathbf{x}_+(\mathbf{X}_g, \mathbf{t})}{\partial \mathbf{t}}$$

and the equilibrium equations (11) are taken into account.

We suppose that displacement is continuous across the reaction front, $\mathbf{x}_-(\Gamma) = \mathbf{x}_+(\Gamma_g)$. Then

$$\mathbf{v}_+^g - \mathbf{v}_- = -(\mathbf{v}_g^\Gamma \cdot \mathbf{F}_+^e - \mathbf{v}^\Gamma \cdot \mathbf{F}_-^e) = -\mathbf{v}^\Gamma \cdot (g\mathbf{F}_+^e - \mathbf{F}_-^e) \tag{18}$$

By (12), (14) and (18):

$$\int\limits_{\Gamma_g} \mathbf{N}_g \cdot (\mathbf{S}_+^g)^\mathsf{T} \cdot \mathbf{v}_+^g\, d\Gamma_g - \int\limits_{\Gamma} \mathbf{N} \cdot \mathbf{S}_-^\mathsf{T} \cdot \mathbf{v}_-\, d\Gamma = \int\limits_{\Gamma} \mathbf{N} \cdot \mathbf{S}_-^\mathsf{T} \cdot (\mathbf{v}_+^g - \mathbf{v}_-)\, d\Gamma =$$

$$= -\int\limits_{\Gamma} \mathbf{N} \cdot (g^3 (\mathbf{S}_+^g)^\mathsf{T} \cdot \mathbf{F}_+^e - \mathbf{S}_-^\mathsf{T} \cdot \mathbf{F}_-^e) \cdot \mathbf{v}^\Gamma\, d\Gamma$$

where it is taken into account that the reaction front velocities $\mathbf{v}_g^\Gamma$ and $\mathbf{v}^\Gamma$ with respect to V_g and V configurations, by (5) and (7), are related as $\mathbf{v}_g^\Gamma = g\mathbf{v}^\Gamma$.

From (3)–(3) it follows the the solid constituents potential energy release is given by the expresion

$$\dot{\Pi} \equiv \dot{F}_s - \int_{\Omega_2^a} \mathbf{t}_0 \cdot \mathbf{v}_- \, d\Omega = -\int_\Gamma \mathbf{N} \cdot (g^3 \mathbf{M}_+ - \mathbf{M}_-) \cdot \mathbf{v}^\Gamma d\Gamma \tag{19}$$

where

$$\mathbf{M}_- = \rho_0 f_- \mathbf{E} - \mathbf{S}_-^\mathsf{T} \cdot \mathbf{F}_-^e, \quad \mathbf{M}_+ = \rho_g f_+ \mathbf{E} - (\mathbf{S}_+^g)^\mathsf{T} \cdot \mathbf{F}_+^e$$

are the Eshelby tensors.

The expression (19) can be rewritten as

$$\dot{\Pi} = -\frac{\rho_0}{\nu_- M_-} \int_\Gamma \mathbf{N} \cdot \mathbf{A}_s \cdot \mathbf{v}^\Gamma \, d\Gamma \tag{20}$$

where

$$\mathbf{A}_s = \nu_+ M_+ \widetilde{\mathbf{M}}_+ - \nu_- M_- \widetilde{\mathbf{M}}_- \tag{21}$$

$$\widetilde{\mathbf{M}}_+ = f_+ \mathbf{E} - \frac{1}{\rho_g}(\mathbf{S}_+^g)^\mathsf{T} \cdot \mathbf{F}_+^e, \quad \widetilde{\mathbf{M}}_- = f_- \mathbf{E} - \frac{1}{\rho_0} \mathbf{S}_-^\mathsf{T} \cdot \mathbf{F}_-^e$$

In classical chemistry $A = \sum \nu_k M_k \mu_k$ is a chemical affinity, where ν_k are stoichiometric coefficients taken with the sign "+" if the k-th component is produced due to the chemical reaction and taken with the sign "−" in other case, μ_k is the chemical potential per unit mass of the k-th component [6]. The tensor $\mathbf{A}_s$ in (20) represents the input of solid constituents into the chemical affinity tensor, and the tensors $\widetilde{\mathbf{M}}$ are the chemical potential tensors.

It can be shown that due to kinematic compatibility across the reaction front

$$\mathbf{N} \cdot \mathbf{A}_s = A_N^s \mathbf{N}, \quad A_N^s = \mathbf{N} \cdot \mathbf{A} \cdot \mathbf{N}$$

This gives one more representation of the potential energy release,

$$\dot{\Pi} = -\frac{\rho_0}{\nu_- M_-} \int_\Gamma A_N^s \nu_N^\Gamma \, d\Gamma, \quad \nu_N^\Gamma = \mathbf{v}^\Gamma \cdot \mathbf{N}$$

and A_N can be called a solid constituents input into chemical affinity at the surface element with a normal $\mathbf{N}$. A scalar value in classical chemical affinity expression is replaced by the normal component of the chemical affinity tensor.

The mass balance for A_* takes the form

$$\dot{\rho}_* = \widehat{\rho}_* - \overset{g}{\nabla} \cdot (\rho_* \mathbf{v}_*) \tag{22}$$

where $\mathbf{v}_*$ is a velocity of the component A_* with respect to V_g due to the diffusion, $\widehat{\rho}_* < 0$ is a sink of the component A_*, mass loss due to the chemical reaction. Then, assuming that $f_* = f_-(\rho_*, T)$, we obtain that

$$\dot{F}_* = \int_{V_g^+} (\widehat{\rho}_* \mu_* + \rho_* \mathbf{v}_* \cdot \overset{g}{\nabla} \mu_*) \, dV_g - \int_{\Omega_g} \rho_* \mu_* \mathbf{v}_* \cdot \mathbf{N}_g \, d\Omega - \int_{\Gamma_g} p_* \mathbf{v}_* \cdot \mathbf{N}_g d\Gamma$$

where

$$\mu_* = f_* + \frac{p_*}{\rho_*}, \quad p_* = \rho_*^2 \frac{\partial f_*}{\partial \rho_*} \tag{23}$$

We assume that chemical reactions are localized at the reaction front. Then

$$\int_{V_g^+} \widehat{\rho}_* \mu_* \, dV_g = \int_{\Gamma_g} \widehat{\rho}_* \mu_* \mathbf{v}_g^\Gamma \cdot \mathbf{N}_g \, d\Gamma$$

The reaction front velosity is determined by the A_+ production rate. To produce $\nu_+ M_+$ mass units of A_+ one needs $\nu_* M_*$ mass units of A_* where M_* is a molar mass of A_*. Then to produce $\rho_g \mathbf{v}_g^\Gamma \cdot \mathbf{N}_g \, d\Gamma$ mass units of A_+ one needs

$$\widehat{\rho}_* \mathbf{v}_g^\Gamma \cdot \mathbf{N}_g \, d\Gamma = \frac{\nu_* M_*}{\nu_+ M_+} \rho_g \mathbf{v}_g^\Gamma \cdot \mathbf{N}_g \, d\Gamma$$

mass units of A_*. Thus,

$$\int_{V_g^+} \widehat{\rho}_* \mu_* \, dV_g = -\frac{\nu_* M_*}{\nu_+ M_+} \int_{\Gamma_g} \rho_g \mu_* \mathbf{v}_g^\Gamma \cdot \mathbf{N}_g \, d\Gamma_g = -\frac{\nu_* M_*}{\nu_- M_-} \int_\Gamma \rho_0 \mu_* \mathbf{v}^\Gamma \cdot \mathbf{N} \, d\Gamma \tag{24}$$

where

$$\mathbf{M}_* = \rho_* \mu_* \, \mathbf{E}$$

Finally we obtain the following expression of the dissipation due the chemical reaction front propagation:

$$D_\Gamma = \int_\Gamma \mathbf{N} \cdot (g^3 \mathbf{M}_+ - \mathbf{M}_- - g_*^3 \mathbf{M}_*) \cdot \mathbf{v}^\Gamma \, d\Gamma = \frac{\rho_0}{\nu_- M_-} \int_\Gamma \mathbf{N} \cdot \mathbf{A} \cdot \mathbf{v}^\Gamma \, d\Gamma = \frac{\rho_0}{\nu_- M_-} \int_\Gamma A_N v_N^\Gamma \, d\Gamma$$

where the chemical affinity tensor

$$\mathbf{A} = \nu_+ M_+ \widetilde{\mathbf{M}}_+ - \nu_- M_- \widetilde{\mathbf{M}}_- - \nu_* M_* \widetilde{\mathbf{M}}_*,$$
$$\widetilde{\mathbf{M}}_* = \mu_* \, \mathbf{E}, \quad A_N = \mathbf{N} \cdot \mathbf{A} \cdot \mathbf{N}$$

The reaction front propagation velocity can be given by the kinetic constitutive equation

$$v_N^\Gamma = \Phi \, (A_N) \tag{25}$$

such that $A_N \, \Phi(A_N) < 0$ For example, in a linear thermodynamic approach

$$v_N^\Gamma = -\kappa A_N, \quad \kappa > 0 \tag{26}$$

In a case of chemical equilibrium the rates of direct and reverse chemical reactions are equal, the reaction front does not move,

$$A_N = 0, \quad \Phi(0) = 0 \tag{27}$$

In a case of martensite phase transformation, due to mass balance $g^3 \equiv dV_g/dV_0 = \rho_0/\rho_g$, $g_* = 0$,

$$g^3 \mathbf{M}_+ = \rho_0 f_+(\mathbf{F}_+)\mathbf{E} - \mathbf{S}_+^{\mathsf{T}} \cdot \mathbf{F}_+$$

and (19) becomes a known formula [3] for energy release due to interface boundary propagation.

We presented a simplest consideration of of the reaction front propagation. Introducing the intermediate reference configuration allowed us to express the chemical potentials in terms of stresses related by the constitutive equations of solid constituents of the reaction. Further progress is expected on the way of taking into account cross effects related with interconnections between the solid skeleton and diffusion of a gas constituent.

Acknowledgements

References

[1] Epstein, M., and Maugin, G. A. Thermomechanics of volumetric growth in uniform bodies. Int. J. Plasticity (2000) 16, 951978.

[2] A. Guillou, R.W. Ogden. Growth in soft biological tissue and residual stress development. In: Holzapfel, G.A., Ogden, R.W. (eds.) Mechanics of biological tissue. Springer, Heidelberg (2006)

[3] J.K. Knowles, On the dissipation associated with equilibrium shocks in finite elasticity, J. Elasticity, 9 (1979) 131-158.

[4] Lee, E. H. Elastic-plastic deformation at finite strains. ASME J. Appl. Mech., (1969) 36, 18.

[5] Lubarda V.A. Constitutive theories based on the multiplicative decomposition of deformation gradient: Thermoelasticity, elastoplasticity, and biomechanics. Appl Mech Rev. (2004) 57, No 2, 95-108

[6] P. Glansdorff, I. Prigogine, Thermodynamic theory of structure, stability and fluctuations, Wiley-Interscience, London, NY, Sydney, Toronto.

Alexander B. Freidin, Institute of Problems in Mechanical Engineering of Russian Academy of Sciences, Bolshoy, 61, V.O. St. Petersburg, 199178 Russia

De-spin of a motorised momentum exchange tether

Claudia C. Gandara   Matthew P. Cartmell

claudiaecg@gmail.com

Abstract

This paper focuses on a conceptual de-spin proposal for a symmetrical Motorised Momentum Exchange Tether (MMET). It starts with a study of the spin motion of the system, both for the propulsion tether and the reaction-providing outrigger tether, by summarising numerical computations of the equations of motion implemented in Mathematica$^{\circledR}$ integrator. An operating duty cycle is for the tether determined and a payload release occurs followed by an inspection of the conservation of total momentum. The paper then continues with a de-spin study of the remaining system by means of analysis of a special de-spin release mechanism. A calculation of the conservation of total momentum is performed for this case. The final work is focused on the de-spin of the released payloads, a very important task from the perspective of system re-utilisation.

1   Introduction

Space Tethers provide a mechanical connection between objects in space enabling the transfer of energy and momentum from one object to the other, giving the potential advantage of providing space propulsion without consuming propellant. The motorised tethered system under investigation here was originally developed by Ziegler and Cartmell[1]. Figure 1 shows a symmetric system concept and comprises a dumb-bell tether attached to a central facility, at which point the centre of mass (COM) of the whole system is assumed to be located, and which also carries a drive motor. Two outrigger tethers are attached to the motor stator in order to act as counter-inertias so that Newton's 3$^{\mathrm{rd}}$ law may be satisfied, as required, for the propulsion side to spin up unidirectionally. De-spin features act as a possible additional bonus. The system is assumed here to be operating on a circular orbit around the Earth.

2   Spin dynamics of the symmetrical laden tether

Following the work done by Ziegler on the rigid body dynamics of tethers in space[2], the equations of motion of the tethered satellite can be deduced based on a planar model of analysis such as the one in Figure 2 representing the propulsion system.
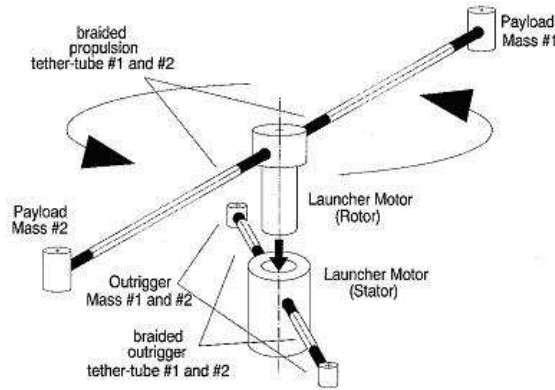
Figure 1: Schematic of symmetrical Motorised Tether concept, as proposed by Ziegler and Cartmell, 1999

We can also use the same model to describe the outrigger system, as both systems have similar physical configurations. The equations of motion can be deduced from Figure 2, starting by describing the system components (two payloads, two tethers, two release mechanisms and the central facility) in Cartesian coordinates and using them to calculate the kinetic and potential energies of the system. The equations of the dumb-bell tether are obtained via the Lagrangian formulation (Equations (1-2)), where the centre of the Earth is set as an absolute origin, an initial torque τ is applied by the motor and the propulsion system is assigned one generalised coordinate ψ, while the outrigger system is also assigned one generalised coordinate β.

$$\frac{d}{dt}\left(\frac{\partial T}{\partial \dot{\psi}}\right) - \frac{\partial T}{\partial \psi} + \frac{\partial U}{\partial \psi} = \tau \tag{1}$$

$$\frac{d}{dt}\left(\frac{\partial T}{\partial \dot{\beta}}\right) - \frac{\partial T}{\partial \beta} + \frac{\partial U}{\partial \beta} = -\tau \tag{2}$$
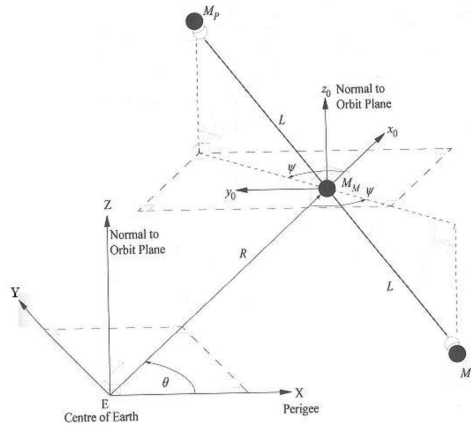
Figure 2: Propulsion system schematic model

3 Orbital performance

The tethered system is assumed to be performing an orbit around the Earth, spinning around its COM and then the instant is taken when the propulsion tether is aligned along the local gravity vector, so that the system velocity can be determined,

$$V_{total} = V_{orbit} + V_{tether} \qquad (3)$$

Providing the payload with a total escape velocity of 10.7 km/s the velocity of the propulsion tether sub-span is given by:

$$V_{tether} = L \, \dot{\psi} \qquad (4)$$

Therefore, the angular velocity $\dot{\psi}$ will increase until it reaches 0.06262 rad/s, in order for the system, as designed, to achieve the required escape velocity V_{total}. The orbital period can also be determined.

$$P = 2 \, \pi \, \sqrt{\frac{r_c^3}{\mu}} \qquad (5)$$

A spin study is carried out by running a specially written piece of code in Mathematica® which gives numerical results by integrating the system's equations of motion. The results are generated using the parameters from Table 1 and the following initial conditions: $\psi = \beta = $ -0.9 rad and $\dot{\psi} = \dot{\beta} = 0$ rad/s. All the necessary conditions are established and the initial spin-up study can now be performed[3].

Parameters	Data	Units
M_p	1000	kg
r_p	0.5	m
L	50000	m
ρ	970	kg/m^3
A	$62.83x10^{-6}$	m^2
M_0	1000	kg
r_0	0.5	m
L_0	25000	m
ρ_0	970	kg/m^3
A_0	$62.83x10^{-6}$	m^2
M_m	5000	kg
r_m	0.5	m
r_c	6870000	m
μ	$3.9877848x10^{14}$	m^3/s^2
τ	3374838	Nm

Table 7: Data values of the dumb-bell tethered system for propulsion, outrigger and main facility

4   Damping the system

It is also desirable to take into account any dissipation in the system due to the bearings in the motor and transmission. These bearings are responsible for the mechanical configuration between the propulsion and outrigger systems. They also dissipate energy into space due to frictional heat. If we take this dissipation into account we will have a system of the type:

$$A \ddot{\psi} + B \psi + C \dot{\psi} = \tau \tag{6}$$

$$A_0 \ddot{\beta} + B_0 \beta + C \dot{\beta} = -\tau \tag{7}$$

Where, A and A_0 represent the mass moments of inertia of the propulsion and outrigger systems respectively, B and B_0 represent the stiffness coefficients, and the damping coefficients of the motor and the stator, C are assumed to be equal, i.e., both generate the same amount of friction, and dissipate the same amount of energy. The damping coefficients are assumed to have a magnitude of $1\text{x}10^7$ Nms. The numerical results take into account the tethered system's orbital coupling, i.e., considering the tether orbiting the Earth with a constant orbital rate as given by:

$$\dot{\theta} = \sqrt{\frac{\mu}{r_c^3}} \tag{8}$$

Figure 3 shows the system in its pure spin condition with a minimum torque required τ, so that the system can increase its angular velocity until it reaches the necessary escape velocity. In this numerical example this corresponds to a time of 206639 sec, i.e. approximately 36.47 orbits. The outrigger system is spinning in the opposite direction to the payload, due to the opposite torque applied.

For a spinning tether, the optimum payload release point is when the tether is aligned along the local gravity vector and when the motion is coplanar with the orbital plane.

The initial spin-up condition provides the time when the payloads must be released. For that time an evaluation of the system motion was made for pragmatic system design data, where the accumulated propulsion spin angle ψ was found to be 6731.42 rad, while the outrigger system responses were found to be β = -23772.11 rad and $\dot{\beta}$ = -0.214469 rad/s. These system responses, corresponding to the payload's release time, are then used as initial conditions for the next phase of the calculation. The data adopted for this investigation is shown in Table 1.

5   Analysis of the system after payload release

The next step consists of evaluating the system after payload release. New studies were carried out in order to analyse the remaining system response for its angular velocities $\dot{\psi}$ and $\dot{\beta}$ and spin angles ψ and β for two cases: for the zero torque condition and for reverse torque.
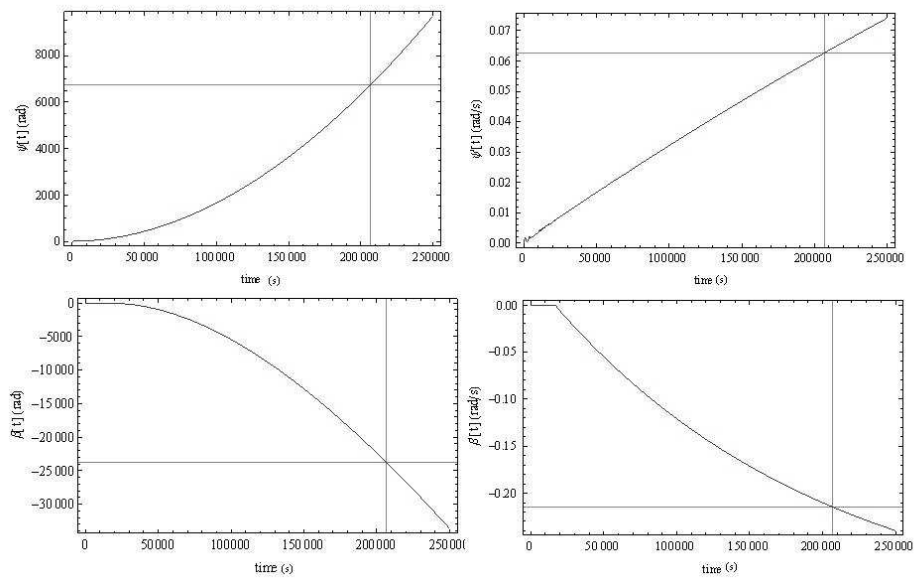
Figure 3: System response for the initial spin-up condition of the damped system

Figure 4 represents the complete angular velocities profile of the damped system for 3 phases of study. The left part of the graph, going from zero until the release time (vertical gridline), represents the first phase, that of initial spin. From the release until a period of 400000 sec has elapsed the dynamics of the remaining system are evaluated.

The second phase corresponds to the payload release and the zero torque condition. This case was studied for a period of 60 sec but further simulations showed that over a longer time of integration; the ripple effect is lessened in the damped system. Due to the instantaneous reduction of the mass moment of inertia on the propulsion side, this led to a change in the acceleration of the remaining system. The propulsion side accelerated more and the outrigger accelerated less than it would have done if the payloads had not been disconnected.

The third phase consists of applying a reverse torque. In the case of the applied reverse torque the propulsion side decelerates until it achieves zero angular velocity and then starts to spin in the opposite direction, the outrigger direction, and finally the remaining system ends up rotating in opposite directions for a time of 293601 sec.

This analysis of the system after payload release has been carried out in order to understand the dynamics of spinning tethered systems, to find a solution for de-spinning of the remaining system after payload release, and a possible way to control this by reducing its unstable behaviour.

From the beginning until it changes its direction of rotation at approximately 51.82 orbits, the outrigger shows a residual post-payload release counter-spin, while the propulsion tether is near its zero angular velocity. This situation happens due to the fact that the payloads themselves had not been de-spun, and so the remaining

system can't be completely stopped without involving the use of some sort of external energy.
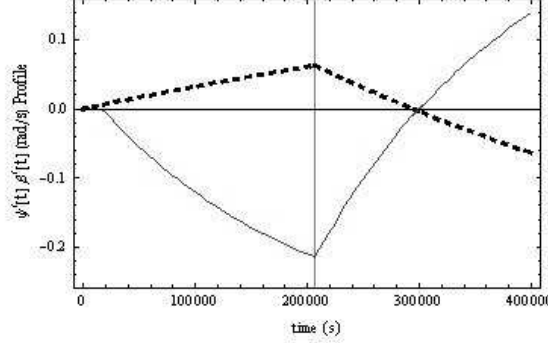
Figure 4: Angular velocities profile of the damped system (dashed plot - propulsion angular velocity, $\dot{\psi}$, and thin plot - outrigger angular velocity, $\dot{\beta}$)

6   Momentum conservation

The conservation of momentum was analysed with respect to the system's COM. When a rigid body rotates, its resistance to a change in its rotational motion is dictated by its moment of inertia. The outrigger angular momentum will be conserved since there are no physical modifications to the system throughout all phases of operation. Hence as the payload release occurs from the propulsion system, the system moment of inertia is given by the sum of the moments of inertia of its components; payloads, tethers, release mechanisms and central facility, namely,

$$I_{payload} = \tfrac{1}{2} \, M_p \, r_p^2 + M_p \, (L + d_1)^2 \tag{9}$$

$$I_{tethers} = \tfrac{1}{12} \, \rho \, A \, 2 \, L \, (3 \, r_T^2 + 4 \, L^2) \tag{10}$$

$$I_{mechanism} = \tfrac{1}{4} \, m_A \, d_1^2 + m_A \, L^2 \tag{11}$$

$$I_m = \tfrac{1}{2} \, M_m \, r_m^2 \tag{12}$$

The total mass moment of inertia of the system before payload release is therefore:
$$I_B = I_m + I_{tethers} + 2 \, I_{payload} + 2 \, I_{mechanism} \tag{13}$$

The angular momentum before and after payload release is determined using the numerical results for the angular velocities of the damped system before and after payload release, $\dot{\psi}_B = 0.062620$ rad/s and $\dot{\psi}_A = 0.062602$ rad/s.

$$H_B = I_B \, \dot{\psi}_B \tag{14}$$

$$H_A = I_A \, \dot{\psi}_A + 2 \, H_R + 2 \, H_T \tag{15}$$

243

Although the payloads are disconnected from the system and therefore have not been de-spun, they have angular momentum due to post-release rotation, H_R, and angular momentum due to post-release translation, H_T.

Therefore,

$$I_A = I_m + I_{tethers} + 2\, I_{mechanism} \tag{16}$$

$$H_R = I_{payload}\, \dot{\psi}_B \tag{17}$$

$$H_T = M_p\, L\, r_p\, \dot{\psi}_B \tag{18}$$

The system's angular momentum is found to be conserved such that $H_B = H_A$ at an order of magnitude of 6.34×10^{11} Nms.

7 Analysis of the system de-spin

The work carried out by Cartmell et $al.$[4] was the precursor to the development of a scale model of the motorised momentum exchange propulsion tether, and the definition for a new idea for the study of the de-spin of payloads after release. According to the experimental work carried out, it was confirmed that the payloads would continue to spin as they translated away tangentially from their release points, and work was initiated to investigate if it would be possible to mitigate this. From this work, it was proposed that a staggered release of each payload, by means of a specially designed double release point mechanism, could be capable of imparting an opposing spin onto the payload as it is released. This device could be used to neutralise the spin of the payload without major interference with the translational velocity that the spin has given it.

Figure 5 represents the release mechanism and in, phase 1 the propulsion tether is spinning attached to the mechanism and the payload D. Phase 2 represents de-spinning when the mechanism is activated by the 3 hinges (A, B and C) in order to release the payload providing the system with two counter motions.

The interest in payload de-spin is that the system could be used as part of a two-way interplanetary payload exchange system. After the release the upper payload could be injected into a rescue orbit, and therefore it is desirable for the payload to have only a translational motion. Being in a rescue orbit allows the payload to be captured next time it comes round to the same orbital position.

The mechanism can be modified into a 2D model such as the one shown in Figure 6, where d_1 is the release mechanism radius, l_2 is the payload radius and θ_1 and θ_2 add to the system two degrees of freedom (DOF). This scheme only represents the upper model. The complete model for de-spin defines a system with a total of 5 DOF: ψ, θ_{1u} and θ_{1l} for the upper and lower mechanisms and θ_{2u}, θ_{2l} for the upper and lower payloads.
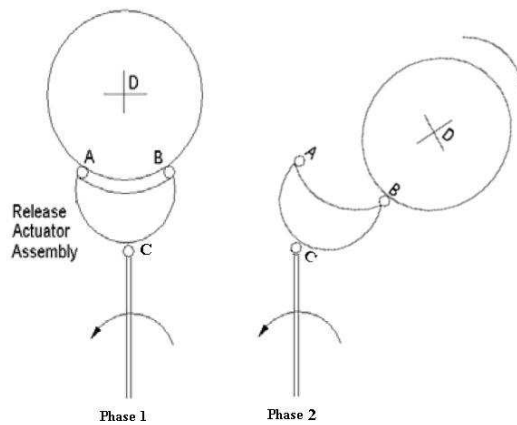
Figure 5: De-spin mechanism [3]
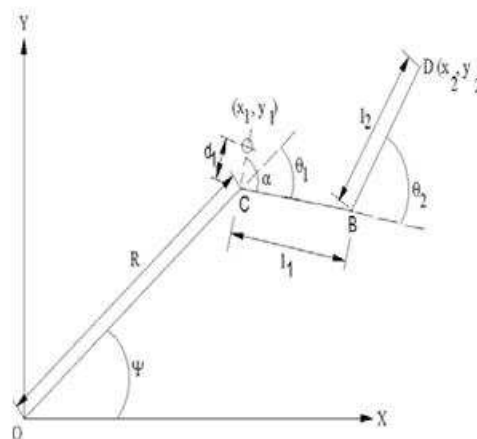
Figure 6: Release mechanism 2D analytical model [3, 4]

8   Payload de-spin

After analysing the system's equations of motion for the de-spin model, the numerical results are then generated in Mathematica$^{\circledR}$ using mechanism parameters obtained from those used by Cartmell *et al.*[4], switching off the torque and introducing new initial conditions: $\theta_{1u} = \theta_{1l} = 0.3$ rad, $\theta_{2u} = \theta_{2l} = 0.6$ rad with zero initial angular velocities.

Performing the system de-spin evaluation, Figure 7 shows that the upper and lower payloads display symmetrical dynamical behaviour and that they are de-spun 0.078 sec after their release. This means that after performing the initial spin and finding the time when the payloads must be released (206639 sec), the torque is switched-off and the release mechanisms are activated defining the system as having 5 DOF, and then the de-spin analysis shows that the payloads are de-spun after 0.078 sec , i.e., the payloads will simply translate after that.
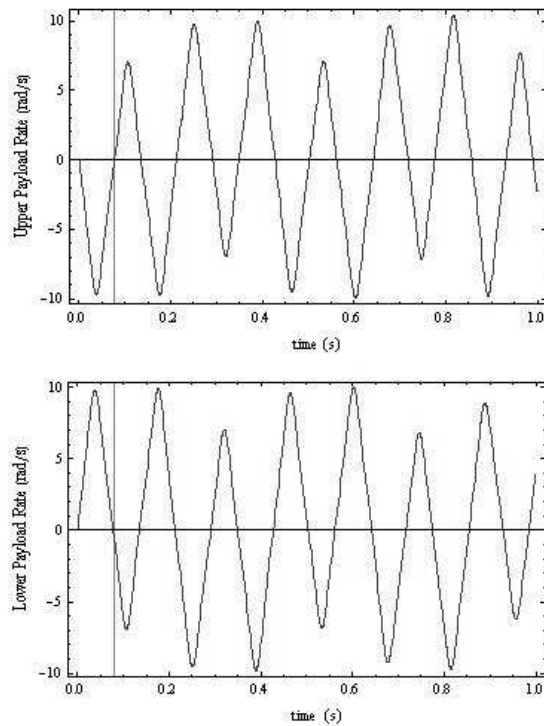
Figure 7: Payload angular velocity evaluation

9 Damping in the release mechanisms

After payload release the remaining system will continue to spin without stopping, the release mechanisms will also be oscillating about their equilibrium point (hinge C), and this will potentially contribute to the system's unstable behaviour. System instability is not desirable; therefore, a suitable damping coefficient must be assigned to the mechanisms with a minimum value capable of damping the oscillatory behaviour. In practice, the system would be damped by means of viscous dampers fitted at the joints within the mechanism.

A new evaluation of the fully laden system was then performed to see how damping the mechanisms would affect the payload de-spin. Results from Figure 8 show that the de-spin time was delayed up to 0.21 sec after payload release, for the system design data applied in this paper. Note that a full numerical investigation of the whole design parameter space would inevitably alter this value, but the functionality of the damping is still convincingly demonstrated in this restricted numerical example.

10 Momentum conservation

Momentum conservation is calculated by analysing the system's numerical results computed for the payload de-spin, with those computed after payload release for the system with damped mechanisms[3]. Conservation is expected for the propulsion system due to the transfer of momentum between the release mechanisms and the
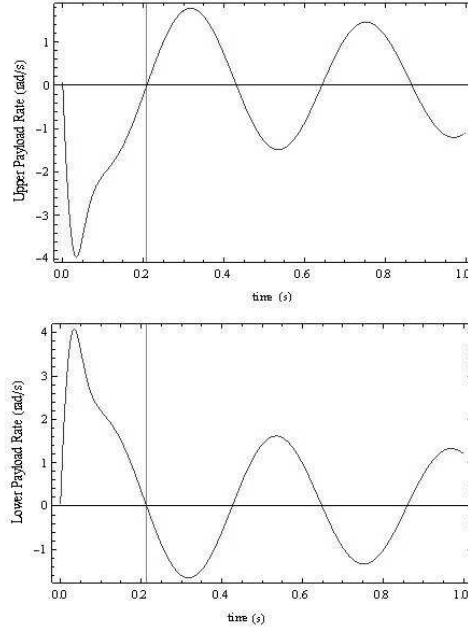
Figure 8: Payload angular velocity evaluation for the damped mechanism

payloads.

The angular momentum before payload release is given by the sums of the products between the system's mass moments of inertia components with their respective angular rates using the numerical results for the angular velocities of the system with damping: $\dot{\psi}_B = 0.062620$ rad/s, $\dot{\psi}_A = 0.062619$ rad/s, $\dot{\theta}_{1B} = 0.164614$ rad/s, $\dot{\theta}_{1A} = 0.062225$ rad/s and $\dot{\theta}_{2B} = 0.101994$ rad/s.

$$H_B = (I_{tethers} + I_m)\, \dot{\psi}_B + 2\, I_{mechanism}\, (\dot{\psi}_B + \dot{\theta}_{1B}) \\ + 2\, I_{payload}\, (\dot{\psi}_B - \dot{\theta}_{1B} + \dot{\theta}_{2B}) \tag{19}$$

Where $\dot{\psi}_B - \dot{\theta}_{1B} + \dot{\theta}_{2B}$ is the payload angular rate. The angular momentum after payload release will be given by the total mass moments of inertia of the remaining system plus the payload translation component.

$$H_A = (I_{tethers} + I_m)\, \dot{\psi}_A + 2\, I_{mechanism}\, (\dot{\psi}_A + \dot{\theta}_{1A}) + 2\, H_T \tag{20}$$

Comparing H_B with H_A, the propulsion system's angular momentum is conserved at an order of magnitude of 3.2×10^{11} Nms.

11   Conclusions

A dumb-bell tether composed of propulsion and outrigger systems, each one laden with two end masses, such as shown in Figure 1; on an Earth-centred reference frame, was investigated. All the work carried out took into account the mechanical dynamics of the planar MMET system. The Lagrangian equations of motion for

the system were derived integrated in order to obtain numerical results. All the calculations were carried out for a damped system with a damping coefficient of 1×10^7 Nms; taking into account the dissipation due to the bearings in the motor.

From the two cases presented, for spin and de-spin; the spin study comprised three phases: the initial spin-up, analysis of the system after payload release, switching-off the torque and analysis applying a reverse torque. Regarding certain initial conditions, and for the system parameters presented, it was found that the time to release the payloads was 206639 sec, i.e., after performing 36.47 orbits. After payload release the payloads will be spinning and translating as they move away from the remaining system. Applying a reverse torque, in order to stop the system, showed that the remaining system couldn't be completely stopped without involving the use of some sort of external energy. To allow system reutilisation the solution to this problem seems to be to use the motor torque to slowly de-spin the system. This method will not stop the system from spinning but can get near that as it can be set to a desirable velocity in order to allow the attachment of other payloads, by continuing to de-spin the propulsion tethers to absolute zero speed so that new payloads can be attached, and then to lose some of the outrigger back-spin by exchanging momentum with the propulsion tethers. This will leave the whole system spinning together, but more slowly, and this time with the propulsion system spinning in reverse, in the outrigger direction. The system's momentum conservation for the spin case was checked before and after payload released and it was found to be conserved, at an order of magnitude of 6.34×10^{11} Nms.

The investigation continued with a study of the de-spin motion provided by the de-spin mechanism with three spherical hinges as originally developed by Cartmell *et al.*[4], with the overall propulsion system comprising a 5 DOF model giving the payloads two counter motions in order to de-spin as they are released. From the payload rate graphs, Figure 7 shows that both payloads de-spin at a time of 0.078 sec after being released. In practice they will translate through space. To reduce the remaining system's unstable behaviour the de-spin mechanisms were damped. A suitable damper was introduced with a suggested value of 1×10^3 Nms. The system response was affected and payload's de-spin time was delayed to 0.21 sec. Conservation of momentum was checked regarding the damped system with 5 DOF. Although the analysis was more complex, the momentum conservation was found to be of the order of 3.2×10^{11} Nms given the fact that the payloads were de-spun, and therefore $H_R = 0$.

Acknowledgements

References

[1] Ziegler, S. W., Cartmell, M. P., "Using motorised tethers for payload orbital transfer", Journal of Spacecraft and Rockets, Vol. 38, No. 6, pp. 904-13, 2001.

[2] Ziegler, S. W., "The rigid-body dynamics of tethers in space", PhD. Dissertation, Department of Mechanical Engineering, University of Glasgow, 2003.

[3] Gandara, C. C., "De-spin of a motorised momentum exchange tether", MSc. Thesis, Department of Aerospace Engineering, University of Glasgow, September 2008.

[4] Cartmell, M. P., Ziegler, S. W., Neill, D. S., "On the performance prediction and scale modelling of a motorised momentum exchange propulsion tether", AIP Conference Proceedings, No. 654, pp. 571-9, 2003.

Claudia C. Gandara and Matthew P. Cartmell, Department of Mechanical Engineering, University of Glasgow, Glasgow, G12 8QQ, Scotland, UK

Dynamics of phase transformations in a spherical elastic body

Serge N. Gavrilov   Ekaterina V. Shishkina

serge@pdmi.ras.ru

Abstract

The dynamic processes in a spherical elastic body composed of a material, which is capable of undergoing phase transitions, are under consideration. The radius of the sphere is supposed to be sufficiently large. We use a model of an elastic body with non-convex strain energy potential [1–13]. It is supposed that the unique phase boundary is spherical and separates two stable phases. It's position is an unknown quantity. Admissible motions of the phase boundary are sought for. It is assumed that the phase boundary moves at a variable speed. The motion is caused by a non-equilibrium initial condition for the phase boundary position. As a result of the study we derive the set of equations at the phase boundary. For a particular case (when the material in the "inner" phase is incompressible) we obtain an analytical non-self-similar solution of the problem and investigate its properties. The results obtained in the framework of this full dynamic approach are compared with the results obtained in the framework of the kinetic (quasi-static) approach. It is demonstrated that the quasi-static approach [12,13] correctly describes the phase boundary motion only in the case of strong dissipation at the phase boundary.

1   Introduction

In the paper we deal with dynamic processes in elastic bodies, capable of undergoing phase transformations. We use a model of an elastic material with non-convex strain energy potential [1-13]. It is known that the problem of elastostatics for a material of such a kind can have solutions with discontinuous deformation gradients [12]. In the framework of the model, the surfaces of the strain discontinuity are considered as the phase boundaries, and the domains of continuity are considered as zones, which are occupied by different phases of the material. The solution of both statical and dynamical problems are generally non-unique, therefore an additional thermodynamic boundary condition at the phase boundary is required [1-7].

2   The governing equations

We considers dynamics of phase transformations in an elastic sphere of a sufficiently large radius with the unique spherical phase boundary. This is is the three-dimensional dynamical spherically symmetrical problem.

In linear elasticity according to the Hooke low the relationship between the stress tensor $\boldsymbol{\sigma}$ and the strain tensor $\boldsymbol{\varepsilon}$ is

$$\boldsymbol{\sigma} = \lambda\theta\mathbf{I} + 2\mu\boldsymbol{\varepsilon} = k\theta\mathbf{I} + 2\mu\mathbf{e} \tag{1}$$

Here λ, μ are the Lame constants, $k = \lambda + \frac{2}{3}\mu$ is the bulk modulus, $\mathbf{I}$ is the identity tensor, $\theta = \operatorname{tr}\boldsymbol{\varepsilon}$, $\mathbf{e} = \operatorname{Dev}\boldsymbol{\varepsilon}$. Here symbols "tr" and "Dev" denote trace and deviator for the tensor of the second rank, respectively. Represent the stress tensor $\boldsymbol{\sigma}$ as follows:

$$\boldsymbol{\sigma} = -p\mathbf{I} + \mathbf{s}, \tag{2}$$

where $\mathbf{s} = \operatorname{Dev}\boldsymbol{\sigma}$; $-p$ is the pressure. In accordance with the Hooke low(1) one can write

$$-p = k\theta, \tag{3}$$
$$\mathbf{s} = 2\mu\mathbf{e} \tag{4}$$

Consider the hypothetical material with piecewise-linear pressure-strain dependency with a "falling down" part of the graph (Fig. 1). We assume that deviatoric compo-
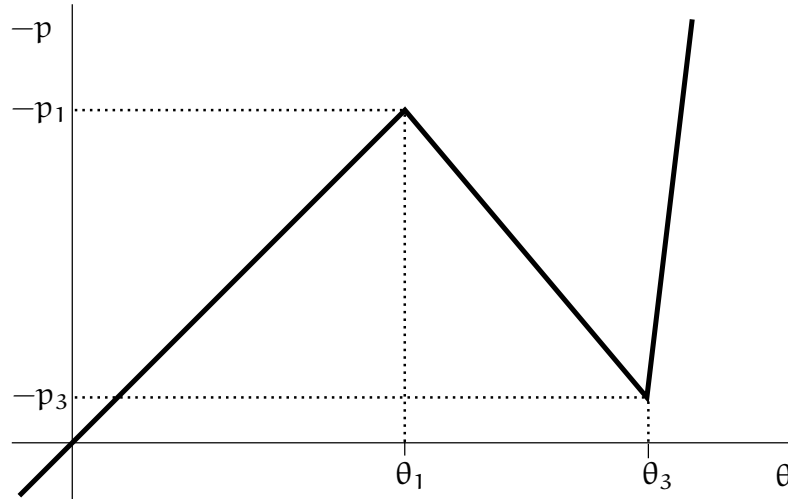
Figure 1: The pressure-strain curve for the hypothetical material, capable of undergoing phase transformations

nents of stress and strain tensors in the hypothetical material are still satisfy Eq. (4). One can see that non-monotonicity in stress-strain relation implies non-convexity of the elastic potential for the material. Thus, in our material discontinuous strain fields can exist.

3 Mathematical formulation

Since the problem is spherically symmetric, the displacement $\mathbf{u}(\mathbf{r})$ can be represented in the form

$$\mathbf{u}(\mathbf{r}) = u(r)\,\mathbf{e}_r, \tag{5}$$

where $\mathbf{e}_r = r^{-1}\mathbf{r}$. In what follows, we consider only motions of the sphere such that for all t there exists a unique phase boundary at a position $l(t)$ in the sphere, which separates stable phases 1 and 3. Here $l(t)$ is an unknown continuous and smooth function.

Without loss of generality we assume that for $r < l(t)$ the material is in the phase state 3 ($\theta > \theta_3$), and for $r > l(t)$ the material is in the phase state 1 ($\theta < \theta_1$). For the material in the phase state 1 the governing equations (3)–(4) (where $k = k_1 \equiv k_+$) should be used. For the material in the phase state 3 one should use Eq. (4) and the relation

$$-p = -p_3 + k_3(\theta - \theta_3), \tag{6}$$

where $k_3 \equiv k_-$. Here and in what follows, we adopt the notation $[\mu] = \mu_+ - \mu_-$, $\mu = (\mu_+ + \mu_-)/2$, $\mu_\pm = \mu|_{r \to l(t)\pm0}$, for any arbitrary function $\mu(r, t)$.

By the use of spherical coordinates (r, ϑ, φ) the Hooke low (1) can be rewritten in the following form:

$$\sigma_r = \lambda\theta + 2\mu\frac{\partial u}{\partial r}, \tag{7}$$

$$\sigma_\vartheta = \sigma_\varphi = \lambda\theta + 2\mu\frac{u}{r}, \tag{8}$$

where

$$\theta = \frac{\partial u}{\partial r} + \frac{2u}{r}. \tag{9}$$

The equation for the dynamics of an elastic body in case of spherically symmetric problem is [14,15]

$$\frac{\partial^2 u}{\partial r^2} + \frac{2}{r}\frac{\partial u}{\partial r} - \frac{2u}{r^2} = \frac{1}{c_\pm^2}\frac{\partial^2 u}{\partial t^2}, \tag{10}$$

where

$$c_\pm^2 = \frac{\lambda_\pm + 2\mu}{\rho}, \tag{11}$$

$$\lambda_\pm = k_\pm - \frac{2}{3}\mu. \tag{12}$$

Here ρ is the mass density for the material of the sphere, which is assumed to be the same for all phase states. Equation (10) is valid both in the "outer" ($r > l(t)$, $c = c_+$) and in the "inner" ($r < l(t)$, $c = c_-$) domains of strains continuity.

At $r = l$ the following boundary conditions should be fulfilled:

$$[u] = 0, \tag{13}$$

$$[\sigma_r] = -\rho \dot{l}[\dot{u}]. \tag{14}$$

At $r = 0$ the boundedness condition

$$u\big|_{r=0} = O(1) \tag{15}$$

has to be satisfied. At $r = R$ we formulate the following boundary conditions:

$$u\big|_{r=R} = u_0 = \text{const} \qquad \text{or} \qquad \sigma_r|_{r=R} = \sigma_0 = \text{const}. \tag{16}$$

To find the unknown phase boundary position $l(t)$ one needs to formulate an additional constitutive equation (so-called thermodynamical boundary condition). It can be shown (see e.g. [2, 7]), that the second law of thermodynamics localized to the infinitesimal layer $[l(t) - 0; l(t) + 0]$ containing the phase boundary leads to the following inequality

$$-\mathcal{F}\dot{l} \geq 0. \tag{17}$$

Here

$$\mathcal{F} = -([W] - \langle \boldsymbol{\sigma} \rangle \cdot \cdot [\boldsymbol{\varepsilon}]) \tag{18}$$

is the configurational (material, thermodynamical) force on the phase boundary,

$$W = \int \sigma(\varepsilon) \, d\varepsilon \tag{19}$$

is the strain energy per unit length of the bar. Inequality (17) follows from full dynamical consideration, which involves the inertia forces. The possible point of view is that Eq. (17) is an important, and perhaps unique, restriction on the constitutive equation structure. The following kinds of the additional thermodynamical condition are most widespread in the literature:

$$\mathcal{F} = 0; \tag{20}$$

$$\dot{l} = -\gamma^{-1}\mathcal{F}. \tag{21}$$

Here $\gamma > 0$ is a material constant associated with dissipation at the phase boundary. We will call relations (20) and (21) the non-dissipative condition and the simplest dissipative condition, respectively. In statics all used constitutive equations can be reduced to condition (20). It may be noted that Eq. (20) is the limit case for Eq. (21) as $\gamma \to +0$.

Besides Eq. (21) one should also formulate the initial condition:

$$l(0) = l_0. \tag{22}$$

In what follows, we assume that l_0 does not coincide with the equilibrium position $l = l^{\text{st}}$ of the phase boundary.

4 Strains at the phase boundary

Consider one-parameter family A_l of static problems formulated for Eq. (10) with boundary conditions (13)–(16). In the framework of a problem A_l the phase boundary is fixed ($\dot{l} = 0$) at a prescribed position l. For strain and stress for the problem A_l one has, respectively: $\mathbf{u} = \mathbf{u}^{\text{st}}$, $\boldsymbol{\varepsilon} = \boldsymbol{\varepsilon}^{\text{st}}$, $\boldsymbol{\sigma} = \boldsymbol{\sigma}^{\text{st}}$. In dynamics for displacement $\mathbf{u}(t)$, strain $\boldsymbol{\varepsilon}(t)$, and stress $\boldsymbol{\sigma}(t)$ we can put:

$$\mathbf{u} = \mathbf{u}^{\text{st}} + \tilde{\mathbf{u}}, \tag{23}$$

$$\boldsymbol{\varepsilon} = \boldsymbol{\varepsilon}^{\text{st}} + \tilde{\boldsymbol{\varepsilon}}, \tag{24}$$

$$\boldsymbol{\sigma} = \boldsymbol{\sigma}^{\text{st}} + \tilde{\boldsymbol{\sigma}}. \tag{25}$$

Configurational force $\mathcal{F}$ can also be represented as a sum of static and dynamic components:

$$\mathcal{F} = \mathcal{F}_0 + \tilde{\mathcal{F}}. \tag{26}$$

Let us represent $\tilde{\mathbf{u}}$ in the following form [14,15]:

$$\tilde{\mathbf{u}} = \frac{\partial \phi}{\partial r}, \tag{27}$$

where $\phi(r, t)$ is some potential function. Substituting representation (27) into Eq. (10) yields

$$\frac{\partial^2}{\partial r^2}\left(\frac{\partial}{\partial r}(r\phi)\right) - \frac{1}{c^2}\frac{\partial^2}{\partial t^2}\left(\frac{\partial}{\partial r}(r\phi)\right) = 0. \tag{28}$$

Equation (28) is the wave equation, therefore it's general solutions can be expressed in the D'Alembert form. Hence the radiation conditions for Eq. (28) leads to the following relations formulated at the phase boundary ($r = l$) (see [8, 10]):

$$\frac{\partial}{\partial r}\left(\frac{\partial}{\partial r}(r\phi_-)\right) - \frac{1}{c_-}\frac{\partial}{\partial t}\left(\frac{\partial}{\partial r}(r\phi_-)\right) = 0, \tag{29}$$

$$\frac{\partial}{\partial r}\left(\frac{\partial}{\partial r}(r\phi_+)\right) + \frac{1}{c_+}\frac{\partial}{\partial t}\left(\frac{\partial}{\partial r}(r\phi_+)\right) = 0. \tag{30}$$

Conditions (29), (30) are valid for times $t < (R - l_0/c_+) \equiv t_*$ (e.g., until the moment of the time, when the wave reflected from the outer boundary of the sphere comes back to the phase boundary). In what follows, we do not take into account the wave reflections, so the results are valid for small enough times only.

Now we can formulate four boundary conditions at the phase boundary, namely, Eqs. (13), (14), (29), (30). Taking into account Eq. (7) for σ_r, and relations (23)–

(25), one can write the following set of boundary conditions at the phase boundary:

$$\left[\frac{\partial\tilde{u}}{\partial t}\right] + i\left[\frac{\partial\tilde{u}}{\partial r}\right] = -i\left[\frac{\partial u^{st}}{\partial r}\right],\tag{31}$$

$$\left[c^2\frac{\partial\tilde{u}}{\partial r}\right] - i^2\left[\frac{\partial\tilde{u}}{\partial r}\right] + \left[\frac{2\lambda}{\rho}\frac{\tilde{u}}{l}\right] = i^2\left[\frac{\partial u^{st}}{\partial r}\right],\tag{32}$$

$$2\frac{\tilde{u}_-}{l} + \frac{\partial\tilde{u}_-}{\partial r} - \frac{1}{c_-}\left(\frac{\partial\tilde{u}_-}{\partial t} + \frac{1}{l}\frac{\partial\phi_-}{\partial t}\right) = 0,\tag{33}$$

$$2\frac{\tilde{u}_+}{l} + \frac{\partial\tilde{u}_+}{\partial r} + \frac{1}{c_+}\left(\frac{\partial\tilde{u}_+}{\partial t} + \frac{1}{l}\frac{\partial\phi_+}{\partial t}\right) = 0.\tag{34}$$

It is important that in some particular cases this set of equations is resolvable with respect to radial strains. In what follows, we consider one of such cases, namely the case when the material in phase state 3 is assumed to be incompressible:

$$\lambda_3 \equiv \lambda_- \to +\infty.\tag{35}$$

Hereby, the corresponding bulk modulus is also infinitely large:

$$k_3 \equiv k_- \to +\infty.\tag{36}$$

For the spherically symmetrical problem the above assumption means that the material in phase state 3 behaves as a rigid one. The strain tensor has the form

$$\varepsilon = \varepsilon_0 \mathbf{I},\tag{37}$$

where $\varepsilon_0 = \theta_3/3 = $ const. In what follows, we use the notations: $\lambda = \lambda_+$, $k = k_+$, $c = c_+$.

The boundary conditions (31)–(34) at the phase boundary ($r = l$) for the particular case under consideration are:

$$\frac{\partial\tilde{u}_+}{\partial t} + i\frac{\partial\tilde{u}_+}{\partial r} = -i\left(\frac{\partial u^{st}_+}{\partial r} - \varepsilon_0\right),\tag{38}$$

$$\frac{\partial\tilde{u}_+}{\partial r} + \frac{1}{c}\frac{\partial\tilde{u}_+}{\partial t} = 0.\tag{39}$$

$$(c^2 - i^2)\frac{\partial\tilde{u}_+}{\partial r} - i^2\left(\frac{\partial u^{st}}{\partial r} - \varepsilon_0\right) = \rho^{-1}\tilde{\sigma}_{r-}.\tag{40}$$

Resolving the set of equations (38)–(40), we get

$$\tilde{\varepsilon}_+(l) = \frac{i}{c - i}\left(\varepsilon^{st}_{r+}(l) - \varepsilon_0\right),\tag{41}$$

$$\tilde{\sigma}_{r-}(l) = \rho c i\left(\varepsilon^{st}_{r+}(l) - \varepsilon_0\right).\tag{42}$$

5 Statics

Before we consider the dynamic formulation, let us treat the following static problems.

5.1 The first static boundary value problem

Assume that for the sphere of radius R the following boundary conditions are prescribed: at the phase boundary $(r = l)$:

$$u(l) = \varepsilon_0 l, \tag{43}$$

at the outer radius $(r = R)$ of the sphere:

$$u(R) = u_0 = 0. \tag{44}$$

The strain energy W_- for the material in the rigid phase state is constant:

$$W_- = \gamma_0, \tag{45}$$

$$\gamma_0 = \frac{3}{2}(3\lambda + 2\mu)\varepsilon_0^2 - \alpha^2, \tag{46}$$

where α^2 is a parameter, which depends on the parameters of the pressure-strain curve (see Fig. 1):

$$\alpha^2 = \frac{(k\theta_3 + p_3)(k\theta_3 + p_1)}{2k}, \qquad \alpha > 0. \tag{47}$$

The equilibrium equation for the elastic sphere in terms of displacements is:

$$\frac{\partial^2 u}{\partial r^2} + \frac{2}{r}\frac{\partial u}{\partial r} - \frac{2u}{r^2} = 0. \tag{48}$$

Hence, for the material in the elastic zone we have

$$u_+ = C_1 r + \frac{C_2}{r^2}, \tag{49}$$

where C_1, C_2 are arbitrary constants.
Satisfying boundary conditions (43), (44), we obtain:

$$u_+ = -\frac{\varepsilon_0 X^3}{1 - X^3}r + \frac{\varepsilon_0}{1 - X^3}\frac{l^3}{r^2}. \tag{50}$$

Here

$$X = l/R. \tag{51}$$

Radial component ε_{r+} of strain is given by:

$$\varepsilon_{r+} = -\frac{\varepsilon_0 X^3}{1 - X^3} - 2\frac{\varepsilon_0}{1 - X^3}\frac{l^3}{r^3}. \tag{52}$$

Taking into account the Hooke low (7), we get the expression for the radial component σ_{r+} of stress in the elastic zone:

$$\sigma_{r+} = -(3\lambda + 2\mu)\frac{\varepsilon_0 X^3}{1 - X^3} - 4\mu\frac{\varepsilon_0}{1 - X^3}\frac{l^3}{r^3}. \tag{53}$$

The limit value for strain energy in the elastic phase at the phase boundary W_+ is:

$$W_+ = \frac{\lambda\theta_+(l)^2}{2} + \mu(\varepsilon_{r+}(l)^2 + \varepsilon_{\phi+}(l)^2 + \varepsilon_{\theta+}(l)^2). \tag{54}$$

Due to the requirement for the compatibility of deformations at the phase boundary it is possible to find the components ε_φ, ε_ϑ of the strain tensor:

$$\varepsilon_{\varphi+} = \varepsilon_{\vartheta+} = \varepsilon_0. \tag{55}$$

Hence, for the strain energy W_+ we have

$$W_+ = \frac{1}{2}\lambda(\varepsilon_{r+}(l) + 2\varepsilon_0)^2 + \mu(\varepsilon_{r+}(l)^2 + 2\varepsilon_0^2). \tag{56}$$

The configurational force is given by Eq. (18). In the problem under consideration $[\boldsymbol{\varepsilon}] = [\varepsilon_r]\mathbf{e_r}\mathbf{e_r}$, therefore

$$\mathcal{F} = \mathcal{F}_0 = -\left([W] - \sigma_r(l)\left(\varepsilon_{r+}(l) - \varepsilon_0\right)\right). \tag{57}$$

Taking into account Eqs. (45), (46), (50)–(53), (56), we obtain the expression for the configurational force:

$$\mathcal{F}_0 = -\frac{1}{2(X^3-1)^2}(2\alpha^2X^6 - 4\alpha^2X^3 - 18\mu\varepsilon_0^2 - 9\lambda\varepsilon_0^2 + 2\alpha^2). \tag{58}$$

Resolving the equation

$$\mathcal{F}_0 = 0, \tag{59}$$

we get the following possible equilibrium positions of the phase boundary:

$$l_1 = R\left(1 + \frac{3\sqrt{2}}{2}\frac{|\varepsilon_0|}{\alpha}\sqrt{(\lambda+2\mu)}\right)^{1/3}, \tag{60}$$

$$l_2 = R\left(1 - \frac{3\sqrt{2}}{2}\frac{|\varepsilon_0|}{\alpha}\sqrt{(\lambda+2\mu)}\right)^{1/3}. \tag{61}$$

It is clear that the restriction

$$0 < l < R \tag{62}$$

should be fulfilled. One has:

$$l_1 > R. \tag{63}$$

At the same time we can always choose parameter α such that root l_2 is satisfy the restriction (62).

In the framework of the quasi-static approach [12–13] to the investigation of the phase transformations the motion of the phase boundary is given by the following low:

$$\dot{l} = -\gamma^{-1}\mathcal{F}_0. \tag{64}$$

Linearization of Eq. (64) in a neighborhood of the equilibrium position $l = l^{st} = l_2$ leads to the relationship:

$$\dot{l} = -A_0(l - l^{st}), \tag{65}$$

where

$$A_0 = \left.\frac{\mathcal{F}_{0l}'(l^{st})}{\gamma}\right|_{l=l^{st}, \dot{l}=0} > 0. \tag{66}$$

It is easy to show that

$$\left.\frac{d\mathcal{F}_0}{dl}\right|_{l=l_2} > 0. \tag{67}$$

Hence, the equilibrium position $l = l_2$ of the phase boundary is stable.

5.2   The second static boundary value problem

Now we formulate the following boundary conditions for the sphere of radius R: at the phase boundary $r = l$:

$$u(l) = \varepsilon_0 l, \tag{68}$$

at the outer radius $r = R$ of the sphere:

$$\sigma_r(R) = \sigma_0 = 0. \tag{69}$$

For the strain tensor and strain energy in the rigid phase one should use Eqs. (37) and (46), respectively. Solving the equilibrium equation (48) for the sphere we obtain that displacement u_+ in the elastic phase is given by Eq. (49). Taking into account the Hooke low (7) we obtain the expression for radial stress σ_{r+} in the elastic zone:

$$\sigma_{r+} = (3\lambda + 2\mu)C_1 - 4\mu\frac{C_2}{r^3}. \tag{70}$$

Satisfying boundary conditions (68), (69), we get

$$u_+ = \frac{4\mu\varepsilon_0 X^3}{(3\lambda + 2\mu) + 4\mu X^3}r + \frac{(3\lambda + 2\mu)\varepsilon_0 X^3 R^3}{(3\lambda + 2\mu) + 4\mu X^3}\frac{1}{r^2}, \tag{71}$$

$$\varepsilon_{r+} = \frac{4\mu\varepsilon_0 X^3}{(3\lambda + 2\mu) + 4\mu X^3} - \frac{2(3\lambda + 2\mu)\varepsilon_0 X^3 R^3}{(3\lambda + 2\mu) + 4\mu X^3}\frac{1}{r^3}, \tag{72}$$

$$\sigma_{r+} = \frac{4(3\lambda + 2\mu)\mu\varepsilon_0 X^3}{(3\lambda + 2\mu) + 4\mu X^3} - \frac{4(3\lambda + 2\mu)\mu\varepsilon_0 X^3 R^3}{(3\lambda + 2\mu) + 4\mu X^3}\frac{1}{r^3}, \tag{73}$$

where

$$X = l/R. \tag{74}$$

Taking into account Eqs. (54), (55), we find that the limit value for strain energy in the elastic phase at the phase boundary ($r = l$) is given by Eq. (56). The

configurational force is given by Eq. (57). Hence, by virtue of Eqs. (45), (46), (56), (57),(71)–(73) we get the expression for the configurational force:

$$
\mathcal{F}_0 = -\frac{1}{2(3\lambda + 2\mu + 4\mu X^3)^2}(32\mu^2\alpha^2 X^6 + 16\mu\alpha^2(3\lambda + 2\mu)X^3 - 252\lambda\varepsilon_0^2\mu^2 -
$$
$$
72\varepsilon_0^2\mu^3 + 8\mu^2\alpha^2 - 270\varepsilon_0^2\lambda^2\mu + 18\lambda^2\alpha^2 + 24\mu\lambda\alpha^2 - 81\varepsilon_0^2\lambda^3). \quad (75)
$$

Solving the equation $\mathcal{F}_0 = 0$, we obtain the following equilibrium positions of the phase boundary:

$$
l_1 = R\left(-\frac{3\lambda + 2\mu}{4\mu} + \frac{3\sqrt{2}(3\lambda + 2\mu)|\varepsilon_0|}{8\mu\alpha}\sqrt{(\lambda + 2\mu)}\right)^{1/3}, \quad (76)
$$

$$
l_2 = R\left(-\frac{3\lambda + 2\mu}{4\mu} - \frac{3\sqrt{2}(3\lambda + 2\mu)|\varepsilon_0|}{8\mu\alpha}\sqrt{(\lambda + 2\mu)}\right)^{1/3}. \quad (77)
$$

One can see that root $l_2 < 0$, root l_1 can be positive for some values of parameters, but

$$
\left.\frac{d\mathcal{F}_0}{dl}\right|_{l=l_1} < 0. \quad (78)
$$

This means that the equilibrium position is unstable. It can be shown that for non-trivial boundary condition at the outer boundary of the sphere ($\sigma_0 \neq 0$) stable equilibrium positions of the phase boundary are also absent.

6 Dynamic addition to the configurational force

Consider the dynamic problem and obtain dynamic correction to the configurational force. We begin from representation Eqs. (23)–(25) for displacements, strain and stress tensors, respectively. For the rigid phase $\boldsymbol{\varepsilon}_- = 0$, $\boldsymbol{\varepsilon}_-^{\text{st}}$ is given by Eq. (37). Since at the phase boundary ($r = l$):

$$
[\varepsilon_\varphi] = [\varepsilon_\vartheta] = 0, \quad (79)
$$

the dynamic addition is

$$
\tilde{\boldsymbol{\varepsilon}}_+ = \tilde{\varepsilon}_+\,\mathbf{e_r}\mathbf{e_r}. \quad (80)
$$

Let us find the dynamic addition for strain in the elastic zone. On the one hand,

$$
\theta_+ = \left(\frac{du_+^{\text{st}}}{dr} + 2\frac{u_+^{\text{st}}}{r}\right) + \left(\frac{d\tilde{u}_+}{dr} + 2\frac{\tilde{u}_+}{r}\right) = \theta_+^{\text{st}} + \tilde{\theta}_+. \quad (81)
$$

On the other hand,

$$
\theta_+ = \varepsilon_{r+}^{\text{st}} + \tilde{\varepsilon}_+ + 2\varepsilon_0 = \theta_+^{\text{st}} + \tilde{\varepsilon}_+. \quad (82)
$$

Hence, $\tilde{\theta}_+ = \tilde{\varepsilon}_+$.

The strain energy in the elastic zone at $r = l + 0$ is given by Eq. (54). Let us rewrite it in the form:

$$W_+ = W_+^{st} + \tilde{W}_+, \tag{83}$$

$$W_+^{st} = \frac{\lambda(\theta_+^{st})^2}{2} + \mu(\varepsilon_{r+}^{st})^2 + 2\varepsilon_0^2, \tag{84}$$

$$\tilde{W}_+ = \lambda\theta_+^{st}\tilde{\varepsilon}_+ + \frac{\lambda\tilde{\varepsilon}_+^2}{2} + 2\mu\varepsilon_{r+}^{st}\tilde{\varepsilon}_+ + \mu\tilde{\varepsilon}_+^2. \tag{85}$$

For the strain energy in the rigid zone at $r = l - 0$ one has:

$$W_- = W_-^{st}, \qquad \tilde{W}_- = 0, \tag{86}$$

Hence, the jump of energy is

$$[W] = [W^{st}] + \tilde{W}_+. \tag{87}$$

The term $\langle \boldsymbol{\sigma} \rangle \cdot\cdot\, [\boldsymbol{\varepsilon}]$ in Eq. (18) for the configurational force $\mathcal{F}$ can be written in the form:

$$\langle \boldsymbol{\sigma} \rangle \cdot\cdot\, [\boldsymbol{\varepsilon}] = \langle \sigma_{r+}^{st}\left(\varepsilon_{r+}^{st} + \tilde{\varepsilon}_+\right)\rangle \left(\varepsilon_{r+}^{st}(l) - \varepsilon_0\right) + \langle \sigma_{r+}^{st}\left(\varepsilon_{r+}^{st} + \tilde{\varepsilon}_+\right)\rangle\tilde{\varepsilon}_+. \tag{88}$$

From the Hooke low (7) it follows that

$$\sigma_{r+} = \sigma_{r+}^{st} + (\lambda + 2\mu)\tilde{\varepsilon}_+ = \sigma_{r+}^{st} + \tilde{\sigma}_{r+}. \tag{89}$$

Thus, for the term $\langle \boldsymbol{\sigma} \rangle \cdot\cdot\, [\boldsymbol{\varepsilon}]$ we obtain:

$$\langle \boldsymbol{\sigma} \rangle \cdot\cdot\, [\boldsymbol{\varepsilon}] = \sigma_r^{st}(l)\left(\varepsilon_{r+}^{st}(l) - \varepsilon_0\right)$$
$$+ \frac{1}{2}\left((\lambda + 2\mu)\tilde{\varepsilon}_+(l) + \tilde{\sigma}_{r-}(l)\right)\left(\varepsilon_{r+}^{st}(l) - \varepsilon_0 + \tilde{\varepsilon}_+(l)\right) + \sigma_r^{st}(l)\tilde{\varepsilon}_+(l). \tag{90}$$

Substitution of Eqs. (87), (90) into Eq. (18) for the configurational force leads to the expression:

$$\mathcal{F} = \mathcal{F}_0 - \left(\tilde{W}_+ - \frac{1}{2}\left((\lambda + 2\mu)\tilde{\varepsilon}_+(l) + \tilde{\sigma}_{r-}(l)\right)\left(\varepsilon_{r+}^{st}(l) - \varepsilon_0 + \tilde{\varepsilon}_+(l)\right) - \sigma_r^{st}(l)\tilde{\varepsilon}_+(l)\right), \tag{91}$$

where

$$\mathcal{F}_0 = -\left([W^{st}] - \sigma_r^{st}(l)\left(\varepsilon_{r+}^{st}(l) - \varepsilon_0\right)\right) \tag{92}$$

is the static component of the configurational force.
Taking into account Eqs. (85), (92) and the expression:

$$\theta_+^{st}(l) = \varepsilon_{r+}^{st}(l) + 2\varepsilon_0, \tag{93}$$

we get for $\tilde{\mathcal{F}}$:

$$\tilde{\mathcal{F}} = \frac{1}{2}(\lambda + 2\mu)\varepsilon_{r+}^{st}(l)\tilde{\varepsilon}_+(l) - \frac{1}{2}(3\lambda + 2\mu)\tilde{\varepsilon}_+(l)\varepsilon_0$$
$$+ \frac{1}{2}\tilde{\sigma}_{r-}(l)\left(\varepsilon_{r+}^{st}(l) - \varepsilon_0 + \tilde{\varepsilon}_+(l)\right) + \sigma_r^{st}(l)\tilde{\varepsilon}_+(l). \tag{94}$$

Substituting Eqs. (41), (42) into Eq. (94), we obtain:

$$\tilde{\mathcal{F}} = \frac{\dot{\mathfrak{l}}}{c - \dot{\mathfrak{l}}} \left(\varepsilon_{r+}^{st}(\mathfrak{l}) - \varepsilon_0 \right) \left(\frac{1}{2}(\lambda + 2\mu)\varepsilon_{r+}^{st}(\mathfrak{l}) - \frac{1}{2}(3\lambda + 2\mu)\varepsilon_0 \right.$$
$$\left. + \frac{1}{2}\rho c^2 \left(\varepsilon_{r+}^{st}(\mathfrak{l}) - \varepsilon_0 \right) + \sigma_r^{st}(\mathfrak{l}) \right). \quad (95)$$

7 Solving of the dynamic problem

Let us treat the solution of the problem considered in section 5.1 as initial condition for the dynamic problem. Hence, the static component of the configurational force $\mathcal{F}_0$ is given by Eq. (58). Taking into account Eqs. (52), (53), (95), we get the expression for the dynamic component

$$\tilde{\mathcal{F}} = \frac{6\varepsilon_0^2 \dot{\mathfrak{l}}}{(c - \dot{\mathfrak{l}})(1 - X^3)^2}(2\lambda + 5\mu + X^3(\lambda + \mu)). \quad (96)$$

Thus,

$$\mathcal{F} = \mathcal{F}_0(\mathfrak{l}) + \tilde{\mathcal{F}}(\mathfrak{l}, \dot{\mathfrak{l}}) = -\frac{1}{2(X^3 - 1)^2}(2\alpha^2 X^6 - 4\alpha^2 X^3 - 18\mu\varepsilon_0^2 - 9\lambda\varepsilon_0^2 + 2\alpha^2)$$
$$+ \frac{6\varepsilon_0^2 \dot{\mathfrak{l}}}{(c - \dot{\mathfrak{l}})(1 - X^3)^2}(2\lambda + 5\mu + X^3(\lambda + \mu)). \quad (97)$$

Substituting the expression for the configurational force into the dissipative condition (21), we obtain the equation of motion for the phase boundary. If $\tilde{\mathcal{F}}'_{\dot{\mathfrak{l}}} \neq 0$ then it follows from the implicit function theorem that Eq. (21) can be represented in the form:

$$\dot{\mathfrak{l}} = -\Phi(\mathfrak{l}), \quad (98)$$

where

$$\Phi'_{\mathfrak{l}} = \frac{\mathcal{F}'_{\mathfrak{l}}}{\mathcal{F}'_{\dot{\mathfrak{l}}} + \gamma}. \quad (99)$$

The stability of the phase boundary motion in a neighborhood of the equilibrium position depends on a sign of function $\Phi'_{\mathfrak{l}}$ at $\mathfrak{l} = \mathfrak{l}^{st} = \mathfrak{l}_2$, where $\mathfrak{l}_2$ is given by Eq. (61). It is easy to show that:

$$\Phi'_{\mathfrak{l}} = \frac{\mathcal{F}_{0\mathfrak{l}}'}{\tilde{\mathcal{F}}'_{\dot{\mathfrak{l}}} + \gamma}\bigg|_{\mathfrak{l}=\mathfrak{l}^{st}, \dot{\mathfrak{l}}=0}. \quad (100)$$

Recall that $\mathcal{F}_{0\mathfrak{l}}'\big|_{\mathfrak{l}=\mathfrak{l}^{st}} > 0$ (see Eq. (67)). At the same time, for $\tilde{\mathcal{F}}$ (See Eq.(96)) one has:

$$\tilde{\mathcal{F}}'_{\dot{\mathfrak{l}}}\big|_{\mathfrak{l}=\mathfrak{l}^{st}, \dot{\mathfrak{l}}=0} \equiv g = \frac{6\varepsilon_0^2}{c\left(1 - \left(\frac{\mathfrak{l}^{st}}{R}\right)^3\right)^2} \left(2\lambda + 5\mu + \left(\frac{\mathfrak{l}^{st}}{R}\right)^3 (\lambda + \mu) \right) > 0. \quad (101)$$

Let us note that $\mathfrak{g}$ is a material constant. Linearization of equation of motion (98) for the phase boundary in a neighborhood of the equilibrium position $\mathfrak{l} = \mathfrak{l}^{\mathrm{st}}$ leads to the following equation:

$$\dot{\mathfrak{l}} = -A(\mathfrak{l} - \mathfrak{l}^{\mathrm{st}}), \tag{102}$$

where

$$A = \left.\frac{\mathcal{F}_{0\mathfrak{l}}'(\mathfrak{l}^{\mathrm{st}})}{\mathfrak{g} + \gamma}\right|_{\mathfrak{l}=\mathfrak{l}^{\mathrm{st}}, \dot{\mathfrak{l}}=0} > 0. \tag{103}$$

Hence, in the framework of the dynamic approach as well as in the framework of the quasi-static one the motion of the phase boundary in a neighborhood of the equilibrium position is stable. Comparison of Eqs. (102), (103) with Eqs. (65), (66), respectively, shows that the quasi-static approach correctly describes the motion of the phase boundary in a neighborhood of the equilibrium position only in the case of strong dissipation at the phase boundary ($\gamma \gg \mathfrak{g}$).

In the same way one can consider the dynamic formulation for the initial static problem formulated in Section 5.2.

8   Conclusion

The dynamic processes in a spherical elastic body composed of a material, which is capable of undergoing phase transitions, are investigated. The radius of the sphere is assumed to be sufficiently large. We use a model of an elastic body with non-convex strain energy potential [1–13]. It is supposed that the unique phase boundary is spherical and separates two stable phases. We consider the particular case, when the material in the "inner" phase is incompressible. In this case the strains at the phase boundary are obtained and the stability of the phase boundary motion is investigated. The motion is caused by a non-equilibrium initial condition for the phase boundary position. The low of the phase boundary motion in a neighborhood of the equilibrium position is found. It is demonstrated that both the dynamic and the quasi-static approaches give us the same decisions concerning the character of stability of the phase boundary equilibrium position. These conclusions are formulated under the assumption that perturbations of the phase boundary position are centrally symmetrical. The quasi-static approach correctly describes the transient process of the relaxation of the phase boundary position to the equilibrium position only in the case of strong dissipation at the phase boundary.

Acknowledgements

References

1. Abeyaratne R. R., Knowles J.K. // Int. J. Solids Structures. 1988. V. 24. P. 1021–1044.

2. Abeyaratne R., Knowles J.K. // Arch. Rath. Mech. Anal. 1991. V. 114. P. 119–154.

3. Abeyaratne R., Knowles J.K. // Physica D. 1994. V. 79. P. 269–288.

4. Morozov N.F., Osmolovkiy V.G. // Izvestia RAN, Mekhanika Tverdogo Tela (Mechanics of Solids). 1994. N1. P. 38–41.

5. Knowles J.K. // Int. J. Solids Structures. 1995. V. 32. P. 2703–2710.

6. Rosakis Ph., Knowles J.K. // J. Mech. Phys. Solids. 1997. V. 45. P. 2055–2081.

7. Gurtin M.E. Configurational Forces as Basic Concepts of Continuum Physics. New York: Springer-Verlag, 2000.

8. Gavrilov S.N. // ZAMM. 2007. V. 87, N2. P. 117–127.

9. Gavrilov S.N. // Doklady Physics. 2006. 413 N3, P. 329–336

10. Gavrilov S.N., Shishkina E.V. On the extension of a bar capable of undergoing phase transitions // Proceedings of XXXIV International Summer School – Conference "Advanced Problems in Mechanics", IPME RAS, 2007.

11. Sten'kin B.V. // Vestnik SPbGU. Ser.1, 1995, v. 4 (N22). P. 85–90.

12. Nazyrov I.R., Freidin A.B. // Izvestia RAN, Mekhanika Tverdogo Tela (Mechanics of Solids). 1998. N 5. P. 52–71.

13. Eremeyev V.A., Freidin A.B., Sharipova L.L.// PMM Journal of Applied Mathematics and Mechanics. V. 71, N1. 2007. P. 66–92.

14. Achenbach J. D. Wave Propagation in Elastic Solids. Amsterdam: North-Holland, 1973.

15. Eringen A.C., Suhubi E.S. Elastodynamics. V. 2. Linear theory. New York: Academic Press, 1975.

Serge N. Gavrilov, Ekaterina V. Shishkina, IPME RAS, V.O., Bolshoy pr. 61, St. Petersburg, Russia

Structural phase transitions imaging in shape memory alloys by photoacoustic microscopy

Alexei L. Glazov   Kyrill L. Muratikov   Vladimir I. Nikolaev
Sergei A. Pulnev
klm.holo@mail.ioffe.ru

Abstract

Near surface modifications of Cu-Al-Ni shape memory single crystal alloys are investigated by photoacoustic microscopy methods. The feasibility of visualization of the early stages of the loading-induced martensitic transformation is demonstrated. The peculiarities of phase transitions near Vickers indented areas detected in Cu-Al-Ni alloys by photoacoustic microscopy are investigated. The advantages of the photoacoustic images over the corresponding optical images are analyzed.

The main purpose of this article is to analyze in details the opportunities to use photoacoustic (PA) microscopy for investigation of phase transitions in shape memory alloys under different conditions. Shape memory alloys offer unique physical properties and may find wide applications in microelectromechanical systems and novel medical devices. The unique properties of these materials are attributed mainly to the effect of high reversible strain that arises at martensitic-austenitic phase transitions. Their mechanical properties are strongly related to the distribution of the martensitic and austenic phases, which may substantially vary with mechanical stresses and temperature. Therefore, in order to optimally design microelectromechanical systems and medical devices and to improve the performance of a small-scale material system, it requires the knowledge of deformations in shape-memory alloys at microscopic level.

At present the phase states in shape-memory materials are examined mainly with optical microscopy methods [1]. However, the authors emphasized that a specimen etching and digital processing of optical images are necessary often to increase the efficiency of optical discrimination between the phases. Moreover, optimal visualization of the phases requires the use of different etchants. It was also noted that even digital processing cannot provide reliable discrimination of the phases if the optical contrast is low.

In our previous study we have investigated the possibility of the PA microscopy application for imaging martensitic transformations in single-crystal Cu-Al-Ni shape memory alloys. We obtained PA and optical images of specimens in initial and loaded states. It is important that we could obtain PA and optical images simultaneously and immediately with the application of a given load. It was shown [2]
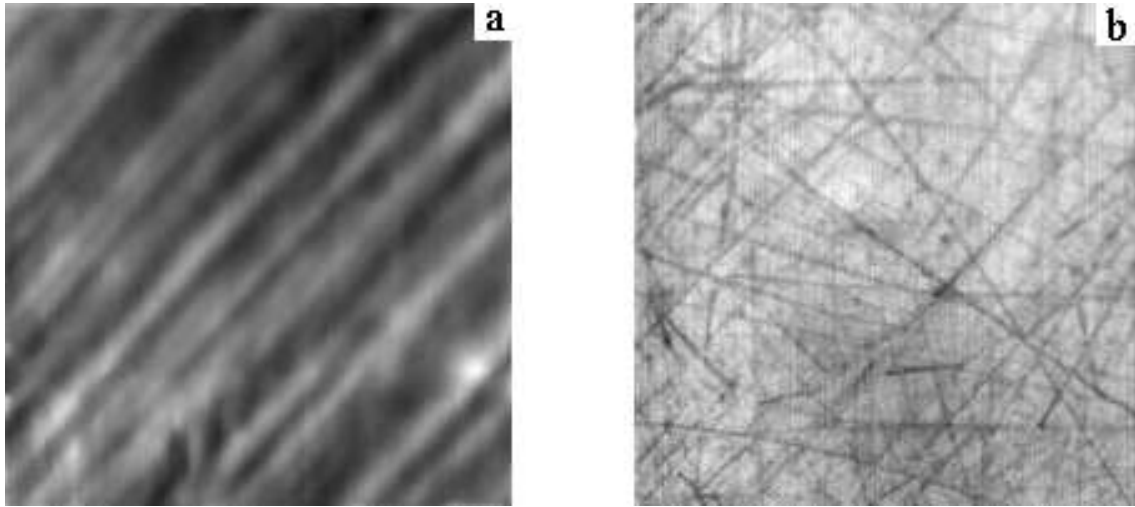
Figure 1: (a) The PA piezoelectric image of a part of Cu-Al-Ni sample; (b) optical image of the same area. The image area is $1 \times 1 \text{mm}^2$.

that the PA microscopy can be applied for visualization and examining martensitic transformations in Cu-Al-Ni shape-memory alloys. The obtained PA images had high spatial resolution and high contrast which were sufficient for the direct observation of the appearance and development of the martensitic phase in specimens under load without any pretreatment.

The main purpose of this work consists in application of the PA microscopy for imaging phase transition peculiarities near Vickers indented areas in Cu-Al-Ni alloys. It is known that the indentation of materials creates high stress under indenters that can cause stress-induced phase transformations. It is also important that some inelastic strains and stress field arise near the indented area. Therefore, thePA imaging of indented areas in Cu-Al-Ni alloys may provide important information about phase transitions in these materials in stressed and strained states. Application of external stresses and heating of samples may give us additional information about phase transitions in Cu-Al-Ni alloys.

PA images were taken with a setup using a pumping argon laser with a maximum output of 1 W. The radiation was modulated by an acoustooptic modulator and focused into a spot of diameter $2 \mu \text{m}$ on the specimen surface. The light power was about 50mW at the surface. The modulation frequency was close to the ultimate value (for the given setup) in order to raise the resolution. In our case it was about 140kHz which corresponded to thermal wavelength of no longer than $15 \mu \text{m}$. The PA images were taken by scanning the specimen mounted on an automated x-y table with a minimal step of $2.5 \mu \text{m}$. Thus, the resolution of the PA images dependent on the thermal wavelength was no worse than $15 \mu \text{m}$.

Prior to the indentation the PA and optical images of the investigated region of the sample were obtained. All optical images were obtained by using laser scanning mode of operation of our setup. In experiments with loading the uniaxial compressive stress was applied to the sample in the direction parallel to its surface. Specially designed small-size strain gauge was used for measuring the applied load.
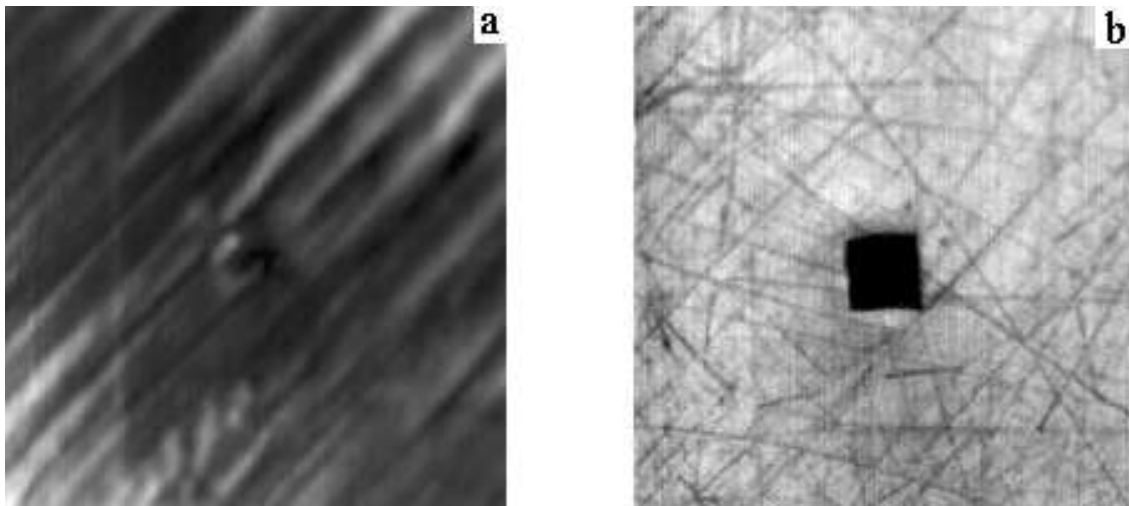
Figure 2: The PA piezoelectric (a) and optical (b) images of the Cu-Al-Ni sample with a Vickers indentation. The indentation load is $49N$. The image area is $1 \times 1mm^2$.

The example of the PA and optical images of the sample in the initial state is shown in Fig.1. One can see lamellar structure of the sample in the initial state. As it was shown in our previous work [2] the bright regions in this PA image correspond to martensitic domains in Cu-Al-Ni alloys. It is also seen that in the optical image of this region (Fig.1b) different phases of Cu-Al-Ni alloy are not visible. However, in contrast with the PA image the scratches from the surface polishing are better seen in the optical image. In Fig.2 the PA and optical images of the same region are represented after indentation. First of all the PA images in Figs.1a and 2a demonstrate that indentation do not influence on the lamella's direction. Some domain splitting and modification of the domain contrast near Vickers indentation are clearly seen in Fig.2a. They reflect the phase transformations in these regions.

The behavior of the PA and optical images during external uniaxial loading of the samples were studied at various loads. In our experiments as a rule the contrast of the PA signal from different phases of Cu-Al-Ni alloy increases with the load. Simultaneously images of new phase domains appear already at small pressures. But unlike the situation with other investigated materials [3], we did not observe clear changes of stress distribution inside the indentation prints, for example along diagonals. The structure of these regions in anisotropic material is more complicated. The optical images begin to change only at relatively large pressures. In this experiment we observed new stripes in optical images for pressures above $65MPa$. Fig.3 presents the PA and optical images of the chosen indented area under uniaxial pressure $73MPa$.

To understand these peculiarities of the obtained images the annealing of Cu-Al-Ni sample was made. It was heated up to the temperature of about $200 \deg C$ and slowly cooled. The PA and optical images of the indented area after annealing are shown in Fig.4. One can see that PA image after annealing has more homogeneous character than in initial and loaded states except of the region near the indentation. The brightness of the available lamellar domains after annealing in Fig.4 is lower in
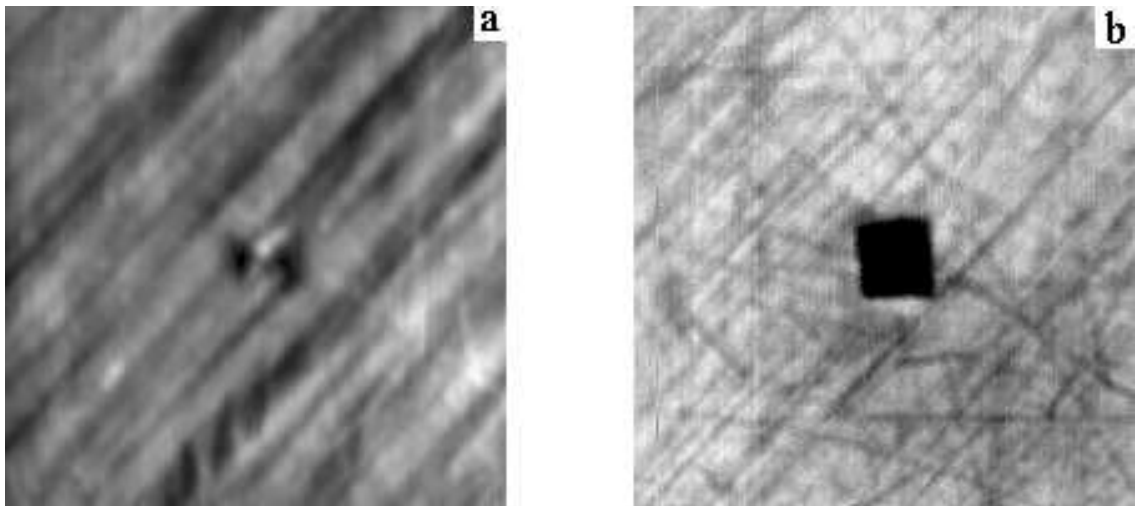
Figure 3: The PA piezoelectric (a) and optical (b) images of the Cu-Al-Ni sample with the Vickers indentation under the external loading of 73MPa applied in left-right direction.
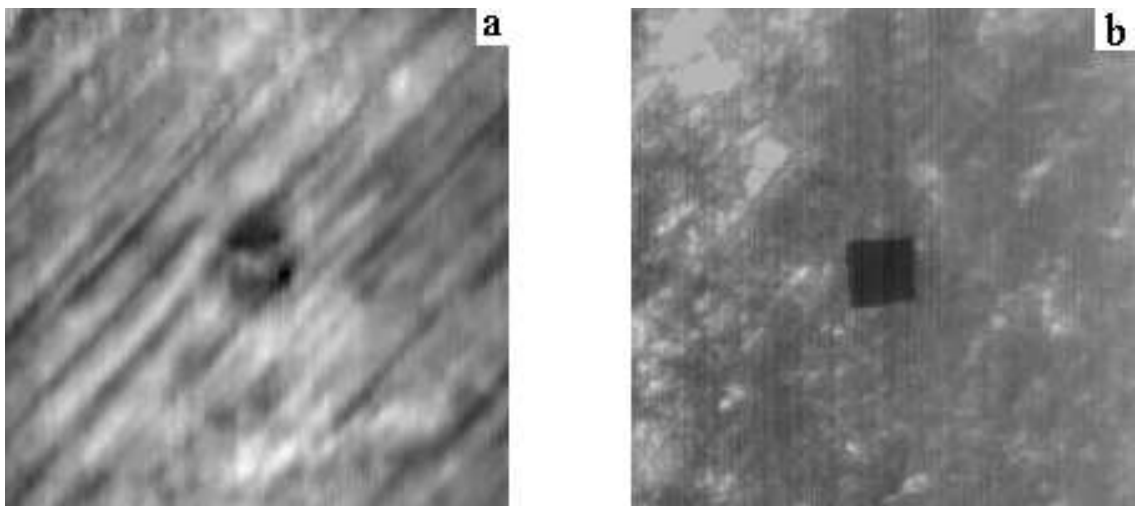
Figure 4: The PA piezoelectric (a) and optical (b) images of the Cu-Al-Ni sample with the Vickers indentation after annealing.

comparison with the loaded state. It means that the austenite phase is predominant in Cu-Al-Ni sample after annealing. Some domain structure which is still presented in this image is due to the presence of the defect region produced by indentation. One more reason of this situation may be related with the fact that PA images reflect the near surface structure of a sample. It is known that near surface phase transitions in Cu-Al-Ni alloys may differ from the volume phase transitions and have incomplete character. Therefore, some residual phase structure may be presented in the PA images of these alloys.

It is also interesting to note that the PA image of the indentation has sufficiently blurry structure while the optical image is almost the same as in the initial state. One may see additionally that polishing scratches almost disappear in the optical

images after annealing. These peculiarities of the obtained images can be explained using results of the paper [4]. In this paper the behavior of the indent recovery in the depth δ_D and lateral δ_L directions in Cu-Al-Ni alloys was investigated with a heating stage. It was demonstrated that for this alloy $\delta_D > \delta_L$. It means that recovery of the material under heating is more effective in the depth direction. This fact is demonstrated by our results in Fig.4 because the PA images more sensitive to the depth modifications of the indented area while the optical images are determined mainly by the lateral characteristics of the indentation. The optical images demonstrate that the lateral recovery of the indent is almost negligible for the used level of indentation loading. This recovery model also well explains the disappearance of polishing scratches after annealing. Typical width and depth of these scratches lie in the micrometer scale. At this scale recovery coefficient δ_D is about $0.7 - 0.8$ [4].

The presented results demonstrate that PA microscopy is the effective tool for investigation of phase transitions in Cu-Al-Ni alloys with the shape memory effect.

Acknowledgements

References

[1] M.L. Castro and R. Romero. J. Microsc. 216, 1 2004.

[2] K.L.Muratikov, A.L.Glazov, V.I.Nikolaev, S.A.Pul'nev. Technical Physics. 51, 809 2006.

[3] K.L.Muratikov, A.L.Glazov. J. Thermal Stresses, 4, 322 2009.

[4] C. Liu, Y.P. Zhao, T. Yu. Materials and Design, 26, 465 2005.

Alexei L. Glazov, Ioffe Physical-Technical Institute, Polytekhnicheskaya 26, 124021 St.Peterburg, Russia

Kyrill L. Muratikov, Ioffe Physical-Technical Institute, Polytekhnicheskaya 26, 124021 St.Peterburg, Russia

Vladimir I. Nikolaev, Ioffe Physical-Technical Institute, Polytekhnicheskaya 26, 124021 St.Peterburg, Russia

Sergei A. Pulnev, Ioffe Physical-Technical Institute, Polytekhnicheskaya 26, 124021 St.Peterburg, Russia

Load-transfer from semi-infinite strip to wedge-shaped plate taking into account the non-homogeneous ageing factor

Vahram N. Hakobyan
vhakobyan@sci.am

Abstract

Some problems on interaction of homogeneous or by power law non-homogeneous semi-infinite strip with arbitrary opening angle wedge-shaped plate when they are made of inherent ageing materials with different ages are considered.

The solutions of all investigated problems are reduced at first to the solving of two-dimension singular integral equation with respect to tangential contact stress, acting under strip and then to the solving of difference equation with respect to Mellin transformants of contact stress using Mellin integral transformation. Then the problem solving is reduced to the solution of differential-difference equation with time-dependent coefficients under certain initial conditions, taking into account the solution of appropriate instant elastic problems and N.Kh.Arutyunyan creep-kernel properties. The closed solution of the latest equation is built by using of Laplace two-sided operator.

1 Statement of problem and governing equations

The generalized plane stress state of wedge-shaped plate, strengthened by the semi-infinite thin inclusion, is investigated in three cases within the framework of creep theory of non-homogeneously ageing materials.

In first case it is assumed that the wedge-shaped plate with arbitrary angle-opening α , is strengthened in border $\phi = 0$ by thin semi-infinite inclusion with h width and plate is deformed under the action of horizontal concentrated load p_0, applied at the end-point of inclusion at the moment τ_0. It is supposed that another border of plate $\phi = \alpha$ is free of stress.

In second and third cases it is supposed that wedge-shaped plate with arbitrary angle-opening 2α is strengthened by semi-infinite thin inclusion with h width along the midline $\phi = 0$. This plate is deformed under action of horizontal concentrated load p_0 at the end of inclusion in second case and in point $r = a$ of inclusion in third case. In second case, it is assumed that the sides $\phi = \pm\alpha$ of wedge-shaped plate are free of stresses and rigidly restrained in third case. In all cases it is assumed that materials of inclusions and wedges possess of creeping property,

which is characterized by non-homogeneous ageing [1]. Furthermore, the inclusions are interpreted as one-dimension continuums and normal stresses are neglected in contact zone.

It is required to determine the distribution law of contact stresses $\tau(x, t)$ acting under inclusions and the coefficients of stress intensity at the end-points of inclusions. Let $C_1(t, \tau)$ denotes creeping measure of inclusions, τ_1 is the age, which is constant by length and $E_1 = \text{const.}$ is the module of instant elastic deformation. $C_2(t, \tau)$, τ_2 and $E_2(t) = E_2 = \text{const.}$ denote the corresponding characteristics for wedges. It is also assumed that the coefficients of lateral contraction $\nu_1(t)$ and $\nu_2(t)$ for materials of wedges are the same and constant for elastic deformation, i.e. $\nu_2(t, \tau) = \nu_1(t) = \nu = \text{const.}$

In order to derive the governing equations of mentioned problems, the deformations of inclusions in r-direction and points of midline $\phi = 0$ of viscoelastic wedges are expressed by the unknown $\tau(x, t)$ contact stresses.

Under these assumptions and using the expressions for deformations of corresponding elastic problems [2], [3] and on the basis of [1] the following can be written:

$$\varepsilon_{r,j}^{(1)}(r, t) = -\frac{1}{E_1 A_s}(1 - L_1)\left[h \int_0^r \tau(r_0, t)\, dr_0 - \Omega_j(r) p_0\right] \quad (j = 1, 2, 3); \quad (1.1)$$

$$\Omega_j(r) = 1 \ (j = 1, 2); \quad \Omega_3(r) = H(r - a). \quad (1.2)$$

$$\varepsilon_{r,j}^{(2)}(r, t) = -\frac{1}{E_2}(1 - L_2)\frac{d}{dr}\int_0^\infty R_j(r, r_0)\tau(r_0, t)\, dr_0 \quad (j = 1, 2, 3). \quad (1.3)$$

Here,

$$R_j(r, r_0) = \frac{1}{2\pi i}\int_{c-i\infty}^{c+i\infty}\frac{L_j(p, \alpha)}{p}\left(\frac{r_0}{r}\right)^p dp;$$

$$L_2(p, \alpha) = \frac{4}{(1 + \varepsilon)^2}\frac{\varepsilon \sin^2(p\alpha) + p^2 \sin^2(\alpha) - (1 + \varepsilon)^2/4}{\sin(2p\alpha) + p\sin(2\alpha)}; \quad (1.4)$$

$$L_3(p, \alpha) = \frac{8}{(1 + \varepsilon)^2}\frac{\varepsilon^2 \sin^2(p\alpha) - p^2 \sin^2(\alpha)}{\varepsilon \sin(2p\alpha) - p\sin(2\alpha)}; \ L_1(p, \alpha) = \frac{\sin(2p\alpha) - p\sin(2\alpha)}{\sin^2(p\alpha) - p^2 \sin^2(\alpha)} \ .$$

Here, $H(t)$ denotes well-known function of Heaviside, and index j=1,2,3 shows the corresponding problem. Temporal operators L_k (k=1,2) acts on arbitrary function in the following way:

$$(1 - L_k)\phi(t) = \phi(t) - \int_{\tau_0}^t K_k(t + \rho_k, \tau + \rho_k)\phi(\tau)\, d\tau;$$

$$K_k(t, \tau) = E_k\frac{\partial C_k(t, \tau)}{\partial \tau}; \ C_k(t, \tau) = \phi_k(\tau)\left[1 - \exp(-\gamma(t - \tau))\right];$$

$$\rho_k = \tau_k - \tau_0; \ k = 1, 2.$$

Without loss of generality, it is assumed that $\rho_1 = 0$ and $\rho_2 = \rho$.
Then, using the contact-conditions of inclusions with wedge-type plate

$$\varepsilon_{r,j}^{(1)}(r, t) = \varepsilon_{r,j}^{(2)}(r, t) \quad (0 \leqslant r < \infty \ j = 1, 2, 3) \tag{1.5}$$

the two-dimensional integral equations are obtained:

$$\frac{1}{E_2}(1 - L_2)\frac{d}{dr}\int_0^\infty R_j(r, r_0)\,\tau(r_0, t)\,dr_0 = \frac{1}{E_1 A_s}(1 - L_1)\left[h\int_0^r \tau(r_0, t)\,dr_0 - P_0\Omega_j(r)\right]; \tag{1.6}$$

For all the condition

$$h\int_0^\infty \tau(r_0, t)\,dr_0 = P_0. \tag{1.7}$$

for contact stresses should be satisfied. Let introduce the following dimensionless values [4]:

$$r = \frac{E_1 A_s}{E_2 h}x; \ r_0 = \frac{E_1 A_s}{E_2 h}s; \ \tau\left(\frac{E_1 A_s}{E_2 h}x, t\right) = \frac{E_2 P_0}{E_1 A_s}\tau_0(x, t).$$

Then (1.6) and (1.7) rewrite in form:

$$(1 - L_2)\frac{d}{dx}\int_0^\infty R_j(x, s)\,\tau_0(s, t)\,ds - (1 - L_1)\left[\int_0^x \tau_0(s, t)\,ds - \Omega_j(x)\right] = 0; \tag{1.8}$$

$$\int_0^\infty \tau_0(s, t)\,ds = 1. \tag{1.9}$$

Thus, the solution of considered problem is reduced to the solving of two-dimensional integro-differential equations (1.8) under condition (1.9).

2 Governing equations solving

In order to build the solutions of equations, the Mellin transforms of unknown contact stresses are considered:

$$T_0(p, t) = \int_0^\infty \tau_0(s, t)\,s^{p-1}ds, \tag{2.1}$$

They are regular functions of p-variable in strip $0 < b < \operatorname{Re} p < 2$ $(b < 1)$ [4]. After multiplication both sides of (1.8) by x^p and integration in interval $0 < x < \infty$, the difference equations are obtained as a result

$$(1 - L_1)T_0(p + 2, t) - (p + 1)L_j(p, \alpha)(1 - L_2)T_0(p + 1, t) =$$

$$= (1 - L_1)\omega_j(p + 2) \qquad (j = 1, 2, 3); \tag{2.2}$$

and condition (1.9) becomes

$$T_0\left(1,t\right)=1\,.\tag{2.3}$$

Note, that equations (2.2) are true in strip of regularity $-1+b<\operatorname{Re}p<0$ and functions $\omega_j\left(p\right)$ are the following:

$$\omega_{1,2}\left(p\right)=0;\quad\omega_3\left(p\right)=a^{p-1}\,.\tag{2.4}$$

After substituting $t=\tau_0$ in (2.2) the equations, describing corresponding problems of momentary-elastic deformation are obtained. Here, the solutions for homogeneous equations in form [3] of corresponding momentary-elastic problems are used:

$$T_0^*\left(p+\frac{3}{2},\tau_0\right)=H_j\left(p\right)U_j\left(p\right)\quad\left(j=1,2,3\right);\tag{2.5}$$

$$H_j\left(p\right)=\left[M_j\left(0,\alpha\right)\right]^{p+1/2}\frac{\pi\left(p+1/2\right)}{\cos\left(\pi p\right)};\quad M_j\left(p,\alpha\right)=pL_j\left(p,\alpha\right);$$

$$U_j\left(p\right)=\prod_{k=1}^{\infty}\frac{\Gamma\left(p+1/2+p_k^{(j)}\right)\Gamma\left(p-1/2+t_k^{(j)}\right)}{\Gamma\left(p-1/2+p_k^{(j)}\right)\Gamma\left(p+1/2+t_k^{(j)}\right)}\left(\frac{t_k^{(j)}}{p_k^{(j)}}\right)^{2p}\times$$

$$\times\prod_{k=1}^{\infty}\frac{\Gamma\left(p+1/2+\bar{p}_k^{(j)}\right)\Gamma\left(p-1/2+\bar{t}_k^{(j)}\right)}{\Gamma\left(p-1/2+\bar{p}_k^{(j)}\right)\Gamma\left(p+1/2+\bar{t}_k^{(j)}\right)}\left(\frac{\bar{t}_k^{(j)}}{\bar{p}_k^{(j)}}\right)^{2p};$$

Here, $p_k^{(j)}$ $\left(j=1,2,3\right)$ are zeros for functions $\sin\left(2p\alpha\right)-p\sin\left(2\alpha\right)$, $\varepsilon\sin^2\left(p\alpha\right)+p^2\sin^2\left(\alpha\right)-\left(1+\varepsilon\right)^2/4$ and $\varepsilon^2\sin^2\left(p\alpha\right)-p^2\sin^2\left(\alpha\right)$ respectively, and are zeros of functions $t_k^{(j)}$ $\left(j=1,2,3\right)$ are zeros of functions $\sin^2\left(p\alpha\right)-p^2\sin^2\left(\alpha\right),\ \ \sin\left(2p\alpha\right)+p\sin\left(2\alpha\right)$ and $\varepsilon\sin\left(2p\alpha\right)-p\sin\left(2\alpha\right)$. It being known that

$$\operatorname{Re}\left(p_k,t_k\right)>0;\ \operatorname{Im}\left(p_k,t_k\right)\geqslant0;\ \operatorname{Re}\left(p_k\right)<\operatorname{Re}\left(p_{k+1}\right);\ \operatorname{Re}\left(t_k\right)<\operatorname{Re}\left(t_{k+1}\right).$$

and each zero writes as much as its order.
Using (2.5) the following can be written:

$$\left(p+1\right)L_j\left(p,\alpha\right)=\frac{T_0^*\left(p+2,\tau_0\right)}{T_0^*\left(p+1,\tau_0\right)}\quad\left(j=1,2,3\right)\,.\tag{2.6}$$

The expression $\left(p+1\right)L_j(p,\alpha)$ from (2.6) is substituted in equation (2.2)

$$X\left(p+1,t\right)=\frac{T_0\left(p+1,t\right)}{T_0^*\left(p+1,\tau_0\right)}\quad\left(j=1,2,3\right);\tag{2.7}$$

Then, after replacement of $\left(p+1\right)$ by p in equations the following is obtained:

$$\left(1-L_1\right)X\left(p+1,t\right)-\left(1-L_2\right)X\left(p,t\right)=\left(1-L_1\right)\frac{\omega_j\left(p+1\right)}{T_0^*\left(p+1,\tau_0\right)}\ ;\ \left(j=1,2,3\right)$$

$$\tag{2.8}$$

These equations should be considered under condition

$$X(1, t) = 1. \tag{2.9}$$

It is obvious, that obtained equations (2.8) are difference equations with constant coefficients and regularity strip $(0 < b \leqslant \operatorname{Re} p < 1)$, the solutions of which are usually built by Laplace two-sided transformation. However, in this case the mentioned method is not allowed for application, since $X(p, t)$ does not converge to zero when $\operatorname{Im} p \to \infty$. In order to eliminate this difficulty the function is considered

$$Y(p, t) = X(p, t) / \cos(\pi p). \tag{2.10}$$

It is not difficult to show that this function converges to zero while $\operatorname{Im} p \to \infty$. Moreover, this function is regular in strip $(1/2 < b \leqslant \operatorname{Re} p < 2)$, $(b < 1)$, excepting point $p = 3/2$, in which function has simple pole. The equations are obtained after dividing both sides of equation (2.8) into $\cos \pi (p + 1)$

$$(1 - L_1) Y(p + 1, t) + (1 - L_2) Y(p, t) =$$

$$= (1 - L_1) \frac{\omega_j(p + 1)}{T_0^*(p + 1, \tau_0) \cos \pi (p + 1)} \quad (j = 1, 2, 3); \tag{2.11}$$

and the condition (2.9) becomes

$$Y(1, t) = -1 \tag{2.12}$$

Let multiply both sides of (2.11) by $\exp(pw)$ and integrate over line $(c - i\infty; c + i\infty)$; $(b < c < 1)$. As a result the integral equations are obtained:

$$(1 + e^{-w}) \bar{Y}(w, t) - \int_{\tau_0}^{t} [e^{-w} K_1(t, \tau) + K_2(t + \rho, \tau + \rho)] \bar{Y}(w, \tau) \, d\tau =$$

$$= (1 - L_1) \bar{F}_j(w) e^{-w} - 2i e^{w/2} (1 - L_1) [X(3/2, t) - q_j(3/2)]; \tag{2.13}$$

$$K_n(t, \tau) = E_n \left[\dot{\phi}_n(\tau) - \left(\dot{\phi}_n(\tau) - \gamma \phi_n(\tau) \right) \exp(-\gamma(t - \tau)) \right].$$

$$\bar{Y}(w, t) = \int_{c-i\infty}^{c+i\infty} Y(p, t) e^{pw} dp; \quad \bar{F}_j(w) = \int_{c-i\infty}^{c+i\infty} \frac{\omega_j(p) e^{pw} dp}{\cos(\pi p) T_0^*(p, \tau_0)};$$

$$q_j(p) = \frac{\omega_j(p)}{T_0^*(p, \tau_0)} \qquad (b < c < 1, j = 1, 2, 3);$$

It is not difficult to show that the integral equation (2.13) is equivalent to the differential equation:

$$\ddot{Y}(w, t) + \gamma \left[1 + \frac{E_1 \phi_1(t) e^{-w} + E_2 \phi_2(t + \rho)}{1 + e^{-w}} \right] \dot{Y}(w, t) = -2i \frac{e^{w/2} T(t)}{1 + e^{-w}} \tag{2.14}$$

$$T(t) = \dot{T}_1(t) = \ddot{X}(3/2, t) + \gamma \dot{X}(3/2, t)(1 + E_1 \phi_1(t)).$$

This equation should be considered under the following certain initial conditions:

$$\overline{Y}(w,t) = -\frac{2ie^{3w/2}}{1+e^w}\left[1+\frac{1}{2\pi i}\int_{-\infty}^{\infty}\frac{\overline{F}_j(w)e^{-w}}{1+e^w}dw\right]+\frac{\overline{F}_j(w)}{1+e^w};$$

$$\dot{Y}(w,\tau_0) = \gamma[E_1\phi_1(\tau_0)-E_2\phi_2(\tau_0+\rho)]\frac{\overline{Y}(w,\tau_0)}{1+e^{-w}}-\frac{2ie^{3w/2}}{1+e^w}\Phi_1(1) \qquad (2.15)$$

After integration of the equation (2.14) and taking into account the initial conditions (2.15) Mellin transforms for unknown functions are found. Then, using the inverse transform in cases $j = 1, 2$ the following is obtained:

$$Y(p,t) = -\frac{1}{\pi}\int_{\tau_0}^{t}dt\int_{\tau_0}^{t}Q_1(t,\tau,p)\dot{T}_1(\tau)d\tau+1/\cos(p\pi)-$$

$$-\frac{\gamma}{2\pi}[E_1\phi_1(\tau_0)-E_2\phi_2(\tau_0+\rho)]\int_{\tau_0}^{t}Q_2(\tau,p)d\tau. \qquad (2.16)$$

In case $j = 3$ the inverse transform gives the result:

$$Y(p,t) = -\frac{1}{\pi}\int_{\tau_0}^{t}dt\int_{\tau_0}^{t}Q_1(t,\tau,p)\dot{T}_1(\tau)d\tau+\int_{\tau_0}^{t}Q_3(\tau,p)d\tau+Y(p,\tau_0). \qquad (2.17)$$

Here a_j $(j = 1, 2, 3)$ are known regular functions, the values of which are not shown. Pass on to find not for a while yet unknown function $T_1(t)$. In this order the condition (2.12) is used. Satisfying to this condition in order to find the unknown function $T_1(t)$ the following integral equation Volterra of second kind is obtained, towards to which the method of successive approximations is applied.

$$T_j(t)-\int_{\tau_0}^{t}R_j(t,\tau)T_1(\tau)d\tau = a_j(t); \quad (j = 1-3) \qquad (2.18)$$

Here $R_j(t,r)$ and $Q_j(t)$ $(j = 1-3)$ are known regular functions, the values of which are not shown.

Hence, the following expression is obtained for Mellin transform of unknown contact stresses:

$$T_0(p,t) = T_0^*(p,\tau_0)\{1+$$

$$\int_{\tau_0}^{t}dt\int_{\tau_0}^{t}\exp\left[-\gamma(t-\tau)-\gamma E_1\int_{\tau}^{t}\phi_1(\xi)d\xi\right]{}_1F_1(3/2-p,1,\gamma\phi(t,\tau))dT_1(\tau)+$$

$$+\frac{\gamma}{2}[E_1\phi_1(\tau_0)-E_2\phi_2(\tau_0+\rho)]\int_{\tau_0}^{t}\exp\left[-\gamma(\tau-\tau_0)-\gamma E_1\int_{\tau_0}^{t}\phi_1(\xi)d\xi\right]\times \qquad (2.19)$$

$$\times \left[{}_1F_1\left(3/2 - p, 1, \gamma\phi\left(\tau, \tau_0\right)\right) - (2p-1)\,{}_1F_1\left(3/2 + p, 2, \gamma\phi\left(\tau, \tau_0\right)\right)\right] d\tau\right\}; (j = 1, 2)$$

$$T_0\left(p, t\right) = T_0^*\left(p, \tau_0\right)\cos\left(p\pi\right)\left\{\frac{1}{\cos\left(p\pi\right)}-\right.$$

$$\left.-\frac{1}{\pi}\int_{\tau_0}^t dt\int_{\tau_0}^t Q_1\left(t, \tau, p\right) dT_1\left(\tau\right) + \int_{\tau_0}^t Q_3\left(\tau, p\right) d\tau\right\} j = 3. \qquad (2.20)$$

After definition of functions in cases , it is not difficult to find the contact stresses using the inverse Mellin transformation.

Note, that under assumption $E_1\phi_1\left(t\right) = E_2\phi_2\left(t + \rho\right)$, as it was done in [5], the integral equations Volterra (2.12) have the trivial solutions. It is essentially simplified the expressions for Mellin transforms of contact stresses.

$$T_0\left(p, t\right) = T_0^*\left(p, \tau_0\right), \quad j = 1, 2; \quad T_0\left(p, t\right) = T_0\left(p, \tau_0\right), \quad j = 3.$$

Hence, the distribution of contact stresses in this case is time-independent. This distribution is defined by solving the correspondent instant elastic problem.

From obtained solutions, in general case, it will be clear that they have the same singularity in point $x = 0$ as the solutions of corresponding instant elastic problems, which were investigated in works [2],[3] .

It allows to state that the factor of non-homogeneous ageing does not change the behavior of contact stresses qualitatively. However, the viscoelastic characteristics of contacted bodies have an influence upon contact stresses and their intensity coefficient at the end-point of inclusion. This influence is shown by numerical calculations as stated below.

Numerical example

The numerical analysis is considered for case j=1, when $\alpha = \pi$, i.e. the non-homogeneous visco-elastic half-plane is strengthened by semi-infinite inclusion of the other age. It is assumed that the ageing functions are the same for base and inclusion and they are

$$\phi_1\left(t\right) = \phi_2\left(t\right) = C_0 + A_0/t$$

Numerical values for the physical parameters are the following:
$E_1 = E_2 = 2\cdot 10^{-4}\text{MPa}; C_0 = 9\cdot 10^{-5}\text{MPa}^{-1}; A_0 = 48,2\cdot 10^{-5}\text{MPa}^{-1}\text{day}; \gamma = 0,026\text{day}^{-1}$

Table1 Values of function $T_1^*\left(t\right), \quad \tau_0^* = 0.5$

$\rho^*\backslash t^*$	0.5	0.7	0.9	1.1	1.3
0.5	3.175	3.295	3.295	3.295	3.295
1	3.133	3.292	3.291	3.291	3.291
1.5	3.112	3.290	3.289	3.289	3.289
2	3.10	3.899	3.288	3.288	3.288

Table2 Values of function $T_1^*(t)$, $\quad \tau_0^* = 0.2$

$\rho^* \backslash t^*$	0.2	0.4	0.6	0.8	1
0.5	3.603	4.012	4.012	4.012	4.012
1	3.529	4.000	3.999	3.999	3.999
1.5	3.498	3.999	3.992	3.992	3.992
2	3.482	3.987	3.987	3.987	3.987

The obtained numerical results are shown at Tables 1 and 2. The numerical values of auxiliary function $T_1^*(t) = T_1(t)/\gamma$ for different moments of time $t^* = \gamma t$ in two cases, when the moment of horizontal force $\tau_0^* = \gamma \tau_0$ application has the values 0,2 and 0,5 under various values of half-plane relative age, are shown at Tables 1 and 2. From these tables it becomes clear that at start moments the function $T_1^*(t)$ is increasing up to define value and then it becomes constant. It is another matter the changing of function $T_1^*(t)$ depending on relative age of half-plane, i.e. the values of function $T_1^*(t)$ are decreasing up to define value while age increases and then they are asymptotically converges to the fixed constant. Here, K is the intensity coefficient of contact stresses taking into consideration the factor of non-homogeneous creep and K_1 is the same coefficient in case of corresponding instant elastic problem. These graphs shows that the value K^* converges to fixed asymptotic value, while it is increasing. This value is as great as relative age of half-plane.

References

[1] Arutyunyan N.Kh., Kolmanovski V.B. Theory of creep in non-homogeneous media. Moscow, Nauka, 1983, 336p.

[2] Gulyan K. About solution of two contact problems on load-transfer from semi-infinite stringer towards two wedge-shaped elastic plates. Proceedings of NAS RA, Mechanics, 1976, Vol.29, N6, pp.3-18

[3] Alblas J.B., Kaypers W.J.J. On the diffusion of load from a stiffener into an infinite wedge-shaped. -Appl. Scientific Res.Sect.A, 1965-1966, v. 15,N6, p. 429-439.

[4] Koiter W.T. On the diffusion of load from a stiffener into a sheer.-Quart.J.Mech.and Appl.Math., 1955, v.8, N2, p.164-178.

[5] Gulyan K. About load-transfer from semi-infinite stringer towards two same wedge-shaped plates taking into account non-homogeneous ageing. Yerevan, Proceedings of NAS RA, 1985, pp.135-145.

Vahram N.Hakobyan, Institute of Mechanics, National Academy of Sciences, Armenia, Yerevan 0019, Baghramyan 24B ave.

Complex change of properties of a superficial layer of details Powder metallurgy by a method of vibrating processing

Khaled Hamouda   J. P. Ankudimov   P. J. Ankudimov
A. P. Babichev   M. N. Benallal   D. Saidi   M. A. Djema   T. Sayah
bmnadjib@hotmail.com

Abstract

Majority of the repair enterprises are small industrial collectives equipped with inexpensive multiuse mission equipment. In technology of repair significant volume take mechanical and fit of work, and also washing and clearing operations. In difference from the "know-how" of new items, where on operations shaving and finishing processing the processing) is widely used vibration, in technology of repair of items the application of the indicated method is only in an initial stage. In offered work the outcomes of a research of a possibility of application vibration in technology of repair of automobiles and tractors, chisel equipment, ship mechanisms, medical and home appliances are represented. For want of research of process vibration on operations of clearing of details from scales, gum, corrosion, scale, rigid and fashion gum of contaminations to processing the typical representatives (representative) of details of auto tractor drives piston pin covered with a stratum gum, spherical support, piston rod with oil contaminations were subjected. As a main criterion of efficiency of process the time of full clearing of details on researched parameters is accepted. As have shown outcomes of researches, the process vibration of clearing grows out of joint effect on deleted contaminations of micro impacts of particles of a medium (mechanical effect) and chemical proper-ties technical basic liquid. Among other types processing of large-sized details on which the conditions of vibration clearing were investigated it is necessary to name spider of a gimbals, valves of drives of various types, on which the process of clearing of a surface from gum was treated.

1   Introduction

Constructional and antifrictional general purpose nibs from powders on the basis of iron make the basic part of production of powder metallurgy. More than half of such details falls at a share of motor industry, instrument making, transport and agricultural mechanical engineering. Taking into account the big role of a superficial layer at work of details in units of machines and mechanisms the further development

of technology of reception of powder details probably both on the basis of change of composite structure, and due to formation favorable structures of a material, for example biporosity of the working and a preworking layer [1, 2].

One of effective opportunities of modifying of working surfaces of such details with creation functional gradient layer from one or diverse materials is dosed out superficial - plastic deformation [3]. Thus it is necessary to take into account, that the factor limiting application of constructional powder details is their porosity reaching 18-20 %.

Conditions of operation of the products working in closed premises with adjustable climatic characteristics, and also outside of premises show to details, besides other increased requirements on stability corrosion. These requirements for details of powder metallurgy are especially actual as their raised porosity increases the free surface of metal adsorbing a moisture which undermines from within sheetings, accelerates corrosion processes.

In clause results of researches on drawing on a surface of details from materials are resulted on the basis of iron of powders of zinc and aluminum, and also compositions on their basis, on technological maintenance of hardening, modifying (to curing and superficial defects) by a method of vibrating processing.

2 Method

Process of vibrating processing will consist in consecutive drawing on a surface of processable details of the big number of microimpacts by particles of a vibrating working environment. A basis of process depending on properties of a working environment is mechanical or mechanical operation the smallest particles of metal from a processable surface, smoothing of its microroughnesses, plastic deformation of a superficial layer of processable details. The priority in studying the basic laws of this process belongs to A.P.Babichev [4].

Depending on purpose of technological operation as processing environments abrasive and other nonmetallic materials of various characteristics, metal working bodies of the required form and the sizes can be applied. Processing can be made in the liquid on structure liquid or gaseous environment. Intensity of processing depends on modes of vibration, the characteristic of the processing and technological environment, mechanical properties of a material of processable details, etc. The model of process of vibrating processing represents system of particles of a working environment of the spherical form in diameter D which centers of weights are packed on a square $D \times D$. With the purpose of formalization of process it is accepted, that:

- The system of particles goes along a vertical straight line in a homogeneous gravitational field;

- During movement layers cooperate with each other by means of direct central impacts;

- dissipativ properties of system are described by factor of restoration at impact;

- External influence is transferred the bottom layer from the bottom of the working chamber varying under the harmonious law in a vertical direction;

- Moving particles inside a layer is absent;

- The bottom of the working chamber has radius $R \longrightarrow +\infty$.

Using the basic position of work [5] on dynamics of "columns" we shall receive at impact i and $i+1$ a layer of a parity:

$$(U_{i,1} - V_{i+1,1}).K_y = V_{i+1,2} - U_{i,2}$$

$$V_{i,1} = U_{i,2} + g.t_i''$$

$$U_{i,1} = V_{i,2} - g.t_i'$$

Where: t_i': time of unaccented movement i a layer after impact in i to pair layers; t_i'': time of unaccented movement i a layer after impact in $i+1$ to pair layers.

As speeds of elements of layers are changeable, on intervals of unaccented movement it is accepted, that: $U_{i,1}$ and $U_{i,2}$ speeds of elements i a layer directly before impact in $i+1$ pair layers, $V_{i,1}$ and $V_{i,2}$ speeds of elements i a layer directly before impact in i pair layers.

As shown in work [4], frequency of fluctuations of layers of particles can be accepted to equal frequency of fluctuations of a bottom of the working chamber ω and consequently the period of fluctuation of layers T, moving of layers S_i and amplitude of their fluctuations A_i, will be:

$$T = \frac{2\pi}{\omega}$$

$$t_i' = t_i'' = T$$

$$S_i' + S_{i-1}'' = const$$

$$A_i = \frac{1}{2}.S_i' = \frac{1}{2}.S_i''$$

The valid movement of layers will be as it was already marked to differ from simulated. First, as a result of slanting impacts displacement of layers will take place. Second, each element of a layer tests action of forces of the dry or viscous friction arising owing to different speeds of separate elements. It can lead to to infringement of symmetry of kinematics of movement. For example, time of movement of elements of layers upwards t_i' becomes less time of movement downwards t_i'' however as shown in work [4] it does not break stability of periodically oscillatory movements of environmentWednesday which are the basic source of power influence on a processable surface . . .

The equation of impact of the first layer with a bottom of the working chamber will be expressed by a equation:

$$V_{1,2} - K_{y0}.V_{1,1} = (1 + K_{y0}).A_0.\omega.cos\omega t$$

Where: K_{y0} is the factor of restoration at impact of the first layer with facing a bottom of the working chamber. Properties of a material facing are expedient for choosing so that K_{y0} came nearer to unit.

Loss of energy in i a layer will be expressed by equation:

$$\Delta E_i = \frac{m.(U_{i,1}^2 - U_{i,2}^2)}{2} = \frac{m}{3}.\frac{(1-K_y)}{(1+K_y)}.(n-i).(n+\frac{1}{2}-i).(n+1-i) \qquad (1)$$

Where: m - weight of a particle of a layer, n - number of layers testing periodic fluctuations.

Owing to "dynamic slackness", caused by the big number of elements and them dissipativ properties, the top part of layers includes the elements moving as one element with weight to equal weight of all elements of its components. From a real picture of behaviour such system is distinguished with neglect dissipative properties of the top part and stochastic to fluctuations of speeds which arise in it and are distributed on its elements from top to down, gradually fading [5].

The account of a "languid" part of loading in weight of M under condition of $M > (m \times n)$, using substantive provisions of work [5], result in values of factor of loss of speed:

$$K_{Vi} = \frac{V_i+1}{V_i} = \frac{(l-i)^2 + 2.(l-n)^2.(n-i-1)\frac{1-K_y}{1+K_y}}{(l-i+1)^2 + 2.(l-n)^2.(n-i)\frac{1-K_y}{1+K_y}} \frac{l-i+1}{l-i} \qquad (2)$$

where: $l = \frac{H}{D}$, H: height of loading of layers.

The maximal values of speed of first layer $V_{1,2}$ depending on a phase of impact with a bottom of the chamber, a material of particles and facings of the chamber are in limits:

$$A.\omega \leq V_{1,2} < 3A.\omega$$

Knowing laws of change of speed of particles of a working environment (2) and losses of energy (1) on layers from bottom to top it is possible to estimate probability of that each point of a surface of a detail will receive even one impact by a particle of environment by energy $E_d \leq E_{d_0}$ sufficient for change of its porosity at equiprobable hit of a detail in i a layer of particles of environment and the general number of fluctuations of layers equal f_τ, where τ duration of processing.

$$P(1 \leq x < \tau.f) = 0.5 - \Phi_0(t_k) \qquad (3)$$

where: $\Phi_0(t) = \frac{1}{\sqrt{2\pi}}.\int_0^t \exp(-\frac{x^2}{2})dx$ represent integral of probabilities

$$t_k = \frac{1 - \tau.f.p_{B3}}{\sqrt{\tau.f.p_{B3}.(1-p_{B3})}}$$

$$p_{B3} = p_{B1}.p_{B2}$$

p_{B1}: Geometrical probability of a covering of a square of packing $D \times D$ traces of processing (prints in diameter d_0) for one fluctuation of the working chamber ($p_{B1} \approx 0.78\frac{d_0^2}{D^2}$).

p_{B2}: Probability of impact about a surface of a detail a layer of particles of a working environment possessing energy $E \geq E_{d_0}$, dependent basically from amplitude-frequency modes of vibration and characteristics of particles of a working environment ($p_{B2} = 1 - F(E_{d_0})$), where $F(E_d)$ is the function of distribution of energy on layers, particles of environment.

The submitted dependences allow to use them for an estimation of power opportunities. Generally details of powder metallurgy are exposed to same technological operations as well as a detail from compact materials. Thus interaction of particles of the processing environment with a surface of a detail influences and such important parameter as porosity of a superficial layer. For revealing interrelation of a degree of change of porosity of a surface at individual its contact to a particle of the working environment having a level of kinetic energy E_d besides earlier made we shall enter the following assumptions:

- Hardness of a particle is more than hardness of a material of a surface;

- The roughness of a particle is absent;

- Depth of introduction of a particle is much less than radius of curvature of a surface in a point of contact, but more than height of its microroughnesses;

- Introduction of a particle occurs on a normal to a surface.

Picture of change of porosity on depth of deformation h_{nl} of a superficial layer of a detail it is possible to present in the following kind.

In an initial condition the structure of a material is submitted as particles close to the spherical form, connected among themselves by the "bridges" of interpartial contact formed as a result of sintering of a material. The relative density of such material will be characterized by the attitude of volume of a firm part of system of the caked particles to total amount of system.

$$\nu = \frac{V_{m,\Phi}}{V_0}$$

Porosity of such system will be expressed as

$$\theta = 1 - \nu$$

Also will lay in limits

$$0 \leq \theta \leq 1$$

At interaction of particles of the processing environment with a surface traces as prints which, covering, all surface, create tensely - deformed a condition on thickness are formed. At full shelter of a surface prints it is possible to assume, that compression of all layers on thickness will correspond on the average to deformation of axial compression under one print. For dynamic methods the dependence offered [4], connecting a zone of plastic deformation with the size of a plastic print $h_{nl} = k_{nl}.d$ (for iron and his alloys $k_{nl} = 1.5$) is known.

However for vibrating processing details from powder materials this dependence gives the overestimated values of depth of plastic deformation. Our researches show, that depth of plastic deformation at grasps all some layers of particles a layer. Change of microhardness testifies to this on thickness of samples from a powder of iron fraction $\approx 100 \mu m$.

Without the big damage for accuracy depth of a zone of plastic deformation can be accepted: $h_{nl} = k_{nl}.a_p$, where a_p is the average size of particles of an initial powder of sintered material $k_{nn} = 1..3$.

It is obvious, that deformation of particles of a powder and filling pore will decrease in process of removal from a surface in depth of a material, and the volume of a firm part of system $V_{m\varphi}$ does not vary, but only leaves volume of a restored print.

Proceeding from a full covering prints in diameter d all surface, the density of an initial powder material in volume of a zone of plastic deformation will be expressed by equation:

$$\nu_0 = \frac{V_{m,\varphi}}{V_0} \approx \frac{V_{m,\varphi}}{\pi . \frac{d^2}{4} . (h + h_{nl})}$$

Where h - depth of a restored print. Density of a superficial layer of a powder material equation :

$$\nu = \frac{V_{m,\varphi}}{V} \approx \frac{V_{m,\varphi}}{\pi . \frac{d^2}{4} . h_{nl}}$$

Change of porosity of a superficial layer, proceeding from linearly decreasing concentration of a firm part of the system which have been squeezed out from volume restored on depth will be:

$$\Delta\theta = \theta - \theta_0 = \frac{2h}{h_{nl}(\theta - 1)(1 - \frac{x}{h_{nl}})}$$

Where x - distance of the deformed layer from a surface.

Thus, knowing a required level of kinetic energy of particles of processing rendering essential influence on condensation of a superficial layer of details from powder materials (decreasereduction in porosity), it is possible, using dependences (1), (2), (3) to define area amplitude-frequency (A_0, f) and time τ modes of vibrating processing with required probability of that the given power influence will be rendered on all surface of a detail.

Calculations show, that at energy particles of working environment $E_{d_0} \approx 10^{-3}...10^{-2}J$ appreciable change of porosity of a superficial layer occurs already after $15-20$ minutes of vibrating processing. On rice 4 dependence of change of porosity on depth of samples from material $PK6,3$ with the size of particles of an initial powder $100 microns$ revealed metal graphic a method and a confirming opportunity effective (up to 2 times) condensation of the superficial layer shown on depth up to $150 microns$ is shown.

3 Experiments

During shock interaction of the firm granulated working environment, with a surface of details at vibrating processing conditions for connection of particles disperse metal included in the environment with a processable surface on the mechanism of "cold" welding by pressure are created. The analysis of modern representations about mechanisms of connection of materials in a firm phase shows, that in dependence of by nature connected materials and thermo deformation conditions of formation of coverings from a powder on cintered metal substrate without fusion coupling (adhesion) of the last can arise for the account particles of a powder owing to allocation of heat at impact, mechanical fastening of particles and microroughnesses of a surface in absence or presence of wetting on sites of contact, action molecular

or nuclear, in particular metal communications. Topochimical reaction, connection of materials without fusion goes in 3 stages [6]:

- Formation of physical contact;

- Activization of contact surfaces;

- Volumetric interaction;

According to these representations the nature of formation of connection between materials in firm is uniform. Distinction consists only in kinetic courses of the separate stages, determined by conditions of heating, character and a degree of deformation influence and features of development relaxation processes. The big influence on materials renders a degree of their plastic deformation which should be more than some minimal size providing clearing of connected surfaces, formation of units preservation of these units after removal of loading. According to academician A.P.Semenova aluminum is easily connected metal in a firm phase: among themselves it incorporates at a degree of deformation of $53 - 58\%$, at a degree of deformation of $60 - 62\%$ while copper incorporates to copper among themselves at a degree of deformation of $74 - 76\%$, cadmium at 80% of deformation, tin more than 80% of deformation, connection of less plastic materials even more inconveniently. Transition from the static appendix of power influence to dynamic and presence in contact of tangential forces generally reduces a necessary degree of deformation as in the first case heat removal from a zone of deformation decreases, and in the second destruction is facilitated. The major factor influencing process of connection of materials in a firm phase is the temperature as she influences and conditions of formation of physical contact, and on conditions of clearing of a surface, and on conditions of formation of the active centers, and, at last, on conditions of preservation of connection at removal of loading. The role of temperature is not limited to only mechanical decrease in resistance of a material to plastic deformation as mechanical properties of metals and alloys are in more complex dependence on temperature and can have zones of fragility at average and low temperatures. Film at low temperatures practically do not influence process as connections of a pressure required for formation considerably surpass pressure of their destruction. However formation of the active centers is sharply accelerated with rise in temperature so even at homogeneous temperatures is appreciably lower $0,4$ (temperature) appreciably moving of vacancies and deployed atoms. For realization of process of drawing of coverings from powder materials the existing equipment - vibrating machine tools are subject to modernization by equipment by their special working chambers, allowing to heat up weight of loading (a working environment and details) to necessary temperatures. With the purpose of experimental studying features of formation of anticorrosive metal coverings on sintering powder materials on the basis of iron (PK6,3) researches on studying influence of conditions on process of reception of coverings of zinc, aluminum and compositions on their basis have been lead. As raw material for reception of coverings powders of aluminum and zinc which rendered on samples with use of laboratory vibrating installation in a working heat chamber to the chamber in capacity of $25 \mathrm{dm}3$ applying as the working shock environment steel spheres in diameter of $1,5 - 14 \mathrm{mm}$ and amplitude-frequency modes - amplitude

$1, 5 \ldots 3\text{mm}$, frequency $15 \ldots 25\text{Hz}$ served. Aluminum covering. Process of formation of a covering begins at temperature above 100°C. Below this temperature is not present conditions for burning out of organic substances and evaporation of the moisture adsorbed by a surface of details and particles of a powder. The powder does not occur to a surface, it is crushed, undergoes qualitative changes and turns to a dark grey dust and organic connections of aluminum. Rise in temperature up to $120 - 150^{\text{o}}\text{C}$ results in reception on a surface of samples of a light aluminum covering which thickness depends on amplitude-frequency modes, durations of processing, and also quantity and a way of submission of a powder in the working chamber. The temperature 250°C essentially does not change conditions of formation of coverings, however his surface has more dark color. Rise in temperature up to 300°C results in reception of coverings of grey color which at storage on air strongly darken as against received at lower temperatures. The aluminum covering well adjoins to the basic metal, copying his roughnesses. Intermediate layers between it and a basis are not present. It is necessary to note, that the big stability of a powder of aluminum oxidation allows to carry out process of drawing of a covering without hermetic sealing the working chamber and without application of the regenerative or inert gas environment.

4 Conclusion

Vibrating processing in an interval $20 - 200^{\text{o}}\text{C}$ in open or in untight closed working chamber does not allow to receive a qualitative zinc covering. Particles of a zinc covering to a processable surface occurs in separate points between which there is a uncovered metal. At temperature is higher 200°C there is the intensive oxidation of a powder making impossible process of processing. Therefore the technology of reception of a zinc covering provides processing in tightly closed chamber (without access of air) with addition in structure of a zinc powder, substances at which decomposition from heating the regenerative atmosphere, for example chloride ammonium is formed. It complicates technology a little and makes coverings similar with diffusion. In this connection the circumstance had been lead researches on revealing an opportunity of reception of zinc - aluminum coverings by vibrating processing in a temperature range of aluminizing. On the first way into structure of an aluminum powder entered zinc powder (30% on volume). The mechanism of formation, structure of such covering and modes of processing do not differ from corresponding at drawing aluminum, however particles of zinc powder reduce harmful influence of porosity of only aluminum covering. On the second way received two-layer coverings by introduction in the working chamber at first the zinc - aluminum powder consisting of 80% of zinc and 20% of aluminum, and then after processing within 60 minutes of only aluminum powder. Such covering has a sublayer enriched with zinc, preventing harmful contact of aluminum to iron on which there is the top layer of aluminum proof in various environments. The thickness of coverings determined by a weight method on increase of weight of samples after processing, or to reduction of their weight after coverings, and also metal graphic on micropolishing changes from $3 - 5$ till $20 - 30$ a micron. The suggested technology - the combined process of vibrating processing with surfaces powders of zinc and aluminum allows to raise

corrosion resistance of details of powder metallurgy and to condense their superficial layer, having reduced his porosity and having increased strength properties. Process is tested on powder products of instrument making, motor industry.

References

[1] Metal powders and powder materials: the Directory. J.V.Levinsky // Autor. B.N.Babich, E.V.Vershinina, V.G.Ljulko, etc.; - M.: EKOMET, 2005. - 520.

[2] Powder metallurgy. Composite materials. Under red. V.Shatta., Metallurgy, 1983.-520 with.

[3] V.G.Ankudimov P.Y., Beljaev A.G., etc. Vibrating superficial - plastic processing of powder antifrictional materials on the basis of iron. Modern problems of mechanics and physical and chemical processes of cutting. Materials international conf. Kiev 2002.

[4] Babichev A.P., Babichev I.A.bas of vibrating technology. Rostov on Don, Publishing center DSTU.1998.-624.

[5] Kobrinskij A.E., Kobrinskij A.A. shock-vibrating systems. Dynamics and stability.M. Science 1973.-591 with.

[6] Radomyselskij I.D., Serdjuk G.G., Cherban N.I., etc. Constructional powder materials, technics, 1985.-152 with.

K. Hamouda, T. Sayah, University of Sciences and Technology of algiers, Algeria.

A Babichev, Y.P. Ankudimov, P.Y. Ankudimov, Don State Technical University, Russia.

M.N. Benallal, University of Khemis Miliana, Algeria.

D. Saidi, Ecole Nationale Polytechnique, Algeria.

M.A. Djema, University of Boumerdes, Algeria.

A unified graphic environment dedicated to SES code for optimization of fire ventilation strategies in subway networks

Luca Iannantuoni   Giovanni Manzini

luca.iannantuoni@polimi.it

Abstract

To avoid difficulties regarding the use of the Subway Environment Simulation (SES) code to properly size and locate ventilation shafts in subway networks to answer to common fire safety engineering tasks, a specific tool has been developed to assist the generation, visualization, manipulation and diagnostic of simulations.

1 Introduction

In order to improve the planning, design and construction of subway ventilation systems, with a focus on the fire safety engineering tasks, the Subway Environment Simulation (SES) code is widely used to properly size and locate ventilation shafts, evaluate tunnel geometries (different transversal and longitudinal lengths), fan sizes and model the heat and smoke transport resulting from fires and other sources.

Performing such kind of numerical simulations, difficulties and criticalities have been identified, many of them regarding the user interface with the code, that has then been provided with a dedicated pre and post-processing tool, named proSES. The paper will explain the rationale behind its development and its verification. It is supported by a graphical interface which provides a unified environment for the visualization, manipulation, generation and diagnostic of SES simulations.

It is possible to represent the network directly by a graph, significantly reducing the time to prepare the input file and decreasing errors concerned with typing and model description. Results are extracted from the output ascii files to generate automated reports to easily compare great number of simulations, both with plots or animations. The tool is written in Python, therefore it is platform independent, and it makes an extensive use of external libraries.

SES and proSES respond to the needs of ventilation designers, but a general approach was used, in order to customize it for different kind of purposes, for example to generate dynamic boundary conditions that can be applied for simulations with other codes (2D or 3D lumped parameters or CFD ones) applied to a portion of the entire network. This tool has been developed for Metropolitana Milanese S.p.A., a

tunnel engineering company operating worldwide, which uses it to optimize ventilation strategies in underground lines.

2   The SES code

The Subway Environment Simulation (SES)[1] is a one-dimensional, incompressible, turbulent, slug-flow model, developed with a designer-oriented approach, providing estimates of airflows, temperatures, and humidity, as well as air conditioning requirements, for both operating and proposed multiple-track subway systems [1]. It provides a dynamic simulation of the bi-directional operation of multiple trains throughout different arrangement of stations, tunnels, ventilation shafts, and fan shafts.

The capabilities of the SES program are comprehensive, allowing the user to simulate a variety of train propulsion and braking systems; various systems of environmental control (including forced air ventilation, station air conditioning, and track-way exhaust); airflows in any given network of interconnected tunnels, stations and underground walkways; any desired sequence of train operation (named routes), including the mixing of trains with different operating characteristics and schedules; various steady-state and non-steady-state heat sources including fire sources; emergency situations with trains stopped in tunnels and air movement solely by mechanical ventilation and buoyant forces [1].

It has been validated in model tests and in actual practice and it is applicable to a variety of subway operating and design configurations and has been demonstrated to be a cost-effective tool for evaluating the performance of most types of environmental control strategies.

A part of computational issues, the main criticalities of the SES software are regarding the user interface, which doesn't give to to the user, during the input management phase, a sufficiently clear representation of the network. This lead to errors due to wrong typesetting and misunderstanding because of the complexity of the model, and long time is required for the verification of the input.

Moreover, the input manager provided with the code has not any feature to simplify parametric studies, that are very important to explore a huge amount of different solutions, changing the great number of independent variables, like geometrical properties, route and train characteristic, fire and fan sizes.

In fact, the SES code is usually very fast on common desktop computers and the user is prone to increment the number of different cases in order to forecast the better solution.

Another criticality is inherent the output file storing the results, that is not readable with common text processing scripts because it is a printed oriented ascii file. The values of variables are not saved in a proper manner (like comma separated values) thus extracting output data would be a very tricky task.

This limits extremely slow down the time dedicated to the description of the network, and the analysis of results, therefore a really long time is required to process any

---

[1]The SES code has been developed by the Department of Transportation of United States of America and it has been released as executable for Windows[TM]platform.

simulation.

3 The proSES tool main features

We have developed[2] a complementary tool to the SES code in order to easy set-up, modify and run multiple cases and to generate plots and animations to rapidly compare and show results of simulations.

An interactive graph allows a visual representation of the network elements (tunnels, stations, vent shafts..) and their relative connections through junctions. Nodes and segments are then described using prototypes, so their properties values can be easily modified in any time, simplifying the generation of different inputs for parametric studies, as shown in figure 1.
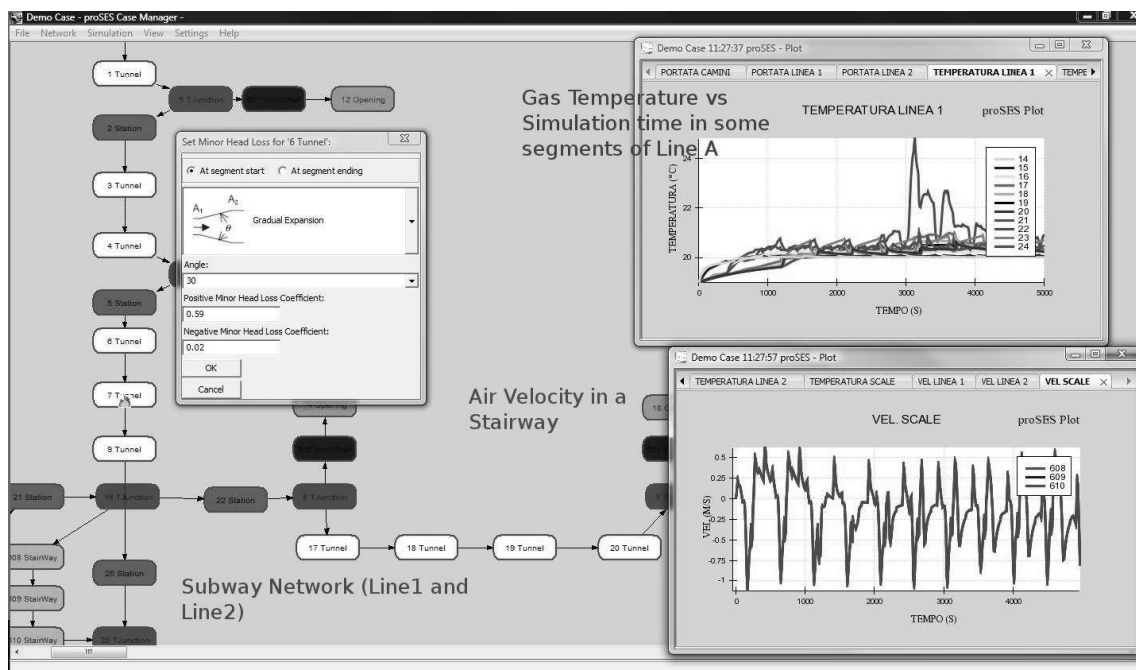
Figure 1: A frame of the proSES tool showing the interactive graph and plots of results.

It is possible to define routes independently from the actual train performance option selected, and a plenty of features assist the user to cover every aspect of the pre-processing phase.

It is possible to extract the output data to generate automated reports and also to generate animations to easily compare different solutions as shown in figure 4

The tool uses Python as a glue programming language [2], [3], [4] and the wxPython [5] graphic library as porting of the wxWidget cross-platform one. For the three dimensional animation the VTK library [6] was chosen, so the post-processor Paraview [7] could be used to visualize the dataset and save animations.

---

[2]Programming: Luca Iannantuoni; Verification: Giovanni Manzini
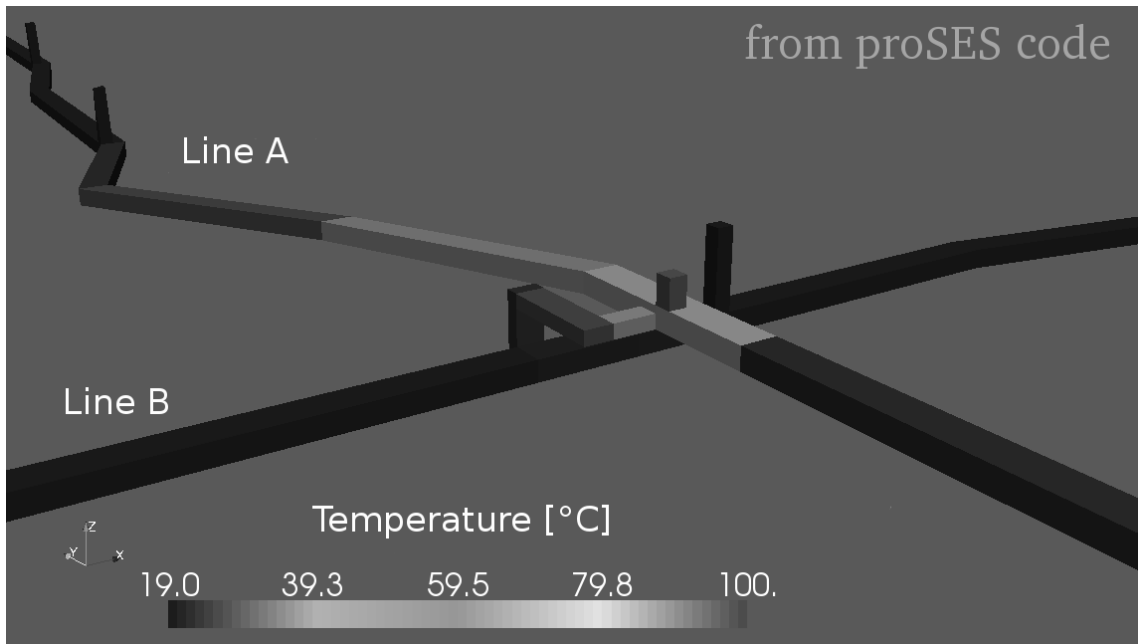
Figure 2: A frame of an animation showing the transient state of a ventilation strategy applied to a subway network in a fire scenario.

4 Mentions about fire safety applications

4.1 Generalities

The SES fire model is intended for use in a trial-and-error fashion to select the emergency ventilation system capacities. The interactions are between the tunnel air velocity and a design air velocity criterion which precludes the backing of smoke against the ventilating air stream (backlayering). The critical air velocity criterion is a function of the fire heat release rate, the tunnel width, the average tunnel slope, and the temperature of the hot gases leaving the fire.

A typical application of the fire model consists in iterating the simulation process to predict the tunnel fresh air velocity and hot smoke temperatures to determine whether the critical air velocity is less than the predicted one. Various tunnel geometries, fire sizes, ventilation strategies and fans are usually taken into account, leading to a huge number of different cases to be computed. With the proSES tool this kind of study is much more faster and reliable, because it provides a unified graphic environment covering every aspects of this kind of application.

A brief description of one study that was performed by SES and ProSES inside a Fire Safety analysys carried out for Metropolitana Milanese is reported below. The aim of the analysis was the effectiveness assessment of different fire protection ventilation strategies applied to driverless metro lines [8]. Mainly, the attention was focused on the smoke backlayering phenomena [9], [10]. Moreover, a fundamental attention was dedicated to the presence of smoke and high air – smoke temperature values inside the volumes of egress paths (platform, corridor, atrium, stairways).
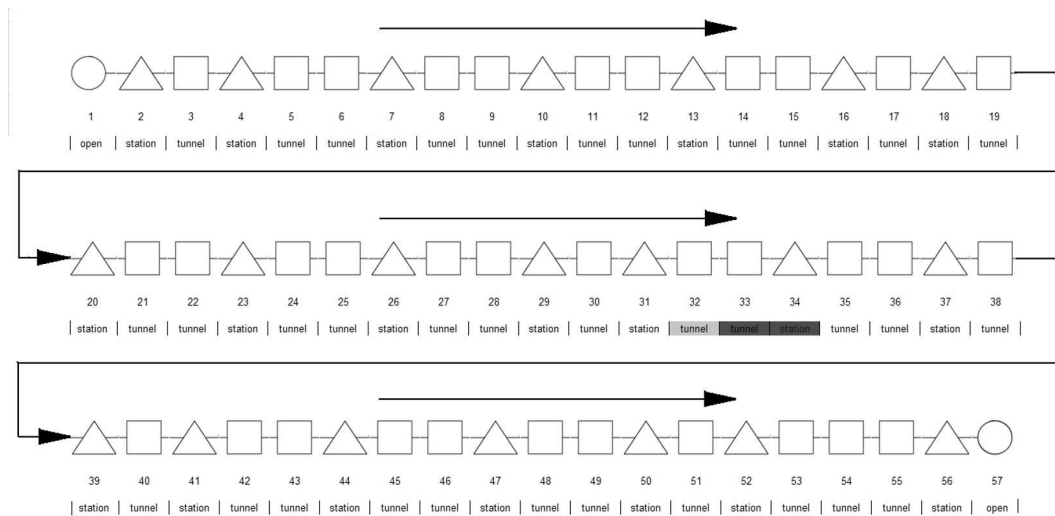
Figure 3: Example of subway line, with indication of fire positions (the fire starts when the train is inside tunnel segment num. 32 and this train stops in station num. 34).

4.2 Case study

The analysis has been focused on the metro line, described in figure 3, that was composed only by single track segments (group 1 cases) or by double track segments (group 2 cases). The main data of such example metro lines are: $L = 12.8\text{km}$, number of stations= 21, the area of tunnel in station is 12.70m^2 for a single track and 35.45m^2 for a double track, the area of tunnel out of station is 14.25m^2 for the single track and 37.00m^2 for the double track, the segment slope goes from -2.80% to $+2.33\%$.

In all cases the progressive stops of trains after the fire detection has been simulated. The ventilation strategies simulated have been both of fire protection type and normal (no fire type), with the aim to predict also the consequences of a failure in the activation of the fire protection strategy.

Many fire protection ventilation strategies are push-pull type with num. 1 or num. 2 tunnel ventilation shaft active to supply fresh air (push mode) and num. 1 or num. 2 tunnel ventilation shaft active in exhaust mode (pull mode) to do a longitudinal ventilation in the fire segment.. Alternatively, just the pull type fan is activated (only num. 1 tunnel ventilation shaft active in exhaust smoke/ pull mode and num. 1 or num. 2 tunnel ventilation shaft are left open with the fan stopped).

In fact, such configurations guarantee a higher value of ventilation flow velocity inside the tunnel segment interested by the fire. The fires considered have been characterized by the following HRR maximum values: 1 (HRR= 5 MW), 2 (HRR= 10 MW), 5 (HRR= 25 MW). For example, figure 4 represent the air-smoke temperatures of different volumes of station when a push-pull strategy is applied along the tunnels and a push or pull ventilation is applied nearby the station platform. The most effectiveness of platform extraction strategy in pull mode is evidenced by the *confinement* of high air/smoke temperatures close to station platform.
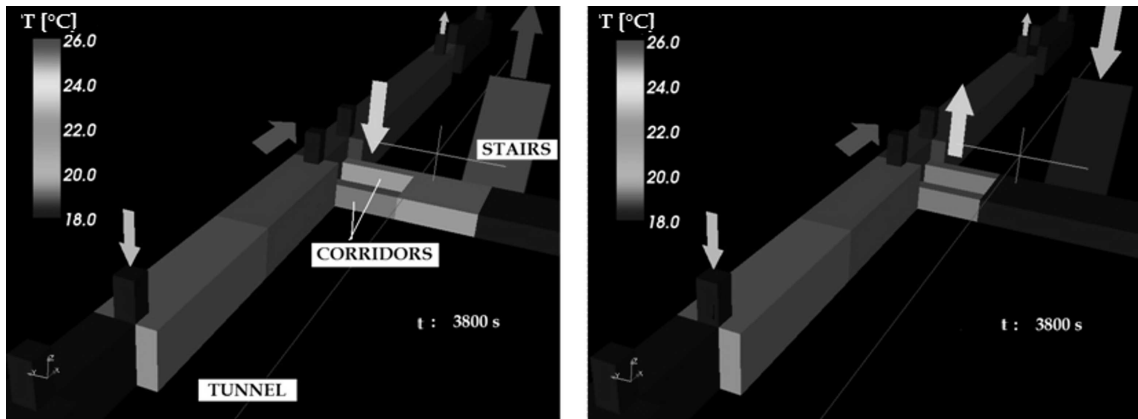
Figure 4: Air/smoke temperature of segments, Single track line, peak hour headway, 1D (SES+proSES) simulation, Fire 5 ($HRR_{MAX} = 25MW$), tunnel ventilation shafts volumetric flow= $300.000 m^3/h$. Tunnel push-pull ventilation strategy and platform push (left image) or pull (right image) of $100.000 m^3/h$. Tunnel of station and outside the station, platform, corridors, atrium and stairways are represented.

5   Conclusions

As shown, proSES tool and SES can be effectively used together in order to verify and optimize fire ventilation strategies in subway networks.

Overall, the analysis carried out for Metropolitana Milanese has evidenced a good usefulness of the proSES as complementary tool to SES, to determine or verify the effectiveness of fire protection ventilation strategies. Mainly, the rapidity in pre and post processing with such a tool and the improved control on errors associated have been demonstrated crucial aspects for the correctness and completeness of calculations. Obviously, because of the code which we have used (SES), it was not possible to do calculations of ventilation effects on burning rate and on production of contaminants like CO, HCN and soot.

6   Future developments

We are currently developing our own code for fluid dynamic simulation of underground transportation networks (subway, rail and road tunnels) which will be integrated in a future release of the presented pre and post-processing tool named proSES. Probably this next release (although minor release will go on to be developed for Windows [TM]platform) should work also on Linux platforms; in fact we have choose Python as programming language, guaranteeing cross-platform development together with the graphical libraries used.

7 Acknowledgements

The authors are grateful to Ing. Eugenio Galli[3] for his fundamental support as subway network designer, Ing. Donato Andrea Paradiso[4] for the effort in doing tests and debugging and Prof. Pierangelo Andreini[5] for the continuous support and precious suggestions.

References

[1] SES User's Manual, U.S. Department of Transportation 2002

[2] Mark Lutz, David Ascher, Programming in Python, 3nd Ed., O'Reilly 2004;

[3] Alex Martelli, David Ascher, Python Cookbook, 2nd Ed., O'Reilly 2005;

[4] Roger S. Pressman, Software Engineering, a practitioner's approach, McGraw-Hill 2005;

[5] Noel Ruppin, Robin Dunn, wxPython In Action, Manning 2006;

[6] The Visualization Toolkit User's Guide, Kitware Inc 2004;

[7] Squillacote, The ParaView Guide, Kitware Inc 2006;

[8] Daniel Gabay, Thematic Network Fire in Tunnels – FIT, Technical Report – Part 2, Fire Safe Design – Metro tunnels, Rapporteur Metro Tunnels, RATP, 2003;

[9] Oka Y., Atkinson G. T., Control of smoke flow in tunnel fires, Fire Safety Journal 25, 1995;

[10] Wu Y., Bakar M. Z. A., Control of smoke flow in tunnel fires using longitudinal ventilation systems - a study of the critical velocity, Fire Safety Journal 35, 363–390, 2000.

Thermal deformation in powder strip fusion

Mohammad Issa Ahmad   Valerij Vasil'evich Chigarev
Aleksandr Grigor'evich Belik
bayan20042002@yahoo.com

Abstract

SPowder bands have great application when different abrasion-resistant alloys are used and thus, in build-up fusion when powder bands the surfaced layer is characterized by chemical heterogeneousness. The appearance of such a chemical heterogeneousness on the surfaced layer in mechanized electric arc welding with powder bands can be due to envelope construction, welding condition or its formulation. Fusion of the shell cause buttons of melting metal, which contact only partly the core, besides, considering short duration of the processes. It is expect that low degree of alloying at button stage would result in chemical heterogeneousness of distribution in the surfaced layer. In this work it was found that chemical homogeneity of surfaced metal coat depends on electrode metal mass transfer in the process of powder strip welding. Metal heterogeneousness applied by powder strip fusion is caused by some core components, that occur in weldpool melt omitting button stage. Such particles have considerably lower temperature, which changes the solidification rate in the joints of weldpool. Attempt was made to find quantity expression of core components appearing in weldpool in an unfused state.

1 Introduction

Powder bands have great application when different abrasion-resistant alloys are to be used [1]. In build-up fusion with powder bands the surfaced layer is characterized by chemical heterogeneousness. The appearance of such a chemical heterogeneousness on the surfaced layer in mechanized electric arc welding with powder bands can be due to envelope construction, welding condition or its formulation [2,3,4]. While examining the nature of powder strip fusion in application of different abrasion-resistant alloys, we should pay attention to the fact of separate shell and core fusion, that is very important, if we deal with metallurgical processes at the button stage. Fusion of the shell cause buttons of melting metal, which contact only partly the core, besides, considering short duration of the processes, we can expect low degree of alloying at button stage. This type of fusing processes and electrode metal transfer would result in chemical heterogeneousness of distribution in the surfaced layer [2]. In this work we came to the conclusion, that chemical homogeneity of surfaced metal coat depends on electrode metal mass transfer in the process of powder

strip welding. Metal heterogeneousness applied by powder strip fusion is caused by some core components, that occur in weldpool melt omitting button stage. Such particles have considerably lower temperature, that change the solidification rate in joints of weldpool. In [5, 6] we make an attempt to find quantity expression of core components appearing in weldpool in an unfused state. Heterogeneousness of chemical composition in surfaced metal is also due to fusing irregularity of the shell and the core of a powder strip. Probability of such mass transfer of electrode material depends on welding current distribution between the shell and the core of the powder strip. It was registered, that welding current passing through the core of powder strip is (1,11 - 2,5) 104 times less, than passing through the shell [2]. Which obviously means, that welding current passes practically through the shell of the powder strip, as shell - core boundary resistance is 4-9 ohm, and the resistance of shell metal is $\approx 3,6 \cdot 10^4$ ohm [2]. Such energy distribution in powder strip welding causes the increase of current density. That, in its turn, is the causal factor of local shell melting and hogging.

2 Thermal deformation in powder strip fusing

Thermal deformation in the metal shell in the process of powder strip fusion can be explained by changing of its volume and linear parameters due to the temperature increase. Under the fusion by powder strip, it is obvious to expect the extension of the length and width of the sell perimeter at the throat of welder due to its heating by passing welding current. The throat of powder strip in abrasion-resistant alloys fusion is usually about $40 - 120 mm$. Under the fusion of powder strip, the shell is being heated by passing current till the butt in temperature interval from the temperature of the environment till the melting point, which is ensured by the heat separated by the passing current at the throat. Knowing the temperature value of a powder strip shell heating at the welding throat at the melting point, we can calculate the length change and volume expansion of shell metal [7]. So, the length extension of powder strip shell under its fusion with the heat of passing welding current at the throat will be:

$$\Delta \ell_T = \alpha \ell_0 (T - T_0) \tag{1}$$

where $\Delta \ell_T$— the increase of the powder strip throat length due to welding current heating, mm; ℓ_0— the initial length of powder strip throat, mm; T_0— the initial temperature of metal shell, Cº; T— the temperature of metal shell heating due to the passing welding current at powder strip fusion, Cº; α metal shell linear extension coefficient, $1/Cº$.

The same conditions cause volume extension of the metal shell. Volume increase of the powder strip metal shell at its throat due to the current heating is defined as follows:

$$\Delta V = \beta \ell_0 V_0 (T - T_0) \tag{2}$$

where ΔV the increase of the powder strip throat volume, mm^3; ΔV_0 the powder strip throat volume before its melting, mm^3; β coefficient of volume extension,

Metals	$\alpha.10^{-6}, 1/C°$	$\beta.10^{-6}, 1/C°$
aluminum	23.9	71.7
copper	16.9	50.7
steel	11.0	33.0

Table 8: Linear and volume extension coefficients for metals.

$1/C°$. Total throat length of the powder strip taking into account the changes due to the welding current heating can be found:

$$\ell = \ell_0(1 + \mathtt{alpha}(T - T_0)) \tag{3}$$

$$\ell = \ell_0 + \Delta\ell \tag{4}$$

The linear coefficient of extension β and volume expansion are known for different metals and given in Table 1 [7]. Thus, the length change of the powder strip throat due to its heating by the passing welding current in the process of fusion can be calculated, if we know the real temperature of shell heating.

3 Experimental program

3.1 Materials and Sample Preparation

There have been held some research work in order to evaluate the temperature of the heated powder strip shell. The research experimental program was accepted analogical to works [7, 8] and is shown in Fig.1. The temperature was measured in the middle part of the powder strip shell and, at the same level, in the locking devise with the help of chromel-alumel thermocouple ϕ 0,15 mm. A part of powder strip with the steel 08KP shell and copper 1000 mm was joint into welding circuit. The welding current was regulated by ballast rheostats and was passing through the researched electrode during some definite period of time, meanwhile the temperature and current values were registered by the oscillograph K-I2-22.
We carried out experimental work for temperature measuring in the heated metal of powder strip shell at the welding throat. The circuit for temperature evaluation was the same, but thermocouples were posed in the middle part of the powder strip shell The procedure of powder strip shell temperature measurement at the welding throat in the process of fusion can be seen in Fig. 2. The welding throat length is 60 mm. Welding current 550-600 A, voltage - 32 V. Chosen values are the most characteristic average values for the named process, which are most commonly used in welding with different powder strips.

4 Results and discussion

According to the results of research analysis, heating temperature around the shell perimeter is irregular. In lock joints the heating is higher, than in the middle of
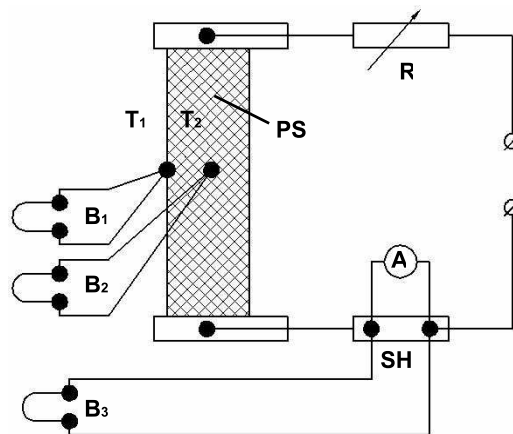
Figure 1: Scheme of a circuit for powder strip temperature measurement, where R ballast rheostats Pb-300, B_1, B_2, B_3 oscillograph loops; A-Amperemeter; SH shunt; PS powder strip; T_1, T_2 thermocouples.
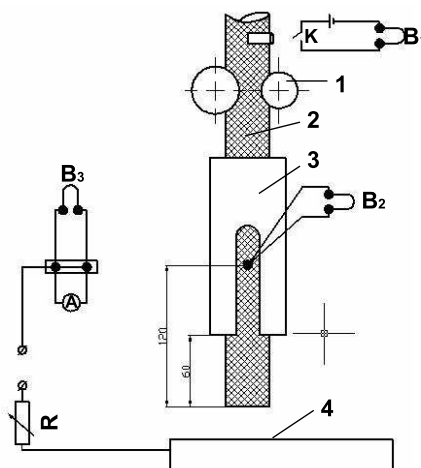
Figure 2: Temperature change in the powder strip shell in the process of melting, where K-finite switch; 1—charged rollers; 2—powder strip, 3— lead wire, 4—plate.

powder strip shell. The authors of the research under [8] explain the phenomenon by the difference in current passing along the perimeter of the powder strip shell. In lock joints welding current passes with 30% higher intense, than in the other part of the perimeter. With the increase of current density there grows temperature difference in the shell perimeter. Lock joint of the powder strip shell is formed by several layers of the metal strip, so that makes influence on welding current passage. With the current density lower $30A/mm^2$, temperature difference of heating between the lock joint and the middle of the shell is up to $100C^o$. At the

current density up till $40 \text{A}/\text{mm}^2$ the difference can be up to 250°. With the increase of electrical resistivity of the shell metal the heating intense also grows. The results of temperature dependence on current passage duration are in Fig. 3.
The results of temperature measurement at the welding throat heating by the welding current in fusion process are displayed in Fig. 4.
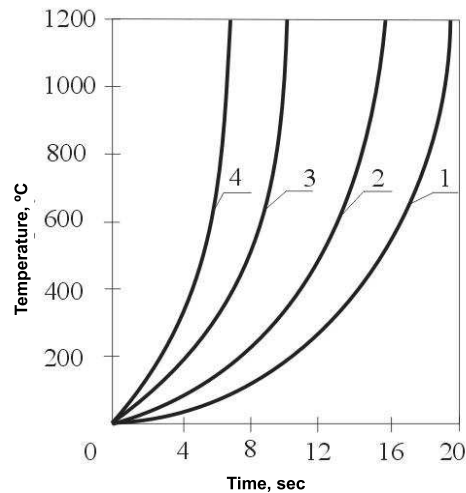
Figure 3: Temperatures of the powder strip shell, where 1—heating of the middle part of the shell, 2—- heating of the lock joint of copper shell, 3—heating of the middle part of steel shell, 4—heating of the lock joint of steel shell.
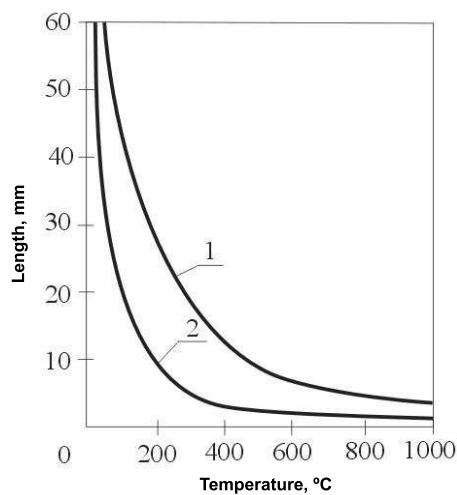
Figure 4: Temperature distribution at the throat of powder strip under fusion, where 1—temperature of the steel shell; 2—temperature of the copper shell.

The research analysis allows us to draw to the conclusion, that the temperature at the throat of powder strip under the fusion for the steel shell can be estimated in

the interval of $400 - 600C°$ and for copper shell $300 - 400C°$. The received values are supposed to be optimal and change with stuff composition, shell thickness, the degree of shell and core squeezing. That is why it is necessary to estimate heating temperature at the welding throat of each powder strip. On the grounds of our experimental data of heating temperatures at the throat of powder strips shells at fusing point we calculated its length alteration by the equation (1). The heating temperature at the throat of the powder strip with the length equal to 60mm, according to the experiments with the steel shell, was assumed as $500C°$, and with the copper shell $350C°$. Length alteration of the throat length in the powder strip with steel shell was $\Delta\ell_T^{st}$ which was calculated as:

$$\Delta\ell_T^{st} = 11 \times 10^{-6} \times 60(500 - 20) = 0.32\text{mm}$$

Length alteration of the throat length in the powder strip with copper shell was $\Delta\ell_T^{cu}$ in calculation:

$$\Delta\ell_T^{cu} = 16.9 \times 10^{-6} \times 60(350 - 20) = 0.33\text{mm}$$

Thus, total length of the throat of powder strip with lengthening for different metals was as follows:

$$\Delta\ell_{st} = 60 + 0.32 = 60.32\text{mm}$$

$$\Delta\ell_{cu} = 60 + 0.33 = 60.33\text{mm}$$

Parameter alteration in the shell due to its heating by the passing welding current at the welding throat of the powder strip in fusion can be estimated as follows

$$P = P_0(1 + \alpha(T - T_o)) \tag{5}$$

where P - shell perimeter, mm; P_o - shell perimeter before fusion, mm. For the powder strip shell, exposed in Fig. 1 (see, [1]) the initial perimeter is equal to $P_o = 46\text{mm}$. Perimeter alteration of the shell due to the heating by passing welding current in fusion can be estimated as:
For steel, $P = 46(1 + 11 \times 10^{-6}(500 - 20)) = 46.24\text{mm}$
For copper, $P = 46(1 + 16.9 \times 10^6(350 - 20)) = 46.26\text{mm}$
As we can see from the calculation, the perimeter of the powder strip shell also changes due to the heating by passing welding current in the process of fusion. Volume alteration of the metal shell at the welding throat of powder strip can be defined according to the formula (2). The initial volume of metal shell at the throat at $\ell = 60\text{mm}$ and thickness of the shell $\delta = 0.4\text{mm}$ will be:

$$V_0 = P\ell\delta; \tag{6}$$

$$V_0 = 46 \times 60 \times 0.4 = 1104\text{mm}^3$$

Alteration of the volume will be:
for steel $\Delta V_{st} = 1104.33 \times 10^{-6}(500 - 20) = 17.49\text{mm}^3$
for copper $\Delta V_{cu} = 1104.5067 \times 10^{-6}(350 - 20) = 18.47\text{mm}^3$.

5   Conclusions

All the carried out estimations prove, that in fusing process at the throat of powder strip there is certain thermal deformation, conditioned be welding current redistribution between the shell and the core. Such alterations of welding throat length, shell perimeter and volume mass of metal cause shell deformation, that leads to breaking the contact between the core and the shell, which, in its turn, may cause fusion irregularity of the shell and the core at the throat of powder strip. The character of fusion and masstransfer of electrode metal in the process of powder strip welding can be influenced by the degree of tightening under the compression of the shell and the core while being produced. As it was displayed, duo rolling mill may cause stresses that would lead to crushing of core components, their compaction, it is obviously change the contact surfaces [10]. Powder strip, as it was noted earlier, is a composite material, where the shell is a solid body and the core is particulate. The core has its mechanical characteristics, mainly that of compression resistance, though partly of stretching stress resistance. Under rolling as the main technological process of core compression in powder strip production, outer presser is balanced by the equal and oppositely directed inner elastic forces. When the pressure is removed, inner elastic forces eliminate, and the powder strip core converges to expansion. This phenomenon, called elastic aftereffect, can be observed in powder fragmentation compression, when the substance preserves its elastic properties. Elastic aftereffect can cause the alteration of electric characteristics of the powder strip. If we know the temperature of the powder strip shell at the throat at the moment of fusion, we can estimate its length alteration and volume expansion of the metal shell, which is the main cause of irregular melting of the shell and, its turn, chemically heterogeneous surfaced layer.

References

[1] Chigarev V.V.; Production and application of powder bands for abrasion-resistant alloys fusion / V.V Chigarev // Machine Welding.- 1994.- No.2, pp.51-52.

[2] Oparin L.I.; Research on alloying elements distribution in surfaced metal / L.I. Oparin, I.I. Frumin // Machine Welding. - 1969. - No.5, pp. 21-23.

[3] Yuzvenko Y.A.; Chemical heterogeneousness of the surfaced layer / Yuzvenko Y.A., B.A. Gorpenyuk, V.L. Korbut // Machine Welding. -1978. - No.3, pp. 22-26.

[4] Patskevich I.R; Welding arc features in powder strip fusion / I.R. Patskevich, A.M. Rykov, V.A. Solovskoy // Welding Fabrication. 1971. - No.4, pp. 27-29.

[5] Patskevich I.R; Metal alloying features in powder strip fusion / I.R. Patskevich, L.A. Heifets // Machine Welding. - 1970. - No.2, pp.13 -15.

[6] Chigarev V.V.; Design-experiment evaluation in the process of fusion and electrode metal transfer / V.V. Chigarev, A.G. Belik, Y.V. Sergienko // Machine Welding.- 2006.- No.6, pp.8-11.

[7] Samokhvalov Y.A., Detail draftsman' manual / Y.A. Samokhvalov, A.Y. Levitsky, V.D. Grigorash. - 3rd issue., revised. - A.: Technology, 1978. - 592 p.

[8] Koletchko A. A. ; Issues of powder strip welding productiveness under open arc welding /A.A. Kolechko, A.V. Zarechensky, A.S. Surzhikov // Welding Fabrication. -1978. - No.8, pp. 35-37.

[9] Fartushny V.G.; Welding throat heating features / V.G. Fartushny, A.A. Kolechko // Machine Welding.- 1979.- No.6, pp.37-39.

[10] Chigarev V.V.; Contact stresses specification in rolling of powder electrode strips / V.V. Chigarev, V.I. Kaplanov // Machine Welding.- 1986.- No.7, pp.19-21.

Mohammad Issa Ahmad, Mechanical Engineering Dept., Al-Huson Univ. College, Al-Balqa' Applied University Al-Salt, Jordan
Chigarev V. V. , Metallurgy and Welding technologies at Priazovsky State Technical University, Mariupol, Ukraine
Belik A.G. , Metallurgy and Welding technologies at Priazovsky State Technical University, Mariupol, Ukraine

Hydrodynamical characteristics of the stationary 'single cell' of the slug flow

Oleg N. Kashinsky   Alexander S. Kurdyumov   Pavel D. Lobanov

kashinsky@itp.nsc.ru, kurdumov@itp.nsc.ru, lobanov@itp.nsc.ru

Abstract

A single cell of the gas-liquid slug flow was studied. The flow around an stationary gas bubble in a downflow of liquid and under its bottom was measured. The values of the wall shear stress and its pulsations were measured by the electrodiffusion method depending on a distance from the bubble nose. It is shown that in a liquid film around a bubble, turbulent pulsations are damped in comparison with a single-phase liquid flow. In the bottom part of a bubble, where vortices are detached, turbulent pulsations exceed significantly the single-phase ones.

1   Introduction

The slug flow of gas-liquid mixture takes place in a wide range of liquid and gas flow rates. It is characterized by the motion of liquid slugs separated by gas Taylor bubbles. The investigation of slug flow is important for the development of modern heat and mass exchange apparatus, power engineering and nuclear industry.

An intensive investigation of the slug flow structure in a scientific literature shows the great interest for such type of flows [1-7]. The gas phase characteristics were presented firstly: the Taylor bubble length distribution, it rise velocities and bubble alternation. The bubble rise velocity in stagnant flow is presented in [1]. The interaction between two consecutive Taylor bubbles in a vertical pipe was investigated in [2]. It is shown that the velocity of the trailing bubble is higher that the leading bubble one. This effect is caused by the trailing bubble nose deformation and decreasing of this bubble hydraulic resistance in the leading bubble wake. Statistical characteristics of the slug flow are presented in [3, 4].

The liquid phase characteristics are of a great interest for engineering purposes. The modern experimental technique allows determination of the liquid velocity vectors, the turbulence structure of the flow, the liquid layer thickness under the bubble and wall shear stress. The structure of the liquid flow around single Taylor bubble rising in the pipe is presented in [5] using PIV method. The experimental study of the hydrodynamic characteristics of upward slug flow was conducted in [6, 7] using electrodiffusional technique.

In the continuous slug flow these local averaged and pulsation characteristics of the liquid phase can be obtained with ensemble averaging technique. Such approach

allows to determine only average values of the flow parameters and does not allow to obtain the dependency of fluctuational characteristics of the flow in relation to the axial coordinate for an arbitrary slug.

The investigation of the characteristics of distribution of phases relative to the distance from the bubble nose is also of significant interest. To perform such studies either the Taylor bubble or its simulator was maintained in the downward liquid flow, the origin of the bubble was fixed by gas nozzle or the holder. Such studies were performed by Delfos et. al. [8] to determine the gas entrainment from the stationary slug in downward liquid flow and by Kockx et. al. [9] to investigate the flow structure in the liquid film around the gas slug.

The flow structure near the pipe wall over a stationary Taylor bubble in the downward liquid flow is presented in this paper. Investigation of this object allows to determinate fluctuating characteristics of the flow and wall shear stress coefficients when the distance from the bubble nose is precisely defined. The Taylor bubble with surrounded liquid slugs is a 'single cell' of a downward slug flow. The stationary Taylor bubbles appear in the regime of "gas hanging" in which the rise velocity of the bubble is equal to the average velocity of liquid. The Taylor bubble rise velocity was evaluated by formula:

$$U_0 = 0.35\sqrt{gD}, \tag{1}$$

were U_0 is the Taylor bubble rise velocity, D is the diameter of the pipe and g is the acceleration due to gravity.

2 Experimental Setup

The flow structure was studied using an electrodiffusonal technique [10]. Miniature wall shear stress probes were used. Experiments were made in a vertical pipe 20 mm i.d. Experiments were performed when the liquid temperature was 25^0 C. The temperature was maintained by the controlling system. The physical properties of the test liquid in our experiments were similar to the distilled water. To produce the Taylor bubble, the gas was supplied to the flow through a capillary tube centered relatively channel axis. The bubble length was varied by changing the gas flow rate. In order to measure the distribution of wall shear stress along the bubble the point of gas injection was traversed along the tube. The Taylor bubble length was determined by video processing. To avoid an optical distortions glass tube was mounted in the square box filled with immersion liquid. The estimated error of measurements was 7 % for the wall shear stress and 3 % for the Taylor bubble lehgth.

3 Results and Discussion

A Taylor bubble length effect on the wall shear stress τ was investigated at first (Figure 1). Here X is the distance from the bubble nose. The negative values of X correspond to the single phase region up to the bubble nose. The bubble length was varied in the range of 10÷120 millimeters. Single-phase wall shear stress values were detected at 30 mm upward the bubble nose. The wall shear stress increases
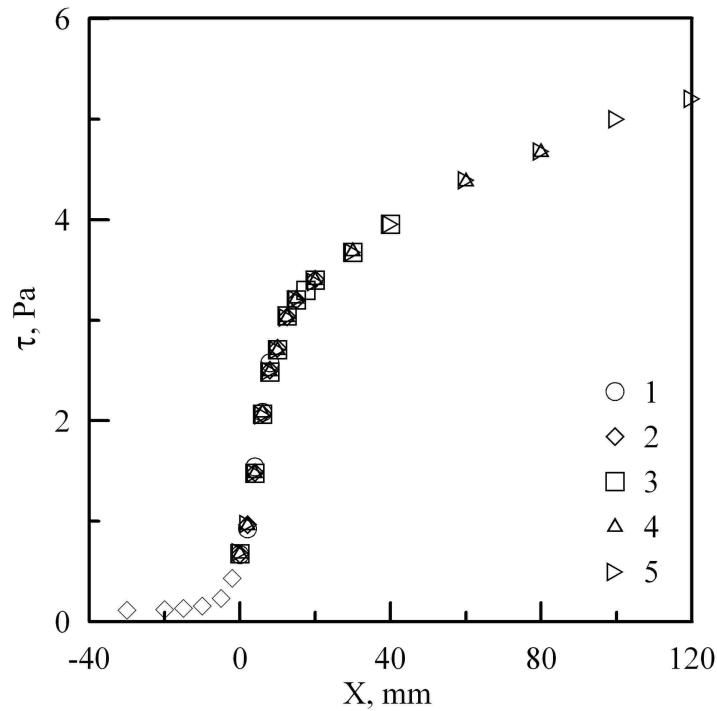
Figure 1: A Taylor bubble length effect on the wall shear stress: 1 – L=20 mm, 2 – L=40 mm, 3 – L=60 mm; 4 – L=80 mm; 5 – L=120 mm.

while approaching the bubble nose. The streamlines modification and the liquid velocity increase at this region were shown in previous experimental and theoretical works of other authors [5, 11]. In the region of the slug nose a sharp increase of wall shear stress takes place. It happens because the slug nose has a spherical shape and the liquid film thickness decreases significantly while the flow rate remains constant. Around the slug the liquid film thickness and the wall shear stress changes smoothly. The study of wall shear stress distribution for long slugs was also performed in this study. Fig. 2 shows the value of wall shear stress for a slug 500 mm long. The values of wall shear stress increases up to the distance from the slug nose of about 200 mm. At this distance from the bubble nose the flow around the bubble is stabilized and does not depend on X. A good agreement is observed in this region with the wall shear stress values calculated from the limiting film thickness given by the formula [12]:

$$\sigma = \left[\frac{3\nu V_L}{2g} \left(\frac{D}{2} - \sigma \right) \right]^{1/3}, \tag{2}$$

were σ is the film thickness, ν is the kinematic viscosity of liquid, V_L – is the velocity of the liquid. The establishment of stabilized thickness of the liquid film around the slug was shown also in [9]. The model accounting for the intensity of surface waves to determine the thickness of the liquid layer flowing around the slug was also presented in this paper. The model describes satisfactory the data presented.
Electrodiffusional technique allows investigating the turbulence structure of the flow near the pipe wall. It was shown in our work that the structure of the probe signal
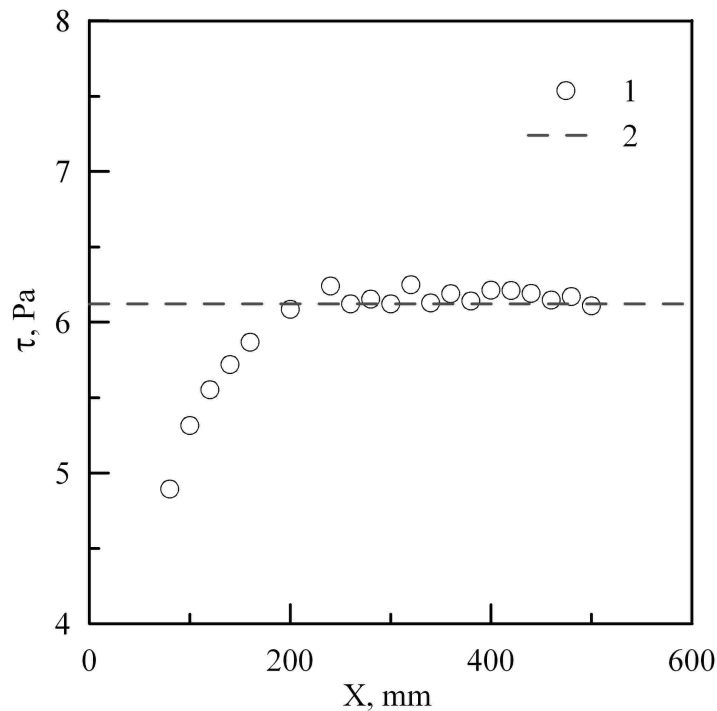
Figure 2: The wall shear stress in the stabilized film zone: dots – experiment; dashed line – eq. 2.

is strongly depending on the region of the flow (Figure 3). At the initial region of the bubble, reduction of turbulence fluctuations of the flow is observed. The liquid velocity acceleration in the liquid film around the bubble is the reason of this trend. High wall shear stress values and low values of its fluctuations compared to a single phase flow were recorded in the region behind the gas slug (Figure 3a). In the stabilized liquid film an increasing of turbulence fluctuations is observed. The bubble bottom oscillation result in a quasi periodical alternation of regions with high and low levels of fluctuations detected in the liquid downstream the bubble bottom in an annular vortex zone of the flow (Figure 3b). The disturbance of the wall shear stress, the wall shear stress fluctuations produced by the Taylor bubble in compare to the single phase values holds for the distance of more than 20 tube diameters from the bubble bottom.

4   Conclusions

The investigation of the hydrodynamics of a single stationary gas slug in downward liquid flow was performed along with the flow structure behind the slug bottom. The information on the fluctuational structure of the flow around the slug was obtained. This information can hardly be obtained in real slug flow. It was shown that the flow disturbance starts at the distance of about 20 mm before the slug due to the deformation of liquid flow by the slug. The shear stress at the tube wall increases and its relative fluctuations decrease. In the liquid film around the slug the wall
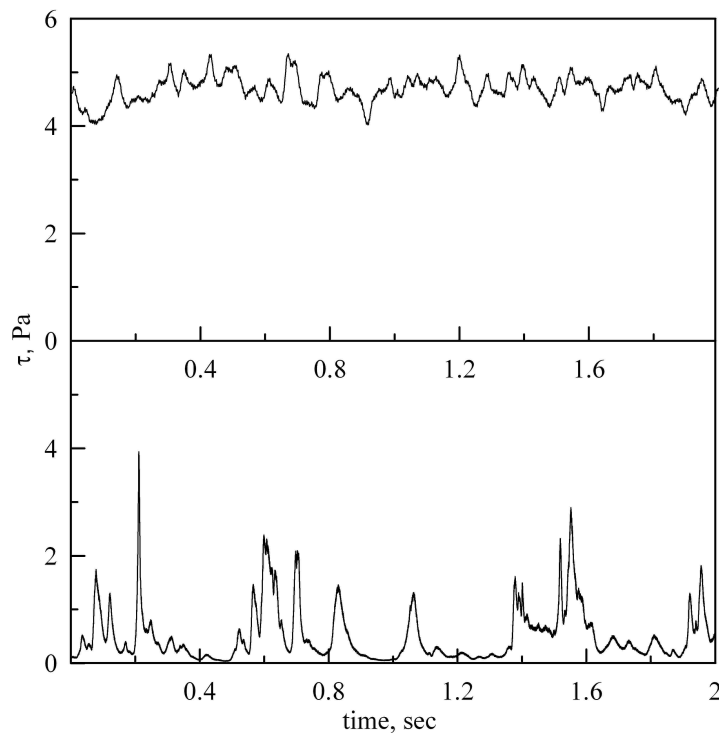
Figure 3: Wall shear stress probe signal: a— in the central part of bubble; b— in the vortex zone behind the bubble bottom.

shear stress may be several tens of times higher than the single phase value, the flow laminarization takes place due to the liquid acceleration. It was shown that the wall shear stress around the bubble depends on the distance from the slug nose and is independent of the slug length. A complex flow structure was observed behind the slug bottom which is characterized by the alternation of regions with high wall shear stress and its fluctuations and the regions with low values of these parameters. The flow perturbation by the single gas slug propagates at the distance of more than 20 pipe diameters.

Acknowledgements

References

[1] Nicklin D.J., Wilkes M.A., Davidson J.F. Two-phase flow in vertical tubes. Trans. Inst. Chem. Eng. 1962. Vol. 40. pp. 61-68.

[2] Aladjem Talvy C., Shemer L., Barnea D. On the interaction between two consecutive elongated bubbles in a vertical pipe. Int. J. Multiphase Flow. 2000. Vol. 26. pp. 1905-1923.

[3] Van Hout R., Barnea D., Shemer L. Evolution of statistical parameters of gas-liquid slug flow along vertical pipes. Int. J. Multiphase Flow. 2001. Vol. 27. pp. 1579-1602.

[4] Shemer L. Hydrodynamic and statistical parameters of slug flow. Int. J. Heat and Fluid Flow. 2003. Vol. 24. pp. 334-344.

[5] S. Nogweira, R.G. Sousa, A.M.F.R. Pinto, M.L. Riethmuller, J.B.L.M. Campos, Simultaneous PIV and pulsed shadow technique in slug flow: a solution for optical problems. Experiments In Fluids. 2003. Vol. 35 pp. 598-609.

[6] Nakoryakov V.E., Kashinsky O.N., Kozmenko B.K. Experimental study of gas-liquid slug flow in a small-diameter vertical pipe. Int. J. Multiphase Flow. 1986. Vol. 12. pp. 337-355.

[7] Nakoryakov V.E., Kashinsky O.N., Petukhov A.V., Gorelic R.S. Study of local hydrodynamic characteristics of upward slug flow. Exp. In Fluids. 1989. Vol. 7. pp. 560-566.

[8] Delfos R., Wisse C.J., Oliemans R.V.A. Measurement of air-entrainment from a stationary Taylor bubble in a vertical tube. Int. J. Multiphase Flow. 2001. Vol. 27. pp. 1769-1787.

[9] Kockx J.P., Nieuwstadt F.T.M., Oliemans R.V.A., Delfos R. Gas entrainment by a liquid film falling around a stationary Taylor bubble in a vertical pipe. Int. J. Multiphase Flow. 2005. Vol. 31. pp. 1-24.

[10] Nakoryakov V.E., Kashinsky O.N., Burdukov A.P., Odnoral V.P. Local characteristics of upward gas-liquid flows. Int. J. Multiphase Flow. 1981. V. 7. pp. 63-81.

[11] Zheng D., He X., Che D. CFD simulations of hydrodynamic characteristics in a gas–liquid vertical upward slug flow. Int. J. Heat Mass Transfer. 2007. Vol. 50. pp. 4151-4165.

[12] Batchelor G.K. An introduction to fluid dynamics. Cambridge University Press, 1999. p. 615.

Kutateladze Insitute of Thermophysics SB RAS, 630090, Akad. Lavrent'ev Avenue, 1, Novosibirsk, Russia

Longitudinal permeability of porous fibrous medium for the power-law fluid flow

Piotr Kedzia

piotr.m.kedzia@doctorate.put.poznan.pl

Abstract

In the paper a flow of the power-law fluid along the regular cluster of fibres is considered. The results were obtained by a fundamental solution method for Newtonian fluid. The solution for velocities of non-Newtonian fluid flow was achieved by the iteration process . In a consequence, permeability decreases when the radius of fibres increases.

1   Introduction

The fluid flow in porous media is observed in many situations like geology, medicine, industry and so on. Especially, fluid flow in fibrous media is very important. Examples of applications of fluid flow through porous fibrous media are given in papers [2, 5, 6]. This paper deals with a non-Newtonian fluid flow in such media. The power-law model for fluid is considered.

The governing equation of power-law fluid flow may be written in the form of a nonlinear equation. The velocity profile of the fluid flow has been obtained by three methods: the method of fundamental solution, the radial basis function and the Picard iteration method. If the velocity profile is known, it is easy to find the permeability of porous fibrous media for power-law fluid flow.

2   Newtonian fluid flow

Let us consider the regular cluster of infinite fibres of radius R and distance between them $2a$. Suppose that z axis is the parallel to axis of fibre. The problem has the symmetry, hence we restrict to the area shown in Fig. (1).

The Navier-Stokes equations, that govern the Newtonian fluid flow of the viscous fluid are as follows:

$$
\begin{aligned}
\frac{\partial u}{\partial t} + u\frac{\partial u}{\partial x} + v\frac{\partial u}{\partial y} + w\frac{\partial u}{\partial z} &= -\frac{1}{\rho}\frac{\partial p}{\partial x} + \frac{\mu_0}{\rho}\left(\frac{\partial^2 u}{\partial x^2} + \frac{\partial^2 u}{\partial y^2} + \frac{\partial^2 u}{\partial z^2}\right), \\
\frac{\partial v}{\partial t} + u\frac{\partial v}{\partial x} + v\frac{\partial v}{\partial y} + w\frac{\partial v}{\partial z} &= -\frac{1}{\rho}\frac{\partial p}{\partial y} + \frac{\mu_0}{\rho}\left(\frac{\partial^2 v}{\partial x^2} + \frac{\partial^2 v}{\partial y^2} + \frac{\partial^2 v}{\partial z^2}\right), \\
\frac{\partial w}{\partial t} + u\frac{\partial w}{\partial x} + v\frac{\partial w}{\partial y} + w\frac{\partial w}{\partial z} &= -\frac{1}{\rho}\frac{\partial p}{\partial x} + \frac{\mu_0}{\rho}\left(\frac{\partial^2 w}{\partial x^2} + \frac{\partial^2 w}{\partial y^2} + \frac{\partial^2 w}{\partial z^2}\right),
\end{aligned}
\tag{1}
$$
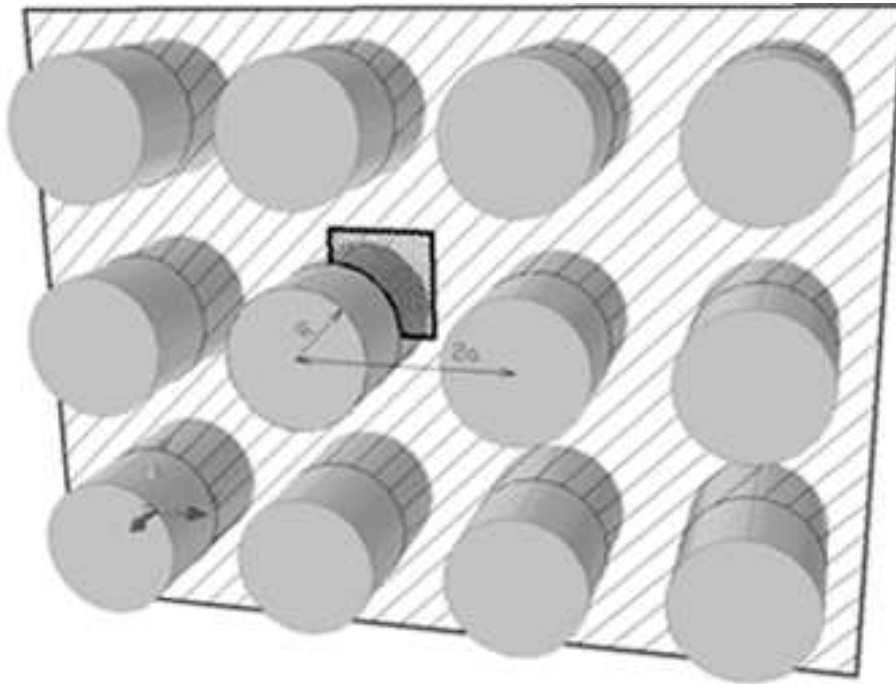
Figure 1: Geometry of the problem.

where (u, v, w) is the velocity vector, p is the fluid pressure, ρ is the density and μ_0 is the dynamic viscosity. Suppose, that fluid is noncompressible, so

$$\frac{\partial u}{\partial x} + \frac{\partial v}{\partial y} + \frac{\partial w}{\partial z} = 0. \tag{2}$$

Our aim is now to find the flow along the fibres. Hence two elements of the velocity vector are 0. Let us assume, that nonzero element is w. If the flow is steady, then the equations (1-2) are as follows

$$
\begin{aligned}
0 &= -\frac{1}{\rho}\frac{\partial p}{\partial x}, \\
0 &= -\frac{1}{\rho}\frac{\partial p}{\partial y}, \\
w\frac{\partial w}{\partial z} &= -\frac{1}{\rho}\frac{\partial p}{\partial x} + \frac{\mu_0}{\rho}\left(\frac{\partial^2 w}{\partial x^2} + \frac{\partial^2 w}{\partial y^2} + \frac{\partial^2 w}{\partial z^2}\right)
\end{aligned}
\tag{3}
$$

and

$$\frac{\partial w}{\partial z} = 0. \tag{4}$$

From (3) and (4) we have

$$\frac{\partial^2 w}{\partial x^2} + \frac{\partial^2 w}{\partial y^2} = \frac{1}{\mu_0}\frac{dp}{dz}, \tag{5}$$

where the right hand side is the ordinary derivative, because the pressure p does not depend on x and y (see first two equations in (3)).

The boundary conditions for problem (5) result from Fig. (2) as follows:
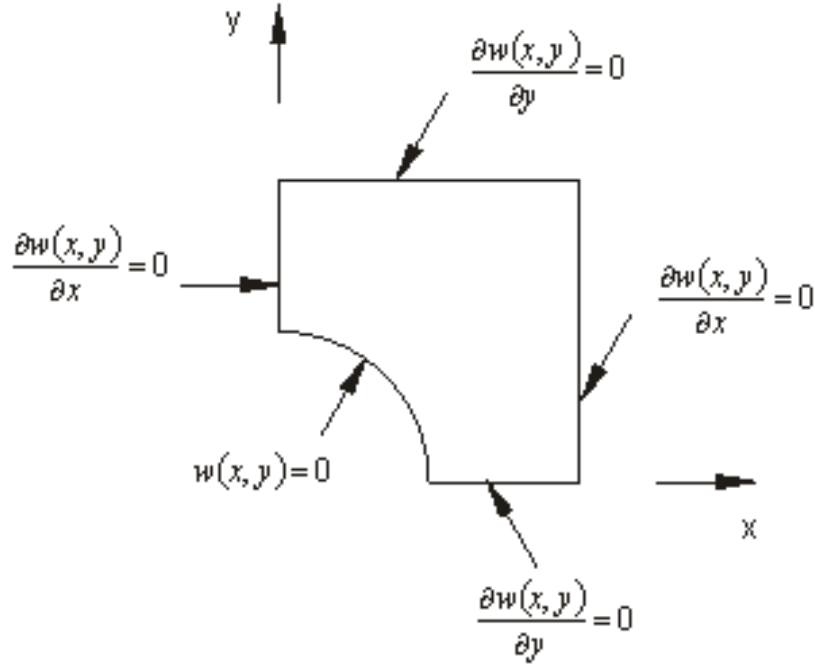
Figure 2: Boundary conditions.

1. $w(x, y) = 0$ for $\Gamma : x^2 + y^2 = R^2$ (the boundary of the fibre),

2. $\dfrac{\partial w(x, y)}{\partial x} = 0$ for $x = 0$ and $x = a$ (the left hand side and the right hand side of the area),

3. $\dfrac{\partial w(x, y)}{\partial y} = 0$ for $y = 0$ and $y = a$ (the bottom side and the top side of the area).

Let us introduce the dimensionless variables:

$$X = \frac{x}{a}, \ Y = \frac{y}{a}, \ W(X, Y) = -\frac{w(x, y)}{\frac{a^2}{\mu_0} \frac{dp}{dz}}, \tag{6}$$

so that, Eq. (5) can be rewritten to the form

$$\frac{\partial^2 W}{\partial X^2} + \frac{\partial^2 W}{\partial Y^2} = -1. \tag{7}$$

The dimensionless boundary conditions are as follows:

1. $W(X, Y) = 0$ for $\tilde{\Gamma} : X^2 + Y^2 = \dfrac{R^2}{a^2}$ (the boundary of the fibre),

2. $\dfrac{\partial W(X, Y)}{\partial X} = 0$ for $X = 0$ and $X = 1$ (the left hand side and the right hand side of the area,
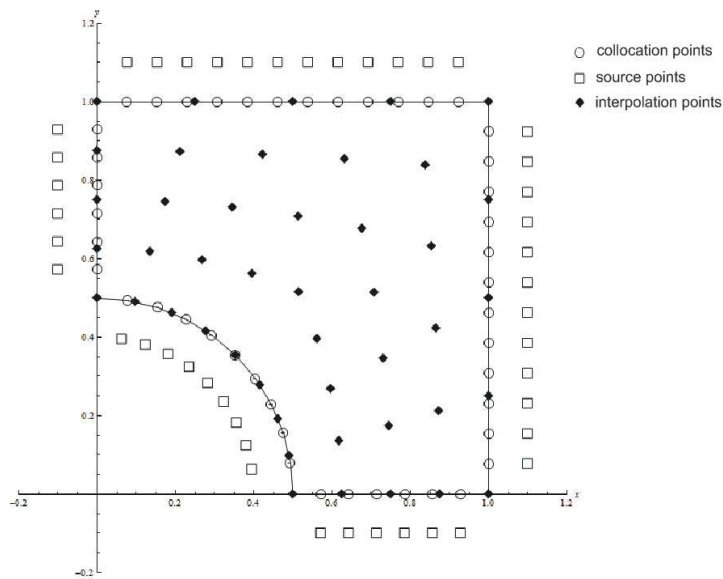
Figure 3: Collocation, source and interpolation points.

3. $\dfrac{\partial W(X, Y)}{\partial Y} = 0$ for $Y = 0$ and $Y = 1$ (the bottom side and the top side of the area).

The solution of (7) has been obtained by the method of fundamental solution (MFS) and reads

$$W(X, Y) = \sum_{j=1}^{N} c_j \ln \sqrt{(X - X_j)^2 + (Y - Y_j)^2} - \frac{1}{4} \left(X^2 + Y^2 \right). \tag{8}$$

c_j coefficients are determined with the help of the boundary collocation method with N collocation points. The collocation and source points are generated during calculations. The source, collocation and interpolation points are presented in Fig. (3).

3   Non-Newtonian fluid flow

In the case of the non-Newtonian fluid, the dynamic viscosity is not constant. In this paper the power-law fluid model has been used with the viscosity in the form:

$$\mu(\gamma) = \beta \gamma^{n-1}, \tag{9}$$

where β is the consistency factor, n is the power-law index and

$$\gamma = \sqrt{\left(\frac{\partial w}{\partial x} \right)^2 + \left(\frac{\partial w}{\partial y} \right)^2}. \tag{10}$$

The equation of motion for the power-law fluid then reads

$$\frac{\partial}{\partial x} \left[\mu(\gamma) \frac{\partial w}{\partial x} \right] + \frac{\partial}{\partial y} \left[\mu(\gamma) \frac{\partial w}{\partial y} \right] = \frac{dp}{dz}. \tag{11}$$

If we use dimensionless variables (6) and

$$E\left(\chi\right) = \frac{\mu\left(\gamma\right)}{\mu_0}, \quad B = \frac{\beta}{\mu_0}\left(\frac{a}{\mu_0}\frac{dp}{dz}\right)^{n-1}, \tag{12}$$

Eq. (11) can be written in the dimensionless form as

$$\frac{\partial}{\partial X}\left[E\left(\chi\right)\frac{\partial W}{\partial X}\right] + \frac{\partial}{\partial Y}\left[E\left(\chi\right)\frac{\partial W}{\partial Y}\right] = -1, \tag{13}$$

where

$$\chi = \frac{\gamma}{\frac{a}{\mu_0}\frac{dp}{dz}} = \sqrt{\left(\frac{\partial W}{\partial X}\right)^2 + \left(\frac{\partial W}{\partial Y}\right)^2}. \tag{14}$$

Finally, from (13) it can be written as follows

$$\frac{\partial^2 W}{\partial X^2} + \frac{\partial^2 W}{\partial Y^2} = -\frac{1}{B}\chi^{1-n} - (n-1)\xi, \tag{15}$$

where

$$\xi = \frac{\left(\frac{\partial W}{\partial X}\right)^2\frac{\partial^2 W}{\partial X^2} + 2\frac{\partial W}{\partial X}\frac{\partial W}{\partial Y}\frac{\partial^2 W}{\partial X\partial Y} + \left(\frac{\partial W}{\partial Y}\right)^2\frac{\partial^2 W}{\partial Y^2}}{\left(\frac{\partial W}{\partial X}\right)^2 + \left(\frac{\partial W}{\partial Y}\right)^2}. \tag{16}$$

The dimensionless boundary conditions are the same as for Newtonian fluid flow. The solution of Eq. (15) has been obtained using radial basis function (RBF) and MFS using the iteration process.

3.1   Algorithm steps

Step 1 Interpolation with multiquadrics
In the paper the multiquadrics function $\phi\left(r_i\right) = \sqrt{r_i^2 + c^2}$, with shape parameter $c = 0.001$ was chosen to interpolate the right hand side of Eq.(15). Interpolation function has the form

$$f\left(X, Y\right) = \sum_{i=1}^{NI} a_i\phi\left(r_i\right), \tag{17}$$

where NI is the number of the interpolation points and a_i are calculated during interpolation. In the first iteration the solution for the Newtonian fluid flow is used to interpolate the right hand side of Eq. (15). In other case the solution from the previous iteration is used.

Step 2 Current solution
The solution in the current step reads

$$W\left(X, Y\right) = \sum_{i=1}^{NI} a_i\psi\left(r_i\right) + \sum_{j=1}^{N} c_j \ln\sqrt{\left(X - X_j\right)^2 + \left(Y - Y_j\right)^2}. \tag{18}$$

c_j coefficients have been obtained with the help of the boundary collocation method.

Step 3 Algorithm is finished, if the maximum difference between values of the velocity in two sequence iterations is smaller than some value. In the other case, algorithm goes to Step 1 or stops after some number of iterations.

4 Permeability of the fibre structure

The permeability of the porous medium is described by the Darcy law in the form:

$$\frac{Q}{A} = -\frac{\kappa}{\mu}\frac{P_b - P_a}{L}, \tag{19}$$

where Q is the total discharge, κ is the permeability, A is the cross-section area, $P_b - P_a$ is the pressure drop over the length L. In this paper the Darcy law we assume as

$$q_z = -\frac{\kappa_\parallel}{\mu}\frac{dp}{dz}, \tag{20}$$

where q_z is the flux along z axis, $\kappa_\parallel$ is the permeability along the regular cluster of fibres.

The dimensionless average flow velocity has been obtained from the (18) by

$$W_A = \frac{\displaystyle\iint_A W(X, Y)\, dA}{\displaystyle\iint_A dA} = \frac{1}{A}\iint_A W(X, Y)\, dA. \tag{21}$$

According to Eq. (6) can be written

$$q_z = w_A = -W_A \frac{a^2}{\mu}\frac{dp}{dz}, \tag{22}$$

where w_A is the average flow velocity.
So that

$$-\frac{\kappa_\parallel}{\mu}\frac{dp}{dz} = -W_A \frac{a^2}{\mu}\frac{dp}{dz} \tag{23}$$

and in the consequence

$$\kappa_\parallel = W_A a^2. \tag{24}$$

Let's take the dimensionless permeability $\hat{\kappa}_\parallel$ as

$$\hat{\kappa}_\parallel = \frac{\kappa_\parallel}{a^2} = W_A. \tag{25}$$

Fig. (4) presents the behaviour of the dimensionless permeability for several values of n and dimensionless radius r.
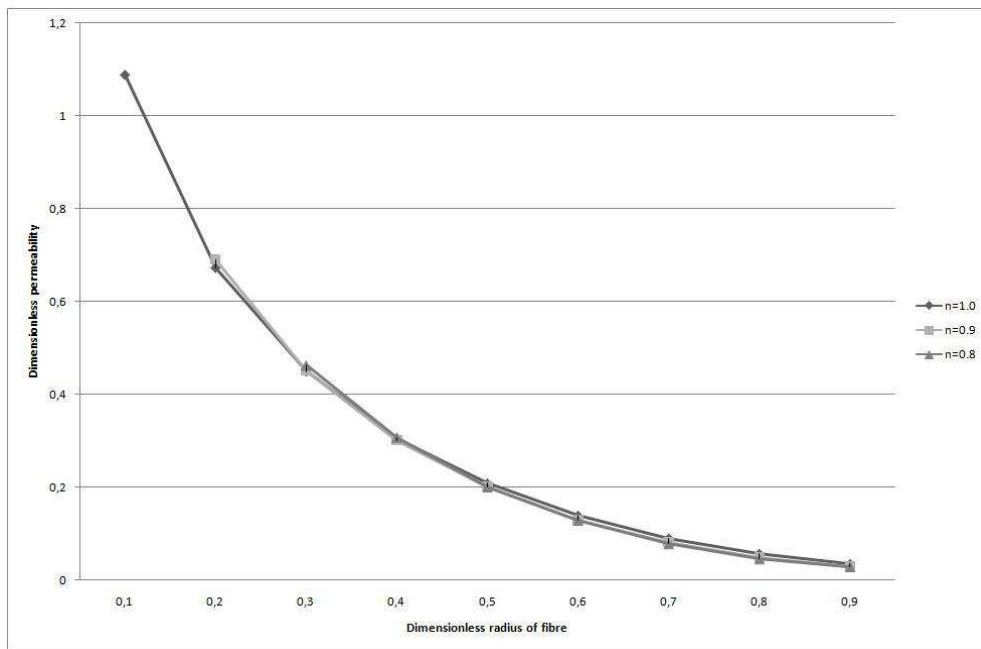
Figure 4: The dimensionless permeability for several values of n and dimensionless radius r.

The dimensionless permeability for several values of n along dimensionless radius r of the fibre is shown below, in Table 1. $\text{err}(n)$ is an error on the boundary.

Table 1. The dimensionless permeability.

r	n					
	1.0	$\text{err}(n)$	0.9	$\text{err}(n)$	0.8	$\text{err}(n)$
0.1	1.08771	$5.583 \cdot 10^{-12}$	—	—	—	—
0.2	0.67206	$9.014 \cdot 10^{-11}$	0.68932	$1.654 \cdot 10^{-10}$	—	—
0.3	0.44901	$9.865 \cdot 10^{-10}$	0.45028	$1.470 \cdot 10^{-9}$	0.46273	$1.614 \cdot 10^{-9}$
0.4	0.30494	$2.964 \cdot 10^{-14}$	0.30062	$1.914 \cdot 10^{-11}$	0.30702	$2.244 \cdot 10^{-11}$
0.5	0.20775	$2.963 \cdot 10^{-12}$	0.20016	$1.535 \cdot 10^{-14}$	0.19993	$6.370 \cdot 10^{-11}$
0.6	0.13841	$1.224 \cdot 10^{-12}$	0.12813	$2.059 \cdot 10^{-12}$	0.12780	$1.531 \cdot 10^{-10}$
0.7	0.08953	$3.419 \cdot 10^{-13}$	0.08048	$1.159 \cdot 10^{-11}$	0.07720	$2.322 \cdot 10^{-11}$
0.8	0.05597	$5.535 \cdot 10^{-13}$	0.04875	$1.039 \cdot 10^{-12}$	0.04470	$2.378 \cdot 10^{-12}$
0.9	0.03431	$8.947 \cdot 10^{-13}$	0.02921	$4.821 \cdot 10^{-11}$	0.02748	$1.847 \cdot 10^{-14}$

5   Concluding remarks

In this paper the new method of solution of the problem of power-law fluid flow along the regular cluster of fibres has been presented. Firstly the velocity profile was found for the Newtonian fluid flow. In the consequence the permeability of porous fibrous media along the cluster of fibres has been obtained.

The iteration process called the Picard iteration method has been used. The convergence was achieved for dimensionless radius r higher than 0.3. Some results have been obtained for smaller radius, as well.

Acknowledgements

References

[1] Woods J.K., Spelt P.D.M., Lee P.D., Selerland T., Lawrence C.J., Creeping flows of power-law fluids through periodic arrays of elliptical cylinders, *J. Non-Newtonian Fluid Mech.* **111** (2003) 211-228.

[2] Vijaysri M., Chhabra R.P., Eswaran V., Power-law fluid flow across an array of infinite circular cylinders: a numerical study, *J. Non-Newtonian Fluid Mech.* **87** (1999) 263-282.

[3] Liu T-J., Fully developed flow of power-law fluids in ducts. *Industrial Engineering Chemical Fundations,* **22** (1988) 183-186.

[4] Liu G.R., Mesh Free Methods, *CRC Press*, Boca Raton, 2003.

[5] Tamayol A., Bahrami M., Analytical determination of viscous permeability of fibrous porous media, *Int. J. of Heat and Mass Transfer*, **52** (2009) 2407-2414.

[6] Zhong W.H., Currie I.G., James D.F., Creeping flow through a model fibrous porous medium, *Experiments in fluids,* **40** (2006) 119-126.

[7] Vakilha M., Manzari M.T., Modeling of Power-law Fluid Flow Through Porous Media Using Smoothed Particle Hydrodynamics, *Transp Porous Med* **74** (2008) 331-346.

[8] Kolodziej J.A., Review of application of boundary collocation methods in mechanics of continuum media, *Solid Mechanics Archives*, **12** (1987) 187-231.

[9] Drummond J.E., Tahir M.I., Laminar viscous flow through regular arrays of parallel solid cylinders, *Int. J. Multiphase Flow,* **10** (1984) 515.

Piotr Kedzia, Poznan University of Technology, Institute of Applied Mechanics, Piotrowo 3, 60-965 Poznan, Poland

Equilibrium forms of the free surface of nonlinearly viscous band under uniaxial tension

Ilya Keller

kie@icmm.ru

Abstract

Large deformations in metal specimens under uniaxial tension in conditions of high-temperature creep and especially of superplasticity are accompanied by the macroscopic second-order surface effects [1-4]. At the free surface of a specimen under deformation one can observe multiple formations of stationary and movable necks with small fixed amplitudes. To our knowledge, no systematic study has been made to gain insight into this phenomenon although the problem is of considerable practical importance. An important point is that the specific nature of the free surface shape evolution, during which the surface disturbances are "frozen", provides stability of the specimen tension process up to abnormally high values. Investigation of conditions responsible for initiation and sustaining of such regimes may lead to a new method of classification and identification of viscoplastic constitutive relations, going beyond the limits of the specimen principle, and to formulation of the superplasticity definition conceivable for mechanicians

This work is concerned with the problem of an infinite nonlinear-viscous band with free lateral boundaries under quasi-static tension, i.e. "necking" problem. The nonlinear rheological relations of Reiner-Rivlin fluid are taken as the constitutive ones. Stability of the straight-line free boundaries of such a band is studied in work [5]. In this work, equilibrium curvilinear free boundary contours are found. Evolution of small axially symmetric disturbances of straight-line free boundaries is investigated by the method of a small parameter. The first term in uniformly convergent asymptotic series satisfies the non-autonomous linear equations of the parabolic type including an arbitrary quantity $\mathfrak{m}$, which is a parameter of material sensitivity to the strain rate. Using the equivalent (leaving the structure of the Lie algebra unchanged) time inverting transformations, this equation, independently from the arbitrary element, can be reduced to a linear heat conduction equation, which has an infinite dimensional algebra of point symmetries. The self-similar stationary solutions of localized and distributed character found exist in some ranges of the parameter $\mathfrak{m}$, which provide the balance between kinematic and physical nonlinearities. The stability of these solutions has not been determined.

The equilibrium of nonlinear-viscous band under quasi-static uniaxial tension is governed by the following equations:

$$\sigma_{x,x} + \tau_{xy,y} = 0, \qquad \tau_{xy,x} + \sigma_{y,y} = 0, \tag{1}$$

$$\sigma_x = -p + \tau\xi^{-1}u_{,x}, \quad \sigma_y = -p - \tau\xi^{-1}u_{,x}, \quad \tau_{xy} = \tau\xi^{-1}(u_{,y}+v_{,x})/2, \quad (2)$$

$$u_{,x} + v_{,y} = 0, \qquad\qquad\qquad\qquad\qquad\qquad\qquad\qquad\qquad (3)$$

where x, y are the Cartesian orthogonal coordinates (x-axis coincides with the band axis), $\sigma_x, \sigma_y, \tau_{xy}$ are the components of the stress tensor, p is hydrostatic pressure, u, v are the components of the displacement rate along the x and y coordinates, $\tau = \sqrt{(\sigma_x - \sigma_y)^2 + 4\tau_{xy}^2}$ and $\xi = \sqrt{(u_{,x})^2 + \frac{1}{4}(u_{,y}+v_{,x})^2}$ are the stress and the strain rate intensities energetically conjugated in a two-dimensional case, the comma denotes partial derivative. The material function $\tau(\xi)$ is supposed to be an arbitrary element determining the form of a solution for the shape of the free boundary of the band in tension.

At the current time, the basic motion, which is that of uniform tension of a band along the generating line with the deformation rate ξ_0, is given by

$$b_{,t} = -\xi_0 b, \qquad\qquad\qquad\qquad\qquad\qquad\qquad\qquad\qquad (4)$$

where b is the current transverse dimension of the undisturbed band. Disturbances of the rectilinear free boundaries are assumed to be symmetric with respect to the axial line which allows us to consider only one boundary: $y(x, t) = b(t) + \eta(x, t)$, where $\eta < 0$ is the boundary disturbances. Using an implicit form of the equation $g = b + \eta - y \equiv 0$ we can write the components of the external normal $n_x = g_{,x}/|\nabla g| = \eta_{,x}/|\nabla g|$, $n_y = g_{,y}/|\nabla g| = -1/|\nabla g|$ to the free boundary and the static boundary conditions

$$\eta_{,x}\sigma_x - \tau_{xy} = 0, \quad \eta_{,x}\tau_{xy} - \sigma_y = 0. \qquad\qquad\qquad\qquad (5)$$

Using (4) and the definitions $dx/dt \equiv u, dy/dt \equiv v$ (d/dt denotes time derivative respectively a fixed material particle), the kinematic condition at the free boundary $dg/dt = 0$, implying its materiality, is written as

$$\eta_{,t} + u\eta_{,x} - v - \xi_0 b = 0. \qquad\qquad\qquad\qquad\qquad\qquad (6)$$

This condition introduces a time derivative into the examined problem which means that the band under quasistatic tension can be in equilibrium at certain evolution of its free boundaries. Let us consider the disturbances vanishing at infinitely distant band ends

$$\eta(x \to \pm\infty) \to 0. \qquad\qquad\qquad\qquad\qquad\qquad\qquad (7)$$

Substitution of (2) and (3) into (1) leads to the equilibrium equations expressed in terms of the displacement rates

$$\tau^{-1}\xi p_{,x} - (m-1)\xi^{-1}[\xi_{,x}u_{,x} + \xi_{,y}(u_{,y}+v_{,x})/2] - u_{,xx} - (u_{,yy}-u_{,xx})/2 = 0,$$
$$\tau^{-1}\xi p_{,y} - (m-1)\xi^{-1}[\xi_{,y}u_{,x} + \xi_{,x}(u_{,y}+v_{,x})/2] + u_{,xy} - (u_{,xy}+v_{,xx})/2 = 0,$$
$$\xi_{,x} = \xi^{-1}[u_{,x}u_{,xx} + (u_{,y}+v_{,x})(u_{,xy}+v_{,xx})/4],$$
$$\xi_{,y} = \xi^{-1}[u_{,x}u_{,xy} + (u_{,y}+v_{,x})(u_{,yy}-u_{,xy})/4],$$

316

where $\tau'\xi/\tau = d\ln\tau/d\ln\xi \equiv m$ is the sensitivity to the strain rate. This quantity is constant for the power law $\tau(\xi)$. At small disturbances all coefficients at highest derivatives in the equations above written are assumed to be constants corresponding to the basic motion. So, in the expressions for these coefficients it is necessary that $u_{,y} = v_{,x} = 0$, $u_{,x} = \xi_0$ so that the system reduces to

$$2\tau^{-1}\xi p_{,x} - (2m-1)u_{,xx} - u_{,yy} = 0, \quad 2\tau^{-1}\xi p_{,y} + (2m-1)u_{,xy} - v_{,xx} = 0. \quad (8)$$

Following the method commonly used for treatment of the layer or band problem [6, 7], the unknown fields are represented in the form of power series in the transverse coordinate

$$p = \sum_{n=0}^{\infty} p_n(x)y^n, \; u = \psi_{,y} = \sum_{n=1,3,}^{\infty} n\psi_n(x)y^{n-1}, \; v = -\psi_{,x} = -\sum_{n=1,3,}^{\infty} \psi'_n(x)y^n, \quad (9)$$

which take into account the axial symmetry of the disturbed velocity field, and ψ is the stream function. In the first terms of the series the basic motion and the disturbance components are distinguished

$$p_0 = -\tau_0 + \pi, \quad \psi_1 = \xi_0 x + \phi \quad (10)$$

where $\tau_0 = \tau(\xi_0)$. System (8), using (9)-(10), imposes constraints on the functions p_n, ψ_n

$$y^0: \quad \kappa\pi_{,x} - (2m-1)\phi_{,xx} - 6\psi_3, \quad p_1 = 0;$$
$$y^1: \quad p_{1,x} = 0 \quad 2\kappa p_2 + 6(2m-1)\psi_{3,x} + \phi_{,xxx};$$
$$y^2: \quad \kappa p_{2,x} - 3(2m-1)\psi_{3,xx} - 60\psi_5, \quad p_3 = 0;$$
$$y^3: \quad p_{3,x} = 0 \quad 4\kappa p_4 + 20(2m-1)\psi_{5,x} + \psi_{3,xxx}$$

etc. ($\kappa \equiv 2\tau_0^{-1}\xi_0$), which allow these functions to be resolved in terms of π and ϕ

$$p = -\tau_0 + \pi + \tau_0\xi_0^{-1}(2m-1)my^2\phi_{,xxx} - (2m-1)/2y^2\pi_{,xx} + O(y^4),$$
$$u = \xi_0 x + \phi - (2m-1)/2y^2\phi_{,xx} + \xi_0\tau_0^{-1}y^2\pi_{,x} + O(y^4), \quad (11)$$
$$v = -\xi_0 y - \phi_{,x}y + (2m-1)/6y^3\phi_{,xxx} + \xi_0\tau_0^{-1}/3y^3\pi_{,xx} + O(y^5).$$

In the following, the terms, having higher order of smallness than the explicitly written terms, are omitted. Their retention leads to appearance of additional dispersion terms in the equation of free boundary evolution.

Expressions (11) are substituted into boundary conditions (5), (6) bearing in mind that at the free surface $y = b + \eta$. Non-dimensionalization of the variables

$$x = b\overline{x}, \; \eta = b\overline{\eta}, \; y = b(1+\overline{\eta}), \; t = \xi_0^{-1}\overline{t}, \; \phi = \xi_0 b\overline{\phi}, \; \pi = \tau_0\overline{\pi},$$

leads to a system of the boundary equations for three unknown functions $\eta(x,t), \phi(x,t), \pi(x,t)$ (the overscribed bar is dropped):

$$\eta_{,x}(2 - \pi + \phi_{,x}) + m(1+\eta)\phi_{,xx} - (1+\eta)\pi_{,x} = 0,$$
$$m\eta_{,x}(1+\eta)(\phi_{,xx} + \pi_{,x}) - \phi_{,x} + \pi = 0, \quad (12)$$
$$\eta_{,t} + \eta_{,x}[x + \phi + (2m-1)/2(\pi_{,x} - \phi_{,xx})(1+\eta)^2] + \eta +$$
$$\quad + (1+\eta)\phi_{,x} + (1+\eta)^3(1/3\pi_{,xx} - (2m-1)/2\phi_{,xxx}) = 0.$$

At small disturbances this system reduces by the multiscale method to a weakly nonlinear form [6,8], for which purpose the desired variables are represented in the form of series expansion in terms of the small parameter ε

$$\eta = \varepsilon^s \eta_0 + \varepsilon^{2s} \eta_1 + \ldots, \quad \phi = \varepsilon^q \phi_0 + \varepsilon^{2q} \phi_1 + \ldots, \quad \pi = \varepsilon^p \pi_0 + \varepsilon^{2p} \pi_1 + \ldots, \quad (13)$$

where $\eta_0, \phi_0, \pi_0, \eta_1, \phi_1, \pi_1$ are the functions of independent variables $x, t, \chi \equiv \varepsilon x, \tau \equiv \varepsilon t$, having order of ε^0. Taking $s = q = p = 1$ one obtains a meaningful model

$$2\eta_{0,x} + m\phi_{0,xx} - \pi_{0,x} = 0, \quad \pi_0 + \phi_{0,x} = 0, \quad (14)$$

$$\eta_{0,t} + x\eta_{0,x} + \eta_0 + \phi_{0,x} - \frac{2m-1}{6}\phi_{0,xxx} + \frac{1}{3}\pi_{0,xx} = 0, \quad (15)$$

$$2\eta_{1,x} + m\phi_{1,xx} - \pi_{1,x} = \frac{2m}{m+1}\eta_{0,x} + \frac{2(m+3)}{m+1}\eta_0\eta_{0,x}, \quad (16)$$

$$\pi_1 + \phi_{1,x} = -\phi_{0,\chi} - 2(\eta_{0,x})^2, \quad (17)$$

$$\eta_{1,t} + x\eta_{1,x} + \eta_1 + \phi_{1,x} - \frac{2m-1}{6}\phi_{1,xxx} + \frac{1}{3}\pi_{1,xx} = -\eta_{0,\tau} - x\eta_{0,\chi} - \quad (18)$$

$$-\phi_{0,\chi} - \frac{6m+1}{3(m+1)}\eta_{0,xx} - \eta_{0,x}\phi_0 + \frac{2}{m+1}\eta_0^2 - \frac{2m+1}{m+1}(\eta_0\eta_{0,x})_{,x}.$$

After using conditions (7), system (14)-(15) reduces to the following equations:

$$\eta_{0,t} + \kappa_1\eta_0 + x\eta_{0,x} + \kappa_2\eta_{0,xx} = 0, \quad \kappa_1 \equiv \frac{m-1}{m+1}, \quad \kappa_2 \equiv \frac{2m+1}{3(m+1)}, \quad (19)$$

$$\pi_0 = -\phi_{0,x} = \frac{2}{m+1}\eta_0. \quad (20)$$

Equation (19) admits a Lie point group with the infinitesimal operator $\omega \exp(t)\partial_x + \partial_t$, where ω is an arbitrary constant. The invariant $x - \omega \exp(t)$ of the operator leads to exponentially self-similar substitution

$$\eta_0 = f(\zeta), \quad \zeta \equiv x - \omega \exp(t). \quad (21)$$

In the basic motion, an arbitrary material point, having in the actual (disturbing) band configuration at time $t = 0$ the space coordinate x_*, will have the space coordinate $x = x_* \exp(t)$ at any subsequent time t. By assuming in (21) that $\omega = x_*$ one can readily show that the contour $f(\zeta)$ is stationary in the reference system ζ, moving as a rigid body with a material point located at the origin of coordinates, whereas with respect to the reference system ζ the *material* undergoes tension. Substitution of (21) leads to the equation for f

$$\kappa_2 f_{,\zeta\zeta} + \zeta f_{,\zeta} + \kappa_1 f = 0, \quad (22)$$

which by applying the transformations $f = \exp(-\frac{1}{4}\bar{\zeta}^2)\bar{f}$, $\zeta = \kappa_2^{1/2}\bar{\zeta}$ can be reduced to a standard form of the parabolic cylinder equation $\bar{f}_{,\bar{\zeta}\bar{\zeta}} - (\frac{1}{4}\bar{\zeta}^2 + \frac{1}{2} - \kappa_1)\bar{f} = 0$ [9].

A solution of this equation is conveniently expressed in terms of the confluent hyper-geometric function Φ, after which the solution of equation (22) takes the following form:

$$f(\zeta) = a \exp(-\frac{\zeta^2}{2\kappa_2})\Phi(\frac{1-\kappa_1}{2}, \frac{1}{2}, \frac{\zeta^2}{2\kappa_2}) + b\zeta \exp(-\frac{\zeta^2}{2\kappa_2})\Phi(\frac{2-\kappa_1}{2}, \frac{3}{2}, \frac{\zeta^2}{2\kappa_2}), \quad (23)$$

where $a(\chi, \tau)$, $b(\chi, \tau) \sim \varepsilon^0$. This solution at $\zeta \to \pm\infty$ has the asymptotic $f(\zeta) \sim \zeta^{-\kappa_1}$ [9]. Hence, at $m < -1$ or $m > 1$, when $\kappa_1 > 0$ and knowingly $\kappa_2 > 0$, the above solution meets the boundary conditions $f(\zeta \to \pm\infty) \to 0$, viz. we have a localized solution.

To ensure that the localized functions η_0, ϕ_0, π_0 describe the disturbances η, ϕ, π to an accuracy of orders ε^1, series (13) should converge uniformly, viz., the decreasing rate of the function η_1 should not be lower than that of η_0: $\eta_1 \sim \zeta^{-\delta}$ at $\zeta \to \pm\infty$, where $\delta \geq \kappa_1 > 0$. To this end, from the right-hand side of the equation for η_1 entering in (16)-(18) one needs to eliminate $\eta_{0,\tau}$ and $\chi\eta_{0,\chi}$, which leads to the solution $a(\chi, \tau) \equiv a$, $b(\chi, \tau) \equiv b$. This solution leaves open the question on stability of the localized solution (21),(23). To solve this problem it is necessary to consider the other terms of the series (13) and their dependence on slower variables.

A localized contour of the function $f(\zeta)$ is formed by a linear combination of the even $(a \neq 0, b = 0)$ and the odd $(a = 0, b \neq 0)$ components. Their asymptotic character is similar, so the symmetric disturbance case $(a = -1, b = 0)$ will be considered further. On the interval $m > 1$ a localized solution is of unimodal form (fig. 1, a) whereas in the limit $m \to \infty$ there occurs the Gaussian function $f(\zeta) = a \exp(-\frac{\zeta^2}{2\kappa_2})$. For the values of the parameter $m < -1$ in the vicinity of the point $m = -1$ a localized solution exists in the form of group soliton (fig. 1, b). As the parameter m recedes from this point the oscillations disappear gradually (fig. 1, c) and in the limit $m \to -\infty$ there again occurs the Gaussian function.

At $m = 1$ (rheology of linear-viscous fluid) equation (22) loses the term $\kappa_1 f$. Its solution is a kink (fig. 1, d), described by the probability integral $f(\zeta) = b\sqrt{\frac{\pi\kappa_2}{2}}erf(\frac{1}{\sqrt{2\kappa_2}}\zeta)$ and does not satisfy the locality conditions (7). However, if instead of (21) we use the ansatz $\eta_0 = f(x - x_* \exp(t)) - f(x + x_* \exp(t))$ we obtain a solution in the form of the distributed, uniformly stretched neck of fixed depth, whose edges have invariable contour and are motionless with respect of the Lagrangian coordinates $\pm x_*$.

The solution of equation (22), which is stationary and localized with respect to self-similar variable, can be viewed as a result of the balance between the leading terms $\zeta f_{,\zeta}$ and $\kappa_2 f_{,\zeta\zeta}$. The former originates from the nonlinear term of the kinematic boundary condition (6) and the latter results from retaining in the velocity component approximations (12), the terms of higher than the first order in the transverse coordinate (note, that the author of [7] also arrived at the conclusion that the hypothesis of plane sections provides no possibility for the existence of localized solutions). The existence of the localized solution is determined by some interval of m, which is a measure of physical non-linearity of the model. The leading terms have the lowest order $p = 2$ of the expression, starting from which the solution is represented in terms of series: $f = \exp(-\zeta^p)\sum_{n=0}^{\infty} f_n \zeta^n$.
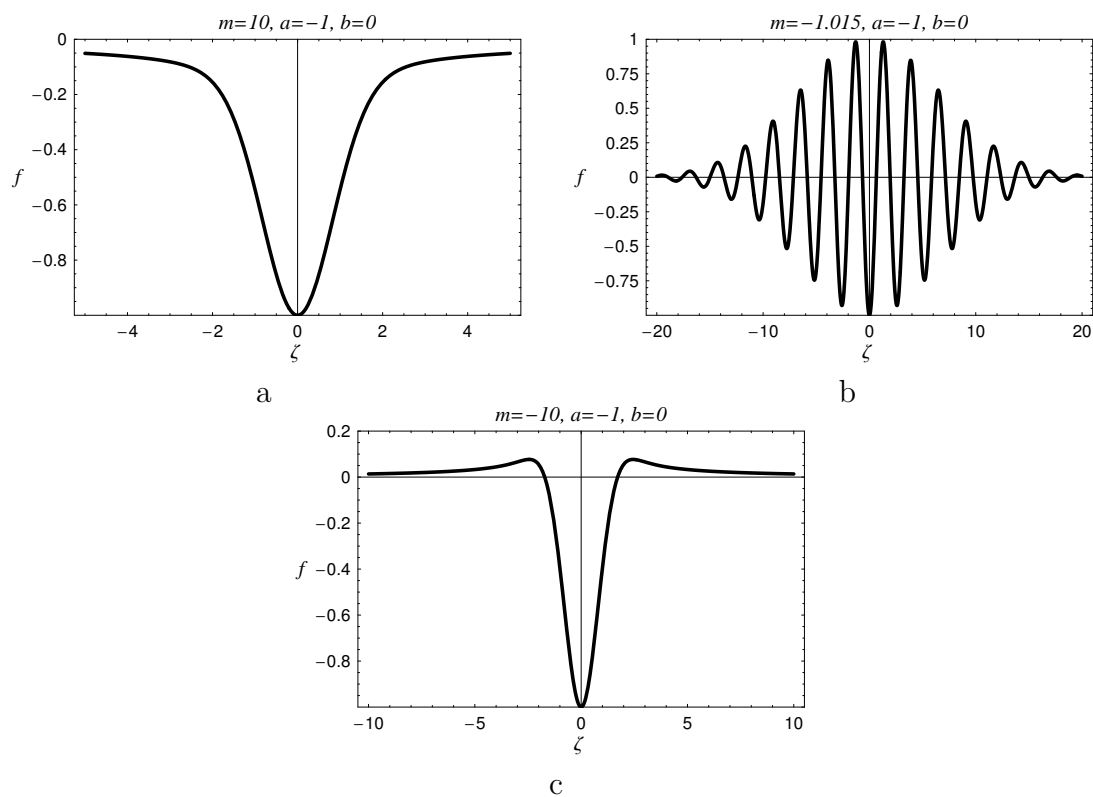
Figure 1: Forms of localized solutions.
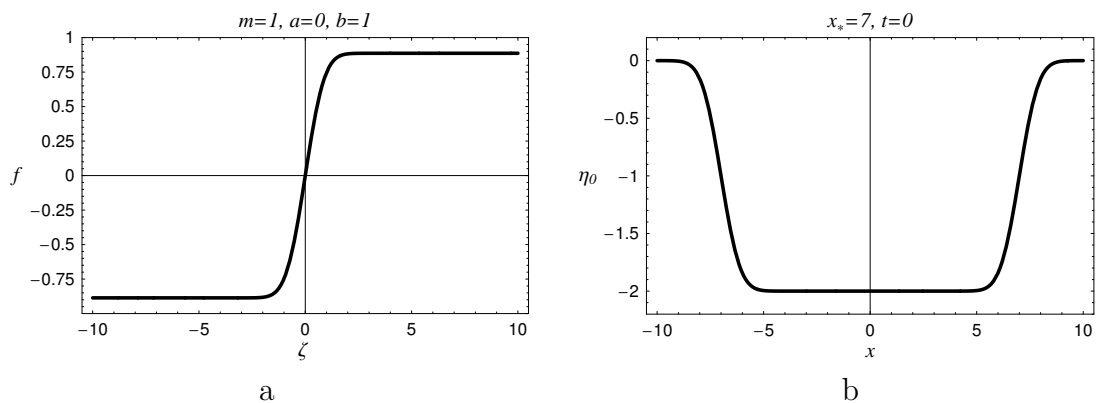
Figure 2: Forms of distributed solutions.

From (12) and (20) it follows that the boundary disturbance is proportional to the elongation rate disturbance of opposite sign, which is averaged over the cross-section of the band. In particular, in the neck region $\eta_0 < 0$ some increase in the extension rate is observed.

Solution (23) allows us to estimate the shape of the neck at $m > 1$. Power series expansion beginning from the terms $f(\zeta) = -1 + \frac{\kappa_1}{2\kappa_2}\zeta^2 + O(\zeta^4)$ takes place in the vicinity of the point $\zeta = 0$. The neck width λ at half its height is derived from the equation $-1 + \frac{\kappa_1}{8\kappa_2}\lambda^2 \approx -\frac{1}{2}$, from which $\lambda = 2\sqrt{\frac{\kappa_2}{\kappa_1}}$. At the values of m slightly higher than unity

$$\lambda \sim \frac{2}{\sqrt{m-1}} + O(\sqrt{m-1}), \tag{24}$$

which corresponds to very flat necks. According to (24), the observed typical values of $\lambda \sim 100$ [4, fig. 6] correspond to $(m-1) \sim 10^{-4}$. In stationary creep experiments (including superplasticity regimes) the most commonly observed values are $0 < m < 1$. Therefore in order that could be identified by a current profile of the lateral surface of the tensile specimen one needs to seek other weakly disturbed equilibrium contours described by equation (19). A systematic search for partial solutions of the differential equation can be realized through studying the structure of its symmetries.

General results on group classification of the linear parabolic equations in partial derivatives with two unknown variables have been obtained by L. V. Ovsiannikov and presented in [10]. Equation (19) is closely related to the equation of heat conduction

$$\overline{\eta}_{,\overline{t}} - \overline{\eta}_{,\overline{xx}} = 0, \tag{25}$$

to which it is reduced by equivalence transformations

$$\overline{\eta} = \exp(\kappa_1 t)\eta_0, \quad \overline{x} = \kappa_2^{-1/2}\exp(-t)x, \quad \overline{t} = \frac{1}{2}\exp(-2t), \tag{26}$$

preserving the algebraic structure of point symmetries of this equation [10], [11: 1.3.3.2]. An optimal system of the finite-dimensional subalgebras in the infinite-dimensional Lie algebra assumed by equation (25) is constructed in [12]. Each of these subalgebras corresponds to a partial solution of equation (25), related by transformations (26) with some unnecessarily localized evolving equilibrium contour of the free boundary. The structure of the Lie algebra in equation (25) does not depend on the arbitrary element of this equation whose role is played by sensitivity to the strain rate m. It means that the problem of group classification of equation (25) with respect to the arbitrary element has a trivial solution. Furthermore, classification and identification of nonlinear-viscous relations is impossible without finding all localized limited solutions in an infinite set of solutions invariant in the corresponding subalgebras of the optimal system and determining the their existence conditions dependently from m. Equation (19) can be meet in quantum mechanics, and some localized solutions of equation (19) and (25) are given in [11: 1.1, 1.3.1.2].

Acknowledgements

References

[1] Presnyakov A.A., Aubakirova R.K. Superplasticity of Metallic Materials (in Russian). Nauka, Alma-Ata, 1982.

[2] Padmanabhan K.A., Vasin R.A., Enikeev F.U. Superplastic Flow: Phenomenology and Mechanics. Springer-Verlag: Berlin-Heidelberg, 2001.

[3] Chumachenko E.N., Smirnov O.M., Tsepin M.A. Superplasticity: Materials, Theory, and Processes (in Russian). URSS, Moscow, 2005.

[4] Wray P. J. Tensile Plastic Instability at an Elevated Temperature and its Dependence upon Strain Rate. J. Appl. Phys. 1970, V. 41. No. 8. P. 3347-3352.

[5] Keller I. E., Trusov P. V., Shishkina O. V., Davydov D. V. An Approach to Testing Constitutive Relations of Superplasticity, Based on Stability. J. Appl. Mech. Tech. Phys. 2007, V.48. No.6. P. 915-921.

[6] Dodd R. K., Eilbeck J. C., Gibbon J. D., Morris H. C. Solitons and Nonlinear Wave Equations, Academic Press, London, 1982.

[7] Porubov A.V. Amplification of Nonlinear Strain Waves in Solids. World Scientific, Singapore, 2003.

[8] Nayfeh A.H. Introduction to Perturbation Techniques. John Wiley and Sons: New York, 1981.

[9] Handbook of Mathematical Functions / Ed. M. Abramowitz and I.A. Stegun. Nat. Bureau of Standards, 1964.

[10] Ovsiannikov L. V. Group Analysis of Differential Equations. Academic Press: New York, 1982.

[11] Polyanin A. D. Handbook of Linear Partial Differential Equations, Boca Raton: Chapman and Hall/CRC, 2002.

[12] Kuzmina A.A. An Optimal System of Finite-Dimensional Subalgebras of the Lie Algebra allowed by the Heat Equation. Sib. Zh. Ind. Mat. 2004, V. 7. No. 2. P. 88-98.

Ilya Keller, Institute of continual media mechanics RAS, Perm, Russia

Description of elastic properties of diamond using angular atomic interaction

S. S. Khakalo   A. M. Krivtsov   O. S. Loboda

akrivtsov@bk.ru

Abstract

Model of diamond taking into account angular interaction between its atoms is presented. Formulae representing the stiffness tensor in terms of the parameters of angular atomic interaction are derived. Obtained results are compared with the experimental data. Comparison with the model based on the moment atomic interaction is made.

1 Description of the model. Derivation of the coefficients

Diamond is one of the allotrope forms of carbon, mineral with a complex crystal structure. Diamond is orthotropic material so it has 3 mutual perpendicular planes of symmetry. The scheme of the diamond crystal is shown in Fig. 1 where cube faces act as planes of symmetry.
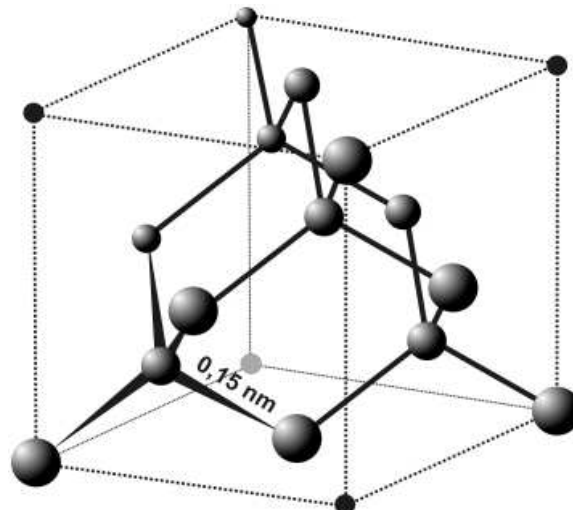
Figure 1: Fragment of the diamond crystal lattice.

Let us consider model of the diamond lattice, depicted in Fig. 2. It represents the ideal biatomic crystal lattice, which atoms are located in the center and vertices of a perfect tetrahedron.
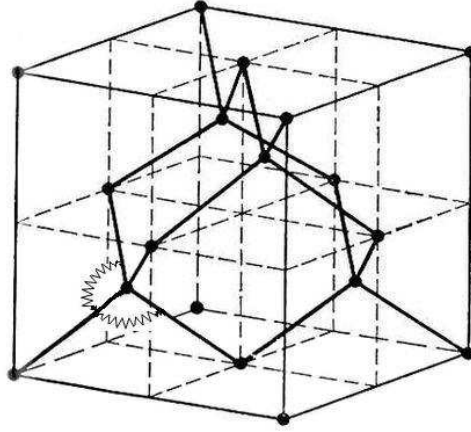
Figure 2: Model of the diamond lattice.

Interaction between atoms are described using longitudinal springs with stiffness c and angular springs with stiffness γ. The elementary cell of such lattice contains two atoms. These atoms are named as atoms of the first and second type. Atoms of each type form a simple crystal lattice, and these lattices are congruent. We choose one of the atoms of the first type as a reference atom. It is postulated that each atom interacts only with the nearest ones. From fig. 2 it is seen that each atom is surrounded by 4 nearest neighbours. Corresponding interactions are numbered from 1 to 4. Let us use an orthonormal basis with vectors perpendicular to the planes of symmetry of the lattice. Then the unit vectors directed to the nearest atoms can be represented as:

$$\mathbf{n}_1 = \frac{1}{\sqrt{3}}(\mathbf{i} - \mathbf{j} + \mathbf{k}), \qquad \mathbf{n}_2 = \frac{1}{\sqrt{3}}(-\mathbf{i} + \mathbf{j} + \mathbf{k})$$

$$\mathbf{n}_3 = \frac{1}{\sqrt{3}}(\mathbf{i} + \mathbf{j} - \mathbf{k}), \qquad \mathbf{n}_4 = \frac{-1}{\sqrt{3}}(\mathbf{i} + \mathbf{j} + \mathbf{k}).$$

In the work [1] the following formulae for an orthotropic material were obtained:

$$^4\mathbf{C} = \kappa \mathbf{e}_k \mathbf{e}_k \mathbf{e}_k \mathbf{e}_k + \lambda \mathbf{J}_1 + \mu \mathbf{J}_{23}, \tag{1}$$

where

$$\mathbf{J}_1 \stackrel{\text{def}}{=} \mathbf{e}_k \mathbf{e}_k \mathbf{e}_n \mathbf{e}_n, \qquad \mathbf{J}_{23} \stackrel{\text{def}}{=} \mathbf{e}_k \mathbf{e}_n \mathbf{e}_n \mathbf{e}_k + \mathbf{e}_k \mathbf{e}_n \mathbf{e}_k \mathbf{e}_n.$$

Here $^4\mathbf{C}$ is macroscopic stiffness tensor; $\mathbf{J}_1$ and $\mathbf{J}_{23}$ are isotropic tensors of the 4th rank; κ, λ and μ are the generalized Lame parameters; $\mathbf{e}_k$ and $\mathbf{e}_n$ are unit vectors of any arbitrary basis.

Macroscopic stiffness tensor is derived in [1] using the expression for the deformation energy of the material

$$W = \frac{1}{2}\varepsilon \cdot\cdot {}^4\mathbf{C} \cdot\cdot \varepsilon, \qquad {}^4\mathbf{C} = {}^4\mathbf{C}^* - {}^3\mathbf{C} \cdot {}^2\mathbf{C}^{-1} \cdot {}^3\mathbf{C}^\mathsf{T}, \tag{2}$$

where

$$
{}^4\mathbf{C}^* = \frac{2}{V_0}\left(H_1\sum_{\alpha=1}^{4}\mathbf{n}_\alpha\mathbf{n}_\alpha\mathbf{n}_\alpha\mathbf{n}_\alpha + H_2\sum_{\alpha,\beta=1}^{4}{}'\,\mathbf{n}_\alpha\mathbf{n}_\alpha\mathbf{n}_\beta\mathbf{n}_\beta + \right.
$$

$$
\left. + H_3\sum_{\alpha,\beta=1}^{4}{}'\,(\mathbf{n}_\alpha\mathbf{n}_\beta\mathbf{n}_\beta\mathbf{n}_\alpha + \mathbf{n}_\alpha\mathbf{n}_\beta\mathbf{n}_\alpha\mathbf{n}_\beta)\right),
$$

$$
{}^3\mathbf{C} = \frac{1}{V_0}H_4\sum_{\alpha=1}^{4}\mathbf{n}_\alpha\mathbf{n}_\alpha\mathbf{n}_\alpha, \qquad {}^2\mathbf{C} = \frac{2}{V_0}H_5\sum_{\alpha=1}^{4}\mathbf{n}_\alpha\mathbf{n}_\alpha, \qquad V_0 = \frac{16\sqrt{3}}{9}a^3.
$$

Here W is energy of deformation of the material; ε is strain tensor; ${}^4\mathbf{C}^*$, ${}^3\mathbf{C}$ and ${}^2\mathbf{C}$ are intermediate stiffness tensors; V_0 is volume of an elementary cell of the crystal; a is length of the internuclear bond. The prime at a sum means that summation is conducted on the adjacent bonds only.

Formulae for H_k from [1] in the case of diamond take form:

$$
H_1 = \frac{1}{2}ca^2 - \frac{9}{8}c_\gamma a^2, \qquad H_2 = \frac{1}{8}c_\gamma a^2, \qquad H_3 = \frac{9}{8}c_\gamma a^2,
$$

$$
H_4 = ca^2 - 4c_\gamma a^2, \qquad H_5 = \frac{1}{2}ca^2 + 4c_\gamma a^2,
$$

where $c_\gamma = \dfrac{\gamma}{a^2}$ is the effective stiffness of the angular interaction.

We substitute obtained coefficients H_k and values of vectors $\mathbf{n}_k$ from expression (1) in formulae for intermediate stiffness tensors (4). With the help of the obtained formulae the macroscopic stiffness tensor (3) for diamond can be found. Representing this tensor in form (2) we obtain the following expressions for the generalized Lame parameters:

$$
\kappa = \frac{3\sqrt{3}}{16a}c_\gamma\frac{72c_\gamma - 7c}{c + 8c_\gamma}, \qquad \lambda = \frac{\sqrt{3}}{12a}(c - 6c_\gamma), \qquad \mu = \frac{3\sqrt{3}}{32a}c_\gamma\frac{15c - 8c_\gamma}{c + 8c_\gamma}. \quad (3)
$$

The formulae for elastic constants [3] expressed through generalized Lame parameters take the form:

$$
C_{11} = \kappa + \lambda + 2\mu, \qquad C_{12} = \lambda, \qquad C_{44} = \mu, \qquad K = \frac{\kappa + 3\lambda + 2\mu}{3},
$$

$$
E = \frac{(\kappa + 2\mu)(\kappa + 3\lambda + 2\mu)}{\kappa + 2\lambda + 2\mu}, \qquad \nu = \frac{\lambda}{\kappa + 2\lambda + 2\mu}, \qquad \eta = \frac{2\mu}{\kappa + 2\mu},
$$

where C_{11}, C_{12}, C_{44} are stiffness tensor coefficients; K is the bulk modulus; E is Young modulus; ν is Poisson ratio; η is the anisotropy parameter.

Then by substituting relations for the generalized Lame parameters (6) in the formulae above we obtain:

$$C_{11} = \frac{\sqrt{3}}{12a}(c + 12c_\gamma), \qquad C_{12} = \frac{\sqrt{3}}{12a}(c - 6c_\gamma), \qquad C_{44} = \frac{3\sqrt{3}}{32a}c_\gamma\frac{15c - 8c_\gamma}{c + 8c_\gamma} \tag{4}$$

$$K = \frac{\sqrt{3}}{12a}c, \qquad E = \frac{9\sqrt{3}}{4a}\frac{cc_\gamma}{c + 3c_\gamma}, \qquad \nu = \frac{1}{2}\frac{c - 6c_\gamma}{c + 3c_\gamma}, \qquad \eta = \frac{1}{8}\frac{15c - 8c_\gamma}{c + 8c_\gamma}. \tag{5}$$

2 Comparison with experimental data

Experiment #	1	2	3	4	5
C_{11}, GPa	1079	1076	1076	1100	950
C_{12}, GPa	124	275	125	330	390
C_{44}, GPa	578	519	576	440	430
$\tilde{C}_{44}$, GPa	428	433	427	438	356
error, %	26	16.5	25.9	0.4	17.2
c, N/m	472	578	472	626	615
c_γ, N/m	57	478	56	46	33
c_γ/c, %	12	8.2	12	7.3	5.4

Tab. 1: Experimental and calculated data

In tab. 1 the experimental values for the stiffness tensor components [2] are presented. Such variability of data is caused by various experimental techniques. Coefficients c and c_γ are calculated using the experimental values of C_{11}, C_{12} and formulae (8). Substituting the obtained values in the formula (8) for C_{44} we find the calculated value $\tilde{C}_{44}$. From Tab. 1 it is visible that the maximum divergence of calculated value $\tilde{C}_{44}$ from the experimental data is 26% and minimum is 0.4%. Considering so essential differences in the experimental data the divergence in the obtained values for C_{44} is acceptable. Thus, the given method of calculation gives good coincidence with the experimental values of elastic constants.

3 Comparison with the model based on the moment interaction between atoms

3.1 Moment interaction

The following formulae [3] fulfill:

$$C_{11} = \frac{\sqrt{3}}{12a}(c_A + 2c_D), \qquad C_{12} = \frac{\sqrt{3}}{12a}(c_A - c_D), \qquad C_{44} = \frac{3\sqrt{3}}{8a}\frac{c_A c_D}{c_A + 2c_D},$$

$$K = \frac{\sqrt{3}}{12a}c_A, \qquad G = C_{44} = \frac{3\sqrt{3}}{8a}\frac{c_A c_D}{c_A + 2c_D}, \qquad \nu = \frac{(c_A - c_D)(c_A + 2c_D)}{2c_A^2 + 2c_D^2 + 5c_A c_D},$$

$$^2\mathbf{C} = \frac{4}{3V_0}(c_A + 2c_D)\mathbf{E}, \tag{6}$$

where $^2\mathbf{C}$ is the intermediate stiffness tensor of 2nd rank; c_A and c_D are the longitudinal and transversal stiffness of the bonds.

Condition for the macroscopic stability of a material is the positivity of the bulk modulus K and the shear modulus G

$$K > 0, \qquad G > 0 \qquad \Rightarrow \qquad c_A > 0, \qquad \left| \begin{matrix} c_D > 0 \\ c_D < -\dfrac{c_A}{2} \end{matrix} \right. \tag{7}$$

This condition of stability admits negative values for transversal stiffness of the bonds.

A condition for the microscopic stability is the positivity of the coefficient:

$$c_A + 2c_D > 0 \tag{8}$$

From (12) and (13) follows

$$c_A > 0, \qquad c_D > 0. \tag{9}$$

Let us present Poisson ratio as a function of c_D/c_A

$$\nu = \frac{(c_A - c_D)(c_A + 2c_D)}{2c_A^2 + 2c_D^2 + 5c_A c_D} = \frac{1 + \dfrac{c_D}{c_A} - 2\dfrac{c_D^2}{c_A^2}}{2 + 5\dfrac{c_D}{c_A} + 2\dfrac{c_D^2}{c_A^2}} \tag{10}$$

The bounding values for ν are

$c_A \ll c_D \qquad \Rightarrow \qquad \nu \approx -1$

$c_A = c_D \qquad \Rightarrow \qquad \nu = 0 \qquad\qquad \Rightarrow \qquad -1 < \nu < \dfrac{1}{2}$

$c_A \gg c_D \qquad \Rightarrow \qquad \nu \approx \dfrac{1}{2}$

From the obtained results it is clear that the model based on the moment atomic interaction gives wide enough area of the admissible values for Poisson ratio, witch include the experimental value [2] $\nu = 0.07$ for diamond.

3.2 Angular interaction

In the first part of this paper the following relations were obtained:

$$C_{11} = \frac{\sqrt{3}}{12a}(c + 12c_\gamma), \qquad C_{12} = \frac{\sqrt{3}}{12a}(c - 6c_\gamma), \qquad C_{44} = \frac{3\sqrt{3}}{32a}c_\gamma\frac{15c - 8c_\gamma}{c + 8c_\gamma},$$

$$K = \frac{\sqrt{3}}{12a}c, \qquad G = C_{44} = \frac{3\sqrt{3}}{32a}c_\gamma\frac{15c - 8c_\gamma}{c + 8c_\gamma}, \qquad \nu = \frac{1}{2}\frac{c - 6c_\gamma}{c + 3c_\gamma},$$

where c is stiffness of the bond, c_γ is the effective stiffness of the angular interaction. If we accept $c_A = c$, $c_D = 6c_\gamma$ then the formulae (10) and (17) for moment and angular interaction will coincide, but only for coefficients C_{11} and C_{12}. However this dose not fulfill for C_{44}.

Using conditions of the macroscopic stability $K > 0, G > 0$ and conditions of the microscopic stability $H_5 > 0$ we obtain the following inequalities

$$c > 0, \qquad 0 < c_\gamma < \frac{15}{8}c. \tag{11}$$

Let us present Poisson ratio as a function of c_γ/c

$$\nu = \frac{1}{2}\frac{c - 6c_\gamma}{c + 3c_\gamma} = \frac{1}{2}\frac{1 - 6\frac{c_\gamma}{c}}{1 + 3\frac{c_\gamma}{c}} \tag{12}$$

The bounding values for ν are

$c \approx \frac{8}{15}c_\gamma \qquad \Rightarrow \qquad \nu \approx -\frac{41}{53}$

$c = c_\gamma \qquad \Rightarrow \qquad \nu = -\frac{5}{8} \qquad\qquad \Rightarrow \qquad\qquad -\frac{41}{53} < \nu < \frac{1}{2}$

$c \gg c_\gamma \qquad \Rightarrow \qquad \nu \approx \frac{1}{2}$

Thus, it is visible that the model based on the angular atomic interaction also gives the wide area of the admissible values of Poisson ratio, which covers experimental value. However the lower boundary for Poisson ratio is different for these two models.

4 Conclusion

In the given work the model of diamond using angular atomic interaction was considered. Formulae for the macroscopic stiffness tensor coefficients C_{11}, C_{12}, C_{44}, the bulk modulus K, Young modulus E, Poisson ratio ν, and the anisotropy parameter η in the terms of the stiffness of the bond c and the effective stiffness of angular interaction c_γ were derived. By using the experimental data and the derived formulae the stiffness values of the interatomic bonds c and c_γ were obtained. Comparison with the model based on the moment interaction between atoms was made. It was shown that the considered models give almost identical areas of values for Poisson ratio, and these areas include the experimental value.

References

[1] *Krivtsov A.M.* Elastic properties of monoatomic and diatomic crystals.: tutorial. - SPb., Polytechnic University, 2009. - p.124.

[2] *Novikov N.V.* Physical properties of diamond. Handbook. Kiev 1987.

[3] *Berinskiy I.E., Dvas N.G., Krivtsov A.M., Kudarova A.M., Kuzkin V.A., Le-Zakharov A.A., Loboda O.S., Neigebauer I.I., Podolskaya E.A.* Elastic and thermal properties of crystals.: tutorial. - SPb., Polytechnic University, 2009. - p.135.

Sergej Khakalo, Department of Theoretical Mechanics, St. Peterburg State Polytechnical University, Politechnicheskaya, 29, St. Peterburg, 195251, Russia

One-dimensional models of filtration with regard to thermal expansion and volume viscosity

Anna G. Knyazeva

anna@ispms.tsc.ru

Abstract

Modeling of the processes in two phase medium has numerous technical applications and is possible on the base of averaged models and with the help pf more complex models - tow temperature, two velocities etc. The authors of most of known papers neglect the phenomenon of thermal expansion and volume viscosity. Nevertheless, if the phases have different rheology properties, taking into consideration these phenomena can lead to interesting effects. For example, it is known that compressibility of the gases is principal in comparison with incompressibility of solid skeleton. The thermal expansion phenomena in this case appear by different ways for various phases, especially if the current is accompanied by chemical conversion. Particularly it leads to new conversion regimes in modern burners based on filtration combustion. Now we stop on the simple models, following from general thermodynamical conceptions, without their detailed investigation. Let us, that all particular models contain physical parameters possessing clear physical sense and known from experiment.

1   Introduction

Filtration theory studies the motion of gases and liquids into porous media and is constructed on the base of the conception that porous medium and filling it fluid is continuum. Let determine the basic parameters of porous media which will be used further. The porosity $m = V_p/V$ and gapness and $a = S_p/S$ are equivalent characteristics, if the medium is isotropic. Here V_p is pore volume, V is summary volume including the pore volume and volume occupying by solid skeleton, S_p is square in the section related to pores, and S is the section square.

We determine the authentic gas (liquid) velocity $\mathbf{v} = (Q/S_p)\mathbf{n}$ and filtration rate $\mathbf{w} = (Q/S)\mathbf{n}$, where Q is gas discharge (consumption), $\mathbf{n}$ is normal to the section. Hence

$$\mathbf{w} = \frac{S_p}{S}\mathbf{v} = a\mathbf{v} \tag{1}$$

Basic relation of filtration theory establishes the connection between filtration rate vector and pressure field which causes the filtration motion. For many situations

one can assume that filtration rate field is continuous, and physical parameters of fluid and skeleton are constant. But it is not possible to neglect the pressure change even for negligible small gradient because the motion absent when the pressure is constant [1,2]. Against this affirmation, majority of filtration combustion theories are developed without taking into consideration of pressure change.

The classical filtration law was ascertained experimentally by Anry Darcy for slow motions and can be presented in the form

$$\mathbf{w} = -\frac{k}{\mu}\nabla p \tag{2}$$

where k is the permeability, and μ is "viscosity" - friction coefficient.

There are the generalizations of this law for complex media and quick currents.

2 Basic equations for one phase no isothermal filtration

To construct the simplest model of no isothermal filtration, including chemically reacting fluids, we should write the basic equations. These equations are known. Firstly, the continuity equation contains the source for mass from skeleton

$$\frac{\partial}{\partial t}m\rho = -\nabla \cdot \rho\mathbf{w} + \sigma.$$

If the volume source for mass is absent and porosity is constant, this equation takes usual form

$$\frac{\partial}{\partial t}m\rho = -\nabla \cdot \rho a\mathbf{v} \quad \text{or} \quad \frac{\partial}{\partial t}\rho = -\nabla \cdot \rho\mathbf{v}. \tag{3}$$

The motion equation can be presented like this

$$\rho\frac{\partial \mathbf{w}s^{-1}}{\partial t} + \rho\frac{\mathbf{w}}{a}\nabla\left(\frac{\mathbf{w}}{a}\right) = \nabla p + \rho(\mathbf{F}_1 + \mathbf{F}_2),$$

where $\mathbf{F}_1 = -(1/\rho)\nabla(gz)$ is gravity force, $\mathbf{F}_2$ is internal friction force proportional to filtration rate.

For slow current or for so called creeping current this equation id simplifies

$$\rho\frac{\partial \mathbf{w}a^{-1}}{\partial t} = \nabla p + \rho(\mathbf{F}_1 + \mathbf{F}_2),$$

and takes the form

$$\nabla p = -\rho(\mathbf{F}_1 + \mathbf{F}_2) \quad \text{or} \quad \mathbf{w} = -\frac{k}{\mu}[\nabla p + \rho\mathbf{F}_1] \tag{4}$$

for stationary filtration regimes. The Darcy law (2) follows from (4).

Naturally, p is summary pressure including "reverse" and "viscous" parts [3]

$$p = p^e + p^V.$$

The energy equation for fluid with the reactions can be presented in the form

$$T\rho\left(\frac{\partial s}{\partial t} + \frac{\mathbf{w}}{a}\nabla s\right) = -\nabla\cdot\left(\mathbf{J}_T - \sum_{k=1}^{n} g_k\mathbf{J}_k\right) - p^V\nabla\cdot\frac{\mathbf{w}}{a} - B - \sum_{k=1}^{n} g_k\sigma_k, \qquad (5)$$

that follows from usual balance equation for internal energy analogously [4,5]. Here s is local entropy, $\mathbf{J}_T$ is the heat flux due to thermal conduction, $\mathbf{J}_k$ are mass fluxes due to diffusion processes, σ_k are sources for components in chemical reactions, g_k are their chemical potentials, B describes the heat exchange with solid skeleton. We should write the balance equations for components

$$\rho\left(\frac{\partial C_k}{\partial t} + \frac{\mathbf{w}}{a}\nabla C_k\right) = -\nabla\cdot\mathbf{J}_k + \sigma_k, \qquad (6)$$

where C_k are mass concentrations.

It is necessary now to determine the values $\mathbf{J}_T, \mathbf{J}_k, p^V, \sigma_k$ and s.

From chemistry we have

$$\sigma_k = \sum_{j=1}^{r} \nu_{kj}M_k\varphi_j,$$

where φ_j are chemical reaction rates, M_k are molar masses, ν_{kj} stoichiometric coefficients.

With the help of Gibbs equation, we find [4,6]

$$T\frac{ds}{dt} = C_\gamma\frac{dT}{dt} + \alpha_T\beta_T^{-1}T\frac{d\gamma}{dt} + \sum_{k=1}^{n} Ts_k\frac{dC_k}{dt},$$

where C_γ is thermal capacity for constant volume, $\gamma = \rho^{-1}$, β_T is isothermal compressibility coefficient, α_T is thermal expansion coefficient, we com to the thermal conductivity equation

$$C_\gamma\rho\left(\frac{\partial T}{\partial t} + \frac{\mathbf{w}}{a}\nabla T\right) = -\nabla\cdot\left(\mathbf{J}_T - \sum_{k=1}^{n} h_k\mathbf{J}_k\right) - (p^V + \alpha_T\beta_T^{-1}T)\nabla\cdot\frac{\mathbf{w}}{a} - \sum_{k=1}^{n} h_k\sigma_k - B, \quad (7)$$

when we take into consideration continuity equation.

The pressure p^e follows from state equation.

To find the expressions for $\mathbf{J}_T, \mathbf{J}_k, p^V, \varphi_j$, we could use the Onsager theory or experimental laws. The first way was described in details in thermodynamical literature [7-9]. For example, when the unique reaction goes in the fluids, "the reagent converts to the product", and φ is the reaction rate, we have [4,5]

$$p^V = -\kappa_V\nabla\cdot\mathbf{v} + \gamma_V A, \quad \varphi = -\gamma_V\nabla\cdot\mathbf{v} + k_{ch}A, \qquad (8)$$

where κ_V - is coefficient of volume viscosity, k_{ch} - reaction rate constant, A is chemical affinity; the coefficient γ_V describes the viscosity appearance due to chemical reaction and the reaction rate dependence on medium mobility. Let us notice, that

this physical phenomena are observed in the literature, but the attempts to determine this coefficient are absent.

But then, the investigations of interrelation between thermal conduction and diffusion together with motion medium and chemical reactions are occurred often.

Now we take the approximation of independent diffusion and heat conduction, when one can to write

$$\mathbf{J}'_{\mathsf{T}} = -\mathbf{J}_{\mathsf{T}} - \sum_{\mathsf{k}=1}^{\mathsf{n}} h_{\mathsf{k}} \mathbf{J}_{\mathsf{k}} = -\lambda \nabla \mathsf{T}, \quad \mathbf{J}_{\mathsf{k}} = -\rho D_{\mathsf{k}}(\mathsf{T}) \nabla C_{\mathsf{k}}. \tag{9}$$

The papers absent where volume viscosity of fluids and thermal expansion are taken into consideration when the filtration problems are studied. Though these phenomena could be principal, for example, when the natural gas or gas mixture are burned in the porous reactors, when fluids flow in the fractured ground etc., especially for slow filtration rate. Let discuss what simples models follows from above.

3   Examples of the simplest models

Naturally, we can obtain from above the known filtration models, well investigated in the literature [1,2,10]. First of all, there is the class of the isothermal one-phase filtration models for one-component fluids. "New" physical effects lead to new model appearance.

1. Really, it is known very well, when the liquid is incompressible, medium is isotropic, porosity is constant and temperature does not change, we have the equations

$$\nabla \cdot \mathbf{v} = 0, \quad \mathbf{v} = -\frac{k}{\mu a} \nabla p^e,$$

for **stationary filtration regime**. These equations give the Laplace equation for pressure

$$\triangle p^e = 0. \tag{10}$$

2. When the gas moves along the porous media, we can not neglect the compressibility in comparison with the solid skeleton [1,10]. In this case, we come to the equations

$$\nabla \cdot \rho \mathbf{v} = 0, \quad \mathbf{v} = -\frac{k}{\mu a} \nabla p^e, \quad p^e = \rho M^{-1} RT,$$

if we take $\kappa_V = 0$. These three equations allow obtaining

$$\nabla \cdot p^e \nabla p^e = 0, \quad \text{or} \quad \nabla \cdot \rho \nabla \rho = 0, \tag{11}$$

and to construct some analytical solutions for one-axis currants.

3. We could write for no ideal gas [6]

$$dp^e = -\frac{\rho}{\beta_T} d\gamma \equiv \frac{1}{\beta_T \rho} d\rho,$$

if temperature is constant and the composition does not change, or

$$\nabla p^e = \frac{1}{\beta_T \rho} \nabla \rho = 0. \tag{12}$$

Instead (10) we shall find $\triangle \rho = 0$ or $\nabla \cdot \nabla p^e + \beta_T (\nabla p^e)^2 = 0$ (for constant properties).
For ideal gas $\beta_T \sim p_e^{-1}$. In this case we obtain known result (11).
If homogeneous gas strainers through plane layer, we come to the problem

$$\frac{d^2 p_e}{dx^2} + \beta_T \left(\frac{dp_e}{dx}\right)^2 = 0,$$

$$x = 0: \quad p_e = p_1, \qquad x = L: \quad p_e = p_2.$$

The solution of this problem has the form

$$p_e = \beta_T^{-1} \left[\ln(x + C_1) C_2\right],$$

where C_1, C_2 are integration constants, depending on p_1, p_2, L.
Hence,

$$V = \frac{k}{\mu a} \frac{1}{\beta_T} \frac{1}{x + C_1} = \frac{k}{\mu a} \frac{1}{\beta_T} \frac{1 - \exp\left[-(p_1 - p_2)\beta_T\right]}{L + x\left(1 - \exp\left[-(p_1 - p_2)\beta_T\right]\right)}$$

filtration rate in the direction x.
It is not difficult to show that we obtain

$$V = \frac{k}{\mu a} \frac{1}{\beta_T} \frac{p_1 - p_2}{L_1}$$

if $\beta \to 0$, that is the medium is incompressible.
4. Let $\kappa_V \neq 0$. In this case we use the continuity equation $\nabla \cdot \rho \mathbf{v} = 0$, from which the relation

$$\frac{\nabla \rho}{\rho} = -\frac{\nabla \cdot \mathbf{v}}{\mathbf{v}} \tag{13}$$

follows. Hence, from (12) we have

$$\nabla p^e = -\frac{1}{\beta_T} \frac{\nabla \cdot \mathbf{v}}{\mathbf{v}}.$$

Because

$$p^V = -\kappa_V \nabla \cdot \mathbf{v} \quad \text{and} \quad \mathbf{v} = -\frac{k}{\mu a}\left[\nabla p^e + \nabla p^V\right],$$

we come to the equation for velocity

$$\beta_T \kappa_V \mathbf{v} \nabla (\nabla \cdot \mathbf{v}) + \nabla \cdot \mathbf{v} - \mu a \beta_T k^{-1} \mathbf{v} \mathbf{v} = 0. \tag{14}$$

For example, for plane porous layer, the problem on velocity distribution takes the
form

$$\varepsilon V\frac{d^2V}{dx^2} + \frac{dV}{dx} - \delta V^2 = 0, \tag{15}$$

$$x = 0: \quad V = V_1, \qquad x = L: \quad V = V_2, \tag{16}$$

where ε, δ - parameters including fluid properties, $\varepsilon = \beta_T \kappa_V$; $\delta = \mu a \beta_T k^{-1}$;
The equation (15) reminds of oscillation equation.
5. Let $T = \text{const}$, chemical reactions are absent, state equation has the form (12),
but gas mixture contains two components. When filtration rate is small, we can
not neglect the difference between individual rates of species. But two component
mixture motions can be described using one diffusion equation

$$\rho\left(\frac{\partial C}{\partial t} + \mathbf{v}\nabla C\right) = \nabla \cdot (D\rho\nabla C).$$

For stationary filtration regime, we come to stationary diffusion problem. For gas
phase ones assumed $D\rho \approx \text{const}$. Then the concentration distribution can be found
independently after velocity field determination. One dimensional problem takes the
form

$$V(x, \varepsilon, \delta)\frac{dC}{dx} = D\frac{d^2C}{dx^2}, \tag{17}$$

$$x = 0: \quad C = C_1, \qquad x = L: \quad C = C_2,$$

Generally speaking, when gas mixture is no ideal, instead (12) we should use the
state equation in the form

$$dp^e = \frac{1}{\beta_T}\left(\frac{d\rho}{\rho} + \triangle\alpha dC\right), \tag{18}$$

where $\triangle\alpha = \alpha_2 - \alpha_1$, $\alpha_k = \frac{1}{\gamma}\left(\frac{\partial\gamma}{\partial C}\right)_T$ is volume concentration expansion coefficient
(it is analogy for α_T) for k - component. Then it is not succeeded to divide the
problem into two parts. In this case, for one dimensional plane filtration we obtain
two coupling nonlinear equations: (17) and

$$\varepsilon V\frac{d^2V}{dx^2} + \frac{dV}{dx} - \delta V^2 - \triangle\alpha \cdot V\frac{dC}{dx} = 0. \tag{19}$$

The boundary conditions stay the same, (16).
The more complex problem has appear when we take into consideration that dif-
fusion flux is proportional to gradient of chemical potential that in turn depends
on volume change or pressure change. This effect connects with pressure diffusion
phenomenon and is worthy of notice also.
6. The situation will more complex, when $T \neq \text{const}$. For stationary filtration
regime we obtain the equation system

$$\nabla \cdot (\rho\mathbf{v}) = 0,$$

$$\mathbf{v} = -\frac{k}{\mu a}\nabla p,$$

$$\rho\mathbf{v}\nabla C = \nabla \cdot (D\rho\nabla C),$$

$$C_\gamma\rho\mathbf{v}\nabla T = \nabla \cdot (\lambda\nabla T) - \left(p^V + \alpha_T\beta_T^{-1}T\right)\nabla \cdot \mathbf{v} - B$$

from above. To describe the heat exchange with the solid skeleton, the thermal conductivity equation for solid body is necessary. Because the velocity for solid body equals to zero and it is incompressible, we write

$$\nabla \cdot (\lambda_s\nabla T_s) + B_s = 0,$$

where index "s" relates to solid skeleton.

The items B and B_s in thermal conductivity equations can be presented in the form

$$B = \frac{\alpha}{m}(T - T_s), \quad B_s = \frac{\alpha}{1 - m}(T - T_s).$$

There are some particular cases in this case.

If fluid is incompressible, we have $\nabla \cdot \mathbf{v} = 0$. Than analogously to previous, the no isothermal diffusion problem and motion problem are separated. We can determine the temperature and concentration fields after velocity field. That way has been used in the combustion filtration problems [11].

When $p^V = 0$ ($\kappa_V = 0$) we have $p = p^e$. Assume that gas mixture is uniform. Using state equation following from Gibbs equation

$$dp^e = \frac{1}{\beta_T}(\alpha_T T - \rho d\gamma) \equiv \frac{1}{\beta_T}\left(\alpha_T T + \frac{d\rho}{\rho}\right),$$

we come to the system of one dimensional equations

$$
\begin{aligned}
&\frac{d^2\rho}{dx^2} + \alpha_T\frac{d}{dx}\rho\frac{dT}{dx} = 0,\\
&\frac{dV}{dx} = \frac{\mu a\beta_T}{k}V^2 + \alpha_T V\frac{dT}{dx},\\
&C_\gamma\rho V\frac{dT}{dx} = \lambda\frac{d^2T}{dx^2} - \frac{\alpha_T}{\beta_T}T\frac{dV}{dx} - B,\\
&\lambda_s\frac{d^2T_s}{dx^2} + B_s = 0.
\end{aligned}
\tag{20}
$$

The heat exchange conditions should be given on the surfaces of the layer through the filtration goes.

Now we come to special class of the filtration models - filtration combustion.

When filtration rate is not too big, influence degree of called effect the same; it can lead to new conversion regime appearance. Some results were discussed in [12]

4   Conclusion

All presented above and mentioned models were constructed on the base of the conception of irreversible thermodynamics. On of basic principle of thermodynamics consist of coupling effects taking into consideration. Now it was shown that any coupling effect is able to result to new model which turns unexplored but possesses large possibilities.

References

[1] Basniev K.S., Kochina I.N., Vfrsimov V.N. Underground hydromechanics / Nedra (Moskow) 1993. 416 p.

[2] Barenblatt G.I., Entov V.M., Ryzhik V.M. Liquids and gases motion in natural layers / Nedra (Moskow) 1984. 208 p.

[3] Diarmati I. Irreversible thermodynamics. Field theory and variation principles / Mir (Moskow) 1974. 128 p.

[4] Knyazeva A.G. Irreversible processes modeling in the materials with large square of internal surfaces // Physical mesomecanics. 2003. V.6. N 5, pp.11-27.

[5] Knyazeva A.G. Diffusion and rheology in local-reversible thermodynamics. / Mathematical modeling of the system and the process. Herald of the Permian state technical university. 2005. issue. 13. pp.45-60.

[6] Putilov K.A. Thermodynamics. Nedra (Moskow) 1993.366 p.

[7] Gurov K.P. Phenomenological thermodynamics of irreversible processes / Nauka (Moscow) 1978. 128 p.

[8] De Groot S., Masur P. Irreversible thermodynamics / Mir (Moscow) 1964. 456 p.

[9] Prigogin I., Kondepudi D. Modern Thermodynamics. From thermal engines to dissipative structure / Mir (Moscow) 2002. 462 p.

[10] Masket Homogeneous fluids currants in porous medium / Moscow – Izhevsk: Institute of computer-aided investigation. 2004. 640 p.

[11] Heat waves propagation in heterogeneous media / Nauka (Novosibirsk) 1988. 286 p.

[12] Knyazeva A.G. Thermodynamical model of viscous heat-conducting gas and its application to combustion processes modeling. / Mathematical modeling of the system and the process. Herald of the Permian state technical university. 2006. issue. 14. pp.92-108.

Anna. G. Knyazeva, Academichesky Ave., 2/4, Tomsk, Russia

Longitudinal strain solitary waves in an auxetic rod

P. Kolat   B. Maruszewski

piotr.kolat@doctorate.put.poznan.pl

bogdan.maruszewski@put.poznan.pl

Abstract

The paper deals with propagation of solitary waves in an auxetic material. That unusual material characterizes with negative Poisson's ratio. It means, that it becomes thicker when stretched and thinner when compressed. The double dispersive equation has been solved by the Crank-Nicolson method. Numerical results concerning wave propagation in the cylindrical rod made of the auxetic material have been presented for solutions resulting from different initial conditions.

1 Introduction

Fast industrial development forces new solutions concerning constructions and materials. The latter ones have to satisfy not only strength of materials conditions, but follow many other properties, which as a consequence lead to new materials and smart structures that are proper for modern technologies. One of the results coming from such an activity are investigation at materials of negative Poisson's ratio commonly called auxetics [10]. They characterize peculiar feature: if they are extended in one direction instead of becoming compressed along remaining ones, they are also extended. Such unexpected property causes that they have been already used in many new engineering constructions [11, 12].
Auxetic materials one can find in nature: α-crystobalit, for instance [16]. However, fast development of materials science allows engineers to design and produce auxetics from conventional materials (foams and polymers [14, 15]). In 1987 Lakes [10], as a first produced auxetic foam of Poisson's ratio equal to $-0,7$. Materials with negative Poisson's ratio have been widely used to create layered composites, because of their resistance to shear [11, 13]. The car and aircraft industries are very much interested to use auxetics in their produce [12].
Successful experiments on solitary waves propagating in solids causes their practical use in nondestructive testing, since their profile becomes unchanged during propagation. An example of such testing is a test on the delamination of layered composites consisted of foams or polymers of negative Poisson's ratio [9].

2 Basing equations

From among several nonlinear equations which describe solitary waves propagation the most popular are Korteweg-de Vries [4] and Boussinesq [5] equations. In the present paper we consider an infinite, isotropic, elastic and circular rod. The double dispersive equation (DDE) governing considered waves propagation reads[1]:

$$u_{tt} - au_{xx} - c_1(u^2)_{xx} - b_1 u_{xxtt} + b_2 u_{xxxx} = 0, \tag{1}$$

where $u(x, t)$ denotes the deformation and coefficients are equal to:

$$a = \frac{E}{\rho_0}, c_1 = \frac{\beta}{2\rho_0}, b_1 = \frac{\nu(\nu - 1)R^2}{2}, b_2 = -\frac{\nu ER^2}{2\rho_0}, \tag{2}$$

$$\beta = 3E + l(1 - 2\nu)^3 + 4m(1 - 2\nu)(1 + \nu) + 6n\nu^2, \tag{3}$$

ρ is the density, E is Young's modulus, l, m, n are Murnaghan's constants, R is the rod radius and β denotes the nonlinearity coefficient. Since coefficients in DDE depend on Poisson's ratio we could estimated its influence on solitary waves propagation.

Difference method

To use the difference method for solving DDE, the space and time steps have been denoted by Δx and Δt in space (x, t), respectively. The DDE solution was approximated in the nodes as $U_i^n = U(\Delta xi, \Delta tn)$ with $0 \leq i \leq (M = L/\Delta x)$ and $0 \leq n \leq (N = T/\Delta t)$, where M and N denote the number of space and time steps, L is the rod length and T is the total calculation time. On using Crank-Nicolson method [3, 6, 7, 8] to solve DDE we get:

$$\delta_t^2 U_i^n - \frac{a}{2}\left(\delta_x^2 U_i^{n+1} + \delta_x^2 U_i^{n-1}\right) - \frac{c_1}{2}\left(\delta_x^2\left(U_i^{n+1}\right)^2 + \delta_x^2\left(U_i^{n-1}\right)^2\right) \tag{4}$$

$$-b_1\delta_t^2 U_i^n \delta_x^2 U_i^n + \frac{b_2}{2}\left(\delta_x^4 U_i^{n+1} + \delta_x^4 U_i^{n-1}\right) = 0.$$

After some algebraic manipulations we obtain the penta-diagonal system:

$$sU_{i-2}^{n+1} + dU_{i-1}^{n+1} + eU_i^{n+1} + dU_{i+1}^{n+1} + sU_{i+2}^{n+1} = p \tag{5}$$

with the coefficients:

$$
\begin{aligned}
s &= \frac{b_2}{2(\Delta x)^4}, \\
d &= -\frac{2b_2}{(\Delta x)^4} - \frac{b_1}{(\Delta t)^2(\Delta x)^2} - \frac{a}{2(\Delta x)^2}, \\
e &= \frac{1}{(\Delta t)^2} + \frac{a}{(\Delta x)^2} + \frac{2b_1}{(\Delta t)^2(\Delta x)^2} + \frac{3b_2}{(\Delta x)^4}.
\end{aligned}
\tag{6}
$$

The right hand side of (5) equals to:
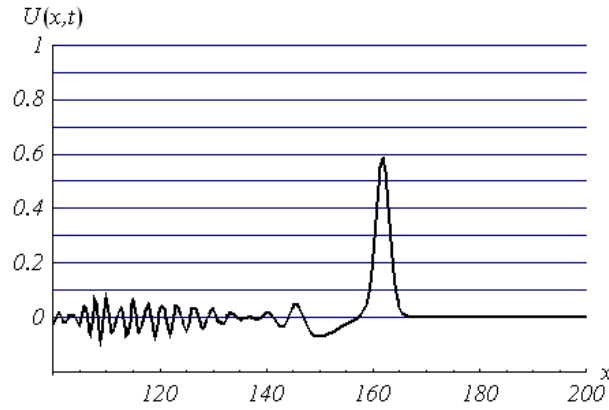
Figure 1: Solitary wave in the rod of negative Poisson's ratio $\nu = -0,8$ with initial condition (11)
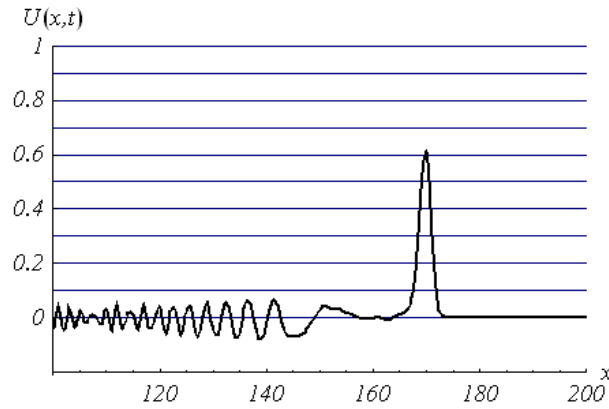
Figure 2: Solitary wave in the rod of positive Poisson's ratio $\nu = 0,4$ with initial condition (11)

$$p = -\frac{1}{\Delta t^2}(U_i^{n-1} - 2U_i^n) + \frac{a}{2\Delta x^2}(U_{i-1}^{n-1} - 2U_i^{n-1} + U_{i+1}^{n-1}) \qquad (7)$$

$$+\frac{b_1}{\Delta t^2 \Delta x^2}(U_{i-1}^{n-1} - 2U_{i-1}^n - 2U_i^{n-1} + 4U_i^n + U_{i+1}^{n-1} - 2U_{i+1}^n)$$

$$-\frac{b_2}{2\Delta x^4}(U_{j-2}^{n-1} - 4U_{j-1}^{n-1} + 6U_j^{n-1} - 4U_{j+1}^{n-1} + U_{j+2}^{n-1})$$

$$+\frac{c_1}{2\Delta x^2}((U_{j-1}^{n+1})^2 - (2U_j^{n+1})^2 + (U_{j+1}^{n+1})^2)$$

$$+\frac{c_1}{2\Delta x^2}((U_{j-1}^{n-1})^2 - (2U_j^{n-1})^2 + (U_{j+1}^{n-1})^2).$$

The nonlinear terms of (7) where approximated by Picard's iterations [3, 6, 7]. The calculation have been stopped after achieving demanded accuracy on each time level:

$$\|U_i^{n+1} - U_i^n\| \le 10^{-5}. \qquad (8)$$

The set of equation (5) has been solved with the help of QR decomposition method with the following initial conditions:

$$u(x,0) = f(x), \qquad (9)$$

$$u_t(x,0) = g(x)$$

340

Figure 3: Solitary wave in the rod of negative Poisson's ratio $\nu = -0,8$ with initial condition (12)
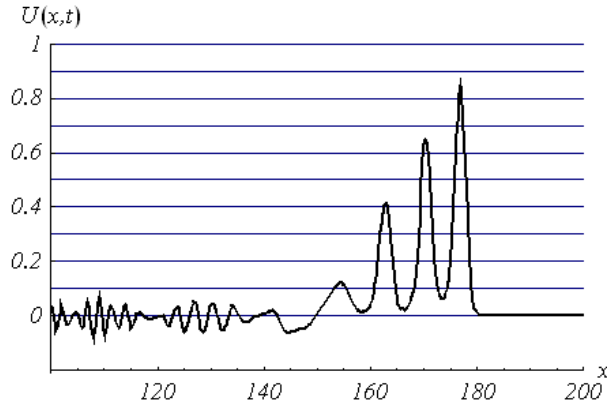
Figure 4: Solitary wave in the rod of positive Poisson's ratio $\nu = 0,4$ with initial condition (12)

for $0 \leq x \leq L$ and boundary conditions [2]:

$$u(0,t) = u(L,t) = 0, \tag{10}$$
$$u_x(0,t) = u_x(L,t) = 0$$

for $0 \leq t \leq T$.

Numerical results

Equation 1 has been solved with the help of difference method for the following data:$\rho = 1050[\text{kg/m}^3]$, $E = 35100000[\text{Pa}]$, $l = -2000000[\text{Pa}]$, $m = -3700000[\text{Pa}]$, $n = -3100000[\text{Pa}]$, $R = 0,1[\text{m}]$. The values of the space and time steps have been taken as: $\Delta x = 1$, $\Delta t = 0.0015$ and calculations were made for 200 space and time steps.

The first simulation deals with a case where the initial rectangular sharp pulse has been introduced as an initial condition in the form:

$$f(x) = \begin{cases} 1 \text{ for } L/2 - 2 \leq x \leq L/2 - 2 \\ 0 \text{ for } x \in \langle 0, L/2 - 2\rangle \cup \langle L/2 - 2, L\rangle \end{cases} \tag{11}$$
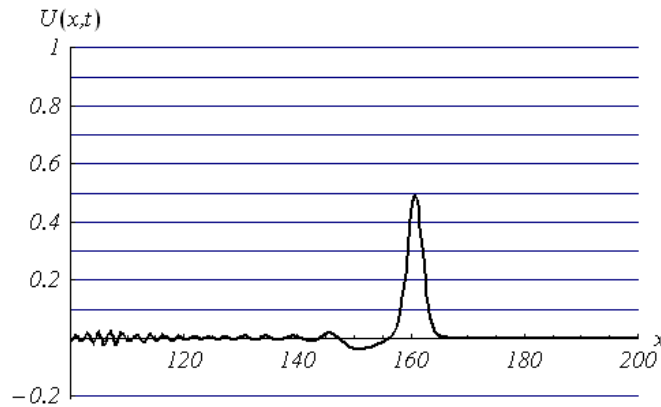
Figure 5: Solitary waves in rod of negative Poisson's ratio $\nu = -0,8$ with initial condition (13)
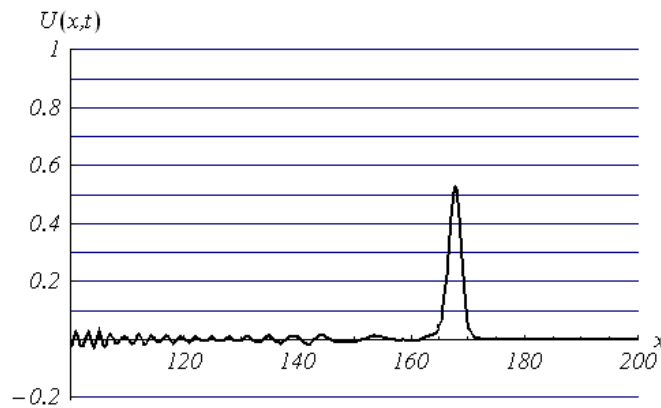
Figure 6: Solitary waves in rod of positive Poisson's ratio $\nu = 0,4$ with initial condition (13)

with initial velocity equal to zero.

The initial deformation (11) being assumed in the center of the rod begins to run splitting to two solitary waves propagating in two opposite directions [2]. For the sake of simplicity in below figures only one half of the soliton profile is presented for $n = 200$. The second one is symmetric to that.

In Fig. 1 the longitudinal mode of solitary waves is presented. It propagates with the constant profile leaving behind an oscillating wave package. In the auxetic materials that propagation is accompanied by a compression area close to the main pulse. However if Poisson's ratio increases, that area disappears.

Comparing results presented in Fig. 1 and 2 we conclude that in the auxetic material the solitary wave has lower amplitude and velocity but its profile is more massive. Moreover, in nonauxetic material there is no compression area.

The second simulation has been done for the initial rectangular massive pulse in the following form:

$$f(x) = \begin{cases} 1 \text{ for } L/2 - 6 \le x \le L/2 + 6 \\ 0 \text{ for } x \in \langle 0, L/2 - 6 \rangle \cup \langle L/2 + 6, L \rangle \end{cases} \tag{12}$$

The obtained results differ from those concerning the first simulation (Fig. 1). It is
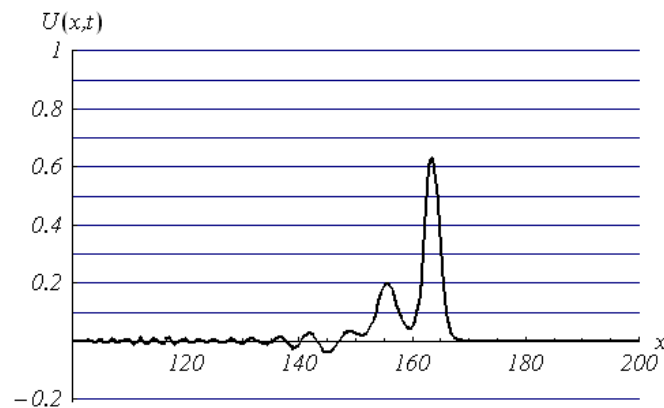
Figure 7: Solitary wave in the rod of negative Poisson's ratio $\nu = -0,8$ with initial condition (14)

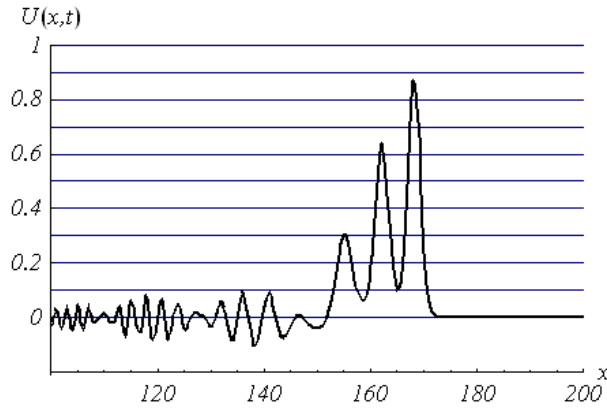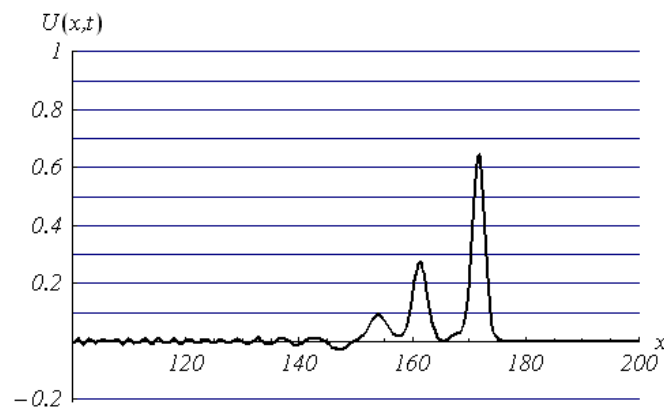Figure 8: Solitary wave in the rod of positive Poisson's ratio $\nu = 0,4$ with initial condition (14)

seen in Fig. 3 that this time the initial rectangular massive pulse is the reason of a train of three solitary waves. Moreover those waves propagate faster with higher amplitude.

Similar situation is observed in Fig. 4 comparing to Fig. 2. This time the train of four solitary pulses propagates faster with more sharp profile of pulses than for the auxetic material. The number of pulses in the train depends not only on width of the initial pulse but also on the Poisson's ratio. It is worth to be noted that the greatest difference in amplitude has been observed for the third pulse in the train of solitary waves comparing auxetic to conventional materials.

The third simulation has been done for the initial triangular sharp pulse in the form:

$$
f(x) = \begin{cases} \frac{1}{3}(x - L/2 + 3) & \text{for } L/2 - 3 \leq x \leq L/2 \\ -\frac{1}{3}(x - L/2) + 1 & \text{for } L/2 < x \leq L/2 + 3 \\ 0 & \text{for } x \in (0, L/2 - 3) \cup (L/2 + 3, L) \end{cases} \tag{13}
$$

Properties of the solitary waves propagating due to initial condition (13) are almost the same as due to condition (11). The only difference is such that the triangular profile of the initial pulse forces waves of lower amplitude of the main pulse. Also compression area occurs for auxetic material (comparing to Fig. 1 and 2)

343

The last simulation concerns the initial triangular massive pulse, i. e.:

$$f(x) = \begin{cases} \frac{1}{6}(x - L/2 + 6) \text{ for } L/2 - 6 \leq x \leq L/2 \\ -\frac{1}{6}(x - L/2) + 1 \text{ for } L/2 < x \leq L/2 + 6 \\ 0 \text{ for } x \in (0, L/2 - 6) \cup (L/2 + 6, L) \end{cases} \quad (14)$$

As well as in the case of the second simulation if the initial pulse profile is more massive the train of solitary waves occurs. Then the number of pulses is bigger in nonauxetic material than in the auxetic one (cf. Figs. 7 and 8 and Figs. 3 and 4)

Conclusions

All the results obtained in this paper confirm stronger damping properties of auxetics than observed in classical materials.

If the profile shape of the initial pulse is more massive the number of train pulses propagating in material with negative Poisson's ratio decreases.

In auxetic material the compression area is observed behind the solitary waves from sharp initial pulse.

The shape (rectangular and triangular) of the initial pulse influences only amplitudes of the solitary waves.

Acknowledgements

References

[1] V. Porubov, Amplification of Nonlinear Strain Waves in Solids, *Word Scientific*, Singapore, 2003.

[2] A. M. Samsonov, Strain Solitons in Solids and How to Construct Them, *Chapman&Hall/Crc*, New York 2001.

[3] H. El-Zoheiry, Numerical study of the improved Boussinesq equation, *Chaos, Solitons and Fractals* **14** (2002) 377-384.

[4] V. I. Erofeev, N. V. Klyueva, Solitons and Nonlinear Periodic Strain Waves in Rods, Plates and shells (A Review), *Acoustical Physics*, **48**, no. 6 (2002) 643-655.

[5] M. P. Soerensen, P. L. Christiansen, P. S. Lomdahl, Solitary waves on nonlinear elastic rods I, *J. Acoust. Soc. Am.* **76** (3), September 1984.

[6] B. Feng, T. Kawahara, T. Mitsui, Solitary-waves propagation and interactions for a sixth-order generalized Boussinesq equation, *Int. J. Mathematics Mathematical Sciences* **9** (2005), 1435-1448.

[7] H. El-Zoheiry, Numerical investigation for the solitary waves interaction of the "good" Boussinesq equation, *Appl. Num. Math.* **45** (2003) 161-173.

[8] K. Djidjeli, W. G. Price, E. H. Twizell, Y. Wang, Numerical methods for the solution of the third- and fifth-order dispersive Korteweg-de Vries equation, *J. Com. Appl. Math.* **58** (1995) 307-336.

[9] G. V. Dreiden, K. R. Khusnutdinova, A. M. Samsonov, I. V. Semenova, Longitudinal strain solitary waves in a two-layered polymeric bar (to appear).

[10] R. Lakes, Foam Structures with Negative Poisson's Ratio, *Science*, **235**, 1987, 1038-1040.

[11] K. E. Evans, A. Alderson, Auxetic Materials: Functional Materials and Structures from Lateral Thinking!, *Adv. Materials* 2000, **12**, no. 9.

[12] Q. Liu, Materials with negative Poisson's ratios and potential applications to aerospace and defence, *DSTO Defence Science and Technology Organization*, August 2006.

[13] K. L. Alderson, V. R. Simkins, V. L. Coenen, P. J. Davies, A. Alderson, How to make auxetic fibre reinforced composites, , *Phys. Stat. Solidi (b)* **242**, no. 3, 2005, 509-518.

[14] R. S. Weber, K. L. Alderson, K. E. Evans, Novel Variations in the Microsture of the Auxetic Microporous Ultra-High Molecular Weight Polyethylene. Part 1: Processing and Microstructure, *Polymer Eng. Sci.*, **40**, no. 8, August 2000.

[15] R. S. Weber, K. L. Alderson, K. E. Evans, Novel Variations in the Microsture of the Auxetic Microporous Ultra-High Molecular Weight Polyethylene. Part 2: Mechanical Properties, *Polymer Eng. Sci.*, **40**, no. 8, August 2000.

[16] H. Kimizuka, H. Kaburaki, Molecular dynamics of the high-temperature elasticity of SiO2 polymorphs: Structural phase transition and elastic anomaly, *Phys. Stat. Solidi (b)* **242**, no. 3, 2005, 607-620.

Piotr Kolat, Poznan University of Technology, Piotrowo 3, 60-965 Poznan, Poland
Bogdan Maruszewski, Poznan University of Technology, Piotrowo 3, 60-965 Poznan, Poland

Imitation modelling of fase transition from axial modes to tangential modes in cylindrical tank

Vitaly Kolykhalin   Sergey Neganov

cap-007@mail.ru

Abstract

Possibilities of application of methods of architectural acoustical diagnostics for control of state of pouring heavy fuel oil (mazut) off from the railway containers are considered. The relative noise levels corresponding of different fuel oil volumes registered by the microphone fixed inside of air phase of railway tank wagon are estimated. The noisemeter signals are analyzed and distinctions of sound-absorbing coefficients of the steel and of the oil are taken care of by a corresponding choice of acoustical diagrams for the empty tank wagon and tank wagon with some fuel oil. Results are proved possibility of method of acoustical diagnostics practical using.

1   Introduction

The volume of rail transportation of fuel oil on highways of the Russian Federation recently has considerably increased, therefore a process of loading and the unloading of railway tanks should be accelerated for exception of idle time. So the residue of fuel oil into tank after unloading must be minimal. The main industrial problem consists of that there is a hardening fuel oil residues in the solid form and has more than half of tank weight. So the exact estimation of the residues should not exceed more then 5...10 percents from all substances. In this case the usual visual control it leads to significant expenses of time and does not provide of the necessary accuracy. The existing technological process of a warming up of substance provides washing out of cold solid fuel oil by jets of the hot liquid black oil +90 deg C which move through two atomizers.Some parts of the fuel oil cool down on the tank walls in the different forms despite of external heating . There is an opportunity to use the "own" source of noise unlike considered before acoustic methods with a "reference" external source of noise [1] and other methods of the remote control of fuel oil volumes in some capacities. It is the noise of a pair of jets which inject some fuel oil through two atomizers under stationary pressure on a surface of the hardening substance.

The complication of ultrasonic field measuring finds out each encompass factor for analysis: ultrasonic oscillation in a fluid, ultrasonic oscillation of air, oscillation of a cylindrical metallic border witch is installed on a foundation with damping elements

of construction and having an open sight hole.

Uniquely to solve the problem in view of these factors is impossible. There is a problem to select of a physical analog to describe those regularities quantitatively. The mane purpose of the work is to describe on the constructed physical model using data witch was obtained experimentally.

2 Measuring spectrum of levels of sound pressure

2.1 The sound source is located in an aerial medium

The acoustic spectrums corresponding to different levels of the sound pressure are registered in wide or narrow strips depending on the some quantity of the residue. The level of pressure Po is measured in the empty tank and the level of pressure Pi is measured in the tank filled partially.

$$\Delta N = 20 \lg \frac{Pi}{Po} \tag{1}$$

The attitude of levels of pressure Po and Pi calculate on the equation (1).

As the result of experimental researches of specific dependence N from the various quantities of the oil rest is obtained. So the spectrums of the relative levels of noise in the rang of $100 \ldots 10000$ Hz account for maximum and minimum quantities of the oil rest in tanks. The equation is noticeably carried out at measurements of spectrums of levels of sound pressure in case of when a source of noise is jet of the hydromonitor [1].

2.2 The statement of the problem

Thus there are some channels of scattering the sound energy: the damping properties of the black oil surface, the exit of the energy through the open tank hole, the energy of scattering through the metallic border and basic damping elements of construction (sprocket, railway rails) etc.

3 Approximate model

3.1 The statement and the solution of the problem

At the first stage the model has the form witch is obviously simplified one when the equation of Helmholtz is solved by a method of dividing of variables:

$$(\Delta + \kappa^2)P(x, y, z) = 0 \tag{2}$$

If the eigen frequency of the system "tank-oil" coincides with one of source harmonic it is possible to expect magnification of amplitude in a spectrum which was experimentally obtained.

These splashes will be rounded owing to the absorption of the system. To calculate fundamental frequencies the elementary model is selected.It has the absolutely rigid walls.

In case of boundary

$$\left.\frac{dP}{dx}\right|_{x=0,2a} = 0, \left.\frac{dP}{dy}\right|_{y=0,2b} = 0, \left.\frac{dP}{dz}\right|_{z=0,2d} = 0 \tag{3}$$

we obtain the dispersing equation

$$\omega_{n,m,p}^2 = \frac{1}{4}c^2\pi^2\left[\left(\frac{n}{a}\right)^2 + \left(\frac{m}{b}\right)^2 + \left(\frac{p}{d}\right)^2\right] \tag{4}$$

3.2 Numerical calculations

For fixed m,n,p the eigen frequencies as function of level of fuel oil d are calculated

$$\omega_{n,m,p} = \sqrt{G}\sqrt{1 + \frac{p}{d^2}} \tag{5}$$

where d is the oil product level in tanks and G,p are constants.

The solution of an inhomogeneous problem with a point source located in the point x_o, y_o, z_o can be obtained in the form :

$$\left(\Delta + \kappa^2\right)P\left(x,y,z\right) = F\delta\left(x - x_0\right)\delta\left(y - y_0\right)\delta\left(z - z_0\right) \tag{6}$$

$$P\left(x,y,z\right) = \frac{F_c^2}{abd}\sum_{n,m,p=0}^{\infty}\frac{\cos\lambda_n x_0 \cos\lambda_p z_0 \cos\lambda_m y_0}{\omega^2 - \omega_{m,n,p}^2}\cos\lambda_n x \cos\lambda_p z \cos\lambda_m y \tag{7}$$

At the second stage the simplified cylindrical model of the railway tank is estimated. Let's appreciate of Helmholtz equation (2) applying the method of dividing of variables in a cylindrical system of coordinates in case of rigid boundary conditions:

$$\left.\frac{dp_c\left(r,\varphi,z\right)}{dr}\right|_{r=a} = 0, \left.\frac{dp_c\left(r,\varphi,z\right)}{dz}\right|_{z=H} = 0 \tag{8}$$

The botton side has boundary conditions :

$$-\left.\frac{dp_c}{dz}\right|_{r=z} = \frac{\rho}{z}\frac{dp_c}{dt} \tag{9}$$

Then we can be obtain

$$\left(\Delta - \frac{1}{c^2}\frac{d^2}{dt^2}\right)\tilde{P}\left(r,\varphi,z,t\right) = F\delta\left(\bar{X}_c - \bar{X}_{ucm}\right)f(t) \tag{10}$$

Solving the problem it would be possible to find out eigen frequencies $\varphi_{m,j,k}$

$$\varphi_{m,j,k}\left(r,\varphi,z\right) = \cos\mu_k z \cdot J_m\left(\lambda_{m,j,k}r\right)\cos m\varphi \tag{11}$$

where J_m are Bessel functions.

General solution of the homogeneous problem in the empty tank

$$p_{\bar{n}}(t) = \frac{C\delta\left(\bar{X}_c - \bar{X}_{ucm}\right)}{2\pi j}\int_{A-j\infty}^{A+j\infty}\frac{e^{pt}\hat{F}(p)dp}{p^2 + \omega_{\bar{n}}^2 + \beta_i} \tag{12}$$

4 Conclusion

As the eigen frequencies depend on the various quantities of the solid oil residue, the method of dividing of variables is inapplicable so problem could be solved numerically (for example, finite element method). The constructed analytical solution of the problem is correct for the whole interval of frequencies. But the most interesting experimental results in the area of medium frequencies acoustical waves were fixed. The geometrical forms and boundary-contact conditions must be strongly pointed and the next step will be to take account of the impedance of surface of solid residue.

References

[1] V. M. Kolykhalin. Different methods of acoustical diagnostics of solid rest of oil product in tank wagons,Conference ELPIT-2005 (Russian Academy of Science, Samara, 2005), pp.97-101.

[2] L. L. Beranec. Acoustic measurements,2nd edition,New York-London,1969.

Changes in the orientation state of polymer molecules in the space between filler particles

Lyudmila A. Komar   Alexander L. Svistkov

komar@icmm.ru

Abstract

For the analysis of formation of polymeric layers with particular properties that arise near filler particles in a filled elastomeric material, a mathematical model has been developed. The model is based on the hypothesis that the oriented regions of the polymer are able to influence the orientation state of neighboring regions.

Modeling of the layer formation proceeds in time. The problem is solved in two-dimensional statement. The model involves the parameter that takes into account the layer extent and velocity. It is assumed that this parameter depends on the number of topological nodes per volume unit.

The periodicity cell of the elastomeric material filled with rigid spherical particles is examined. Formation of layers in the space between particles and away from it is modeled. The results of numerical simulation have indicated that in the material near filler particles there occur regions where polymeric molecules are in uniaxial and biaxial states.

1   Continuum, probabilistic and discrete modeling

The layers of 2 to 10 nm (and more) thick that occur near the surface of filler particles play a large part in the formation of the mechanical properties of polymer nanocomposites. Despite the longstanding efforts of scientists to elucidate the cause of formation of these layers and to understand the mechanism of their influence on the mechanical properties of the material, the problem still remains to be solved. There is no answer to the question as to why the thickness of the layers formed near the surface of filler particles is so large that it achieves several nonometers. In the current study an attempt has been made to construct a mathematical model capable of providing the answer to this question.

For constructing the model, it is essential to determine mathematical parameters best suited to our study. The establishment of these parameters requires information about the preferential orientation of polymer links. To gain it, we use the notion of the orientation tensor. However, before proceeding to the description of the oriented state of the bulk medium, it is necessary to introduce the characteristic of the oriented state of a single link of one of the polymeric chains. Let all links of all polymer chains have a through enumeration: the first link of the first chain is

designated as 1, and the last link of the last chain as N. The index j, running the values from 1 to N, takes the numbers of all links of all polymer chains.

As a characteristic of orientation of the polymer chain link with number j, we offer to use the tensor $\boldsymbol{\tau}_j \otimes \boldsymbol{\tau}_j$, in which $\boldsymbol{\tau}_j$ denotes a unit vector defining the space orientation direction of the j-th link. Clearly, a change in the direction of the vector $\boldsymbol{\tau}_j$ to the opposite produces no effect on the values of the tensor $\boldsymbol{\tau}_j \otimes \boldsymbol{\tau}_j$. The proposed tensor is suitable for our purpose because its averaged value can be found for all possible links of polymer chains and the result of such averaging will not be equal to a zero tensor. It gives an estimate of the oriented state of the polymer. Its eigenvectors and eigenvalues have a clear physical meaning. The eigenvectors of the averaged tensor $\boldsymbol{\tau}_j \otimes \boldsymbol{\tau}_j$ define the space directions along which the chain links are mainly oriented and the directions along which the links are rarely oriented. The eigenvalues of this tensor give a quantitative estimation of the orientation degree of polymer chains in corresponding directions. We assume that the interaction energy of the i-th and j-th links of polymer chains is represented as a potential:

$$u_{ij} = u_0\, w_1(r_{ij})\, w_2(\boldsymbol{\tau}_i \cdot \boldsymbol{\tau}_j),$$

where u_0 is a depth of energy well (or well depth), $w_1(r_{ij})$ is a Lenard-Jones potential energy function. Dependence of energy of interaction u_{ij} from a corner between directions of links of polymeric chains we shall set as

$$w_2(\boldsymbol{\tau}_i \cdot \boldsymbol{\tau}_j) = (\boldsymbol{\tau}_i \cdot \boldsymbol{\tau}_j)^2 - \frac{1}{3} = \boldsymbol{\tau}_i \otimes \boldsymbol{\tau}_i \cdot \boldsymbol{\tau}_j \otimes \boldsymbol{\tau}_j - \frac{1}{3}.$$

The energy of interaction of the i-th link with the other links is defined as

$$\sum_{j=1, j\neq i}^{N} u_{ij} = u_0 \sum_{j=1, j\neq i}^{N} w_1(r_{ij})\, w_2(\boldsymbol{\tau}_i \cdot \boldsymbol{\tau}_j) = \frac{u_0}{C_N} \left(\frac{1}{3} - \boldsymbol{\tau}_i \otimes \boldsymbol{\tau}_i \cdot \left\langle \boldsymbol{\tau}_j \otimes \boldsymbol{\tau}_j \right\rangle_V \right),$$

where value of a constant C_N is determined from a discrete normalization condition

$$C_N \sum_{j=1, j\neq i}^{N} \rho(r_{ij}) = 1,$$

where $\rho(r_{ij}) = -w_1(r_{ij})\, H(r_{ij} - l_{ef})$ is weight factor, $H(\cdot)$ is a function of Heaviside, l_{ef} is effective value of link ($l_{ef} = 0.58$ nm).

We should use the space averaging $\left\langle \boldsymbol{\tau}_j \otimes \boldsymbol{\tau}_j \right\rangle_V$, which in a discrete statement can be obtained as

$$\left\langle \boldsymbol{\tau}_j \otimes \boldsymbol{\tau}_j \right\rangle_V = C_N \sum_{j=1, j\neq i}^{N} \rho(r_{ij})\, \boldsymbol{\tau}_j \otimes \boldsymbol{\tau}_j,$$

and which in a continuum statement can be obtained as

$$\left\langle \boldsymbol{\tau}_j \otimes \boldsymbol{\tau}_j \right\rangle_V = C_V \int_V \rho(r)\, \mathbf{O}\, dV,$$

here value of a constant C_V is determined from a continuum normalization condition

$$C_V \int_V \rho(r)\, dV = 1.$$

We assume that there is a continuous twice differentiated tensor function $\mathbf{O}(t, \mathbf{x})$, which provides calculation of the energy of interaction of the i-th link with the remaining material, as it is usually fulfilled in the context of probability and discrete models.

It is easy to demonstrate that the requirement of equivalence of continuum averaging and discrete averaging for an arbitrary bounded doubly differentiable tensor function will be fulfilled under following conditions

$$C_N \sum_{j=1, j \neq i}^{N} \rho(r_{ij}) \, (x_k^j - x_k^i)^2 = C_V \int_V \rho(r) \, \Delta x_k^2 \, dV.$$

For correct tetrahedron structure we can have

$$C_V \int_V \rho(r) \, \Delta x_i^2 \, dV \approx 0.323, \qquad C_V = 0.047.$$

2 Main causes of change in the orientation tensor with time

The following assumption will be used for constructing the model to describe the formation of layers near filler particles.

In a considered point of a material a speed of change of orientation tensor is defined by two reasons: (a) the orienting effect of neighboring points of the medium on the point in question and (b) the effect of thermal motion of polymer chains, which tends to bring the material to the unoriented state. On the basis of these hypotheses the evolution equation of the orientation tensor $\mathbf{O}$ will have view

$$\frac{1}{b} \frac{D\mathbf{O}}{Dt} = a \left(\langle \boldsymbol{\tau}_j \otimes \boldsymbol{\tau}_j \rangle_V - \mathbf{O} \right) + \left(\frac{\mathbf{I}}{3} - \mathbf{O} \right),$$

where $D\mathbf{O}/Dt$ is the objective derivative with respect to time, $\mathbf{I}$ is the unit tensor, b is speed orientation parameter, a is function from $\mathbf{O} \cdot \mathbf{O}$, which will calculated from the following schema of reasonings.

In an equilibrium condition is carried out

$$\langle \boldsymbol{\tau}_j \otimes \boldsymbol{\tau}_j \rangle_V \cdot \langle \boldsymbol{\tau}_i \otimes \boldsymbol{\tau}_i \rangle_\Gamma = \langle \boldsymbol{\tau}_j \otimes \boldsymbol{\tau}_j \rangle_V \cdot \mathbf{O}.$$

With the use of the Gibbs distribution, it is possible to calculate the average of the distribution for the tensor $\boldsymbol{\tau}_i \otimes \boldsymbol{\tau}_i$

$$\langle \boldsymbol{\tau}_i \otimes \boldsymbol{\tau}_i \rangle_\Gamma = \int_\Gamma \boldsymbol{\tau}_i \otimes \boldsymbol{\tau}_i \, C \exp \left\{ -\frac{u_0}{c_B \theta C_V} \left(\frac{1}{3} - \boldsymbol{\tau}_i \otimes \boldsymbol{\tau}_i \cdot \langle \boldsymbol{\tau}_j \otimes \boldsymbol{\tau}_j \rangle_V \right) \right\} \, d\Gamma,$$

where u_o is the material constant, c_B is the Boltzmann constant, and θ is the temperature.

Evolution of the orientation tensor $\mathbf{O}$ is transformed into the following equation under equilibrium condition

$$\langle \boldsymbol{\tau}_j \otimes \boldsymbol{\tau}_j \rangle_V = \mathbf{O} + \frac{1}{a}\left(\mathbf{O} - \frac{\mathbf{I}}{3}\right).$$

In this case value of function $a(\mathbf{O} \cdot \mathbf{O})$ should be defined from a condition

$$\left[\mathbf{O} + \frac{1}{a}\left(\mathbf{O} - \frac{\mathbf{I}}{3}\right)\right] \cdot \mathbf{O} = \left[\mathbf{O} + \frac{1}{a}\left(\mathbf{O} - \frac{\mathbf{I}}{3}\right)\right] \cdot \langle \boldsymbol{\tau}_i \otimes \boldsymbol{\tau}_i \rangle_\Gamma.$$

Solution of this equation is represented on Fig. 1.

a   b
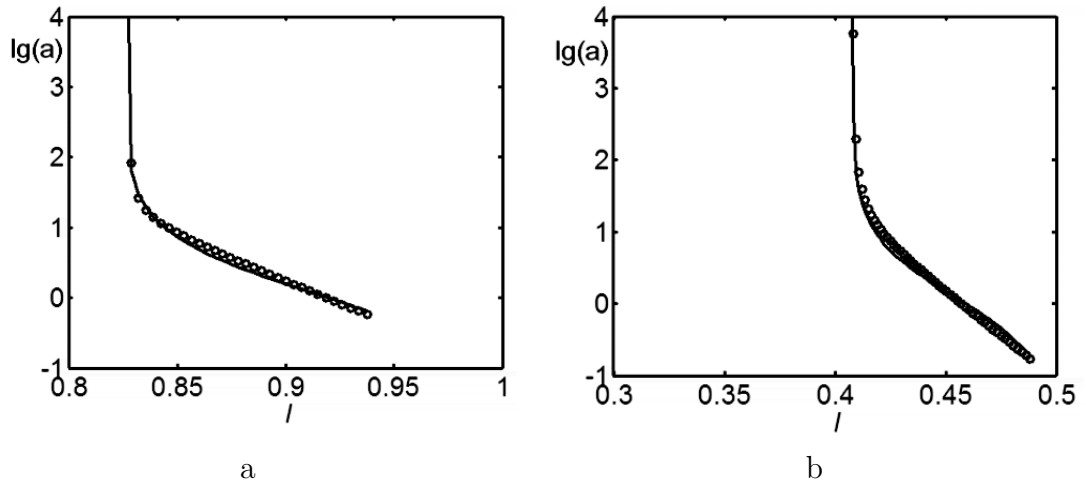
Figure 1: Dependence of parameter a from argument I for uniaxially (a) and biaxially (b) oriented states. Parameter I iqual to $\mathbf{O} \cdot \mathbf{O}$

After decomposition of function $\mathbf{O}$ in a vicinity of a considered point we receive

$$\langle \boldsymbol{\tau}_j \otimes \boldsymbol{\tau}_j \rangle_V = \mathbf{O} + C_\Delta \sum_{i=1}^{3} \frac{\partial^2 \mathbf{O}}{\partial x_i^2},$$

where

$$C_\Delta = \frac{1}{2} C_V \int_V \rho(r) \, \Delta x_i^2 \, dV.$$

For correct tetrahedron structure $C_\Delta = 0,161$.
Ultimately, the evolution equation of the orientation tensor $\mathbf{O}$ takes the form

$$\frac{1}{b}\frac{D\mathbf{O}}{Dt} = a\, C_\Delta \sum_{i=1}^{3} \frac{\partial^2 \mathbf{O}}{\partial x_i^2} + \left(\frac{\mathbf{I}}{3} - \mathbf{O}\right).$$

3 Features of modelling of polymer molecules orientation on the surface of filler particle and in the space between filler particles

In polymeric materials close to a surface of active filler particles and in spaces between these particles the polymeric layers of various character can appear. For example, on border of a polymeric layer a process of connection to it of new links of polymeric chains occurs as a result of orientation of these links under influence of already generated layer and can be taken into account in the evolution equation of orientation tensor by introduction in it of a source of orientation. Changes in the orientation state of polymer molecules in the space between filler particles too can arise. Such changes have absolutely other character. For example, they can arise under influence of any external loading. In this case an uniaxially oriented layer will be formed.

Changes in the orientation state of polymer molecules can be described by the following equation

$$\frac{1}{b}\frac{D\mathbf{O}}{Dt} = a\, C_\Delta \sum_{i=1}^{3}\frac{\partial^2 \mathbf{O}}{\partial x_i^2} + \left(\frac{\mathbf{I}}{3} - \mathbf{O}\right) + (f_u + f_b)\left(\mathbf{O} - \frac{\mathbf{I}}{3}\right),$$

where functions f_u and f_b depend on parameter I. Functions f_u and f_b affect formation of a layer in the field of polymer in which polymeric chains have uniaxially and biaxially oriented direction accordingly. In addition this functions are distinct from zero only in a nonequilibrium condition.

Let's set functions f_u and f_b in the following kinds

$$f_u = g_u\,(I_u^{\max} - I)(I - I_u^{\min}), \qquad I_u^{\min} < I < I_u^{\max},$$

$$f_b = g_b\,(I_b^{\max} - I)(I - I_b^{\min}), \qquad I_b^{\min} < I < I_b^{\max},$$

where g_u and g_b are constants. Values $I_u^{\max}$ and $I_b^{\max}$ are equal to values of parameter I at which function $a(I)$ has the maximal values at uniaxially and biaxially oriented state accordingly (Fig. 1). On the other hand, values $I_u^{\min}$ and $I_b^{\min}$ are equal to values of parameter I at which function $a(I)$ has the minimal values at uniaxially and biaxially oriented state accordingly.

4 Examples of formation of layers

Let's come out with the assumption, that in a zone of formation of biaxially oriented area (near to a source of orientation) there is a change of speed orientation parameter b under the law

$$b = b_1 \exp(-b_2 t),$$

where b_1 and b_2 are constants.

Results of calculation of process of formation of a layer in time in one-dimensional statement are shown in Fig. 2. Process formation of a layer has frontal character. Lines of movement of front are represented in figure with equal step on time $\Delta t =$
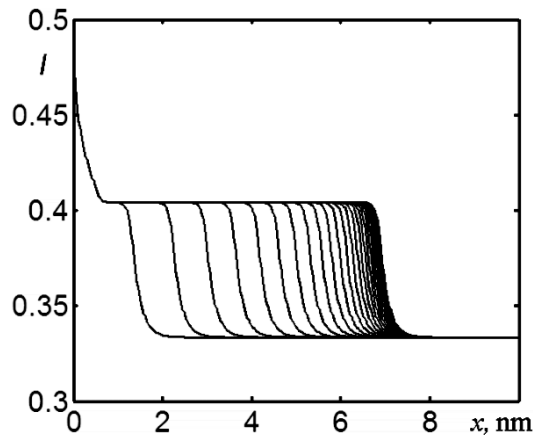
Figure 2: Example of formation of a layer in time in one-dimensional statement in the vicinity of filler surface

10 s. First line corresponds to time $t_1 = 10$ s and extreme right line corresponds to time $t_1 = 300$ s. At such values of constants at the presence of a source of orientation the maximal thickness of a layer is equal 8 nanometers approximately. Thus the clear-cut border between strictly oriented area and area with strict chaos is observed.
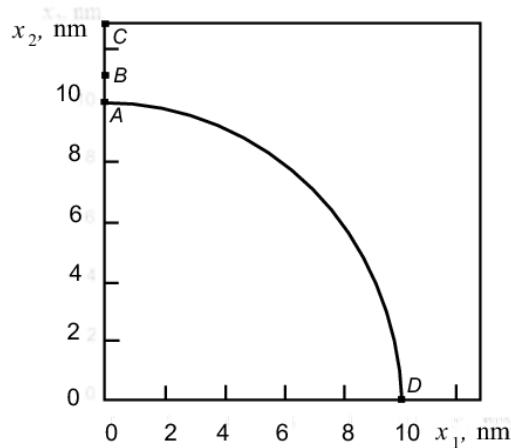
Figure 3: The fragment of the filled polymer containing a spherical filler particle

Let's consider one more example. We apply the evolution equation for modelling change of orientational state of polymer molecules under condition of presence of two sources of orientation f_u and f_b. Under influence of the first source f_u the molecules are oriented in uniaxial direction, but under influence of the second source f_b the molecules are oriented in biaxial direction. The fragment of the filled polymer containing a spherical filler particle is considered (Fig. 3). The radius of a particle R is equal 10 nanometers. Thickness of a gap between particles is equal $0.2R$. Let the source f_u operates along line BC and source f_b operates along line AD.
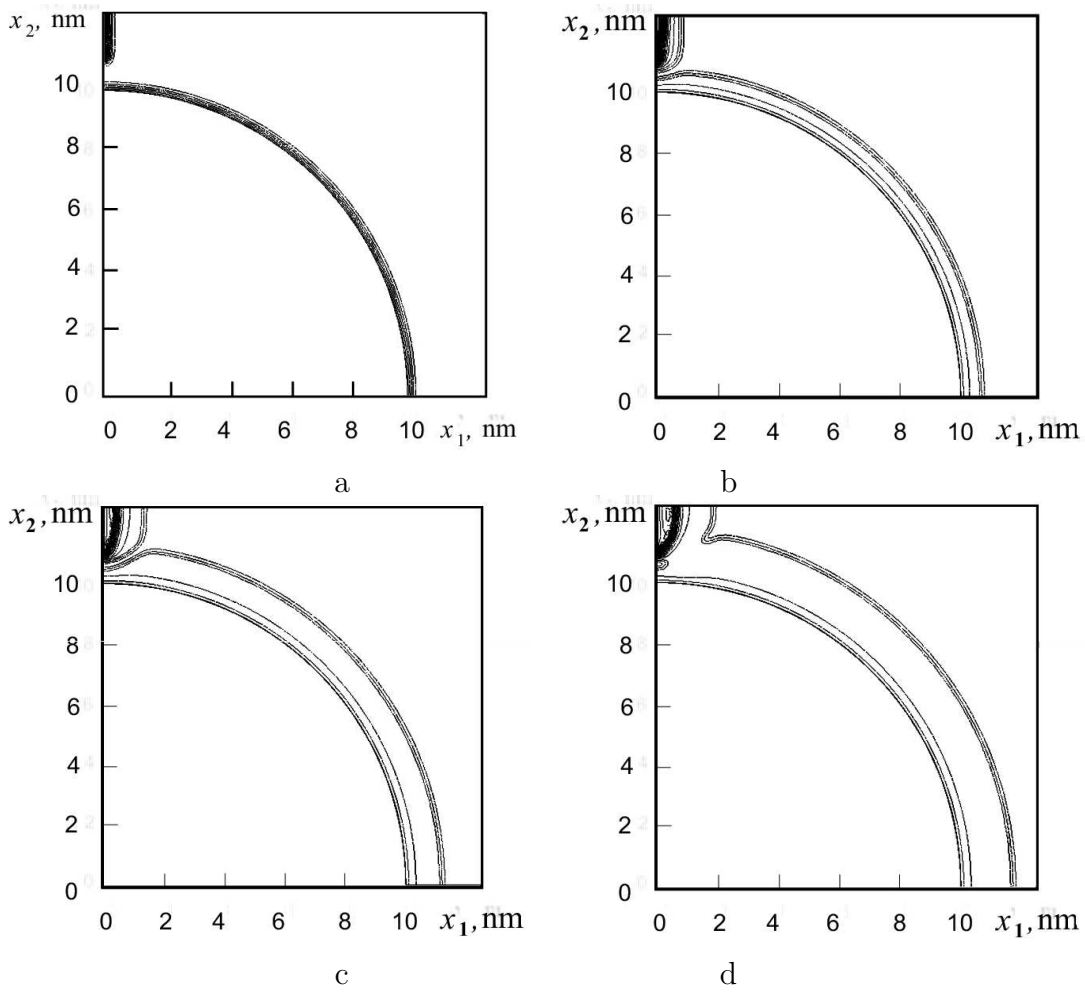
Figure 4: Formation of layer in space between of fillers particles. Time: 100 s (a); 400 s (b); 700 s (c); 1000 s (d)

Results of calculation of this process are shown in Fig. 4. Here we can see layers with uniaxial and biaxial direction in time: 100 s (a); 400 s (b); 700 s (c); 1000 s (d).

Acknowledgements

Lyudmila A. Komar, Perm, Russia
Alexander L. Svistkov, Perm, Russia

Multilevel approach to description of deformation and fracture of brittle porous materials on the basis of movable cellular automaton method

Igor S. Konovalenko   Aleksey Yu. Smolin

igkon@ispms.tsc.ru

Abstract

An approach to multilevel description of deformation and fracture of brittle porous media on the basis of movable cellular automaton method was proposed. The media characterized by pore size distribution function having one maximum were considered. The core of this approach consists in finding the automaton effective response function by means of direct numerical simulation of representative volume of the porous medium. A hierarchical model of mechanical behavior of ceramics under compression and shear loading was developed. A method of taking into account heterogeneity in space distribution of strength properties of porous media was proposed. The main point of this method consists in changing inter-automaton interaction parameters in random directions. It was shown, that the proposed method of taking into account heterogeneity in space distribution of strength properties opens up a wide vistas in multilevel description of porous media with hierarchical porous structure.

Introduction

Porous materials are characterized by hierarchical pore structure and complex mechanical behavior at fracture [1, 2]. To study and describe these materials the information about their structure and mechanical properties on a few scale levels is needed. One way of getting this information is a numerical simulation. In the framework of one-level approach direct accounting for peculiarities of structure and mechanical behavior of material on each scale level seems to be impossible. As a result, the goal of this investigations is the development of multilevel approach and corresponding hierarchical model for describing deformation and fracture of nanostructure porous ceramics under compression and shear on the basis of movable cellular automaton method (MCA) [3]. The calculations were performed for a model material with mechanical properties of nanocrystalline $ZrO_2(Y_2O_3)$ (yttria-stabilized zirconia) with the average pore size comparable with the grain size and one maximum in its pore size distribution function [1]. Building up a hierarchical

model was performed by several stages. At the first stage to find automaton effective response function on macroscopic scale level the calculation were performed with explicit taking into account the structure of material on micro level (this is the scale level where pores structure of model specimens with the size of 6÷120 μm was defined explicitly). The representative volume of porous medium on this scale level was found. At the second stage the calculations performed on the macro-level for "continuous-solid" specimens. The porous structure data on lower scale level was taked into account via the effective response function found at the first stage. One way of taking into account heterogeneity, inherent to porous materials on macroscopic level, is a scatter of mechanical parameters of automaton, for example strength one. The main point of this method consists in changing inter-automaton interaction parameters (the value of inter-automaton interaction criterion) in random directions for randomly chosen automata. The third stage was a verification of the developed model.

1 Finding the representative volume of porous medium and corresponding effective response functions on the macroscopic scale level

On "micro-scale" level the representative volume was determined by means of convergence analysis of elastic and strength properties of the model porous specimens with their size increase. Mechanical behavior of six groups of porous ceramics specimens under uniaxial compression and simple shear was performed. All specimens in each group had the same geometrical size, but different pore space distribution. Each group consisted of five specimens. Square specimens under consideration had dimension (square side) of 6, 12, 36, 60, 90 and 120 μm according to the groups. It was supposed that all pores in ceramics under investigation, as well as the model material, had spherical shape. The pore size of the model material, according to maximum in ceramics pore size distribution function [1], was 1.8 μm. Diameter of movable cellular automata, according to the average grain size [1], was 0.6 μm. Pore structure of model specimens was made by moving away an automaton randomly and its six nearest neighbors (fig. 1,a). The total porosity in all the samples was 15%. The simple-shear loading was simulated by setting equal velocities in horizontal direction to all automata in the upper layer. The value of this velocity gradually increased from 0 to 1 m/s in sinusoidal manner and then remained constant. The automata in the bottom layer were fixed. This regime ensured a quasi-static character of loading and allowed dynamic effects to be avoided until the first damage appears. All samples had periodic boundary conditions in the direction of loading. The uniaxial compression loading was simulated by setting equal velocities in vertical direction (up to 1 m/s) to all automata in the upper layer. The velocities of automata in the bottom layer were set to zero. Displacement in horizontal direction were allowed to automata in the bottom and upper layers. The lateral surfaces of specimen were free. The problem was solved under plane strain conditions. The response function of automata corresponded to the diagram of loading for nanocrystalline $ZrO_2(Y_2O_3)$ with total porosity of 2% and an average pore size comparable

with the grain size [1]. Shear modulus of movable cellular automaton G = 30.8 GPa, Poisson ratio ν = 0.3. Inter-automaton bond fracture criterion used for intensity of shear stresses.

a)   b)   c)
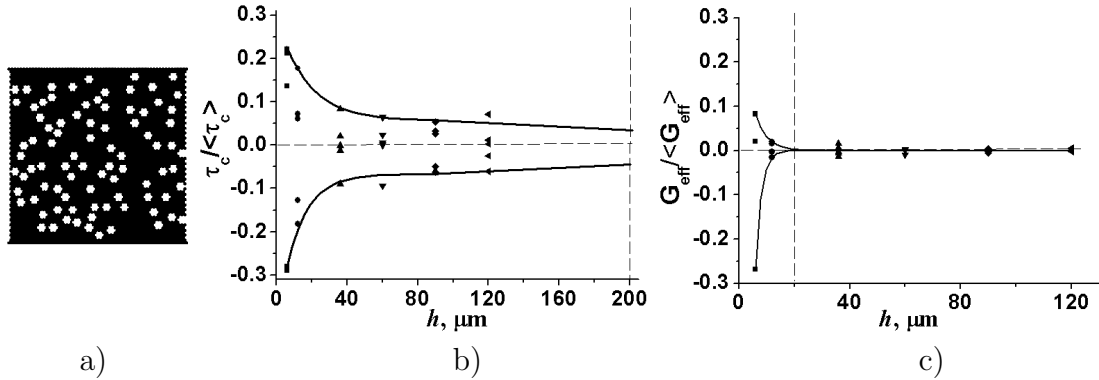
Figure 1: Initial structure of a model specimen with 60 μm sides (a); relative shear strength τ_c deviation (b) and shear modulus G_{eff} deviation (c) of model specimens from corresponding mean values $< G_{eff} >$ and $< \tau_c >$

Convergence analysis of mechanical properties for model specimens with increase of their size was performed in terms of estimated deviation of effective elastic modulus of specimen E_{eff} and its strength σ_c (parameters of diagram of loading) from corresponding mean values in the groups $< E_{eff} >$, $< \sigma_c >$. The specimen size, for which deviation did not exceed 3% for E_{eff} and 20% for σ_c, was accepted as the size of representative volume. Simulation results showed nonlinear convergence of strength and elastic properties of model specimens. Simulation results for case of shear loading is presented in fig. 1,b,c. Relative deviation of E_{eff}, G_{eff}, σ_c and τ_c of model specimens with 60 μm sides from corresponding group average was 1.85, 0.94, 13.7 and 9.3%. These values did not exceed of the desired limits. Thus, it was shown, that porous specimens with 60 μm sides is the representative volume of the model media under consideration. The values of $< E_{eff} >$ and $< \sigma_c >$ were taken as characteristics of response function of automata on macroscopic level.

2   Numerical simulations on macrolevel with implicit taking into account strength properties heterogeneity

On macrolevel the calculations were performed for square "continuous-solid" specimens with 6 mm side. Diameter of movable cellular automata was 6 mm. Information about structure and strength properties of material from micro– to macrolevel was transferred by means of response functions with corresponding characteristics of loading diagrams for representative volumes of material on microlevel. Loading conditions and assumption about stress state are similar with that at the first stage. Heterogeneity of space distribution of strength properties of material on macrolevel was taking into account at the model by means of changing two of six inter-automaton interaction parameters (the value of inter-automaton interaction

criterion) in random directions. The choice of automaton was performed in random manner also. Parameters, characterizing the mentioned heterogeneity on macrolevel, are 1) fraction of automata in the specimen ξ, for which threshold value of inter-automaton bond strength σ is changed, 2) the relative quantity of its changing φ, for randomly chosen bond of isolated automaton, as well as 3) the number of such bonds N for this automaton.

Four groups of model specimens were simulated. Value of ξ was varied as 1, 5, 10 and 15%, correspondingly, and N = 2. The φ varied from -15% to $+50\%$. Each group of specimens contained three subgroups. Every subgroup includes five specimens with equal combinations of σ varying. There were three combinations of φ value under consideration: -10% and -10%, -10% and 10%, -15% and 50% for the first and the second randomly chosen inter-automaton bonds correspondingly.

3   Model verification

We considered the model as successfully verified (i.e the model is valid for ceramics under investigation) if the simulation results satisfied the following criteria: 1) Linear diagram of loading for model specimens, that is typical for porous brittle materials. 2) Qualitative compatibility of the fracture patterns of equal-sized macro-specimens with explicit and implicit description of porous structure. 3) Fit strength properties of specimens a certain interval whose limits was found on the basis of approximate estimator. Performed calculations and comparison of simulated diagrams of loading of model specimens [2] with corresponding diagrams of brittle porous bodies under shear and compression loading [1] revealed their good qualitative compatibility. Thus, the first verification criterion of the model is satisfied. Direct verification of the second criterion satisfaction is not available nowadays owing to vast computational resources needed. In this connection the simulation results of mechanical behavior of brittle porous macroscopic specimens with lower size and explicit description of pores structure from [2] were taken for comparison with the simulation results obtained in this study. Typical fracture pattern of model specimens, represented as inter-automaton bond net at the time of first macrocrack propagation, are presented in fig. 2. Under uniaxial compression the specimens were broken-down because of generating therein the asymmetrical system of inclined macrocracks in conjugated directions (fig. 2,a,b). In case of shear loading the specimens were broken-down because of generating therein both inclined and horizontal macrocrack system (fig. 2,c,d).

One can see from the pattern of generated damages and macrocracks, that the model material with implicit description of porosity equal to 15% and heterogeneously distributed strength properties corresponds to both real [1] and model [2] porous brittle media with small value of porosity (5–10%) and explicit descriprion of pores in the model. It should be noted, that complete correspondence of fracture patterns of the model specimens under consideration and that with explicit description of porous structure is impossible. The reason of this is the fact, that difference in the inner structure of specimens substantially determines the difference in processes, taking place in specimens under mechanical loading. In accordance with these factors we would consider the satisfaction of the second verification criterion of the proposed
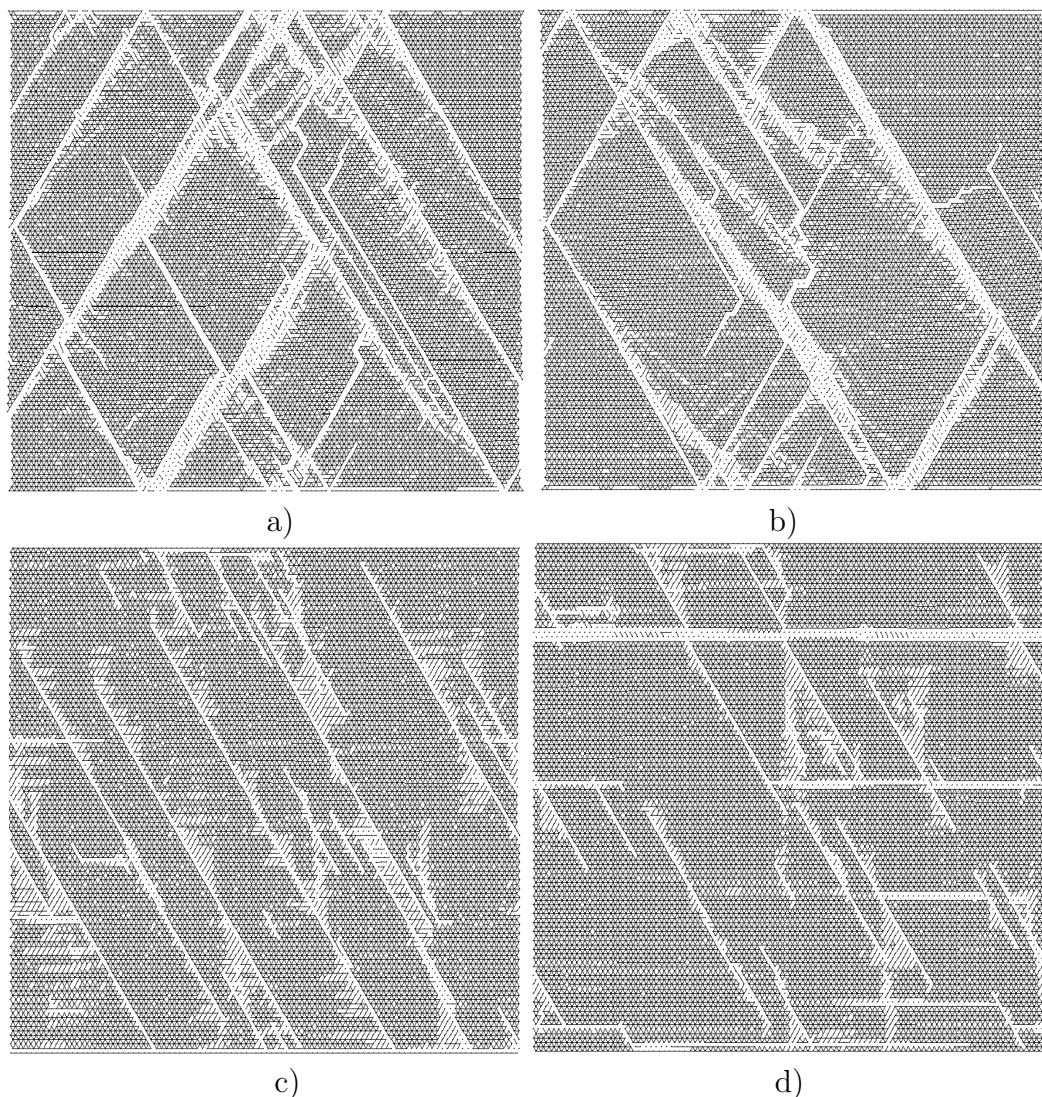
model.

Figure 2: Fracture pattern of model specimens with the same combination of φ values (for specimen (a,b) and (c,d)) in the moment of the macrocrack system nucleation under uniaxial compression (a,b) and shear (c,d). For specimens (a,c) $\xi = 15\%$, and (b, d) – $\xi = 5\%$

To verify the satisfaction of the third verification criterion of model the variation interval of σ_c for groups of specimens with equal value of parameters ξ, φ and N is determined on the basis of the following considerations. The upper limit of σ_{c_max} variation interval corresponded to the strength of macro-specimen without "changed" inter-automaton bonds σ_0 and was equal 500 and 166 MPa in case of uniaxial compression and simple-shear respectively. When deleting inter-automaton bonds for $\xi\%$ of automata as well as taking into account possible change of strength of representative volume (by $\theta\%$), low limit of σ_{c_min} variation interval is described by the expression $\sigma_{c\_min} = \sigma_{c\_max} \cdot (1 - \frac{\xi}{100})(1 - \frac{\Theta}{100})$. Since inter-automaton bonds were not broken at the model, but loosed at $\varphi\%$ in strength, then σ_c of model specimens had to vary in the interval $\sigma_{c\_min} \leq \sigma_c \leq \sigma_{c\_max}$. Simulation results showed, that

turndowns of strength of model specimens σ_c in the case of $\xi = 5\%$ and $\xi = 15\%$ under uniaxial compression and simple-shear loading hit the variation intervals of σ_{c_min} and σ_{c_max}. Thus, the third verification criterion of the proposed model was satisfied.

Conclusions

Thus, on the basis of simulation results we may conclude, that a multy-level approach proposed in this study on the basis of movable cellular automaton method and corresponding hierarchical model developed allow describing of deformation and fracture of brittle porous media under mechanical loading. It was shown, that the proposed method of taking into account heterogeneity of space distribution of strength properties opens up wide vistas in multilevel description of porous media with the hierarchical porous structure. The proposed approach allow predicting the properties of ceramics depending on peculiarities of its pores structure and could serve for development of new brittle porous materials.

Acknowledgements

References

[1] S. N. Kul'kov, S. P. Buyakova, and V. I. Maslovskii, Vestn. Tomsk. Gos. Univ., No. 13, 34 (2003). (in Russian)

[2] Ig.S. Konovalenko. Theoretical investigation of deformation and fracture of porous materials for medical applications and biomechanical constructions. – Diss. cand. phys.-math. Sci., (2007), Tomsk, 174 p. (Institute of Strength Physics and Materials Science SB RAS). (in Russian)

[3] S. G. Psakhie, G. P. Ostermaier, A. I. Dmitriev, et al., Fiz. Mezomekh. 3 (2), 5 (2000). (In Russian)

Igor S. Konovalenko, pr. Academicheskii 2/4, Tomsk, 634021 Rissia
Aleksey Yu. Smolin, pr. Academicheskii 2/4, Tomsk, 634021 Rissia

Influence of structural defects on properties of non-closed nanostructures

Ivan S. Konovalenko   Konstantin P. Zolnikov   Sergey G. Psakhie

ivkon@ispms.tsc.ru

Abstract

Molecular dynamics simulation of non-closed nanostructure behavior is carried out. These structures are formed by self-rolling of nano-sized bilayer Ni-Cu metallic films. Without external actions edges of nano-sized films make weakly damped harmonic oscillations during formation process. Dependences of amplitude and oscillation frequency of nanostructures from initial film sizes are investigated. Optimal geometric parameters of initial films, at which they oscillate with maximal amplitude, are determined. Peculiarities of film composition influence on non-closed nanostructure oscillation are revealed. It is shown that layer composition changing and defect saturation of initial film can purposefully have effect on amplitude, frequency of oscillation or on both these parameters simultaneously. Obtained results are of interest from the point view of nanodevice developing for different purposes.

1   Introduction

Considerable interest in nanostructure investigation is due to their new properties, which significantly differ from macro-sized materials ones [1, 2]. In many respects this is related with increasing of surface atom fraction. An investigation of behavior peculiarity of nanostructures under external actions has both fundamental and applied character. Specifically, nanostructures can be used as components of nano- and micro-devices of different types and purposes.

At present there are two manners of nanostructure fabrication: regulated formation of precise nanoobjects from atoms, and using already pre-composed building blocks with larger sizes, for example, multilayered crystal films. Lack of reliable assembler of nanoobjects from individual atoms makes the second manner more perspective [3]. For nano-sized films creation the method of Molecular-Beam Epitaxy (MBE) is used. MBE is based on epitaxialy growth atomic layers on a substrate surface with precise up to one atomic monolayer. At that, formed film has ideal crystal structure duplicating the substrate one. Under following chemical etching of "sacrificial layer" the film begins to detach from substrate and to roll by reason of appearing of force moments in it. The shape of formed nanostructure depends on chemical and layer composition as well as geometrical sizes of initial film. Fundamentally important fact of nanostructure generation on the basis of above mentioned manner is high

degree of multilayer film crystal order. At the same time the crystal order can be broken by a number of reasons (due to some peculiarities of etching and drying at formation of nanostructures, or at utilizing them, if they are used as components of different nanodevices). Therefore the main goal of the present researches is influence investigation of crystal order disruption of initial films on properties of non-closed nanostructures, formed on their basis.

2 Computer-aided experiment statement

The calculations are carried out by means of molecular-dynamics method. The system, under investigation, is Cu-Ni. In consequence of process transience and small sizes of studied objects computer simulation, in particular, molecular-dynamics method allows obtaining the information which is hard-hitting in experimental investigations. The necessity of explicit taking into account of atomic structure discreteness of simulated objects makes molecular-dynamics method the efficient one in investigation of nanostructure behavior and properties [4, 5]. Interatomic interactions are described by the many-body potentials calculated by the embedded atom method [6, 7, 8] which allows to characterize elastic and surface properties as well as energy parameters of point defects of studied system.

The choice of Cu and Ni as a chemical elements used for bilayered film composition is due to the fact, that they have the identical crystal structure and mismatch between lattice constants near 2.5%. In addition, the Cu-Ni phase diagram shows the continuous number of solid solutions. Such characteristics of these metals and peculiarities of their phase diagram allow in practice to put on a substrate large number of Cu and Ni atomic layers and form on the base of generated films nanostructures with different shapes and properties [3, 9].

For bilayered nanostructure formation the simulated film is conventionally divided into two layers with the equal thickness. One layer is consisted of Ni atoms, and the other one – of Cu atoms. Each layer contains 4 atomic planes. The lattice constant either of the two layers is given by the average value of equilibrium lattice constants of these metals. Thus, initial metallic film is strained (Ni layer is stretched and Cu layer is compressed). It is noted, that chemical etching process is not taken into account, because its real duration is too long for molecular-dynamics calculation. The length of simulated film is equal to 100 lattice parameters. Along two axes free surfaces are simulated and along the third direction periodic boundary conditions are set. The simulated film contains 12000 atoms.

3 Simulation results

Without external actions simulated bilayered nanofilm begins rolling in Ni layer side. This process is due to the initial assumed stretching of Ni layer and compressing of Cu layer. After reaching of the position, shown in Fig. 1,a, when free edges of the film are maximum brought together, the simulated nanostructure beings unbending to the position close to initial one (Fig. 1,b). After that the "bending-unbending" film process with periodically reaching of the two extreme positions is

occurred. Without external resisting forces the oscillations have weakly damped character that is related with dissipative processes. Oscillations damping is due to the internal friction effect, which gives rise to gradual transformation of mechanical oscillation energy into thermal motion of atoms. The substance of this effect can be explained by the fact, that in certain time moment the stretched film layer has less temperature then the compressed one. The temperature gradient arises, which leads to heat transfer and conversion of mechanical energy into thermal one, hence, to the oscillation damping.

3.1 Influence of geometrical sizes of initial films on nanostructure properties

Properties of nanostructures depend on not only from boundary and initial conditions but also from their geometrical sizes. For the purpose of investigation of geometrical factor influence on nanostructures behavior initial bilayered films with different thickness are simulated. Either of the two layers (Cu and Ni) consists of 5, 10, 15, 20 and 25 atomic planes. For all investigated specimens these values of film lengths are used that the normalized amplitude of non-closed nanostructure oscillations (maximum distance changing between the oscillating film edges divided by its initial length) is equal to 70%. The oscillations with amplitude more then this one can lead to nonreversible structural reconfiguration and closing of free edges of nanostructure during afore-said process. Results show that the normalized amplitude of simulated nanostructures has linear dependence on the initial film length.

Calculation results show that oscillations amplitude (Am) of free edges of non-closed nanostructure with constant film thickness depends on its initial length. The simulated non-closed nanostructures, either of the two layers contains 15 atomic planes (the first layer consists of Cu atoms and the second layer - Ni atoms), are shown in Fig. 2. Length increasing of simulated nanostructure with constant film thickness leads to increasing of the oscillation amplitude. The oscillation amplitude dependences on the initial film length are depicted in Fig. 3,a. The oscillation amplitude in the initial film length units is represented. In accordance with obtained results the normalized oscillation amplitude of simulated nanostructures increases nonlinearly with growth of their length.
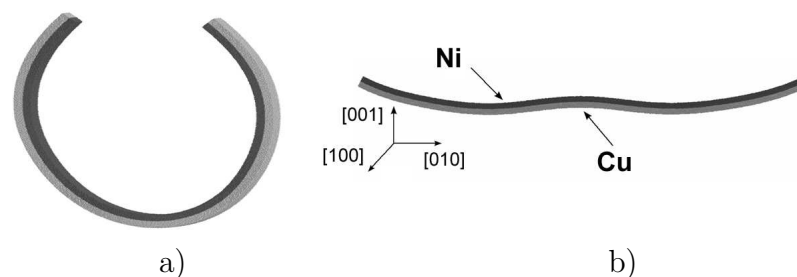
Figure 1: Extreme positions of simulated non-closed nanostructure. Free edges of the film are: a) maximum brought together; b) maximum moved apart. Coordinate axes are shown in accordance with crystallographic directions of initial film
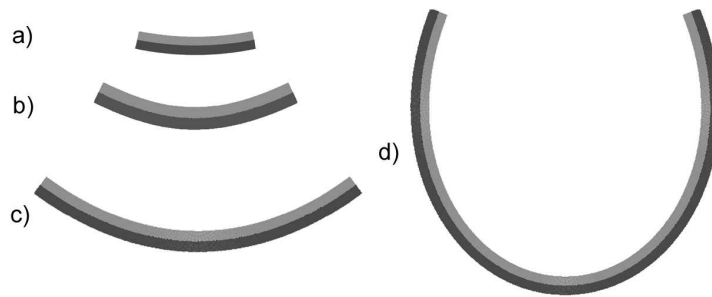
Figure 2: Non-closed nanostructures with different initial film length L: a) 35.7 nm, b) 49.9 nm, c) 89.2 nm, d) 206.9 nm at the points, when their free edges are maximum brought together. Layer of Ni are marked by light color and layer of Cu – by dark color

Fig. 3,b demonstrates the dependences of oscillation frequency variation on initial film lengths. The curve 1 corresponds to the film which layers (Cu and Ni) contain 15 atomic planes and the curve 2 – the film which layers (Cu and Ni) contain 10 atomic planes. It is seen that oscillation frequency decreases quickly enough with initial film length increasing. Results analysis shows that for lengths more then 40 nm (curves in Fig. 3,b) are well described by relation $\sim 1/L^2$, that is in a good agreement with investigation [9]. If the film length is less then the mentioned one the studied dependence is disrupted by reason of increasing influence of structure discontinuity.

Fig. 4 shows the oscillation amplitude and frequency dependence of bilayered film on its thickness. Each point on the curves corresponds to the film, which oscillates with normalized amplitude 70%. One can see that the oscillation frequency decreases nonlinearly with increasing of film thickness h (Fig. 4,a). The oscillation amplitude growths with increasing of h (Fig. 4,b) and can be described by linear function inside investigated thickness region.
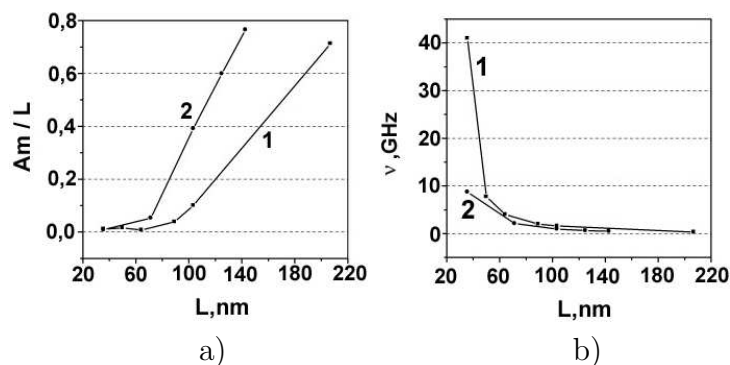
Figure 3: The influence of length L of non-closed nanostructure on: a) oscillation amplitude Am, which are normalized to initial film length L, b) oscillation frequency ν. The results are presented for different film thickness (in atomic planes of Cu and Ni layers): 1) 15, 2) 10

The behavior of non-closed nanostructures under heating is investigated. The initial non-closed nanostructure is relaxed to 200K and then heated up to 300K or up to

500K by means of atom velocities scaling in order to study the transformation of supplied thermal energy into mechanical oscillation energy of its free edges. The efficiency estimation of this transformation is carried out.

The simulation of heating process is carried out for films with following sizes: the lengths are equal to 50, 100, 150 and 200 lattice spacing and the sicknesses are equal to 4, 6, 8 and 10 monolayer for each kind of atoms. The efficiency of thermal energy transformation (η) into mechanical oscillation energy of all simulated films is calculated for different temperatures: 300K (Fig. 5,a), 500K (Fig. 5,b). This value is estimated as the fraction of thermal energy transformed into mechanical oscillations.
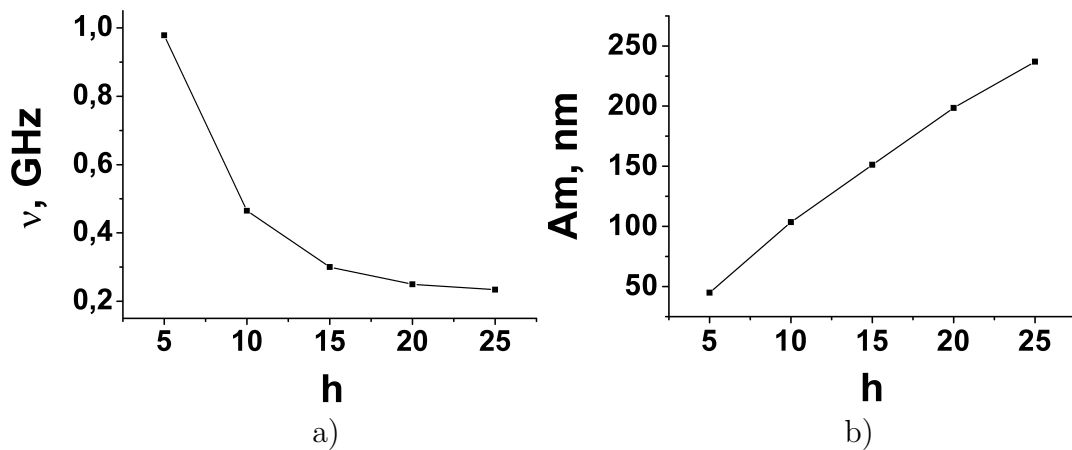
Figure 4: Oscillation frequency (a) and amplitude (b) dependences of bilayered film on its thickness

As demonstrated in Fig. 5,a the transformation efficiency of thermal energy under heating increases with growth of heating temperature. Thus the variation of geometrical parameters of initial film allows purposefully having effect on transformation efficiency of thermal energy into energy of mechanical oscillations.

3.2 Influence of structural defects and layers composition on properties of non-closed nanostructures

Eigenfrequencies and amplitudes of harmonic oscillations of non-closed nanostructures, which are formed on the basis of bilayered crystal films, depend not only on its length, sickness, chemical and layers compositions, but also on defects presence in crystal layers. Two percent of vacancies were put into initial film in order to investigate of defect influence on oscillation process (Fig. 6).The geometrical sizes of initial film are chosen such way that the normalized oscillation amplitude is nearly to 70%. Vacancies are located in random manner into central third part of the film. Presence of a large number of vacancies leads to appearance of additional volume and following stress relieving. Despite the geometrical sizes of the film are not changed, its oscillation amplitude is significantly decreased. Bended and unbended positions of simulated films with ideal crystal and defect structure are shown in Fig. 6.

Formation of different initial film layer configuration can be the efficient manner to change kinematical characteristics of non-closed nanostructures. For that, the

367

a)   b)
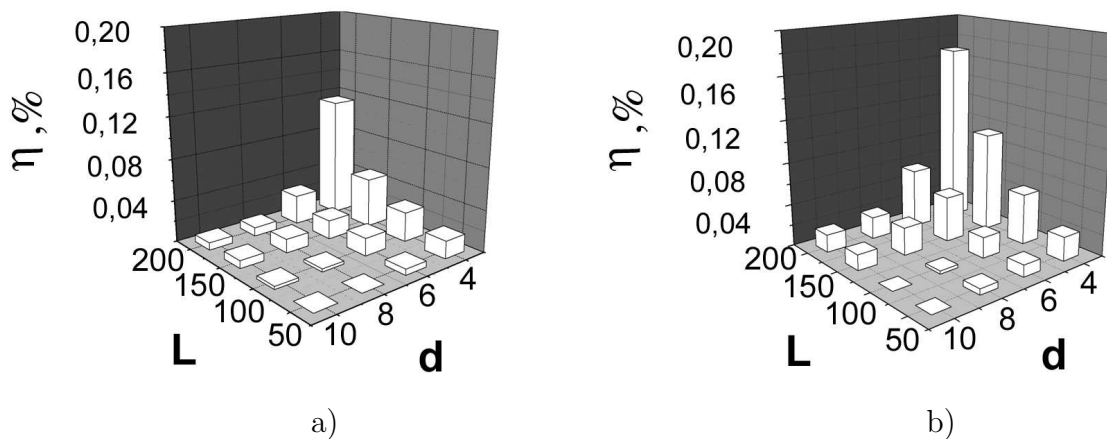
Figure 5: The dependence of transformation efficiency of thermal energy into mechanical one for non-closed nanostructures on different lengths L and thicknesses d of the initial film (d is expressed as atomic plane number, L – as lattice constant number) under heating up to temperatures: a – T = 300K; b – T = 500K

behavior of non-closed nanostructures with following layer configuration is investigated. One sort of atoms is changed by another one in the atomic plane near the layer interface of the initial film. Thus, the atom sort is substituted "artificially" in the central third part of atomic plane. The dependence of distance changing between non-closed nanostructure free edges on time is presented in Fig. 7.
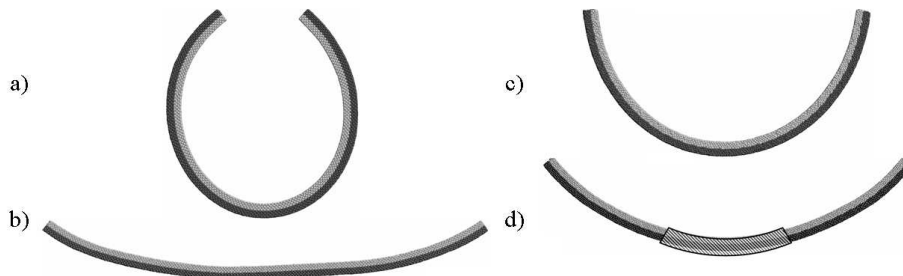
Figure 6: Non-closed nanostructures with ideal crystal order (a, b) and with ∼ 2% vacancy saturation (c, d) in extreme positions of free edges: a, c – maximum brought together; b, d – maximum opened. Layers of Ni are marked by light color and layers of Cu – by dark color. Hatched part of the film contains ∼ 2% of vacancies

It is seen, that vacancy insertion into initial crystal film leads to the amplitude decreasing (Fig. 7). At that, nanostructure oscillation frequency doesn't change practically and curve describing distance between free edges has many "breaks", which are smoothed with time. It is noted that "breaks" are also observed on the curve of non-closed nanostructure with ideal crystal structure at stage of the oscillation formation.

Changing of layer composition of non-closed nanostructure leads not only to amplitude revising but also to variation of free edge oscillation frequency. Thus, substitution of Cu atoms of central third part of atomic plane from Cu layer, which lies on layers interface, for Ni atoms results in oscillation changing of free edges

368

of non-closed nanostructure (Fig. 7, III curve). For this layer composition the oscillation amplitude of free edges decreases approximately by 32% and oscillation frequency diminishes roughly by 15%. Amplitude-frequency characteristics of non-closed nanostructures with various layers configuration and crystal order disruption are demonstrated in Fig. 8.
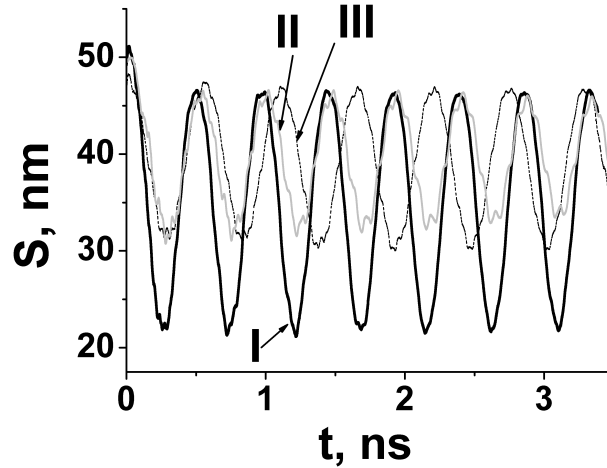
Figure 7: Dependence of distance changing between free edges of non-closed nanostructures on time (I – ideal crystallite; II – ~ 2% vacancy saturation; III – one Ni atomic plane insertion)

4 Conclusions

So, performed calculations show that nano-sized structures formed on the basis of bilayered crystal films without external actions make weakly damped harmonic oscillations. It is determined that amplitude and frequency of mechanical oscillations depend on geometrical sizes (length and thickness of initial film). The increasing of initial nano-film length provided that its thickness constancy results in the oscillation frequency decreasing. The simultaneous proportional increasing of length and thickness of initial crystal film leads to the linear growth of the oscillation amplitude. Therefore, kinematical properties of non-closed nano-sized structures can be changed purposefully by variation of their geometrical parameters. It is shown that aforesaid parameter changing influences on transformation efficiency of thermal energy supplied to the non-closed nanostructure into mechanical oscillation one.

It is shown that kinematical characteristics of simulated nanostructures can be varied by the selection of layer composition of the intial bilayer film. In particular, the thickness variation of initial film layers which are consisted of different sort atoms can significantly influence on the amplitude and the oscillation frequency of free edges. The substitution Cu atoms by Ni ones results in higher changing of amplitude then frequency one in simulated nanostructures. Inverse atom substitution leads to insignificant amplitude changing and great decreasing of frequency oscillation (Fig. 8). Vacancy insertion in the initial film results in considerable amplitude

changing, whereas oscillation frequency remains practically changeless in comparison with nanostructure with ideal crystal lattice.

Nanostructure	Amplitude, nm	Frequency, GHz	Initial film
with ideal crystal structure	24,6	2,13	
Cu atoms are changed by Ni atoms in central plane	16,7 (32%)	1,82 (15%)	
Ni atoms are changed by Cu atoms in central plane	24,2 (2%)	1,75 (18%)	
with ~2% vacancy saturation	12,0 (51%)	2,14 (0%)	

Figure 8: Amplitudes and frequencies of different non-closed nanostructure oscillations

The results of simulations are of interest of components developing with required geometrical sizes and kinematical characteristics for nanodevices for different functional purposes.
Calculation is done with use of supercomputer "SkifSyberia" located at Tomsk State University.

References

[1] C. Poole, F. Owens, Nanotekhnologii. Mir materialov i tekhnologij. (Tekhnosfera, Moscow, 2005).

[2] E. Vogel, Nature nanotech. V.2 (1), 25 (2007).

[3] Yu.V. Nastaushev, V.Ya. Prinz, S.N. Svitasheva, Nanotech. V.16 (6), 908 (2005).

[4] S.G. Psakhie, K.P. Zolnikov, S.Yu. Korostelev, A.V. Jeleznjakov, Iv.S. Konovalenko, Fiz. Mezomekh. 11 (6), 17 (2008).

[5] S.G. Psakhie, K.P. Zolnikov, Iv.S. Konovalenko, Fiz. Mezomekh. 9 (Special issue), 9 (2006).

[6] M.S. Daw, M.I. Baskes, Phys. Rev. B29 (12), 6443 (1984).

[7] S.M. Foiles, M.I. Baskes, M.S. Daw, Phys. Rev. B33.(12), 7983 (1986).

[8] J. Cai, Y.Y. Ye, Phys. Rev. B54 (12), 8398 (1996).

[9] S.G. Psakhie, K.P. Zolnikov, Iv.S. Konovalenko, Syntez I svojstva nanokristal-licheskikh I substrukturnikh materialov, 147 (Ed. by A.D. Korotaev, Tomsk State University Press, Tomsk, 2007).

Ivan S. Konovalenko, pr. Academicheskii 2/4, Tomsk, 634021 Rissia
Konstantin P. Zolnikov, pr. Academicheskii 2/4, Tomsk, 634021 Rissia
Sergey G. Psakhie, pr. Academicheskii 2/4, Tomsk, 634021 Rissia

FEM simulation of fatigue damage, crack nucleation and growth in a pre-damaged material

Igor K. Korolev   Alexander B. Freidin   Sergei V. Petinov

i.korolev82@gmail.com, afreidin@yandex.ru, spetinov@mail.ru

Abstract

A FEM-based procedure of fatigue crack growth simulation in the field of progressive damage is developed. A specific finite element grid is suggested which allows saving information on accumulated damage and "natural" tracing of growing crack; otherwise it is timely and laborious using the standard FEM-procedures. The basic principles of meshing are formulated and following these principles a two-level finite element grid was designed. Further, fatigue behavior of a notched plate with imbedded randomly distributed defects is analyzed. The plate is assumed a composition of finite elements representing material elements with randomly distributed fatigue resistance parameters. Defects in material structure are modeled by elements with negligibly small stiffness. The fatigue properties of the material elements are described by parameters of the Basquin (S-N) equation. The damage evolution and the traces of growing cracks in the plate are assessed at different phases of fatigue life.

The procedure developed is deemed an effective mechanism that allows both to model the crack formation from a defect and its further propagation accordingly the damage accumulation during all period of cyclic loading. It provides also reducing substantially the influence of the mesh geometry on the progressive crack extensions.

1   Introduction

Simulation of fatigue crack growth in conjunction with the damage accumulation, based on coupled action of mechanisms of slip in material grains and stress field has been attracting attention through the past decades, e.g., [1]. One of effective ways of modeling the crack propagation is the use of finite-element method (FEM). Application of FEM for the analysis of crack propagation when the crack path may be affected by the inhomogeneous development of damage or by specifics of the stress field immediately assumes an operative reorganization of a finite element grid during the crack extensions. It allows avoiding the influence of the finite element grid topology on the crack trajectory. This is because the initial grid can not adequately describe the re-distribution the stress and strain field around the tip of the growing crack.

However, applicability of such approach is limited by a class of problems where there
is no correlation between the crack path and the previous history of damage accumu-
lation in material. When dependence of the crack extensions on the pre-history of
damage should be accounted for, the re-design of the FE mesh is unacceptable since
it leads to deleting the information on the developing degradation of the material.
This work is focused on the design of finite element grid which, on the one hand,
would allow naturally to save the information on the fatigue damage in material
(finite elements) prior to failure and to model by this the whole process of fatigue
crack development using the unique finite element mesh, and on the other hand,
would minimize the influence of the mesh topology on the traces of fatigue cracks.
Based on the formulated principles the original structure of FE grid is developed
and verification of its consistency is presented.

2   Basics of the approach and development of the specific mesh type

The crack initiation and propagation is modeled based solely on assumption that
the damage accumulation in material elements controls the process. As an example,
the fatigue process is analyzed in a formally elastic plate with a central circular
hole under cyclic zero-to-tension loading. First, the analysis is addressed to the
homogeneous material modeled with the finite element mesh differing by topology.
Fatigue process is modeled by the sequence of damage accumulation in FE's using
the Palmgren-Miner rule [2]:

$$D = \sum_i \frac{n_i}{N_i} \tag{1}$$

where D is the accumulated damage in an element, $n_i = n(S_i)$ is the number of
load cycles with the stress range S_i , $N_i = N(S_i)$ is the number of cycles prior to
failure of the "i" element with the stress range S_i.
Values of $N(S_i)$ are obtained from the S-N curve for the plate material approximated
by the Basquin equation [3]:

$$N(S) = C/S^m \tag{2}$$

where and m – the material empirical "constants", to be obtained from the exper-
imental data, S - the stress range.
By substitution (2) into (1) the damage accumulated in every of the elements:

$$D = \sum_i \frac{n_i}{N_i} = (1/C) \sum_i n_i S_i^m \tag{3}$$

Successive failure of elements, i.e. when the damage in a sequential element becomes
$D = 1$, is defined by decreased stiffness of the element by several decimal orders (
"killing" of elements), and succession of failures indicates the crack extension. Rapid
acceleration of the progress of damage, characterized by the crack growth rate, was
regarded the indication of the plate failure. This scenario was realized in the case

when the crack origination was assumed at the notch root, but at a certain distance from the axis of symmetry.

First, a standard regular finite element mesh is used. Fig.1 shows the initial stage of the crack extensions and the final state with well-developed crack under cyclic loading (the cyclic load is applied far from the fragment shown, in "infinity").
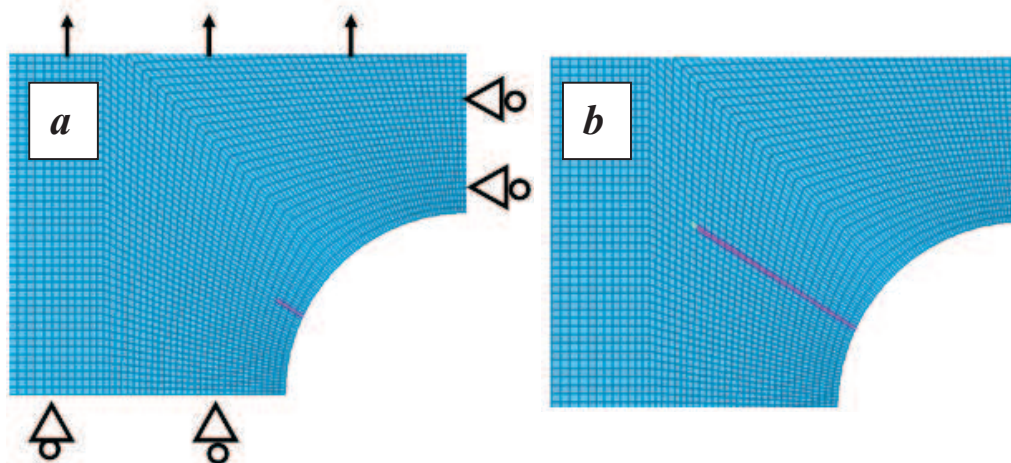
Figure 1: Crack growth simulation by the mechanism of the damage accumulation. Regular FE mesh

Fig.1, a, b show that crack follows strictly the mesh nodal line, inclined to the direction of loading and direction of the maximum principal stress. Due analysis (by using finer mesh at assumed crack tip) indicates that the most intensive damage at every of the crack increments develops in successive element located directly ahead the crack tip, i.e. along the grid nodal line. It may be explained by modeling the crack extensions by successive "killing" of elements.

Keeping with the modeling of fatigue cracks by the damage accumulation principle, the following requirements for the meshing can be formulated in order to minimize the influence of the grid topology on the trajectory of growing crack:

1. The crack tip should be provided "freedom" to turn under the influence of the local stress field, accompanied by the accumulated fatigue damage in successive elements.

2. The isotropy of the grid is desired. Any specified nodal lines in the mesh would control the crack extensions.

Respectively, a cell structure of the mesh was derived meeting the above requirements. A cell of the mesh structure is shown in Fig.2.

The cell consists of "blocks-circles"; in the center of "circles" there are triangular elements which allow for deviation of the crack tip. By this in the center of every of the "block-circles" the crack path would be corrected accordingly the local stress field; further, the crack would extend towards the next "block-circle". Thus, the crack trace would be represented by a zigzag line. If the size of the grid cell is small enough then the trajectory will be slightly differing from the "true" one.Also this cell is consistent with the requirement to the mesh isotropy, since there is no predominant direction, nodal point line, capable of controlling the crack path.
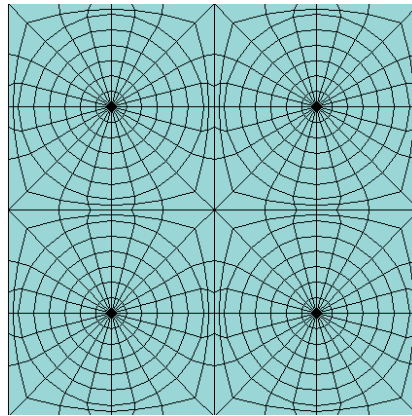
Figure 2: A cell of the proposed isotropic mesh type

This mesh type was applied for the above crack growth analysis. Figs.3, 4 present
the results of simulation of fatigue crack extensions under uniaxial cyclic loading
for different directions of applied cyclic load. Fig.3, a shows that the simulated
crack propagation in general satisfactorily follows orientation of the planes normal
to the maximum principal stress flow, apart from the area where the mesh is ori-
ented. When the plate is loaded in horizontal direction (Fig.3, b) the initial "defect"
(black line) occurs inactive, and the crack is initiated by the damage accumulation
mechanism in the "proper" location.
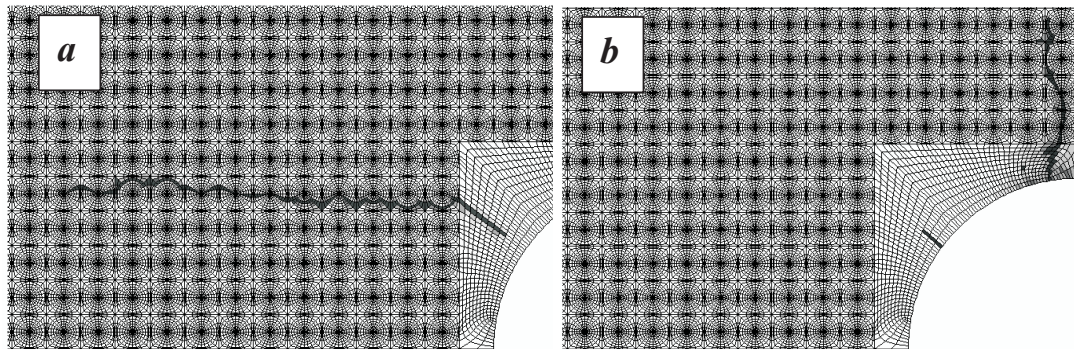
Figure 3: Fatigue crack simulated under uniaxial cyclic loading: (a) cyclic load is
applied in vertical direction; (b) - horizontal direction of cyclic loading

Another example of "calibration" of the suggested procedure is the simulation of
fatigue crack propagation under the in-phase biaxial loading. Fig.4 shows the results
of the crack modeling: it is seen again that in general the crack trajectory complies
with the Sih's principle - it grows normally to direction of the maximum principal
stress.
However, the applied mesh type provides the wavy character of the crack path: the
mesh makes the damage accumulation preferred along the boundaries of the mesh
cells. To allow for the better crack trace simulation the proposed meshing would
need in further optimization so that the damage accumulation and respective crack
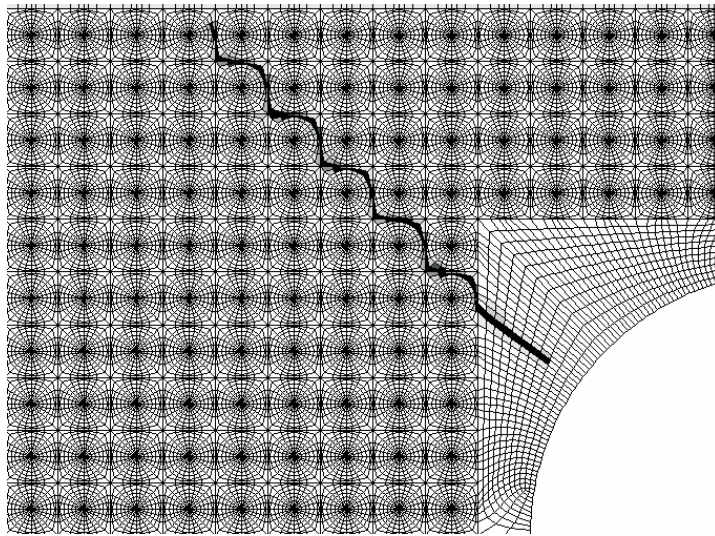
Figure 4: Development of fatigue crack under biaxial cyclic loading (the in-phase cyclic loads are applied both in horizontal and in vertical direction with equal amplitudes)

extensions would be less dependent on the properties of cells.

By applying the trial-and-error method an improved grid is developed which combines the advantages of the previous one and allow eliminating the revealed shortcomings. A cell with improved FE sub-structure is presented in Fig.5. This cell
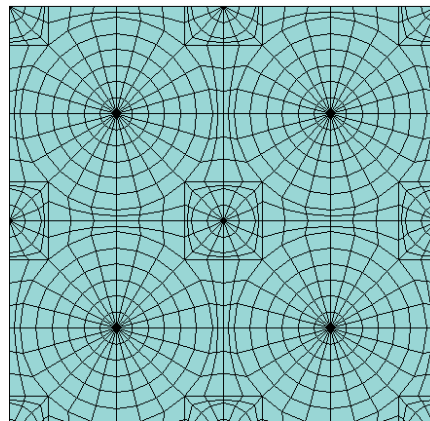
Figure 5: A cell of the improved finite element grid

type has a two-level structure. The first level consists of "large blocks-circles"; in the center of these "circles" there are triangular elements which allow for trajectories of growing crack to deviate under influence of stress flow and accumulated damage in the part surrounding the crack tip. The second level consists of "small blocks-circles"; in the center of "circlets" there are also located triangular elements. The second level allows the crack to turn if it would extend along the edge of a "large circle".

By this, the proposed topology of the modified finite-element grid for modeling the crack propagation would allow a trajectory to turn accordingly the local stress flow; the less wavy deviations are also expected. The two-level cell structure has to be better suited for the modeling fatigue crack morphology when the damage summation procedure is applied.

The modified mesh type was used to simulate behavior of initial micro-crack-like defects in material structure under cyclic loading. The defects and "fatigue properties" (coefficient C in (2)) of "material elements" (finite elements) were randomly distributed in a rectangular thin plate, as shown in Fig.6, a; cyclic load is applied in vertical direction (at "infinity"). It is seen that a defect in the intensive damage
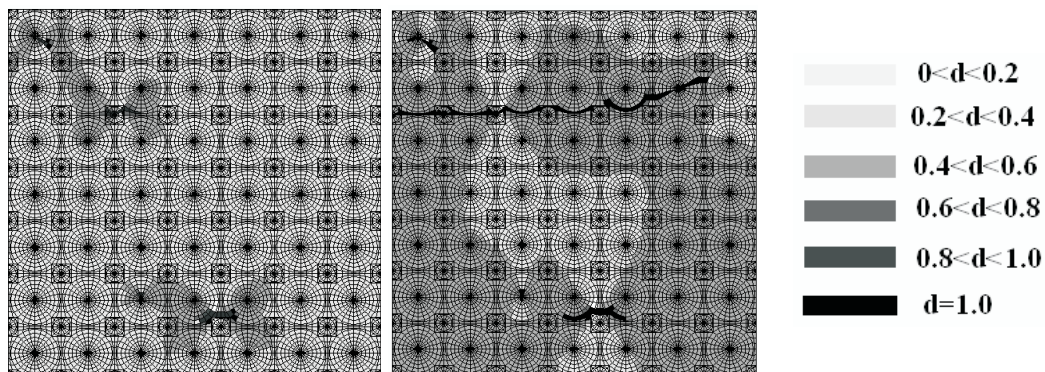
Figure 6: Development of defects in material structure into the propagating crack: (a) initial defects; (b) evolution of defects under cyclic loading; right hand - the damage intensity legend

area became an "active" one, which turned into the propagating crack; the other defects remained "dormant".

The trajectory of crack initiated at the "active" defect, shown in Fig.6, in general, is controlled by the stress flow; its deviation from the straight line perpendicular to the loading direction may be explained by the different (randomized) rate of the damage in "material" elements and partly, by the sensitivity to the progress of damages induced by the defect in the lower part of the plate. It is seen in this example that the influence of grid topology on the crack trajectory can be essentially reduced. Also, the modified meshing provides the better smoothness of the crack morphological features and makes it possible to trace the step-by-step damage accumulation, further formation of fracture nucleus near initial cracks/defects and their propagation.

3   Verification of the developed grid consistency

The given in above examples may not be convincing in accuracy of the proposed approach. To add, a standard problem is considered to make comparison of stress intensity factors calculated in the cases:

–

- when the crack is simulated using the proposed approach

- when the regular mesh with singular elements is applied and

- SIF's obtained from the hand book sources, e.g., [4]

A rectangular plate with symmetrical edge cracks loaded in direction perpendicular to the crack planes is assumed. Fig.7 shows the geometry; due to the symmetry, a 1/4 of the plate with respective boundary conditions is considered. A crack is located in the right bottom corner.
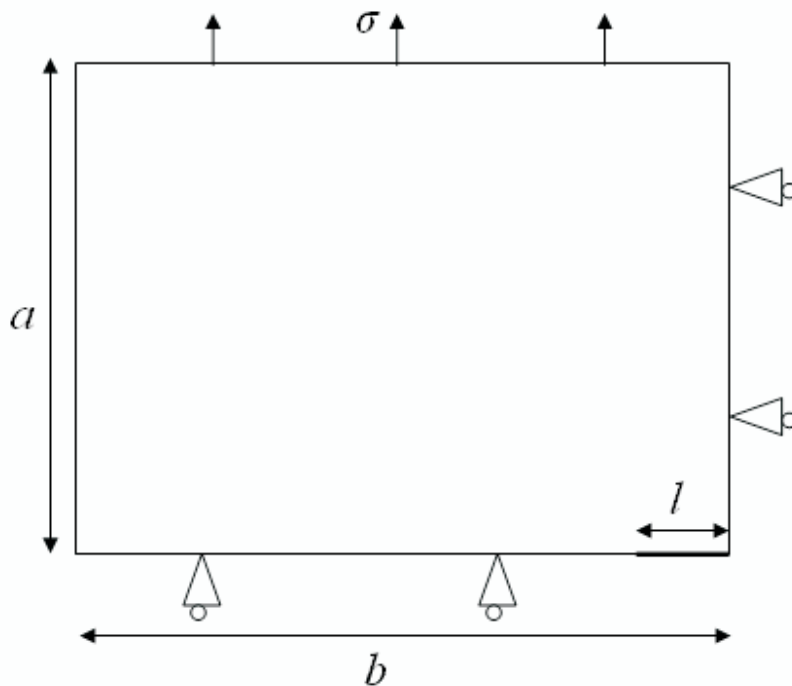
Figure 7: Edge crack propagation modeling

The plate dimensions are: $2 = 2b = 7 * 2l = 28$ mm, initial crack length is: $2l = 4$ mm, the size of grid cells is 2 mm; the plate is loaded by static stress $\sigma = 1$ MPa. According to the handbook data [4] stress intensities (K_I^I) for the plate with symmetrical cracks at the edges are given by:

$$K_I^I = \sigma\sqrt{\pi l} \cdot F_I(\alpha), \ \alpha = l/b, \ F_I(\alpha) = \sqrt{\sec(\alpha\pi/2)}$$

When the proposed modified meshing is applied, the stress intensities, , can be estimated by using the extrapolation to the crack tip technique [5]:

$$K_I^{grid} = \lim_{r\to 0} \sigma\sqrt{2\pi r}$$

where r - the distance of the reference point from the crack tip, $\sigma = \sigma(r)$ is the (maximum principal) stress at the reference point range. In case the plate with edge cracks is modeled by regular mesh with singular elements, stress intensities (K_I^{sin}) are calculated by means of a procedure built in a software based on the method of nodal displacements. Respectively, the SIF values are as follows:

- handbook data [4] : $K_I^I = 80.3\mathrm{kPa} \cdot \sqrt{m}$

- regular mesh with singular elements: $K_I^{sin} = 81.6\mathrm{kPa} \cdot \sqrt{m}$

- proposed modified meshing technique: $K_I^{grid} = 78.5\mathrm{kPa} \cdot \sqrt{m}$

The example shows that relative difference of the results does not exceed 2.5% which can be regarded favorable for the proposed approach together with the assumed isotropic meshing.

4 Conclusion

A simple approach allowing for simulation of the fatigue crack initiation and growth in a non-uniform field of progressing fatigue damages is developed based on application of the principles of FE meshing which provide realistic crack extensions independent of the mesh geometry.

Acknowledgements

References

[1] *Ellyin F* Fatigue Damage, Crack Growth and Life Prediction. Chapman & Hall, London, 1997

[2] *Miner, MA* Cumulative Damage in Fatigue. Journal of Applied Mechanics, 1945, Vol. 12, Trans. ASME Vol. 67, pp. A159-A164

[3] *Basquin, OH* . The Exponential Law of Endurance Tests. Proc. of ASTM, 1910, Vol.10, Part II, p.625

[4] *Murakami, Y., ed.* Stress Intensity Factors Handbook. In 2 volumes. Pergamon Books Ltd, 1987

[5] *Aamodt, B* Application of the Finite Element to Fracture Mechanics. Dep. of Structural Mechanics, NTH, Trondheim, 1974.

Igor K. Korolev, Institute of Problems in Mechanical Engineering, RAS, 199178, V.O., Bolshoy pr., 61, St.Petersburg, Russia

Nonstationary vibrations of 3-layered thermoviscoelastic thin-walled structures

Vladimir A. Kovalev   Sergey A. Lychev

lychev@ipmnet.ru

Abstract

This paper deal with laminated thin-walled structures. The laminated structures considered herein consist of three layers. The following assumptions are assumed. The thickness of inner layer is sufficient grater then others. The kinematic relations for the inner layer are in the form of Mindlin-Reissner shell theory, for the outer layers are in the form of membrane theory. The deformations of the whole layered structure obey the polyline hypothesis. The material of outer layers are suppose to be thermoelastic isotropic, whereas that of inner one being isotropic thermoviscoelastic. A variational principle for 3-layered thermoviscoelastic thin–walled structures is obtained. The variational technique is utilized to derive the equations of motion and heat conduction as well as appropriate boundary and initial conditions. The boundary conditions are in the most general form, corresponding to elastic fixing of boundary edges. A closed solution of the dynamic problem for finite 3-layered viscoelastic thin–walled structures is obtained. The solution is of the form of spectral expansion based on complete biorthogonal sets of eigenfunctions corresponding to mutual adjoint pairs of operator pencils.

1 Variational principle

We construct the variational statement of the problems with the use of the following well-known assertion [1]: if a linear operator $\mathcal{A}$ with domain $\mathcal{D}$ is self-adjoint with respect to a symmetric bilinear form $\langle ., . \rangle$ and if this bilinear form is nondegenerate, i.e., satisfies the condition

$$\left(\forall \mathbf{u} \in \mathcal{D} \ \langle \mathbf{u}, \boldsymbol{v} \rangle = 0 \right) \Rightarrow \boldsymbol{v} = \mathbf{0},$$

then the stationary points of the quadratic functional

$$\mathcal{I}[\mathbf{u}] = \frac{1}{2} \langle \mathbf{u}, \mathcal{A}[\mathbf{u}] \rangle$$

defined on the same domain $\mathcal{D}$ are exactly the solutions of the equation

$$\mathcal{A}[\mathbf{u}] = \mathbf{0}.$$

That is, the extension of variational formalism to novel problems depends on an appropriate definition of bilinear forms. Noticeable progress in this field was obtained by Gurtin [2], Tonti [3], and Belli and Morosi [4]. They proposed the use of the convolution as a bilinear form. It can be proved that the equations of motion and heat conduction generates the differential operators, which are self adjoint with respect to the convolution bilinear form. This permits one to obtain a well-defined variational statement for linear dynamic elasticity, thermoelasticity and viscoelasticity.

We recall that the convolution product of two functions $u(t)$, $v(t)$ is defined as

$$\langle u(t), v(t) \rangle = \int_0^T u(T-t)\, v(t)\, dt. \tag{1}$$

We note that hereafter variable T corresponds to the current time, whereas t and τ denote preceding moments of time. It follows from the definition (1) and the rule of integration by parts that

$$\langle u, v \rangle = \langle v, u \rangle, \quad \langle \dot{u}, v \rangle = \langle u, \dot{v} \rangle + u(T)v(0) - u(0)v(T), \tag{2}$$

where the dot stands for differentiation with respect to t. For simplicity we use the following notion for the convolution products of vector and tensorial fields

$$\langle \mathbf{u}(t)\cdot\mathbf{v}(t) \rangle = \int_0^T \mathbf{u}(T-t)\cdot\mathbf{v}(t)\, dt, \quad \langle \mathbf{A}(t):\mathbf{B}(t) \rangle = \int_0^T \mathbf{A}(T-t):\mathbf{B}(t)\, dt, \text{ ets.}$$

In the following we shall use the velocity $\mathbf{v}$ and the temperature θ as basic functions. According to [4] the variational formulation to the problem has the form

$$\delta \mathcal{F} = 0,$$
$$\mathcal{F}[\mathbf{v}, \theta] = \int_V \left(\mathcal{L}_{\text{mech}} + \mathcal{L}_{\text{therm}} + \mathcal{L}_{\text{inter}} - \frac{\rho}{2}\mathbf{v}(T)\cdot\mathbf{v}_0 - \frac{c}{2}\theta(T)\theta_0 \right) dV. \tag{3}$$

Here item $\mathcal{L}_{\text{mech}}$ characterize pure mechanical deformation

$$\mathcal{L}_{\text{mech}} = \frac{1}{2}\left(\rho\langle \mathbf{v}\cdot\dot{\mathbf{v}} \rangle - 2\rho\langle \mathbf{K}\cdot\mathbf{v} \rangle + 2\mu\langle \boldsymbol{\varepsilon}:\dot{\boldsymbol{\varepsilon}} \rangle + \lambda\langle \mathbf{E}:\boldsymbol{\varepsilon}, \mathbf{E}:\dot{\boldsymbol{\varepsilon}} \rangle \right), \tag{4}$$

item $\mathcal{L}_{\text{therm}}$ characterize pure heat conduction

$$\mathcal{L}_{\text{therm}} = \frac{1}{2}\left(2\langle \varpi, \theta \rangle - c\langle \theta, \dot{\theta} \rangle - k\langle \boldsymbol{\nabla}\theta\cdot\boldsymbol{\nabla}\theta \rangle \right), \tag{5}$$

item $\mathcal{L}_{\text{inter}}$ characterize the coupling effects

$$\mathcal{L}_{\text{inter}} = -\beta\langle \theta, \mathbf{E}:\dot{\boldsymbol{\varepsilon}} \rangle, \tag{6}$$

and $\mathbf{v}_0$, θ_0 are initial values for velocity any temperature correspondingly. In the Eq. (4)–(6) we use the following notation: $\boldsymbol{\varepsilon}$ is the strain tensor, which may be expressed in the terms of velocities as follows:

$$\boldsymbol{\varepsilon} = \frac{1}{2}\int_0^t \left(\boldsymbol{\nabla}\otimes\mathbf{v}(\tau) + (\boldsymbol{\nabla}\otimes\mathbf{v}(\tau))^* \right) d\tau,$$

$\mathbf{K}$ is an externally applied body forces per unit mass, ϖ is an external rate of supply of heat per unit mass, ρ is a mass density, μ, λ are the Lamé elastic modulus, k is a heat conductivity, c is a specific heat, β is a thermomechanical modulus.

Direct calculation shows that the Euler–Lagrange equations corresponding to the functional (3) are equivalent to the equation of motion and heat conduction of isotropic thermoelastic solid [4].

The generalization of the variational principle (3) to the thermoviscoelastic case is based on the refinement of the item $\mathcal{L}_{\text{mech}}$ as follows:

$$\mathcal{L}_{\text{mech}} = \frac{1}{2} \left(\rho \langle \mathbf{v} \cdot \dot{\mathbf{v}} \rangle - 2\rho \langle \mathbf{K} \cdot \mathbf{v} \rangle + 2 \langle \mathcal{M}[\varepsilon] : \dot{\varepsilon} \rangle + \langle \mathcal{L}[\mathbf{E} : \varepsilon], \mathbf{E} : \dot{\varepsilon} \rangle \right),$$

where $\mathcal{M}, \mathcal{L}$ — differential operators

$$\mathcal{M}[\varepsilon] = \mu \varepsilon + \sum_{k=1}^{N} \mu_k \frac{\partial^k}{\partial t^k} \varepsilon, \quad \mathcal{L}[\mathbf{E} : \varepsilon] = \lambda \mathbf{E} : \varepsilon + \sum_{k=1}^{N} \lambda_k \frac{\partial^k}{\partial t^k} \mathbf{E} : \dot{\varepsilon}.$$

A straightforward computation readily shows that the corresponding Euler–Lagrange equations are equivalent to the equations of viscoelastic motion and heat conduction of the thermoviscoelastic solid. This proves that the proposed variational principle is well–posedness.

2 Thermoelastic thin–walled structures

Now we are in a position to construct a variational statement for thin–walled structures, taking into account the Mindlin-Reissner kinematic hypothesis [5]. Denote by α, β, ζ the appropriate curvilinear coordinates, by $\boldsymbol{e}^\alpha, \boldsymbol{e}^\beta, \boldsymbol{e}^\zeta$ corresponding local basis and suppose that the thin–walled structure is the body bounded by two coordinate surfaces $\zeta = C_1$, $\zeta = C_2$, $C_2 > C_1$. The distance between this surfaces (thickness) $h = C_2 - C_1$ is small with respect to general dimensions of the structure. According to the accepted kinematic hypothesis the velocity $\mathbf{v}$ and the temperature θ may be represent as expansions with respect to variable ζ:

$$\mathbf{v} = \mathfrak{u} + \zeta \mathfrak{v}, \quad \mathfrak{v} \cdot \boldsymbol{e}^\zeta = 0; \quad \theta = \mathfrak{a} + \zeta \mathfrak{b}, \tag{7}$$

where $\mathfrak{u} = \mathfrak{u}(\alpha, \beta)$ and $\mathfrak{v} = \mathfrak{v}(\alpha, \beta)$ are the translate displacements and twists of shell normals. Taking into account this relations we get the expansion of the strain tensor ε

$$\varepsilon = \int_0^t \mathbf{def}\,\mathbf{v}(\tau)\,d\tau, \quad \mathbf{def}\,\mathbf{v} = \mathbf{def}\,\mathfrak{u} + \zeta \mathbf{def}\,\mathfrak{v} + \frac{1}{2} \left(\mathfrak{v} \otimes \boldsymbol{e}^\zeta + \boldsymbol{e}^\zeta \otimes \mathfrak{v} \right). \tag{8}$$

According to the stress hypothesis of Mindlin-Reissner theory we put the density of pure mechanical item $\mathcal{L}_{\text{mech}}$ (5) as follows:

$$\mathcal{L}_{\text{mech}} = \frac{1}{2} \left(\rho \langle \mathbf{v} \cdot \dot{\mathbf{v}} \rangle - 2\rho \langle \mathbf{K} \cdot \mathbf{v} \rangle + 2\mu \langle \varepsilon : \mathbf{G} : \dot{\varepsilon} \rangle + \lambda \langle \mathbf{E} : \varepsilon, \mathbf{E} : \dot{\varepsilon} \rangle \right), \tag{9}$$

where $\mathbf{G}$ is shear correction tensor [7] ($\varkappa$ is the coefficient of transversal shear [5])

$$\mathbf{G} = 1 + (\varkappa - 1)\left(\mathbf{G}_0 + \mathbf{G}_0^{(2143)}\right), \quad \mathbf{G}_0 = \boldsymbol{e}^\alpha \otimes \boldsymbol{e}^\zeta \otimes \boldsymbol{e}^\alpha \otimes \boldsymbol{e}^\zeta + \boldsymbol{e}^\beta \otimes \boldsymbol{e}^\zeta \otimes \boldsymbol{e}^\beta \otimes \boldsymbol{e}^\zeta.$$

Here $\mathbf{1}$ is the tensorial unit and $\mathbf{G}_0^{(2143)}$ is the tensorial isomer with dyadic permutation 2413. Substituting expressions (7) and (8) into Eq. (9) we get the $\mathcal{L}_{\text{mech}}$ in expanded form. Here we write out the third and forth items:

$$\boldsymbol{\varepsilon} : \mathbf{G} : \dot{\boldsymbol{\varepsilon}} = \int\limits_0^t \mathbf{def}\,\mathfrak{u}\,d\tau : \mathbf{G} : \mathbf{def}\,\mathfrak{u} +$$

$$+ \frac{\varkappa}{2}\left(\int\limits_0^t \mathbf{def}\,\mathfrak{u}\,d\tau : (\mathfrak{v}\otimes \boldsymbol{e}^\zeta + \boldsymbol{e}^\zeta \otimes \mathfrak{v}) + \int\limits_0^t (\mathfrak{v}\otimes \boldsymbol{e}^\zeta + \boldsymbol{e}^\zeta \otimes \mathfrak{v})\,d\tau : \mathbf{def}\,\mathfrak{u} + \int\limits_0^t \mathfrak{v}\,d\tau \cdot \mathfrak{v}\right) +$$

$$+ \zeta\left(\int\limits_0^t \mathbf{def}\,\mathfrak{v}\,d\tau : \mathbf{def}\,\mathfrak{u} + \int\limits_0^t \mathbf{def}\,\mathfrak{u}\,d\tau : \mathbf{def}\,\mathfrak{v}\right) + \zeta^2 \int\limits_0^t \mathbf{def}\,\mathfrak{v}\,d\tau : \mathbf{def}\,\mathfrak{v},$$

$$\mathbf{E} : \boldsymbol{\varepsilon}\,\mathbf{E} : \dot{\boldsymbol{\varepsilon}} =$$

$$= \int\limits_0^t \boldsymbol{\nabla}\cdot\mathfrak{u}\,d\tau\,\boldsymbol{\nabla}\cdot\mathfrak{u} + \zeta\left(\int\limits_0^t \boldsymbol{\nabla}\cdot\mathfrak{v}\,d\tau\,\boldsymbol{\nabla}\cdot\mathfrak{u} + \int\limits_0^t \boldsymbol{\nabla}\cdot\mathfrak{u}\,d\tau\,\boldsymbol{\nabla}\cdot\mathfrak{v}\right) + \zeta^2 \int\limits_0^t \boldsymbol{\nabla}\cdot\mathfrak{v}\,d\tau\,\boldsymbol{\nabla}\cdot\mathfrak{v}.$$

Evidently,

$$\boldsymbol{v}\cdot\dot{\boldsymbol{v}} = \mathfrak{u}\cdot\dot{\mathfrak{u}} + \zeta\left(\mathfrak{u}\cdot\dot{\mathfrak{v}} + \dot{\mathfrak{u}}\cdot\mathfrak{v}\right) + \zeta^2\mathfrak{v}\cdot\dot{\mathfrak{v}},$$

$$\mathbf{K}\cdot\boldsymbol{v} = \mathbf{K}\cdot\mathfrak{u} + \zeta\mathbf{K}\cdot\mathfrak{v}.$$

We get the densities of pure thermal (5) and coupling items (6) in the same way:

$$\mathcal{L}_{\text{therm}} = \langle \varpi, \mathfrak{a}\rangle - \frac{c}{2}\langle \mathfrak{a}, \dot{\mathfrak{a}}\rangle - \frac{k}{2}\langle \boldsymbol{\nabla}\mathfrak{a}\cdot\boldsymbol{\nabla}\mathfrak{a}\rangle +$$

$$+ \zeta\left\{\langle \varpi, \mathfrak{b}\rangle - \frac{c}{2}\left\langle \mathfrak{a}, \dot{\mathfrak{b}}\right\rangle - \frac{c}{2}\langle \dot{\mathfrak{a}}, \mathfrak{b}\rangle - k\langle \boldsymbol{\nabla}\mathfrak{a}\cdot\boldsymbol{\nabla}\mathfrak{b}\rangle\right\} - \zeta^2\left\{\frac{c}{2}\left\langle \mathfrak{b}, \dot{\mathfrak{b}}\right\rangle + \frac{k}{2}\langle \mathfrak{b}, \mathfrak{b}\rangle\right\},$$

$$\mathcal{L}_{\text{inter}} = -\beta\langle \mathfrak{a}, \boldsymbol{\nabla}\cdot\mathfrak{u}\rangle - \zeta\beta\left(\langle \mathfrak{b}, \boldsymbol{\nabla}\cdot\mathfrak{u}\rangle + \langle \mathfrak{a}, \boldsymbol{\nabla}\cdot\mathfrak{v}\rangle\right) - \zeta^2\beta\langle \mathfrak{b}, \boldsymbol{\nabla}\cdot\mathfrak{v}\rangle.$$

Consequently all items of functional (3) have the form of expansion with respect to a small parameter ζ. Now we are in a position to reformulate the problem in the terms of average stress and temperature fields by integrating the density of the functional (3) with respect to variable ζ. If the mean surface is congruent with the

middle surface of the structure, then we get the formula

$$
\begin{aligned}
\mathcal{F}_{\mathrm{red}} = \int\limits_{\Omega} \Bigg\{ &\frac{h\rho}{2}\left\langle \mathbf{u}\cdot\dot{\mathbf{u}}\right\rangle - h\rho\left\langle \mathbf{K}\cdot\mathbf{u}\right\rangle + h\mu\left\langle \int\limits_0^t \mathbf{defu}\,d\tau : \mathbf{G} : \mathbf{defu}\right\rangle + \\
&+\frac{\mu\varkappa}{2}\left\langle \int\limits_0^t \mathbf{defu}\,d\tau:\left(\mathbf{v}\otimes\mathbf{e}^\zeta + \mathbf{e}^\zeta\otimes\mathbf{v}\right)\right\rangle + \frac{\mu\varkappa}{2}\left\langle \int\limits_0^t \left(\mathbf{v}\otimes\mathbf{e}^\zeta + \mathbf{e}^\zeta\otimes\mathbf{v}\right)\,d\tau:\mathbf{defu}\right\rangle + \\
&+\mu\left\langle \int\limits_0^t \mathbf{v}\,d\tau\cdot\mathbf{v}\right\rangle + \frac{h\lambda}{2}\left\langle \int\limits_0^t \boldsymbol{\nabla}\cdot\mathbf{u}\,d\tau, \boldsymbol{\nabla}\cdot\mathbf{u}\right\rangle + h\left\langle \varpi, \mathfrak{a}\right\rangle - \frac{hc}{2}\left\langle \mathfrak{a}, \dot{\mathfrak{a}}\right\rangle - \frac{hk}{2}\left\langle \boldsymbol{\nabla}\mathfrak{a}\cdot\boldsymbol{\nabla}\mathfrak{a}\right\rangle - \\
&-h\beta\left\langle \mathfrak{a}, \boldsymbol{\nabla}\cdot\mathbf{u}\right\rangle + \frac{h^3\rho}{24}\left\langle \mathbf{v}\cdot\dot{\mathbf{v}}\right\rangle + \frac{h^3\mu}{12}\left\langle \int\limits_0^t \mathbf{defv}\,d\tau:\mathbf{defv}\right\rangle + \frac{h^3\lambda}{24}\left\langle \int\limits_0^t \boldsymbol{\nabla}\cdot\mathbf{v}\,d\tau, \boldsymbol{\nabla}\cdot\mathbf{v}\right\rangle - \\
&-\frac{h^3c}{24}\left\langle \mathfrak{b}, \dot{\mathfrak{b}}\right\rangle + \frac{h^3k}{24}\left\langle \mathfrak{b}, \mathfrak{b}\right\rangle - \frac{h^3\beta}{12}\left\langle \mathfrak{b}, \boldsymbol{\nabla}\cdot\mathbf{v}\right\rangle - \\
&-\frac{h\rho}{2}\mathbf{u}(T)\cdot\mathbf{u}_0 - \frac{h^3\rho}{24}\mathbf{v}(T)\cdot\mathbf{v}_0 - \frac{hc}{2}\mathfrak{a}(T)\mathfrak{a}_0 - \frac{h^3c}{24}\mathfrak{b}(T)\mathfrak{b}_0 \Bigg\}\,dA. \qquad (10)
\end{aligned}
$$

Using the standard variational technique we obtain the variation of the functional (10). Further the Gauss divergence theorem with respect to material variables and the rule of integration by parts with respect to time t give the following:

$$
\begin{aligned}
\delta\mathcal{F}_{\mathrm{red}} = \\
= \oint\limits_{\Gamma}\boldsymbol{\mathcal{N}}\cdot\Bigg\{ &\left\langle \left(\int\limits_0^t h\left[2\mu\mathbf{defu}\!:\!\mathbf{G} + \mu\varkappa\left(\mathbf{v}\otimes\mathbf{e}^\zeta + \mathbf{e}^\zeta\otimes\mathbf{v}\right) + \lambda\boldsymbol{\nabla}\cdot\mathbf{u}\boldsymbol{\mathcal{E}}\right]d\tau - h\beta\mathfrak{a}\boldsymbol{\mathcal{E}}\right)\cdot\delta\mathbf{u}\right\rangle + \\
&+\left\langle \left(\int\limits_0^t \frac{h^3}{12}\left[2\mu\mathbf{defv} + \lambda\boldsymbol{\nabla}\cdot\mathbf{v}\boldsymbol{\mathcal{E}}\right]d\tau - \frac{h^3\beta}{12}\mathfrak{b}\boldsymbol{\mathcal{E}}\right)\cdot\delta\mathbf{v}\right\rangle - \left\langle hk\boldsymbol{\nabla}\mathfrak{a}, \delta\mathfrak{a}\right\rangle - \left\langle hk\boldsymbol{\nabla}\mathfrak{b}, \delta\mathfrak{b}\right\rangle \Bigg\}\,d\Gamma + \\
+\int\limits_{\Omega}\Bigg\{ &\left\langle h\left(\rho\left[\dot{\mathbf{u}}-\mathbf{K}\right] - \int\limits_0^t \left[2\mu\boldsymbol{\nabla}\cdot\mathbf{defu}\!:\!\mathbf{G} + \mu\varkappa\boldsymbol{\nabla}\cdot\left(\mathbf{v}\otimes\mathbf{e}^\zeta + \mathbf{e}^\zeta\otimes\mathbf{v}\right) + \lambda\boldsymbol{\nabla}\boldsymbol{\nabla}\cdot\mathbf{u}\right]d\tau + \beta\boldsymbol{\nabla}\mathfrak{a}\right)\cdot\delta\mathbf{u}\right\rangle + \\
&+\left\langle \left(\frac{h^3\rho}{12}\dot{\mathbf{v}} + \int\limits_0^t \left[2h\mu\varkappa\mathbf{defu}\cdot\mathbf{e}^\zeta + 2h\mu\mathbf{v} - \frac{h^3\mu}{6}\boldsymbol{\nabla}\cdot\mathbf{defv} - \frac{h^3\lambda}{12}\boldsymbol{\nabla}\boldsymbol{\nabla}\cdot\mathbf{v}\right]d\tau + \frac{h^3\beta}{12}\boldsymbol{\nabla}\mathfrak{b}\right)\cdot\delta\mathbf{v}\right\rangle + \\
&+\left\langle \left(h\varpi - hc\dot{\mathfrak{a}} + hk\boldsymbol{\nabla}^2\mathfrak{a} - h\beta\boldsymbol{\nabla}\cdot\mathbf{u}\right), \delta\mathfrak{a}\right\rangle + \left\langle \left(-\frac{h^3c}{12}\dot{\mathfrak{b}} + \frac{h^3k}{12}\boldsymbol{\nabla}^2\mathfrak{b} - \frac{h^3\beta}{12}\boldsymbol{\nabla}\cdot\mathbf{v}\right), \delta\mathfrak{b}\right\rangle - \\
&-\frac{h\rho}{2}\delta\mathbf{u}(T)\cdot(\mathbf{u}_0 - \mathbf{u}(0)) - \frac{h^3\rho}{24}\delta\mathbf{v}(T)\cdot(\mathbf{v}_0 - \mathbf{v}(0)) - \\
&-\frac{hc}{2}\delta\mathfrak{a}(T)(\mathfrak{a}_0 - \mathfrak{a}(0)) - \frac{h^3c}{24}\delta\mathfrak{b}(T)(\mathfrak{b}_0 - \mathfrak{b}(0)) \Bigg\}\,dA.
\end{aligned}
$$

By using the fundamental lemma of calculus of variations, we obtain the Euler–

Lagrange equations

$$h\rho\left[\dot{\mathbf{u}}-\mathbf{K}\right]-\int_0^t h\left[2\mu\boldsymbol{\nabla}\cdot\mathbf{def}\,\mathbf{u}:\mathbf{G}+\mu\varkappa\boldsymbol{\nabla}\cdot\left(\mathbf{v}\otimes\mathbf{e}^\zeta+\mathbf{e}^\zeta\otimes\mathbf{v}\right)+\lambda\boldsymbol{\nabla}\boldsymbol{\nabla}\cdot\mathbf{u}\right]\,d\tau+h\beta\boldsymbol{\nabla}\mathfrak{a}=\mathbf{0},$$

$$\frac{h^3\rho}{12}\dot{\mathbf{v}}+\int_0^t\left[2h\mu\varkappa\left(\mathbf{def}\,\mathbf{u}\cdot\mathbf{e}^\zeta+\mathbf{v}\right)-\frac{h^3\mu}{6}\boldsymbol{\nabla}\cdot\mathbf{def}\,\mathbf{v}-\frac{h^3\lambda}{12}\boldsymbol{\nabla}\boldsymbol{\nabla}\cdot\mathbf{v}\right]\,d\tau+\frac{h^3\beta}{12}\boldsymbol{\nabla}\mathfrak{b}=\mathbf{0},$$

$$h\varpi-hc\dot{\mathfrak{a}}+hk\boldsymbol{\nabla}^2\mathfrak{a}-h\beta\boldsymbol{\nabla}\cdot\mathbf{u}=0,$$

$$-\frac{h^3c}{12}\dot{\mathfrak{b}}+\frac{h^3k}{12}\boldsymbol{\nabla}^2\mathfrak{b}-\frac{h^3\beta}{12}\boldsymbol{\nabla}\cdot\mathbf{v}=0,$$

the natural boundary conditions ($\boldsymbol{\mathcal{E}}=\mathbf{e}^\alpha\otimes\mathbf{e}^\alpha+\mathbf{e}^\beta\otimes\mathbf{e}^\beta$):

$$\boldsymbol{\mathcal{N}}\cdot\left(\int_0^t h\left[2\mu\mathbf{def}\,\mathbf{u}:\mathbf{G}+\mu\varkappa\left(\mathbf{v}\otimes\mathbf{e}^\zeta+\mathbf{e}^\zeta\otimes\mathbf{v}\right)+\lambda\boldsymbol{\nabla}\cdot\mathbf{u}\boldsymbol{\mathcal{E}}\right]\,d\tau-h\beta\mathfrak{a}\boldsymbol{\mathcal{E}}\right)\Bigg|_\Gamma=\mathbf{0},$$

$$\boldsymbol{\mathcal{N}}\cdot\left(\int_0^t\frac{h^3}{12}\left[2\mu\mathbf{def}\,\mathbf{v}+\lambda\boldsymbol{\nabla}\cdot\mathbf{v}\boldsymbol{\mathcal{E}}\right]\,d\tau-\frac{h^3\beta}{12}\mathfrak{b}\boldsymbol{\mathcal{E}}\right)\Bigg|_\Gamma=\mathbf{0},$$

$$hk\boldsymbol{\mathcal{N}}\cdot\boldsymbol{\nabla}\mathfrak{a}|_\Gamma=0,$$

$$hk\boldsymbol{\mathcal{N}}\cdot\boldsymbol{\nabla}\mathfrak{b}|_\Gamma=0$$

and the natural initial conditions

$$\mathbf{u}|_{t=0}=\mathbf{u}_0,\quad \mathbf{v}|_{t=0}=\mathbf{u}_0,\quad \mathfrak{a}|_{t=0}=\mathbf{u}_0,\quad \mathfrak{b}|_{t=0}=\mathbf{u}_0.$$

We stress that in the contrast with conventional variational principles (for example Hamilton's principle) the initial conditions yield from the variational statement in the same way as boundary conditions.

3 Three–layered structures

To obtain an equations of motion and heat conduction of the 3-layered thin–walled structures we assume the following. The thickness of inner layer h_1 is sufficient grater then others (h_2, h_3). The kinematic relations for the inner layer are in the form of Mindlin-Reissner shell theory, for the outer layers are in the form of membrane theory. The deformations of the whole layered structure obey the polyline hypothesis.

Taking into account above mentioned assumptions we represent the velocities and the temperature in inner (1) and outer (2,3) layers as follows

$$\mathbf{v}^1=\mathbf{u}+\zeta\mathbf{v},\quad \mathbf{v}^2=\mathbf{u}-h_-\mathbf{v},\quad \mathbf{v}^3=\mathbf{u}+h_+\mathbf{v},\quad \mathbf{v}\cdot\mathbf{e}^\zeta=0;$$
$$\theta^1=\mathfrak{a}+\zeta\mathfrak{b},\quad \theta^2=\mathfrak{a}-h_-\mathfrak{b},\quad \theta^3=\mathfrak{a}+h_+\mathfrak{b}.$$

Here h_+, h_- are the distance from the average surface to the medium surfaces of outer layers.

The expansion of strain tensor with respect to small parameter ζ, corresponding to inner or outer layers, are the following:

$$\boldsymbol{\varepsilon}^{k} = \int\limits_{0}^{t} \mathbf{def}\boldsymbol{v}^{k}(\tau)\,d\tau, \quad \mathbf{def}\boldsymbol{v}^{1} = \mathbf{def}\mathfrak{u} + \zeta\mathbf{def}\mathfrak{v} + \frac{1}{2}\left(\mathfrak{v}\otimes\boldsymbol{e}^{\zeta} + \boldsymbol{e}^{\zeta}\otimes\mathfrak{v}\right),$$

$$\mathbf{def}\boldsymbol{v}^{2,3} = \mathbf{def}\mathfrak{u} \mp \mathsf{h}_{\mp}\mathbf{def}\mathfrak{v}. \quad (11)$$

.

Taking into account Eq. (11) we get the density of pure mechanical item $\mathcal{L}_{\mathrm{mech}}$

$$\mathcal{L}_{\mathrm{mech}} = \frac{1}{2}\Big(\rho^{1}\left\langle\boldsymbol{v}^{1}\!\cdot\!\dot{\boldsymbol{v}}^{1}\right\rangle - 2\rho^{1}\left\langle\mathbf{K}\!\cdot\!\boldsymbol{v}^{1}\right\rangle + 2\mu^{1}\left\langle\boldsymbol{\varepsilon}^{1}\!:\!\mathbf{G}\!:\!\dot{\boldsymbol{\varepsilon}}^{1}\right\rangle + \lambda^{1}\left\langle\mathbf{E}\!:\!\boldsymbol{\varepsilon}^{1},\mathbf{E}\!:\!\dot{\boldsymbol{\varepsilon}}^{1}\right\rangle +$$

$$+ \rho^{2}\left\langle\boldsymbol{v}^{1}\!\cdot\!\dot{\boldsymbol{v}}^{2}\right\rangle - 2\rho^{2}\left\langle\mathbf{K}\!\cdot\!\boldsymbol{v}^{2}\right\rangle + 2\mu^{2}\left\langle\boldsymbol{\varepsilon}^{2}\!:\!\dot{\boldsymbol{\varepsilon}}^{2}\right\rangle + \lambda^{2}\left\langle\mathbf{E}\!:\!\boldsymbol{\varepsilon}^{2},\mathbf{E}\!:\!\dot{\boldsymbol{\varepsilon}}^{2}\right\rangle +$$

$$+ \rho^{3}\left\langle\boldsymbol{v}^{3}\!\cdot\!\dot{\boldsymbol{v}}^{3}\right\rangle - 2\rho^{3}\left\langle\mathbf{K}\!\cdot\!\boldsymbol{v}^{3}\right\rangle + 2\mu^{3}\left\langle\boldsymbol{\varepsilon}^{3}\!:\!\dot{\boldsymbol{\varepsilon}}^{3}\right\rangle + \lambda^{3}\left\langle\mathbf{E}\!:\!\boldsymbol{\varepsilon}^{3},\mathbf{E}\!:\!\dot{\boldsymbol{\varepsilon}}^{3}\right\rangle\Big) \quad (12)$$

and the same way we get the expansions of $\mathcal{L}_{\mathrm{therm}}$ and $\mathcal{L}_{\mathrm{inter}}$ (the upper indexes in material modulus denotes the number of the layer). The detailed expression of functional (10), corresponding Euler–Lagrange equations and boundary conditions are similar to the equations, obtained in section 3. The distinction in the formulas, which determine the average coefficients in equations and boundary conditions, cause by the special position of mean surface, see [7].

4 Thermoviscoelastic structures

In this section the material of outer layers are suppose to be thermoelastic isotropic, whereas that of inner one being isotropic thermoviscoelastic. To obtain an equations of motion and heat conduction of such thermoviscoelastic thin–walled structure we define the pure mechanical item in the functional (3) as follows:

$$\mathcal{L}_{\mathrm{mech}} = \frac{1}{2}\Bigg(\rho^{1}\left\langle\boldsymbol{v}\!\cdot\!\dot{\boldsymbol{v}}\right\rangle - 2\rho^{1}\left\langle\mathbf{K}\!\cdot\!\boldsymbol{v}\right\rangle + 2\mu^{1}\left\langle\boldsymbol{\varepsilon}\!:\!\mathbf{G}\!:\!\dot{\boldsymbol{\varepsilon}}\right\rangle + \lambda^{1}\left\langle\mathbf{E}\!:\!\boldsymbol{\varepsilon},\mathbf{E}\!:\!\dot{\boldsymbol{\varepsilon}}\right\rangle +$$

$$+ \sum_{k=1}^{N} 2\mu_{k}\left\langle\frac{\partial^{k}}{\partial t^{k}}\boldsymbol{\varepsilon}\!:\!\mathbf{G}\!:\!\dot{\boldsymbol{\varepsilon}}\right\rangle + \sum_{k=1}^{N}\lambda_{k}\left\langle\mathbf{E}\!:\!\frac{\partial^{k}}{\partial t^{k}}\boldsymbol{\varepsilon},\mathbf{E}\!:\!\dot{\boldsymbol{\varepsilon}}\right\rangle + \dots\Bigg),$$

where the items corresponding to the outer layers are omitted (they are like that in (12)). This brings about some obvious transformations of the functional (10) and the Euler–Lagrange equations.

5 Representation of the solution

The initial boundary value problem generated by equations boundary and initial conditions obtained in previous sections can be formulated in the form of Cauchy

initial problem with operator coefficients in the following form:

$$\dot{\boldsymbol{\chi}} = (\mathbf{u}, \mathbf{v}), \quad \mathcal{L}(\boldsymbol{\chi}, \theta) = \mathbf{f}, \quad \mathcal{L}(\boldsymbol{\chi}, \theta) = \sum_{k=0}^{N} \mathcal{A}_k \frac{\partial^k}{\partial t^k}(\boldsymbol{\chi}, \theta).$$

The formulated initial-boundary value problem is nonsymmetrical. It generates the pair of mutual adjoint polynomial operator pencils, defined in the space of square integrable complex value vector–functions with scalar product $\langle ., . \rangle_\mu$

$$\mathcal{L}_\nu = \sum_{k=0}^{N} \nu^k \mathcal{A}_k, \quad \mathcal{L}_\nu^* = \sum_{k=0}^{N} \overline{\nu}^k \mathcal{A}_k^*.$$

The obtained solutions are of the form of expansions based on sets of eigenfunctions $\mathbf{k}_i$, $\mathbf{k}_j^*$, which may be found as the solutions of mutual conjugate boundary value problems

$$\mathcal{L}_\nu \mathbf{k}_i = \mathbf{0}, \quad \mathcal{L}_\nu^* \mathbf{k}_j = \mathbf{0}, \quad \mathbf{k}_i = (\boldsymbol{\chi}_i, \theta_i), \quad \mathbf{k}_j^* = \left(\boldsymbol{\chi}_j^*, \theta_j^*\right).$$

The solution represents in the form [6]

$$\mathbf{y} = \sum_{i=1}^{\infty} \left[\left\langle \sum_{n=1}^{N} \sum_{m=n}^{N} \nu_i^{(m-n)} \mathcal{A}_m^* \mathbf{k}_i^*, \mathbf{y}_0^{(n-1)} \right\rangle_\mu \exp(\nu_i t) - \right.$$
$$\left. - \int_0^t \langle \mathbf{f}(\tau), \mathbf{k}_i^* \rangle_\mu \exp\left(\nu_i(t - \tau)\right) d\tau \right] \mathbf{k}_i \mathcal{Q}_i^{-1},$$

where

$$\mathbf{y} = (\boldsymbol{\chi}, \theta), \ \mathbf{y}_0^0 = (\boldsymbol{\chi}_0, \theta_0), \ \mathbf{y}_0^1 = \left(\dot{\boldsymbol{\chi}}_0, \dot{\theta}_0\right), \ldots \ Q_i = \langle \mathcal{A}_1 \mathbf{k}_i, \mathbf{k}_i^* \rangle_\mu + 2\nu_i \langle \mathcal{A}_2 \mathbf{k}_i, \mathbf{k}_i^* \rangle_\mu.$$

We stress that the corresponding eigenvalues are complex numbers. In the common case of elastic boundary fixing the eigenvalues may be computed numerically as the roots of corresponding transcendental equation. The algorithmic procedure destined to localize the roots is proposed. The special classes of boundary conditions are single out. These conditions are generated by auxiliary canonical scalar operators with boundary conditions of Dirichlet and Neumann types. The eigenvalue sequences of auxiliary operators for canonical domains are well known and even tabulated. That is the eigenvalues of the problem under consideration may be computed in exact form as the roots of algebraic equation with coefficients, depended on eigenvalues of auxiliary operators.

Acknowledgements

References

[1] Vainberg M M 1964 *Variational Methods in the Study of Nonlinear Operators.*

[2] Gurtin M E 1964 *Arch. Rat. Mech.* **16:1** 34–50.

[3] Tonti E 1973 *Annali di Matematica Pura ed Applicata* **95:1** 331–359.

[4] Belli G and Morosi C 1974 *Meccanica* **9:4** 239–243.

[5] Reissner E 1964 *J. App. Mechanics* **31** 233–238.

[6] Lychev S A 2008 *Mech. Solids* **43** 769-784

[7] Lychev S A and Saifutdinov Yu N 2005 *Vestnik SSU* **6(40)** 70–88 (in Russian).

Kovalev V.A. Moscow City Government University of Management st. Sretenka 28, Moscow, Russia, Russian Federation
Lychev S.A. Institute for Problems in Mechanics of the Russian Academy of Sciences, prosp. Vernadskogo 101, block 1, Moscow, Russian Federation

Influence of viscosity of the liquid on the vibrational hydrodynamic top

Nick Kozlov

kozlovn@pspu.ru

Abstract

In the present work an influence of viscosity of the liquid on the "vibrational hydrodynamic top" [1] is experimentally investigated. The question is excitation of intensive motion of a light cylindrical body in a rotating cavity with liquid at the vibration influence. Viscosity strengthens the interaction between the solid and the cavity walls, but at the same time reduces the average vibrational flows. In the absence of vibrations the viscosity increase results in the reduction of intensity of the differential rotation of the solid, and also in decrease of the thresholds of existence of the centrifuged state of the system and its stabilization. Vibrations influence the behaviour of the system in the resonant areas. In case of low-viscous liquids the resonant curve has a strongly asymmetric shape with a large hysteresis area. The viscosity results in decrease of the rotation speed of the solid, the resonant curve obtains more symmetric shape, and the hysteresis is absent.

1 Introduction

In behaviour of rotating multiphase systems the forces of inertia play an important role. Thus, at vibrations, perpendicular to the axis of rotation, in a centrifuged liquid layer with a free surface an azimuthal inertial wave, which is giving rise to an average current, is excited [2]. In case when the cavity is filled with liquid and light granular matter, the differential rotation of the light phase is observed, as well as, under certain conditions, transformation of the interface from the form of the circular cylinder to a polygonal prism [3].

In [1] is found a differential motion of the light solid body in a rotating cavity with liquid – the "vibrational hydrodynamic top". It can be induced both by external vibrational influence and by the gravity field. In the first and second cases the effect differs in magnitude and conditions of existence. At rotation of the cavity in the gravity field the centrifuged solid performs lagging rotation in relation to the cavity. The intensity of the lagging increases with decrease of the speed of the cavity rotation until the solid rises in a threshold way to the cylindrical wall of the cavity. At influence on the rotating system with vibrations, normal to the cavity axis, more intensive motion of the solid is revealed. It can be both outstripping and lagging. Vibrational excitation of intensive motion of the solid in the cavity frame has a

resonant character and is determined by the ratio of the vibration and rotation frequencies $n = f_v/f_r$. There are two resonant areas: outstripping motion ($n \approx 2$) and lagging motion ($n \approx 0.5$). They are mirror-symmetric and are determined by the relative radius of the solid and its relative density [1].

In the present work the influence of viscosity of the liquid on the "vibrational hydrodynamic top" is experimentally investigated.

2 Experimental setup and techniques

The transparent cylindrical cavity *1* (Fig.1) with the light cylindrical solid body *2* inside is filled with liquid and is installed on the platform of the electrodynamic vibrator *3*. The rotation is imposed to the cavity from the stepper motor *4* by means of the flexible transmission *5*. The detailed description of the setup is presented in the work [4].
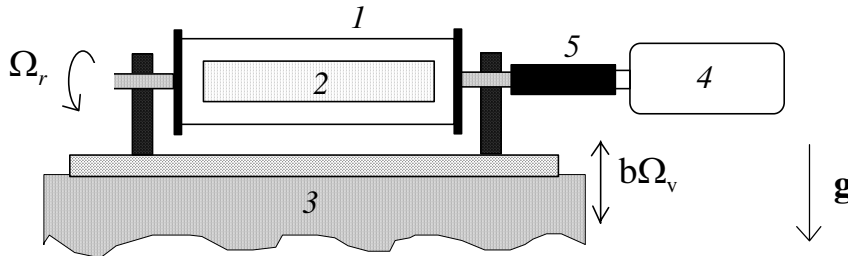

Figure 1: The schema of the experimental setup.

The cavity length $L = 9.9$ cm, diameter $2R_2 = 5.0$ cm; the body length $l = 9.3$ cm, diameter $2R_1 = 3.0$ cm. The density of the solid $\rho_s = 0.54$ g/cm^3. The cavity rotation speed varies from 0 to 20 rps. The frequency and the amplitude of vibrations are constant, $f_v = 25.0$ Hz, $b = 0.3$ mm.

The working liquids are water and water-glyceric solutions of various concentration. The range of viscosity ν is from 1 to 50 cSt, the density of liquids ρ_L changes from 1 up to 1.20 g/cm^3. The viscosity of the liquid is measured with a capillary viscosimeter; the ambient temperature is controlled during experiment.

The cavity is set at rotation, and at achievement of the threshold frequency of rotation the body takes a steady position in the center of the cavity, i.e. is centrifuged. The end-walls of the solid and the cavity do not adjoin. All observations are carried out at a centrifuged state of the solid. The rotation speed of the cavity is changed fluently first with increasing step, and then with decreasing one.

The rotation speed of the cavity is measured with an opto-relay registering the rotation of the interrupter bolted on the cavity axis, and a tachometer. The rotation speed of the solid is measured using the synchronization with the flicker frequency of a stroboscopic lamp. At small speeds the stroboscope is synchronized on the cavity rotation, and a stop watch is used to measure the average period of the solid body revolution. The error of measurements does not exceed 0.1 rps. In case of measurement of the speed by the average period the error does not exceed 5 percent.

For the measurement of the vibration amplitude an accelerometer fixed on the platform of the vibrator is used, the signal from which is processed on an oscilloscope.

3 Experimental results

After centrifugation the solid takes a steady position in the center of the cavity and rotates slower (in the laboratory frame). In the cavity frame the rotation speed of the solid is negative: $\Delta f = f_s - f_r$, where f_s is the rotation speed of the solid, f_r – that of the cavity. At the further increase of the rotation speed of the cavity the curve $\Delta f(f_r)$ approaches zero from below. In the threshold a, the outstripping motion of the solid is excited in a resonant way, and the sign of Δf becomes positive. In case of the low-viscous liquids a finite-amplitude transition to the intensive outstripping motion is observed (Fig.2, curves 1, 2). At large values of viscosity the excitation occurs in a soft way (curve 3).
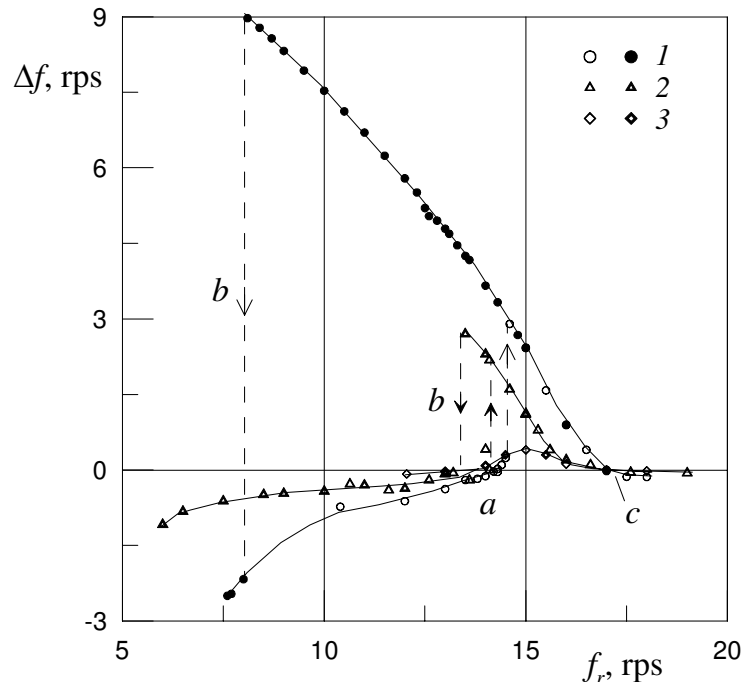
Figure 2: The speed of the average differential rotation of the solid in dependence on the cavity rotation rate.

In the viscous liquid at the subsequent increase of f_r the speed of the average outstripping rotation grows and reaches the maximal value. In the low-viscous liquid the increase of the rotation speed of the solid occurs at downturn of the rotation speed of the cavity, the maximum of intensity is reached in the threshold b where then there is a collapse of the intensive motion and transition to the non-excited state. The hysteresis area limited by transitions a and b, decreases with the increase of viscosity in the certain range (curves 1, 2) and is not observed in cases concerning the high viscosity (a curve 3). At the approach to the resonant area from above of the rotation speed in the threshold c there is a soft excitation.

Outside the resonant area the curve $\Delta f(f_r)$ coincides with the case of the absence of vibrations [1]. The gravity influence on the rotating cavity results in the excitation of the average lagging rotation of the solid, which intensity decreases with the increase of viscosity. Simultaneously, the area of existence of the centrifuged state of the solid increases (Fig.2).

On Fig.2 the speed of the average differential rotation of the solid is presented in dependence on the rotation speed of the cavity. The viscosity equals 1.1 (*1*), 5.8 (*2*), 27.7 (*3*) cSt.

At large viscosities, the resonant "bell" has the symmetric shape, the hysteresis area is absent, and the point of the maximum of the speed is between the thresholds of the resonant area. In the low-viscosity liquids the resonant area essentially increases due to the hysteresis area and obtains a strictly asymmetric form with the maximum in the threshold of the collapse of the average differential rotation.

The maximal speed of rotation of the solid monotonously decreases with the increase of viscosity (Fig.3). The points are presented on the plane $\nu, \Delta f_{max}$ in the logarithmic scale.

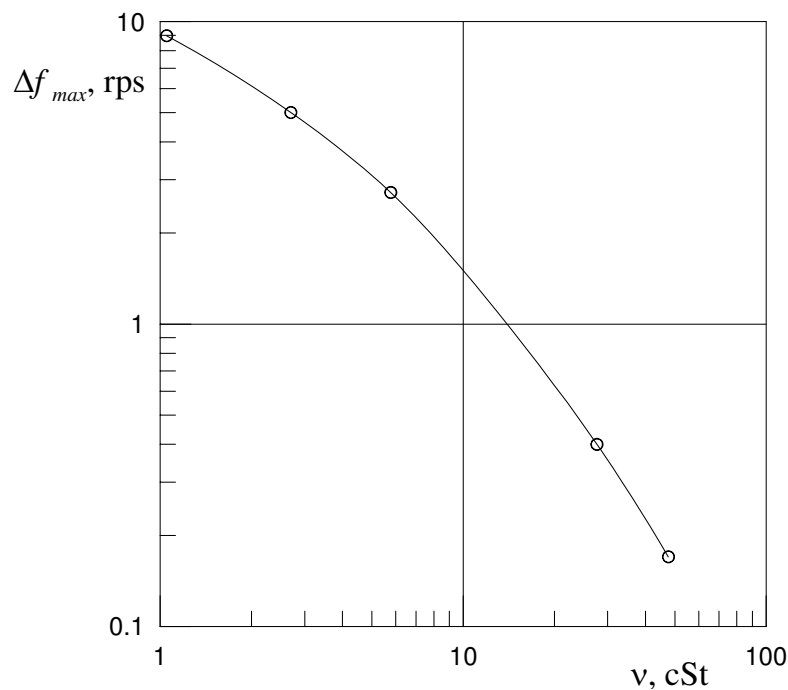Figure 3: The maximal rotation speed of the solid versus the liquid viscosity.

4 Analysis

The mechanism of excitation of intensive differential rotation of the light non-deformable solid is due to generation of the average vibrational force in the viscous boundary layers formed on cylindrical walls of the solid and the cavity. The influence of the external oscillating force field on the considered system results in circular

oscillations of the light body in the cavity frame, which is the propagation of an azimuthal inertial wave in the coaxial liquid layer. Oscillations of the liquid caused by it result in generation of the average vibrational force in the boundary layers, which is directed tangentially and gives rise to the average stationary azimuthal flow in the liquid layer. The light solid is free to the tangential displacement, therefore the vibrational force applied to its surface produces the intensive differential rotation. The force, formed on the wall of the cavity, has the same direction and is applied to the surface of the cavity. Its contribution to the differential rotation of the light body is small in comparison with the force formed on the surface of the solid [1]. However, its action is noticeable in the laboratory frame by the change of the rotation speed of the cavity. Thus, at vibrations in the resonant area after a disconnection of the transmission of the motor from the cavity, the latter continues to rotate for a long time, essentially greater than in the absence of vibrations.

In the linear theory of the hydrodynamic top submitted in [1], [5], expression of the vibrational torque applied to the unit of length of the body is written in the following way:

$$M_v = (1/2)\pi\rho_L\delta R_1((1 + R^2)/(1 - R^2))^2 b_s^2 \Omega_{osc}^2 \ (1)$$

Here $\delta = \sqrt{2\nu/\Omega_{osc}}$ – the width of the Stokes boundary layer, $R = R_1/R_2$ – the relative radius of the solid, b_s – the amplitude of the body oscillations, Ω_{osc} – the radian frequency of the body oscillations in the cavity frame. Also, the vibrational torque can be calculated using the average on the period rotation speed of the solid in the cavity frame:

$$M_v = 4\pi\nu\rho_L(2\pi\Delta f R_1^2 R_2^2)/(R_2^2 - R_1^2),$$

which corresponds to the approximation of a viscous laminar flow in case of rotation of the internal one of two coaxial cylinders [6]. For this the condition is used, that the average vibrational torque (1) is equilibrated by the moment of the viscous forces in the liquid, since the motion is stationary.

On Fig.4 is shown the dependence of the dimensionless average vibrational torque $M = M_v/(\rho_L h R_1^2 b \Omega_v^2)$ on the dimensionless frequency $\omega = \Omega_{osc} h^2/\nu$. Here $\Omega_v = 2\pi f_v$, $\Omega_{osc} = \Omega_v - \Omega_r$, $h = R_2 - R_1$. The dashed lines stand for the finite-amplitude transitions, as in the Fig.2. The viscosity equals 1.1 (*1*), 2.7 (*2*), 5.8 (*3*), 27.7 (*4*), 47.6 (*5*) cSt.

The curves obtained at different viscosities split on the chosen plane. It is quite natural, as the resonant frequencies of the body in the rotating cavity are determined by the dimensionless frequency of vibrations $n \equiv \Omega_v/\Omega_r$ or the dimensionless frequency of the body oscillations in the cavity frame $n - 1 = \Omega_{osc}/\Omega_r$. The width of the hysteresis area grows with increase of the dimensionless frequency, as well as the width of the resonant area as a whole. At small values of ω the hysteresis is absent. The maximal value of the vibrational torque changes nonmonotonely with dimensionless frequency. In case of high ω the dependence $M_{max}(\omega)$ is of the form of a function with a negative degree (Fig.5), which is in qualitative agreement with the expression (1) that can be written as

$$M = (\pi/\sqrt{2})((1 + R^2)/(1 - R^2))^2(b_s^2/R_1 b)(\Omega_{osc}/\Omega_v)^2 \omega^{-1/2} \ (2)$$
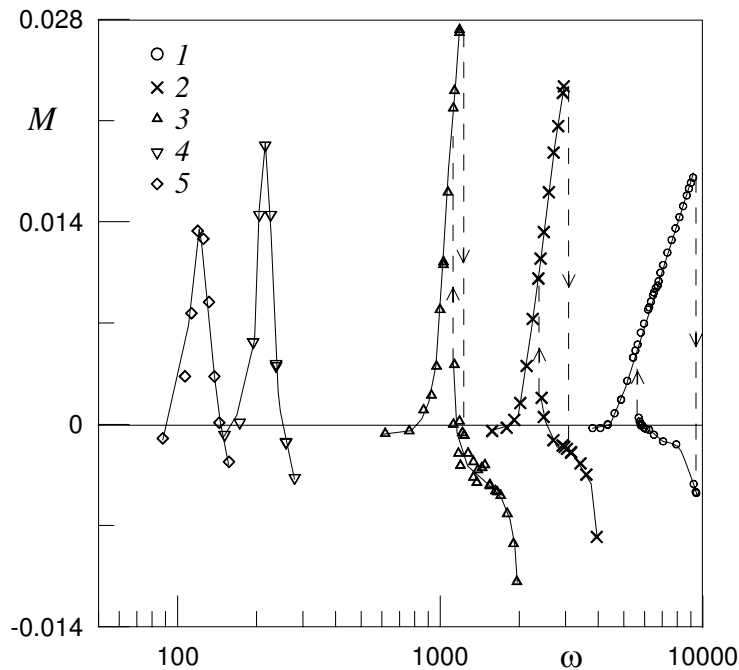
Figure 4: The dimensionless vibrational torque versus the dimensionless frequency.

Within the limits of small values of the dimensionless frequency the viscous interaction is amplified, preventing the excitation of the differential rotation. At $\omega \to 0$ the torque should also tend to zero, as it is observed on the graph. At very high values of ω the liquid should behave as an ideal one, i.e. nonviscous, that excludes a possibility of generation of the average flow induced by the oscillations of the liquid in the viscous boundary layers. It agrees with the decrease of the torque on the graph in the high-frequency limit.

The presence of the point of maximum on the plane ω, M_{max} has the physical sense, which consists in that the reduction of the dimensionless frequency in the certain limits strengthens viscous interaction of the solid and the liquid, but then begins to suppress the average vibrational effect.

The vibrational torque applied to the cavity wall

$$M_v' = (1/2)\pi\rho_L\delta R_2(4R^2/(1-R^2))^2 b_s^2\Omega_{osc}^2 \quad (3)$$

The ratio of (3) to (1) in the conditions of the present experiment gives $M_v'/M_v \approx 0.79$. Thus, the full torque applied to the cavity wall is equal 1.79 of the torque measured on the speed of the differential rotation of the solid.

5 Conclusion

In this work the influence of viscosity of the liquid on the "vibrational hydrodynamic top" is investigated. It is found, that the increase of viscosity stabilizes the centrifuged state of the light solid body, increasing the area of its existence. At
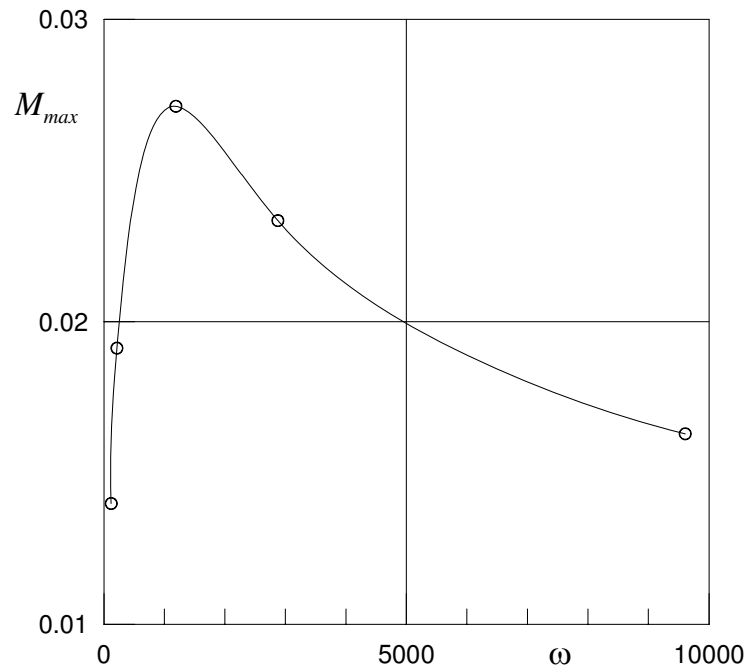
Figure 5: The maximal torque depending on the dimensionless frequency.

the same time the narrowing of the resonant area is observed, as well as the reduction and/or disappearance of the hysteresis area. Beyond, "the resonant bell" changes its form, becoming more symmetric simultaneously with disappearance of the hysteresis area. The increase of viscosity results in reduction of intensity of the average differential rotation of the solid. The maximal speed of the body decreases monotonously with the growth of viscosity.

However the change of the average vibrational torque occurs nonmonotonely. For the peak value of the force momentum depending on the dimensionless frequency there is the point of maximum that indicates the existence of a mode of vibrations optimal for the management of the rotation speed of the cavity.

Vibrations allow to operate the motion of a light solid inclusion in the rotating liquid, accelerating or decelerating its rotation. Vibrations also allow controlling the rotation of the cavity containing a solid body and liquid.

Acknowledgements

References

[1] Kozlov V.G., Kozlov N.V. Vibrational Dynamics of a Light Body in a Liquid-Filled Rotating Cylinder // Fluid Dynamics. 2008. Vol. 43. No 1. P. 9-19.

[2] Ivanova A.A., Kozlov V.G. and Polezhaev D.A. Vibrational dynamics of a centrifuged fluid layer // Fluid Dynamics. 2005. V. 40. No 2. P. 297-304.

[3] Salnikova A., Kozlov N., Ivanova A., Stambouli M. Dynamics of rotating two-phase system under transversal vibration // Microgravity Sci. Technol. 2009. V. 21. P. 83-87.

[4] Kozlov Nick. Light solid in rotating cavity filled with liquid under vibration // Convective flows. Perm: PSPU, 2005. Vol. 2. P. 163-171. (in Russian)

[5] Kozlov Nick. On the neture of the "vibrational hydrodynamic top" // Convective flows. Perm: PSPU, 2007. Vol. 3. P. 97-114. (in Russian)

[6] Landau L.D., Lifschitz E.M. Theoretical Physics. V. 6. Hydrodynamics. M.: Nauka, 1986. 736 p. (in Russian)

Nick Kozlov, Perm State Pedagogical University, Perm, Russia

Hydrodynamic interaction of a cylindrical solid with a boundary of cavity subjected to vibration

Victor G. Kozlov   Vitaliy D. Schipitsyn
kozlov@pspu.ru vital13@bk.ru

Abstract

Interaction of a light cylindrical solid body with an upper boundary of a rectangular cavity filled with viscous liquid and subjected to high-frequency horizontal vibration is experimentally investigated. It is found that at some intensity (frequency) of vibration the cylindrical body is pushed away from the cavity boundary and gets a stable position at a short distance from it. With increase of the vibration frequency the average motion of the body along the axis of vibration appears. The direct and reverse transitions (repulsion of the body from the boundary and its return, and also the excitation of its motion) with intensification and decreasing of the vibration frequency appear in a threshold way, a hysteresis in these transitions is observed in experiments with viscous fluids. The character of oscillation of the body with respect to the cavity is investigated using the high speed video recording: before the repulsion, after the repulsion and in the case of tangential motion of the solid.

1   Introduction

The repulsion of a spherical solid from a boundary of a cavity filled with viscous liquid and subjected to vibration is found in [1]. The lift force has the opposite direction to the well-known Bjerknes force of vibrational attraction between a solid and a boundary. The topic of the paper is the experimental research of the interaction of a light cylindrical solid and a wall of a rectangular cross section cavity filled with viscous liquid. It is found that cylindrical body orientates across the horizontal axis of vibration and then repulses from the boundary by threshold and takes a steady position at a definite distance from it. The increase of vibrational action results in the threshold excitation of the tangential solid motion along the axis of vibration. The tangential motion of the solid is caused by the asymmetry of its oscillation. The interaction of a solid with a cavity wall and tangential motion are studied using the high-speed camera.

2   Experimental setup

The rectangular cell *1* (fig.1, *a*) containing the cylindrical solid *2* and filled with a water-glycerol mixture is fastened horizontally on the platform of the mechanical
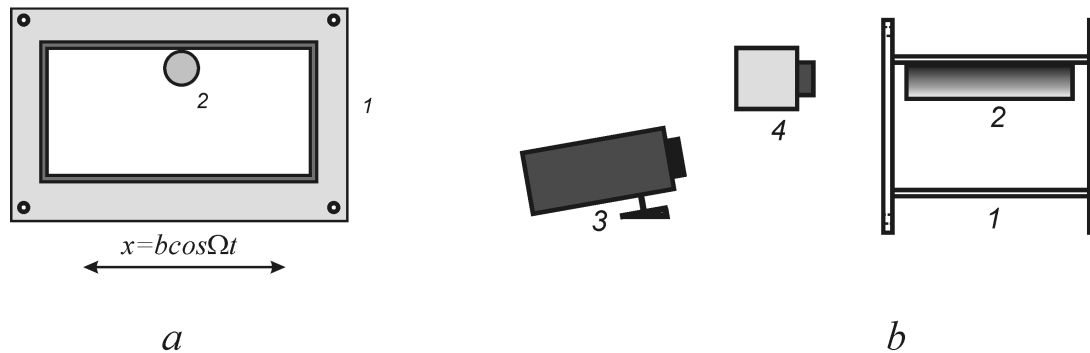
Fig. 1

vibrator (for detailed information [1]). The platform performs horizontal transla-tional oscillation according the low $x_c = b \cos \Omega t$. Fig. 1, b (side view) shows the schematic drawing of the experimental setup. The observation is made at strobo-scopic light and/or steady illumination 3. The registration of the solid motion is made by high-speed camera "Basler A402k" 4 connected to the personal computer. The image data are stored on the hard disc and analyzed by PC software.

The cell is a rectangular parallelepiped made of plexiglas with inside dimensions $12.00 \times 5.50 \times 9.50$ cm^3. The solid is an ebonite tube with an external diameter $d = 0.61$, 1.23 or 2.00 cm and the length 8.00 cm. The end-walls of the tube are covered by thin lavsan films with a reflective markers to observe the angular oscillation of solid about its center of rotation. The density of the solid is $\rho_S = 0.66$ g/cm^3. The ranges of the vibrational frequency f and the amplitude b are $0 - 25$ Hz and $0.1 - 5.0$ cm.

The glycerol concentration in water-glycerol mixtures varies. It allows to change the kinematic viscosity in the range $\nu = 0.1 - 7.8$ St, the fluid density varies in the range $\rho_L = 1.00 - 1.26$ g/cm^3.

3 Experimental results

In the absence of vibration the light cylindrical body has a steady position near the upper boundary of the cavity. The increase of vibrational frequency f at definite amplitude b results in the threshold repulsion of the solid from the boundary in viscous liquids ($\nu = 7.8 - 1.5$ St). During the period the solid performs longitudinal oscillation at definite distance from the wall. The further rise of f brings to the growth of the gap width between the solid and the boundary to some definite value. In low-viscous liquids ($\nu = 1.4 - 0.4$ St) the solid repulses from the wall to the smaller distance; and there is a threshold excitation of the mean tangential motion of the body along the cavity wall. The direction of the motion changes to the opposite one near the end-walls of the cavity. So, the solid performs periodical motion from left side of the cavity to the right one and vice versa. At the same time the cylinder rotates about its axis. While the body moves from the left to the right with respect to the cavity it rotates counterclockwise and vice versa in case of opposite motion. It is found that the gap width varies at different phases of oscillation. The decrease
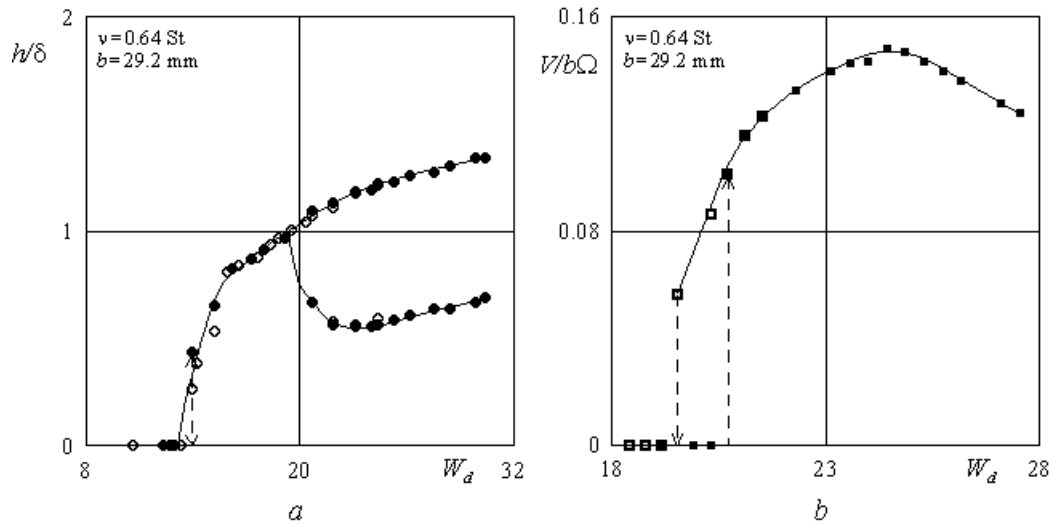
Fig. 2

of vibrational frequency results in the threshold disappearance of the solid motion. The further reduction of f brings to the zero gap width between the solid and the wall.

The task is to determine the threshold frequencies of the solid repulsion from the wall and its return to it; and critical frequencies of the appearance and the disappearance of the mean solid motion.

The gap width defines the radius of the repulsive force. In the limit of high vibrational frequency the solid dynamics is determined by vibrational parameter $W_d = (b\Omega)^2/(gd)$ and dimensionless frequency of vibration $\omega = \Omega d^2/\nu$, which is proportional to the ratio of the cylinder diameter d and the thickness of viscous boundary layer $\delta = \sqrt{2\nu/\Omega}$ [1].

Fig. 2, a shows the dependence of the dimensionless gap width on the parameter W_d. One can see that the gap width does not exceed 2 (filled and empty circles correspond to the increase and the reduction of W_d). The threshold of the body repulsion and its return to the boundary is at $\omega = 351$, $W_d = 14$; the thresholds of appearance and disappearance of the motion are at $\omega = 425$, $W_d = 20$ and $\omega = 413$, $W_d = 19$.

The mean motion excitation is attended by the loss of the symmetry of the solid oscillation. The two branches at $W_d > 20$ (fig. 2, a) demonstrate the gap width in the left and right positions of solid. At the beginning the dimensionless velocity of tangential motion $V/b\Omega$ increases with W_d (fig. 2, b) and then it begins to decrease (filled and empty squares correspond to the increase and decrease of W_d). The data in fig. 2 correspond to the experiment with a solid of the diameter $d = 2.00$ cm.

The points of the critical transitions in experiments with liquids of different viscosity ($\nu = 0.4 - 5.8$ St) and solids of different diameters ($d = 2.00, 1.23, 0.61$ cm) are in good agreement on the plane ω, W_d (fig.3).

The curves of the oscillating solid transitions have two branches: the repulsion (curve 1) at W_d growth and the return of the solid to the boundary (curve 2) at W_d reduction; the motion excitation (curve 3) and the motion disappearance (curve 4). In the limit $\omega > 300$ the hysteresis is absent and the threshold value of W_d is
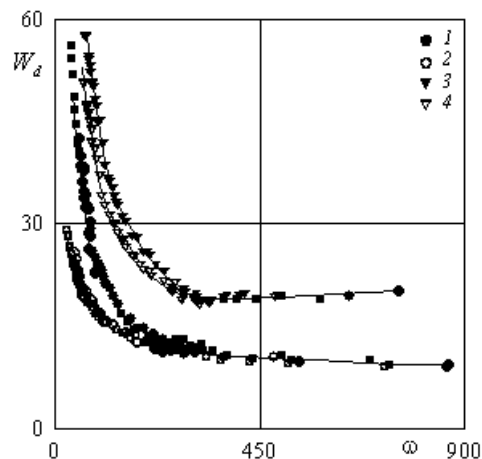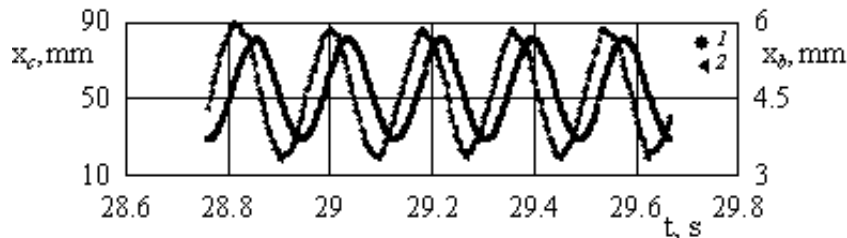
399

Fig. 3

Fig. 4

almost constant.

4 The motion of solid

We use a high-speed camera "Basler A402k" to study the oscillations and the tangential motion of the solid and its interaction with the boundary. The solid motion is studied at different frequencies f and some amplitude b. The frame rate is 380 Hz. The image analysis makes possible to study the oscillation of the solid with respect to the cavity. Fig. 4 shows the dependences of the cavity coordinate x_c in the laboratory frame (1) and the coordinate of the body center x_b in the cavity frame (2) on time (body diameter $d = 1.23$ cm, liquid viscosity $\nu = 0.65$ St, $f = 5.5$ Hz, $b = 26.3$ mm). If the solid is close to the boundary (in continuous touch with the boundary) it performs the oscillation of relatively small amplitude and with some phase-displacement between x_b and x_c.

Fig. 5 shows the dependence of the oscillation characteristics on time in the regime when the body is repulsed from the wall and the tangential motion is absent ($f = 9.4$ Hz, $b = 27.6$ mm).

The cavity sinusoidal vibration x_c (fig. 5, a) results in the solid oscillation x_b along the axis of vibration (fig. 5, b), the oscillations of the cavity and the solid are practically in-phase. The gap width varies during the solid motion and reaches the maximal value in the left and the right body positions (fig. 5, c).

The angular body oscillation (fig. 5, d) and the cavity vibration are not in-phase. In a few experiments one could also observe the relatively slow mean rotation of the
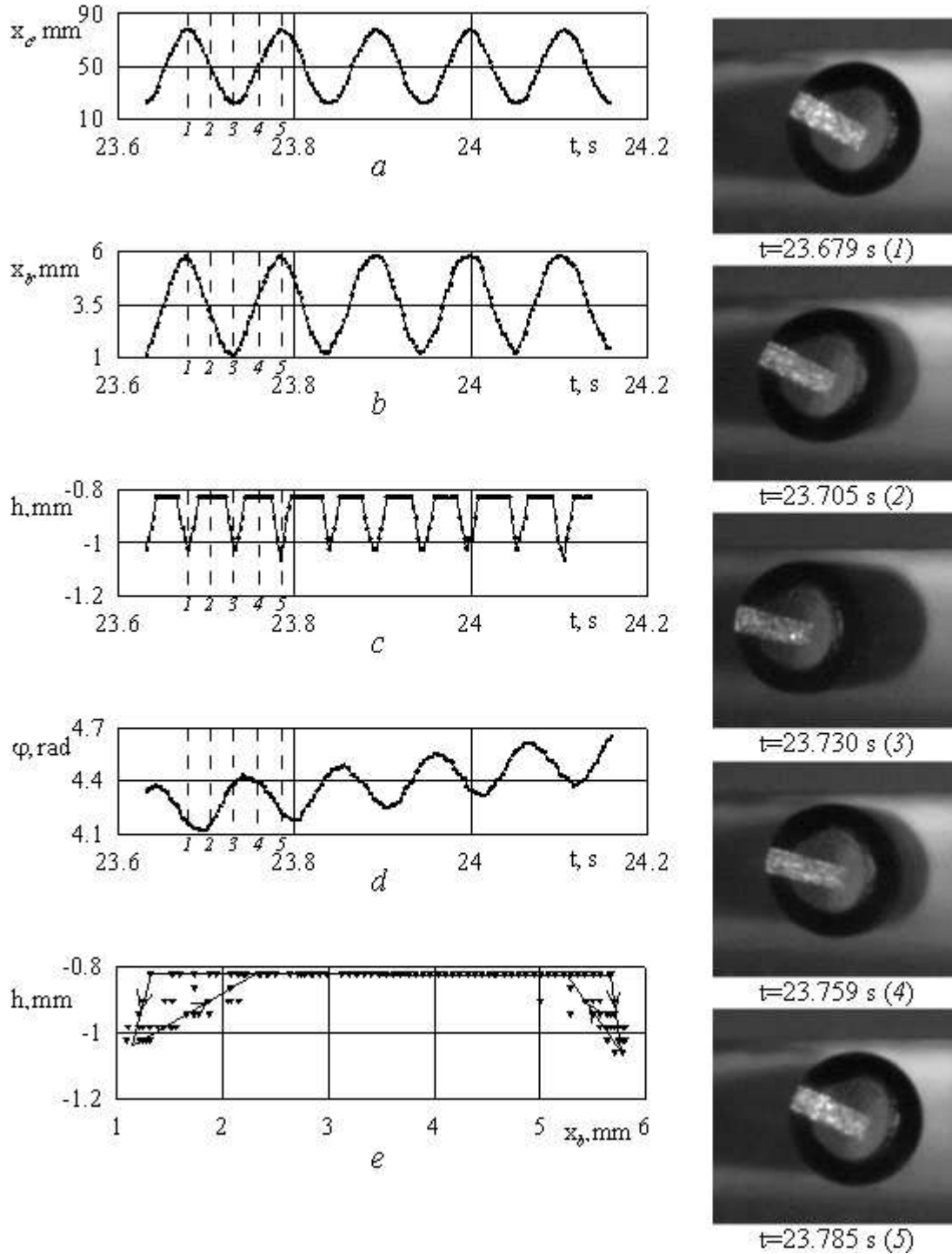
400

Fig. 5, 6
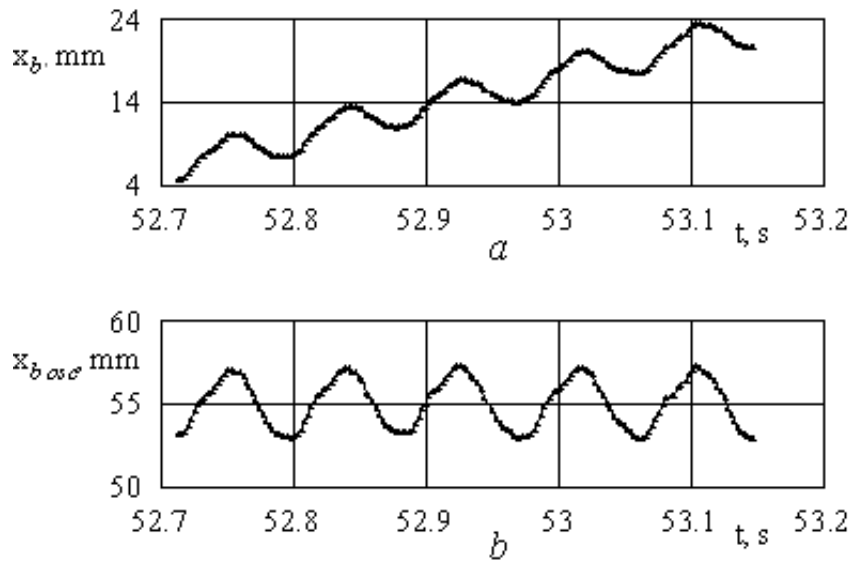
Fig. 7
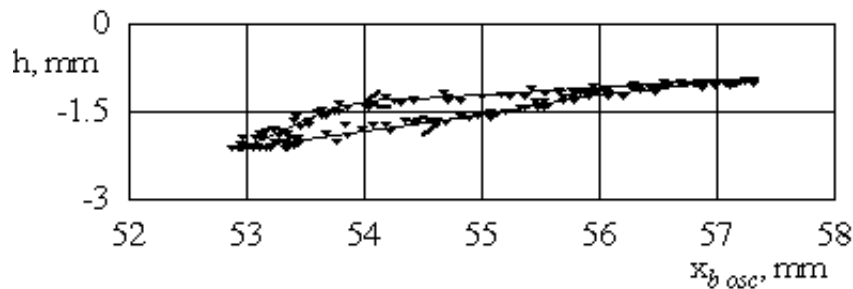
Fig. 8

solid in the absence of the mean motion.

Fig. 5, *e* demonstrates the trajectory of the solid with respect to the cell. One can see that the gap width is nearly constant during the period; it slightly increases in the right and left positions. In general the trajectory is symmetric.

Fig. 6 demonstrates the images of the solid in different phases of the period. The number of an image (*1 - 5*) in fig. 6 corresponds to the marks in fig. 5.

Discuss the regime of mean tangential motion of the solid along the axis of vibration. Consider the case of left-to-right motion. Fig. 7, *a* shows the dependence of coordinate of the solid on time ($f = 11.4$ Hz, $b = 28.4$ mm). It is evident that the body performs both the oscillation and the averaged motion. During the period the solid drifts for a definite distance. Fig. 7, *b* shows the dependence of the oscillating component of displacement of the cylinder on time.

The gap width as function of oscillational coordinate component is shows in Fig. 8 ($f = 11.4$ Hz, $b = 28.4$ mm). One can see that the trajectory of the oscillational motion (in the cavity frame) is asymmetric.

During the period the gap width varies. If the body is in left position then the gap is larger than the one is in the right position. The trajectory of the oscillating motion looks like a loop. The body moves along the trajectory counterclockwise, and the phase displacement between the oscillation of the solid and the cavity vibration is

402

Fig. 9

nearly zero. The angular oscillation of the solid and the cavity vibration are not in-phase. If the solid moves from left to right the rotation is counterclockwise. The angular velocity is significantly larger than the one in the subcritical regime.
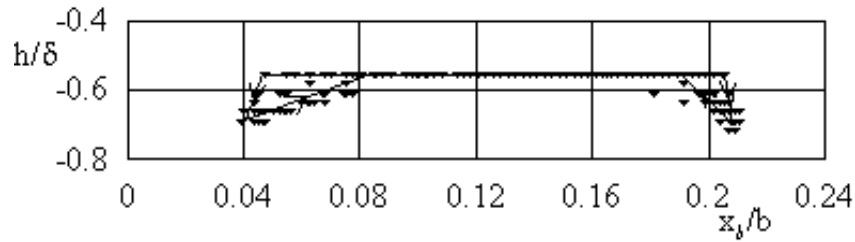
If the mean tangential motion goes from right-to-left then the trajectory has a reflection symmetry to the one in fig. 8, and the body perform the mean clockwise rotation.

5   Discussion

The body dynamics is determined by the interaction between the body, liquid and the cavity walls. In the high-frequency limit $\omega \gg 1$ the oscillation of light cylinder and the cavity vibration ought to be in-phase. The data in fig. 5 correspond to $\omega = 137$, $W_d = 22$, the data in fig. 8 and 9 - $\omega = 166$, $W_d = 34$. Relatively high frequency brings to nearly synchronous oscillations of the solid and the cavity; the phase displacement could be found only if the cylinder touches the boundary (fig. 4). If the solid - boundary interaction is nonviscous then the solid is attracted to the boundary. The experimental results demonstrate the opposite effect - repulsion of the solid, so it is determined by the viscous interaction. It is confirmed by the fact that the order of magnitude of the gap width is comparable with the Stokes layer thickness $\delta = \sqrt{2\nu/\Omega}$. It makes possible to introduce the dimensionless units of the gap width h/δ and the amplitude of body oscillation in the cavity frame x_b/b. Consider the regime when the solid is repulsed from the boundary and there is no tangential motion of it. Fig. 9 shows the dependence of the dimensionless gap width on the dimensionless cylinder coordinate ($\omega = 137$, $W_d = 22$). So, the gap width slightly varies in the course of a period. The trajectory demonstrates that the magnitude of the dimensionless gap width is nearly 0.6, it becomes larger in left and right positions ($h/\delta \approx 0.7$).

The trajectory of the upper solid edge in the regime of the tangential motion ($\omega = 166$, $W_d = 34$) is shown in fig. 10.

The dimensionless gap width varies during the period. In the left position of the cell the gap width ($h/\delta \approx 1.5$) is larger than in the right one ($h/\delta \approx 0.7$). At the same time the magnitude of the amplitude of the solid horizontal oscillation is comparable to the one in the previous regime. The trajectory looks like a loop. The direction of the tangential motion changes near the end-walls of the cavity; in this case the trajectory of the oscillational motion has the reflection symmetry, the intensity of the tangential motion remains the same.

The comparison of the trajectories in different regimes confirms that the asymmetry

403
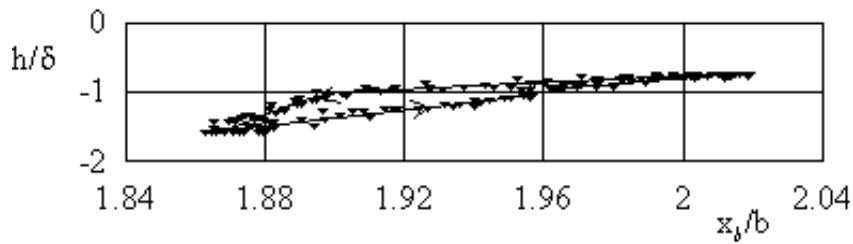
Fig. 10

of the solid oscillation is the reason of its tangential motion. The motion is absent while the oscillation is symmetric. The appearance of the asymmetry results in the excitation of tangential motion of the solid. The loop shape determines the direction of the cylinder motion. If the gap width in the left position is greater than in the right one then the solid moves to the right, and vice versa.

Compare the dimensionless gap width in the subcritical and overcritical regimes. The gap width is twice larger in the regime of the tangential motion; the amplitude of the horizontal oscillation with respect to the cavity is nearly the same in both cases.

6 Conclusion

The vibrational interaction between a light cylinder and a horizontal boundary of a cavity filled with viscous liquid is experimentally investigated. The repulsion of the solid and its tangential motion are found and analyzed. The thresholds of the solid repulsion and the excitation of the mean motion are presented on the plane ω, W_d. The results of the experiments with liquids of different viscosity correspond to each other on the plane of these parameters. It is found that the excitation of the tangential motion is determined by the asymmetry of the solid oscillation. The radius of action of the repulsive force is comparable with the thickness of the viscous Stokes layer.

Acknowledgements

References

[1] Ivanova A.A., Kozlov V.G., Kuzaev A.F. Vibrational hydrodynamical interaction of sphere with cavity boundary // Fluid Dynamics. 2008. Vol. 43. N 2. P. 194-202.

Victor G. Kozlov, Perm State Pedagogical University, Russia
Vitaliy D. Schipitsyn, Perm State Pedagogical University, Russia

Regimes of transformation in intermetallic systems with inert particles in conditions of controllable coating synthesis on base

Olga N. Kryukova   Anna G. Knyazeva

okruk@ispms.tsc.ru

Abstract

In this work the numerical investigation of transformation regimes realized in given technology condition was carried out. The system named "inert wolfram particles in matrix and nickel-aluminium on base" was decided as a model system. Coating was made on iron base. In calculations a thickness base and coating, volume fraction of inert particles in previously made powder layer and parameters of electron-beam influence are varied.

Parameters areas characterized for different synthesis regime was found under detailed parametric model investigation.

1   Introduction

Methods of powder metallurgy have a peculiar possibilities to produce materials and compositions with distinct properties in combination with application of concentrated energy fluxes. For example, electron-beam treatment allows to improve exploitation properties of the details with traditional coatings essentially. As a result of electron-beam heating the structure of coating and base is modificated. Hardness and wearlessness of coating material is improved. If previously made coating contains inert particles, then distinct of transformation regimes is realized. In this case, as a result of heat treatment, accompanied by chemical transformations in coating matrix, the composite is formed. Composite properties depend both on part of inert filler and synthesis regime.

2   The mathematical formulation of the problem

Let us assume that on the surface of the parallelepiped-shaped sample the coating containing chemically reacting components and inert inclusions with volume fraction η_p is deposited. Sizes of the coating (1) and the sample (2) are specified (Fig. 1). An effective energy source moves along the slab surface in the line of the OX-axis at the rate of V, cm/s. Energy in the effective source is distributed under the law

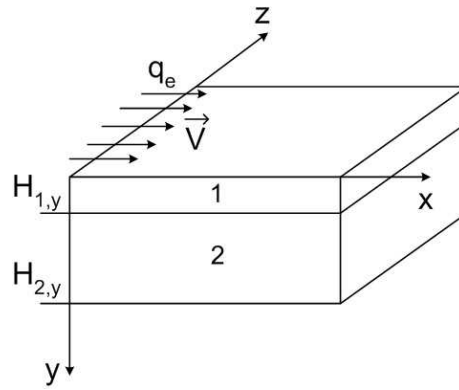$$q_e(x, y, t) = q_0 \exp\left(-(x - Vt)^2/a_t^2\right), \tag{1}$$

Figure 1: Illustration on the problem definition.

where q_0 – is a maximal power density of the source, Vt/cm^2, a_t is effective radius of the source, cm. The source is evenly distributed in the z-direction.

Thus the problem of electron-beam treatment includes the two-dimensional heat conduction equations for the coating (2) and the substrate (3)

$$c_1\rho_1\frac{\partial T_1}{\partial t} = \left[\frac{\partial}{\partial x}\left(\lambda_1\frac{\partial T_1}{\partial x}\right) + \frac{\partial}{\partial y}\left(\lambda_1\frac{\partial T_1}{\partial y}\right)\right] + q_{ch}(a, T)(1-\eta_p), \tag{2}$$

$$c_2\rho_2\frac{\partial T_2}{\partial t} = \left[\frac{\partial}{\partial x}\left(\lambda_2\frac{\partial T_2}{\partial x}\right) + \frac{\partial}{\partial y}\left(\lambda_2\frac{\partial T_2}{\partial y}\right)\right], \tag{3}$$

where c_1, ρ_1, λ_1 and c_2, ρ_2, λ_2 – are thermophysical properties of the coating and the substrate.

Let a chemical reaction in the reagent (with volume fraction $1-\eta_p$) can be described by the general scheme $A \rightarrow B$. Then the change of the product fraction or conversion degree a in the coating follows from the equation

$$\frac{\partial a}{\partial t} = k_0\varphi_1(a)\varphi_2(T), \tag{4}$$

where $\varphi_1(a)$ is a kinetic function, $\varphi_2(T) = \exp(-E_a/RT)$. Then $q_{ch} = Q_{ch,0}k_0\varphi_1(a)\varphi_2(T)$, $Q_{ch,0}$ – is total heat emission of the reaction, J/mol.

Boundary and initial conditions enclose the set of equations (3), (4)

$$x = 0, H_x: \quad -\lambda_i\frac{\partial T_i}{\partial x} = \sigma\varepsilon(T_i^4 - T_0^4); \quad i = 1, 2, \tag{5}$$

$$y = 0: \quad -\lambda_1\frac{\partial T_1}{\partial y} = q_e - \sigma\varepsilon(T_1^4 - T_0^4), \tag{6}$$

$$y = H_{1,y} + H_{2,y}: \quad -\lambda_2\frac{\partial T_2}{\partial x} = \sigma\varepsilon(T_2^4 - T_0^4), \tag{7}$$

$$y = H_{1,y}: \quad \lambda_1\frac{\partial T_1}{\partial y} = \lambda_2\frac{\partial T_2}{\partial y}; \quad T_1 = T_2, \tag{8}$$

where (8) is the condition of ideal contact on the back of the slab ($y = H_{1,y}$).

At zero time the temperature is specified

$$t = 0: \quad T_1(x, y, 0) = T_0, \quad a = 0. \tag{9}$$

As the coating is the composite which contains inert nonmelting inclusions (or particles with very high melting temperature) with volume fraction η_p and properties c_p, ρ_p, λ_p then the properties of the coating can be written as follows:

$$c_1\rho_1 = c_p\rho_p\eta_p + c_m\rho_m(1 - \eta_p), \quad \lambda_1 = \lambda_p\eta_p + \lambda_m(1 - \eta_p),$$

where c_m, ρ_m, λ_m are heat capacity, density and heat conductivity of the matrix. Heat capacities of the material of the matrix and the substrate experience considerable change in the vicinity of the melting temperatures. It is reflected in the following dependencies:

$$\begin{aligned}
(c_m\rho_m) &= (c_m\rho_m)_{eff} + L_{ph,m}\rho_{s,m}\delta(T - T_{ph,m}), \\
(c_2\rho_2) &= (c_2\rho_2)_{eff} + L_{ph,2}\rho_{s,2}\delta(T - T_{ph,2}),
\end{aligned} \tag{10}$$

where

$$(c_m\rho_m)_{eff} = \begin{cases} c_{s,m}\rho_{s,m}, & T < T_{ph,m}, \\ c_{l,m}\rho_{l,m}, & T \geq T_{ph,m}, \end{cases} \quad (c_2\rho_2)_{eff} = \begin{cases} c_{s,2}\rho_{s,2}, & T < T_{ph,2}, \\ c_{l,2}\rho_{l,2}, & T \geq T_{ph,2}, \end{cases}$$

δ is Dirac delta-function; $L_{ph,m}$, $L_{ph,2}$ – are melting (crystallization) heats of the matrix and the substrate, J/mol; $T_{ph,m}$, $T_{ph,2}$ – are melting (crystallization) temperatures of the matrix and the substrate, K; index "l" –corresponds to liquid phase; "s" –to solid phase.

3 Problem definition in nondimensional variables

Let us change over to dimensionless variables

$$\tau = \frac{t}{t_*}, \quad \xi = \frac{x}{x_*}, \quad \eta = \frac{y}{x_*}, \quad \theta = \frac{T - T_0}{T_* - T_0},$$

where $x_* = h_S$ –is a spatial scale, $t_* = k_0^{-1}$ and a temperature scale, T_* have been defined as a temperature of "solid-phase" reaction products

$$T_* = T_0 + \frac{Q_{ch,0}}{c_m\rho_m}.$$

Then mathematical statement of the problem takes on form

$$f_1\frac{\partial\theta_1}{\partial\tau} = \frac{1}{\delta}f_2\left(\frac{\partial^2\theta_1}{\partial\xi^2} + \frac{\partial^2\theta_1}{\partial\eta^2}\right) + \varphi(a, \theta)(1 - \eta_p); \tag{11}$$

$$f_5\frac{\partial\theta_2}{\partial\tau} = \frac{1}{\delta}K_{\lambda b}\left(\frac{\partial^2\theta_2}{\partial\xi^2} + \frac{\partial^2\theta_2}{\partial\eta^2}\right); \tag{12}$$

$$\frac{\partial a}{\partial t} = \varphi(a, \theta); \tag{13}$$

$$\xi \to 0: \quad \frac{\partial \theta_1}{\partial \xi} = -S_k \frac{f_3}{f_2}; \quad \xi \to X_\xi: \quad \frac{\partial \theta_2}{\partial \xi} = -S_k \frac{f_3}{K_{\lambda b}}; \tag{14}$$

$$\eta \to 0: \quad \frac{\partial \theta_1}{\partial \eta} = \frac{1}{f_2}(S_k f_3 - S_r f_4); \quad \eta \to Y_{1,\eta} + Y_{2,\eta}: \quad \frac{\partial \theta_2}{\partial \eta} = -S_k \frac{f_3}{K_{\lambda b}}; \tag{15}$$

$$\eta \to Y_{1,\eta}: \quad f_2 \frac{\partial \theta_1}{\partial \eta} = K_{\lambda b} \frac{\partial \theta_2}{\partial \eta}; \quad \theta_1 = \theta_2; \tag{16}$$

$$\tau = 0: \quad \theta = 0, \quad a = 0, \tag{17}$$

where

$$f_1 = \left\{ 1 + \frac{Q_{ph,m}}{A\sqrt{\pi}} \exp\left[-\left(\frac{\theta - \theta_{ph,m}}{A\sqrt{\pi}}\right)^2 \right] \right\}(1 - \eta_p) + \eta_p K_{cp};$$

$$f_2 = 1 - \eta_p + \eta_p K_{\lambda p};$$

$$f_3 = (\theta + \gamma)^4 - \gamma^4;$$

$$f_4 = \exp\left(-(\xi - \bar{V}\tau)^2/\delta_1\right);$$

$$f_5 = \left\{ 1 + \frac{Q_{ph,2}}{A_1\sqrt{\pi}} \exp\left[-\left(\frac{\theta - \theta_{ph,2}}{A_1\sqrt{\pi}}\right)^2 \right] \right\} K_{cb};$$

$$\varphi(a, \theta) = \varphi_1(a)\varphi_2(\theta);$$

$$\varphi_1(a) = 1 - a; \quad \varphi_2(\theta) = \exp\left[-\frac{\gamma}{\beta(\gamma + \theta)} \right];$$

$$\delta = \frac{h_s^2}{\kappa_m t_*}; \quad S_r = \frac{h_s q_0}{Q_{ch,0}\kappa_m}; \quad S_k = \frac{\varepsilon\sigma(T_* - T_0)^3 h_s}{\lambda_m}; \quad \beta = \frac{RT_0}{E_a}; \quad \gamma = \frac{T_0}{T_* - T_0};$$

$$Q_{ph,m} = \frac{L_{ph,m}\rho_m}{c_m \rho_m (T_* - T_0)}; \quad Q_{ph,2} = \frac{L_{ph,2}\rho_2}{c_m \rho_m (T_* - T_0)}; \quad \delta_1 = \left(\frac{a_t}{h_s}\right)^2;$$

$$\theta_{ph,m} = \frac{T_{ph,m} - T_0}{T_* - T_0}; \quad \theta_{ph,2} = \frac{T_{ph,2} - T_0}{T_* - T_0}; \quad \bar{V} = \frac{h_s V}{t_*}; \quad \kappa_m = \frac{\lambda_m}{c_m \rho_m};$$

$$K_{cb} = \frac{c_2 \rho_2}{c_m \rho_m}; \quad K_{cp} = \frac{c_p \rho_p}{c_m \rho_m}; \quad K_{\lambda b} = \frac{\lambda_2}{\lambda_m}; \quad K_{\lambda p} = \frac{\lambda_p}{\lambda_m};$$

$$A = \frac{\sigma_0}{T_* - T_0}; \quad A_1 = \frac{\sigma_{0,1}}{T_* - T_0}; \quad X_\xi = \frac{H_x}{h_s}; \quad Y_{1,\eta} = \frac{H_{1,y}}{h_s}; \quad Y_{2,\eta} = \frac{H_{2,y}}{h_s}.$$

It is obvious, that not all the parameters are required for qualitative investigation of the model. Thus, without loss of generality we can take

$$Q_{ph,m} = Q_{ph,2} = Q_{ph}; \quad \theta_{ph,m} = \theta_{ph,2} = \theta_{ph};$$
$$K_{cb} = K_{cp} = K_c; \quad K_{\lambda b} = K_{\lambda p} = K_\lambda; \quad A = A_1.$$

Transformation modes of intermetallic systems with inert particles will depend on the parameters Q_{ph} which is the ratio of melting heat to heat storage in warm layer; δ which is the ratio of substrate thickness to the typical heat scale; S_r which
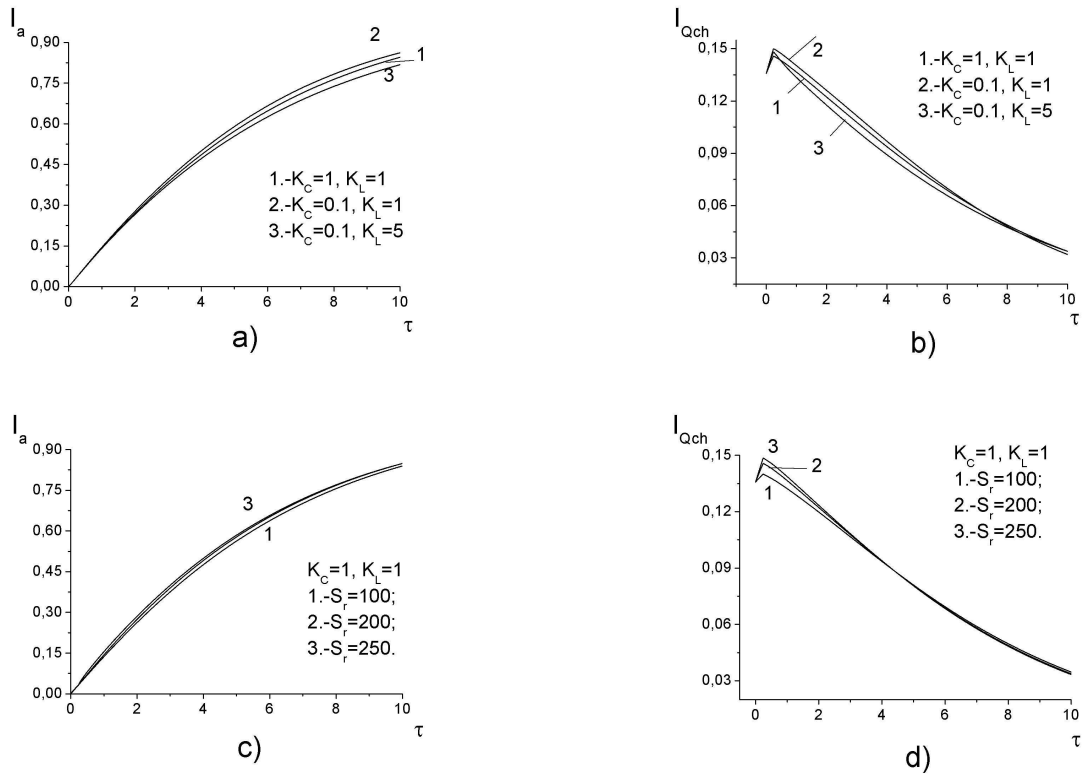
Figure 2: Dependencies of integrated conversion degree I_a and integrated heat release in chemical reaction I_{Qch} from time for different values of the parameters K_c, K_λ, S_r).

is the ratio of heat accumulated in the substrate of thickness h_S while heating by the flux q_0 to chemical heat emission; S_k which is dimensionless parameter of heat loss; β which is the ratio of the temperature characterizing external heating to the activation temperature E_a/R of the dilution process; θ_{ph}; K_c and K_λ.

Using literary data on the properties of different substances (Ni, Al, W, Fe) and varying source parameters (q_0, V) we can define domains of variation of dimensionless parameters:

$S_k = 10^{-10} \div 10^{-5}$; $\quad \eta_p = 0.05 \div 0.8$; $\quad S_r = 0 \div 500$; $\quad \beta = 0.001 \div 1$; $\quad \gamma = 0.01 \div 10$; $\quad Q_{ph} = 0.01 \div 10$; $\quad \theta_{ph} = 0.1 \div 10$; $\quad K_c = 0.1 \div 10$; $\quad K_\lambda = 0.1 \div 10$; $\delta = 0.05 \div 10^5$; $\quad \bar{V} = 50 \div 10^5$.

4 Analysis of the results of the numerical investigation

For numerical problem solution (12) - (14) with conditions (15) - (20), an absolutely stable implicit difference scheme and double-sweep method are used.

Coating formation regimes of basic material depend on energy parameters characterizing external source and melt of substances.

The analysis of numerical calculation results show that in process of heat treatment

409
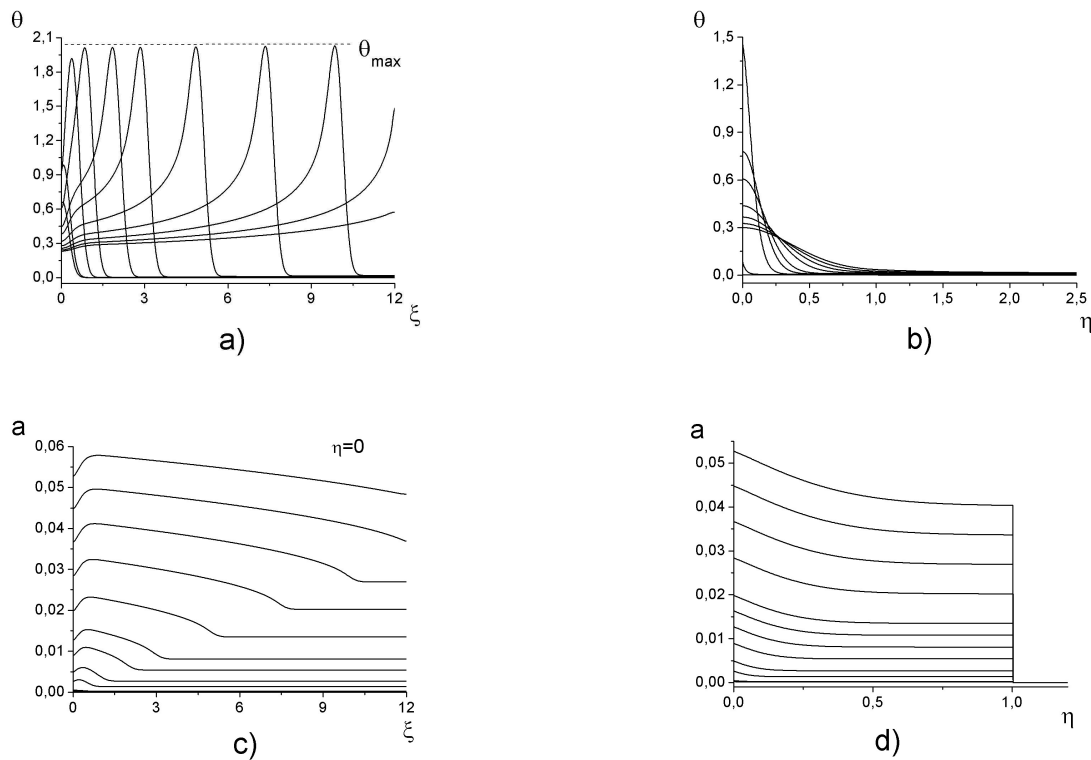
Figure 3: The distribution of temperature and conversion degree (a, c) - along axis $O\xi$, (b, d) - along axis $O\eta$ in serial time moments. $K_c = 0.1, K_\lambda = 1, S_r = 200, S_k = 10^{-8}, Q_{ph} = 0.1, \theta_{ph} = 2, \gamma = 2, \delta = 5, \beta = 0.5$.

of the plate in investigated field of the parameters a quasi stationary regime not establishes. In the specimen by finite size coating synthesis flow in a nonsteady regime. In order to judge on the quasistationarity or nonstationarity of the technological process it can be characterized additionally by integrated conversion degree

$$I_a = \frac{1}{X_\xi} \int_0^1 \left(\int_0^{X_\xi} a(\xi, \eta) d\xi \right) d\eta,$$

integrated heat release in chemical reaction

$$I_{Qch} = \frac{1}{X_\xi} \int_0^1 \left(\int_0^{X_\xi} Q_{ch}(\xi, \eta) d\xi \right) d\eta$$

in dependence on conditions of synthesis that is of interest for technology immediately (fig.2). But even those values not allow talk about a presence of quasi stationary stages, that distinguish this model from [1].
Integrated conversion degree and heat release in reactions most depend on ratio of thermophysical properties of the coating and the base, that shown in fig. 2, a, b.
Examples of the temperature distributions along axis $O\xi$ (on the surface) and the temperature distributions along axis $O\eta$ (along specimen depth) for different time moments in fig. 3 are demonstrated for illustration of process dynamics. Only

410
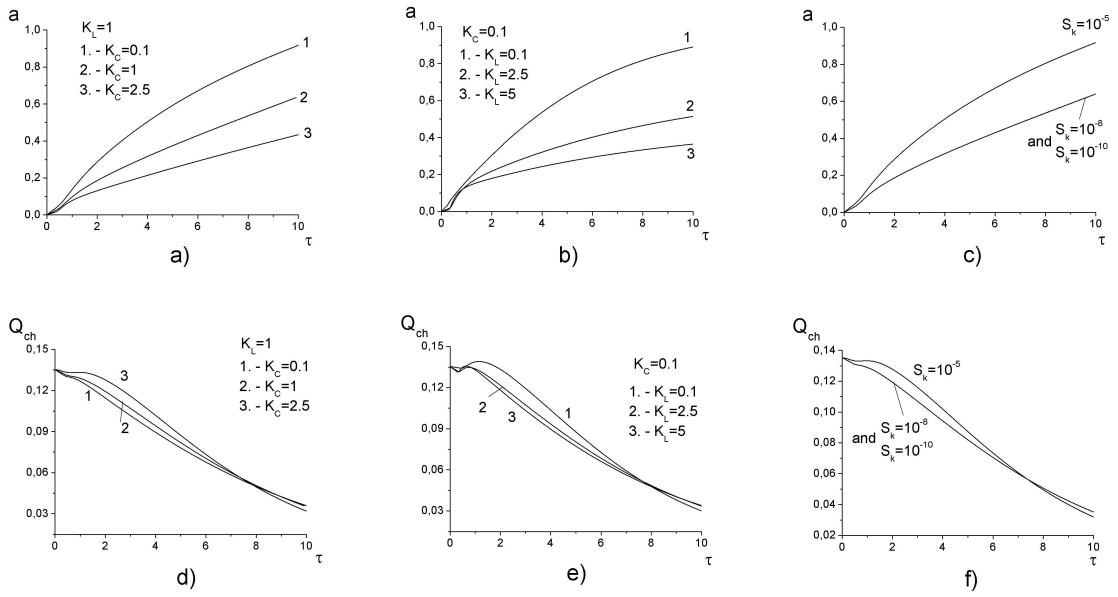
Figure 4: Dependencies of conversion degree (a, b, c) α and heat release in chemical reaction (d, e, f) Q_{ch} from time for different values of the parameters K_c, K_λ, S_k; $Q_{ph} = 0.1, \theta_{ph} = 2, \gamma = 2, \delta = 5, \beta = 0.5$.

weak change of maximal temperature with time $\theta_{max}(\tau)$ point to some approach to quasistationary (fig. 3, a). As source moving along a plate, synthesis proceed in all volume irregularly and not followed out (fig. 3, c, d). In this case we can talk about value α_f towards the end treatment process and about value $\langle \alpha_f \rangle$ depend on model parameters.

Influence of some parameters on conversion degree at point $\xi = \xi_{max}$ versus τ and on chemical thermal flax is illustrated in fig. 4.

With increase K_c more quantity of heat is required on heating therefore conversion degree decrease (fig. 4, a). With increment of thermal conductivity of the base with respect to coating heat faster leave outside coating. It reduces a conversion degree (fig. 4, b). Obviously, with increase of heat loss completeness degree of reaction is increased, also (fig. 4, c). In any case chemical thermal flax decrease versus time in the investigated area of parameters (fig. 4, d, e, f) and is not great versus external heating. It means that synthesis flow in controllable regime.

5 Conclusions

Thus, in this work the model of a controllable coating synthesis on the base is formulated and is investigated. A parametric investigation was carried out.

411

References

[1] Kryukova O.N., Knyazeva A.G. Critical conditions of particle solution in the molten bath during electron-beam modification of metal surface // Proceeding 9th International Conference on Modification of Materials with Particle Beams and Plasma Flows. Tomsk. Russia, 21-26 September 2008, pp. 186-189.

Olga N. Kryukova, Academichesky Ave., 2/4, Tomsk, Russia
Anna G. Knyazeva, Academichesky Ave., 2/4, Tomsk, Russia

Role of viscosity in continuum mechanics approach to describe flow through porous media

Ilya V. Kudinov   Nikolay V. Evseev

ilya.kudinov@gmail.com

Abstract

Question about magnitude of viscous stresses in fluid phase in continual description of filtration process is under consideration. This question directly relates to applicability limits of the Darcy's law, which uses scalar pressure instead of full stress tensor to characterize fluid stress state. Manifestation of viscous effects on macroscopic (averaged) velocity field is studied in the case of flow through channel filled with a porous medium. This problem was investigated by direct numerical modeling based on the Navier-Stokes equation. We used regular arrays of spheres as model porous media. In addition two configurations with porosity varying along the cross-section were considered to reproduce near-wall perturbations in porous structure. Based on microscopic fields found in the numerical experiments, viscous dissipations and seepage velocity profiles were calculated. The results obtained prove applicability of the Darcy's law and validity for neglecting viscous part of macroscopic stress tensor even for high porosities (upto 0.9). Also discussed is nonmonotonic shape of seepage velocity profiles observed experimentally and its connection to the question discussed.

1   Introduction

Flow through porous media could be described on macroscopic scale in the frame of continuum mechanics by introducing multiple interacting continua characterized by volume-averaged quantities [1]. Most of the models based on continual approach employ Darcy's law as momentum balance equation:

$$\mathsf{V} = -\frac{\mathsf{k}}{\mu}\nabla\mathsf{P} \tag{1}$$

where V is seepage velocity (averaged over a unit cross-section), μ is viscosity, $\nabla\mathsf{P}$ is macroscopic pressure gradient applied to the saturating fluid, k is permeability of the medium.

In this equation viscosity is present explicitly as a multiplier. However fluid stress state is described only by scalar pressure field, viscous stresses represented by non-diagonal terms of stress tensor being omitted. Such a contradictory role of viscosity in the Darcy's law was discussed by several authors (see for example [2]), starting

from the classical works of N.E. Zhukovsky who derived equation (1) from the Euler's equation for inviscid fluid but taking into account solid-fluid frictional force proportional to the viscosity. A typical argumentation for this derivation is that contact solid-fluid viscous interaction greatly exceeds internal viscous stresses inside fluid, which could be neglected on macroscale.

However such reasoning becomes doubtful in many situations, particularly for high-porosity media and high-viscosity liquids. Question about correctness of neglecting deviator part of the fluid stress tensor is non-trivial in these cases. Remark that it is not a purely academic question, it has a practical concern as well. Nowadays most of the commercial hydrodynamic simulators in oil industry are based on the Darcy's law, so that their applicability to model heavy-oil transport is controversial.

In a general case it is difficult to evaluate macroscopic viscous effects analytically. There are two different points of view on the subject. According to the first one [3], buckling, convergence and divergence of steamlines in porous media (as compared with void space) may lead to a more intensive liquid mixing, thus providing an increased effective macroscopic viscosity. Following this approach porous medium may be considered as a source of pulsation disturbances of velocity field that give rise to additional vicsous stresses similar to Reynolds stresses in turbulent regime of flow. According to the second position [4], the described analogy with Reynolds stresses is not comletely correct because power of viscous dissipation on solid-liquid interface prevails over power of the mixing produced. This implies that macroscopic manifistation of viscous properties is limited to the friction (flow-resistance) force.

In the present work question about macroscopic viscous effects is addressed by means of direct numerical simulation. In particular, we consider seepage velocity profiles for flow through channel filled with high-porosity particulate media. Evolution of the profile which characterizes magnitude of viscous effects is observed as porosity increases.

2 Method of modeling

We consider stationary isothermal flow of a Newtonian fluid through spatially-periodic arrays of spherical grains. Typically grains have equal radii and are arranged in nodes of a simple cubic lattice thus constituting a uniform isotropic medium. The medium is placed between two horizontal impermeable planes (Fig. 1). Additionally, two cases with porosity variation in near-wall region are addressed. Porosity variation is achieved by decreasing particles' radii or increasing distances between them.

Our approach is to determine pore-scale fluid velocity field by solving hydrodynamic equations and then to find seepage velocity profile via direct averaging of the microscopic field. Mass and momentum balance equations governing isothermal viscous flow are as follows

$$\frac{\partial \rho}{\partial t} + \frac{\partial (\rho v_i)}{\partial x_i} = 0 \tag{2}$$

$$\frac{\partial (\rho v_i)}{\partial t} + \frac{\partial}{\partial x_j} (\rho v_i v_j - p_{ij}) = -\rho \frac{\partial \varphi}{\partial x_i}, \ p_{ij} = \tau_{ij} - p \delta_{ij} \tag{3}$$
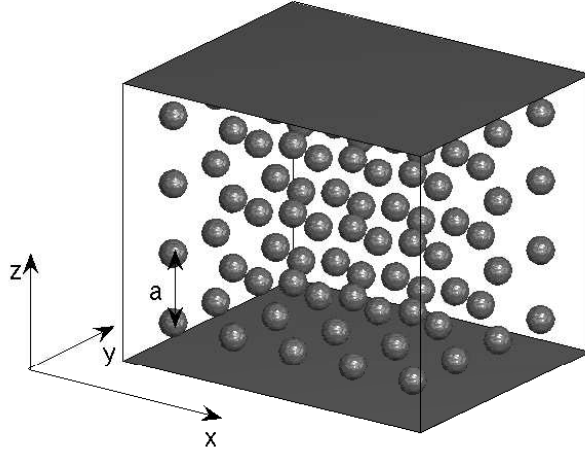
414

Figure 1: Channel filled with idealized porous medium - cubic lattice of spheres of radius r with lattice period a.

where ρ is mass density, v_i is velocity component along axis i ($i, j = 1 \ldots 3$), φ is external bulk force potential, p_{ij} and τ_{ij} are full stress tensor and viscous stress tensor respectively, p is pressure, δ_{ij} stands for unity tensor. Summation is assumed for repeating indices.

For a Newtonian fluid viscous stress tensor has the following classical form

$$\tau_{ij} = \left(\eta - \frac{2}{3}\mu\right)\frac{\partial v_k}{\partial x_k}\delta_{ij} + \mu\left(\frac{\partial v_i}{\partial x_j} + \frac{\partial v_j}{\partial x_i}\right) \qquad (4)$$

here η and μ represent bulk and shear viscosities respectively. To close the model we use equation of state for slightly compressible liquid:

$$p = E(\rho - \rho_0)/\rho_0 \qquad (5)$$

where E is inverse compressibility (measured in Pa), ρ_0 is equilibrium mass density. No-slip boundary condition is applied at grains' surfaces and confining walls

$$v_i|_{surface} = 0, \; v_i|_{z=0} = 0, \; v_i|_{z=H} = 0 \qquad (6)$$

According to the spatial periodicity of the porous structure, velocity and density fields are presumed to be spatially-periodic as well, that is

$$v_i|_{x=0} = v_i|_{x=L}, \; v_i|_{y=0} = v_i|_{y=L}, \; \rho|_{x=0} = \rho|_{x=L}, \; \rho|_{y=0} = \rho|_{y=L} \qquad (7)$$

System of equations (2–7) presents a closed problem which was solved numerically by means of a finite-volume method on a regular orthogonal grid. Explicit numerical scheme which provided 2nd order approximation in space and 1st order approximation in time was employed. We used staggered grids for different variables (velocity components and density) [5]. Adaptive time-step was applied to prevent possible instability development. Stationary solutions were obtained by the relaxation method.

	I	II	III	IV
a, mm	2.5	3.75	5.0	6.25
ϕ	0.73	0.92	0.97	0.98
δ_f, Pa/s	9.87×10^{-11}	1.07×10^{-9}	3.19×10^{-9}	8.06×10^{-9}
$\langle \delta_\nu \rangle$, Pa/s	7.68×10^{-11}	1.06×10^{-9}	3.36×10^{-9}	7.76×10^{-9}
$\delta_f / \langle \delta_\nu \rangle$	1.28	1.00	0.95	1.04

Table 9: Characteristics of the lattices: period a, porosity ϕ, filtration dissipation δ_f, averaged viscous dissipation $\langle \delta_\nu \rangle$.

In all the computations numerical viscosity was negligible in comparison with the values of physical viscosities.

Correctness of the numerical procedure was verified in two test cases with known analytical solutions: flow through a cylindrical pipe (Poiseuille's flow) and flow over a single spherical body. For the both problems numerical solution converged to the analytical one as mesh was refined. Based on this preliminary study discretization of a sphere by 4 computational cells per radius was selected as the minimal one giving satisfactory accuracy. Further computations were performed using this particular discretization.

3 Numerical experiments

Arrays of spheres addressed in the present work consisted of 100 particles in the direction normal to the walls. In order to obtain each seepage velocity value, we applied averaging over a cross-section containing 10 particles, so that seepage velocity profile had 10 points. Four different lattices of spheres were considered with porosity varied from 0.73 to 0.98 (parameters of the lattices are presented in Table 9). Such porosity range was chosen as it covered transition zone from a flat seepage velocity profile to a quasi-parabolic one. Therefore lower porosity region seemed to be unpromising to observe any macroscopic viscosity effect. All the computations were carried out for $\rho_0 = 1000 \, \text{kg/m}^3$, $\mu = 0.1 \, \text{Pa} \cdot \text{s}$, $\eta = 0.1 \, \text{Pa} \cdot \text{s}$, $E = 10^4 \, \text{Pa}$. Radius of spheres was equal to $1 \, \text{mm}$, macroscopic pressure gradient was $10^{-2} \, \text{Pa/m}$. Such small magnitude of ∇P guarantied creeping regime of flow without any non-Darcy effect.

The obtained pore-scale velocity distributions (Fig. 2) show that influence of the external boundary is localized in its immediate vicinity even for porosity 0.98. Fig. 2 demonstrates that at a very short distance from the wall (2-3 pore channels) a universal microscopic velocity field, independent from the external boundary and the same in the whole inner region, is formed. On the macroscopic scale this leads to a flat profile of the averaged velocity (see Fig. 3), wall effect being visible only at points that are in direct contact with the boundary. Particular view of this wall effect is strongly dependent on details of the averaging procedure. For example, averaging over a smaller or larger cross-section area would give profiles that differ in the near-wall region but coincide in the inner region.

Flat seepage velocity profiles indicate that at macroscopic scale viscosity does not affect flow pattern, it just reduces flow rate. In order to better understand relations
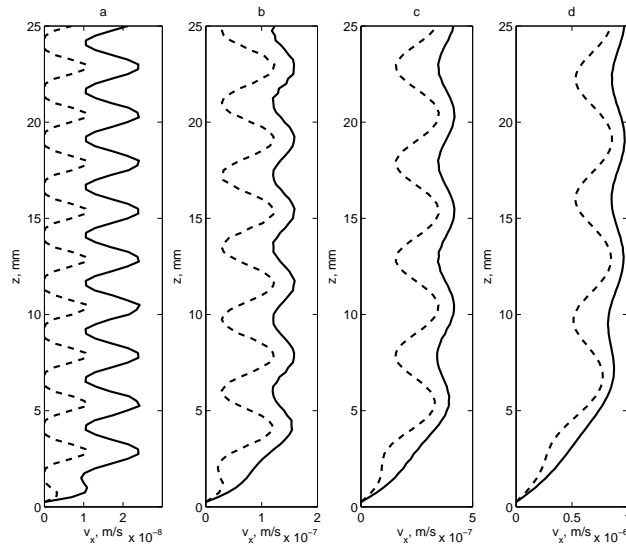
Figure 2: Minimal (dashed line) and maximal (solid line) values of v_x in a vertical section located in the middle between spheres. Near-wall region is shown for the lattices with porosity 0.73 (a), 0.92 (b), 0.97 (c) and 0.98 (d).
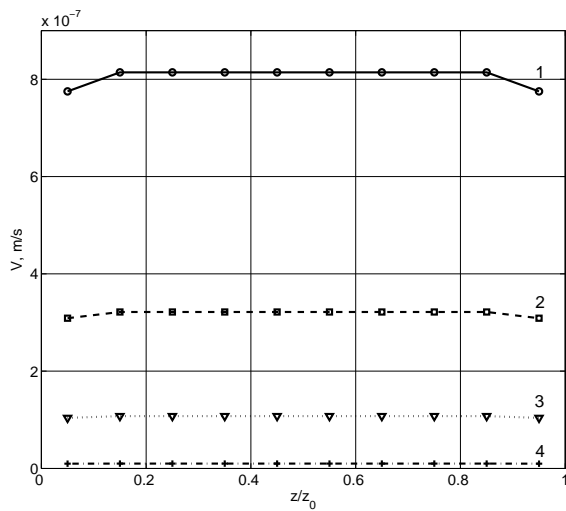

Figure 3: Seepage velocity profiles for the lattices with porosity 0.98 (line 1), 0.97 (line 2), 0.92 (line 3) and 0.73 (line4).

between micro-scale viscous effects and macro-scale ones we calculated viscous dissipation (loss of fluid energy in a unit volume per second) at the two scales. In the framework of the continual approach dissipation of filtration is defined as [6]

$$\delta_f = -V\nabla P \tag{8}$$

which could be rewritten using the Darcy's law as

$$\delta_f = \frac{k}{\mu}(\nabla P)^2 \tag{9}$$

On the other hand, at the micro-scale viscous dissipation is defined by the following formula

$$\delta_\nu = \frac{\mu}{2} \int \left(\frac{\partial \nu_i}{\partial x_j} + \frac{\partial \nu_j}{\partial x_i} \right)^2 dV \tag{10}$$

Based on the numerical results viscous dissipation (10) along with filtration dissipation (9) were calculated for the four porous structures considered. The corresponding values are shown in Table 9. Note that from a computational point of view an additional interpolation step was required to calculate expression (10) which probably led to a decreased accuracy. Therefore one should consider the presented values of $\langle \delta_\nu \rangle$ as evaluative ones.

The data obtained indicate no prominent trend for $\delta_f / \langle \delta_\nu \rangle$ as a function of porosity. However this ratio was close to unity in all the cases thus proving that filtration dissipation is dominantly governed by viscous friction on pore walls rather than inside pore space. Indeed, δ_f as it is defined by (8) characterizes power of the flow-resisting force, while averaged δ_ν directly quantifies all the viscous losses on grains' surfaces as well as in a bulk fluid. Consequently, approximate equality of δ_f and $\langle \delta_\nu \rangle$ implies that solid-fluid frictional dissipation is prevailing in flows through porous media.

4 Discussion and conclusions

The performed numerical experiments on the idealized porous media have shown that even for high porosity (greater than 0.9) averaged velocity field corresponds to inviscid fluid flow, *i.e.* seepage velocity profiles are flat and insensitive to the external boundaries. Let us highlight that at the same time the liquid passing through the medium is essentially viscous and micro-scale velocity distribution in each individual pore is close to Poiseuille's parabolic profile (see Fig. 2).

In spite of high porous space connectivity in the cases considered, hydrodynamic link between pores is insufficient to propagate disturbances (as those ones exerted by external boundaries) at macroscopically visible distances. The main reason for such a behavior is that viscous dissipation at solid-fluid contacts predominates over viscous dissipation inside the fluid itself. Furthermore, even for high porosity media
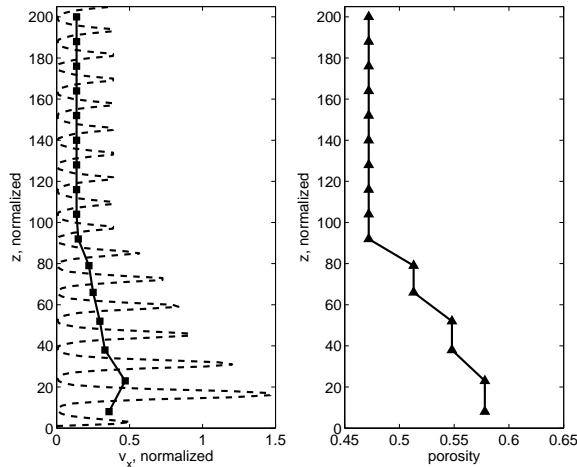
Figure 4: Pointwise velocity (dashed line), averaged over 1 lattice cell velocity (square marker) and porosity (triangle marker) profiles for the lattice with the near-wall perturbance (case a). Bottom half containing 16 spheres is shown.

specific surface area of pore walls is greater than that of external confining walls, thus making dissipation at the internal interphase boundary determinative.

The point of view [3], according to which flow mixing in a porous sample gives rise to some kind of macroscopic effective viscosity, was not validated by the numerical experiments. According to our opinion, the proposed analogy between velocity pulsations in porous media and those ones taking place in turbulent flows is not quite adequate due to the presence of the solid phase. The directly calculated viscous and filtration dissipations demonstrate that fluid momentum loss at contacts with solids is superior than momentum exchange via mixing which is responsible for the effective viscosity. Moreover, time averaging procedure employed by Reynolds when introducing the turbulent stress tensor is not equivalent to the space averaging used in the continual description of heterogenuous systems.

Work [3] was inspired partially by a set of publications on experimentally observed effect of non-monotonic flow rate distribution in pipes filled with a granular material (see for example [7]). It was found that flow rate (measured in the empty pipe downstream from the granular pack) has a maximum at a short distance from the tube wall, decreasing gradually toward the center, and sharply toward the wall. This flow rate peak was attributed to porosity increase (and thus permeability increase) in the boundary layer due to wall-induced perturbations of the granular pack structure. However, flow rate drop in the very close vicinity of the wall was interpreted by some researchers as a violation of the Darcy's law.

To verify the numerical procedure against the experimental data, two cases with the porosity increasing in the boundary layer were addressed. We have considered lattice of 32 spheres per channel diameter (as it was in [7]) with a modified near-wall region: slightly shrinking particles (a), or slightly growing inter-particle gaps (b). For the both cases close results that are in a qualitative agreement with the experimental profiles have been obtained (see Fig. 4). Reproduction of the flow rate

peak phenomenon is an additional argument for the model correctness, however it has no direct concern to the question considered in the present paper. Flow rate profile (as it was understood in [7]) could not be regarded as the Darcy's seepage velocity profile, since the ratio of mean grain size to the pipe diameter is not small enough. It contradicts the basic assumption of the continual approach, which requires existence of the meso-scale λ such that $l \ll \lambda \ll L$ where l is the characteristic pore length, λ is the size of volume of averaging, L is the characteristic length of flow. Therefore, the presented data on flow rate peak effect could not be interpreted as the effective viscosity manifestation or Darcy's law failure.

As a main conclusion of the work, applicability of the Darcy's law, which neglects the deviator part of the fluid stress tensor, was proven for high porosity (up to 0.9) media. Furthermore, as the averaged velocity profile was found to be more or less independent from the velocity profile in an individual pore, it seems warrantable to use the Darcy's law when filtrating liquid has a more complex rheology than the newtonian one.

Acknowledgements

References

[1] Nigmatulin R.I. Dynamics of multiphase media. M.: Nauka, 1987 [in Russian]

[2] Basniev K.S., Dmitriev N.M., Rosenberg G.D. Hydromechanics of oil and gas. M.-Izhevsk: IKI, 2005 [in Russian]

[3] Shirko I.V., Parfus V.O. Viscous properties of flows of an incompressible liquid in an anisotropic heterogeneous granular medium // *Theor. Found. Chem. Eng.*, V. 38, N. 6, 2004

[4] Kondaurov V.I. Mechanics and thermodynamics of a saturated porous medium. M.: MFTI, 2007 [in Russian]

[5] Patankar S. Numerical heat transfer and fluid flow. N.Y.: Hemisphere, 1980

[6] Coussy O. Poromechanics. Chichester: Wiley, 2004

[7] Schwartz C.E., Smith J.M. Flow distribution in packed beds // *Ind. Eng. Chem.*, V. 45, N. 6, 1953

Ilya V. Kudinov, Moscow Institute of Physics and Technology, Institutsky per. 9, 141700 Dolgoprudny, Russia

Nikolay V. Evseev, Schlumberger Moscow Research, per. Ogorodnaya sloboda 5A, 101000 Moscow, Russia

Equivalent thermo-mechanical parameters for perfect crystals with arbitrary multibody potential

Vitaly A. Kuzkin

kuzkinva@gmail.com

Abstract

Derivation of equivalent thermo-mechanical parameters for perfect crystals in the case of arbitrary interatomic potential is conducted. The approach based on the averaging of equations of motion is considered. Long wave approximation is used to make link between the discrete system and equivalent continuum. Macroscopic thermo-mechanical parameters such as Piola and Cauchy stress tensors, heat flux are represented via microscopic parameters.

1 Introduction

Determination of the connection between parameters of discrete and continual systems is one of the challenging problems for modern physics. In spite of the intensity and time period of investigations in this direction the problem is far from its final solution. At the beginning the problem was only of a fundamental interest. However, practical interest is increasing now. The increase is caused by fast development of discrete [1, 2] and discrete-continual [3, 4] methods of simulation of mechanical behavior of bodies under mechanical and thermal loadings. Various methods of transition from discrete system to equivalent continual exist. Long wave assumption is used in [5]. The concept of quasicontinuum is proposed in [6]. Localization functions are used in [7, 8, 9]. These approaches give the opportunity to spread mechanical parameters determined in lattice nodes on all volume of the body. Decomposition of motions on slow macroscopic and fast thermal is used for description of thermal properties. There are different approaches for decomposition. In papers [7, 8, 9] the decomposition of particles' velocities is conducted by the use of localization functions. As a result, the dependencies of stress tensor and heat flux on parameters of the discrete system were obtained and analyzed. Another approach was proposed in [10]. Fourier transformation was used for decomposition of displacements and velocities of particles. Different methods of decompositions were discussed. It was noted that the result of the decomposition is not unique. It should depend on characteristic time and spatial scales of the problem.
The approach based on averaging of equations of motions and application of long wave assumption [5] was proposed in papers [11, 12]. It was used for derivation of expressions for stress tensors for ideal crystals in book [11]. Only pair potentials were

considered. Thermal motion was neglected. The influence of thermal oscillations on mechanical properties was considered in [11, 12] for one dimensional case. Proposed approach gives opportunity to conduct analytical derivations. In particular, equation of state in Mie-Gruneisen form was obtained in papers [11, 12, 13].

Different assumptions about interatomic potentials were used in all papers mentioned above. This fact decreases the range of applications of results of these papers. In the present paper derivations are conducted for arbitrary many-body potential. It is assumed that the energy per one particle depends on all vectors connecting this particle with its neighbors. The approach proposed in works [11, 12] is used for transition from discrete system to equivalent continual. Equations of motion of particles are derived. The connection of Cauchy and Piola stress tensors and heat flux with parameters of discrete systems is determined. The symmetry of obtained Cauchy stress tensor is proved. Comparison with known expressions for Cauchy stress tensor is discussed.

2 Hypotheses

Let us consider discrete system of interacting particles which form perfect simple crystal lattice in $d = 1, 2$ or 3 dimensions. Two main principles are used for transition from discrete system to equivalent continual: decomposition of motions of particles on slow macroscopic and fast thermal [10, 11], and long wave assumption [5]. First let us focus on decomposition. In practice different types of averaging such as time averaging, spatial averaging are used for decomposition. In paper [10] it was noted that unique decomposition is impossible because there are no rules for the choice of the period of averaging, size of representative volume, etc. These parameters should depend somehow on time and spatial scales of the considered problem. According to the opinion of the author of the present paper derivations should not be based on the particular method of decomposition. In addition results should not change qualitatively with replacement of the method of averaging. Therefore let us consider average component $\left\langle f \right\rangle$ and thermal component $\widetilde{f}$ of physical value f that are connected by the following expression

$$f = \left\langle f \right\rangle + \widetilde{f}, \qquad \widetilde{f} \stackrel{\text{def}}{=} f - \left\langle f \right\rangle. \tag{1}$$

Also long wave assumption will be used [5]. The idea of the assumption is as follows: average component of any physical value is assumed to be slowly changing in space on distances of order of interatomic distance. Then average component can be considered as continual function of space variable and can be expanded into power series with respect to interatomic distance. Resulting series should converge rapidly. Exactly this assumption allows to make transition from discrete system to continuum.

3 Kinematics

Let us use Lagrangian (material) description of equivalent continuum and consider the reference and actual configurations of discrete and continual systems. Let us

take an unstrained configuration of crystal lattice as the reference one for discrete system. Let us denote radius-vectors of equivalent continuum in reference and actual configurations as $\underline{r}$ and $\underline{R}$ respectively. Two ways for identification of the particles will be used. On the one hand, the position of the particle is determined by its radius-vector. On the other hand, let us use local numbering. Starting with one reference particle let us mark all its neighbors by index α. Let us denote vector connecting the reference particle with its neighbor number α as $\underline{a}_\alpha$. The numbering will be conducted in such a manner that $\underline{a}_\alpha$ has the following property

$$\underline{a}_\alpha = -\underline{a}_{-\alpha}. \tag{2}$$

The same vectors in actual configuration $\underline{\mathcal{A}}_\alpha$ will be represented as a sum of averaged component $\underline{A}_\alpha$ and thermal component $\underline{\tilde{A}}_\alpha$. The connection between vectors $\underline{a}_\alpha$ and $\underline{A}_\alpha$ in long wave approximation is as follows

$$\underline{A}_\alpha = \underline{R}(\underline{r} + \underline{a}_\alpha) - \underline{R}(\underline{r}) \approx \underline{a}_\alpha \cdot \overset{\circ}{\nabla} \underline{R}, \tag{3}$$

where $\overset{\circ}{\nabla}$ is nabla-operator in the reference configuration. Note that equation (3) is similar to equation for connection between vectors $d\underline{R}$ and $d\underline{r}$ in continual mechanics [18].

Let us consider properties of introduced numbering system. If $f(\underline{r})$ is a physical value which corresponds to the particle with radius-vector $\underline{r}$ in the reference configuration. Then $f_\alpha(\underline{r})$ is the same physical value for particle α. Thus the following two expressions are equivalent

$$f_\alpha(\underline{r}) \equiv f(\underline{r} + \underline{a}_\alpha). \tag{4}$$

In the framework of this approach physical value in point $\underline{r}$ can be represented in three different ways.

$$f(\underline{r}) = f_\alpha(\underline{r} - \underline{a}_\alpha) = f_{-\alpha}(\underline{r} + \underline{a}_\alpha) \tag{5}$$

4   Balance of momentum

Let us assume that potential energy per one particle is represented by the following expression

$$\Pi = \Pi(\{\underline{\mathcal{A}}_\alpha\}_{\alpha \in \Lambda}), \tag{6}$$

Here $\{\underline{\mathcal{A}}_\alpha\}_{\alpha \in \Lambda}$ is the set of all vectors $\underline{\mathcal{A}}_\alpha$ for the given particle; Λ is the set of all numbers of particles which interact with the given particle. Potential energy per particle can be represented in the form (6) for the majority of commonly used potentials. In particular, equation (6) is satisfied for pair potentials, embedded atom potential [14], Stillinger-Weber potential [15], Tersoff potential [16].

Let us derive the equation of motion of the particle with radius-vector $\underline{r}$ in the reference configuration. For the sake of simplicity let us consider the case when

volumetrical forces are absent. Denote radius-vector of the particle in the current moment of time by $\underline{R}_t$. The following identity is satisfied for $\underline{R}_t$

$$\underline{R}(\underline{r}) = \left\langle \underline{R}_t \right\rangle. \tag{7}$$

Let us denote potential energy per particle α as Π_α, where $\Pi_\alpha = \Pi(\{\underline{\mathcal{A}}_\beta(\underline{r}+\underline{a}_\alpha)\}_{\beta\in\Lambda})$. Using Lagrange approach one can obtain the equation of motion of the reference particle

$$m\underline{\ddot{R}}_t = -\frac{\partial}{\partial \underline{R}_t}\left(\Pi + \sum_\alpha \Pi_\alpha\right) \quad \Rightarrow \quad m\underline{\ddot{u}}_t = -\frac{\partial \Pi}{\partial \underline{u}_t} - \sum_\alpha \frac{\partial \Pi_\alpha}{\partial \underline{u}_t}, \tag{8}$$

where $\underline{u}_t$ is the current displacement of the particle, summation is conducted on the set Λ. Calculating derivatives in equation (8) one can obtain

$$\frac{\partial \Pi}{\partial \underline{u}_t} = \sum_\alpha \frac{\partial \underline{\mathcal{A}}_\alpha}{\partial \underline{u}_t} \cdot \frac{\partial \Pi}{\partial \underline{\mathcal{A}}_\alpha} = -\sum_\alpha \frac{\partial \Pi}{\partial \underline{\mathcal{A}}_\alpha},$$
$$\left[\frac{\partial \Pi_\alpha}{\partial \underline{u}_t}\right](\underline{r}) = \sum_\beta \frac{\partial \underline{\mathcal{A}}_\beta(\underline{r} + \underline{a}_\alpha)}{\partial \underline{u}_t(\underline{r})} \cdot \left[\frac{\partial \Pi}{\partial \underline{\mathcal{A}}_\beta}\right](\underline{r} + \underline{a}_\alpha) = \left[\frac{\partial \Pi}{\partial \underline{\mathcal{A}}_{-\alpha}}\right](\underline{r} + \underline{a}_\alpha). \tag{9}$$

Here relation $\underline{\mathcal{A}}_\alpha(\underline{r}) = -\underline{\mathcal{A}}_{-\alpha}(\underline{r} + \underline{a}_\alpha)$ was used. Square brackets mean that all expressions in brackets are calculated in one point. Substituting the result into equation of motion (8) one obtains

$$m\underline{\ddot{u}}_t = \sum_\alpha \underline{F}_\alpha, \qquad \underline{F}_\alpha \overset{\text{def}}{=} \frac{1}{2}\left(\underline{\mathcal{F}}_\alpha(\underline{r}) - \underline{\mathcal{F}}_{-\alpha}(\underline{r} + \underline{a}_\alpha)\right), \qquad \underline{\mathcal{F}}_\alpha \overset{\text{def}}{=} 2\frac{\partial \Pi}{\partial \underline{\mathcal{A}}_\alpha}. \tag{10}$$

Here $\underline{F}_\alpha$ is the force acting between the given particle and particle α. One can prove that the third Newton's law is satisfied for $\underline{F}_\alpha$, i.e. $\underline{F}_\alpha(\underline{r}) = -\underline{F}_{-\alpha}(\underline{r} + \underline{a}_\alpha)$. In the case of pair interactions one has

$$\underline{\mathcal{F}}_\alpha(\underline{r}) = -\underline{\mathcal{F}}_{-\alpha}(\underline{r} + \underline{a}_\alpha) \quad \Rightarrow \quad \underline{F}_\alpha = \underline{\mathcal{F}}_\alpha. \tag{11}$$

Note that $\underline{\mathcal{F}}_\alpha$ can be considered as a force only in this particular case. One can verify this statement on the example of embedded-atom potential [14].

Now let us obtain equation of balance of momentum for equivalent continuum. Let us average (10) and apply long wave assumption. Then the right side of equation (10) take form

$$\frac{1}{2}\sum_\alpha \left\langle \underline{\mathcal{F}}_\alpha(\underline{r}) - \underline{\mathcal{F}}_{-\alpha}(\underline{r} + \underline{a}_\alpha) \right\rangle = \frac{1}{2}\sum_\alpha \left\langle \underline{\mathcal{F}}_\alpha \right\rangle(\underline{r}) - \frac{1}{2}\sum_\alpha \left\langle \underline{\mathcal{F}}_\alpha \right\rangle(\underline{r} - \underline{a}_\alpha) \approx$$
$$\approx \frac{1}{2}\sum_\alpha \left\langle \underline{\mathcal{F}}_\alpha \right\rangle(\underline{r}) - \frac{1}{2}\sum_\alpha \left\langle \underline{\mathcal{F}}_\alpha - \underline{a}_\alpha \cdot \overset{\circ}{\nabla} \underline{\mathcal{F}}_\alpha \right\rangle(\underline{r}) = \frac{1}{2}\overset{\circ}{\nabla} \cdot \left(\sum_\alpha \underline{a}_\alpha \left\langle \underline{\mathcal{F}}_\alpha \right\rangle\right), \tag{12}$$

Substituting the result into averaged equation (10) and dividing both parts by the volume of elementary cell in the reference configuration one obtains

$$\rho_0 \underline{\ddot{u}} = \overset{\circ}{\nabla} \cdot \left(\frac{1}{2V_0}\sum_\alpha \underline{a}_\alpha \left\langle \underline{\mathcal{F}}_\alpha \right\rangle\right), \qquad \rho_0 \overset{\text{def}}{=} \frac{m}{V_0}. \tag{13}$$

Comparing equation (13) with equation of motion of continual media in Piola form [18] one can conclude that ρ_0 is a density of equivalent continuum in the reference configuration, expression for Piola stress tensor has the following form

$$\underline{\underline{P}} = \frac{1}{2V_0} \sum_\alpha \underline{a}_\alpha \left\langle \mathcal{F}_\alpha \right\rangle. \tag{14}$$

Let us derive the expression for Cauchy stress tensor. One can show that in actual configuration formula (12) has the following form

$$\frac{1}{2V} \sum_\alpha \left\langle \mathcal{F}_\alpha(\underline{R}) - \mathcal{F}_{-\alpha}(\underline{R} + \underline{A}_\alpha) \right\rangle = \frac{1}{2V} \sum_\alpha \underline{A}_\alpha \cdot \nabla \left\langle \mathcal{F}_\alpha \right\rangle =$$
$$= \nabla \cdot \left(\frac{1}{2V} \sum_\alpha \underline{A}_\alpha \left\langle \mathcal{F}_\alpha \right\rangle \right) - \sum_\alpha \nabla \cdot \left(\frac{1}{2V} \underline{A}_\alpha \right) \left\langle \mathcal{F}_\alpha \right\rangle. \tag{15}$$

Here ∇, V are nabla-operator and volume of elementary cell in actual configuration. Using formula (3) and Piola's identity [18] one can show that the second term in the right side of equation (15) is equal to zero. Then substituting (15) into equation of motion (10) one obtains

$$\rho \underline{\ddot{u}} = \nabla \cdot \left(\frac{1}{2V} \sum_\alpha \underline{A}_\alpha \left\langle \mathcal{F}_\alpha \right\rangle \right), \qquad \rho \overset{\text{def}}{=} \frac{m}{V}. \tag{16}$$

Comparing equation (16) with equation of motion of continuum in Cauchy form one can obtain the following expression for Cauchy stress tensor $\underline{\underline{\tau}}$:

$$\underline{\underline{\tau}} = \frac{1}{2V} \sum_\alpha \underline{A}_\alpha \left\langle \mathcal{F}_\alpha \right\rangle. \tag{17}$$

In the case of the absence of thermal motion in the crystal with pair potential the result coincides with expressions proposed in papers [11, 17].

5   Balance of moment of momentum

One can see that tensor $\underline{\underline{\tau}}$ is not symmetrical in the general case. It is known from continual mechanics [19] that the symmetry of Cauchy stress tensor follows from equation of balance of moment of momentum for elementary volume. In discrete case elementary cell plays the role of elementary volume. Let us write down averaged equation of moment of momentum for elementary cell. Moments will be calculated with respect to the center of the cell determined by vector $\underline{R}$.

$$m \left\langle \underline{\widetilde{u}} \times \underline{\dot{\widetilde{u}}} \right\rangle^{\cdot} = \frac{1}{2} \left\langle \underline{\widetilde{u}} \times \sum_\alpha \left(\mathcal{F}_\alpha(\underline{r}) - \mathcal{F}_{-\alpha}(\underline{r} + \underline{a}_\alpha) \right) \right\rangle. \tag{18}$$

Let us use the following relation

$$\left\langle \underline{\widetilde{u}}(\underline{r}) \times \mathcal{F}_{-\alpha}(\underline{r} + \underline{a}_\alpha) \right\rangle = \left\langle \underline{\widetilde{u}}_{-\alpha} \times \mathcal{F}_{-\alpha} \right\rangle (\underline{r} + \underline{a}_\alpha). \tag{19}$$

Substituting formula (19) into equation (18) and using long wave assumption one can obtain

$$\mathsf{m}\left\langle \widetilde{\underline{\mathsf{u}}} \times \dot{\widetilde{\underline{\mathsf{u}}}} \right\rangle^{\cdot} = -\frac{1}{2} \sum_\alpha \left\langle \widetilde{\underline{\mathsf{A}}}_\alpha \times \underline{\mathcal{F}}_\alpha \right\rangle + \frac{1}{2} \overset{\circ}{\nabla} \cdot \sum_\alpha \underline{\mathsf{a}}_\alpha \left\langle \widetilde{\underline{\mathsf{u}}}_\alpha \times \underline{\mathcal{F}}_\alpha \right\rangle. \qquad (20)$$

where the relation $\widetilde{\underline{\mathsf{A}}}_\alpha = \widetilde{\underline{\mathsf{u}}}_\alpha - \widetilde{\underline{\mathsf{u}}}$ was used. Let us represent the first expression in the right side in the following form

$$-\frac{1}{2} \sum_\alpha \left\langle \widetilde{\underline{\mathsf{A}}}_\alpha \times \underline{\mathcal{F}}_\alpha \right\rangle = -\frac{1}{2} \sum_\alpha \left\langle \underline{\mathcal{A}}_\alpha \times \underline{\mathcal{F}}_\alpha \right\rangle + \frac{1}{2} \sum_\alpha \underline{\mathcal{A}}_\alpha \times \left\langle \underline{\mathcal{F}}_\alpha \right\rangle. \qquad (21)$$

Dividing both parts of (21) by V and using the expression (17) for Cauchy stress tensor one obtains

$$-\frac{1}{2\mathsf{V}} \sum_\alpha \left\langle \widetilde{\underline{\mathsf{A}}}_\alpha \times \underline{\mathcal{F}}_\alpha \right\rangle = -\frac{1}{2\mathsf{V}} \sum_\alpha \left\langle \underline{\mathcal{A}}_\alpha \times \underline{\mathcal{F}}_\alpha \right\rangle + \underline{\underline{\mathsf{E}}} \cdot \times \underline{\underline{\tau}}. \qquad (22)$$

Substituting the right side of equation (22) into equation (20) one has

$$\underline{\underline{\mathsf{E}}} \cdot \times \underline{\underline{\tau}} = \frac{1}{2\mathsf{V}} \sum_\alpha \left\langle \underline{\mathcal{A}}_\alpha \times \underline{\mathcal{F}}_\alpha \right\rangle + \rho \left\langle \widetilde{\underline{\mathsf{u}}} \times \dot{\widetilde{\underline{\mathsf{u}}}} \right\rangle^{\cdot} - \frac{1}{2\mathsf{V}} \sum_\alpha \underline{\mathsf{a}}_\alpha \cdot \overset{\circ}{\nabla} \left\langle \widetilde{\underline{\mathsf{u}}}_\alpha \times \underline{\mathcal{F}}_\alpha \right\rangle. \qquad (23)$$

Let us consider the right side of equation (23). The first term is equal to zero for the majority of known potentials. This statement is proved in the appendix in the case when potential energy per particle is represented in form

$$\Pi = \Pi(\{\underline{\mathcal{A}}_\alpha\}_{\alpha \in \Lambda}, \{\underline{\mathcal{A}}_\beta \cdot \underline{\mathcal{A}}_\gamma\}_{\beta, \gamma \in \Lambda}). \qquad (24)$$

In other words, potential energy depends on the distances between particles and angles between bonds of the particle with its neighbors. The second term in equation (23) is equal to zero only on the average over the space. In order to show this let us conduct the following reasoning. Obviously, the following identity is satisfied

$$\rho \left\langle \widetilde{\underline{\mathsf{u}}} \times \dot{\widetilde{\underline{\mathsf{u}}}} \right\rangle^{\cdot} = \rho \left\langle (\underline{\mathsf{R}} + \widetilde{\underline{\mathsf{u}}}) \times \dot{\widetilde{\underline{\mathsf{u}}}} \right\rangle^{\cdot}. \qquad (25)$$

The right side of this equation is the derivative of the part of moment of momentum which corresponds to thermal motion. Moment of momentum is calculated with respect to the origin of coordinates. Let the averaging operator incudes spatial averaging over significantly big volume and let us assume that thermal motion does not lead to macroscopic rotation of the volume. Then expressions (25) are equal to zero. As a result the following identity is satisfied on the average over space.

$$\underline{\underline{\tau}}^A = -\frac{1}{2\mathsf{V}} \sum_\alpha \underline{\mathsf{a}}_\alpha \cdot \overset{\circ}{\nabla} \left\langle \widetilde{\underline{\mathsf{u}}}_\alpha \underline{\mathcal{F}}_\alpha \right\rangle^A. \qquad (26)$$

Here index A means an antisymmetrical part of the tensor. One can see that the antisymmetrical part of the stress tensor (17) has the same order as terms which are

neglected in long wave approximation. Therefore $\underline{\underline{\tau}}^A$ is small in comparison with the symmetrical part and stress tensor can be considered as approximately symmetrical. Thus, averaging operator proposed above can not be arbitrary. It should include spatial averaging. Otherwise tensor $\underline{\underline{\tau}}$ will not be symmetrical and the usage of formula (17) in calculations can lead to incorrect results. Note that all reasoning mentioned above is satisfied only for the potentials that can be represented in form (24). Evidently one cannot prove that the first term in equation (23) is equal to zero in the case if arbitrary potential like (6). Therefore stress tensor (17) is not symmetrical in the general case.

6   Comparison with known expressions for Cauchy stress tensor

Different expressions connecting Cauchy stress tensor with parameters of discrete systems are proposed in literature. Relatively full reviews on this topic can be found in papers [9], [17]. In paper [9] it was shown that the majority of known expressions can be represented in the form proposed in paper [7]. Let us find the relation between this expression and formula (17). Let us write down the equation of thermal motion of the reference particle. It has the following form

$$
m\ddot{\widetilde{\underline{u}}} = \frac{1}{2} \sum_\alpha \left(\widetilde{\underline{\mathcal{F}}}_\alpha(\underline{r}) - \widetilde{\underline{\mathcal{F}}}_{-\alpha}(\underline{r} + \underline{a}_\alpha) \right).
\tag{27}
$$

Multiplying both part of the given equation by $\widetilde{\underline{u}}$ and averaging it one obtains

$$
m\left\langle \widetilde{\underline{u}}\,\dot{\widetilde{\underline{u}}} \right\rangle^{\cdot} - m\left\langle \dot{\widetilde{\underline{u}}}\,\dot{\widetilde{\underline{u}}} \right\rangle = -\frac{1}{2} \sum_\alpha \left\langle \widetilde{\underline{A}}_\alpha \widetilde{\underline{\mathcal{F}}}_\alpha \right\rangle + \frac{1}{2} \sum_\alpha \underline{a}_\alpha \cdot \overset{\circ}{\nabla} \left\langle \widetilde{\underline{u}}_\alpha \widetilde{\underline{\mathcal{F}}}_\alpha \right\rangle.
\tag{28}
$$

The derivation of this formula is similar with the derivation of equation (20). Dividing both parts by volume V and using expressions (17), (21) one can obtain

$$
\rho\left\langle \widetilde{\underline{u}}\,\dot{\widetilde{\underline{u}}} \right\rangle^{\cdot} - \rho\left\langle \dot{\widetilde{\underline{u}}}\,\dot{\widetilde{\underline{u}}} \right\rangle = \underline{\underline{\tau}} - \frac{1}{2V} \sum_\alpha \left\langle \underline{\mathcal{A}}_\alpha \underline{\mathcal{F}}_\alpha \right\rangle + \frac{1}{2V} \sum_\alpha \underline{a}_\alpha \cdot \overset{\circ}{\nabla} \left\langle \widetilde{\underline{u}}\,\underline{r}\,a1\,\widetilde{\underline{\mathcal{F}}}_\alpha \right\rangle.
\tag{29}
$$

On the one hand this expression can be used for the proof of symmetry of Cauchy stress. Thereto one can calculate vector invariant of both parts of equation (29). On the other hand one can consider stationary state of the crystal[6]. In this case one obtains

$$
\underline{\underline{\tau}} = \frac{1}{2V} \sum_\alpha \underline{A}_\alpha \left\langle \underline{\mathcal{F}}_\alpha \right\rangle = \frac{1}{2V} \sum_\alpha \left\langle \underline{\mathcal{A}}_\alpha \underline{\mathcal{F}}_\alpha \right\rangle - \rho\left\langle \dot{\widetilde{\underline{u}}}\,\dot{\widetilde{\underline{u}}} \right\rangle.
\tag{30}
$$

Thus in the particular case formulae (17) is similar with the expression used in papers [7, 9].

---

[6]In such state the average components of all physical values are constant in time and space

7 Balance of energy

For the sake of simplicity let us consider the case when volumetrical forces and volumetrical heat sources are equal to zero. Derivations will be conducted in the reference configuration. In this case averaged specific total energy per volume V_0 has the following form

$$\rho_0 \mathcal{E} = \frac{1}{2}\rho_0 \Big\langle (\underline{\dot{u}} + \underline{\dot{\tilde{u}}})^2 \Big\rangle + \frac{1}{V_0}\Big\langle \Pi(\{\underline{\mathcal{A}}_\alpha\}_{\alpha\in\Lambda}) \Big\rangle, \tag{31}$$

Here $\mathcal{E}$ is mass density of the total energy. Let us represent $\mathcal{E}$ as sum of densities of kinetic $\mathcal{K}$ and internal $\mathcal{U}$ energies. $\mathcal{K}$ is kinetic energy of average motions. $\mathcal{U}$ is potential energy plus kinetic energy of thermal motion. Then $\mathcal{K}$ and $\mathcal{U}$ has the following form

$$\rho_0 \mathcal{E} = \rho_0 \mathcal{K} + \rho_0 \mathcal{U}, \quad \rho_0 \mathcal{K} = \frac{1}{2}\rho_0 \underline{\dot{u}}^2, \quad \rho_0 \mathcal{U} = \frac{1}{2}\rho_0 \Big\langle \underline{\dot{\tilde{u}}}^2 \Big\rangle + \frac{1}{V_0}\Big\langle \Pi(\{\underline{\mathcal{A}}_\alpha\}_{\alpha\in\Lambda}) \Big\rangle. \tag{32}$$

Differentiating $\mathcal{K}$ and $\mathcal{U}$ with respect to time one obtains

$$\rho_0 \dot{\mathcal{K}} = \rho_0 \underline{\ddot{u}} \cdot \underline{\dot{u}} = \left(\overset{\circ}{\nabla} \cdot \underline{\underline{P}} \right) \cdot \underline{\dot{u}},$$

$$\rho_0 \dot{\mathcal{U}} = \rho_0 \Big\langle \underline{\dot{\tilde{u}}} \cdot \underline{\ddot{\tilde{u}}} \Big\rangle + \frac{1}{2V_0}\sum_\alpha \Big\langle \underline{\mathcal{F}}_\alpha \Big\rangle \cdot \underline{\dot{\mathcal{A}}}_\alpha + \frac{1}{2V_0}\sum_\alpha \Big\langle \underline{\mathcal{F}}_\alpha \cdot \underline{\dot{\tilde{\mathcal{A}}}} \Big\rangle. \tag{33}$$

Where differentiation rule for multivariable function was used: $\dot{\Pi} = \sum_\alpha \frac{\partial \Pi}{\partial \underline{\mathcal{A}}_\alpha} \cdot \underline{\dot{\mathcal{A}}}_\alpha$. Let us consider terms in right side of (33) separately. The first term in the right side of equation (33) can be transformed as follows

$$\rho_0 \Big\langle \underline{\dot{\tilde{u}}} \cdot \underline{\ddot{\tilde{u}}} \Big\rangle = \frac{1}{2V_0}\sum_\alpha \Big\langle (\underline{\mathcal{F}}_\alpha(\underline{r}) - \underline{\mathcal{F}}_{-\alpha}(\underline{r} + \underline{a}_\alpha)) \cdot \underline{\dot{\tilde{u}}}(\underline{r}) \Big\rangle =$$

$$= \frac{1}{2V_0}\sum_\alpha \Big\langle \left[\underline{\mathcal{F}}_\alpha \cdot \underline{\dot{\tilde{u}}} \right](\underline{r}) - \left[\underline{\mathcal{F}}_{-\alpha} \cdot \underline{\dot{\tilde{u}}}_{-\alpha} \right](\underline{r} + \underline{a}_\alpha) \Big\rangle \approx \tag{34}$$

$$\approx -\frac{1}{2V_0}\sum_\alpha \Big\langle \underline{\mathcal{F}}_\alpha \cdot \underline{\dot{\tilde{\mathcal{A}}}} - \underline{a}_\alpha \cdot \overset{\circ}{\nabla} \left(\underline{\mathcal{F}}_\alpha \cdot \underline{\dot{\tilde{u}}}_\alpha \right) \Big\rangle.$$

The second term can be represented as follows

$$\frac{1}{2V_0}\sum_\alpha \Big\langle \underline{\mathcal{F}}_\alpha \Big\rangle \cdot \underline{\dot{\mathcal{A}}}_\alpha = \frac{1}{2V_0}\sum_\alpha \Big\langle \underline{\mathcal{F}}_\alpha \Big\rangle \cdot (\underline{\dot{u}}(\underline{r} + \underline{a}_\alpha) - \underline{\dot{u}}(\underline{r})) \approx \underline{\underline{P}} \cdot\cdot \left(\underline{\dot{u}} \overset{\circ}{\nabla} \right). \tag{35}$$

Substituting results of derivations (34), (35) into equation (33) one can obtain the following expression for $\rho_0 \dot{\mathcal{U}}$:

$$\rho_0 \dot{\mathcal{U}} = \underline{\underline{P}} \cdot\cdot \left(\underline{\dot{u}} \overset{\circ}{\nabla} \right) + \overset{\circ}{\nabla} \cdot \left(\frac{1}{2V_0}\sum_\alpha \underline{a}_\alpha \Big\langle \underline{\mathcal{F}}_\alpha \cdot \underline{\dot{\tilde{u}}}_\alpha \Big\rangle \right). \tag{36}$$

428

Let us compare equation (36) with equation of balance of energy for continuum [19]. Let us demand the equivalence of discrete system and continuum. Then heat flux in the reference configuration $\underline{h}$ has the following form

$$\underline{h} = -\frac{1}{2V_0} \sum_\alpha \underline{a}_\alpha \left\langle \underline{\mathcal{F}}_\alpha \cdot \dot{\tilde{\underline{u}}}_\alpha \right\rangle. \tag{37}$$

Using equation for connection between fluxes in different configurations [20]

$$\underline{H} = \frac{V_0}{V} \left(\underline{R} \overset{\circ}{\nabla} \right) \cdot \underline{h},$$

one obtains the expression for heat flux in actual configuration $\underline{H}$:

$$\underline{H} = -\frac{1}{2V} \sum_\alpha \underline{A}_\alpha \left\langle \underline{\mathcal{F}}_\alpha \cdot \dot{\tilde{\underline{u}}}_\alpha \right\rangle. \tag{38}$$

8 Conclusion

Generalization of approach for transition from discrete system to equivalent continuum proposed in [11] was conducted. Two main principles were used for transition: decomposition of motions into continual and thermal parts, and long wave assumption [5]. The decomposition was conducted by means of averaging operator of general type. Kinematics of discrete system was considered. Connection between vectors connecting neighboring atoms in two configurations was obtained. It was shown that the connection is similar with equation for vectors $d\underline{r}$ and $d\underline{R}$ which is used in continual mechanics. Potential of general type was used for description of interactions. It was proposed to represent potential energy per particle as function of all vectors connecting the given particle with its neighbors. Equation of motion for some particle was obtained. Transition from this equation to equation of motion for continual system was conducted. Expressions connecting Cauchy and Piola stress tensor with parameters of discrete system were obtained. It was shown that in general case the discrete analog of Cauchy stress tensor can be unsymmetrical. The symmetry was proven in the case when potential energy per particle depends on distances between the particle and her neighbors and angles between bonds created by the particle. Also it was shown that spatial averaging is required for symmetry of the stress tensor. Thus it was proven that averaging operator can not be taken arbitrary. It was shown that expression for Cauchy stress tensor is similar with expression proposed in papers [7, 9]. Equation of balance of energy was considered. The given equation was transformed to the form similar to equation of balance of energy for continuum. As a result the expression for connection between heat flux and parameters of discrete system was obtained.

9 Appendix

It was shown that the fulfilment of the following expression is necessary for the symmetry of the discrete analog of Cauchy stress tensor

$$\sum_\alpha \underline{\underline{A}}_\alpha \times \underline{\mathcal{F}}_\alpha = 0. \tag{39}$$

For the sake of simplicity averaging operator will be omitted in this paragraph. In the case of pair interactions $\underline{\mathcal{F}}_\alpha$ is force between the reference particle and particle number α. Obviously $\underline{\mathcal{F}}_\alpha$ and $\underline{\mathcal{A}}_\alpha$ are collinear therefore identity (39) is satisfied. Let us show that the identity (39) is satisfied in the case when potential energy per particle has form (24). Substituting (24) into (39) one obtains

$$
\begin{aligned}
\sum_\alpha \underline{\mathcal{A}}_\alpha \times \underline{\mathcal{F}}_\alpha &= 2\sum_\alpha \underline{\mathcal{A}}_\alpha \times \left(\sum_\varepsilon \frac{\partial \Pi}{\partial \mathcal{A}_\varepsilon} \frac{\mathrm{d}\mathcal{A}_\varepsilon}{\mathrm{d}\underline{\mathcal{A}}_\alpha} + \sum_{\beta,\gamma} \frac{\partial \Pi}{\partial(\underline{\mathcal{A}}_\beta \cdot \underline{\mathcal{A}}_\gamma)} \frac{\mathrm{d}\underline{\mathcal{A}}_\beta \cdot \underline{\mathcal{A}}_\gamma}{\mathrm{d}\underline{\mathcal{A}}_\alpha} \right) = \\
&= 2\sum_\alpha \underline{\mathcal{A}}_\alpha \times \sum_{\beta,\gamma} \frac{\partial \Pi}{\partial(\underline{\mathcal{A}}_\beta \cdot \underline{\mathcal{A}}_\gamma)} \left(\delta_{\alpha\beta}\underline{\mathcal{A}}_\gamma + \delta_{\alpha\gamma}\underline{\mathcal{A}}_\beta \right),
\end{aligned}
\tag{40}
$$

where δ is Kronecker's symbol. Using the definition of Kronecker's symbol one can conduct the following transformations

$$
\begin{aligned}
\sum_\alpha \underline{\mathcal{A}}_\alpha \times \underline{\mathcal{F}}_\alpha &= 2\sum_{\alpha,\gamma} \frac{\partial \Pi}{\partial(\underline{\mathcal{A}}_\alpha \cdot \underline{\mathcal{A}}_\gamma)} \underline{\mathcal{A}}_\alpha \times \underline{\mathcal{A}}_\gamma + 2\sum_{\alpha,\beta} \frac{\partial \Pi}{\partial(\underline{\mathcal{A}}_\alpha \cdot \underline{\mathcal{A}}_\beta)} \underline{\mathcal{A}}_\alpha \times \underline{\mathcal{A}}_\beta = \\
&= 2\sum_{\alpha,\beta} \frac{\partial \Pi}{\partial(\underline{\mathcal{A}}_\alpha \cdot \underline{\mathcal{A}}_\beta)} \underline{\mathcal{A}}_\alpha \times \underline{\mathcal{A}}_\beta + 2\sum_{\alpha,\beta} \frac{\partial \Pi}{\partial(\underline{\mathcal{A}}_\beta \cdot \underline{\mathcal{A}}_\alpha)} \underline{\mathcal{A}}_\beta \times \underline{\mathcal{A}}_\alpha = 0,
\end{aligned}
\tag{41}
$$

where the the following relation was used $\frac{\partial \Pi}{\partial(\underline{\mathcal{A}}_\beta \cdot \underline{\mathcal{A}}_\alpha)} = \frac{\partial \Pi}{\partial(\underline{\mathcal{A}}_\alpha \cdot \underline{\mathcal{A}}_\beta)}$.

Thus in the case when potential energy per particle is given by the formula (24) the identity (39) is satisfied.

10   Aknowlegments

References

[1] M.P. Allen, D.J. Tildesley. Computer Simulation of Liquids. Clarendon Press, Oxford, (1987), 385 p.

[2] R.W. Hockney, J.W. Eastwood. Computer simulation using particles. Taylor & Francis Group, New York, (1988), 541 p.

[3] G.J. Wagner, W.K. Liu. Coupling of atomistic and continuum simulations using a bridging scale decomposition. J. Comput. Phys. **190**, (2003), pp. 249–274, .

[4] R.E. Rudd, J.Q. Broughton. Coarse-grained molecular dynamics: Nonlinear finite elements and finite temperature. Phys. Rev. B **72**, 144104, (2005).

[5] M. Born, K. Huang. Dynamical theory of crystal lattices. Oxford: Clarendon Press, (1988).

[6] I.A. Kunin Theory of elastic media with microstrucrutes. Springer-Verlag, (1982).

[7] R.J. Hardy. Formulae for determining local properties in molecular-dynamics simulations: Shock waves. Journal of Chemical Physics, **76**, (1982), pp. 622–628.

[8] E.B. Webb, J.A. Zimmerman, S.C. Seel. Reconsideration of Continuum Thermomechanical Quantities in Atomic Scale Simulations. Mathematics and Mechanics of Solids, **13**, (2008), pp. 221-266.

[9] J.A. Zimmerman, E.B. Webb, J.J. Hoyt, R.E. Jones, P.A. Klein, D.J. Bammann. Calculation of stress in atomistic simulation. Modelling Simul. Mater. Sci. Eng. **12**, (2004), pp. 319–332.

[10] M. Zhou. Thermomechanical contimuum representation of atomistic deformation at arbitrary size scales. Proc. R. Soc. A **461**, (2005), pp. 3437–3472.

[11] A.M. Krivtsov. Deformation and fracture of bodies with microstructure. M.:FML. (2007), 302 p.[in Russian]

[12] A.M. Krivtsov. From nonlinear oscillations to equation of state for simple discrete systems. Chaos, Solitons & Fractals **17**, 79, (2003).

[13] A.M. Krivtsov, V.A. Kuzkin. Derivation of equations of state for perfect crystals with simple structure. Mechanics of Solids, (2009) [paper in press]

[14] S.M. Foiles, M. S. Daw, M. I. Baskes. Embedded-atom-methodfunctions for fcc metals Cu, Ag, Au, Ni, Pd, Pt, and their alloys. Phys. Rev. B, **33**, No. 12, (1986), p. 7983.

[15] F.H. Stillinger, T.A. Weber. Computer simulation of local order in condensed phases of silicon. Phys. Rev. B, Vol. 31, No. 8, (1985), p. 5262.

[16] J. Tersoff. New empirical model for structural properties of silicon. Phys. Rev. Lett, Vol. 56, No. 6, (1986), p. 632.

[17] M. Zhou. A new perspective of atomic level virial — on continuum molecular system equivalence. Proc. R. Soc. A **459** (2003) pp. 2347–2392.

[18] A.I. Lurie. Nonlinear theory of elasticity. North-Holland. Amsterdam. (1990), 617 p.

[19] V.A. Palmov. Vibrations of elasto-palstic bodies. Springer-Verlag, Berlin, (1998).

[20] V.I. Kondaurov, V.E. Fortov. Foundations of thermo-mechanics of condensed matters. M.: Izd. MFTI, (2002), 336 p.[in Russian].

Vitaly A. Kuzkin, Laboratory for "Discreet Models in Mechanics", Institute for Problems in Mechanical Engineering RAS, Bolshoy pr. V.O. 61, St.-Petersburg, Russia.

Investigation of thin wall sheet hydro-forming for complicated shape part in aircraft industry

L. H. Lang   B. S. Liu   G. C. Gu   J. N. Duan   E. Lyamina

lang@buaa.edu.cn

Abstract

The thin wall sheet hydro-forming of oil tank upper shoe of aeroengine was simulated in Eta.Dynaform and confirmed in experiment to optimize the processing parameters. The generating causes of wrinkle and fracture were investigated, in which the influences of chamber fluid pressure, blank holder gap and blank size on the forming limit were involved. It is proved that the simulated results give a reasonable agreement with the experiment.

Keywords: sheet hydro-forming; complicated shape part; parameters optimization

1 Introduction

As an innovative forming technology, sheet hydro-forming technology forms a part by applying a certain pressure liquid instead of die to compel the blank coating punch to get the desired shape part[1]. Due to many advantages of sheet hydro-forming, such as high drawing ratio, high quality surface finish, high dimensional precision, high forming limit etc. compared with conventional stamping, it has been widely used in automotive, aerospace, aircraft industries in recent years, which caters for the demand of less production cost, light weight and high quality [2]-[3]. Hein and Vollertsen[4] investigated another class of hydro-forming process based on the use of sheet metal pairs instead of tubes, in which simulation and experiments had concentrated on the feasibility of one particular process of the hydro-forming of unwelded sheet metal pairs and the influence of various parameters on the forming procedure. Kreis and Hein[5] developed a manufacturing system integrating the process steps of hydro-forming, mechanical trimming, laser beam welding and hydrocalibrating for sheet metal pairs. Shin and Kim et al[6] discussed the welded blank hydro-forming (WBH) technology in the aspects of formability and the engine mount bracket and the subframe were analyzed and manufactured for the application of the technology. Lang[7] carried out the experimental program to study the effect of main process parameters such as the initial pressure, sheet thickness, sheet material properties, punch load, and drawing ratio on the drawing performance, and the results were discussed in detail. Palumbo et al [8] investigated the simulation and production of the complex shape with cylinder and square compounded. The experiment of thin wall

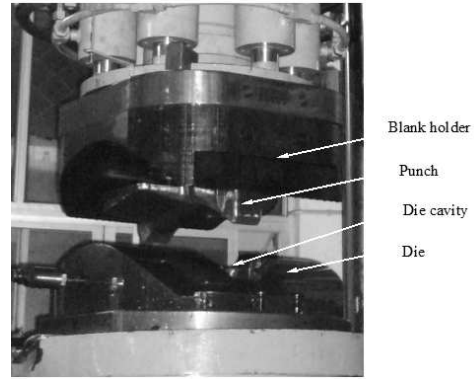Figure 1: 550ton double action sheet hydro-forming machine.

Figure 2: Molds assembly for experiment.

oil tank shoe for aircraft was carried out on a 5500KN double-action sheet hydro-forming machine developed in Beihang University, as shown in Fig. 1, in which processing optimization parameters and quality evaluation method are investigated.

2 Tools and materials

The test facility for sheet metal forming in the study with master cylinder 3300KN and blank holder force 2000KN can realize the control of variable blank holding force, non-uniform cavity pressure, adjustable speed from 5 to 15mm/s, maximum pressure 100.0MPa and 150MPa for pre-bulging and die cavity pressure respectively. The SS304 sheet with 0.5mm thickness is selected as the material, corresponding properties are shown in Tab. 1. The molds layout and structure can be found in Fig. 2.

Mechanical properties for SS304 sheet

Material	SS304
Yield stress, $\sigma_{0.2}$(MPa)	357
Strength stress, σ_b(MPa)	652
Elongation, σ_b(%)	42
Strain harding value, n	0.347
Harding coefficient, K	134

3 Model

3.1 Part and 3D model

As shown in Fig. 3-4, the separation angles between side and bottom are 60° and 90°, the radius for flange face and underside face are 400mm and 370mm respectively, the axial length is 450mm and longitude length is 500mm. The part is difficult to be formed because of the complicated shape with the characteristics of different taper side walls, different radii of curvature, un-symmetry structure, a sunk bulging and

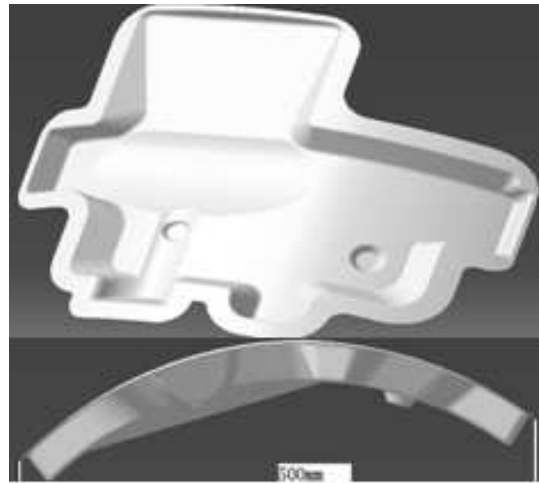Figure 3: The part by conventional drop stamping.

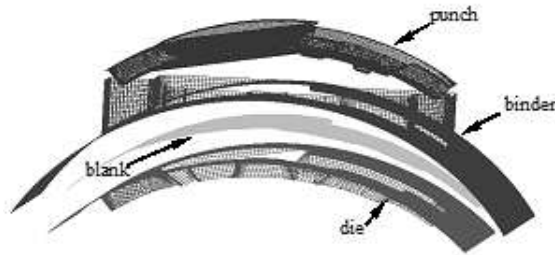

Figure 4: 3D model for oil tank thin wall part.

Figure 5: FE model.

two heaves with small round end in the underside face. And the thickness is only 0.5mm, called the ultra-thin sheet, which makes the main defects more significantly on the account of dimensional effect compared with thick ones, such as fracture early occurring caused by inadequate blank feeding and wrinkle severely cased by less holder force. Fig. 3 gives us a view of final part by conventional drop stamping, in whose forming process a number of intermittent passes are needed to pre-press, then beat for wrinkle-smoothing, continue forming, and calibrate ongoing until final part finished, which causes a heave cost of equipments and manpower. We can see the part in Fig. 3 is in a low quality for surface finish and mechanical properties distribution. Actually, sheet hydro-forming can effectively enhance the formability and control the thinning flooding of deformation region owing to friction maintaining effect and oil flooding lubrication, which makes the part sheet forming in one pass realize.

3.2 FE model

Successful simulation technologies for sheet forming make it the requisite tool in the products manufacturing for panel beating. In this study, the commercial FEM
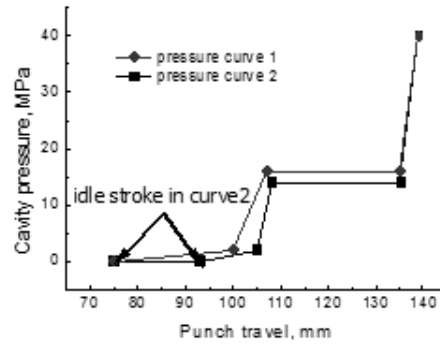
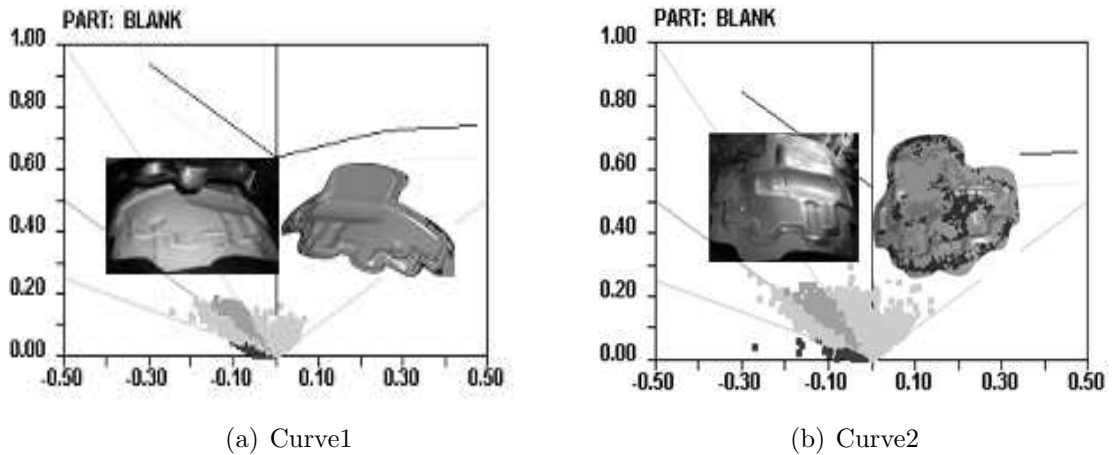Figure 6: Diagram for cavity pressure versus punch travel.

(a) Curve1
(b) Curve2

Figure 7: The FLD of curve1 and curve2 in the pre-bulging stage.

software eta.Dynaform with the key solver LS-Dyna is used to analyze sheet hydro-forming process. The FE model can be found in Fig. 5, firstly, blank is pre-bended in double curvature shape and can be approximately attached to the die surface; then, blank holder goes down to fix the blank on the die with the force of 500KN; continually, the punch goes down, oil is injected into die cavity and intensified to finish pre-bulging; oil is intensified ongoing for shape calibration with the punch further going down. The model is dispersed with rigid four nodes quadrilateral, Belytschko-Lin-Tsay element with five integration points through the shell thickness. The tools (namely punch, binder, die) are viewed as rigid body, meanwhile the blank is deformable. Mises yield criterion is used here for the isotropic blank assumption. Penalty contact interfaces were used to enforce the intermittent contact and sliding boundary condition. A friction coefficient = 0.25 was used for the interface between the blank and the punch, and = 0.15 for the blank and the other tools. The die and the blank holder were constrained fully and the punch could move only along the Z-direction, corresponding to the central axis of the punch.

4 Results and discussion

4.1 Cavity liquid pressure and punch travel

The cavity liquid pressure is one of the key processing parameters in hydro-forming. The following job is to analyze the influence of pressure load curve on formability and quality evaluation. The punch travel and two pressure load curves are concerned. Forming pressure versus punch travel is as following designed according to equipment condition: punch moves down with a speed of 1000mm/s after binder holds the blank firstly at the feeding distance of 25mm or 30mm, where the pressure generating time is also different, curve1 begins at the time of punch travel in 75mm while curve2 in 93mm, and then punch goes down continually 3mm or 7mm against 2MPa counter pressure at a velocity of 600mm/s, now liquid pressure is intensified to 14MPa and 16MPa respectively for the forming stage and last 40MPa is needed to calibrate the small round corner of the two heaves.

In pre-bulging stage, the main difference between curve1 and curve2 is the position of punch opposite blank, curve1 leaves the more distance than curve2, so material storing is too much and finally causes severe wrinkling, which makes the bad formability and large strain, see Fig. 6 (a). By contrast, curve2 perform a good formability and uniform strain distribution, which can be found in Fig. 6(b). So suitable pre-forming height is necessary and makes an important basis for the on-going forming. Fig.7 represents the thickness variation trend with the relation to what time enforcing pressure to blank. We can see earlier pre-bulging in curve1 indicative of severe thickness thickening tendency makes the worse influence on the thickness homogenization control, while curve2 gasps more suitable pre-bulging time than curve1, however point A in two curves behaves more or less the same. So what time liquid pressure should be exerted is also an important factor to be concerned. In the forming stage, lower cavity liquid pressure causes the blank muffling punch inadequate, the friction maintaining effect take less influence, leaving a large relative sliding between punch and blank. At last, the blank will become thinning even crack with the punch deeply going down. In another aspect, the lower pressure will bring about the free material in the non-contacting mold region of part wrinkle. The phenomenon will eliminate as the pressure rises, however ultra-high pressure easily makes the part early bursting with the lack of insufficient deformation time for metal. We can observe the wrinkling and fracture results of simulation and experiment in Fig.8.

4.2 Blank holder gap and Blank size

A number of simulation investigations find that blank holder gap and blank shape size also sensitively affect the part quality. The following study is on the basis of the gaps between blank holder and die of 0.53mm(1.06 times thickness) and 0.6mm (1.2 times thickness), which is an indirect reflect of the influence of holder force on formability. In Fig.9 (a), blank cracks at the end of forming with the 0.53 gab, while in the case of 0.6mm, the corner fractures and the bottom wrinkles. So the suitable blank holder gab is also needed. We can find the influence of gab on forming limit in Fig.10. As the gab is 1.13-1.17 times of thickness, the forming is safe and
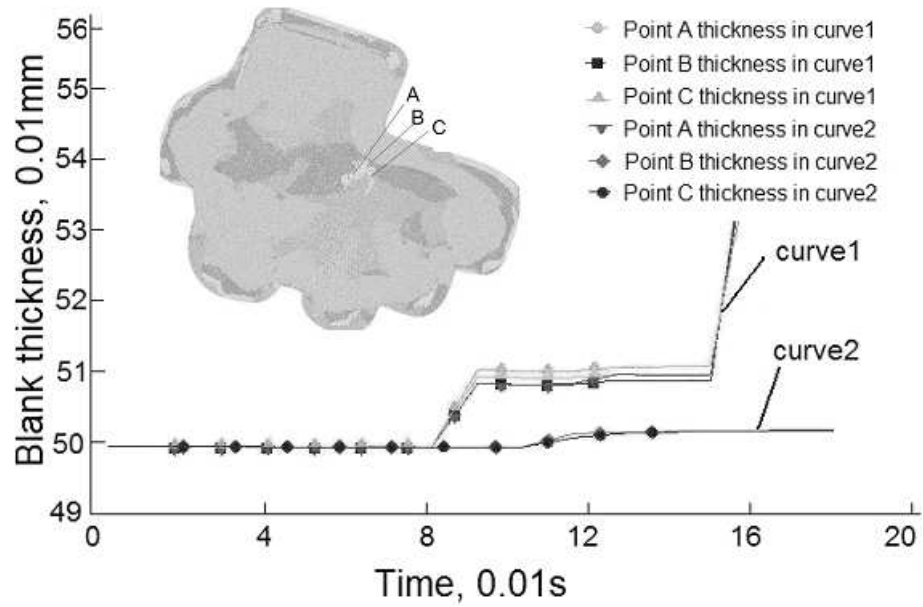
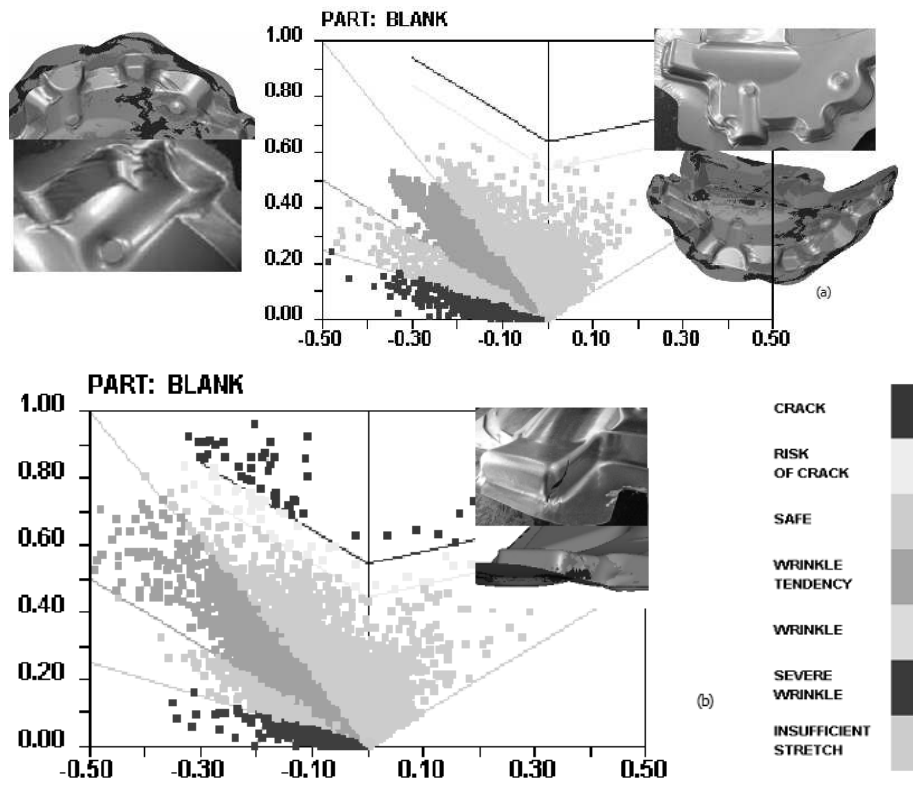Figure 8: The thickness tendency at wrinkling risk point.
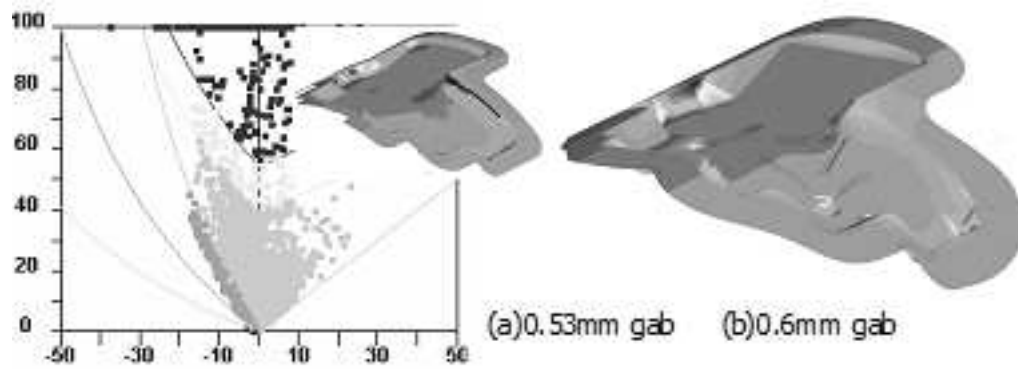

Figure 9: Wrinkle and fracture.

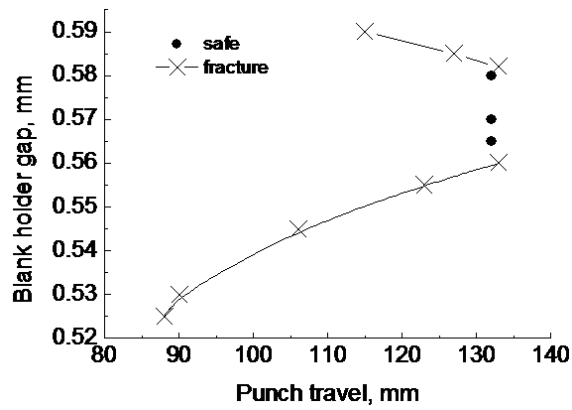Figure 10: Forming defects cased by blank holder gab.

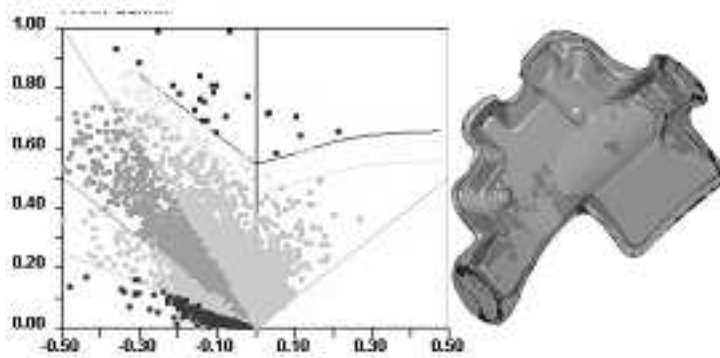Figure 11: The influence of gab on formability.

Figure 12: The influence of blank size on formability.

Figure 13: The final part.

can be formed in a good quality; while gab less than 1.13 times of blank thickness, the thickened material at flange in the initiative forming get the difficulties to flow, finally causes fracture; drawing limit of part increases as the gab enlarges, but under the circumstance of more than 1.17 times of thickness, the blank holder force is inadequate to restrain the flange wrinkle with the feeding of blank, for which fracture and wrinkle probable occur, and finally causes the forming fail.

Suitable blank shape and size should be optimized for good formability under the design requirement of 25mm margin left. The better blank shape is shown in Fig.12, the margin should be left as small as possible in the range of greater than 25mm at the venue with small corner, which makes material feeding easily. Too large and too small blank are both inadvisable, Fig.11 show the simulation result for forming with small blank, where fracture occurs and the part is unqualified for the wrong dimension.

5   Conclusions

The oil tank upper shoe is investigated here in both simulation and experiment, where simulation shows a reasonable agreement with experiment. Compared with conventional sheet stamping, the advantages of sheet hydro-forming are obviously, especially surface finish, we can find it in Fig. 3 and Fig. 12. Some influencing factors on formability are studied, which can be concluded as follows.

1.The blank shape and size play an important role on forming limit, much bigger size causes large tensile stress, easily bringing about fracture, while the part fails in the forming process frequently at the case of blank with smaller size with the failure style of wrinkle and insufficient flange. Blank shape and size adjustment is an effective and convenient way to improve forming quality.

2.In forming, blank holder gab less than 0.56mm (1.12 times thickness) results in part fracture because of material difficult to flow; in the context of greater than 0.59mm (1.18 times thickness), wrinkling tendency sharply increased, and severe wrinkle makes the part flange storing too much material which also causes fracture finally.

3.Cavity liquid pressure influences the part forming quality significantly, the adjustment of pressure and punch travel should be optimized, good coordination of which can enhance the forming limit remarkable. Curve2 in Fig.7 is better than curve1 for forming.

Acknowledgements

References

[1] K Nakamura, T Nakagwa, H Amino. Various application of hydraulic counter pressure deep drawing[J]. Journal of Materials Processing Technology, 1997, 71(1): 160-167.

[2] L H. Lang, G C. GU, T. Li, X B. Zhou. Numerical and experimental confirmation of the calibration stage's effect in multi-operation sheet hydro-forming using poor-formability materials[J]. Journal of materials processing technology, 2008(201):97-100.

[3] X J Liu, W Yan, W L Guo. Numerical simulation of aluminum-magnesium alloy cup's forming by hydrodynamic deep drawing with double loading paths. The Chinese Journal of Nonferrous Metals, 2008(4):698-702.

[4] P. Hein, F. Vollertsen. Hydro-forming of sheet metal pairs. Journal of Materials Processing Technology 87(1999) 154-164.

[5] O. Kreis, P. Hein. Manufacturing system for the integrated hydro-forming, trimming and welding of sheet metal pairs. Journal of Materials Processing Technology 115(2001) 49-54.

[6] Y. S. Shin, H. Y. Kim, B. H. Jeon, S. I. Oh. Prototype tryout and die design for automotive parts using welded blank hydro-forming. Journal of Materials Processing Technology 130-131(2003). 121-127.

[7] L H. Lang, T. Li, D Y. An, C L. Chi, K B Nielsen, J. Danckert. Investigation into hydromechanical deep drawing of aluminum alloy-Complicated components in aircraft manufacturing. Materials Science and Engineering A 499 (2009) 320-324.

[8] G. Palumbo, S. Pinto, L. Tricarico. Numerical/experimental analysis of the sheet hydro forming process using cylindrical, square and compound shaped cavities. Journal of Materials Processing Technology 155-156 (2004) 1435-1442

Investigation of thin wall sheet hydro-forming for complicated shape part in aircraft industry

L. H. Lang, B. S. Liu, G. C. Gu, J. N. Duan, School of Mechanical Engineering and Automation, Beihang University, Xue Yuan Road 37, 100191 Beijing, China

E. Lyamina, Institute for Problems in Mechanics of Russian Academy of Sciences, 101-1 Prospect Vernadskogo, 119526 Moscow, Russia

Vibration analysis of filament winder machines with sprung feeler rollers

Suleiman E. AL-Lubani   Abdullah F. Al-Dwairi

Omar M. Al-Araidah

slubani@huson.edu.jo   dwairy@just.edu.jo   alarao@just.edu.jo

Abstract

This paper presents a dynamic analysis of textile winders used to wind different kinds of filament such as thread or yarn onto cylindrical bobbins. The type of winder under study is currently in common use in the production of threads from synthetic fibers.

The paper begins with a description of the winder to show its main components and their functions. A dynamic model of the machine is then developed based on certain simplifying assumptions. It is shown that the system can be represented by a two-degree-of-freedom model. The paper studies natural and forced vibrations of the model by first neglecting the effects of friction to get a rough estimate of the system's behavior. A more accurate model is then developed by including the effects of viscous and dry friction in the mechanism and the damping properties of some of the its components.

The analysis is conducted on quite real data from typical designs. Design recommendations are given for selecting various design parameters of the system to ensure its vibration stability. In particular, conditions for the winder to operate in a self-centering mode and its design as a vibration absorber are obtained.

1   Introduction

Winder machines are widely used in the textile industry to wind different kinds of filament onto bobbins or spindles of cylindrical form. For the winding operation to proceed successfully, it is often required to use a pressing cylinder (roller) that come into contact with the bobbin and that is driven by the winding through friction between their contacting surfaces. The function of the roller differs from one application to another. While the roller is mainly used to ensure a compact and smooth winding, it is also used as a sensor (feeler) of the current diameter and/or the rotational speed of the bobbin with the filament. In any of the above applications, for the roller to perform its function successfully, it must remain in a permanent and reliable contact with the winding; the roller should not slip relative to the package surface or loose contact with it.

In practice, the main cause of contact loss between the winding and the pressing roller is due to vibrations of the latter. It is therefore necessary to investigate vibration behavior of the system so as to identify the key design variables that govern these vibrations. The need for such studies becomes clear if one recalls that winding speeds in today's synthetic thread manufacturing reach 8000 m/min [1].

This paper presents an analytical study of the dynamic behavior of a typical winding machine. The system is shown to be well represented by a two-degrees-of-freedom system. Natural and forced vibrations are first investigated by neglecting friction and damping effects to get an approximate view of the system's behavior. The effect of friction and damping properties of the system are then introduced to obtain a more accurate model. The study reveals optimum motion parameters corresponding to given conditions of operation. The operating conditions assumed here are those typically met in the manufacture of synthetic fibers.
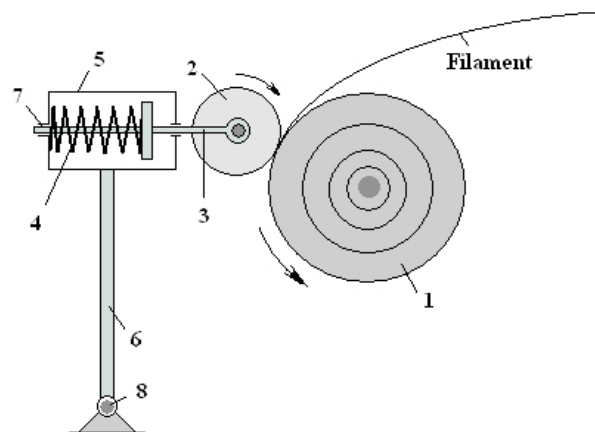
2   System Modeling

Fig. 1: Winder Machine. 1- filament package, 2- feeler roller, 3- rod, 4- spring, 5- case, 6- lever,7- guide, 8- pivot

The winder machine under study is schematically shown in Fig. 1. Textile filament is wound up onto package 1. Feeler roller 2 is driven by friction with the package and hence works as a follower. The roller is mounted on rod 3 which in turn is mounted in guides 7 of case 5. Case 5 is fixed on lever 6 pivoted to the ground by pin 8.

For this stage of analysis, we shall first build a rough model of the system by making the following simplifying assumptions:

1. Amplitudes of vibration of case 5 are small in comparison with the length of lever 6 and hence motion of case 5 can be considered rectilinear.

2. Friction in guides 7 is negligible.

3. All the components of the system, except for the spring and the package, are solid.

4. Motions of all the system's elements occur in parallel planes.

5. The outer layer of the wound product is elastic, but with no damping properties.

6. The moment M, with which roller 2 is pressed to the package is constant. Consequently, the pressing force Q is constant too.

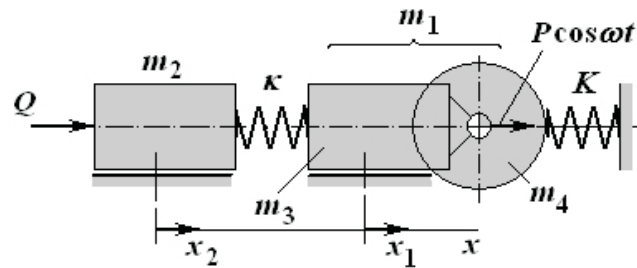Under the above assumptions, the system can be modeled as shown in Fig. 2.

Fig. 2. Simplified dynamic model of the winder

The following notations are used in the above model: K – stiffness of the outer layer of the filament winding, k – stiffness of spring 4, m_1- total mass of roller 2 with rod 3, m_2 – total mass of components 5,6 and 7; m_3 - mass of rod 3, m_4 – mass of roller 2, ω – rotational speed of roller 2, x_1 and x_2 – coordinates of masses m_1 and m_2, respectively. In addition, eccentricity of the roller's center of mass will be designated by e.

Dynamic analysis of this model yields the following equations of motion [2, 3, 4]:

$$
\begin{aligned}
m_1\ddot{x}_1 +_(k + K)x_1 - kx_2 &= m_4 e\omega^2 \cos \omega t \\
m_2\ddot{x}_2 + k(x_2 + x_1) &= 0.
\end{aligned}
\tag{1}
$$

Equations (1) are second-order linear differential equations in x_1 and x_2. Integration of this system yields x_1 and x_2 as functions of time.

3 Natural vibrations

To study the natural vibrations of the system, we set the right-hand sides of (1) to zero. This leads to the following system of homogeneous equations:

$$
\begin{aligned}
m_1\ddot{x}_1 +_(k + K)x_1 - kx_2 &= 0 \\
m_2\ddot{x}_2 + k(x_2 + x_1) &= 0
\end{aligned}
\tag{2}
$$

Equations (3) are known to have a general solution of the form [5, 6]:

$$
\begin{aligned}
x_1 &= A_1 \sin(\omega t + \beta) \\
x_2 &= A_2 \sin(\omega t + \beta)
\end{aligned}
\tag{3}
$$

444

Double differentiation of (3) yields:

$$\ddot{x}_1 = -A_1\omega^2\sin(\omega t + \beta)$$
$$\ddot{x}_2 = -A_2\omega^2\sin(\omega t + \beta)$$

(4)

Substituting from (4) and (3) into (2) and dividing through by $\sin(\omega t + \beta)$ gives:

$$(k + K - m_1\omega^2)A_1 - kA_2 = 0$$
$$-kA_1 + (k - m_2\omega^2)A_2 = 0$$

(5)

Equating the determinant of the system of (4) to zero yields the following frequency equation [2, 3, 4]:

$$\omega^4 - (\frac{k+K}{m_1} + \frac{k}{m_2})\omega^2 + \frac{kK}{m_1 m_2} = 0$$

(6)

Equation (5) is quadratic in ω^2. This leads to two real and positive values for ω^2. Calling them $\omega_1{}^2$ and $\omega_2{}^2$, the values of ω^2 from Eq. (5) are:

$$\omega_{1,2}^2 = \frac{1}{2}(\frac{k+K}{m_1} + \frac{k}{m_2}) \pm \sqrt{(\frac{k+K}{2m_1} + \frac{k}{2m_2})^2 - \frac{kK}{m_1 m_2}}$$

(7)

Equation (6) yields four solutions which are $\pm\,\omega_1$ and $\pm\,\omega_2$. Since the solutions in Eq. (3) are harmonic, the negative signs merely change the signs of the arbitrary constants and would not lead to new solutions. Hence, the natural frequencies are ω_1 and ω_2.

For the filament winder under study, typical values of the design variables in the right-hand side of Eq. (6) are: $m_1 = 3$ kg, $m_2 = 6$ kg, $k = 800$ N/m, and $K = 24000$ N/m. For these values, the natural frequencies are $\omega_1 = 91$ s^{-1} and $\omega_2 = 11$ s^{-1}. These are the natural frequencies of vibration of the system's masses without roller's rotation. These frequencies hence are independent of the roller's diameter.

4 Forced vibrations

Amplitudes of forced vibrations can be found based on Eqs. (1) which are known to have a steady-state solution of the form:

$$x_1 = A_1 \cos \omega t$$
$$x_2 = A_2 \cos \omega t$$

(8)

Substituting from Eq. (7) into Eq. (1) and rearranging terms yields the steady-state amplitudes of vibration of the two masses m_1 and m_2 as:

$$A_1 = \frac{m_4 e\omega^2 (k - m_2\omega^2)}{(K + k - m_1\omega^2)(k - m_2\omega^2) - k^2}$$
$$A_2 = \frac{m_4 e\omega^2 k}{(K + k - m_1\omega^2)(k - m_2\omega^2) - k^2}$$

(9)

445

Figure 3 is a plot of these amplitudes as functions of the roller's rotational speed ω, for a roller's eccentricity of $e = 0.5$ mm. At a filament supply speed of 3000 m/min and a roller's diameter of 60 mm, the roller rotates at $\omega = 1670$ rad/s. Under these conditions the amplitudes are $A_1 = 0.333$ mm and $A_2 = 0.017$ mm.
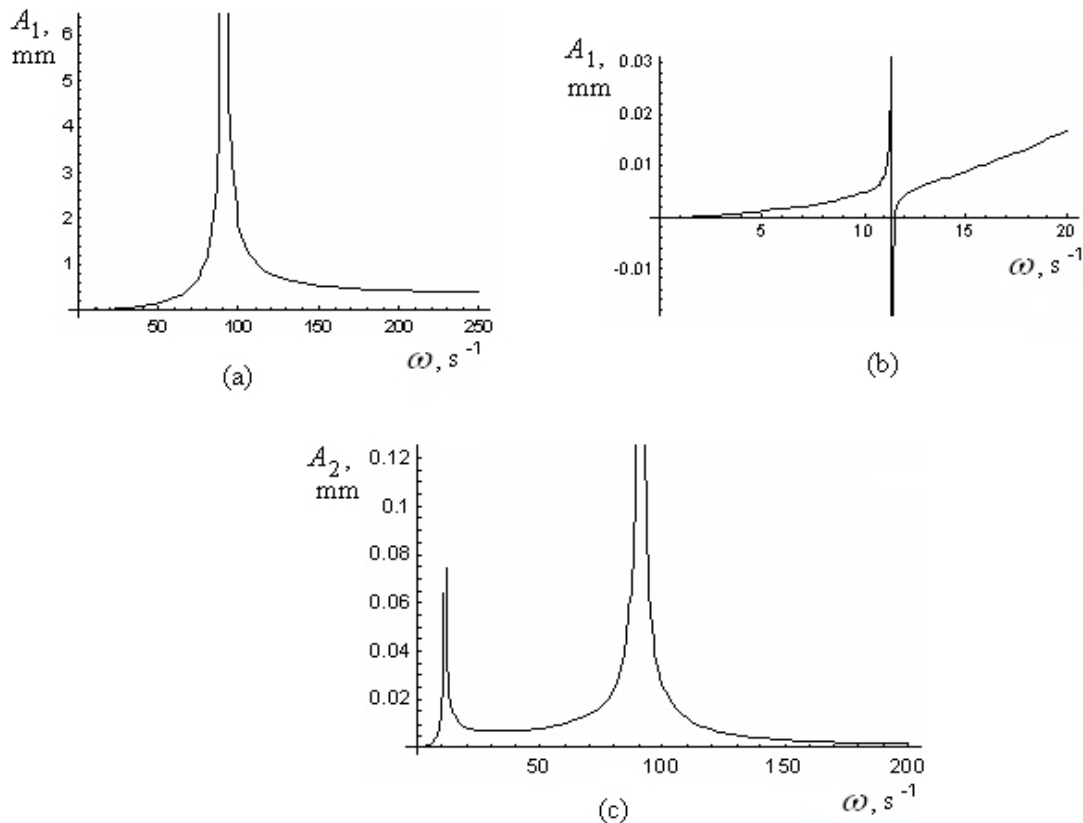

Fig. 3: Amplitude-frequency characteristic of the model

Figures 3(a) and (b) pertain to mass m_1 while Fig. 3(c) pertains to m_2. As seen from Fig. 3 (b) and (c), the first resonance takes place within the frequency range from 10 to 20 s $^{-1}$, while the second resonance occurs in the range 80 - 100 s $^{-1}$, i.e., in the vicinities of the system's natural frequencies. At roller's rotational speeds exceeding 300 s $^{-1}$, the roller rotates in a self-centering mode and the amplitudes of vibration are independent of further increase of the roller's speed.

5   The Effect of Friction

The dynamic model considered above was simplified to allow a rough estimate of the vibration of case 5 and that of roller 2. In order to get a more accurate analysis, we shall reestablish the effects of friction and damping in the system. We shall here account for the effect of viscous and dry friction in guides 7 hinge 8 and for the damping properties of the outer layer of the filament package.
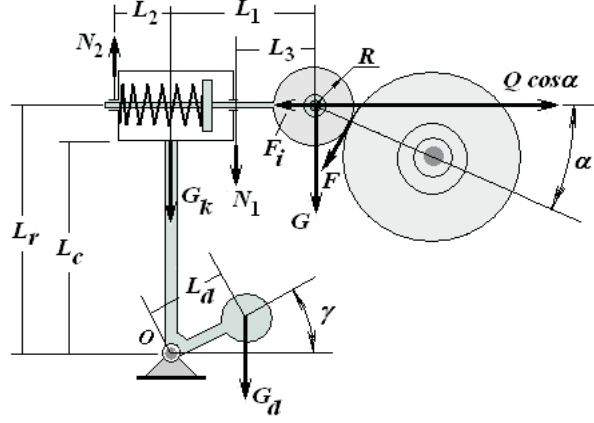
446

Fig.4. To the force analysis of the system

Figure 4 illustrates force elements acting on the system. The force Q with which the roller is pressed to the package is given by:

$$Q = \frac{\sum M_o}{L_r \cos \alpha} = \frac{M_{Gr} + M_d + M_{Gk} + M_F - M_{cf}}{L_r \cos \alpha} \qquad (10)$$

where M_o is the resultant moment about axis O; M_{Gd}, M_{Gr}, M_{Gc} are moments of counterweight G_d, roller's weight G_r, and combined weight G_c of case 5 and lever 6 respectively; M_F is the moment of friction forces between roller and package surfaces; M_{cf} is the constant component of the moment of friction about axes O; also, see the linear and the angular dimensions shown in Fig. 4. A static force analysis of the mechanism would show that

$$
\begin{aligned}
M_{Gd} &= G_d L_d \cos \alpha; \\
M_{Gr} &= G_r L_r \cos \alpha; \\
M_{Gk} &= -G_c L_c \cos \alpha; \\
M_F &= Q f \cos \alpha \, (R \cos \alpha + L_1).
\end{aligned}
\qquad (11)
$$

Substituting from Eqs. (10) into (9) yields the pressing force Q as

$$Q = \frac{G_r L_r \cos \alpha + G_d L_d \cos \alpha + G_c L_c \cos \alpha - M_{cf}}{L_r \cos \alpha - f \cos \alpha (L_1 + R \cos \alpha)} \qquad (12)$$

The referred mass m_2 of the parts moving as a whole is:

$$m_2 = m_c \left(\frac{v_c}{v_M}\right)^2 + m_d \left(\frac{v_{Gd}}{v_M}\right)^2 \qquad (13)$$

where v_M is the referred linear speed of the parts moving together and v_c and v_{Gd} are linear speeds of case 5 together with lever 6 and load G_d.
Recall that

$$v_c = v_M = \omega_M L_c; \; v_d = \omega_M L_d \qquad (14)$$

447

Substituting this into Eq. (21) gives:

$$m_2 = \frac{1}{L_r^2}(m_c L_c^2 + m_d L_d^2) \tag{15}$$

The expanded model of the system is shown in Fig. 5. For this model, differential equations of steady-state motion in view of friction and damping effects are of the following general form [3, 2, 4]:

$$m_1\ddot{x}_1 + b_n(\dot{x}_1 - \dot{x}_2) + b_m\dot{x}_1 + k(x_1 - x_2) + kx_1 = F(t) \\ m_2\ddot{x}_2 + b_n(\dot{x}_2 - \dot{x}_1) + b_m\dot{x}_1 + k(x_2 - x_1) = Q \tag{16}$$

where $F(t)$ is the periodic force exerted on the roller by the package due to the rotation of the latter and b_m, b_n, b_b are coefficients of viscous friction.
Since the spring elements in the model are assumed linear, we have:

$$x_1 = \frac{1}{K}Q \\ x_2 = (\frac{1}{k} + \frac{1}{K})Q \tag{17}$$
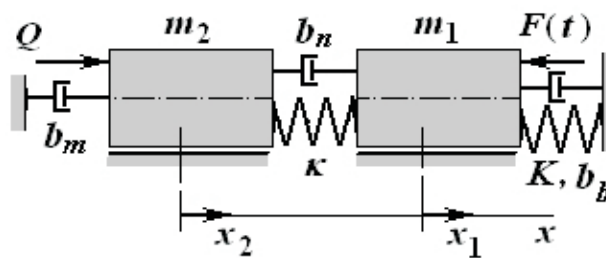
Fig 5. Expanded dynamic model of the winder

Each of the coordinates x_1 and x_2 consists of a constant (static) and a variable (dynamic) component. Considering the variable components, we conclude that in order to suppress the roller's vibration, the referred mass m_2 and the spring constant k should be selected such that they work together as a dynamic vibration absorber. Thus, the condition for vibration suppression is the equality:

$$\frac{k}{b_n^2 + k^2} = \frac{m_2}{b_m^2 + \omega^2 m_2^2} \tag{18}$$

Suppression of vibrations is achieved more effectively if the coefficients b_m and b_n are small. With $b_m \approx 0$ and $b_n \approx 0$, Equation (17) reduces to:

$$k = \omega^2 m_2 \tag{19}$$

The spring constant k recommended in Eq. (18) is optimum for suppression of vibrations only if the system does not involve resistance forces proportional to speed. If such forces are present, then k must be found from Eq. (17) such that:

$$k = \frac{1}{2}(\frac{b_m^2}{m_2} + \omega^2 m_2) \pm \sqrt{\frac{1}{4}(\frac{b_m^2}{m_2} + \omega^2 m_2)^2 - b_m^2 \omega^2} \qquad (20)$$

Since rod 3 is a two-support cantilever loaded with the roller's weight G_r at its end, the support reactions N_1 and N_2 of guide 7 are found to be:

$$N_1 = G_r \cos\alpha \, (1 + \frac{L_3}{L_1 + L_2 - L_3})$$
$$N_2 = \frac{G_r \cos\alpha \, L_3}{L_1 + L_2 - L_3} \qquad (21)$$

Denoting by f_g the friction coefficient that accounts for both viscous and dry friction in guide 7, the friction force F_7 in the guide is given by:

$$F_7 = f_g(N_1 + N_2) = m_4 g f_g \cos\alpha \frac{L_1 + L_2 + L_3}{L_1 + L_2 - L_3} \qquad (22)$$

Equation (21) involves six design variables of the winder that can be used to control the friction forces.

For a 250-mm diameter package with a slightly elliptical cross-section, if the filament winding speed is 3000 m/min, the rotational speed of the package will be 400 rad/s and the corresponding excitation frequency ω_{exc} thus is 800 rad/s.

For typical values of $m_1 = 5$ kg and $K = 24000$ N/m we have:

$$\omega_{exc} m_1 - \frac{K}{\omega_{exc}} = 800 \times 5 - \frac{24000}{800} = 3970 \text{ N} \cdot \text{s/m} \qquad (23)$$

Equation (22) shows that at typical values of m_1, K, and ω_{exc}, the force of inertia of the roller is by two orders of magnitude higher than the restoring force of the surface layer of the filament package. That is:

$$m_1 \ddot{x}_1 >> K x_1 \qquad (24)$$

The difference between the inertia and the restoring forces in the system will increase with further increase of the filament supply speed and energy regeneration in the system will be negligible.

6 Conclusion

The paper presents a typical winder machine modeled as a two-degrees-of-freedom system. Vibration behavior of the model was studied at two levels of sophistication: with and without friction and damping effects. For typical values of the design

parameters of the system, the system's stiffness is relatively low and resonant vibrations may arise at low speeds of filament supply not exceeding 400 m/min., i.e., at the starting phase. Beyond this range the system operates in a self-centering mode. The external excitation frequency is shown to be much higher than any of the system's natural frequencies. Moreover, the restoring force due to the elasticity of the package surface was shown to be negligible compared to the inertia forces in the system. Finally, design conditions under which the feeler roller mechanism operates as a vibration absorber are discussed.

References

[1] Seimens Company website http://www.automation.siemens.com/mc/textiles/en /9965bd61-9a1c-43e2-bc6f- 1ff72832b2fd/index.aspx

[2] Kelly S. Graham Fundamentals of Mechanical Vibrations,McGraw-Hill, 2000, 672 pages.

[3] Pangavhane D. R.,and Ahirrao N. S., Mechanical Vibrations, Satya Prakashan Publishers, 2003, 216 pages.

[4] Inman D. J., Engineering Vibration, Pearson Prentice Hall, third edition, 2008, 669 pages.

[5] Diprima R. C., Elementary Differential Equations, John Wiley and Sons, Inc., seventh edition, 2003, 592 pages.

[6] Nagle R. K., and Staff E. B., Fundamentals of Differential Equations, Pearson Addison Wesley, 2004, 660 pages.

Suleiman E.Lubani,Mechanical Engineering Department Al-Huson College of Engineering Al-Balqaa Applied University P.O. Box 50, Al-Huson 19117, Jordan
Abdullah F. Al-Dwairi,Industrial Engineering Department Jordan University of Science and Technology P.O. Box 3030, Irbid 22110, Jordan dwairy@just.edu.jo
Omar M. Al Araidah,Industrial Engineering Department Jordan University of Science and Technology P.O. Box 3030, Irbid 22110, Jordan alarao@just.edu.jo

Calculation of thermal stresses on composite material on base glass and metal

Olga N. Lubimova   Ekaterina A. Gridasova
berms@mail.ru

Abstract

Constructing of mathematical models and researches on new composite materials production still remain to be actual tasks of continuum mechanics. In this work we offer a new mathematical model of one of the steps in production of a new composite material which has a cylindrical shape produced by diffusion welding of glass and metal. Mr. Pikul V.V. has offered a new way to make the glass layer stronger [1] . He has also invented a new composite material - glass-metal-composite, which consists of the glass layer cased inside metal coat. The new way of producing this material offers a much better connection between the glass layer and metal coat, which prevents the inside layer from the environmental influence.

The glass-metal-coat production technology development consists of a number of researches on continuum mechanics and mathematical modelling, which allows counting residual stresses and deformations during the production of glass and metal, based composite materials. Melted glass is pouring on the inside area of cylindrical cover made of aluminum set in centrifuge machine using different kinds of special accessories. The melted glass evenly divides through the area of the aluminum cover. At this time the process of diffusion welding under high temperatures starts. The material is being cooling till the glass base state T_g temperature after the melted glass layer is divided, which is close to the temperature of aluminum melting. The aluminum melt is sprayed to the inner surface at the temperature T_a with a thickness less than the thickness of the aluminum exterior layer at the temperature of glass transition. The isothermal soaking and stress relaxing are having place to be held in order to normalize the glass properties after the process of aluminum graining at the temperature of glass transition. The composite material is being cooling till the environment temperature.

When describing the cooling process, we need to divide the task into two temperature intervals: 1) $[T_m, T_g]$, $t \in [0, t_1]$; 2) $[T_g, T_e]$, $t \in [t_1, t_2]$. On each interval we face thermal conductivity process, which has place in fixed number of layers, but the equation of thermal conductivity has different coefficients in every layer (price wise-impure environment). The function $T(r, z, t)$ can be written the following way:

$$T(r,z,t) = \begin{cases} T_1(r,z,t), & r_0 \le r < r_1 \ - \ \text{the inside aluminum temperature}, \\ T_2(r,z,t), & r_1 \le r < r_2 \ - \ \ \text{the glass temperature}, \\ T_3(r,z,t), & r_2 \le r < r_3 \ - \ \text{the exterior aluminum temperature}, \end{cases}$$

where $t \geq 0$, $0 \leq z \geq l$.

The equation of thermal conductivity has a following view, according to the heat production at the change of aluminum state:

$$\frac{\partial T_k}{\partial t} = a_k \left(\frac{\partial^2 T_k}{\partial r^2} + \frac{1}{r} \frac{\partial T_k}{\partial r} + \frac{\partial^2 T_k}{\partial z^2} \right) + \frac{Q_k}{c_k \rho_k},$$

where $k = 1, 2, 3 -$ is the number of the layer, a_k, ρ_k, $c_k -$ coefficients of thermal diffusivity, specific heat capacity and density of the concrete layer at the $[T_m, T_g]$, $Q_2(T, t) = 0$ interval, the $Q_3(T, t)$ function, which is characterizing warming wasting at aluminum transition from hard to liquid. Aluminum starts melting, when some temperature T_a is reached and its temperature becomes constant. All the temperature, which is given to it later, goes for the aluminum melting process, that's why it becomes constant. At the second temperature interval $Q_k(T, t)$.

At first time meaning some conditions are being performed for each interval:

$$T_2|_{t=0} = T_m, \quad T_3|_{t=0} = T_e, \quad T_1|_{t=t_1} = T_a, \quad T_2|_{t=t_1} = T_g, \quad T_3|_{t=t_1} = T_g,$$

We suppose that at the first interval there is an unideal heat contact because of infusible oxide film, that aluminum has:

$$\lambda_2 \frac{\partial T_2}{\partial r}|_{r=r_2} = -\lambda_3 \frac{\partial T_3}{\partial r}|_{r=r_2}, \quad \lambda_2 \frac{\partial T_2}{\partial r}|_{r=r_2} = \frac{1}{R}(T_3 - T_2)|_{r=r_2},$$

where $R -$ is the coefficient of contact resistance, which is counted experimentally, $\lambda_k -$ is the coefficient of thermal conductivity. We suppose that at the second temperature interval the bias surfaces of glass layer have ideal heat contact. The heat exchange between bias surfaces of the composite material is being held by the Newton law, that's why the boundary conditions have a view of the third degree. The boundary condition can be written the following way because of the function $T(r, z, t)$ is symmetrical to the flatness of perpendicular axis of generatrix:

$$\frac{\partial T_k}{\partial z}|_{z=0} = 0, \quad \lambda_k \frac{\partial T_k}{\partial z}|_{z=l} = \theta_k (T_k - T_e)|_{z=l},$$

where, $\theta_k -$ are the coefficients of the heat exchange of glass and aluminum.

The most interesting part are the residual stresses and strain in the ready composite material, because of isothermal soaking the process of production.

Aluminum is going to have plastic properties at the $[T_m, T_*]$ temperature interval and glass is going to be visco-elastic. The T_* temperature is the temperature, which makes aluminum to become elastic. Then residual strain can be written the following way:

$$\varepsilon_{ij} = \varepsilon_{ij}^p + \varepsilon_{ij}^v + \varepsilon_{ij}^E,$$

where the upper indexes p, v, E, $-$ are the signs of plastic, visco-elastic and elastic strains, for the aluminum layer $\varepsilon_{ij}^v = 0$, for the glass layer $\varepsilon_{ij}^p = 0$.

The tension, strains, their deviators, speed and etc. of the glass and metal based composite material can be written the same way the temperature is, as the piecewise-continuo functions. The tension increase must meet the equations of balance.

$$\dot{\sigma}_{ij,j}^{(k)} + \dot{F}_i^{(k)} = 0.$$

The tensor of tension $\sigma_{ij}^{(k)}$ and strain $\varepsilon_{ij}^{(k)}$ are use to be the sum of its middle meanings $\sigma^{(k)}$, $\varepsilon^{(k)}$ and deviators $s_{ij}^{(k)}$, $e_{ij}^{(k)}$ which are counted by the following formulas:

$$\sigma^{(k)} = \frac{1}{3}\sigma_{ii}^{(k)}, \quad \varepsilon^{(k)} = \frac{1}{3}\varepsilon_{ii}^{(k)},$$
$$s_{ij}^{(k)} = \sigma_{ij}^{(k)} - \delta_{ij}\sigma^{(k)}, \quad e_{ij}^{(k)} = \varepsilon_{ij}^{(k)} - \delta_{ij}\varepsilon^{(k)},$$

where δ_{ij} — is the symbol of Kroneker.
The speed of components of deviator of aluminum and glass consists of plastic, elastic and visco-elastic components:

$$\dot{e}_{ij}^{(k)} = \begin{cases} \dot{e}_{ij}^{(1)} = \dot{e}_{ij}^{(1)\,p} + \dot{e}_{ij}^{(1)\,E}, \\ \dot{e}_{ij}^{(2)} = \dot{e}_{ij}^{(2)\,v}, \\ \dot{e}_{ij}^{(3)} = \dot{e}_{ij}^{(3)\,p} + \dot{e}_{ij}^{(3)\,E}. \end{cases}$$

The connection on the speed of the tensor of strain change and the tensor of tensions is written the following way using the equations of visco-elastic environment of Maxwell:

$$\varepsilon_{ij}^{(2)} = \frac{s_{ij}^{(2)}}{\eta(T)},$$

where $\eta(T)$ — is the coefficient of the dynamic glass viscosity, which can be written through the Fulcher — Tamman equation:

$$\lg\eta(T) = A + \frac{B}{T - T_0},$$

where A, B, T_0 — are the experimental constants.
The connection on tensions and strains in the elastic are is held by the Duamel — Neymann law:

$$\sigma_{ij}^{(k)} = \frac{E_k}{1 + \nu_k}\varepsilon_{ij}^{(k)} + \delta_{ij}\Big(\frac{E_k\nu_k}{(1 + \nu_k)(1 - 2\nu_k)}\varepsilon_{ii}^{(k)} - \frac{E_k}{1 - 2\nu_k}\int_{T_0^k}^{T}\alpha_k(T)\,dT\Big),$$

where α_k — is the coefficient of the linear widening, $k = 1$ and $k = 3$.
We can write the law of stream which is associated with the condition of stream by Mizess [2], because the experiments show that this condition describe the plastic

materials behavior pretty good:

$$\dot{e}_{ij}^{(k)p} = 0, \ \ \text{if} \ \ \frac{1}{2}s_{ij}^{(k)}s_{ij}^{(k)} < K^2(T)$$

$$\text{or, if} \ \ \frac{1}{2}s_{ij}^{(k)}s_{ij}^{(k)} = K^2(T) \ \ \text{and} \ \ \dot{s}_{ij}^{(k)}s_{ij}^{(k)} - 2KK'\dot{T} < 0;$$

$$\dot{e}_{ij}^{(k)p} = \gamma s_{ij}^{k}, \ \ \text{if} \ \ \frac{1}{2}s_{ij}^{(k)}s_{ij}^{(k)} = K^2(T)$$

$$\text{and} \ \ \dot{s}_{ij}^{(k)}s_{ij}^{(k)} - 2KK'\dot{T} = 0, \ \ \gamma \geq 0,$$

where $K(T)$ is the limit of stream of aluminum in conditions of clear shift at the temperature T,

$$K' = \frac{dK}{dT}, \ \ \gamma = \frac{1}{2K^2}s_{ij}^{(k)}\dot{e}_{ij}^{(k)p},$$

so that the γ measure is proportional to power, which is used for plastic strain of the element in the unit of volume.

As a result of the relaxing of tensions after the process of the glass transition we can consider that all the tensions and displacements during the process of cooling are equal to 0.

The boundary conditions on the inside bound $r = r_0$:

$$\sigma_{33}^{(1)}|_{r=r_0} = 0, \ \ \sigma_{13}^{(1)}|_{r=r_0} = 0.$$

At the bound, where $r = r_3$ we can see the following, because the aluminum coat is fixed:

$$\frac{\partial u_1^{(3)}}{\partial r}|_{r=r_3} = 0, \ \ \frac{\partial u_3^{(3)}}{\partial r}|_{r=r_3} = 0,$$

where $u_1^{(3)} = u_r$, $u_3^{(3)} = u_z$ are the elements of the displacement tensor for the exterior aluminum layer.

The boundary conditions on the surface of the inside glass layer are the geometrical and power conditions of coupling with the exterior aluminum surfaces:

$$u_1^{(1)}|_{r=r_1} = u_1^{(2)}|_{r=r_1}, \ \ u_1^{(2)}|_{r=r_2} = u_1^{(3)}|_{r=r_2},$$

$$u_3^{(1)}|_{r=r_1} = u_3^{(2)}|_{r=r_1}, \ \ u_3^{(2)}|_{r=r_2} = u_3^{(3)}|_{r=r_2},$$

$$\sigma_{13}^{(1)}|_{r=r_1} = \sigma_{13}^{(2)}|_{r=r_1} = \tau_{13}^{+}, \ \ \sigma_{13}^{(2)}|_{r=r_2} = \sigma_{13}^{(3)}|_{r=r_2} = \tau_{13}^{-},$$

$$\sigma_{33}^{(1)}|_{r=r_1} = \sigma_{33}^{(2)}|_{r=r_1} = \tau_{33}^{+}, \ \ \sigma_{33}^{(2)}|_{r=r_2} = \sigma_{33}^{(3)}|_{r=r_2} = \tau_{33}^{-}.$$

The boundary conditions on the end openings of the cylindrical cover we can write considering that the is a hard fixing of the cover on the end openings:

$$\frac{\partial u_1^{(k)}}{\partial z}|_{z=l} = 0, \ \ \frac{\partial u_3^{(k)}}{\partial z}|_{z=l} = 0.$$

The boundary conditions in the middle cross-section can be found through the symmetry of tangent displacements:

$$u_1^{(k)}|_{z=0} = 0, \ \ \frac{\partial u_3^{(k)}}{\partial z}|_{z=0} = 0.$$

References

[1] Pikul V.V., Naumov L.A.,Goncharuk V.K. All about composite material on base glass and metall. Perspective materials, N 3, 2008, p . 3-9.

[2] B.Boley,J.Weiner. Theory of thermal stresses. New York.London.John Wiley and Sons,INC,1960, 520 p.

Olga N. Lubimova, Vladivostok, Russia
Ekaterina A. Gridasova, Vladivostok, Russia

Influence of creep on cyclic loading behavior of thick spherical vessels

H. Mahbadi   M. R. Eslami

h_mahbadi@yahoo.com

Abstract

Influence of creep on cyclic loading behavior of thick spherical vessels is studied in this article. Ratcheting or shakedown behaviors of the vessel under load and deformation controlled conditions are compared for the cases which creep is included and excluded. Kinematic hardening theory of plasticity based on the multi-linear Prager and Armstrong-Frederick models is assumed to evaluate multi-axial nonlinear strains in the plastic region. An iterative incremental method is used to solve the governing equations due to the nonlinearity and load history dependency of the problem. Based on the obtained results an interaction diagram is proposed to predict ratcheting or shakedown behavior of the thick spherical vessels.

1 Introduction

Cyclic loading of structures result into either structural shakedown or ratcheting. Theoretical prediction of ratcheting and shakedown behavior depends on the hardening model assumed to obtain the results. Two general hardening theories used for plastic analysis of structures are the isotropic and kinematic hardening theories. The isotropic hardening theory always predict shakedown behavior, if creep is not considered (Mahbadi and Eslami [1]). The result of the kinematic hardening model, on the other hand, is different. Bari [2] evaluated the performance of a number of constitutive models to predict the ratcheting response of beams made of carbon steel material for a set of uniaxial and biaxial loading histories. His investigations show that for uniaxial stress-controlled history, the linear Prager kinematic hardening [3] and multilinear models produce closed hysteresis loops and, hence, cannot simulate the ratcheting response. The Prager model overpredicts ratcheting strains during the initial cycles, which are followed by shakedown after a few more cycles for all biaxial loading cases. The nonlinear kinematic hardening model (Armstrong and Frederick [4]), overpredicts the ratcheting responses for both uniaxial and biaxial loading histories considered in this study.

It is possible to relate the structural behavior to the stress category in cyclic loading condition. According to the BS5500 unfired fusion welded pressure vessels code [5], the sum of primary and secondary stresses are responsible for ratcheting or shakedown behavior of structures. Based on this code, a *primary stress* is a stress

produced by mechanical loadings only and so distributed in the structure that no redistribution of load occurs as a result of yielding. It is a normal or a shear stress developed by the imposed loading that is necessary to satisfy the simple laws of equilibrium of external and internal forces and moments. The basic characteristic of this stress is that it is not self limiting. Primary stresses that considerably exceed the yield strength will result in failure, or at least in gross structural distortion. A thermal stress is not classified as a primary stress. A *secondary stress* is a normal or a shear stress developed by the constraint of the adjacent parts or by self-constraint of a structure. The basic characteristic of a secondary stress is that it is self limiting. Local yielding and minor distortions can satisfy the conditions that cause the stress to occur and failure from one application of the stress is not to be expected. Eslami and Shariyat [6] proposed a technic to distinguish the primary and secondary stresses. Eslami and Mahbadi [7] classified the loading of structures into the load controlled and deformation controlled types. They showed that the load controlled cyclic loading of structures results to ratcheting while the deformation controlled cyclic loading of structures results into the shakedown behavior.

In this paper, the influence of creep on cyclic loading behavior of thick spherical vessels under load and deformation controlled cyclic loadings is investigated. The vessel's material is assumed to be isotropic and homogeneous and obey nonlinear strain hardening law in plastic range. Secondary creep law is considered to obtain the creep strains in elevated temperature. The kinematic hardening theory based on the Prager and Armstrong-Frederick models with von Mises associated flow rule are used to predict ratcheting or shakedown behavior of thick spherical vessels. An effective incremental iterative method is used to analyze structural behavior under cyclic loading conditions. Using the Prager and Armstrong-Frederick kinematic hardening models, cyclic loading results of vessel under various types of loads, including creep at the end of each load cycle, is compared with those which creep is excluded.

2   Mathematical Formulation

Consider a thick sphere of inside radius a and outside radius b under internal pressure P_i and external pressure P_o. A radial temperature distribution $T(r)$ is assumed for the sphere resulting into a spherical symmetry condition. The dimensionless quantities are:

$$
\begin{array}{cccccc}
S_r = \dfrac{\sigma_r}{\sigma_0} & S_\theta = \dfrac{\sigma_\theta}{\sigma_0} & S_\phi = \dfrac{\sigma_\phi}{\sigma_0} & e_r = \dfrac{\epsilon_r}{\epsilon_0} & e_\theta = \dfrac{\epsilon_\theta}{\epsilon_0} & e_\phi = \dfrac{\epsilon_\phi}{\epsilon_0} \\[2ex]
e_r^p = \dfrac{\epsilon_r^p}{\epsilon_0} & e_\theta^p = \dfrac{\epsilon_\theta^p}{\epsilon_0} & e_\phi^p = \dfrac{\epsilon_\phi^p}{\epsilon_0} & e_r^c = \dfrac{\epsilon_r^c}{\epsilon_0} & e_\theta^c = \dfrac{\epsilon_\theta^c}{\epsilon_0} & e_\phi^c = \dfrac{\epsilon_\phi^c}{\epsilon_0} \\[2ex]
e_r^{Res} = \dfrac{\epsilon_r^{Res}}{\epsilon_0} & e_\theta^{Res} = \dfrac{\epsilon_\theta^{Res}}{\epsilon_0} & e_\phi^{Res} = \dfrac{\epsilon_\phi^{Res}}{\epsilon_0} & p_i = \dfrac{P_i}{\sigma_0} & p_o = \dfrac{P_o}{\sigma_0} & \tau = \dfrac{E\alpha T}{(1-\nu)\sigma_0} \\[2ex]
\rho = \dfrac{r}{a} & \beta = \dfrac{b}{a}
\end{array}
\tag{1}
$$

where σ_r, σ_θ, and σ_ϕ are the radial, tangential, and meridian stresses, respectively. Similarly, ϵ_r, ϵ_θ, ϵ_ϕ are the total strains, ϵ_r^p, ϵ_θ^p, ϵ_ϕ^p are the plastic strains, ϵ_r^c, ϵ_θ^c, ϵ_ϕ^c are the creep strains, and ϵ_r^{Res}, ϵ_θ^{Res}, ϵ_ϕ^{Res} are the residual strains in the

radial, tangential, and axial directions, respectively, σ_0 is the yield stress and ϵ_0 is the yield strain. The Poisson's ratio is denoted by ν. The inclusion of the residual strains in the stress-strain relations is unique and important, as the relations are capable to be used for the cyclic loading analysis. The governing equations are as follow:

Compatibility and equilibrium equations are:

$$\frac{de_\theta}{d\rho} = \frac{e_r - e_\theta}{\rho} \tag{2}$$

$$\frac{dS_r}{d\rho} = \frac{2(S_\theta - S_r)}{\rho} \tag{3}$$

Stress-strain relationship:

$$e_r = S_r - \nu(S_\theta + S_\phi) + (1 - \nu)\tau + e_r^p + e_r^c + e_r^{Res}$$
$$e_\theta = S_\theta - \nu(S_r + S_\phi) + (1 - \nu)\tau + e_\theta^p + e_\theta^c + e_\theta^{Res} \tag{4}$$

The boundary conditions are

$$S_r(1) = -p_i$$
$$S_r(\beta) = -p_o \tag{5}$$

From the spherical symmetry

$$S_\theta = S_\phi$$
$$e_\theta = e_\phi \tag{6}$$

From the incompressibility condition

$$e_r^p + e_\theta^p + e_\phi^p = 0$$
$$e_r^c + e_\theta^c + e_\phi^c = 0 \tag{7}$$

or

$$e_r^p = -2e_\theta^p$$
$$e_r^c = -2e_\theta^c \tag{8}$$

The same relation exist between the residual strains, provided the previous load cycles are spherically symmetric

$$e_r^{Res} = -2e_\theta^{Res} \tag{9}$$

Solving the governing equations, the radial and tangential stresses are

$$S_r = \frac{1}{1 - \nu}\int_1^\rho \frac{e_r^p}{\rho}d\rho + \frac{1}{1 - \nu}\int_1^\rho \frac{e_r^c}{\rho}d\rho + \frac{1}{1 - \nu}\int_1^\rho \frac{e_r^{Res}}{\rho}d\rho$$
$$-\frac{2}{\rho^3}\int_1^\rho \tau\rho^2 d\rho + \frac{C_2}{\rho^3} + C_1 \tag{10}$$

$$S_\theta = \frac{1}{1 - \nu}\int_1^\rho \frac{e_r^p}{\rho}d\rho + \frac{e_r^p}{2(1 - \nu)} + \frac{1}{1 - \nu}\int_1^\rho \frac{e_r^c}{\rho}d\rho + \frac{e_r^c}{2(1 - \nu)}$$
$$+\frac{1}{1 - \nu}\int_1^\rho \frac{e_r^{Res}}{\rho}d\rho + \frac{e_r^{Res}}{2(1 - \nu)} + \frac{1}{\rho^3}\int_1^\rho \tau\rho^2 d\rho - \tau - \frac{C_2}{2\rho^3} + C_1 \tag{11}$$

where the constants of integration are given as

$$C_1 = -p_i - C_2$$
$$C_2 = \frac{\beta^3}{\beta^3 - 1}(p_o - p_i) - \frac{1}{1-\nu}\int_1^\beta \frac{e_r^p}{\rho}d\rho - \frac{1}{1-\nu}\int_1^\beta \frac{e_r^c}{\rho}d\rho$$
$$-\frac{1}{1-\nu}\int_1^\beta \frac{e_r^{Res}}{\rho}d\rho - \frac{2}{\rho^3}\int_1^\beta \tau\rho^2 d\rho \qquad (12)$$

3 Hardening Model

Different kinematic hardening models are available for the plastic analysis of structures. The Prager kinematic hardening model [3] is proposed for the linear strain hardening materials. The Armstrong and Frederick [4] modified the Prager model so that the transformation of yield surface in the stress space is different during loading and unloading. This is done by assuming different hardening modulus in loading and unloading conditions. Assuming the von Mises yield criterion, the flow rule for kinematic hardening model may be written in the following form

$$d\epsilon_{ij}^p = \frac{1}{H}\langle \frac{\partial f}{\partial \sigma_{ij}} \cdot d\sigma_{ij}\rangle \frac{\partial f}{\partial \sigma_{ij}} \qquad (13)$$

where $\langle f(x)\rangle = f(x)$ when $f(x) > 0$, and $\langle f(x)\rangle = 0$ when $f(x) \leq 0$.

3.1 Prager Model

The back stress tensor for the Prager kinematic hardening model is defined as follow:

$$da_{ij} = Cd\epsilon_{ij}^p \qquad (14)$$

where H is the plastic modulus and C is a multiplier, both positive non-constant values.

3.2 Armstrong-Frederick Model

In this model, da_{ij} is found from the following equation

$$da_{ij} = \frac{2}{3}Cd\epsilon_{ij}^p - \gamma a_{ij}|d\epsilon_p| \qquad (15)$$

where C and γ are two material constants in the Armstrong-Frederick kinematic hardening model and are found from the uniaxial strain controlled stable hysteresis curve.

4 Creep Equations

The flow rules for creep is based on the Levy-Mises equations

$$d\epsilon_{ij}^c = s_{ij}d\lambda \qquad (16)$$

It can be shown that the constant $d\lambda$ in terms of the effective stress and increment of effective creep strains becomes

$$d\lambda = \frac{3}{2}\frac{d\epsilon_c}{\sigma_e} \qquad (17)$$

The effective creep strain, when von Mises yield criteria is used, is defined as

$$d\epsilon_c = \sqrt{\frac{2}{3}d\epsilon_{ij}^c d\epsilon_{ij}^c} \qquad (18)$$

The creep strain is a function of stress, where the constitutive law of creep is used to define the functional relationship.

5 Numerical Solution

The method of analysis used in this paper is based on an incremental iterative method. Considering the complexities incurred by the assumed kinematic hardening theories and loading history dependency of the problem, the proposed method is quite capable and unique to handle the cyclic loading calculations. This method may be used for the analysis of uniaxial as well as multiaxial states of loading. The detailed description of the numerical method for uniaxial loading is given in Mahbadi and Eslami [8]. The method described in [8] is extended to the case of mutiaxial states of stress in [9]. To evaluate the creep strains in the vessel due to the cyclic loading, the method presented by Eslami et al. [10] and [11] is used.

According to the equivalent stress and strain definitions, these values are always positive and hence they cannot predict compressive behavior of equivalent stress and strains. For this reason, equivalent stress versus equivalent strain curves produced by plastic analysis module of commercial FEM softwares may not be used for cyclic loading analysis of structures. In the proposed incremental iterative method, two different coordinate axes showing the loading and unloading behaviour of the structure are defined. A coordinate system is initially fixed at the origin, showing the loading curve. At the end of the loading curve, we may fix the second coordinate system with opposite coordinate directions showing the unloading curve. In the second coordinate system the equivalent stress, as the result of unloading, is always positive and is increasing. The final residual stresses are obtained by adding up the stresses in the second coordinate system to those in the first system, where proper changes of sign are considered (Jiang [12]). This method may be used to assign the correct sign to the equivalent stress and strain.

6 Results and Discussion

Two types of loads are checked to show their ratcheting or shakedown behavior as the result of cyclic loading. These are namely the *load controlled* and *deformation controlled* types. Load controlled cyclic loading is one which primary stresses are dominant, while in the deformation controlled cyclic loading the secondary stresses are dominant. Definitions of primary stresses and secondary stress are given in

Table 10: Vessel properties

Properties	Nomenclature	Value	Unit
Modules of elasticity	E	173.2	GPa
Yield stress	σ_0	241	MPa
Poison ratio	ν	0.3	-
Thermal expansion	α	10.8E-6	1/°C
Creep law coefficient	b_1	7.28528E-10	1/s
Creep law power	n_1	3.5	-
Creep law power	Q/R	29840	°K
Outside to inside ratio	b/a	1.5	-
Prager model coefficient	m	2631	MPa
Prager model coefficient	n	0.35	-
Armstrong-Frederic model coefficient	C	55.3	GPa
Armstrong-Frederic model coefficient	γ	280	-

the introductory section. Their applications to the spherical vessel structures are investigated and its behavior under these two types of loads is studied in this section. For all examples in this article, the vessels properties are assumed to be as given in Table (1). For this material, the stress-strain curve equation which is used to evaluate the plastic strains is considered to be as follow:

$$\sigma = \sigma_0 + m\epsilon_p^n \qquad (19)$$

It is assumed that creep strains follow the power law equation:

$$\dot{\epsilon} = b_1 \sigma^{n1} e^{\frac{-Q}{RT}} \qquad (20)$$

To check the numerical algorithm, results obtained from the proposed method are compared with those obtained form the commercial FEM software [13] and are shown in Figs. (1) and (2) for loading up to the plastic region and creep relaxation, respectively. In Fig. (1) the vessel is loaded with inside pressure up to 300 MPa. The critical pressure to bring the inside surface of the vessel up to the plastic region is 114 MPa. In figures (1-a) and (1-b) stress and strain distributions along the radius of the sphere is compared with the results of commercial FEM software.
In Fig. (2) the inside pressure of the sphere is cycled between 0 to 280 MPa. Due to cycling of the mechanical loads with nonzero mean value, the case is considered to be load controlled cyclic loading. For this problem, the normalized equivalent stress versus normalized equivalent strain at the inside surface of the vessel is plotted in Fig. (2-a). The vessel is assumed to experience creep for 1000 hr at 200 °C uniform temperature at the end of loading and unloading curves per each load cycle. The normalized equivalent strain at the end of each load cycle versus the number of cycles for the Prager and Armstrong-Fredereick kinematic hardening models are compared in Fig. (2-b) for different cases, where creep is included and excluded. As seen from the figure, when creep is not considered the Prager model (P-model) predicts shakedown, while the Armstrong-Fredereick model (AF-model) predicts ratcheting
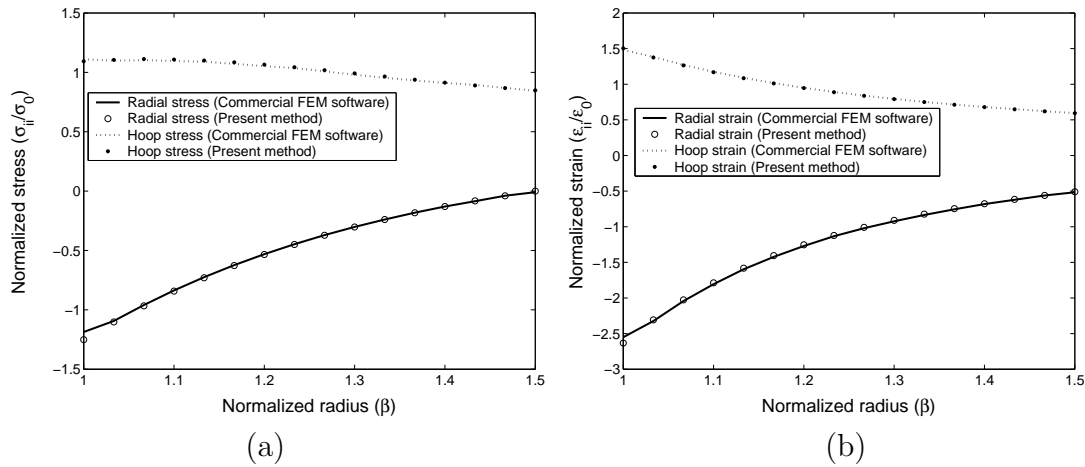
Figure 1: Plastic analysis verification of the proposed method for a thick sphere with the commercial FEM software. (a) stress components distribution along radius, (b) strain components distribution along radius.

for the same problem. When creep is included, both models predict ratcheting, although the rate of ratcheting is different. These results are well compared with the analytical results of Mahbadi et al. given in referesnces [9] and [14] for a thick sphere based on the AF-model exculding creep, and isotropic hardening theory including creep, repectively. The experimental results of Hassan and Kyriakides show ratcheting for load controlled cyclic loading of beam structures [15]. Analytical results based on the Chaboche and AF-models show the same behavior for load controlled cyclic loading of beam structures for both cases where creep is included and excluded [8, 16, 17].
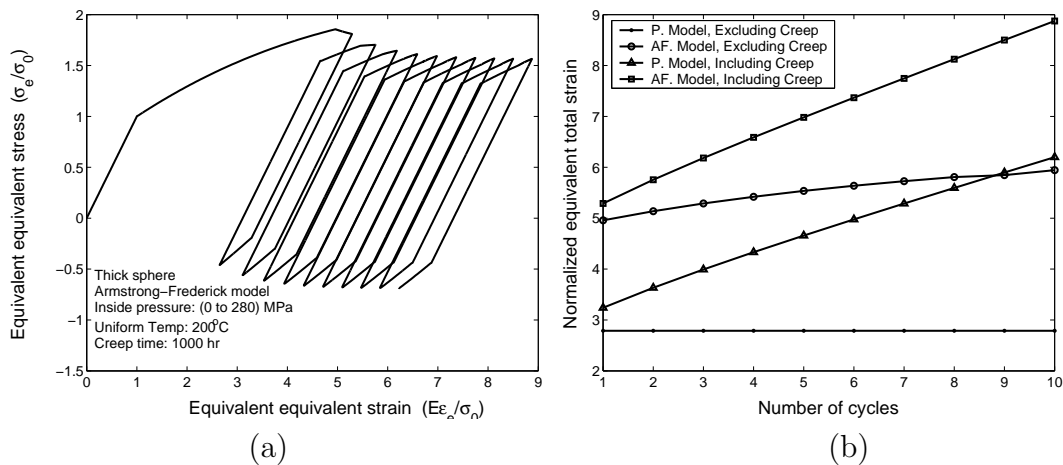

Figure 2: Inside pressure cyclic loading of a thick sphere

The next problem is a thick sphere with inside cycled temperatures between -70

to 250°C, while the outside surface temperature is kept at 0. While the assumed thermal boundary conditions may seem to be unrealistic, the reason for their choice is to have reversed plasticity during unloading and at the mean time to be elevated enough to excite creep. Due to the assumed boundary conditions, the resulting stresses are pure deformation controlled thermal stresses. The critical temperature difference which brings the thick sphere up to the yield point is 144°C and the mean temperature on the inside surface is 160°C. A 1000 hr creep time is considered at the end of both loading and unloading curves per each load cycle. Figure (3-a) shows the normalized equivalent stress versus the normalized equivalent strain at inside surface of the vessel up to 10 cycles of load, using the AF-model including creep. In Fig. (3-b) the normalized equivalent strain based on the AF-model and P-model versus the number of cycles, where creep deformation is included and excluded, is plotted. The figure shows that when creep is not considered, the P-model predicts shakedwon, while the AF-model predicts ratcheting to shakedown. When creep is considered, both models predicts ratcheting to shakedown behavior. Analytical results given in the references [9] and [14] show the same behavior for a thick sphere under deformation controlled cyclic loading. Experimental results of reference [15] and analytical results of [8, 16, 17] show the same behavior for a beam structure under deformation controlled cyclic loading.
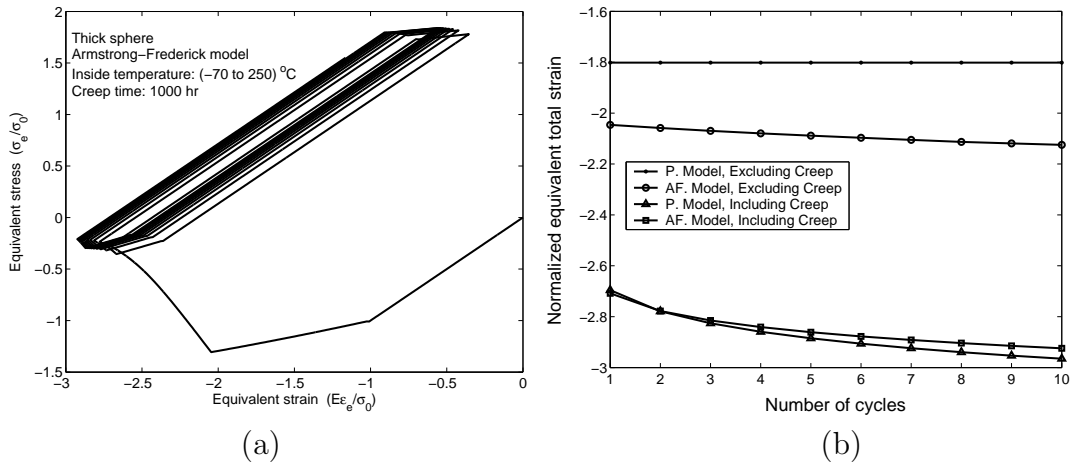

Figure 3: Inside temperature cyclic loading of a thick sphere

Now consider the case where both inside and outside radii of the thick sphere experience cyclic surface pressure in turn, respectively. In this example, the inside surface is cycled with the internal pressure from 0 to 200 MPa and after unloading the internal pressure, the external surface is cycled from 0 to 100 MPa of external pressure. At uniform temperature of 200°C, creep time is considered to extend to 1000 hr per half cycle of internal and external loads. Due to the cycled mechanical loads, the case may be considered as load controlled cyclic loading. Also, it may be classified as non-proportional cyclic loading, since the cyclic loads on the inside and outside surfaces are not in the same phase. In Fig. (4-a) the normalized equivalent stress versus the normalized equivalent strain based on the AF-model including

creep is plotted. Ratcheting is achieved due to the cyclic pressure on inside and out-side surfaces of the sphere. Comparison among the P and AF-models for the cases where creep is included and excluded is shown in Fig. (4-b). As it may be seen from the figure, ratcheting is obtained for all cases, where ratcheting rate for the P-model excluding creep is low with respect to the other cases. The same results are found in references [9] and [14] for a thick sphere under the same loading condition of this problem.
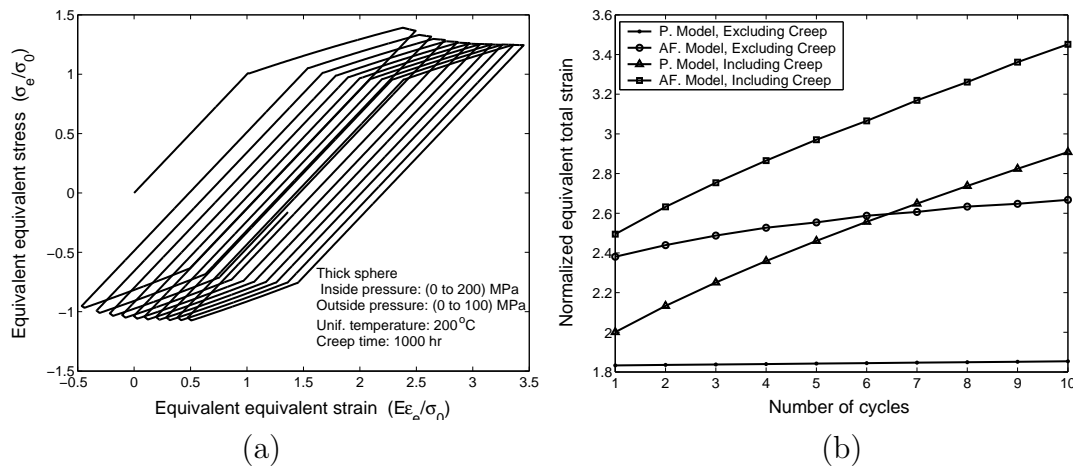

(a)   (b)

Figure 4: Inside/outside pressure cyclic loading of a thick sphere

The next example shows cyclic loading of a thick sphere, where in turn experiences cyclic temperature of 0 to 220°C and 0 to 160°C on its inside and outside sur-faces, respectively. Creep time is considered to be 1000 hr. Figure (5-a) shows the normalized equivalent stress versus the normalized equivalent strain at inside surface of the vessel and based on the AF-model with creep included. According to the figure, ratcheting is obtained as the result of temperature cycling on the inside and outside surfaces of the vessel. In Fig. (5-b) the normalized equivalent strain is plotted versus the number of load cycles, using the AF and P models for cases where creep is included and excluded. Again all cases show ratcheting, with lowest ratcheting rate corresponds to the P-model excluding creep. References [9] and [14] show ratcheting, when the same loading conditions of this problem are considered. This is an example which shows thermal ratcheting of the vessel. The thermal loads in this example may be classified as the load controlled type.

Problems (2) through (5) are repeated for various loading amplitude, vessel thick-ness and creep conditions. The same ratcheting or shakedown behavior is obtained for the repeated conditions. To summarize the results, an interaction diagram for a thick vessel under combination of load and deformation controlled cyclic loading is plotted in Fig. (6). Three regions are distinguished, the elastic, elastic shakedown, and reversed plasticity-ratcheting regions. The vertical axis is the normalized defor-mation controlled stress and the horizontal axes is the normalized load controlled stress. When the sum of the load and deformation controlled cycled stresses are less than the yield stress, the behaviour is elastic. When the sum of these stresses
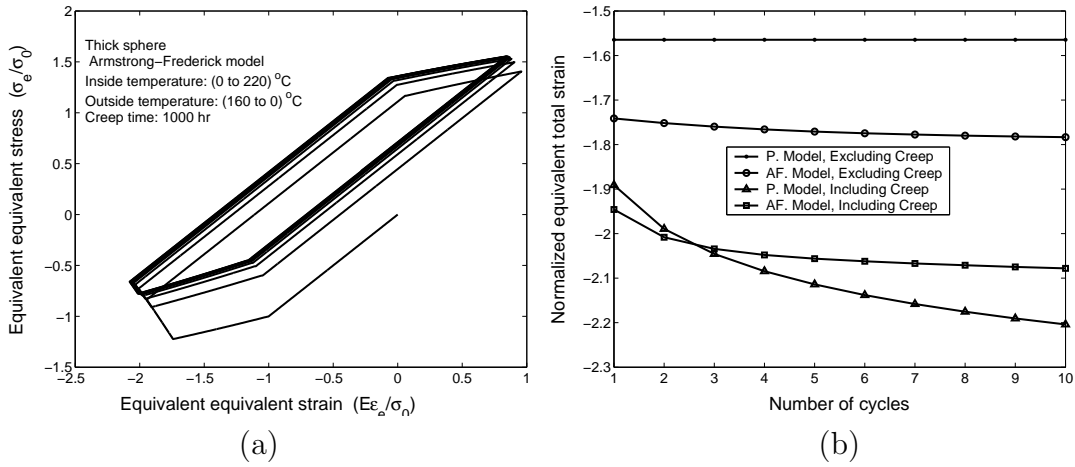
Figure 5: Inside/outside temperature cyclic loading of a thick sphere
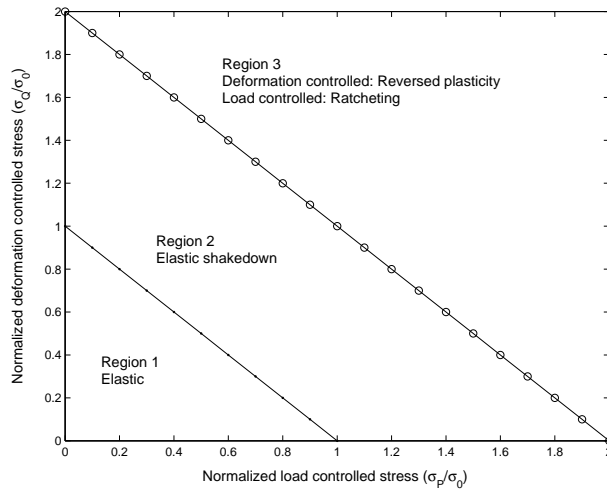

Figure 6: The interaction diagram for deformation controlled cyclic loading versus load controlled cyclic loading

is larger than the yield stress, but lower than twice the yield stress, the behaviour is in the elastic shakedown region. For the sum of the load and deformation controlled stress larger than twice the yield stress, the situation is reverse plasticity for deformation controlled stress, and ratcheting for the load controlled stress.

7   Conclusion

In this paper influence of creep on cyclic loading behavior of thick spherical vessels is investigated. Armstrong-Frederick kinematic hardening model is used to perform plastic analysis during the cyclic loading of the structure. Due to complexities incurred by the nonlinearity of the problem, a numerical iterative method is proposed

which is quite capable to obtain the multidimensional state of stresses caused by cyclic thermal and mechanical loads in plastic region. Results obtained using the Armstrong-Frederick kinematic hardening model is compared with those obtained with the Prager model and are shown on an interaction diagram.

It is concluded that when creep is not considered, Prager kinematic hardening model predicts revresed plasticity for all combination of loadings where stress range are twice the yield stress. Solving the same problems with the Armstrong-Frederick model shows that ratcheting is achieved for load controlled cyclic loading while reversed plasticity is achieved for deformation controlled cyclic loading.

When creep is considered, both models predict the same ratcheting or shakedown behavior. Both models predicts ratcheting for load controlled cyclic loading and reversed plasticity for deformation controlled cyclic loading when the stress range is larger than twice the yield stress. The ratcheging rate predicted by the Armstrong-Frederick model is larger than those predicted with the Prager model.

References

[1] Mahbadi, H., and Eslami, M.R., Load and Deformation Controlled Cyclic Loading of Beams Based on Isotropic Hardening Model, Transactions of Iranin Society of Mechanical Engineering, Vol. 3, No. 1, pp. 28-46, 2002.

[2] Bari, S., Constitutive Modeling for Cyclic Plasticity and Ratcheting, A Thesis Submitted in Partial Fulfillment of the Requirements for the Degree of Doctor of Philosophy, under the Guidance of Dr. Tasnim Hassan, January 2001.

[3] Prager, W., A New Method of Analyzing Stresses and Strains Work-Hardening Plastic Solids, Journal of Applied Mechanics, pp. 493-496, December 1956.

[4] Armstrong, P.J., and Frederick, C.O., A Mathematical Representation of the Multiaxial Bauschinger Effect. CEGB Report No. RD/B/N 731, 1966.

[5] BS5500 Specifications for Unfired Fusion Welded Pressure Vessels, Appendix A, British satandard, 1997 Edition.

[6] Eslami, M.R., and Shariyat, M., A Techinque to Distinguish the Primary and Secondary Stresses, ASME Journal of Pressure Vessel Technology, Vol. 117, pp. 1-7, August 1995.

[7] Eslami, M.R., and Mahbadi, H., Cyclic Loading of Thermal Stresses, Journal of Thermal Stresses, Vol. 24, No. 6, pp. 577-603, 2001.

[8] Mahbadi, H., and Eslami, M.R., Cyclic Loading of Beams Based on the Prager and Frederick-Armstrong Kinematic Hardening Models, International Journal of Mechanical Sciences, Vol. 44, pp. 859-879, 2002.

[9] Mahbadi, H., and Eslami, M.R., Cyclic Loading of Thick Vessels Based on the Prager and Armstrong-Frederick Kinematic Hardening Model, IMechE, International Journal of Pressure Vessels and Piping, Vol. 83, pp. 409-419, 2006.

[10] Eslami, M.R., Creep Relaxation of Beam of General Cross Section Subjected to Mechanical and Thermal Loads, Trans. ASME, J. Mech., Design, Vol. 100, No. 4, pp. 626-629, , Oct. 1978.

[11] Eslami, M.R., Creep Analysis of Spherical Vessels Subjected to Inside Pressure and Royal Temperature Variations, Proceedings, Int. Conf. Nonlinear Mech. Shanghai, China, Oct. 28-31, 1985.

[12] Jiang, W., New Kinematic Hardening Model, Journal of Engineering Mechanics, Vol. 120. No. 10, pp. 2000-2020, October 1994.

[13] ANSYS, Educational Program Rev. 5.6, Swanson Analysis Systems, 1997.

[14] Mahbadi, H., and Eslami, M.R., Load and Deformation Controlled Cyclic Loading of Thick Vessels Based on the Isotropic Hardening Model, Transaction of Iranian Society of Mechanical Engineering, Vol. 4, No. 1, pp. 5-25, 2003.

[15] Hassan, T., and Kyriakides, S., Ratcheting in Cyclic Plasticity, Part 1: Uniaxial Behavior, International Journal of Plasticity, Vol. 8, pp. 91-116, 1992.

[16] Mahbadi, H., and Eslami, M.R., Bree Diagram for Cyclic Loading of Beams Based on the Chaboche Kinematic Hardening Model, Proceedings of ASME/ESDA2002, 6th Biennial Conference on Engineering Systems Design and Analysis, Istanbul, Turkey, July 8-11, 2002.

[17] Mahbadi, H., Gowhari, A.R. and Eslami, M.R., Elastic-Plastic-Creep Cyclic Loading of Beams Based on the Prager Kinematic Hardening Model, IMechE, International Journal of Strain Analysis, Vol. 39, No. 2, pp. 127-136, 2004.

H. Mahbadi, ME Dept., Islamic Azad University, Central Tehran Branch, IRAN
M.R. Eslami, ME Dept., Amirkabir University of Technology, Tehran, IRAN

Limiting phase trajectories and superharmonic resonance in Duffing oscillator

Leonid I. Manevitch   Elina L. Manevitch

lmanev96@yahoo.com

Abstract

We present an analytical study of non-stationary vibrations in the forced oscillator with cubic nonlinearity. Special attention is paid to limiting phase trajectories (LPT), introduced by the first of the authors, and corresponding to the most intensive energy exchange between the oscillator and the source of energy. It is shown that the dynamical transition in the undamped system occurs at a certain value of the parameter, which characterizes nonlinearity. This transition leads to a qualitative change of both phase plane structure and temporal behavior of oscillator. The adequate description of non-stationary vibrations of both undamped and damped oscillators in the conditions of 1:3 resonance is achieved using the non-smooth basic functions.

1   Introduction

Secondary resonances in Duffing oscillator as well as principal resonance were subjects of numerous studies [1, 2]. However, these studies mainly dealt with the stationary vibrations, where a simple analytical consideration is possible. As for non-stationary process, it was studied before only numerically because of the mathematical complications, especially for damped systems. However, an analytical study of this fundamental problem is important in order to understand the regularities in the behavior of nonlinear systems.

In this problem we deal with intensive energy exchange between the oscillator and the source of energy. The adequate mathematical tool for description of such processes was introduced in [3] in application to coupled oscillators and oscillatory chains. This conception turned out to be efficient also for the case of 1:1 resonance in Duffing oscillator [4]. We apply the proposed method to the study of superharmonic resonance.

2   Model

The system under consideration is described by the following equation of motion:

$$m\frac{d^2U}{dt^2} + 2n\frac{dU}{dt} + c_1 u + c_3 u^3 = f \sin \omega t \qquad (1)$$

In dimensionless form we have:

$$\ddot{u} + 2\gamma\,\varepsilon\,\dot{u} + u + 8\beta\,\varepsilon u^3 = 2F\sin\bar{\omega}\tau_0 \tag{2}$$

where $\omega_0 = \sqrt{\dfrac{c_1}{m}}$, $2\varepsilon\,\gamma = \dfrac{2n}{\sqrt{c_1 m}}$, $8\,\beta\varepsilon = \dfrac{c_3 r_0^2}{c_1}$, $u = \dfrac{U}{r_0}$, $2F = \dfrac{f}{c r_0}$, $\tau_0 = t\omega_0$,

$\bar{\omega} = \dfrac{\omega}{\omega_0}$. Eq. (2) is equivalent to the following system of two first-order equations

$$\begin{aligned} \frac{dv}{d\tau_0} + 2\gamma\,\varepsilon\,v + u + 8\beta\,\varepsilon\,u^3 &= 2F\sin\bar{\omega}\tau_0 \\ \frac{du}{d\tau_0} &= v. \end{aligned} \tag{3}$$

Let us introduce the following conjugate functions [2, 8]:

$$\psi = v + iu; \quad \psi^* = v - iu. \tag{4}$$

Multiplying the second equation (3) by i and adding it to the first equation, we obtain:

$$\frac{d\psi}{d\tau_0} - i\psi + \gamma\,\varepsilon\,(\psi + \psi^*) + i\beta\,\varepsilon\,(\psi - \psi^*)^{\,3} = 2F\sin\bar{\omega}\tau_0. \tag{5}$$

Let us introduce, alongside with the "fast" time τ_0, the slow times $\tau_1 = \varepsilon\tau_0$, $\tau_2 = \varepsilon^2\tau_0$, and so on. In accordance with the procedure of multiple scale expansions we present a solution as a series

$$\psi_1 = \psi_0 + \varepsilon\psi_1 + \varepsilon^2\psi_2 + \ldots, \tag{6}$$

where

$$\frac{d}{d\tau_0} = \frac{\partial}{\partial\tau_0} + \varepsilon\frac{\partial}{\partial\tau_1} + \varepsilon^2\frac{\partial}{\partial\tau_2} + \ldots \tag{7}$$

Substitution of the expansion (6) into Eq. (5) and selection of the terms of the same order of ϵ lead to the following relations:

$$\epsilon^0: \quad \frac{\partial\psi_0}{\partial\tau_0} - i\psi_0 = -iF\left(e^{i\bar{\omega}\tau_0} - e^{-i\bar{\omega}\tau_0}\right) \tag{8}$$

$$\epsilon^1: \quad \frac{\partial\psi_0}{\partial\tau_1} + \frac{\partial\psi_1}{\partial\tau_0} - i\psi + \gamma\,(\psi_0 + \psi_0^*) + i\beta\,(\psi_0 - \psi_0^*)^3 = 0 \tag{9}$$

The solution of Eq. (8) can be presented in the form

$$\psi_0 = \varphi\,(\tau_1, \ldots)\,e^{i\tau_0} + \Lambda\left[(1 + \bar{\omega})\,e^{i\bar{\omega}\tau_0} - (1 - \bar{\omega})\,e^{-i\bar{\omega}\tau_0}\right] \tag{10}$$

where $\Lambda = \dfrac{F}{1 - \bar{\omega}^2}$. Then Eq. (9) takes the following form:

$$\begin{aligned} \frac{\partial\psi_1}{\partial\tau_0} \; - \; & i\psi_1 = -\frac{\partial\varphi}{\partial\tau_1}e^{i\tau_0} - \gamma\,\left(\varphi\,e^{i\tau_0} + 2\bar{\omega}\Lambda e^{i\bar{\omega}\tau_0}\right) - i\beta\,\Big[\big(\varphi^3\,e^{3i\tau_0} \\ & - \; 3\,|\varphi|^2\,\varphi\,e^{i\tau_0}\big) + 6\Lambda\left(\varphi^2 e^{i(2+\bar{\omega})\tau_0} - 2\,|\varphi|^2\,e^{i\bar{\omega}\tau_0} - \varphi^2 e^{i(2-\bar{\omega})\tau_0}\right) \\ & + \; 12\Lambda^2\varphi\left(e^{i(1+2\bar{\omega})\tau_0} - 2e^{i\tau_0} + e^{i(1-2\bar{\omega})\tau_0}\right) \\ & + \; 8\Lambda^3\left(e^{3i\bar{\omega}\tau_0} - 3e^{i\bar{\omega}\tau_0}\right)\Big] + \text{c.c.} = 0 \end{aligned} \tag{11}$$

where c.c. denotes conjugate terms.

Let us now consider the case when

$$\bar{\omega} = \frac{1}{3} + s\varepsilon \tag{12}$$

Since secular terms in the fast time should be absent, function $\varphi\left(\tau_1, \tau_2, \ldots\right)$ can be found as the solution of the following equation:

$$\frac{\partial \varphi}{\partial \tau_1} + \gamma\varphi - i\beta\left(3\left|\varphi\right|^2\varphi + 24\Lambda^2\varphi - 8\Lambda^3 e^{3is\tau_1}\right) = 0. \tag{13}$$

The complex solution of this equation can be presented in the polar form:

$$\varphi = a\, e^{i\delta}. \tag{14}$$

Substituting expression (14) into (13) and separating real and imaginary parts, after simple transformation we get the system of two real equations

$$
\begin{aligned}
\frac{d\xi}{d\tau_1} &= -\gamma\xi - 8e^*s\sin\Delta \\
\xi\frac{d\Delta}{d\tau_1} &= 3e^*s\xi\left(\xi^2 + 8\right) - 8e^*s\cos\Delta - 3\xi s
\end{aligned}
\tag{15}
$$

where $\xi = \dfrac{a}{\Lambda}$, $\quad e^* = \dfrac{\Lambda^2\beta}{s}$, $\Delta = \delta - 3s\tau_1$. Then if damping is absent this system is integrable and its integral has the following form:

$$H = 3e^*\left(\frac{\xi^4}{4} + 4\xi^2\right) - 3\frac{\xi^2}{2} - 8e^*\xi\cos\Delta = \text{const.} \tag{16}$$

Let us consider first the equilibrium points of the system (15). These points correspond to stationary superharmonic vibrations, therefore the following conditions are satisfied: $\dfrac{d\xi}{d\tau_1} = 0$, $\dfrac{d\Delta}{d\tau_1} = 0$. This means that $\Delta = 0$ or $\Delta = \pi$ (we eliminate an exact resonance when s=0), and the amplitude is determined by the following algebraic equation:

$$\xi^3 + \mu\xi \mp \nu = 0 \tag{17}$$

where $\mu = 8 - 1/e^*$, $\nu = 8/3$. If we introduce parameter $D = \nu^2/4 + \mu^3/27$, then the solution of Eq. (17) depends on the sign of D. If $D < 0$, the equation has 3 real roots, and in the case of $D > 0$ there are 1 real and 2 conjugated roots. Transition between these two cases appears when $D = 0$, and the corresponding relationship between parameters is $\nu^2 = -4\mu^3/27$, or $e_s^* = 1/(8 + 2\sqrt[3]{6}) \approx 0.0859$. Then the stationary point's amplitude is determined by the positive root of Eq. (17), namely: $\xi_0 = 2\sqrt[3]{4/3} \approx 2.2013$ and $\xi_\pi = \sqrt[3]{4/3} \approx 1.1006$ for here $\Delta = 0$ and $\Delta = \pi$, respectively.

We are focusing now on the determination of LPTs, where integral (16) must equal zero because LPT passes through the point $\xi = 0$. Hence we have the following equation:

$$\xi\left(e^*\left(\frac{\xi^3}{4} + 4\xi\right) - \frac{\xi}{2} - \frac{8}{3}e^*\cos\Delta\right) = 0 \tag{18}$$

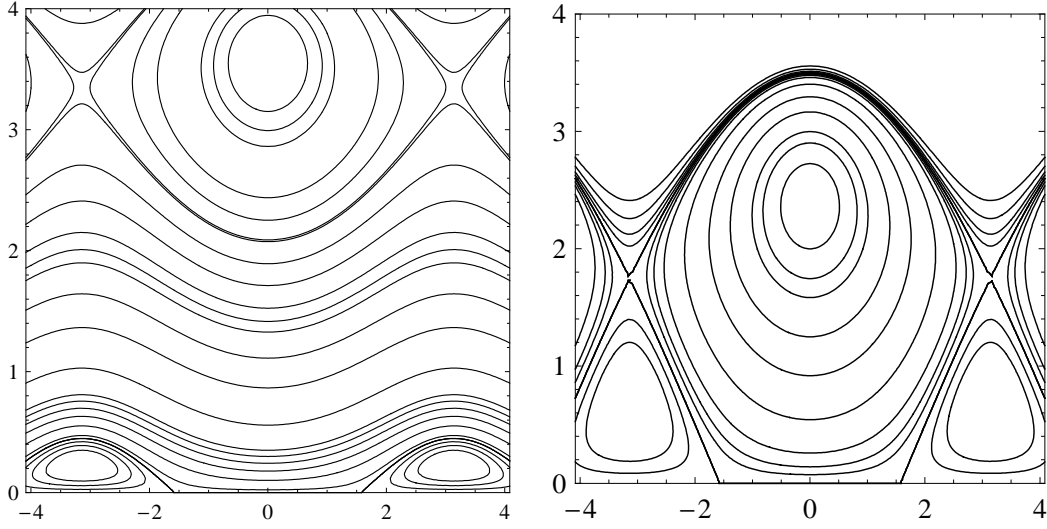Figure 1: (**a**, left) $e^* < e^*_{\text{LPT}}$; (**b**, right) $e^* = e^*_{\text{LPT}}$. Coordinates (Δ, ξ).

It is clear that Eq. (18) has two branches. One of them is $\xi = 0$, and the other one corresponds to LPT and follows from the solutions of the cubic equation in (18) with Δ values corresponding to the maximum of the amplitude. To find these values we have to satisfy the condition $\dfrac{\mathrm{d}\xi}{\mathrm{d}\Delta} = 0$. From system (15) with $\gamma = 0$ we can find:

$$\frac{\mathrm{d}\xi}{\mathrm{d}\Delta} = -\frac{8e^*\xi\sin\Delta}{3e^*\left(\xi^3 + 8\xi\right) - 3\xi - 8e^*\cos\Delta} \tag{19}$$

It is now obvious that the amplitude has its maxima when $\Delta = k\pi (k = 0, \pm 1, \ldots)$, and because of the periodicity it is again sufficient to study only cases $\Delta = 0$ and $\Delta = \pi$. Then from Eq. (18) we have the following conditions:

$$\xi^3 + 2\xi\left(8 - \frac{1}{e^*}\right) \mp \frac{32}{3} = 0, \quad (\Delta = 0, \pi) \tag{20}$$

In this case parameter e^*_{LPT}, corresponding to the transition between different types of roots, satisfies the condition $D = \dfrac{256}{9} + \dfrac{8}{27}\left(8 - (e^*_{\text{LPT}})^{-1}\right)^3 = 0$. Hence we have $e^*_{\text{LPT}} = \dfrac{1}{8 + 6\sqrt[3]{4/9}} \approx 0.0795$. Corresponding maximal amplitudes in the system are:

$$\begin{aligned}
\xi_{\text{LPT}} &= 4\sqrt[3]{\frac{2}{3}} \approx 3.4943 \text{ for } \Delta = 0 \\
\xi_{\text{LPT}} &= 2\sqrt[3]{\frac{2}{3}} \approx 1.7472 \text{ for } \Delta = \pi
\end{aligned} \tag{21}$$

We now see that $e^*_{\text{LPT}} < e^*_s$, which means that the qualitative transition in the system will occur when the system reaches the vicinity of e^*_{LPT}. Stationary points here can be found by substituting e^* in (17) for e^*_{LPT}. Then parameter D is negative
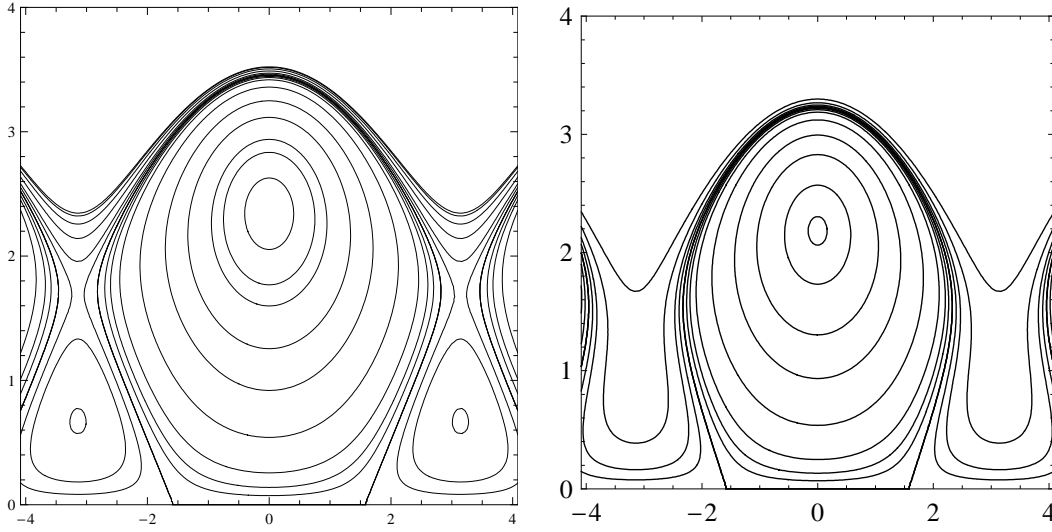
Figure 2: (**a**, left) $e^*_{\mathrm{LPT}} < e^* < e^*_s$; (**b**, right) $e^* > e^*_s$. Coordinates (Δ, ξ).

and the positive roots are as follows:

$$\xi = 2\sqrt{2}\sqrt[3]{\frac{2}{3}}\cos\frac{\pi}{12} \approx 2.3867 \text{ in the case } \Delta = 0 \tag{22}$$

$$\xi_1 = 2\sqrt[3]{\frac{2}{3}} \approx 1.7472, \ \xi_2 = 2\sqrt{2}\sqrt[3]{\frac{2}{3}}\cos\frac{5\pi}{12} \approx 0.6395 \text{ in the case } \Delta = \pi$$

It is clear from the comparison of formulas (21) and (22) that the stationary point lies on the LPT when $\Delta = \pi$.

We now observe the transformation of LPT from encircling the "non-resonance" center (Fig. 1a) to encircling the "resonance" center (Fig. 2a).

We also see the qualitative change in temporal behavior of both amplitude of vibration ξ and phase shift Δ between the external force and oscillator (Figs. 3,4). The transformation leads to the essential increasing of period and amplitude when the process resembles vibro-impact oscillators (Fig. 5). The discussed transition occurs at critical value of parameter $e^* = e^*_{\mathrm{LPT}}$ when the unstable stationary point turns out to be located on LPT. This means that LPT coincides with the separatrix, separating the stable stationary points.

When $e^* = e^*_{\mathrm{LPT}}$, we observe the second topological transformation of the phase plane (Fig. 1b) with further approach to the saw-tooth behavior (Fig. 5).

To clarify the reason of the described transformation of the solution corresponding to LPT let us derive the equation of second order for ξ by excluding variable Δ. After simple transformations, we obtain from Eqs. (18) and (15) for LPT:

$$\frac{d^2\xi}{d\tau_1^2} + \mu_1\xi - \mu_2\xi^3 + \mu_3\xi^5 = 0 \tag{23}$$

where $\mu_1 = 9s^2\left(16e^{*2} - 4e^* + \frac{1}{4}\right)$, $\quad \mu_2 = 36e^*s^2\left(\frac{1}{8} - e^*\right)$, $\quad \mu_3 = \frac{27}{16}(e^*s)^2$.

The stationary points of Eq. (23) satisfy the next algebraic equation:

$$\xi\left(\mu_3\xi^4 - \mu_2\xi^2 + \mu_1\right) = 0 \tag{24}$$
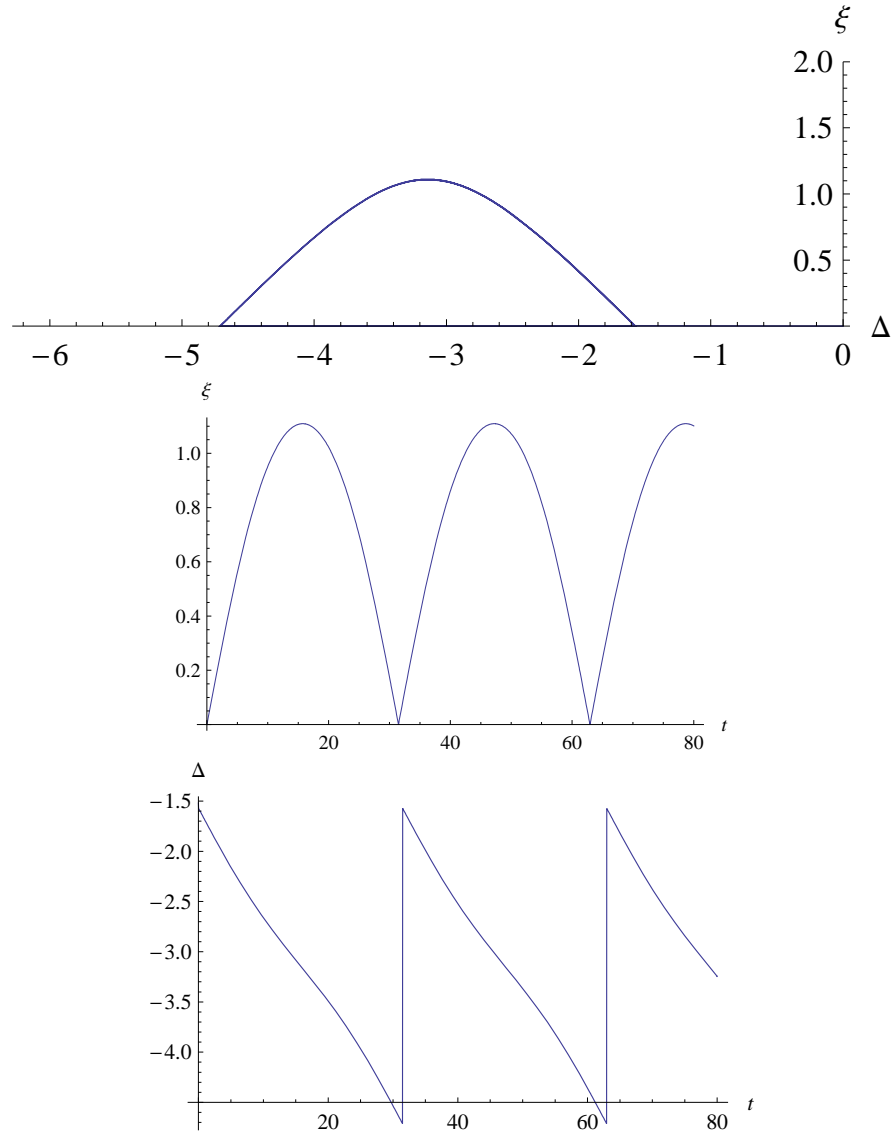
Figure 3: The case $e^* < e^*_{\mathrm{LPT}}$.

Its solutions are $\xi_1 = 0$ and $\xi^2_{2-4} = \dfrac{\mu_2 \pm \sqrt{\mu_2^2 - 4\mu_1\mu_3}}{2\mu_3}$. Taking into account that $0 \leq \xi \leq \xi_{\max}$, as follows from (21), we can construct the phase plane for Eq. (23) (Fig. 6).

Dealing with LPTs we suppose that $\xi = 0$ when $\tau_1 = 0$. If the phase trajectory is located inside the separatrix the case is non-resonant, because there is no essential energy exchange between the oscillator and the source of energy. When we pass the separatrix, the phase trajectories tend to become almost straight lines as the initial value of $\dfrac{d\xi}{d\tau_1}$ increases.

Taking into account that $\xi \leq \xi_{\max}$, we understand that the adequate description of the process can be obtained after the change of temporal variable, because the almost straight trajectory has to "turn" in the opposite direction when $\xi = \xi_{\max}$. So, until the first topological transition we deal with energy localization near the

473

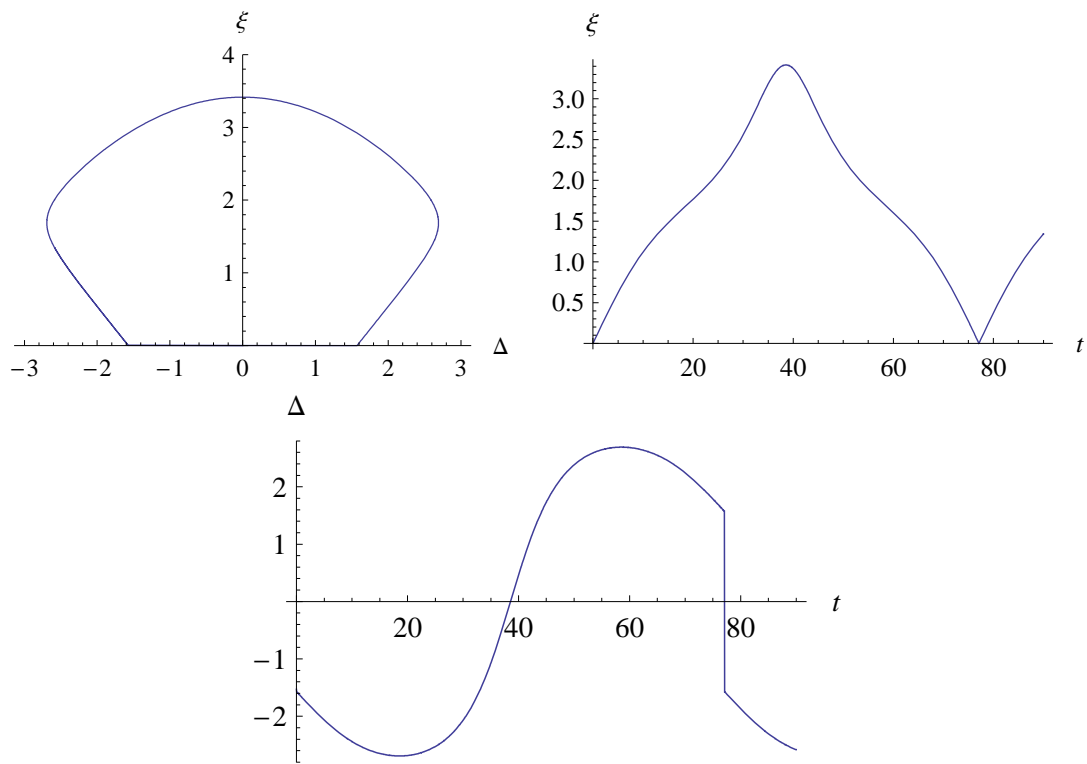Figure 4: The case $e_{\text{LPT}}^* < e^* < e_s^*$.
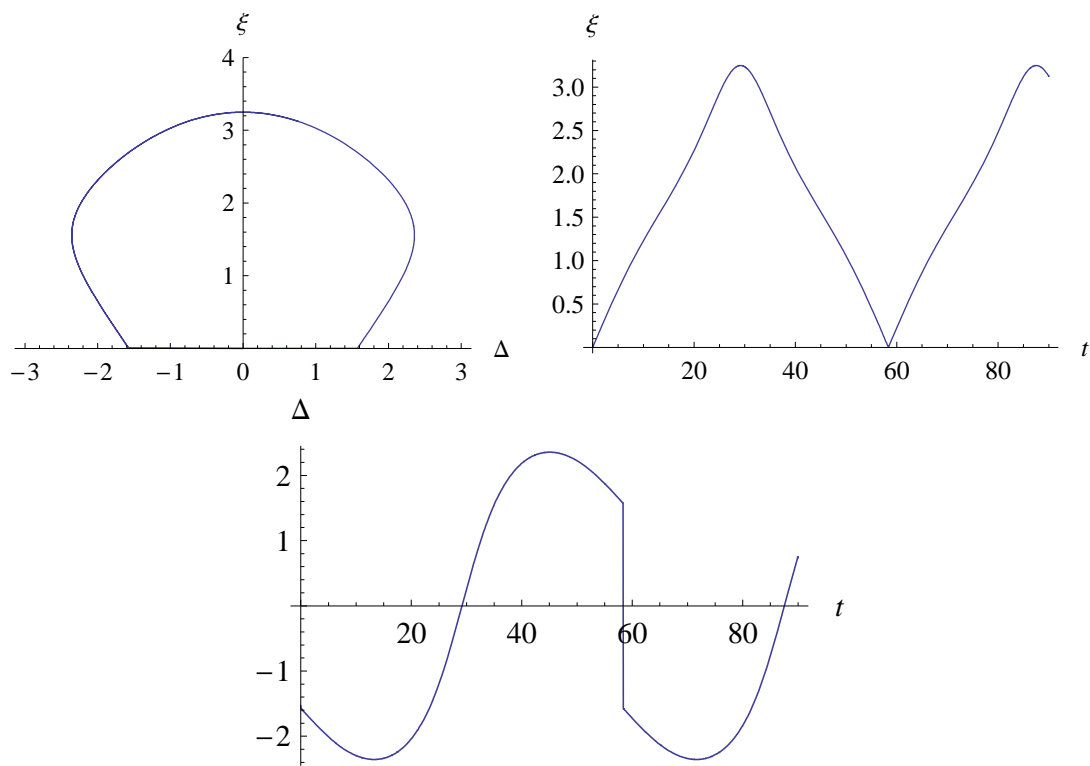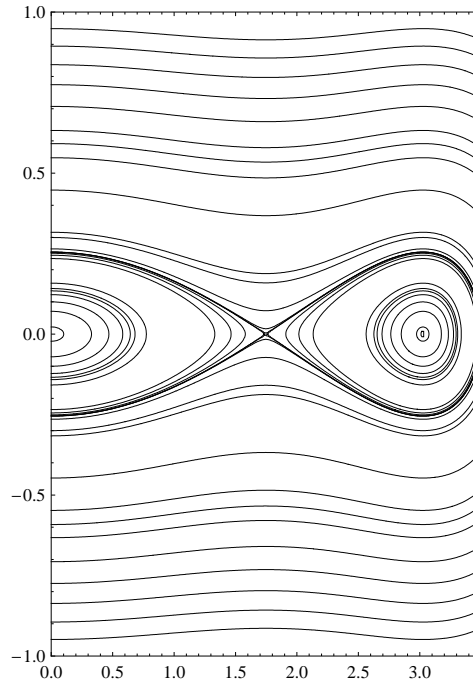

Figure 5: The case $e^* > e_s^*$.

Figure 6: Phase plane for Eq. (23) in coordinates $(\xi, \dfrac{d\xi}{d\tau_1})$.

non-resonant stationary state. After the transition we observe an intensive energy exchange between the oscillator and the source of energy. This exchange is described in the chosen coordinates similarly to the description of the vibro-impact process. It is practical to consider here a special non-smooth basis $\tau(\tau_1)$ and $e(\tau_1)$. This basis was introduced in [5,6,7] for studying the vibrations close to vibro-impact ones, and was used in [2] for the description of LPT in 2DoF system. According to the procedure of this method, we introduce fast and slow times as follows:

$$
\begin{aligned}
t_1 &= \omega(t^0)\tau_1 \\
t^0 &= \gamma\tau_1 \\
\tau &= \tau(t_1) = \frac{2}{\pi}\arcsin\left(\sin\frac{\pi t_1}{2}\right)
\end{aligned}
$$

Then amplitude and phase may be represented in the following form:

$$
\begin{aligned}
\xi(\tau_1) &= X_1(\tau, t_0) + e(t_1)Y_1(\tau, t_0) \\
\Delta(\tau_1) &= X_2(\tau, t_0) + e(t_1)Y_2(\tau, t_0)
\end{aligned}
\tag{25}
$$

where $e(t_1) = \dfrac{d\tau}{dt_1}$. Then

$$
\begin{aligned}
\frac{d\xi}{d\tau_1} &= e\frac{\partial X_1}{\partial \tau}\omega + \gamma\frac{\partial X_1}{\partial t^0} + \frac{\partial Y_1}{\partial \tau}\omega + e\gamma\frac{\partial Y_1}{\partial t^0} \\
\frac{d\Delta}{d\tau_1} &= e\frac{\partial X_2}{\partial \tau}\omega + \gamma\frac{\partial X_2}{\partial t^0} + \frac{\partial Y_2}{\partial \tau}\omega + e\gamma\frac{\partial Y_2}{\partial t^0}
\end{aligned}
\tag{26}
$$

providing that $Y|_{\tau=1} = 0$.

Substituting (25) and (26) into system (15) and grouping terms with and without e, we obtain the following system:

$$
\begin{aligned}
&\omega\frac{\partial Y_1}{\partial \tau} + F\sin X_2 \cos Y_2 = -\varepsilon(\gamma\frac{\partial X_1}{\partial t^0} + \gamma X_1)\\
&\omega\frac{\partial X_1}{\partial \tau} + F\sin Y_2 \cos X_2 = -\varepsilon(\gamma\frac{\partial Y_1}{\partial t^0} + \gamma Y_1)\\
&\omega X_1\frac{\partial Y_2}{\partial \tau} + \omega Y_1\frac{\partial X_2}{\partial \tau} + s_1 X_1 - \alpha X_1^3 - 3\alpha X_1 Y_1^2\\
&\quad + F\cos Y_2 \cos X_2 = -\varepsilon(\gamma X_1\frac{\partial X_2}{\partial t^0} + \gamma Y_1\frac{\partial Y_2}{\partial t^0})\\
&\omega X_1\frac{\partial X_2}{\partial \tau} + \omega Y_1\frac{\partial Y_2}{\partial \tau} + s_1 Y_1 - \alpha Y_1^3 - 3\alpha Y_1 X_1^2\\
&\quad - F\sin Y_2 \sin X_2 = -\varepsilon(\gamma X_1\frac{\partial Y_2}{\partial t^0} + \gamma Y_1\frac{\partial X_2}{\partial t^0})
\end{aligned}
\tag{27}
$$

where $F = 8e^* s$, $s_1 = 3s - 24e^* s$, and $\alpha = 3e^* s$. Parameter ε is introduced here only for convenience of the main terms selection and has to be finally set equal to unity. Now we seek the solution of system (27) in the form of the following series expansions:

$$
\begin{aligned}
X_n(\tau, t^0) &= X_{n0} + \varepsilon X_{n1} + \varepsilon^2 X_{n2} + \dots\\
Y_n(\tau, t^0) &= Y_{n0} + \varepsilon Y_{n1} + \varepsilon^2 Y_{n2} + \dots\\
\omega(t^0) &= \omega_0 + \varepsilon\omega_1 + \omega_2\varepsilon^2 + \dots
\end{aligned}
\tag{28}
$$

where $n = 1, 2$. Then at ε^0 we obtain the following system:

$$
\begin{aligned}
&\omega_0\frac{\partial X_{10}}{\partial \tau} + F\sin Y_{20} = 0\\
&\omega_0 X_{10}\frac{\partial Y_{20}}{\partial \tau} + s_1 X_{10} - \alpha X_{10}^3 + F\cos Y_{20} = 0\\
&X_{20} = Y_{10} = 0
\end{aligned}
\tag{29}
$$

System (29) is integrable, being equivalent to system (15) without damping. Its integral is similar to (18). Using this integral we can derive the second-order differential equation for $X_{10}(\tau, t^0)$ similar to equation (23)

$$
\frac{\partial^2 X_{10}}{\partial \tau^2} + \frac{1}{\omega_0^2}(\mu_1 X_{10} - \mu_2 X_{10}^3 + \mu_3 X_{10}^5) = 0
\tag{30}
$$

We now seek the solution of Eq. (30) in the form of the following series [5]:

$$
\begin{aligned}
X_{10} &= X_{10,0} + X_{10,1} + \dots\\
1/\omega_0^2 &= \lambda_0(1 + \rho_1 + \dots)
\end{aligned}
\tag{31}
$$

In the first approximation we obtain:

$$
\begin{aligned}
X_{10,0} &= A_0(t^0)\tau\\
\lambda_0 &= (6\mu_1 - 3\mu_2 A_0^2 + 2\mu_3 A_0^4)/12
\end{aligned}
\tag{32}
$$

where an arbitrary function A_0 has to be determined from the initial conditions. In the next approximation we obtain:

$$
\begin{aligned}
X_{10,1} &= -\frac{\lambda_0}{2}\left(\frac{\mu_1\tau^3}{3} - \frac{\mu_2\tau^5}{10} + \frac{\mu_3\tau^7}{21}\right)\\
\rho_1 &= -\frac{\int_0^1 X_1(\tau)[\mu_1 A_0 - 3\mu_2 A_0^3\tau^2 + 5\mu_3 A_0^5\tau^4]d\tau}{\int_0^1 [\mu_1 A_0\tau - \mu_2 A_0^3\tau^3 + \mu_3 A_0^5\tau^5]d\tau}
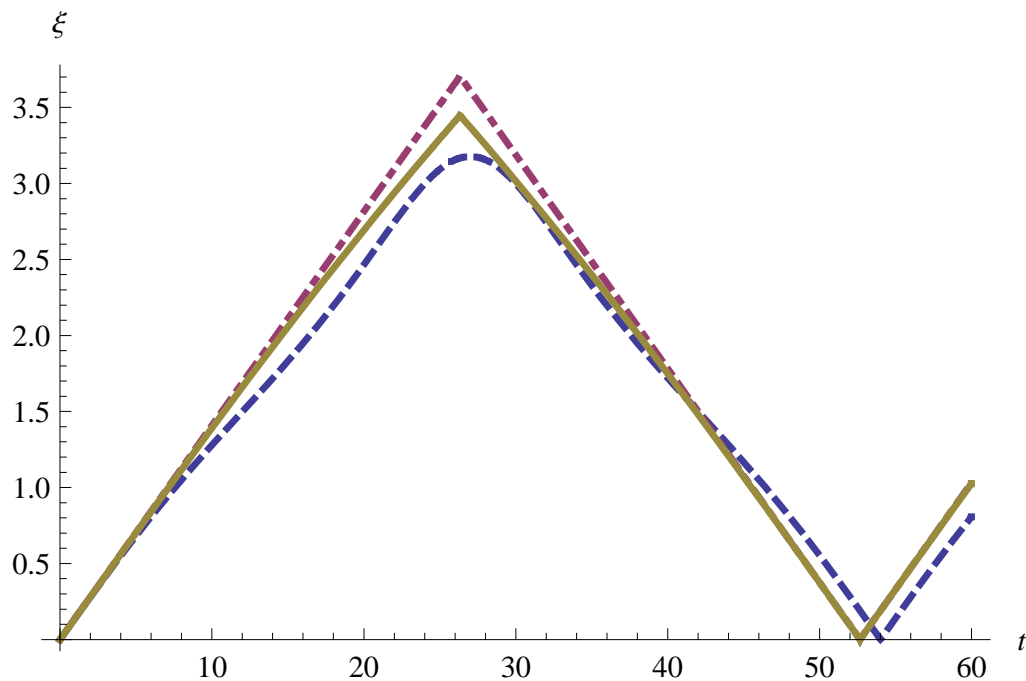\end{aligned}
\tag{33}
$$

Figure 7: Dashed line represents the numerical solution, dotted and dashed line corresponds to the first approximation, and continuous line represents the second approximation for LPT.

Y_{20} can be determined from (18) in the new variables, namely:

$$\cos Y_{20} = \frac{\alpha X_{10}^3}{4F} - \frac{s_1 X_{10}}{2F} \tag{34}$$

It is sufficient to retain only two terms in the approximation corresponding to LPT. They are shown in Fig. 7. The next approximation for system (27) will allow us to estimate the effect of damping, which provides the transition from LPT to stationary state in the time τ_1 or to steady-state oscillations in the time τ_0.

3 Conclusions

1. The concept of a Limiting Phase Trajectory (LPT) turns out to be an adequate tool for analytical treatment of intensive energy exchange between the oscillator and the external force in the conditions of superharmonic resonance.

2. Despite more complicated nature of this resonance in comparison with 1:1 resonance, principal regularities are the same in both cases.

3. After corresponding change of variables non-smooth basic functions provide an efficient description of nonstationary nonlinear oscillations.

4. Analytical results are confirmed by the numerical calculations.

References

[1] Nayfeh, A.H. Introduction to Perturbation Methods, Wiley, NY, 1981.

[2] Manevich, A.I. and Manevitch, L.I. The Mechanics of Nonlinear Systems with Internal Resonances, Imperial College Press, London, 2005.

[3] Manevitch, L.I. New approach to beating phenomenon in coupled nonlinear oscillatory chains. In: Proceedings of 8th Conference on Dynamical Systems - Theory and Applications, v.7, pp.119-136, 2005, Lodz and Arch. Appl. Mech. v. 77, p. 301-312, 2007.

[4] Manevitch, L.I. and Musienko, A.I. Transient forced vibrations of Duffing oscillator. In: Nonlinear phenomena in polymer and low-dimensional systems. Moscow, Nonlinear Dynamics, 2008 (to be published).

[5] Vakakis, A. F., Manevitch, L.I., Mikhlin, Yu.V., Pilipchuk, V.N., and Zevin, A.A. Normal modes and localization in nonlinear systems. Wiley, NY, 1996.

[6] Pilipchuk, V.N. Transformation of oscillating systems by means of a pair of nonsmooth periodic functions. Dokl. Akad. Nauk Ukr. SSR, Ser. A, 87, 30-40, 1985.

[7] Manevitch, L.I, Mikhlin, Yu.V., and Pilipchuk, V.N. Method of normal vibrations for essentially nonlinear systems. Moscow, Nauka, 1989.

[8] Manevitch, L.I. The description of localized normal modes in a chain of nonlinear coupled oscillators using complex variables. Nonlinear Dynamics, 25, 95-109, 2001.

Leonid I. Manevitch, Institute of Chemical Physics, Russian Academy of Sciences, Moscow, Russia
Elina L. Manevitch, University of Illinois at Urbana-Champaign, Urbana, IL, USA

Non-stationary vibrations of a nonlinear oscillator under random excitation

L. I. Manevitch   D. S. Shepelev   A. S. Kovaleva
lmanev@chph.ras.ru deshep@mail.ru a.kovaleva@ru.net

Abstract

Whilst periodic and random stationary vibrations of a strongly nonlinear oscillator have been well-studied for centuries, the theoretical analysis of non-stationary processes is still a daunting task. Recently it has been shown [1], [2] that the difficulties of the theoretical analysis for deterministic non-stationary vibrations may be obviated by using the concept of limiting phase trajectories (LPTs). The LPT concept is of great help in the case of an intensive energy exchange between the oscillator and a source of the periodic excitation. This approach allows finding an analytical approximation for a non-stationary response corresponding to the most intensive energy pumping from the source of energy into the oscillator and calculating the required statistical parameters of the response. The present paper extends the LPT approach to a nonlinear oscillator subjected to a harmonic excitation with random amplitude.

1   Introduction

The topic discussed in the paper is closely related to a well-known problem of vibration attenuation in structures. The task is to construct an effective absorber "taking" the energy from the structure and thus diminishing dangerous vibration. The effectiveness of nonlinear absorbers in suppressing undesired vibration was proved long ago, see, e.g. [3]. However, non-uniqueness of periodic solutions in a nonlinear system is a serious shortcoming in the development of nonlinear vibration protection. This paper analyzes the energy pumping from a source of harmonic forcing into an sdf Duffing oscillator under the condition of primary 1:1 resonance. It is well known that a nearly-resonance excitation may induce 2 stable periodic solutions of small and large amplitudes. The quasi-linear solution of small amplitude should be avoided as it corresponds to intensive vibrations of the structure and small oscillations of the absorber. The nonlinear solution of large amplitude is associated with the effective energy pumping from the source of energy into the oscillator; it is considered as a required mode of operation. The purpose of the paper is to define a parameter of nonlinearity and a critical amplitude of excitation ensuring intensive vibration of the nonlinear system.

479

The paper is organized as follows. In Section 2 we discuss the method of limiting phase trajectories (LPTs), demonstrate typical LPTs, and calculate critical values of the nonlinearity parameter guaranteeing the existence of large nonlinear oscillations. In Section 3 we demonstrate that the envelope of large oscillations can be described with help of a simple saw-tooth approximation. Section 4 extends this approach to a system with a harmonic excitation of random amplitude.

2   Equations of motion

We investigate nearly-resonance dynamics of a nonlinear non-dissipated oscillator subjected to a weak harmonic excitation. The dimensionless equation of motion is reduced to the form

$$\frac{d^2 u}{dt^2} + u + 8\varepsilon\alpha u^3 = 2\varepsilon F \sin[(1 + \varepsilon s)t + \theta], \tag{1}$$

where ε is a small parameter, $0 < \varepsilon \ll 1$; the detuning parameter s describes deviations of the excitation frequency from the natural frequency of a generic linear system ($\alpha = 0$); F is the amplitude of the excitation, θ is a constant phase. In this Section, we consider F and θ as pregiven deterministic parameters. We recall that the maximum energy pumping from the source of excitation into the oscillator corresponds to the initial conditions $u(0) = (0) = 0$; an orbit corresponding to these initial conditions is said to be *the limiting phase trajectory* (LPT) [1].
Following the approach developed in [4], we introduce the change of variables

$$\varphi = e^{-it}(\frac{du}{dt} + iu), \varphi^* = e^{it}(\frac{du}{dt} - iu), \tag{2}$$

where $i = \sqrt{-1}$; the asterisk denotes the complex conjugate variable. Note that representation (2.2) is convenient for problems of the energy exchange, as the functions φ and φ^* depend both on the displacement and the velocity of the system. Using the two-scale expansion procedure [5], we seek an asymptotic expansion in the form

$$\varphi(t, \varepsilon) = \varphi_0(\tau_0, \tau_1) + \varepsilon\varphi_1(\tau_0, \tau_1) + \ldots, \tag{3}$$

where $\tau_0 = t$ is the fast (natural) time and $\tau_1 = \varepsilon t$ is the slow time associated with the rate of the response envelope; the functions $\varphi_{1,2}(\tau_0, \tau_1)$ are supposed to be periodic in τ_1. The derivatives with respect to time are expressed in term of the new time scales as

$$\frac{d}{dt} = \frac{\partial}{\partial\tau_0} + \varepsilon\frac{\partial}{\partial\tau_1}, \frac{d^2}{dt^2} = \frac{\partial^2}{\partial\tau_0^2} + 2\varepsilon\frac{\partial^2}{\partial\tau_0\partial\tau_1}... \tag{4}$$

Substituting (2) - (4) into (1) and equating coefficients of like powers of ε, we obtain $\partial\varphi_0/\partial\tau_0$. This implies that the function φ_0 depends on the 'slow' times only. Then, equating the coefficients of order ε, we obtain

$$\frac{\partial\varphi_0}{\partial\tau_1} + \frac{\partial\varphi_1}{\partial\tau_0} + i\alpha(\varphi_0^3 e^{-2i\tau_0} - 3|\varphi_0|^2\varphi_0+ \tag{5}$$

$$3|\varphi_0|^2\varphi_0^* e^{-2i\tau_0} - (\varphi_0^*)^3 e^{-4i\tau_0}) = -iF[e^{is(\tau_1+\theta)} - e^{-i(2\tau_0+s\tau_1+\theta)}].$$

The condition of periodicity requires eliminating secular terms from (5). This leads to the equation for $\varphi_0(\tau_1)$

$$\frac{\partial \varphi_0}{\partial \tau_1} - 3i\alpha|\varphi_0|^2\varphi_0 = -iFe^{is(\tau_1+\theta)}. \tag{6}$$

We can circumvent complex-valued functions φ_0 and φ_0^* by introducing the polar variables. Denote $\varphi_0 = ae^{i\delta}$, $\varphi_0^* = ae^{-i\delta}$, where $a > 0$, $\delta = \Delta + s\tau_1 + \theta - \pi/2$. Using the polar variables, we transform (6) into the system

$$\frac{da}{d\tau_1} = F\cos\Delta, \quad a\frac{d\Delta}{d\tau_1} = -sa + 3\alpha a^3 - F\sin\Delta. \tag{7}$$

It is easy to prove that system (7) possesses the integral of motion

$$H = sa^2 - \frac{3}{2}\alpha a^4 + 2aF\sin\Delta = \text{Const}, \tag{8}$$

which describes the phase trajectories in the plane (a, Δ). A constant in the right-hand side of (6) depends on the initial conditions of motion. Recall that the LPT, corresponding to the most intensive energy pumping from an external source into the oscillator, satisfies the initial condition $a = 0$, or by (8), $H = 0$. Stationary states associated with the steady-state vibration can be found from the equations

$$\frac{da}{d\tau_1} = 0, \frac{d\Delta}{d\tau_1} = 0, \tag{9}$$

or

$$\Delta = \pm\pi/2, f(a) = sa - 3\alpha a^3 = -F\text{sgn}\Delta. \tag{10}$$
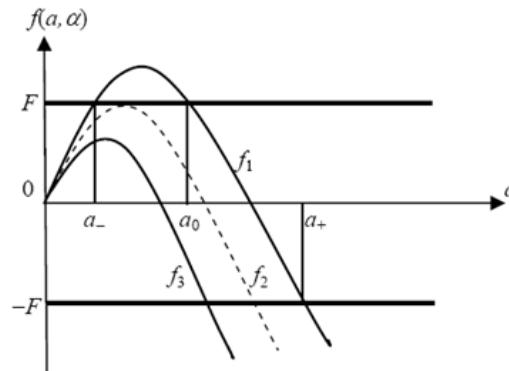

Figure 1: Roots of Eqs (10): $\alpha < \alpha^*$ (f_1), $\alpha = \alpha^*$ (f_2) and $\alpha > \alpha^*$ (f_3)

The discriminant D of Eq.(10) takes the form

$$D = \frac{1}{9\alpha^2}(\frac{F^2}{4} - \frac{s^3}{81\alpha}). \tag{11}$$

If $D < 0$, Eq. (10) has 3 different real roots (curve 1 in Fig. 1); if $D > 0$, Eq. (10) has a single real and two complex conjugate roots (curve 3). In the intermediate

case $D = 0$ two real roots merge together (curve 2). This yields the critical value of the parameter α

$$D(\alpha) = 0, \quad \alpha^* = \frac{4s^3}{81F^2}. \tag{12}$$

A straightforward investigation proves that, in case $\alpha < \alpha^*$ (weak nonlinearity) there exist two stable centres: $C_- : (-\pi/2, a_-)$, $C_+ : (\pi/2, a_+)$, and an intermediate unstable hyperbolic point $O : (-\pi/2, a_0)$, but in case $\alpha > \alpha^*$ (strong nonlinearity) there exists only a unique stable centre $C_+ : (\pi/2, a_+)$. Bounded oscillations in the left half-plane are associated with the quasilinear dynamics of the system; oscillations in the right half-plane correspond to the strongly nonlinear motion.

Now we define a LPT for system (7). The equation of the LPT

$$H = sa^2 - \frac{3}{2}\alpha a^4 + 2aF \sin \Delta = 0 \tag{13}$$

has the solution $a = 0$ for an arbitrary Δ and three non-degenerate solutions $(a.\Delta)$. Note that only an orbit starting at $a = 0, \Delta = 0$ can be considered as the LPT. Phase portraits in Figs 2a, 3a demonstrate the transformation of the LPT from encircling the non-resonance "quasi-linear" center of relatively small oscillations (Fig. 2) to encircling the "resonance" center of large oscillations associated with the maximum energy absorption (Fig. 3). Fig. 2b and Fig. 3b show the shape of $a(\tau_1)$ corresponding to the LPTs of small and large oscillations, respectively. Note that the variables $a(\tau_1)$ and $\Delta(\tau_1)$ found by Eqs (7) and (13) can be interpreted as the envelope and the phase of the LPT.
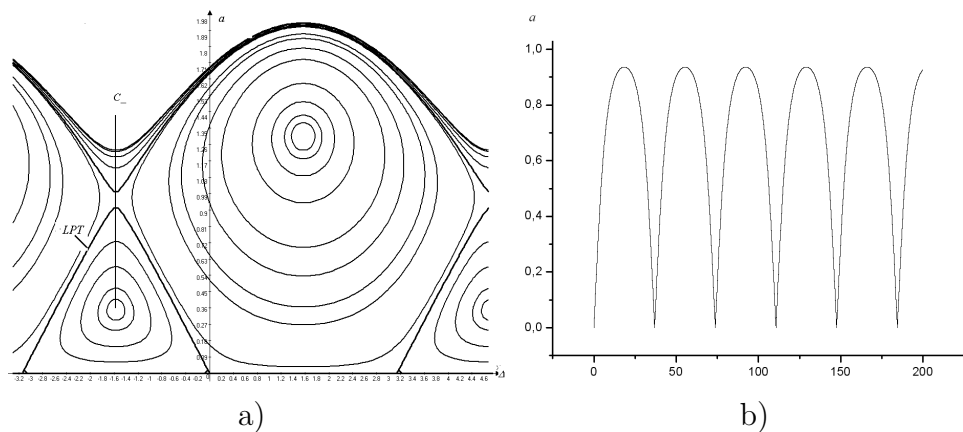

a)   b)

Figure 2: Phase portrait (a) and plots of $a(\tau_1)$ (b) for quasi-linear oscillations: $s = 0.4, F = 0.13, \alpha = 0.093$

We find a critical value $\alpha_{cr} < \alpha^*$ ensuring the transition from small to large oscillations. In the critical case, stable orbits, encircling the centers and C_+, and a trajectory, passing through the unstable point, coalesce at a point $M : (a_M, \Delta_M)$ corresponding to the maximum of an orbit encircling C_-. The maximum condition (9) gives $\Delta_M = -\pi/2$ for any a_M. Recall that the point M lies on the LPTs and, hence, condition (13) holds. In case $\Delta_M = -\pi/2$, the determinant of Eq. (13) is

$$D = \frac{4}{\alpha^2}(F^2 - \frac{2s^3}{81\alpha}). \tag{14}$$

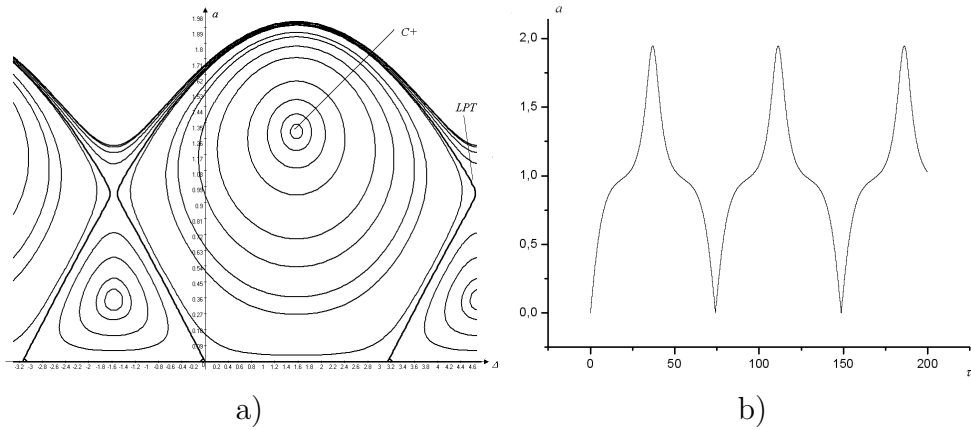a)   b)

Figure 3: Phase portrait (a) and plots of $a(\tau_1)$ (b) for strongly nonlinear oscillations: $s = 0.4, F = 0.13, \alpha = 0.094$

As above, we consider the condition $D = 0$. This yields the critical value of the parameter α

$$\alpha_{cr} = \frac{2s^3}{81F^2} = \frac{\alpha^*}{2}. \tag{15}$$

The parameter α_{cr} corresponds to boundary between small ($\alpha < \alpha_{cr}$) and large ($\alpha > \alpha_{cr}$) oscillations. In particular, for $s = 0.4, F = 0.13$ we obtain $\alpha_{cr} = 0.0935$. Note that Fig. 2 and Fig. 3 are plotted for $\alpha < \alpha_{cr}$ and $\alpha > \alpha_{cr}$, respectively.

If $\alpha = 2\alpha_{cr} = \alpha^*$, the above-mentioned coincidence of the stable and unstable points in the left half-plane results in the topological transformation of the phase portraits, with evident saw-tooth form of $a(\tau_1)$ (Fig. 4).
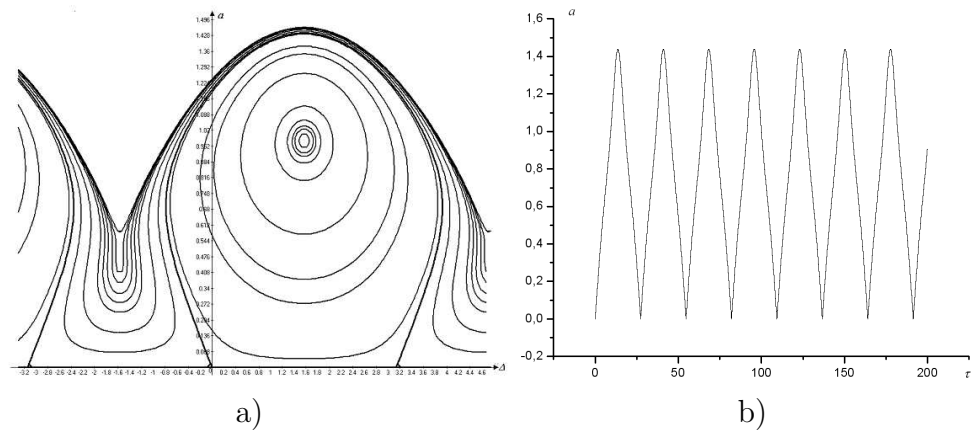

a)   b)

Figure 4: Phase portrait (a) and plots of $a(\tau_1)$ (b): $s = 0.4, F = 0.13, \alpha = 0.187$

3   Vibro-impact approximations of motion

Numerical simulations (Figs 3, 4) demonstrate that the saw-tooth form of the envelope $a(\tau_1)$ for the LPT of large oscillations is similar to a vibro-impact process [2].
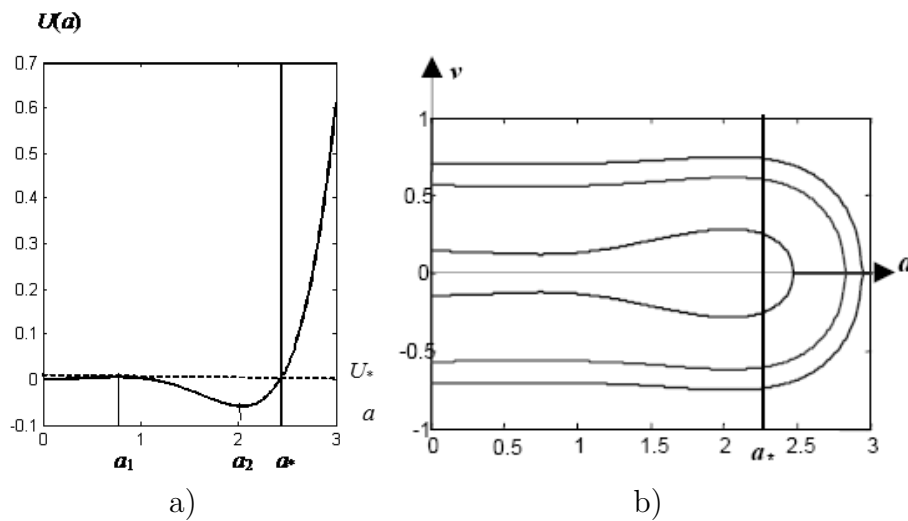
Figure 5: Potential $U(a)$ (a) and phase trajectories (b): $s = 0.4, \alpha = 0.1, F = 0.18; F = 0.58; F = 0.75$

Here we give only a brief insight into the strongly nonlinear dynamics; details and a mathematically rigorous discussion can be found e.g. in [6], [7], and references therein.

Using (13), we eliminate the phase Δ from Eq. (7). This results in the second order equation for $a(\tau_1)$

$$\frac{d^2 a}{d\tau_1^2} + Q(a) = 0. \tag{16}$$

with the initial conditions: $\tau_1 = 0 : a = 0, da/d\tau_1 = F$. In (16) we denote

$$Q(a) = \frac{dU}{da} = \frac{a}{4}(\frac{3}{2}a^2 - s)(\frac{9}{2}a^2 - s). \tag{17}$$

Equation (16) can be interpreted as the equation of a conservative oscillator with potential

$$U(a) = \frac{9}{32}(\alpha a)^2(a^4 - \frac{16}{9}\frac{s}{\alpha}a^2 + \frac{4}{9}\frac{s^2}{\alpha^2}) \tag{18}$$

and total energy

$$E = \frac{v^2}{2} + U(a) = F^2; v = \frac{da}{d\tau_1} \tag{19}$$

Potential $U(a)$ has a maximum at $a_1 = (2s/9\alpha)^{1/2}$ and a minimum at $a_2 = (2s/3\alpha)^{1/2}$. The potential barrier corresponds to $U_* = U(a_1) = U(a_*)$ (Fig. 5a). As may be seen in Fig. 5b, trajectories of large oscillations are weakly sensitive to the shape of the potential. A high energy orbit is close to the straight line until it reaches the point a_*. If the time of motion along the remainder of the orbit is much less than the time needed to reach a_*, the periodic function $a(\tau_1)$ is approximated by the periodic solution of the equation

$$\frac{d^2 a_{\lim}}{d\tau_1^2} = 0 \tag{20}$$

484

satdfying the impact conditions: $\tau_1 = 0 : a_{\lim} = 0$, $da_{\lim}/d\tau_1 = F; \tau_1 = T/2 - 0 :$ $a_{\lim} = a_*$, $da_{\lim}/d\tau_1 = F; \tau_1 = T/2 + 0$, $a_{\lim} = a_*$, $da_{\lim}/d\tau_1 = -F$, with the periodic extension to the intervals $kT < \tau_1 < (2k + 1)T/2$, $(2k + 1)T/2 < \tau_1 < (k + 1)T$, $k = 0, 1, ...$;the period $T = 2a_*/F$. The periodic solution of Eq. (20) takes the form

$$a_{\lim}(\tau_1) = F\tau_1, 0 < \tau_1 < T/2, \quad a_{\lim}(\tau_1) = F(T - \tau_1), T/2 < \tau_1 < T, \tag{21}$$

etc. It has been shown [8], [9] that solution (21) can be rewritten as

$$a_{\lim}(\tau_1) = a_*|\arcsin(\sin\frac{\pi\tau_1}{T})|. \tag{22}$$

Formula (22) gives a unified representation of $a_{\lim}(\tau_1)$ and, therefore, of the function $a(\tau_1) \approx a_{\lim}(\tau_1)$ on the infinite time interval.

It remains to compare (21), (22) with the results of simulation (Fig. 5). The direct calculation of the potential $U(a)$ and the magnitude a_* for $\alpha = 0.187$ leads to $a_* \approx 1.44, T \approx 23$. This proves good agreement of the theory with numerical simulation.

Note that the above derivation presents only rough ideas of the vibro-impact approximations; a rigorous mathematical consideration can be found in [6].

4 An oscillator subjected to a harmonic excitation with random amplitude

In this section we assume that the parameters s and α are fixed but the amplitude F and the phase θ are random parameters uniformly distributed within the intervals $\Phi : [F_-, F_+]$ and $\Theta : [0, 2\pi]$, respectively. The task is to calculate statistical parameters of the generated random process $a(\tau_1)$.

Now we find an amplitude F_{cr} guaranteeing the maximum pumping of energy into the oscillator with fixed parameters s and α. From (15) we obtain

$$F_{cr} = \frac{1}{9}(\frac{2s^3}{\alpha})^{1/2}. \tag{23}$$

If $F > F_{cr}$, the LTP encircles the centre C_+; if $F < F_{cr}$, the LTP encircles the centre C_-. This implies that, if F_{cr} is beyond the interval Φ, all samples of the process exhibit similar behavior, and the probability of occurrence of large (small) oscillations is equal either 1 or 0. If $F_{cr} \in \Phi$, different samples of the process may exhibit different behavior. The probability of occurrence of large and small oscillations is obviously equal $P_l = (F_+ - F_{cr})/(F_+ - F_{cr})$ and $P_s = (F_{cr} - F_{c-})/(F_+ - F_{cr})$, respectively.

As an example, we investigate the oscillator with detuning $s = 0.4$ and $\alpha_1 = 0.03$ (weak nonlinearity), $\alpha_2 = 0.095$ (an intermediate case), $\alpha_3 = 0.187$ (strong nonlinearity). Critical amplitudes corresponding to the parameters $\alpha_1, \alpha_2, \alpha_3$ are, respectively $F_{1cr} = 0.23, F_{2cr} = 0.13, F_{3cr} = 0.09$. The amplitude F is supposed to be uniformly distributed within the interval $[0.1, 0.15]$. Numerical simulation was performed with a step $\delta F = 0.1$. The space average $Ea(\tau_1)$ is calculated by averaging over 15 samples,

4.1 The regular behaviour

1. Consider the weakly nonlinear system with $\alpha = 0.03$, $F_{cr} = 0.23$; in this case $F_- < F < F_+ < F_{cr}$. Samples of the process $a(\tau_1)$ and the space average $Ea(\tau_1)$ are presented in Figs 6a and 6b, respectively. As expected, shapes of all samples are similar to the function $a(\tau_1)$ corresponding to small oscillations (Fig. 2b).
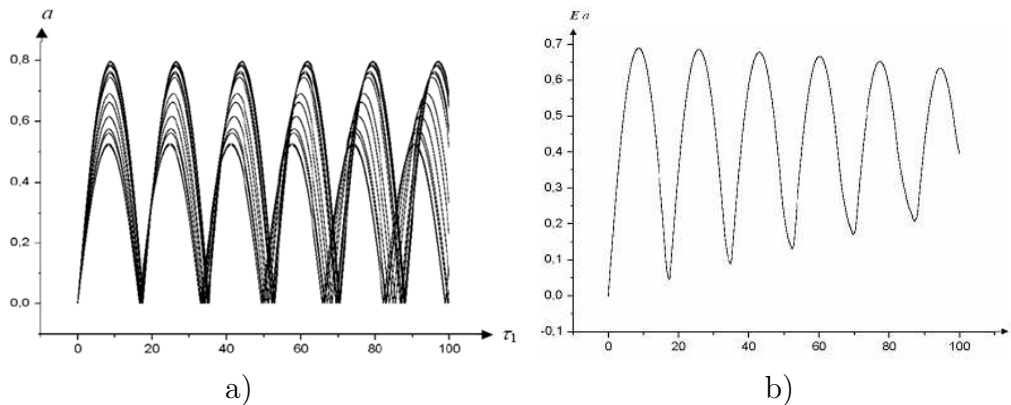

a)   b)

Figure 6: Plots of $a(\tau_1)$ (a) and the mean value $Ea(\tau_1)$ (b): $s = 0.4$, $\alpha = 0.03$, $Fcr = 0.23$, $F \in [0.1, 0.15]$

2. Consider the strongly nonlinear system with $\alpha = 0.187$, $F_{cr} = 0.09$. In this case $F_{cr} < F_- < F < F_+$. Samples of the process $a(\tau_1)$ and the space average $Ea(\tau_1)$ are presented in Figs 7a and 7b. The saw-tooth shape of every sample is similar to the shape of the function $a(\tau_1)$ corresponding to large oscillations (Fig. 5).
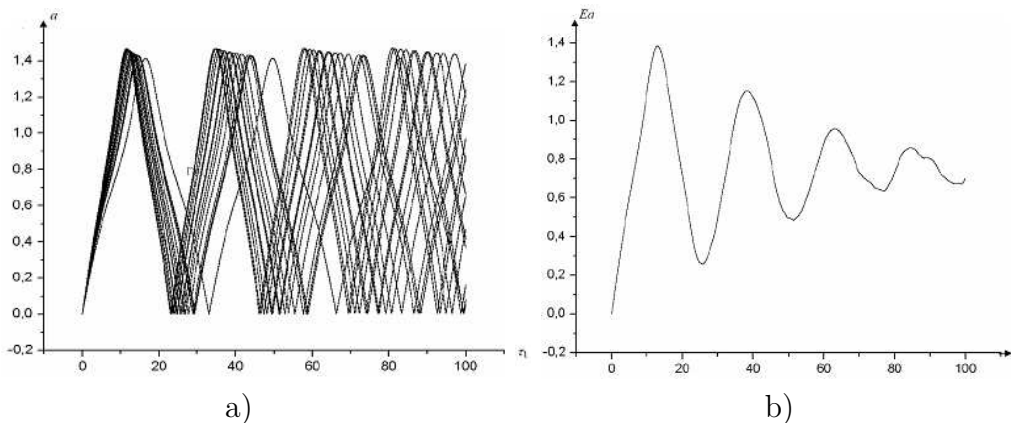

a)   b)

Figure 7: Plots of $a(\tau_1)$ (a) and the mean value $Ea(\tau_1)$ (b): $s = 0.4$, $\alpha = 0.187$, $Fcr = 0.09$, $F \in [0.1, 0.15]$

Variations in the amplitude F entail the change in the initial inclination $da/d\tau_1 = F$ and the period $T = 2a_*/F$. As seen in Figs 6, 7, samples of $a(\tau_1)$ fill the plane with some degree of symmetry with respect to the time average $< a(\tau_1) > = \bar{a}$. This allows presuming the ergodic properties of the process $a(\tau_1)$. We prove the necessary condition of ergodicity, namely, the convergence $Ea(\tau_1) \to \bar{a}$ as $\tau_1 \to \infty$ for the saw-tooth function $a(\tau_1)$. We recall that (21), (22) can be represented as

486

the Fourier series

$$a(\tau_1) = a_0 + \sum_{n=1}^{\infty} a_n \cos(n\omega\tau_1), \omega = 2\pi/T = \pi F/a_*, \tag{24}$$

where

$$a_0 = \tfrac{2}{T} \int_0^{T/2} a(s)ds, a_n = \tfrac{2}{T} \int_0^{T/2} a(s)\cos(n\omega s)ds. \tag{25}$$

Substituting (21) into (25), we obtain after standard transformations

$$a_0 = \frac{a_*}{2}, a_{2k+1} = -\frac{8a_*}{[(2k+1)\pi]^2}, a_{2k} = 0, \tag{26}$$

and, therefore,

$$\bar{a} = a_0 = \frac{a_*}{2} \tag{27}$$

Note that the frequency $\omega = \pi F/a_*$ is uniformly distributed within the interval $[\Omega_+, \Omega_-]$ of length $\Delta\Omega = \Omega_+ - \Omega_-$. where $\Omega_\pm = \pi F_\pm/a_*$. This allows calculating the mean value as

$$E[\cos(n\omega\tau_1)] = \tfrac{1}{\Delta\Omega} \int_{\Omega_-}^{\Omega_+} \cos(n\omega\tau_1)d\tau_1 = \tfrac{1}{n(\Delta\Omega)\tau_1}[\sin(n\Omega_+\tau_1) - \sin[(n\Omega_-\tau_1)]$$

and, therefore,

$$E\{\cos[(2k+1)\omega\tau_1]\} \underset{\tau_1\to\infty}{\to} 0. \tag{28}$$

It follows from (24), (27) that

$$Ea(\tau_1) \underset{\tau_1\to\infty}{\to} a_0 = \bar{a} \tag{29}$$

with rate of convergence of order $1/\tau_1$.

4.2   The irregular behavior

We now consider an intermediate situation, $\alpha = 0.095, F_{cr} = 0.13, F_- < F_{cr} < F_+$. A typical behavior of the system is shown in Fig. 8.
Considering the distribution of the parameter F, we find a set of small amplitudes with small periods and a few numbers of large amplitudes with large periods (Fig. 8a) with irregular average $Ea(\tau_1)$ (Fig.8b). In this case $a(\tau_1)$ cannot be considered as an ergodic process.
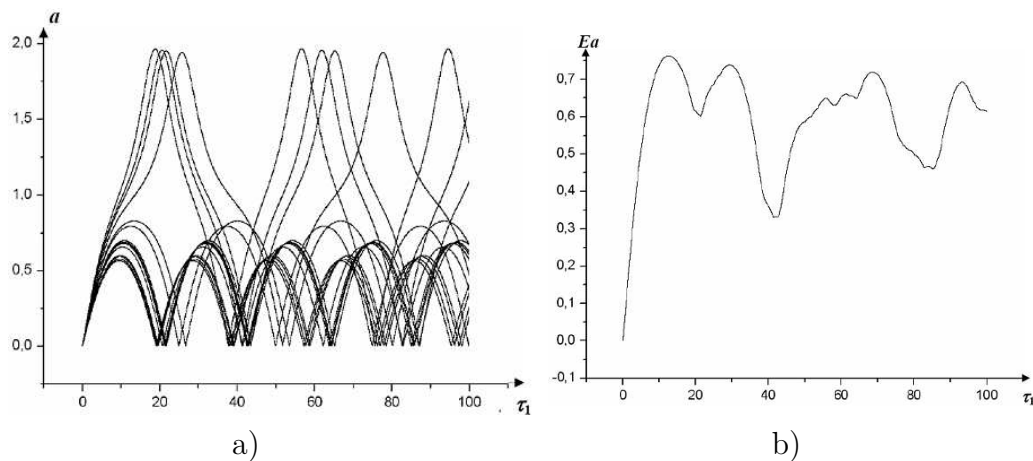
Figure 8: Plots of $a(\tau_1)$ (a) and the mean value $Ea(\tau_1)$ (b): $s = 0.4$, $\alpha = 0.095$, $Fcr = 0.13$, $F \in [0.1, 0.15]$

5 Conclusion

This paper has demonstrated the effectiveness of the LPTs approach in the study of strongly nonlinear dynamics for an sdf Duffing oscillator subject to a quasi-resonance harmonic excitation. We have found the critical parameters of nonlinearity and forcing ensuring the most intensive energy pumping from the source of energy to the oscillator and demonstrated the validity of a simple non-smooth approximation for the LPT. In addition, we have extended the LPTs approach to a system with a harmonic excitation of random amplitude. The clearness and simplicity of this approach may constitute a promising alternative to previously developed methods of non-linear mechanics.

6 Acknowledgements

References

[1] Manevitch, L. I. (2007). New approach to beating phenomenon in coupled non-linear oscillatory chains. Arch. Appl. Mech. 77(5), 301-312.

[2] Manevitch, L. I. and Musienko, A. I. (2008). Transient forced vibrations of Duffing oscillator. In: International Conference "Nonlinear Phenomena in Polymer Solids and Low-dimensional Systems", 7-10 July, 2008, Moscow, Russia, pp. 114-127. IChPh RAN.

[3] Kolovsky, M.Z. (1999). Nonlinear Dynamics of Active and Passive Systems of Vibration Protection. Springer, Berlin.

[4] Manevitch, L. I. (2001). The description of localized normal modes in a chain of nonlinear coupled oscillators using complex variables. Nonlinear Dynamics 25, 95-109.

[5] Nayfeh, A. H. (1973). Perturbation Methods. Wiley, New York.

[6] Vakakis, A. F., Manevitch, L. I., Mikhlin, Yu. V., Pilipchuk, and V. N., Zevin, A. A. (1996). Normal Modes and Localization in Nonlinear Systems. Wiley, New York.

[7] Babitsky, V.I. and Krupenin, V.L. (2001). Vibration of Strongly Nonlinear Discontinuous Systems. Springer, Berlin.

[8] Manevitch, L. I. (2009). Vibro-impact models for smooth non-linear systems. In: R. Ibrahim, ed. Proceedings of the International Symposium on Vibro-Impact Dynamics of Ocean Systems, 2-3 October, 2008, Troy, MI, USA. Springer, New York (to appear).

[9] Pilipchuk, V. N. (1988). A transformation for vibrating system based on a non-smooth pair of functions, Doklady AN Ukr, SSR, ser. A, 4, pp. 37–40 (in Russian).

L. I. Manevitch, Semenov Institute of Chemical Physics, Russian Academy of Sciences, 4, Kosygina str., Moscow 119991 Russia, e-mail: lmanev@chph.ras.ru

D.S. Shepelev, Lomonosov Moscow State University, Leninskie Gory, Moscow, 119992, Russia, e-mail: deshep@mail.ru

A.S. Kovaleva, Space Research Institute, Russian Academy of Sciences, 84/32, Profsoyuznaya str., Moscow 117997 Russia, e-mail: a.kovaleva@ru.net

A new piezoceramic material for a sandwich type transducer used for NDT of civil engineering strucures

C. Miclea   C. Tanasoiu   T. Tanasoiu   C. F. Miclea   A. Iuga
M. Cioangher   L. Amarande   C. T. Miclea   M. Susu   C. David
I. Voicu   V. Malczanek

cmic@infim.ro

Abstract

Nondestructive testing (NTD) of materials and structures by ultrasonics has now become a classical test method for many important influencing factors. The essential tool in ultrasonic detection is the ultrasonic transducer, which basically consists of a piezoelectric element housed in a special case, which while excited by a very short electrical signal is transmitting an ultrasonic pulse. The same piezoelectric element can in turn generate an electrical signal when it receives an ultrasonic signal. The efficiency of the NDT method depends on the ultrasonic transducer which further depends on the piezoelectric element used. Consequently, we developed a new piezoelectric material by doping the basic PZT composition with Sr, Ba, Ni, Nb, Sb, and W ions in small quantities, between 1 and 5 % at. The obtained materials have rather high values for the piezoelectric parameters like k_p, ε_r, d_{33} and Q_m. Therefore, they can be used for the construction of high performance piezoelectric transducers designed for NDT of different materials and structures. Difficulties arise at low frequencies since the transducers would require large piezoceramic elements and consequently high voltage signals. To avoid these difficulties we designed and constructed a rather simple piezoceramic active element of sandwich type. This consists in a number of piezoceramic discs, glued together, with the polarization in opposition and electrically connected in parallel. This construction allows the transducer to be made at the desired working frequency. In our case the sandwich piezoactive element was made using eight discs of 25 mm diameter and 1.8 mm thickness, so that the whole construction had the resonant frequency at 60 kHz. Transducers made with such sandwich like elements for different low frequencies as well as their performances for NDT are presented and discussed in the present work. They can be successfully used for NDT, either in trough transmission or pulse-echo arrangements.

1 Introduction

Among the methods used for testing materials and different engineering structures the nondestructive testing (NDT) methods are the most preferable ones because they can evaluate the material and structures capabilities in situ during service and even more can monitor them within longer periods of time. Ultrasonic testing (UT) methods occupy an important place among the NDT methods as the problems of testing the physical and mechanical properties of materials and structure can be easily solved with their help. To be effective, the UT methods make use of high performance ultrasonic transducers [1, 2]. Such transducers represent devices that may convert one form of energy (in this case electrical) into another one (mechanical) or vice versa by means of one or more piezoelectric active elements capable of undertaking the converse piezoelectric effect [3, 4]. The performances of a piezoelectric transducer essentially depend on both the quality of the piezoelectric material used and the transducer design. High efficiency for emitter and sensitivity for receiver are fundamental characteristics that need to be maximized in a high performance transducer. Both are directly dependent on the electromechanical coupling factor in such a way that a high k is always desirable. In addition, high values of permittivity and elastic compliances can also be favorable in obtaining adequate practical values for electrical impedance at resonance frequency of the piezoelectric active element. On the other hand the mechanical quality factor Q_m can be a determinant parameter for practical transducers. A low Q_m can assure a good transfer of acoustic energy into the load [1, 3, 5, 6]. The most used piezoelectric materials for ultrasonic transducers are the PZT based piezoceramics made of doped solid solutions of lead zirconate - lead titanate [7, 8, 9, 10, 11, 12]. The material properties can be tailored as a function of the dopants used in order to have the optimum characteristics for any specific application. The effect of different dopants on the material characteristics is generally known [11, 12, 13, 13, 14, 15, 16]. Consequently, for the purpose of this investigation we need to develop a new PZT type material with characteristics required by a high performance transducer to be used for inspection and NDT investigation of different structures.

2 Experimental

2.1 Material synthesis

The basic material we used in this experiment was the well known PZT, doped with a number of elements that can enhance the material characteristics needed for the transducer. Thus, we used Sr and Ba in small amounts to replace Pb in order to increase the polarisability and the room temperature dielectric constant [14]. Furthermore, Zr and Ti were partially replaced by Nb, Ni, Bi and Sb in order to increase the electromechanical coupling factor k and the charge constant d_{33} [11, 15, 16, 17, 18]. We have also added a small amount of W in order to keep the mechanical quality factor Q_m at lower values. Finally, small excess of PbO was used in order to both compensate for the PbO losses during sintering [19, 20] and to enhance densification at lower sintering temperatures [21, 22, 23, 24].

Consequently, the final chemical formula of the material investigated was the following: $Pb_{0.90}Sr_{0.05}Ba_{0.05}[Zr_{0.45}Bi_{0.03}Ni_{0.05}Nb_{0.05}Sb_{0.02}W_{0.01}Ti_{0.39}]O_3$. The material was prepared from high purity oxides (over 99.8 %) from Merck, Riedel de Haen and Fluka by using the conventional mixed oxide route slightly modified at the milling stage of the calcined product as should be shown further. The stoichiometric amounts of oxides were intimately mixed for 3 hours by means of a planetary ball mill in methanol and after drying were double calcined for 2 hours at 850 and 900 ºC respectively with an intermediate milling of half an hour. A small amount of 2 wt % PbO was now added to the calcined product and this mixture was subjected to a prolonged milling stage of 24 hours in a Retsch 400 PM planetary ball mill in order to acquire a fine nanometric scale powder with a higher reactivity during sintering. The milled powder was analyzed structurally by X-ray (Siemens Kristalloflex diffractometer) and morphologically by SEM microscopy (Hitachi S-2600 N model microscope). The powder thus obtained was uniaxially pressed into disc shaped samples of different diameters and sintered in sealed alumina crucibles at 1250 ºC for 6 hours. The morphostructure of the sintered samples was also investigated by electron microscopy. Next, the sintered samples were mechanically processed by abrasion, ultrasonically cleaned, dried and chemically electroded with nickel electrodes. Next the samples were poled in a silicon oil bath at 220 ºC under an electric field of 3 kV/mm and cooled down to room temperature still being under the influence of the electric field. Twenty four hours after poling the samples were characterized from the dielectric and piezoelectric point of view by resonance spectroscopy using an Agilent 4294A impedance analyzer.
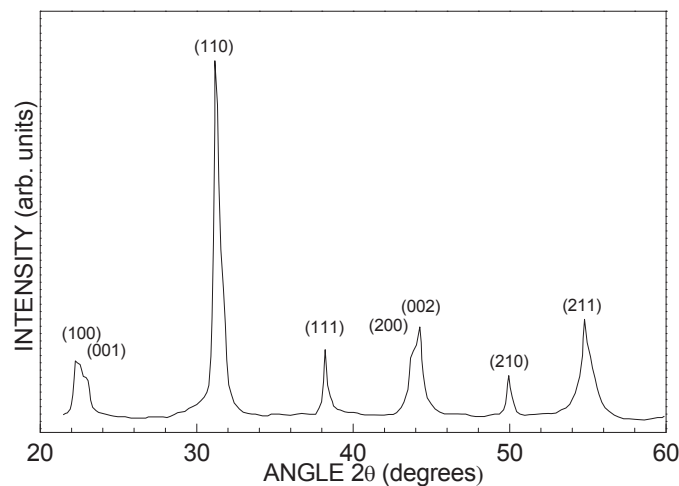
2.2 Results

Figure 1: *The X-Ray patterns obtained of the calcined powder of the PZT material used in the present investigation*

Figure 1 shows the X-ray diffractogram of the calcined powder of the material investigated. Only the peaks corresponding to the well known perovskite phase are present and no other foreign phase was detected. This means that the calcining

temperature and time were enough to complete the solid state reaction between
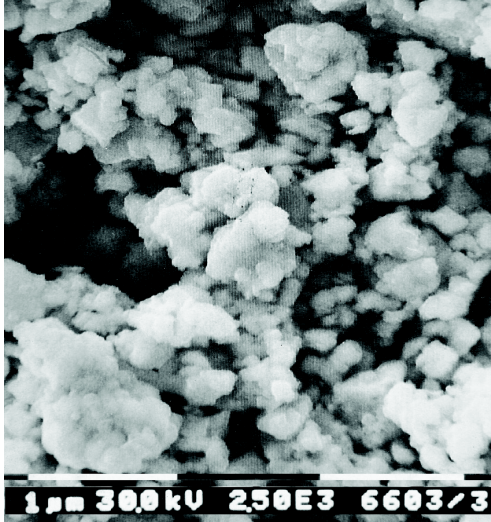the oxides involved and that all of them correspondingly reacted to form one single
phase.

Figure 2: *SEM micrograph illustrating
the morphostructure of the calcined and
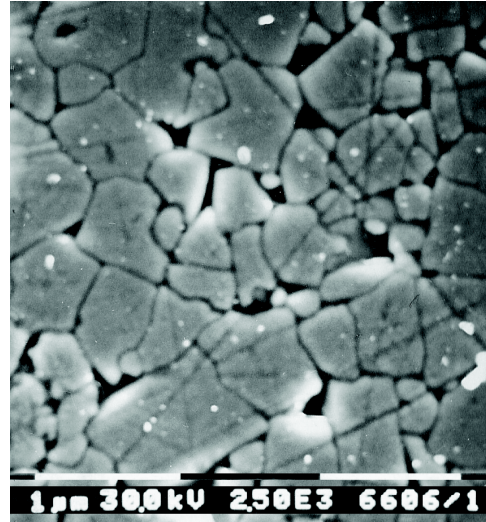milled powder of the PZT material in-
vestigated*

Figure 3: *SEM micrograph showing the
structure of a sintered sample on a pol-
ished and thermally etched surface*

The morphology of the calcined and milled powder is shown in the SEM micrograph
of figure 2. One can see the rather uniform shapes and sizes distribution of the
powder particles though some agglomerates are still visible. The particles are within
the nanoscale range with an average grain size of about 200 nm. The structure of
the pressed and sintered samples is illustrated in the micrograph shown in fig. 3
on a polished and thermally etched surface. One can see that the samples are well
enough densified and the crystallite grain size is just submicrometric though few
crystallites with greater sizes, up to around 1 μm can be distinguished. The main
characteristics of the material were determined on standard samples and the values
of the measured parameters are listed in table 1.

The values reported in the table represent the average values for ten measured
samples for which the differences were within ± 2 %. These values are typical
for a soft type piezoelectric material and they are better than those for the usual
commercial materials. Consequently, we have used this material for the construction
of a special piezoelectric transducer of high efficiency.

2.3   The transducer

A piezoelectric transducer, in its elementary form, consists of a piezoactive element,
generally a disc shaped element, incorporated in a way or another into a case that
serves as housing to protect it. This element vibrates, when excited with an electrical
signal, in the mode allowed by the direction of the polarization axis at a frequency
that depends on the physical dimensions of it. For low frequency working range the

Table 11: Parameters

Parameter	Symbol	Units	Measured value
Density	ρ	g/cm^3	7.72
Relative dielectric constant	ε_r	-	1620
Dielectric losses	$tg\delta$	-	0.014
Planar coupling factor	k_p	-	0.65
Charge constant	d_{33}	pC/N	485
Charge constant	d_{31}	pC/N	-180
Voltage constant	g_{33}	10^3 Vm/N	25.8
Voltage constant	g_{31}	10^3 Vm/N	-11.8
Mechanical quality factor	Q_m	-	63
Curie temperature	T_C	^{o}C	355

thickness of the element must be very large and in this case the piezoactive element becomes inconvenient. For many materials and structures the investigation must be carried out at rather low frequency [25, 26], but because of the high wave attenuation the dimension of the piezoactive element should become very big and this will imply a very high power generator to work at high voltages and this becomes undesirable. To overcome these difficulties a solution is provided by using a "sandwich" type piezoactive element made of a number of thinner discs glued together and having the polarization direction in opposition. Such multielement sandwich type transducer incorporates an even number of piezoceramic discs. The sandwich type piezoactive element, glued on a steel cylinder acting as backing material has two main advantages: 1) the electrical connection are disposed in derivation, thus each disc receiving the whole emf of the driver, much smaller compared to the case of single thick element and consequently a considerable simplification of the electronics can be achieved; 2) the working frequency of such a transducer can be simply
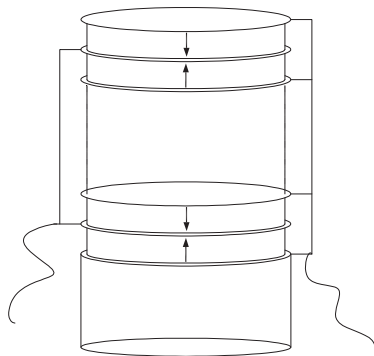

Figure 4: *The schematic arrangement of a piezoactive element made from a number of thin disks glued together on a backing steel block*
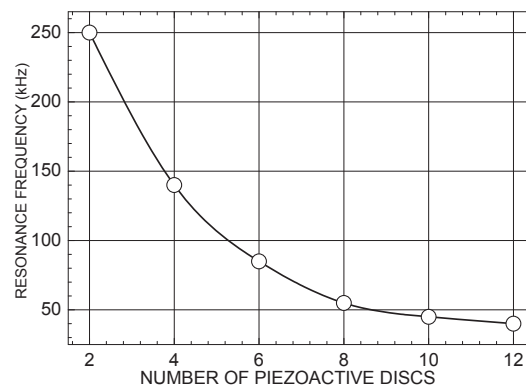

Figure 5: *The experimental points (circles) and the calculated curve (full line) of the resonance frequency versus the number of thin disk in a sandwich type piezoactive element*
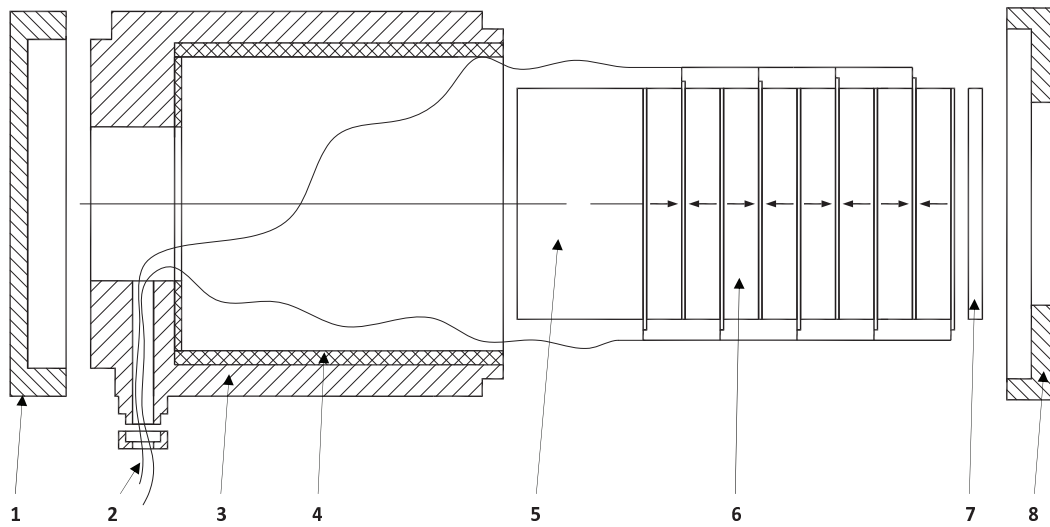
494

Figure 6: *The schematic view of the sandwich type transducer: 1-end cap; 2-electrical connections; 3-outer case; 4-inner electrical isolation; 5-backing steel block; 6-piezoactive thin disc; 7-protection plate; 8-end cap.*

chosen by taking the right number of thin piezoactive elements. Figure 4 show the schematic of a sandwich type piezoactive elements and figure 5 illustrates the experimental resonance frequency of such a sandwich element as a function of the number of thin discs. The discs used in this experiment for the sandwich type piezoactive element have a diameter of 25 mm a thickness of 1.8 mm. The resonance frequencies were measured after gluing each pair of two discs to the previously stacked ones which were already glued on a backing steel block with a diameter of 26 mm and a thickness of 15 mm.

One can see from figure 5 that the frequency resonance decreases with increasing number of disc pairs. The decreasing can be described by a law approximated by a fifth order polynomial function of the form:

$$F = a + b_1 x + b_2 x_2 + b_3 x_3 + b_4 x_4 + b_5 x_5, \tag{1}$$

where the constants a and b_n ($n = 1, 2..5$) have the following values:

$$a = 85.01; \ b_1 = 301.25; \ b_2 = -199.79; \ b_3 = 84.54; \ b_4 = -5.21 \text{ and } b_5 = 0.21. \tag{2}$$

The curve described by the equation 1 is shown as a solid line in figure 5. For the practical construction of the transducer we choose the sandwich structure with four pairs of discs (eight thin piezoceramic discs) corresponding to a resonant frequency of 60 kHz. The schematic view of the transducer is illustrated in figure 6.

2.3.1 The characteristics of the transducer

The electrical characteristics of this transducer were determined by means of an impedance gain/phase analyzer type Agilent 4294A. The electrical spectra are shown

in figure 7. The resonance frequency is situated around 60 kHz with a minimum impedance of 22 Ω and the antiresonance frequency at 71 kHz with a maximum impedance of 28 kΩ . The quality factor Q can be easily calculated by means of the formula:

$$Q = f_W/\Delta f, \tag{3}$$

where f_W is the working frequency which correspond to the resonance frequency, $\Delta f = f_a - f_r$ is the bandwidth of the oscillation spectrum and f_r and f_a are the resonance and antiresonance frequencies. The estimated value of Q is 5.5. There is another way to calculate Q by means of the formula:

$$Q = X/R, \tag{4}$$

where X is the reactance and R the resistance of the electrical branch of the equivalent circuit of the transducer. The reactance is given by:

$$X = 2\pi f_W L - \frac{1}{2\pi f_W C_b}, \tag{5}$$

where L and C_b are the inductance and capacitance of the electrical branch of the equivalent circuit. The equivalent circuit with its characteristics, as determined by the impedance analyzer gave the following values: R = 30.4 Ω, L = 9.94 mH and $C_b = 1.5$ nF so that the estimated value of Q was 5.44 in good agreement with the value estimated with 3.

As concerns the acoustical characteristics, they were determined by using a pair of transducers, one emitter and one receiver, and measuring the ultrasonic output by means of the gain phase analyzer. The transmitted ultrasonic wave within the working range is shown in figure 8. The shape of the acoustical spectrum is that of a product of two lorentzians, each corresponding to a single mode.

The data from this figure allow calculating the relative bandwidth at 1.5 dB under the resonance peak and the corresponding Q number with the formula:

$$Q = \frac{\omega}{\Delta\omega_{1.5dB}} \tag{6}$$

Using the experimental values for w and $\Delta\omega_{1.5dB}$ we obtained for Q a value of 50 which seems a reasonable value for a pair of transducers working in tandem conditions.

3 Conclusion

A new piezoceramic material based on doped PZT was prepared. The dopants used were Sr, Ba, Ni, Nb, Sb, Bi and W, with doping levels ranging between 1 and 5 % at. The piezoelectric parameters of the resulting material were high enough so as to make it suitable for a high performance piezoelectric transducer to be used for NDT of different materials and structures.
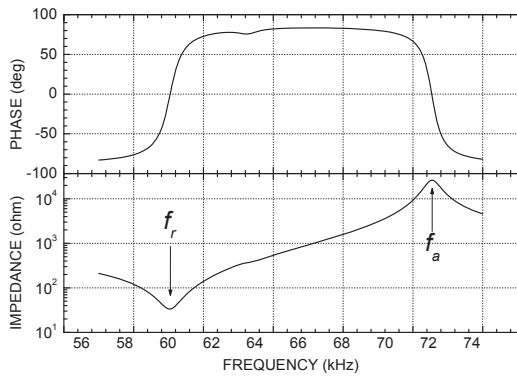
Figure 7: *7 The characteristic electrical spectra of the transducer showing the phase and impedance versus frequency*
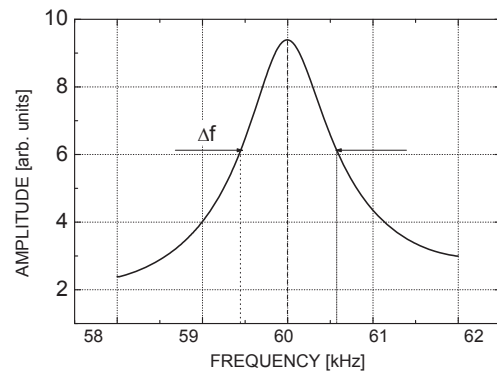
Figure 8: *The characteristic acoustical spectrum of a pair of transducer working in the trough-transmission arrangement*

A sandwich type piezoelectric transducer working at 60 kHz was designed and constructed for different materials inspections and NDT investigations. The transducer is a composite structure made of eight piezoceramic discs of 25 mm diameter and 1.8 mm thickness glued together, with polarization in opposite directions and then glued on a steel cylinder which plays the role of backing material. The transducer can work either in the through transmission or pulse-echo arrangement.

4   Acknowledgements

References

[1] G. Bradfield, Ultrasonic transducers. Introduction to ultrasonic transducers. Part A, Ultrasonics **8**, 112-123 (1970).

[2] B. Hamonic, I. Decarpigni (ed), Power sonic and ultrasonic transducer design, Springer Verlag, Berlin, (1988).

[3] J. Gallego-Juarez, Piezoelectric ceramics and ultrasonic transducers, J. Phys. E: Sci. Instr. **22**, 804-816 (1989).

[4] H. Banno, Piezoelectric transducers and piezoelectric ceramics, Encyclopedia of advanced materials, Ed. R. Cahn, Pergamon Press, Oxford UK, (1995).

[5] D. Berlincourt, D. Curran, H. Jaffe, Piezoelectric materials and their function in transducers, Physical acoustics 1A, Acad Press, New York (1964).

[6] C. Desilet, J. Fraser, G. Kino, The design of efficient piezoelectric transducers, IEEE Trans. Sonics and Ultrasonics SU-**25**, 115-125 (1978).

[7] B. Jaffe, R. Roth, S. Marzullo, Piezoelectric properties of lead zirconate - lead titanate solid solution ceramics, J. Appl. Phys. **25**, 809-810 (1954).

[8] H. Jaffe, D. Berlincourt, Piezoelectric transducer materials, Proc. IEEE **53**, 1372-1386 (1965).

[9] T. Kojima, A review of piezoelectric materials for ultrasonic transducers, Proc. Int. Conf. Ultrasonic, 888-895 (1987).

[10] O. Mattiat (ed), Ultrasonic transducer materials, Plenum Press, New York (1971).

[11] B. Jaffe, W. Cook, H. Jaffe, Piezoelectric Ceramics, Acad. Press. New York (1971).

[12] G. Haertling, Ferroelectric Ceramics: History and Technology, J. Am. Cer. Soc. **82**, 797-818 (1999).

[13] D. Berlincourt, Piezoelectric ceramic compositional development, J. Acoustic. Soc. Am. **91**, 3034-3040 (1992).

[14] L. Eyrand, B. Guiffard, L. Lebrun, D. Guyomar, Interpretation of the softening effect in PZT ceramics near the morphotropic phase boundary, Ferroelectrics **350**, 51-60 (2006).

[15] A. Albareda, R. Perez, J. Garcia, D. Ochoa, V. Gomis, J. Eiras, Influence of donor and acceptor substitutions on the extrinsic behavior of PZT ceramics, J. Eur. Cer. Soc. **27**, 4025-028 (2007).

[16] S. Takahashi, Effect of impurity doping in PZT ceramics, Ferroelectrics **41**, 143-156 (1982).

[17] C. Miclea, C. Tanasoiu, C. F. Miclea, L. Amarande, A. Gheorghiu, F. Sima, Effect of iron and nickel substitution on the piezoelectric properties of PZT type ceramics, J. Eur. Cer. Soc. **25**, 2397-2400 (2005).

[18] J. Garcia, R. Perez, A. Albareda, J. Eiras, Nonlinear dielectric and piezoelectric response in undoped and Nb and Fe doped PZT ceramic system, J. Eur. Cer. Soc. **27**, 4029-4032 (2007).

[19] C. Miclea, C. Tanasoiu, C. F. Miclea, Effect of small amounts of PbO on the piezoelectric properties of soft type PZT ceramics, J. Optoelectronic Adv. Mater. **1**, 59-65 (1999).

[20] L. Amarande, C. Miclea, C. Tanasoiu, Effect of excess PbO on the structure and piezoelectric properties of Bi modified PT ceramics, J. Eur. Cer. Soc. **22**, 1269-1275 (2002).

[21] T. Futakuchi, K. Tanino, K. Furukawa, M. Adachi, A. Kubawata, Low temperature sintering of PZT ceramics with addition of PbO-Bi2O3, Jpn. J. Appl. Phys. **35**, 5113-5116 (1996).

[22] G. Zhilun, L. Longtu, G. Suhka, Z. Xiaowen, Low temperature sintering of lead based piezoelectric ceramics, J. Am. Cer. Soc. **72**, 486-491 (1989).

[23] C. Wang, L. Wu, PbO-Bi2O3 a new sintering agent for PZT ceramics, Jpn. J. Appl. Phys. **32**, 3209-3213 (1993).

[24] E. Nielsen, E. Ringgaard, M. Kosec, Liquid phase sintering of PZT using PbO-WO3 additive, J. Eur. Cer. Soc. **22**, 1847-1855 (2002).

[25] J. Krautkramer, H. Krautkramer, Ultrasonic testing of materials, The 4th edition of Springer Verlag Berlin (1990).

[26] B. Zombori, In situ NDT of built in wooden members, The 12th Int. Symp. NDT of wood **6**, 134-145 (2001).

C. Miclea, National Institute for Materials Physics, Bucharest-Magurele, ROMANIA

C. Tanasoiu, National Institute for Materials Physics, Bucharest-Magurele, ROMANIA

T. Tanasoiu, National Institute for Materials Physics, Bucharest-Magurele, ROMANIA

C.F. Miclea, National Institute for Materials Physics, Bucharest-Magurele, ROMANIA

A. Iuga, National Institute for Materials Physics, Bucharest-Magurele, ROMANIA

M. Cioangher, National Institute for Materials Physics, Bucharest-Magurele, ROMANIA

L. Amarande, National Institute for Materials Physics, Bucharest-Magurele, ROMANIA

C.T. Miclea, Hyperion University, Str. Calarasi 169, sector 3, Bucharest, ROMANIA

M. Susu, Hyperion University, Str. Calarasi 169, sector 3, Bucharest, ROMANIA

C. David, Hyperion University, Str. Calarasi 169, sector 3, Bucharest, ROMANIA

I. Voicu, Hyperion University, Str. Calarasi 169, sector 3, Bucharest, ROMANIA

V. Malczanek, Fairleigh Dickinson University, NJ, USA

Atomic force microscopy of the structure of filled rubber compounds

Ilya Morozov

ilya.morozov@gmail.com

Abstract

Mechanical properties of elastomeric composites in particular carbon blacks and silicas filled rubbers considerably depend on the uniformity of filler distribution and sizes of its clusters in an end-product, i.e. on the quality of mixing of composite components. The more uniform distribution and is smaller sizes of clusters, the larger area of a filler surface interacts with the polymer chains. Insufficient mixing and crushing of filler granules leads to strong filler-filler interactions. In this case the non-uniform distribution of stress during deformation takes place. Breakage of large clusters is the cause of strong change of dynamic module and hysteresis losses. All these factors negatively affect the mechanical behavior of rubber compounds. A technique for quantitative analysis of filled rubber microstructure by atomic force microscopy (AFM) is presented.

1 Introduction

Carbon black (CB), one of the main components of rubber composites (tires, insulators, conveyer belts, etc), is preferably delivered in the form of granules of diameter 1-2 mm. During mixing of the polymer and the fillers, the carbon granules are broken down, and the CB structures (aggregates and agglomerates) are distributed throughout the material. The more uniform the distribution of clusters is and the smaller their sizes are, the larger is the filler surface area that interacts with the binder.

Insufficient mixing and grinding of granules lead to strong filler-filler interactions. In this case, stresses are distributed non-uniformly during deformation. Breakage of large-size clusters results in an essential change in the dynamic modulus of the material, which, in turn, causes high hysteresis losses. All these factors adversely affect the mechanical properties of the end product. Hence, the deciding factor that influences the quality of filled rubbers, all other factors being equal, is the degree of filler dispersion. As the filler distribution in the material gets more uniform, the scattering in particle sizes decreases, improving thus the mechanical characteristics of the filled rubber.

Atomic force microscope provides a powerful, yet rather simple, way to study the nanostructure of materials, in particular, filled elastomers [1]. This study presents

methods for qualitative analysis of the structure of filled rubbers. The proposed approach includes two stages: 1) Processing of AFM images for further statistic analysis of the structure of clusters. 2) Analysis of quantitative estimates of the filler distribution in the material, its sizes, areas, volume fraction and compactness. The obtained characteristics give us insight into the microstructure of elastomeric composites.

2   Experiment and image analysis

For AFM imaging, three industrial tire rubbers manufactured at the "Scientific-Research Institute of Tire Industry" (Moscow) were prepared with next CBs: N220(1), N330(2), N339(3). In all cases filler volume fraction was 0.2 and the binder was natural rubber.

The materials were imaged in a close contact mode using Nano-DST (nominal radius of the tip <10nm). For statistics, from each rubber 10 images of 15x15 μm with resolution 1024x1024 points in plane were obtained and analyzed by our procedures written in Matlab.

The surface structure obtained by AFM is a complex three-dimensional relief. If we observe only such part of the AFM-image that is higher as some height h above the zero level, the relief will be separated into 'islands'. As we cannot define whether this 'island' is part of CB aggregate or agglomerate any structural feature of the AFM image, whose cross-section A is larger than 0.01 μm^2, is called a cluster. The smaller objects of the surface relief are excluded from the analysis, since the probes of the microscope are unable to provide the reliable images of small (<20 nm) features in the xy-plane. For obtained images the following height dependences are constructed:

1. The average compactness [2] of the cluster cross-section $c(h)$:

$$c(h) = \frac{2\sqrt{\pi}}{N(h)} \sum_{k=1}^{N(h)} \frac{\sqrt{(A_k(h))}}{P_k(h)} \qquad (1)$$

where $N(h)$ - number of clusters; $A_k(h)$, $P_k(h)$ are the area and perimeter of the k-th cluster cross section. Equation (1) shows how much the shape of the circle and some figure are different. For circle $c \equiv 1$, the smaller is c, the less compact is the profile of the cluster cross-section.

2. The volume fraction of clusters $\phi(h)$:

$$\phi(h) = \frac{V|_h^{h+20}}{20 * 10000} \qquad (2)$$

By equation (2) we calculate the volume fraction of the material in the layer 20 nm above h. To determine A and P we examine the clusters that do not intersect the image edge. Figure 1 illustrates cross-sections of the specimen with contours of separate clusters. Figure 2 presents the dependences of c and ϕ on the relative height h/h_{max}, where h_{max} is the maximum height over the zero level. As one can see (fig. 2) for $h = h^*[0.45...0.52]h_{max}$, the compactness is minimal and volume
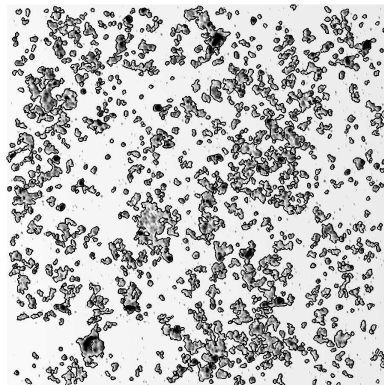
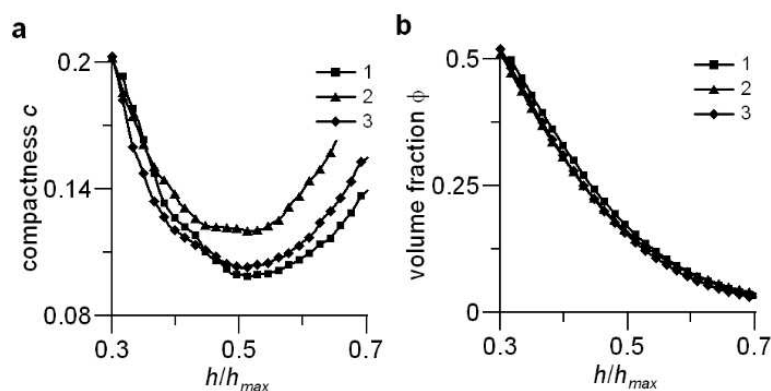Figure 1: Upper part of one of the AFM images: $h \geq 0.5 h_{max}$.

Figure 2: Example of picture obtained after cutting off the lower part of the image for $h = 0.5 h_{max}$.

fraction of clusters close to the filler volume fraction 0.2. At small heights we observe compact and dense clusters with high volume fraction. Such objects cannot truly represent shape of CB clusters in rubber which are known for its branchy structure [3]. Only from some height $h = h^*$ we can suggest that the relief structure is closest to the filler geometry. Therefore, our further analysis of AFM images is concerned with the study of the upper part of the relief: $h \geq h^*$.

3 Results

For the analysis of cluster distribution in obtained images, we use Morishita's index [4]:

$$I_\delta = q \sum_{i=1}^{q} \frac{n_i(n_i - 1)}{N(N-1)} \qquad (3)$$

The image is separated into q squares, the clusters are replaced by the points coinciding with geometric center of the clusters; n_i is the number of points in the i-th square; N - total number of clusters. Reference dependencies $I_\delta(q)$ and obtained curves are presented in Fig. 3. Figure 3 illustrates the following kinds of cluster
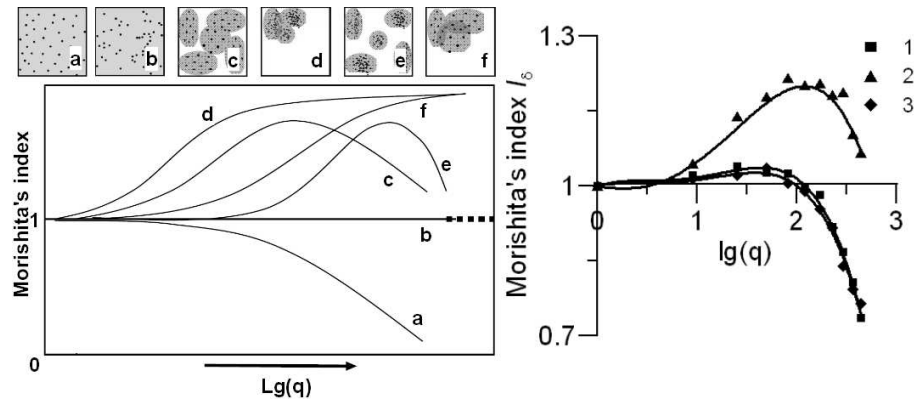
502

Figure 3: Morishita's index.

distribution: a) - uniform distribution; b) - random distribution) c-f) - different cases of agglomeration. The obtained dependences $I_\delta(q)$ lead to a conclusion that the largest non-uniformities in cluster distribution are observed in specimen 2, which corresponds to the case e) of small cluster agglomerates inside which the clusters are distributed uniformly [4]. For specimens 1, 3, the cluster distribution is considered to be uniform, the case a), and with weakly pronounced non-uniformities - the case c) or the case e).

Figure 4 gives distribution histograms for cluster cross sections at $h = h^*$. The
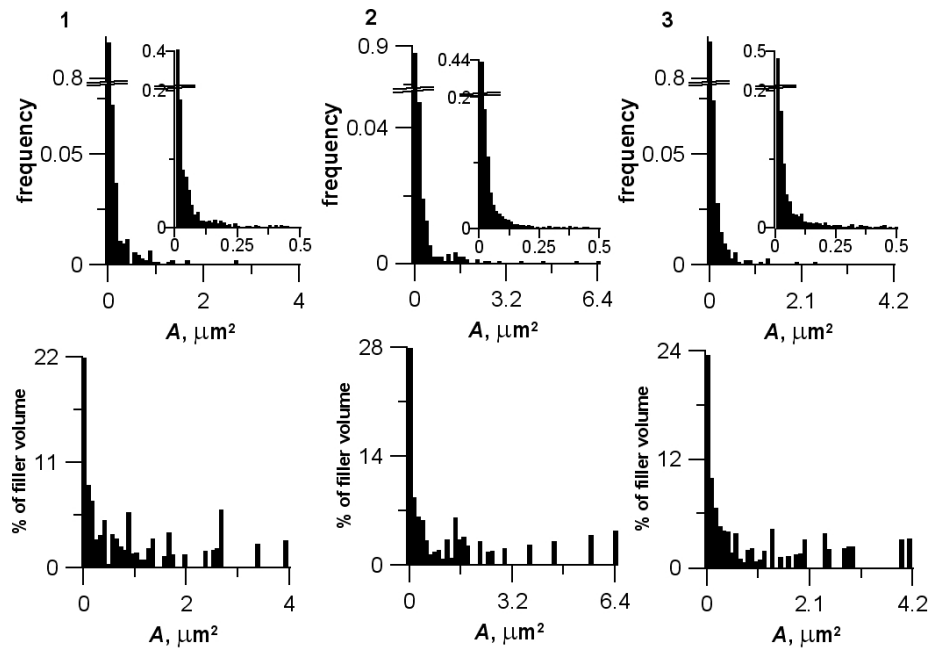
Figure 4: Cluster compactness versus their diameter.

histograms in Figure 4 show that more than 90% of clusters have an area $< 1\mu m^2$. However, there are also separate large-size objects of area 4...6.5 μm^2, which is compatible with the area of all small-size clusters. We suggest that the observed large-size clusters are parts of CB granules that have not been broken completely. Figure 4 also shows the contribution of cluster volumes, calculated using expres-

sion (2), to their observed total volume depending on their cross-section area. It follows from measurements that from 17 (material 1) to 23% (material 2) of the total volume fractions of fillers are large-size objects ($A > 2\mu m^2$). The sizes and number of large-size clusters are important mixing-quality indices. The higher are these characteristics, the smaller is the filler area wetted by the polymer, and the stronger are the filler-filler interactions.

To define the cluster shapes, we construct the plots of their compactness c on the diameter d (Fig. 5). The cluster diameter is calculated as a doubled mean length of the radius-vector from the center of the cross-section up to the most distant point when measuring the polar angle 0 to 2π with the step $2\pi/16$. As one can see, the
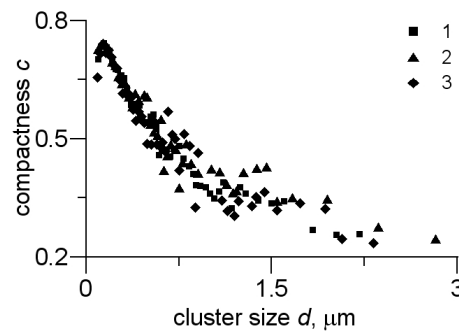

Figure 5: Distribution of cluster cross sections and contribution of clusters with respective areas to the filler volume.

compactness of small-size clusters is most pronounced. This fact is consistent with the data confirming that the primary aggregates are dense formations consisting of 9 sintered particles [5]. Joining of several aggregates into one agglomerate leads to formation of more branchy structures having less compactness.

It is also seen from Figure 5 that the largest clusters can be observed in specimen 2. This indicates again that the mixing quality in specimen 2 differs poorly from the remaining two specimens.

It is known that the CB generates fractal structures in the material [6]. The perimeter P_k and the cross-section area A_k of the k-th cluster are related by the fractal relationship:

$$P_k = \mu_p(\sqrt{A_k})^{D_p} \tag{4}$$

where μ_p is a constant, and D_p is the fractal dimension of the perimeter. The volume V_k and diameter d_k of the cluster are related as:

$$V_k = \mu_m(d_k)^{D_m} \tag{5}$$

where μ_p is a constant, and D_m is the mass fractal dimension. The cluster volume above h^* is denoted by V_k. Figure 6 presents the obtained experimental values and lines approximating these values in logarithmic coordinates. As shown in Figure 6, the dependences $P(A)$ and $d(V)$ within the entire size scale governed by fractal relationships. For primary aggregates D_p and D_m, the values 1.28 and 2.43 (N220), 1.28 and 2.40 (N330), 1.30 and 2.40 (N339) [6] are valid. The corresponding values
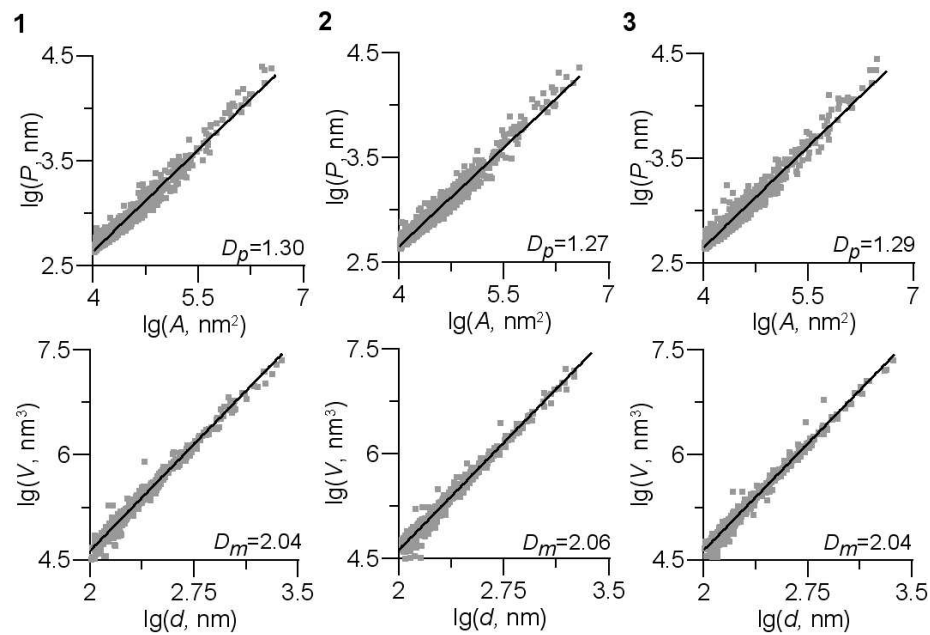
Figure 6: Fractal relationships.

are supposed to be equal with accuracy to decimals. The same values have been obtained for specimens under study. Differences can be caused by many factors: agglomeration, binder layer, manufacture peculiarities, etc.

4 Summary

A method for analyzing filled rubber structures by AFM has been developed. Statistic treatments of AFM mages have been carried out for several filled rubbers. The analysis of the cross-section of the relief has indicated that the compactness reaches its minimum and volume fraction of clusters equal to the filler fraction at the height $h^* = 0.45...0.5$ of the maximum height above the zero level. In the further analysis of the surface features, the value h^* is taken to be a zero level. The uniformity of cluster distribution in the material has been is evaluated using Morishita's index. It is shown that the cluster distribution in materials 1 and 3 is almost uniform, while in 2 one can observe heterogeneities as agglomeration of small units. Examination of cross-sections reveals that more than 90% of clusters are relatively small (less than 2 μm^2), and the rest of clusters of area reaching 6.4 μm^2 (material 2) comprise 23% of the total filler volume fraction. Cluster distribution and sizes are significant product-quality indices. The more non-uniform the cluster distribution is and the larger are the clusters themselves, the stronger is the filler-filler interaction, the more non-uniform is the stress field, and the greater is the amount of hysteresis losses under cyclic loading conditions. Under these aspects, the 2nd material has the worst mechanical characteristics.

Acknowledgements

References

[1] Johnson L.L. Atomic force microscopy (AFM) for rubber // Rubber chemistry and technology. 2008. V. 81. pp. 359-383.

[2] J. Bogaert, R. Rousseau, P. Van Hecke, I. Impens. Alternative area-perimeter ratios for measurement of 2D shape compactness of habitats // Applied mathematics and computation. 2000. V. 111. pp. 71-85.

[3] Kohjiya S., Katoh A., Suda T., Shimanuki J., Ikeda Y. Visualisation of carbon black networks in rubbery matrix by skeletonisation of 3D-TEM image // Polymer. 2006. V. 47 pp. 3298-3301.

[4] L. Karasek, M. Sumita. Review: characterization of dispersion state of filler and polymer-filler interactions in rubber carbon-black composites // Journal of materials science. 1996. V. 31. pp. 281-289.

[5] J.B. Donnet, E. Custodero, T.K. Wang. Atomic force microscopy of carbon black aggregates // Kautschuk Gummi Kunststoffe. 1995. V. 49. pp. 274-279.

[6] Herd C.R., McDonald G.C., Hess W.M. Morphology of carbon-black aggregates: fractal versus euclidean geometry // Rubber chemistry and technology. 1991. V. 65. pp. 107-129.

Ilya Morozov. Russia, 614013 Perm, street Academ. Koroleva, 1. Institute of continuous media mechanics UB RAS.

Solution of contact problems using p-extension finite elements

István Páczelt   Attila Baksa

mechpacz@uni-miskolc.hu

Abstract

The normal elastic contact problems are solved by the variational principles using total potential energy or Hellinger-Reissner functional with augmented Lagrangian technique. For solution of contact problems the p-extension of the finite element method is used. Discretization of the domain with p-extension finite elements is advantageous, since it results in fast convergence and the high order mapping assures accurate geometry for bodies. When the p-extension is used the accuracy is typically high enough for the singularities to induce oscillations in the numerical solutions. In this case the mesh is adjusted during the iteration process in order to align the nodal points in 2D or the sides of the elements in 3D to the border of the contact domain, allowing the jumps in the derivatives to be represented in the discretized problem. The boundaries of the elements are positioned – using a special algorithm – in such a way, that each element in the contact domain will either be in contact, or separate along its full domain. In 3D the border of contact zone is interpolated by B-splines. The last part of this paper a problem is investigated, when the minimum of the wear dissipation power at the contact surface gives the wear rate which characterize the steady wear process.

1   Introduction

The rapid progress in the computer sciences and information technology, the increase of computational speed, and improvements in graphical user-interface software provide new opportunities for modeling physical phenomena with a high degree of reliability and usefulness. The solution of contact problems is difficult because the actual contact zone is unknown a priori and must be determined by iterative procedure which seeks to satisfy not only equation of motion but also one or more inequality conditions. Another source of difficulty is that the stress changes very substantially over short distances at the boundaries of the contact zone. Therefore the development of efficient and reliable procedures for the numerical treatment of contact is an important and challenging problem.
Number of methods have been published on the field of the mechanical contact since the appearance of the Hertzian contact theory. Applying the electronic computers,

better and better numerical processes have been worked out after the late sixties. The paper by Fridman and Chernina [2] was an important contribution to the numerical treatment of contact. This work seems to be open of numerical contact mechanics. Its further development could take into regard the relative rigid body displacements of the contacting bodies [9]. One direction for solution of contact problem is using the Mathematical programming method [1]. In the case of FEM special iteration technique was used first in [19], Lagrangian multiplier technique in [10], [4] and penalthy method in [6]. The combination of the two methods was applied in [16]. A good review of the static mechanical contact problems is given in [22] and detailed discussion of contact problems has been presented in books by Laursen [7] and Wriggers [21].

The error of a finite element solution depends on the element size (h), and on polynomial level (p) of the approximation. The majority of the finite element applications are using the h-extension of the FEM. The solution accuracy is improved adaptively in [20]. Relatively few papers have been dealt with the application of the p-extension method [17] for mechanical contact problems. The high-quality approximation properties of the p-extension make it possible to detect the presence of singularity, even weak singularity, by numerical means. This is possible theoretically but not feasible in practice with the h-version. The application of the augmented Lagrangian technique was investigated first in [11] concerning the solution accuracy. The contact conditions of the p-extension elements are checked in the Gauss or Lobatto integration points. As a result of adaptive remesh the whole sides of the elements are either in the contacting region or in the separation region. This preferable mesh performs no oscillation in the solution. In this paper it is assumed that the displacements and deformations are small, as well as the adhesion, friction and dynamic effects between the contacting bodies can be neglected.

2   Formulation of the contact problem

Let us consider the contact problem of two elastic bodies ($e = 1, 2$). The surfaces of the bodies will be separated into three regions: $S_u^{(e)}$ denotes that part of the body where displacements $\mathbf{u_o}$ are given, in $S_t^{(e)}$ the traction $\mathbf{t_o}$ is applied, while $S_c^{(e)}$ represents that part of the bodies where contact is expected. The $S_c^{(e)}$ part of the body is called the proposed zone of the contact. The bodies are loaded with the body force $\mathbf{b}^{(e)}$. We are interested in finding the displacement vector field $\mathbf{u}^{(e)}$, strain $\mathbf{A}^{(e)}$ and stress $\mathbf{T}^{(e)}$ tensor fields.

For the examination of the contact/separation conditions in the proposed zone of contact we shall consider the projection of the displacement in a prescribed direction only (e.g., normal to the surface $\mathbf{n_c} = \mathbf{n}^{(1)}$). The contact normal vector $\mathbf{n_c}$ determines the points Q_1, Q_2 on the corresponding surfaces S_c^1 and S_c^2, where the two surfaces may contact with each other. Therefore the contact surface will be denoted by S_c. The elastic displacements in the normal direction is denoted by $u_n^{(e)} = \mathbf{u}^{(e)} \cdot \mathbf{n_c}$, the normal contact stress is $\sigma_n^{(e)} = \mathbf{n}^{(e)} \cdot \mathbf{T}^{(e)} \cdot \mathbf{n}^{(e)}$ and the contact pressure is $p_n = -\sigma_n^{(1)} = -\sigma_n^{(2)} \geqslant 0$.

The initial gap between the contacting surfaces is denoted by h, and after deformation the gap is $d = d(\mathbf{u}) = u_n^{(2)} - u_n^{(1)} + h \geq 0$. In the normal direction the Signorini

contact conditions are valid: $d \geq 0, p_n \geq 0, \; p_n \, d = 0$ for $\mathbf{r} \in S_c$. From the condition of frictionless contact we have zero tangential stress $\tau^{(e)} = 0 \; \mathbf{r} \in S_c^{(e)}$.

2.1 Principles based on the total potential energy and Hellinger-Reissner functional

For investigation of normal contact problem we can use the principle of minimum potential energy $\Pi(\mathbf{u})$ subject to two types of kinematic conditions: $\mathbf{u} = \mathbf{u_o}$ on $\mathbf{r} \in S_u$ and $d \geq 0$ on $\mathbf{r} \in S_c$. If we use the Hellinger-Reissner functional [14] we have only kinematical constraints for contact conditions: $d \geq 0$ on $\mathbf{r} \in S_c$. Formally

$$\min\{\Pi(\mathbf{u}) \, | \quad \mathbf{u} = \mathbf{u_o}, \quad \mathbf{r} \in S_u, \quad d \geq 0, \quad \mathbf{r} \in S_c\}, \tag{1}$$

$$\min\{\Pi_R(\mathbf{u}, \mathbf{T}) \, | \quad d \geq 0, \quad \mathbf{r} \in S_c\} \tag{2}$$

which must be solved satisfying the variational inequality $\delta\Pi \geq 0$ or $\delta_u\Pi_R \geq 0$ and $\delta_T\Pi_R = 0$. The detailed mathematical discussion of this variational inequality and other variational principles can be found in books [3], [8] and in the paper [18]. Practically, instead of the problems (1) and 2 we can use another method. Combining the Lagrangian method and penalty method we have the augmented Lagrangian functional in the next form:

$$\mathcal{L}^{AU} = \mathcal{L}^{AU}(\mathbf{u}) = \Pi(\mathbf{u}) - \int_C p_n d(\mathbf{u}) \, dS + \frac{1}{2}\int_C c_n (d(\mathbf{u}))^2 \, dS \; , \tag{3}$$

$$\mathcal{L}_R^{AU} = \mathcal{L}_R^{AU}(\mathbf{u}, \mathbf{T}) = \Pi_R(\mathbf{u}, \mathbf{T}) - \int_C p_n d(\mathbf{u}) \, dS + \frac{1}{2}\int_C c_n (d(\mathbf{u}))^2 \, dS, \tag{4}$$

where c_n means the penalty term and p_n is the Lagrangian multiplier, which is kept to be constant during an iteration loop, $C \subset S_c$ is the real contact domain. From the variational equation

$$\delta_u\mathcal{L}^{AU} = 0 \; \text{ or } \delta_u\mathcal{L}_R^{AU} = 0, \tag{5}$$

and we have a formula for the normal contact stress

$$\sigma_n^{(1)}\left(\mathbf{u}^{(1)}\right) = \sigma_n^{(2)}\left(\mathbf{u}^{(2)}\right) = -\left(p_n - c_n d(\mathbf{u})\right) \; = \sigma_n^{(1)}\left(\mathbf{T}^{(1)}\right) = \sigma_n^{(2)}\left(\mathbf{T}^{(2)}\right). \tag{6}$$

During the iteration process, the contact pressure is updated using the formula

$$p_n^{[k]} = \left\langle p_n^{[k-1]} - c_n d\left(\mathbf{u}^{[k]}\right)\right\rangle \tag{7}$$

where the operation $< \cdot >$ is defined by $\langle p_n \rangle = \frac{1}{2}(p_n + |p_n|)$ and $x^{[k]}$ means the value of x in iteration step k. In the $(k+1)$th iteration loop the contact surface is subjected by $p_n^{[k]}$ as an external load in the variational formula:

$$\delta_u\mathcal{L}^{AU}\left(\mathbf{u}^{[k+1]}\right) = \delta\Pi\left(\mathbf{u}^{[k+1]}\right) - \int_C \delta d(\mathbf{u})\left(p_n^{[k]} - c_n d\left(\mathbf{u}^{[k+1]}\right)\right) \, dS = 0, \tag{8}$$

$$\delta_u \mathcal{L}_R^{AU} \left(\mathbf{u}^{[k+1]}, \mathbf{T}^{[k+1]} \left(\mathbf{u}^{[k+1]} \right) \right) = \tag{9}$$

$$\delta_u \Pi_R \left(\mathbf{u}^{[k+1]}, \mathbf{T}^{[k+1]} \left(\mathbf{u}^{[k+1]} \right) \right) - \int_C \delta d \left(\mathbf{u} \right) \left(p_n^{[k]} - c_n d \left(\mathbf{u}^{[k+1]} \right) \right) dS = 0$$

because from the next variational equation $\delta_T \mathcal{L}_R^{AU} = 0$ we have possibility to gain the relation for $\mathbf{T}^{[k+1]} = \mathbf{T}^{[k+1]} \left(\mathbf{u}^{[k+1]} \right)$. Using p-extension finite elements [17], [11], $c_n \sim 100E - 1000E$ is recommended, where E is the Young modulus.

2.2 Discretized functionals

After the approximation by finite elements technique the discretized form of the $\mathcal{L}^{AU}$, $\left(\mathcal{L}_R^{AU} \right)$ functionals are written as:

$$\mathcal{L}^{AU} = \mathcal{L}^{AU} \left(\mathbf{q} \right) = \sum_e \left\{ \frac{1}{2} \mathbf{q}^{(e),T} \mathbf{K}^{(e)} \mathbf{q}^{(e)} - \mathbf{q}^{(e),T} \mathbf{f}^{(e)} \right\} + \frac{1}{2} \mathbf{q}^T \widetilde{\mathbf{C}} \mathbf{q} + \mathbf{q}^T \left(\mathbf{f}_h - \mathbf{f}_p \right). \tag{10}$$

The algebraic system of equation associated with (10) can be written as follows:

$$\begin{bmatrix} \mathbf{K}^1 + \widetilde{\mathbf{C}}^{11} & -\widetilde{\mathbf{C}}^{12} \\ -\widetilde{\mathbf{C}}^{21} & \mathbf{K}^2 + \widetilde{\mathbf{C}}^{22} \end{bmatrix} \begin{bmatrix} \mathbf{q}^{(1)} \\ \mathbf{q}^{(2)} \end{bmatrix}^{[k+1]} = \begin{bmatrix} \mathbf{f}^{(1)} + \mathbf{f}_h^{(1)} - \mathbf{f}_p^{(1),[k]} \\ \mathbf{f}^{(2)} - \mathbf{f}_h^{(2)} + \mathbf{f}_p^{(2),[k]} \end{bmatrix}, \tag{11}$$

in which the matrix $\mathbf{K}^{(i)}$ is the stiffness matrix, $\widetilde{\mathbf{C}}^{ij}$ is modified to fulfill the contact / separation conditions, the vectors $\mathbf{f}^{(i)}, \mathbf{f}_h^{(i)}, \mathbf{f}_p^{(i),[k]}$ are calculated from given load, initial gap and contact pressure respectively, $\mathbf{q}^{(i)}$ is the parameter vector for displacement.

The iterative *Kalker* procedure [5], [11] with the control of the sign of p_n can be applied for solving (11). The contact conditions are checked in the Gauss or Lobatto integration points of the contact elements during the solution of (11). In the knowledge of the updated contact pressure $p_n^{[k+1]}$ we have new penalty (contact) matrix $\widetilde{\mathbf{C}}$, and new vectors $\mathbf{f}_h$ and $\mathbf{f}_p$. The $(k+1)th$ displacements are obtained from the solution of (11). The procedure is terminated when the following condition is fulfilled: $\int_{S_c} \left| p_n^{[k+1]} - p_n^{[k]} \right| dS / \int_{S_c} p_n^{[k+1]} dS \le 10^{-4}$

Remarks:

1. Since $d(\mathbf{u})$ is computed in local coordinate system, the elements, which have boundaries on the contact surface, must be transformed from global coordinate system to the local one. The transformation is performed by least squares fitting [11].

2. One of the advantages of the p-version is that for smooth problems only coarse meshes are needed, since the error in energy norm decreases exponentially when the polynomial degree of elements is increased [17]. When the p-extension is used then accuracy is typically high enough for singularities to induce oscillations in the numerical solutions. The oscillations are minimized when nodes are located at the boundary of the contact zone. In the contact problems when the ends of contact zone are not situated in nodal points then the derivatives of the shape functions cannot have the appropriate jumps there. By moving the nodal points to the ends of the real contact zone C, the jump in the derivatives can be represented in the discretized problem. First idea of the positioning technique can be found in [11].

3   Positioning the nodal points

The positioning of the nodal points is performed in one or two phases, depending on the predefined tolerance. The first phase is a rough positioning of contact point to ensure that contact exists in each integration point of the contacting elements (see Fig. 1).
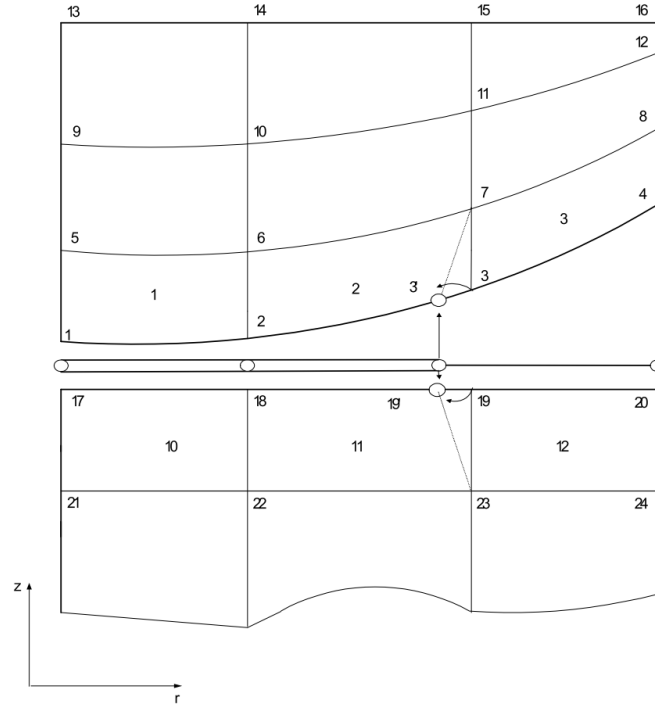

Figure 1. The new positions of the nodal points (3', 19') of the contacting bodies are found by a projection of the nodal points of the contacting elements in normal direction.

In the second phase the border points are moved in order to increase the accuracy. Search to find the end points of contact region with iteration process. The next efficient indicator may be used to monitor the fine adjustment of the nodal points: contact pressure at the contact border point (zero value is sought) $I_1 = \min |c_n \cdot d(r_P)|$, where r_P is the coordinate of the computed contact border point.
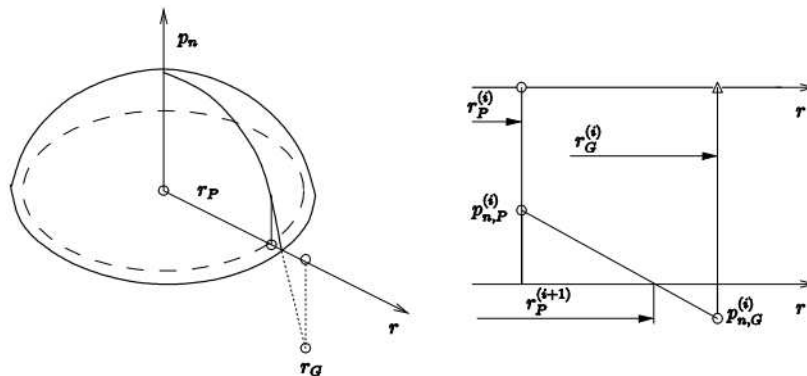

Figure 2. Position of the new border point P along the line r

In the three-dimensional problem it is supposed that contact domain is a single-connected. The border of contact domain will be given by Non-Uniform Rational B-spline curves or shortly by NURBS [13]. Along the border 8 interpolation points are used for calculation of control points of NURBS. The spline is closed curve. The interpolation points are chosen by the contact search algorithm was mentioned before. In Fig. 2 the iteration is demonstrated for position of the contact border points along the line r. Using the i-th iteration, the contact pressure is calculated in the points P and G and the new position is defined from linearization between the two states. Because $p_{n,G}^{(i)} \leq 0$ this point is in the gap region.

4 Examples

4.1 Example 1

Let us consider the contact problem of cylindrical bodies with the following geometrical data: inner radius $r_i^{(1)} = r_i^{(2)} = 20mm$, external radius $r_e^{(1)} = r_e^{(2)} = 120mm$, height $b = b^{(1)} = b^{(2)} = 100mm$. We suppose that the surface of the lower body is flat and the meridian curve of the upper body is parabolic. Kinematic load is applied on the top of the upper body by prescribing the displacement to $w_o = -0.15mm$. The initial gap function is determined by the shape for the upper body, $h = 0.0004 \cdot (r - 70)^2$ mm. The Young's modulus $E = 2 \cdot 10^5 N/mm^2$ and Poisson's ratio $\nu = 0.3$ are used in the constitutive equations.

Using the $p = 8$ polynomial order approximation, the initial mesh $(12 * 5)$ is demonstrated in the Fig. 3a. Using the positioning technique, the first modified and last modified mesh is illustrated in Fig. 3b,d. Final mesh at the left side of contact end zone is in Fig. 3c. The mesh is geometrically graded at the vicinity of the contact/gap border points. The calculated normal stress is demonstrated in the Fig. 4. At the end of contact zone we find a little oscillation. The oscillation of the contact pressure is restricted to the first element in the gap region, whilst the values are smaller than 1 on the rest of the elements.
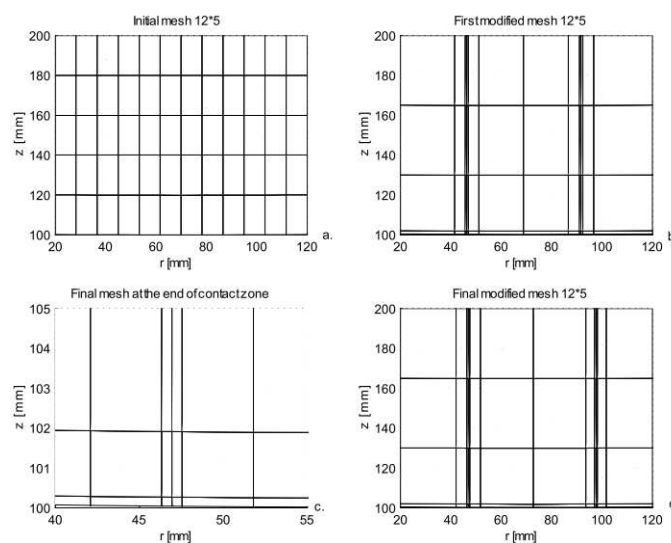

Figure 3. Remeshing procedure
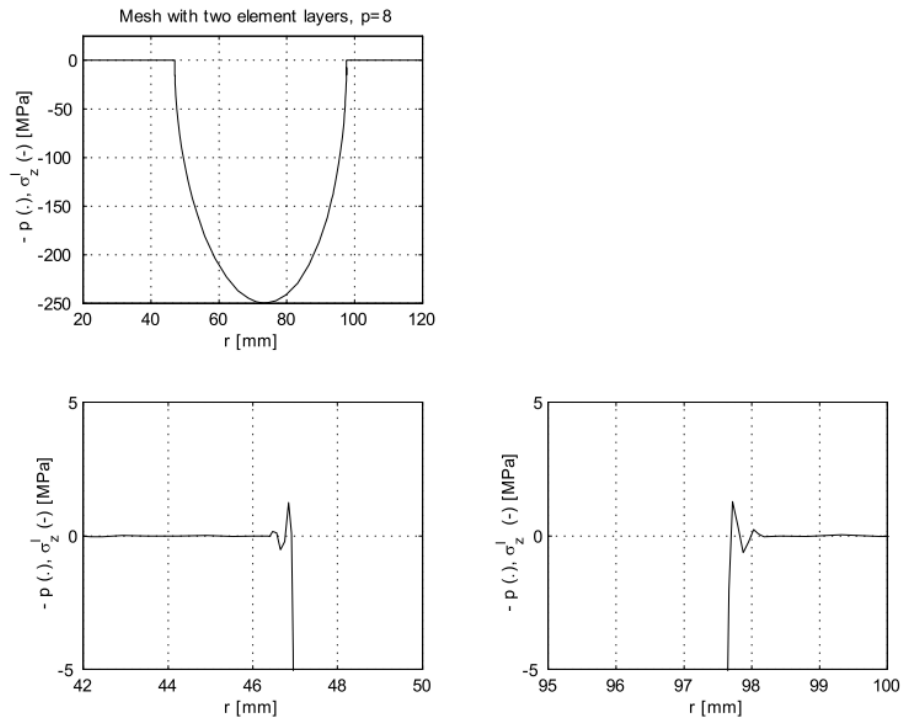
Figure 4. Distribution of normal stress
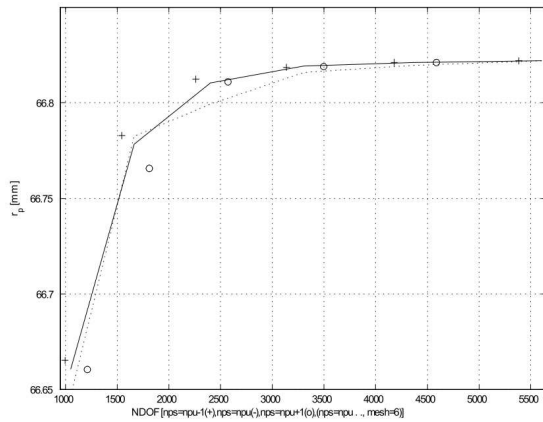
Figure 5. Convergence of the radius of contact border r_p at the different npu and nps
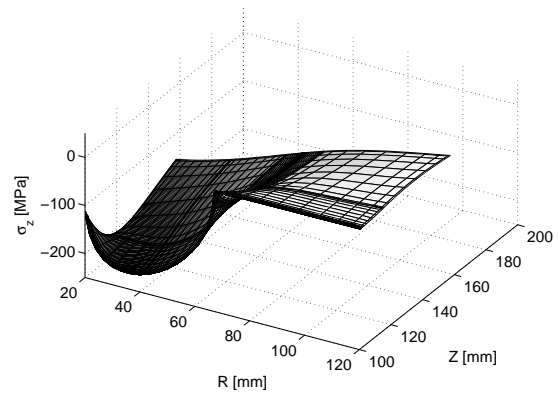
Figure 6. Distribution of σ_z in the upper body

4.2 Example 2

Let us consider the same cylindrical bodies with new initial gap $h = 0.0004 \cdot (r - 20)^2$. For the Hellinger-Reissner variational principle, choosing different polynomial order for approximation of **u** (npu) and for **T** (nps) the border point of contact zone has a convergency according to Fig. 5. Here nps=npu-1 (+), nps=npu (-), nps=npu+1 (o) and npu≤ 8, nps≤ 8, NDOF = unknown for approximation of **u**. The dotted line (...) illustrates the results of minimization of the total potential energy Π. Quickest convergency is establised by nps=npu-1. The normal stress σ_z is demonstrated in Fig. 6.

513

4.3 Example 3

Consider the contact of rigid sphere with radius $R = 800\mathrm{mm}$ and elastic block with the geometrical data: height is $5\mathrm{mm}$, and its size is $100 \cdot 100\mathrm{mm}$. The material parameters for block $E^{(2)} = 2.1 \cdot 10^5 \mathrm{MPa}, \upsilon^{(2)} = 0.3$. The upper body is loaded on its top by a prescribed displacement $w_0 = -5 \cdot 10^{-3}\mathrm{mm}$.

The initial and final mesh in the plane xy is shown in Fig 7. In the z direction only one element used. The polynomial order of the finite element is equal to 8. The results for straight bordered elements are demonstrated in Fig. 8a, 9a. Results are not acceptable because the normal displacement and pressure has not smooth distribution. If the spline bordered elements are applied (Fig. 7b), then results have very good smooth distribution (Fig. 8b, 9b). The calculated radius is $r_P = 2.168\mathrm{mm}$, and $\max p_n = 408\mathrm{MPa}$.
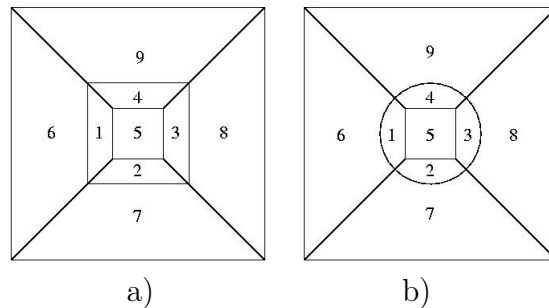

a)   b)

Figure 7. Original and modified mesh
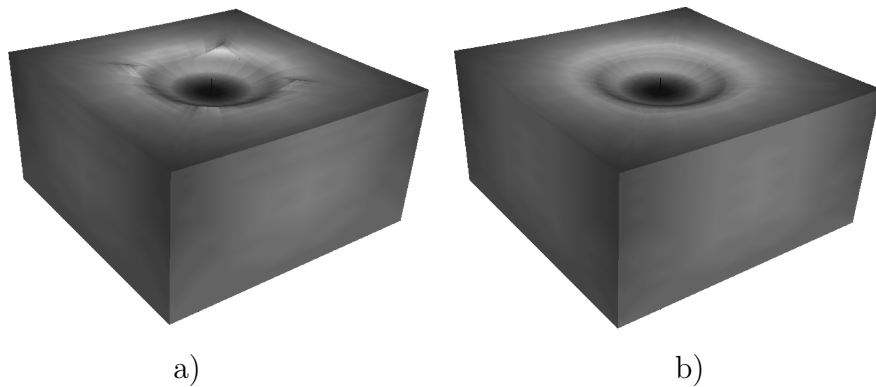

a)   b)

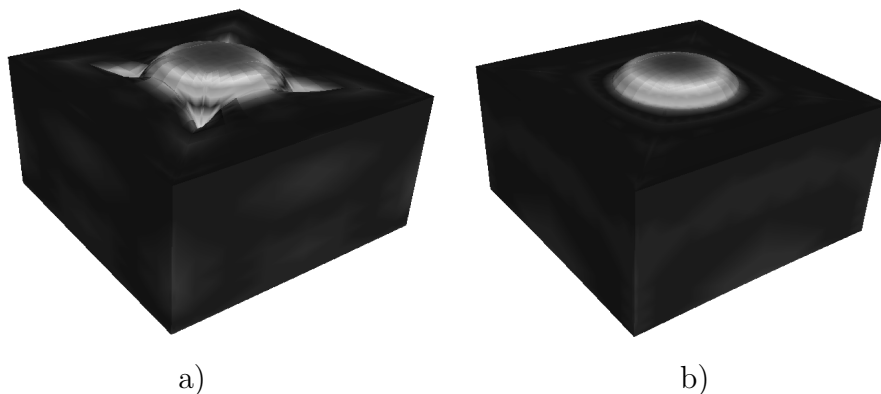Figure 8. Normal displacement at the original and modified mesh

a)   b)

Figure 9. Normal stress at the original and modified mesh

5 Investigation of the steady wear process

In the analysis of wear problem, usually the elastic portion of relative tangent velocity is much smaller than the rigid body motion induced velocity, thus the effect of elastic component of tangent relative velocity can be neglected in the wear analysis. Assume the isotropic normal wear rule in the form [12]

$$\dot{w}_{n,i} = \beta_i \, p_n^{b_i} \, v_r^{a_i}, i = 1, 2 \tag{12}$$

The material parameters β_i, a_i, b_i specify the wear rates of two contacting bodies and $v_r = \left\| \dot{\mathbf{u}}_\tau \right\|$ is the relative velocity between two bodies. In general contact conditions the vector of wear rate is not normal to the contact surface [12] and has tangential components. This vector specifies the shape transformation and tangential motion of the worn material. To analyze this transformation, let us define first the contact stress of interaction of bodies B_1 and B_2, thus

$$\mathbf{t}^c = \mathbf{t}_1^c = -\mathbf{t}_2^c = -p_n(\mathbf{n}_c \pm \mu \, \mathbf{e}_{\tau 1}) - \mu_d p_n \mathbf{e}_{\tau 2} = -p_n \rho_c^\pm \tag{13}$$

where μ is the friction coefficient specifying the shear stress in sliding direction and μ_d is the friction coefficient associated with transverse wear velocity. The unit vectors $\mathbf{e}_{\tau 1}$, $\mathbf{e}_{\tau 2}$, $\mathbf{n}_c$ constitute the local reference triad on S_c, Fig. 10. Here $\mathbf{n}_c$ is the unit normal to the contact surface of body B_1, $\mathbf{e}_{\tau 1}$ is the tangent unit vector coaxial with the sliding velocity v_r and $\mathbf{e}_{\tau 2}$ is the transverse tangent unit vector.
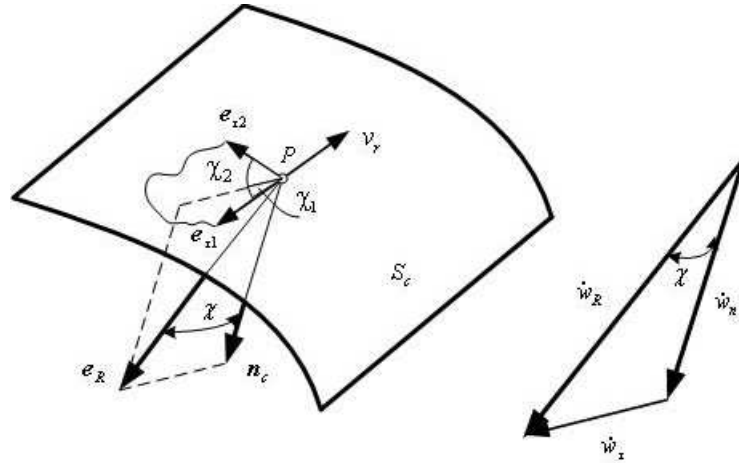
Figure 10. Reference frame and wear rate vectors on the contact surface S_c : coaxiality of $\dot{w}_R$ and $\mathbf{e}_R$.

In the paper [12] a *Fundamental assumption* was introduced: in the steady state the wear rate vectors $\dot{\mathbf{w}}_i \, i = 1, 2$ are collinear with the rigid body wear velocity of B_1, thus

$$\dot{\mathbf{w}} = \dot{\mathbf{w}}_1 + \dot{\mathbf{w}}_2 = \dot{\mathbf{w}}_R = \dot{\mathbf{w}}_{1,R} + \dot{\mathbf{w}}_{2,R} = \dot{w}_R \mathbf{e}_R, \; \mathbf{e}_R = \frac{\dot{\lambda}_F + \dot{\lambda}_M \times \Delta \mathbf{r}}{\left\| \dot{\lambda}_F + \dot{\lambda}_M \times \Delta \mathbf{r} \right\|} \tag{14}$$

and $\dot{\lambda}_F$ and $\dot{\lambda}_M$ are the relative translation and rotation velocities induced by wear, $\Delta\mathbf{r}$ is the position vector with respect to a reference point. The normal and tangential wear rate components now are

$$\dot{w}_n = \dot{w}_R \cos\chi, \ \dot{w}_\tau = \dot{w}_R \sin\chi = \dot{w}_n \tan\chi \tag{15}$$

where χ is the angle between n_c and e_R . The wear rate components in the tangential directions are

$$\dot{w}_{\tau 1} = \dot{w}_R \cos\chi_1 \sin\chi, \ \dot{w}_{\tau 2} = \dot{w}_R \sin\chi \ \sin\chi_1 \tag{16}$$

where the angle χ_1 is shown in Fig. 10. The contact surface does not evolve in time and is specified. The wear velocity associated with rigid body motion does not vanish and is compatible with the specified boundary conditions. The steady state is reached at which the contact stress is fixed with respect to the moving contact domain. Assuming the body B_1 to play the role of an indenter and the body B_2 executing sliding motion, the contact surface will be fixed on B_1 and translating on B_2. The stress state at a material point of B_1 on S_c will be fixed and vary at a contacting material point of B_2 due to translation motion. It has been shown that the steady state conditions can be obtained from minimization of the generalized wear dissipation power for the case of wear of two bodies

$$D_w^{(q)} = \sum_{i=1}^{2} \left(\int_{S_c} (\mathbf{t}_i^c \cdot \dot{\mathbf{w}}_i)^q \, dS \right)^{1/q} = \sum_{i=1}^{2} C_i^{1/q} \tag{17}$$

where q is the control parameter, usually > 0. Assume that the contact pressure p_n and the friction induced shear stress $\tau_n = \mu\, p_n$ satisfy the global equilibrium conditions for the body B_1, so we have for force $\mathbf{f} = \mathbf{0}$ and moment $\mathbf{m} = \mathbf{0}$. Introducing the Lagrangian functional at $b = b_1 = b_2$ is

$$L_D^{(q)} = L_D^{(q)}(p_n, \dot{\lambda}_F, \dot{\lambda}_M) = D_w^{(q)}(p_n) + (b+1)(\dot{\lambda}_F \cdot \mathbf{f} + \dot{\lambda}_M \cdot \mathbf{m}) \tag{18}$$

and satisfying the stationary condition of (18), the contact pressure distribution has the following form

$$p_n = \frac{\dot{\lambda}_F \cdot \rho_c^\pm + (\dot{\lambda}_M \times \Delta r) \cdot \rho_c^\pm}{\left[(\beta_1 v_r^a)^q C_1^{\frac{1-q}{q}} + (\beta_2 v_r^a)^q C_2^{\frac{1-q}{q}} \right]} (1 \mp \mu \tan\chi \cos\chi_1 - \mu_d \tan\chi \sin\chi_1)^{-q})^{\frac{1}{(b+1)q-1}} \tag{19}$$

Let us note that the orientation angle $\chi = \chi(\dot{\lambda}_F, \dot{\lambda}_M)$ depends on Lagrangian vectors and equilibrium equations $\mathbf{f} = \mathbf{0}$ and $\mathbf{m} = \mathbf{0}$ are highly nonlinear, that is the Lagrangian vectors $\dot{\lambda}_F, \dot{\lambda}_M$ specifying the wear velocities can be calculated by applying Newton-Raphson technique. It was shown in [12] that for $q = 1$ the optimal solution corresponds to the steady state condition for wear process of arbitrary shape of contact surface. Thus, this condition can be directly specified from (19) instead of integration of the normal wear rule (12) for the whole transient wear process until the steady state is reached.

5.1 Example: Drum braking system

Consider a drum braking system of Fig. 11a, when the shoe has the form of ring with constant thickness $t = 10mm$ and height $h = 20mm$ and the uniform distributed load is concentrated at the shoe centre. The uniform vertical traction equals $\widetilde{p} = 49.5$ MPa and the resultant force is $F_0 = 10$ kN. The shoe is allowed to translate along vertical end supports at $x = \pm 100mm$ and interacts with the rotating drum of radius $R_0 = 200mm$ with angular velocity $\omega = 1$ rad/s. In our case the rigid wear velocity of upper shoe equals $\lambda_F = -\lambda_F \, \mathbf{e}_z$ and the wear rate vector is collinear with $\mathbf{e}_z$ The steady wear state is reached for $q = 1$ and following contact pressure distribution has a simple form

$$p_n = A \left(\cos \alpha \right)^{1/b} \tag{20}$$

where A is calculated from equilibrium for body B_1. The pressure distribution is symmetric with respect to z-axis and does not depend on the friction coefficient. Easy to derive the formulae for vertical wear rate

$$\dot{w}_R = \dot{\lambda}_F = A^b \sum_{i=1}^{2} \beta_i \left(R_0 \omega \right)^{a_i} = \text{const} \tag{21}$$

Fig. 11b present the optimal gap shape in vertical direction for different values of the friction coefficient for the case when the thermal distortion is not accounted for and the disk rotates in the anticlockwise direction. It is seen that the effect of friction on the contact shape is very significant.
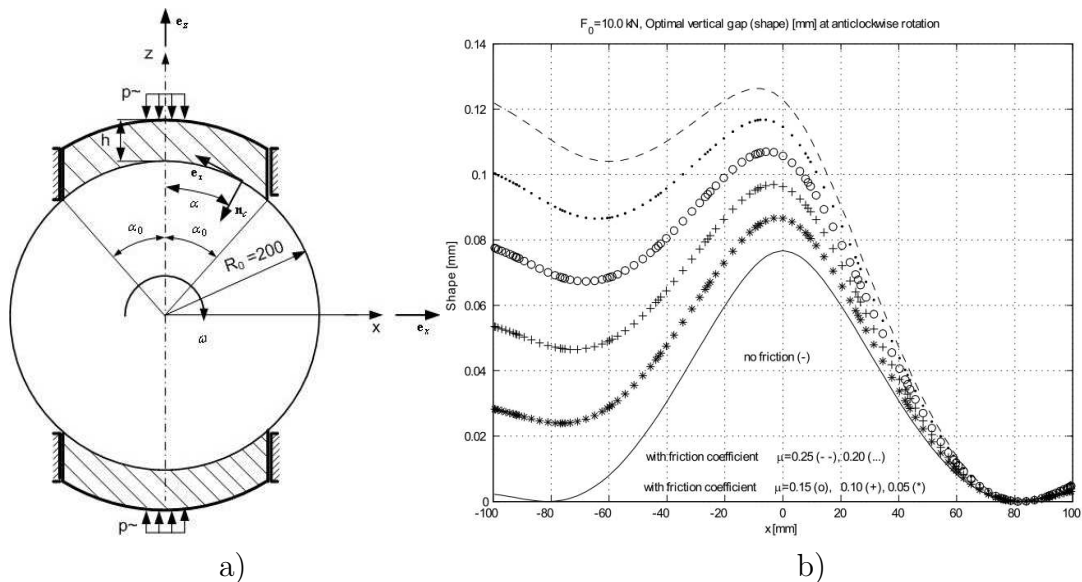

a)   b)

Figure 11. Drum brake: a) geometry and load, b) vertical shape in the steady state wear process for different values of friction coefficient μ

Acknowledgements

References

[1] T. F. Conry and G. A. Seireg, A Mathematical Programming Method for Design of Elastic Bodies in Contact, ASME, J. Appl. Mech., 1971, 38, pp. 387-392.

[2] V. M. Fridman and V. S. Chernina,Iteration Methods Applied to the Solution of Contact Problems of Bodies (in Russian), Mehanika Tverdogo Tela AN, USSR, 1967 1, pp. 116-120.

[3] J. Haslinger and P. Neittaanmaki, Finite Element Approximation for Optimal Shape Design, John Wiley and Sons, London, 1988.

[4] T. R. J. Hughes and R. L. Taylor and at.al., A Finite Element Method for a Class of Contact Impact Problems, Comput. Meths. Appl. Mech. Engng., 1976 8, pp. 249-276.

[5] J. Kalker, Three-dimensional Elastic Bodies in Rolling Contact, Academic Publisher, Dordrecht, 1990.

[6] N. Kikuchi and J. T. Oden and G. F. Carcey eds., Finite Elements: Special Problems in Solid Mechanics, Vol.4, Prentice Hall, Englewood, 1984.

[7] T. A. Laursen, Computational Contact and Impact Mechanics, Springer, Berlin, 2002.

[8] J. T. Oden and N. Kikuchi, Contact Problem in Elasticity: A Study of Variational Inequalities and Finite Element Methods, SIAM, Philadelphia, 1988.

[9] I. Páczelt, Iterational Method Applied to the Solution of Contact Problems of Elastic Systems Having Elements in Unilateral Relation (in Russian), Acta Tech. Hung., 1974, 76, pp. 217-241.

[10] I. Páczelt, Solution of Elastic Contact Problems by the Finite Element Displacement Method, Acta Tech. Hung., 1976, 82, pp. 353-375.

[11] I. Páczelt and B. A. Szabó and T. Szabó, Solution of Contact Problem using the hp-version of Finite Elements, Computer Math. Applic., 1999, 38, pp. 49-69.

[12] I. Páczelt and Z. Mróz, On the analysis of steady sliding wear process, Tribology International, 2009, 42, pp. 275-283.

[13] L. Piegl and W. Tiller, The NURBS book, Springer, Berlin, 1995.

[14] L. A. Rozin, Set-up of variational problems for elastic systems (In Russian), Izd. Leningradskogo Universiteta, Leningrad, 1978.

[15] J. C. Simo and T. A. Laursen, An Augmented Lagrangian Treatment of Contact Problems Involving Friction, Comp. Struct., 1992, 42 7, pp. 97-116.

[16] J. C. Simo and P. Wriggers and R. L. Taylor, Perturbed Lagrangian Formulation for the Finite Element Solution of Contact Problems, Comput. Meth. Appl. Mech. Engng., 1985, 50, pp. 163-180.

[17] B. A. Szabó and I. Babuska, Finite Element Analysis, John Wiley & Sons, New York, 1991.

[18] J. I. Telega, Variational Principles for Mechanical Contact Problems (in Russian), Advances of Mechanics, 1987, 10, pp. 3-95.

[19] E. A. Wilson and B. Parsons, Finite element analysis of contact problems using differential displacements, Int. J. Numer. Meth. Engng., 1970, 2, pp. 387-395.

[20] P. Wriggers, Finite Elements for Thermomechanical Contact and Adaptive Finite Element Analysis of Contact Problems, CISM Course: Contact Problems: Theory, Methods, Applications, Udine, 1977, pp. 1-66.

[21] P. Wriggers, Computational Contact Mechanics, John Wiley & Sons Ltd,New York, 2002.

[22] Z. H. Zhong and J. Mackerle, Static Contact Problems a Review, Eng. Comput., 1992, 9, pp. 13-37.

István Páczelt, Department of Mechanics, University of Miskolc, H-3515 Miskolc-Egyetemváros, Hungary

Attila Baksa, Department of Mechanics, University of Miskolc,H-3515 Miskolc-Egyetemváros, Hungary

Propagation peculiarities of spherically converging waves in materials under uniform impact loading

N. A. Parfenov   K. P. Zolnikov   S. G. Psakhie

kiro@sibmail.com

Abstract

Molecular dynamics investigation of structural response peculiarities of copper crystallite under high rate impact loading was carried out. It was shown that structural rearrangements take place at the front of the converging wave. As well as the effect of the crystal structure on the character of propagation of spherically converging waves was study.

1   Introduction

It is known that the high rate energy loading of material can change internal structure, physicochemical properties, as well as initiate chemical reactions, increase diffusion processes and so on [1, 2, 3]. High rate energy loading is usually conducted by nonlinear effects. One of these effects is generation of solitary waves in material [4]. These waves propagate for a long distance without changes their shape and amplitude in materials with ideal crystal structure. Also these waves can pass through each other and then restore their initial characteristics. Solitary waves are characterized by a microscopic wavelength that measures a few lattice parameters and the velocity of these waves depends on their amplitude, in particular: the higher the amplitude, the higher the velocity. In the region of the wave, the material is in compressed state. Note that the higher the velocity of a solitary wave, the higher is the degree of compression of the material i n the region of the wave. Depending on time duration of loading, more than one solitary wave with different amplitude can generate in a material. In this work the peculiarities of solitary wave's generation, propagation and stability are investigated. One of the purposes of this work is computer simulation of nonlinear response of materials with perfect and disorder crystal structure under uniform pulse compression. Peculiarities of generation, propagation and stability of solitary waves in copper spherical specimens under uniform pulse loading are investigated in this work.

2   Calculation formalism and loading scheme

The molecular dynamics method was used for solving problems formulated in this work. In order to describe atomic interaction the embedded atom method was used

[5, 6]. The specimens under study were spherical copper crystallites. The simulated
specimens contained from 20 000 to 2 000 000 atoms. The atoms of copper were
placed in points of perfect FCC lattice with the value of the lattice parameter
a=3.639A. Due to the smallness of simulated specimens, externally they were shaped
as regular polyhedrons. The external pulse loading was prescribed by displacing the
sub-surface layer towards the center of the crystallite. The displacement rate of the
sub-surface layer was varied from 250 m/s to 2 000 m/s. Depending on the rate, the
loading time was selected so that degree of straining was the same, in particular, it
war sufficient to cause atomic displacement in sub-surface layer equal to 1% of the
lattice parameter. All calculations were carried out at the temperature close to 0 K.

3   Calculation results and discussion

The calculations showed that under uniform pulse loading of the crystallites under
study spherical converging waves form in them. Fig. 1(a) and fig. 1(b) present the
atomic velocity distribution for the central part of loaded specimen (the thickness
of the central part is equal to several lattice parameters) at different points of time.

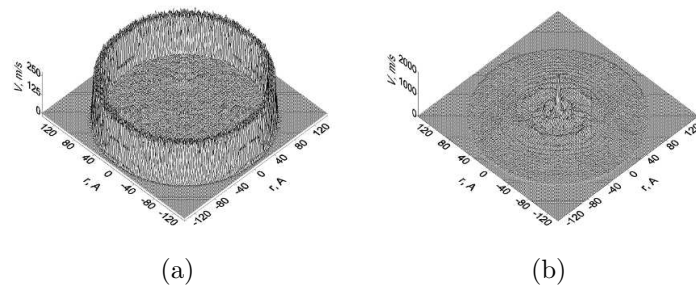(a)   (b)

Figure 1: Distribution of atomic velocities in the loaded crystallite containing
780 000 atoms at different points of time for a compression rate of 250 m/s

Along the vertical axis in fig. 1(a) and fig. 1(b) are depicted the atomic veloci-
ties and along two other axis – their coordinates. The initial point of time of the
atomic velocities distribution and the point of time when the spherically converg-
ing wave reaches the center of the specimen are shown in fig. 1(a) and fig. 1(b),
respectively. Note that the amplitude of the spherical converging wave in the center
of the specimen was increased by a factor of 7-8 compared to the initial rate of
loading. Propagation peculiarities of the spherically converging waves and the in-
crease in their amplitude in their focusing range depend on the rate of pulse loading.
Fig. 2(a) depicts the dependence of the amplitude of a wave reaching the center on
the rate of loading. The calculations demonstrate that with an increase in the rate of
pulse compression the increase in the wave amplitude in the center of the specimen
is slowed down (fig. 2(a)). For the same uniform pulse compression intensity, the
degree of focusing of spherical converging solitary waves in the dependent on the size
of the simulated crystallite. Fig. 2(b) shows the dependence of the amplitude of a
spherically converging wave that have reached the center on the simulated specimen
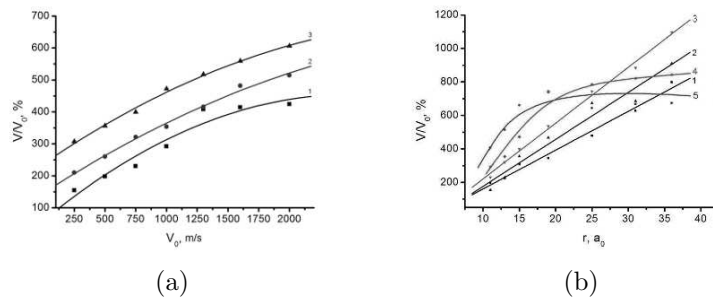radius.

(a) (b)

Figure 2: Dependence of the wave amplitude in the specimen center (V) on the pulse-loading rate (V_0) (a) and the crystallite radius r (b) (a_0 - copper lattice parameter). Curves 1, 2 and 3 correspond to the specimens containing 22 000, 37 000 and 55 000 atoms, respectively (a). Curves 1–5 correspond to pulse loading at a rate of 250 m/s, 500 m/s, 750 m/s, 1 000 m/s, and 2 000 m/s, respectively (b)

It follows from the calculations performed that the tilt of the curves in fig. 2(b) is controlled by the loading intensity: the higher the rate of pulse loading of the crystallite the lager the tilt. For the pulse loading rates up to $750\tilde{m}$/s the dependence of the amplitude of a spherically converging wave on the radius is linear (Curves 1–3 in fig. 2(b)). For higher loading intensities (Curves 4 and 5), starting from a certain distance from the crystallite surface, the distribution pattern of the spherically converging wave is changed. Note that the growth in the wave amplitude in the specimen center is decreased. It is very likely that for larger crystallites the curves corresponding to lower rates of pulse loading would also deviated from a linear dependence. An analysis of the calculation results demonstrated that this deviation of the wave amplitude increase from linearity is associated with the structural rearrangements developing in the crystal specimen. These rearrangements start at the front of the converging wave where the minimum distance between the atoms reaches a certain threshold value. Fig. 3 depicts how the inter-atomic distance at the front of a spherically converging wave varies as it propagates in the specimen.

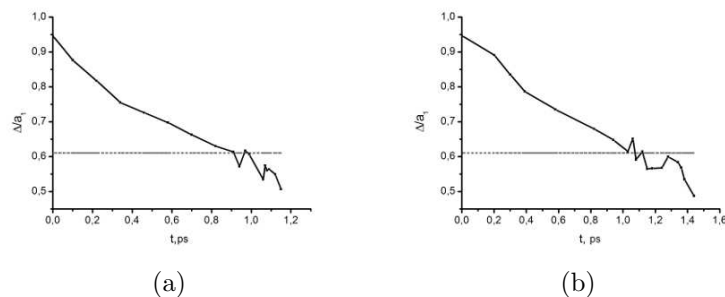
(a) (b)

Figure 3: Dependence of the inter-atomic distance at the wave front on time for crystallites containing 500 000 (a) and 780 000 (b) atoms, respectively, under uniform pulse compression at 2 000 m/s (Δ - distance between the atoms at the wave front, a_1 - radius of the first coordination sphere)

The results of calculations show that the increase in the wave amplitude deviates

from linearity or even slows down starting from the point where the atoms at the wave front approach each other to a distance less than 0.6 radius of the first coordination sphere. The specimen structure at the point of time when the wave reaches the center was investigated in this work. There are 3 regions can be distinguished in the central part of the specimen fig. 4: the region recovered initial structure after the wave had passed - 1; the region, where structure defects were generated after the wave had passed - 2; the region with disordered structure - 3.
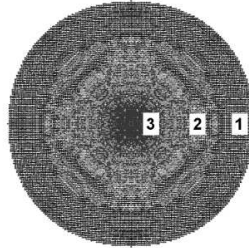
Figure 4: The central part of the specimen at the point of time when the wave reached the center. Specimen containing 780 000 atoms for a compression rate of 2 000 m/s

It should be noted that the pressure, the temperature and the atomic density in the region 3 were considerably increased after the wave had reached the center of the simulated crystallite.
The wave reflected from the specimen center led to an appearance of greater straining pressure and as a result the pore was formed in the specimen center fig. 5.
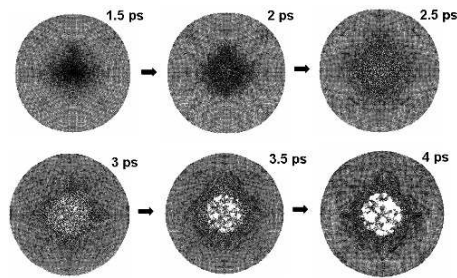
Figure 5: The pore formation in the specimen center at different points of time

In order to study the effect of the crystal structure on the character of propagation of spherically converging waves, the initial specimen was melted and then cooled close to 0 K. As a result of this treatment, the specimen with disordered structure is formed. After that, the specimen was subjected to the same uniform compression as in the case of a crystal specimen. The comparison was performed for the specimens containing 500 000 atoms. The compression rate was as high as 2 000 m/s. Distribution of atomic velocities in the loaded specimen with the disordered structure at different points of time are illustrated in fig. 6(a) and fig. 6(b). Fig. 6(a) depicts the initial point of time of the distribution of atomic velocities under uniform compression. The point of time where the spherically converging wave reaches the center of the specimen is shown in fig. 6(b).

(a)   (b)
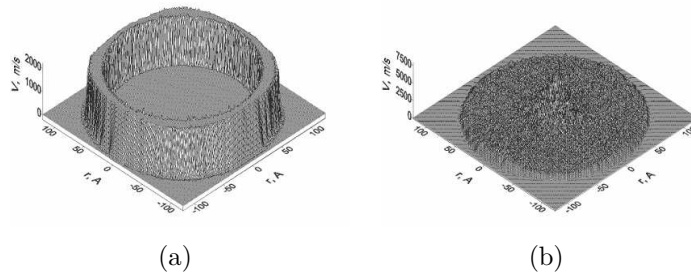
Figure 6: Distribution of atomic velocities in the loaded specimen with the disordered structure containing 500 000 atoms at different points of time for a compression rate of 2 000 m/s

After the spherically converging wave has reached the center, its amplitude increased by a factor of 3.5–4.0 compared to that at the initial point of loading. The dynamics of an increase in the spherically converging waves for the specimens of the same size having crystal and disordered structure is given in fig. 7.
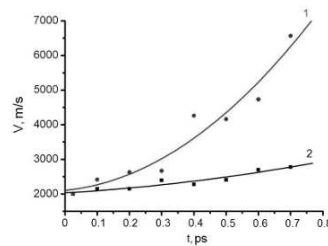
Figure 7: Dependence of the wave amplitude on time in the specimens with perfect (curve 1) and disordered (curve 2) crystal structure

Fig. 7 shows that the increase of the wave amplitude in specimen with the perfect crystallite structure is greater than the increase of the wave amplitude in specimen with the disordered one. Largely such behavior is connected with intensive energy dissipation due to disordered structure.

4   Summary

Based on the calculations performed, we can draw a conclusion that spherically converging waves generated in the specimens could give rise to structural rearrangements in the case of critical compressions at the wave front. As the intensity of pulse compression is increased, an increase in the amplitude of a spherically converging wave that reaches the center of the specimen is slowed down. The pattern of propagation of the spherical solitary waves depends both on the pulse loading intensity and on the size of the simulated crystallite. Probably specimens with a perfect crystal structure are more appropriate for obtaining a high pressure and temperature under uniform pulse compression as compared with disordered one.

References

[1] Kannel G.I., Razorenov S.V., Utkin A.V., Fortov V.E. Shock wave phenomena
in condensed matter// Moscow 1996. P.230-242. /in Russian

[2] Zolnikov K.P., Uvarov T.Yu., Psakhie S.G. Non-Linear Effect and Solitary-
Waves Induced by Intense Pulsed Affects. //Proceedings of 11-th Conference
on Radiation Physics and Chemistry of Condensed Matter Tomsk. (Ed. by
D.Vaisburd). 2000. V.1. P.349-351

[3] Psakhie S.G., Zolnikov K.P., Kadyrov R.I., Rudenskii G.E., Vassiliev S.A.,
Sharkeev Yu.P. About nonlinear mechanism of energy transformation at ion
implantations// Journal of Materials Science & Technology. 1999. V.15. N6.
P.1-2.

[4] Psakhie S.G., Zolnikov K.P., Korostilev S.U. About nonlinear matter response
under high rate deformation. Atomic level //PJTF 1995. V.21. N13. P.1-5./in
Russian

[5] Daw M.S., Baskes M.I. Embedded atom method: Derivation and application
to impurities, surfaces, and other defects in metals// Phys. Rev. 1984. V.B29.
N12. P.6443-6453.

[6] Foiles S.M., Baskes M.I., Daw M.S. Embedded-atom-method for the fcc metals
Cu, Ag, Au, Ni, Pd, Pt, and their alloys// Phys. Rev. 1986. V.B33. N12.
P.7983-7991.

N.A Parfenov, 2/1, pr. Akademicheskii, Tomsk, 634021, Russia
K.P. Zolnikov, 2/1, pr. Akademicheskii, Tomsk, 634021, Russia
S.G. Psakhie, 2/1, pr. Akademicheskii, Tomsk, 634021, Russia

Viscoelastic model of rubber compound and algorithm of definition of material constants using experimental data under complex cyclic loadings, including stress relaxation and creep

A. G. Pelevin   A. L. Svistkov   A. A. Adamov

pelevin@icmm.ru

Abstract

Rubbers are generally referred to as nanocomposites, which can be stretched to five or more times their initial length and return after unloading to nearly original state. The paper considers a structural phenomenological model of rubber based on the results of experiments on complex cyclic loadings of rubber specimens including relaxation and creep.

The material model is represented schematically in Fig. 1. Each element on this scheme corresponds to a specific constitutive equation. The scheme demonstrates the way in which these elements can be combined into a single system [1]. Separate blocks of the elements are used to model the behavior of specific parts of the material at the nanolevel .

The work introduces the algorithm for calculation of the model constants. A search for the desired constants is realized in a step-wise manner and incorporates refinement of the model at each step. The results obtained at the previous steps are kept unchanged at the next step. The experiments proposed in the work (cyclic loading with relaxation and creep) allow us to gain a deeper insight into viscoelastic behavior of rubbers.

The peculiarities of the model behavior were determined based on the analysis of the experimental data for two identical specimens. Each of the specimens was subjected to seven cycles of deformation including extension, relaxation, unloading to a zero stress and creep. At the first cycle of deformation the first specimen was stretched to two times and the second specimen - to three times of its original length. At next cycles the maximal elongations of the first specimen were 1.4, 1.5, 1.6, 1.7, 1.8, 1.9 and those of the second specimen were 1.5, 1.75, 2, 2.25, 2.5, 2.75. After completion of all cycles the specimens were stretched up to rupture. The elongation and unloading rate $| \dot{\lambda} |$ was equal to 1/30 sec^{-1}. Relaxation occurred during 30 minutes.
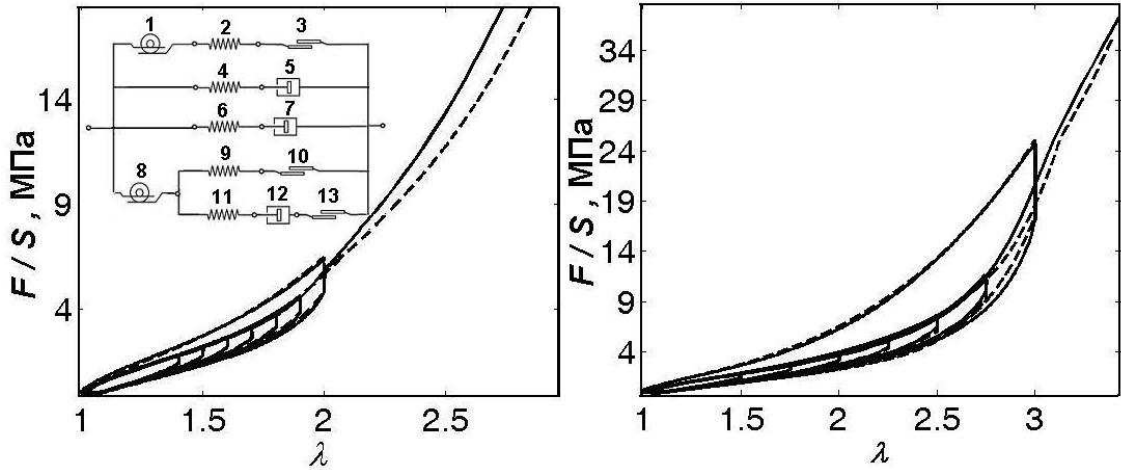
Figure 1: The sheme of model used for calculation and the results of two experiments. Solid line - experimental data, dashed line - theoretical predictions

Step 1

Find the constants, of the elastic element and the transmission ratio ν_1 in the transmission element numbered 1 for the second and next cycles of loading.

At this step we are dealing with the elastic properties of the model. For search of the constants we use only lower points of relaxation with elongation less than 1.8. The elastic properties of the specimen are defined by elastic and transmission elements of the scheme (Fig. 1). At lower points of relaxation the viscous processes have already completed which means that under these conditions the model under consideration provides the same mathematical description of the material behavior as does the model in Fig. 2. The transmission element in the model serves to increase the rate of deformation tensor by ν_k times and to decrease simultaneously the Cachy stress tensor by ν_k times $\mathbf{T}_k^{\text{left}} = \nu_k \mathbf{T}_k^{\text{right}}$, $\mathbf{D}_k^{\text{left}} = \frac{1}{\nu_k} \mathbf{D}_k^{\text{right}}$ where ν_k is the non-negative function of the state parameters (the transmission ratio), and k is the number of the transmission element [1]. The potential of second elastic element is represented by the following formula

$$w = w_2 = c_1^{(2)} \left(\sum_{i=1}^{3} (\lambda_i^{(2)})^2 - 3 \right) + c_2^{(2)} \left(\sum_{i=1}^{3} (\frac{1}{\lambda_i^{(2)}})^2 - 3 \right),$$

where $\lambda_1^{(2)}$, $\lambda_2^{(2)}$, $\lambda_3^{(2)}$ are values of stretch ratios for second elastic element, w is potential of material under cosideration. For the j-th elastic element, the material time derivative of the stretch tensor $\dot{\mathbf{V}}_j$ is calculated by equation:

$$\frac{2}{\nu_j} \mathbf{Y}_j^{0.5} \mathbf{D}_j \mathbf{Y}_j^{0.5} = \dot{\mathbf{Y}}_j - \mathbf{Y}_j \mathbf{W}_R^\mathsf{T} - \mathbf{W}_R \mathbf{Y}_j,$$

$$\nu_1$$

$\mathbf{W}_R = \dot{\mathbf{R}} \ \mathbf{R}^\mathsf{T}$, $\mathbf{Y}_j = \mathbf{V}_j^{\frac{2}{\nu_k}}$, $\nu_k > 0$, where $\mathbf{R}$ is the rotation tensor in the polar decomposition $\mathbf{F} = \mathbf{V}\mathbf{R}$ of the deformation gradient of the medium $\mathbf{F}$ into the
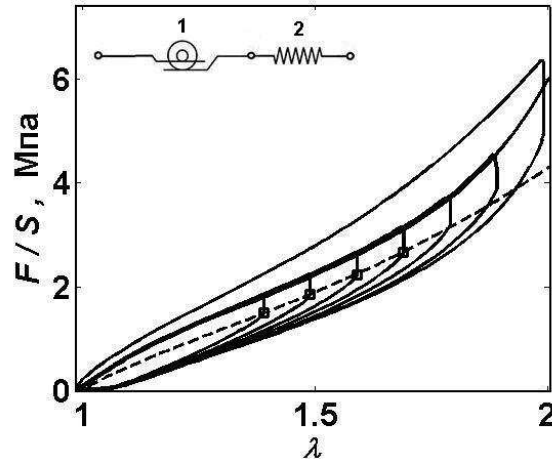
Figure 2: The scheme of model and the obtained results. Solid line - experimental data, dashed line - theoretical predictions, thick points - correspond to the state after cessation of relaxation processes

left stretch tensor $\mathbf{V}$ and the rotation $\mathbf{R}$; ν_k is the transmission ratio of the k-th transmission element connected on the left with the considered elastic element.

Step 2

Find the constant κ_3 and the relationship for ν_1 under first loading.
At this step we consider elastic-plastic properties of the specimen during the first cycle of loading. Plastic properties of the specimen are defined by the plastic element. All plasticity processes of the material occur only during the first cycle of loading. Variation of the elastic properties with the growth of the specimen damage is taken into account by changing the transfer number ν_1 of the transmission element. Thus we obtain a mathematical description of the material behavior shown in Fig. 3. Peculiarities of the plastic element behavior are defined by the proportional relation $\sqrt{\mathbf{D}_n \cdot \mathbf{D}_n} = \kappa_n \sqrt{\mathbf{D} \cdot \mathbf{D}}$, where n is the number of the plastic element. The symbol κ_n designates the non-negative function of state parameters [1].
The difference between loading and unloading is due to the influence of the plastic element and variation in the elastic properties during the first cycle of loading. During next cycles the elastic properties remain intact and therefore loading and unloading will fit the same curve and coincide with the unloading curve of the first cycle.

Step 3

Find two constants - ν_9, c_9 and the relationship κ_{10} for determining the fiber properties.
At this step we enter into the model the specimen properties resulted from formation
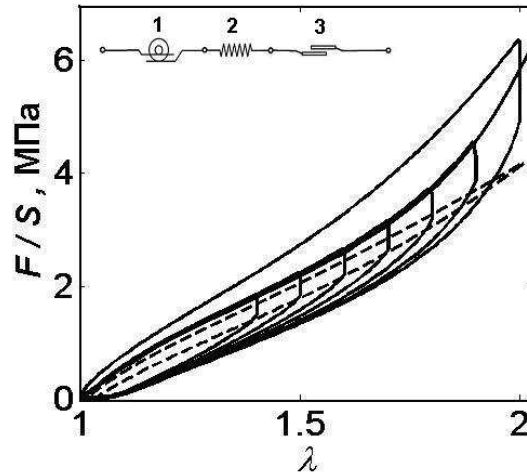
Viscoelastic model of rubber compound and algorithm of definition of material
constants using experimental data under complex cyclic loadings, including stress
relaxation and creep

Figure 3: The scheme of model and the obtained results. Solid line - experimental
data, dashed line - theoretical predictions, thick points - correspond to the state
after cessation of relaxation processes

of high-strength fibers between the filler particle aggregates of the rubber. To find
constants we use the first cycle of loading and all lower points of relaxation. Taking
into account the fact of fiber formation we obtain good coincidence of the lower
points of relaxation for elongation longer than 1.8. Then three elements describing
this process are added to the model (Fig. 4).

$$w = w_2 + w_9,$$

where w_9 the potential of the elastic element describing formation of fibers is ex-
pressed as

$$w_9 = \begin{cases} 0, & \text{when } \xi_9 < 0, \\ c_9 \xi_9, & \text{when } \xi_9 \geq 0. \end{cases}$$

where $\xi_9 = (\lambda_1^{(9)} - 1)(\lambda_2^{(9)} - 1)(\lambda_3^{(9)} - 1)$
The term w_9 has non-zero values only in the case when one of the stretch ratios of
the corresponding elastic element is larger than 1. With this technique, the model
can be used to take into account the fact that the generated fibers are only stretched,
while under compression they sag, exhibiting no resistance (Fig. 5)

Step 4

Find the constants of two Maxwell elements (four constants - $c_1^{(4)}$, $c_2^{(4)}$, $c_1^{(6)}$, $c_2^{(6)}$ for
4 and 6 elastic elements and two relationships η_k for 5 and 7 viscous elements).
At this step we add viscoelastic properties to the material. The constants are defined
using the whole deformation history of the specimen until rupture occurs. The model
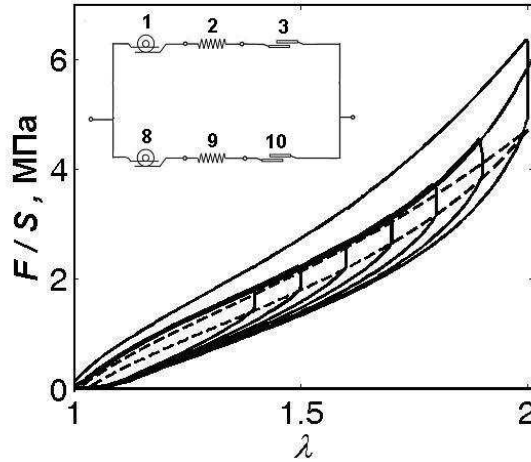is rearranged as follows:

Figure 4: The scheme of model and the obtained results. Solid line - experimental data, dashed line - theoretical predictions, thick points - correspond to the state after cessation of relaxation processes

The deviator of the Cauchy stress tensor of the k-th viscous element is calculated by the formula from the theory of nonlinear viscous fluids $\mathrm{dev}\,\mathbf{T}_k = 2\eta_k \mathbf{D}_k$, where the shear viscosity coefficient is the non-negative function of state parameters $\eta_k \geq 0$.

$$w = w_2 + w_4 + w_6 + w_9,$$

where w_4, w_6 the potential of the $4, 6$-th elastic elements is defined by the following formula:
$$w_j = c_1^{(j)}\left(\sum_{i=1}^3 (\lambda_i^{(j)})^2 - 3\right) + c_2^{(j)}\left(\sum_{i=1}^3 (\tfrac{1}{\lambda_i^{(j)}})^2 - 3\right), \quad j = 1, 2, 3$$

Step 5

Find constant c_{11} for 11 element and two relationships η_{12}, κ_{13} determining viscous properties of he fibers.
Here we add viscous properties to the fibers of the material. The model has taken the final form (Fig. 1).

$$w = w_2 + w_4 + w_6 + w_9 + w_{11},$$

where w_{11} the potential of the 11 elatic element describing formation of fibers is expressed as

$$w_{11} = \begin{cases} 0, & \text{when } \xi_{11} < 0, \\ c_{11}\xi_{11}, & \text{when } \xi_{11} \geq 0. \end{cases}$$

where $\xi_{11} = (\lambda_1^{(11)} - 1)(\lambda_2^{(11)} - 1)(\lambda_3^{(11)} - 1)$. The deviator of the Cauchy stress tensor of the 12-th viscous element is calculated by the formula from the theory of nonlinear viscous fluids $\mathrm{dev}\,\mathbf{T}_{12} = 2\eta_{12}\mathbf{D}_{12}$, where the shear viscosity coefficient is
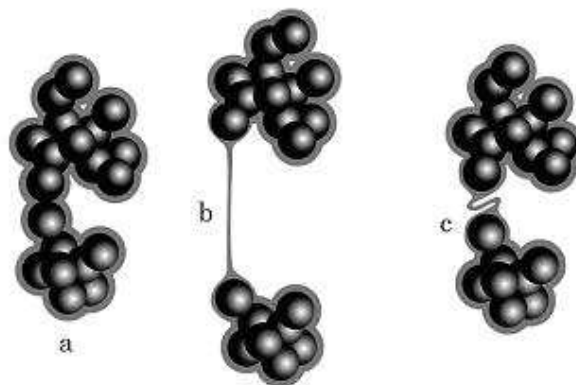
Figure 5: Illustration of fiber formation from the layers near filler particles in material stretching and fiber sag on external unloading
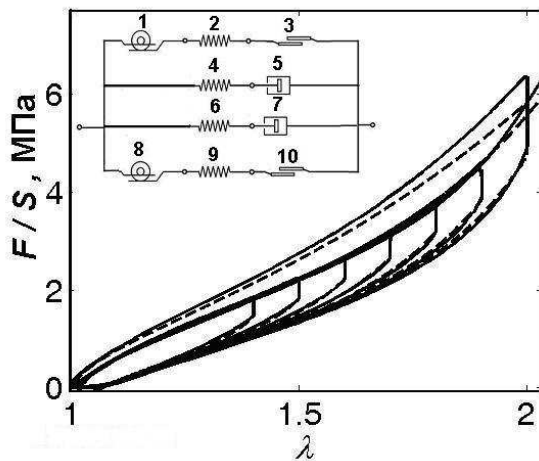
Figure 6: The scheme of model and the obtained results. Solid line - experimental data, dashed line - theoretical predictions, thick points - correspond to the state after cessation of relaxation processes

the non-negative function of state parameters $\eta_{12} \geq 0$. Peculiarities of 13-th plastic element behavior are defined by the proportional relation $\sqrt{\mathbf{D}_{13} \cdot \mathbf{D}_{13}} = \kappa_{13}\sqrt{\mathbf{D} \cdot \mathbf{D}}$,

Conclusion

A method based on a step-wise search for the model constants has been proposed to describe viscoelastic properties of rubbers. The system of constitutive equations takes into account the peculiarities of the material behavior at the structural level. The obtained theoretical results describe with sufficient accuracy the behavior of rubber.

References

[1] Svistkov A. L., Lauke B., Heinrich G. Modeling of viscoelastic properties and softening of rubber materials // Proceedings of 5th European conference "Constitutive models for rubbers" - Paris, 2007. - P. 113-118.

Axially symmetric problem of interaction between a soft orthotropic shell and a rigid body enveloped by the shell

Ekaterina Polyakova   Vitaly Lutov   Victor Chaikin
ekpol@mail.ru lutoww@mail.ru v_chaikin@mail.ru

Abstract

This study is focused on the research of the deflected mode of a soft orthotropic elastic shell enveloping a solid of rotation. It is supposed that one set of lines of orthotropy coincides with meridians of a body, and the another one - with its parallels, and that the stress-strain state of the shell is axially symmetric. The estimation of the deformed state of the shell is reduced to the minimization problem of energy functional. The solution of the latter problem is obtained by means of the projective method, being represented by a linear combination of a set of coordinate functions with some coefficients, subjected to definition. These coefficients are found from a system of non-linear equations by the method of continuation by parameter. The technique proposed is illustrated on a special case. The results of numeric calculations are presented.

1   Introduction

The problems concerning the interaction between soft shells and rigid bodies arise at designing of clothing, engineering of technical, household and medical goods [1], [2]. The soft elastic shells are used for protection of mobile and immobile detached connections of machines, devices, pipelines from external corrosiveness, toxic and other aggressive environments. The extensive use of soft shells of medical purpose, such as fixative elastic bands, bandages, compressing stockinet etc., is observed nowadays.
A variety of conditions of exploitation and functional demands to soft shell products cause the necessity of adequate design and proper choice of shell's materials. The last problem can be effectively solved on the basis of the results of stress-strain state analysis of the soft shell enveloping a rigid body [1], [3], [4], [5].
This paper presents an analysis of the deflected mode of a soft orthotropic elastic shell enveloping a solid of rotation. It is supposed that one set of lines of orthotropy coincides with meridians of a body, and the another one - with its parallels, and that the deflected mode of the shell is axially symmetric. The cylindrical coordinates of any shell's particle, corresponding to an undeformed state of the shell, are taken

as the material (Lagrangian) coordinates. In view of mentioned suppositions the definition of the strained state of the shell reduces to estimation of deformations of its meridians.

The extensional strains of meridional and parallel shell's elements are considered as the measures of the shell deformation. Thus, the potential energy of deformation is presented by the sum of deformation energies of the shell parallels and meridians, and in general terms, meridians and parallels are endowed with elasticity coefficients, depending on coordinates. The estimation of the deformed state of the shell is then reduced to the minimization problem of energy functional. The solution of the latter problem can be obtained by means of the projective method, being represented by a linear combination of a set of coordinate functions with some coefficients, subjected to definition. These coefficients are found from a system of nonlinear equations by the method of prolongation by parameter [6]. The technique proposed is illustrated on a special case. The results of numeric calculations are presented.

2 Basic assumptions. Potential energy of soft shell deformation

Let us assume that the soft shell in its undeformed state is a part of the sphere of radius ρ, symmetrical with respect to equatorial plane. The origin of rectangular Cartesian coordinate system $O_1\xi\eta\zeta$ coincide with the centre of the sphere; $O_1\xi$-axis and $O_1\eta$-axis belong to equatorial plane specified above (figure 1, a). At such choice of Cartesian system coordinates of the shell's points, laying on the upper and lower edges of the shell, are $\zeta = h$ and $\zeta = -h$ respectively. We assume that material (Lagrangian) coordinates any shell's particle coincide with its cylindrical coordinates φ and ζ when the shell is in undeformed state.

In view of mentioned suppositions it is possible to indicate the location of any shell's particle corresponding to Lagrangian coordinates (φ, ζ) by its radius-vector $\mathbf{r}_0$:

$$\mathbf{r}_0(\varphi, \zeta) = \sqrt{\rho^2 - \zeta^2} \cos \varphi \, \mathbf{i} + \sqrt{\rho^2 - \zeta^2} \sin \varphi \, \mathbf{j} + \zeta \mathbf{k}, \tag{1}$$

where $\mathbf{i}$, $\mathbf{j}$, $\mathbf{k}$ are basis vectors of system $O_1\xi\eta\zeta$.

Calculation of the coefficients of the first quadratic form yields

$$g_{11}^0 = \left(\frac{\partial \mathbf{r}_0}{\partial \zeta}\right)^2 = \frac{\rho^2}{\sqrt{\rho^2 - \zeta^2}}, g_{12}^0 = \frac{\partial \mathbf{r}_0}{\partial \zeta} \cdot \frac{\partial \mathbf{r}_0}{\partial \varphi} = 0, g_{22}^0 = \left(\frac{\partial \mathbf{r}_0}{\partial \varphi}\right)^2 = \rho^2 - \zeta^2. \tag{2}$$

Suppose that the soft shell of the specified type is pulled on a spherical surface of radius R, where $R \geq \rho$, and that the origin of Cartesian coordinate system coincide with the centre of the sphere (figure 1, b).

It the present study, it is accepted that meridians and parallels of the shell surface in its undeformed state after deformation are disposed on meridians and parallels of the sphere respectively. In this case the stress-strain state of the shell is axially symmetric, and the definition of the displacements of the shell's particles reduces to determination of function $z = z(\zeta)$.
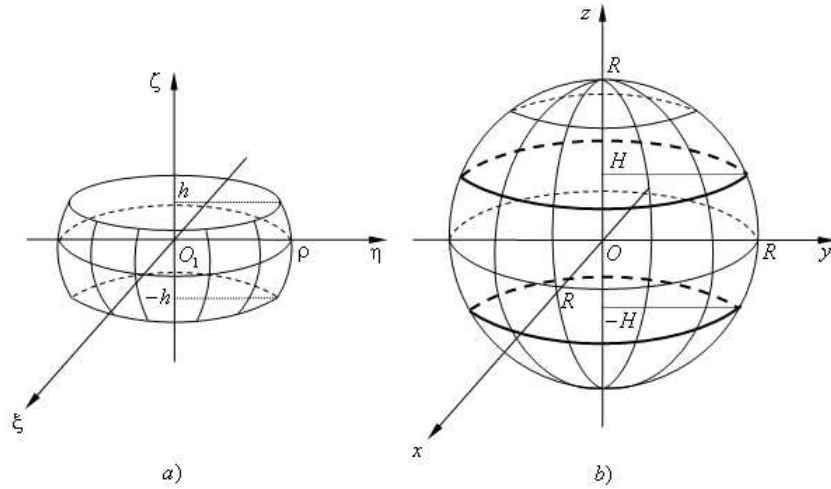
Figure 1. The soft shell in undeformed (a) and deformed (b) states.

For the sake of simplicity let us consider the deformed state of the shell to be symmetric with respect to plane $\mathsf{O}xy$, so that $z(\pm h) = \pm H$. Radius-vector $\mathbf{r}$ of arbitrary shell's particle, indicated by Lagrangian coordinates (φ, ζ), can be represented in the form

$$\mathbf{r}(\varphi, \zeta) = \sqrt{R^2 - (z(\zeta))^2} \cos \varphi \mathbf{i} + \sqrt{R^2 - (z(\zeta))^2} \sin \varphi \mathbf{j} + z(\zeta)\mathbf{k}. \tag{3}$$

The coefficients of the first quadratic form of the shell surface in the deformed state will be

$$g_{11} = \left(\frac{\partial \mathbf{r}}{\partial \zeta} \right)^2 = \frac{R^2}{R^2 - (z(\zeta))^2} \left(\frac{dz}{d\zeta} \right)^2, \tag{4}$$

$$g_{12} = \frac{\partial \mathbf{r}}{\partial \zeta} \cdot \frac{\partial \mathbf{r}}{\partial \varphi} = 0,$$

$$g_{22} = \left(\frac{\partial \mathbf{r}}{\partial \varphi} \right)^2 = \sqrt{R^2 - (z(\zeta))^2}.$$

The extension strains ε_1 and ε_2 of the elements lying on coordinate lines $\varphi = \mathsf{const}$ and $\zeta = \mathsf{const}$ are defined by expressions

$$\varepsilon_1(\zeta) = \sqrt{\frac{g_{11}}{g_{11}^0}} - 1 = \frac{R}{\rho} \left| \frac{dz}{d\zeta} \right| \sqrt{\frac{\rho^2 - \zeta^2}{R^2 - (z(\zeta))^2}} - 1, \tag{5}$$

$$\varepsilon_2(\zeta) = \sqrt{\frac{g_{22}}{g_{22}^0}} - 1 = \sqrt{\frac{R^2 - (z(\zeta))^2}{\rho^2 - \zeta^2}} - 1.$$

It is reasonable to suppose that in the deformed state the meridional elements are extended, therefore function $z = z(\zeta)$ is monotonically increasing. If the shell edges are free, we have $\varepsilon_1(\zeta)|_{\zeta = \pm h} = 0$, whence

$$\left(\frac{R}{\rho}\frac{dz}{d\zeta}|_{\zeta=\pm h}\right)^2 \frac{\rho^2 - h^2}{R^2 - (z(\pm h))^2} = 1. \tag{6}$$

We assume that the required function $z = z(\zeta)$ can be represented in the form

$$z(\zeta) = A\zeta + B\eta(\zeta), \tag{7}$$

where $\eta(\zeta)$ is a given odd function, A, B are coefficients, which have to be defined. From (6) we obtain

$$\left(\frac{R}{\rho}\right)^2 \left(A + B\frac{d\eta}{d\zeta}|_{\zeta=\pm h}\right)^2 \frac{\rho^2 - h^2}{R^2 - (Ah + B\eta(h))^2} = 1. \tag{8}$$

Let us introduce parameter $\mu = \frac{R-\rho}{\rho}$ and assume that $\eta(\zeta) = \zeta^3$. In this case equation (8) yelds

$$(1+\mu)^2(A + 3Bh^2)^2(\rho^2 - h^2) = (1+\mu)^2\rho^2 - (Ah + Bh^3)^2. \tag{9}$$

It is assumed that in undeformed state the soft shell material has the structure corresponding to orthogonal net with meshes, which sides lie on coordinate lines of the surface. Elasticity coefficients $k_1(\zeta)$ and $k_2(\zeta)$ of the elements, lying on coordinate lines $\zeta = \mathrm{const}$ and $\varphi = \mathrm{const}$ respectively, are supposed to depend on Lagrangian coordinate ζ.

The potential energy of deformation is given by

$$U = \pi\rho \int_{-h}^{h} (k_1(\zeta)\varepsilon_1^2(\zeta, A(B, \mu), B, \mu) + k_2(\zeta)\varepsilon_2^2(\zeta, A(B, \mu), B, \mu))d\zeta, \tag{10}$$

where $A(B, \mu)$ is considered to be defined from boundary condition (9).

3 Energy functional minimization

As far as the potential energy of deformation achieves minimum value in the equilibrium state of the shell on the sphere surface, one obtains the following equation for definition of $B(\mu)$:

$$\frac{dU}{dB} = 2\pi\rho \sum_{i=1}^{2} \int_{-h}^{h} k_i(\zeta)\varepsilon_i(\zeta, A(B, \mu), B, \mu)\left(\frac{\partial\varepsilon_i}{\partial A}\frac{\partial A(B, \mu)}{\partial B} + \frac{\partial\varepsilon_i}{\partial B}\right)d\zeta = 0. \tag{11}$$

The latter equality is fulfilled under $A = 1$, $B = 0$, $\mu = 0$, since in this case $\varepsilon_1(\zeta, A(B, \mu), B, \mu) = 0$ and $\varepsilon_2(\zeta, A(B, \mu), B, \mu) = 0$.

536

In order to obtain a differential equation for $B(\mu)$, one should carry out the derivative of (11) with respect to μ. Finally, we obtain the differential equation

$$\frac{dB(\mu)}{d\mu} = F(\mu) \tag{12}$$

under initial condition $B(0) = 0$, where

$$F(\mu) = \frac{D(\mu)}{C(\mu)}, \tag{13}$$

$$
\begin{aligned}
D(\mu) = &-\sum_{i=1}^{2} \int_{-h}^{h} k_i(\zeta) P(\zeta) \left[\left(\frac{\partial \varepsilon_i}{\partial A} \frac{\partial A}{\partial \mu} + \frac{\partial \varepsilon_i}{\partial \mu} \right) \left(\frac{\partial \varepsilon_i}{\partial A} \frac{\partial A(B,\mu)}{\partial B} + \frac{\partial \varepsilon_i}{\partial B} \right) + \right. \\
&+ \left. \varepsilon_i(\zeta, A, B, \mu) \left(\left(\frac{\partial^2 \varepsilon_i}{\partial A^2 \partial \mu} + \frac{\partial^2 \varepsilon_i}{\partial A \partial \mu} \right) \frac{\partial A}{\partial B} + \frac{\partial \varepsilon_i}{\partial A} \frac{\partial^2 A}{\partial A \partial B \partial \mu} + \frac{\partial^2 \varepsilon_i}{\partial A \partial B} \frac{\partial A}{\partial \mu} + \frac{\partial^2 \varepsilon_i}{\partial B \partial \mu} \right) \right] d\zeta,
\end{aligned} \tag{14}
$$

$$
\begin{aligned}
C(\mu) = &\sum_{i=1}^{2} \int_{-h}^{h} k_i(\zeta) P(\zeta) \left[\left(\frac{\partial \varepsilon_i}{\partial A} \frac{\partial A(B,\mu)}{\partial B} + \frac{\partial \varepsilon_i}{\partial B} \right)^2 + \varepsilon_i(\zeta, A, B, \mu) \times \right. \\
&\times \left. \left(\left(\frac{\partial^2 \varepsilon_i}{\partial A^2} \frac{\partial A}{\partial B} + \frac{\partial^2 \varepsilon_i}{\partial A \partial B} \right) \frac{\partial A}{\partial B} + \frac{\partial \varepsilon_i}{\partial A} \frac{\partial^2 A}{\partial B^2} + \frac{\partial^2 \varepsilon_i}{\partial A \partial B} \frac{\partial A(B,\mu)}{\partial B} + \frac{\partial^2 \varepsilon_i}{\partial B^2} \right) \right] d\zeta.
\end{aligned} \tag{15}
$$

The differential equation (12) can be easily solved numerically by the method of polygonal lines. Let $\mu_k = (k-1)\Delta\mu$, where $\Delta\mu$ is arbitrary small quantity, $k = 1, 2, \ldots$. The value $B(\mu_k)$ is determined by recurrence formula

$$B(\mu_{k+1}) = B(\mu_k) + F(\mu_k)\Delta\mu \tag{16}$$

under the assumption $\mu_1 = 0$, $B(\mu_1) = 0$.

4   Stress-strain state analysis

The next calculations consist in determination of $A(B(\mu), \mu)$, ε_1, ε_2, $\sigma_{11} = k_1\varepsilon_1$ and $\sigma_{22} = k_2\varepsilon_2$ on the base of equalities (9), (7), (5), that can be easily realized under arbitrarily defined characteristics of the shells materials.

Analytical results can be obtained for shells with nonstretchable meridians. In this case the solution of the problem is based on the analysis of the stress equilibrium equations [1] that in tangential stresses absence take the following form:

$$\frac{d}{dz}\left(\sigma_{11}\sqrt{R^2 - z^2}\right) + \sigma_{22}\frac{z}{\sqrt{R^2 - z^2}} = 0, \quad \sigma_{11} + \sigma_{22} = Rp. \tag{17}$$

Taking in consideration the latitude α on the sphere, one obtains

$$z = R \sin \alpha, \quad \frac{d}{dz} = \frac{d}{d\alpha} \Big/ \frac{dz}{d\alpha} = \frac{1}{R \cos \alpha} \frac{d}{d\alpha}. \tag{18}$$

Then the first of equilibrium equations (17) is expressed as

$$\frac{d}{d\alpha}(\sigma_{11} \cos \alpha) + \sigma_{22} \sin \alpha = 0. \tag{19}$$

Let us determine stresses σ_{22} under the assumption that the shell meridians are non-stretchable. Let be the distance from the sphere equator to some parallel, counted along the meridian. The latitude α depends on the sphere radius: $\alpha = s/\rho$ for the parallel formed by some thread of the undeformed shell and $\alpha = s/R$ for the parallel formed by the same thread after shell deformation. It's quite evident that the extension strain ε_2 of the thread mentioned above and corresponding stress σ_{22} are given by

$$\varepsilon_2 = \frac{R \cos(s/R)}{\rho \cos(s/\rho)} - 1 \tag{20}$$

and

$$\sigma_{22} = k_2 \varepsilon_2 = k_2 \left(\frac{R \cos(s/R)}{\rho \cos(s/\rho)} - 1 \right) = k_2(\alpha) \left(\frac{R}{\rho} \frac{\cos \alpha}{\cos(\alpha R/\rho)} - 1 \right). \tag{21}$$

Substitution of (21) into (19) and the following integration yield the quadrature expression for σ_{11}:

$$\sigma_{11} = \frac{1}{\cos \alpha} \int_{\alpha}^{L/R} k_2(\tau) \left(\frac{R}{\rho} \frac{\cos \tau}{\cos(\tau R/\rho)} - 1 \right) \sin \tau d\tau, \tag{22}$$

where L is the half of meridian length.

The latter integral (22) can be easily calculated numerically if stiffness $k_2(\alpha)$ is preassigned. The typical estimated functions $\sigma_{11}(\alpha)$ under $k_2(\alpha) = a + b\alpha^n$ for different n values are shown in Figure 2.

In order to define maximal value σ_{11}^{max} of meridional stresses one should substitute $\alpha = 0$ into (22). Figure 3 shows graphs of σ_{11}^{max} as a function of L/R under $k_2(\alpha) = a + b\alpha^n$ for different n values.

For sufficiently narrow shells approximate analytical estimates can be obtained. Particularly, if $k_2 = const$, it can be shown that

$$\sigma_{11}^{max} = \frac{1}{2} k_2 \left(\frac{R}{\rho} - 1 \right) \frac{L^2}{R^2}, \tag{23}$$

The second of equilibrium equations (17) under the defined σ_{11} and σ_{22} allows to determine easily the shell pressure on the sphere.
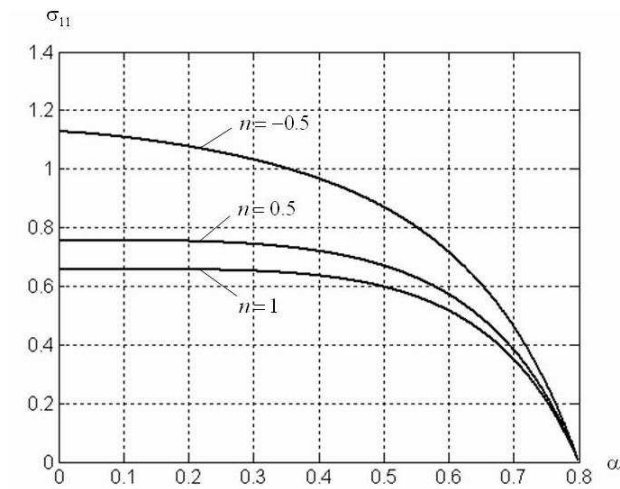
Figure 2. The relation $\sigma_{11}(\alpha)$ graphs.
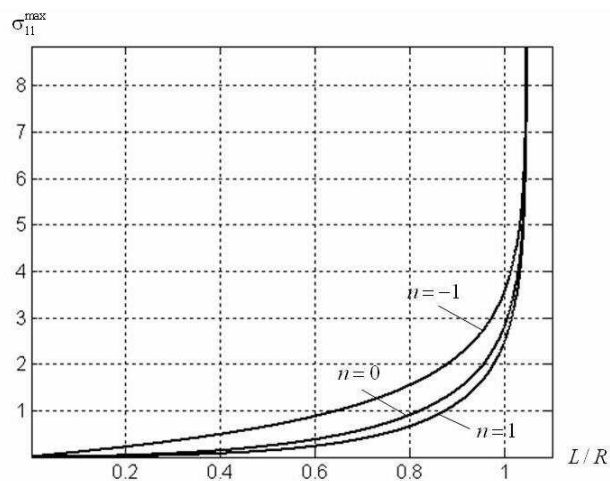
Figure 3. Graphs of maximal meridional stress σ_{11}^{max} as a function of L/R.

5   Conclusion

In this paper an analysis of stress-strain state of a soft orthotropic elastic shell enveloping a solid of rotation has been presented. The main results are the following.

1. The technique of calculation of axially symmetric stress-strain state of the shell pulled on the defined surface of a rigid body has been proposed. The estimation of the deformed shell state has been reduced to the minimization problem of energy functional.

2. For the special case of the soft shell pulled on a spherical surface calculation relations for stresses and the shell pressure on the sphere have been obtained. The results of numeric calculations have been presented.

Acknowledgements

References

[1] Polyakova E.V., Chaikin V.A. Applied problems of mechanics of soft shells and fabrics. Monograph. St.-Petersburg, SPSUTD, 2006, 193 p. (Russian)

[2] Shirihin V.N., Ionova V.F., Shalnev O.V., Kotlyarenko V.I. Elastic mechanisms and constructions. Monograph. Irkutsk, IrSTU, 2006, 286 p. (Russian)

[3] Wempner G., Demosthenes G. T. Mechanics of solids and shells: Theories and approximations. CRC PRESS, 2003. 521 p.

[4] Steigmann D. J. Elements of the theory of elastic surfaces // Nonlinear Elasticity: Theory and Applications / Ed. by I.B. Fu, R.W. Ogden. Cambridge: Cambridge Univ. Press, 2001. P. 268– 304.

[5] Libai A., Simmonds J. G. The nonlinear theory of elastic shells. 2nd ed. Cambridge: Cambridge Univ. Press. 1998. 560 p.

[6] Grigoluk E.I., Shalashilin V.I. Problems of nonlinear deformation. Method of prolongation by parameter in nonlinear problems of mechanics of deformable rigid body. Moscow, Nauka, 1988. 232 p. (Russian)

Ekaterina Polyakova, Vitaly Lutov, Victor Chaikin, St. Petersburg State University of Technology and Design, Bolshaya Morskaya St. 18, St.-Petersburg, 191186, Russia

The self-synchronization of two coaxed unbalanced vibroexciters with inner degree of freedom and the "asleep" gyroscope problem

Mary A. Potapenko

m.potap@mail.ru

Abstract

The question about possibility of provision of synphase rotation of two unbalanced rotors of vibration plant in selfsynchronizing regime is discussed. In this case under consideration only the antiphase rotating. This rotating is a natural stable regime. The possibility of using for this aim the vibroexciters with additional degree of freedom of rotors is studied. The simulation data and the well-known problem of "asleep" gyroscope is compared.

1   Description Of The Plant

We consider a free solid body fixed by means of springs with certain characteristics and realizing plane oscillations. On the bearer two coaxed unbalanced masses with one rotating degree of freedom are fixed. Within each of debalances a definite additional mass which can oscillate along the debalance's axis is fixed.Fig.1
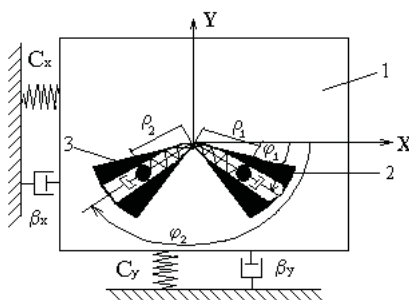
Figure 1: A vibrostand with two debalances having mobile centers of mass

Thereby the vibrostand has two translational degrees of freedom, x and y, each i - debalance having one rotational φ_i and one translational degree of freedom, ρ_i defined by displacement of the additional mass from the axis of rotor. Let us consider the equation of motion obtained in [1] for a plant with two vibroexciters, each having two inner degrees of freedom:

$$[I + m_0\varepsilon^2 + m(r + \rho_s)^2 + m\sigma_s^2)]\ddot{\varphi}_s + K_s(\dot{\varphi}_s - \omega) + 2m[(r + \rho_s)\dot{\rho}_s + \sigma_s\dot{\sigma}_s]\dot{\varphi}_s-$$

$$-[m_0\varepsilon + m(r + \rho_s)](\ddot{x}\sin\varphi_s + \ddot{y}\cos\varphi_s) - m\sigma_s(\ddot{x}\cos\varphi_s - \ddot{y}\sin\varphi_s)+$$

$$+m[(r + \rho_s)\ddot{\sigma}_s - \sigma_s\ddot{\rho}_s] = 0 \qquad\qquad (\ s = 1, 2\ )$$

$$M\ddot{x} = \sum_{i=1}^{2}[m_0\varepsilon + m(r + \rho_i)](\ddot{\varphi}_i\sin\varphi_i + \dot{\varphi}_i^2\cos\varphi_i)-$$

$$-m\sum_{i=1}^{2}[\ddot{\rho}_i - \sigma_i\ddot{\varphi}_i - 2\dot{\sigma}_i\dot{\varphi}_i]\cos\varphi_i+$$

$$+m\sum_{i=1}^{2}[(\dot{\rho}_i - \sigma_i\dot{\varphi}_i)\dot{\varphi}_i + \ddot{\sigma}_i + \dot{\rho}_i\dot{\varphi}_i]\sin\varphi_i - \beta_x\dot{x} - C_x x$$

$$M\ddot{y} = \sum_{i=1}^{2}[m_0\varepsilon + m(r + \rho_i)](\ddot{\varphi}_i\cos\varphi_i - \dot{\varphi}_i^2\sin\varphi_i) + m\sum_{i=1}^{2}[\ddot{\rho}_i - \sigma_i\ddot{\varphi}_i-$$

$$-2\dot{\sigma}_i\dot{\varphi}_i]\sin\varphi_i + m\sum_{i=1}^{2}[(\dot{\rho}_i - \sigma_i\dot{\varphi}_i)\dot{\varphi}_i + \ddot{\sigma}_i + \dot{\rho}_i\dot{\varphi}_i]\cos\varphi_i - \beta_y\dot{y} - C_y y$$

$$\ddot{\rho}_s + \beta_\rho\dot{\rho}_s + \omega_\rho^2\rho_s = \sigma_s\ddot{\varphi}_s + 2\dot{\sigma}_s\dot{\varphi}_s + (r + \rho_s)\dot{\varphi}_s^2 - (\ddot{x}\cos\varphi_s - \ddot{y}\sin\varphi_s)$$

$$\ddot{\sigma}_s + \beta_\sigma\dot{\rho}_s + \omega_\sigma^2\sigma_s = -(r + \rho_s)\ddot{\varphi}_s - 2\dot{\rho}_s\dot{\varphi}_s + \sigma_s\dot{\varphi}_s^2 + (\ddot{x}\sin\varphi_s + \ddot{y}\cos\varphi_s)$$

where $\beta_\rho = \frac{h_\rho}{m}; \beta_\sigma = \frac{h_\sigma}{m}; \ \omega_\rho^2 = \frac{C_\rho}{m}; \ M = M^0 + 2m_0 + 2m, \ \omega_\sigma^2 = \frac{C_\sigma}{m}.$

Here m_o is additional movable mass in the unbalanced mass; m is the mass of the debalance; M is the mass of the whole plant; ε is the eccentricity or the value of displacement of the center of masses of the unbalanced mass from its axis of rotation; r is length of an unstressed spring inside the rotor; ρ is the displacement of the movable mass from the rest or the movable mass radius in the stabilized regime; I is the central moment of inertia of the whole system; x is the abscissa of the bearer or the horizontal displacement; y is the ordinate of the bearer or the vertical displacement; ω_ρ is angular velocity (frequency of the mass's intrinsic oscillations) of mobile mass; ω is synchronizable (steady) angular velocity of the rotor; φ is the angle of the rotation of rotor from the rest; β_x, β_y are coefficients of the damping of oscillations of the bearer along corresponding axes; K is the coefficient of electric damping of the motor; ω_i is the intrinsic (angular) velocity of the unbalanced mass; σ_s are numbers that equal 1 or -1; the first case corresponds to the debalance's rotation in positive direction and the second case corresponds to the clockwise direction.

2 The Stationary Regime of Motion of The System

Now, investigate the case when the rotor has only one inner degree of freedom, related with the possibility of displacement of an additional mass radially and elastic and demping forces of all springs of the system are taken into account.

For the stationary synpfase regime of motion of equal vibroexciters, i.e. $\varphi_1 = \varphi_2 = \omega t$; $\rho_1 = \rho_2 = \rho = \mathrm{const}$, the system of equations assumed the form

$$
\begin{aligned}
& [m_0\varepsilon + m(r+\rho_s)](\ddot{x}\sin\omega t + \ddot{y}\cos\omega t) = K(\omega - \omega_s) \\
& M\ddot{x} = 2[m_0\varepsilon + m(r+\rho)]\omega^2\cos\omega t - \beta_x\dot{x} - C_x x \\
& M\ddot{y} = 2[m_0\varepsilon + m(r+\rho)](-\omega^2\sin\omega t) - \beta_y\dot{y} - C_y y \\
& \omega_\rho^2\rho = (r+\rho)\omega^2 - (\ddot{x}\cos\omega t + \ddot{y}\sin\omega t)
\end{aligned}
\tag{1}
$$

where $\omega_\rho^2 = \dfrac{C_\rho}{m}$; $M = M^0 + 2m_0 + 2m$

For the stationary regime we receive from the second and third equations:

$$
x = \frac{2(m_0\varepsilon + m(r+\rho))\omega^2(C - M\omega^2)}{(M\omega^2 - C)^2 + \beta^2\omega^2}\cos\omega t + \frac{2(m_0\varepsilon + m(r+\rho))\omega^3\beta}{(M\omega^2 - C)^2 + \beta^2\omega^2}\sin\omega t
\tag{2}
$$

$$
y = \frac{2(m_0\varepsilon + m(r+\rho))\omega^3\beta}{(M\omega^2 - C)^2 + \beta^2\omega^2}\cos\omega t + \frac{2(m_0\varepsilon + m(r+\rho))\omega^2(M\omega^2 - C)}{(M\omega^2 - C)^2 + \beta^2\omega^2}\sin\omega t
$$

After the differentiation and the substituting from the second equation for stationary regime we can express ρ :

$$
\rho = \frac{r\omega^2[(M\omega^2 - C)^2 + \beta^2\omega^2] - 2\omega^4(m_0\varepsilon + mr))(M\omega^2 - C)}{(\omega_\rho^2 - \omega^2)[(M\omega^2 - C)^2 + \beta^2\omega^2] + 2\omega^4 m(M\omega^2 - C)}
\tag{3}
$$

This equation is an analytical expression for the coordinate ρ of the additional mass in the steady-state regime.

3 The Expression for The Displacement of The Movable Mass

Changing the nominator and the denominator of the fraction and taking into account that $\frac{m_0}{M}$ and $\frac{m}{M}$ are small, where as $\frac{C}{\omega^2}$ and $\frac{\beta}{\omega^2}$ tend to zero, we receive

$$
\rho \approx r\frac{1}{\frac{\omega_\rho^2}{\omega^2} - 1}, \qquad \omega_\rho \neq \omega
\tag{4}
$$

From here one can see, that for $\omega_\rho < \omega$ value of ρ is positive, i.e. the movable mass move from the axe of rotation, but for $\omega_\rho > \omega$ approach to it.

On the Fig. 2 the changing during the time difference of the phases of rotating and displacement of center of the mass of bearer without additional masses in debalances is shown. The curves correspond to these parameters: $M_0 = 2$ kg, $m_0 = 1$ kg, $r = 0.01$m, $\varepsilon = 0.035$m, $\beta_x = 84$, $C_x = C_y = 12.6\,\frac{H}{m}$, $\omega_s = 300\,\frac{rad}{c}$.
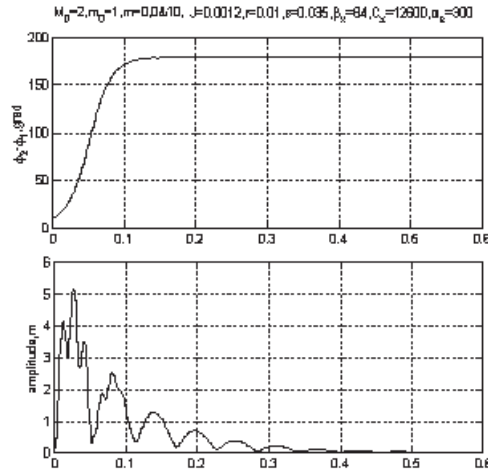
Figure 2: The behaviour of the plant without the movable masses

4 The Conditions of Temporary Stability by Blekchman-Sperling

Let us return to the first equation (1) and transform it identically using $\frac{1}{1+x} \approx 1-x$. As a result we receive

$$\omega \approx \omega_s\{1 - \frac{2\beta[m_0\varepsilon + m(r + \rho)]^2}{M^2K}\} \tag{5}$$

Combining (3) and (5) express ω

$$\omega^2 \approx \frac{\rho}{r + \rho}\omega_\rho^2\{1 - \frac{2\beta[m_0\varepsilon + m(r + \rho)]^2}{M^2K}\}^2 \tag{6}$$

Check if the 3rd condition of temporary stability [1]

$$\omega^2 \left[1 + \frac{2(m_0\varepsilon + m(r + \rho))^2 - 4mM(r + \rho)^2}{MI^O}\right] < \omega_\rho^2 \tag{7}$$

Then, after substitution and identical transformations [2]
we receive:

$$1 - \frac{4m(r + \rho)^2}{I^O} < \frac{r + \rho}{\rho} \tag{8}$$

which always fulfils, i.e. $m, I^0 > 0$.

To satisfy the 1st and the 2nd conditions that

$$\omega < \frac{\omega_\rho}{\sqrt{e'^*}}$$

$$\omega < \frac{\omega_\rho\sqrt{M}}{\sqrt{M - 2m}}$$

choose an appropriate ω_ρ and other initial data.

It is always possible to meet 1st condition: $\omega > \omega_\rho$ and 2nd condition of temporary stability by choosing an appropriate ω_ρ and other initial data.
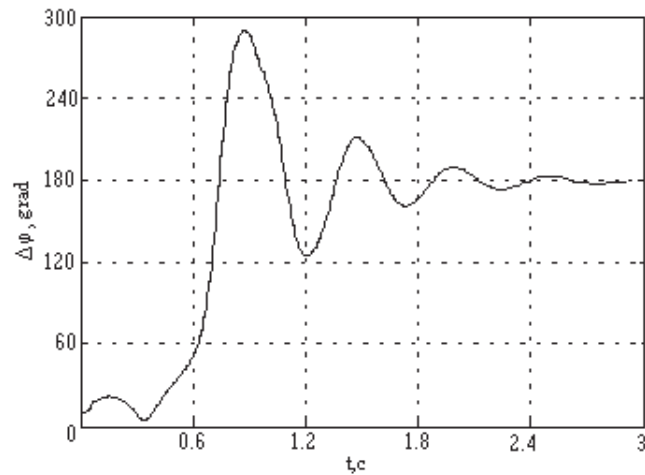
Figure 3: The behaviour of the plant with inner degrees of freedom in debalances

On the Fig. 3 the results of the modeling with same initial data as Fig.2 with additional movable masses $m = 0.1; \varepsilon = 0.035$ in the debalances are presented.

5 An Analogy with the Problem of "asleep" gyroscope

These results are resemble with the solution of the classical problem of "asleep" gyroscope or the rotating shell.
In these systems the stable is provided also by means of gyroscope members, without it the gyroscope and shell are unstable.
In classical textbook [3] the necessary condition of stable of "asleep" gyroscope is reduced:

$$I_3^2 \omega_z^2 > 4lGI_1 \tag{9}$$

Here ω_z is the projection of angle velocity to the axe z; I_1, I_3 are the main moments of inertia; G is the force of gravity; l - the distance from the center of mass C to point of rest.
Usually it's assumed, that satisfaction of the condition (9) provide the stable of the system. If the condition breaks then the shell is down as a result of decreasing of velocity of rotating ω_z for the forces of friction.

Conclusion

The system of six non linear differential second order equations, describing the behaviuor of two coaxed undebalanced vibroexciters with inner degree of freedom, fixed on softlyisolated rigid body is researched by numerical methods. It is shown that the unstable synphase regime of selfsynchronizing with two debalances transforms into temporary (hyroscope) stability by means of the introduce the inner degree of freedom in each of the debalances. The comparison with results of the classical problem "asleep" gyroscope is presented.

References

[1] Blekhman I.I. Selected Topics in Vibrational Mechanics, World Scientific, 2004.

[2] Potapenko M.A.The study of self-synchronization of vibroexciters with inner degree of freedom using numerical methods, Physcon'09, September 1-4, University of Catania at Sicily, Italy, 2009.

[3] Lojcjanskij L.G., Lurie A.I. The Theoretical Mechanics, Moscow, 1957.

Mary A. Potapenko, Kuibitsheva str, 22-8, S.Petersburg, Russia.

Elastic tube subjected to pressure and general corrosion

Yulia G. Pronina

DearJuly@gmail.com

Abstract

The stress in real metal structures can vary with time even under permanent external load. It takes place due to dimensional changes of structure elements induced by surface corrosion. This paper is concerned with the uniform mechanochemical corrosion of the linearly elastic cylindrical tube subjected to external and internal pressure. Assuming that changes of inner and outer radii of the tube are quasi-static, we base our investigation on G. Lame's solution. Corrosion rate depends on many factors. In neutral and alkalescent environments or when tension is less than certain threshold, mechanical stress has no influence on corrosivity. In the circumstances, values of stress-components at any instant are determined by G. Lame's formulae with given laws of corrosive wear in time. In other cases, according to most experimental data, the rate of general corrosion is linear with stress (when stress increases beyond a given threshold) and is inversely as exponent of time (if closed oxide layer leads to the inhibition of corrosion). Then the problem is reduced to the ordinary differential equation. Analytical solutions of the basic equation in different cases are found.

Taking into account synergetic interaction of general corrosion with mechanical stresses, the life-time of a tube can be assessed. For the criterion of the onset of breaking the approach of the chosen limiting stress in the pipe can be used. However buckling or chance failure can occur before a fracture stress is reached. To determine the reason and the instant of failure, estimating functions are suggested. Various functions are introduced to assess the strength margin, stability factor, damage accumulation, accident risk and so on. The calculations performed in proposed manner have shown that increasing the exponent b of inhibition of corrosion leads to considerable prolongation of the service life of a tube.

1 Introduction

Most damage issues in machines and structures are due to material degradation induced by an operating environment. It is well known that corrosion activity may be intensified by mechanical stresses. Such corrosion is said to be a mechanochemical one. The research in this area has been conducted by numerous authors. This

paper is concerned with surface mechanochemical corrosion. A comprehensive review of models and calculations of structures taking into account corrosive wear was given e.g. in [1], [2]. One of the first in the field is the article [3] concerned with mechanochemical corrosion of a thin-walled cylindrical shell under longitudinal force. In the work [4] the lifetime of a loaded pipe has been assessed under the assumption of the exponential dependence of corrosion rate on stress. According to [2],[5] corrosion rate depends on stress linearly. Using this relation the corrosive wear of a nonlinearly elastic tube subjected to pressure and temperature has been simulated in book [2]. In this paper the equal-rate mechanochemical corrosion of a thick-walled tube subjected to internal and external pressure is discussed [6]. The analitical solution of the problem of a linearly elastic tube under pressure and longitudinal force has been found in [7].

2 Problem statement

The surface corrosion of an elastic tube subjected to internal p_r and external p_R pressure is investigated. Inner and outer tube radii at initial instant $t = 0$ are denoted by r_0 and R_0 ($r_0 < R_0$). The action of the ends of the cylinder is not taken into account. Changes of the tube radii are assumed to be quasi-static. Corrosion rates at inner and outer boundaries are given by expressions [2],[5]:

$$v_r = \frac{dr}{dt} = \frac{d[r_0 + \delta_r]}{dt} = [a_r + m_r\sigma_1(r)]\exp(-bt) \quad \text{when } |\sigma_1(r)| \geq |\sigma_r^{th}|, \qquad (1)$$

$$v_R = -\frac{dR}{dt} = -\frac{d[R_0 - \delta_R]}{dt} = [a_R + m_R\sigma_1(R)]\exp(-bt) \quad \text{when } |\sigma_1(R)| \geq |\sigma_R^{th}| \quad (2)$$

correspondingly. Here b, a_r, a_R, m_r, m_R are observable quantities, and $a_r = v_r^0 - m_r\sigma_r^{th}$, $a_R = v_R^0 - m_R\sigma_R^{th}$; σ_r^{th}, σ_R^{th} are threshold stresses (as a matter of fact, which are different for traction and compression); v_r^0, v_R^0 are the initial corrosion rates at $|\sigma_1(r)| < |\sigma_r^{th}|$, $|\sigma_1(R)| < |\sigma_R^{th}|$; σ_1 is a maximum principal stress. It is necessary to assess a life-time of tube concerned.

3 Basic equations

The problem of a tube under pressure has been disscused by numerous writers including G. Lame. The stress-components are expressed, by reference to polar coordinates ρ, θ, by the equations

$$\sigma_{\theta\theta}(\rho) = -p_r - \frac{p_R - p_r}{R^2 - r^2}\left(R^2 + \frac{r^2R^2}{\rho^2}\right), \qquad (3)$$

$$\sigma_{\rho\rho}(\rho) = -p_r - \frac{p_R - p_r}{R^2 - r^2}\left(R^2 - \frac{r^2R^2}{\rho^2}\right), \qquad (4)$$

$$r \leq \rho \leq R, \quad 0 \leq \theta < 2\pi.$$

The maximum principal stress is the circumferential one $\sigma_1 = \sigma_{\theta\theta}$. When $r = 0$, $p_r = 0$, $p_R = p$ or $p_r = p_R = p$, there is a homogeneous stress $\sigma_{\theta\theta} \equiv \sigma_{\rho\rho} \equiv -p$ in a tube irrespective of corrosion.

In neutral and alkalescent environments or when load is less than threshold, stress has no influence on corrosion rate. In that cases the stress-components at any instant are determined by the above equations (3), (4) with given lows of $r(t)$, $R(t)$.

Now let the absolute values of stresses $\sigma_1(r)$, $\sigma_1(R)$ be greater than the thresholds and $\sigma_1(r) \neq \sigma_1(R)$. The greatest tension is the circumferential tension at the inner surface $\rho = r$. So we are to observe its amount $\sigma_{\theta\theta}(r) = \sigma_1(r)$. It will be convenient to rewrite the formula (3) in the form

$$\sigma_1(r) = \sigma_{\theta\theta}(r) = p_r \frac{\eta^2 + 1}{\eta^2 - 1} - 2p_R \frac{\eta^2}{\eta^2 - 1}, \tag{5}$$

$$\sigma_1(R) = p_r \frac{2}{\eta^2 - 1} - p_R \frac{\eta^2 + 1}{\eta^2 - 1} = \sigma_1(r) - p_r + p_R, \tag{6}$$

where

$$\eta = \frac{R}{r} = \frac{R_0 - \delta_R}{r_0 + \delta_r}. \tag{7}$$

The formulae (1), (2) and (6) give

$$Rm_r + rm_R = m_R \left(r_0 + \frac{a_r}{-b} \left[\exp(-bt) - 1 \right] \right) + m_r \left(R_0 - \frac{A_R}{-b} \left[\exp(-bt) - 1 \right] \right) \tag{8}$$

where

$$A_R = a_R - m_R (p_r - p_R). \tag{9}$$

On differentiating the expression (5) with respect to t, and using (1), (2), (7)–(9), we can obtain the ordinary differential equation for $\sigma_1(r)$ [6]

$$\frac{d\sigma_1(r)}{dt} = \frac{\sqrt{[\sigma_1(r) + p_r][\sigma_1(r) - p_r + 2p_R]}}{p_r - p_R} \times$$

$$\times \frac{[A_R + m_R \sigma_1(r)]\sqrt{\sigma_1(r) - p_r + 2p_R} + [a_r + m_r \sigma_1(r)]\sqrt{\sigma_1(r) + p_r}}{\left[m_R \left(r_0 - \frac{a_r}{-b} \right) + m_r \left(R_0 + \frac{A_R}{-b} \right) \right] \exp(bt) + m_R \frac{a_r}{-b} - m_r \frac{A_R}{-b}} \times$$

$$\times \left[m_r \sqrt{\sigma_1(r) + p_r} + m_R \sqrt{\sigma_1(r) - p_r + 2p_R} \right]. \tag{10}$$

The initial conditions to be satisfied at $t = 0$ are

$$\sigma_1(r)|_{t=0} = \sigma_1^0(r) = p_r \frac{\eta_0^2 + 1}{\eta_0^2 - 1} - 2p_R \frac{\eta_0^2}{\eta_0^2 - 1}, \qquad \eta_0 = \frac{R_0}{r_0}. \tag{11}$$

4 Solutions of the basic equations

The integral of the equation (10), satisfying the conditions (11), is

$$t = -\frac{1}{b} \ln \left\{ 1 - b\frac{m_R r_0 + m_r R_0}{m_R a_r - m_r A_R} \left(\exp\left[(m_R a_r - m_r A_R)\, F(\sigma_1(r))\right] - 1 \right) \right\},$$
(12)

where

$$F(\sigma_1(r)) = (p_r - p_R) \int_{\sigma_1^0(r)}^{\sigma(r)} \frac{1}{\sqrt{[\sigma_1 + p_r][\sigma_1 - p_r + 2p_R]}} \times$$

$$\times \frac{1}{[A_R + m_R \sigma_1[\sqrt{\sigma_1 - p_r + 2p_R} + [a_r + m_r \sigma_1]\sqrt{\sigma_1 + p_r}} \times$$

$$\times \frac{d\sigma_1}{m_r\sqrt{\sigma_1 + p_r} + m_R\sqrt{\sigma_1 - p_r + 2p_R}}.$$

When corrosion is one-sided the solution can be simplified. For example, if $p_R = p > 0$, $p_r = 0$, $a_r = m_r = 0$ (external corrosion) the result may be written in the form

$$t = -\frac{1}{b} \ln\{1 - bF(\sigma_1(r))\} \quad \text{when} \quad b \neq 0,$$

$$t = F(\sigma_1(r)) \quad \text{when} \quad b = 0,$$

where
— if $\quad 2p > |A_R/m_R|$

$$F(\sigma_1(r)) = -\frac{r_0}{m_R\,(A_R/m_R - 2p)} \left(\sqrt{\frac{\sigma_1(r)}{\sigma_1(r) + 2p}} - \eta_0 + \frac{p}{\sqrt{A_R/m_R\,(A_R/m_R - 2p)}} \times \right.$$

$$\left. \times \left[\ln \frac{\sqrt{A_R/m_R\,(A_R/m_R - 2p)\,\sigma_1[\sigma_1 + 2p]} + \sigma_1\,(p - A_R/m_R) - pA_R/m_R}{\sigma_1 + A_R/m_R} \right]_{\sigma_1^0(r)}^{\sigma_1(r)} \right),$$

— if $\quad 2p < \left|\dfrac{A_R}{m_R}\right|$

$$F(\sigma_1(r)) = -\frac{r_0}{m_R\,(A_R/m_R - 2p)} \left(\sqrt{\frac{\sigma_1(r)}{\sigma_1(r) + 2p}} - \eta_0 + \frac{p}{\sqrt{A_R/m_R\,(A_R/m_R + 2p)}} \times \right.$$

$$\left. \times \left[\ln \frac{\sqrt{A_R/m_R\,(A_R/m_R + 2p)\,\sigma_1[\sigma_1 + 2p]} + \sigma_1\,(p - A_R/m_R) - pA_R/m_R}{\sigma_1 + A_R/m_R} \right]_{\sigma_1^0(r)}^{\sigma_1(r)} \right).$$
(13)

Here it is necessary to take the real branch of the function $\ln(x)$. It is to be noted that in that case $m_R < 0$ since $\sigma_1(r) < 0$.

5 Tube thickness determination

The solutions of the basic equations give us the time-to-stress relation. Using the equation (7), (8) and reverse formula (5) we can derive the tube thickness dependence on t and $\sigma_1(r)$:

$$h = R - r = \left\{ m_r R_0 + m_R r_0 - \frac{1}{b} \left[\exp(-bt) - 1\right](m_R a_r - m_r A_R) \right\} \times$$

$$\times \frac{\sqrt{\sigma_1(r) + p_r} - \sqrt{\sigma_1(r) - p_r + 2p_R}}{m_r \sqrt{\sigma_1(r) + p_r} + m_R \sqrt{\sigma_1(r) - p_r + 2p_R}}$$

and the dependences of radii r and R on t and $\sigma_1(r)$.

When stress has no influence on corrosion rate:

$$v_r = v_r^0 \exp(-b_r t), \qquad v_R = v_R^0 \exp(-b_R t),$$

the pipe wall thickness is determined by the expression

$$h = R_0 - r_0 - \frac{v_r^0}{b_r}[1 - \exp(-b_r t)] - \frac{v_R^0}{b_R}[1 - \exp(-b_R t)].$$

If the rates of external and internal corrosion are constant we obtain

$$h = R_0 - r_0 - (v_R + v_r)t.$$

6 Lifetime assessment

Taking into account synergetic interaction of general corrosion with mechanical stresses, lifetime of a tube may be assessed. Failure can be due to a variety of reasons. To determine the reason and the instant of failure, estimating functions are suggested. Following the L. Kachanov approach [8], different kinds of damage are represented by scalar functions changing in the interval $[0, 1]$ (or $[-\infty, 1]$) and mounting to 1 in the moments of fault related to concrete criteria. To assess the strength margin, functions of the type $\Pi_s = \dfrac{f(\sigma, \epsilon)}{\sigma_s} \leq 1$ may be used. For the maximum stress criterion we can write $\Pi_s = \dfrac{\sigma_1(t)}{\sigma_s(t)}$, where $\sigma_s(t)$ is limiting stress that may change in time. In that case if $\sigma_s = \text{const}$ the time to rupture is evaluated by the formulae (12)–(13) with the σ_s for $\sigma_1(r)$.

Functions to assess the stability factor are of the form $\Pi_{cr} = \dfrac{\sigma_1(t)}{\sigma_{cr}(t)} \leq 1$, where σ_{cr} is buckling stress depending on the tube sizes and mechanical quantities. For example, in the case of thin-wall medium-length cylindrical shell under external pressure, the estimating functions can be given by expression $\Pi_{cr} = \dfrac{\sigma_1(r)L}{Ch}\sqrt{\dfrac{R}{h}}$, where L is length, R is mean radius, h is thickness of the shell, C is constant depending on grip conditions and mechanical properties [9]. The amounts of $\sigma_1(r)$, R and h at any time t are given by the above equations. Stability of thin-walled shells under

conditions of the corrosive action have been investigated by many scientists, e.g. [10], [11].

Damage being due to different reasons, to assess damage accumulation numerous functions can be proposed. For instance, according to Bailey's principle, the time to destruction t^* is determined by the equation $\Pi_d = \int\limits_0^{t^*} \dfrac{dt}{\tau[\sigma(t)]} = 1$, where $\tau[\sigma(t)]$ is the working life of the material under stress σ.

Furthermore, failure may be determined apparently by accidental circumstances. For such assessment we can introduce estimating function as being equal to probability i.e. accident risk. It is to be emphasized that unreliability function depends on other estimating functions.

The graphs of all these functions are plotted and compared with each other. The curve being the first to run up to 1 determines the most probable reason of breakdown and the durability of an item. Calculations performed in proposed manner have shown that increasing the exponent b of inhibition of corrosion leads to considerable prolongation of the service life of a tube. When b is relatively high corrosion can practically stop before any critical state is reached.

Acknowledgements

References

[1] I. G. Ovchinnikov, Yu. M. Pochtman. Calculation and rational design of structures subjected to corrosive wear (review). Materials Science. V. 27. N 2, 105–116, 1992.

[2] G. A. Naumova, I. G. Ovchinnikov. Strength calculations of compound frameworks and pipeline structures with taking into account corrosion damages [in Russian]. Saratov State University, Saratov, 2000.

[3] V. M. Dolinskii. Calculation of stressed pipes subjected to corrosion. Khim. Neft. Mashinostr., No. 2, 18–21, 1967.

[4] E. M. Gutman, R. S. Zainulin, A. T. Shatalov, et al. Strength of gas industry pipes under corrosive wear conditions [in Russian]. Nedra, Moscow, 1984.

[5] P. A. Pavlov, B. A. Kadyrbekov, V. A. Kolesnikov. Strength of steels in corrosive media [in Russian], Nauka, Alma-Ata, 1987.

[6] Yu. G. Pronina. Estimation of the stability of an elastic tube under the pressure of corrosive environments. Vestnik St. Petersburg University [in Russian], Ser. 10, N 3, 55-63, 2006.

[7] Yu. G. Pronina. Lifetime prediction for the elastic tube subjected to uniform surface corrosion under the longitudinal force and pressure [in Russian]. Deformation and fracture of materials, N 2, 41–44, 2009.

[8] L. M. Kachanov. Introduction to continuum damage mechanics. Martinus Nijhoff Publishers, Dordrecht, Netherlands, 1986.

[9] A. S. Vol'mir. Stability of elastic systems [in Russian]. Fizmatgiz, Moscow, 1963.

[10] V. G. Karpunin, S. I. Kleshchev, and M. S. Kornishin. Endurance of plates and shells under conditions of the corrosive action of a medium, in: Strength and Endurance of Structures [in Russian]. Naukova Dumka, Kiev, 35–44, 1980.

[11] E. Gutman, J. Haddad, R. Bergman. Stability of thin-walled high-pressure vessels subjected to uniform corrosion. Thin-Walled Structures, 38, 43-52, 2000.

Yulia G. Pronina, Universitetskii pr. 35, 198504, Saint-Petersburg, Russia

Two-liquid system in a rotating cylinder under transversal vibrations

A. N. Salnikova   N. Kozlov   M. Stambouli

salnikova@pspu.ru

Abstract

Mean dynamics of two immiscible liquids of different density in the rotating horizontal cylinder performing oscillations perpendicular to the axis of rotation is investigated. Experiments are carried out at frequency of vibrations comparable with the rotation frequency when the influence of the Coriolis force on liquid oscillations is essential. Outstripping and lagging azimuthal motion of the interface in respect to the cavity is found. It is generated by an inertial wave arising in a resonant way. The azimuthal motion leads to excitation of an axial liquid current and to an axisymmetric change of the cylindrical form of the light liquid column. In case of intensive vibrations the relief in the form of hills directed along the rotation axis is formed on the interface due to Kelvin–Helmholtz instability. Self-oscillations – periodical formation and collapse of the relief – are investigated in the system under certain conditions. It is shown, that the dynamics of two-liquid system is substantially determined by the ratio of vibration and rotation frequencies.

1   Introduction

Vibrational dynamics of multiphase systems under rotation acquires peculiar properties due to the influence of inertia forces, especially Coriolis force. Study of centrifuged liquid layer at simultaneous action of rotation and transversal vibrations [1] finds out an intensive azimuthal motion of the liquid in the cavity frame. This motion is generated by inertial wave arising in the system in a resonant way. Analogical effect exerts in a differential rotation of light solid in liquid [2] and light granular matter in liquid [3] in rotating horizontal cylinder performing transversal vibrations. In the latter work a transformation of the circular form to a poligonal one is also observed. Study of rotating two-liquid system under the longitudinal vibrations [4] shows that vibrations are capable to provide generation of intensive mean flows in a liquid and, hence, they give possibility to manage mass transfer – process which is crucial in many chemical technologies. In present work the dynamics of two immiscible liquids in a rotating horizontal cylinder subjected to vibration normal to the rotation axis is studied experimentally.
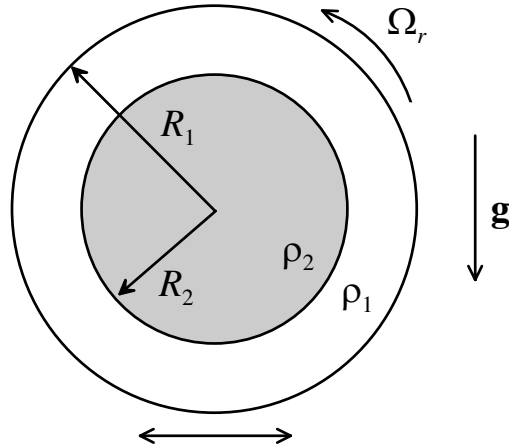
Figure 1: Experimental model

2   Experimental procedure

Experiments are carried out with plexiglass cylinders of radius $R_1 = 2.5$ cm and different lengths: $L = 15.2, 7.4, 4.2$ cm. Two pairs of immiscible liquids are investigated: fluorinert ($\rho_1 = 1.85$ g/cm^3, $\nu_1 = 0.02$ St) and castor oil ($\rho_2 = 0.96$ g/cm^3, $\nu_2 = 17$ St), water and transformer oil ($\rho_2 = 0.88$ g/cm^3, $\nu_2 = 0.60$ St). The interfacial tension of the first pair of liquids $\sigma = 6.0 \pm 0.3$ dyne/cm, the second pair – $\sigma = 38.0 \pm 3.0$ dyne/cm. Description of an experimental setup could be found in [3].

A cavity filled with the immiscible liquids in the ratio 1:1 is fixed on a table of the vibrator and is set in rotation. After transition of the liquids in centrifuged state (Fig.1, R_2 – radius of the interface) transversal vibrations are set. At definite Ω_r and constant amplitude b the vibration frequency Ω_v is fluently increased (decreased) by step of $0.7 - 3.1 \text{s}^{-1}$. For an establishment of a stationary mode of the liquid motion a delay of few minutes is made before measurements for each step. Speed of rotation and parameters of vibrations vary in intervals $\Omega_r = 0 - 0.94$ rad/s, $\Omega_v = 0 - 188$ s^{-1}, $b = 1.8 - 5.5$ mm.

Rate of the azimuthal motion of the phases interface in the cavity frame $\Delta\Omega = 2\pi/T$ is studied. Rubber particles of the size about 1 mm are situated on the interface to visualize the streams. The period T of rotation of the markers in the cavity system is measured by means of a stop-watch in stroboscopic light with frequency Ω_r. The error of measurement of T does not exceed 5 percent.

The form of the light liquid column is studied on photos, in particular the effective diameter of the column D in the central part of the cavity and near to the end walls is determined. The measurement error of D does not exceed 6 percent. Photos are received for water and transformer oil in a cavity of length $L = 4.2$ cm. On the pictures the cavity rotates counter-clockwise.
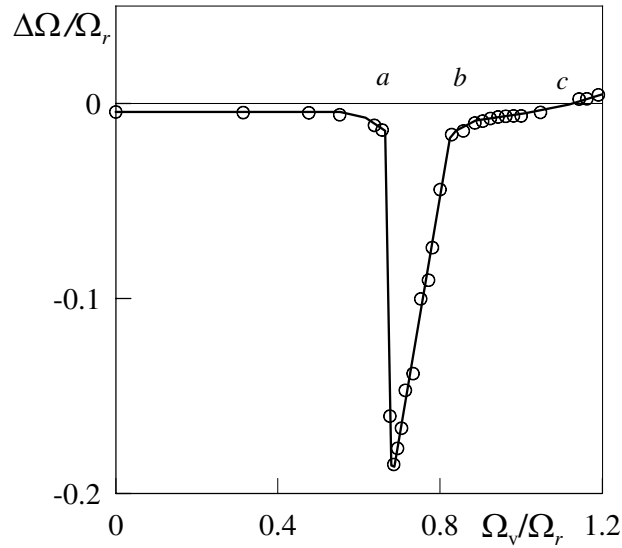
Figure 2: Relative speed of the light liquid column versus the dimensionless frequency

3 Experimental results

At rest the less dense liquid is in the upper part of the cavity. At rotation the heavy liquid is distributed near the cylindrical cavity wall under the action of centrifugal inertia force, and light liquid forms the coaxial cylinder of diameter D_0 in the central part of the cavity. The light liquid column makes the circular oscillations induced by gravity in the cavity frame. At that time the interface moves slowly in the direction of the oscillations, i.e. opposite to the cavity rotation. The dependence of relative speed of the light liquid column $\Delta\Omega/\Omega_r$ on dimensionless frequency of vibrations Ω_v/Ω_r (fluorinert and castor oil, $L = 15.2$ cm, $\Omega_r = 65.9$ rad/s, $b = 2.2$ mm) is presented on Fig.2; negative values $\Delta\Omega/\Omega_r$ on the graph correspond to the lagging motion of the interface, $\Delta\Omega/\Omega_r = 0$ – to the solid-state rotation of the liquid together with the cavity.

Under the action of transversal vibrations of small intensity the speed of the motion and the cylindrical shape of the column remain. The amplitude of circular oscillations of the light liquid column increases with vibration frequency. At achievement of critical frequency the intensity of the lagging motion of the interface sharply grows (Fig.2 point a). The light liquid column gets a shape of a dumbbell: it is narrowed in the middle part of the cavity and extends to the end-walls (Fig.3 a). Reorganization takes several seconds. Markers form a ring in the bottleneck of the light liquid column, usually in the middle of the cavity. The whole column performs intensive circular oscillations with the largest amplitude in the middle part of the cylinder. The area of contact of a column with an end face increases, on the Fig.3 c (view from the end-wall side) one can see a translucent strip of a liquid – the thin layer of light liquid existing just near to an end face.

In cavities of different lengths the liquid behaves in the similar way. However in case of a short cavity all effects are more pronounced, in particular, narrowing of
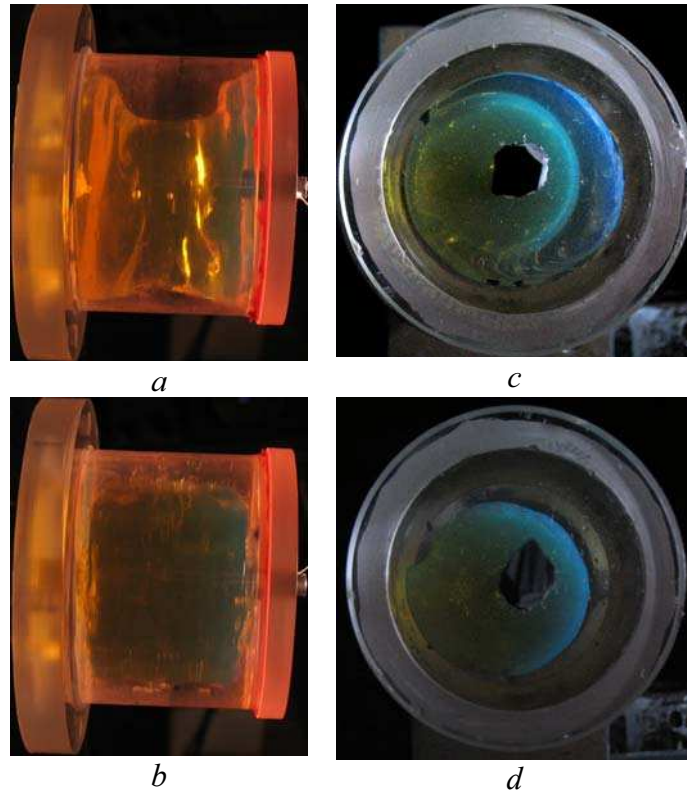
Figure 3: Interface shape at different frequencies of vibration

the light liquid column in the middle part of the cavity.

On Fig.4 is shown the dependence of dimensionless effective diameter of the light liquid column D/D_0 in the central part of the cavity (points 1) and near the end-walls (2) on relative frequency of vibrations Ω_v/Ω_r (water and transformer oil, $L = 4.2$ cm, $\Omega_r = 78.5$ rad/s, $b = 2.5$ mm). Areas I, II, III differ both by the type of motion and the interface shape. At lagging motion (area I) the diameter of the light liquid column in the middle part of the cavity is less than the diameter of a column near the end-walls.

The amplitude of the column oscillations decreases with the vibration frequency, the lagging motion is slowed down (Fig.2). The diameter of the light liquid column in the central part of the cavity increases, and diminishes near to the end-walls. At further increase of the frequency the intensity of lagging motion becomes the same, as in the absence of vibrations (Fig.2 point b, Fig.4 II). The weak lagging motion induced by gravity (oscillating in the cavity frame) is observed in some range of vibration frequencies close to the frequency of rotation. The interface takes the cylindrical form: points 1 and 2 in the area II coincide.

Study of the thresholds of the appearance and disappearance of the vibrational lagging motion versus the rotation rate finds out the growth of critical vibration frequency with increase of Ω_r.

At achievement of the critical vibration frequency the column of the light liquid again starts to perform circular oscillations, this time – in the direction of the cavity
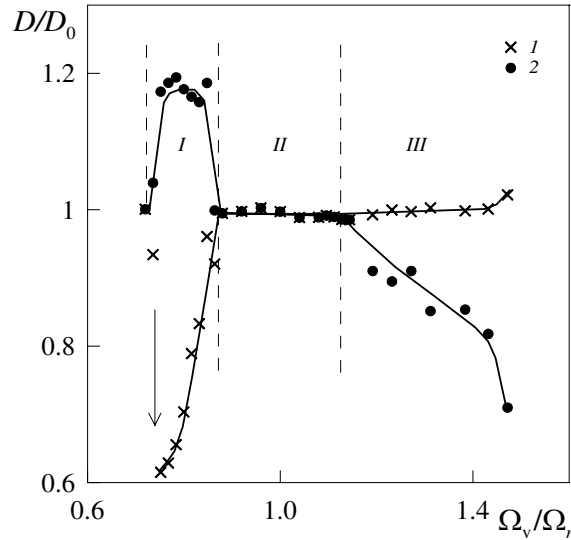
Figure 4: Dimensionless effective diameter of the light liquid column in the central part of the cavity (point *1*) and near the end-walls (*2*) versus the relative frequency of vibrations

rotation. On the interface of the liquids the outstripping motion is excited (Fig.2 *c*). The change of the shape of the light liquid column is observed which is opposite to the case of the lagging rotation – narrowing towards the end-walls (Fig.3 *b*, and Fig.4 *III*). Narrowing occurs in a small area directly near the end-walls, so the small mass of the light liquid withdrawn from the end-walls cannot change the diameter of the rest of the column essentially. It explains the insignificant increase in diameter of the light liquid column in the center while the diameter of the column at the end-walls considerably diminishes (Fig.4 *III*). Intensity of oscillations and speed of the outstripping motion increase with vibration frequency. At fast rotation of the liquid column the situation is possible when the light liquid does not adjoin to the cavity end-walls.

A transition from 2D motion of the liquid to three-dimensional one is specific for the resonance corresponding to the outstripping motion. The markers move on a spiral trajectory that complicates the measurement of their speed. For this reason on Fig.2 only the beginning of the outstripping motion is presented, when the speed is low and markers move on a circular trajectory.

In resonant areas when the oscillations of the light liquid column reach the high intensity, an azimuthal wave with a crest is formed on the interface. The slopes of the crest have a different steepness. Depending on the direction of the wave propagation in the cavity frame two shapes of the interface are observed. They differ by a relative position of the crest slopes (Fig.3 *c*, *d*). With growth of the relative rotation speed the height of the crest increases.

At $\Omega_v \approx 2\Omega_r$ the interface gets the shape close to cylindrical, and continues to rotate intensively in the direction of the cavity rotation. However with a small increase of frequency ($\Omega_v > 2\Omega_r$) a 2D relief appears on the interface in case of the large amplitudes of vibration (Fig.5). The relief has a shape of hills extended along the

rotation axis (Fig.5 a). At first the form of normal cross-section of the light liquid column is approached to an oval that corresponds to relief with two hills. With Ω_v the number of hills increases. At large amplitude of vibrations the height of hills reaches significant value (Fig.5 b) in this case the self-oscillations manifesting in periodic relief formation and destruction are observed. Reaching the certain height, the hills suddenly disappear, the interface becomes cylindrical. But in one or two seconds a relief with the same quantity of hills appears again.
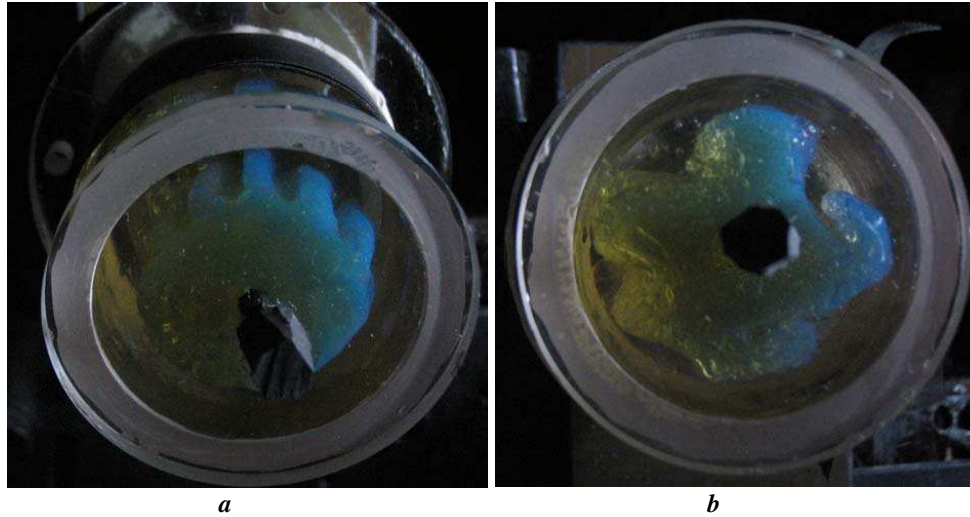

a $\qquad\qquad\qquad\qquad\qquad\qquad\qquad$ b

Figure 5: Quasisteady relief on the interface

The curves of the threshold excitation (Fig.6 points 1) and disappearance (2) of lagging flows for water and the transformer oil, presented on the plane of dimensionless parameters $\Omega_r R_2^2/\nu_2$, Ω_v/Ω_r, demonstrate the increase of relative frequency of vibrations with the dimensionless speed of rotation. The hysteresis in transitions is not found.

The intensive lagging and outstripping flow of liquid is characterized by nonlinear transformation of the shape of the wave, manifesting itself in the formation of a specific crest with the slopes of different steepness (Fig.3). The similar phenomenon is revealed at studying the vibrational dynamics of a centrifuged liquid layer [1] where the two-dimensional azimuthal wave extending on a free surface of a liquid is observed as a hill on the liquid surface.

The comparison of azimuthal inertial waves with known gravitational ones [7] demonstrates their analogy. In particular the crest is formed in the front part of the wave if one consider its propagation concerning the cavity along the surface of the heavy liquid. Thus the direction of mean flow of liquid coincides with the direction of wave propagation.

The transport of the markers along the interface towards its central area in case of lagging motion specifies the existence of axial streams of the liquid. Near the interface the flows are directed from the end faces of the cavity towards the center. In case of outstripping rotation of interface the axial flows have an opposite direction. Axial flow is generated in the viscous Ekman layers arising near the end faces of the cylinder at the presence of relative rotation [8]. The Coriolis force causing radial

motion of the liquid in the Ekman layers also determines the shape of the interface.
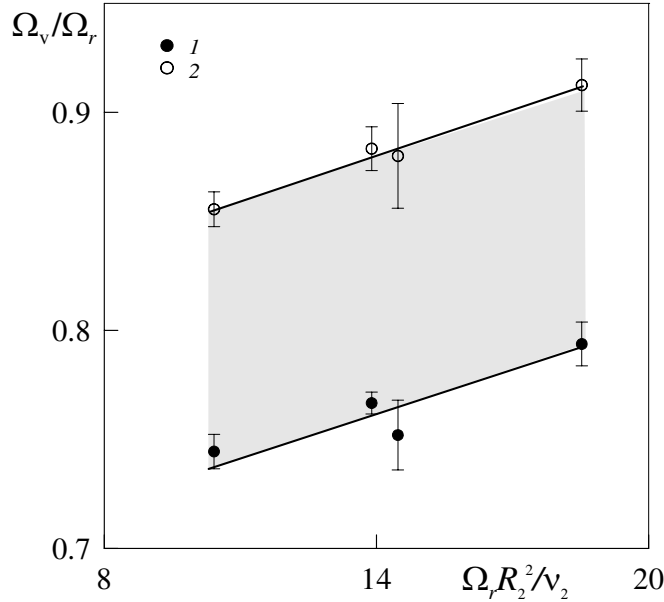

Figure 6: The area of resonant excitation of lagging streaming

The quasisteady relief existing at rather high frequencies of vibrations $\Omega_v/\Omega_r > 2$ is formed as a result of instability of tangential discontinueties of velocity on the interface of immiscible liquids of different density (Kelvin–Helmholtz instability) [9]. The relief excitation occurs in case of intensive oscillation of liquids near the interface which are possible in resonant conditions.

The resonant frequency depends on the form of the interface, the eigenfrequencies of oscillations of the layers of different geometry are various. The consequence of this dependence are self-oscillations of the interface, occurring in the case when the relief achieves the large height and the shape of the interface border strongly differs from the initial, cylindrical one. The significant change of the interface shape results in the displacement of resonant area, that is the reason of the relief disappearance. However, as soon as the relief disappears and the column of a light liquid gets the cylindrical shape the system comes back to the resonant area and the conditions for existence of the relief appear again.

4 Conclusion

The dynamics of immiscible liquids of different density in the rotating horizontal cylinder subjected to transversal vibrations is experimentally investigated. The lagging and outstripping azimuthal flows of two liquids interface in the cavity frame, which are generated by an inertial azimuthal wave, are revealed and arise in the cavity in the resonant way. The direction of flow is determined by the relative frequency of vibrations Ω_v/Ω_r. The lagging current exists at $\Omega_v/\Omega_r < 1$, the outstripping one – at $\Omega_v/\Omega_r > 1$. The intensive azimuthal flow is accompanied

with the axisymmetrical change of the shape of the light liquid column and with the axial flows which are caused by action of viscous Ekman layers.

It is revealed that at intensive vibrations the relief with the shape of the hills extended along the axis of rotation is formed on the interface. The Kelvin–Helmholtz instability lays in the basis of the relief formation. The spatial period of the relief decreases with the increase of the vibration frequency. Under the certain conditions the self-oscillations of the system manifesting itself in the periodic formation and destruction of the relief are observed.

Acknowledgements

References

[1] Ivanova A.A., Kozlov V.G. and Polezhaev D.A. Vibrational dynamics of a centrifuged fluid layer // Fluid Dynamics. 2005. V. 40. No. 2. P. 297-304.

[2] Kozlov V.G. and Kozlov N.V. Vibrational dynamics of a light body in a liquid-filled rotating cylinder // Fluid Dynamics. 2008. Vol. 43. No. 1, p. 9-19.

[3] Salnikova A., Kozlov N., Ivanova A., Stambouli M. Dynamics of rotating two-phase system under transversal vibration // Microgravity Sci. Technol. 2009. V. 21. P. 83-87.

[4] Ivanova A.A. and Sal'nikova A.N. Dynamics of a two-fluid system in a rotating horizontal cylinder under longitudinal vibration // Fluid Dynamics. 2007. V. 42. N 3. P. 369-375.

[5] Batchelor G. K. An introduction to fluid dynamics. M.: Mir, 1973. 760 p.

[6] Phillips O.M. Centrifugal waves // J. Fluid Mech. 1960. V. 7. P. 340-352.

[7] Lighthill J. Waves in fluids. M.: Mir, 1981. 598 p.

[8] Greenspan H.P. The theory of rotating fluids. L.: Gismeteoizdat, 1975. 304 p.

[9] Ivanova A.A., Kozlov V.G. and Evesque P. Interface dynamics of immiscible fluids under horizontal vibration // Fluid Dynamics. 2001. V. 36. No 3. P. 362-368.

Kozlov Nick, Perm State Pedagogical University, Perm, Russia
Salnikova A.N., Perm State Pedagogical University, Perm, Russia
Stambouli M., Ecole Centrale Paris,France

Computer modelling for initiation and synchronization processes of oscillation of ciliated cells' cilia

Elena N. Selivanova

elle_s@list.ru

Abstract

Mucociliary transport is an important way of clearance of respiratory passages from infectious agents and minor particles. Based on theoretical researching, experiments, mathematical and computer models of ciliated cells' motion behavior development of new methodologies for treating diseases of respiratory passages are possible. Considering this, the development of mathematical and computer models, sufficiently describing the physical properties and characteristics for this kind of structures, becomes relevant. In this case object of modeling is single ciliated cell of human respiratory passages' epithelium. Now it is known that cilia's motions are synchronized within ciliated cell and moreover within group of cells. Motion of cilia provides mucociliary transport. Changing in cilia's motion parameters leads to problems in transport's working and in the following might lead to respiratory diseases. Cilia are surrounded with inter-cilia fluid, produced by ciliated cells. On the surface of this fluid there is layer of mucus, produced by beaker cells and glands of mucous membrane. Type of cilia's movement can be described as paddle motion. This motion can be divided in two phases - effective stroke and recovery stroke. During phase of effective movement cilia get straight and their ends dive into mucus layer. And mucus and upper part of inter-cilia fluid are moving at this moment. There are different theories concerning the mechanism of cilia's movement coordination. They can be divided in three groups: neural-alike way of excitation wave transfer, process of cilia's interaction viscous fluid and mechanism of wave transfer triggered by contact of cilia.

This work represents and simulates mechanism of motion initiation and synchronization due to performance of membrane transport systems and calcium ion as coordinating agent of this process. Cilium is presented as mathematical model of system consisted of solid bodies, connected with flexible linkages. Signal for conformation changing of specific protein (dynein) is increase of calcium ion concentration at the bottom of the cilia (kinetosome). Calcium concentration is regulated by calcium pumps (proteins) that are integrated into the cells membrane. Signal for synchronization of cilia's beatings is supposed to be calcium concentration changing in the inter-cilia fluid (and concerned with wave-alike movements of fluid). Apparently there are parts of

ciliated cells that are responsible for direction and frequency of cilia's beating
and that work according to signals of neural system. These signals can be
presented as local short-time changing of electric potential of cell's membrane
at the cilia, defining the paddle motion.

1 Structure of cilium

Cilium is flexible membrane extensions of the cell. It is surrounded with inter-cilia
fluid, produced by ciliated cells. The thickness of its layer is about $7 - 10\mu m$.[2] On
the surface of this fluid there is layer of mucus (thickness is $0.5 - 2\mu m$)[2], produced
by beaker cells and glands of mucous membrane.

Cilium consists of central bundle of microtubules, called the axoneme, in which nine
outer doublet microtubules surround a central pair of singlet microtubules. This
characteristic "9 + 2" arrangement of microtubules is seen when the axoneme is
viewed in cross section with the electron microscope. Each doublet microtubule
consists of A and B tubules. The bundle of microtubules comprising the axoneme is
surrounded by the plasma membrane. Regardless of the organism or cell type, the
axoneme is about $0.25\mu m$ in diameter, but it varies greatly in length, from a few
microns to more than $2mm$ [4].

At its point of attachment to the cell, the axoneme connects with the basal body
(kinetosome). It's cylindrical structure consisting nine triplet microtubules. Each
triplet contains one complete A tubule, fused to the incomplete B tubule, which in
turn is fused to the incomplete C tubule. Basal body of cilium plays an important
role in initiating the growth of the axoneme.

Within the axoneme, the two central singlet and nine outer doublet microtubules
are continuous for the entire length of the structure. Doublet microtubules, which
represent a specific protein - tubulin, are found only in the axoneme. Permanently
attached to the A tubule of each doublet microtubule is an inner and an outer row
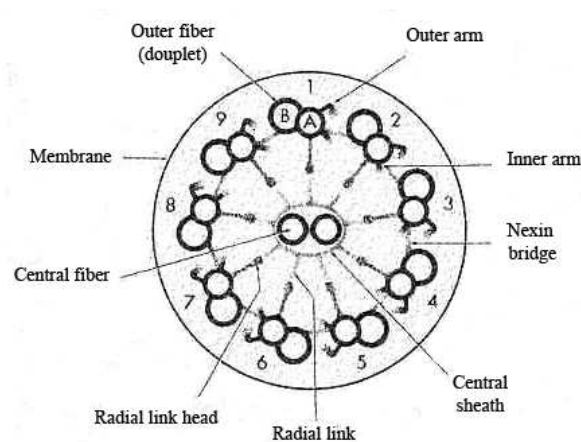of dynein arms.

Figure 1: Sturcture of cilium

Ciliary beating are produced by controlled sliding of outer doublet microtubules.
Dynein arms generate the sliding forces in axoneme upon condition of presence of

sufficient amount of ATP molecules and calcium ions.

2 Movements of the cilia and its mechanism

Type of cilia's movement can be described as bend ("paddle") motion. This motion can be divided in two phases - effective stroke and recovery stroke. During phase of effective movement cilia get straight and their ends dive into mucus layer. And mucus and upper part of inter-cilia fluid are moving at this moment [2]. Duration of these two phases is different – effective stroke's duration is 3-6 times shorter than recovery's [2].
Movement spreads from one cilium to another. Cilia movements are synchronized in one cell and more over in the group of cells. It can be archived with the existence of special regulation mechanisms coordinating dynein molecules activity. There are different theories concerning the mechanism of cilia's movement coordination. They can be divided in three groups:

1. neural-alike way of excitation wave transfer;

2. process of cilia's interaction viscous fluid;

3. mechanism of wave transfer triggered by contact of cilia [2].

In present work the calcium ion is considered to be coordinating agent. Signal for dynein arms tension is increasing of calcium ion concentration in liquid around cilia. Calcium concentration is regulated by calcium pumps (proteins that are integrated into the cell's membrane).
Let's take more detailed look at cilium's beating. Due the signal of nervous system there is short-term increase of charge on the basal body's membrane that leads to opening on calcium channels. That is initiation of cilium's beating.
More detailed than effective and recovery stroke, cilium's beating can be divided in four phases:

1. Phase "Bend". Calcium ions are going through channel in cell's membrane and moving up to the negative charged axoneme. At first axoneme charge doesn't change due to participation of ion in ATP hydrolyze (that is the reason of conformation changes in dynein and tension of dynein arms). Then negative charge of the axoneme is neutralized and there's increase of calcium concentration appears at the basal body. Then the channel closes.

2. Phase "Relaxation". Reduction of ATP molecules begins, followed by release of calcium ions going into inter-cilia fluid though calcium channels in axoneme's membrane. With inter-cilia fluid calcium ions are transported to the next cilium and initiate bend phase there, after crossing the threshold of the ions concentration. Tension of dynein arms decrease and due to this rigidity of cilium decreases too. Cilium starts to behave like string.

3. Phase "Return". Flow of calcium ions going out of cilium's plasmolemma generates opening of calcium pump (that is situated at the other side of cilia)
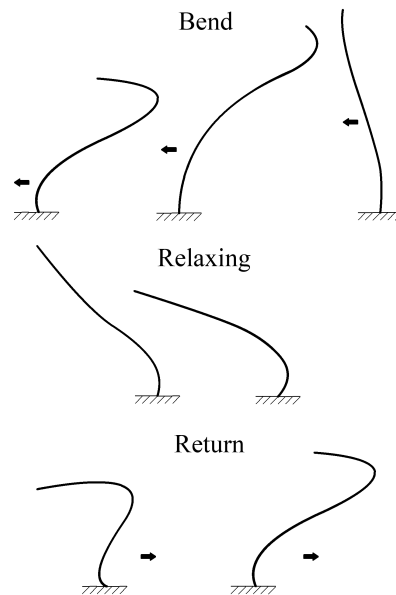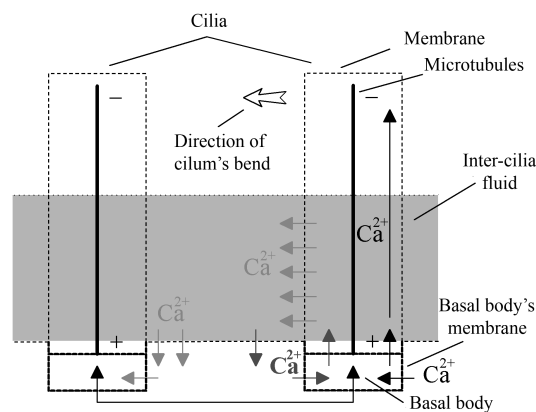
Figure 2: Phases of cilium beating

Figure 3: Mechanism of cilium beating

4. Then goes another phase of relaxation and then new bend.

Flow of the ions through the channel in biological membrane can be also controlled not only with changing of calcium ions' concentration but with changing of its thickness.

Signal for synchronization of cilia's beatings is supposed to be calcium concentration changing in the inter-cilia fluid (and concerned with wave-alike movements of fluid).

3   Information and computer model of cilium

Cilium is concidered as mathematical model of system consisted of solid bodies, connected with flexible linkeges [1].

Scheme of synchronization shows the conception of cilia's beating mechanism. Understanding of this process requires detailed analysis of contractile proteins' behavior

and performing complex experiment experiments to find waves of calcium ions in ciliary liquid and comparing them with wave fluctuations in information-computer model.

Model was realised using Mathlab Simulink. It consists of two impulse generating blocks (triggering potential, two blocks "OR"(that choose type for control of open-close state of right and left channels – by potential changing or changing of thickness of the membrane), two logical blocks "AND" that simulate left right channels, ten logical blocks "AND" simulating tense of dynein arms in the bend phase, two logic blocks "AND" simulating dynein arms tense in the return phase. Delay blocks:

- Delay of calcium ions in the channels controlled by triggering potential (τ_1)

- Delay of calcium ions in the channels controlled by changing of the membrane thickness (τ_2)

- Delay of calcium ions due to diffusion up to the end of axoneme (between axoneme elements) (τ_3)

- Delay of calcium ions due to diffusion from right channel to the left (τ_4)

- Delay of calcium ions due to diffusion from left channel to the right (τ_5)

Next time characteristics are proposed in this model:

- Cycle of beating $T_c = 1/f_k = 0.2s$;

- Duration of bend phase $T_b = 9\tau_3$;

- Duration of relaxing phase after bend: $T_{rb} = \tau_3$

- Duration of relaxing phase after return: $T_{rr} = \tau_2 + \tau_5$

Correlation of phases duration is known from experiments [5]:

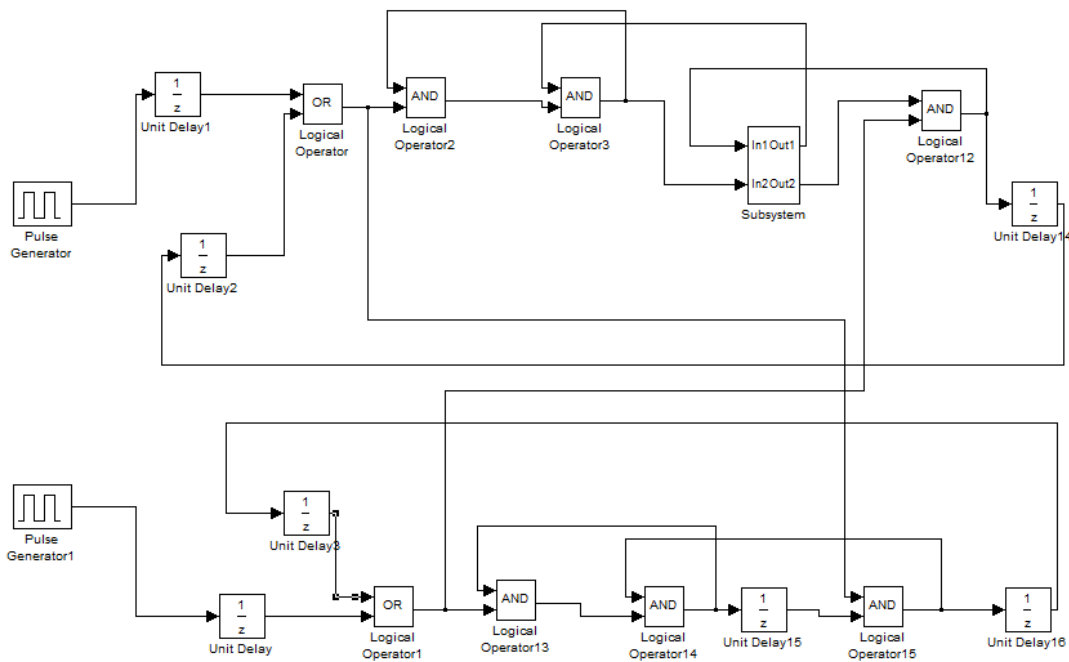$$T_b + T_{rb} + T_{rr} = (4 - 6) \cdot T_c$$

Figure 4: Computer model of cilium
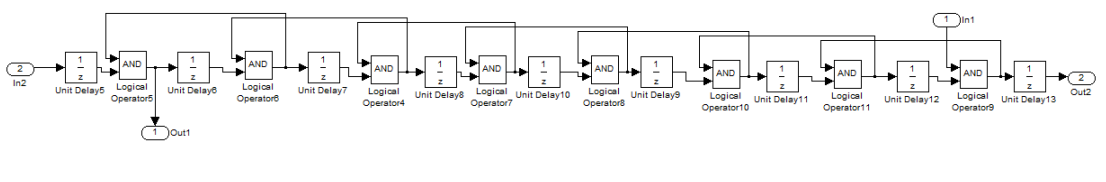
Figure 5: Subsystem

4   Conclusions

This work describes strucrure and mechanism of cilium beating motion concidering membrane transport systems and calcium ion as coordinating agent of this process. Its initiation and synchronization processes are modelled in Matlab Simulink. Hydradinamics is no taken into consideration. Researching of these processes will be continued in future and result will be published in next articles.

References

[1] *Alekseev D.C., Badu E.I., Gorodetskiy A.E., Dubarenko V.V., Kuchmin A.Yu., Tarasova I.L.* Modelling of cilia systems of ciliated cells/ Mathematical modeling 2008

[2] *Shabalin V.V.* Biomechanics of ciliated cell's cilia motion // Scientific-technical journal of SPbSTU, 1998, Vol. 2-3., St.Petersburg

[3] *Johnson N.T., Villalon M., Royce F.H., Hard R., Verdugo P.* Autoregulation of beat frequency in respiratory ciliated cells: demonstration by viscous loading// Am. Rev. Respir. Dis. 1991 Vol. 144.

[4] *Johnson K. A. 1985.* Pathway of the microtubule-dynein ATPase and structure of dynein: a comparison with actomyosin. Annu. Rev. Biophys. Biophys. Chem., 14, 161-188

[5] *Pluzhnikov M.S., Shanturov A.G.* Schneiderian membrane. Mechanisms of homeostasis and homokinetics. Saint-Petersburg 1995. pp. 6-12.

Elena N. Selivanova, Institute for Problems in Mechanical Engineering RAS, Saint-Petersburg, Russia

Some problems of drag reduction for motion in water with developed cavitation

Vladimir V. Serebryakov

serebrvv@public.icyb.kiev.ua

Abstract

The article gives the analysis of the most general conformities to the law at motion of locomotive facilities in a liquid. Basic attention is spared the problems of drag reduction. For illustration of general conformities the elementary models of motion with developed cavitaion are used on the basis of laws of conservation of energy and impulse.

1   Introduction

A process of motion of different locomotive facilities in a liquid is the complicated enough mechanical system, different a considerable variety for the different types of objects. That not, less this process in considerable part has a lot of general conformities to the law of based on the fundamental laws of conservation of energy and impulse. One of basic priorities at motion in a liquid there is a problem of minimum expenses of energy providing motion related to the problems of diminishing of resistance motion. The most general conception in this area was formulated an academician L.I. Sedov in 1971 on the international IUTAM symposium in Leningrad of "Unsteady flows in water with high speed". This conception after was most full developed in works of V.M. Ivchenko and his collaborators [5, 6]. Application of developed cavitation presents one of the most interesting and effective facilities of decline resistance at motion in water. The system of realization of this motion is one of the most complicated systems, plugging in itself a row there are enough difficult processes of formation of cavity, problems of gas injection and loss et al. However the row of elementary models, evidently illustrating the basic physical features of this process on the whole is here developed. It allows simply enough on the basis of elementary models and also laws of conservation of energy and impulse to analyze basic high-quality conformities to the law and ways of increase of efficiency of motion of locomotive mean in general case, including also the case of motion with developed cavitation.

2   Simplest models of supercavitation

Supercavitation flow give the possibility isolated body against water avoids of high viscose resistance and thank to it to reach very small drag as compared to continuous flow. The process of creating of slender axisymmetric cavity can be explained with help of simple model of radial flow [1, 10], Fig.1. In the case of prolate cavities cavitator size is small and its drag is practically independent on cavity form and cavity form is independent on cavitator form and is defined by cavitator drag only. Moving cavitator push motionless fluid to asides and it's work is transformed into kinetic energy of mainly radial near cavity flow in the each motionless section which cavitator passed. In doing so real zone of perturbations contained main part of energy and impulse of flow is concentrated in the finite region limited with surface $r = \psi(x,t)$ with wide some more as compared to semi-length of the cavitator and cavity surface. This fact make cavity as alike on wake of definite type. Further the expansion of the cavity section together with radial flow near cavity is occurred by inertia under action pressure difference in the undisturbed flow and in cavity. In doing so the expansion process weakly enough depends on surface $r = \psi(x,t)$ form $(x,t$ — prolong coordinate, time) and the less the more slender is surface of cavitator and cavity. Cavity section reach maximal radius in the middle part and further start to be decreased under outer pressure action. Decreasing of the cavity section is finished in the back unstable zone of cavity with chaotic flow and all energy of radial flow is transformed into energy of wake behind cavity.
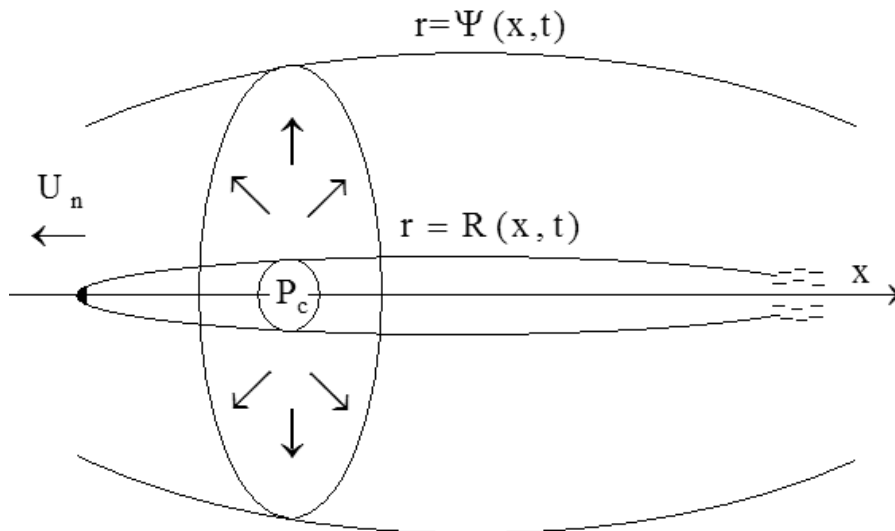

Figure 1: Radial flow model.

The least cavitational drag coefficient per cavity middle section C_D (the body close enough inserted in cavity) are reached for maximally prolonged (slender) cavities and possibility of it decreasing are limited by maximal aspect ratios of the bodies from the point of view of it's strength. Basic parameter of cavitation flow is cavitation number $\sigma = \dfrac{2\Delta P}{\rho U_\infty^2}$, where ΔP — pressure difference between hydrostatic pressure in flow and pressure in cavity what for vapor cavities is near zero, ρ — water mass

density, U_∞ — speed of undisturbed flow. Cavitation Number σ in the case of disc type cavitators defines cavity aspect ratio λ, which quickly is increased along σ decreasing. One of the basic mathematical statements of supercavitation is classical problem on the base of ideal incompressible fluid for potential of speeds defining by Laplace under boundary conditions not penetration and given pressure on the unknown before solution cavity surface. The classic theory is presented by Number of well known books [1, 3, 8], including development one of the most hopeful method of nonlinear numerical computation [4]. The most important for application the slender cavities are so they provide minimal drag. For this case theory can be simplified on the base of known Slender Body Theory and the Linearized Theory of Axisymmetric Supercavitation on this base have been developed [9]–[14]. This theory at present really is as base of number practical methods and simplest heuristic models for prediction of supercavitation.

3 Elementary equations of the axisymmetric cavity

Elementary equations for axisymmetric cavity really express radial flow cavitation model Fig.1 and are developed as first order equations of linearized theory on the base of Slender Body Hydrodynamics. Simplest variant of the equations for slender steady axisymmetric cavity $r = R(x)$ in the case of small (disc type cavitators) [9]–[14] is:

$$a)\mu\frac{d^2R^2}{dx^2} + \sigma = 0, \qquad \frac{dR^2}{dx}\Big|_{x=0} = R_n^2\sqrt{\frac{2c_d}{k\mu}}, \qquad R^2\big|_{x=0} = 0$$

$$b)R^2 = R_n\sqrt{\frac{2c_d}{\mu k}}x - \frac{\sigma}{2\mu}x^2 \qquad\qquad (1)$$

$$c)R_k = R_n\sqrt{\frac{c_d}{k\sigma}}, \qquad L_k = R_n\frac{\sqrt{2\mu c_d/k}}{\sigma}, \qquad \lambda = \sqrt{\frac{2\mu}{\sigma}} = 2\frac{\ln\lambda/\sqrt{e}}{\lambda^2}.$$

The solution of the system (1a) at the case of $\sigma = const$ is presented by ellipsoidal cavity form (1b) and defines known dependencies (1c) for cavity maximal radius R_k cavity semi-length L_k and also cavity aspect ratio $\lambda = \frac{L_k}{R_k}$. In the system (1a) cavitator drag D is defined by known dependence $D = c_d\pi R_n^2\rho U_\infty^2/2$, R_n, c_d — radius, drag coefficient of cavitator. Cavitator sizes here are neglected. For defining of first initial conditions the energy conversation laws is used instead of matching. It is supposed that cavitator work is transformed in the energy of radial flow at the moment when cavitator pass this motionless section of fluid. Equations (1) include 2 characteristic values μ and k having clear physics: μ characterize mass of expanding cavity sections, k — prolong transmission of energy along the flow sections. Basic idea of equations (1a) receiving is that we use simplest to the limit equation for cavity form, but in doing so we use values of main coefficient here μ, k on the base of more accurate second order approaches. Second order expressions for this values are defined by slowly enough changing dependencies on λ and σ:
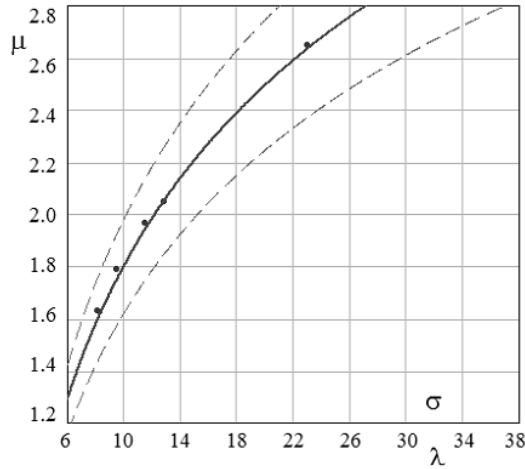
Figure 2: Inertial coefficient $\mu(\sigma), \mu(\lambda)$. Solid line — μ dependence (2); dashed line 10% difference with μ; dotted line $\mu = \sigma\lambda^2/2$ — numerical calculations [4]
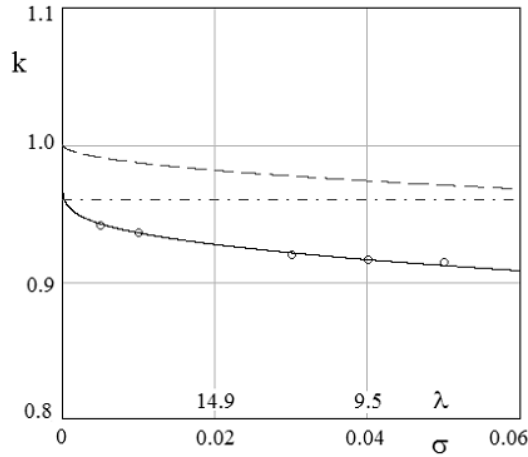

Figure 3: Values $\mu(\sigma), k(\lambda)$. Solid line — dependence (3); dotted line — experiment H. Reichard; circles — numerical calculations [4].

$$\mu = \ln\frac{\lambda}{\sqrt{e}} \simeq \ln\sqrt{\frac{\ln2/\sigma}{e\sigma}}\bigg|_{\lambda\approx8\div15} \approx \ln\sqrt{\frac{1.5}{\sigma}} \sim 2, \tag{2}$$

$$k = 1 - \frac{2\ln2/\sqrt{e}}{\ln\lambda} \approx 1 - \frac{2\ln2/\sqrt{e}}{\ln4/\sigma}\bigg|_{\lambda\approx8\div15} \sim 0.93 - 0.94, \tag{3}$$

and for characteristic range of changing of λ, σ can be used for estimations as definite constants. Calculation μ, k as compared to nonlinear numerical prediction [4] are illustrated by Fig. 2,3. Equations (1a) can be expressed in the form of energy conversation for each motionless fluid section. Main energetic dependencies are
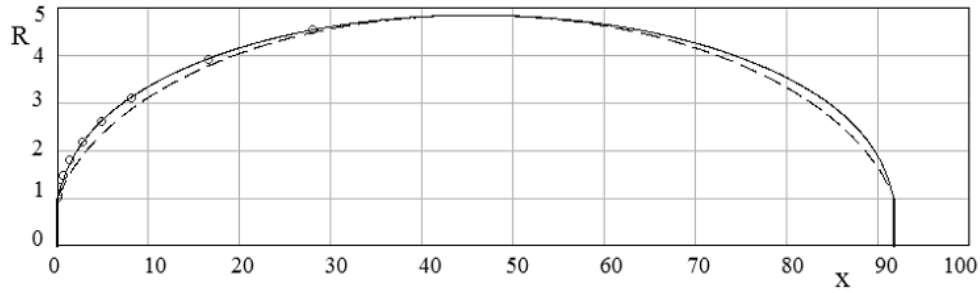
572

Figure 4: Ellipsoidal cavity for accuracy $\sigma = 0.04$; dashed line — equations (3,5); Circles — nonlinear numerical calculation [4]

done below:

$$a)E_k = \pi\frac{\mu\rho}{4}U_\infty^2\left(\frac{dR^2}{dx}\right)^2, \qquad b)Ek = \pi\frac{\mu\rho}{4}U_\infty^2\left(\frac{dR^2}{dx}\right)^2|_{x=0} = \frac{D}{k},$$

$$c)k\pi\frac{\mu\rho}{4}\frac{d}{dx}U_\infty^2\left(\frac{dR^2}{dx}\right)^2 + \pi\frac{dR^2}{dx}\Delta P(x) = 0, \tag{4}$$

$$d)E_{kx} + E_{px} = \pi\frac{\mu\rho}{4}U_\infty^2\left(\frac{dR^2}{dx}\right)^2 + \pi R^2\Delta P = \frac{D}{k}.$$

Dependence (4a) defines kinetic energy of fluid in the section of the flow near cavity in particular in the steady case. Energy what is given by cavitator to the fluid section for the initial moment is defined by expression (4b). Equation (1a) in general case can be presented as energy conservation equation in each motionless fluid equation (4c). In the case of constant pressure difference ΔP this is total kinetic E_{kx} and potential energy E_{px} conservation equation in each motionless section (4d). More accurate variant of these equations with rough estimation of the cavity near disc type cavitator is:

$$\mu_c\frac{d^2R^2}{dx^2} + \sigma = 0, \qquad \frac{dR^2}{dx}|_{x=0} = R_n\sqrt{\frac{2(c_d - k\sigma)}{k\mu_c}}, \qquad R^2|_{x=0} = R_n^2, \tag{5}$$

where $\mu_c = \eta\mu, \eta = c_d/(c_d - k\sigma)$. Accuracy of equations (1, 5) as compared to nonlinear numerical prediction [4] is illustrated by Fig 4. Some violations in the forward cavity part is due to that parabolic asymptotic for $\sigma \to 0$ of the solutions on the base of equations (1a) rough enough approximate more complicated real asymptotic [3, 7]. There are similar equations for prediction of unsteady supercavitation too [9]–[14]. It is need to note that number of key results on the base of Linearized Theory and in particular on the base of the simplest model Fig. 1 and equations (1-5) are confirmed by numerous experiments and received earlier as separate results in known researches by H. Rechardt, G. Birkhoff, P Garabedian, G. Logvinovich, L. Epshtein and another ones.

4 Cavitational drag

Drag of disc type cavitators is defined by known dependencies:

$$D = D(\sigma) = c_d(\sigma)\pi R_n^2 \frac{\rho U_\infty^2}{2}, \qquad c_d = c_{d0}(1+\sigma), \qquad \text{disk}: \quad c_{d0} \sim 0.82-0.83. \quad (6)$$

where c_{d0} is cavitator drag coefficient for $\sigma = 0$. For slender cavitator drag coefficient is defined by dependence:

$$\text{a) } c_d = \left(c_{d0}(1+\sigma) - \frac{\sigma}{2\mu}\left(\ln\bar{L} + \frac{2}{3}\right) + \sigma \right),$$

$$\text{b) } c_d \sim c_{d0}(1+\sigma), \qquad c_d \sim c_{d0} + \sigma, \tag{7}$$

which cover 2 known for more limited ranges dependencies 7b) and 7c). Here: $\bar{L} = \bar{L}_c + 1, \bar{L} = L_c/l, L_c, l$ — cavity and cavitator lengths. Asymptotic approximation for slender cone drag coefficient c_{d0} until cone semi angle $\gamma < 50^\circ$ is:

$$c_{d0} \approx 2\text{tg}^2\gamma\ln\left(\frac{3}{2e}\frac{(1+(4/3)\text{tg}\gamma)}{\text{tg}\gamma}\right). \tag{8}$$

More informative the drag coefficients per definite cavity section are. This is drag coefficient for forward part of the cavity C_{D0} under $\sigma = 0$ for motion in the forward part of the cavity and drag coefficient per middle cavity section C_D:

$$C_{D0} = \frac{1}{8}\frac{\ln(4\lambda_f/\sqrt{e})}{\lambda_f^2}, \qquad C_D = k\sigma = \frac{2}{\lambda^2}\ln\frac{\lambda}{2}, \tag{9}$$

More universal is dependence for C_{DF} per interstitial forward part of cavity until maximal body section touched by cavity C_{DF} with aspect ratio of this part λ_f:

$$D = C_{DF}\pi R_N^2\frac{\rho U_\infty^2}{2}, \qquad C_{DF} = k\mu_x\frac{[1+2\lambda_f^2\sigma/\xi\mu]^2}{8\lambda_f^2}, \qquad \xi = \sqrt{\frac{\mu_x}{\mu}},$$

$$\mu_x = 0.5\ln\left(\frac{16}{e}(\lambda_f^2+1)\left(1 - \frac{2\lambda_f^2\sigma/\mu}{1+2\lambda_f^2\sigma/\mu}\right)^2\right). \tag{10}$$

Where R_N — cavity radius in the touched by cavity body maximal section, λ_f aspect ratio of this forward part of cavity, $e \sim 2.72...$ For $\mu_x = \mu, \xi = 1$ C_{DF} expression [10] is defined on the base of ellipsoidal cavity form. Values for C_{DF} under given aspect ratios $\lambda_f = 8, \lambda_f = 16$ are illustrated by Fig. 5.

5 Main ways for drag reduction

One of basic ways of diminishing of cavitation drag is a maximally possible increase of body aspect ratio dense entered in a cavity or use of the mode of motion in the front area of cavity at the considerably less coefficients of resistance. In both cases it can be arrived at the considerable increase of gas injection and loss which very quickly grows at the increase of the cavity aspect ratio and also by the increase of movement
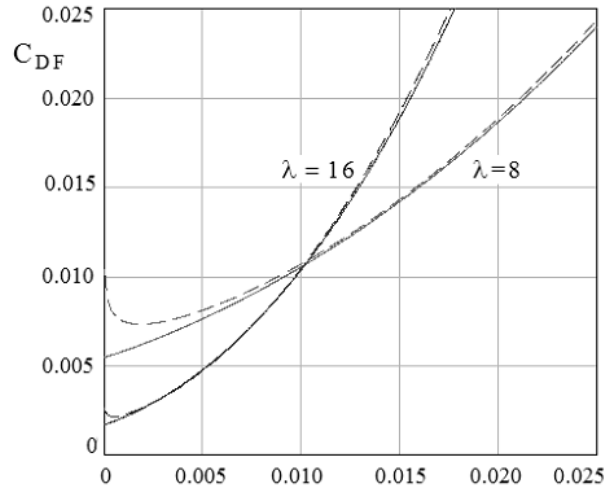
Figure 5: Values of C_{Df} depend on given σ, λ_f. Solid line — dependencies (10); dashed line — dependence (10) for $\mu_x = \mu$.

speeds to their optimum values. Physically energy of cavitation resistance is lost in dulled end of cavity where a loss of stability of flow is with formation of chaotic flow of liquid of transforming energy cavitation flow in energy of wake after a cavity. One of basic ways of diminishing of resistance at motion of body densely entered in a cavity there is the use of the proper closers in the back-end of body. In an ideal model the law of Dalamber–Euler takes a place during complete indemnification of resistance. However in reality even partial realization of a compensate force is related to considerable difficulties in connection with instability of flow in the blunted back-end of cavity. At the variable along length number of cavitation, in particular in the case of vertical cavities, was found out possibility of existence of cavities with sharpening in a back point [16]. From one side the blunt of back-end of cavity is diminished by possibility of origin of instability in this area. From other side accordance with dependence (4a) means possibility of shorting of cavity without the losses of energy in wake. It was found out analogical possibility also in the case of ordinary cavities with a partition, separating the back-end of cavity with the more high pressure $\sigma_2 < 0$ as compared to the forehand of cavity $\sigma_1 > 0$ [13]. Solutions in both cases of vertical cavity and cavity of part by a partition with different pressures in each of parts easily are defined on the basis of equations (1a). Conditions of existence of points of sharpening in the back-ends of vertical cavity and in the case of more high pressure in the back section of ordinary cavity got as dependencies:

$$a) \sigma Fr_L^2 = \frac{4}{3}, \qquad b) \sigma_2 = -\frac{\sigma_1}{2} \frac{(\bar{L}_1 - 1)^2}{\bar{L}_1 (1 - \bar{L}_1/2)}, \tag{11}$$

where: $Fr_L = U_\infty / \sqrt{gL}$, $\bar{L}_1 = L_1/L_k$ define distance until section where second cavity part under $\sigma_2 < 0$ is started, $L = 2L_k$ — cavity length. Fig. 6 illustrates vertical cavity form with sharpening at the cavity end as compared to form of ordinary cavity Realization of pressure value in the back-end of cavity greater as compared to hydrostatical pressure in a stream can be related to the considerable
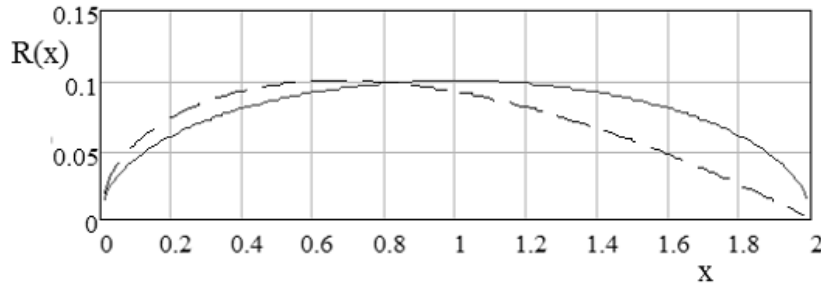
Figure 6: Vertical cavity with sharp end — dash as compared to ordinary cavity — solid.
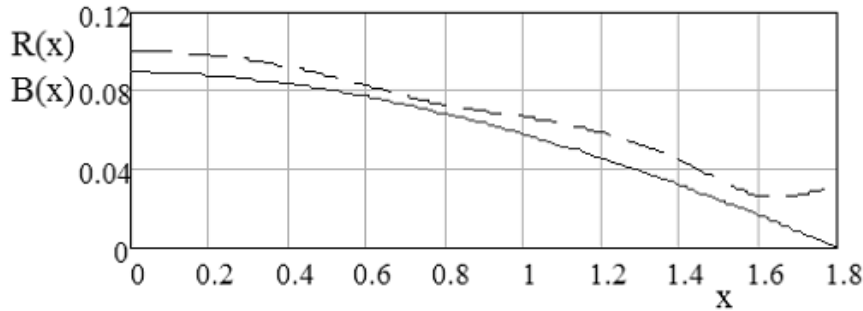

Figure 7: Cavity with account of gas layer. Dashed line — $r = R(x)$ cavity form; solid line — $r = B(x)$ rigid surface form.

problems. One of possible ways for realization of flowing around of back-end of cavity with sharpening and accordingly with indemnification of resistance there can be application of back hard sharp cowling the surface of which is insulated from water by flowing around of high speed flow of gas a thin layer. Simplest approximate approach on the base of model of ideal transonic flow of gas can be defined by system of equations:

$$
\begin{aligned}
&a) \left(\frac{2k}{k-1}\right)\left(\frac{P_{c1}}{\rho_{c1}}\right)\left(\frac{P_c}{P_{c1}}\right)^{\frac{k-1}{k}} + U_c^2 = \left(\frac{2k}{k-1}\right)\left(\frac{P_{c1}}{\rho_{c1}}\right) + U_{c1}^2, \\
&b)(R^2 - B^2)\rho_{c1}U_{c1} = (R_1^2 - B_1^2)\rho_{c1}U_{c1}, \\
&c)\rho_c = \rho_{c1}\left(\frac{P_c}{P_{c1}}\right)^{\frac{1}{k}}, \qquad d)P_c = P_\infty + \mu\frac{\rho U_\infty^2}{2}\frac{d^2R^2}{dx^2}.
\end{aligned}
\tag{12}
$$

Here: $r = B(x)$ is the rigid surface in the cavity equation, k is the adiabatic coefficient, $\rho_c, \rho_{c1}, U_c, U_{c1}, P_c, P_{c1}$ are gas mass density, speed, pressure at arbitrary and initial locations. System (12) for a given cavity form $r = R(x)$ is transformed to the equation defining the surfaces $r = B(x)$. For a given $r = B(x)$, the system solution is transformed to the ODE for the cavity form. The system of equations (12) approximately describe the gas layer flow where prolong speed and pressure is as constant along radius and is defined by pressure on the cavity surface. For very high initial speeds $P_{c1}/\rho_{c1}U_{c1}^2 \to 0$ the nonlinear equation is simplified to the

576

equation (σ_1 correspond to the initial section):

$$\frac{d^2R^2}{dx^2} + \frac{\sigma_1}{\mu} - \frac{2}{\mu}\frac{P_{c1}}{\rho U_\infty^2}\left(\left(\frac{R_1^2 - B_1^2}{R^2 - B^2}\right)^k - 1\right) = 0. \tag{13}$$

It is need to note the qualitative nature of equations (12-13). Significant influence of viscosity and centrifugal forces on lateral pressure gradients is possible here. Limited is adiabatic approximation. The ideal gas model has limited applicability for super overheated vapor only and heat and mass transfer and phase changes can be significant here. Further perfection of the model is required. Fig. 7 illustrates calculation results based on equation (13) in the case of air for: $k \sim 1.4, \sigma_1 \sim 0.04, 2P_{c1}/\rho U_\infty^2 \sim 0.02, R'|_{x=0} = 0$, where $\mu \sim 2$ is used for a rough estimation. As follow from calculation results for sufficiently high gas speeds: it is possible to significantly control cavity form, however due to gas compressibility we have an elastic system where high frequency oscillations and waves on the cavity appearance are possible and can disturb flow at the cavity end with violation of flow stability. Thus, oscillations can appear even in the case of cylindrical rigid surfaces, but it can suppose that in the case of rigid surface form similar as cavity form under constant pressure for $\sigma < 0$ (11b) this oscillations can be maximally increased. For decreasing of energy expenses the way to utilize in mover mechanic energy of the wake can be used too. Propulsion coefficient η_u here can be defined by dependence:

$$\eta_u = \eta/(1 - k\eta)_{\eta\to 0} \sim \eta(1 + \kappa\eta) \tag{14}$$

Here κ is part of energy of drag what can be extracted from the wake as mechanic energy and utilized in mover. For small propulsion coefficients this way of drag reduction can not be effective enough.

6 Ideal movers approximate dependencies

For very high speed over $\sim 50\mathrm{m/s}$ even supercavitating propellers become not effective. Application of supercavitation regime give the possibility considerable decrease drag in a lot of time but require especial hydro jet movers. It can be movers of different types used on the base of gas, vapor, vapor-water drops mix, multiphase fluid and ie. Main information about very high speed movers is presented by number of books and another sources: [2, 5, 6] and others. The hydro jet mover force F can be defined in general case by known approximate B. Stechkin [15] dependence:

$$F = \dot{m}_i U_n + \dot{m}_e(U_n - U_\infty) + (P_n - P_\infty)A_n. \tag{15}$$

Here $\dot{m}_i, \dot{m}_e$ - masses of flowing per second from nozzle which are contained in the moving vehicle $\dot{m}_i$ and got of outer water $\dot{m}_e, U_n, P_n$, accordingly are: speed of jet, pressure in the nozzle end section with square A_n. This equation is generalized also for case of outer fluid inlet from wake behind body by V. Ivchenko [5, 6]. In the case of calculated nozzle regime under essential pressure for motion in continuous flow third term here is absent. One of the main efficiency criteria here is propulsion coefficient:

$$\eta = \left(\frac{2}{1 + U_j/U_\infty}\right)\left(\frac{I_i - i_m}{I_i}\right), \tag{16}$$

where U_∞ — motion speed, U_j — final jet speed, I_i — initial enthalpy per unite of mass, i_m missed with jet enthalpy. This dependence is maximally general and valid both for gas, vapor, mix water vapor hydro jet movers.

Optimization for the most effective mover work in general case defines next system of dependencies for optimal values under given missed enthalpy i_m:

$$\text{a) } \bar{U}_j = 1 + \sqrt{2\bar{i}_m}, \qquad \text{b) } \bar{I}_{iopt} \approx \sqrt{2\bar{i}_m}(1 + \sqrt{2\bar{i}_m}), \qquad \text{c) } \eta_{opt} = \frac{1}{1 + \sqrt{2\bar{i}_m}}. \quad (17)$$

where: $\bar{U}_j = U_j/U_\infty$, $\bar{I}_{iopt} = I_{opt}/U_\infty^2$, $\bar{i}_m = i_m/U_\infty^2$. In doing so optimal propulsion coefficient is achieved in the case of optimal jet speed what is provided by optimal initial value of enthalpy.

7 Main efficiency criteria - optimization

One of basic initial values is a drag coefficient per the most section of body touched a cavity surface (10). This coefficient is universally suitable estimations of drag both at the dense inscribing in a cavity and at motion in the front area of cavity. His simplest variant is here defined on the basis of ellipsoid cavity form.

$$C_{DF} = \frac{k\mu}{8} \frac{[1 + 2\lambda_f^2\sigma/\mu]^2}{\lambda_f^2}. \tag{18}$$

Here λ_f is aspect ratio of part of body to his maximal section, rounded a cavity. For rough understanding of sizes the values $k \sim 0.93 - 0.95$, $\mu \sim \ln 0.7\lambda \sim 0.5\ln 1/\sigma \sim 2.2$ are suitable. More general is presentation of body drag D and units of his volume D/V_b in a kind:

$$D = C_{VF}V_b^{2/3}\frac{\rho U_\infty^2}{2}, \qquad \frac{D}{V_b} = \frac{C_{VF}}{\sqrt[3]{V_b}}\frac{\rho U_\infty^2}{2}, \qquad C_{VF} = \sqrt[3]{\frac{\pi}{\kappa_p^2}}\frac{k\mu}{8}\frac{[1 + 2\lambda_f^2\sigma/\mu]^2}{(\lambda_f^2)^{4/3}}, \quad (19)$$

where C_{VF} — coefficient of volume, κ — relation volume of body to the volume of the paraboloid entered in a cavity . Most characteristic values of coefficient of volume at motion in the front area of cavity $\sigma \to 0$ and at the dense writing into a cavity:

$$C_{V0} = \sqrt[3]{\frac{\pi}{\kappa_p^2}}\frac{k\mu}{8}\frac{\ln 4\lambda_f/\sqrt{e}}{\lambda_f^2} \approx \sqrt[3]{\frac{\pi}{\kappa_p^2}}\frac{k}{8}\frac{\mu}{\lambda_f^2}, \qquad C_V = \frac{3}{4}\sqrt[3]{\frac{2\pi}{3}}\frac{k\sigma}{\sqrt[3]{\kappa_c^2\mu}}, \qquad (20)$$

where: κ_c — relation of body volume per cavity volume. Optimization of expenses of energy on unit of length of way E_X conducted on the basis of dependence and structure of its function for optimization to on σ:

$$\text{a) } E_X = \frac{D}{\eta} = \frac{k}{4}\frac{[1 + 2\lambda_f^2\sigma/\mu]^2}{2\sigma\lambda_f^2/\mu}\left(1 + \sqrt{2\tilde{i}_m}\sqrt{\sigma}\right)\Delta P\pi R_N^2,$$

$$\text{b) }\frac{(1 + b\sigma)^2}{b\sigma}(1 + c\sqrt{\sigma}), \qquad \text{c) } 3bc\left(\sqrt{\sigma}\right)^3 + 2b\left(\sqrt{\sigma}\right)^2 - c\sqrt{\sigma} - 2 = 0.$$
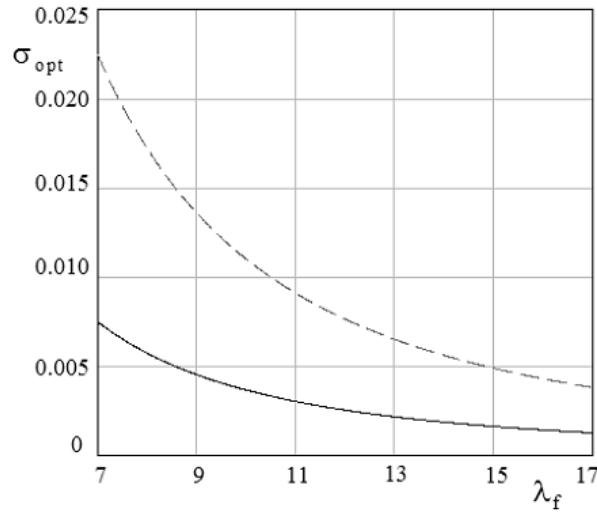
$$(21)$$

Figure 8: Optimal cavitation numbers $\sigma = \sigma(\lambda_f)$ for $\tilde{i}_m = 0$ and $\tilde{i}_m \gg 0$

Where $\tilde{i}_m = \rho i_m / \Delta P$. Here taken into account only cavitation drag and estimations of losses of energy during realization of motion are based on the maximally idealized model in supposition of the use of optimized movers. At the given $\tilde{i}_m, \Delta P$ there are two typical cases. At small $\tilde{i}_m \to 0$ motion providing the minimum expenses of energy takes a place in the first half of cavity subject to the condition: $2\sigma\lambda_f^2/\mu = 1$. At the considerable values of jet enthalpy $\tilde{i}_m \to \infty$ motion providing the minimum expenses of energy takes a place at greater speed and in the front area of considerably longer cavity subject to the condition $2\sigma\lambda_f^2/\mu = 1/3$. Got on the basis of maximal idealized models and laws of conservation of energy and impulse have general character. Probably, these dependencies are reflected by high-quality tendencies for the sufficient wide type of the movers systems and need clarification and addition in every case.

8   Conclusions

The most characteristic possibilities of diminishing of resistance and expenses of energy are probed at motion in water on the basis of maximal the idealized models and laws of conservation of energy and impulse. The got dependencies of the most general character can be utilized for a high-quality estimation at development of methods of calculation of wide class of movers facilities and systems.

References

[1] Birkhoff G., Zarantonello E., Jets, wakes and cavities. - New York: Academic Press, 1957.

[2] Greiner L. Hydrodynamics and Power of Underwater Vehicles -1967, COMPASS PUBLICATIONs, Inc. 383p.

[3] Gurevich M.I. Theory of jets of ideal fluid, NAUKA, Moscow, 1978. (Russ.)

[4] Gusevsky L. G. Numerical Analysis of Cavitation Flows, (Preprint of CO of AS USSR, Institute of Thermo physics, N 40-79), 1979. (Russ.)

[5] Ivchenko V.M. Foundations of hydro-jet motion theory. - In book: Modern questions of hydrodynamics. -, 1967 NAUKOVA DUMKA, Kiev, pp. 155-178. (Russ.)

[6] Ivchenko V. M., Grigoriev V. A. Prichodiko N.A., "Optimal Hydro-jet Propulsion Systems" -1985, under general edition by Ivchenko V. M, KRASNOYARSK STATE UNIVERSITY, 220 p. (Russ.)

[7] Levinson N. "On the asymptotic shape of the cavity behind an axially nose moving through an ideal fluid" // Annals of Mathematics. vol.47. N.4. -1946.

[8] Logvinovich G. V Hydrodynamics of Flows with Free Boundaries, Kiev, NAUKOVA DUMKA, 1969. (Russ.)

[9] Serebryakov V.V. Asymptotic solution for slender axisymmetric cavity. // J. DAN of Ukraine. SSR, No. 12, 1973, pp. 1119-1122. (Russ.)

[10] Serebryakov V.V. Ring model for calculation of axisymmetric flows with developed cavitation. // J. Hydromechanics - 1974, No. 27, pp. 25-29.(Russ.)

[11] Serebryakov V. V. About one variant of the equations of the principle of independent of cavity expansion. // J. Hydromechanics - 1976, No.34, pp. 45-48. (Russ.)

[12] Serebryakov V.V. Models of the Supercavitation Prediction for High-Speed Motion in Water. // Proceedings of International scientific school "High speed Hydrodynamics - 2002, Chebocsary, pp.71-92 (Invited lecture)

[13] Serebryakov V. V. Drag and Drag Reduction Problems for High Speed Motion in Water with Supercavitation. // Proceedings of ISSDR - 2005, Busan, pp.183-198.

[14] Serebryakov V.V. Some problems of hydrodynamics for high speed motion in water with supercavitation, proceedings of int. conf. SuperFAST2008, St. Petersburg, 2008, Russia,12p.

[15] Stechkin B.S. - 1958, Theory of jet engines. Part I and Part II. - ZHUKOVSKY WAR-AIR-ENGINEERING ACADEMY Moscow. (Russ.)

[16] Yefremov I.I. Serebryakov V.V. On forms of slender cavities for small cavitation numbers in plane and axisymmetric flows. // J. Hydromechanics - 1978, No. 38, pp. 82-85 (Russ.)

Vladimir V. Serebryakov, Institute of Hydromechanics of NASU 8/4 Zheliabov Str., 03680, Kiev, Ukraine.

Investigation and mathematicle modelling of dynamic properties of polyethylene

Vladimir V. Shadrin   Ludmila A. Komar   Gennadiy P. Bashin

shadrin@icmm.ru

Abstract

The paper deals with an experimental study of the dynamic properties of filled and unfilled polyethylene. Two components of the complex modulus, storage and loss moduli, have been investigated. Estimation of internal heating of the specimen caused by harmonic vibrations has been done. The experimental results agree well with the theoretical predictions obtained by the phenomenological model describing the behavior of the material under study.

One of the promising ways of improving the mechanical properties of polyethylene is its reinforcement with nanoparticles of other materials. Addition of a rather small amount of filling particles essentially increases the elasticity modulus and strength of the obtained composite and improves its resistance to ignition.

In this work, the influence of filling clay nanoparticles on the elasticity modulus of polyethylene under tension was studied experimentally. The experiments were made using a highly sensitive measuring instrument for dynamic mechanical analysis DMA/SDTA861^e manufactured by Swiss company METTLER TOLEDO. The dynamic mechanical analysis of the specimens was performed in the frequency range from 0,1 to 100 Hz, and in the force range from 0,5 to 17,5 N at the room temperature of about 25°C. The frequency and the amplitude of tensile dynamic load varying under the sinusoidal law were the parameters, which were changed during the experiments. The objective of experimental investigation was to define two components of the complex modulus: the real part (storage modulus) and the imaginary part (loss modulus)[1]. The obtained results were used to determine the dependence of the Yung modulus of the examined material on the variable parameters.

The experiments were made for plane specimens of length 10,5 mm, width 4 mm and thickness 2 mm. The polymer under investigation was a nanocomposite including layer clay filler which was a mixture of a plenty of thin silica plates 1nm thick and with transverse dimension varying from 30 nm to several microns. The filler fraction of the total material mass was 3% .

Figures 1 and 2 show the dependence of the elasticity modulus for filled and unfilled polyethylene on loading frequency. The test were performed for three levels of tensile deformation: 0,35 μm, 3,5 μm and 35 μm, which correspond to 0,003%, 0,033% and 0,333% for deformation. Each loading was repeated 5 times. The experiment error was 7%.

The plots show that (fig. 1 and 2):

— frequency increase from 0,1 Hz to 100 Hz causes an increase in the storage modulus and a decrease in the loss modulus by 30–40%;

— the storage modulus of the filled polyethylene is 40% higher than that of the unfilled polyethylene over the whole frequency range;

— the loss modulus weakly depends on the content of the filler in polyethylene.
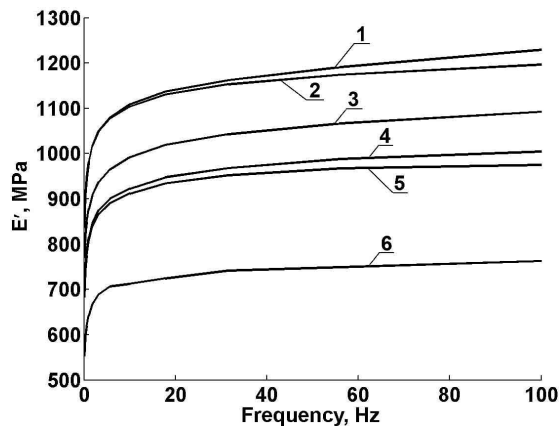

Figure 1: Storage modulus versus frequency of dynamic tensile load;
1,2,3 — filled polyethylene; 4,5,6 — unfilled polyethylene; 1,4 — tensile amplitude of 0.35 μm; 2,5 — tensile amplitude of 3.5 μm; 3,6 — tensile amplitude of 35 μm.

a   b
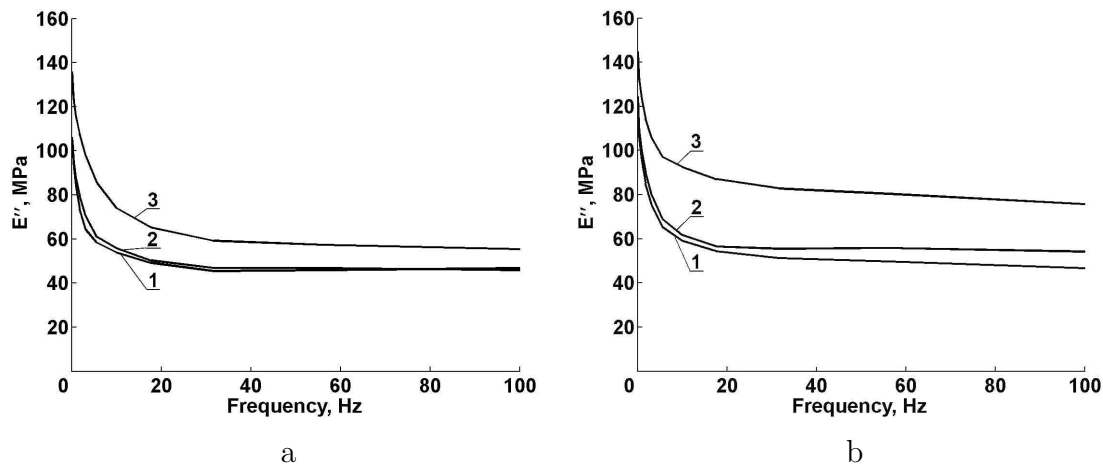
Figure 2: Loss modulus versus frequency of dynamic tensile load;
a — for filled polyethylene, b — for unfilled polyethylene;
1 — at the amplitude 0,35 μm; 2 — at the amplitude 3,5 μm; 3 — at the amplitude 35 μm.

Figures 3 give the results of experimental investigation of the elasticity modulus versus the amplitude of the tensile force for filled and unfilled polyethylene. The frequency of loading was set at two levels. Each loading was repeated 5 times.
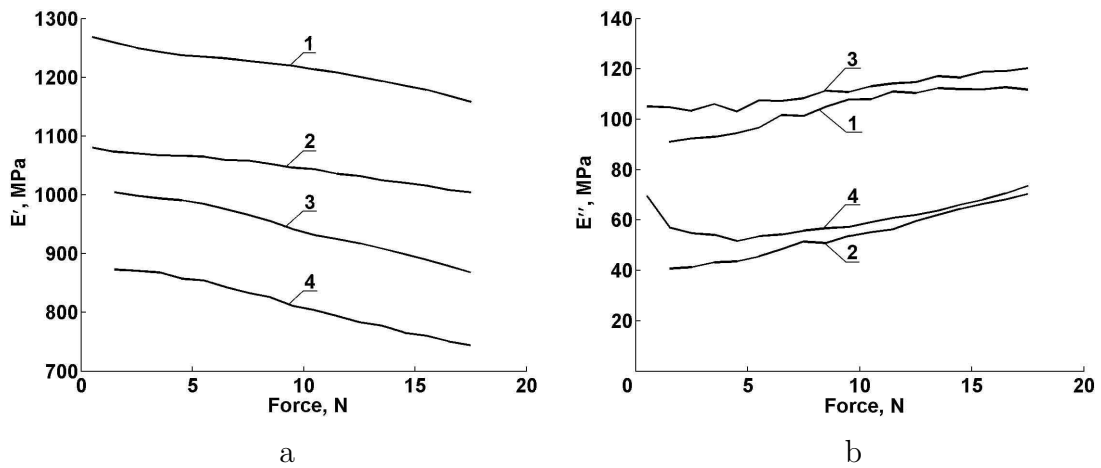
Figure 3: The storage modulus (a) and the loss modulus (b) versus amplitude of dynamic load;
1 — at frequency of 100 Hz and 2 — at frequency of 1 Hz for filled polyethylene;
3 — at frequency of 100 Hz and 4 — at frequency of 1 Hz for unfilled polyethylene.

A repeated series of tensile tests were carried out first at the amplitude of 3,5 μm followed by a series of tests at large deformation amplitude of 35 μm, after which the tests were again realized at the deformation amplitude of 3,5 μm — in total there were 15 cycles of tension — compression loads at deformation amplitudes of 3,5 and 35 μm. Figs. 4–5 show the curves of the first test of the original specimen during the fist loading cycle consisting of 5 subsequent loading steps and the curves of the last test. The curves were constructed by experimental points. As it is seen from the plots, after long-run tests the values of E', E'' and loss factor, $\tan\delta$ remained practically unchanged, i.e. no softening of the material was observed (the Mullins effect was lacking)(fig. 4 and 5).
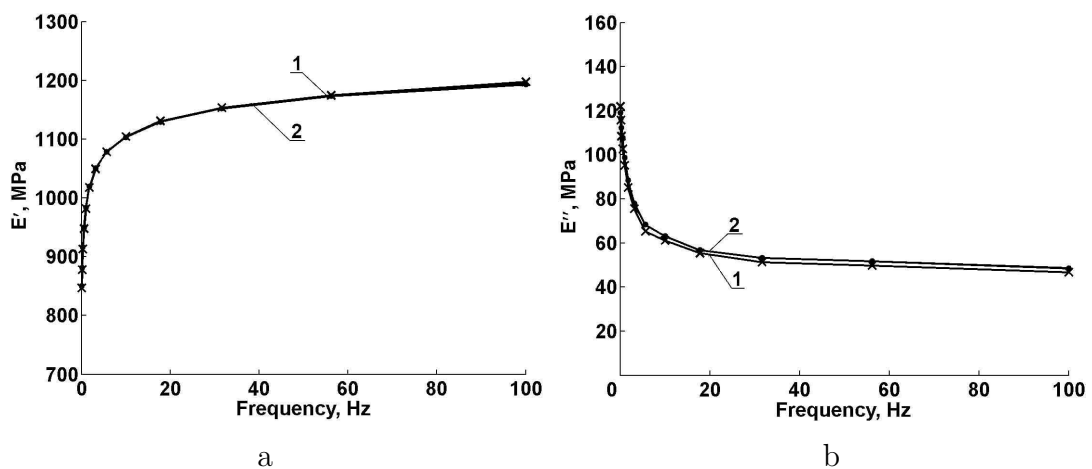

Figure 4: Variation of the storage modulus (a) and the loss modulus (b) of the filled polyethylene under repeated tension; 1 — first test, 2 — repeated test.
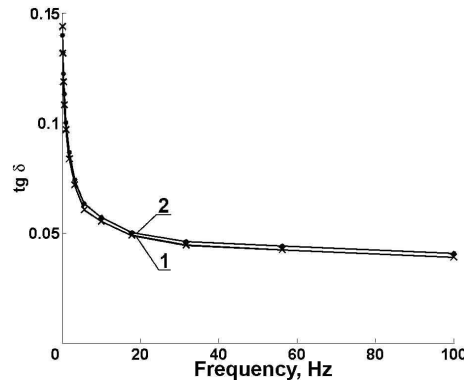
Figure 5: Variation of the loss factor, $\tan\delta$ for filled polyethylene
under repeated tension; 1 — first test, 2 — repeated test.

The viscoelastic behavior of polyethylene under cyclic load is described with good accuracy by the phenomenological model (Fig. 6) [2]. It consists of two elastic and one viscous element. Each element corresponds to one or two tensor equations. The system gives an idea of how they can be combined into a system of constitutive equations determining the properties of the material. The model has been developed for a medium with finite deformations. It has been used to simulate the dependence of the heat generation rate on the amplitude and frequency of material deformation under cyclic loading conditions.
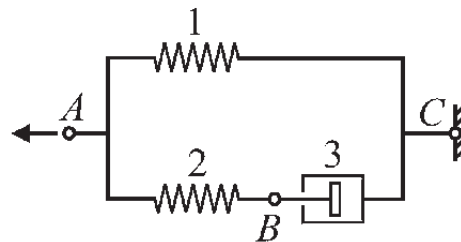
Figure 6: The symbolic circuit of phenomenological
model of polymeric material.

The temperature variation strongly affects the polymer properties [3]. In the specimen, heat transfer to the environment occurs through the specimen surface. At large thickness of the specimen the temperature in its center might be essentially higher than at the boundaries. Due to this temperature difference the mechanical behavior of the material near the specimen boundary differs markedly from that at the center. Therefore it appears rather important to determine the specimen thickness, at which the temperature field of the specimen under cyclic deformation will be uniform and equal to the ambient temperature

$$c_\rho \rho \frac{\partial \theta}{\partial t} = k \frac{\partial^2 \theta}{\partial x^2} + f,$$

where is a specific heat, is a material density and is a thermal conductivity, is the amount of heat released per unit time and unit volume, is temperature. For polyethylene we use the following values:

$$c_\rho = 2 \cdot 10^3 \frac{J}{kg \cdot K}, \quad \rho = 0,92 \frac{kg}{m^2}, \quad k = 0,33 \frac{J}{s \cdot m \cdot K}.$$

The results of the calculations are shown in Fig. 7. The calculations have been made for the case, in which the deformation frequency is 100 Hz and the amplitude of grip displacements is 35 μm. These are the limiting characteristics of the DMA/SDTA861^e device, which are most unfavorable for heating of the specimen during the experiment.
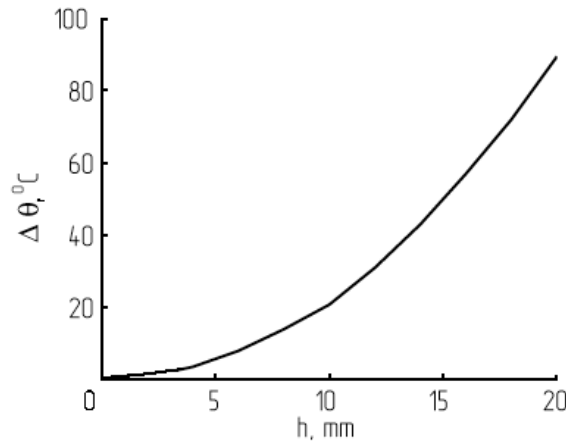
Figure 7: Temperature difference $\Delta\theta$ between the center of the polyethylene specimen and the environment versus thickness of the specimen h under cyclic deformation.

The data shown in the figure supports the view that investigation of the viscoelastic behavior of the specimen under dynamic load should be made for a specimen whose thickness is not higher than 2 mm. Only in this case the temperature difference inside the specimen will not exceed 0,8 °C, so that when studying the polyethylene properties nonuniformity of the temperature field can be neglected.

During the experiment, the specimen temperature measurements were made (Fig. 8). In the present experiment, the temperature of the 2-mm-thick specimen increases by 0,25 °C, which has no effect on the properties of the examined specimen. The obtained results are therefore thought to indicate the properties of the material at ambient temperature, i.e., at temperature measured at the beginning of the experiment. The observed temperature variation can be attributed to the fact that during the experiment the vibration modes are stopped and switched.

Figure 8: Temperature measurement during the experiment.

The analysis of the results described in this study led us to the following conclusions:

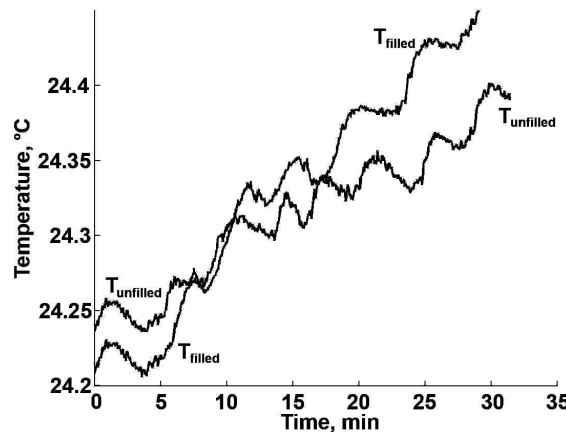— at temperature 25 °C within the entire range of frequencies and amplitudes, the storage modulus of the filled polyethylene is approximately 40% higher than that of the unfilled polyethylene, whereas the loss modulus is almost the same;

— with increase in frequency from 0,1 Hz to 100 Hz, the storage modulus increases, and the loss modulus is 40% lower than its original value;

— with increase in frequency from 0,5 Hz to 17,5 Hz, the storage modulus decreases, and the loss modulus is of the order of magnitude of 10% greater than its original value;

— in the region of small deformations there are no changes in the properties of the polyethylene specimen subjected to multiple extension;

— in order to exclude the undesirable heating of the tested specimens, it is necessary to control their temperature. For instance, the specimen thickness in dynamic tests must not exceed 2 mm at deformation frequency of 100 Hz and amplitude of 35 μm — if these conditions are satisfied, the specimen temperature will be equal to 0,8 °C within the steady-state temperature regime.

Acknowledgements

References

[1] Kabanov V.A. et. al. Polymer Encyclopedia — M.: Soviet Encyclopedia, 1977. Vol. 3. — 1152 p. (in russian)

[2] Svistkov A.L., Lauke B. Structural-phenomenological simulation of the mechanical behavior of rubbers // Polym. Sci., Ser. A, 2008. V. 50, No. 5. — P. 591–599. (in english)

[3] Lykov A.V. Heat/mass transfer: Book of reference. — M.: Energya, 1978. — 480 p. (in russian)

Vladimir V. Shadrin, Institute of Continuous Media Mechanics, Perm, Russia
Ludmila A. Komar, Institute of Continuous Media Mechanics, Perm, Russia
Gennadiy P. Bashin, Perm State University, Perm, Russia

An approach to modeling of elastic-plastic continuum within the framework of discrete element approach

Evgeny V. Shilko   Alexey Yu. Smolin   Sergey V. Astafurov
Sergey G. Psakhie
shilko@ispms.tsc.ru

Abstract

The authors propose an approach to develop formalism of discrete element method for simulation of isotropic elastoplastic media with use of uniform packing of equal size elements (particles). It is based on building associations between the components of stress/strain tensor and the inter-element forces/displacements. The proposed associating allows one to rewrite relations of the corresponding plasticity model in terms of forces and displacements or their increments. The developed approach to formulation of mechanical interaction of elements seems to be general for all realizations of DE method and provides potential possibility to realize various models of elastoplastic or viscoelastoplastic media in the framework of this method.

1   Introduction

At the present time methods of discrete approach in mechanics are known to be reliable tools for simulation of deformation and fracture of condensed media of various nature. Depending on the application field and the problem under consideration, these methods could be divided into two main types: particle methods (PM) and cellular automaton (CA) methods.

The latter are mainly used to study thermodynamic processes connected with change of material phase state on cells fixed in space [1] while methods belonging to the first group are applied mostly to investigate mechanical (or thermomechanical) aspects of material behavior (including fracture) under complex external actions. Particle methods are based on presentation of simulated material or media as an ensemble of interacting bodies (particles) having final size and defined shape. Evolution of ensemble is governed either by Newton's equations of motion [2] or system of equations for potential energy minimization [3]. At present time "newtonian" approach is known as a discrete element method (DEM) and successfully used for simulation of deformation and fracture of materials and media in various fields of material science, geomechanics and civil engineering [2, 4, 5]. An important fundamental problem of DEM is development particle interaction force/potential, which provides

element ensemble response conforming to simulated material or media. In spite of considerable progress in DEM, up to now two-particle forces are mainly used for description of particle interaction [4, 5, 6]. This leads to a series of problems, which are solved via stochastic dense packing of nonuniform-sized elements [4], definition of particle interaction constants using lattice approximation of continuum [6] etc. Also note that application of pair interaction makes difficult correct simulation of irreversible strain accumulation in ductile materials, whose plasticity is provided by mechanisms of crystal lattice scale.

Most of listed (and other) problems are successfully solved within the framework of continuum mechanics based numerical methods (FEM, FDM and so on). Isotropic behavior and required characteristics of mechanical response of model medium therewith are readily achieved even on uniform grids. Analysis of state of the art shows that similar success can be achieved in the framework of DEM with use of many-body interaction forces/potentials.

An approach to building the expressions for normal and tangential interaction of discrete elements simulating isotropic elastoplastic medium is proposed in the paper. The approach is realized within the framework of two-dimensional version of the movable cellular automaton (MCA) method, which integrates possibilities of the CA approach and the DEM. Capabilities of developed formalism are shown by the example of deformation plasticity theory.

2 General formalism of the MCA method

Movable cellular automaton (MCA) method is based on conventional concept of cellular automata [1]. It is a result of CA concept development by means of incorporation of some basic postulates and relations of DEM [7, 9]. The concept of the MCA method is based on the introduction of new type of states, viz., the state of a pair of automata (let us next call them also as elements), into that of classical cellular automata. Overlap of automata h_{ij} is used as a simplest controlling parameter of the new type of states (Fig. 1). Note that the notion of element overlap was adopted from DEM formalism [4, 5].
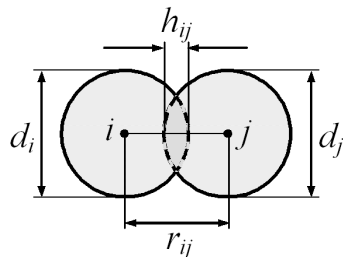
Figure 1: Parameters of spatial relation of the pair of cellular automata i and j: overlap h_{ij} (a) and distance between automata mass centers r_{ij} (b). d_i is size of the automaton i.
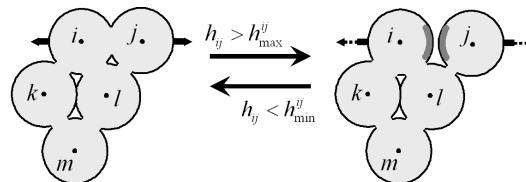
Figure 2: Schematic presentation of switching between linked (at the left) and unlinked (at the right) steady stationary states of the pair of movable cellular automata i and j.

For the simplest case, interacting pair can be considered as a "virtual" bistable

cellular automaton [1]. Two steady stationary states, which characterize bistable automaton, are associated with presence (*linked* state) and absence (*unlinked* state) of chemical bond between elements of the pair (Fig. 2). The simplest criterion of switching between steady states is connected with reaching specified threshold value of pair overlap (threshold values for direct and reverse switching can be different). Note that when simulating real materials, complex state controlling parameters, which depend on a group of variables including h_{ij}, are used.

Set of "virtual" bistable automata forms spatially distributed active medium. Authors showed in some previous papers that description of spatial interaction of movable cellular automata can be based both on bistable cellular automaton formalism and excitable cellular automaton formalism. Famous Wiener-Rosenblueth model of excitable active medium [10] was used by authors to describe propagation of mechanical perturbations in the medium consisting of pairs of interacting elements. On basis of this model the following equation describing mechanical interaction of movable cellular automata i and j was derived under the assumption that ensemble of elements simulates Voight medium [9]:

$$\frac{d^2 h_{ij}}{dt^2} = \frac{p_{ij}}{m_{ij}} + \sum_{k \neq j} C(ij, ik) \frac{p_{ik}}{m_{ik}} + \sum_{l \neq i} C(ij, jl) \frac{p_{jl}}{m_{jl}}, \tag{1}$$

where $m_{ij} = (m_i m_j / (m_i + m_j))$, m_i and m_i are masses of cellular automata i and j; p_{ij} is two-particle normal interaction force depending only on h_{ij}; $C(ij,ik)$ is the coefficient associated with perturbation transfer from the pair i-k to the pair i-j. It is seen in (1) that normal interaction of movable automata i and j has many-body form and is defined by superposition of two-particle forces of interaction of considered two automata with neighbors.

To take into account tangential interaction of finite size cellular automata the developed model was extended via introduction of the second state controlling parameter l_{shear}^{ij} (in addition to h_{ij}) connected with relative tangential displacements of interacting automata (Fig. 3). Features of tangential (as well as of normal) interaction of movable cellular automata in many respects depends on dimension of the problem. The case of plane motion of three-dimensional objects (quasi-two-dimensional approximation) is considered in the paper. In the framework of this approximation the following equation for l_{shear}^{ij} was derived on the basis of analysis similar to carried out for h_{ij}:

$$\frac{d^2 l_{shear}^{ij}}{dt^2} = \frac{F_{tang}^{ij}}{m_{ij}} = \frac{s_{ij}}{m_{ij}}, \tag{2}$$

where s_{ij} is two-particle tangential interaction force depending only on l_{shear}^{ij}. It is seen in (2) that F_{tang}^{ij} is written in pair form unlike many-body form of F_{norm}^{ij}.

Movable cellular automaton is a finite size object. Hence possibility of its rotation under the action of moments of tangential forces is physically founded and taken into account in described model [7, 9]. The method of calculation of normal and tangential (shear) relative velocities of considered pair i-j is described in [4, 7].

As in DEM, dynamics of automaton mass centers is governed by Newton-Euler motion equations.
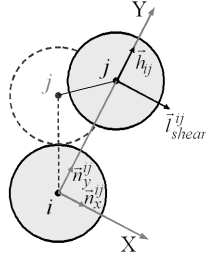
Figure 3: Components h_{ij} and l_{shear}^{ij} of relative displacement vector in the instantaneous local coordinate system concerned with current spatial position of the pair i-j. Dashed line outlines previous relative position of automata.
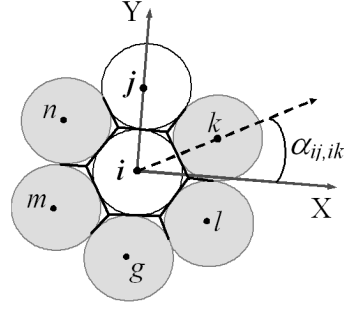

Figure 4: Definition of angle $\alpha_{ij,ik}$ between line connecting mass centers of automata in the pair i-k and x-axis of instantaneous local coordinate system of the pair i-j.

3 Description of isotropic elastoplastic medium with MCA formalism

Stress-strain state of isotropic linearly elastic medium is described on the basis of generalized Hooke's law [11]:

$$
\begin{cases}
\sigma_\alpha = \varphi \varepsilon_\alpha + (K - \varphi)\varepsilon_m = \varphi \varepsilon_\alpha + (1 - \varphi/K)\sigma_m \\
\tau_{\alpha\beta} = \dfrac{\varphi}{2}\gamma_{\alpha\beta}
\end{cases}
, \tag{3}
$$

here $\alpha, \beta = x, y, z$; σ_α and ε_α are diagonal components of stress and strain tensors; $\tau_{\alpha\beta}$ and $\gamma_{\alpha\beta}$ are off-diagonal components; $\varepsilon_m = (\varepsilon_x + \varepsilon_y + \varepsilon_z)/3$ is mean strain; K is bulk modulus; $\sigma_m = K\varepsilon_m$; $\varphi = 2G$ (G is shear modulus).

The form and the matter of equations (3) are analogous to equations (1)-(2) describing normal and tangential interaction of cellular automata. What's more, as is shown in [8], when assigning $p_{ij} = E_i S_{ij} h_{ij}/d_i$ (here E_i is Young modulus of material filling the cellular automaton i, S_{ij} is area of contact between automata i and j) and $d_i \to 0$, equation (1) transforms to Hooke's law for corresponding diagonal component of stress tensor in local coordinate system of considered pair. This argues for the possibility of correct simulation of mechanical response of isotropic linearly elastic medium by ensemble of finite size elements. Using results of [8] as the base, authors proposed more accurate model of interaction of movable cellular automata. This improved model is based on the following four statements:

1. In the local coordinate system of considered pair i-j (Fig. 3) strain tensor components ε_{yy} and ε_{xy} are associated with normal (ε_{ij}) and shear ($\gamma_{ij}/2$) relative displacements normalized by automaton size. These are calculated in an incremental fashion:

$$
\begin{cases}
\Delta\varepsilon_{ij} = \dfrac{\Delta r_{ij}}{(d_i + d_j)/2} = \dfrac{\Delta q_{ij}}{d_i/2} + \dfrac{\Delta q_{ji}}{d_j/2} = \Delta\varepsilon_{i(j)} + \Delta\varepsilon_{j(i)} \\
\Delta\gamma_{ij} = \dfrac{V_{shear}^{ij}\Delta t}{r_{ij}} = \Delta\gamma_{i(j)} + \Delta\gamma_{j(i)}
\end{cases}
, \tag{4}
$$

where symbol Δ indicates increment of the value, q_{ij} and q_{ji} are distances from mass centers of automata i and j to center of contact area ($q_{ij} + q_{ji} = r_{ij}$), $\varepsilon_{i(j)}$ and $\varepsilon_{j(i)}$ are strains of automata i and j in i-j pair, $\Delta\gamma_{i(j)}$ and $\Delta\gamma_{j(i)}$ are contributions of automata i and j to the total value $\Delta\gamma_{ij}$; Δt is time step of numerical scheme of integration of Newton-Euler motion equations.

2. In the local coordinate system of the pair i-j stress tensor components σ_{yy} and σ_{xy} are associated with specific normal (σ_{ij}) and shear (τ_{ij}) forces, which are defined as follows:

$$\begin{cases} F^{ij}_{norm} = \sigma_{ij} S_{ij} \\ F^{ij}_{tang} = \tau_{ij} S_{ij} \end{cases} \tag{5}$$

3. Association for stress tensor component σ_{xx} cannot be found considering i-j pair independently of surrounding automata. In the simplest case it can be defined following the procedure in [8]. Nevertheless, more correct approximation is based on definition of average stresses in the bulk of cellular automaton. If surface of the automaton i can be presented as a sum of contact areas, then expression for average σ_{xx} in the bulk of automaton i in local coordinate system concerned with i-j pair can be written in the following form [4, 5]:

$$\sigma^{i(j)}_{xx} = \frac{1}{V_i} \sum_{k=1}^{N_i} q_{ik} S_{ik} \cos(\alpha_{ij,ik})[\cos(\alpha_{ij,ik})\sigma_{ik} + \sin(\alpha_{ij,ik})\tau_{ik}], \tag{6}$$

where N_i is number of neighbors of automaton i, V_i is the volume of automaton i, $\cos(\alpha_{ij,ik})$ is defined as shown in the Fig. 4.

4. In the framework of quasi-two-dimensional realization of the MCA method stress tensor component σ_{zz} could be found from (6) using plane stress state ($\sigma^{i(j)}_{zz} = 0$) or plane strain state ($\Delta\sigma^{i(j)}_{zz} = \frac{K-\varphi}{2K-\varphi}(\Delta\sigma_{ij} + \Delta\sigma^{i(j)}_{xx})$) approximation. In both cases $\sigma^{i(j)}_{xz} = \sigma^{i(j)}_{yz} = 0$.

Described statements give the possibility to calculate normal and shear forces of interaction of cellular automata whose ensemble simulates isotropic linearly elastic medium. Forces are calculated with use of combined force-displacement algorithm (it is suggested that all pairs of interacting automata are *linked*):

1. Force of normal interaction of the automata i and j ($F^{ij}_{norm} = F^{ji}_{norm}$), as well as strains $\varepsilon_{i(j)}$ and $\varepsilon_{j(i)}$, are calculated in an incremental fashion by solving the following system of equations:

$$\begin{cases} \Delta\sigma_{ij} = \Delta\sigma_{ji} = \varphi_i \Delta\varepsilon_{i(j)} + \left(1 - \frac{\varphi_i}{K_i}\right)\Delta\sigma^{i(j)}_m = \varphi_j \Delta\varepsilon_{j(i)} + \left(1 - \frac{\varphi_j}{K_j}\right)\Delta\sigma^{j(i)}_m \\ \Delta\varepsilon_{i(j)} d_i/2 + \Delta\varepsilon_{j(i)} d_j/2 = \Delta r_{ij} \end{cases}, \tag{7}$$

where symbol Δ hereinafter indicates increment of corresponding parameter during one time step Δt, φ_i and K_i are constants of material filling the bulk of the automaton i, values of $\Delta\sigma^{i(j)}_m$ and $\Delta\sigma^{j(i)}_m$ are taken from previous time step. Note that mean stress for automaton i in i-j pair can be written as follows: $\sigma^{i(j)}_m = (\sigma_{ij} + \sigma^{i(j)}_{xx} + \sigma^{i(j)}_{zz})/3$. Value of $\sigma^{j(i)}_m$ is calculated in the same way.

2. Tangential (shear) interaction force in i-j pair ($F_{tang}^{ij} = F_{tang}^{ji}$) as well as strains $\gamma_{i(j)}$ and $\gamma_{j(i)}$ are calculated in pair approximation according to (2) and (3):

$$\begin{cases} \Delta\tau_{ij} = \Delta\tau_{ji} = \dfrac{\varphi_i}{2}\Delta\gamma_{i(j)} = \dfrac{\varphi_j}{2}\Delta\gamma_{j(i)} \\[2mm] \Delta\gamma_{i(j)} + \Delta\gamma_{j(i)} = \dfrac{V_{shear}^{ij}\Delta t}{r_{ij}} \end{cases}. \tag{8}$$

Proposed association of force- and deformation-related characteristics of automaton (discrete element) interaction with local values of stress and strain tensor components (in the volume "belonging" to interacting pair) seems to be general for all realizations of DE methods and provides potential possibility to implement various models of elastoplastic or viscoelastoplastic media. In particular, authors applied proposed approach to realize two basic models: deformation plasticity theory with elastic unloading (DPT) and incremental plasticity theory (IPT). Implementation of the DPT is based formally on the same expressions (3)-(8) as were used for the model of linear elasticity. The main difference is connected with variable value of modulus within the framework of DPT [11]. In this situation φ characterizes not the automaton as a whole, but automaton part "belonging" to considering pair ($\varphi_i \to \varphi_{i(j)}$). If the DPT is realized in an incremental fashion, current value of $\varphi_{i(j)}$ is defined by the expression:

$$\varphi_{i(j)}^n = \begin{cases} \dfrac{2}{3}\dfrac{\Delta(\sigma_{int}^{i(j)}(\varepsilon_{int}^{i(j)}))}{\Delta\varepsilon_{int}^{i(j)}}, \text{when following the loading surface} \\[3mm] 2G, \text{when being inside the loading surface} \end{cases} \tag{9}$$

where n is the number of current time step, $\sigma_{int}^{i(j)}$ is stress intensity for automaton i in i-j pair:

$\sigma_{int}^{i(j)} = \frac{1}{\sqrt{2}}\sqrt{(\sigma_{xx}^{i(j)} - \sigma_{ij})^2 + (\sigma_{ij} - \sigma_{zz}^{i(j)})^2 + (\sigma_{zz}^{i(j)} - \sigma_{xx}^{i(j)})^2 + 6\tau_{ij}^2}$.

Defining relationship $\sigma_{int} = \Phi(\varepsilon_{int})$ for each considered material is assigned. Current value of $\varepsilon_{int}^{i(j)}$ could be calculated directly or using $\sigma_{int}(\varepsilon_{int})$ curve.

So, implementation of the DPT in the MCA method is based on modified version of expressions (4)-(8). Modification includes use of $\varphi_{i(j)}$ instead of φ_i and definition of $\varphi_{i(j)}$ on each time step according to (9). Implementation of IPT is carried out similarly, however expressions (7)-(9) has to be replaced by other relations.

Testing of developed approach showed that ensemble of interacting movable cellular automata demonstrates macroscopically isotropic mechanical response even in case of uniform packing of equal-size elements. Comparison of results of a series of tests (including uniaxial compression/tension, biaxial loading, shearing strain, local impulsive loading of homogeneous elastic and elastoplastic samples) with results of FDM simulation with use of the same plasticity models showed their close fit. This argues for correctness of proposed approach and gives grounds for its application to simulation of heterogeneous elastoplastic materials and media.

Note that expressions (3)-(9) hold true for *linked* pairs of cellular automata. *Linked → unlinked* switching of the pair state (Fig. 2) corresponds to fracture phenomenon. Criteria of fracture are quite different and depend on physical mechanisms of material deformation. Use of described above approach makes possible

direct use of conventional multiparametric fracture criteria (Huber-Mises-Hencky,
Drucker-Prager, Mohr-Coulomb, Podgorski etc.), which are written in tensor form.
However, unlike deformation processes, fracture pattern of homogeneous isotropic
material simulated by ensemble of discrete automata depends to a great extent on
packing of automata. So, various methods of both direct and indirect taking into
account of heterogeneous internal structure of real materials have to be used for
correct simulation of material response and fracture [4].

Linked → *unlinked* transition of the pair state is accompanied by change of char-
acter of automaton interaction. Particularly, normal interaction of *unlinked* pair is
calculated in the same way as for *linked* state, however *unlinked* pair carries only
compressive load ($\sigma_{ij} < 0$) and becomes noninteracting at $\sigma_{ij} = 0$. Expression (8)
cannot be applied to *unlinked* (chemically unbonded) pairs and has to be replaced
by other relations, which take into account dry or viscous friction of surfaces of
interacting automata (at $\sigma_{ij} < 0$) [4].

4   Future trends in development of the approach

An important problem of simulation of heterogeneous materials and media is as-
signment (definition) of interaction of different components (grains, phases, parts
of a structure and so on). Solution of this problem is based, among other factors,
on taking into account physical-mechanical properties of interfacial region (grain
boundary or bonding interfacial layer).

Two methods of taking into account interfaces are well known. First method is
connected with direct simulation of interfacial regions by "layers" of automata with
specific mechanical properties [12]. Main shortcoming of this method is connected
with necessity of considerable decrease of automaton size, when simulating hetero-
geneous material containing thin interfaces. The second method was proposed by
P.A. Cundall [4] and consists in introduction of the "third body" (bonding layer of
predefined thickness). Strains and force response of bonding layer are calculated in
parallel with interaction of particles themselves. These two interactions are inde-
pendent and function in parallel. Capabilities of described above approach make
possible formulation of more rigorous model of interaction of the pair of automata
with bonding interfacial layer. Improved model is based on modification of (4), (7)-
(9) or similar expressions corresponding to considered rheological model. Modified
version of these expressions contains three strain components which correspond to
strains of automata themselves and strain of interfacial layer. Moreover relations
(7)-(8) consist of three expressions instead of two: two expressions correspond to
Newton's second law for the pairs "automaton i - layer" and "layer - automaton
j" while the third expression sums deformation contributions of all three bodies
to amount of change of h_{ij} or l_{shear}^{ij}. At present time improved model is under
development and seems to be perspective evolution of formalism of the MCA/DE
method.

Acknowledgements

References

[1] Mikhailov A.S. Foundations of Synergetics I. Distributed Active Systems, second ed. Springer, Berlin, 1994.

[2] Cundall P.A., Strack O.D.L. // Geotechnique. 1979. V.29. N 1. P.47-65.

[3] Jing L. // Int. J. Eng. Geol. 1998. V.49. P.371-381.

[4] Potyondy D.O. etc. // Int. J. Rock Mech. Min. Sci. 2004. V.41. P.1329-1364.

[5] Martin C.L., Bouvard D. // Acta Mater. 2003. V.51. P.373-386.

[6] Wang G. etc. // Comp. Mat. Sci. 2009. V.44. P.1126-1134.

[7] Psakhie S.G. etc. // Rus. Phys. J. 1995. V.58. P.1157-1168.

[8] Psakhie S.G. etc. // Phys. Mesosmech. 2000. V.3. N 3. P.89-92.

[9] Psakhie S.G. etc. // Theor. Appl. Fract. Mech. 2001. V.37. P.311-334.

[10] Wiener N. etc. // Arch. Inst. Cardiol. Mex. 1946. V.16. N 3-4. P.205-265.

[11] Lubliner J. Plasticity Theory. Macmillan Publishing, New York, 1990.

[12] Psakhie S.G. etc. // Tech. Phys. 2007. V.52. PP.1523-1526.

Evgeny Shilko, ISPMS SB RAS, Akademicheskii pr. 2/4, Tomsk, Russia, 634021
Alexey Smolin, ISPMS SB RAS, Akademicheskii pr. 2/4, Tomsk, Russia, 634021
Sergey Astafurov, ISPMS SB RAS, Akademicheskii pr. 2/4, Tomsk, Russia, 634021
Sergey Psakhie, ISPMS SB RAS, Akademicheskii pr. 2/4, Tomsk, Russia, 634021

Mathematical models for two-phase combustion in streaming flows

N. N. Smirnov   V. F. Nikitin   V. R. Dushin
ebifsun1@mech.math.msu.su

Abstract

The paper presents the results of theoretical investigations of combustion and detonation initiation in heterogeneous polydispersed mixtures. The problems of fuel droplets atomization, evaporation and combustion being the key factors for ignition delays and shock waves attenuation evaluation in heterogeneous mixtures and the non-equilibrium effects in droplets atomization and phase transitions were taken into account. The effects of droplets size non-uniformity and spatial distribution non-uniformity on mixture ignition and flame acceleration were investigated for mild initiation of detonation by spark ignition followed by deflagration to detonation transition.

1   Introduction

Combustion processes in heterogeneous mixtures differ greatly from that in homogeneous mixtures, because they are governed not only by chemistry but also by physical processes of combustible mixture formation, such as droplet atomization, evaporation and diffusive mixing of fuel vapor with an oxidant [1].

The model applies both deterministic methods of continuous mechanics of multiphase flows to determine the mean values of parameters of the gaseous phase and stochastic methods to describe the evolution of polydispersed particles in it and fluctuations of parameters [2]. Thus the influence of chaotic pulsations on the rate of energy release and mean values of flow parameters can be estimated. The transport of kinetic energy of turbulent pulsations at the same time obeys the deterministic laws being the macroscopic characteristic.

The motion of polydispersed droplets (particles) is modeled making use of a stochastic approach. A group of representative model particles is distinguished each of them representing a number of real particles. Motion of these particles is simulated directly taking into account the influence of the mean stream of gas and pulsations of parameters in gas phase, as well as evaporation and atomization.

Investigating the behavior of individual droplets in a heated air flow allowed to distinguish two scenarios for droplet heating and evaporation. Small droplets undergo successively heating, then cooling due to heat losses for evaporation, and then rapid heating till the end of their life time. Larger droplets could directly be heated up to

a critical temperature and then evaporate rapidly. Atomization of droplets interferes the heating and evaporation scenario.

The onset of detonation in case of a mild ignition of dispersed mixtures at ambient pressures and temperatures comes via galloping combustion mode with increasing amplitude finally bringing to an overdriven regime, which then evolves into a self-sustaining one [3]. Generally speaking, convective combustion in dispersed mixture could lead either to a galloping mode, or to onset of detonation. For large droplets and small ignition energy only galloping combustion modes could be attained.

Non-uniform spatial distribution of droplets has a strong influence on predetonation time (in most cases time is increasing) and much smaller effect on predetonation length. Different types of spatial non-uniformity inhibit deflagration to detonation transition, or direct initiation of detonation, while in case of turbulent flame initiation by spark ignition spatial non-uniformity could serve a promoting factor.

Most of rocket and aviation engines have pulverized in air fuels combustion serving the base of their working cycle. Thus combustible mixtures formation and deflagration or detonation initiation in poly-dispersed fuel - air mixtures are the key aspects providing different limitations for operation of those engines. Onset of detonation being very dangerous for conventional engines could, however, serve the basis for creating new generation of engines - pulse detonating engines (PDE). Dispersed mixtures having been formed by different pulverizers could not be spatially uniform. However, in most experimental and theoretical investigations the ignition characteristics of uniformly distributed in space mixtures were studied. To achieve uniform droplet distribution and to avoid gravitational separation of the mixture having been formed investigations under microgravity conditions are performed [1]. The goal of the present research was, however, to investigate sensitivity of detonation onset to mixture parameters non-uniformity (spatial non-uniformity of dispersed phase, size distribution function, etc.) for both strong and mild initiation. Special attention was paid to peculiarities of droplet interaction with a high enthalpy flow.

2 Mathematical model for polydispersed mixture combustion

The mathematical models for simulating turbulent chemically reacting flows in heterogeneous mixtures were described in details in [2 - 4]. Combustion processes in heterogeneous mixtures differ greatly from that in homogeneous mixtures, because they are governed not only by chemistry but also by physical processes of combustible mixture formation, such as droplet atomization [3, 4], evaporation and diffusive mixing of fuel vapor with an oxidant. The model applies both deterministic methods of continuous mechanics of multiphase flows to determine the mean values of parameters of the gaseous phase and stochastic methods to describe the evolution of polydispersed particles in it and fluctuations of parameters. Thus the influence of chaotic pulsations on the rate of energy release and mean values of flow parameters can be estimated. The transport of kinetic energy of turbulent pulsations at the same time obeys the deterministic laws being the macroscopic characteristic. The motion of polydispersed droplets (particles) is modeled making use of a stochastic

approach. A group of representative model particles is distinguished each of them representing a number of real particles. Motion of these particles is simulated directly taking into account the influence of the mean stream of gas and pulsations of parameters in gas phase [2, 3], as well as evaporation and atomization. Thus a great amount of real particles (liquid droplets) was modeled by an ensemble of model particles. Each model particle was characterized by a vector of values, representing its location, velocity, mass, number of real particles represented by the given model one and other properties. The number of model particles was 25000 each representing up to hundred thousand real particles (depending on mass fraction of fuel). The number of cells was of the order of thousand. Thus the minimal average number of model particles per a grid node was provided guaranteeing sufficient accuracy of fluxes between phases evaluation. The momentum equation for a single droplet motion in the gas flow has the following form [2, 3]

$$m\frac{d\vec{u}}{dt} = m\vec{g} - \phi\nabla p + \vec{f}_d, \quad \frac{d\vec{r}}{dt} = \vec{u}, \quad \vec{f}_d = \frac{C_d}{2}\rho_E\frac{\pi d^2}{4}(\vec{v}-\vec{u})|\vec{v}-\vec{u}|, \qquad (1)$$

the drag coefficient being the function of Reynolds number

$$C_d = \left(\frac{24}{Re} + \frac{4,4}{\sqrt{Re}+0,42}\right)\beta K, \quad Re = \frac{\rho|\vec{v}-\vec{u}|d}{\mu}, \quad \beta = \sqrt{\frac{\rho}{\rho_s}\left(2-\frac{\rho}{\rho_s}\right)}, \quad K = \left(\frac{T}{T_s}\right)^{\frac{4}{5}},$$

$$\frac{\rho_s}{\rho} = \begin{cases} \left(1+\frac{\gamma-1}{2}M^2\right)^{1/(\gamma-1)}, & M < 1; \\ \frac{(\gamma+1)M^2}{(\gamma-1)M^2+2}\left(1+\frac{\gamma-1}{2}\cdot\frac{(\gamma-1)M^2+2}{2\gamma M^2-(\gamma-1)}\right)^{1/(\gamma-1)}, & M \geq 1. \end{cases} \qquad (2)$$

The energy equation for a droplet has the following form [2]

$$m\frac{de}{dt} = q + Q_s, \quad \text{where} \quad e = c_{vs}T_s + h_f^0. \quad Q_s = \frac{dm}{dt}h_L \qquad (3)$$

where h_L is the latent heat of evaporation, Q_s - the energy of phase transitions. Heat flux to a single droplet from the surrounding gas flow is determined as follows [7]:

$$q = \begin{cases} \pi d\lambda \cdot Nu \cdot (T - T_s), & Re < 1000; \\ \pi d^2\rho\,|\vec{v}-\vec{u}|\cdot St\cdot(H_r - H_w), & Re \geq 1000. \end{cases}$$

$$Nu = 2 + 0,16Re^{2/3}Pr^{1/3}, \quad St = \frac{C_d}{2}Pr^{-2/3}, \qquad (4)$$

The non-equilibrium evaporation model is used to determine the evaporation rate [3]

$$\dot{m} = \pi d\cdot\rho D\cdot Nu\cdot\log\left(\frac{1-Y_e}{1-Y_w}\right), \quad Y_w = \frac{W_N P_0}{Wp}\exp\left[\frac{H_b}{R}\left(\frac{1}{T_b(P_0)} - \frac{1}{T_s}\right)\right] - \dot{m}\frac{\sqrt{2\pi RT_s}}{\pi\delta_e pd^2}. \qquad (5)$$

The dynamic interaction of liquid droplets with the gaseous flow could bring to instability of the interface in the shear flow and atomization of droplets. The criterion for liquid droplets instability is that of the critical Weber number [5]: $We = \dfrac{\rho v_{rel}^2 d}{\sigma}$, where σ is the surface tension at the interface, v_{rel} is relative velocity of a droplet versus gas. On exceeding the critical value of the Weber number droplets break up due to vibrational instability takes place. On essentially surpassing the critical Weber number other mechanisms start playing essential roles in the break up process that brings to formation of fine mist [3, 5, 7]. These main characteristics of the atomization process could be taken into account by the following approximate formula [3] determining mean diameters of droplets d_a originating in atomization of initial droplets (diameter d):

$$
d_a = \begin{cases}
d = \left(\dfrac{6\alpha_2}{\pi n}\right)^{1/3}, & We < We_*; \\
\dfrac{dWe_*}{We}, & We_* \le We \le We_{**}; \\
d_*, & We > We_{**}; \\
We_* = 12(1 + Lp^{-0.8}), & We_{**} = 350;
\end{cases}
\tag{6}
$$

where n is the number of droplets per volume unit, α_2 - volumetric fraction of the droplet phase, We_* - the critical Weber number, $Lp = \dfrac{d\rho_c\sigma}{\mu_c^2}$ - the Laplace number, ρ_c , μ_c - liquid density and viscosity.

To determine the mean diameter of droplets d_* after the breakup of a type of an explosion ($We > We_{**}$) one needs to evaluate the part of the accumulated by a droplet energy spent for the breakup. The assumption, that the breakup energy was spent for the formation of new free surface makes it possible to evaluate the number N and the mean diameter d_* of the formed droplets:

$$
N = \left(1 + \frac{E_*}{\sigma\pi d^2}\right)^3; \quad d_* = \frac{d}{1 + \dfrac{E_*}{\sigma\pi d^2}} \quad E_* = A_{drag} - \sum_{i=1}^{N_*} \frac{m_i v_{i*}^2}{2}
\tag{7}
$$

Where the breakup energy is evaluated as the difference between the work of the drag forces separating small droplets from the initial one, and the kinetic energy of fragments' scattering. Thus main assumption of the model is the following: work of drag forces in separating pieces of droplets is spent for additional free surface formation and relative kinetic energy of fragments.

Assuming that the initial droplet is split into N_* equal droplets ($N_* = \dfrac{d^3}{d_*^3}$) having equal velocities of radial expansion of the cloud v_* and the separation of droplets takes place after the droplet is moved away at a distance d_*, one obtains the following formulas:

$$
A_{drag} = \frac{1}{8}N_*\rho C_d v_{rel}^2 \pi d_*^2 d_*; \quad d_* = \frac{d}{1 + \dfrac{1}{4}\left(\dfrac{1}{2}C_d\rho v_{rel}^2 - \dfrac{1}{3}\rho_c v_*^2\right)\dfrac{d}{\sigma}}.
\tag{8}
$$

The mean velocity of the cloud expansion v_* could be evaluated based on the condition of matching the two formulas for d_a at $We = We_{**}$. The reason to perform that matching is that both formulas for breakup regimes were obtained from experiments, thus, indirectly the expansion of the cloud of droplets after the breakup should have been taken into account. On the other hand, the dependence of characteristic droplets diameters on the Weber number should be continuous. In modeling droplets breakup in a gas flow the inertia of the process should be taken into account. Fragmentation does not take place instantaneously: it needs time for small droplets to separate from the initial one, i. e. it needs a definite time for the liquid bridges between the droplets to be established, elongated and broken [3]. Then, finally the first order estimates give the following formula:

$$
\begin{aligned}
d_* &= \frac{dWe_*}{\frac{1}{8}C_d(We - We_{**})We_* + We_{**}}, \\
t_* &= \frac{d}{v_{rel}}\frac{We_*}{We}\left(1 + \frac{3}{8}C_d\frac{\rho}{\rho_c}\left(1 - \frac{4}{C_dWe_*}\right)\right).
\end{aligned}
\tag{9}
$$

Coalescence of droplets due to collisions is neglected. This assumption is valid for rarefied mixtures. In present simulations we'll study mixtures, wherein volume fraction of fluid is 10^{-3}, which provides the probability of collision 10^{-6}.

3 Numerical investigation of gas-droplet interaction in streaming flows

In order to evaluate the influence of different factors on the rate of droplet evaporation and mixture formation in heterogeneous detonation, let us investigate the problem of droplet interaction with the streaming gas flow taking into account mechanical drag, atomization of droplets, non-equilibrium heat and mass transfer. A series of model problems was regarded, in which gas flow and droplet initially had different relative velocities and temperatures, and then relaxation took place. Those model problems are similar to that encountered in shock wave initiation of detonation in combustible dispersed fuel-air mixtures. The two-phase flow becomes strongly non-equilibrium behind the shock wave, because due to mechanical inertia droplets keep their speed practically constant and gas accelerates on passing the shock wave. Besides, due to thermal inertia, temperature inside droplets practically does not change, while gas temperature increases instantaneously behind the shock wave. Due to that reason gas temperature in all the numerical experiments was assumed to be higher than the boiling temperature for liquid droplets.

The thermophysical properties for gas and droplets were assumed similar for all numerical experiments: ambient pressure $p = 1,013$ bar, temperature $T=1000$ K, gaseous phase - air, liquid - n-decane ($C_{10}H_{22}$). Initial droplet temperature was assumed to be $T=300$ K.

The relaxation processes for droplets of different diameters were regarded. Numbered lines on the successive figures correspond to the following initial diameters of droplets: 1 - 1 μm; 2 - 5 μm; 3 - 10 μm; 4 - 50 μm; 5 - 100 μm; 6 - 500 μm; 7 - 1000 μm.
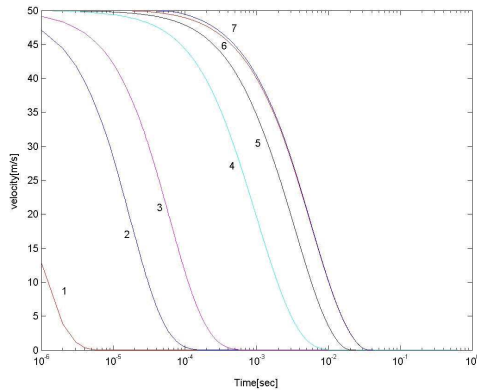
Figure 1: Velocity relaxation versus time for droplets of different diameters. $V_0 = 50\text{m/s}$, taking into account atomization.
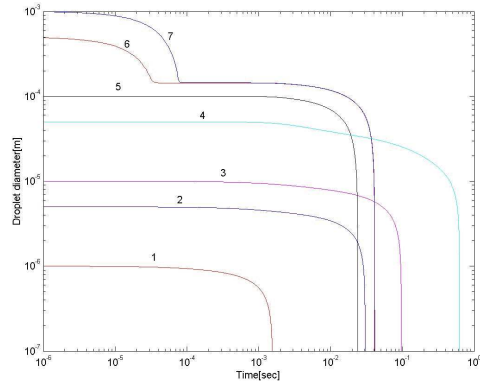

Figure 2: Droplet diameter variation versus time for droplets of different initial diameters. $V_0 = 50\text{m/s}$, taking into account atomization.
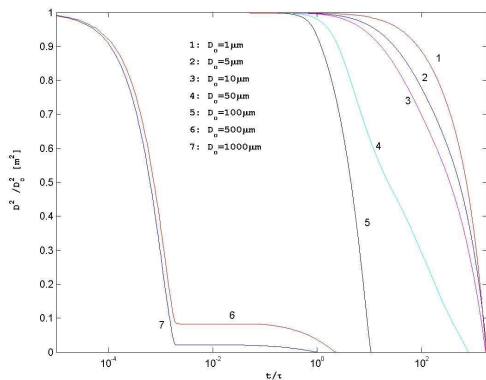

Figure 3: Relative surface area variation versus time for droplets of different diameters. $V_0 = 50\text{m/s}$, taking into account atomization.
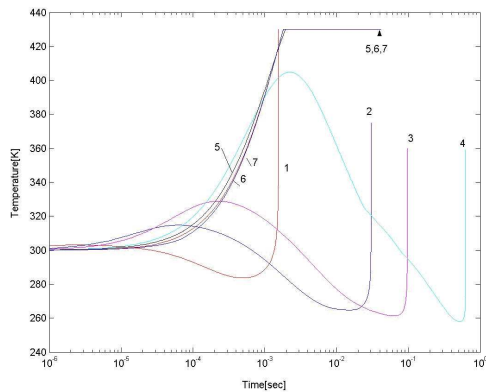

Figure 4: Mean droplet temperature variation versus dimensional time in seconds (a) and dimensionless time (b) for droplets of different diameters. $V_0 = 50\text{m/s}$, taking into account atomization.

Figs. 1-5 illustrate parameters of droplets variation in the process of mechanical and thermal relaxation for the set of numerical experiments assuming initial velocity difference to be equal to 50 m/s. Fig. 1 illustrates velocity relaxation. It is seen that on decreasing initial droplet radius the relaxation process turns to be faster. The decrease of the relaxation time is monotonic. Some curves begin lower than 50 m/s because the relaxation process is too fast for small droplets, and the time scale on the x-axis is logarithmic beginning from a definite small value. Large droplets undergo atomization until their diameter gets smaller. That is the reason for the 6-th and 7-th curves in Figs. 1 and 2 to converge into one, because atomization terminates on reaching by all droplets one and the same diameter.
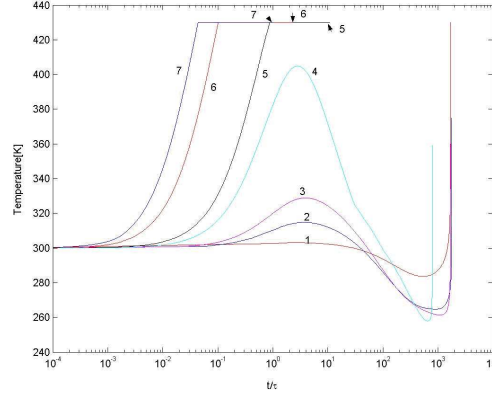
Figure 5: Mean droplet temperature variation versus dimensional time in seconds (a) and dimensionless time (b) for droplets of different diameters. $V_0 = 50 m/s$, taking into account atomization.

Fig. 2 illustrates droplet diameter variation due to evaporation. It is seen from the figure that evaporation time increases with the increase of initial droplet diameter, but the increase does not take place monotonically: the increase of life time (curves 1, 2, 3, 4) changes for a decrease (curves 4, 5) and then comes back to an increase (curves 5, 6, 7). That testifies the effect of manifestation of different mechanisms depending on the characteristic size of droplets.

One could distinguish the characteristic deceleration time τ (velocity decreases e times) for each droplet. This time depends on droplet initial mass m_0, relative gas velocity v_0 and drag f_d.

$$\tau = \frac{v_0}{a_0}, \quad \text{where} \quad a_0 = \frac{f_d(t = 0)}{m_0}. \tag{10}$$

The time being normalized to this value, and droplet diameter being normalized to its initial value allow us to obtain the dependences for relative surface area of a droplet versus normalized time, which is present in Fig. 3. It is seen that all the curves could be split into two families: curves for droplets of small initial radii, and curves for droplets of relatively large initial radii. The obtained result testifies that droplet evaporation process in the stream of air, probably, follows two different scenario. Curves 6 and 7 diverge in Figs. 3 and 4b because relative values versus normalized time are shown there. Thus having one and the same physical diameter droplets 6 and 7 have different relative values as they had different initial size.

Fig. 4 illustrates droplet temperature variation versus dimensional time in seconds. The dynamics of droplet heating is the following. For small droplets (curves 1, 2, 3, 4) in the very beginning the temperature increases due to external heating. On rapid decrease of droplet relative velocity (Fig. 1) evaporation in the stream of gas brings to a decrease of temperature. Then on decreasing droplet radius heat fluxes growth brings to an increase of temperature until the droplet disappears. The first increase of temperature is higher for larger droplets, which relative velocity decreases much slower than for small droplets. Very large droplets follow different scenario:
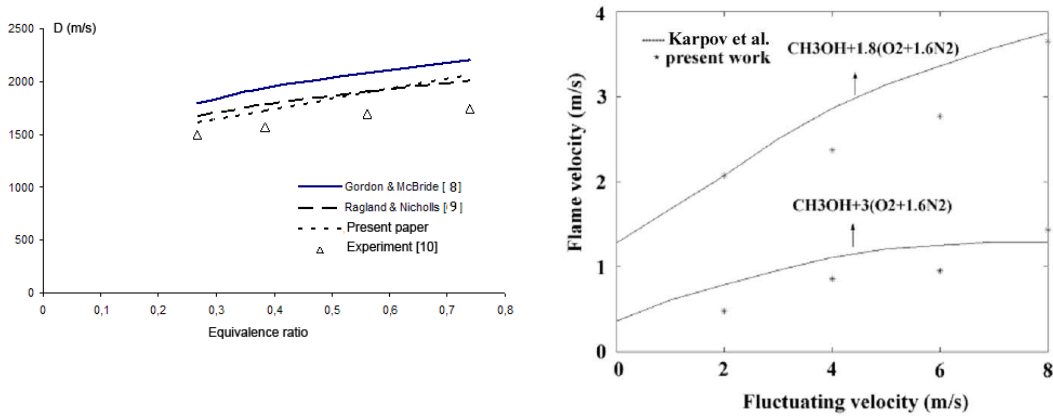
601

Figure 6: Detonation velocities in n-decane ($C_{10}H_{22}$)-oxygen two-phase mixture (a) and turbulent flame velocity in one-phase (b) mixture developed in numerical simulations and in physical experiments.

The first increase of their temperature goes as high as up to the critical value. Then evaporation takes place at a critical temperature very rapidly. Arrows with numbers in Fig. 4 indicate the end of droplet life time. That is the reason for a larger droplet (curves 5 in Figs. 2 and 4) to have a shorter life time.

Fig. 5 illustrates droplet temperature variation versus normalized time t/τ. As it is seen from the figure all maxima and minima of temperature correspond to nearly the same normalized time moments independently on initial droplet radius. The difference between the two scenarios for droplet behavior in the stream of heated air could be clearly distinguished from this figure: small droplets are first slightly heated, then cooled down due to high evaporation rate, and then undergo sharp temperature increase on increasing heat flux to small droplets; large droplets are gradually heated up to the boiling temperature and then evaporate at this temperature.

4 Non-uniform sprays combustion.

Numerical investigations of detonation initiation in dispersed hydrocarbon fuel - air mixtures after mild ignition via DDT and by shock waves of different intensities were performed in tubes of cylindrical geometry. The tube diameter was 20 mm, the tube length was 2 m. The flow was assumed to have the following initial turbulence characteristics: energy $k = 0.1$ J/kg, the mixing length $l = 0.01$ m, mean velocity $u = 0$, initial temperature 300 K. The number of model particles used in calculations was 25000. Validation of numerical scheme was performed based on comparing the obtained results of numerical simulations for the detonation wave velocities in dispersed mixtures with available experimental data [7]. Fig. 6a illustrates detonation velocities in hydrocarbon-oxygen two-phase mixtures developed in numerical simulations and in experiments [8-10]. Liquid n-decane ($C_{10}H_{22}$) fuel was used. Fig. 6b illustrates turbulent flame propagation velocities versus velocity pulsation in gaseous mixtures of CH_3OH, O_2 and N_2. (Curves - experiments [11], dots
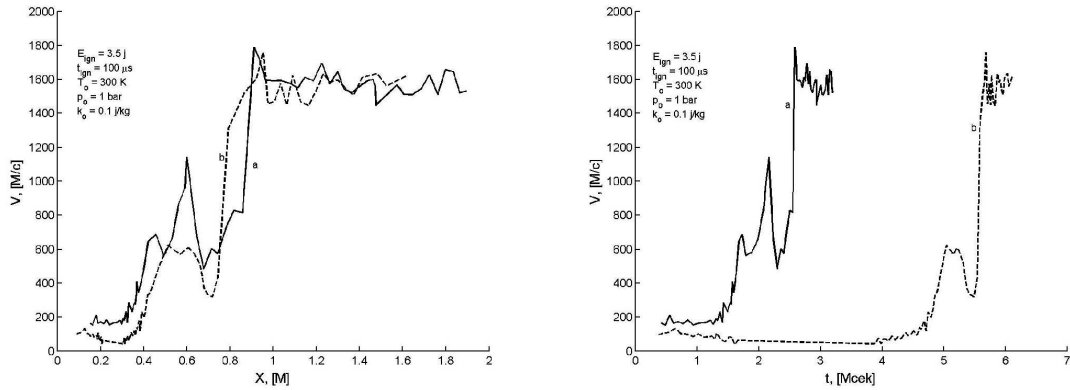
Figure 7: The effect of spatial non-uniformity of mean droplet concentration distribution (a – uniform, b – non-uniform, mean fuel concentration is decreasing along x-axis) on the onset of detonation in polydispersed mixtures. Velocity versus axial coordinate and versus time diagrams.

- numerical computations). Satisfactory coincidence of theoretical and experimental data could serve a macroscopical validation for the developed model.

To simulate hydrocarbons the following parameters were taken: $\rho = 850$ kg/m3; $H = 43$ MJ/kg; $h_L = 200$ kJ/kg; $W = 140$ kg/kmol. The share of water in hydrocarbon decomposition was assumed to be $\zeta = 0.2$. The mean droplets diameter was assumed 50 μm, minimal diameter - 10 μm, maximal - 100 μm. The droplets size distribution function was assumed to be a triangular one. The initial droplets volume concentration $\alpha = 0.001$.

Numerical modeling of two phase mixture ignition and combustion was carried out to understand better the deflagration to detonation transition (DDT) processes. Submicron particles did not play any role in the present study, as their lifetime was negligibly small being below the limit of accuracy of numeric scheme. The size of droplets accounted by the model is the one larger then minimal size evaporating within one time step. Reaction rate of smaller (submicron) particles cannot influence simulations, as the total energy release of their burning out is distributed within the computational cell within one time step. The effect of droplet size distribution function on the DDT process was investigated in [4]. Here we'll study the effect of droplet spatial distribution on the onset of detonation. As it was shown in [2] droplet spatial non-uniformity promotes ignition and combustion onset. In particular, the presence of concentration gradient in droplet spatial distribution lowers the minimal ignition concentration in the zone of energy release. The successive results illustrate the combustion zone averaged axial velocity variation versus time and tube length for different spatial distributions of droplets.

For one and the same fuel content ($\rho_0 = 0.8$ kg/m3) and similar droplet size distribution function the spatial non-uniformity along the longitudinal co-ordinate was investigated. The values of other ignition characteristics were also similar: $T_0 = 300K, p_0 = 1bar, k_0 = 0.1j/kg, E_{ign} = 3.5j, t_{ign} = 100\mu s$ Figure 7 presents the comparison of results obtained for homogeneous (a) and non-homogeneous (b) spatial distribution of droplets. In case (b) mean fuel concentration is decreasing along x-axis.
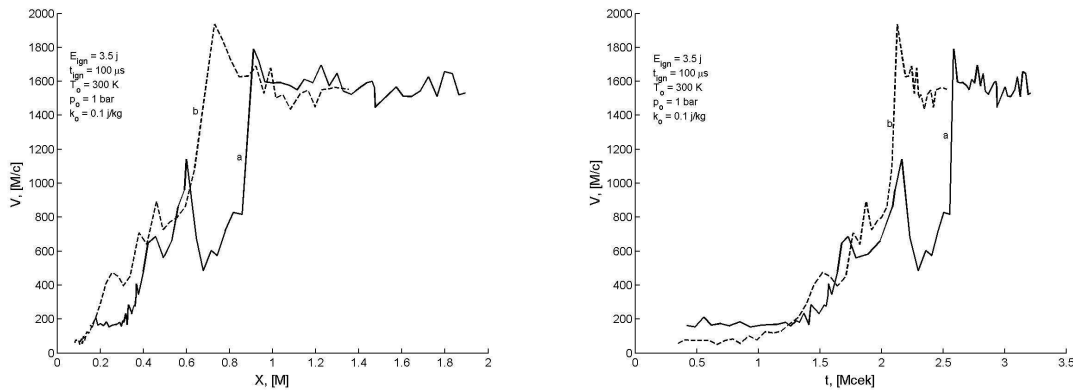
Figure 8: The effect of increasing along the axis mean droplet concentration (a – uniform, b – non-uniform) on the onset of detonation in polydispersed mixtures. Velocity versus axial coordinate and versus time diagrams.
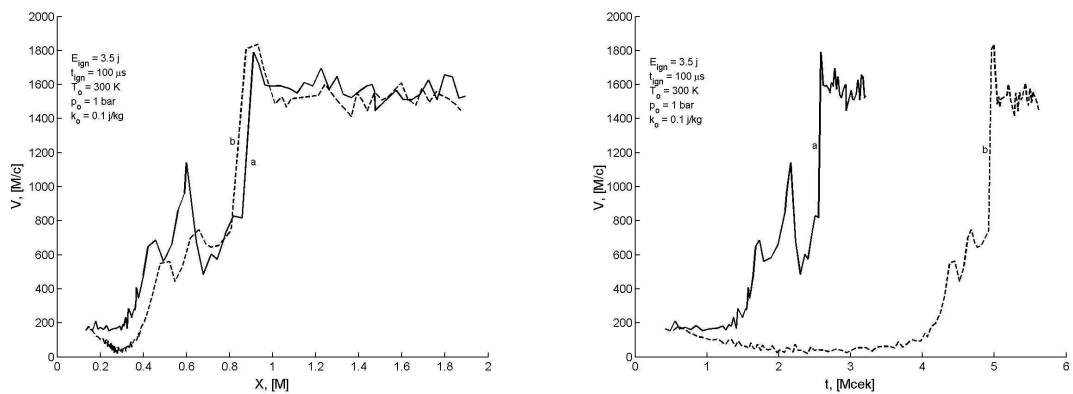

Figure 9: The effect of spatial non-uniformity of mean droplet concentration distribution in radial direction (a – uniform, b – minimum on the axis) on the onset of detonation in polydispersed mixtures. Velocity versus axial coordinate and versus time diagrams.

For the case (a) the turbulent flame propagation in the mixture is very non-monotonic. Velocity first stays at the level of 200 m/s, then it increases up to 700 m/s, again decreases to 600 m/s then increases to 1100 m/s and decreases to 500 m/s again, and then increases up to 1800 m/s and decreases to an average self-sustaining velocity of 1600 m/s with periodical oscillations near that value. It is seen, that in the beginning some galloping combustion mode is established, which turns to be unstable with increasing amplitude of oscillations until finally an overdriven regime is formed, after which mean velocity cannot go down below the self-sustaining one. Detonation in poly-dispersed fuel-air mixture is named a self-sustaining propagation of shock induced ignition. Comparison with cellular gaseous detonation does not seem legible, because cellular structure is an attribute of gaseous detonation, but by no means its definition.

Results of numerical simulations show that pre-detonation length remains practically the same for different spatial distribution of condensed matter (Figure 7 c). It seems
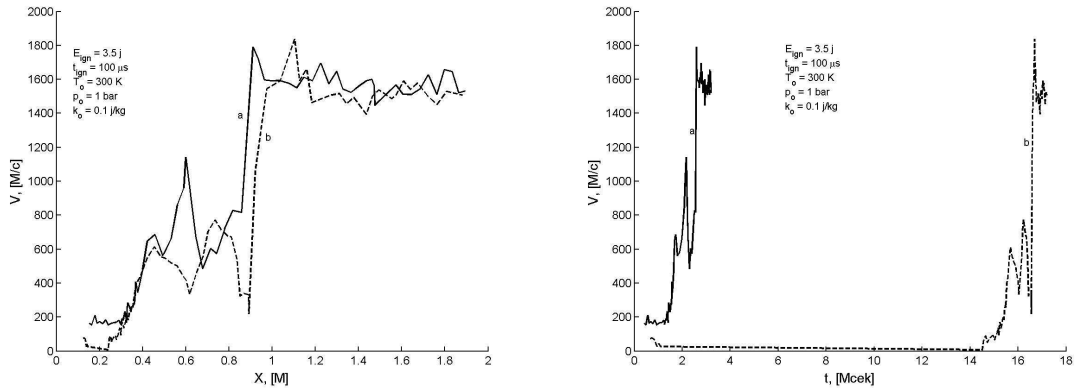
Figure 10: The effect of spatial non-uniformity of mean droplet concentration distribution in radial direction (a – uniform, b – maximum on the axis) on the onset of detonation in polydispersed mixtures. Velocity versus axial coordinate and versus time diagrams.

to be even a little shorter for the case of the increased fuel concentration in the beginning of the tube. While velocity versus time diagrams show essential increase of pre-detonation time. This effect is due to a serious decrease of flame propagation velocity in the ignition section (50 - 100 m/s), which takes place because of the increased heat losses to heat the increased mass of droplets.

Figs. 8-10 illustrate DDT process after ignition in the non-uniform mixture with increasing along the axis mean fuel content (Fig. 8), decreasing in the radial direction (minimal in the center - Fig. 9, maximal in the center - Fig. 10). Comparison of results shows, that for the increasing fuel concentration along the axis pre-detonation length and time practically do not depend on such type of non-uniformity, while for both cases of radial non-uniformity (minimal in the center, or maximal in the center) pre-detonation times grow due to initial decrease of mean axial flame propagation velocity. When fuel concentration is maximal in the ignition zone more time is needed to heat all the droplets, which increases ignition delay, when fuel concentration is minimal in the ignition zone at the axis, propagation velocity is limited by lean conditions, which brings to ignition delay due to the increase of evaporation time to guarantee the necessary vapor concentration.

The results of simulations based on the developed model show that the zone of increased density of droplets behind shock waves appear, which was first discovered numerically by Korobeinikov [6] and named the ρ-layer. Later, the formation of ρ-layers in dusty gases was confirmed experimentally. The present results show that for liquid droplets ρ-layers are formed as well behind shock waves despite droplets atomization. After ignition of dispersed mixture either turbulent combustion wave is formed lagging behind the attenuating shock wave, or a self-sustaining detonation wave. The spatial non-uniformity of droplet distribution in the radial direction for this type of initiation also inhibits the onset of detonation.

Figs. 11-12 and 13-14 illustrate successive stages for droplets concentration and mixture temperature in the problem of spray ignition in shock wave. The mean droplets diameter was assumed 100 μm, minimal diameter - 10 μm, maximal - 200
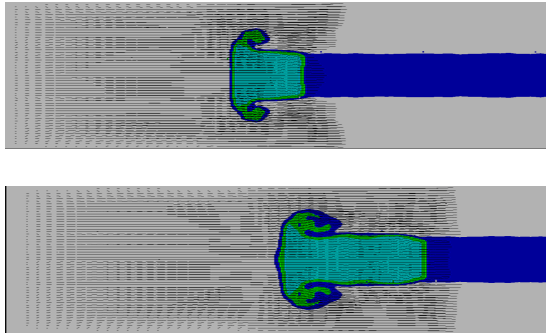
Figure 11: Spray density evolution. Initial density was $\rho_0 = 5.0 \mathrm{kg/m^3}$
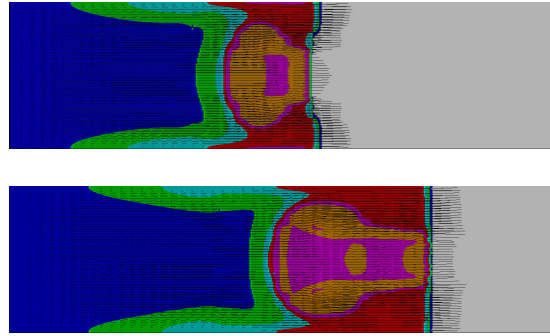

Figure 12: Mixture temperature evolution. Initial spray density was $\rho_0 = 5.0 \mathrm{kg/m^3}$
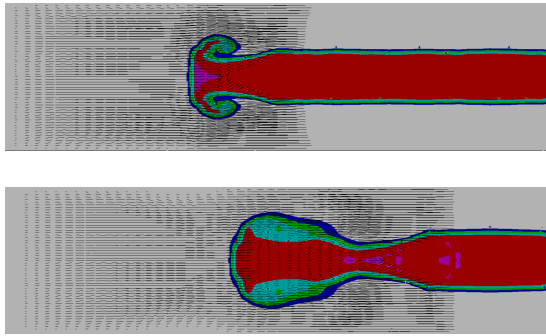
Figure 13: Spray density evolution. Initial density was $\rho_0 = 20.0 \mathrm{kg/m^3}$
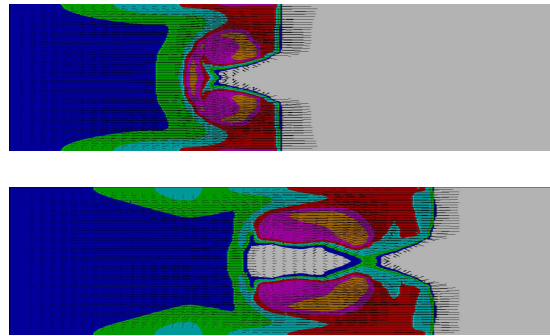
Figure 14: Mixture temperature evolution. Initial spray density was $\rho_0 = 20.0 \mathrm{kg/m^3}$

μm. Spray density was $\mathrm{errror}\rho = 5.0$ kg/m3 for the case illustrated in Figs. 11-12, and $\mathrm{errror}\rho = 20.0$ kg/m3 for the case illustrated in Figs. 13-14. The process was initiated by the shock wave of one and the same intensity in both cases. Comparison of results shows, that for the lower spray density onset of detonation takes place, while for higher density some kind of forced galloping combustion takes place, wherein chemical reactions take place mostly not inside the spray layer, but rather on the sides of it. That peculiarity is due to the lack of oxidant inside the dense spray. The picture is similar to gas-film detonation, wherein fuel and oxidant were spatially separated in the beginning [7].

5 Conclusions

Investigating the behavior of individual droplets in a heated air flow allowed to distinguish two scenarios for droplet heating and evaporation. Small droplets undergo successively heating, then cooling due to heat losses for evaporation, and then rapid heating till the end of their life time. Larger droplets could directly be heated up to a critical temperature and then evaporate rapidly. Atomization of droplets interferes the heating and evaporation scenario.

The onset of detonation in case of a mild ignition of dispersed mixtures at ambient

pressures and temperatures comes via galloping combustion mode with increasing amplitude finally bringing to an overdriven regime, which then evolves into a self-sustaining one. Generally speaking, convective combustion in dispersed mixture could lead either to a galloping mode, or to onset of detonation. For large droplets and small ignition energy only galloping combustion modes could be attained.

Non-uniform spatial distribution of droplets has a strong influence on predetonation time (in most cases time is increasing) and much smaller effect on predetonation length. Different types of spatial non-uniformity inhibit deflagration to detonation transition, or direct initiation of detonation, while in case of turbulent flame initiation by spark ignition spatial non-uniformity could serve a promoting factor. Strong spatial non-uniformity could bring to formation of different detonation modes, which are typical for non-premixed systems.

Acknowledgements

References

[1] Smirnov N.N., Pushkin V.N., Dushin V.R., Kulchitskiy A.V. Microgravity investigation of laminar flame propagation in monodisperse gas-droplet mixtures. Acta Astronautica, 2007, vol. 61, 626-636.

[2] N.N. Smirnov, V.F. Nikitin, J.C. Legros, Ignition and combustion of turbulized dust - air mixtures. Combust. Flame, 123, (1/2), (2000), 46 - 67.

[3] N.N. Smirnov, V.F. Nikitin, A.V. Kulchitskiy, J.C. Legros, V.M. Shevtsova. Detonation Initiation in Pulse Detonating Devices, In G.D.Roy, P.J.Strikowski (Eds.) Proc. Thirteenth ONR Propulsion meeting, Univ. of Minnesota, Minneapolis, 2000, p. 213-232.

[4] Smirnov N.N. Nikitin V.F. Khadem J. Aliari Shourekhdeli Sh. Onset of Detonation in Polydispersed Fuel-Air Mixtures. Proceedings of the Combustion Institute. 2006, vol. 31, pp. 832-841.

[5] B.J. Azzopardi, G.F. Hewitt, Maximum drop sizes in gas-liquid flows. Multiphase Sci.&Tech., 9, (1997), 109-204.

[6] V.P. Korobeinikov, On arising in dusty gas of zones with high concentration of particles. Archivum Combustionis, 9, (?), (1989), 149-152.

[7] N.N. Smirnov, Combustion and detonation in multiphase media. Initiation of detonation in dispersed-film systems behind a shock wave. Int.J.Heat Mass Transfer, 1988, vol. 31, No 4, pp. 779–793.

[8] Gordon S. and McBride B. Computer program for calculation of complex chemical equilibrium compositions, rocket performance, Incident and Reflected shocks, and Chapman-Jouguet detonation. NASA sp-273, 1971.

[9] K.W.Ragland, E.K.Dabora and J.A.Nicholls Observed structure of spray detonations. Physics of fluids, Vol. 11, 1968.

[10] M.J.Tang, J.A.Nicholls, M.Sichel and Z.C.Lin, The direct initiation of detonation in decane-air and decane-oxygen sprays. Gas dynamics laboratories, report No. UM-018404-1, October 1983.

[11] Karpov V.P., Politenkova G.G., Severin E.S., Turbulent burning of alcohol. Combustion, Explosion, Shock waves, 22, N 4: 12-14, 1986.

[12] Smirnov N.N. Nikitin V.F. Khadem J. Aliari Shourekhdeli Sh.Onset of Detonation in Polydispersed Fuel-Air Mixtures. Proceedings of the Combustion Institute. 2006, vol. 31, pp. 832-841.

Smirnov N.N., Nikitin V.F., Dushin V.R., Faculty of Mechanics and Mathematics, Moscow M.V. Lomonosov State University, Moscow 119992, Leninskie Gory 1, RUSSIA

Resistance and lift forces in thin body motion in compressible fluid parallel to free surface

M. N. Smirnova

wonrims@inbox.ru

Abstract

The two-dimensional problem of thin body motion in compressible fluid near free surface is regarded. The fluid is assumed occupying infinite semi-space, gravity is neglected as compared with fluid inertia. The solution was obtained for a problem of infinite span wing motion in compressible fluid at a definite depth, constant velocity and inclination angle. The solution allows determining drag and lift forces in the limiting cases. It was shown that on Mach number tending to unity both forces infinitely increase. For relatively thin fluid layer above the moving wing the resistance force depends on body thickness, inclination and Mach number, while for relatively thick fluid layer the force depends on wing length, inclination angle and Mach number as well.

1   Introduction

The problem is relevant to surface or underwater high velocity gliding of thin wing, which is often used to reduce resistance of the glider. During the motion in water the wing having a definite angle of attack produces a lift force, which leads to suspending of a boat thus reducing the overall resistance to the resistance of the wing. The goal of the overall solution was in developing analytical formulas for evaluating the lift and drag forces. Another important application is determining resistance force being the function of the depth in underwater motion of a bullet or shell.

Similar problems arise in cutting or slicing solid materials by a rigid cutter under the condition inertia forces play dominating role. The possible application of the problem of thin body motion near the free surface at a negative attack angle is description of the motion of a rigid cut slicing plasticized medium. Knowing exact solutions for the cut one could determine resistance forces being the function of its velocity, cutting angle and depth thus developing optimal conditions for material processing.

The problem of fluid streaming rigid bodies in the presence of free surface of water of infinite and finite depth was regarded within the frames of linear [1-4] and non-linear [5, 6] statements, and found its generalized classical solution in [7]. High speed streaming flows accounting for fluid compressibility were investigated in [8-10].
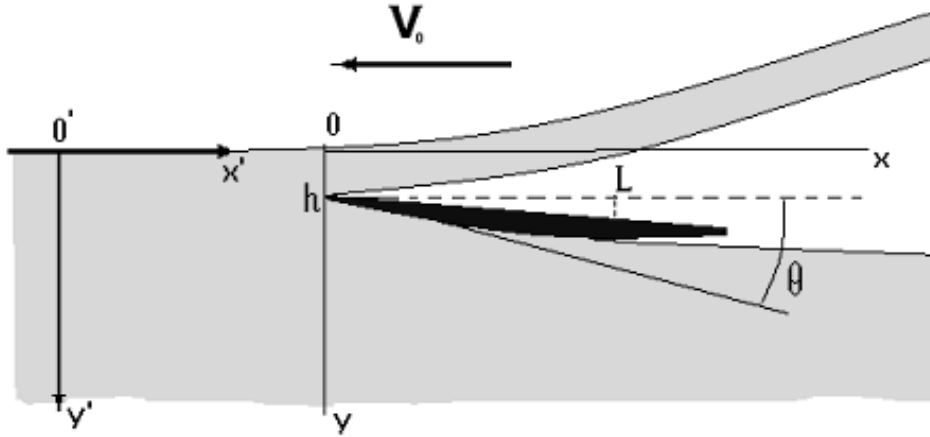
609

Figure 1: Thin body streaming by a compressible fluid at a depth h, constant velocity V_0 parallel to free surface and inclination angle θ. Flow separation from the upper surface.

2   Mathematical statement of the problem

The two-dimensional problem of fluid streaming thin body motion of infinite span with velocity parallel to the free surface is regarded under the assumption of flow separation from the upper surface of the body (Fig. 1) or lower surface of the body (Fig.2). Pressures on free surface and in the cavity are assumed equal to vapor ambient pressure. Fluid is assumed to be ideal, depth – infinite, mass forces – negligibly small, flow field – plane. Velocity field in fluid is assumed to be potential

$$\vec{V} = \vec{V_0} + \text{grad}\varphi, \tag{1}$$

fluid will be regarded as linear compressible

$$P = P_0 + a^2(\rho - \rho_0), \quad a^2 = \left(\frac{dP}{d\rho}\right)_{\rho_0}, \tag{2}$$

$$P = P(\rho), \quad ds = 0 \rightarrow dP = \left(\frac{dP}{d\rho}\right)_{\rho_0} d\rho$$

where $\varphi(x,y,t)-$ disturbance velocity potential, P, $\rho-$ fluid pressure and density, P_0, ρ_0 pressure and density in quiescent fluid, $a-$ sonic velocity.
Fluid flow satisfies continuity equation

$$\frac{d\rho}{dt} + \rho \, \text{div}\vec{V} = 0, \tag{3}$$

pressure is determined by Cauchy-Lagrange integral

$$\frac{\partial\varphi}{\partial t} + \frac{(\text{grad}\varphi)^2}{2} + \int \frac{dP}{\rho} = c(t). \tag{4}$$

Flow induced variations of density and velocity are considered small values.

$$\rho'/\rho = (\rho - \rho_0)/\rho \ll 1; \quad u_x/V_0 \ll 1; \quad u_y/V_0 \ll 1,$$

where u_x, u_y— disturbance velocity components.

Then it follows from continuity equation (3), integral (4) and relationships (1), (2) neglecting small values of the orders higher than one, flow potential φ under the condition of steady-state flow satisfies the equation

$$V_0^2 \frac{\partial^2 \varphi}{\partial x^2} = a^2 \left(\frac{\partial^2 \varphi}{\partial x^2} + \frac{\partial^2 \varphi}{\partial y^2} \right), \tag{5}$$

and fluid pressure is determined

$$P - P_0 = \rho_0 V_0 \frac{\partial \varphi}{\partial x}. \tag{6}$$

Boundary conditions should be satisfied on free surfaces and on the body surface contacting fluid. On free surfaces constant pressure is assumed, on the fluid-body contact streaming condition of the equality of normal velocity component.

The obstacle being thin and inclination angle being small all disturbances could be considered small, and boundary conditions take the form

$$y = 0, \quad P - P_0 = 0;$$

$$y = h^-, \ 0 < x \quad P - P_0 = 0;$$

$$y = h^+, \ 0 < x < L \quad u_y = \frac{\partial \varphi}{\partial y} = V_0 \sin \theta; \tag{7}$$

$$y = h^+, \ L < x \quad P - P_0 = 0.$$

Substituting in (7) dynamical equation (6) boundary conditions look as follows

$$y = 0, \quad \frac{\partial \varphi}{\partial x} = 0; \quad y = h^-, \ 0 < x \quad \frac{\partial \varphi}{\partial x} = 0;$$

$$y = h^+, \ 0 < x < L \quad \frac{\partial \varphi}{\partial y} = V_0 \sin \theta; \quad y = h^+, \ L < x \quad \frac{\partial \varphi}{\partial x} = 0. \tag{8}$$

Thus equation (5) with boundary conditions (8) present a closed form statement of the problem.

3 Problem solution

We assume the flow to be subsonic. Then on introducing dimensionless parameter $\alpha = \sqrt{1 - M^2}$, where $M = V_0/a$— Mach number and dimensionless functions and variables

$$\varphi^* = \frac{\pi \varphi}{a h}; \quad p^* = \frac{P - P_0}{\rho_0 a^2}; \quad l = \frac{L \pi}{h \alpha}; \quad x^* = \frac{\pi x}{\alpha h}; \quad y^* = \frac{\pi y}{h}, \tag{9}$$

equations and boundary conditions take the form

$$\frac{\partial^2 \varphi^*}{\partial x^{*2}} + \frac{\partial^2 \varphi^*}{\partial y^{*2}} = 0, \quad p^* = \frac{M}{\alpha} \frac{\partial \varphi^*}{\partial x^*},$$
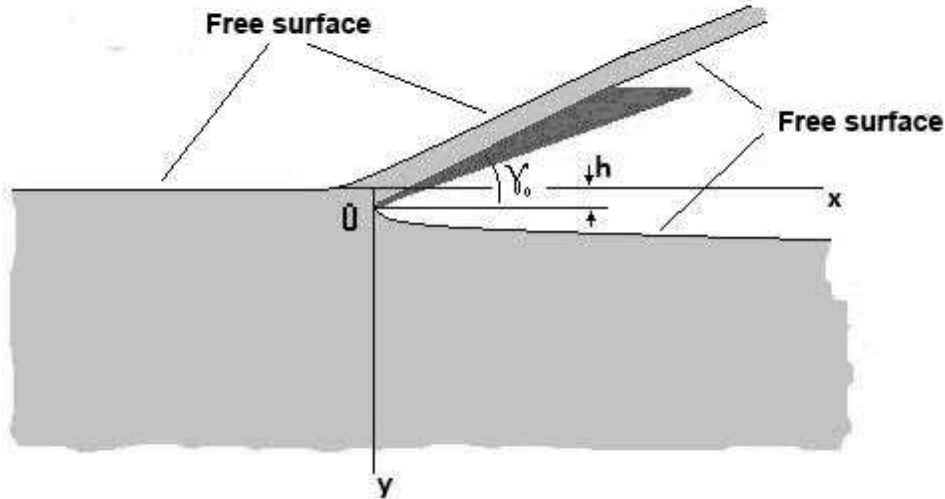
Figure 2: Thin body streaming by a compressible fluid at a depth h, constant velocity V_0 parallel to free surface and inclination angle θ. Flow separation from the bottom surface.

$$y^* = 0, \quad \frac{\partial \varphi^*}{\partial x^*} = 0; \quad y^* = \pi^-, \, 0 < x^* \quad \frac{\partial \varphi^*}{\partial x^*} = 0;$$

$$y^* = \pi^+, \, 0 < x^* < l \quad \frac{\partial \varphi^*}{\partial y^*} = M \cdot \gamma(x^*) \frac{1}{\alpha}; \tag{10}$$

$$y^* = \pi^+, \, l < x^* \quad \frac{\partial \varphi^*}{\partial x^*} = 0.$$

$$\sin \theta \approx tg\theta = \frac{dy}{dx}; \quad tg\theta = \frac{1}{\alpha} \frac{dy^*}{dx^*} = \frac{1}{\alpha} \gamma(x^*).$$

In successive derivations star in dimensionless value symbols will be omitted. The problem is reduced to developing analytical function in the domain $y > 0$ with a cut $y = \pi$, $x > 0$, satisfying boundary conditions (10). The solution will be developed in the form of a real part for the analytical function of complex variable $\varphi(x, y) = \text{Re}\Phi(z)$, $z = x + iy$.

Thus development of the analytical function is reduced to Riemann – Hilbert problem. The latter for a special function type is reduced to Dirichlet problem. The solution for the Dirichlet problem is given by Schwarz integral. In case inclination angle is constant this integral can be taken in elementary functions. The projections of forces are given by the following formulas:

$$X = \frac{\rho a^2 h M^2 \gamma_0^2 (\sqrt{u_0^{\mp}} - 1)^2}{2\alpha^2} \quad Y = \frac{\rho a^2 h M^2 \gamma_0 (\sqrt{u_0^{\mp}} - 1)^2}{2\alpha}$$

- flow separation singularity at the front edge of the plate,

$$X = -\frac{\rho a^2 h M^2 \gamma_0^2 (2\sqrt{u_0^{\mp}} - 3u_0^{\pm} + u_0^{\pm 2})}{\alpha^2 u_0^{\pm}} \quad Y = -\frac{\rho a^2 M^2 \gamma_0^2 (2\sqrt{u_0^{\mp}} - 3u_0^{\pm} + u_0^{\pm 2})}{\alpha u_0^{\pm}}$$
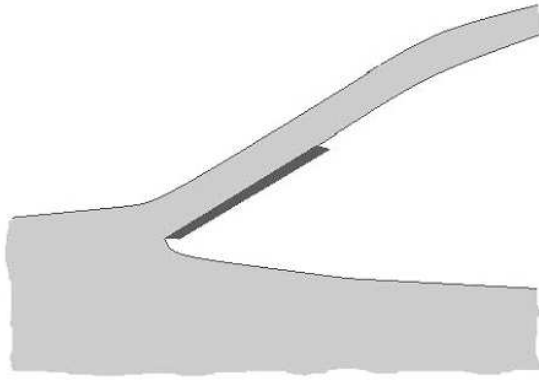
Figure 3: Free surface shape for the case of flow separation from the bottom surface, singularity located at front edge.
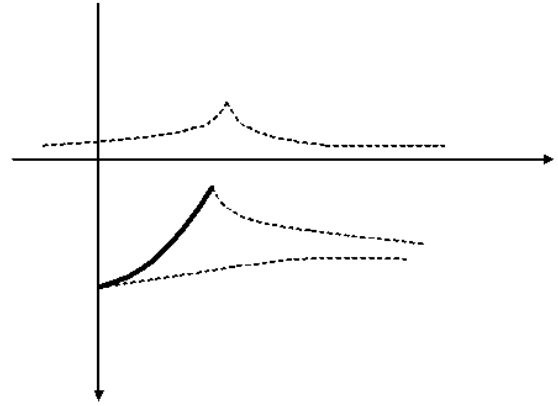
Figure 4: Free surface shape for the case of flow separation from the bottom surface, singularity located at rear edge.

- flow separation singularity at the front edge of the plate. The projection X represents the drag force, and projection Y – lift force, where $u_0^{\pm}$ are roots of algebraic equation

$$l = u_0 - \ln |u_0| - 1.$$

Sign plus stands for case of flow separation from the upper side of the plate (Fig. 1), while sign minus stands for the case of flow separation from the bottom side of the plate (Fig. 2).

4   Results and discussion

Analysis of obtained results shows the following asymptotic behavior of the solution depending on the ratio of body length and fluid layer thickness.
In case fluid separation takes place from the bottom of the body two flow scenarios are possible having singularity on the front edge (fig. 3) and on the rear edge (Fig. 4).
The front edge separation case has the following asymptotic solutions:

$$1)\quad \frac{h}{L} \to 0:\ X = \frac{\rho a^2 h M^2 \gamma_0^2}{2\alpha^2};\quad Y = \frac{\rho a^2 h M^2 \gamma_0}{2\alpha},$$

$$2)\quad \frac{h}{L} \to \infty:\ X = \frac{\pi \rho a^2 M^2 \gamma_0^2 L}{4\alpha^3};\quad Y = \frac{\pi \rho a^2 M^2 \gamma_0 L}{4\alpha^2}.$$

The rear edge separation case has the following asymptotic solutions:

$$1)\quad \frac{h}{L} \to 0:\quad X = -\frac{\rho a^2 h M^2 \mathrm{tg}^2\theta}{\alpha^2}\left(\sqrt{\frac{2\pi L}{\alpha h}} - 3 + \frac{2\alpha h}{\pi L}\right) \to 0;$$

$$Y = -\frac{\rho a^2 M^2 \mathrm{tg}\theta}{\alpha}\left(\sqrt{\frac{2\pi L}{\alpha h}} - 3 + \frac{2\alpha h}{\pi L}\right) \to \infty;$$

Figure 5: Free surface shape for the case of flow separation from the upper surface, singularity located at the front edge.

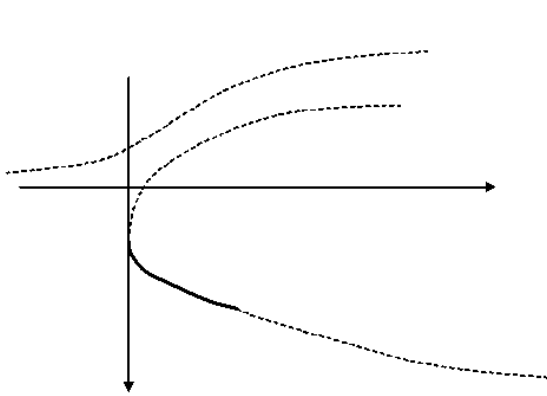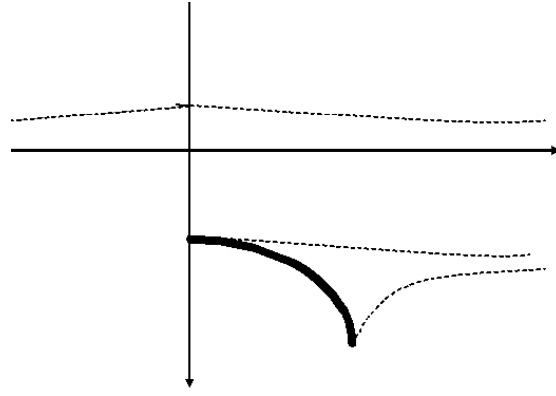Figure 6: Free surface shape for the case of flow separation from the upper surface, singularity located at the rear edge.

$$2)\quad h/L \to \infty:\quad X = \rho a^2 M^2 \gamma_0^2 \frac{3\pi L}{2\alpha^3};\quad Y = \frac{3\rho a^2 M^2 \gamma_0 \pi L}{2\alpha^2}.$$

In case fluid separation takes place from the upper side of the body two flow scenarios are possible having singularity on the front edge (fig. 5) and on the rear edge (Fig. 6).

The front edge separation case has the following asymptotic solutions:

$$1)\quad \frac{h}{L} \to 0:\quad X = \frac{\rho a^2 h M^2 \gamma_0^2}{2\alpha^2}\left(\sqrt{\frac{L\pi}{h\alpha}} - 1\right)^2;\quad Y = -\frac{\rho a^2 M^2 \gamma_0 \pi L}{2\alpha^2};\qquad (11)$$

$$2)\quad h/L \to \infty:\quad X = \rho a^2 M^2 \frac{\gamma_0^2 \pi L}{2\alpha^3};\quad Y = -\frac{\rho a^2 M^2 \gamma_0 \pi L}{2\alpha^2}.$$

The rear edge separation case has the following asymptotic solutions:

$$1)\quad \frac{h}{L} \to 0:\quad X = \rho a^2 h M^2 \gamma_0^2 \left(2\sqrt{\frac{h\alpha}{L\pi}} - 3 + \frac{L\pi}{h\alpha}\right);$$

$$Y = -\rho h a^2 M^2 \frac{\gamma_0}{\alpha}\left(2\sqrt{\frac{h\alpha}{L\pi}} - 3 + \frac{L\pi}{h\alpha}\right);$$

$$2)\quad h/L \to \infty:\quad X = \rho a^2 M^2 \gamma_0^2 \frac{3\pi L}{\alpha};\quad Y = -\frac{\rho a^2 M^2 \gamma_0}{\alpha^2} 3\pi L.$$

The two possible scenarios of the flow could be relevant to motion of plates, which have different curvature. The linearized problem statement does not take into account curvature of the plate. However, analysis of results shows, that singularity at the front or at the rear edge could occur due to additional effect of plate curvature as shown in Figs. 3-4 and 5-6.

The solution (11) for the depth h being exactly equal to zero gives the following formulas:

$$X = \frac{\rho V_0^2 \gamma_0^2 L\pi}{2(\sqrt{1 - M^2})^3},\quad Y = -\frac{\rho V_0^2 \gamma_0 \pi L}{2(1 - M^2)},$$

which for incompressible fluid ($M \to 0$) provides exact matching with classical solution for a gliding plate [7].

5   Conclusions

The solution was obtained for a problem of infinite span wing motion in compressible fluid at a depth h, constant velocity V_0 and inclination angle. Both cases of positive and negative inclination were regarded, which means flow separation from the upper side and bottom side of the wing. The solution allows determining drag and lift forces in the limiting cases. It was shown that on Mach number tending to unity both forces infinitely increase, for relatively thick fluid layer above the moving wing the resistance force does not depend on the layer thickness, but depends on body length and inclination angle, and for relatively thin fluid layer forces depend on layer thickness.

Analysis of the obtained solution shows that it could describe the fluid flow induced by wings of both positive and negative curvature, which could have singularity at the rear or at the front edge.

Acknowledgements

References

[1] Gurevich M.I., Yanpolskii A.R. On motion of a gliding plate. Techniques of the aviation fleet, 1933, 10.

[2] Haskind M.D. Plane problem on gliding over the surface of heavy fluid. Proc. Acad. Sci. USSR, Tech.Sci. Ser., 1943, 1-2.

[3] Gurevich M.I. Gliding of a circle segment over the surface of heavy fluid. TsAGI Tech. Papers, 1937, 153, $1 - 6$.

[4] Chaplyguin Yu.S. Gliding on the surface of fluid of final depth. Journ. Applied Math. and Mech., 1941, 5, 2.

[5] Chaplyguin Yu.S. Gliding of a flat plate of infinite span over the surface of heavy fluid. TsAGI Tech. Papers, 1942, 508.

[6] Green A. E. The gliding of a plate on a stream of finite depth. Proc. Cambridge Phil. Soc., 1935, 31, 4.

[7] Sedov L.I. Plane problems of hydrodynamics and aerodynamics. Moscow: Science Publ., 1980.

[8] Smirnova M.N. , A.V. Zvyaguin. Motion of a rigid body in compressible fluid with a free surface. Proc. 6-th IASME/WSEAS Conference, Rhodes, 2008, 1, 61-66.

[9] Zvyaguin A.V., Smirnova M.N. Motion of a slender body near the free surface of compressible fluid. Moscow University Mechanics Bulletin, 2009, 64, 2, 5-15.

[10] Smirnova M.N., Zvyaguin A.V. Fluid flow interaction with an obstacle near free surface. Acta Astronautica 64 (2009) 288–294.

M.N. Smirnova, Faculty of Mechanics and Mathematics, Moscow M.V. Lomonosov State University, Moscow 119992, Leninskie Gory 1, RUSSIA

Description of rotation in the movable cellular automaton method

Aleksey Yu. Smolin
asmolin@ispms.tsc.ru

Abstract

The problem of rotation description in particle method is discussed. It is shown that taking into account rotation either as a degree of freedom or via motion of neighboring particles allows describing classical continuum. To describe more complex media it is required to realize the both ways and to consider rotational degree of freedom as independent rotation.

Introduction

Rotation takes place in the nature at any scale level from elementary particles to galaxies. In physical mesomechanics, which studies a solid under mechanical loading as a multilevel self-organizing system, rotation of structure elements of the material is considered as an important part of deformation mechanism [1, 2]. In the movable cellular automaton (MCA) method, a discrete method for simulation material behavior at meso- and macroscale, rotation is taken into account as an independent degree of freedom of an automaton in addition to translation motion of its centroid [3]. This approach has been used from the very beginning of the method development as a postulate [4]. When automaton size tends to zero, the MCA method would describe some continuum. It was shown that using linear response function for automata tends to the Hook's law for the result continuum when automaton size vanishes [5]. But rotation was not taken into account in that paper and therefore it has been still undetermined what a continuum the MCA method describes when automaton size vanishes: a classical one, where an elementary point has no rotational degree of freedom or a micropolar one, where an elementary volume has nonzero inertia moment and is characterized by independent rotation [6, 7].

The results obtained by simulation using the MCA method showed that it allows describing behavior of classical continuum. It gave a basis to couple the MCA method with numerical methods of continuum mechanics naturally to study the problem where local regions of severe deformation could be explicitly defined a priori while the other regions are deformed slightly [8]. It should be noted that deformation of continuum here was governed by hyper-elastic law and stress computation took rotation of Lagrangian mesh cell into account [9]. Because the nodes of the mesh only translated, to took rotation into account distortions of the corresponded cells was considered.

Thus, there are two approaches for taking into account rotation under deformation. The first one describes it explicitly and leads to increase of the phase space dimension; the second one describes it implicitly as a result of collective behavior of the elements of the model media.

Therefore it is an urgent problem to study peculiarities of the both approaches for taking into account rotation and to reveal their advantages and disadvantages. In this paper the both approaches are considered in the framework of the movable cellular automaton method.

1 Taking into account rotation as independent degree of freedom in the framework of MCA method

Note, that description of rotation in the MCA method is adopted basically from discrete element method [10] where an element rotation is described explicitly due to its finite size. At that there is a moment of forces acting among automata and applied in their contacts in the right side of the Euler equation (for rotational velocity). But for correct describing of motion of the media, not an ensemble of particles, it is required to add a moment which resists to relative rotation of the elements to the moment of inter-element forces. Let us explain it in detail.

Let us consider calculation of the force resisting shear deformation in movable cellular automata in 3D. As is well known [11], any point of rotating rigid solid has the same rotational velocity $\vec{\omega}$ and its translational velocity is described by the formula

$$\vec{v}_{A} = \vec{v}_{O} + \vec{\omega} \times \vec{r}_{OA}$$

where $\vec{v}_{A}$ and $\vec{v}_{O}$ are translational velocities of the points A and O in any inertial coordinate system, $\vec{r}_{OA}$ is the vector connecting points O and A. In case of rotation of automaton pair as a rigid body (without deformation) this formula can be written as follows (fig. 1):

$$\vec{v}_{j} - \vec{v}_{i} = \vec{\omega}_{ij} \times \vec{r}_{ij},$$

where $\vec{r}_{ij} = (\vec{r}_{j} - \vec{r}_{i})$, $\vec{\omega}_{ij}$ is rotational velocity of the pair as a whole (rigid body). If premultiply both sides of this equation by vector $\vec{r}_{ij}$ and neglect rotation about pair axis (i.e. $\vec{\omega}_{ij} \cdot \vec{r}_{ij} = 0$), then one can obtain the following formula for $\vec{\omega}_{ij}$:

$$\vec{\omega}_{ij} = \frac{(\vec{r}_{j} - \vec{r}_{i}) \times (\vec{v}_{j} - \vec{v}_{i})}{r_{ij}^{2}} = \frac{\vec{n}_{ij} \times (\vec{v}_{j} - \vec{v}_{i})}{r_{ij}},$$

where $\vec{n}_{ij}$ is the unit vector directed from the center of automaton i to the center of automaton j.

Instantaneous rate of shear strain of automaton i under its interaction with automaton j can be defined as a ratio of tangential velocity in the contact point to the distance q_{ij} from the center of automaton i to its contact with automaton j:

$$\vec{\omega}_{ij}^{sh} = \frac{\vec{V}_{ij}^{\tau}}{q_{ij}} = \frac{q_{ij}(\vec{\omega}_{ij} - \vec{\omega}_{i}) \times \vec{n}_{ij}}{q_{ij}} = (\vec{\omega}_{ij} - \vec{\omega}_{i}) \times \vec{n}_{ij}.$$
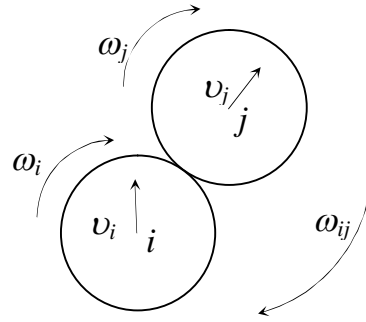
Figure 1: Rotation of a pair of automata.

Angular value of shear strain of automaton i at time T is defined by the integral

$$\vec{\gamma}^{ij} = \int_0^T \vec{\omega}_{ij}^{sh}(t)\,dt = \vec{\theta}_{ij} - \vec{\theta}_i, \tag{1}$$

where $\vec{\theta}_{ij}$ is vector of rotation of the pair axis relative to the initial position.

For small deformation we can use linear (Hook's) law to compute the resistance force:

$$\vec{f}_{ij}^e = -(G_i\vec{\gamma}_{ij} + G_j\vec{\gamma}_{ji}) \times \vec{n}_{ij}, \tag{2}$$

where G_i is the shear modulus of the material of automaton i. Equation (2) describes the pair tangential force produced by shear strain of each automata of the pair.

From equations (1) and (2) one can see, that in case of rotation of automata with velocities of the same value but in the opposite directions ($\theta_{ij} = 0$ and $\theta_i = -\theta_j$)), the shear resisting force (2) does not prevent such motion. But the medium, described by such automata is subjected to deformation and has to resist it. In case of linear elastic media the resulting moment should be proportional to the difference of rotation vectors in the pair $\vec{\theta}_j - \vec{\theta}_i$. The question is: what is the aspect ratio? Which elastic modulus we can use for this moment? If consider a pair as a brick of a medium, then such deformation may be considered as bending of a beam. In strength of materials the resulting moment is defined by the Young's modulus [12]. But if we consider a pair of automata as a couple of disks, then the aspect ratio should be equal to the shear modulus. Test computations showed that in case of uniaxial tension–compression and simple shearing strain the value of the aspect ratio to calculate the moment resisting to relative rotation practically has no effect on stress-strain diagrams. It could be explained by the fact that in such tests we register only forces and the role of the moments defined by this modulus is to eliminate a mismatch in automata rotation. Resulting moments on the surface where loading is applied are not analyzed usually. But it should be noted that in case of simple shear strain and using periodic boundary conditions in the direction of shear, the moments resulting among the surface automata are mutually vanish.

2 Taking into account rotation as cooperative motion of medium elements

Numerical methods of classical continuum mechanics give solution of motion equations as displacement or translation velocities of mesh nodes and do not consider rotation of these nodes. Rotations in the medium can be computed from consideration of strain of the mesh cells containing the node examined. Obviously, this approach should allow computing rotation in the MCA method also. To do so, rotation velocity of an element may be considered as an average rotation velocity of all its neighbors interacting with it. It is very simple to do it in 2D because rotation is described by a scalar here. An average rotational velocity is defined by the formula

$$\omega_i = \frac{\sum_j \omega_{ij}}{N},$$

where ω_{ij} is rotational velocity of the axis of pair i–j, N — number of automata interacting with automaton i.

In 3D rotation is described by an orthogonal tensor or vector having three independent components. The problem how to determine average rotation may be formulated as follows. There are points $j = 1..N$, defined by vectors $\vec{r}_{ij}$, starting at the fixed point i. Each point j moves relative to point i with velocity $\vec{v}_{ij}$. This motion can be represented as rotation of a solid having j points about point i. Real motion of each point j is a sum of such average rotation of a solid and deformation of this solid. The problem: to determine rotational velocity $\vec{\omega}_i$ of this solid.

As is well known [11], angular momentum of a rigid body rotating about an axis defined by the unit vector $\vec{n}_\omega$, is determined by the following expression

$$K = \sum_j r_j \times m_j v_j = \sum_j m_j v_j \rho_j = \sum_j m_j \omega \rho_j^2 = J\omega,$$

where $\rho_j = |\vec{n}_\omega \times \vec{r}_j|$ is a distance from the axis of rotation to point j, J is the moment of inertia of the body with respect to axis $\vec{n}_\omega$. Then the requirement that motion of the set of points $j = 1..N$ corresponds to rotation of a solid on average can be expressed as equality of the corresponding moments of inertia:

$$\omega \sum_j m_j \rho_j^2 = \sum_j r_{ij} \times m_j v_{ij},$$

Taking into account that all automata has the same mass and $\vec{r}_{ij} \times \vec{v}_{ij} = r_{ij}^2 \vec{\omega}_j$ we can express the sought rotational velocity as follows

$$\vec{\omega}_j = \frac{\sum_j r_{ij}^2 \vec{\omega}_j}{\sum_j |\vec{n}_\omega \times \vec{r}_{ij}|^2}.$$

Computations with rotation taken into account in such way showed that in this case we have the same behavior as in case of taking into account rotation explicitly. At least compression–tension tests, shear and the Lamb's problem did not reveal any significant dissimilarity.

3 Advantages of taking into account rotation as independent degree of freedom

In spite of similarity of the results in both approaches it should be noted that taking into account rotation as independent degree of freedom allows modeling more complicated medium with implicit describing its internal structure. For example, it was shown that stress tensor for such medium in general is a nonsymmetrical one, as it should be for a Cosserat medium with bending torsion [7]. More of that, it is possible to get a constitutive equation for micropolar medium describing a granular media based on computations by discrete element method (with explicit rotation) [13].
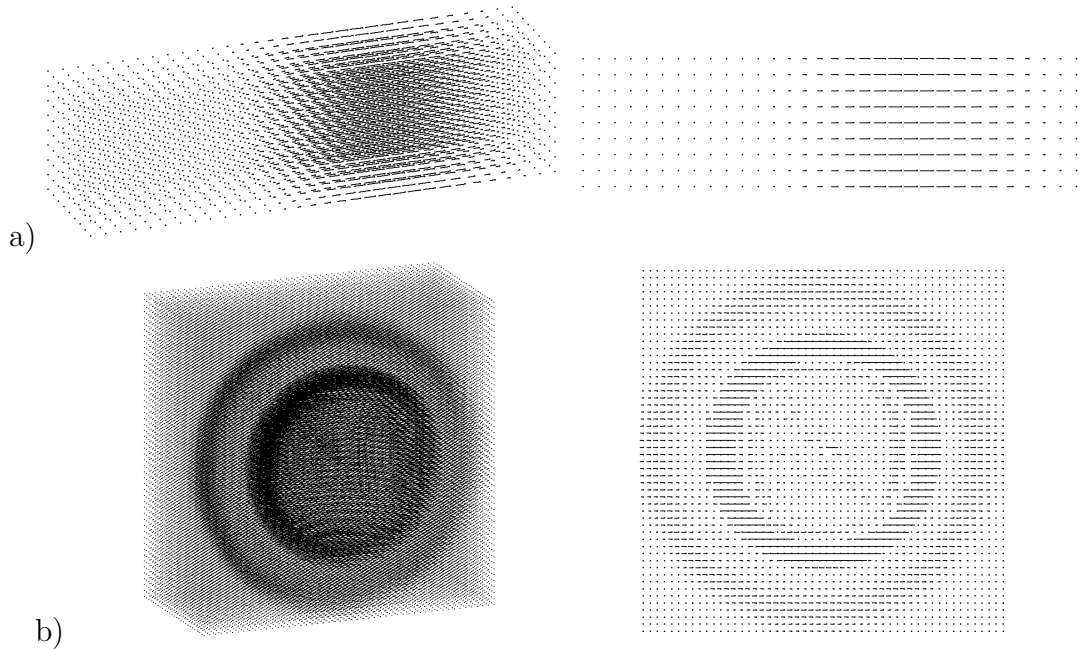
Figure 2: Plane (a) and spherical (b) waves of longitudinal rotation as vector field of rotational velocities of movable cellular automata (3D images are shown at the left, cross section at the right).

Taking into account rotation by the both approaches simultaneously gives the possibility to model a Cosserat medium by the MCA method if consider rotational degree of freedom as independent rotation. Of course, this leads to necessity of introducing additional elastic moduli, which are considered in the theory of micropolar media and can be defined experimentally [7]. As is well known, a new type of elastic waves are possible in such a medium, for example longitudinal rotation wave. Fig. 2 shows development of plane and spherical waves of longitudinal rotation, computed by the MCA method. The plane wave is initialized by setting all the automata at right face of the prism the same rotational velocity, the spherical one — by setting rotational velocity to the automaton in the center of the cubic body. In spite of bell-shaped (positive) initial signal in both case the initial direction of rotation remains only for the plane wave. In case of point source the resulting wave consists of two regions of opposite rotation just as a spherical longitudinal elastic wave consists of a

compression region followed by an expansion region [14].

For modeling classical medium, taking into account rotation as motion of surrounding neighbors would be more correct. But disadvantage of this approach is an ambiguity in computation of rotation as an average motion in case of breaking one ore more bonds with neighbors or in case of formation of a new bond that may occur under severe deformation. But the MCA method is widely used for successful modeling namely such processes.

4 Significance of taking into account rotation for MCA method

Let us consider how significant is rotation for the MCA method. For this purpose we analyzed the problem of elastic waves generation and propagation in a half-space from the point source on the surface (the Lamb's problem) solved by the MCA method with taking into account rotation and without it (fig. 3). According to symmetry of the problem we considered a quater of cubic steel sample with the size of $0.25 \times 0.25 \times 0.25$ m ($\rho = 7800$ kg/m^3, $\nu_P = 5.95$ km/s, $\nu_S = 3.19$ km/s). The automaton size was 0.0025 m. Symmetric boundary conditions was applied on the planes $X = 0$ and $Y = 0$, the other faces of the cube were free. Initial pulse of velocity was applied in the origin of coordinates (shown in fig. 3 by the arrow) as a "bell" of sine curve during 5 μs. All the results in fig. 3 shown at 40μs in $Y = 0$ plane.

As a result of such loading the longitudinal P and transverse (shear) S elastic waves are formed at some distance from the source in the medium. These waves propagate with different velocities. Free surface of the body cause generation of the conical and surface waves. The conical wave C forms in the region of interaction of the longitudinal wave with the free surface, it connects the longitudinal and transverse wave fronts. Near the free surface a little behind the transverse wave a Rayleigh wave R propagates, it has elliptical polarization and significantly decays by depth.

The computation show that the results obtained without rotation taken into account depend on the packing of automata used. More of that, Rayleigh's wave in that case vanishes and the shear wave propagates immediately after the longitudinal wave with the same velocity, that is a qualitatively wrong result (fig. 3,c–d). It has to be noted that close packing in 2D has larger order of symmetry and provides qualitatively correct results (fig 3,b), there is just a difference in wave velocities. Taking into account rotation provides simulation result to be not depending on the used packing of automata and physically correctness of elastic waves description for continuum (fig 3,e–f).

The second example, demonstrating necessity of taking into account rotation in the MCA method is a result of simulation of simple shear, shown in fig. 4. Here there are only plots for FCC packing because the diagrams for cubic packing agree closely with them. It is seen that without rotation taken into account the inclination of the diagrams is two time grater than the shear modulus $G = 79$ GPa. This is because the displacement Δx in that case totally corresponds to shear strain $\gamma_{ij} = \gamma = \Delta x/h$, while according to the formula of small strain tensor $\varepsilon_{ij} = 1/2(\partial u_y/\partial x + \partial u_x/\partial y)$
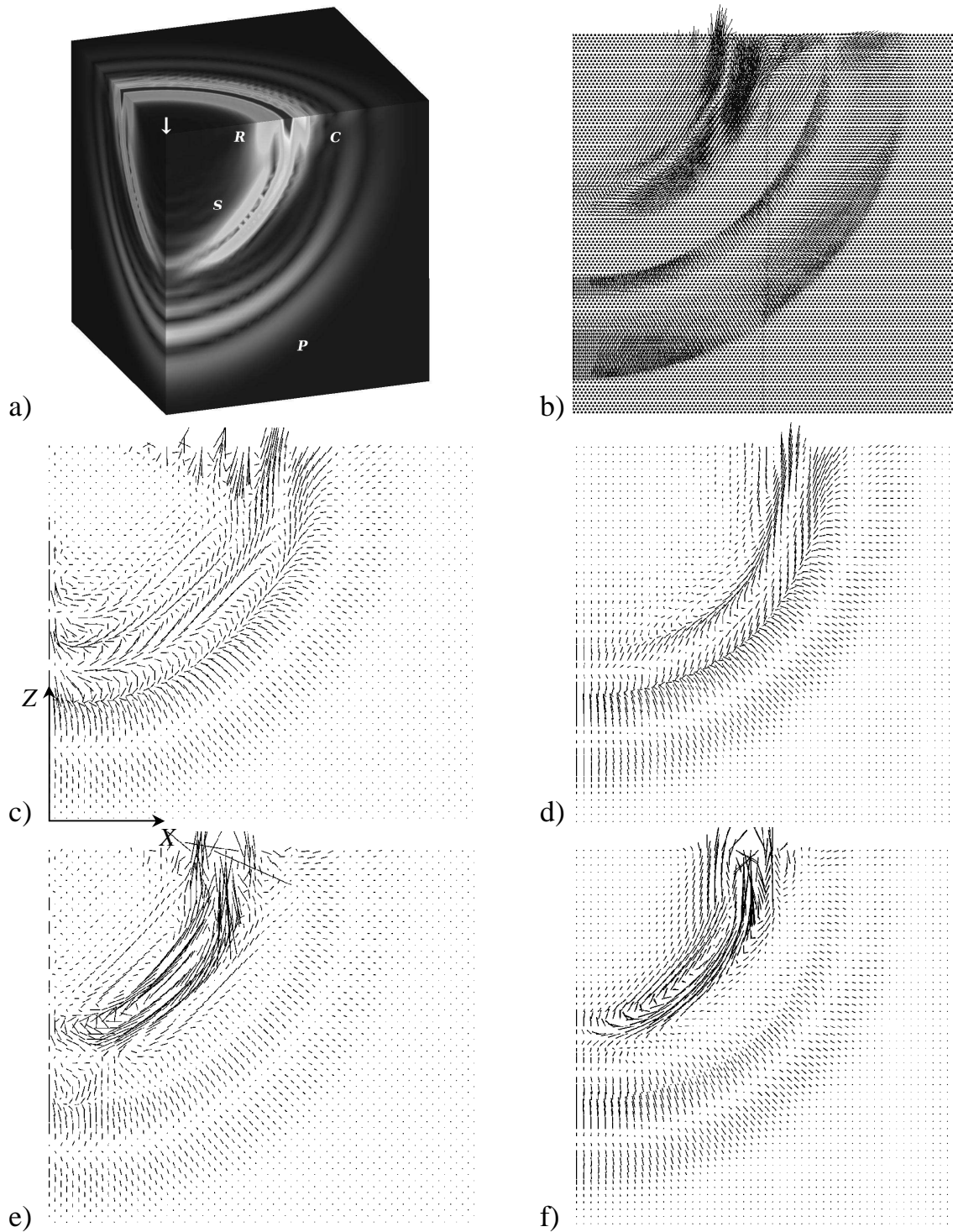
Figure 3: Movable cellular automata velocity field for the Lamb's problem and various models and packings: a,f — cubic packing with rotation of automata, b — close packing without rotation taken into account, c — FCC packing without rotation, d — cubic packing without rotation, e — FCC packing with rotation.

under simple shear it is to be equal to $\varepsilon_{ij} = 0.5\gamma$. I.e. a sample under simple shear is deformed with the shear strain equal to 0.5γ and rotates as a whole on the same

angle. Indeed, the computation shows that in case of rotation is taken into account all automata of the sample under simple shear are rotated on the angle equal to 0.5γ and shear strain in all pairs have the same value.
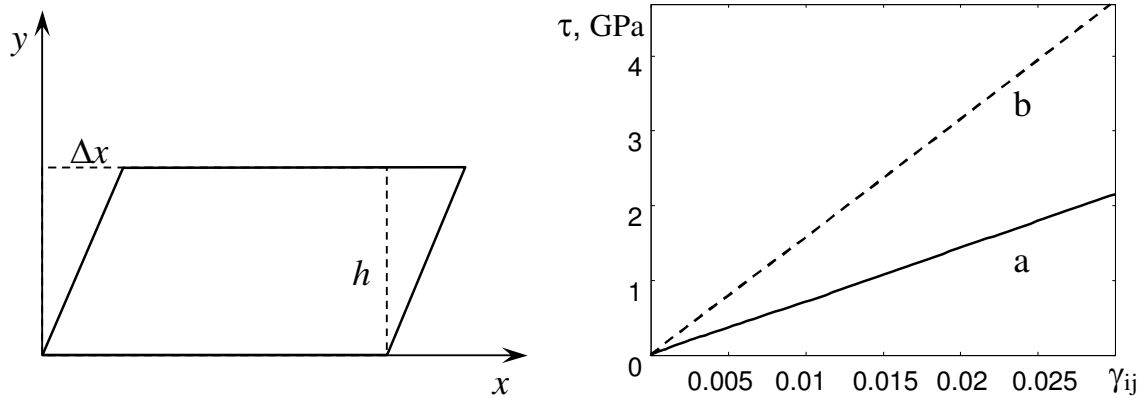
Figure 4: Scheme of sample loading and corresponding loading diagrams for simple shear. The curve (a) corresponds to FCC packing with rotation taken into account, (b) — FCC without rotation.

Conclusions

Thus, the study conducted shows that rotation of automata taken into account as independed degree of freedom or via motion of neighboring automata allows correct describing classical continuum by the movable cellular automata method. To describe more complex media (for example Cosserat continuum) it is required to realize the both ways and to consider rotational degree of freedom as independent rotation.

Acknowledgements

References

[1] Panin V.E., Likhachev V.A., Grinyaev Yu.V. Strukturnye urovni deformacii tverdykh tel.– Novosibirsk: Nauka, Sib. div, 1985.– 230 p. (in Russian)

[2] Panin V.E. Fundamentals of physical mesomechanics // Physical mesomechanics.– 1998.– V. 1, No 1.– P.5–22. (in Russian)

[3] Psakhie S.G., Dmitriev A.I., Shilko E.V., et al. Method of movable cellular automata as a new trend in discrete computational mechanics. I. Theoretical

description // Physical mesomechanics.– 2000.– V. 3, No 2.– P. 5–15. (in Russian)

[4] Psakhie S.G. Horie Ya., Korostelev S.Yu. et al. Method of Movable Cellular Automata as a Tool for Simulation Within the Framework of Mesomechanics // Russian Physics Journal.– 1995.– V. 38, No 11.– P. 1157–1168.

[5] Psakhie S.G., Chertov M.A., Shilko E.V. Interpretation of the parameters of the method of movable cellular automata on the basis of continuum description // Physical mesomechanics.– 2000.– V. 3, No 3.– P. 89–92.

[6] Cosserat E. et F. Theórie des Corps Deformables. – Paris: Librairie Scientifique A. Hermann et Fils., 1909. – 230 p.

[7] Erofeev V.I. Wave processes in solids with microstructure. – Moscow: Moscow state univ., 1999. – 328 p. (in Russian)

[8] Psakhie S.G., Smolin A.Yu., Stefanov Yu.P. et all. Modeling the behavior of complex media by jointly using discrete and continuum approaches // Tech. Phys. Lett.– 2004.– V. 30.– P.712–714.

[9] Wilkins M.L. Calculation of elastic-plastic flow / Methods in computational physics, V. 3, ed. by B. Alder, S. Fernbach and M.V.Rotenberg.– New York:Academic Press, 1964.– P. 211–263.

[10] Cundall P.A., Strack O.D.L. A discrete numerical model for granular assemblies // Geotechnique.– 1979.– V.29, No. 1.– P. 47–65.

[11] Landau L.D. Lifshits E.M. Theoretical physics V.1. Mechanics.– Moscow: Nauka, 1988.– 216 p. (in Russian)

[12] Aleksandrov A.V., Potapov V.D., Derzhavin B.P. Strength of materials: a Course for univ.– Moscow: Vysshaya shkola, 2001.– 560 p. (in Russian)

[13] Walsh S.D.C., Tordesillas A.A. thermomechanical approach to the development of micropolar constitutive models of granular media // Acta Mechanica.– 2004.– V. 167, No 3–4.– P. 145–169.

[14] Zel'dovich Ya.B., Raizer Yu.P. Physics of shock waves and high-temperature hydrodynamics phenomena. Moscow: Nauka, 1966.– 686 p. (in Russian)

Aleksey Yu. Smolin, pr. Academicheskii 2/4, Tomsk, 634021 Rissia

Dynamic properties of nonlinear system with oscillating pendulum

V. S. Sorokin

slavos87@mail.ru

Abstract

Analysis of motion of nonlinear mechanical systems, containing pendulums is the generic problem for studying the internal resonance effect. Furthermore, investigations of this type are useful in search for systems with high efficiency coefficient. Specifically, paradoxical high magnitudes of the efficiency coefficient of the considered system have been reported in different references.

In the present work, the motion of the system of two coupled mathematical pendulums is examined. A harmonic load is applied to one of the pendulums. The deflection of one pendulum and the angle of rotation of another one are introduced as generalized coordinates. The motion of the system is examined for excitation close to the eigenfrequency of one of the pendulums in the case of internal parametric resonance (the eigenfrequency of one pendulum is twice as large as the eigenfrequency of another). The iterative method is used to solve this problem [1].

This work is initiated by the paradox results reported in [2-3]. It also be pointed out that a similar mechanical system with two degrees of freedom has been considered in [4] using the method of multiple scales.

1 Model system and equations of motion

The two degrees of freedom system consists of two coupled pendulums as shown in Figure 1.
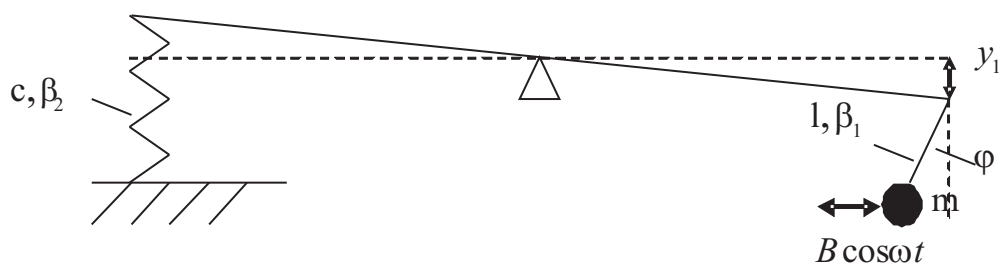

Figure 1: The model mechanical system

A pendulum is suspended at the edge of another one. The opposite edge of the second pendulum is supported by a spring element with the stiffness c and a dissipative element with the coefficient of viscous damping β_2.

The equations of motion of this system have the following form:

$$ml^2\ddot{\varphi} + \beta_1\dot{\varphi} + ml(g - \ddot{y}_1)\varphi = B\cos\omega t \tag{1}$$

$$m\ddot{y}_1 + \beta_2\dot{y}_1 + cy_1 - ml(\varphi\ddot{\varphi} + \dot{\varphi}^2) = mg \tag{2}$$

Here y_1 is the deflection of the right edge of the first pendulum, φ is the angle of rotation of the second pendulum, l is the length of the second pendulum, β_1 is the coefficient of viscous damping of the dissipative element connected to the second pendulum; B is the amplitude and ω is the frequency of excitation. Time differentiation is denoted by dot.

It is expedient to introduce the scaled parameters: $A = \frac{B}{ml^2}$, $2n_1 = \frac{\beta_1}{ml^2}$, $\lambda^2 = \frac{g}{l}$, $2n_2 = \frac{\beta_2}{m}$, $q^2 = \frac{c}{m}$. And the scaled variable: $y = \frac{y_1}{l} - \frac{g}{lq^2}$. Then equations (1-2) acquire in the nondimensional form:

$$\ddot{\varphi} + 2n_1\dot{\varphi} + (\lambda^2 - \ddot{y})\varphi = A\cos\omega t \tag{3}$$

$$\ddot{y} + 2n_2\dot{y} + q^2 y - (\varphi\ddot{\varphi} + \dot{\varphi}^2) = 0 \tag{4}$$

2 Solution of the problem

As already mentioned, the case of combined external $\omega \approx \lambda$ and parametric resonance $q \approx 2\lambda$ is considered. In solving equations (3-4), dissipation is not regarded as small.

The governing equations are transformed as:

$$\ddot{\varphi} + \lambda^2\varphi = \varepsilon\ddot{y}\varphi + A\cos\omega t - 2n_1\dot{\varphi} \tag{5}$$

$$\ddot{y} + q^2 y = \varphi\ddot{\varphi} + \dot{\varphi}^2 - 2n_2\dot{y} \tag{6}$$

Here the bookkeeper ε is introduced to mark the weakly nonlinear term in equation (5). The problem is solved by iterative method with regular expansion of solution in powers of the parameter ε:

$$\varphi(t) = \varphi_0 + \varepsilon\varphi_1$$

$$y(t) = y_0 + \varepsilon y_1$$

Accordingly to the method, φ_0 and y_0 are determined from equations:

$$\ddot{\varphi}_0 + 2n_1\dot{\varphi}_0 + \lambda^2\varphi_0 = A\cos\omega t \tag{7}$$

$$\ddot{y}_0 + 2n_2\dot{y}_0 + q^2 y_0 = \varphi_0\ddot{\varphi}_0 + \dot{\varphi}_0^2 \tag{8}$$

The functions φ_1 and y_1 are found from:

$$\ddot{\varphi}_1 + 2n_1\dot{\varphi}_1 + \lambda^2\varphi_1 = \ddot{y}_0\varphi_0 \tag{9}$$

$$\ddot{y}_1 + 2n_2\dot{y}_1 + q^2 y_1 = \varphi_0\ddot{\varphi}_1 + \varphi_1\ddot{\varphi}_0 + 2\dot{\varphi}_0\dot{\varphi}_1 \tag{10}$$

As follows from (7):

$$\varphi_0 = A_1\cos(\omega t - \psi_1) \tag{11}$$

Here the amplitude A_1 and the phase ψ_1 are:

$$A_1 = \frac{A}{\sqrt{(\lambda^2 - \omega^2)^2 + (2n_1\omega)^2}} \qquad \mathrm{tg}\,\psi_1 = \frac{2n_1\omega}{\lambda^2 - \omega^2} \tag{12}$$

Then equation (8) is transformed as:

$$\ddot{y}_0 + 2n_2\dot{y}_0 + q^2 y_0 = -\omega^2 A_1^2 \cos(2(\omega t - \psi_1)) \tag{13}$$

Solution of equation (13) is:

$$y_0 = A_2\cos(2\omega t - \psi_2) \tag{14}$$

Here the amplitude A_2 and the phase ψ_2 are:

$$A_2 = \frac{\omega^2 A_1^2}{\sqrt{(q^2 - 4\omega^2)^2 + (4n_2\omega)^2}} \qquad \mathrm{tg}(\psi_2 - 2\psi_1) = \frac{4n_2\omega}{q^2 - 4\omega^2} \tag{15}$$

Now equations (9-10) should be solved. Equation (9) is written in the following form:

$$\ddot{\varphi}_1 + 2n_1\dot{\varphi}_1 + \lambda^2\varphi_1 = -2\omega^2 A_2 A_1(\cos(3\omega t - \psi_1 - \psi_2) + \cos(\omega t - \psi_2 + \psi_1)) \tag{16}$$

Its solution is:

$$\varphi_1 = B_1\cos(3\omega t - \psi_3) + B_2\cos(\omega t - \psi_4) \tag{17}$$

Here the amplitudes B_1 and B_2 and the phases ψ_3 and ψ_4 are:

$$B_1 = \frac{2\omega^2 A_2 A_1}{\sqrt{(\lambda^2 - 9\omega^2)^2 + (6n_1\omega)^2}} \qquad \mathrm{tg}(\psi_3 - \psi_1 - \psi_2) = \frac{6n_1\omega}{\lambda^2 - 9\omega^2} \tag{18}$$

$$B_2 = \frac{2\omega^2 A_2 A_1}{\sqrt{(\lambda^2 - \omega^2)^2 + (n_1\omega)^2}} \qquad \mathrm{tg}(\psi_4 + \psi_1 - \psi_2) = \frac{2n_1\omega}{\lambda^2 - \omega^2} \tag{19}$$

Equation (10) is written in the following form:

$$\ddot{y}_1 + 2n_2\dot{y}_1 + q^2 y_1 = -\omega^2 A_1(8B_1\cos(4\omega t - \psi_1 - \psi_3) + \\ + 2B_1\cos(2\omega t - \psi_3 + \psi_1) + 2B_2\cos(2\omega t - \psi_1 - \psi_4)) \tag{20}$$

The solution is:

$$y_1 = C_1\cos(4\omega t - \psi_5) + C_2\cos(2\omega t - \psi_6) + C_3\cos(2\omega t - \psi_7) \tag{21}$$

Here:

$$C_1 = \frac{8\omega^2 A_1 B_1}{\sqrt{(q^2 - 16\omega^2)^2 + (8n_2\omega)^2}} \qquad \mathrm{tg}(\psi_5 - \psi_1 - \psi_3) = \frac{8n_2\omega}{q^2 - 16\omega^2} \tag{22}$$

$$C_2 = \frac{2\omega^2 A_1 B_1}{\sqrt{(q^2 - 4\omega^2)^2 + (4n_2\omega)^2}} \qquad \text{tg}(\psi_6 + \psi_1 - \psi_3) = \frac{4n_2\omega}{q^2 - 4\omega^2} \qquad (23)$$

$$C_3 = \frac{2\omega^2 A_1 B_2}{\sqrt{(q^2 - 4\omega^2)^2 + (4n_2\omega)^2}} \qquad \text{tg}(\psi_7 - \psi_1 - \psi_4) = \frac{4n_2\omega}{q^2 - 4\omega^2} \qquad (24)$$

The final result is the following:

$$\varphi = A_1 \cos(\omega t - \psi_1) + \varepsilon(B_1 \cos(3\omega t - \psi_3) + B_2 \cos(\omega t - \psi_4)) \qquad (25)$$

$$y = A_2 \cos(2\omega t - \psi_2) + \varepsilon(C_1 \cos(4\omega t - \psi_5) + C_2 \cos(2\omega t - \psi_6) + \\ + C_3 \cos(2\omega t - \psi_7)) \qquad (26)$$

3   The energy conservation in this system

In the paper [3], it is suggested that the efficiency of this system may exceed unity, i.e., some 'additional energy' is produced. This statement can be easily disqualified with the solution (25-26) presented in the previous section. So, the work of external forces is written as:

$$A_{in} = \int_0^T M \cdot \dot\varphi \, dt + \int_0^T M_1 \cdot \dot y_1 \, dt \qquad (27)$$

Here $M = B \cos \omega t$ - is the moment of external forces applied to the inertial element m, and $M_1 = -ml(\omega^2 A_1^2 \cos(2(\omega t - \psi_1)))$ is the force acting at the pendulum with a spring from the other pendulum, $T = \frac{2\pi}{\omega}$ is the period of oscillations.
The energy losses due to dissipation are defined as:

$$A_{out} = \int_0^T \beta_1 \dot\varphi \cdot \dot\varphi \, dt + \int_0^T \beta_2 \dot y_1 \cdot \dot y_1 \, dt \qquad (28)$$

Employing the formulas (25)-(26) we obtain the following expression for the work of external forces:

$$A_{in} = \pi B(A_1 \sin \psi_1 + \varepsilon B_2 \sin \psi_4) + 2\pi\omega^2 ml^2 A_1^2 (A_2 \sin(2\psi_1 - \psi_2) + \\ + \varepsilon C_2 \sin(2\psi_1 - \psi_6) + \varepsilon C_3 \sin(2\psi_1 - \psi_7))$$

The energy losses are found to be:

$$A_{out} = \pi\beta_1\omega(A_1^2 + \varepsilon^2(9B_1^2 + B_2^2) + 2\varepsilon A_1 B_2 \cos(\psi_1 - \psi_4)) + \\ + 4\pi l^2 \beta_2 \omega(A_2^2 + 2\varepsilon A_2(C_2 \cos(\psi_2 - \psi_6) + C_3 \cos(\psi_2 - \psi_7)) \\ + \varepsilon^2(4C_1^2 + C_2^2 + C_3^2 + 2C_2 C_3 \cos(\psi_6 - \psi_7)))$$

With the use of expression for B, we obtain the work of external forces in the form:

$$A_{in} = \pi ml^2 \omega(2n_1 A_1^2 + 8n_2 A_2^2 + O(\varepsilon)) \qquad (29)$$

The energy dissipation is:

$$A_{out} = \pi ml^2 \omega(2n_1 A_1^2 + 8n_2 A_2^2 + O(\varepsilon))$$

Therefore:

$$A_{out} - A_{in} \sim O(\varepsilon) \qquad (30)$$

Just as an illustrative example, the dependence of the external work per cycle upon excitation frequency is shown in Figure 2 for $l = 1$ sm, $m = 1$ kg, $\lambda = 1$ 1/s, $q = 2$ 1/s, $n_1 = 0.2$ 1/s, $n_2 = 0.2$ 1/s, $A = 0.1$ 1/s^2. As is seen, maximum of the work is attained at the excitation frequencies, which slightly differ from the eigenfrequency of the pendulum.
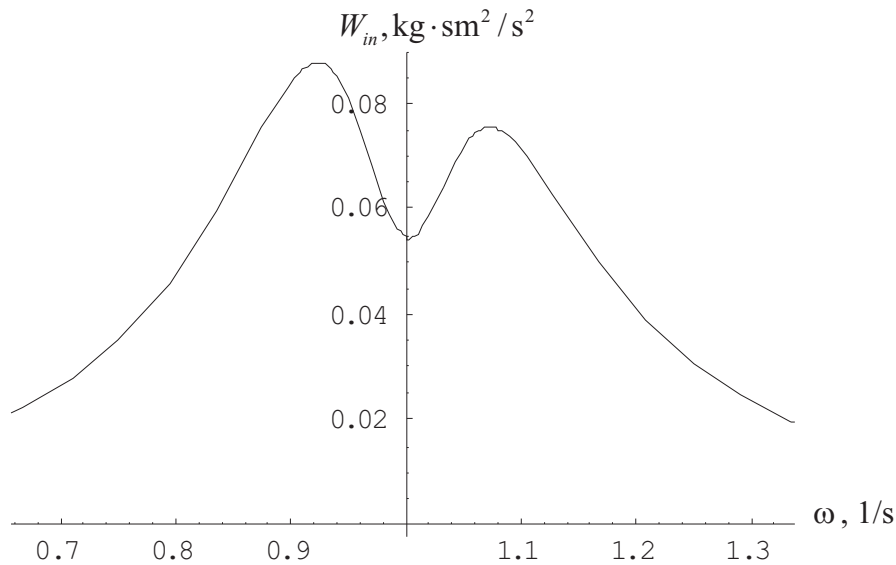
Figure 2: The dependence of the external work per cycle upon excitation frequency

4 Validation of the reported results

It should be noted that the obtained formulas are valid for relatively large viscous damping coefficients $(n_1, n_2 > 0.2\omega)$, because in solving equations (5-6) these coefficients have been assumed to be of the same order of magnitude as λ^2.

The reported results have been verified in numerical experiment by means of Matematica 5.2 [5].

For numerical experiment, the following parameters are used $\lambda = 1.1$ 1/s, $q = 2.1$ 1/s, $n_1 = 0.25$ 1/s, $n_2 = 0.25$ 1/s, $\omega = 1$ 1/s, $A = 0.1$ 1/s^2. Then formulas (12), (15), (18), (19) and (22)-(24) give the following results: $A_1 = 0.1844$, $A_2 = 0.0314$, $\psi_1 = 1.173$, $\psi_2 = 0.39$, $B_1 = 0.00146$, $B_2 = 0.0214$, $C_1 = 0.0002$, $C_2 = 0.0005$, $C_3 = 0.0073$.

In Figure 3 the time dependence of the displacement y is presented for the time interval $[100; 125]$ seconds with analytical solution plotted as a dashed line and the numerical solution plotted as a solid line.

In Figure 4 the time dependence of the angle of rotation φ for the time interval $[100; 125]$ seconds is presented in the same way.
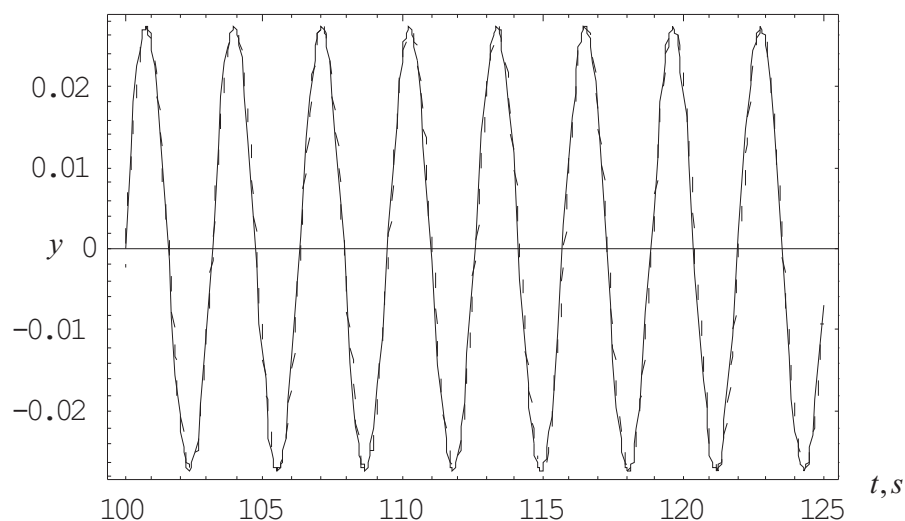
Figure 3: The time dependence of the displacement y
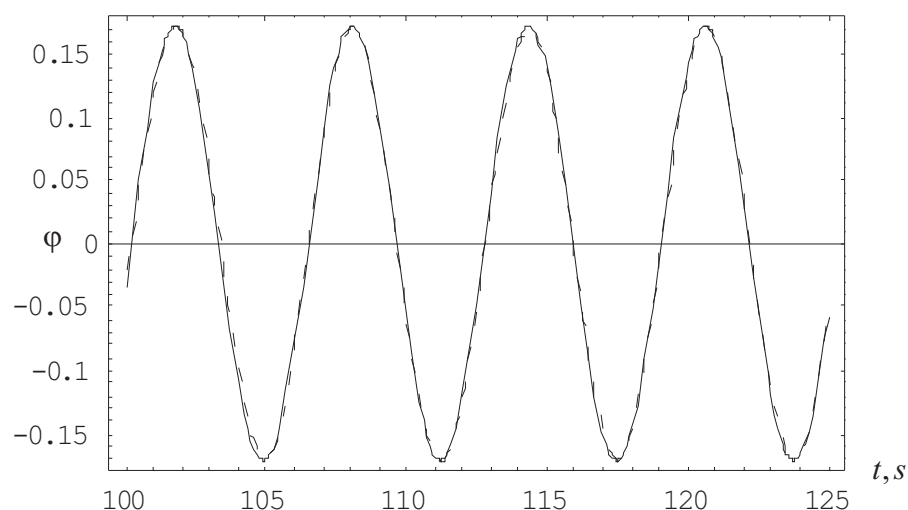
Figure 4: The time dependence of the angle of rotation φ

Obviously, there is an excellent agreement between analytical and numerical results.

5 Conclusion

Relatively simple formulas are obtained to describe the harmonically excited motion of a mechanical system, which consists of two coupled pendulums. These formulas suggest that the system is involved in the motion with the frequencies twice and three times larger than the excitation frequency. The presence of the third harmonic may be particularly pronounced at the large amplitude excitation. Furthermore, the expressions for external force work and for work of dissipation forces are obtained.

Acknowledgements

References

[1] Amosov A.A., Dubinskii Y. A., Kopchenova N.P. Computational methods for the engineers. - M.: Mir, 1998.

[2] Milkovic V. www.veljkomilkovic.com

[3] Panic L. On the track of the energy surplus of a two-stage mechanical oscillator by Veljko Milkovic, 2008.

[4] Thomsen J.J. Vibrations and Stability. Advanced Theory, Analysis and Tools. Springer, 2003.

[5] Wolfram S. Mathematica: a system for doing mathematics by computer. Reading, MA: Addison-Wesley Publishing Co., 1991

Sorokin V.S., V.O., 22 linya, 3, Saint-Petersburg, 199106, Russia

Motion of a body with variable volume (a gas bubble) in an oscillating fluid

V. S. Sorokin   I. I. Blekhman

slavos87@mail.ru

Abstract

As has been shown in a number of publications [1-5] a solid and deformable particle in a standing wave field in the fluid may either sink or rise in the direction opposite to Archimedes force. The considered mechanism of 'reverse' motion of a particle may be called gradient-induced, because it is produced by the space- and time-variability of the vibration field in a fluid or elastic continuum.

In references [6-7], it has been also shown that the velocity of motion of a deformable particle in a uniformly vibrating fluid may significantly reduce due to the nonlinearity in the fluid resistance force to the motion of the particle at large Reynolds numbers.

In this paper, motion of a deformable body (an air bubble) in an incompressible viscous fluid exposed to harmonic oscillations is studied. Isothermal variation in the size of a body due to pressure pulsations in a fluid are taken into account. As a result, fluid's reaction varies with the same period. It generates vibrational forces, which may act at the deformable body with a mass density less than the mass density of the ambient fluid (for instance, a gas bubble) so that the body sinks rather than rises up. The ranges of parameters, at which this effect occurs, are determined.

Range of sizes of gas bubbles and range of excitation frequencies, when a gas bubble should be modeled as a deformable body are given.

The effect considered in the present paper may be regarded as a special case of the more general effect of vibrational locomotion or transposition [8], generated by deformability of elements of the system.

The problem is solved within the concept of vibrational mechanics by means of the method of direct separation of motions [8]. Explicit formula for the mean velocity of a deformable body is derived. Reported results are validated by comparison with results of numerical integration of original equations of motion of a body.

1   A model of a bubble

For analysis of motion of a gas bubble in a fluid, we adopt the model, which accounts for vibration-induced variations in its volume. The model is a spherical shell of variable radius as schematically shown in Figure 1.
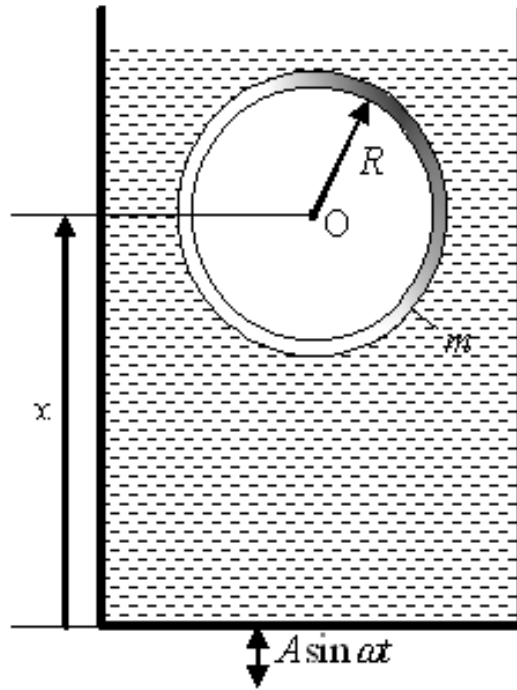
Figure 1: The model of a gas bubble in a fluid

In the course of the motion of a bubble in a fluid, its volume pulsates due to the pressure variation. In this paper, we assume that these pulsations are isothermal and, therefore, they are governed by the formula:

$$P_t V_b = \text{Const} \tag{1}$$

Here P_t is the total pressure exerted by a fluid at the bubble, V_b is the volume of the bubble. The total pressure acting at the bubble is written as:

$$P_t = P_e + \rho h(g - A\omega^2 \sin \omega t) \tag{2}$$

Here P_e is some constant 'outside' pressure, ρ is the density of the fluid, g is the gravitational acceleration, h is the height of the fluid column from the point considered, A is the amplitude, and ω is the frequency of the oscillations of the vessel. Then we obtain from equation (1) that:

$$V_b = \frac{\text{Const}}{P_e + \rho g h - \rho h A \omega^2 \sin \omega t} \tag{3}$$

As seen from equation (3) the volume of the bubble V_b is some periodic function with a period of $T = \frac{2\pi}{\omega}$. For $P_e + \rho g h \gg \rho h A \omega^2$ we can employ the following approximation of this function:

$$V_b = V_{b0}(1 + B_V \sin \omega t) \tag{4}$$

Here V_{b0} is the quiescent bubble volume. B_V is the amplitude of the relative volume change of the bubble, determined from expression:

$$B_V = \frac{\rho h A \omega^2}{P_e + \rho g h} \tag{5}$$

2 Governing equations

Equation of motion of a bubble has the following form:

$$(m + m_0)\ddot{x} = -F(\dot{x}) + (m - \rho V_b)(A\omega^2 \sin \omega t - g) \tag{6}$$

Here x is the coordinate of the center of the bubble, m is the mass of the bubble, m_0 is the added mass of a fluid, defined by the formula $m_0 = \chi V_b \rho$, with χ being an added mass coefficient, with the magnitude of $\chi = 1/2$.

The resistance force to gas bubble motion $F(\dot{x})$ is introduced in the general form. We note that the sign of $F(\dot{x})$ coincide with the sign of velocity of a gas bubble $\dot{x}$. Thus, for a rising bubble, we have $F(\dot{x}) > 0$, and for a sinking bubble we have $F(\dot{x}) < 0$.

3 Solution of the problem by the method of direct separation of motions

To solve the problem, we use the concept of vibrational mechanics and the method of direct separation of motions [8]. Solution of the equation of motion is sought in the form:

$$x = X(t) + \psi(t, \tau)$$

Where X is the slow component of the motion ψ is the fast component of the motion with the period 2π on the non-dimensional fast time $\tau = \omega t$. It's averaged over period τ magnitude vanishes:

$$\langle \psi(t, \tau) \rangle = 0$$

Here for any $h = h(t, \tau)$, T is the period of fast time τ, we define $\langle h(t, \tau) \rangle = \frac{1}{T} \int\limits_0^T h d\tau$, with t taken as a constant.

Substitution to the governing equation (6), yields the following system of equation for the variables X and ψ:

$$m\ddot{X} + \tfrac{1}{2}\rho V_{b0}(\ddot{X} + \left\langle \ddot{\psi} B_V \sin \omega t \right\rangle) = -\langle F(\dot{X} + \dot{\psi}) \rangle - \\ -mg - \tfrac{1}{2}\rho V_{b0} B_V A\omega^2 + \rho V_{b0} g \tag{7}$$

$$m\ddot{\psi} + \tfrac{1}{2}\rho V_{b0}(\ddot{\psi} + \ddot{X} B_V \sin \omega t) = -F(\dot{X} + \dot{\psi}) + \langle F(\dot{X} + \dot{\psi}) \rangle + \\ +mA\omega^2 \sin \omega t - \rho V_{b0} A\omega^2 \sin \omega t + \rho V_{b0} g B_V \sin \omega t \tag{8}$$

We should solve equation of fast motion (8) first. The essential advantage of the method of direct partition of motions is a possibility to solve the equations of fast motions in an approximate manner, if, as is typical, the equation of slow motion is the one of primary interest. In this case, in the course of solving equation (8),

we assume that the resistance force $F(\dot{X} + \dot{\psi})$ is negligibly small in comparison to the other forces, i.e. to inertia and external excitation. We also observe that the product $\ddot{X}B_V$ is much smaller than $\ddot{\psi}$ and, therefore, it may be also neglected. Then equation of fast motion is reduced to the following form:

$$m\ddot{\psi} + \frac{1}{2}\rho V_{b0}\ddot{\psi} = mA\omega^2\sin\omega t - \rho V_{b0}A\omega^2\sin\omega t + \rho V_{b0}gB_V\sin\omega t \qquad (9)$$

Steady-state solution of this equation is:

$$\psi = -B\sin\omega t \qquad (10)$$

With B defined by the formula:

$$B = \frac{(m - \rho V_{b0})A\omega^2 + \rho V_{b0}gB_V}{\omega^2(m + {}^1\!/_2\rho V_{b0})} \qquad (11)$$

Now, to derive equation of slow motion, we employ the expression $\left\langle \ddot{\psi}B_V\sin\omega t \right\rangle = \frac{B\omega^2}{2}B_V$ so that equation (7) acquires the form:

$$m\ddot{X} + \frac{1}{2}\rho V_{b0}(\ddot{X} + \frac{B\omega^2}{2}B_V) = -\langle F(\dot{X} + \dot{\psi})\rangle - mg - \frac{1}{2}\rho V_{b0}B_VA\omega^2 + \rho V_{b0}g \quad (12)$$

4 The velocity of the steady state motion and the parameters of the system, when a bubble sinks rather than rises

In a stationary (steady-state) motion of a bubble, $\dot{X} = \dot{X}_* = \text{const}$. Then the velocity $\dot{X}_*$ is found from equation:

$$\frac{1}{4}\rho V_{b0}B\omega^2B_V = -\langle F(\dot{X}_* + \dot{\psi})\rangle - mg - \frac{1}{2}\rho V_{b0}B_VA\omega^2 + \rho V_{b0}g \qquad (13)$$

It yields:

$$\langle F(\dot{X}_* + \dot{\psi})\rangle = -\frac{1}{4}\rho V_{b0}B\omega^2B_V - mg - \frac{1}{2}\rho V_{b0}B_VA\omega^2 + \rho V_{b0}g \qquad (14)$$

Expression $\langle F(\dot{X}_* + \dot{\psi})\rangle$ gives the mean magnitude of the resistance force averaged in the period $T = \frac{2\pi}{\omega}$. Now we employ the assumption that the velocity of a bubble $\dot{x} = \dot{X} + \dot{\psi}$ in the motion considered preserves its sign, i.e. $\left|\dot{X}\right| > |B|\,\omega$ and $\text{sign}(\dot{X} + \dot{\psi}) = \text{sign}\dot{X}$. Then the sign of $\langle F(\dot{X}_* + \dot{\psi})\rangle$ should coincide with the sign of the velocity of steady-state motion of the bubble $\dot{X}_*$. Therefore, if right hand side of equation (14) is positive, then the bubble moves upwards along the x-axis and if it is negative, the bubble moves downwards.

It yields the condition of bubble's sinking in the following form:

$$\frac{1}{4}\rho V_{b0}B\omega^2B_V + mg + \frac{1}{2}\rho V_{b0}B_VA\omega^2 > \rho V_{b0}g \qquad (15)$$

Now we determine the velocity of steady-state motion of the bubble $\dot{X}_*$. Its magnitude is controlled by the adopted model of the fluid resistance. In the general case, it may be formulated as [9-11]:

$$F(\dot{x}) = 4\rho R^2 \Psi(\mathrm{Re})\dot{x}^2 \mathrm{sgn}\dot{x} \tag{16}$$

Here R is the radius of the bubble, and $\Psi(\mathrm{Re})$ is the resistance coefficient, dependent on Reynolds number $\mathrm{Re} = 2\rho R\dot{x}/\mu\,\mathrm{sgn}\dot{x}$ (μ is the dynamic viscosity of the fluid). This dependence is provided by classic Rayleigh diagram [3,9-10]. In our study, we assume Reynolds numbers to be very small ($\mathrm{Re} < 1$), and we set the resistance coefficient to:

$$\Psi(\mathrm{Re}) = \frac{3\pi}{\mathrm{Re}} \tag{17}$$

Then the formula for resistance force (16) reduces to the Stokes formula [3]:

$$F(\dot{x}) = 6\pi\mu R\dot{x} \tag{18}$$

The radius of the bubble depends on the fast time $\tau = \omega t$ and it obeys the equation:

$$\frac{4}{3}\pi R^3 = V_{b0}(1 + B_V \sin\omega t) \tag{19}$$

Inasmuch as B_V is small, the variation in the radius may be given as:

$$R = R_0(1 + B_R \sin\omega t) \tag{20}$$

With R_0 as a mean radius of the bubble in the period $T = \frac{2\pi}{\omega}$, and B_R is the amplitude of its relative variation in time. Obviously, equation (19) yields:

$$R_0 = \frac{3}{4\pi}\sqrt[3]{V_{b0}}; \quad B_R = \frac{B_V}{3} \tag{21}$$

So we obtain:

$$\langle R\dot{x} \rangle = R_0(\dot{X} + \langle \dot{\psi} B_R \sin\omega t \rangle) \tag{22}$$

However, $\langle \dot{\psi}\sin\omega t \rangle = 0$, and, therefore, the period-averaged resistance force is:

$$\left\langle F(\dot{X}_* + \dot{\psi}) \right\rangle = 6\pi\mu R_0 \dot{X}_* \tag{23}$$

Finally, the steady-state velocity of the motion of the bubble is defined by the simple formula

$$\dot{X}_* = \frac{1}{6\pi\mu R_0}\left(-\frac{1}{4}\rho V_{b0}B\omega^2 B_V - mg - \frac{1}{2}\rho V_{b0}B_V A\omega^2 + \rho V_{b0}g\right) \tag{24}$$

5   Discussion of the obtained results

In the reported analysis, we have adopted the simplest model of pulsation of the volume and the radius of a bubble exposed to oscillations of the external pressure. As the result, these pulsations have appeared to be in phase with the pressure pulsations and have not contributed to vibrational force via the force $F(\dot{x})$ of fluid resistance to the motion of a bubble. Sinking of the bubble in this situation is produced only due to pulsations of the added mass and Archimedes force.

However, if the approximation (4) of formula (3) is not employed and equation for the dynamics of the radius of a bubble [4] is used, then the volume pulsations of a gas bubble become shifted from the pressure pulsations. In turn, it should produce a contribution to the vibrational force via the force $F(\dot{x})$ of fluid resistance to the motion of a bubble.

Moreover, if a nonlinear dependence of the fluid resistance force $F(\dot{x})$ on velocity $\dot{x}$ is employed (i.e., if large Reynolds numbers ($Re > 1000$) are considered), see [9-11], then the vibrational force is also amplified via the force $F(\dot{x})$ of fluid resistance to the motion of a bubble.

For frequencies $\omega < 200 \; 1/s$, a bubble should be considered as compressible if its radius exceeds 2 mm [5].

So, the condition of sinking of a bubble in the fluid is formulated by the inequality (15). It may be re-formulated as follows:

$$(m + \eta m_0)g + \delta m_0 A \omega^2 > m_0 g \tag{25}$$

Where

$$m_0 = \rho V_{b0}; \quad \delta = \frac{1}{2}B_V + \frac{m - m_0}{4m + 2m_0}B_V; \quad \eta = \frac{m_0}{4m + 2m_0}B_V^2 \tag{26}$$

If we neglect the mass of the bubble, then, as follows from formulas (26): $\delta = 0$, $\eta = \frac{1}{2}B_V^2$. Respectively, the condition (25) reduced to:

$$\frac{1}{2}B_V^2 > 1 \tag{27}$$

However, the amplitude of relative volume change of the bubble B_V is defined by the formula (5), under condition that $P_e \gg \rho h A \omega^2$, and, therefore, $B_V \ll 1$. Thus, the condition (27) is not held.

Therefore, in the framework of the adopted assumptions, it is not possible to claim that a bubble should sink. However, in the flotation theory the practically relevant situation is when a solid particle is attached to the bubble, so that its mass is not equal to zero. Then the condition (25) may hold true for some combinations of parameters. For example, if $m = \frac{1}{2}m_0$, then, taking into account that $B_V \ll 1$, the condition (25) gives:

$$\frac{A\omega^2}{g} > \frac{4}{3B_V} \tag{28}$$

So, the condition (28) holds true for $A\omega^2 \gg g$.
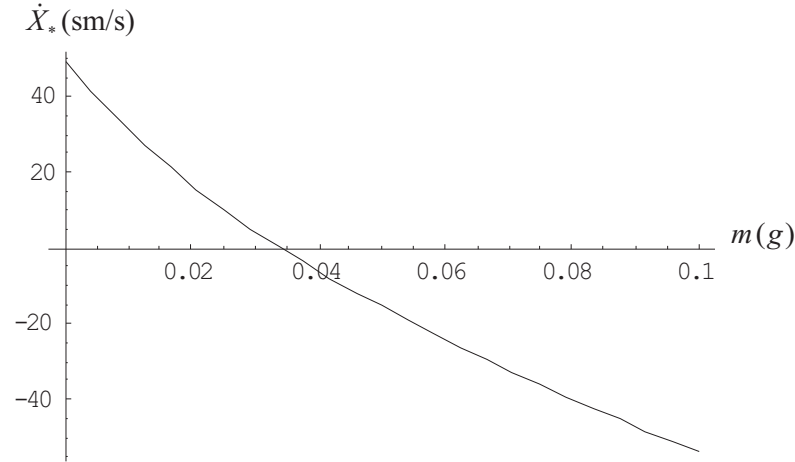
Figure 2: Velocity of steady state motion of the bubble versus its mass
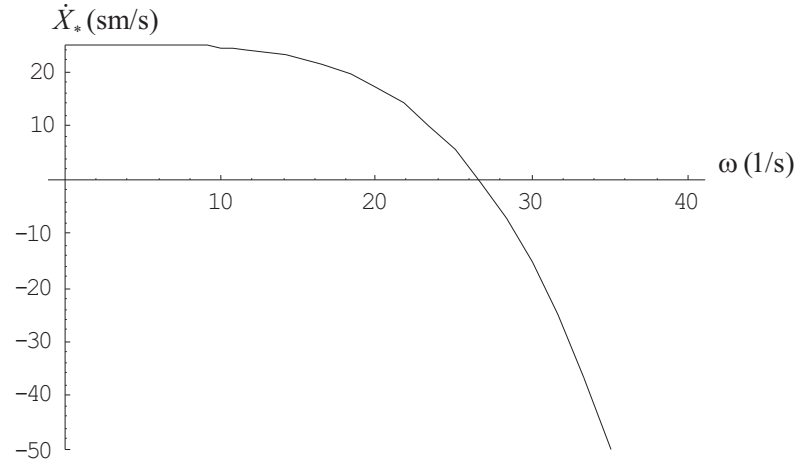
Figure 3: Velocity of steady state motion of the bubble versus excitation frequency

To summarize this discussion, we conclude that the effect of bubble sinking in a fluid is feasible when a fluid-filled vessel is exposed to intensive vibrations.

Utilizing the introduced notations, formula (24) for the velocity of steady state motion of a bubble may be transformed as:

$$\dot{X}_* = k((m + (\eta - 1)m_0)g + \delta m_0 A \omega^2) \tag{29}$$

where $k = -\frac{1}{6\pi\mu R_0}$.

Parametric studies of the dependence of the steady state velocity of a bubble are illustrated in Figures 2-3. In Figure 2, the dependence of the velocity $\dot{X}_*$ on the mass of the bubble (or the mass of a particle attached to the bubble) m for the excitation frequency $\omega = 30 \, 1/s$ is shown. Other parameters of the system are: $\rho = 1 \, \text{g/sm}^3$, $V_{b0} = 0.1 \, \text{sm}^3$, $A = 0.2 \, \text{m}$, $g = 10 \, \text{m/s}^2$, $h = 0.1 \, \text{m}$, $P_e = 150 \cdot 10^3 \, \text{kg/(m} \cdot \text{s}^2)$, $6\pi\mu R_0 = 2 \, \text{g/s}$. In Figure 3, the dependence of the velocity $\dot{X}_*$ on the excitation frequency ω is shown for the bubble with the mass $m = 0.05 \, \text{g}$.

Figure 4: The time dependence of the velocity of the bubble ($m = 0.05\,g$; $\omega = 30\,1/s$)

As seen from Figures 2-3, the magnitude of velocity of a bubble in its steady state motion decreases, when its mass (or the mass of an attached particle) grows and when excitation frequency grows. Thus, a bubble should sink rather than rise at certain combinations of parameters.

6   Comparison with numerical experiments

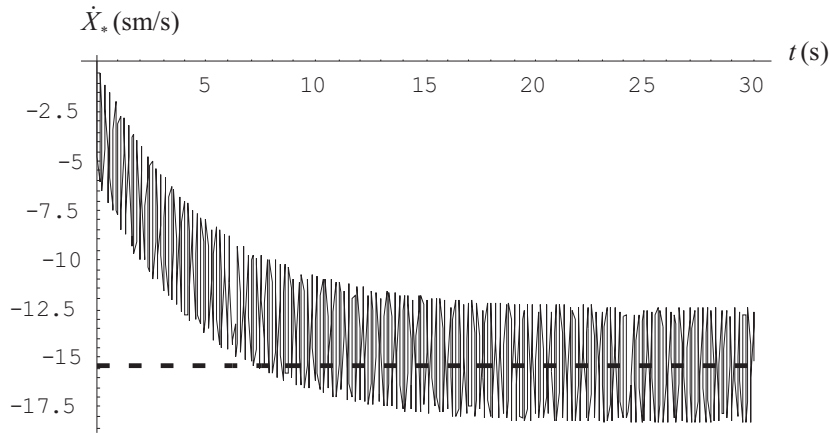The reported results have been validated in numerical experiments. Equation of motion (10) with conditions(8), (9), (22) taken into account has been numerically integrated by means of Mathematica 5.2, and the results have been compared with the analytical predictions. The parameters have been chosen as follows: $\rho = 1\,g/sm^3$, $V_{b0} = 0.1\,sm^3$, $A = 0.2$ m, $g = 10\,m/s^2$, $h = 0.1$ m, $P_e = 150 \cdot 10^3\,kg/(m \cdot s^2)$, $6\pi\mu R_0 = 2\,g/s$.

For $m = 0.05\,g$ and $\omega = 30\,1/s$, formula (33), predicts $\dot{X}_* = -15.4\,sm/s$. The straight dashed line in Figure 4 displays this analytical solution. The continuous curve displays results of numerical integration. As is seen, there is a good agreement between analytical and numerical results.

For $m = 0.025\,g$ and $\omega = 37\,1/s$, formula (33) predicts: $\dot{X}_* = -25.1\,sm/s$. The straight dashed line in Figure 5 displays this analytical solution. The continuous curve displays results of numerical integration.

So, the results of numerical integration validate approximate analytical solution.

7   Conclusion

Simple formula is derived for the velocity of a gas bubble in its steady state motion in an oscillating viscous incompressible fluid exposed to vibration. The variation in the volume of the bubble induced by the pressure pulsations is accounted for. It is assumed that volume pulsations of the bubble are harmonic and isothermal. It is
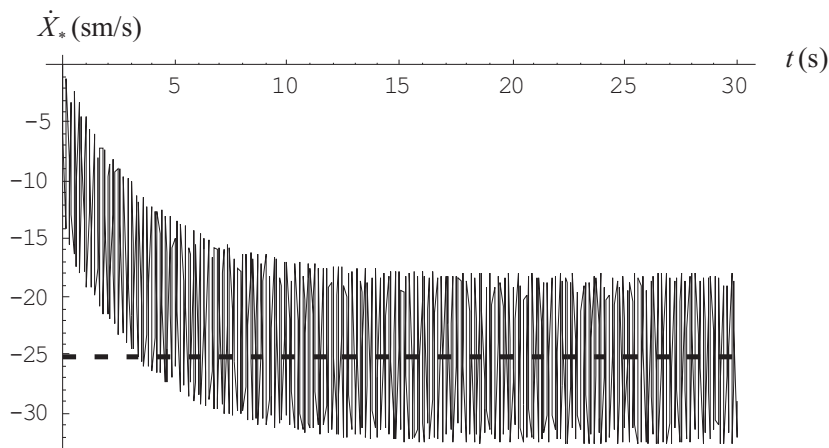
Figure 5: The time dependence of the velocity of the bubble ($m = 0.025\,g$; $\omega = 37\,1/s$)

demonstrated that in certain excitation conditions (for some excitation frequencies and amplitudes of vibrations of the vessel) a gas bubble sinks, rather than rises. The analytical results are validated in numerical experiments.

Acknowledgements

References

[1] Buchanan R. H., Jameson G.J. Cycling migration of bubbles in vertically vibrating liquid columns.-Ind. Eng. Chem. Fundamen., 1(2), 1962, 82-86.

[2] Crum L.A., Eller A.I. Motion of bubbles in a stationary sound field.- The Journal of the Acoustical Society of America, Vol. 48, N 1(2), 1970, 181-189.

[3] Houghton G. The behavior of particles in a sinusoidal velocity field.-Proceedings of the Royal society of London, series A, Vol. 272., 3, 1962, 33-43.

[4] Ganiev R.F., Ukrainskii L.E. Nonlinear wave mechanics and technologies (in Russian), Regular and chaotic dynamics, Moscow, 2008, p. 712.

[5] Blekhman I.I., Vaisberg L.A., Blekhman L.I., Vasilkov V.B., Yakimova K.S "Anomalus" phenomena in fluid under vibration.- Doklady Physics, 2008, v. 53, N 10, pp. 520-524.

[6] Blekhman I.I., Sorokin V.S. On motion of a solid particle and a gas bubble in oscillating fluid (in Russian), Enrichment of raw materials, N 3, 2007, 20-23.

[7] Sorokin V.S. Motion of a deformable particle in an oscillating medium: continuous model, Proceeding of the APM 2008, 2008, 621-629.

[8] Blekhman I.I. Vibrational Mechanics, World Scientific, Singapore, 2000, p. 510.

[9] Bogdanov O.S. Handbook on enrichment of raw materials (in Russian), 2nd Edition, extended and corrected, Nedra, Moscow, Russia, 1982, p. 400.

[10] Kisevalter B.V. Theory of gravitational enrichment processes (in Russian), Nedra, Moscow, Russia, 1979

[11] Bogdanovich A.M. Theoretical background and methods of efficient separation in gravitational enrichment of raw materials (in Russian), Doctoral Degree Thesis, ZAO Mekhanobr engineering, Saint Petersburg, 2002

Sorokin V.S., V.O., 22 linya, 3, Saint-Petersburg, 199106, Russia

Influence of volumetric changes on synthesis in the solid phase

S. N. Sorokova   A. G. Knyazeva

s_sorokova@tpu.ru

Abstract

In this work the synthesis regimes in the solid phase are analyzed taking into account the coupling of heat transfer and deformation processes. In example investigated the models of the volumetric synthesis and the coating formation in conditions of electron beam processing. The comparative analysis of models was shows that the interrelation between thermal and mechanical processes not results to new quantitative and to qualitative results.

1 Introduction

Solid phase synthesis provides wide possibilities for producing a variety of materials. The mechanical stress unavoidable accompany of chemical reactions can influence on conditions of synthesis in the solid phase as a result of high temperature gradients and cause to change of properties during reactions that is actively investigated and used in chemistry solid-phase materials [1].

In this work the influence of interaction of the internal mechanical processes and heat-and-mass transfer on conditions of synthesis in the solid phase are investigated an example of synthesis model in volume in conditions of controlled heating and model of coating formation in conditions of electron-beam treatment. Influence of connected of thermal and mechanical processes in various conditions of synthesis appears various.

2 Sintering of powders in conditions of controlled heating

2.1 Problem formulation

Application of sintering of pressing powders the $Ti - TiAl_3$ allows obtaining admissible properties of sintered specimen and decreasing of the cost price of their manufacturing in conditions of industrial production [2]. For the purposeful choice of technological regimes of sintering it is necessary theoretical and experimental research of laws of structure formation, phase structure and physic mechanical properties of the material at sintering.

Let's consider the process of sintering of pressing powders the $Ti--TiAl_3$ in the form of the parallelepiped with the sizes $l_1 \times l_2 \times l_3$ in the vacuum furnace at regulated heating. As layer heat thickness in scores of times the dimension of the sample we can neglect distribution of temperature in the sample. Then the three-dimensional heat conduction equation may be integrated by volume sample, taking into account the heat-exchange condition on surface contacting to an environment. In this case we come to "zero-dimensional" of problem definition [3] which includes the heat balance equation

$$V_0 c \rho \frac{dT}{dt} = -\varepsilon_T \sigma_T \left(T^4 - T_e^4 \right) S_n - 3KT\alpha_T V_0 \frac{d\varepsilon_{kk}}{dt} + V_0 W_1 \qquad (1)$$

where T is temperature; T_e is temperature of walls of the vacuum chamber which changes under the certain law; t is time; c, ρ are the effective heat capacity and density respectively; W_1 — is the heat release due to chemical reactions; $\varepsilon_{kk} = \varepsilon_{11} + \varepsilon_{22} + \varepsilon_{33}$ is the first invariant of strain tensor; $K = \lambda + \frac{2}{3}\mu$ is the bulk modulus, λ, μ are the Lame coefficients; ε_t is the emissity; S_n is the total surface area of sample; V_0 is its volume, α_T — is thermal expansion coefficient.

We consider that components of stress and strain are connected with changes of temperature and concentration the Djuamelya–Neyman generalized relationship [4]:

$$\sigma_{ij} = 2\mu\varepsilon_{ij} + \delta_{ij}\left[\lambda\varepsilon_{kk} - K\omega\right] \qquad (2)$$

where δ_{ij} – Kronecker delta, ω is the relative change of local volume owing to change of temperature and concentration of the components participating in reactions [5]

$$\omega = 3\left[\alpha_T(T - T_0) + \sum_{l=1}^{n} \alpha_l(y_l - y_{l,0})\right], \qquad (3)$$

where $\alpha_l = M_l \bar{\alpha}_l / \rho$, $\bar{\alpha}_l$ is the concentration expansion coefficients[5]; the index zero relates to the initial condition; M_l are the mass concentrations of components. According to state diagram of the system $Ti - Al$ [6], we can write the six chemical reactions

$$TiAl_3 \rightarrow TiAl + 2Al; \; Ti + Al \rightarrow TiAl; \; 2Ti + TiAl_3 \rightarrow 3TiAl;$$
$$2Ti + TiAl \rightarrow Ti_3Al; \; 3Ti + Al \rightarrow Ti_3Al; \; Ti_3Al \rightarrow 2Ti + TiAl.$$
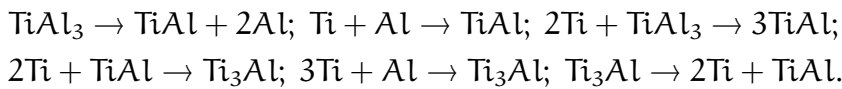
in the area of atomic concentration which interesting from the practical point of view. We determine the mass concentrations of reactants and reaction products as:

$$y_1 = [TiAl_3], \; y_2 = [Ti], \; y_3 = [Al], \; y_4 = [TiAl], \; y_5 = [Ti_3Al],$$

Then, according [7] and on base of mass action law, we shall obtain

$$\frac{dy_1}{dt} = -y_1\varphi_1 - y_2^2 y_1 \varphi_3, \qquad (4)$$

$$\frac{dy_2}{dt} = -y_2 y_3 \varphi_2 - 2y_1 y_2^2 \varphi_3 - 2y_2^2 y_4 \varphi_4 - 3y_3 y_2^3 \varphi_5 + 2y_5 \varphi_6, \qquad (5)$$

$$\frac{dy_3}{dt} = 2y_1\varphi_1 - y_2y_3\varphi_2 - y_2^2y_3\varphi_5, \tag{6}$$

$$\frac{dy_4}{dt} = y_1\varphi_1 + y_2y_3\varphi_2 + 3y_1y_2^2\varphi_3 - y_2^2y_4\varphi_4 + y_5\varphi_6, \tag{7}$$

$$\frac{dy_5}{dt} = y_2^2y_1\varphi_4 + y_3y_2^3\varphi_5 - y_5\varphi_6 \tag{8}$$

where we take into account that all chemical reactions are inhibited by the layer of the product $y = y_4 + y_5$ [7]:

$$\varphi_i = k_i \exp\left(-\frac{E_{ai}}{RT}\right)\exp(-my)y^{-n}, \ i = 1, 2, 3,$$

m, n are the stagnation parameters; k_i, E_{ai} — pre-exponential factor and activation energy.

As the sample is free from action of external forces we have $\sigma_{kk} = 0$. Therefore, the bulk deformations are obtained from relation (2):

$$\varepsilon_{kk} = \omega = \frac{\rho^{-1} - \rho_0^{-1}}{\rho_0^{-1}} = \frac{V^{-1} - V_0^{-1}}{V_0^{-1}} \ \text{or} \ \frac{V}{V_0} = \frac{1}{1 + \varepsilon_{kk}}. \tag{9}$$

Substituting (9) expression in the heat conduction equation (1) and considering (3) and assembling similar composed, we obtain

$$c_{eff} = \frac{dT}{dt} = -\varepsilon_T\sigma_T(T^4 - T_e^4)S_n + W_{eff}, \tag{10}$$

where $c_{eff} = V_o c\rho + 3D\alpha_T$; $D = 3KT\alpha_T V_0$. The total heat source W_{eff} due to chemical reactions (including change of volume during reaction) subject to equations (4) – (8) write down in form

$$W_{eff} = V_0\rho \sum_{i=1}^{5} \frac{h_i}{m_i}\frac{dy_i}{dt} - 3D\sum_{i=1}^{5}\alpha_i\frac{dy_i}{dt} = \sum_{j=1}^{n}\omega_j, \ j = 1 - 6,$$

where

$$\omega_1 = Q_1'y_1\varphi_1; \ \omega_2 = Q_2'y_2y_3\varphi_2; \ \omega_3 = Q_3'y_1y_{2_2}\varphi_3;$$

$$\omega_4 = Q_4'y_4y_{2_2}\varphi_4; \ \omega_5 = Q_5'y_3y_{2_3}\varphi_5; \ \omega_6 = Q_6'y_5\varphi_6; \tag{11}$$

where $Q' = VQ_j - 3D\Delta Q_j$; $Q_j = \frac{\rho}{m}\sum_{k=1}^{n}h_k\nu_{ki}$; $\Delta Q_j = \sum_{k=1}^{n}\alpha_k\nu_{ki}$.
Initial conditions take the form

$$t = 0: \ T = T_o, \ y_1 = y_{10}, \ y_2 = y_{20}, \ y_3 = 0, \ y_4 = 0, \ y_5 = 0. \tag{12}$$
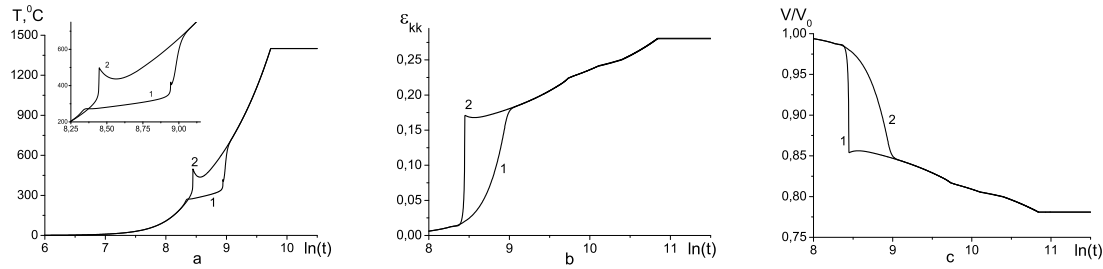
Figure 1: Temperature (a), volumetric deformations (b) and relative change of volume (c) during heating and sintering for connected (1) and unconnected (2) formulations of a problem.

2.2 Numerical investigation

The problem (10), (4) – (8), (12) was solved numerically with use of Runge–Qutta method for a thermal part of the problem and implicit Euler's method for the kinetic part of the problem. Simulation veracity is confirmed by comparison with known analytical solutions for extreme particular cases, qualitative comparison with experiment [2] on character of change locally volume and temperature of the sample. Parameters of the model were determined by special methods [3, 7].

It has appeared that for the given system and for the chosen area of change technological parameters the account of the connected character of processes (when the factor D in the equation of heat conductivity (11) is distinct from zero) leads to downturn of temperature during synthesis (fig. 1, a). Additional expenses of energy for volumetric deformations in the sample lead to appearance of plateau on the temperature curve, not connected with phase transition (compare curves 1 and 2 on fig. 1, a). The local maximum on temperature curves (fig. 1, a) is connected with allocation of heat in the first chemical reaction [5] for the connected model the local maximum also appears on the kinetic curve for TiAl (fig. 2,a). In consideration of decrease of temperature chemical reactions in volume occur more slowly (fig. 2).

Not looking at changes in kinetics process of sintering, the account of coherent character of different physical processes in the chosen area of change of parameters at calculations is not reflected in a final chemical compound of pressing and relative change of final volume.

3 Formation of coating structure during electron-beam treatment with use solid phase synthesis

3.1 Problem formulation

The joining formation or transient regions between the materials are rarely formed during the synthesis of a coating on a substrate [8]. To form the transient region, additional heat treatment is required. However, the substrate that removes heat from the heating region may considerably affect the regimes of reaction initiation
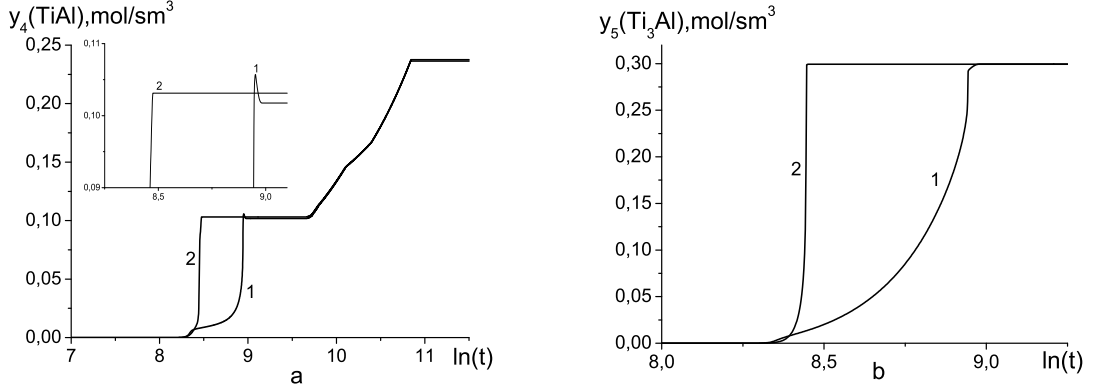
Figure 2: Change of phases concentration TiAl (a) and $\mathsf{Ti_3Al}$ (b) in time during heating and sintering for connected (1) and un connected (2) formulations.

and layer-by-layer propagation in the solid phase.

We shall assume that the surface of a thin plate has been covered with a single–layer coating. To a first approximation the elements re-allocation on plate thickness with coating can not considered. We can neglect elements redistribution along the plate thickness assuming that this slow process happens after coating synthesis that is during cooling stage. The plate is free from external forces action. According to [9], one can believe, that the conditions correspond to plane stressed state. Let consider that external source moving along the coating surface with the rate V, heats the surface in the axis direction perpendicular to motion direction uniformly. Described conditions realize when the scanning electron beam flared-out into line is used and scanning thickness exceeds the specimen thickness. Under action of external energy source, the chemical reactions initiate in the coating. The coating and substrate are thermally thin, that allows integrating all equations along the specimen thickness. As a result we come to one dimensional problem formulation which is analogous to [8] and includes thermal conductivity equation coupling with the stresses

$$c_{eff}\frac{\partial T}{\partial x_1} = \left(\lambda_{T,b}(\delta(k_{\lambda,T} - 1) + 1)\frac{\partial T}{\partial x_1}\right) - D_1(A - 3B)\frac{\partial \sigma_{22}}{\partial t} - \qquad (13)$$

$$- \sigma_0\varepsilon_{eff}\frac{(T^4 - T_0^4)}{h_c + h_b} + \frac{q_e(t, x_1)}{h_c + h_b} + W_{eff},$$

the kinetic equation system for $\mathsf{Ti} - \mathsf{TiAl_3}$ (4) – (8) and equations for determination of the stress and strain tensor components succeeding of problem solution on mechanical equilibrium of the plate free from action of external forces [4]

$$\sigma_{22} = \sigma_{33} = \qquad (14)$$

$$= \left[\left(\frac{4}{L_x} - \frac{6x_1}{L_x^2}\right)(I_1 + I_2) + \left(\frac{12x_1}{L_x^3} - \frac{6}{L_x^2}\right)(I_3 + I_4) - \tilde{\varepsilon}^T - \tilde{\varepsilon}^L\right](A - B)^{-1},$$

$$\varepsilon_{11} = \varepsilon_{33} = -B\sigma_{22} + \tilde{\varepsilon}^T + \tilde{\varepsilon}^{(l)}, \quad \varepsilon_{22} = (A - B)\sigma_{22} + \tilde{\varepsilon}^T + \tilde{\varepsilon}^{(l)}, \qquad (15)$$

647

where

$$\delta = h_c/(h_c + h_b); \ 1 - \delta = h_b/(h_c + h_b);$$

$$c_{eff} = c_b \rho_b \left(\delta \left(k_c - 1\right) + 1\right) + 3D\alpha_{T,b} \left[\delta \left(k_\alpha - 1\right) + 1\right];$$

$$D_1 = 3\alpha_{T,b}K_b \left(\delta \left(k_V k_\alpha - 1\right) + 1\right) T; \ \tilde{\varepsilon}^T = \alpha_{T,b} \left(T - T_0\right) \left[\delta \left(k_\alpha - 1\right) + 1\right];$$

$$\tilde{\varepsilon}^{(l)} = \delta \sum_{l=1}^{5} \alpha_l \left(y_l - y_{l,0}\right); \ A = \frac{1}{2\mu_b} \left(\delta \left(\frac{1}{k_\mu} - 1\right) + 1\right);$$

$$B = \frac{\lambda_b}{6\mu_b K_b} \left(\delta \left(\frac{k_\lambda}{k_\mu k_V} - 1\right) + 1\right);$$

$$k_{\lambda,T} = \lambda_{T,c}/\lambda_{T,b}; \ k_c = c_c \rho_c/c_b \rho_b; \ k_V = K_c/K_b; \ k_\alpha = \alpha_{T,b}/\alpha_{T,c};$$

$$k_\lambda = \lambda_c/\lambda_b; \ k_\mu = \mu_c/\mu_b; \ k_\rho = \rho_c/\rho_b;$$

subscripts "c" – correspond to the effective properties of the coating; subscripts "b" – correspond to the effective properties of the base.

The total heat source W_{eff} due to chemical reactions in the heat conduction equation record to similarly previous case where ω_i are determine under the formula (11) in which it is accepted that $Q'_i = \delta Q_i - 3\delta D_1 \Delta Q_i$. At the initial time, we have the conditions

$$t = 0: \quad T(x, 0) = T_0, \quad y_1 = y_{10}, \quad y_2 = y_{20}, \quad y_3 = y_4 = y_5 = 0, \quad \sigma_{22} = 0,$$

$$\varepsilon_{11} = \varepsilon_{22} = \varepsilon_{33} = 0.$$

3.2 Numerical investigation

The problem was solved numerically using an implicit difference scheme that is second-order accurate in space and first-order accurate in time with linear sweep. In each time step, the first stage is to solve the heat conduction equation (13). The second stage is the solution of the kinetic problem (4) - (8). The third stage is to describe the stress and strain components (14) - (15) where integrals were calculated on method of trapezoids. The thermodynamic and physical properties are known from the experimental date or are calculated of special shape [8, 10].

Figure 3 dependences on time of stress (a) and strain components (b)-(c) in section $x_1 = 5$ sm (i.e. in the center of plate) are shown calculated for two limiting cases: factor $D_1 \neq 0$ (curve 1) and factor $D_1 = 0$ (curve 2). Dependence of temperature on time is not resulted, as the account of connected processes in model leads to its minor change. The account of connected of heat-conduction process and deformations in model is essentially influenced on value of the stress and strain components and also on their qualitative behaviors. So from fig. 3, b, it is visible that in the connected model stress component do not change the sign. In unconnected model change of sign is observed.

From distributions on length of the plate of temperature and concentration of phases Ti, TiAl$_3$ and Ti$_3$Al (fig. 4) it is visible that the account of coherence of mechanical and thermal processes leads to decrease of temperature in the location of source
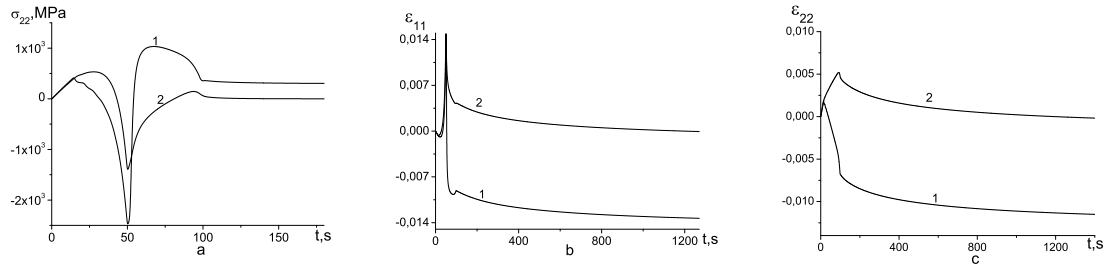
Figure 3: Distributions of stress component σ_{22} (a) and strain components (b, c) in time in section $x_1 = 5$ sm the problems received numerically for different formulations.
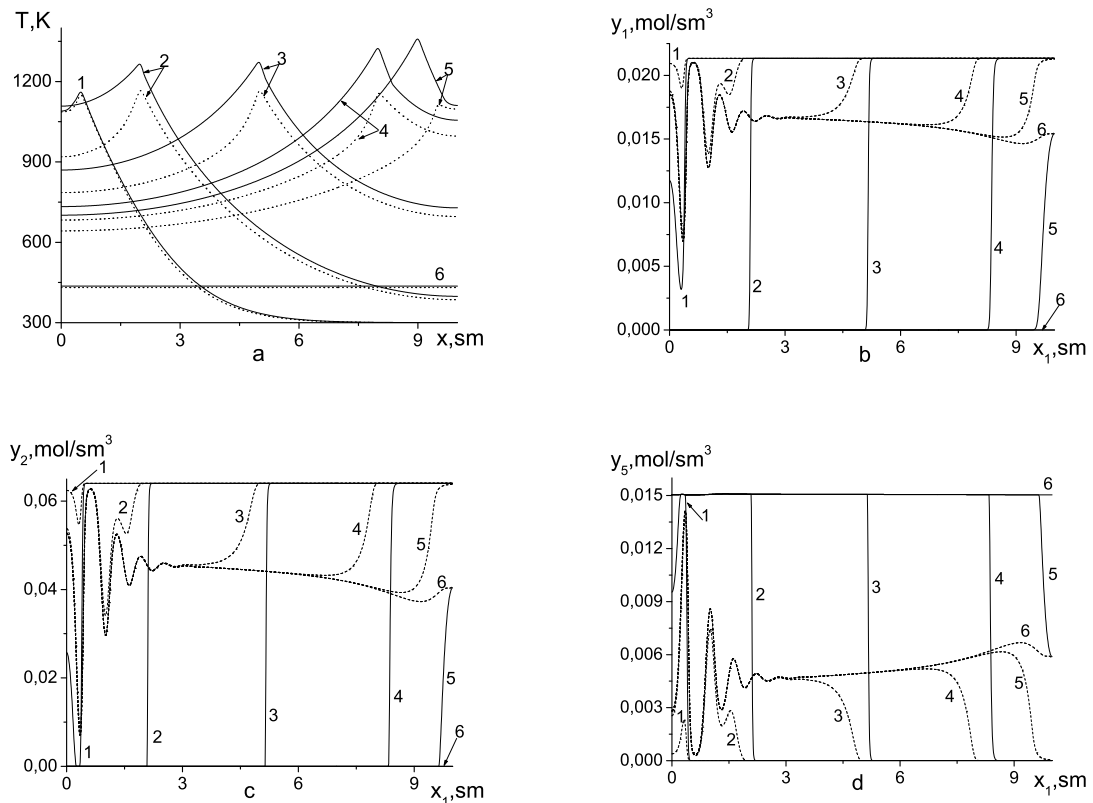
Figure 4: Distribution of temperatures (a) and concentration of components (b) - (d) along a plate during the various moments of time: 1. $t = 10s$, 2. $t = 50s$, 3. $t = 200s$, 4. $t = 400s$, 5. $t = 600s$, 6. $t = 800s$ (continuous curves - unconnected model; dotted - the connected model)

$x_1 = Vt$. It leads to decrease of temperature and in front of reaction. There are the additional expenses of the energy connected with creation of is strain – stress condition owing to what there is no full synthesis (compare continuous and dotted curves). Essential heterogeneity of concentration in the beginning of the plate for

the connected problem statement interpreted of low temperatures in the reaction zone in initial stage of processing process and decelerating of reactions by product layer [7]. Similar heterogeneity is observed and in distributions of stress and strain components.

4 Conclusion

Within the limits of sintering model in the chosen area of change of physical parameters it is shown that the account of the connected character of physical processes essentially influences dynamics of sintering process, but is not reflected in the final chemical compound of pressing and relative change of its volume.
Within the limits of model of the covering synthesis on substrate the basic role of the connected character of thermal, mechanical and chemical processes for structure of the covering and for sizes of pressure and the deformations accompanying process of synthesis is revealed, it speaks about the various roles of mechanical processes in modes of transformation under various technological conditions.

References

[1] Tretiyakov Y.D. Solid-phase reaction. M.: Chemistry, 1978.

[2] Pribytkov G.A., Andreeva I.A., Korjova V.V.//Russia journal "The fundamental problems of modern materials science". 2007. V.4. N 2. P. 128–133.

[3] Sorokova S.N., Knyazeva A.G., Pribytkov G.A. // The collection of reports of XIII International scientifically-practical conference of students, post-graduate students and young scientists "Modern technics and technologies". Vol. 2. – P. 212–214.

[4] Boley B., Weiner J. Theory of thermal stresses. 1964.

[5] Sorokova S.N., Knyazeva A.G. // Physical Mesomechanics. 2008. – Vol. 11. – N 12. – P. 95–103.

[6] Mishin Y., Herzig Chr. Acta mater. 48 (2000). P. 589–623.

[7] Merzhanov A.G. Theory of Gasless Combustion. Preprint. Chernogolovka. 1973.

[8] Sorokova S.N., Knyazeva A.G. // Theoretical foundations of chemical engineering. – 2008. – Vol. 42. – N 4. – P. 457–465.

[9] Sedov L.I. Continuum mechanics. 1994.

[10] Karapetyants M. Kh. Chemical Thermodynamics. Moscow: Chemistry, 1975.

S.N. Sorokova, Tomsk Polytechnic University, Tomsk, Russia
A.G. Knyazeva, Institute of strength physics and materials science SB RAS, Tomsk, Russia

Analysis of buckling behaviour the 3D spacer fabrics under axial compression

Oleg Stolyarov

oleg.stolyarov@rambler.ru

Abstract

This paper deals with experimental and analytical studies on buckling of three dimensional spacer fabrics consisting of two outer layers combined by spacer yarns. Depending on different structural parameters such as thickness of the spacer fabrics, the amount of the spacer yarns per square cm, spacer yarn properties and spacer yarn laying angle, different factors that affect the buckling behavior of spacer fabrics are observed. The basic factors affected the buckling behavior of spacer fabrics were determined. It is shown that buckling of spacer yarns in fabric is a very complex phenomenon that involves interactions between the two outer layers of spacer fabrics. Different mechanisms can cause buckling the spacer yarns to fail in carrying a compression load are discussed.

1   Introduction

The textile industry manufactures various types of fabrics. Among them, 3-D spacer fabrics occupy an important position because of their unique properties. Spacer fabrics are state of the art of structures and they are very unlike to the traditional textile fabrics. They consist of two outer layers combined by spacer yarns (Figure 1). They have been already used in many areas and present different advantages especially for the technical applications. The compression behavior of spacer fabrics is one of their main characteristics and therefore it must be taking into account in various tasks. The construction of spacer fabrics provides a textile which has spacers in the middle of its structure [1].

The spacer fabrics can be produced by different textile technologies as weaving or knitting. The most commonly technology used for manufacturing the spacer fabrics is knitting. Both weft knitting and the warp knitting processes can be used for production of spacer fabrics. Buckling behavior of spacer fabrics is especially important for multi-layers textiles used in the field of composites reinforcements for lightweight constructions and load-bearing building applications. Research to study of spacer fabrics has been performed for many years. In work [2], the characteristics of different spacer fabrics including low-stress mechanical properties, air permeability and thermal conductivity were investigated. It was shown that low-stress mechanical properties revealed that all tensile, bending and compression properties of spacer
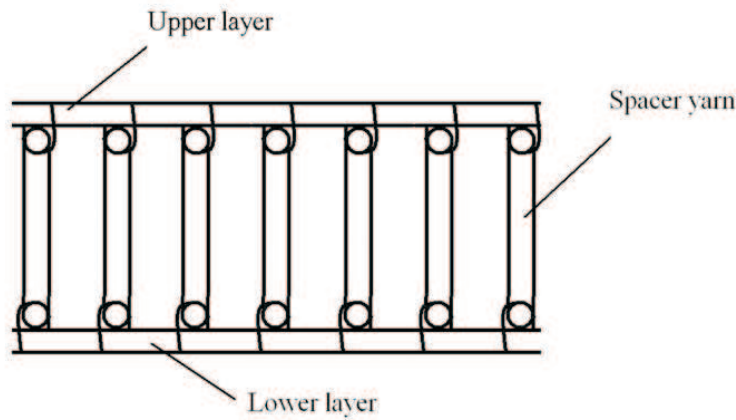
Figure 1: The elements of the spacer fabrics.

fabrics are greatly depending on the type of spacer fabric (warp knit or weft knit), the type of spacer yarn used (monofilament or multifilament), the yarn count of the spacer yarn, the stitch density and the spacer yarn configuration. Some authors [3] investigated the possibility of using warp knitted spacer fabrics for cushion application instead of common polyurethane foam that used in seats, sofas and mattresses, etc. The results show that the warp knitted spacer fabrics have better pressure relief properties, higher air permeability, and lower heat resistance than PU foam, and thus could be used to substitute. In work [4] the transverse impact of 3D biaxial spacer weft-knitted reinforced fabric was developed and investigated. Andreas Roye and Thomas Gries [5] investigated the possibility to use completely new type of 3-D-fabric – warp knitted spacer fabrics for concrete applications. The double needle bar raschel technology has been improved by inserting straight reinforcement yarns inserted bi-axially on both sides of the textile. In the paper [6] a model of transverse deformation in a textile product consisting of two external layers combined with spacer yarn in the middle layer are presented.

There are many studies of the properties of spacer fabrics, but there are no sufficiently broad published studies on the buckling behavior. Understanding the buckling behavior of spacer fabrics is important for the rational development of structural elements reinforced with spacer fabrics.

2 Buckling

In engineering, buckling is a failure mode characterized by a sudden failure of a structural member subjected to compressive stresses, where the actual compressive stress at the point of failure is less than the ultimate compressive stresses that the material is capable of withstanding. This mode of failure is also described as failure due to elastic instability [7].

The critical force P_{cr} for prismatic bar in axial compression within elastic part is

determined by the Euler equation:

$$P_{cr} = \frac{\pi^2 EI}{l_r^2},\tag{1}$$

where E is a modulus of elasticity of the bar material; I is a minimum moment of inertia of the cross-sectional area F of the bar; $l_r = \mu l$ is reduced length of the bar (the length at which a bar with hinged ends is equivalent in stability to the bar with given end conditions); l is a true length of the bar; μ is a length reduction factor depending on the end conditions and type of loading.

The moment inertia of an annular section of the spacer yarn is

$$I = \frac{\pi D^4}{64},\tag{2}$$

where D is a diameter of spacer yarn, mm.

The cross sectional area of the bar is

$$F = \frac{\pi D^2}{4}.\tag{3}$$

The radius of inertia of the cross section is

$$i = \sqrt{\frac{I}{F}}.\tag{4}$$

Slenderness ratio of the bar λ is determined by the equation

$$\lambda = \frac{\mu l}{i}.\tag{5}$$

The μ influences on the length at which a bar with hinged ends is equivalent in stability to the bar with given end conditions. Figure 2 illustrates the case of compression of spacer yarn at corresponding value of factor $\mu = 1$.
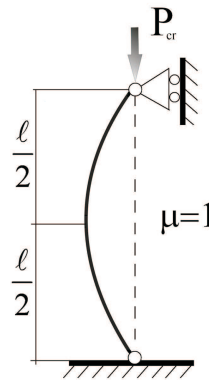

Figure 2: The case of compression of spacer yarn at corresponding value of factor $\mu = 1$.

3 Experimental

In this study, the spacer fabrics were produced on a double needle bar Rachel machine, on the basis of a Karl Mayer HDR 6-7 DPLM at the Institute fur Textilltechnik der RWTH Aachen (Germany). The four different types of spacer fabrics were produced from PES and PP monofilament yarns. The characteristics and tensile properties of spacer yarns are listed in the table 1 and the characteristics of spacer fabrics are presented in table 2. The spacer fabrics investigated has different structural parameters such as thickness of the spacer fabrics, the amount of the spacer yarns per square cm, spacer yarn properties and spacer yarn laying angle. The samples SF2 in comparing with SF3 has additional system of laying up glass yarns in biaxial direction. Then the samples were cut into round shapes with diameter from 70 to 190 mm. The fabrics were conditioned and measured in the dry relaxed state.

Table 1. Tensile properties of the spacer yarns used in 3D - fabrics

N	Spacer yarn	Diameter, mm	Force at break, N	Elongation at break,%	Tensile stress, MPa	Tensile modulus, MPa
1	PES	0.25	29.3	24.5	600	10000
2	PP	0.3	38.6	27.0	545	3800

Table 2. Characteristics of the spacer fabrics investigated

Name	Type of spacer yarn used	Thickness of the spacer fabrics	Amount of the spacer yarns per 100 cm^2
SF1	PES	20	1760
SF2	PES	20	192
SF3	PES	20	192
SF4	PP	20	800

The compression test was performed on a Zwick/Roell 2.5 material testing machine. The force-compression diagrams were obtained with a 20 - mm sample base and clamp movement of 10 mm/min. No fever than three specimens were tested. It should be noted that compression were calculated from crosshead displacement. Typical force-compression diagrams are shown in figure 2. When the compression load on a spacer fabric is applied, the spacer yarn loaded in the same manner until will fail by buckling.

4 Results and discussion

The force-compression diagrams of spacer fabric are presented in figures 4 and 5. All of them show the typical behaviour under axial compression as it was mentioned above. In the first part, there is elastic part where the spacer yarns work within the proportional limit. Then at some point the buckling of spacer fabric occur.

The values of moment inertia, the radius of inertia of the cross section, slenderness ratio and critical force for all samples were calculated using equations (1)–(5). The first three samples have the PES spacer yarn and the fourth sample has the PP yarn. The points at which the spacer fabrics have failed by buckling or loss the stability
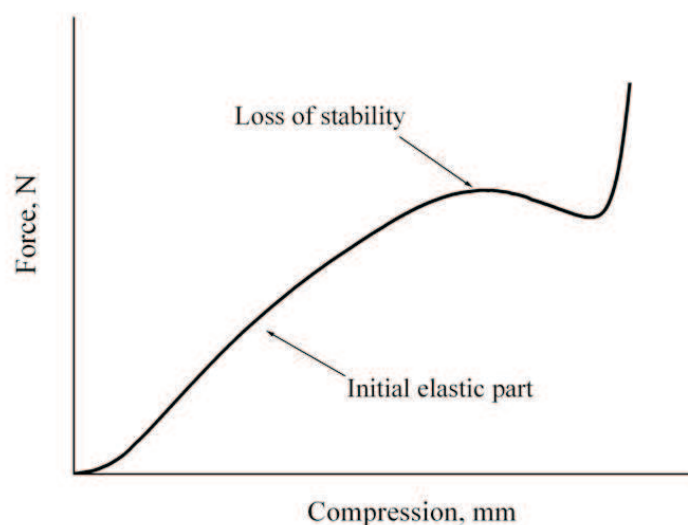
Figure 3: Typical response curves of spacer fabrics in axial compression.

were determined from force-compression curve. The critical force that applies for single spacer yarn was calculated taking into account the number of yarns in cross-sectional area of spacer fabric.

Table 3. The properties of the spacer fabrics investigated

Name	The moment inertia of an annular section, m^4	The radius of inertia of the cross section, mm	Slenderness ratio of the bar λ	Loss of stability (from force - compression curve), N	Critical force P_{cr} , N
SF1	$1.92 \cdot 10^{-16}$	$6.25 \cdot 10^{-2}$	320	115.3	140.0
SF2	$1.92 \cdot 10^{-16}$	$6.25 \cdot 10^{-2}$	320	19.8	22.8
SF3	$1.92 \cdot 10^{-16}$	$6.25 \cdot 10^{-2}$	320	18.1	22.8
SF4	$3.97 \cdot 10^{-16}$	$7.5 \cdot 10^{-2}$	260	11.3	14.8

The difference between critical force obtained from force-compression curve and calculated by equation (1) is within the range of 13 – 23%. Such big difference can be explained by the nonlinear behavior of spacer fabric under axial compression. Also, the slenderness ratio of spacer yarn is greater than 260. Usually short steel columns have the slenderness ratio not more than 50 and an intermediate length steel column has a slenderness ratio ranging from 50 to 200. The deviation from the pure Euler behaviour can include the no straight spacer yarn geometry and nonlinear stress-strain behavior of spacer yarn polymer materials. Another factor that may be affected from this equation is the effect of length on critical load. Clearly, empirical equation for buckling must been developed to agree with experimental data.

5   Conclusions

The experimental and analytical studies on buckling behaviour of spacer fabrics under uniaxial loading condition are investigated by using analytical and experimental approaches. The force-compression diagrams of spacer fabric are obtained.
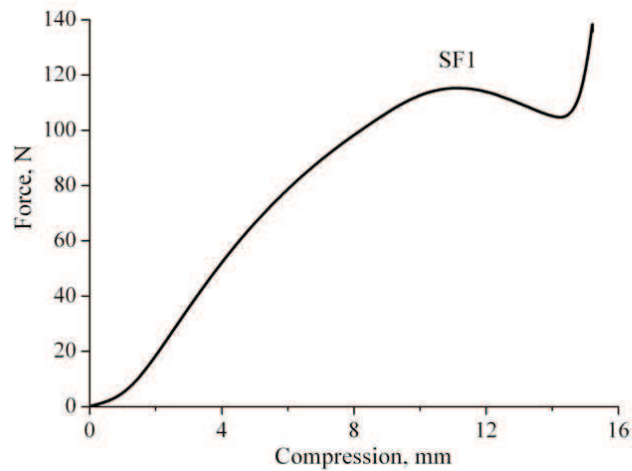
Figure 4: Force-compression curve of spacer fabric (SF1).
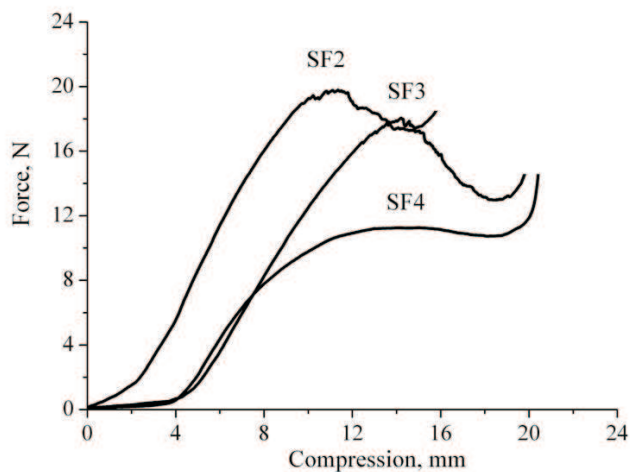
Figure 5: Force-compression curve of spacer fabrics (SF2, SF3, SF4).

Depending on different structural parameters such as thickness of the spacer fabrics, the amount of the spacer yarns per square cm, spacer yarn properties and spacer yarn laying angle, critical force that affect the buckling behavior of spacer fabrics are observed. It is shown that buckling of spacer yarns in fabric is a very complex phenomenon that involves interactions between the two outer layers of spacer fabrics.

Acknowledgements

References

[1] Mecit, D. Development and defining of a characterization method for 3D spacer fabrics considering concrete applications, Diplomarbeit, Institut für Textiltechnik der RWTH Aachen, 2005, p. 97.

[2] Joanne Yip, Sun-Pui Ng, Study of three-dimensional spacer fabrics: Physical and mechanical properties, Journal of materials processing technology, 206, 2008, 359-364.

[3] Xiaohua Ye, Hong Hu and Xunwei Feng Development of the Warp Knitted Spacer Fabrics for Cushion Applications Journal of Industrial Textiles, 37, 2008, 213-223.

[4] Yuanwan Liu, Lihua Lv, Baozhong Sun, Hong Hu and Bohong Gu, Dynamic Response of 3D Biaxial Spacer Weft-knitted Composite under Transverse, Journal of Reinforced Plastics and Composites, 25, 2006, 1629-1641.

[5] Andreas Roye and Thomas Gries, 3-D Textiles for Advanced Cement Based Matrix Reinforcement, Journal of Industrial Textiles, 37, 2007, 163-173.

[6] Marek Musiol, Analysis of transverse deformability of spacer products, AUTEX Research Journal, Vol. 5, N 1, 2005, 67-70.

[7] Timoshenko, S. P., and Gere, J. M., Theory of Elastic Stability, 2 ed., McGraw-Hill, 1961.

Oleg Stolyarov, St. Petersburg State University of Technology and Design, Bolshaya Morskaya St. 18, St.-Petersburg, 191186, Russia

Hybrid algorithms applied to inverse spectral problems for hydromechanical systems

V. D. Sulimov   P. M. Shkapov

spm@bmstu.ru

Abstract

Problems of nuclear reactor diagnostics are formulated as inverse spectral problems. Incompleteness of registered spectral data and presence of multiple frequencies result in the error function being non-convex and non-differentiable. As the function has numerous local minima, it is necessary to use global optimization methods. A novel global optimization algorithm combining a Metropolis-based algorithm and deterministic gradient techniques is introduced. Smoothing approximations are inserted during the local search that makes it possible to expand the approach on the class of non-differentiable problems. Implementations of the hybrid algorithm are discussed. Results of computational experiments are presented to illustrate the efficiency of the approach.

1 Introduction

It is the practice to distinguish two kinds of extremal problems for dynamic systems, they are problems of optimization and diagnostics. Both of them are formulated as inverse spectral problems [1]. Dynamic numerical investigation and analysis generally requires a mathematical model representing the physical behaviour of the object under consideration. The model may be used to determine responses to service dynamic loads, assess object integrity including seismic analysis, and also to study the impact of required design modifications or system fault diagnostics. Reliable computer modeling in system dynamics is very important for studies related to the safety of equipment components in the nuclear power industry. Computer dynamic model updating is a powerful means to produce these reliable models [2]. The method uses an initial computer model and measured spectral data of the equipment components to modify physical parameters of the initial computer model. Vibration monitoring methods are cost-effective and reliable tools for early failure detection and preventive maintenance in the up-to-date nuclear power industry. One of the most severe accidents in nuclear power generation is loss of coolant, where the re-circulating coolant of the pressurized water reactor may flash into steam [3]. The standard reactor instrumentation can register signals caused by pressure fluctuation of the coolant. The program seeks interpretations of the registered spectra and useful data

extraction for diagnostics. Computational models of a VVER-1000 reactor are applicable to analysis of various operational occurrences, abnormal events, and design scenarios and provide a significant analytical capability for the specialists working in the field nuclear power safety. In what follows, methods of solving diagnostics problems for computational models of the reactor equipment components and of the coolant flow in the primary circuit are under consideration.

Possible occurrence of anomalies in the phase constitution of the coolant can be detected owing to changes in dynamical characteristics of the two-phase flow. Mathematical models for numerical analysis of acoustical oscillations in two-phase coolant have been developed [4]. As the normal state of the coolant and anomalous one are characterized by different spectra, then it is necessary to minimize simultaneously individual differences between spectral components. These differences can be described by an appropriate error function. The inverse spectral problem is formulated using the vector of relative acoustic velocities in the coolant flowing throw the specified zones. The goal is to find a set of controlling variables, which will minimize the error function and determine current phase constitution of the coolant. In the general case it is necessary to solve the inverse problem using inaccurate incomplete experimental data. It is well known that the above problem is often ill posed, so that small perturbations in the data can result in large changes of the solution. Regularization technique is a standard method of transforming the initial problem into well-posed form. Implementation of special procedures is required for finding regularization parameters.

The inverse problems here are solved for perfect but incomplete spectral data. The results of the direct problem solutions have been confirmed by using the finite-element code ANSYS®. Incompleteness of the measured spectral data results in the error function being non-convex. As the error function has numerous local minima, it is necessary to use global optimization methods. On account of possible presence of multiple frequencies in registered spectra the error function may not be differentiable everywhere. Up-to-date methods for solving global optimization problems are Metropolis-based algorithms: the stochastic Particle Collision Algorithm PCA [5] and the hybrid algorithm NMPCA that combines stochastic and deterministic optimization methods [6]. The hybrid algorithm performs as follows: first, a wide search in the solution space is carried out using a stochastic optimization algorithm (the PCA), and then scanning the promising areas is made with a deterministic local search technique (Nelder-Mead Simplex). This searching is performed iteratively until a certain number of fitness function evaluations is reached. However, it is well-known that the convergence theory for Nelder-Mead simplex method is far from completion; so the method can fail to converge or converge to non-stationary points [7]. Another modern approach to search global solutions on base of diagonal partitions and a set of Lipschitz constants is proposed in [8]. As an alternative to the NMPCA a novel hybrid algorithm is introduced. This algorithm combines the PCA and the deterministic gradient techniques with smoothing approximations for fitness functions.

The plan of the remainder of this paper is as follows. The section following contains statement of the diagnostics problem. Section 3 provides brief descriptions of the hybrid global optimization algorithms. In section 4 successful computational exper-

iments for identifying anomalies of the VVER-1000 equipment components and the phase constitution of the coolant in the primary circuit are presented to illustrate peculiarities of the approaches. Section 5 gives conclusions and discussion on further work.

2 Formulation of the problem

It is supposed that a set of performance index values associated with computational model of the VVER-1000 equipment components or of pressure fluctuations in the primary circuit is defined by a set of controlling variables [4]. Experimental spectral data registered by reactor instrumentation may be incomplete. So the goal is to determine vectors of controlling variables using only restricted data on natural frequencies of the coolant flow in the circuit. The standard approach is to set the inverse spectral problem and then to solve the corresponding least squares problem

$$\min_{x \in X \subset \mathbb{R}^n} f(x),$$

where $f(x) = \sum_{i=1}^{N} \alpha_i (\zeta_i(x) - \zeta_i^*)^2$; x, X — the vector of controlling variables and its feasible domain of the error function $f(x)$ respectively; α is a vector of weighted coefficients (the additional vector α is introduced in order to provide a match with the computational model); N is the number of eigenvalues under consideration; $\zeta_i(x)$ and ζ_i^* denote the eigenvalues that correspond to computed (solutions of the direct problem) and to measured natural frequencies of the coolant flow oscillation respectively;

$$X = \left\{ x_i \,|\, x_i^L \leq x_i \leq x_i^U; \ i = \overline{1,n} \right\};$$

here x_i^L, x_i^U — the lower and upper bounds on the ith controlling variable.

As practical observations show, the error function in the considered problem is often multiextremal. Therefore, it is necessary to turn to methods of global optimization. It is clear that if the measured spectral data exactly match to the computational model then the solution of the minimization problem will cause error function to take its global minimum value of zero. Let us suppose that there is a unique solution of the ill-posed inverse spectral problem and that this corresponds to the global minimum of the error function. However, the fact is that the theoretical question of the uniqueness of solutions of the problem may not be relevant to practical applications in which there is the additional complication of accuracy of experimental measurements. Furthermore, some complications may arise due to incompleteness of measured spectral data, influence of the two-phase interference on the flow dynamics, the presence of noise, etc. Within the scope of this work we take it as a convenient and reasonable assumption that global minimization of the error function in the above inverse problem will yield correct identification of the coolant phase constitution anomalies from the flow spectral pattern.

3 3. Stochastic global optimization algorithms

3.1 The Nelder-Mead Particle Collision Algorithm (NM-PCA)

The modern Particle Collision Algorithm [5] has some essential advantages in relation to well known stochastic global optimization algorithms such as the Genetic Algorithms, Simulated Annealing, Fast Simulated Annealing, etc. Specifically, the PCA does not require any additional parameters other than the number of iterations; the algorithm is extremely easy to implement and can be applied to both continuous and discrete optimization problems. The PCA performs using the analogy with nuclear particle collision reactions, in particular scattering and absorption. So, a particle that hits a high-fitness "nucleus" would be "absorbed" and would explore the boundaries. Otherwise, a particle that hits a low-fitness region would be scattered to another region. This reasoning makes it possible to simulate the exploration of the search space and the exploitation of the most promising areas of the fitness landscape throw successive scattering and absorption collision events. The original PCA works as follows. First an initial configuration is chosen, then a modification of the old configuration into a new one is implemented. The qualities of the two configurations are compared. A decision then is made on whether the new configuration is acceptable. If it is, the current configuration acts as the old configuration for the next step. If it is not acceptable, the algorithm proceeds with a new change of the old configuration. It is pertinent to note that acceptance of current trial solution with certain probability may avoid the convergence to local optima.

However, the PCA is in its early stages. In spite of its advantages over Genetic Algorithm and Simulated Annealing in solving test problems, practical application of the PCA is restricted because of solutions remain too expensive. As possible development, the local search procedure in the algorithm could be improved. It seems promising to use gradient methods for local minimization of the error function. But in so doing the problem of non-differentiability of the function should be taken into account. A hybridization of the stochastic PCA and the Nelder-Mead Simplex algorithm was introduced in [6]. The last method does not require any gradient information. During processing two procedures are performing: a wide search in the solution space using the stochastic PCA and a local search in the promising areas with the deterministic simplex algorithm. The local search procedure is performed iteratively until a certain number of fitness function evaluations being reached.

3.2 The smoothing technique for local optimization

Inverse problems are considered to be substantially difficult because of the kinks connected with presence of the multiple frequencies in registered spectra of the diagnosing object or of acoustical oscillations in two-phase coolant. The difficulty motivated the development of algorithms for the solution of the minimization problem via some smooth approximation, which could be minimized by using any of the efficient classical approaches for smooth optimization. Several approximations to

smooth out the kinks may be introduced. One of them results in a continuously differentiable approximate fitness function, whereas another one leads to a twice continuously differentiable approximate function. These approximations replace the original function in some neighborhoods of directional differentiability points. Moreover, this approach preserves such important property of the original function as its convexity. It is clear that the approach makes it possible to implement efficient gradient techniques in the solution process. Two-parametric smoothing approximations were successfully used to solve problems of multi-criterion optimization of mechanical and hydro-mechanical systems with continuous but not everywhere differentiable functions.

Suppose now that the problem only has constraints on the variations of the individual coordinates, i.e. the problem is of the form [9]

$$\min_{x}\{f(x) : a_j \leq x_j \leq b_j, \ j = 1, \ldots, n\}.$$

Real numbers a_j, b_j, ε, $0 < \varepsilon < 1$, and parameters of the approximation [10] $p < 0$, $q > 0$ are chosen.

For this problem, it is sensible to use all the constraints in the auxiliary problem. Thus, for simple constraints, the algorithm has the following form:

0. A point x^0 is chosen so that $a_j \leq x_j^0 \leq b_j$, $j = 1, \ldots, n$.

1. If the point x^k has already been constructed, the vector $h^k = h(x^k)$ is calculated (solution of the quadratic subproblem).

2. Determine the first number $r = 0, 1, \ldots$, in which for $\alpha = (1/2)^r$ the inequality

$$\tilde{f}(p, q, x^k + \alpha h^k) \leq \tilde{f}(p, q, x^k) - \varepsilon \alpha \|h^k\|^2$$

is satisfied. If such $r = r_0$ is determined, then set $\alpha_k = 2^{-r_0}$, $x^{k+1} = x^k + \alpha_k h^k$. The algorithm returns to 1.

3. Stopping criterion: $h^k = 0$.

3.3 The hybrid algorithm (PCAHS)

The proposed hybrid algorithm (named here PCAHS) combines the stochastic PCA and deterministic gradient techniques. Smoothing approximations are introduced during the local search that makes it possible to expand the approach on the class of non-differentiable problems. In this new version of the global optimization algorithm the local search mechanism is a standard deterministic linearization method. In general case the error function is not differentiable everywhere, so the implementation of the smoothing technique may be quite pertinent. Solutions of some benchmarks show the computational efficiency of the hybrid algorithm. The pseudo code description of the operating version of the PCAHS under development is as follows.

    0. Generate an initial solution *Old_Config*
       Best Fitness = Fitness *(Old_Cofig)*
   1. Main loop
     For $n = 0$ to # iterations
       Perturbation ( )

      If Fitness *(New_Cofig)* > Fitness *(Old_Cofig)*
        If Fitness *(New_Cofig)* > *Best Fitness*
          Best Fitness := Fitness *(New_Cofig)*
        End If
        Old_Config := *New_Config*
        Exploration ( )
      Else
        Scattering ( )
      End If
    End For

2. Exploration ( )
    For $n = 0$ to # iterations
      Small Perturbation ( )
        Local search using smoothing approximation
        Check stopping criterion:
        Find global solution *Best Fitness*
        Else continue
        If Fitness *(New_Config)* > *Best Fitness*
          Old_Config := *New_Config*
        End If
    End For
    Return

3. Scattering ( )
    $p_{scatt} = 1 -$ (Fitness (New_Cofig)) / (*Best Fitness*)
    If p_{scatt} > random(0, 1)
      Old_Config := random solution
    Else
      Exploration ( )
    End If
    Return

4. Small Perturbation ( )
    For i=0 to ## iterations
      Upper = Random (1.0, 1.0 + δ)**Old_Config[i]
      If (*Upper* > Superior Limit [i])
        Upper = Superior Limit [i])
      End If
      Lower = Random (1.0-δ, 1.0)**Old_Config[i]
      If (*Lower* < Interior Limit [i])
        Lower = Interior Limit [i])
      End If
      Rnd = Random (0, 1)
      New_Config[i] = *Old_Config*[i] * ((*Upper* – *Old_Cofig*)*Rnd) –
        ((*Old_Cofig* - *Lower*)**(1 - Rnd)*)
  End

The approximate solution of the regularized inverse problem is connected with searching some unknown variables $x \in X \subset R^n$ determining the computational model of the object and minimizing the error function $f(x, \zeta_\delta) = \mu_D^2 (A(x), \zeta_\delta) + \alpha s(x)$. Here ζ — stands for measured data, $\zeta \in D$ is an element of the metrical

data space D; δ is an error of measurements; $\zeta_\delta = \zeta + \delta\zeta$; μ_D is a distant function, $\mu_D(\zeta_\delta, \zeta) \leq \delta$; $A(\cdot)$ is the direct modeling operator; $s(x)$ is a stabilizing functional; α is a parameter of regularization. The unknown real parameter α is defined from the following condition: $\mu_D(A(x_\alpha), \zeta_\delta) = \delta$, where x_α is the element at which the functional $f(x, \zeta_\delta)$ reached its minimum. The process is constructed iteratively as follows: $x_{n+1} = x_n - k_n^\alpha l^\alpha(x_n)$; here n is a current number of the current iteration; real coefficient k_n^α is determined by minimization of the parametric functional with respect to this coefficient; $l^\alpha(x_n)$ is the direction of the steepest ascent of the parametric functional. Stopping criterion: $\delta f(x_N) \leq \varepsilon_0$, where ε_0 is a specified level.

4   Computational results

In this section two numerical examples of hybrid algorithm PCAHS applications to inverse spectral problems for VVER-1000 equipment are presented. First example is devoted to identification of anomalies in a state of steam pipe supporting units. In the second example diagnostics of the coolant phase constitution in the primary circuit is carried out.

The computations were performed for identification of anomalies in a state of steam pipe diagnostics of the coolant phase constitution in the VVER-1000 primary circuit. Appearance of the second phase is possible: in a coolant heating zone (pressure tank of the pressurizer), in an exit volume of the reactor pressure vessel (RPV), in a core barrel of the RPV, in exit volumes of main circulating pumps. In order to formulate the inverse problems two vectors of relative acoustic velocities in a coolant flowing throw the specified zones are introduced.

Example 1. The object under consideration is a steam pipe from the connection with the second circulating loop steam collector to the support on the wall of the airtight zone. Spacing supporting units bound the vertical displacements of the pipe only. The stiffness of each spacing unit is $c = 40.0$ MN/m. Anomalous state of the object is characterized by decrease of the stiffness characteristics. The spectra corresponding to normal state and anomalous one of the object are given. It is convenient to introduce the following controlling variables: $x_i = (c_i/c) \cdot 100\%$, where $c_i \leq c$ is the current stiffness of the ith supporting unit. First we consider the problem for known spectral data presented in Table 1. Here we have: i — mode number; ω_i — natural ith frequency of the object oscillation under normal conditions; ω_i^* — natural ith frequency of the object oscillation with abnormal state of the supporting units.

Table 1: Given spectral data for Example 1

i	1	2	3	4	5
ω_i, Hz	13.1	23.0	26.1	27.0	34.8
ω_i^*, Hz	8.42	21.8	24.6	26.9	33.3

Let the anomalous state of the supporting units be characterized be the following vector of controlling variables: $x_i^* = 100\%$, $i = \overline{1,3}$, $x_4^* = 0$; $x_5^* = 100\%$. The error function in this example is determined using five lower spectral components. Controlling parameters dependence on the number of final iterations Niter of the
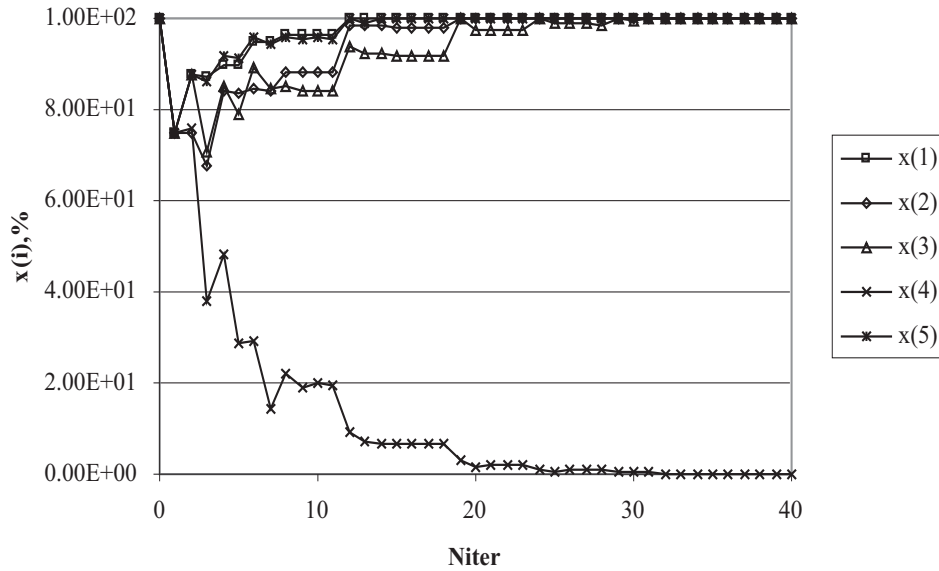
Figure 1: Number of final iterations of the PCAHS vs. relative velocities (Example 1)
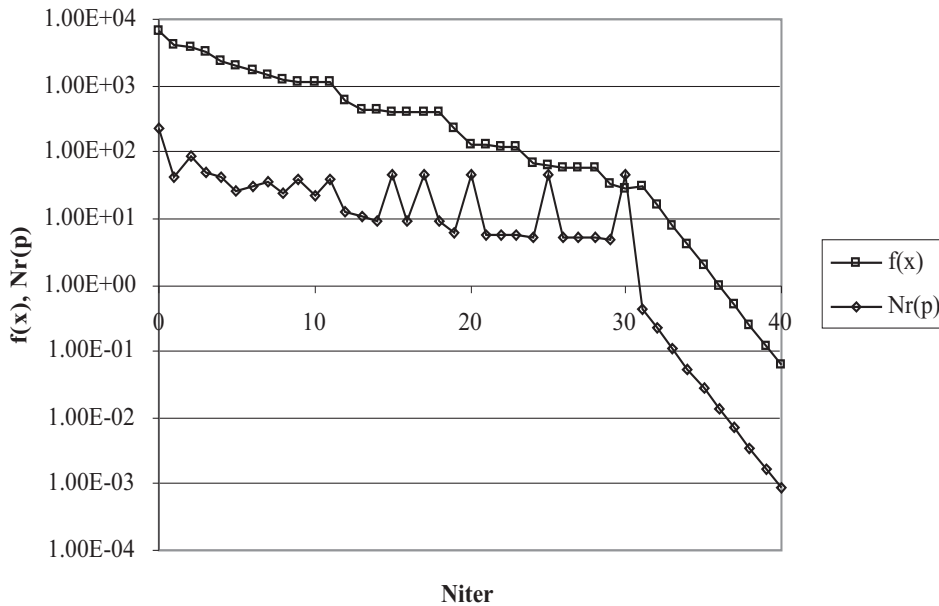

Figure 2: Number of final iterations of the PCAHS vs. error function and search gradient norm (Example 1)

hybrid algorithm PCAHS is shown in Fig. 1; the analogous dependences for the error function $f(x)$ and the search gradient norm $N(p)$ are presented too, see Fig. 2. The results obtained by the hybrid algorithm after forty iterations are as follows: $x_i^{40} \approx 100\%$, $i = \overline{1,3}$; $x_4^{40} \approx 0.861 \cdot 10^{-3}\%$; $x_5^{40} \approx 100\%$; $f(x^{40}) \approx 0.616 \cdot 10^{-1}$. It is clear, that the inaccuracy of the relative acoustical velocity is less than 1%. Consequently, these results show that the coolant phase constitution anomaly is conditioned by boiling process in the coolant heating zone.

Example 2. Let now the anomalous coolant state constitution be characterized by second vector of controlling variables: $x_1^* = x_4^* = 100\%$; $x_2^* = 81\%$; $x_3^* = 72.9\%$. The error function is determined using ten lower spectral components. Table 2
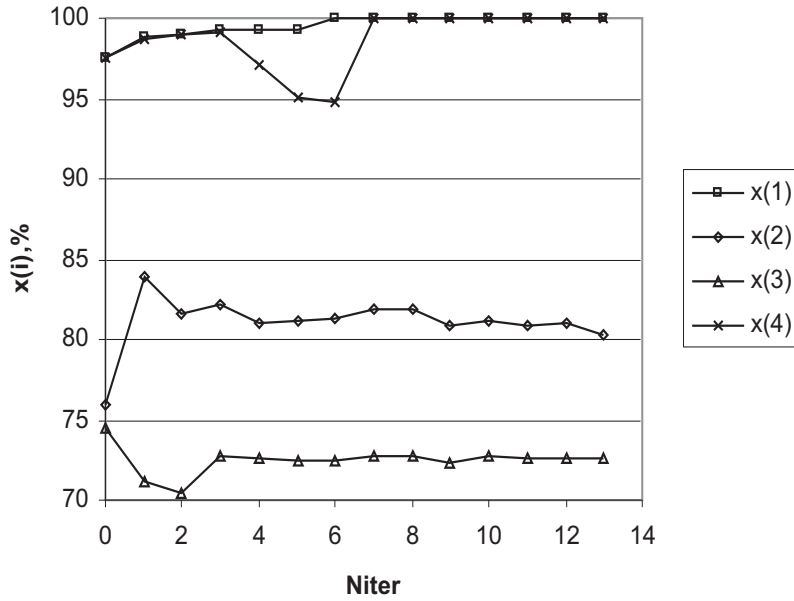
Figure 3: Number of final iterations of the PCAHS vs. relative velocities (Example 2)
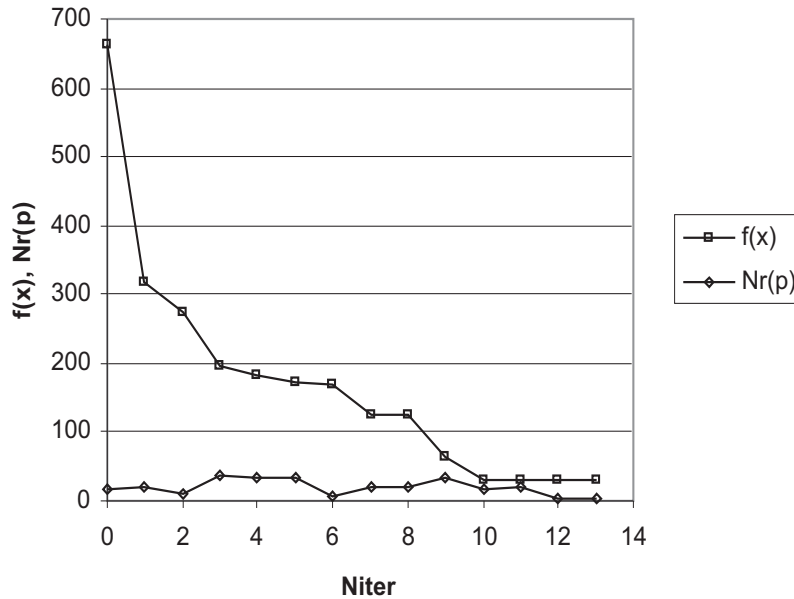
Figure 4: Number of final iterations of the PCAHS vs. error function and search gradient norm (Example 2)

displays the known spectral data for the second inverse problem. Here we have: i — mode number; ω_i — natural ith frequency of the coolant oscillation under normal conditions (without appearance of the second phase in the coolant); ω_i^* — natural ith frequency of the coolant oscillation with the availability of anomalies in coolant phase constitution.

Table 2: Given spectral data for Example 2

i	1	2	3	4	5	6	7	8	9	10
ω_i, Hz	0.89	6.77	9.82	15.44	15.96	18.94	24.55	26.69	27.07	30.52
ω_i^*, Hz	0.86	6.77	9.07	15.26	15.96	18.93	24.55	26.66	26.85	28.61

The reached approximate solution is: $x_1^{13} \approx x_4^{13} \approx 100\%$; $x_2^{13} \approx 79.87\%$; $x_3^{13} \approx 73.74\%$. Fig. 3 and Fig. 4 illustrate the solution history (final iterations of the hybrid algorithm). The inaccuracy of the relative acoustical velocity computing is about 1%. As follows from the results obtained in this example the coolant phase constitution anomaly is conditioned by boiling process in the exit volume of the reactor pressure vessel and in the core barrel of the RPV.

5 Conclusions

A novel hybrid algorithm PCAHS combining the stochastic algorithm PCA and determining gradient techniques is presented. Smoothing approximations are introduced during the local search that makes it possible to expand the approach on the class of non-differentiable problems. The PCAHS was used for solving inverse spectral problems in connection with model determining anomalies of the VVER-1000 equipment components and coolant phase constitution diagnostics. Computational experiments show the principal applicability of the proposed hybrid algorithm for solving the above diagnostic problems. The future work will be devoted to increasing the computational efficiency of tools for solution the inverse spectral problems.

Acknowledgements

References

[1] V. Isacov. Inverse problems for PDE. Springer-Verlag, Berlin et al., 2005.

[2] Göge D., Link M. Assessment of computational model updating procedures with regard to model validation // Aerospace Science and Technology. – 2003. – V. 7, N 1. – P. 47-61.

[3] A. Poullikkas. Effects of two-phase liquid-gas flow on the performance of nuclear reactor cooling pumps. Progress in Nuclear Energy 42, 3–10, 2003.

[4] V.G. Kinelev, P.M. Shkapov, V.D. Sulimov. Application of global optimization to VVER-1000 reactor diagnostics. Progress in Nuclear Energy 43, 51–56, 2003.

[5] W.F. Sacco, C.R.E. de Oliveira, C.M.N.A. Pereira. Two stochastic algorithms applied to nuclear reactor core design. Progress in Nuclear Energy 48, 525–539, 2006.

[6] W.F. Sacco, H.A. Filho, N. Henderson, C.R.E. de Oliveira. A Metropolis algorithm with Nelder-Mead Simplex applied to nuclear reactor core design. Annals of Nuclear Energy 35, 861–867, 2008.

[7] K.I.M. McKinnon. Convergence of the Nelder-Mead simplex method to a non-stationary point. SIAM J. Optimization 9, 148–158, 1998.

[8] Y.D. Sergeev, D.E. Kvasov. Global search based on efficient diagonal partitions and a set of Lipschitz constants. SIAM J. Optimization 16, 910–937, 2006.

[9] B.N. Pshenichnyj. 1994. The Linearization Method for Constrained Optimization. Springer-Verlag, Berlin et al., 1994.

[10] V.D. Sulimov, P.M. Shkapov, P.M. Smoothing approximation in problems of vector non-differentiable optimization of mechanical and hydro-mechanical systems. Vestnik MGTU. Estestvennye Nauki 2, 17–30, 2006 (in Russian).

V.D. Sulimov, Baumanskaya 2$^{\mathrm{nd}}$ *str. 5, Moscow, 105005, Russia.*
P.M. Shkapov, Baumanskaya 2$^{\mathrm{nd}}$ *str. 5, Moscow, 105005, Russia.*

Structural-phenomenological modelling of softening and recovery of mechanical properties of elastomer nanocomposite

A. L. Svistkov   A. G. Pelevin   A. A. Adamov
svistkov@icmm.ru

Abstract

The method of constructing the system of constitutive equations was applied to develop the model describing the behaviour of rubber compounds. We simulated the effect of softening of the material after the first stretching (Mullins effect), viscoelastic properties and recovery of mechanical behavior after the long rest and thermostating.

Rubbers are elastomeric nanocomposites that have long been used in industry and are of great practical importance. The incorporation of active fillers in rubber compounds increases by an order of magnitude the strength of the material compared to the unfilled elastomer and increases breaking deformations [1]. These materials have a number of features essential for the understanding of their behavior. In particular, near filler particles there appear polymer layers with special characteristics. During the failure of rubber compounds, at the tip of a macrorupture there occur fibers joining the edges of this macrorupture [2], where the polymer chains are in the oriented state [3]. The formation and disappearance of the oriented regions explain the hysteresis phenomena in the material subject to cyclic loading [4, 5]. On this basis, we put forward the following hypothesis: during deformation, between the aggregates of filler particles there appear uniaxially oriented fibers caused by the slippage of polymers chains from the layers near the active filler into the gaps between particles. In the present paper, we offer the structural-phenomenological model able to accurately describe the mechanical behavior of the medium taking into account the process of fiber formation at the nano-level of the material.

The mathematical model describing the mechanical behavior of the material is schematically represented in Fig. 1. The system of constitutive equations is constructed in correspondence with following rules:

1. To each point of the scheme the rate of deformation tensor of this point is assigned, which plays the role of a tensor parameter necessary for construction of the mathematical model.

2. The Cauchy stress tensor and the rate of deformation tensors are assigned to the elastic, viscous and plastic elements of the scheme.

3. For each transmission element the Cauchy stress tensor for the left and right points are used.

4. It is assumed that the rate of deformation tensor of the left point of the scheme coincides with the rate of deformation tensor $\mathbf{D}$ of the medium, and the rate of deformation tensor of the right point of the scheme is equal to zero.

5. The rate of deformation tensor of elastic, viscous and plastic elements is calculated as the difference between the rate of deformation tensors of the left and right points of these elements.

6. The material is assumed to be incompressible. The trace of any rate of deformation tensor in the model is equal to zero.

7. The Cauchy stress tensor $\mathbf{T}$ of the medium is equal to the sum of the Cauchy stress tensors of elastic elements and the left points of transmission elements connected with the left point of the scheme.

8. The sum of the Cauchy stress tensors of elastic, viscous and plastic elements and the right points of transmission elements connected on the left with any inner point of the scheme is equal to the sum of the Cauchy stress tensors of elastic, viscous and plastic elements and the left points of transmission elements connected on the right with this point of the scheme.
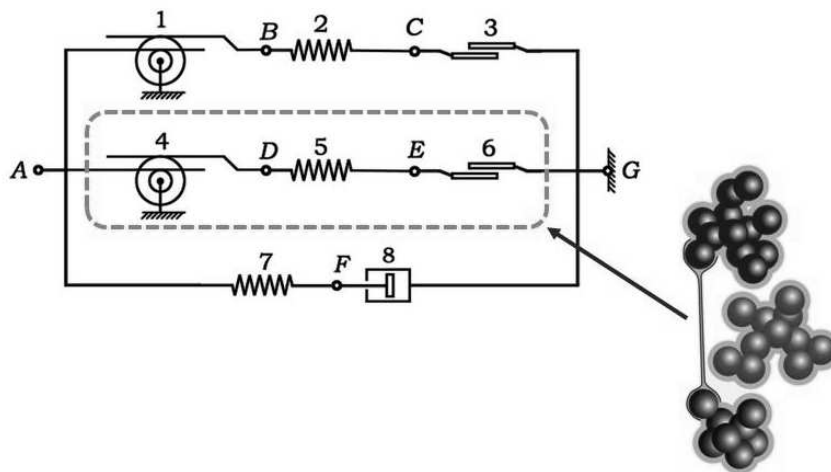

Figure 1: Scheme of mechanical behavior of rubber compound. Elements in dashed box simulate mechanical properties of high-strength fibers

Our investigation focuses on the study of isothermal processes. To describe the properties of elements shown in the scheme, the known formulas from continuum mechanics are used. For calculation of the Cauchy stress tensors $\mathbf{T}_i$ of elastic elements, we take the mass density of free energy f, which is the function of stretch ratios of all elastic elements

$$f = f(\theta, ..., \lambda_1^{(i)}, \lambda_2^{(i)}, \lambda_3^{(i)}, ...),$$

where $\lambda_1^{(i)}$, $\lambda_2^{(i)}$, $\lambda_3^{(i)}$ are the stretch ratios for the i-th elastic element. This means that the deviator of the Cauchy stress tensor of the i-th elastic element should be

calculated by the formula of the nonlinear elasticity theory

$$\mathrm{dev}\mathbf{T_i} = \mathrm{dev}\left(\rho \sum_{k=1}^{3} \lambda_k^{(i)} \frac{\partial f}{\partial \lambda_k^{(i)}} \, \mathbf{n}_k^{(i)} \otimes \mathbf{n}_k^{(i)} \right),$$

$$\mathrm{dev}(\cdot) = (\cdot) - \frac{1}{3}\,\mathrm{tr}(\cdot),$$

where ρ is the mass density of the material, and $\mathbf{n}_1^{(i)}$, $\mathbf{n}_2^{(i)}$, $\mathbf{n}_3^{(i)}$ form an orthonormal triple of eigenvectors of the stretch tensor $\mathbf{V_i}$ of the elastic element. $\mathbf{V_i} = \lambda_1^{(i)} \mathbf{n}_1^{(i)} \otimes \mathbf{n} + \lambda_2^{(i)} \mathbf{n}_2^{(i)} \otimes \mathbf{n}_2^{(i)} + \lambda_3^{(i)} \mathbf{n}_3^{(i)} \otimes \mathbf{n}_3^{(i)}$.

For the i-th elastic element, the material time derivative of the stretch tensor $\dot{\mathbf{V}}_i$ is calculated by equation:

$$\frac{2}{\nu_m}\,\mathbf{Y_i}^{0.5}\mathbf{D_i}\mathbf{Y_i}^{0.5} = \dot{\mathbf{Y}}_i - \mathbf{Y_i}\mathbf{W_R^T} - \mathbf{W_R}\,\mathbf{Y_i}, \qquad (1)$$

$$\mathbf{W_R} = \dot{\mathbf{R}}\,\mathbf{R^T},$$

where

$$\mathbf{Y_i} = \mathbf{V_i}^{\frac{2}{\nu_m}}, \qquad \nu_m > 0,$$

$\mathbf{R}$ is the rotation tensor in the polar decomposition $\mathbf{F} = \mathbf{VR}$ of the deformation gradient of the medium $\mathbf{F}$ into the left stretch tensor $\mathbf{V}$ and the rotation $\mathbf{R}$; ν_m is the transmission ratio of the m-th transmission element connected on the left with the considered elastic element. If the left point of the elastic element coincides with the left point of the scheme then transmission ratio ν_m is equal to unity.

The known equations of the nonlinear elastic theory describing the time variation of stretch ratios of the i-th elastic element

$$\dot{\lambda}_k^{(i)} = \lambda_k^{(i)} \mathbf{n}_k^{(i)} \otimes \mathbf{n}_k^{(i)} \cdot \mathbf{D_i}, \qquad k = 1, 2, 3$$

and the rate of work in this element

$$\mathbf{T_i} \cdot \mathbf{D_i} = \rho \sum_{k=1}^{3} \frac{\partial f}{\partial \lambda_k^{(i)}} \, \dot{\lambda}_k^{(i)}$$

are the consequences of equation (1) in the case when the parameter ν_m is a constant

$$\nu_m = \mathrm{const.}$$

In the general case, parameters ν_k can be the time decreasing functions. They are convenient to use for modeling the growth of damages in the medium.

The deviator of the Cauchy stress tensor of the j-th viscous element is calculated by the formula from the theory of nonlinear viscous fluids

$$\mathrm{dev}\,\mathbf{T_j} = 2\eta_j \mathbf{D_j},$$

where the shear viscosity coefficient is the non-negative function of state parameters $\eta_j \geq 0$.

The deviator of the Cauchy stress tensor of the plastic element is calculated by the formula of the plastic flow theory

$$\mathbf{D}_n = \sqrt{\frac{\mathbf{D}_n \cdot \mathbf{D}_n}{\operatorname{dev} \mathbf{T}_n \cdot \operatorname{dev} \mathbf{T}_n}} \, \operatorname{dev} \mathbf{T}_n, \tag{2}$$

where n is the number of the plastic element. For modeling the plastic flow process, it is necessary to exclude the ambiguity in expression (2). To this end, it is offered to use the mathematical expression which links the rate of deformation tensor of the plastic element with the rate of deformation tensor of the medium:
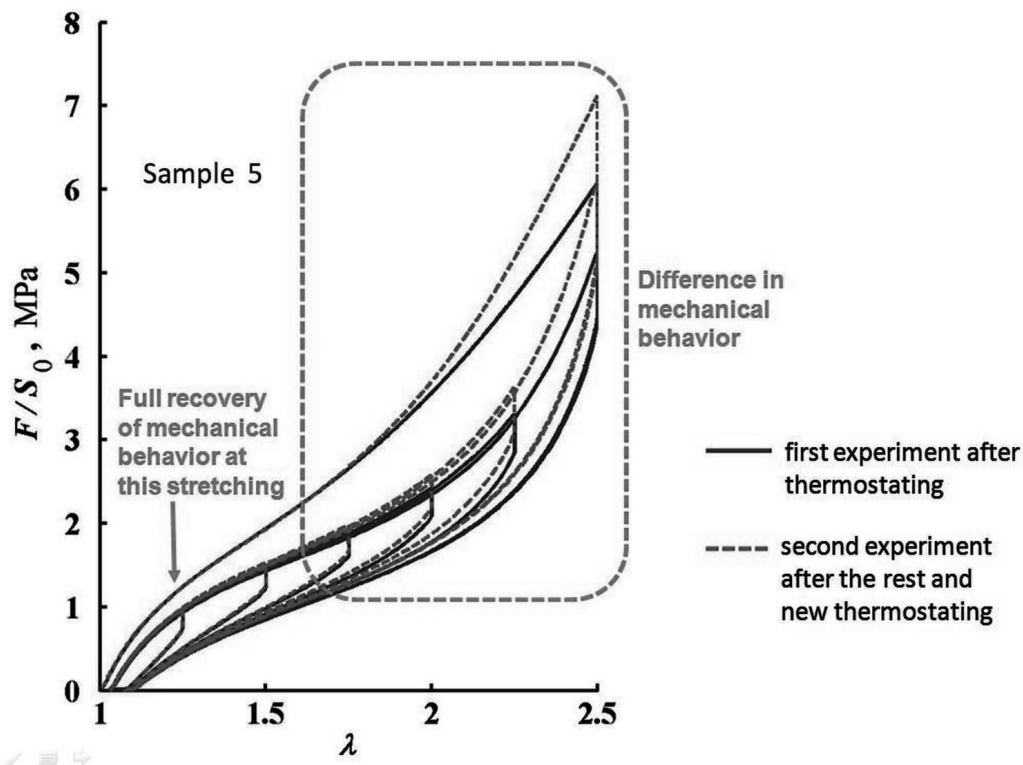

Figure 2: Difference in mechanical behavior of rubber compound in first experiment after thermostating and in second experiment after long rest and new thermostating

The symbol κ_n designates the non-negative function of state parameters. When calculating, we assume that plastic flow is possible under the following condition:

$$\max \operatorname{inv}(\mathbf{T}_n) = \operatorname{inv}(\mathbf{T}_n), \tag{3}$$

where

$$\operatorname{inv}(\mathbf{T}_n) = \sqrt{\operatorname{dev} \mathbf{T}_n \cdot \operatorname{dev} \mathbf{T}_n},$$

i.e., when the invariant of stresses in the appropriate plastic element is equal to the maximum of this invariant in the considered element during the whole deformation history of the medium.
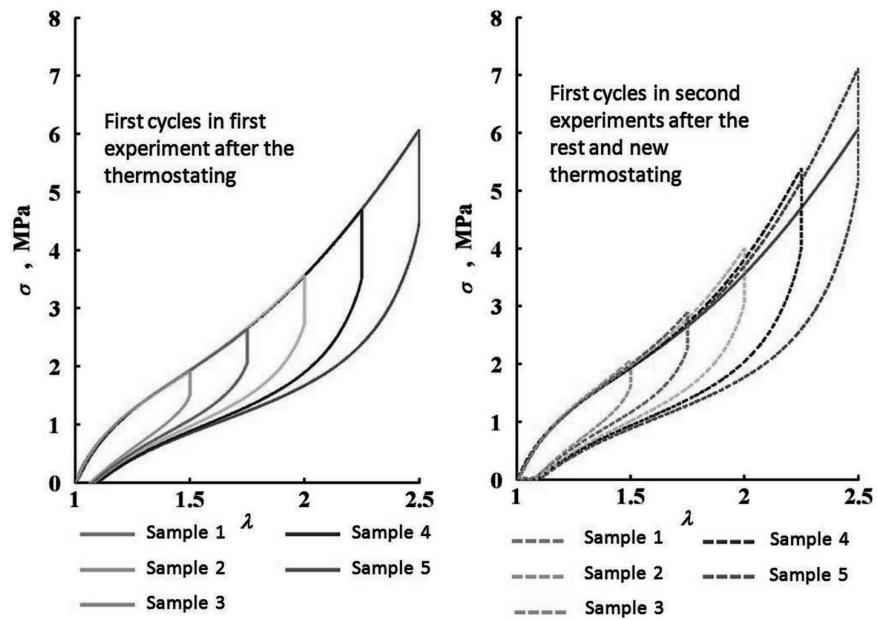
672

Figure 3: First cycles of deformation of samples in the first experiments after thermostating (left plot) and in the second experiment after long rest and new thermostating (right plot)
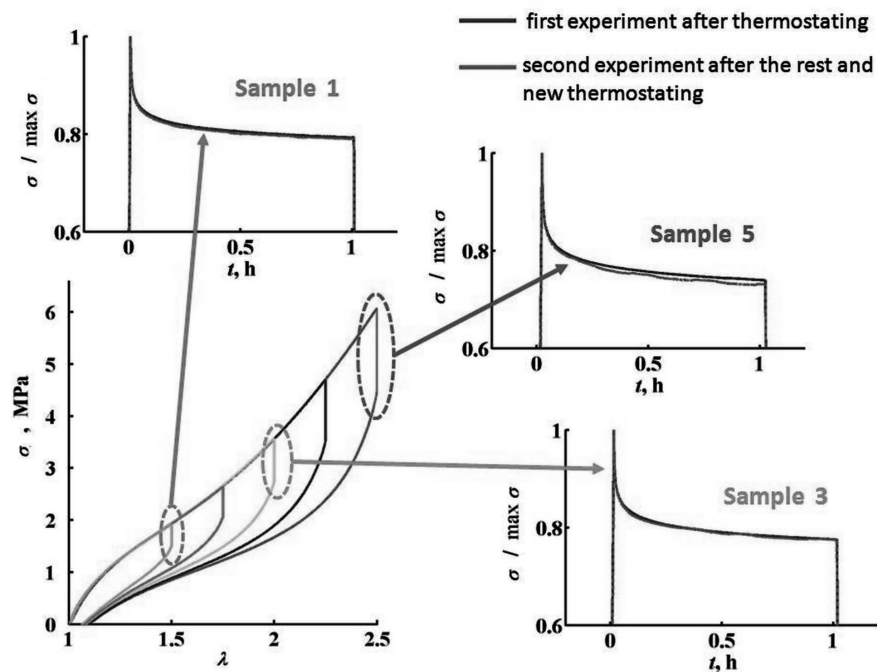

Figure 4: Relaxation curves of samples in the first experiments (continuous lines) and in the second experiment (dashed lines)

The transmission element in the model serves to increase the rate of deformation tensor by ν_m times and to decrease simultaneously the Cachy stress tensor by ν_m times

$$\mathbf{T}_m^{\text{left}} = \nu_m \mathbf{T}_m^{\text{right}}, \qquad \mathbf{D}_m^{\text{left}} = \frac{1}{\nu_m} \mathbf{D}_m^{\text{right}},$$

where ν_m is the non-negative function of the state parameters (the transmission ratio), and k is the number of the transmission element.

The necessity to introduce transmission elements into the model stems from the following. In the initial state, the particle aggregates of carbon black in rubbers touch each other, forming a filler network. We put forth a hypothesis that during deformation the polymer chains slipped off from the polymer layers near the filler particles into the gaps between aggregates, where high-strength fibers are formed as a polymer in the uniaxially oriented state (Fig. 1). The strength of these fibers is a thousandfold higher than the strength of the elastomeric material without a filler (binder strength). This increases the macroscopic strength of rubbers (filled elastomers) by an order of magnitude. For example, the strength of spider cobweb is 2000-4000 MPa and the strength of non-crystallizing elastomeric materials is 4-10 MPa. We reason that such a relationship between strengths will also appear when comparing the strengths of oriented fibers and the binder.

The fact that during deformation polymer chains slipped off into the gaps between aggregates clarifies the deformation growth at the moment of rupture of filled elastomers compared to the unfilled material. In the course of deformation, the neighboring particle aggregates of carbon black move away at a large distance from each other, and other aggregates come into the gaps between them. However, the material is not destroyed in this case. After removing the external load, the material reverts to its primary state. This may take place only in the case when fibers are able to elongate by several tens of times. The macroscopic deformations of the material do not exceed the stretch ratios of 4-7. This distinction between the macroscopic deformations and the deformation of separate elements of the material on structural level can be taken into account by the transmission elements introduced in the model.

We simulated the effect of softening of the material after the first stretching (Mullins effect), viscoelastic properties and recovery of mechanical behavior after the long rest and thermostating (Fig. 2 – Fig. 4). We found that all difference in mechanical behavior of rubber compound in first experiment after thermostating and in second experiment after long rest and new termostating was produced by plastic element with number six. It means from our viewpoint that only hight-strength fibers remember the long history of deformation of the material.

Acknowledgements

References

[1] Kraus, G., Reinforcement of elastomers by Carbon Black, Advance of Polymer Science, 8, 155-237, 1971.

[2] Le Cam, J.-B. Huneau, B. Verron, E. Gornet L., Mechanism of Fatigue Crack Growth in Carbon Black Filled Natural Rubber, Macromolecules, 37, 5011-5017, 2004.

[3] Trabelsi, S. Albouy, P.-A. Rault, J., Stress-Induced Crystallization around a Crack Tip in Natural Rubber, Macromolecules, 36, 9093-9099, 2003.

[4] Toki, S. Sics, I. Ran, S. Liu, L. Hsiao, B.S., Molecular orientation and structural development in vulcanized polyisoprene rubbers during uniaxial deformation by in situ synchrotron X-ray diffraction, Polymer, 44, 6003-6011, 2003.

[5] Toki, S. Sics, I. Ran, S. Liu, L. Hsiao, B.S. Murakami, S. Tosaka, M. Kohjiya, S. Poompradub, S. Ikeda, Y. Tsou, A.H., Strain induced molecular orientation and crystallization in natural and synthetic rubbers under uniaxial deformation by in-situ synchrotronv X-ray study, Rubber Chemistry and Technology, 77, 317-335, 2004.

Svistkov A. L., Institute of Continuous Media Mechanics, Russian Academy of Science, Academika Koroleva Street, 1, 614013, Perm, Russian Federation

Numerical simulation of heat propagation from deepen pipeline with accounting filtration properties of soils

Natalia A. Vaganova

vna@imm.uran.ru

Abstract

Mathematical model of heat propagation from an underground source is considered with accounting of physical factors such as filtration of water in soil and a solar radiation. This problem leads to solution of heat diffusivity equation and equation of water filtration in soil with nonlinear boundary conditions. In the presentation the methods and algorithms of computation of the problem is considered.

1   Introduction

One of methods of investigation of thermal fields in different media is direct numerical simulation of thermal diffusivity processes. Soil is a complex structure which includes solid particles, water and air with water vapour. We will consider two basic ways of heat transfer: thermal conductivity in solids and groundwater flow which filtrates through pores in soil. Purpose of this work is elaboration of models, computational algorithms and codes to investigate temperature distribution with taking into consideration humidity of soil, water flow trough soil and also solar radiation and evaporation on earth surface.

2   Heat propagation with accounting water filtration in ground

In [1] thermal diffusivity processes was considered in 3D origin where the heat source is a pipeline with a constant temperature. It is supposed that heat flow from the earth (upper) surface is caused by solar energy and difference of temperatures between earth and air. There are considered two components of heat propagation processes: thermal diffusivity and filtration of water in soil.

Let the pipeline be inside of a parallelepiped (Fig. 1). At the time moment $t = 0$ a temperature $T(t,x,y,z)$ is given, for example,

$$T(0, x, y, z) = T_0(z) = T_{air} + (T_{bot} - T_{air})z, \tag{1}$$

where T_{air} is temperature of air, T_{bot} is temperature at the bottom of the parallelepiped. Assume that at the lateral area heat flow equals to zero and at the bottom temperature is fixed.
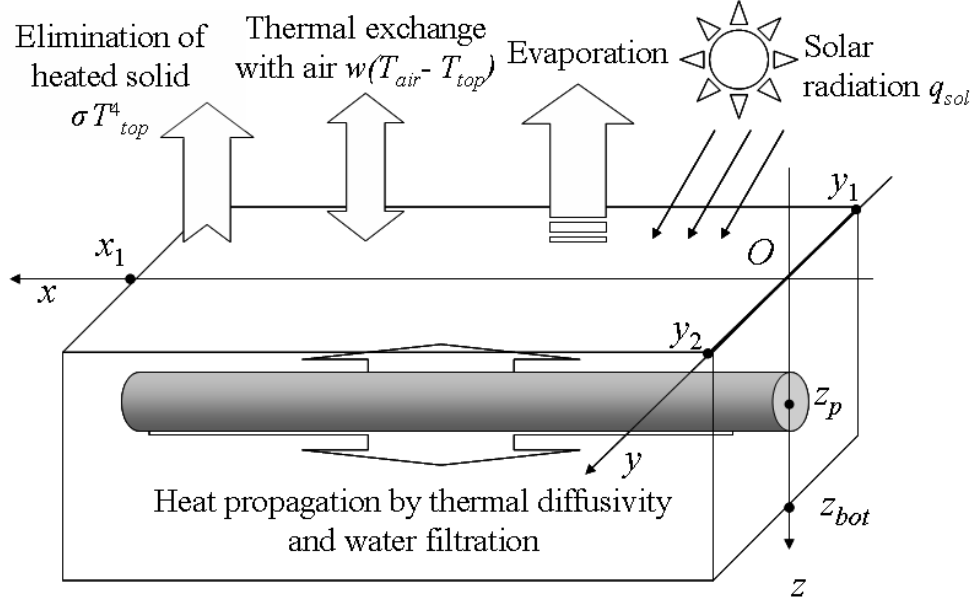

Figure 1: Model of heat distribution.

For heat distribution in soil we have

$$\frac{\partial T}{\partial t} + \text{div} (\overrightarrow{V} T) = \lambda \triangle T. \tag{2}$$

where $\lambda = \kappa/\rho c_v$ — thermal conductivity coefficient, κ — heat conductivity, ρ — density, c_v — specific heat, $\overrightarrow{V}$ — vector of velocity of water filtration in soil. Boundary condition at the pipeline has the form:

$$\lambda \frac{\partial T}{\partial \mathbf{n}} = \varepsilon(x) \left(T\Big|_{pipe} - T\Big|_{media} \right) \mathbf{n}, \tag{3}$$

where $\mathbf{n}$ is normal vector to the surface.
Boundary conditions at upper surface is

$$\gamma_{sol} q_{sol} v_{sol} + w_{top} \left(T_{air} - T|_{z=0} \right) = \sigma (T|_{z=0})^4 - km\rho_f (Q + c_v T) \frac{\partial h}{\partial z} + \kappa \frac{\partial T}{\partial z}\Bigg|_{z=0}, \tag{4}$$

where m is porosity of soil, ρ_f is density of flow, Q is thermal capacity of evaporation. Let Darcy low be used for the considered soils (for example, sand, clay and others). Let $h = h(x, y, z)$ be a potential, then

$$V_x = -k \frac{\partial h}{\partial x}, \qquad V_y = -k \frac{\partial h}{\partial y}, \qquad V_z = -k \frac{\partial h}{\partial z}. \tag{5}$$

Let assume that the flow is incompressible [2] and the soil is uniform, then we obtain

$$\frac{\partial^2 h}{\partial x^2} + \frac{\partial^2 h}{\partial y^2} + \frac{\partial^2 h}{\partial z^2} = 0. \tag{6}$$

Boundary condition for $h(x, y, z)$ at upper and lower surfaces of the considered parallelepiped include evaporation at the soil surface, are proportional to absorbed solar radiation, and have the form

$$\frac{\partial h}{\partial z} = -\frac{\gamma}{k} T(t, x, y, 0). \tag{7}$$

At the lateral surfaces it is assumed that

$$\frac{\partial h}{\partial x} = \frac{\partial h}{\partial y} = 0. \tag{8}$$

Boundary condition at the pipeline has the form ($\vec{V} = 0$):

$$\frac{\partial h}{\partial x} = \frac{\partial h}{\partial y} = \frac{\partial h}{\partial z} = 0. \tag{9}$$

3   Numerical results

To compute heat distribution (2) in a three-dimensional domain (fig. 1) the finite-difference method with splitting by spatial dimensions is used. Computations are carried out on orthogonal grid, uniform or adapted by layers. The pipeline position is exactly defined and additional grid points are inserted. Basic equation is approximated by an implicit finite-difference pattern in each of spatial dimensions. System of linear difference equations has a three-diagonal form and may be solved by a sweep method.

In the following table the parameters of computations are presented.

| Parameter	Units	Value
Air temperature	K	278.15
Soil temperature	K	278.15
Pipeline temperature	K	303.15
Soil density	kg/m^3	1800
Heat conductivity	Wt/m K	0.7
Specific heat	J/kg K	880
Water density	kg/m^3	1000
Specific heat of evaporation	Wt/m K	2625.0
Specific heat of water	J/kg K	4.12
Size of area	m	$1 \times 10 \times 4$
Pipeline diameter	m	0.5
Depth of pipeline	m	0.9
Computational time	24 hours	20

(a) (b)
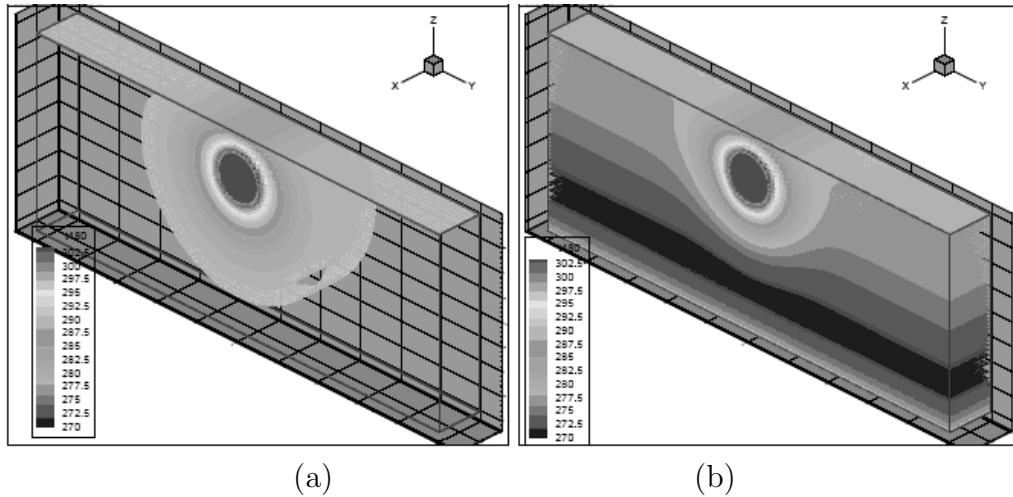
Figure 2: Temperature distribution: (a) — without filtration, (b) — with filtration
of water in soil

(b)

(a)
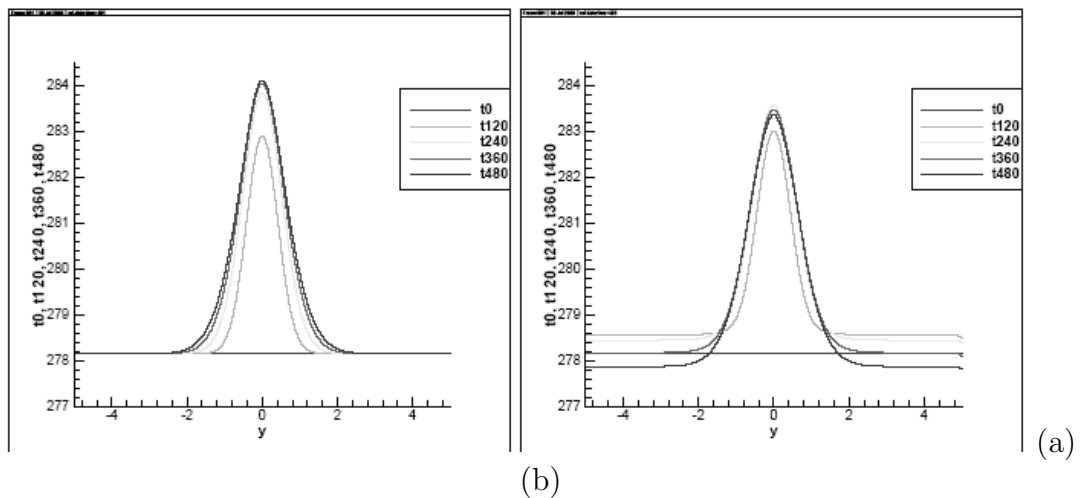
Figure 3: Profiles of temperature on the ground across pipeline: (a) — without
filtration, (b) — with filtration of water in soil

In Figures 2 and 3 the computed temperature distribution is presented.

Thus problem of simulation of heat propagation in soil with taking into account flow
which filtrates through pores in soil amounts to numerical solution of the problem
(2), (5), (6) with initial conditions (1) and boundary conditions (3), (4) (7)–(9). A
number of numerical experiments will allow to verify the presented mathematical
model of heat propagation.

Acknowledgements

References

[1] N.A.Vaganova. Simulation of heat propagation from deepen pipeline with accounting filtration and solar radiation. Proc. of APM-2008

[2] Polubarinova-Kochina P.Ya.Theory of groundflow water. M: Gostehizdat. 1952. (in Russian)

Natalia A. Vaganova
Institute of Mathematics and Mechanics UrB RAS, S. Kovalevskaya str. 16, Ekaterinburg, 620219, Russia

Modelling a chemical reaction front propagation in elastic solids: 1D case

Elena N. Vilchevskaya   Alexander B. Freidin

vilchevska@gmail.com, alexander.freidin@gmail.com

Abstract

We specify a 3D-model of a chemical reaction front in a nonlinear elastic solids for 1D-case to clarify how material, chemical and loading parameters affect chemical reactions and how chemical reactions affect stresses and strains. We consider a bar where a chemical reaction of oxidation type takes place. We suppose that the chemical reaction is localized at the reaction front and is sustained by a diffusion of an oxidizing gas constitute through the solid oxide. Stress controlled and displacement controlled bar undergoing chemical reactions is considered. We derive the dependence of chemical affinity on the chemical reaction parameters, elasticity modules of reactive materials and stress. We demonstrate that the stress action on the oxidation process depends on a parameter that is a combination of chemical reaction parameters and elastic modulus of solid constitutes.

1   Kinematics and stresses

Consider a bar where a chemical reaction of oxidation type takes place. Let $l(t)$ is a current bar length. We suppose that a chemical reaction is localized at the transformation front

$$x^{\Gamma} = x^{\Gamma}(t), \qquad x^{\Gamma} \in (0, l(t)).$$

The segment $[0, x^{\Gamma})$ is occupied by a material produced by a chemical reaction

$$\nu_- A_- + \nu_* A_* \to \nu_+ A_+ \tag{1}$$

where A_-, A_+ and A_* are chemical formulae of reacting constituents, ν_-, ν_* and ν_+ are stoichiometric coefficients. We assume that A_- and A_+ are solids and A_* is a gas. An example of the reaction (1) is the oxidation of silicon

$$\mathrm{Si} + \mathrm{O}_2 \to \mathrm{SiO}_2 \quad (\nu_- = \nu_* = \nu_+ = 1) \tag{2}$$
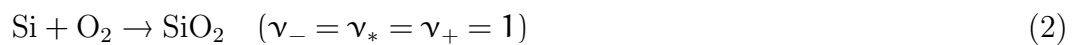
The segment $[0, x^{\Gamma})$ serves as a transport (diffusion) zone for oxidizing substance A_*. We assume that the diffusion of A_* occurs only in ν_+ until the chemical reaction front is reached by molecules of A_*. That means that the segment $(x^{\Gamma}, l]$ is occupied by an initial material A_-. We consider ν_+ as a solid skeleton for diffusing A_*. For

simplicity sake we assume that diffusion of A_* does not affect strains in the skeleton. We also neglect the influence of skeleton deformations on partial pressure of the gas constituent A_*.

Two stress free configurations can be related with the bar (Fig. 1). The reference configuration

$$X_0 \in [0, X_0^\Gamma] \cup [X_0^\Gamma, L_0]$$

presents a stress free bar made from an initial material A_-. The segment $[X_0^\Gamma, L_0]$ is an image of $[x^\Gamma, l]$.

The intermediate configuration

$$X_g \in [0, X_g^\Gamma] \cup [X_g^\Gamma, L_g]$$

is a stress free bar occupied by A_+. The segment $[0, X_g^\Gamma)$ is a stress free image of $[0, x^\Gamma)$, X_g^Γ is the image of x^Γ.

The segments $(x^\Gamma, l]$ and $(X_0^\Gamma, L_0]$ consist of the same material points A_-. Although material points of segments $[0, X_g^\Gamma)$ and $[0, X_0^\Gamma)$ present different materials, A_- and A_+ respectively, the distances between corresponding points of the segments are related by the chemical reaction (1). Indeed, the linear stress free element $dX_0 = \nu_- M_-/\rho_0$ transforms into the linear stress free element $dX_g = \nu_+ M_+/\rho_g$ where ρ_0 and ρ_g are densities of A_- and A_+ per unit length in stress free states. Then

$$dX_g = g\, dX_0, \quad g = \frac{dX_g}{dX_0} = \frac{\nu_+ M_+}{\nu_- M_-}\frac{\rho_0}{\rho_g} \tag{3}$$

and the parameter g depends on the molar masses, stoichiometric coefficients and densities.

Thus, the current state of a bar is determined by two mapping onto two stress free states:

$$x_- = x(X_0, t) \qquad X_0 \in (X_0^\Gamma, L_0] \tag{4}$$

$$x_+ = x(X_g, t) \qquad X_g \in [0, X_g^\Gamma) \tag{5}$$

where linear elements of the reference and intermediate configurations are related by (3).
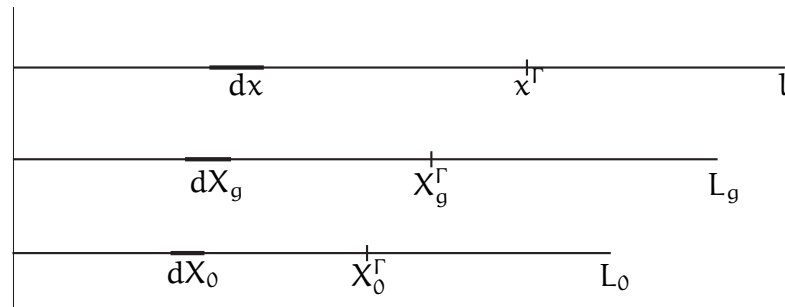

Figure 1: Current, intermediate and reference configurations

Mappings (4), (5) correspond to strains

$$\varepsilon_- \equiv \overset{0}{\varepsilon}_- = \frac{\partial x_-}{\partial X_0}, \qquad \varepsilon_+ \equiv \overset{g}{\varepsilon}_+ = \frac{\partial x_+}{\partial X_g}, \qquad \overset{0}{\varepsilon}_+ = \frac{\partial x_+}{\partial X_0} = g\,\overset{g}{\varepsilon}_+ \tag{6}$$

Decomposition $(6)_3$ Lee decomposition if g presents plastic strains [1] or growth ("transplant") strain (see, e.g. [2, 3, 4] and reference therein).

Further assume that the process is isothermal, and materials A_- and A_+ are elastic. Then ε_- and ε_+ are elastic strains and free energy densities per mass

$$f_- = f_-(\varepsilon_-), \qquad f_+ = f_+(\varepsilon_+)$$

Stresses acted on A_- and A_+ and calculated with respect to reference and intermediate configurations

$$S_-^0 = \frac{\rho_0}{\Omega_0}\frac{\partial f_-}{\partial \varepsilon_-}, \qquad S_+^g = \frac{\rho_g}{\Omega_g}\frac{\partial f_+}{\partial \varepsilon_+}$$

where Ω_0 and Ω_g the cross-section areas in the reference and intermediate configurations. Further we use tractions

$$\sigma_-^0 = \Omega_0 S_-^0, \qquad \sigma_+^g = \Omega_g S_+^g$$

Since the material transformation occurs only along the bar axe, $\Omega_0 = \Omega_g$. Then the tractions calculated with respect to reference and intermediate configurations are equal,

$$\sigma_-^0 = \sigma_-^g \equiv \sigma_- = \rho_0\frac{\partial f_-}{\partial \varepsilon_-}, \qquad \sigma_+^g = \sigma_+^0 \equiv \sigma_+ = \rho_g\frac{\partial f_+}{\partial \varepsilon_+} \tag{7}$$

Partial pressure p_*^g of A_* referred to V_g configuration is determined by the constitutive equation

$$p_*^g = \rho_*^2\frac{\partial f_*}{\partial \rho_g^*} \tag{8}$$

where ρ_g^* is partial density of A_* per unit length in the intermediate configurations, $f_* = f_*(\rho_*)$ is free energy density of A_* per unit mass.

2 Dissipation inequality

The free energy of the bar

$$F = \int_0^{x^\Gamma} \rho_+ f_+(\varepsilon_+)\,dx + \int_{x^\Gamma}^l \rho_- f_-(\varepsilon_-)\,dx + \int_0^{x^\Gamma} \rho^* f_*(\rho^*)\,dx =$$

$$\int_0^{X_g^\Gamma} \rho_g f_+(\varepsilon_+)\,dX_g + \int_{X_0^\Gamma}^{L_0} \rho_0 f_-(\varepsilon_-)\,dX_0 + \int_0^{X_g^\Gamma} \rho_g^* f_*(\rho_g^*)\,dX_g =$$

$$\int_0^{X_0^\Gamma} g\rho_g f_+(\varepsilon_+)\,dX_0 + \int_{X_0^\Gamma}^{L_0} \rho_0 f_-(\varepsilon_-)\,dX_0 + \int_0^{X_g^\Gamma} \rho_g^* f_*(\rho_g^*)\,dX_g$$

where ρ_- and ρ_+ are densities of A_- and A_+ per unit length in the current configuration, ρ^* and ρ_g^* are partial densities of A_* per unit length in the current and the intermediate configurations.

The potential energy of the solid constituents

$$\Pi = \int_0^{x^*} \rho_+ f_+(\varepsilon_+)\, dx + \int_{x^*}^l \rho_- f_-(\varepsilon_-)\, dx - \sigma\,(l - L_0)$$

By boundary conditions $V_+(0) = \partial x_+(X_g, t)/\partial t|_{X_g=0} = 0$. Then, by (7),

$$\dot{\Pi} = \sigma\left(V_+(X_g^\Gamma) - V_-(X_0^\Gamma)\right) + (g\rho_g f_+ - \rho_0 f_-)V_0^\Gamma$$

where

$$V_- = \frac{\partial x_-(X_0, t)}{\partial t}, \qquad V_+ = \frac{\partial x_+(X_g, t)}{\partial t}$$

are velocities of A_- and A_+ with respect to reference configurations.

By boundary conditions $V_+(0) = \partial x_+(X_g, t)/\partial t|_{X_g=0} = 0$. Then

$$\dot{\Pi} = \sigma\left(V_+(X_g^\Gamma) - V_-(X_0^\Gamma)\right) + (g\rho_g f_+ - \rho_0 f_-)V_0^\Gamma$$

To derive so called second order compatibility condition on the moving reaction front we note that

$$x_+(X_g^\Gamma + \Delta X_g^\Gamma, t + \Delta t) = x_+(X_g^\Gamma, t) + \left.\frac{\partial x_+(X_g, t)}{\partial X_g}\right|_{X_g^\Gamma} \Delta X_g^\Gamma + \left.\frac{\partial x_+(X_g, t)}{\partial t}\right|_{X_g^\Gamma} \Delta t$$

$$x_-(X_0^\Gamma + \Delta X_0^\Gamma, t + \Delta t) = x_-(X_0^\Gamma, t) + \left.\frac{\partial x_-(X_0, t)}{\partial X_0}\right|_{X_0^\Gamma} \Delta X_0^\Gamma + \left.\frac{\partial x_+(X_0, t)}{\partial t}\right|_{X_0^\Gamma} \Delta t$$

By the continuity, $x_+(X_g^\Gamma, t) = x_-(X_0^\Gamma, t), x_+(X_g^\Gamma + \Delta X_g^\Gamma, t + \Delta t) = x_-(X_0^\Gamma + \Delta X_0^\Gamma, t + \Delta t)$. Then

$$V_+(X_g^\Gamma) - V_-(X_0^\Gamma) = -(\varepsilon_+ V_g^\Gamma - \varepsilon_- V_0^\Gamma) = -(g\varepsilon_+ - \varepsilon_-)V_0^\Gamma$$

and, finally, we have

$$\dot{\Pi} = (g(\rho_g f_+ - \sigma\varepsilon_+) - (\rho_0 f_- - \sigma\varepsilon_-))V_0^\Gamma = \frac{\rho_0}{\nu_- M_-}\left(\nu_+ M_+ \mu_+ - \nu_- M_- \mu_-\right)V_0^\Gamma$$

where

$$\mu_+ = f_+ - \frac{1}{\rho_g}\sigma\varepsilon_+, \qquad \mu_- = f_- - \frac{1}{\rho_0}\sigma\varepsilon_-.$$

In the case of the phase transformation $g = \rho_0/\rho_g$ and we would have

$$\dot{\Pi} = (\rho_0[f] - \sigma[\varepsilon])V_0^\Gamma.$$

The mass balance for A_* takes the form

$$\dot{\rho}_g^* \equiv \frac{\partial \rho_g^*(X_g, t)}{\partial t} = \widehat{\rho}_* - \frac{\partial \rho_g^* V_g^*}{\partial X_g} \tag{9}$$

where V_g^* is a diffusion velocity of the constituent A_* in the intermediate configuration, $\widehat{\rho}_* < 0$ is a sink of the constituent A_* due to the chemical reaction. Then

$$\frac{d}{dt} \int_0^{X_g^\Gamma} \rho_g^* f_*(\rho_g^*) \, dX_g = \int_0^{X_g^\Gamma} \dot{\rho}_g^* \mu_* \, dX_g + \rho_g^* f_*|_{X_g^\Gamma} V_g^\Gamma$$

where

$$\mu_* = f_* + \frac{p_*}{\rho_g^*},$$

By (9),

$$\int_0^{X_g^*} \dot{\rho}_g^* \mu_* \, dX_g = \int_0^{X_g^*} (\widehat{\rho}_* \mu_* + \rho_g^* V_g^* \frac{\partial \mu_*}{\partial X_g}) \, dX_g - \rho_g^* V_g^* \mu_*|_0^{X_g^\Gamma}$$

Note that $\rho_g \dot{X}_g^*$ is mass production of A_+ per unit time. According to (1), to produce such an amount of A_+ one have to use

$$\frac{\nu_* M_*}{\nu_+ M_+} \rho_g \dot{X}_g^*$$

mass units of A_* where M_* is molar mass of A_*. Assuming that chemical reactions are localized at the reaction front we get:

$$\int_0^{X_g^*} \widehat{\rho}_* \mu_* \, dX_g = \widehat{\rho}_* \mu_*|_{X_g^\Gamma} = - \frac{\nu_* M_*}{\nu_+ M_+} \rho_g \mu_*\Big|_{X_g^\Gamma} \dot{X}_g^\Gamma =$$

$$- \frac{\nu_* M_*}{\nu_+ M_+} g \rho_g \mu_*\Big|_{X_g^\Gamma} V_0^\Gamma = - \frac{\nu_* M_*}{\nu_- M_-} \rho_0 \mu_*\Big|_{X_g^\Gamma} V_0^\Gamma$$

Since we assume that the diffusion of A_* takes place only in ν_-, the velocity of the component A_* at the chemical reactions front coincides with the velocity of the reaction front. Then $V_g^* = V_g^\Gamma$, and finally we have the expression of the dissipation function

$$D = \frac{\rho_0}{\nu_- M_-} \left(\nu_+ M_+ \mu_+ - \nu_- M_- \mu_- - \nu_* M_* \mu_* \right) V_0^\Gamma + \int_0^{X_g^*} \rho_g^* V_g^* \frac{\partial \mu_*}{\partial X_g} \, dX_g$$

The derived value

$$A = \nu_+ M_+ \mu_+ - \nu_- M_- \mu_- - \nu_* M_* \mu_* \tag{10}$$

is chemical affinity.

If materials A_- and A_+ are linear-elastic then

$$f_\pm(\varepsilon_\pm) = \gamma_\pm + \frac{1}{2} C_\pm \varepsilon_\pm^2 = \gamma_\pm + \frac{1}{2} \sigma_\pm \varepsilon_\pm, \qquad \sigma_\pm = C_\pm \varepsilon_\pm$$

where C_- and C_+ are elasticity modules of the bar made of A_- and A_+, respectively, and $\gamma_\pm$ are free energies of stress free A_- and A_+. Then

$$\nu_- M_- \mu_- = \frac{\nu_- M_-}{\rho_0} \left(\gamma_- - \frac{1}{2} \sigma \varepsilon_- \right), \quad \nu_+ M_+ \mu_+ = \frac{\nu_+ M_+}{\rho_g} \left(\gamma_+ - \frac{1}{2} \sigma \varepsilon_+ \right)$$

and

$$A = \gamma_* + \left(\frac{\nu_- M_-}{\rho_0} \varepsilon_- - \frac{\nu_+ M_+}{\rho_g} \varepsilon_+ \right) \frac{\sigma}{2} - \nu_* M_* \mu_* = \tag{11}$$

$$\gamma_* + \nu_- M_- G \frac{\sigma^2}{2\rho_0 C_-} - \nu_* M_* \mu_*$$

where

$$\gamma_* = \frac{\nu_+ M_+}{\rho_g} \gamma_+ - \frac{\nu_- M_-}{\rho_0} \gamma_-, \quad G = 1 - g \frac{C_-}{C_+} \tag{12}$$

By (11) and (12), the influence of stress on the chemical affinity depends on the parameter G that in turn depends on the chemical reaction molar parameters and elasticity modules of reacting materials.

3 Mechanochemical kinetics of the diffusion controlled chemical reaction front propagation

The chemical reaction rate [5]

$$\omega = \vec{\omega} \left\{ 1 - \exp\left(\frac{A}{RT} \right) \right\} \tag{13}$$

where

$$\vec{\omega} = k_* c, \quad c = \rho_* / \rho_g \tag{14}$$

is a rate of direct chemical reaction, k_* is a reaction parameter. Not far from chemical equilibrium $|A/(RT)| \ll 1$ and

$$\omega = -k_* c \frac{A}{RT} \tag{15}$$

The equilibrium concentration c_{eq} satisfies the condition $A = 0$ that, by (11), take the form of the equation for $c_{eq} = c_{eq}(\sigma)$,

$$\gamma_* + \nu_- M_- G \frac{\sigma^2}{2\rho_0 C_-} - \nu_* M_* \mu_*(c_{eq}, p^*) = 0 \tag{16}$$

Further we assume that

$$M_* \mu_* = \eta(T) + RT \ln(c)$$

Then, by (15) and (16) not far from the chemical equilibrium

$$\frac{A}{RT} = \nu_* \frac{c - c_{eq}}{c_{eq}}, \quad \omega = k_* \nu_* (c - c_{eq}) \tag{17}$$

Now we can proceed to the diffusion and the reaction front coupled considerations. In the steady-state approximation

$$D \frac{\partial^2 c}{\partial X_g^2} \equiv D \frac{\partial^2 \tilde{c}}{\partial X_g^2} = 0, \qquad X_g \in [0, X_g^\Gamma] \tag{18}$$

686

where $\tilde{c} = c - c_{eq}$. We assume that the concentration of the oxidizing component A_* is given at the left end of the bar, $c = c_0$ at $X_g = X_0 = 0$ and, thus,

$$\tilde{c} = c_0 - c_{eq} \quad \text{at } X_g = X_0 = 0 \tag{19}$$

The oxidizing component concentration at the reaction front $X^\Gamma(t)$ is controlled by the balance of the oxidant influx due to the diffusion and the "deflux" due to the reaction. By $(15)_2$,

$$D\frac{\partial \tilde{c}}{\partial X_g} + k_* \nu_* \tilde{c} = 0 \quad \text{at } X_g = X_g^\Gamma. \tag{20}$$

If the problem (18)–(20) is solved then the position of the reaction front can be found from the kinetic equation

$$V_g^\Gamma = -D \left.\frac{\partial \tilde{c}}{\partial X_g}\right|_{X_g^\Gamma} = \frac{\nu_+ M_+}{\nu_* M_*}\frac{1}{\rho_g} = \frac{k_* \nu_+ M_+}{\rho_g M_*}(c_* - c_{eq})$$

where c_* is the concentration of the oxidant A_* at the chemical reaction front, c_{eq} is the concentration of the oxidant A_* that would be equilibrium at the acting stress. The kinetic equation can be written as

$$V_0^\Gamma = \frac{k_* \nu_- M_-}{\rho_0 M_*}(c_* - c_{eq}) \tag{21}$$

We emphasize that the condition (19) and the equation (21) include the concentration c_{eq} that depends on stress through (16). The stress in turn may depend on the position of the reaction front. Thus the loading law is to be added to the relationships (18)–(20). Further two cases will be considered:
(i) σ is given by the boundary condition,
(ii) the average strain $\varepsilon_0 = (x(L_0) - L_0)/L_0$ is given by the boundary condition.
The following notation is used

$$\eta_* = \gamma_* - \nu_* \eta(T), \quad w = \frac{\sigma^2}{2C_-}$$

The oxidation is possible only if the initial concentration is greater than the equilibrium concentration, $c_0 > c_{eq}$. Fig. 2 demonstrates the dependence of c_{eq} on w at various η_* for the case $G < 0$, corresponding the oxidation of polysilicon. ($M_{Si} = 28$, $M_{SiO_2} = 60$, $C_{Si}/C_{SiO_2} \simeq 1.3$, $\rho_{Si}/\rho_{SiO_2} \simeq 1.1$, then $g \simeq 2.36$) Given c_0, at $\eta_* < \eta_c(c_0)$ there exists threshold value

$$w_0 = \frac{\rho_0}{\nu_- M_- G}\left(\eta_*(T) + \nu_* RT \ln(c_0)\right)$$

such that the oxidation is blocked if $w < w_0$. If $\eta_* > \eta_c(c_0)$ then threshold effect disappears.
If $G > 0$ (Fig. 3) then for every η and c_0 there exists w_0 (w_0^a, w_0^b, etc.) such that the oxidation is blocked if $w > w_0$.
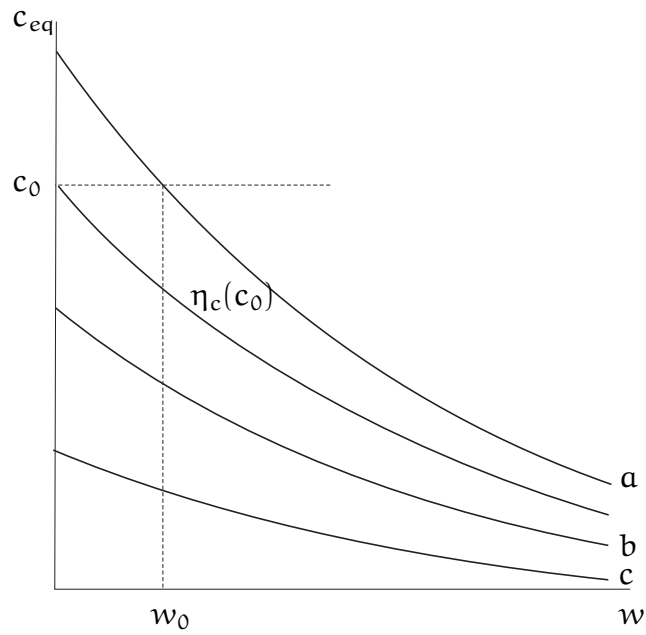
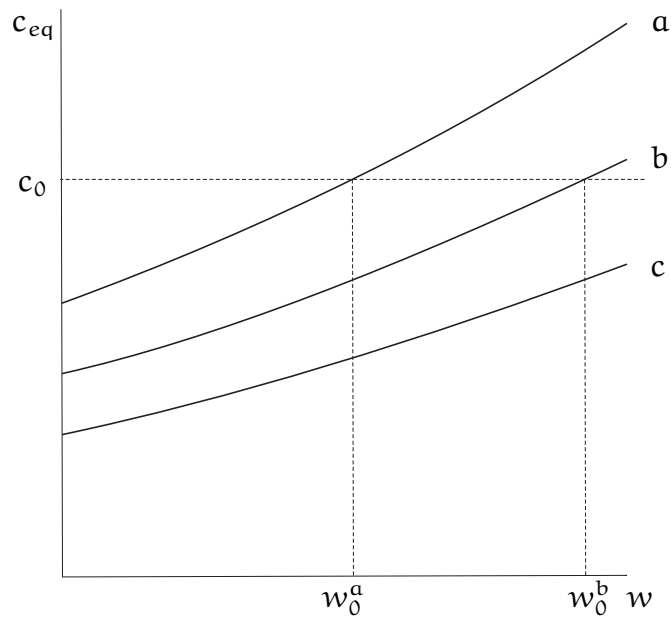Figure 2: Dependence of the equilibrium concentration on w at $G < 0$, $\eta_*^a < \eta_*^b < \eta_*^c$

Figure 3: Dependence of the equilibrium concentration on w at $G > 0$, $\eta_*^a < \eta_*^b < \eta_*^c$
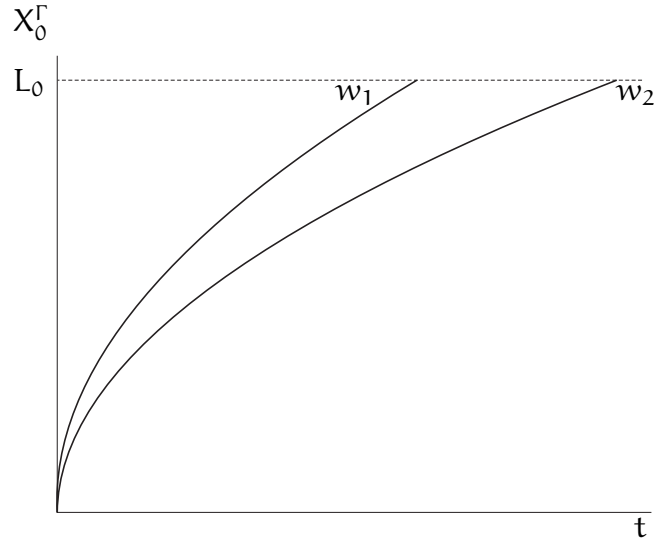
Figure 4: Oxide zone growth at given external stress, $w_1 > w_2$ if $G < 0$, and $w_1 < w_2$ if $G > 0$

Thus, the character of the stress influence on the oxidation process depends on combination of material parameters and chemical reaction parameters.

Fig. 4 demonstrates the oxide zone growth at given external stress. If $G < 0$ then stresses accelerate the chemical reaction front. On the contrary, if $G > 0$ then stresses decelerate the chemical reaction front. If the average stain $\varepsilon_0 = (x(L_0, t) - L_0)/L_0$ is given then strains ε_-, ε_+ and the relative position

$$\xi_\Gamma = X_0^\Gamma/L_0 \in [0, 1]$$

of the reaction front are related as

$$(1 - \xi_\Gamma)\varepsilon_- + g\xi_\Gamma\varepsilon_+ + (g - 1)\xi_\Gamma = \varepsilon_0 \tag{22}$$

The stress depends on ε_0 and the reaction front position as

$$\sigma = C_-\frac{\varepsilon_0 - (g - 1)\xi_\Gamma}{1 - \xi_\Gamma G} \tag{23}$$

Given ε_0, (23) describes the stress evolution during the front propagation. Since $G < 1$ by (12) and $\xi_\Gamma \in [0, 1]$, the denominator in (23) is positive. If $\varepsilon_0/(g - 1) \in [0, 1]$ then the stress changes the sign due to the reaction front propagation at

$$\xi_\Gamma = \varepsilon_0/(g - 1) \in [0, 1]$$

If $\varepsilon_0 \geq \varepsilon_0^s = g - 1$ then the stress does not change the sign. Note that value ε_0 can be large even if ε_- and ε_+ are small because of the input of the chemical reaction represented by the term in (22) (recall that in a case of silicon oxidation $g \simeq 2.4$). There is another characteristic strain

$$\varepsilon_0^c = \frac{g - 1}{G} : \quad \frac{\partial \sigma}{\partial \xi_*} < 0 \quad \text{if} \quad \varepsilon_0 < \varepsilon_0^c, \qquad \frac{\partial \sigma}{\partial \xi_*} > 0 \quad \text{if} \quad \varepsilon_0 > \varepsilon_0^c.$$
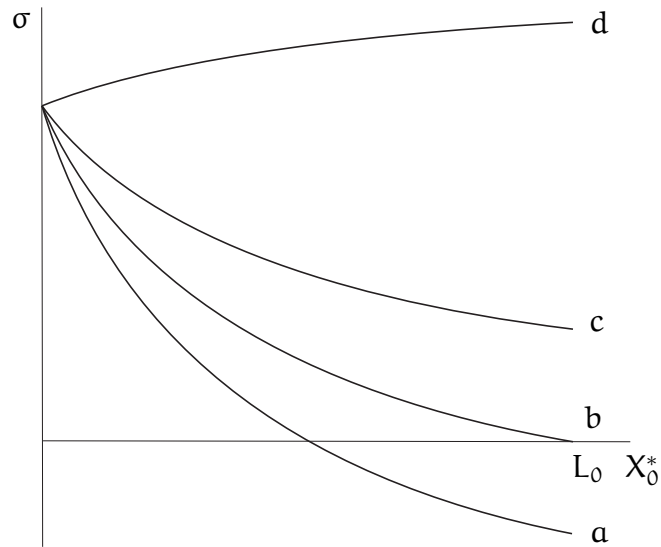
Figure 5: Dependencies of stress on the oxide zone size at various external strains ε_0: a $-\varepsilon_0 < \varepsilon_0^s$, b $-\varepsilon_0 = \varepsilon_0^s$, c $-\varepsilon_0^s < \varepsilon_0 < \varepsilon_0^c$, d $-\varepsilon_0 > \varepsilon_0^c$

The stress dependencies on the reaction front position at various strains are shown in Fig. 5. The evolution of stress due to oxide growth leads to changes of the equilibrium oxidant concentration c_{eq} and this in turn changes the solution of the diffusion problem (18)–(21) and affect the front propagation. The reaction front kinetics is shown in Fig. 6.
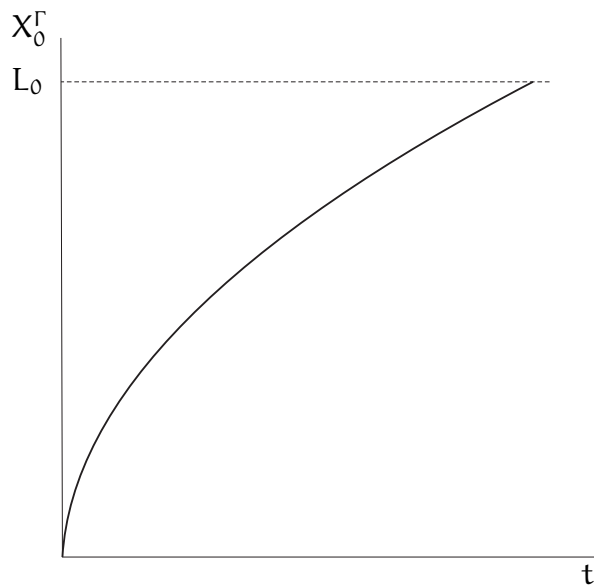

Figure 6: Oxide growth kinetics at given strain.

4   Conclusions

A deformable bar sustaining chemical transformations of oxidizing type is considered. An intermediate configuration reflected chemical transformations is introduced. The expression of the dissipation due to the chemical reaction front propagation is obtained. It is demonstrated that stresses affect the chemical affinity through a parameter that depends on molar masses and the stoichiometric coefficients of the reaction and elastic modules of reacting substances. If we neglect the interconnections between the diffusion of a gas component and deformations of a solid component, then stresses affect the diffusion and chemical reaction front kinetics through the equilibrium concentration of the gas component. Stress controlled and displacement controlled chemical reactions are considered. It is shown that stresses relax or grow due to the chemical reaction front propagation in a case of the displacement control (the constraint effect), depending on external strain, and chemical and elastic parameters.

Acknowledgements

References

[1] Lee, E. H. Elastic-plastic deformation at finite strains. ASME J. Appl. Mech., (1969) 36, 18.

[2] Epstein, M., and Maugin, G. A. Thermomechanics of volumetric growth in uniform bodies. Int. J. Plasticity (2000) 16, 951978.

[3] Lubarda V.A. Constitutive theories based on the multiplicative decomposition of deformation gradient: Thermoelasticity, elastoplasticity, and biomechanics. Appl Mech Rev. (2004) 57, No 2, 95-108

[4] A. Guillou, R.W. Ogden. Growth in soft biological tissue and residual stress development. In: Holzapfel, G.A., Ogden, R.W. (eds.) Mechanics of biological tissue. Springer, Heidelberg (2006)

[5] P. Glansdorff, I. Prigogine, Thermodynamic theory of structure, stability and fluctuations, Wiley-Interscience, London, NY, Sydney, Toronto.

Elena N. Vilchevskaya, Alexander B. Freidin, Institute of Problems in Mechanical Engineering of RAS, Bolshoy, 61, V.O. St. Petersburg, 199178 Russia

Thermal convection in a rotating horizontal cylindrical layer

Alexey A. Vjatkin   Alevtina A. Ivanova

Vjatkin_aa@pspu.ru a.ivanova@pspu.ru

Abstract

Thermal convection in a horizontal cylindrical layer of fluid rotating around its own axis is experimentally investigated. Two cases are realized: heating of external border of the layer and the case when the internal border has the higher temperature. It is revealed that thermal convection of liquid could be excited in both cases. It is shown that convection is determined by the action of two different mechanisms: the first - well-known mechanism of centrifugal thermal convection, the second - thermovibrational one, connected to the oscillations of nonisothermal liquid concerning the cavity, which are caused by the gravity field rotating in the cavity frame. The thermovibrational mechanism is responsible for the excitation of convection in a layer which is heated from inside. The threshold of excitation and the structure of convective currents depending on the frequency of rotation and difference of temperatures of the layer borders as well as heat transfer in overcritical area are investigated.

1 Introduction

In case of higher temperature of external border of quickly rotating cylindrical liquid layer the occurrence of centrifugal convection [1] in the shape of rolls extended along the axis which size is comparable with the thickness of the layer is observed. In [2] it was found that in a rotating horizontal annulus with decrease of rotation velocity there is a change of convective modes: the excitation of long-wave structures is observed. Convective structures of the same type are also observed in the case to high temperature of internal border of the layer when centrifugal force plays a stabilizing role. In this case the convection arises in a threshold way at decrease of rotation frequency and is accompanied with the critical increase of heat flux through the layer. The thermovibrational mechanism of mean thermal convection in a cavity rotating around the horizontal axis was earlier studied experimentally in a plane layer [3]; the influence of rotation on the thermal vibrational convection was investigated theoretically in [4]. It was shown that mean thermal convection in a cavity rotating around the horizontal axis besides the well known centrifugal Rayleigh number $Ra = \Omega^2 R \beta \Theta h^3 / \nu \chi$ is characterized by the modified vibrational parameter
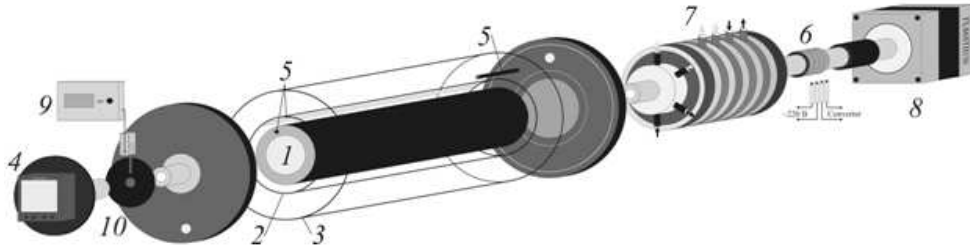
Fig. 1

$R_v = (g\beta\Theta h)^2/2\nu\chi\Omega^2$. Here β, ν and χ - coefficients of volumetric expansion, kinematic viscosity and thermal conductivity of liquid, Θ - a characteristic temperature difference, $\Omega \equiv 2\pi n$ - angular velocity of rotation (n - rotation frequency).

2   Experimental setup and technique

The layer is formed by the cylinders *1* and *2* (Fig. 1). The internal aluminium cylinder has a diameter $d = 60$ mm, the external one is made of a plexiglass pipe with a thickness of a wall 3 mm. The thickness of a layer $h = 7$ mm, its length $l = 230$ mm. The temperature of the borders is set by a liquid (water) pumping through the internal cavity heat-exchanger *1* (T_1) and in a shirt between the cylinders *2* and *3* (T_3). For the temperature measurement the device "Thermodat" *4* with an accuracy of measurement 0.1 K is used; the copper thermometers of resistance *5* measuring the temperature of the borders of a layer serve as gauges. The electric collector *6* serves for electric feed of "Thermodat" and reading its data. The data are transferred to the computer and displayed in real time. The uniformity of temperature of the borders of the layer is provided with a high charge of the water transferred from jet thermostats to rotating cavity by means of a liquid collector *7*. All the elements of the installation are rotating around the horizontal axis by means of a step-by-step engine *8*. The engine is connected to the sound generator. Windings of the engine are switched in such a manner that the big momentum of momentum is created on a shaft, thus the uniform rotation in all the frequency range is provided (instability of speed of rotation does not exceed 0.001 rps). The rotation frequency varies in an interval $n = 0.1 - 0.5$ rps and is controlled by means of the digital tachometer *9* counting the revolutions of a disk *10*.

The distilled water serves as f working liquid. A technique of experiments is the following. With the help of the thermostats the temperatures of internal border of a layer T_1 and of a liquid in a water shirt T_3 are defined, the cavity is subject to rotation with the definite high enough frequency. During the experiment the rotation velocity n is decreases step by step. The temperature of external border of the layer T_2 is measured on each step after the coming to the stationary regime of convection. The experiments are repeated at various values of temperature T_1 and T_3. The aluminium powder with a small amount of surface active surfactants is added in a working liquid for visualization of convective structures.

3   Results of experiment

The temperature of external border T_2 of a layer as function of rotation frequency n for the case when the internal border of the layer has higher temperature is shown in Fig. 2. At rather large n the temperature does not change with reduction of rotation velocity (area 2), the thermal flux is close to the molecular one. It happens due to the stabilizing action of a centrifugal force. At some critical value n the increase in a thermal flux through the layer is observed. It is connected to the threshold excitation of convective rolls extended along the axis (Fig. 3a). The gauge located on the external layer border registers the oscillations of the temperature (the shaded area) caused by slow azimuth drift of convective rolls.
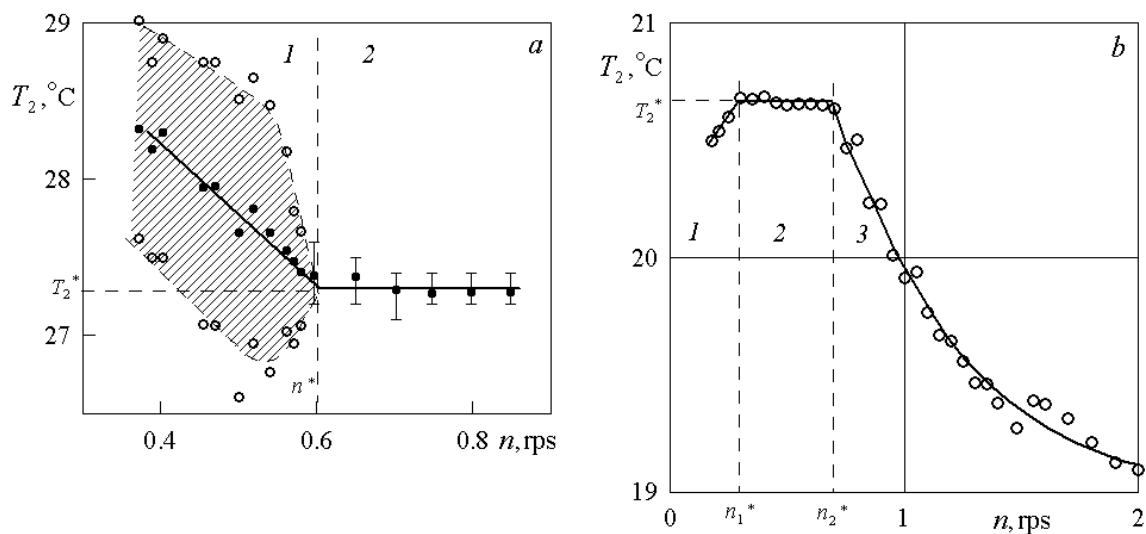

Fig. 2

The rolls drift in the direction opposite to the direction of rotation. At further reduction of velocity n there is a change of convective modes - the vortical system periodic along an axis appears (Fig. 3b). It is possible to determine the threshold values of temperature T_2^* and speed n^* on the critical change of behavior of the average value T_2.

In a case when the external border of the layer has higher temperature at relatively large speed of rotation the advanced centrifugal convection is observed (Fig. 2b, area 3). The intensity of convection reduces with decreasing the n. At some value n_1^* the convection disappears (area 2). The convective rolls appears again by a threshold way below some critical value n_1^*. The mechanism of excitation of such convection is the same as in the area 1 on Fig. 2a. It is connected to the gravity field rotating in the cavity frame. The presence of interval of frequencies of rotation, where thermal convection is absent (the area 2, Fig. 2b), is observed only at small values of a difference of temperatures of borders of a layer Θ.

The Nusselt parameter Nu which is determined as the ratio of heat flux through the layer and the molecular one (in the absence of convection) at the same Θ value is chosen as the characteristic of heat transfer.

The heat transfer curves at heating the external border have a various kind: the first (Fig. 4, points 1), with the absence of thermal convection in some range
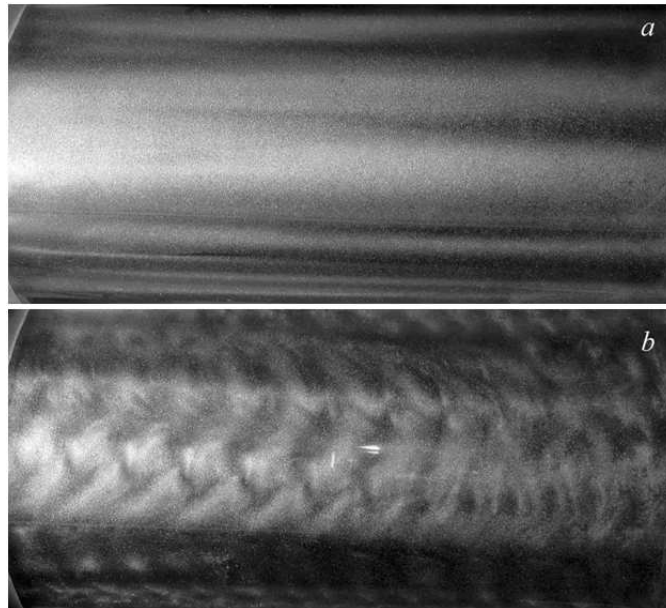
Fig. 3

of frequencies, is found at a small Θ; the second (points *1-3*) - with changing of convective modes for which the parameter is always distinct from the unit. With Θ increase the shape of the curves does not change significantly, the intensity of heat transfer at large Ra aspires to approximately one value. At slow rotation the sharp growth of heat flux through the layer is observed. Points *2-4* correspond to a difference of temperatures $T_3 - T_1 = 8.7, 12.9, 18.0$ and 25.9 K. The threshold of change of convective modes is determined on the minimal value on a curve $Nu(Ra)$.

Fig. 4

4 Discussion of results

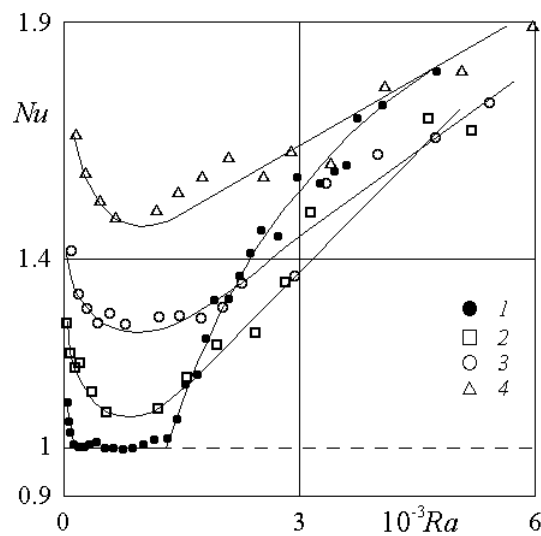The threshold curve of vibrational convection excitation *1* is shown on the plane of dimensionless parameters Ra, R_v (Fig. 5). In the field of negative values Ra (at heating the internal border of the layer) the centrifugal inertia force has a stabilizing effect. The curve *1* corresponds to a threshold of excitation of thermovibrational convection except the area of positive Ra near to the axis - in this case the centrifugal convection manifests itself. The curve *2* shows the border of separation of centrifugal and thermovibrational modes of convection. In the field of the large

Fig. 5

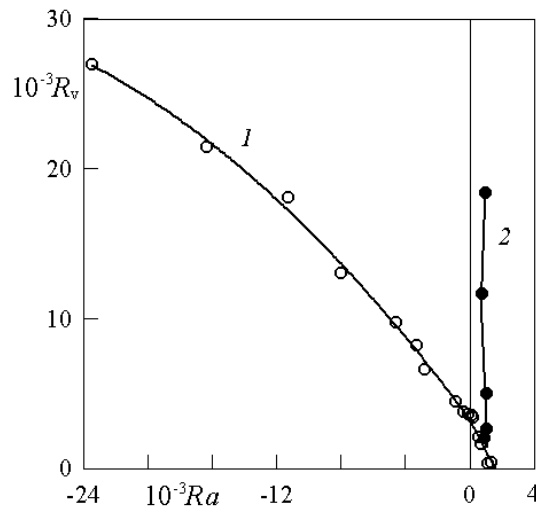Ra the centrifugal force that results in development of a corresponding convection plays the governing role. With decrease of rotation frequency (to the left of the curve *2*) the thermovibrational convection is in charge. The detailed description of the threshold curve (points *1*) and the character of change of the wave-length of convective structures in the investigated range of Ra could be found in [2].
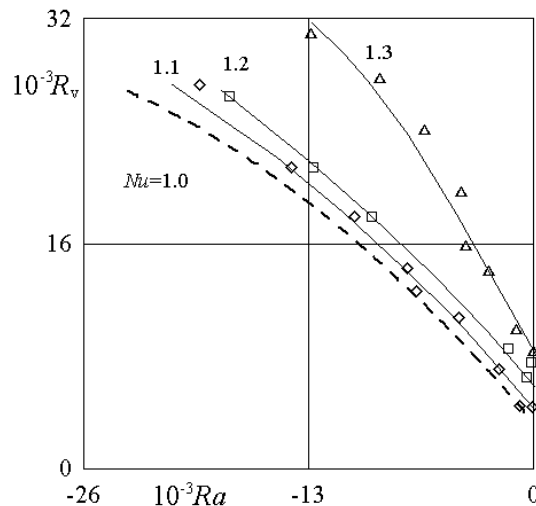

Fig. 6

696

The isolines of constant value of parameter Nu are shown in the Fig. 6. Below the threshold curve (a shaped line) $Nu = 1$, thermal convection is absent, above the line the convective rolls arise (Fig. 3). The average value of temperature oscillations grows with reduction of speed of rotation n (increase of R_v) - the heat flux through the layer increases.

5   The conclusion

Thermal convection in the horizontal annulus of liquid performing steady rotation around its own axis is experimentally investigated. The increase of heat transfer is revealed in case of heating the internal border of the layer, connected with the threshold excitation of thermovibrational convection. The centrifugal convection is found out at heating the layer from external side and rather high speed of rotation n. With decrease of the centrifugal convection is replaced by the thermovibrational one. At a small difference of temperatures Θ the change of the convective modes occurs through a phase of convection absence. With increasing Θ the range of speed of rotation in which the convection is absent (heat transfer corresponds to the molecular one), decreases, and disappears at some definite Θ.

The threshold of excitation of convective flows and the border of separation of different convective modes are investigated depending on the rotation velocity and the temperature difference; the structure of convective flows is studied. The results of research of the threshold of thermal convection excitation and the borders of change of convictive modes and also the values of Nusselt number are submitted on the plane of determining parameters Ra, R_v.

Acknowledgements

References

[1] Gershuni G.Z., Zhukhovitsky E.M. Convective stability of incompressible liquid. M.: Nauka, 1972. 392 p. (Translated in English: Keter Publishing House Jerusalem Ltd., Jerusalem 1976)

[2] Vjatkin A.A., Ivanova A.A., Kozlov V.G. Convective stability of nonisothermal liquid in rotating horizontal annulus // Izv. RAN. MZhG (in press)

[3] Ivanova A.A., Kozlov V.G., Rylova V.V. Thermal convection in a plane layer rotating about a horizontal axis // Fluid Dynamics. 2003. Vol. 38. N 1. P. 9-17.

[4] Kozlov V.G. Thermal vibrational convection in rotating cavities // Fluid Dynamics. 2004. Vol. 39. N 1. P. 3-11.

Alevtina A. Ivanova, Perm State Pedagogical University, Russia

Alexey A. Vjatkin, Perm State Pedagogical University, Russia

Use of acoustic parameter measurements for evaluating the reliability criteria of machine parts and metalwork

Lev B. Zuev   Boris S. Semukhin   Alexey G. Lunev

lbz@ispms.tsc.ru

Abstract

A new method for non-destructive evaluation of the mechanical properties of structural materials has been developed. This is based on measurements of the ultrasound propagation velocity in deforming materials. Preliminarily investigations were carried out in order to relate the ultrasound propagation velocity to the mechanical characteristics of the deforming material. A detailed description of suitable devices intended for ultrasound propagation velocity measurement to a high accuracy is presented. Using Zr base alloys as an example, it is shown that the method can be used for monitoring zirconium billets from which nuclear reactor fuel cladding is fabricated by cold rolling.

1 Experimental justification of the method

It was established previously [1, 2] that the ultrasound propagation rate measured directly for tensile metal specimens would depend on total deformation (see Fig. 1 obtained for the tested brass specimen), flow stress and material structure. Similar data were obtained also for small total strains by M. Kobayashi [3]. However, our attention was focused in particular on the form of ultrasound rate dependence on flow stress obtained (Fig. 2). This consists of three linear sections that can be described [1] by the following equation

$$V_S = V_0 + \xi\sigma \tag{1}$$

were the empirical constants V_0 and ξ, have different values for the different stages of the flow process. From Fig. 1 follows that x can be both positive and negative. However, the proportionality $V_S \sim \sigma$ is always fulfilled within a single stage with the correlation coefficient being ~ 0.9.

The goal of the present study is to verify that Eq. 1 can be used for the evaluation of mechanical characteristics of materials, using the non-destructive method developed. To elucidate the issue, the dependence $V_S(\sigma)$ was obtained for various kinds of alloys (see Table). Using the method of sound pulses autocirculation, the propagation rate of Rayleigh waves was measured directly for flat tensile specimens.
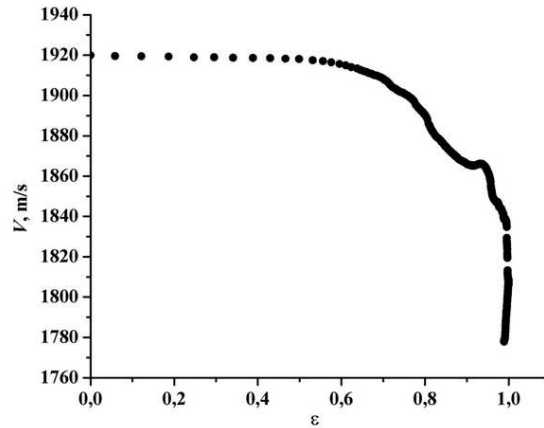
Figure 1: The generalize dependence obtained for steels.

The dependencies $V_S(\sigma)$ obtained for all the test materials have a similar shape. One can easily establish the general form of this dependence (Fig. 2), using the dimensionless variables V_S/V_S^* and σ/σ_B, were V_S^* is the rate of ultrasound propagation in the undeformed material and σ_B is the strength limit of the material.

Table. Chemical composition of the alloys investigated

N	Material	Symbol	C	N	Si	Mg	Mn	Li	Cr	Cu	Ni	Zn	Pb	Zr	Ti	Sn	Nb
1	Steel	▽	0.12	-	0.8	-	2.0	-	$\binom{17.0-}{19.0}$	0.3	$\binom{9.0-}{11.0}$	-	-	-	$\binom{0.5-}{0.8}$	-	-
2	Steel	■	< 0.12	0.008	$\binom{0.5-}{0.8}$	-	$\binom{1.3-}{1.7}$	-	< 0.3	< 0.3	< 0.3	-	-	-	-	-	-
3	Steel	▲	< 0.12	0.008	$\binom{0.8-}{1.1}$	-	$\binom{0.5-}{0.8}$	-	$\binom{0.6-}{0.9}$	$\binom{0.4-}{0.6}$	$\binom{0.5-}{0.8}$	-	-	-	-	-	-
4	Steel	♦	$\binom{0.14-}{0.22}$	-	$\binom{0.12-}{0.3}$	-	$\binom{0.4-}{0.65}$	-	< 0.3	< 0.3	< 0.3	-	-	-	-	-	-
5	Duralumin	⊗	-	-	< 0.5	1.5	-	-	-	4.35	< 0.1	< 0.3	-	-	-	-	-
6	Al-Mg	+	-	-	0.25	$\binom{5.8-}{6.2}$	$\binom{0.1-}{0.25}$	$\binom{1.8-}{2.2}$	-	-	-	-	-	0.1	-	-	-
7	Al-Li	×	-	-	0.15	-	-	$\binom{1.8-}{2.0}$	-	$\binom{2.8-}{3.2}$	-	-	-	0.12	0.12	-	-
8	Brass	•	-	-	< 0.1	-	-	-	-	-	-	$\binom{38.0-}{41.0}$	$\binom{0.8-}{1.9}$	-	-	-	-
9	Zr-Nb	★	-	-	-	-	-	-	-	-	-	-	-	99.0	-	-	1.0
10	Zr-Nb	▼	-	-	-	-	-	-	-	-	-	-	-	97.5	-	1.0	1.0

The above normalization permits pooling of the data obtained for all the materials tested; stages 1 and 2 of the dependence $V_S(\sigma)$ are given by

$$V_S/V_S^* = \kappa_i + \alpha_i \cdot \sigma/\sigma_B \qquad (2)$$

Here $i = 1, 2$ is stage number; the empirical constants κ_i and α_i are independent of the kind of material. It is found that the respective values for stages 1 and 2 are as follows: $\kappa_1 = 1.0 \pm 2 \cdot 10^{-4}$ and $\kappa_2 = 1.03 \pm 10^{-3}$; $\alpha_1 = 6.5 \cdot 10^{-3} \pm 4.7 \cdot 10^{-4}$ and $\alpha_2 = 3.65 \cdot 10^{-2} \pm 3.2 \cdot 10^{-3}$.
From Eq. (2) follows

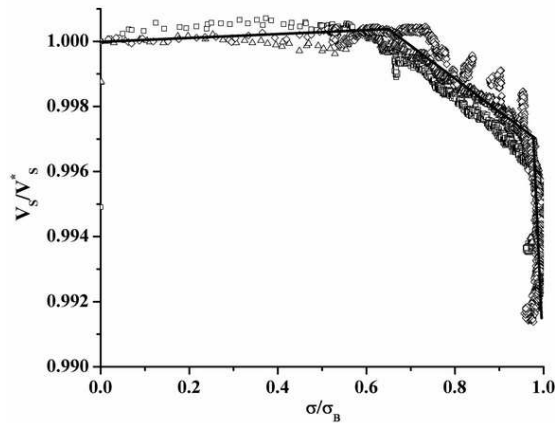$$\sigma_B = \frac{\alpha_i \sigma}{V_S/V_S^* - \kappa_i}. \qquad (3)$$

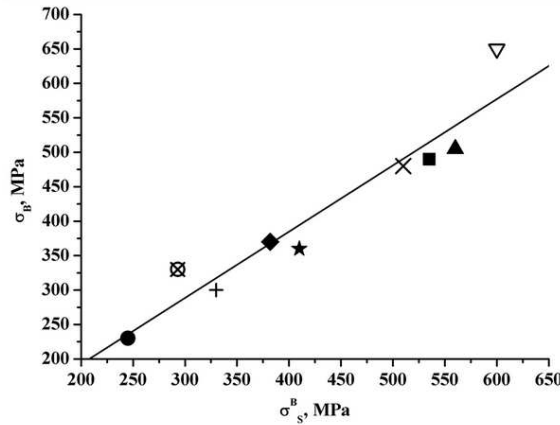Figure 2: The generalize dependence obtained for steels.

Figure 3: The generalize dependence obtained for steels.

This can be used for the estimation of strength limit at small total plastic strains long before specimen failure. To do this, the ultrasound propagation rate, V_S, is measured for stresses in the range $\sigma_{0.2} < \sigma < 0.6\sigma_B$ (here $\sigma_{0.2}$ is proof stress), which initiates small plastic deformation only.

The strength limit values obtained from Eq. 3 (σ_B^S) are matched against those derived conventionally from the curves $\sigma - \varepsilon$ (σ_B) in Fig. 3. The rate, V_S, was measured at the deformation $e \approx 1\%$ for the flow stress $\sigma \approx 0.1\sigma_B$. The values σ_B and σ_B^S are practically equal, i.e. $\sigma_B = 0.96\sigma_B^S$. The correlation coefficient is ~ 0.96.

The above testifies the efficiency of the proposed method for strength limit evaluation in structural materials, which deform at small total plastic strains long before specimen failure. Thus, it is a promising method for structural integrity monitoring of metalwork and machine parts. The nature of the above relation might be addressed on the assumption that material hardening is determined by the internal stress fields, which inhibit dislocation motion [4]. On other hand, with increasing internal stresses, the ultrasound propagation rate would decrease [1, 2]. Thus, the above two values are defined by the same factor; therefore, they are found to be closely related.

2 Equipment designed for ultrasound method application

The units designed for ultrasound method implementation are Acoustic Strain Tester Rapid (ASTR) and Acoustic Non-Destructive Analyzer (ANDA), which are meant for structural integrity inspection of metals and alloys in metalwork and machine parts during long-term service in both regular and severe conditions; the units are made in small lots. The general principle of operation of the units is measurement of Rayleigh wave pulse frequency, using an auto-circulation method [3]. They are simple in operation; frequency measurement is performed to an accuracy of $\sim 3{\cdot}10^{-5}$. The technique of auto-circulation of pulses is based on the excitation of the ultrasonic vibrator by a pulser, which is synchronized by pulses passing through the analyzed medium. The pulse repetition frequency assumes a steady-state value, which is determined by the running time of the pulse in the medium analyzed. Evidently, due to a fixed distance between the piezo-transducers, the pulse repetition frequency would be directly proportional to the ultrasound propagation rate. The pulse repetition frequency is commonly called auto-circulation frequency. A device based on the principle of auto-circulation makes use of longitudinal, transverse or surface (Rayleigh) waves. In the present work Rayleigh surface waves having frequency of 2.5 MHz are used.

The excitation of surface waves in the specimen investigated is performed with the aid of a piezoelectric transducer, which features a waveguide having the shape of a truncated prism, a piezoelectric element and a damper. The piezoelectric transducers, both the excitation source and the receiving one, are installed on a common base and thus form a gage head. The separation between the piezo-transducers is fixed and is taken to be the gage length. To take measurements, the waveguides are pressed firmly to the object tested so as to provide for good contact. Transformer oil is used as contact medium for ultrasonic transmission. However, the space between the transducers should remain free of the contact medium.

3 Use of the ultrasound method to evaluate residual internal stress level

The applications of the proposed method include the estimation of stressed state in zirconium billets used for the manufacture of nuclear reactor fuel cladding. During the cold rolling of Zr-Nb alloy tubes, an intricate distribution of residual internal macro-stresses would form in the worked billet, which enhances the probability of its failure at one of the process stages. When tackling the problems of process optimization, one has to take into account the level and distribution of residual internal macrostresses in worked billets. On account of their large size, however, this is hardly feasible with the aid of conventional methods, e.g. X-ray techniques [5], very much so under process conditions.

The present investigation was carried on using the ASTR unit to determine internal stress levels for worked billets. The measurements were made in a wide range of internal stresses for the deforming specimens of Zr-Nb alloy **9** (see the Table)

in order to relate the internal stresses to the propagation rate of acoustic waves. The most significant results were obtained for the worked billets in which internal stresses varied over a wide range. The present work is aimed at development of non-destructive methods for the determination of residual stresses in thin-wall Zr tubes manufactured by cold rolling [6]. This would help improve the technologies currently employed for tube production. The investigation was carried on for a wide range of specimens, i.e. tubes and round billets made from Zr based alloys **9** and **10**.The lifetime of materials and constructions is in many ways affected by material uniformity and by the stressed state of end products manufactured from the same material.

Therefore, the investigation of residual macro-stresses was performed using the traditional X-ray technique as well the acoustic method developed; the two sets of data obtained by the above two techniques were matched.

It has been found that the magnitude of macro-stresses $\sigma_1 + \sigma_2$ is linearly related to the frequency of auto-circulation f in alloy **9**, i.e.

$$\sigma_1 + \sigma_2 = \sigma_0 - \beta f, \tag{4}$$

where $\sigma_0 = 420$ MPa and $\beta = 0.42$ MPa·s are the constants. The correlation coefficient is ~ 0.7, which allows one to conclude that the above relationship is close to a functional one. Therefore, auto-circulation frequency can be safely converted to stresses using Eq. (4). On the base of the above results, a technique has been developed which is intended for internal stress measurement in Zr alloy tubes.

The macro-stresses, i.e. residual stresses resulting from rolling, were measured with the aid of X-ray technique for round zirconium billets $\varnothing 14.8 \times \varnothing 9.5$ mm. The macro-stresses in the specimens of alloy **10** (see the Table) are found to vary from 400 to 900 MPa (Fig. 4), especially so in the area between a small diameter and a larger one. It should be noted that regions removed far enough from the above area reveal sufficiently smooth and uniform distributions of macro-stresses. The level of stresses in alloy **9** is found to be considerably lower relative to alloy **10**. The low stress jumps in Fig. 4 suggest that alloy **9** worked by rolling is in a more homogeneous state relative to alloy **10**, which might be due the former alloy having greater ductility. The use of appropriate die profile enabled one to reduce considerably the stress jumps in the worked material. To measure the stresses accurately, the test objects shall conform to the following requirements: absence of surface defects, the occurrence of equidistant points marked over the tube envelope and availability of reference sample.

The stress distributions in tubes were determined using a specially designed attachment. This features a stage with two guides, which allow the sample to be aligned in both the beam plane and relative to the goniometer axis. The scanning was performed manually every 20 mm, using the marks over the tube envelope. Figure 5 illustrates the variation in the macro-stresses σ_1 over the tube made from alloy **9**. It can be seen that homogeneous distributions are observed in the range of 200 MPa. To obtain more detailed distribution patterns, recording was performed for four equidistant points marked over the tube envelope. The measurements were made for the ends and middle lengths of the tubes. As is seen from Fig. 5, more uniform distributions of stresses are observed for the middle lengths of the tubes rel-
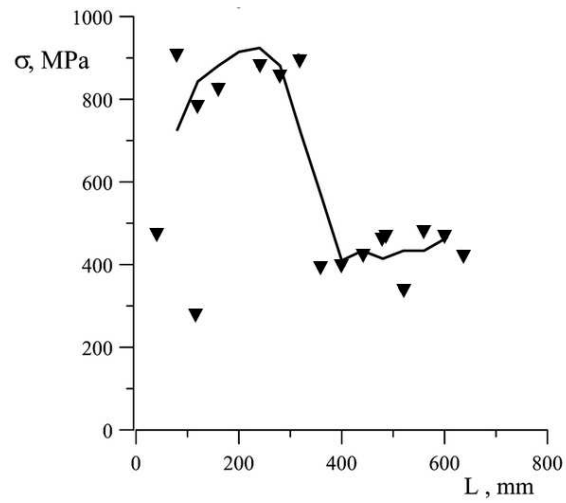
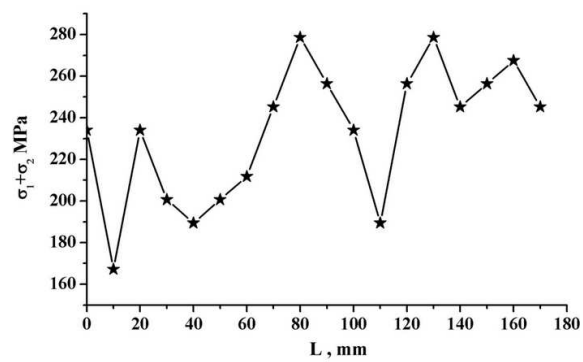Figure 4: The generalize dependence obtained for steels.

Figure 5: The generalize dependence obtained for steels.

ative to the tube ends where stresses may be due partly to material non-uniformity
and partly to the tube deformation by cutting.

4 Conclusions

Thus, the method designed for estimation of mechanical characteristics facilitates
considerably residual stress measurement in real objects. This is based on the re-
lation between the ultrasound rate and the level of residual internal macro-stresses
in tubes and round billets. The modern applications of the ultrasound method also
include
- analysis of stress-strained state of heavily loaded large-sized metalwork;
- evaluation of the remaining lifetime of water-tube boiler parts and pipelines;
- estimation of residual stresses in steels and alloys by welding;
- monitoring of cumulative fatigue damages;
- analysis of chemical heat-treatment (carburizing, nitriding, hydrogen saturation);
- monitoring and evaluation of the remaining lifetime of railway transport parts.

References

[1] L.B. Zuev and B.S. Semukhin. Some acoustic properties of a deforming medium.
Phil. Mag. A42, pp.1183-1193, 2002.

[2] M. Kobayashi, "Ultrasonic nondestructive evaluation of microstructural changes
of solid materials under plastic deformation" Int. J. Plasticity. 19, pp.511-522,
2003.

[3] R. Truel, C. Elbaum and B. Chick. Ultrasonic Methods in Solids State Physics,
Acad. Press, New York, 1969.

[4] R.W.K. Honeykombe, The Plastic Deformation of Metals, E. Arnold Publ. Ltd.,
New York, 1968.

[5] A. Taylor, X-Ray Metallography, J. Wiley and Sons, New York, 1961.

[6] L.B. Zuev, V.I. Danilov and S.A. Barannikova, Plastic Flow Macrolocalization
Physics. Nauka, Novosibirsk, 2008 (in Russuan)

Lev B. Zuev, Academichesky Ave., 2/4, Tomsk, Russia
Boris S. Semukhin, Academichesky Ave., 2/4, Tomsk, Russia
Alexey G. Lunev, Academichesky Ave., 2/4, Tomsk, Russia

Influence of defects distribution and specimen size on fracture initiation

Anton M. Krivtsov

akrivtsov@bk.ru

Abstract

An analytical model for the scale dependence of the fracture initiation is suggested. The model is based on the idea that fracture is a stochastic process, for the bigger specimens probability of joint defects is higher, and this stimulates the fracture. An analytical formula for the strength dependance on the specimen size and defects density was obtained and compared with the molecular dynamics simulation. The results show that generally there is no similarity in fracture of the specimens of the different size and scale. This also prevents from using representative volume for the material strength properties.

1   Introduction

The defect structure of material has essential and sometimes unexpected influence on the strength properties. One of such results [1] is shown in Fig. 1. The figure is obtained by MD (molecular dynamics) simulation of cyclic loading of monocrystal material with randomly distributed defects (vacancies). The density of defects for the specimen in Fig. 1a is 10 times lower then for the specimen in Fig. 1b. The
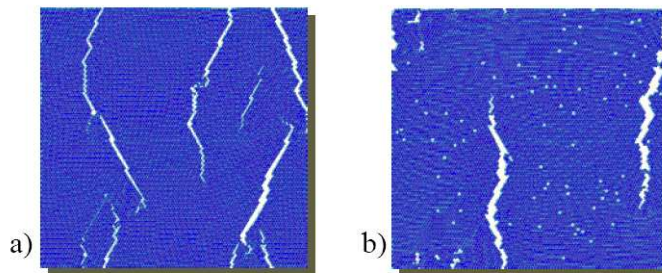

Figure 1: Crack development in crystals: a) 0.1% defects; b) 1.0% defects.

unexpected result is that for the lower density of defects the number of cracks is higher. The explanation of this fact is that for the higher density of defects the crystal contains occasional zones where the defects are very close to each other — these zones initiate the cracks — see Fig. 2. For the lower defects density all
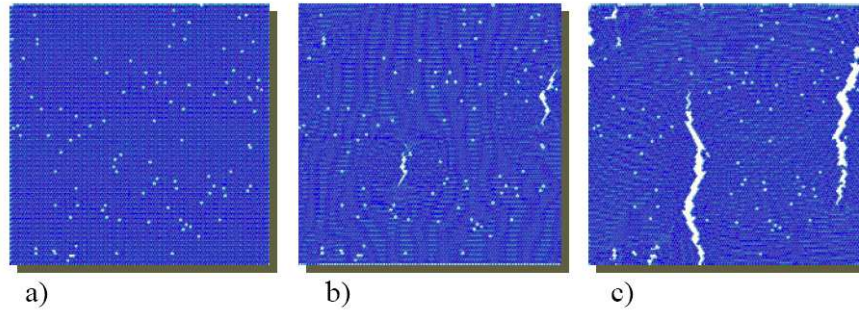
Figure 2: Crack development in crystal with 1% defects

vacancies are separated and all of them initiate cracks. Of course, the material strength in the last case is much higher. However this result can be changed if the bigger specimens would be observed, then even for the low defects density the probability of two defects to appear closely to each other could be high enough, and then they would produce the week zones in which crack would initiate. Thus, the fracture scenario can differ for specimens of different sizes, even if the defects density is equal. The current paper is mainly devoted to study of such phenomenon. Below, an analytical model for the analysis of the scale dependence of the material strength is suggested and compared with the results of MD simulation.

2 Analytical model

Let us consider an ideal crystal, containing randomly distributed defects — vacancies. Each vacancy is formed by removing a single atom from the lattice. The material is weaker in the places, where the vacancies are close to each other. The most dangerous situation is when two vacancies are formed from the neighboring atoms — this structure we will call double vacancy. Let us calculate the probability of formation of the double vacancy.

Let the crystal contain N atoms, each atom has M neighbors. For closed packed lattices $M = 6$ in 2D and $M = 12$ in 3D. Let us remove sequentially atoms from the lattice to form vacancies. The probability that a double vacancy will appear after n atoms are removed will be denoted as ξ_n. Then the following recurrent relation fulfils

$$\xi_{n+1} = \xi_n + (1 - \xi_n)\frac{Mn}{N}. \tag{1}$$

Indeed, the first term ξ_n in the above relation gives the probability that the double vacancy was formed at the step n, the probability of the otherwise is $1 - \xi_n$. Then, the probability that in this situation the new vacancy number $n+1$ will appear near one of the previous vacancies is proportional to the number Mn of atoms neighboring to vacancies, divided by the total number of atoms N. To obtain relation (1) it was assumed that the density of vacancies is low: $n << N$. This assumption allows us to neglect the situation when one atom is a neighbor for two vacancies, and also we neglect that the total number of atoms is decreasing. The mentioned approximations

little bit increase both numerator and denominator in relation (1), therefore together this effects should not give a considerable error. Relation (1) can be rewritten in the form

$$\zeta_{n+1} = (1 - \varepsilon n)\, \zeta_n\,; \qquad \zeta_n \overset{\text{def}}{=} 1 - \xi_n\,, \qquad \varepsilon \overset{\text{def}}{=} M/N. \qquad (2)$$

Here ζ_n is the probability that a pair of double vacancies will NOT appear after n atoms are removed; ε is a small parameter; for any n fulfills: $\varepsilon n < 1$. Since $\zeta_1 \equiv 1$, from the recurrent relation (2) it follows

$$\zeta_{n+1} = \prod_{k=1}^{n} (1 - \varepsilon k) \quad \Rightarrow \quad \ln \zeta_{n+1} = \sum_{k=1}^{n} \ln(1 - \varepsilon k)\,. \qquad (3)$$

Assuming that the number of vacancies is a big value: $n \gg 1$, the last sum can be calculated as

$$\ln \zeta_n \approx \ln \zeta_{n+1} = n \sum_{k=1}^{n} \ln\left(1 - \varepsilon n\, \frac{k}{n}\right) \frac{1}{n} \approx n \int_0^1 \ln(1 - \varepsilon n x)\, dx. \qquad (4)$$

Calculation of the integral gives

$$\ln \zeta_n = -\frac{1}{\varepsilon}(1 - \varepsilon n)\ln(1 - \varepsilon n) - n \quad \Rightarrow \quad \zeta_n = e^{-n}(1 - \varepsilon n)^{-(1 - \varepsilon n)/\varepsilon}. \qquad (5)$$

Let us consider

$$\varepsilon n = \frac{Mn}{N} = Mp\,, \qquad p \overset{\text{def}}{=} \frac{n}{N}. \qquad (6)$$

Here p is porosity. It was already assumed that porosity is small: $p = n/N \ll 1$. For simplification of formula (5) let us assume that $\varepsilon n = Mp \ll 1$. Please note that this assumption gives more strict constriction for the smallness of p, since M is of order of 10. Anyway, for $\varepsilon n \ll 1$ in the first nontrivial approximation from (5) we obtain[7]

$$\ln \zeta_n = -\frac{1}{2}\varepsilon n^2 \quad \Rightarrow \quad \zeta_n = e^{-\frac{1}{2}\varepsilon n^2}. \qquad (7)$$

For the further consideration let us change parameters ε, n to parameters p, N using formulae

$$n = Np\,, \qquad \varepsilon = \frac{M}{N}\,; \qquad \varepsilon n = Mp\,, \qquad \varepsilon n^2 = MNp^2. \qquad (8)$$

Parameters ε, n were more convenient for calculations, however parameters p, N have more clear physical meaning — porosity and total number of particles. Then probability $\xi_n = 1 - \zeta_n$ of the double vacancies appearance can be represented as a function of these quantities:

$$\xi(p, N) = 1 - e^{-n}(1 - Mp)^{-(1 - Mp)N/M}\,, \quad p \ll 1;$$

$$\xi(p, N) = 1 - e^{-\frac{1}{2}MNp^2}\,, \qquad\qquad\qquad p \ll \tfrac{1}{M}; \qquad (9)$$

$$\xi(p, N) = \frac{1}{2}MNp^2\,, \qquad\qquad\qquad\qquad p \ll \sqrt{\tfrac{2}{MN}}.$$

---

[7]For correct result the two-term expansion for $\ln(1 - \varepsilon n)$ is required.

At the left side of each formula the corresponding restriction for the porosity is given. For the first formula this restriction is the weakest. For the second formula it is little bit stronger, however the formula is much simpler. Since the difference in the restrictions is small, then for most cases the second formula can be used instead of the first one; it will be shown later that the error in this case is even less then can be expected. For the last formula in (9) the corresponding restriction is very strong. Thus the last formula is valid only for very low porosity, moreover the bigger is the specimen, the lower should be the porosity. However the last formula has the simplest form and can be easily analyzed. From this formula it follows that the probability for the double vacancy is proportional to the square of porosity and to the total number of particles. The last fact is very important — it means, that specimens of different size can have different mechanisms for fracture. Indeed, if the specimen is small enough, then appearance of join vacancies is unlikely, and the fracture will be initiated from single vacancies. The bigger specimens are likely to have double vacancies — since the fracture will be initiated from them, and this requires much lower stresses, then for the single vacancies in the small specimens. Thus there will be no similarity in fracture of the specimens of the different size and scale. This also means that the representative volume for the material strength properties does not exist. These conclusions follows directly from the third formula in (9), however the first or second formulae from (9) (more exact approximations) lead to the same conclusions — the probability for the double vacancies essentially depends on the total number of particles N.

Let us rewrite the third formula from (9):

$$\xi(p, N) = \frac{1}{2} MNp^2, \qquad p \ll \sqrt{\frac{2}{MN}}. \tag{10}$$

This formula can be also used to estimate the density of the double vacancies in material. If we consider that the material is combination of $N_s \gg 1$ specimens with N particles each, then the number of double vacancies n_2 in such material can be calculated as

$$n_2 = N_s \xi(p, N), \qquad p_2 \stackrel{\text{def}}{=} \frac{n_2}{N_s N}. \tag{11}$$

Here p_2 — is the density of double vacancies in the material. Substituting the above relations to the last formula in (9) we obtain

$$p_2 = \frac{1}{2} Mp^2, \qquad p \ll \frac{1}{M}. \tag{12}$$

Thus the density of the double vacancies is proportional to the square of porosity. The restriction $p \ll 1/M$ was taken from the second formula in (9). Let us show that if the material contains enough particles then it can be divided in specimens with N particles each, so that restriction from (10) will be fulfilled. Using restriction for formula (10) we can obtain inequality for the number of particles in the specimen

$$M \ll N \ll \frac{2}{Mp^2} \quad \Rightarrow \quad p \ll \frac{\sqrt{2}}{M}. \tag{13}$$

The obtained inequality for porosity guarantee that the material can be divided in specimens containing enough particles to use formula (10). But this inequality is weaker then $p \ll 1/M$, therefore it is already fulfilled.

Let us apply the obtained results for estimation of the strength properties of a specimen with N particles and porosity p. Let ε_1 and ε_2 be the critical strains for the fracture initiation from a single vacancy and a double vacancy. Then the critical strain for the specimen can be estimated as

$$\varepsilon(p, N) = \varepsilon_1 \zeta(p, N) + \varepsilon_2 \xi(p, N) = \varepsilon_1 + (\varepsilon_2 - \varepsilon_1)\xi(p, N). \tag{14}$$

The same formula can be written for other critical parameters, e.g. ultimate strength. Using formula (14) we consider fracture as a stochastic process, therefore strength properties should be obtained as average over many tests. When deriving equation (14) we have used the following rude assumptions:

1. Vacancies interact only when they are joined.

2. Junction of more then two vacancies does not exist.

Of course these assumptions are not completely true, especially the first one. However they allow to estimate the dependence of material properties on the porosity and the specimen size, as it will be shown in the next section.

3 Computational model

The simulation procedure applied in this work is conventional MD technique, same as in [2], in more details it is described in [3, 4]. The material is represented by a set of particles interacting through a pair potential $\Pi(r)$. The equations of particle motion have the form

$$m\ddot{\underline{r}}_k = \sum_{n=1}^{N} \frac{f(|r_k - r_n|)}{|r_k - r_n|} \left(\underline{r}_k - \underline{r}_n\right), \tag{15}$$

where $\underline{r}_k$ is the radius vector of the k-th particle, m is the particle mass, N is the total number of particles, and $f(r) = -\Pi'(r)$ is the interparticle interaction force. We use the following notation: a is the equilibrium distance between two particles $(f(a) = 0)$, $D = |\Pi(a)|$ is binding energy, C is the stiffness of the interatomic bond in equilibrium, and T_0 is the period of vibrations of the mass m under the action of a linear force with stiffness C

$$C = -\Pi''(a) \equiv -f(a), \qquad T_0 = 2\pi\sqrt{m/C}. \tag{16}$$

We will use the quantities a and T_0 as microscopic distance and time scales. For a particle of mass m that is in equilibrium in the potential field $\Pi(r)$ its minimum velocity to reach infinity is $v_d = \sqrt{2D/m}$ — so called dissociation velocity. We will use this quantity as a velocity scale. To measure the level of thermal motion in material the velocities deviation Δv (mean-square value of random velocities) will be

used. When Δv approaches dissociation velocity v_d then the thermal motion break the internal bonds in the material resulting in its melting.

Let us consider the classical Lennard–Jones potential:

$$\Pi_{LJ}(r) = D \left[\left(\frac{a}{r} \right)^{12} - 2 \left(\frac{a}{r} \right)^6 \right], \tag{17}$$

where D and a are the binding energy and the equilibrium interatomic distances, introduced earlier. The corresponding interaction force $f(r) = -\Pi'(r)$ has the form

$$f_{LJ}(r) = \frac{12D}{a} \left[\left(\frac{a}{r} \right)^{13} - \left(\frac{a}{r} \right)^7 \right]. \tag{18}$$

In the case of the Lennard–Jones potential, the stiffness C and the binding energy D obey the relation $C = 72D/a^2$; the force (18) reaches its minimum value (the bond strength) at $r = b = \sqrt[6]{13/7}$, where b is the break distance. The corresponding break deformation of the Lennard–Jones bond is $\varepsilon_* = b - a \approx 0.109$. The Lennard–Jones potential is the simplest potential that allows one to take into account the general properties of interatomic interaction: repulsion of particles that approach each other, attraction of particles moving away from each other, and the absence of interaction at large distances between them. For calculations the shortened Lennard–Jones interaction will be used, given by formula

$$f(r) = \left[\begin{array}{ll} f_{LJ}(r), & 0 < r \le b, \\ k(r)f_{LJ}(r), & b < r \le a_{cut}; \end{array} \right. \tag{19}$$

where b is break distance for Lennard-Jones potential, a_{cut} is cut-off distance (for $r > a_{cut}$ the interaction vanishes). The coefficient $k(r)$ is the shape function

$$k(r) = \left[1 - \left(\frac{r^2 - b^2}{a_{cut}^2 - b^2} \right)^2 \right]^2. \tag{20}$$

The cut-off distance will be set as $a_{cut} = 1.4a$, in this case only the first neighbors are interacting for the close-packed structures. In the current paper we study the fracture process in general, therefore, the proposed simplified potential is sufficient. The obtained results can be easily extended to more complex potentials describing the properties of materials more exactly.

In this work, a two-dimensional material will be used, where particles are packed to form an ideal 2D close-packed (triangular) crystal lattice. This is simplified lattice, however its symmetry is same as the symmetry of [111] cross-sections and surfaces of such 3D crystal lattices as FCC and diamond (the last one is the lattice of silicon crystals). For computations square specimens are used, periodic boundary conditions are applied at all boundaries. All specimens are subjected to uniaxial loading by applying a small uniform deformation to positions of all particles and to the periodic boundaries, after each step of deformation a step of MD computation is used. The deformation is changing according the formula

$$\varepsilon(t) = \varepsilon_{max} \frac{t}{t_{max}}, \tag{21}$$

where ε_{max} is the maximum value of strain, t_{max} is the time of computation. The strain is directed along one of the sides of triangles, forming the lattice. The computation parameters are given in the Table 12.

Parameter	Symbol	Value
Number of particles	N	$10^4 \div 10^5$
Porosity	p	$10^{-4} \div 10^{-2}$
Cut-off radius	a_{cut}	$1.4\, a_0$
Initial velocity deviation	Δv	$0.005\, v_d$
Integration step	Δt	$0.02\, T_0$
Calculation time	t_{max}	$50\, T_0$
Maximum strain	ε_{max}	0.1

Table 12: Computation parameters.

4   Results of computations

Fig. 1a shows dependencies of the critical strain on porosity obtained from the computer experiments. Two sizes of specimens are considered: $N = 10\,000$ and $N = 100\,000$. The same graphs obtained analytically using estimation (14) are
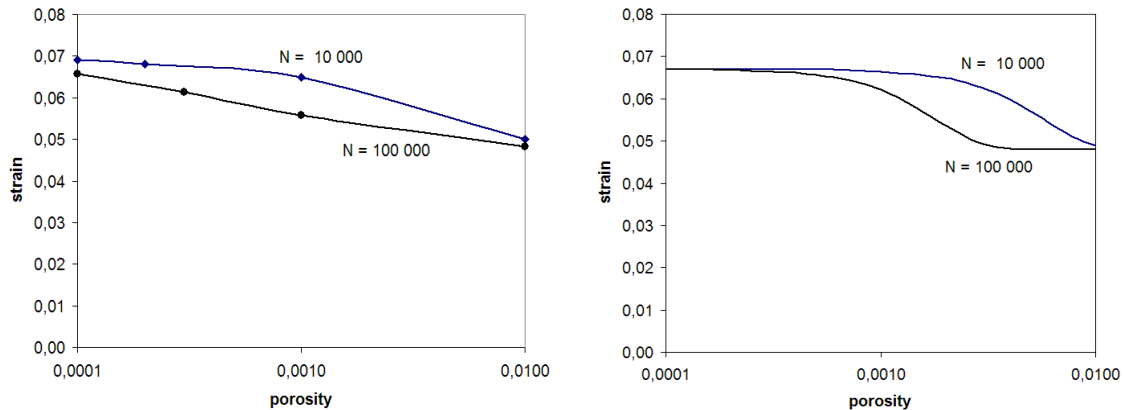

Figure 3: Comparison of results for different sizes of specimens: a) MD computations, b) analytical model.

shown in Fig. 1b. To obtain these graphs first or second formula from (9) can be used, the difference between them is negligible[8]. The values of the parameters used for the analytical calculations are

$$\varepsilon_1 = 0.067\,, \qquad \varepsilon_2 = 0.048\,; \qquad M = 6. \tag{22}$$

Results of the both models, MD and analytical, show the same tendencies: the strength of the bigger specimen is considerably lower, then for the smaller one; the scale effect is smaller for high and low porosities, and it has maximum for the intermediate porosities. The explanation for the last fact is that for low and high porosities both specimens have the similar mechanism for the fracture initiation:

---

[8]The maximum difference between the first and the second formula from (9) while calculating graphs Fig. 3a is lower then 1% for $\xi(p, N)$ calculation and lower then 0.2% for the critical strain calculation.

single vacancies for low porosity and double vacancies for high porosity. In the case of intermediate porosity the situation is scale-dependant, because the smaller specimen is unlikely to have double vacancies in this case, but for the bigger specimen the double vacancies are much more probable.

Thus, qualitatively computational and analytical graphs are similar, but quantitatively they have differences: the computational graphs are more flat, and the maximum scale effect appears at different porosities. Fig. 4a,b shows comparison of computational and analytical models for the small and big specimen respectively. In
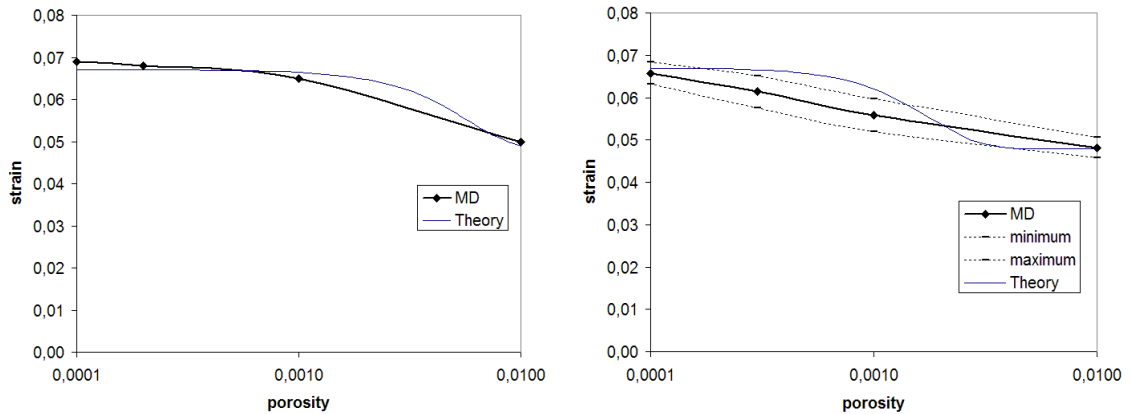

Figure 4: Comparison of results of MD computer experiments and predictions of analytical model: a) $N = 10\,000$, b) $N = 100\,000$.

Fig. 4b together with the average computational result an error corridor obtained for the series of 5 experiments is shown. The theoretical curve gets inside the error corridor for the low and high porosities, but escapes from it for the intermediate porosities. The main explanation for the differences between the computational and analytical models is that the assumption that vacancies interact only when they are joined is too rude. Of course two closely located vacancies interact and such place is likely for fracture initiation. This effect can be also described analytically by the similar method as it was used above for the double vacancies, but such description requires additional calculations and also an estimation of the influence of the distance between the vacancies on the critical strain. For the bigger specimens also appearance of more then two joint vacancies should be taken into account.

5 Conclusions

An analytical model for the scale dependence of the fracture initiation is suggested. The model is based on the idea that fracture is a stochastic process, for the bigger specimens probability of joint defects is higher, and this decreases the material strength. Thus there is no similarity in fracture of the specimens of the different size and scale. This also means that the representative volume for the material strength properties does not exist. Indeed, the bigger is the specimen, the more sophisticated joining of defects can appear in it, giving new mechanisms for the fracture initiation.

The probability for double vacancies was calculated, and the material strength properties as a function of defects density and specimen size were estimated. These results where compared with MD simulations. Results of both models, MD and analytical, show the same tendencies: the strength of the bigger specimen is considerably lower then for the smaller one; the scale effect is smaller for high and low porosities, and it has maximum for the intermediate porosities.

Qualitatively computational and analytical graphs are similar, but quantitatively they have differences: the computational graphs are more flat, and the maximum scale effect appears at different porosities. The explanation for the differences between the computational and analytical models is that the assumption that vacancies interact only when they are joined is too rude, interaction of non-joined vacancies should be taken into account. This effect can be also described analytically by the similar method as it was used in the report for the double vacancies, but such description requires additional calculations and also an estimation of the influence of the distance between the vacancies on the critical strain. For the bigger specimens also appearance of more then two joint vacancies should be taken into account.

Acknowledgements

References

[1] A. M. Krivtsov. MD modeling of low-cycle high-amplitude loading of monocrystal material with defects. Proc. of XXXIII Summer School "Advanced Problems in Mechanics 2005", St. Petersburg, Russia, 2006, 341-346.

[2] A. M. Krivtsov. Molecular dynamics simulation of plastic effects upon spalling. Phys. Solid State **46**, 6 (2004).

[3] Allen M. P. and Tildesley A. K. Computer Simulation of Liquids. – Oxford: Clarendon Press. 1987. 385 .

[4] A. M. Krivtsov. Deformation and fracture of solids with microstructure. Moscow, Fismatlit. 2007. 304 p. (In Russian).

Anton M. Krivtsov, Institute for Problems in Mechanical Engineering Russian Academy of Sciences, Bolshoy pr. V.O., 61, St. Petersburg, 199178, Russia.

Molecular dynamics study of fracture accompanied by chemical reaction

Anton M. Krivtsov

akrivtsov@bk.ru

Abstract

A molecular dynamics model for fracture accompanied by chemical reaction is suggested. Crack initiation and development in specimens subjected to an uniaxial loading is considered. The oxidation of the initial and new specimen surfaces during the fracture process is taken into account. It is postulated that the material properties such as density, stiffness and strength are changing due to the oxidation. Influence of the chemical reaction (oxidation) on the fracture scenario is investigated. Fracture process for the specimens of different shape, with and without predefined defects is studied.

1   Introduction

Molecular dynamics is a powerful tool for modelling of fracture in material with various internal structure and defects distribution. In most of these models only single-phase material is considered. However in the real applications the fracture is closely connected with chemical reactions. In particular, for MEMS made from silicon the oxidation process accompanying the fracture is essential, since the mechanical properties if the silicon dioxide differs essentially from those of the pure silicon [1].

The following model is suggested. The properties of particles adjusting to the surfaces is changed mimicking the difference between the silicon and its dioxide: size of the particles became slightly bigger, the elastic and strength properties became substantially lower then for the initial particles. This change take place immediately and involves as the particles surrounding the original surfaces of the specimen, as the particles laying near the new surfaces provided by the fracture and crack development. Since the size of the particles increases, this can provide separation of the pieces of material — the oxidization induced fracture. In this case fracture and chemical reaction can stimulate each other resulting in a self-generating process. Although mainly we will be studying situations when the fracture is induces by an external load, the possibility and conditions of such self-generation will be considered.

2 Computational model

The simulation procedure applied in this work is similar to that used in [2, 3], in more details it is described in [4, 5]. The material is represented by a set of particles interacting through a pair potential $\Pi(r)$. The equations of particle motion have the form

$$m\ddot{\underline{r}}_k = \sum_{n=1}^{N} \frac{f(|r_k - r_n|)}{|r_k - r_n|} (\underline{r}_k - \underline{r}_n),$$ (1)

where $\underline{r}_k$ is the radius vector of the k-th particle, m is the particle mass, N is the total number of particles, and $f(r) = -\Pi'(r)$ is the interparticle interaction force. We use the following notation: a is the equilibrium distance between two particles ($f(a) = 0$), $D = |\Pi(a)|$ is binding energy, C is the stiffness of the interatomic bond in equilibrium, and T_0 is the period of vibrations of the mass m under the action of a linear force with stiffness C

$$C = -\Pi''(a) \equiv -f(a), \qquad T_0 = 2\pi\sqrt{m/C}.$$ (2)

We will use the quantities a and T_0 as microscopic distance and time scales. For a particle of mass m that is in equilibrium in the potential field $\Pi(r)$ its minimum velocity to reach infinity is $v_d = \sqrt{2D/m}$ — so called dissociation velocity. We will use this quantity as a velocity scale. To measure the level of thermal motion in material the velocities deviation Δv (mean-square value of random velocities) will be used. When Δv approaches dissociation velocity v_d then the thermal motion break the internal bonds in the material resulting in its melting.

Let us consider the classical Lennard–Jones potential:

$$\Pi_{LJ}(r) = D\left[\left(\frac{a}{r}\right)^{12} - 2\left(\frac{a}{r}\right)^{6}\right],$$ (3)

where D and a are the binding energy and the equilibrium interatomic distances, introduced earlier. The corresponding interaction force $f(r) = -\Pi'(r)$ has the form

$$f_{LJ}(r) = Q\left[\left(\frac{a}{r}\right)^{13} - \left(\frac{a}{r}\right)^{7}\right], \qquad Q \stackrel{\text{def}}{=} \frac{12D}{a},$$ (4)

where Q is the interparticle force magnitude. In the case of the Lennard–Jones potential, the stiffness C and the binding energy D obey the relation $C = 72D/a^2$; the force (4) reaches its minimum value (the bond strength) at $r = b = \sqrt[6]{13/7}$, where b is the break distance. The corresponding break deformation of the Lennard–Jones bond is $\varepsilon_* = b - a \approx 0.109$. The Lennard–Jones potential is the simplest potential that allows one to take into account the general properties of interatomic interaction: repulsion of particles that approach each other, attraction of particles moving away from each other, and the absence of interaction at large distances between them. For calculations the shortened Lennard–Jones interaction will be used, given by formula

$$f(r) = \left[\begin{array}{ll} f_{LJ}(r), & 0 < r \leq b, \\ k(r)f_{LJ}(r), & b < r \leq a_{\text{cut}}; \end{array}\right.$$ (5)

where b is break distance for Lennard-Jones potential, a_{cut} is cut-off distance (for $r > a_{cut}$ the interaction vanishes). The coefficient $k(r)$ is the shape function

$$k(r) = \left[1 - \left(\frac{r^2 - b^2}{a_{cut}^2 - b^2} \right)^2 \right]^2 . \tag{6}$$

The cut-off distance will be set as $a_{cut} = 1.4a$, in this case only the first neighbors are interacting for the close-packed structures. For the general study of the fracture process this simplified potential is sufficient. If necessary the obtained results can be extended to more complex potentials describing the properties of materials more exactly.

In case of oxidation it is postulated that the properties of the particle is changing. The diameter and force magnitude for the oxidized particles will be denoted as $\tilde{a}$ and $\tilde{Q}$. For the silicon dioxide it approximately fulfills

$$\tilde{a}/a = 1.1 \,, \qquad \tilde{Q}/Q = 1/3. \tag{7}$$

The vector of interaction force between two original particles can be represented as following

$$\underline{f} = \Phi(r^2)\underline{r} \,, \qquad \Phi(r^2) \overset{\text{def}}{=} f(r)/r. \tag{8}$$

When one or both of the interacting particles are oxidized then the interaction law takes the form

$$\underline{f} = \Phi \left(\lambda(r^2 - \overline{a}^2) + a^2 \right) \underline{r} \,, \qquad \lambda \overset{\text{def}}{=} a^2/\overline{a}^2, \tag{9}$$

where function Φ is calculated using average values for the particle diameter and force magnitude:

$$\overline{a} \overset{\text{def}}{=} (a_1 + a_2)/2 \,, \qquad \overline{Q} \overset{\text{def}}{=} (Q_1 + Q_2)/2; \tag{10}$$

indexes 1 and 2 correspond to the first and the second interacting particle. The law (10) independently of the particles sizes preserve the same width of the potential well.

For simulation a two-dimensional material will be used, where particles are packed to form an ideal 2D close-packed (triangular) crystal lattice. This is simplified lattice, however its symmetry is same as the symmetry of [111] surfaces of 3D crystal lattices, such as FCC and diamond (the last one is the lattice of silicon crystals). For the computations periodic boundary conditions are applied at all boundaries. All specimens are subjected to uniaxial loading by applying a small uniform deformation to positions of all particles and to the periodic boundaries. After each step of deformation a step of MD computation is used. The deformation is changing according the formula

$$\varepsilon(t) = \varepsilon_{max} \frac{t}{t_{max}}, \tag{11}$$

where ε_{max} is the maximum value of strain, t_{max} is the time of computation. The strain is directed along one of the sides of triangles, forming the lattice. The computation parameters are given in the Table 13.

Parameter	Symbol	Value
Number of particles	N	10^5
Cut-off radius	a_{cut}	$1.4\,a$
Initial velocity deviation	Δv	$0.005\,v_d$
Integration step	Δt	$0.02\,T_0$
Maximum strain	ε_{max}	0.15
Strain rate	$\varepsilon_{max}/t_{max}$	$0.002\,T_0^{-1}$
Chemical inflation	$\tilde{a}/a$	$1.10 \div 1.15$
Chemical strengthening	$\tilde{Q}/Q$	$1/3$

Table 13: Computation parameters.

3   Results of computations

The results of the first computer experiment are presented in Fig. 1. A single vacancy placed in the center of specimen is used to initiate a crack. In Fig. 1a no chemical reaction is taken into account. In this case four straight cracks are propagating in crystallographical directions. In Fig. 1b,c the particles adjusting to the crack surfaces are subjected to oxidation that results in change of particle size (chemical inflation) and bond strength. The bond strength for the oxidized material in all experiments is taken three times lower then for the original material. The chemical inflation is 10% for Fig. 1b and it is 15% for Fig. 1c, e.g. $\tilde{a}/a = 1.10$ and $\tilde{a}/a = 1.15$ respectively. In the figures the original material is shown by blue color, the oxide — by cyan, the empty space is white. From Fig. 1b it follows that oxidation stimulates the fracture: initial fracture zone appears in the vicinity of the initial vacancy, where the oxidized material forms an elliptical area; the cracks are producing branches, substantially complicating the crack shape. In Fig. 1c it is visible that when the chemical inflation is increased from 10% to 15% then the amount of the oxidized material is increased in many times. The explanation of this phenomenon is that the break extension of the interatomic bond for the considered interaction potential is 11%. If the chemical inflation rate is greater then this value, then the chemical reactions produces fracture in material. The fracture creates new surfaces, where oxidation takes place, again producing the fracture and so on. Thus we have self-developing process, where the chemical reaction and fracture stimulate each other. If the greater values of the chemical inflation are used then this process can take place without external loading at all, resulting in very fast oxidation of the whole specimen. Also the high chemical inflation can result in the crack closing, since the oxidized material requires more space then the original one. If the oxide would not be weaker then the original material then a self-healing of the material can be realized.

Fig. 2 shows the sequential stages of the fracture process for the specimen with circular hole. The chemical inflation is 10%. No predefined crack is used, the fracture starts just from the inner boundaries of the specimen. From the very beginning several cracks appear, then the branching process produces very complicated, fractal
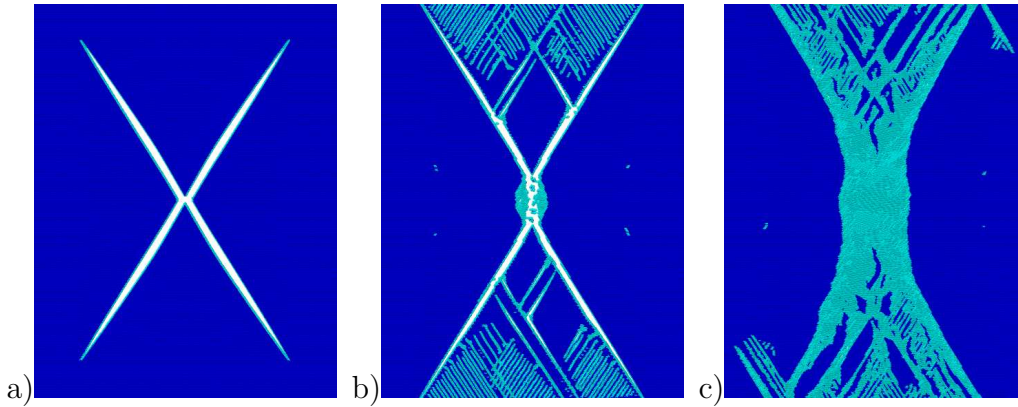
Figure 1: Comparison of the computational results for different rate of chemical inflation: a) no chemical reaction, b) 10% chemical inflation, c) 15% chemical inflation.

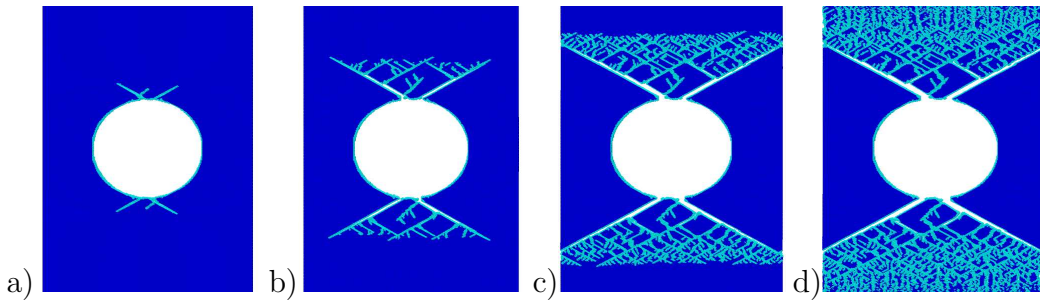structure of the cracks. Zoom-up of the specimen with the developed crack is shown in Fig. 3.

Figure 2: Sequential stages of extension for the specimen with circular hole: a) $\varepsilon = 7\%$, b) $\varepsilon = 10\%$, c) $\varepsilon = 13\%$, d) $\varepsilon = 15\%$.

Comparison with extension of the specimen with a predefined crack is shown in Fig. 4. Figure shows, that the predefined crack localizes the beginning of the fracture in the specified area, however the developed crack due to its branching does not depend much, whether the predefined crack was introduced or not.

Comparison of the results for the different rate of the chemical inflation is shown in Fig. 5. The specimen with a circular hole and predefined crack is used. As for the case of the fracture starting from a single vacancy, increasing the rate of the chemical inflation over the critical value of 11% results in abrupt increase of the oxidized area. The oxide is located not only in the vicinity of the crack, but also it is forming a wide belt around the hole, forming zone of plastic deformation.
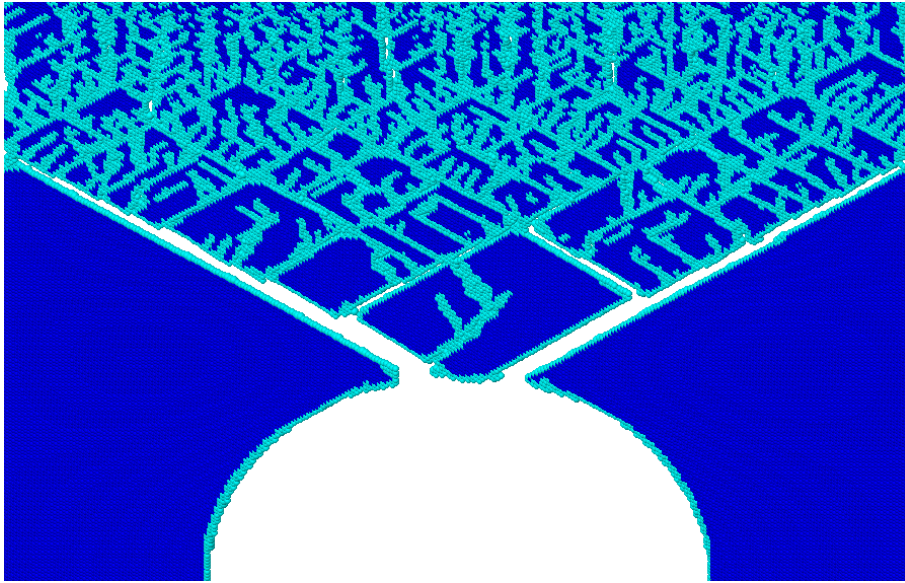
Figure 3: Zoom-up of the specimen with the developed crack, $\varepsilon = 15\%$.

4 Conclusions

A molecular dynamics model for the fracture accompanied by a chemical reaction was suggested. A crack initiation and development in specimens subjected to an uniaxial loading was considered. The oxidation of the initial and new specimen surfaces during the fracture process was taken into account. It was taken into account that the material properties such as density, stiffness and strength are changing due to the oxidation.

The results of the computer experiments show that oxidation stimulates the fracture. The cracks are producing branches, substantially complicating the crack shape. The branching of the cracks forms fractal-like structures: the longer is the fracture process the greater is the number of branches and subbranches.

If the rate of the chemical inflation is over the break extension of the interatomic bond then an abrupt increase of the oxidized area can be observed. The explanation of this fact is that in this case the chemical reactions produces fracture in the material. The fracture creates new surfaces, where oxidation takes place, again producing the fracture and so on. Thus a self-generating process is realized, where the chemical reaction and fracture stimulate each other. For the greater values of the chemical inflation this process can take place without external loading at all, resulting in a very fast oxidation of the whole specimen. Also the high chemical inflation can result in the crack closing, since the oxidized material requires more space then the original one. If the oxide would not be weaker then the original material then the oxidation can result in a self-healing of the material.
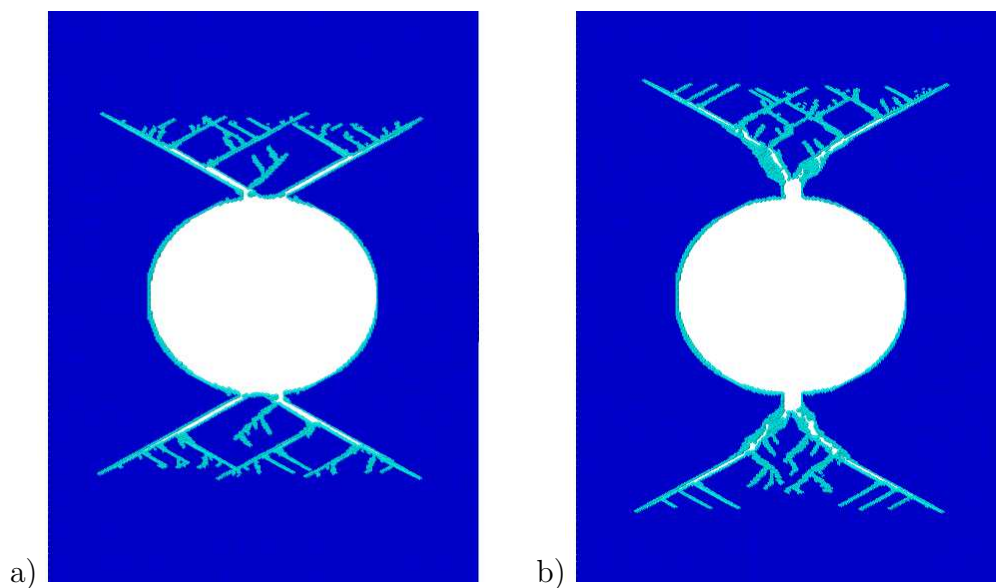
Acknowledgements

Figure 4: Comparison of 10% extension for the specimen: a) without predefined crack, b) with predefined crack.
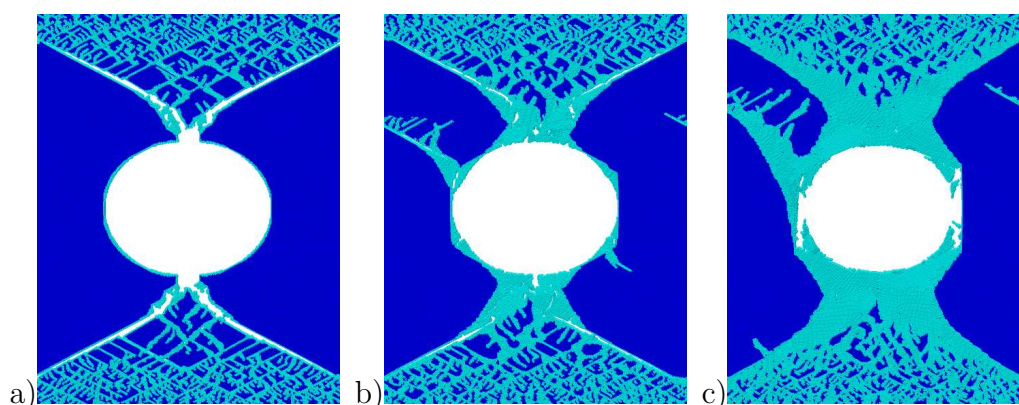

Figure 5: Comparison of results for different chemical inflation: a) 10%, b) 12%, c) 15%.

References

[1] Muhlstein, CL, Brown, SB, and Ritchie, RO. (2001). High-cycle Fatigue and Durability of Polycrystalline Silicon Thin Films in Ambient Air. Sensors and Actuators, A 94. Elsevier, pp.177-188.

[2] A. M. Krivtsov. MD modeling of low-cycle high-amplitude loading of monocrystal material with defects. Proc. of XXXIII Summer School "Advanced Problems in Mechanics 2005", St. Petersburg, Russia, 2006, 341-346.

[3] A. M. Krivtsov. Molecular dynamics simulation of plastic effects upon spalling. Phys. Solid State **46**, 6 (2004).

[4] Allen M. P. and Tildesley A. K. Computer Simulation of Liquids. – Oxford: Clarendon Press. 1987. 385 .

[5] A. M. Krivtsov. Deformation and fracture of solids with microstructure. Moscow, Fismatlit. 2007. 304 p. (In Russian).

Anton M. Krivtsov, Institute for Problems in Mechanical Engineering Russian Academy of Sciences, Bolshoy pr. V.O., 61, St. Petersburg, 199178, Russia.